

IFMBE Proceedings

Ion Tiginyanu · Victor Sontea
Serghei Railean (Eds.)

Volume 77

4th International Conference on Nanotechnologies and Biomedical Engineering

Proceedings of ICNBME-2019,
September 18–21, 2019,
Chisinau, Moldova



IFMBE Proceedings

Volume 77

Series Editor

Ratko Magjarevic, Faculty of Electrical Engineering and Computing, ZESOI, University of Zagreb, Zagreb, Croatia

Associate Editors

Piotr Ładyżyński, Warsaw, Poland

Fatimah Ibrahim, Department of Biomedical Engineering, Faculty of Engineering, University of Malaya, Kuala Lumpur, Malaysia

Igor Lackovic, Faculty of Electrical Engineering and Computing, University of Zagreb, Zagreb, Croatia

Emilio Sacristan Rock, Mexico DF, Mexico

The IFMBE Proceedings Book Series is an official publication of *the International Federation for Medical and Biological Engineering (IFMBE)*. The series gathers the proceedings of various international conferences, which are either organized or endorsed by the Federation. Books published in this series report on cutting-edge findings and provide an informative survey on the most challenging topics and advances in the fields of medicine, biology, clinical engineering, and biophysics.

The series aims at disseminating high quality scientific information, encouraging both basic and applied research, and promoting world-wide collaboration between researchers and practitioners in the field of Medical and Biological Engineering.

Topics include, but are not limited to:

- Diagnostic Imaging, Image Processing, Biomedical Signal Processing
- Modeling and Simulation, Biomechanics
- Biomaterials, Cellular and Tissue Engineering
- Information and Communication in Medicine, Telemedicine and e-Health
- Instrumentation and Clinical Engineering
- Surgery, Minimal Invasive Interventions, Endoscopy and Image Guided Therapy
- Audiology, Ophthalmology, Emergency and Dental Medicine Applications
- Radiology, Radiation Oncology and Biological Effects of Radiation

IFMBE proceedings are indexed by SCOPUS and EI Compendex. They are also submitted for ISI proceedings indexing.

Proposals can be submitted by contacting the Springer responsible editor shown on the series webpage (see “Contacts”), or by getting in touch with the series editor Ratko Magjarevic.

More information about this series at <http://www.springer.com/series/7403>

Ion Tiginyanu · Victor Sontea ·
Serghei Railean
Editors

4th International Conference on Nanotechnologies and Biomedical Engineering

Proceedings of ICNBME-2019, September
18–21, 2019, Chisinau, Moldova

 Springer

Editors

Ion Tiginyanu
Academy of Sciences of Moldova
Chisinau, Moldova

Serghei Railean
Department of Microelectronics
and Biomedical Engineering
Technical University of Moldova
Chisinau, Moldova

Victor Sontea
Department of Microelectronics
and Biomedical Engineering
Technical University of Moldova
Chisinau, Moldova

ISSN 1680-0737

ISSN 1433-9277 (electronic)

IFMBE Proceedings

ISBN 978-3-030-31865-9

ISBN 978-3-030-31866-6 (eBook)

<https://doi.org/10.1007/978-3-030-31866-6>

© Springer Nature Switzerland AG 2020

This work is subject to copyright. All rights are reserved by the Publisher, whether the whole or part of the material is concerned, specifically the rights of translation, reprinting, reuse of illustrations, recitation, broadcasting, reproduction on microfilms or in any other physical way, and transmission or information storage and retrieval, electronic adaptation, computer software, or by similar or dissimilar methodology now known or hereafter developed.

The use of general descriptive names, registered names, trademarks, service marks, etc. in this publication does not imply, even in the absence of a specific statement, that such names are exempt from the relevant protective laws and regulations and therefore free for general use.

The publisher, the authors and the editors are safe to assume that the advice and information in this book are believed to be true and accurate at the date of publication. Neither the publisher nor the authors or the editors give a warranty, expressed or implied, with respect to the material contained herein or for any errors or omissions that may have been made. The publisher remains neutral with regard to jurisdictional claims in published maps and institutional affiliations.

This Springer imprint is published by the registered company Springer Nature Switzerland AG
The registered company address is: Gewerbestrasse 11, 6330 Cham, Switzerland

Preface

This volume presents the Proceedings of the 4th International Conference on Nanotechnologies and Biomedical Engineering (ICNBME), which was held on September 18–21, 2019 in Chisinau, Republic of Moldova. ICNBME-2019 continued the series of international conferences in the field of nanotechnologies and biomedical engineering with the main goal focused at bringing together scientists and engineers dealing with fundamental and applied research for reporting on the latest theoretical developments and applications in the fields involved.

The conference covered a wide range of subjects of primary importance for research and development such as nanotechnologies and nanomaterials; plasmonics and metamaterials; bio-micro/nanotechnologies and devices; biomaterials for medical applications; biomimetics and sensors; biomedical instrumentation; biomedical signal processing; biomedical imaging and image processing; bioinformatics; medical physics and biophysics; molecular; cellular and tissue engineering; clinical engineering; health technology management and assessment; health informatics, e-health and telemedicine; biomedical engineering education; innovation, development and interdisciplinary research; nuclear and radiation safety and security.

The papers included in the Proceedings reflect the results of multidisciplinary research undertaken by about one hundred of groups worldwide. Special attention is paid to the development of novel nanotechnologies and nanomaterials, in particular of bio-nanotechnologies and bio-nanomaterials. New biocompatible materials are proposed for use in regenerative medicine, cellular and tissue engineering. Interesting data on novel chemical and biosensors are reported which are based on nanostructured metal oxides and hybrid nanocomposite materials.

Considerable progress has been achieved at the intersection of nanotechnologies, information technologies, and biomedicine as, for example, in health informatics, biomedical signal, and image processing. New theoretical and experimental results are highlighted in such fields as superconductivity, novel magnetic materials, metamaterials, aeromaterials, optoelectronic and photonic materials, photovoltaic structures, quantum dots, one- and two-dimensional nanomaterials, multifunctional hybrid materials like core-shell structures, etc. The Proceedings reflect the state of the art in controlling the properties of several classes of nanocomposite materials for important future applications in various fields. It is worth to note that the Proceedings include also a number of review papers reflecting the fascinating history and recent achievements in the development of novel solid-state structures as well as nanoelectronic and optoelectronic devices on their basis.

We hope that the papers included in the ICNBME-2019 Proceedings will be of interest for established researchers working in multidisciplinary fields of science and technology, young scientists, students and broad community wishing to get up-to-date information on progress in the fast-developing areas of nanotechnology and biomedical engineering.

Chisinau, Moldova

Acad. Prof. Ion Tiginyanu
Prof. Victor Sontea
Dr. Serghei Railean

4th International Conference on Nanotechnologies and Biomedical Engineering ICNBME-2019, September 18–21, 2019, Chisinau, Republic of Moldova

Organizers

Technical University of Moldova
Academy of Sciences of Moldova
State Medical and Pharmaceutical University “Nicolae Testemitanu”
Moldavian Society of Biomedical Engineering

In Collaboration with

The International Federation for Medical and Biological Engineering (IFMBE)



Sponsored by

European Commission under the Grant #810652 “NanoMedTwin”



National Agency of Research and Development



Committees

Conference Chairs

Ion Tiginyanu	Academy of Sciences of Moldova, Republic of Moldova
Victor Sontea	Technical University of Moldova, Republic of Moldova

International Advisory Committee

Ion Ababii	Nicolae Testemițanu State Medical and Pharmaceutical University, Republic of Moldova
Rainer Adelung	Institute for Materials Science, University of Kiel, Germany
Gert Baumann	Charité Hospital, University of Berlin, Germany
Adriana Velazquez Berumen	World Health Organization, Switzerland
Viorel Bostan	Technical University of Moldova
Serghei Cebotari	Hannover Medical School, Germany
Lee Chow	University of Central Florida, Orlando, USA
Pascal Colpo	Joint Research Center, Italy
Dan Dascalu	Romanian Academy
Yury Dekhtyar	Institute of Biomedical Engineering and Nanotechnologies, Riga Technical University, Latvia
Sergei Dik	Belarusian State University of Informatics and Radioelectronics, Belarus
Franz Faupel	Institute for Materials Science, University of Kiel, Germany
Vladimir Fomin	Institute for Integrative Nanosciences, Germany
Sergey Gaponenko	National Academy of Sciences, Belarus
Boris Gorshunov	Moscow Institute of Physics and Technology, Russia
Nora H. de Leeuw	Cardiff University, United Kingdom
Hans Hartnagel	Technical University Darmstadt, Institute of Microwave Engineering and Photonics, Germany
Nicolae Jula	Military Technical Academy, Romania
Lorenz Kienle	Institute for Materials Science, University of Kiel, Germany
Jan Linnros	Royal Institute of Technology, Sweden
Ratko Magjarević	University of Zagreb, Croatia
Hidenori Mimura	Research Institute of Electronics, Shizuoka University, Japan
Nicolas Pallikarakis	University of Patras, Greece
Thierry Pauporte	Ecole nationale supérieure de chimie de Paris, France
Alexander Pogrebnyak	Sumy State University
Peter Scharff	Technical University Ilmenau
Bogdan Simionescu	Romanian Academy
Bruno Viana	Chimie ParisTech, PSL University, Paris, France
Niels Wessel	Humboldt University of Berlin, Germany

International Program Committee

Artur Buzdugan	Technical University of Moldova
Anatolie Casian	Technical University of Moldova
Radu Ciorap	Grigore T. Popa University of Medicine and Pharmacy, Romania
Anatol Ciubotaru	Republican Clinical Hospital , Republic of Moldova
Călin Corciova	Grigore T. Popa University of Medicine and Pharmacy, Romania
Hariton Costin	Grigore T. Popa University of Medicine and Pharmacy, Iasi, Romania
Ghenadie Curocichin	Nicolae Testemițanu State Medical and Pharmaceutical University, Republic of Moldova
Adrian Dinescu	National Institute for Research and Development in Microtechnology—IMT Bucharest, Romania
Mircea Dragoman	National Institute for Research and Development in Microtechnology—IMT Bucharest, Romania
Constantin Găindric	Academy of Sciences of Moldova, Republic of Moldova
Anca-Irina Galaction	Grigore T. Popa University of Medicine and Pharmacy, Romania
Tatisvili Grigor	Institute of Inorganic Chemistry and Electrochemistry of I. Javakhishvili Tbilisi State
Stanislav Groppa	State Medical and Pharmaceutical University “Nicolae Testemițanu”, Moldova
Andres Hilfiker	Hannover Medical School, Germany
Leonid Kulyuk	Institute of Applied Physics, Moldova
Oleg Lozan	Nicolae Testemițanu State Medical and Pharmaceutical University, Republic of Moldova
Oleg Lupan	Technical University of Moldova
Viorel Nacu	State Medical and Pharmaceutical University “Nicolae Testemițanu”, Moldova
Anatolii Orlov	National Technical University of Ukraine, Kyiv, Ukraine
Gheorghe Rojnovanu	Nicolae Testemițanu State Medical and Pharmaceutical University, Republic of Moldova
Andrei Sarua	University of Bristol, United Kingdom
Anatolie Sidorenko	Ghitu Institute of Electronic Engineering and Nanotechnolo- gies, Moldova
Nicolai Sobolev	University of Aveiro, Portugal
Ian Toma	The George Washington University
Roman Tomashevskiy	Kharkiv Polytechnical Institute, Ukraine
Pavel Topală	Alecu Russo State University of Balti, Republic of Moldova
Vasile Tronciu	Technical University of Moldova
Dumitru Tsiulyanu	Technical University of Moldova
Veaceslav Ursaki	Academy of Sciences of Moldova
Liliana Verestiuc	Grigore T. Popa University of Medicine and Pharmacy, Romania
Victor Vovc	Nicolae Testemițanu State Medical and Pharmaceutical University, Republic of Moldova

Organizing Committee

Sergey Railean	Technical University of Moldova, Head
Nicolai Ababii	Technical University of Moldova
Tudor Braniste	Technical University of Moldova
Vasilii Cretu	Technical University of Moldova
Elena Darii	Technical University of Moldova
Eugenia Groza	State Medical and Pharmaceutical University “Nicolae Testemițanu”
Nicolae Magariu	Technical University of Moldova
Ion Pocaznoi	Technical University of Moldova
Vasile Postica	Technical University of Moldova
Alexandr Sereacov	Technical University of Moldova

Reviewers List

Vladimir Fomin	Postica Vasile	Mihai Macovei
Ian Toma	Roman Tomashevskyi	Elena Achimova
Calin Corciova	Anatolie Sidorenko	Victor Vovc
Artur Buzdugan	Oleg Lupan	Alexander Ushenko
Viorel Nacu	Liliana Verestiuc	Victor Zalamai
Nicolas Pallikarakis	Eduard Monaico	Corneliu-Nicolae Druga
Veaceslav Ursaki	Nicolae Jula	Daria Grabco
Mircea Dragoman	Vasile Tronciu	Ionel Sanduleac
Radu Ciorap	Ghenadie Curocichin	Leonid Kulyuk
Sontea Victor	Nicolae Enaki	

Plenary Speakers Abstracts

New Areas of Research and Applications for GaN

Ion Tiginyanu
tiginyanu@asm.md

Academy of Sciences and Technical University of Moldova, Chisinau, Republic of Moldova

Gallium nitride, a wide-bandgap semiconductor compound ($E_g = 3.4$ eV at 300 K), has in the past two decades registered a fascinating increase in the crystalline quality of epitaxial layers determining its leading role in the development of the modern solid-state lighting industry. Exhibiting an impressive number of unique properties such as high breakdown voltage, high switching frequencies, enhanced power efficiency, high electrical conductivity, excellent thermal stability, and radiation hardness, over the past decade GaN has been remarkably successful in the area of high-power/high-frequency electronic applications and is now considered the second most important semiconductor material after Si. In this paper, we report on new fields of research and applications of gallium nitride.

First, we describe the possibility to fabricate ultrathin GaN-suspended membranes for multifunctional applications. In particular, these suspended membranes were used to fabricate networks of memristor devices exhibiting basic learning mechanisms such as habituation and dishabituation to a certain electrical stimulus [1].

Second, we report on GaN biocompatibility and on the possibility to mark living cells with hollow GaN nanoparticles exhibiting piezoelectric and magnetic properties. We show that the living cells marked by GaN:Fe nanoparticles can be guided in a controlled fashion using applied magnetic fields which is important for use in cell therapy [2].

Third, we report on three-dimensional nanoarchitectures of GaN for nano/microfluidic, microrobotic, and biomedical applications. The three-dimensional nanoarchitectures are based on GaN microtubular structures with nanoscopic thin walls which exhibit dual hydrophobic–hydrophilic behavior [3]. The microtubular structures are shown to self-organize when interacting with water, forming self-healing waterproof rafts with impressive cargo capabilities (cargo up to 500 times heavier than the floating raft). Along with this, we demonstrate self-propelled liquid marbles with exceptional mechanical robustness which may find applications as bioreactors for scalable *in vitro* cell growth. The physical properties of the new material based on three-dimensional GaN architectures will be presented in the context of its prospects for various biomimetic applications. Along with this, the novel material is shown to exhibit shielding capabilities against electromagnetic radiation in X-band [4].

We will discuss the feasibility to use the nano/microtubular structures on GaN for the fabrication of light-driven nano/microengines with performances higher than those inherent to microengines based on arrays of TiO₂ nanotubes [5].

References

1. Dragoman, M., Tiginyanu, I., et al.: Learning mechanisms in memristor networks based on GaN nanomembranes. *J. Appl. Phys.* **124**, 152110 (2018)
2. Braniste, T., Tiginyanu, I., et al.: Targeting endothelial cells with multifunctional GaN/Fe nanoparticles. *Nanoscale Res. Lett.* **12**, 486 (2017)

3. Tiginyanu, I., Braniste, T., et al.: Self-organized and self-propelled aero-GaN with dual hydrophilic-hydrophobic properties. *Nano Energy* **56**, 759 (2019)
4. Dragoman, M., Braniste, T., et al.: Electromagnetic interference shielding in X-band with aero-GaN. *Nanotechnology* **30**, 34LT01 (2019)
5. Enachi, M., Guix, M., et al.: Light-induced motion of microengines based on microarrays of TiO₂ nanotubes. *Small* **12**, 5497 (2016)

Recent Progress of Cold Cathodes: Volcano-Structured Field Emitters and GOS Tunneling Cathodes

H. Mimura

mimura.hidenori@shizuoka.ac.jp

T. Masuzawa

Y. Neo

K. Murakami

M. Nagao

Research Institute of Electronics, Shizuoka University, Hamamatsu, Japan
Research Institute of Electronics, Shizuoka University, Hamamatsu, Japan
Research Institute of Electronics, Shizuoka University, Hamamatsu, Japan
National Institute of Advanced Industrial Science and Technology, Tsukuba, Japan
National Institute of Advanced Industrial Science and Technology, Tsukuba, Japan

Vacuum devices are dominant in high power and high frequency. Though thermal cathodes are widely used in vacuum devices, if the thermal cathodes are replaced with cold cathodes, more superior devices are expected. The conventional cold cathodes with an electron extraction gate are field emitters (FEs). The FEs, however, have two big problems such as current fluctuation and beam divergence. The current fluctuation is suppressed when the FE is operated in ultrahigh vacuum or connected in series to a constant current source such as a field-effect transistor [1, 2]. For the beam divergence, though the double-gated FE with both an electron extraction gate and a focus gate was proposed, the electron emission current was significantly reduced when the electron beam was focused. Recently, we have developed the volcano-structured double-gated field emitter (VDG-FE) [3, 4]. The VDG-FE can focus electron beam without a decrease of the emission current. By using the VDG-FE, we are developing the compact image pickup tube which is applicable to a radiation-tolerant image sensor [5].

As the second topic, I will talk about fabrication of graphene and its application to planar Graphene–Oxide–Si (GOS) tunneling cathodes with an extremely high electron emission efficiency. The MetalOxide–Si (MOS) tunneling cathode is a fine cold cathode, because it has fluctuation free emission current, produces uniform emission from the whole emitter area, and has a highly directional electron beam. Furthermore, the electron emission is almost independent of the ambient gas pressure. However, MOS cathodes have very low electron emission efficiency less than 1% [6]. We synthesized graphene by low-pressure chemical vapor deposition. We have developed GOS tunneling cathodes with an extremely high electron emission efficiency larger than 20% by replacing the poly-Si gate electrode of MOS cathodes with a graphene electrode [7].

References

1. Hashiguchi, G., Mimura, H., Fujita, H.: *Jpn. J. Appl. Phys.* **35** (1996) L84
2. Shimawaki, H., Tajima, K., Mimura, H., Yokoo, K.: *IEEE Trans. Electron Devices* **49** (2002) 1665
3. Neo, Y., Soda, T., Takeda, M., Nagao, M., Yoshida, T., Yasumuro, C., Kanemaru, S., Sakai, T., Hagiwara, K., Saito, N., Aoki, T., Mimura, H.: *App. Phys. Express.* **1** (2008) 053001

4. Neo, Y., Takeda, M., Soda, T., Nagao, M., Yoshida, T., Kenamaru, S., Sakai, T., Hagiwara, K., Saito, N., Aoki, T., Mimura, H.: *J. Vac. Sci. Technol. B* **27** (2009) 701
5. Honda, Y., Nanba, M., Miyakawa, K., Kubota, M., Nagao, M., Neo, Y., Mimura, H., Egami, N.: *J. Vac. Sci. Technol. B* **34** (2016) 052201
6. Mimura, H., Neo, Y., Shimawaki, H., Abe, Y., Tahara, K., Yokoo, K.: *Appl. Phys. Lett.* **88** (2006) 123514
7. Murakami, K., Miyaji, J., Furuya, R., Adachi, M., Nagao, M., Neo, Y., Takao, Y., Yamada, Y., Sasaki, M., Mimura, H.: *Appl. Phys. Lett.* **114** (2019) 213501

Macromolecular Nanovectors for Gene Delivery

Bogdan C. Simionesci

“Petru Poni” Institute of Macromolecular Chemistry of the Romanian Academy, Iasi, Romania
“Gheorghe Asachi” Technical University of Iasi, Iasi, Romania

Several types of polymer-based structures including micelles, polymersomes, nano- and microparticles (-capsules/-spheres), molecular imprinting polymers, dendrimers, nanogels, hydrogels and interpenetrated polymer networks have been developed and tested as potential systems of interest for biomedical applications. Advances in polymer science—focusing on an improved control of polymer molecular weight, polydispersity, structure, properties, and functionality through the synthetic approach—have led to the development of several novel systems designed for drug/gene delivery and tissue engineering, two recently emerging areas with pivotal role for both research/academic community and industry, new niche markets being generated. They yielded the development of tailored polymer materials, engineered to exert distinct biological functions, implying multi-functionality as well as appropriate form/architectural features (with the implication of nanotechnology), and giving rise to specificity and high responsiveness (i.e., stimuli-responsive polymers and polymers capable of molecular recognition).

In this context, the presentation summarizes the challenges in the synthesis of macromolecular compounds to be used as nanovectors/carriers for gene delivery, pointing on synthetic polymers as a possible realistic solution to specific challenges, and outlines the current state of the art, focusing on the newest approaches to improve systems effectiveness and responsiveness. Some recent original results are briefly described and expected future directions are underlined.

Nanosensors: Current Status and Perspectives

Oleg I. Lupan
oleg.lupan@mib.utm.md; ollu@tf.uni-kiel.de

L. Chow
R. Adelung

Department of Microelectronics and Biomedical Engineering, Center for Nanotechnology and Nanosensors
Technical University of Moldova
Chisinau, Republic of Moldova
Institute for Materials Science/Functional Nanomaterials
Kiel University
Kiel, Germany
Department of Physics
University of Central Florida
Orlando, FL, USA
Department of Physics
University of Central Florida
Orlando, FL, USA
Institute for Materials Science/Functional Nanomaterials
Kiel University
Kiel, Germany

Nanosensors play a great role in the world of nanotechnology and are demanded nowadays due to miniaturization of electronic devices in many countries for the development of faster portable diagnostics techniques or sensing systems, as well as interconnected setups for extensive customer applications. Size effect and introducing additives in semiconducting oxides make them suitable for sensing by tuning their selectivity, response, and reliability. The present overview is aimed to summarize our results in this field and reported ones too [1, 2]. It is known that companies developing nanosensors, especially in medical applications should consider a series of characteristics (molecular, toxically, secondary reactions creating side products, etc.). I will demonstrate how networked or single nanowire/nanosensors are built by a new bottom-up approach with electronic [1], chemical [3], physical [2], magnetic properties of emerging semiconducting oxide materials leading to their tuning toward new applications in nanotechnology, nanoelectronics, and biomedical fields. Improvements in the past years were made following new requirements of selectivity, response, reliability, and lower power consumption of the nanosensors [4]. One of the major factors driving the market for nanosensors is increasing demand for nanosensors in homeland security (e.g., detection of biotoxines, radiations, etc). In this work, we report on a single nanowire/nanorod/nanotetrapod nanodevices fabricated by using platinum complex maskless nanodeposition in the dual-beam focused electron/ion beams (FIB/SEM) scientific instrument Dualbeam Helios Nanolab (FEI). The bottom-up method is based on the assembly of nanoscale building blocks to design and growth the desired nanostructure-based sensor. The main advantages of such an approach are the nanomaterial growth control with near-atomic precision and synthesize it with desired/tuned chemical compositions which are not accessible or very expensive with conventional top-down technologies. These nanodevices open absolutely new perspectives for nanoelectronics and biomedical applications. I gratefully acknowledge the support of the Kiel

University, Germany for an invited professor and visiting scientist positions in 2019. This research was partly supported by the Technical University of Moldova. This research was partly supported by the STCU within the Grant 6229.

References

1. Lupan, O., Postica, V., Wolff, N., Polonskyi, O., Duppel, V., Kaidas, V., Lazari, E., Ababii, N., Faupel, F., Kienle, L., Adelung, R.: Localized synthesis of iron oxide nanowires and fabrication of high performance nanosensor based on a single Fe₂O₃ nanowire. *Small* (Weinheim an der Bergstrasse, Germany), **13** (2017), 1602868
2. Lupan, O., Braniste, T., Deng, M., Ghimpu, L., Paulowicz, I., Mishra, Y.K., Kienle, L., Adelung, R., Tiginyanu, I.: Rapid switching and ultra-responsive nanosensors based on individual shell-core Ga₂O₃/GaN:O_x@SnO₂ nanobelt with nanocrystalline shell in mixed phases. *Sensors and Actuators, B: Chemical* **221**, 544–555 (2015)
3. Siebert, L., Lupan, O., Mirabelli, M., Ababii, N., Terasa, M.-I., Kaps, S., Cretu, V., Vahl, A., Faupel, F., Adelung, R.: 3D-printed chemiresistive sensor array on nanowire CuO/Cu₂O/Cu heterojunction nets. *ACS Appl. Mater. Interfaces* **11**, 25508–25515 (2019)
4. Lupan, O., Postica, V., Pauporté, T., Faupel, F., Adelung, R.: UV nanophotodetectors: A case study of individual Au-modified ZnO nanowires. *Sensors and Actuators, A*, **296**, 400–408. (2019). <https://doi.org/10.1016/j.sna.2019.07.040>

Complex Nanostructured Materials

Lorenz Kienle
lk@tf.uni-kiel.de

Institute of Material Science, Synthesis and Real Structure
CAU Kiel
Kiel, Germany

Today's advanced materials are coined by structural, chemical, and functional properties that require combined approaches of cutting-edge methods for their characterization. In order to determine the structures on multiscale, several techniques have to be combined synergistically, e.g., atomic resolution transmission electron microscopy (TEM), X-ray- and Synchrotron-based analyses. In this contribution, several complex nanostructured materials will be discussed with respect to their real structure–property relationships. In case of multilayer materials, the design of sensor devices is enabled via tuning of their layered components. For instance, ultrathin films of FeCo have been magnetically decoupled by layers of TiN to ensure high thermal stability, soft magnetic behavior and a coercive field strength scaling with the individual FeCo layer thickness. In the field of thermoelectrics, chalcogenide-based multilayers are known as the materials of choice for achieving ultralow thermal conductivity. Moreover, these materials are of great interest for fundamental research as demonstrated by the discovery of novel transition metal based heterostructures. In case of telluride-based phase change materials, the interfaces between the nanolayered components themselves are establishing the device function. Via in situ TEM, the atomic processes and defect dynamics interrelated to switching can be examined, enabling the characterization of switching mechanisms. More complex nanoarchitectures can be produced by dedicated syntheses as demonstrated for spark plasma sintered chalcogenides and the laser ablation synthesis of bimetallic core–shell nanoparticles. In the latter case the bimetallic particles, e.g., for the system Au–Fe, can be used as templates for etching experiments thus enabling the preparation of highly porous Au nanoparticles with well-defined porosity distribution.

Topology- and Geometry-Induced Properties of Advanced Nanoarchitectures

Vladimir M. Fomin
v.fomin@ifw-dresdxen.de

Laboratory of Physics and Engineering of Nanomaterials, Department of Theoretical Physics
Moldova State University
Chisinau, Republic of Moldova
Institute for Integrative Nanosciences
Leibniz IFW Dresden
Dresden, Germany

Study of topological matter is one of the fascinating main roads of modern physics. The present overview is aimed at topology- and geometry-driven effects, owing to special geometries of novel micro- and nanoarchitectures fabricated of both conventional and topologically nontrivial materials implemented by the high-tech techniques, in particular, self-organization [1, 2]. I will demonstrate how topology of the quantum fields determines electronic [3], excitonic [4], optical, superconducting [5], magnetic, thermal [6] properties of emerging nanostructured materials leading to their functionalization towards novel applications in advanced nanotechnologies, including biomedical ones [7]. Self-assembled quantum volcanos, which are singly connected, surprisingly exhibit the Aharonov–Bohm behavior in experiment. This is explained by the fact that in a quantum volcano the electron wave functions are identical to the electron wave functions in a quantum ring from a topological point of view. Combination of a geometric potential and an inhomogeneous twist renders an observation of the topology-driven effects in the electron ground-state energy in Möbius rings at the microscale into the area of experimental verification. Advances in the high-tech roll-up fabrication methods have provided qualitatively novel curved superconductor micro- and nanoarchitectures, e.g., nanostructured microtubes and microhelices. Rolling up superconductor Nb nanomembranes into open tubes allows for a new, highly correlated vortex dynamics regime that shows a threefold increase of a critical magnetic field for the beginning of vortex motion and a transition magnetic field between single- and many-vortex dynamic patterns. These results demonstrate pathways of tailoring nonequilibrium properties of vortices and phase slips in curved superconductor nanoarchitectures leading to their application as tunable superconducting flux generators for fluxon-based information technologies. For various micro- and nanoarchitectures, we have found a possibility of efficiently engineering the Seebeck coefficient and electric conductivity in one-dimensional stacks of quantum dots, acoustic phonon energy dispersion in one-dimensional quantum-dot superlattices, cross-section-modulated nanowires, Si wires ranging from nanoscale to microscale, and, more recently, multishell tubular structures, which are promising candidates for an advancement in thermoelectric materials [6]. Soft and reconfigurable swimming microrobots [7], which are fabricated within the high-tech roll-up approach, open new avenues for biomedical applications. I gratefully acknowledge the support of the COST Action “Nanoscale Coherent Hybrid Devices for Superconducting Quantum Technologies” CA16218 and the German Research Foundation (DFG) under grants #FO 956/4-1 and FO 956/5-1.

References

1. Fomin, V. M.: Topology-driven effects in advanced nanoarchitectures. In: Sidorenko, A. (ed.) *Functional Nanostructures and Metamaterials*, pp. 195–220. Springer International Publishing, Cham (2018)
2. Fomin, V. M.: Topology and geometry controlled properties of nanoarchitectures. *Phys. Stat. Sol.—Rapid Research Letters* **13**, 1800595 (2019)
3. Fomin, V. M.: *Physics of Quantum Rings*, 2nd Edition, p. 586. Springer International Publishing, Cham, (2018)
4. Corfdir, P., Marquardt, O., Lewis, R. B., Sinito, C., Ramsteiner, M., Trampert, A., Jahn, U., Geelhaar, L., Brandt, O., Fomin, V. M.: Excitonic Aharonov–Bohm oscillations in core–shell nanowires. *Adv. Mater.* **31**, 1805645 (2019)
5. Rezaev, R. O., Posenitskiy, E. A., Smirnova, E. I., Levchenko, E. A., Schmidt, O. G., Fomin, V. M.: Voltage induced by superconducting vortices in open nanostructured microtubes. *Phys. Stat. Sol.—Rapid Research Letters* **13**, 1800251 (2019)
6. Fomin, V. M.: Tailoring electron and phonon energy dispersion and thermal transport in nano- and microarchitectures. *Moldavian J. Phys. Sci.* **17**, 121–131 (2018)
7. Medina-Sánchez, M., Magdanz, V., Guix, M., Fomin, V. M., Schmidt, O. G.: Swimming microrobots: Soft, reconfigurable and smart, feature article. *Advanced Functional Materials* **28**, 1707228 (2018)

From Transplantation to Organ and Tissue Biofabrication

Axel Haverich
haverich@thg.mh-hannover.de

Department of Cardiothoracic, Transplantation and Vascular Surgery
Hannover Medical School
Hannover, Germany

End-stage diseases lead to permanent organ failure and can occur in all ages. Organ transplantation often appears as a single option to save the patient's life and represents the current standard of care for chronic end-stage disease of many organs. Transplantation of a new organ improves not only the life expectancy but also the quality of life of the patient. However, the main problem in transplantation remains donor organ shortage. Often patients are dying on a waiting list, because not enough organs are available through donation to meet the increasing demand.

To overcome this situation, since years alternative approaches have been intensively investigated by the researchers. The usage of animal organs for human transplantation may solve the problem of organ shortage. However, organ rejection still remains the main problem for xenogenic transplantation. Animal breeding using gene therapy represents ongoing efforts to knock-out from xenogenic tissue the epitopes responsible for hyper-acute rejection.

The past decade's rapid advancement in cell biology and bioengineering opened new perspectives for treatment of end-stage diseases. On the one hand, the efforts are made toward stimulation of endogenous repair mechanisms and tissue regeneration. On the other hand, the idea of biofabrication of new organs is currently pursued by scientists, engineers, and physicians. Active research in the field of biocompatibility and tissue engineering will give the possibility to restore damaged or diseased tissues in vivo and create living tissue and organ replacements.

Engineered Microbots for Biomedical Applications

Mariana Medina Sánchez
m.medina.sanchez@ifw-dresden.de

IFW Leibniz Institute
Dresden, Germany

Micro- and nanotechnologies together with the creation of new materials have facilitated the development of a variety of medical microbots, with low power consumption and certain degree of complexity. Such medical microbots are classified into three main categories, according to their propulsion mechanism: chemical, physical, and biohybrid [1]. The first group are the ones that employ catalytic materials which react with the microbot surroundings, forming subproducts which lead to their forward motion if the asymmetry in any of its forms is present. In this work, catalytic micromotors made by using two-photon lithography, with highly reproducible geometry, are presented as model structures to understand the different propulsion regimes which are present when varying parameters such as medium viscosity, microbot surface tension, or fuel concentration. Physical microbots, on the other hand, need external physical sources to be actuated, for example, magnetic fields, light, or acoustic waves. An application using magnetically driven helical micromotors is shown to capture, transport, and release immotile but living sperm cells, to encounter one of the most common men infertility problems, asthenozoospermia or reduced sperm motility [2]. Therefore, the proposed artificial flagellum is conceived as a sperm prosthesis to help sperm reach the oocyte. Finally, the third category, biohybrid microbots, is constituted by a biological and an engineered component to combine the advantages of both, such as the ability of cells to move through different taxis mechanisms (e.g., chemotaxis, rheotaxis, thigmotaxis), their compliance which allows them to move in intricate and complex cavities and channels in living organisms, and their ability to sense their environment and interact with the surrounding biological tissues. On the other side, the engineered component is used to improve cargo-capacity, as contrast agent for imaging, to perform alternative operations such as micro-drilling, micro-grasping, or synthetic sensing, among others [3]. In this presentation, one of the most known biohybrid systems is presented, the so-called spermbots or sperm-hybrid microbots [4–6]. In this assembly, the sperm is motile and provides the whole system with a natural propulsion mechanism. The synthetic part is used for sperm guidance, release, and cargo-delivery of drugs. All of the above-mentioned microbots have in common the engineered microparts which can also be functionalized with imaging reporters for further in vivo bioimaging, which is a key prerequisite to transfer this technology to in vivo settings. Thus, the use of different materials and structures is shown to improve their contrast and selectivity when visualized below biological tissues [7]. Other current challenges which still remain like microbots biocompatibility, multifunction, and adaptability will also be discussed.

Exploiting the Versatility of Nanostructured Transistors for Biosensing Applications

Bergoi Ibarlucea
bergoi.ibarlucea@tu-dresden.de

Institute for Materials Science and Max Bergmann Center for Biomaterials, Center for Advancing Electronics Dresden (Cfaed)
Technical University of Dresden
Dresden, Germany

Rapid demographic changes demand improved biomedical diagnostic technologies with rapidness, low cost, and high throughput, without sacrificing the sensitivity. Considering the miniature size, scalability of fabrication, and ease of chemical modification, nanoscale ion-sensitive field-effect transistors (FETs) packaged in small chips and integrated with additional circuits and lab-on-a-chip structures are ideal candidates to fulfill the task. In this talk, I will give an overview of the advances that we have achieved in this direction, showing a variety of technologies and solutions for different applications. On the one hand, we have demonstrated the validity of honeycomb-shaped nanowires as sensor material of FETs for microorganism monitoring activity and screening of antibiotic effects [1]. While traditional approaches rely on optical techniques to measure cell growth, it is rather difficult to distinguish between certain bacteriostatic or bactericide agents. We demonstrate how an electrical-based detection of cell metabolic activity can help to tackle this drawback, by measuring the acidification caused by bacteria that are still alive despite the absence of growth upon bacteriostatic treatment. The analysis of the cells' response under various conditions opens the way to perform optics-less minimum inhibitory concentration assays. On the other hand, we have shown high sensitivity in disease diagnostics [2–3], giving steps toward multiplexing of a variety of pathogens in pico- and femtomolar levels. Integration of different sensors on a single chip can be critical to discriminate rapidly the presence of a specific lethal disease showing similar initial symptoms to others. While the most common FET measurement technique during target molecule attachment is based on the shift of the threshold voltage, recently new alternative methodologies have been demonstrated. I will show the relation of memory properties, e.g., memristive properties [4] and gating hysteresis [5], to the presence of attached biomolecules on the dielectric surface. Additionally, I will discuss the integration of microfluidics offering compartmentalization [6]. Encapsulating enzymes in nanoliter droplets enables the electrical monitoring of hundreds of chemical reactions, critical for high-throughput analysis increasing statistics and parallelizing the experiments in a tiny space. Finally, the transfer of nanomaterials to flexible supports by very simple and low-cost techniques will be shown. Bottom-up grown silicon nanowires can be transferred to alternative substrates like plastic foils by a parallel contact printing technique [2], while more hydrophobic materials such as MoS₂ form thin layers on a water tank that remain on the surface after an evaporation process, forming large area sensors [7]. The resulting sensors withstand further mechanical stress than that needed for external body measurements, envisioning their use in wearable devices and smart skins.

References

1. Ibarlucea, B., et al.: Nanowire sensors monitor bacterial growth kinetics and response to antibiotics. *Lab. Chip.* **17**, 4283–4293 (2017)
2. Karanushenko, D., Ibarlucea, B., et al.: Light weight and flexible high-performance diagnostic platform. *Adv. Health. Mater.* **4**, 1517–1525 (2015)
3. Ibarlucea, B., et al.: Lethal disease discrimination using silicon nanowire-based field-effect transistors. In: *Proceedings of 17th IMCS*, pp. 182–183, (2018)
4. Ibarlucea, B., et al.: Ultrasensitive detection of Ebola matrix protein in a memristor mode. *Nano Res.* **11**, 1057–1068 (2018)
5. Ibarlucea, B., et al.: Gating hysteresis as an indicator for silicon nanowire FET biosensors. *Appl. Sci.* **8**, 950 (2018)
6. Schütt, J., Ibarlucea, B., et al.: Compact nanowire sensors probe microdroplets. *Nano Lett.* **16**, 4991–5000 (2016)
7. Zhang, P., Yang, S., Pineda-Gómez, R., Ibarlucea, B., et al.: Electrochemically exfoliated high-quality 2H-MoS₂ for multflake thin film flexible biosensors. *Small* **15**, 1901265 (2019)

Polysaccharide (Nano) Composites

V. Harabagiu
hvaleria@icmpp.ro

R. Rotaru
A. C. Humelnicu

“Petru Poni” Institute of Macromolecular Chemistry
Iasi, Romania

In the last decades, polysaccharides are more and more investigated either as biodegradable and biocompatible matrices for drug delivery and for tissue engineering systems [1, 2] or as renewable substitutes of synthetic polymers (tributary of exhaustible fossil resources), usually combined with different inorganic compounds able to tailor specific properties and high-tech uses [3, 4].

The presentation deals with clean chemical and physical methods for the preparation of chitosan hydrogels for cutaneous repairing, of magnetic or high k cellulose-based composites and of polysaccharide-based polyelectrolyte composite membranes for fuel cell applications. Their specific properties in correlation with their structures are also discussed.

Acknowledgement This work was supported by a grant of the Romanian Ministry of Research and Innovation, PCCDI-UEFISCDI, project number PN-III-P1-1.2-PCCDI-2017-0194/PCCDI/2018, contract no. 25PCCDI, within PNCDI III.

References

1. Peptu, C., Humelnicu, A.C., Rotaru, R., Fortuna, M.E., Patras, X., Teodorescu, M., Tamba, B.I., Harabagiu V. In: van den Broek B., Boeriu, C. (eds.) Chitosan-based drug delivery systems, Wiley Publishing, in press
2. Peptu, C., Rotaru, R., Ignat, L., Humelnicu, A.C., Harabagiu, V., Peptu, C.A., Leon, M.-M., Mitu, F., Cojocaru, E., Boca, A., Tamba, B.I.: *Curr. Pharm. Design* **21**, 6125–6139 (2015)
3. Coseri, S., Spatareanu, A., Sacarescu, L., Socoliuc, V., Stratulat, I.S., Harabagiu, V.: *J. Appl. Polym. Sci.* **133**, 42926–42942 (2016)
4. Rotaru, R., Savin, M., Tudorachi, N., Peptu, C., Samoila, P., Sacarescu, L., Harabagiu, V.: *Polym. Chem.* **9**, 860–868 (2018)

Contents

Nanotechnologies and Nanomaterials

3D-Printed Sensor Array of Semiconducting Oxides	3
L. Siebert, M. I. Terasa, N. Ababii, O. Lupan, and R. Adelung	
Broad-Band Spectroscopy of Nanoconfined Water Molecules	7
M. A. Belyanchikov, M. Savinov, Z. V. Bedran, P. Bednyakov, P. Proschek, J. Prokleska, V. I. Torgashev, E. S. Zhukova, S. S. Zhukov, L. S. Kadyrov, V. Thomas, A. Dudka, A. Zhugayevych, V. B. Anzin, R. K. Kremer, J. K. H. Fischer, P. Lunkenheimer, A. Loidl, E. Uykur, M. Dressel, and B. Gorshunov	
Superposition States of the Two-Dimensional Magnetoexcitons with Dirac Cone Dispersion Law and Quantum Interference Effects in Optical Transitions	13
S. A. Moskalenko, I. V. Podlesny, I. A. Zubac, and B. V. Novikov	
Superconductivity and Weak Ferromagnetism in Inclination Bicrystal Interfaces of Bismuth and Antimony	19
F. M. Muntyanu, K. Nenkov, A. J. Zaleski, and V. Chistol	
Unusual Size Dependence of Acoustic Properties in Layered Nanostructures	23
S. Cojocaru	
Features of Radiative Recombination of Iron-Doped Gallium Antimonide	29
A. Mihalache	
Spin Crossover in Iron(II) Complexes with Mixed Nitrogen-Sulfur Coordination: DFT Modeling	33
S. I. Klokishner and O. S. Reu	
Change in Microstructure and Magnetic Properties of Transition Metal Nitride Thin Films by Substrate Temperature	37
M. Kamp, L. Voß, T. Bichel, M. Hicke, U. Schürmann, and L. Kienle	
Modeling of Charge Transfer Induced Spin Transition in a Linear {FeCoFe} Complex	43
S. M. Ostrovsky and S. I. Klokishner	
Mössbauer Effect in 57Fe-Doped Gallium Antimonide	47
A. Mihalache	
ZnO Nanometric Layers Used in Photovoltaic Cells	53
V. Botnariuc, L. Gorceac, A. Coval, B. Cinic, P. Gaugas, P. Chetrus, I. Lungu, and S. Raevschi	

Resistivity Response to Stress and Strain of a Flexible Bi₂Te₃ Based Thermoelectric Material	57
L. O. Akinsinde, S. Scheitz, L. Zimoch, J. K. Sierck, L. Siebert, R. Adelung, U. Schürmann, M. A. Rübhausen, T. Dankwort, and L. Kienle	
“True” Dose Rate Effect of the ELDRS Conversion Model	61
V. S. Pershenkov, A. S. Bakerenkov, V. A. Telets, V. V. Belyakov, V. A. Felitsyn, and A. S. Rodin	
Modeling of the Valence Tautomeric Transformation in Heterometallic [Cr-Dhbq-Co] Molecules	67
M. A. Roman and S. I. Klokishner	
Fabrication and Application of TEM-Compatible Sample Grids for Ex Situ Electrical Probing	71
O. Gronenberg, N. Carstens, A. Vahl, F. Faupel, and L. Kienle	
Refractive Index in the Region of Excitonic Resonances in TlGaSe₂ Crystals	75
A. V. Tiron	
Optical Activity in Mn Doped As₂S₃ Glasses	79
V. V. Zalamai, A. V. Tiron, M. S. Iovu, and N. N. Syrbu	
Electrical Properties of Thermal Annealed in Vacuum Spray Deposited Al-Doped ZnO Thin Films	83
T. Potlog, I. Lungu, S. Raevschi, V. Botnariuc, S. Robu, S. Worasawat, and H. Mimura	
Growth of P-GaN on Silicon Substrates with ZnO Buffer Layers	89
S. Raevschi, L. Gorceac, V. Botnariuc, and T. Braniste	
TEM and Electrochemical Investigation of Different Morphology Silicon Anodes	93
K. Saleem, U. Schürmann, S. Hansen, H. Cavers, R. Adelung, and L. Kienle	
Adsorption of Lead Ions on Carbonaceous Sorbents of Nutshell Obtained from Secondary Raw Material	97
T. Marsagishvili, G. Tatishvili, N. Ananiashvili, N. Giorgadze, E. Tskhakaia, M. Gachechiladze, J. Metreveli, and M. Machavariani	
Structural and Photoluminescence Properties of Nanoparticles Formed by Laser Ablation of Porous Silicon in Ethanol and Liquid Nitrogen	101
A. V. Skobelkina, F. V. Kashaev, S. V. Zaboltnov, A. V. Kolchin, T. P. Kaminskaya, D. E. Presnov, E. A. Sergeeva, M. Yu. Kirillin, L. A. Golovan, and P. K. Kashkarov	
Electrical and Photoelectrical Properties of Zn_{1-x}Mg_xO Thin Films Obtained by Spin Coating and Aerosol Deposition Method	105
V. Morari, V. Postolache, G. Mihai, E. Rusu, Ed. Monaico, V. V. Ursachi, K. Nielsch, and I. M. Tiginyanu	
Peculiarities of Surface Relief Grating Formation in Nanomultilayer Structures Based on As₂S₃-Se Chalcogenide Glasses	111
A. Meshalkin, O. Paiuk, E. Achimova, A. Stronski, V. Abaskin, A. Prisacar, G. Triduh, A. Korchovy, and P. Oleksenko	
Near-Edge Optical Properties of Layered Tin Sulfide (Selenide) Crystals	117
V. V. Zalamai, A. V. Tiron, E. V. Rusu, E. V. Monaico, and N. N. Syrbu	

Nanostructured Organic Crystals as Prospective Thermoelectric Materials for Infrared Sensors	121
I. I. Sanduleac, S. C. Andronic, and A. I. Casian	
Effects of Green Silver Nanoparticles on CCl₄ Injured Albino Rats' Liver	127
Sh. Kazaryan, M. Petrosyan, L. Rshtuni, V. Dabaghyan, and A. Hovhannisyanyan	
Luminescent Properties on ZnO:Cr Nanocrystals and Thin Layers	133
T. Goglidze, I. Dementiev, E. Goncareenco, N. Nedeoglo, T. Iurieva, and D. Nedeoglo	
Evaluation of Stimulatory, Antifungal and Thermo-Resistant Action of Aqueous Dispersions of Nanoparticles on Seeds of Parental Forms and Reciprocal Hybrids of Winter Wheat	137
S. N. Maslobrod, G. A. Lupashku, S. I. Gavzer, A. I. Gore, and Yu. A. Mirgorod	
Photocatalytic Degradation of Methylene Blue with Composite Nanocrystalline TiO₂+ Diatomite	143
T. Ya. Datsko, V. I. Zelentsov, and D. P. Dvornikov	
Micromechanical Properties and Plastic Deformation Features of the Pb_{1-x}Yb_xTe Ternary Semiconductors	149
D. Z. Grabco, V. Z. Nicorici, Z. A. Barbos, D. Topal, and O. A. Shikimaka	
Quantum Interferences with Equidistant Three-Level Quantum Wells	155
V. Ceban and M. A. Macovei	
Luminescence Properties of a Novel Eu³⁺ Dinuclear Coordination Compound ...	161
V. I. Verlan, I. P. Culeac, O. Bordian, V. E. Zubareva, I. Bulhac, M. S. Iovu, M. Enachescu, N. A. Siminel, and V. V. Nedelea	
Me-ZnP₂ Diodes Sensible to Optical Gyration	167
A. V. Dorogan, S. I. Beril, I. G. Stamov, and N. N. Syrbu	
Applications of Chalcogenides as Electron Transport Layers and Doping Materials in Perovskite Solar Cells	173
M. E. Popa	
Applications of Chalcogenides as Hole Transport Layers and Dopants in Perovskite Solar Cells	177
M. E. Popa	
The Influence of the External Magnetic Field on the Electronic Density of States of Quasi-1D System in the Mixed Phase of Superconductivity and Spin Density Wave	181
M. E. Palistrant, I. D. Cebotari, and S. A. Palistrant	
Elastic Coupling at Epitaxial Multiferroic Interfaces: In Situ X-Ray Studies of Electric Field Induced Strain	187
C. T. Koops, S. B. Hrkac, M. Abes, P. Jordt, J. Stettner, A. Petraru, H. Kohlstedt, V. Hrkac, N. Wolff, L. Kienle, O. H. Seeck, G. Nisbet, O. M. Magnussen, and B. M. Murphy	
Investigation of the Electrochemical Properties of Lithium–Sulfur Cells with Sulfur Electrodes Based on Carbon Inverted Opals	193
N. S. Sukhinina, E. V. Karaseva, V. M. Masalov, E. V. Kuzmina, A. A. Zhokhov, V. S. Kolosnitsyn, and G. A. Emelchenko	

Peierls Structural Transition in Organic Crystals of TTT_2I_3 with Intermediate Carrier Concentration	199
S. C. Andronic, I. I. Sanduleac, and A. I. Casian	
GaN-Based 2D and 3D Architectures for Electronic Applications	203
Vladimir Ciobanu	
The Structure and Chemical Composition of Ga_2O_3 Oxide Prepared by Annealing of Ga_2Se_3 Crystals	207
V. Sprincean, E. Vataavu, L. Dmitroglu, D. Untila, I. Caraman, and M. Caraman	
The Use of Metal Oxide Semiconductors for THz Spectroscopy of Biological Applications	213
H. L. Hartnagel and V. P. Sirkeli	
ZnO-Based Quantum Structures for Terahertz Sources	219
V. P. Sirkeli, H. L. Hartnagel, O. Yilmazoglu, and S. Preu	
Surface Modification of PVDF Copolymer Nanofiber by Chitosan/Ag(NP)/Nanosilica Composite	225
M. Nasir, R. I. Sugatri, and D. M. Agustini	
Recent Progress in GaN-Based Devices for Terahertz Technology	231
V. P. Sirkeli, I. M. Tiginyanu, and H. L. Hartnagel	
Silanized Citric Acid Capped Magnetic Nanoparticles and Influence on Chlorophylls	237
L. Popescu, L. Sacarescu, M. Grigoras, C. Morosanu, D. Creanga, D. Dorohoi, and C. Stan	
Enhancement in Conductivity and Photoresponse of Ga Doped ZnO Nanofibers	243
M. N. Martyshov, A. S. Ilin, V. B. Platonov, P. A. Forsh, and P. K. Kashkarov	
Luminescence of $\beta\text{-Ga}_2\text{O}_3$ Nanoforms Obtained by Oxidation of GaSe Doped with Eu	247
V. Sprincean, D. Untila, A. Chirita, I. Evtodiev, and I. Caraman	
Sensorial and Local Reflectivity Properties of the Columnar ZnO:Eu Films	253
C. Lupan, A. Schütt, A. Birnaz, M. Hoppe, and R. Adelung	
Effects of Heat Treatment on Palladium-Doped Zinc Oxide on Sensory Selectivity	259
N. Magariu	
Mechanical and Wetting Properties of Three-Dimensional Flexible Tetrapodal ZnO Networks ALD-Coated with Al_2O_3	263
A. Gapeeva, M. T. Bodduluri, S. Kaps, F. Rasch, B. Wagner, R. Adelung, and O. Lupan	
Polarization Holographic Recording on Photosensitive Polymers	269
E. Achimova, V. Abaskin, A. Meshalkin, A. Prisacar, L. Loghina, M. Vlcek, and A. Yakovleva	
QDs Doped Azopolymer for Direct Holographic Recording	275
C. Loşmanskii, E. Achimova, V. Abaskin, A. Meshalkin, A. Prisacar, L. Loghina, M. Vlcek, and A. Yakovleva	
Radiative Recombination of Bound Excitons in $\text{MoSe}_2\text{:I}_2$ Layered Crystals	279
N. Siminel, V. Nedelea, K. Sushkevich, A. Siminel, A. Micu, and L. Kulyuk	

Acetone Sensing Properties of Nanostructured Copper Oxide Films on Glass Substrate	285
V. Cretu, N. Ababii, V. Postica, N. Magariu, M. Hoppe, V. Verjbitki, V. Sontea, R. Adelung, and O. Lupan	
Influence of the Growth Temperature on the Properties of the Transparent and Conductive NiO Thin Films Obtained by RF Magnetron Sputtering	291
L. Ghimpu, V. Suman, and D. Rusnac	
Plasmonics and Metamaterials	
Active Spectral Absorption Control in a Tunable Liquid Crystal/Metamaterial Structure by Polarization Plane Rotation	299
A. Bărar, O. Dănilă, D. Mănăilă-Maximean, and V. A. Loiko	
Spectral Investigation of Surface Plasmon Resonance Bands of Silver Nanoparticles Capped with Gallic Acid	305
L. Popescu, G. Ababei, D. Babusca, D. Creanga, C. A. Benchea, N. Lupu, and L. Oprica	
Bio-micro/nano Technologies and Devices	
Cathodoluminescent UV Sources for Biomedical Applications	313
D. I. Ozol, E. P. Sheshin, M. I. Danilkin, and N. Yu. Vereschagina	
European Terahertz Technology for Environmental Monitoring and Bio-friendly Imaging	319
O. Cojocari, M. Hoefle, D. Mopro-Melgar, I. Oprea, and M. Rickes	
Synthesis and Characterization of Self-assembled Submicron Particles Based on Biotinylated N-palmitoyl Chitosan	325
V. Balan, C. I. Moise, and L. Verestiuc	
Biomaterials for Medical Applications	
A Novel Nanocomposite (SR/HA/-nZnO) Material for Medical Application	333
H. Sh. Majdi, A. N. Saud, and M. H. Al-Mamoori	
Influence of MW Irradiation on the Hydroxyapatite/Chitosan Composite Structure and Drug Release Kinetics	343
L. B. Sukhodub, M. O. Kumeda, and L. F. Sukhodub	
Improvement of the Antibacterial Activity of Benzylpenicillin in Combination with Green Silver Nanoparticles Against <i>Staphylococcus aureus</i>	349
S. Ohanyan, H. Grabski, L. Rshtuni, S. Tiratsuyan, and A. Hovhannisyan	
Functionalization of Flavonoids (Quercetin) to Chitosan Matrix and Determination of Antioxidant Activity of Obtained Bio-composites	355
M. Gonta, E. Sirbu, S. Robu, A. Gonta, and L. Mocanu	
Molecular Docking of Compounds Modulating Amyloid Peptide Aggregation Schemes	361
S. Ginosyan, Y. Hambarzumyan, T. Mkrtchyan, H. Grabski, and S. Tiratsuyan	
Use of the Auto Osteomatrix Forte Graft in Total Tympanomastoid Dissection	367
I. Ababii, S. Vetrician, V. Smetanca, and L. Danilov	

Composite Metamaterials for Biological Decontamination of Fluids	373
N. A. Enaki, M. Turcan, S. Bazgan, E. Starodub, T. Paslari, A. Nistreanu, C. Ristoscu, and I. N. Mihailescu	
Study of a Customized Implant in Cranio-Maxillofacial Surgery	379
C. Miron-Borzan, H. Chezan, C. Buciuman, and E. Sabau	
Hydrogels Based on Collagen and Dextran for Bioartificial Tissues	385
Maria Butnaru, A. M. Lucaci, B. P. Cosman, and L. Verestiuc	
Biomimetics and Sensors	
Microelectronic Pyroelectric Measuring Transducers	393
Andriy O. Semenov, S. V. Baraban, O. V. Osadchuk, O. O. Semenova, K. O. Koval, and A. Yu. Savytskyi	
Ionizing Radiation Dose Sensor Based on <i>n</i>-channel MOSFET	399
B. I. Podlepetsky, V. S. Pershenkov, V. V. Belyakov, A. S. Bakerenkov, V. Felitsyn, and A. S. Rodin	
Conductance and Photoconductance of Indium Oxide-Zinc Oxide Composites in the Hydrogen-Containing Atmosphere	405
Alexander S. Ilin, P. A. Forsh, M. I. Ikim, A. V. Koroleva, M. N. Martyshov, L. I. Trakhtenberg, and P. K. Kashkarov	
Biomedical Instrumentation	
Visual Control of Human Locomotion	411
H. N. Rozorinov, N. I. Chichikalo, E. H. Arkhiereieva, and E. Yu. Larina	
Method for Performance Evaluation of Electrostimulation of the Lower Esophageal Sphincter	417
V. Sontea, S. Ungureanu, N. Sipitco, D. Fosa, and V. Vidiborschii	
Profile Forming of Infrared Cabin User's Biomedical Indicators	421
M. M. Mezhenaya, A. V. Vorobey, V. Y. Drapeza, A. N. Osipov, S. K. Dick, and M. X.-M. Thostov	
The Algorithms Modernization of Temperature and Gas Control Systems of Ion Mobility Spectrometer	427
Y. R. Shaltaeva, A. V. Golovin, V. K. Vasilyev, E. A. Gromov, M. A. Matusko, E. K. Malkin, I. A. Ivanov, V. V. Belyakov, and V. S. Pershenkov	
An Optimal Path Planning Proposal for Motion Robots with Specific Constraints Applicable in Biomedical Engineering	433
C. Corciovă, M. Turnea, A. Gheorghită, and D. Arotăritei	
Intelligent System for Monitoring Vital Signs at Patient's Home	439
R. Fuior, D. Andrițoi, C. Luca, and C. Corciovă	
Bio-behavioral Aspects of Patients with Ocular Problems with Implications for Optometric Comfort	447
M. I. Baritz, A. M. Lazar, and M. G. Apostoiaie	

Biomedical Signal Processing

Testing the Heart Rate Coherence Function for Detecting and Identifying Atrial Fibrillation	455
--	-----

Y. Sokol, P. Shapov, M. Shyshkin, and R. Tomashevskiy

Dense Array Electroencephalography-Based Electric Source Imaging of Interictal Epileptiform Discharges	461
---	-----

S. A. Groppa, D. Ciolac, A. Vataman, and V. Chiosa

Cardiorespiratory Coupling: A Review of the Analysis Methods	469
---	-----

V. Tonu, V. Vovc, and N. Enache

Recording of the Breathing Pattern in the Test with Controlled Hyperventilation in Subjects with a Borderline Type Personality Disorder	475
--	-----

S. Lozovanu, I. Moldovanu, V. Vovc, T. Besleaga, and A. Ganenco

Encephalographic Signal LabView Processing	481
---	-----

I. C. Roşca, C. Drugă, I. Şerban, and R. D. Necula

Multifocal Repetitive Transcranial Magnetic Stimulation—A Novel Paradigm in Migraine Treatment	485
---	-----

P. Leahu, S. A. Groppa, M. Bange, S. Scheiter, D. Ciolac, V. C. Chirumamilla, M. Muthuraman, and S. Groppa

Biomedical Imaging and Image Processing

Remodeling of Cortical Structural Networks in Multiple Sclerosis	491
---	-----

D. Ciolac

Polarization Tomography of Synovial Fluids Polycrystalline Layers	497
--	-----

V. V. Protsiuk, V. L. Vasiyk, Y. M. Vasylichshyn, O. G. Ushenko, M. V. Shaplavskiy, O. B. Bodnar, A. V. Dubolazov, Yu. O. Ushenko, and Yu. Ya. Tomka

Differential Muller-Matrix Microscopy of Protein Fractions of Vitreous Preparations in Diagnostics of the Pressure of Death	503
--	-----

Yu. Sarkisova, V. T. Bachinskyi, M. Garazdyuk, O. Ya. Vanchulyak, O. Yu. Litvinenko, O. G. Ushenko, B. G. Bodnar, A. V. Dubolazov, Yu. O. Ushenko, Yu. Ya. Tomka, I. V. Soltys, and S. Foglinskiy

Laser Autofluorescent Microscopy of Histological Sections of Parenchymatous Biological Tissues of the Dead	507
---	-----

O. G. Ushenko, A.-V. Syvokorovskaya, V. T. Bachinsky, O. Ya. Vanchuliak, A. V. Dubolazov, Yu. O. Ushenko, Yu. Ya. Tomka, and M. L. Kovalchuk

Statistical Analysis of Polarization Images of Histological Cuts of Parenchymatic Tissues in Diagnostics of Volume of Blood Loss	513
---	-----

N. Sivokorovskaya, V. T. Bachinskyi, O. Ya. Vanchulyak, O. G. Ushenko, A. V. Dubolazov, Yu. O. Ushenko, Yu. Ya. Tomka, and L. Ya. Kushnerik

Deep Learning in Processing Medical Images and Calculating the Orbit Volume	519
--	-----

V. S. Asipovich, O. N. Dudich, V. L. Krasilnikova, A. A. Karakulko, A. L. Radnionok, P. A. Moroz, A. Y. Nikolaev, M. A. Konovalova, and K. D. Yashin

Sleep-Related Epilepsy Diagnosis: Standard Video-EEG or Video-EEG Telemetry?	523
V. A. Chiosa	
A Real-Time WebGL Rendering Pipeline for MRI Using RayCasting Transfer Functions	529
R. Ciucu, F. Adochiei, I. Adochiei, F. Argatu, C. M. Larco, and L. Grigorie	
Alterations of Brain Structure Linked to Myoclonic Epilepsy	535
A. Vataman	
Bioinformatics	
Mode of Artemisinins' Action on Oxidative Stress, Genomic and G-Quadruplex DNA	543
S. G. Ginosyan, G. V. Chilingaryan, H. V. Grabski, L. A. Ghulikyan, N. M. Ayvazyan, and S. G. Tiratsuyan	
Evaluation of the Quercetin Semisynthetic Derivatives Interaction with ABCG2 and Cyclooxygenase-2	549
A. E. Manukyan	
Information Analysis of Biochemical Parameters for Glucose Tolerance Tests ...	553
Y. I. Sokol, O. V. Chmykhova, V. V. Boyko, P. N. Zamyatin, and D. P. Zamiatin	
Medical Physics and Biophysics	
Theoretical Model of Lipid Peroxidation Kinetics for Complexes of Cytochrome <i>c</i> and Cardiolipin with Participation of Antioxidants	561
E. Yu. Kanarovskii, O. V. Yaltychenko, and N. N. Gorinchoy	
Testing Green Silver Nanoparticles for Genotoxicity, Antioxidant and Anticancer Activity	567
M. Petrosyan, T. Gevorgyan, G. Kirakosyan, L. Ghulikyan, A. Hovhannisyanyan, and N. Ayvazyan	
Influence of Polarization on Electron Localization in the Coated Tetramer Nanoclusters Used as Elements of Biorecognition Systems	573
E. Yu. Kanarovskii and O. V. Yaltychenko	
Use of Physical Methods as an Element of Complex Treatment of Burn Wound Microbiome	579
V. Nagaichuk, R. Chornopyshchuk, O. Yunusova, and M. Onyshchenko	
Molecular, Cellular and Tissue Engineering	
Interaction of Quercetin with LasR of <i>Pseudomonas aeruginosa</i>: Mechanistic Insights of the Inhibition of Virulence Through Quorum Sensing	585
H. V. Grabski and S. G. Tiratsuyan	
Mechanical and Morphological Characterization of Decellularized Umbilical Vessels as Tissue Engineering Scaffolds	589
T. Malcova, L. Globa, A. Vascan, E. Ţugui, A. Stoian, and V. Nacu	
The Procedure of Bone Cells Obtaining, Culture and Identification	595
M. Jian, V. Cobzac, A. Mostovei, and V. Nacu	

Evaluation of the Endothelial Cell Regenerative Proprieties of the Cornea in the Culture Media. Results and Prospects	601
A. Cociug, O. Macagonova, V. Cusnir Jr., V. Cusnir, and V. Nacu	
The Influence of Semiconductor Nanoparticles Upon the Activity of Mesenchymal Stem Cells	607
T. Braniste, V. Cobzac, P. Ababii, I. Plesco, S. Raevschi, A. Didencu, M. Maniuc, V. Nacu, I. Ababii, and I. Tiginyanu	
Clinical Engineering, Health Technology Management and Assessment	
Medical Devices Regulations, Management and Assessment; New Trends New Needs	615
N. Pallikarakis	
Assessment of Human Tissue Transplantation Activities in the Republic of Moldova	621
T. Timbalari, I. Codreanu, O. Lozan, and V. Nacu	
Electro-Acoustical Examination in Noninvasive Monitoring as a Basis for Treatment Selection	627
S. Diacova	
Functional and Morphological Correlations in Prolonged Otitis Media in Childhood	633
S. Diacova, I. Ababii, L. Danilov, M. Maniuc, P. Ababii, V. Gavriluta, and A. Levcenco	
The Review of Bipolar Ion Mobility Spectrometers	639
Y. R. Shaltaeva, A. V. Golovin, V. K. Vasilyev, E. A. Gromov, M. A. Matusko, E. K. Malkin, I. A. Ivanov, V. V. Belyakov, and V. S. Pershenkov	
Assessing the Safety of Using Incubators for Newborns	645
C. Pislaru, V. Şontea, and S. Railean	
Health Informatics, e-health and Telemedicine	
Creation of Regional Telemedicine Diagnostic and Treatment Complex	651
K. V. Kolisnyk, R. S. Tomashevskyi, T. V. Sokol, S. M. Koval, and D. M. Deineko	
Telemedicine—Advanced Technology at the Service of Society	657
E. Arama, S. Maximilian, L. Rotaru, and V. Vovc	
Biomedical Engineering Education	
Static Analysis of the Human Body Balance Following an Induced Vertigo	667
I. Şerban, C. Drugă, A. Tătaru, and B. Braun	
Innovation, Development and Interdisciplinary Research	
Voltage Management of a Remote Load	673
A. Penin, Yu. Savva, and A. Sidorenko	
Steady-State Behaviors of a Quantum Oscillator Coupled with a Three-Level Emitter	677
A. Mirzac and M. A. Macovei	

Integration of Cyber Security in Healthcare Equipment	681
Au. Buzdugan	
Cyber-Physical Systems—Nanomaterial Sensors Based Unmanned Aerial Platforms for Real-Time Monitoring and Analysis (Invited Paper)	685
A. Vaseashta	
Bibliometric Analysis of the Nanotechnology Research Area in the Republic of Moldova	691
A. I. Rosca, I. P. Cojocaru, and A. Gh. Turcanu	
Qualitative Method to Control Toxic Impurities in Drinking Water	697
O. Kulikova, A. Siminel, A. Micu, and N. Siminel	
The Cathepsin D as a Potential Biomarker for Survival Rate in Polytrauma. Pilot Research	703
O. Arnaut, S. Sandru, A. Sauleal, I. Grabovschi, and Gh. Rojnovceanu	
Comparative Study of the <i>p</i>-CdS/<i>n</i>-CdTe Photovoltaic Devices with Depleted Intrinsic Layer	707
A. Al Qassem, L. Gagara, V. Fedorov, I. Lungu, and T. Potlog	
Synthesis and Biological Properties of the Novel Coordination Compound with Rhodanine-3-Acetic Acid	713
A. Vitu, D. Chișca, E. Gorincioi, E. Coropceanu, and P. Bourosh	
Phenomena of Radiative Recombination in Single Crystals of Cadmium Thiogallate with Cadmium (CdGa₂S₄:Cd) or Sulfur (CdGa₂S₄:S) Excess	719
E. Arama, V. Pantea, T. Shemyakova, and V. Vovc	
Design and Evaluation of a Low Cost Electrical Muscle Stimulator (EMS) with Biopac	725
I. Șerban, C. Drugă, I. Tătulea, B. Braun, and R. Necula	
Development of the High-Resolution Scintillator Type Imager Using Si GRID Structures	731
K. Tabata, R. Ohtake, J. Nishizawa, A. Koike, and T. Aoki	
Packing Conditions of Optical Separated CsI:Tl Scintillator by Silicon Collimator	735
R. Ohtake, K. Tabata, J. Nishizawa, A. Koike, and T. Aoki	
Study on Ferroelectric Thin Film Capacitor for AC-Coupled CdTe X-ray Detector	741
M. Hayakawa, H. Nakagawa, K. Sakaida, and T. Aoki	
Aluminium-BSF Versus PERC Solar Cells: Study of Rear Side Passivation Quality and Diffusion Length	745
A. Schütt, O. Lupan, and R. Adelung	
Smart Device for Therapeutic Hypothermia	749
V. Cojocaru, R. Galus, and T. Fedorisin	
Make Innovation Happen: Scientific and Statistic Tools to Accelerate the Way Toward Technology Readiness Level TRL 9—A Deployed Application	755
N. Varachiu	
Investigation into Interlayer Water Structure in Na⁺- and Ca²⁺-Montmorillonite: A Molecular Dynamics Study	761
N. Siminel	

A Positioning Mechanism Based on MEMS-INS/GPS and ANFIS Data Fusion for Urban Life Mobility Improvement	767
L. T. Grigorie, N. Jula, C. L. Corcău, I. R. Adochiei, C. Larco, and S. M. Mustață	
Scattering Indicatrix for Absorbing Porous Medium with Dark Modes	775
V. V. Sergentu, E. V. Monaico, and V. V. Ursaki	
Static Versus Novel Dynamic Biofouling-Testing of Fouling-Release Coatings for Marine Applications: Pros and Cons	779
H. Qiu, I. Hölken, A. Gapeeva, R. Adelung, and M. Baum	
Comparison the Marginal Fit of Metal Coping Cast Made Through Different Methods	785
A. Badarau, A. Gumeniuc, and E. V. Monaico	
Synthesis of New Zinc Phthalocyanine with Block Copolymers in Nanomedicine Applications	789
P. Tiuleanu, S. Robu, V. Prisakari, V. Furtuna, R. Rusnac, and T. Potlog	
Portable Campimeter to Evaluate Visual Field Modifications of Subjects with Low Vision State	793
M. I. Baritz, M. G. Apostoaie, and A. M. Lazar	
Nanotechnological Aspects at Electro-activation of Secondary Dairy Products	799
E. G. Vrabie, M. K. Bologa, I. V. Paladii, V. G. Vrabie, A. Policarpov, V. Gonciaruc, C. Gh. Sprincean, and T. Stepurina	
Nuclear and Radiation Safety and Security	
Evaluation of Radiation Hardness of the Bipolar Devices in the Space Conditions	807
A. S. Rodin, A. S. Bakerenkov, V. A. Felitsyn, V. S. Pershenkov, and V. A. Telets	
Integral Estimate of LSI Radiation Hardness as a Fuzzy Number of Multiplicity of Nodes	811
V. M. Barbashov, N. S. Trushkin, and A. K. Osipov	
Revision of the Curriculum on Nuclear Safety and Security in the Light of Recent International Recommendations	815
Ar. Buzdugan, and Au. Buzdugan	
National Nuclear Security Support Centre and Non-proliferation of Weapon of Mass Destruction	821
Ar. Buzdugan and A. Țurcanu	
Li₂B₄O₇ for Thermoluminescent Dosimetry: A New Life of an Old Material	827
M. I. Danilkin, N. Yu. Vereschagina, A. S. Selyukov, and D. I. Ozol	
Author Index	831

Part I

Nanotechnologies and Nanomaterials

3D-Printed Sensor Array of Semiconducting Oxides

L. Siebert, M. I. Terasa, N. Ababii, O. Lupan, and R. Adelung

Abstract

Sensors start to play an ever increasing role in human life and new technologies for their cost-effective mass production are required. In this work, the one-step 3D-printing of nanoflakes—nanowire covered $\text{Fe}_2\text{O}_3/\text{Fe}-\text{CuO}/\text{Cu}_2\text{O}/\text{Cu}$ microparticles (MPs) with diameters of $\sim 10\ \mu\text{m}$ on the surface of glass substrate successfully forming an ordered net is reported for the first time. 3D-printed Fe–Cu and only Cu MPs-based stripes formed non-planar $\text{CuO}/\text{Cu}_2\text{O}/\text{Cu}$ and $\text{Fe}_2\text{O}_3/\text{Fe}-\text{CuO}/\text{Cu}_2\text{O}/\text{Cu}$ heterojunctions after thermal annealing at $425\ ^\circ\text{C}$ for 4 h in air and were fully covered with nanoflakes of Fe_2O_3 and CuO nanowire net bridging MPs with external Au-contacts. The morphological, chemical and structural investigations were performed in detail, showing the high crystallinity of the 3D printed material. This concept proves to be easily translatable to other semiconducting, metallic or functional microparticles for the rapid fabrication of sensor devices.

Keywords

3D printing • Cu–Fe deposition • Heterojunction • Fe_2O_3 –CuO/ $\text{Cu}_2\text{O}/\text{Cu}$ • Gas sensing

1 Introduction

Nowadays, three-dimensional (3D) printing has attracted a significant amount of attention, for example, for the manufacturing of custom devices or complex and functional parts [1, 2]. Another very important field is the fabrication built from functional nanomaterials or as macro- or microdevices via 3D-printing technologies due to the low-cost and easy processing [3–5].

In this field of biomedical engineering, 3D-printed components or biosensors have gained a significant attention, due to novel design possibilities e.g. for innovative strain sensors [6–8] or full electronic components [9]. The reason for this boom in this new and quite efficient technology is the compatibility with standard techniques from materials science for both the materials preparation as well as the post processing after 3D printing.

In this regard, Direct Ink Writing (DIW) has become a prominent technology, focusing on the fabrication of devices and particle systems from a viscous liquid ink [10, 11]. With this technique, even complex-shaped micro- and nanoparticles can be arranged in 3D or as 2D traces for micro- and nanoelectronics [12]. Here we present the simple integration of semiconducting oxides by DIW of metal particles with subsequent heat treatment to form sensor nets for volatile organic compound (VOC) detection.

2 Experimental

Spheroidal copper particles ($\sim 10\ \mu\text{m}$) and spheroidal iron particles ($\sim 10\ \mu\text{m}$) were obtained from Sigma-Aldrich. For the copper based sensor, the 3 parts by weight of Cu particles were sonicated in 2 parts distilled water for 5 min after which polyethylene oxide (PEO, $M_v = 2,000,000$), obtained from Sigma-Aldrich was added. The solution was stirred until a homogeneous, viscous state was reached for the ink.

L. Siebert (✉) · M. I. Terasa · O. Lupan (✉) · R. Adelung
Functional Nanomaterials, Faculty of Engineering, Institute for
Materials Science, Kiel University, Kaiserstraße 2, Kiel, Germany
e-mail: lesi@tf.uni-kiel.de

O. Lupan
e-mail: ollu@tf.uni-kiel.de

N. Ababii · O. Lupan
Department of Microelectronics and Biomedical Engineering,
Center for Nanotechnology and Nanosensors, Technical
University of Moldova, Chisinau, Republic of Moldova

The concentration of PEO in the final ink was 6% by weights.

For the Cu–Fe based sensor array, both copper and iron particles were sonicated in 96% Ethanol for 5 min. Polyvinyl butyral (PVB) was kindly provided by Kuraray Co. Ltd. and was added and the solution was stirred at room temperature until a homogeneous mixture was obtained. The mixing ratios of the final ink by weights were 3:1:0.5:0.5 (Ethanol:PVB:Fe:Cu). Both inks were printed in a custom-built DIW apparatus. The Cu-based ink was printed with a tapered nozzle (diameter $d = 0.41$ mm) with a constant printing speed of $0.6 \text{ mm}^3 \text{ s}^{-1}$, while the Cu–Fe-based ink was printed with a nozzle diameter of $d = 0.58$ at a speed of $0.46 \text{ mm}^3 \text{ s}^{-1}$. One layer was printed for both variations with a layer height of 0.1 mm. The printing substrate was a standard glass slide. After printing, the objects were dried at room temperature overnight and subsequently heat-treated for 4 h at 425°C in air.

Micro-Raman, X-Ray Diffraction and Scanning Electron Microscopy were done to investigate the structural and morphological properties of the printed constructs.

Micro-Raman was performed at room temperature using a WITec system. A Nd:YAG laser was used which power was set to less than 4 mW.

The wavelength of the laser was $\lambda_{ex} = 532.2$ nm and each spectrum was taken with 10 accumulations at an integration time of 1 s.

XRD was performed on a Seifert 3000 TT unit at 40 kV and 40 mA, with $\text{CuK}_{\alpha 1}$ radiation ($\lambda = 1.540598 \text{ \AA}$).

Additionally, interdigitated gold contacts were sputtered onto the samples (~ 170 nm), to measure the sensor properties. By determining the resistance ratios $\Delta R/R_{air}$, where R_{air} and R_{gas} and $\Delta R = R_{gas} - R_{air}$ are the electrical resistances of the printed sensor in ambient air and under exposure to VOCs, respectively. More details on the sensing experiments can be found in previous works on gas sensing [13, 14].

For all further results and the discussion, the copper-based sample set will be named CuO 3D and the copper-iron-based sample set will be named CuO– Fe_2O_3 3D.

3 Results and Discussion

In Fig. 1a is presented XRD for CuO 3D sample annealed TA at 425°C for 4 h, where detected three phases (CuO monoclinic, Cu_2O and Cu cubic). In XRD was detected mainly CuO (Tenorite) at 2θ of 32.65° , 35.65° , 46.7° , 48.8° , 58.25° , 61.5° , 68.05° , 72.6° , 75.35° , 83.85° , 90.05° and 95.2° , respectively. Reflections at 2θ of 36.5° , 42.35° , 52.75° , 73.35° and 77.7° , are due to Cu_2O (Cuprite) phase. Also, at 2θ of 43.35° , 50.5° and 74.15° were detected reflections of metallic Cu, accordingly.

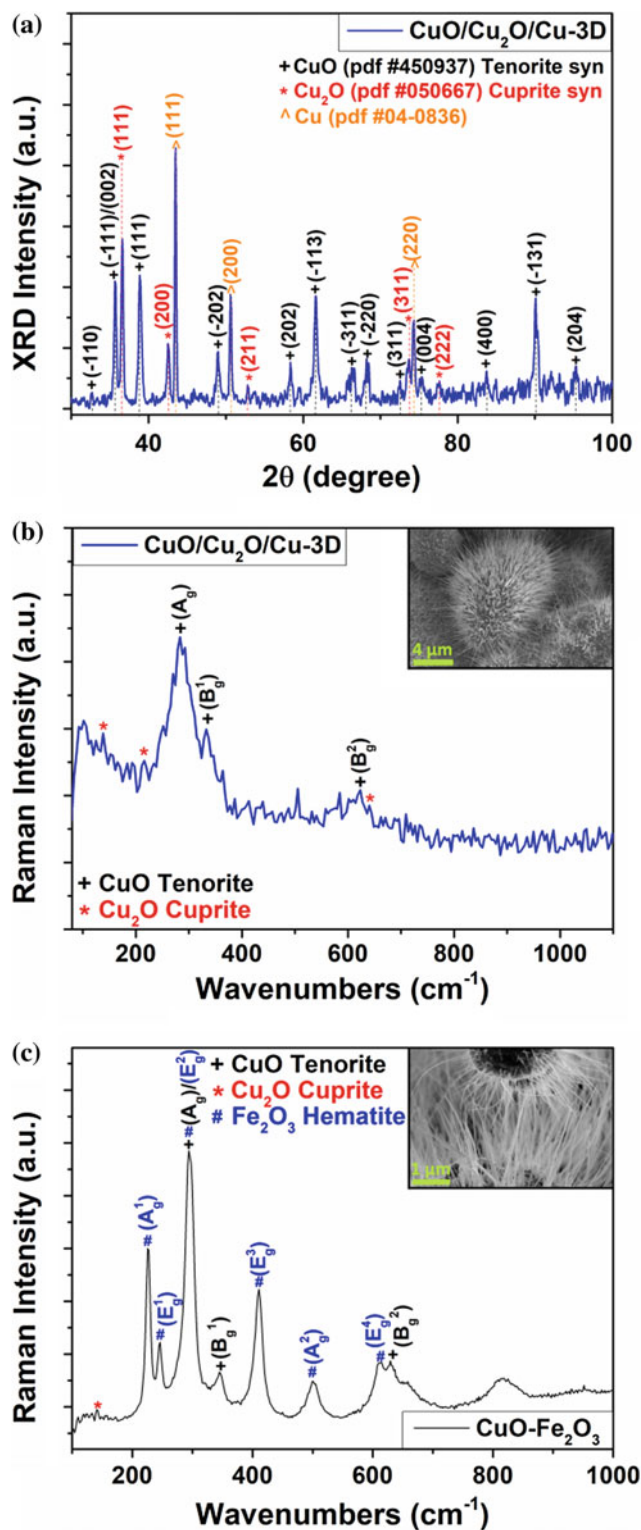


Fig. 1 a XRD patterns of the 3D printed nanowire CuO/Cu₂O/Cu heterojunction net after thermal annealing at 425°C for 4 h in air for CuO 3D-T sample set; b Raman spectra for CuO 3D-T sample set from (a), in insertion is SEM for CuO 3D-T; c Raman spectrum of the 3D printed nanoflakes—nanowire covered $\text{Fe}_2\text{O}_3/\text{Fe}$ –CuO/Cu₂O/Cu microparticles (MPs) heterojunction net after TA at 425°C for 2 h in air

In Fig. 1b is shown micro-Raman for CuO 3D annealed TA at 425 °C for 4 h which confirms Cu₂O and CuO in the printed samples after annealing, where intense modes at 283, 332 and 610 cm⁻¹ are due to CuO (Tenorite) and weaker peaks at 129, 215 and 627 cm⁻¹ are due to Cu₂O (Cuprite). In insertion you can see SEM for CuO 3D samples covered with nanowires on top of CuO/Cu₂O/Cu microparticles (MPs).

In Fig. 1c is shown micro-Raman for CuO–Fe₂O₃ samples TA at 425 °C for 4 h, where modes of Cu₂O, CuO and Fe₂O₃ phases in MPs are observed, namely modes A_g (297 cm⁻¹), B_g¹ (345 cm⁻¹) and B_g² (633 cm⁻¹) corresponds to CuO (Tenorite), mode (143 cm⁻¹) corresponds to Cu₂O as well as A_g¹ (227 cm⁻¹), E_g¹ (246 cm⁻¹), E_g² (297 cm⁻¹), E_g³ (408 cm⁻¹), A_g² (498 cm⁻¹) and E_g⁴ (612 cm⁻¹) which are due to α-Fe₂O₃ (Hematite). In the insertion of Fig. 1c, SEM images can be seen for CuO–Fe₂O₃ nanowires—nanoflakes, which are covering the Cu and Fe MPs.

The gas sensing results are presented in Fig. 2.

Figure 2a shows the gas response for ethanol and 2-propanol on CuO 3D samples. A higher selectivity for 2-propanol can be observed at the operating temperature

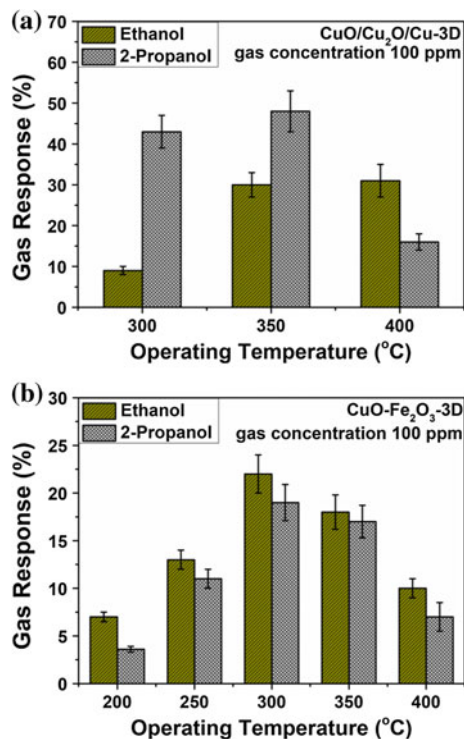


Fig. 2 Gas response to 100 ppm of ethanol and 2-propanol vapors for the 3D-printed sensor on: **a** nanowire CuO/Cu₂O/Cu heterojunction net at OPT of 300, 350 and 400 °C for sensor on CuO 3D; **b** nanoflake-nanowire Fe₂O₃–CuO/Cu₂O/Cu microparticles (MPs) with diameters of 15–25 μm heterojunction net at OPT of 200 °C up to 400 °C for sample set CuO–Fe₂O₃ 3D

(OPT) of 300 °C, whereas ethanol only invokes a low change in resistance. At 350 °C the gas response for 2-propanol slightly increases, while the increase in gas response for the ethanol is a lot higher. When the OPT is set to 400 °C, the gas response for ethanol does not change, while the response for 2-propanol strongly decreases. This shows, that the selectivity towards either VOC can be switched by increasing or decreasing the OPT for 3D printed sensor.

A reason for this behavior might be the desorption of more volatile 2-propanol at higher temperatures, while the less volatile ethanol can still attach onto the nanowires of CuO. Details on the proposed gas sensing mechanism is given in previous works [14, 15].

For the CuO–Fe₂O₃ 3D samples, no such trend can be observed. The selectivity towards either component is not very pronounced and the gas response is generally lower, than for the Cu 3D samples. However, a constant increase of the gas response is found to an OPT of 300 °C. After that, it constantly decreases. Around 300 °C seems to be the optimal temperature range for the detection of VOC for the Fe₂O₃/Fe–CuO/Cu₂O/Cu samples.

Figure 3a shows the dynamic gas response of the optimal OPT for the CuO–Fe₂O₃ 3D samples. The response to the inlet of the gas is immediate, as well as the response to the

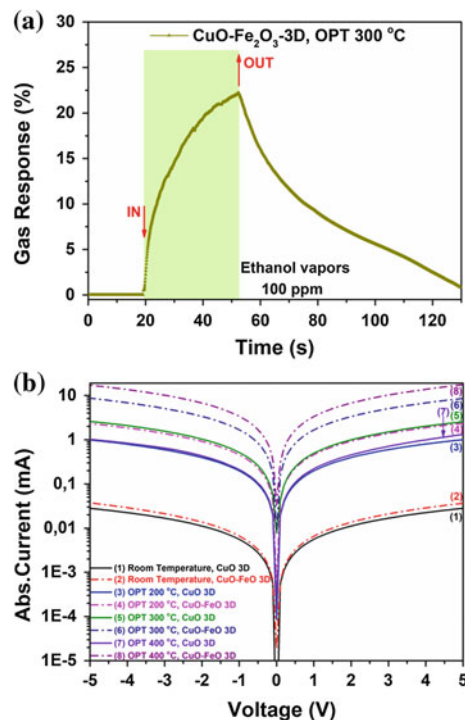


Fig. 3 **a** Dynamic response to 100 ppm of ethanol vapors 3D-T printed nanoflakes—nanowire covered Fe₂O₃/Fe–CuO/Cu₂O/Cu MPs heterojunction net (sample set 3D). **b** Current-voltage characteristics of Fe₂O₃/Fe–CuO/Cu₂O/Cu and CuO 3D sensor at different operating temperature

gas reduction. As can be expected the time constants for both reactions are different, shown by the sharper increase upon gas inlet and the slow decrease on the gas outlet. This is related to the ad- and desorption mechanism, respectively, indicating that the desorption of gas is slower than the adsorption.

In Fig. 3b the I-V-curves with logarithmic display are shown for all samples tested for their gas response with their respective OPT. For the CuO 3D samples, a strong increase in the conductivity can be observed, when the temperature is raised from RT to 200 °C. Another increase can be observed, when the temperature is raised to 300 °C, however a lower conductivity is observed, when the temperature is at 400 °C. This means, that for the nanowire net, the intrinsic conductivity is reached at 300 °C, with no further increase in charge carrier concentration upon temperature increase.

When no higher charge carrier concentration can be reached, the classic mechanism for the temperature dependence in conducting materials is dominant which include scattering of electrons on the vibrating lattice (phonons). With the maximum conductivity at an OPT of 300 °C, it seems obvious that the highest gas response at the same temperature is related to the conductivity. The base conductivity gets lowered by the adsorption of the gas molecules, thus increasing this conductivity results in a higher change in resistance. The same mechanism is not as easily applicable to the CuO-Fe₂O₃ 3D sample set, as its conductivity steadily increases with increasing temperature, indicating that the iron oxide is not in its intrinsic state at 400 °C. The maximum of the sensitivity at 300 °C with respect to the proposed mechanism for the CuO 3D samples indicates that the absorption of gas is mainly governed by the CuO/Cu₂O/Cu heterojunctions and not by the iron oxide. With higher temperatures, the iron oxide shortcuts the copper oxide, leading to conductive pathways not afflicted by the adsorbed gas species.

4 Conclusions

The rapid 3D-printing of CuO/Cu₂O/Cu microparticles (MPs), which possess diameters of 15–25 μm on the sensors substrate surface is successfully reported for the first time. 3D-printed Cu and Cu-Fe MPs-based stripes with high shape fidelity formed non-planar heterojunctions after thermal treatment at 425 °C in air and were fully covered with dense 20 nm thick nanowire or nanoflakes net. The morphological, chemical and structural investigations were performed in detail, showing the high crystallinity of the NWs and 3D-printed CuO/Cu₂O/Cu heterojunctions lines, as

well as the growth of CuO NWs on the surface of microparticles MPs. The gas response can be mainly related to the ability to absorb VOC onto the surface and the general conductivity of the semiconducting parts. When the adsorption is low, an increase in the conductivity can shortcut the gas response on those parts, where the VOCs are adsorbed.

Acknowledgements This work was financially supported by the German Research Foundation (DFG) via the research unit FOR 2093 “Memristive devices for neuronal systems” through project A2. Additional funding was provided under the project “Hot End” (grant number: 16KN021247), by the Federal ministry for Economic Affairs and Energy. Moreover, this research was partly supported by the project Institutional inst-15.817.02.29A funded by the Government of the Republic of Moldova and by the Technical University of Moldova. Dr. Oleg Lupan acknowledges the Alexander von Humboldt Foundation for the research fellowship for experienced researchers 3-3MOL/1148833 STP at the Institute for Materials Science, Kiel University, Germany. The authors would like to thank J. Bahr for the technical assistance and Prof. Tiginyanu for fruitful scientific discussion. Conflict of Interest The authors declare no competing interests.

References

- Xu, Y., Wu, X., Guo, X., Kong, B., Zhang, M., Qian, X., Mi, S., Sun, W.: *Sensors* **17** (Basel, Switzerland) (2017)
- MacDonald, E., Wicker, R.: *Science* **353** (New York, N.Y.) (2016)
- Zhu, W., O'Brien, C., O'Brien, J.R., Zhang, L.G.: *Nanomedicine* **9**, 859 (London, England) (2014)
- Sultan, S., Siqueira, G., Zimmermann, T., Mathew, A.P.: *Curr. Opin. Biomed. Eng.* **2**, 29 (2017)
- Campbell, T.A., Ivanova, O.S.: *Nano Today* **8**, 119 (2013)
- Gowers, S.A.N., Curto, V.F., Seneci, C.A., Wang, C., Anastasova, S., Vadgama, P., Yang, G.-Z., Boutelle, M.G.: *Anal. Chem.* **87**, 7763 (2015)
- Roda, A., Guardigli, M., Calabria, D., Calabretta, M.M., Cevenini, L., Michelini, E.: *The Anal.* **139**, 6494 (2014)
- Muth, J.T., Vogt, D.M., Truby, R.L., Mengüç, Y., Kolesky, D.B., Wood, R.J., Lewis, J.A.: *Adv. Mater.* **26**, 6307 (Deerfield Beach, Fla.) (2014)
- Wu, S.-Y., Yang, C., Hsu, W., Lin, L.: *Microsyst Nanoeng* **1**, 609 (2015)
- Lewis, J.A., Smay, J.E., Stuecker, J., Cesarano, J.: *J Am. Ceram. Soc.* **89**, 3599 (2006)
- Lewis, J.A.: *Adv. Funct. Mater.* **16**, 2193 (2006)
- Skylar-Scott, M.A., Gunasekaran, S., Lewis, J.A.: *Proc. Natl. Acad. Sci. U.S.A.* **113**, 6137 (2016)
- Lupan, O., Postica, V., Wolff, N., Polonskyi, O., Duppel, V., Kaidas, V., Lazari, E., Ababii, N., Faupel, F., Kienle, L., Adelung, R.: *Small* **13**, 1602868 (Weinheim an der Bergstrasse, Germany) (2017)
- Lupan, O., Postica, V., Cretu, V., Wolff, N., Duppel, V., Kienle, L., Adelung, R.: *Phys. Status Solidi RRL* **10**, 260 (2016)
- Lupan, O., Cretu, V., Postica, V., Ababii, N., Polonskyi, O., Kaidas, V., Schütt, F., Mishra, Y.K., Monaico, E., Tiginyanu, I., Sontea, V., Strunskus, T., Faupel, F., Adelung, R.: *Sens. Actuators, B* **224**, 434 (2016)



Broad-Band Spectroscopy of Nanoconfined Water Molecules

M. A. Belyanchikov, M. Savinov, Z. V. Bedran, P. Bednyakov, P. Proschek, J. Prokleska, V. I. Torgashev, E. S. Zhukova, S. S. Zhukov, L. S. Kadyrov, V. Thomas, A. Dudka, A. Zhugayevych, V. B. Anzin, R. K. Kremer, J. K. H. Fischer, P. Lunkenheimer, A. Loidl, E. Uykur, M. Dressel, and B. Gorshunov

Abstract

We have performed broad-band spectroscopic investigations of vibrational and relaxational excitations of water molecules confined to nanocages within artificial beryl

and mineral cordierite crystals. Signatures of quantum critical phenomena within the H₂O molecular network are registered in beryl. In cordierite, a density functional analysis is applied to reconstruct the potential energy landscape experienced by H₂O molecules, revealing a pronounced anisotropy with a potential well of about 10 meV for the molecular dipole moment aligned along the *b*-axis. This anisotropy leads to a strongly temperature dependent and anisotropic relaxational response of the dipoles at radiofrequencies with the activation energies corresponding to the barriers of the rotational potential. At $T \approx 3$ K, we identify signatures of a transition into a glassy state composed by clusters of H₂O dipoles. Rich set of anisotropic and temperature-dependent excitations are observed in the terahertz frequency range which we associate with rotational/translational vibrations.

M. A. Belyanchikov · Z. V. Bedran · E. S. Zhukova · S. S. Zhukov · L. S. Kadyrov · V. B. Anzin · B. Gorshunov (✉)
Moscow Institute of Physics and Technology, 9 Institutskiy per,
141700 Dolgoprudny, Moscow Region, Russia
e-mail: bpgorshunov@gmail.com

M. Savinov · P. Bednyakov
Institute of Physics, Czech Academy of Sciences, 18221 Praha 8,
Czech Republic

P. Proschek · J. Prokleska
Department of Condensed Matter Physics, Faculty of Mathematics
and Physics, Charles University, Prague 2, 12116, Czech Republic

V. I. Torgashev
Faculty of Physics, Southern Federal University, 344090
Rostov-on-Don, Russia

V. Thomas
Institute of Geology and Mineralogy, RAS, 630090 Novosibirsk,
Russia

Novosibirsk State University, 630090 Novosibirsk, Russia

A. Dudka
Shubnikov Institute of Crystallography, “Crystallography and
Photonics”, RAS, 119333 Moscow, Russia

A. Zhugayevych
Solkovo Institute of Science and Technology, 143026 Moscow,
Russia

V. B. Anzin
Prokhorov General Physics Institute, RAS, 119991 Moscow,
Russia

R. K. Kremer
Max-Planck-Institut für Festkörperforschung, 70569 Stuttgart,
Germany

J. K. H. Fischer · P. Lunkenheimer · A. Loidl
Experimental Physics V, University of Augsburg, 86135
Augsburg, Germany

E. Uykur · M. Dressel
Physikalisches Institut, Universität Stuttgart, 70569 Stuttgart,
Germany

Keywords

Nanoconfined water · Spectroscopy · Quantum criticality · Ferroelectricity

1 Introduction

A cutting edge of recent condensed-matter science is the study of phenomena occurring on the nanoscale, where qualitatively new properties can arise not known from the regular macroscopic bulk state of matter. Understanding the nature of the emerging new phases and their relations to the physical, chemical, geometrical, and morphological characteristics of the environment is of great fundamental and technological interest, but is presently still at its infancy. In the studies, special attention is paid to water due to its widespread prevalence and omnipresence on Earth and its critical importance for biological systems and organisms. Although the isolated H₂O molecule seems to be rather simple, bulk water remains one of the least understood liquids. Under the conditions of nanoconfinement, it acquires

an even greater variety of diverse and intriguing properties. Understanding such properties is important for geology, biology, mineralogy, ionic liquids, nanosciences and applications.

An ideal playground for the studies of confined water is provided by hydrated dielectric crystals whose ionic structure contains nanosized cavities with just a single water molecule. Among those systems, especially attractive are beryl $\text{Be}_3\text{Al}_2\text{Si}_6\text{O}_{18}$ and cordierite $(\text{Mg}, \text{Fe})_2\text{Al}_4\text{Si}_5\text{O}_{18}$. Both include channels elongated along the c -axis that contain voids of 5.1 Å diameter, hosting single H_2O quasi-free molecule [1, 2]. The caged H_2O molecules are at a distance of approximately 5–10 Å and are thus free of H-bonds but coupled by electric dipole-dipole forces (the dipole moment of the water molecule is $p = 1.85$ Debye). In hexagonal beryl, water molecules experience a 6-well potential landscape with an amplitude of ≈ 1 meV. In orthorhombic cordierite the potential is fourfold and asymmetric with the deeper wells (≈ 10 meV) for the water dipole moment oriented along the b -axis. In this work we present the first experimental results demonstrating signatures of quantum critical phenomena within the H_2O molecular network within the crystalline matrix of beryl. First detailed measurements of broad-band dielectric spectra of cordierite reveal signatures of a transition into glassy state among clusters of H_2O dipoles. The results are obtained by applying radiofrequency and terahertz spectroscopic techniques supplemented by specific heat measurements and DFT analysis.

2 Experimental Details

All studied crystals were carefully analyzed by X-ray scattering and cut into slices needed for the polarization-dependent measurements. The results are obtained on artificial beryl [3] and mineral cordierite from India (the detailed location is unknown). The spectra of complex dielectric permittivity $\varepsilon^*(\nu) = \varepsilon'(\nu) + i\varepsilon''(\nu)$ were determined at radio and micro ($\nu = 1$ Hz–1.3 GHz) as well as terahertz ($\nu = 0.3$ –3 THz) frequencies in a broad temperature interval $T = 0.3$ –300 K and for three principle polarization directions $E||a$, $E||b$ and $E||c$. At radiofrequencies, we used a Novocontrol Alpha AN High Performance Frequency Analyzer, an Andeen-Hagerling 2500A capacitance bridge and a coaxial reflectometric technique employing an impedance analyzer (Keysight 4991B). For terahertz measurements, a commercial time-domain TeraView 3000 spectrometer was used. The dielectric experiments were complemented by measurements of the heat capacity in the relaxation method employing a PPMS system (Quantum Design). In all experiments, measurements on dehydrated samples allowed us to extract the characteristics determined exclusively by a network of water molecules.

3 Results and Discussion

In Ref. [3], incipient ferroelectricity was reported in a system of water molecules in beryl. It was shown that the ferroelectric phase transition was suppressed by quantum effects (tunneling of the dipole moments within the six-well crystalline potential [5, 6]) that emerge below 10–20 K. Here, we demonstrate that at these low temperatures the properties of the water subsystem reveal signatures of quantum critical behavior. The transition from the classical paraelectric regime to the state where quantum effects dominate is documented by the temperature behavior of the inverse dielectric permittivity, $(\varepsilon')^{-1}$, the parameter that is linked to the state of electrical polarization of the material. In particular, while cooling down below a certain classical-to-quantum regime crossover temperature, the Curie-Weiss behavior $(\varepsilon')^{-1} \sim T$ changes into a different form, $(\varepsilon')^{-1} \sim T^\gamma$, where the critical exponent γ approaches a value of $\gamma = 2$ or $\gamma = 3$ for multi-axial or uniaxial dipoles orientations, respectively [7–9]. Another dielectric indication of the closeness of the system to the quantum-critical point is provided by the existence of a shallow minimum in the temperature dependence of $(\varepsilon')^{-1}$ at the lowest temperatures. This minimum is considered to be caused by the coupling of the critical optical soft modes (lattice vibrations that drive the displacive ferroelectric transitions) to acoustical phonons. A similar minimum was observed, e.g., in the prototypical incipient ferroelectric SrTiO_3 , which is also close to quantum criticality at low temperatures [10]. According to Fig. 1, the observed temperature evolution of the low-frequency inverse permittivity $(\varepsilon')^{-1}$ in hydrous beryl exhibits these two typical signatures of quantum critical behavior in the form of its quadratic (not cubic—see lower inset in Fig. 1) variation with temperature over the 3–12 K interval and a shallow minimum in the $(\varepsilon')^{-1}(T)$ dependence below 3 K.

We thoroughly measured the dielectric response of nanoconfined water molecules in mineral cordierite in order to check for the possibility of a macroscopic ferroelectric phase transition that was not observed in beryl. According to our DFT analysis, the localizing potential is strongly asymmetric in this crystal and the H_2O molecules tend to align their dipole moment along the b -axis. From Fig. 2 it is seen that in the polarization $E||b$ the low-frequency permittivity is fully determined by single-particle excitations observed at terahertz frequencies, as discussed below. In the $E||a$ case, there is a pronounced peak in the $\varepsilon'(T)$ behavior that is caused by a strong temperature dependence of a broad relaxational excitation at radiofrequencies, as demonstrated in Fig. 3.

In Fig. 4 we present the peak frequency of this relaxation as a function of temperature. Though the data shown in Figs. 2, 3 and 4 resemble the dependences typical for relaxor

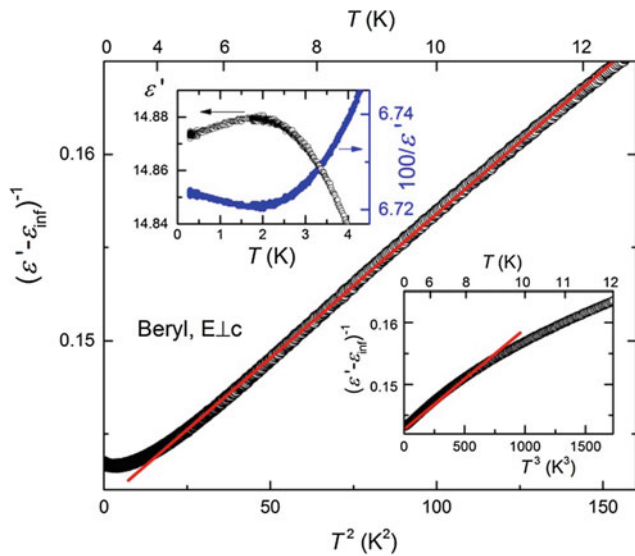


Fig. 1 Temperature dependence of the low-frequency (1 kHz) inverse dielectric permittivity $(\epsilon' - \epsilon_{\text{inf}})^{-1}$ plotted versus temperature squared, of a hydrous beryl crystal measured with $E_{\perp c}$ polarization (dots). The red solid line demonstrates that the dependence is quadratic in temperature in the range 4–12 K and not cubic, as seen in the lower inset. $\epsilon_{\text{inf}} = 7.9$ is the high-frequency contribution to the permittivity from the lattice vibrations and interband transitions [4]. The upper inset shows the temperature dependence of dielectric permittivity and the inverse dielectric permittivity of nanoconfined water in beryl measured with polarization $E_{\perp c}$. At around $T = 2$ K the dependences exhibit a shallow maximum and corresponding minimum, respectively

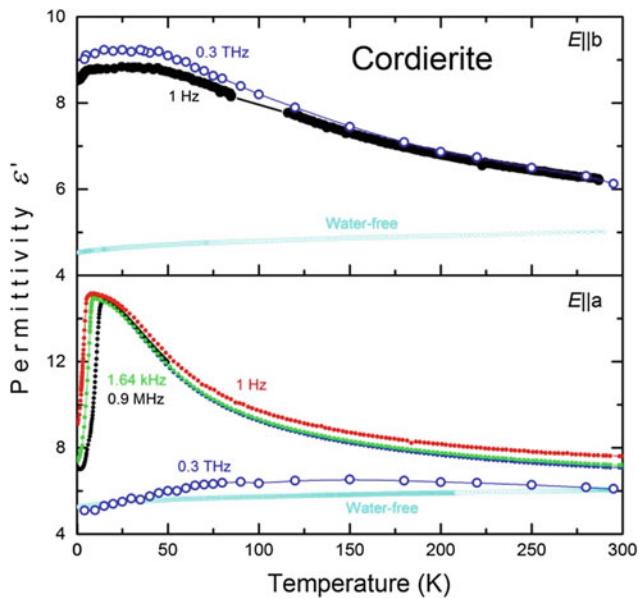


Fig. 2 Temperature dependences of real dielectric permittivity of nanoconfined water in mineral cordierite crystal measured at various frequencies for polarizations $E||b$ (upper panel) and $E||a$ (lower panel). WF denotes the data obtained on water-free (dehydrated) crystal

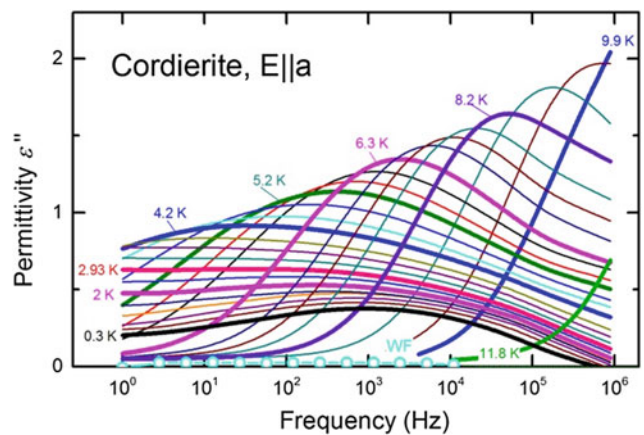


Fig. 3 Temperature-dependent relaxation in the radio-frequency spectra of nanoconfined water molecules in cordierite measured at various temperatures for polarization $E||a$. WF (cyan symbols) denotes the spectrum measured on water-free (dehydrated) crystal

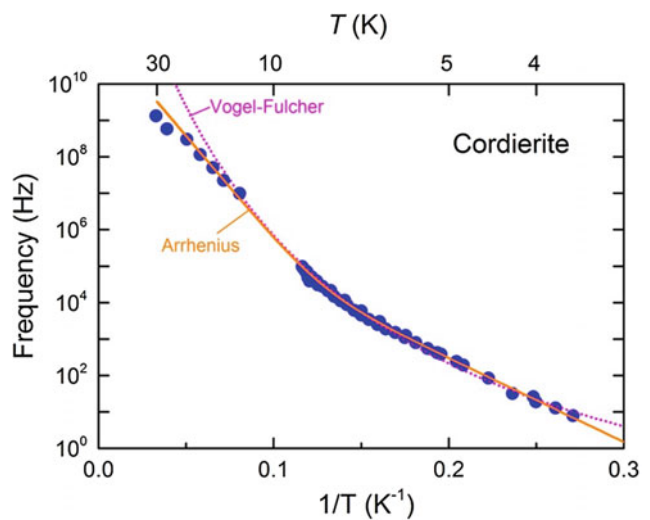


Fig. 4 Temperature dependence of the peak frequency of the relaxational excitation observed in the radio-frequency spectra of hydrous cordierite crystal, see Fig. 3. Solid line describes the data with the Arrhenius expression $A \exp(-E_1/k_B T) + B \exp(-E_2/k_B T)$ (A and B are constants) with two activation energies of 11.2 meV at $T \approx 10$ –30 K and 4.6 meV at $T \approx 4$ –7 K. Dotted line corresponds to the Vogel-Fulcher expression used to describe the dielectric response of relaxor ferroelectrics [11], $f_R = f_0 \exp[-U/kg(T - T_{VF})]$ where U is the activation energy, T_{VF} is the characteristic temperature and f_0 is the attempt frequency

ferroelectrics [10] (see also caption for Fig. 4), we exclude such scenario here for the following reasons: (i) the Vogel-Fulcher fit to the data (Fig. 4) leads to a *negative* divergence temperature $T_{VF} = -10 \pm 1$ K, that is of no physical meaning and (ii) the obtained Vogel-Fulcher attempt frequency $f_0 \approx 10^{16}$ Hz is unreasonably high—one

expects it to be of the order of phonon frequencies, i.e., 10^{12} – 10^{13} Hz. Fitting the temperature dependence of the peak frequency of the relaxational band at $3.5 \text{ K} < T < 30 \text{ K}$ with the Arrhenius expression $A \exp(-E_1/k_B T) + B \exp(-E_2/k_B T)$ (A and B are constants, k_B is the Boltzmann constant) results in the activation energies $E_1 = 11.2 \text{ meV}$ for $3.5 \text{ K} < T < 30 \text{ K}$ and $E_2 = 4.6 \text{ meV}$ for $4 \text{ K} < T < 7 \text{ K}$. We associate these energies with the potential barriers experienced by nanoconfined water molecules.

At lower temperatures, $T < 3 \text{ K}$, we observe a broad relaxation that *hardens* upon cooling (Fig. 3). We connect this behavior to smeared-out polar phase transition into a disordered low-temperature state among the 3D dipolar complexes of H_2O molecules that are coupled along the three crystallographic axes. This transition is also confirmed by an anomaly in the temperature dependence of the specific heat of the water subsystem detected at close temperature of $T \approx 6 \text{ K}$.

Figure 5 displays the terahertz spectra of the optical conductivity of water subsystem in cordierite. The response is strongly anisotropic. For the $E||a$ polarization it is in qualitative agreement with the predictions of the mean-field model described in Nakajima and Naya [12]: during cooling, the spectral weight of hindered rotational modes is transferred to librational oscillations of the dipole moments. The fine structure seen in the terahertz spectra at the lowest temperatures can be connected to transitions between the

tunnel-split energy levels caused by rotational tunneling of the H_2O molecule within the potential.

For the polarization $E||b$ we observe two terahertz excitations that significantly soften while cooling down. We associate them with translational vibrations of H_2O molecules located in the wells of the localizing potential. The softening of these modes should be connected with strong anharmonicity of the localizing potential.

4 Conclusions

Broad-band (radio-frequency up to terahertz) dielectric studies are performed of a network of interacting water molecules each confined to nanocage within the crystal lattice of hydrous beryl and cordierite. In hexagonal beryl, we identify signatures of quantum critical phenomena within the H_2O molecular network. In orthorhombic cordierite, radio-frequency relaxation is observed for the $E||a$ polarization that hardens at low temperatures. This behavior indicates a transition to a glass state within water molecular clusters. Anisotropic sets of excitations are detected at terahertz frequencies, which we assign to complex translational and librational vibrations of confined water molecules.

Acknowledgements We thank G. Untereiner for careful crystal preparation. The study was funded by RFBR (projects 18-32-20186 and 18-32-00286), by RF Ministry of Science and Higher Education (State assignment FSRC «Crystallography and Photonics» and Program 5-100), Deutsche Forschungsgemeinschaft (DR228/61-1) and by the Stuttgart/Ulm Research Center for Integrated Quantum Science and Technology (IQST). E.U. acknowledges the support of the European Social Fund and of the Ministry of Science Research and the Arts of Baden-Württemberg. M.S. and SK acknowledge Czech Science Foundation (Project No. 15-08389S) and MŠMT (Project No. SOLID21—CZ.02.1.01/0.0/0.0/16_019/0000760).

Conflict of Interest The authors declare that they have no conflict of interest.

References

1. Gibbs, G.G., Breck, D.W., Meagher, E.P.: Structural refinement of hydrous and anhydrous synthetic beryl, $\text{Al}_2(\text{Be}_3\text{Si}_6)\text{O}_{18}$ and emerald, $\text{A}_{11.9}\text{Cr}_{0.1}(\text{Be}_3\text{Si}_6)\text{O}_{18}$. *Lithos* **1**, 275–285 (1968)
2. Gibbs, G.V.: The polymorphism of cordierite I: the crystal structure of low cordierite. *Am. Miner.* **51**, 1068–1087 (1966)
3. Thomas, V.G., Klyakhin, V.A.: The specific features of beryl doping by chromium under hydrothermal conditions. In: Sobolev, N.V. (ed.) *Mineral Forming in Endogenic Processes*, pp. 60–67. Nauka, Novosibirsk (1987) (in Russian)
4. Gorshunov, B.P., Torgashev, V.I., Zhukova, E.S., et al.: Incipient ferroelectricity of water molecules confined to nano-channels of beryl. *Nat. Commun.* **7**, 12842 (2016)

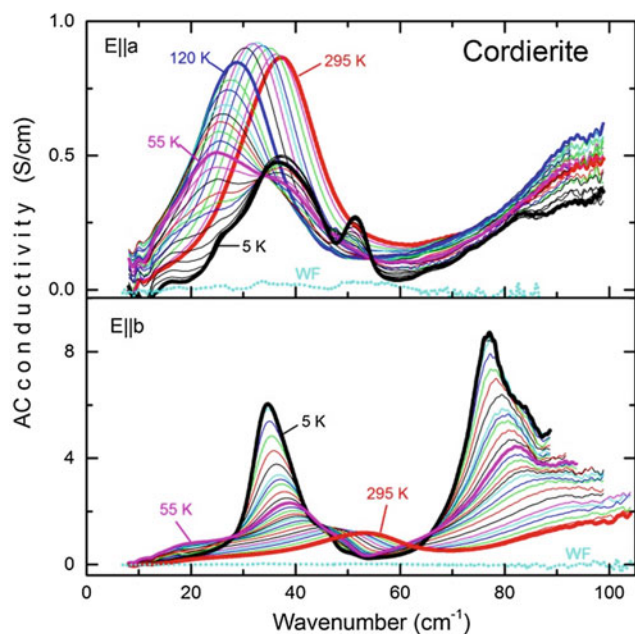


Fig. 5 Terahertz spectra of optical conductivity of nanoconfined water molecules in cordierite crystal measured at different temperatures for polarizations $E||a$ (upper panel) and $E||b$ (lower panel). WF denotes spectra obtained for water-free (dehydrated) crystals

5. Gorshunov, B.P., Zhukova, E.S., Torgashev, V.I., et al.: Quantum behavior of water molecules confined to nanocavities in gemstones. *J. Phys. Chem. Lett.* **4**, 2015–2020 (2013)
6. Kolesnikov, A.I., Reiter, G.F., Choudhury, N., et al.: Quantum tunneling of water in beryl: a new state of the water molecule. *Phys. Rev. Lett.* **116**, 167802 (2016)
7. Khmel'nitskii, D.E., Shneerson, V.L.: Low-temperature displacement-type phase transition in crystals. *Sov. Phys.: Solid State* **13**, 687 (1971)
8. Khmel'nitskii, D.E., Shneerson, V.L.: Phase transitions of the displacement type in crystals at very low temperatures. *Sov. Phys. JETP* **37**, 164 (1973)
9. Rowley, S.E., Spalek, L.J., Smith, R.P., et al.: Ferroelectric quantum criticality. *Nat. Phys.* **10**, 367 (2014)
10. Viana, R., Lunkenheimer, P., Hemberger, J., et al.: Dielectric spectroscopy in SrTiO₃. *Phys. Rev. B* **50**, 601–604 (1994)
11. Cowley, R.A., Gvasaliya, S.N., Lushnikov, S.G., et al.: Relaxing with relaxors: a review of relaxor ferroelectrics. *Adv. Phys.* **60**, 229–327 (2011)
12. Nakajima, Y., Naya, S.: Orientational phase transition and dynamic susceptibility of hindered-rotating dipolar system—a librator-rotator model. *J. Phys. Soc. Jpn.* **63**, 904–914 (1994)

Superposition States of the Two-Dimensional Magnetoexcitons with Dirac Cone Dispersion Law and Quantum Interference Effects in Optical Transitions

S. A. Moskalenko, I. V. Podlesny, I. A. Zubac, and B. V. Novikov

Abstract

The exchange electron-hole (e-h) Coulomb interaction changes essentially the properties of the two-dimensional (2D) magnetoexcitons, whose electron structure is mainly determined by the action of the Lorentz force and by the direct e-h Coulomb interaction. The exchange interaction leads to the mixing of the two bare magnetoexciton states with total angular momentum projections $F = \pm 1$. As a result instead of them two new superposition states one symmetric and another asymmetric appeared. The symmetric state acquired a Dirac cone dispersion law in the range of the small in-plane wave vectors $|\vec{k}_{\parallel}|l_0 < 1$, where l_0 is the magnetic length, with group velocity proportional to the magnetic field strength. The quantum transitions to this state from the ground state of the crystal under the influence of the light with both circular polarizations have the equal probabilities, being strongly dependent on the direction of the light propagation as regards the plane of the layer. The probability is maximal in the Faraday geometry and vanishes in the Voigt one. In difference on it, the asymmetric state is characterized by the usual dispersion law inherited from the bare magnetoexciton states, is dipole active in both circular polarization, but does not depend on the direction of the light propagation. In the case of light with linear polarizations the both symmetric and asymmetric states reveal the quantum interference effects.

Keywords

Magnetoexcitons • Strong magnetic field • Quantum interference • Dirac cone dispersion law • Superposition state

1 Introduction

The role of the exchange electron-hole (e-h) Coulomb interaction in the physics of the two-dimensional (2D) magnetoexcitons is investigated. Up till now only the direct Coulomb e-h interaction of the electrons and holes undergoing the Landau quantization (LQ) in a strong magnetic field perpendicular to the layer, in conditions when the cyclotron energies of the particles are greater than the binding energy of the 2D Wannier-Mott exciton was taken into account. In these conditions the Lorentz force plays a decisive role and determines the dipole structure of the 2D magnetoexciton. The dipole arm \vec{d} is perpendicular to the center-of-mass wave vector \vec{k}_{\parallel} and is proportional to its modulus $d = |\vec{k}_{\parallel}|l_0^2$, where l_0 is the magnetic length. The direct e-h Coulomb interaction determines the binding energy of the magnetoexciton, its ionization potential I_l and the dispersion law, demonstrating an example of a strong interdependence between the relative and the center of mass motions of the e-h pair in the frame of the magnetoexciton bound state [1–3].

The bare magnetoexciton states are characterized by the e-h angular momentum projections $F = s_z^e + j_z^h$ with the four possible values ± 1 and ± 2 . Two of them with $F = \pm 1$ are spin allowed in optical quantum transitions giving rise to the dipole-active, bright excitons in GaAs quantum wells (QWs), whereas the another two are spin forbidden, forming the dark states. The two dipole-active bright magnetoexciton states with $F = \pm 1$ under the influence of the direct Coulomb e-h interaction have the coincident energy levels. Their degeneracy is removed by the influence of the exchange e-h Coulomb interaction. The description in which way it takes place and of the new physical properties arising in these conditions are the main contents of the paper.

S. A. Moskalenko · I. V. Podlesny (✉) · I. A. Zubac
Institute of Applied Physics, Ministry of Education, Culture and Research, 5, Academiei Str., Chisinau, Moldova
e-mail: eboard_mjps@phys.asm.md

B. V. Novikov
Institute of Physics, St. Petersburg, Russia

2 Optical Quantum Transitions from the Ground State of the Crystal to the Superposition Magnetoexciton States. The Interference Effects

Bellow the optical absorption of the photon leading to the excitation of the magnetoexciton superposition states arising under the influence of the exchange electron-hole Coulomb interaction will be investigated. The initial states of the light-matter system are formed from the ground state of the crystal and from the one photon states with different circular and linear polarizations. The photon creation operators with different circular $\vec{\sigma}_{\vec{k}}^{\pm}$ and linear $\vec{s}_{\vec{k}}$ and $\vec{t}_{\vec{k}}$ polarizations look as [2–4]

$$\begin{aligned} (C_{\vec{k},\pm})^{\dagger} &= (C_{\vec{k},\vec{s}_{\vec{k}}} \pm iC_{\vec{k},\vec{t}_{\vec{k}}})^{\dagger} / \sqrt{2}, \\ \vec{\sigma}_{\vec{k}}^{\pm} &= (\vec{s}_{\vec{k}} \pm i\vec{t}_{\vec{k}}) / \sqrt{2}; \quad \vec{k} = \vec{a}_3 k_z + \vec{k}_{\parallel}; \quad \vec{k}_{\parallel} = \vec{a}_1 k_x + \vec{a}_2 k_y, \\ \vec{s}_{\vec{k}} &= \frac{\vec{a}_3 |\vec{k}_{\parallel}|}{|\vec{k}|} - \frac{\vec{k}_{\parallel} k_z}{|\vec{k}| |\vec{k}_{\parallel}|} = \vec{s}_{-\vec{k}}; \quad \vec{t}_{\vec{k}} = \frac{\vec{a}_1 k_y - \vec{a}_2 k_x}{|\vec{k}_{\parallel}|} = -\vec{t}_{-\vec{k}}, \quad (1) \\ (\vec{s}_{\vec{k}} \cdot \vec{k}) &= (\vec{t}_{\vec{k}} \cdot \vec{k}) = (\vec{\sigma}_{\vec{k}}^{\pm} \cdot \vec{k}) = (\vec{s}_{\vec{k}} \cdot \vec{t}_{\vec{k}}) = 0, \\ |\vec{s}_{\vec{k}}|^2 &= |\vec{t}_{\vec{k}}|^2 = |\vec{\sigma}_{\vec{k}}^{\pm}|^2 = 1; \quad k_x \pm ik_y = |\vec{k}_{\parallel}| e^{\pm i\varphi}. \end{aligned}$$

Side by side with the circular polarizations $\vec{\sigma}_{\vec{k}}^{\pm}$ for the light, it is reasonable to introduce the circular polarization $\vec{\sigma}_{\pm 1}$ for the magnetoexcitons in the way

$$\vec{\sigma}_{\pm 1} = (\vec{a}_1 \pm i\vec{a}_2) / \sqrt{2}. \quad (2)$$

Here the unit in-plane vectors \vec{a}_1 and \vec{a}_2 , as well as the perpendicular to the plane unit vector \vec{a}_3 were introduced. The four initial photon states are

$$\begin{aligned} |i_+\rangle &= (C_{\vec{k},+})^{\dagger} |0\rangle; \quad |i_-\rangle = (C_{\vec{k},-})^{\dagger} |0\rangle; \\ |i_s\rangle &= C_{\vec{k},\vec{s}_{\vec{k}}}^{\dagger} |0\rangle; \quad |i_t\rangle = C_{\vec{k},\vec{t}_{\vec{k}}}^{\dagger} |0\rangle, \end{aligned} \quad (3)$$

where $|0\rangle$ is the light-matter vacuum state. The initial states obey to the normalization and orthogonality conditions

$$\begin{aligned} \langle 0 | C_{\vec{k},\pm} (C_{\vec{k},\pm})^{\dagger} | 0 \rangle &= 1; \quad \langle 0 | C_{\vec{k},\pm} (C_{\vec{k},\mp})^{\dagger} | 0 \rangle = 0, \\ \langle 0 | C_{\vec{k},\vec{s}_{\vec{k}}} (C_{\vec{k},\vec{s}_{\vec{k}}})^{\dagger} | 0 \rangle &= 1 / \sqrt{2}; \quad \langle 0 | C_{\vec{k},\vec{s}_{\vec{k}}} (C_{\vec{k},\vec{t}_{\vec{k}}})^{\dagger} | 0 \rangle = \mp i / \sqrt{2}. \end{aligned} \quad (4)$$

The final states of the light-matter system in our case are the superpositions $|\psi_0^{\pm}(\vec{k}_{\parallel})\rangle$ of the 2D magnetoexciton states determined in the way

$$|\psi_0^{\pm}(\vec{k}_{\parallel})\rangle = C_1^{\pm} \left[\hat{\psi}_{ex}^{\dagger}(-1; \vec{k}_{\parallel}) \pm e^{-2i\varphi} \hat{\psi}_{ex}^{\dagger}(1; \vec{k}_{\parallel}) \right] |0\rangle. \quad (5)$$

They obey to the normalization and orthogonality conditions

$$\begin{aligned} \langle \psi_0^{\pm}(\vec{k}_{\parallel}) | \psi_0^{\pm}(\vec{k}_{\parallel}) \rangle &= 1; \quad \langle \psi_0^{\pm}(\vec{k}_{\parallel}) | \psi_0^{\mp}(\vec{k}_{\parallel}) \rangle = 0, \\ \langle 0 | \hat{\psi}_{ex}(\pm 1; \vec{k}_{\parallel}) \hat{\psi}_{ex}^{\dagger}(\pm 1; \vec{k}_{\parallel}) | 0 \rangle &= 1; \quad |C_1^{\pm}| = 1 / \sqrt{2}, \quad (6) \\ \langle 0 | \hat{\psi}_{ex}(\pm 1; \vec{k}_{\parallel}) \hat{\psi}_{ex}^{\dagger}(\mp 1; \vec{k}_{\parallel}) | 0 \rangle &= 0. \end{aligned}$$

It is necessary to underline that the single 2D magnetoexciton states introduced earlier [2, 3] in the form

$$|\psi_{ex}(\pm 1; \vec{k}_{\parallel})\rangle = \hat{\psi}_{ex}^{\dagger}(\pm 1; \vec{k}_{\parallel}) |0\rangle \quad (7)$$

are dipole-active, with different from zero probabilities of the quantum transitions from the ground state of the crystal. In spite of it, their superposition states (5) are subjected to the interference effects influencing essentially on their probabilities of the quantum transitions from the ground state of the crystal. It will be seen from the next calculations.

The Hamiltonian of the light-matter interaction describing the band-to-band quantum transitions with participation of the photons and 2D magnetoexcitons was derived earlier [2–4]. For our purpose only of the following its part is necessary

$$\begin{aligned} \hat{H}_{el-rad}^{abs}(\vec{k}) &= A_{\vec{k}} \left\{ \left[(C_{\vec{k},-})^{\dagger} (\vec{\sigma}_{\vec{k}}^- \cdot \vec{\sigma}_{-1}) + (C_{\vec{k},+})^{\dagger} (\vec{\sigma}_{\vec{k}}^+ \cdot \vec{\sigma}_{-1}) \right] \right. \\ &\times \hat{\psi}_{ex}(-1; \vec{k}_{\parallel}) + \left[(C_{\vec{k},-})^{\dagger} (\vec{\sigma}_{\vec{k}}^- \cdot \vec{\sigma}_1) + (C_{\vec{k},+})^{\dagger} (\vec{\sigma}_{\vec{k}}^+ \cdot \vec{\sigma}_1) \right] \\ &\times \hat{\psi}_{ex}(1; \vec{k}_{\parallel}) \left. \right\}; \quad A_{\vec{k}} = \left(-\frac{e}{m_0} \right) \sqrt{\frac{\hbar}{L_c l_0^2 \omega_{\vec{k}}}} e^{-\frac{|\vec{k}_{\parallel}|^2 l_0^2}{4}} P_{c-v}^*. \end{aligned} \quad (8)$$

The matrix elements describing the optical quantum transitions in the bare magnetoexciton states $\psi_{ex}(\pm 1; \vec{k}_{\parallel})$ are

$$\begin{aligned} \langle i_+ | \hat{H}_{el-rad}^{abs}(\vec{k}) | \psi_{ex}(\pm 1; \vec{k}_{\parallel}) \rangle &= A_{\vec{k}} (\vec{\sigma}_{\vec{k}}^+ \cdot \vec{\sigma}_{\pm 1}), \\ \langle i_- | \hat{H}_{el-rad}^{abs}(\vec{k}) | \psi_{ex}(\pm 1; \vec{k}_{\parallel}) \rangle &= A_{\vec{k}} (\vec{\sigma}_{\vec{k}}^- \cdot \vec{\sigma}_{\pm 1}), \\ \langle i_s | \hat{H}_{el-rad}^{abs}(\vec{k}) | \psi_{ex}(\pm 1; \vec{k}_{\parallel}) \rangle &= \frac{A_{\vec{k}}}{\sqrt{2}} [(\vec{\sigma}_{\vec{k}}^- \cdot \vec{\sigma}_{\pm 1}) + (\vec{\sigma}_{\vec{k}}^+ \cdot \vec{\sigma}_{\pm 1})], \\ \langle i_t | \hat{H}_{el-rad}^{abs}(\vec{k}) | \psi_{ex}(\pm 1; \vec{k}_{\parallel}) \rangle &= \frac{iA_{\vec{k}}}{\sqrt{2}} [(\vec{\sigma}_{\vec{k}}^- \cdot \vec{\sigma}_{\pm 1}) - (\vec{\sigma}_{\vec{k}}^+ \cdot \vec{\sigma}_{\pm 1})]. \end{aligned} \quad (9)$$

The matrix elements describing the optical quantum transitions in the superposition magnetoexciton states $|\psi_0^{\pm}(\vec{k}_{\parallel})\rangle$ are

$$\begin{aligned}
& \langle i_+ | \hat{H}_{\text{el-rad}}^{\text{abs}}(\vec{k}) | \psi_0^\pm(\vec{k}_\parallel) \rangle \\
&= A_{\vec{k}} C_1^\pm \left[\left(\vec{\sigma}_{\vec{k}}^+ \cdot \vec{\sigma}_{-1} \right) \pm e^{-2i\varphi} \left(\vec{\sigma}_{\vec{k}}^+ \cdot \vec{\sigma}_1 \right) \right], \\
& \langle i_- | \hat{H}_{\text{el-rad}}^{\text{abs}}(\vec{k}) | \psi_0^\pm(\vec{k}_\parallel) \rangle \\
&= A_{\vec{k}} C_1^\pm \left[\left(\vec{\sigma}_{\vec{k}}^- \cdot \vec{\sigma}_{-1} \right) \pm e^{-2i\varphi} \left(\vec{\sigma}_{\vec{k}}^- \cdot \vec{\sigma}_1 \right) \right], \\
& \langle i_s | \hat{H}_{\text{el-rad}}^{\text{abs}}(\vec{k}) | \psi_0^\pm(\vec{k}_\parallel) \rangle \\
&= \frac{A_{\vec{k}} C_1^\pm}{\sqrt{2}} \left\{ \left[\left(\vec{\sigma}_{\vec{k}}^- \cdot \vec{\sigma}_{-1} \right) + \left(\vec{\sigma}_{\vec{k}}^+ \cdot \vec{\sigma}_{-1} \right) \right] \right. \\
&\quad \left. \pm e^{-2i\varphi} \left[\left(\vec{\sigma}_{\vec{k}}^- \cdot \vec{\sigma}_1 \right) + \left(\vec{\sigma}_{\vec{k}}^+ \cdot \vec{\sigma}_1 \right) \right] \right\}, \\
& \langle i_t | \hat{H}_{\text{el-rad}}^{\text{abs}}(\vec{k}) | \psi_0^\pm(\vec{k}_\parallel) \rangle \\
&= \frac{A_{\vec{k}} C_1^\pm i}{\sqrt{2}} \left\{ \left[\left(\vec{\sigma}_{\vec{k}}^- \cdot \vec{\sigma}_{-1} \right) - \left(\vec{\sigma}_{\vec{k}}^+ \cdot \vec{\sigma}_{-1} \right) \right] \right. \\
&\quad \left. \pm e^{-2i\varphi} \left[\left(\vec{\sigma}_{\vec{k}}^- \cdot \vec{\sigma}_1 \right) - \left(\vec{\sigma}_{\vec{k}}^+ \cdot \vec{\sigma}_1 \right) \right] \right\}.
\end{aligned} \tag{10}$$

The scalar products between the circular polarization vectors $\vec{\sigma}_{\vec{k}}^\pm$ and $\vec{\sigma}_{\pm 1}$ give rise to the expressions

$$\begin{aligned}
& \left(\vec{\sigma}_{\vec{k}}^\pm \cdot \vec{\sigma}_1 \right) = -\frac{e^{i\varphi}}{2} \left(\frac{k_z}{|\vec{k}|} \mp 1 \right); \\
& \left(\vec{\sigma}_{\vec{k}}^\pm \cdot \vec{\sigma}_{-1} \right) = -\frac{e^{-i\varphi}}{2} \left(\frac{k_z}{|\vec{k}|} \pm 1 \right); \\
& \left(\vec{\sigma}_{\vec{k}}^- \cdot \vec{\sigma}_1 \right) + \left(\vec{\sigma}_{\vec{k}}^+ \cdot \vec{\sigma}_1 \right) = -\frac{k_z}{|\vec{k}|} e^{i\varphi}; \\
& \left(\vec{\sigma}_{\vec{k}}^- \cdot \vec{\sigma}_1 \right) - \left(\vec{\sigma}_{\vec{k}}^+ \cdot \vec{\sigma}_1 \right) = -e^{i\varphi}; \\
& \left(\vec{\sigma}_{\vec{k}}^- \cdot \vec{\sigma}_{-1} \right) + \left(\vec{\sigma}_{\vec{k}}^+ \cdot \vec{\sigma}_{-1} \right) = -\frac{k_z}{|\vec{k}|} e^{-i\varphi}; \\
& \left(\vec{\sigma}_{\vec{k}}^- \cdot \vec{\sigma}_{-1} \right) - \left(\vec{\sigma}_{\vec{k}}^+ \cdot \vec{\sigma}_{-1} \right) = e^{-i\varphi}.
\end{aligned} \tag{11}$$

Substituting the expressions (11) into the matrix elements (9) and (10) we will obtain

$$\begin{aligned}
& \langle i_+ | \hat{H}_{\text{el-rad}}^{\text{abs}}(\vec{k}) | \psi_{ex}(\pm 1; \vec{k}_\parallel) \rangle = -\frac{A_{\vec{k}} e^{\pm i\varphi}}{2} \left(\frac{k_z}{|\vec{k}|} \mp 1 \right), \\
& \langle i_- | \hat{H}_{\text{el-rad}}^{\text{abs}}(\vec{k}) | \psi_{ex}(\pm 1; \vec{k}_\parallel) \rangle = -\frac{A_{\vec{k}} e^{\pm i\varphi}}{2} \left(\frac{k_z}{|\vec{k}|} \pm 1 \right), \\
& \langle i_s | \hat{H}_{\text{el-rad}}^{\text{abs}}(\vec{k}) | \psi_{ex}(\pm 1; \vec{k}_\parallel) \rangle = -\frac{A_{\vec{k}}}{\sqrt{2}} e^{\pm i\varphi} \frac{k_z}{|\vec{k}|}, \\
& \langle i_t | \hat{H}_{\text{el-rad}}^{\text{abs}}(\vec{k}) | \psi_{ex}(\pm 1; \vec{k}_\parallel) \rangle = \mp \frac{i A_{\vec{k}}}{\sqrt{2}} e^{\pm i\varphi}. \\
& \langle i_+ | \hat{H}_{\text{el-rad}}^{\text{abs}}(\vec{k}) | \psi_0^\pm(\vec{k}_\parallel) \rangle \\
&= -\frac{A_{\vec{k}} C_1^\pm e^{-i\varphi}}{2} \left[\left(\frac{k_z}{|\vec{k}|} + 1 \right) \pm \left(\frac{k_z}{|\vec{k}|} - 1 \right) \right], \\
& \langle i_- | \hat{H}_{\text{el-rad}}^{\text{abs}}(\vec{k}) | \psi_0^\pm(\vec{k}_\parallel) \rangle \\
&= -\frac{A_{\vec{k}} C_1^\pm e^{-i\varphi}}{2} \left[\left(\frac{k_z}{|\vec{k}|} - 1 \right) \pm \left(\frac{k_z}{|\vec{k}|} + 1 \right) \right], \\
& \langle i_s | \hat{H}_{\text{el-rad}}^{\text{abs}}(\vec{k}) | \psi_0^\pm(\vec{k}_\parallel) \rangle \\
&= -\frac{A_{\vec{k}} C_1^\pm e^{-i\varphi}}{\sqrt{2}} \frac{k_z}{|\vec{k}|} (1 \pm 1), \\
& \langle i_t | \hat{H}_{\text{el-rad}}^{\text{abs}}(\vec{k}) | \psi_0^\pm(\vec{k}_\parallel) \rangle \\
&= \frac{i A_{\vec{k}} C_1^\pm e^{-i\varphi}}{\sqrt{2}} \frac{k_z}{|\vec{k}|} (1 \mp 1); |C_1^\pm| = \frac{1}{\sqrt{2}}.
\end{aligned} \tag{12}$$

They lead to the square moduli of the matrix elements (12).

$$\begin{aligned}
& \left| \langle i_+ | \hat{H}_{\text{el-rad}}^{\text{abs}}(\vec{k}) | \psi_{ex}(\pm 1; \vec{k}_{\parallel}) \rangle \right|^2 = |A_{\vec{k}}|^2 (k_z / |\vec{k}| \mp 1)^2 / 4, \\
& \left| \langle i_- | \hat{H}_{\text{el-rad}}^{\text{abs}}(\vec{k}) | \psi_{ex}(\pm 1; \vec{k}_{\parallel}) \rangle \right|^2 = |A_{\vec{k}}|^2 (k_z / |\vec{k}| \mp 1)^2 / 4, \\
& \left| \langle i_s | \hat{H}_{\text{el-rad}}^{\text{abs}}(\vec{k}) | \psi_{ex}(\pm 1; \vec{k}_{\parallel}) \rangle \right|^2 = |A_{\vec{k}}|^2 k_z^2 / (2|\vec{k}|^2), \\
& \left| \langle i_t | \hat{H}_{\text{el-rad}}^{\text{abs}}(\vec{k}) | \psi_{ex}(\pm 1; \vec{k}_{\parallel}) \rangle \right|^2 = |A_{\vec{k}}|^2 / 2, \\
& \left| \langle i_{\pm} | \hat{H}_{\text{el-rad}}^{\text{abs}}(\vec{k}) | \psi_0^+(\vec{k}_{\parallel}) \rangle \right|^2 = |A_{\vec{k}}|^2 k_z^2 / (2|\vec{k}|^2), \\
& \left| \langle i_{\pm} | \hat{H}_{\text{el-rad}}^{\text{abs}}(\vec{k}) | \psi_0^-(\vec{k}_{\parallel}) \rangle \right|^2 = |A_{\vec{k}}|^2 / 2, \\
& \left| \langle i_s | \hat{H}_{\text{el-rad}}^{\text{abs}}(\vec{k}) | \psi_0^+(\vec{k}_{\parallel}) \rangle \right|^2 = |A_{\vec{k}}|^2 k_z^2 / |\vec{k}|^2, \\
& \left| \langle i_s | \hat{H}_{\text{el-rad}}^{\text{abs}}(\vec{k}) | \psi_0^-(\vec{k}_{\parallel}) \rangle \right|^2 = 0, \\
& \left| \langle i_t | \hat{H}_{\text{el-rad}}^{\text{abs}}(\vec{k}) | \psi_0^+(\vec{k}_{\parallel}) \rangle \right|^2 = 0, \\
& \left| \langle i_t | \hat{H}_{\text{el-rad}}^{\text{abs}}(\vec{k}) | \psi_0^-(\vec{k}_{\parallel}) \rangle \right|^2 = |A_{\vec{k}}|^2.
\end{aligned} \tag{13}$$

They will determine the probabilities of the eight quantum transitions in the two final superposition states $|\psi_0^{\pm}(\vec{k}_{\parallel})\rangle$ under the absorption of the photon with four different polarizations. To this end the Fermi golden rule can be used. The total probabilities of the quantum transitions in each superposition state for two circular polarizations and for two linear polarizations obey the following sum rules:

$$\begin{aligned}
& \left| \langle i_+ | \hat{H}_{\text{el-rad}}^{\text{abs}}(\vec{k}) | \psi_0^+(\vec{k}_{\parallel}) \rangle \right|^2 + \left| \langle i_- | \hat{H}_{\text{el-rad}}^{\text{abs}}(\vec{k}) | \psi_0^+(\vec{k}_{\parallel}) \rangle \right|^2 \\
& = \left| \langle i_s | \hat{H}_{\text{el-rad}}^{\text{abs}}(\vec{k}) | \psi_0^+(\vec{k}_{\parallel}) \rangle \right|^2 + \left| \langle i_t | \hat{H}_{\text{el-rad}}^{\text{abs}}(\vec{k}) | \psi_0^+(\vec{k}_{\parallel}) \rangle \right|^2 \\
& = |A_{\vec{k}}|^2 k_z^2 / |\vec{k}|^2; \\
& \left| \langle i_+ | \hat{H}_{\text{el-rad}}^{\text{abs}}(\vec{k}) | \psi_0^-(\vec{k}_{\parallel}) \rangle \right|^2 + \left| \langle i_- | \hat{H}_{\text{el-rad}}^{\text{abs}}(\vec{k}) | \psi_0^-(\vec{k}_{\parallel}) \rangle \right|^2 \\
& = \left| \langle i_s | \hat{H}_{\text{el-rad}}^{\text{abs}}(\vec{k}) | \psi_0^-(\vec{k}_{\parallel}) \rangle \right|^2 + \left| \langle i_t | \hat{H}_{\text{el-rad}}^{\text{abs}}(\vec{k}) | \psi_0^-(\vec{k}_{\parallel}) \rangle \right|^2 = |A_{\vec{k}}|^2.
\end{aligned} \tag{14}$$

Looking at the Formulas (13) and (14) one can conclude that the superposition state $|\psi_0^+(\vec{k}_{\parallel})\rangle$ with the Dirac cone dispersion law can be excited only by the incident propagating light with different from zero perpendicular to the plane component $k_z \neq 0$ of its wave vector $\vec{k} = \vec{a}_3 k_z + \vec{k}_{\parallel}$. The probability of the quantum transition is maximal in Faraday geometry $\vec{k}_{\parallel} \parallel \vec{a}_3$ and vanishes in the Voigt geometry $\vec{k}_{\parallel} \perp \vec{a}_3$ with light propagating along the plane of the layer. The probabilities of the quantum transitions in the both circular polarizations $\vec{\sigma}_{\vec{k}}^{\pm}$ are equal. What concerns the light with linear polarizations $\vec{s}_{\vec{k}}$ and $\vec{t}_{\vec{k}}$ the selection rules are

completely different. Due to the quantum interference effects [5–7] the probability of the quantum transition in the linear polarization $\vec{s}_{\vec{k}}$ is enhanced in account of the quantum transition in the linear polarization $\vec{t}_{\vec{k}}$. As a result the former probability is doubled in comparison with the circular polarization case, whereas the latter probability equals to zero.

The selection rules of the quantum transitions in the superposition state $|\psi_0^-(\vec{k}_{\parallel})\rangle$ are much simple, because they do not depend on the direction of the propagating light wave vector \vec{k} . It takes place because the state $|\psi_0^-(\vec{k}_{\parallel})\rangle$ has an ordinary dispersion law common to the single bare magnetoexciton states $|\psi_{ex}(\pm 1; \vec{k}_{\parallel})\rangle$ and does not possess the Dirac cone dispersion law at all.

The probabilities of the quantum transitions in the superposition state $|\psi_0^-(\vec{k}_{\parallel})\rangle$ in both circular polarizations are equal as in the case of the superposition state $|\psi_0^+(\vec{k}_{\parallel})\rangle$. The quantum interference effects [5–7] take place also in the superposition state $|\psi_0^-(\vec{k}_{\parallel})\rangle$. Here the redistribution of the quantum transition probabilities also takes place but in the favor of the linear polarization $\vec{t}_{\vec{k}}$ in account of the probability of quantum transition in the linear polarization $\vec{s}_{\vec{k}}$. As in the case of superposition state $|\psi_0^+(\vec{k}_{\parallel})\rangle$ the probability of the allowed quantum transition in the linear polarization is doubled in comparison with the case of a given circular polarization. Due to the interference effects the quantum transition in the superposition state $|\psi_0^-(\vec{k}_{\parallel})\rangle$ in linear polarization $\vec{s}_{\vec{k}}$ happened to be forbidden, whereas the quantum transition in the superposition state $|\psi_0^+(\vec{k}_{\parallel})\rangle$ is forbidden in the linear polarization $\vec{t}_{\vec{k}}$.

3 Conclusions

The influence of the exchange electron-hole (e-h) Coulomb interaction leads to the formation of two symmetric and asymmetric superpositions consisting of two bare bright magnetoexciton states with total angular momentum projections $F = \pm 1$ and with electron structure determined only by the direct Coulomb e-h interaction. The symmetric superposition state acquires a Dirac cone dispersion law in the range of small in-plane wave vectors $|\vec{k}_{\parallel}| l_0 < 1$, where l_0

is the magnetic length, with group velocity proportional to the magnetic field strength. The quantum transition from the ground state of the crystal in the symmetric state have equal probabilities in both light circular polarizations, but essentially depend on the direction of the light propagation as regards the plane of the layer. They are maximal in the Faraday geometry and vanish in the Voigt one. In difference on it the asymmetric superposition state remains with the same dispersion law inherited from the bare magnetoexciton states, is characterized by the dipole-active quantum transitions in both light circular polarizations, which do not depend on the direction of the light propagation.

The both symmetric and asymmetric superposition states revealed the quantum interference effects [5–7] in the case of light with two linear polarizations. The polarizations have different parities as regards the inversion of the light wave vector \vec{k} . The symmetric (asymmetric) state is allowed in the case of linear polarization with positive (negative) parity and forbidden in the case of linear polarization with negative (positive) parity. The obtained optical results open the possibility to investigate the thermodynamic properties of the 2D Bose gas with Dirac cone dispersion law.

Conflict of Interest The authors declare that they have no conflict of interest.

References

1. Paquet, D., Rice, T.M., Ueda, K.: Two-dimensional electron-hole fluid in a strong perpendicular magnetic field: exciton Bose condensate or maximum density two-dimensional droplet. *Phys. Rev. B* **32**, 5208–5221 (1985). <https://doi.org/10.1103/PhysRevB.32.5208>
2. Moskalenko, S.A., Liberman, M.A., Podlesny, I.V.: Exciton-cyclotron resonance in two-dimensional structures in a strong perpendicular magnetic field and optical orientation conditions. *Phys. Rev. B* **79**, 125–425 (1–18) (2009). <https://doi.org/10.1103/physrevb.79.125425>
3. Moskalenko, S.A., Podlesny, I.V., Dumanov, E.V., Liberman, M. A.: Effects of Rashba spin-orbit coupling, Zeeman splitting and gyrotropy in two-dimensional cavity polaritons under the influence of the Landau quantization. *Eur. Phys. J. B* **88**, 218 (2015). <https://doi.org/10.1140/epjb/e2015-60335-7>
4. Moskalenko, S.A., Podlesny, I.V., Dumanov, E.V., Liberman, M. A., Novikov, B.V.: Dispersion laws of the two-dimensional cavity magnetoexciton-polaritons. *J. Nanophoton.* **10**(3), 036006 (2016). <https://doi.org/10.1117/1.JNP.10.036006>
5. Zhu, S.-Y., Scully, M.O.: Spectral line elimination and spontaneous emission cancellation via quantum interference. *Phys. Rev. Lett.* **76**, 388 (1996). <https://doi.org/10.1103/PhysRevLett.76.388>
6. Martinez, M.A.G., et al.: Quantum interference effects in spontaneous atomic emission: dependence of the resonance fluorescence spectrum on the phase of the driving field. *Phys. Rev. A* **55**, 4483 (1997). <https://doi.org/10.1103/PhysRevA.55.4483>
7. Ceban, V., Macovei, M.A.: Cavity quantum interferences with three-level atoms. *J. Opt. Soc. Am. B* **33**(5), 942–946 (2016). <https://doi.org/10.1364/JOSAB.33.000942>

Superconductivity and Weak Ferromagnetism in Inclination Bicrystal Interfaces of Bismuth and Antimony

F. M. Muntyanu, K. Nenkov, A. J. Zaleski, and V. Chistol

Abstract

Using Quantum Design SQUID magnetometer and Physical Property Measuring System (PPMS), we studied the magnetic and superconducting properties of high-quality inclination crystallite interfaces (CIs) of bicrystals of Sb and Bi. It was found that the CIs with a higher carrier density than single crystalline samples exhibit a superconducting transition with respectively $T_c \leq 10$ K for Sb and $T_c \leq 21$ K for Bi interfaces; the Sb CIs also manifest ferromagnetic hysteresis loops against a paramagnetic background, thereby indicating occurrence of superconductivity and weak ferromagnetism.

Keywords

Antimony • Bismuth • Bicrystal interface • Superconductivity and ferromagnetism

1 Results and Discussion

The high-quality inclination bicrystals of bismuth and antimony were prepared by the horizontal zone recrystallization method. The magnetic and superconducting properties were studied in temperature range 1.6–300 K and magnetic fields

up to 14 T using highly sensitive measurement systems, such as Quantum Design SQUID magnetometer and Physical Property Measuring System.

1.1 Bi Inclination Interfaces

Low temperature studies of Bi small disorientation angles (SDA) nano-width CIs have revealed [1] some surprising results: the observation in high magnetic field of new high frequency SdH quantum oscillations, the detection of Hall quasi-plateaus (~ 3 , ~ 6 , ~ 15 T) together with deep magnetoresistance minima, the discovery of superconductivity of CIs, etc.

Figure 1 shows the typical temperature dependences (including zero-field cooled (ZFC) and field cooled (FC) dependences) of the magnetic moment and the hysteresis loops of inclination bicrystals.

One or two superconducting transition associated with CIs are observed, at that, the low temperature phase with $T_c \leq 4.3$ K assigned to the adjacent layers occur independently or alongside with the second transition (8.4 K $\leq T_c \leq 21$ K) attributed to the central layer. The discovery of superconductivity in nano-width CIs with unexpectedly high transition temperature $T_c \leq 21$ K is an unusual event, because bismuth bulk single crystals do not exhibit superconductivity above 30 mK.

The hysteresis loops of Bi bicrystals unfold against a diamagnetic background and do not significantly change their form with temperature. The ZFC and FC dependences (see Fig. 1b, inset) denote a considerable Meissner signal, a pronounced magnetic flux expulsion, and the superconducting transition starting off at 36 K. Thus, our results show that the inclination bismuth SDA interfaces have fairly high transition temperature $T_c \leq 21$ K, exhibit superconducting hysteresis loops of an almost symmetric shape and occur exclusively against diamagnetic background, typical for strong type-II superconductors. The superconductivity of the Bi interfaces results from the reconstruction of the

F. M. Muntyanu (✉)
Institute of Electronic Engineering and Nanotechnologies,
3/3, Academiei Street, Chisinau, Moldova
e-mail: muntean_teorod@yahoo.com

K. Nenkov
Leibniz-Institut für Festkörper und Werkstofforschung,
Dresden, Germany

A. J. Zaleski
Institute of Low Temperatures and Structural Research,
Polish Academy of Sciences, Wrocław, Poland

V. Chistol
Technical University of Moldova, Chisinau, Moldova
e-mail: chistol_vitalie@yahoo.com

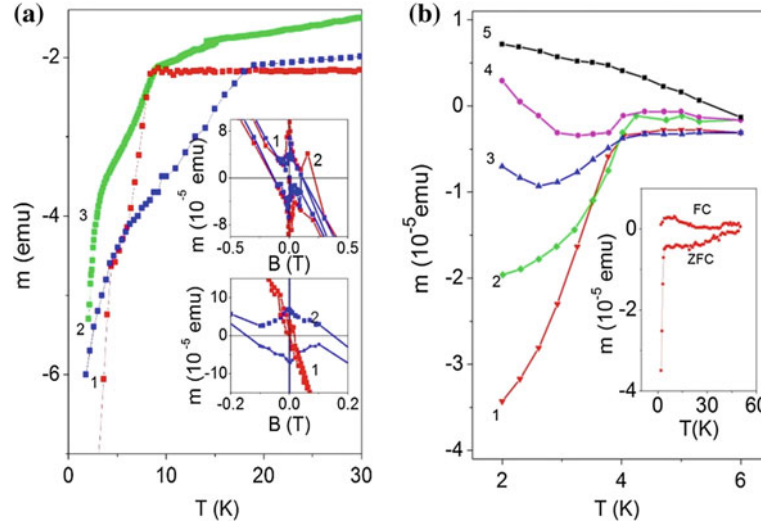


Fig. 1 Magnetic moment versus temperature T and magnetic field B for Bi inclination bicrystals. **a** Temperature dependences $m(T)$ in bicrystals with two superconducting transition: (1) $\theta = 4^\circ$, (2) $\theta = 5^\circ$, (3) $\theta = 4.5^\circ$; the upper inset shows magnetic hysteresis loops in bicrystals with $\theta = 4^\circ$ at 2.1 K (1) and 6 K (2); the lower inset exhibit

magnetic hysteresis loops at 2.1 K of bicrystals with $\theta = 5^\circ$ (1) and $\theta = 2^\circ$ (2). **b** Temperature dependences $m(T)$ in magnetic field of bicrystal with $\theta = 5^\circ$: (1) 0.005 T, (2) 0.01 T, (3) 0.02 T, (4) 0.04 T, (5) 0.08 T; the inset show FC and ZFC curves in bicrystal with $\theta = 4.5^\circ$

rhombohedral crystal structure A7 under deformations. In this case, the Fermi surface (FS) consisting of CIs layers instead changes substantially topology of both isoenergetic surfaces of electrons (FS is less anisotropic and much larger in volume than in bulk) and holes (modifications of the shape, elongation and volume of FS) and the phonon spectra, stimulating electron pair correlation.

1.2 Sb Inclination Interfaces

The Sb semimetal with strong spin-orbit interactions has the topological characteristics [2, 3] with Z_2 invariant $\nu_0 = 1$, just like the $\text{Bi}_{1-x}\text{Sb}_x$ ($0.07 \leq x \leq 0.2$) alloys, which are 3D topological insulators. The rhombohedral single crystalline Sb does not exhibit superconductivity or ferromagnetism. The topological situation entirely changes in the case of small disorientation angle (SDA) nano-width crystallite interfaces (CIs), which are more available in the experimental study than other low-dimensional objects. By varying their inclination angle θ it is possible to change the charge carrier concentration and the number of microstructural defects or the stress states, which leads to the manifestation of new interesting features of several physical phenomena. The ARPES measurements [3, 4] reveal the occurrence of a Sb metallic topologically protected surface state with a single Dirac cone. Antimony undergoes topological nontrivial-to-trivial transitions under

the action of several factors, which make it very attractive for spintronic applications.

We revealed that the SDA Sb interfaces exhibits only one superconducting transition with critical temperature 6.5 K $T_c \leq 10$ K, depending of inclination angle θ of crystallites. This is evident from the Fig. 2a–c which show the temperature dependences of magnetic moment and the real $\chi'(T)$ and imaginary $\chi''(T)$ parts of AC susceptibility at magnetic field directed along the interface plane. From this data, we found that the upper critical field $B_{c2}(T)$ (see inset in Fig. 2a) is linear in a wide range; this feature makes it possible to use the well-known WHH formula [5]. As a result, it was evaluated that for CIs with $\theta = 5^\circ$ and $T_c \sim 6.5$ K the $dB_{c2}/dT \sim 0.04$ T/K, $B_{c2}(0) \sim 0.18$ T and coherence length $\xi(0) \sim 43$ nm. The AC susceptibility dependences show also that, if the CIs temperature approaches T_c , a single sharp drop occurs in $\chi'(T)$ and of a peak in $\chi''(T)$ simultaneously appears; this fact provides still more evidence of the presence of only one superconducting phase.

The $\chi''(T)$ data in the absence of magnetic field clearly indicate the energy dissipation in CIs region. On the other hand, the applied magnetic field suppress superconductivity and pushed the onset of superconducting transition to lower temperature which is typical for strong type-II superconductors.

The field dependences of magnetization show the ferromagnetic hysteresis loops against a paramagnetic background (see lower inset in Fig. 2c), indicating the manifestation of weak ferromagnetism. It can also be

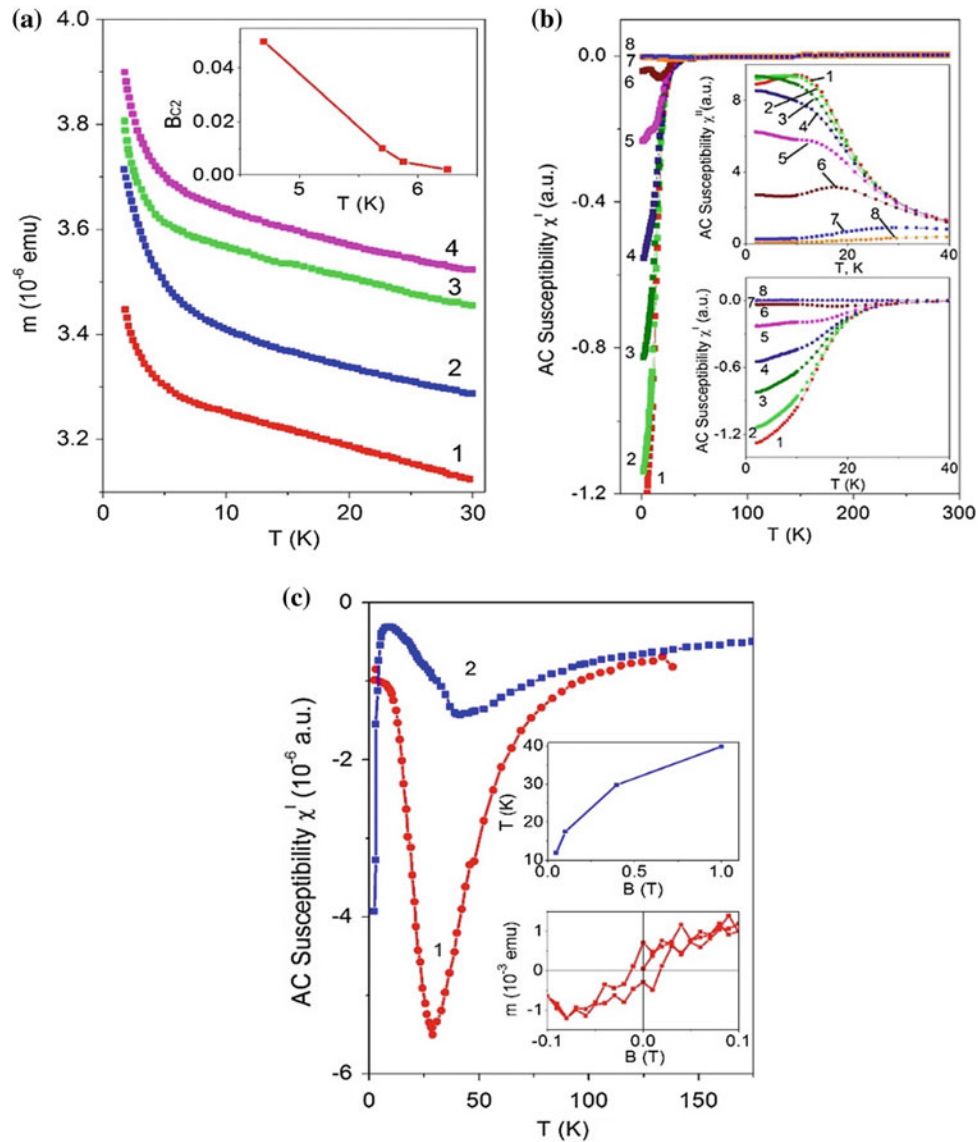


Fig. 2 Magnetic moment and AC susceptibility versus temperature and magnetic field for Sb inclination bicrystals. **a** Sb bicrystal with $\theta = 5^\circ$: (1) 0.002 T, (2) 0.005 T, (3) 0.01 T, (4) 0.05 T; Inset: the dependences of the upper critical field B_{c2} on temperature T . **b** Sb bicrystal with $\theta = 2^\circ$, $f = 1000$ Hz: (1) 0 T, (2) 0.01 T, (3) 0.02 T,

(4) 0.03 T, (5) 0.05 T, (6) 0.1 T, (7) 0.4 T, (8) 1 T. **c** Sb bicrystal with $\theta = 2^\circ$, $f = 1000$ Hz: (1) 0.4 T, (2) 1.0 T; Upper inset shows the temperature dependences of $\chi'(T)$ maximum at different applied fields, lower inset show the magnetic hysteresis loops at 2 K

remarked, that in inclination bicrystals with slightly larger disorientation angles at $T > 25$ K, a diamagnetic maximum of $\chi'(T)$ at $B \geq 0.4$ T appears (see the upper inset in Fig. 1c), which is suppressed and shifted to higher temperatures as the applied field is increased. We believe that these particularities can be attributed to the spin reorientations of charge carriers in magnetic field of some CIs layers [6, 7].

Thus, the Sb nano-width inclination interfaces show a single superconducting transition with $T_c \leq 10$ K; at the same time, they exhibit ferromagnetic hysteresis loops against a paramagnetic background like as 3D TI $\text{Bi}_{1-x}\text{Sb}_x$ ($0.07 \leq x \leq 0.2$) CIs [1, 8].

2 Conclusions

We have experimentally studied the magnetic and superconducting properties of high-quality inclination interfaces of Bi and Sb. One or two superconducting transitions associated with CIs are observed in Bi SDA bicrystals, at that, the low temperature phase with $T_c \leq 4.3$ K assigned to the adjacent layers occur independently or alongside with the second transition ($8.4 \text{ K} \leq T_c \leq 21 \text{ K}$) attributed to the central layer. Only one superconducting transitions are reliably recorded in Sb SDA CIs with critical temperature

$6.5 \text{ K} \leq T_c \leq 10 \text{ K}$. At the same time, the SDA interfaces of Sb show a ferromagnetic hysteresis loop against paramagnetic background. This fact indicates the simultaneous occurrence of superconductivity and weak ferromagnetism. The coexistence of superconductivity and magnetism at Sb SDA interfaces may represent a great interest for the fundamental physics and for future applications in quantum computing and spintronic devices.

Conflict of Interest The authors declare that they have no conflict of interest.

References

1. Muntyanu, F.M., Gilewski, A., Zaleski, A.J., Chistol, V., Munteanu, V., Rogacki, K., Sidorenko, A.: Functional Nanostructures and Metamaterials for Superconducting Spintronics, pp. 1–15. Springer International Publishing AG, part of Springer Nature, Sidorenko, A. (ed.) (2018)
2. Hasan, M.Z., Kane, C.L.: Colloquium: topological insulators. *Rev. Mod. Phys.* **82**, 3045 (2010)
3. Bianchi, M., Guan, D., Strozecka, A., Voetmann, C.H., Bao, S., Pascual, J.I., Eiguren, A., Hofman, P.: Surface states on a topologically nontrivial semimetal: the case of Sb(110). *Phys. Rev. B* **85**, 155431 (2012)
4. Sugawara, K., Sato, T., Souma, S., Takahashi, T., Arai, M., Sasaki, T.: Fermi surface and anisotropic spin-orbit coupling of Sb(111) studied by angle-resolved photoemission spectroscopy. *Phys. Rev. Lett.* **96**, 046411 (2006)
5. Werthamer, N.R., Helfand, E., Hohenberg, P.C.: Temperature and purity dependence of the superconducting critical field, H_{c2} . III. Electron spin and spin-orbit effects. *Phys. Rev.* **147**, 295 (1966)
6. Burkov, A.: Topological semimetals. *Nat. Mater.* **15**, 1145–1148 (2016)
7. Blamire, M.G., Robinson, J.W.A.: The interface between superconductivity and magnetism: understanding and device prospects. *J. Phys.: Condens. Matter* **26**, 453201 (2014)
8. Wang, H., Ma, L., Wang, J.: Tip-induced or enhanced superconductivity: a way to detect topological superconductivity. *Sci. Bull.* **63**, 1141–1158 (2018)

Unusual Size Dependence of Acoustic Properties in Layered Nanostructures

S. Cojocaru

Abstract

Compared to symmetrically stacked layered structures, e.g., sandwich-like, much less is known about acoustic properties in a more general configuration lacking such a symmetry. Structures composed of layers with different characteristics (e.g., metal-insulator) are ubiquitous in nanotechnologies harnessing finite size and quantum effects. Explicit analytic expressions describing acoustic waves in a representative two-layer system are derived and analyzed in the full space of material parameters. An unusual behavior of the spectrum is revealed in the dispersive (long wavelength) region where size effects are most prominent. Velocity of the lowest frequency branch, which becomes the Rayleigh surface wave at shorter wavelengths, is shown to depend in a strongly non-monotonous way on the thickness of the layers in contrast with the expected monotonous evolution of higher frequency branches. The wave pattern of different mode types is discussed in detail. Connection between long (including resonances of the composite plate) and short wavelength (bulk-like, surface and interface guided) regions of the spectrum is established. It is shown that the peculiar behavior of the low energy phonon spectrum induces similar effects in the electron-phonon relaxation and heat transport in composite nanomaterials at low temperatures.

Keywords

Acoustic waves • Phonons in nanomaterials • Ultrathin composite films

1 Introduction

By populating the lowest energy region of the vibration spectrum acoustic waves play a key role in both equilibrium and non-equilibrium properties of nanomaterials, e.g., cooling of hot electrons in nanodetectors [1] or causing an exceptional thermal conductivity in graphene [2]. Their long coherence length and ability of coupling to other degrees of freedom makes them a prospective candidate for transmission of quantum information [3]. As compared to bulk materials behavior of mechanical vibrations at the nanoscale is strongly modified due to confinement and sensitivity to boundary conditions, producing a large variety of spectral branches and wave patterns dependent on geometry, composition and external fields [4]. A great deal of knowledge has been accumulated on the basis of linear elasticity theory for the structures with a symmetric composition, e.g., in layer stacking or periodic superlattices [5]. At the same time, although an asymmetric layout presents a considerable technological interest, its studies are hindered by a higher degree of complexity. The approach outlined in the present work introduces certain simplification which allows to obtain explicit analytic expressions describing acoustic waves in the long wavelength region of the spectrum and to reveal some new features in their behavior.

2 Surface Adapted Basis Set

The displacement field vector satisfies the equations of elastodynamics [4–6].

$$\rho \frac{\partial^2 U_i(\mathbf{r}, t)}{\partial t^2} = \frac{\partial \Sigma_{ij}(\mathbf{r}, t)}{\partial r_j}. \quad (1)$$

Here ρ is mass density and Σ the stress tensor ($i = x, y, z$) which is related to the displacement by known constituent equations. The wave propagates along the x direction of the bilayered plate. The z axis is aligned along the thickness

S. Cojocaru (✉)
Horia Hulubei National Institute for Physics and Nuclear Engineering, Reactorului, Magurele, Romania
e-mail: scojocaru@theory.nipne.ro

($d = d_a + d_b$) of the plate with $z = 0$ fixed at the interface between a and b materials, so that outer surfaces correspond to $z = d_a$ and $z = -d_b$. Solutions of (1) can be expanded into eigenmode series

$$U_i(\mathbf{r}, t) = \sum_n \int u_{i,\gamma}(q, z) \exp(iqx - i\omega_n t) \frac{dq}{2\pi}, \quad (2)$$

where n labels the branches of the spectrum and $\gamma = a, b$ is used to label the layers. We further consider the mixed longitudinal and transverse waves (P + SV polarization) with the aim of finding a relation to Lamb's single layer solutions and their symmetry classification. Then from (1) and (2) one obtains the known equations for the amplitudes $u_{i,\gamma}(q, z)$ and $\sigma_{ij,\gamma}(q, z)$ of the multilayered system [6]. In a standard approach these are solved for the boundary conditions (BC) by representing the amplitudes as a superposition of incoming and outgoing plane waves; that results in a system of eight equations for the coefficients. Instead, it is proposed to choose the basis in such a form as to satisfy the BC on the outer surfaces in an identical way, i.e., even when the solutions are known with an approximation. The BC require zero tension on the outer surfaces and continuity on the interface:

$$\begin{aligned} \sigma_{xz}(zz)(z = d_a) = \sigma_{xz}(zz)(z = -d_b) = 0, \\ u_{x,\gamma}(z = 0) = u_{x,\bar{\gamma}}(z = 0), \sigma_{zx,\gamma}(z = 0) = \sigma_{zx,\bar{\gamma}}(z = 0). \end{aligned} \quad (3)$$

To achieve our construction the amplitudes are expressed in terms of hyperbolic functions with the arguments containing the equations *defining* the outer surfaces. After substitution into Eqs. (1)–(3) one obtains the following expressions

$$\begin{aligned} u_{x,\gamma}(q, z) &= X_\gamma(q) \left(\sinh((z - d_\gamma)q v_\gamma) - \frac{(1 + v_\gamma^2)}{2\omega_\gamma v_\gamma} \sinh((z - d_\gamma)q \omega_\gamma) \right) \\ &\quad + Y_\gamma(q) \left(\cosh((z - d_\gamma)q v_\gamma) - \frac{2}{(1 + v_\gamma^2)} \cosh((z - d_\gamma)q \omega_\gamma) \right), \dots \\ \frac{i\sigma_{zx,\gamma}(q, z)}{2\mu_\gamma q} &= Y_\gamma(q) (\cosh((z - d_\gamma)q v_\gamma) - \cosh((z - d_\gamma)q \omega_\gamma)) \\ &\quad + X_\gamma(q) \left(\sinh((z - d_\gamma)q v_\gamma) - \frac{(1 + v_\gamma^2)^2}{4\omega_\gamma v_\gamma} \sinh((z - d_\gamma)q \omega_\gamma) \right). \\ \omega_\gamma &= \sqrt{1 - (c/\ell_\gamma)^2}, \quad v_\gamma = \sqrt{1 - (c/s_\gamma)^2} \end{aligned} \quad (4)$$

Here

and $c = \omega_\gamma/q$. Respective bulk wave velocities

$$\ell_\gamma = \sqrt{(\lambda_\gamma + 2\mu_\gamma)/\rho_\gamma}, \quad s_\gamma = \sqrt{\mu_\gamma/\rho_\gamma}$$

are given in terms of the Lamé constants for materials a and b . One can see that Eqs. (4) ensure an automatic fulfillment of the first row of BC in (3). So, we are left with the four

unknown parameters $\{X_\gamma, Y_\gamma\}$ which are to be determined from the BC in the second row of (3).

3 Properties of the Solutions

As a consequence, a simple relation between X and Y and the surface amplitudes is obtained

$$\begin{aligned} u_{x,\gamma}(q, z = d_\gamma) &= -Y_\gamma(q) \frac{1 - v_\gamma^2}{1 + v_\gamma^2}, \\ iu_{z,\gamma}(q, z = d_\gamma) &= X_\gamma(q) \frac{1 - v_\gamma^2}{2v_\gamma}. \end{aligned}$$

We therefore may use the continuity at the parametric point “ $a = b$ ” to identify the two classes of solutions, dilatational (D) and flexural (F), as the correspondents of symmetric (S) and antisymmetric (A) Lamb waves in the single layer limit. Indeed, one can verify that our equations remain invariant under the transformations $a \leftrightarrow b$, $z \rightarrow -z$, provided

$$\begin{aligned} D : X_\gamma(q) &= -X_{-\gamma}(q), Y_\gamma(q) = Y_{-\gamma}(q) \\ F : X_\gamma(q) &= X_{-\gamma}(q), Y_\gamma(q) = -Y_{-\gamma}(q) \end{aligned} \quad (5)$$

In the long wavelength region $qd < 1$ for the gapless modes we use Taylor expansion. Taking into account the above transformation properties we find

$$\begin{aligned} D : c_D &= 2\sqrt{\frac{d_a\mu_a(1 - J_a) + d_b\mu_b(1 - J_b)}{d_b\rho_b + d_a\rho_a}}, Y_\gamma(q) \\ &= (c_D^2 - 2s_\gamma^2)/\sqrt{dc_D^2} + O(q^2), \end{aligned}$$

where $J_\gamma \equiv s_\gamma^2/\ell_\gamma^2$, $X_a = -X_b(a \rightleftharpoons b)$.

$$\begin{aligned} F : c_F &= q\sqrt{\frac{4\mu_a\mu_b d_a d_b (1 - J_a)(1 - J_b)d^2 + (\mu_a d_a^2(1 - J_a) - \mu_b d_b^2(1 - J_b))^2}{3(d_a\mu_a(1 - J_a) + d_b\mu_b(1 - J_b))(\rho_a d_a + \rho_b d_b)}}, \\ &= q\sqrt{\frac{4\mu_a\mu_b d_a d_b (1 - J_a)(1 - J_b)d^2 + (\mu_a d_a^2(1 - J_a) - \mu_b d_b^2(1 - J_b))^2}{3(d_a\mu_a(1 - J_a) + d_b\mu_b(1 - J_b))(\rho_a d_a + \rho_b d_b)}}, \end{aligned} \quad (6)$$

$$\begin{aligned} Y_a &= qX_a(d^2\mu_b(1 - J_b) + d_a^2(\mu_a(1 - J_a) - \mu_b(1 - J_b))) \\ &\quad /2(d_a\mu_a(1 - J_a) + d_b\mu_b(1 - J_b)), \\ X_\gamma &= 2s_\gamma^2/\sqrt{dc_F^2}, Y_b = -Y_a(a \rightleftharpoons b). \end{aligned}$$

where expression for c_D was known earlier. To get an insight into the physical behavior contained in (6) and to circumvent the complexity of parametric space we introduce the scaled quantities:

$$\mu = \frac{\mu_b}{\mu_a} \times \frac{1 - J_b}{1 - J_a}, \quad \delta = \frac{d_b}{d_a}, \quad \rho = \frac{\rho_b}{\rho_a}.$$

With these our result can be represented as a ratio to the known Lamb solution for a single layer “reference” material (a) of the same thickness d :

$$\left(\frac{c_D}{c_{S_0}}\right)^2 = \frac{1 + \mu\delta}{1 + \rho\delta}, \quad (7)$$

$$\left(\frac{c_F}{c_{A_0}}\right)^2 = \frac{(1 - \mu\delta^2)^2 + 4\mu\delta(1 + \delta)^2}{(1 + \delta)^2(1 + \mu\delta)(1 + \rho\delta)}. \quad (8)$$

It can be seen that the standard, non-dispersive, behavior of acoustic waves as described by (7) is associated with a monotonous change with material parameters. For instance, when thickness of the added layer increases, the sound velocity either increases or decreases relative to single layer. The dispersive flexural mode (8), in contrast, behaves in a rather non-trivial manner, Fig. 1.

Figure 2 shows the cross section of the surface in Fig. 1 for the specified values of material parameters. Remarkably, the strongest non-monotonicity occurs at the incipient stage (coating) of increasing the thickness of the added layer.

Aside from the gapless solutions in (6), the rest of the spectrum at $q = 0$ consists of gapped modes with diverging phase velocity which correspond to the finite frequencies of plate resonances. The eigenfrequency equations known from earlier works are also reproduced by the present approach:

$$\begin{aligned} \rho_a \ell_a \sin(\omega d_a / \ell_a) \cos(\omega d_b / \ell_b) + \rho_b \ell_b \sin(\omega d_b / \ell_b) \cos(\omega d_a / \ell_a) &= 0, \\ \rho_a s_a \sin(\omega d_a / s_a) \cos(\omega d_b / s_b) + \rho_b s_b \sin(\omega d_b / s_b) \cos(\omega d_a / s_a) &= 0. \end{aligned} \quad (9)$$

Because the two polarizations (P + SV) decouple at $q = 0$, the solutions are split in two categories of plate resonances: thickness-stretch and thickness-shear, respectively.

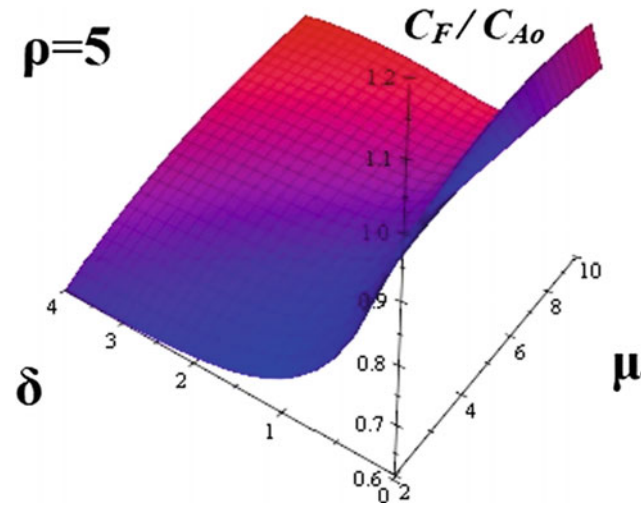


Fig. 1 Velocity of the lowest frequency wave scaled with Lamb A_0 mode in a single layer for $qd < 1$, Eqs. (6) and (8), $\rho = 5$

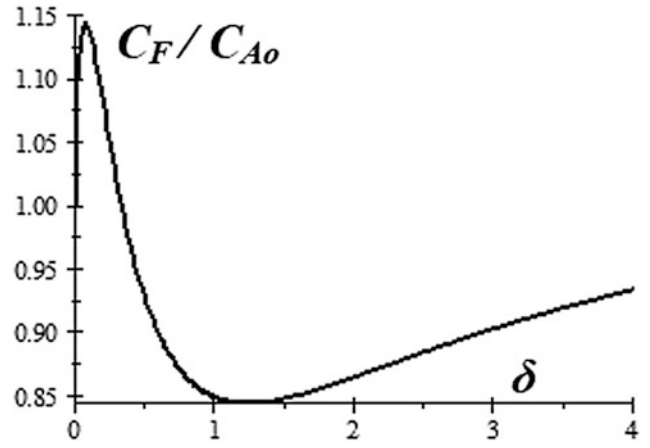


Fig. 2 Evolution of the lowest frequency branch with the ratio of the layer thicknesses for a choice of elasticity parameters with $\mu = 6$ and $\rho = 5$

The non-vanishing components of the amplitudes obtained in the framework of our surface adapted basis are given below.

Thickness-shear:

$$u_{x,\gamma}(z) = G(s) \cos(\omega_n d_{-\gamma} / s_{-\gamma}) \cos(\omega_n (z - d_{\gamma}) / s_{\gamma})$$

Thickness-stretch:

$$u_{z,\gamma}(z) = G(\ell) \cos(\omega_n d_{-\gamma} / \ell_{-\gamma}) \cos(\omega_n (z - d_{\gamma}) / \ell_{\gamma}) \quad (10)$$

Here G are normalization constants. It can be seen that absolute values of the amplitudes reach maxima at the surfaces of the composite plate. Figures 3 and 4 exemplify this property for two lower frequency resonance modes for unspecified couple of materials.

Another feature that can be inferred from these figures is that the amplitudes look like distorted versions of the perfectly symmetric A and S Lamb modes: $A \rightarrow F$ and $S \rightarrow D$. This resemblance turns out to persist throughout the whole spectrum and amounts to a topological equivalence. Namely, the signs of the amplitudes on the outer surfaces for a chosen mode branch remain unchanged upon inclusion of the second layer, while the shape of the amplitude is deformed and the symmetry of the Lamb wave is lost. Thus, for the *flexural* waves we find

$$\begin{aligned} \text{sign}(u_x(qd \ll 1, z = d_a) \times u_x(qd \ll 1, z = -d_b)) &= -1, \\ \text{sign}(u_z(qd \ll 1, z = d_a) \times u_z(qd \ll 1, z = -d_b)) &= +1. \end{aligned}$$

and for the *dilatational* waves, respectively

$$\begin{aligned} \text{sign}(u_x(qd \ll 1, z = d_a) \times u_x(qd \ll 1, z = -d_b)) &= -1, \\ \text{sign}(u_z(qd \ll 1, z = d_a) \times u_z(qd \ll 1, z = -d_b)) &= +1. \end{aligned}$$

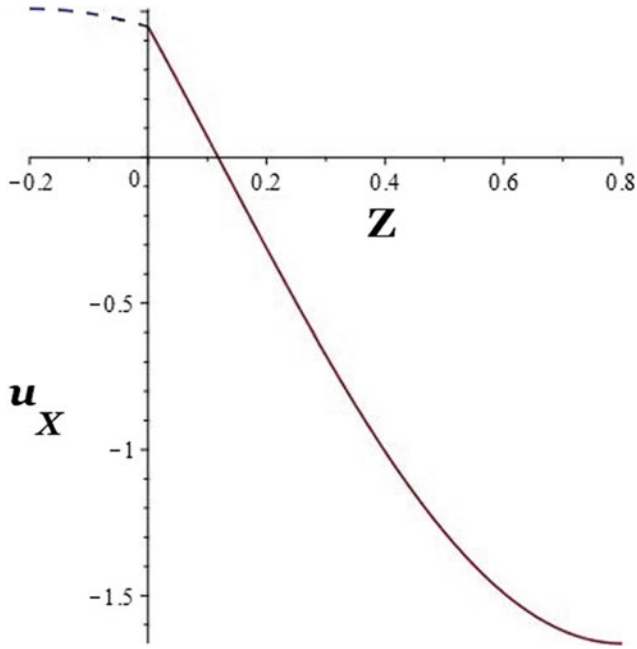


Fig. 3 Amplitude of the thickness-shear lowest resonance mode which, according to (5), is of flexural type (F). Different lines correspond to different layers

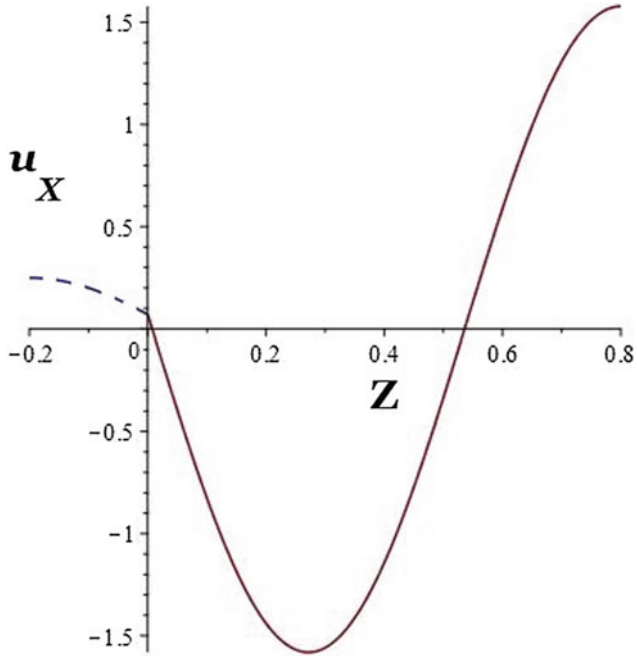


Fig. 4 Amplitude of the thickness-shear resonance mode which, according to (5), is of dilatational type (D)

This conclusion is confirmed by the analysis of solutions for the Eqs. (9, 10) and by observation that F and D modes follow in an alternating order with the increase of ω_n within

each category of solutions (shear, stretch). Whether the above sign pattern remains valid for the full range of wavenumbers requires further investigation, while it is confirmed by the examples considered in our numerical analysis.

The latter has been carried out to explore the continuity of the solution branches between the two limits: $qd \ll 1$ and $qd \gg 1$. It is known that at short wavelengths the multiple branches of spectrum should coalesce into the bulk modes (longitudinal and shear) corresponding to the two materials of the composite plate, to the Rayleigh surface acoustic waves and to the interface guided Stoneley wave. Thus, it has been shown that this limit is also reproduced by our equations. All the branches of the spectrum are ordered according to the value of their velocities at a given wavenumber. For instance, the lowest one is the Rayleigh mode “localized” near the outer surface of the softest of the two materials. If the material parameters satisfy the condition for the existence of the Stoneley wave, then it is this interface guided mode which follows the Rayleigh mode. Otherwise, this position is taken by the shear bulk wave, etc. The mixed P + SV polarization is preserved only by the surface and interface guided modes. A laborious numerical analysis (to be presented elsewhere) shows by branch continuity that the ordering of the eigenmodes in the $qd \gg 1$ limit can be traced to analogous ordering at long wavelengths. In particular, the Rayleigh mode originates in the fundamental flexural mode F_0 while the Stoneley wave has its origin the fundamental dilatational mode D_0 . At intermediate wavenumbers some of the branches demonstrate the phenomenon of avoided crossing. In the respective regions two incoming branches take a sharp turn exchanging not only the directions on the outcome, but also the apparent shape of the wave, the phenomenon first described by Sezawa (see, e.g., [7]). However, we find that despite of this exchange, the sign pattern discussed above remains unchanged, corroborating our finding of this new invariant characteristics of acoustic waves in composite layered structures.

4 Conclusions

The proposed approach gives a fresh and physically appealing perspective on describing wave propagation in layered media. It has allowed to establish a connection between the symmetric and antisymmetric Lamb waves and those of the structures lacking such symmetry. We have demonstrated the existence of a generic feature of the wave pattern at long wavelengths related to the sign of the vibration amplitudes on the outer surfaces. It reveals a

topological equivalence with the waves in a single layer allowing to classify the whole spectrum in terms of dilatational and flexural modes. The complete solution in the full parametric space has uncovered an unusual, strongly non-monotonous, variation of the flexural wave velocity with thickness of the layered structure. This effect has implications for the low energy physics of nanomaterials and can be useful for engineering of their properties. In particular, quantization of the acoustic waves and interaction of the acoustic phonons with electrons would affect the heat transport and electron-phonon interaction in layered nanomaterials, e.g., [8, 9].

Acknowledgements This work has been financially supported by ANCS Romania, Project No. PN 19 06 01 01/2019.

Conflict of Interest The author declares having no conflict of interest.

References

1. Cojocaru, S., Anghel, D.V.: Low-temperature electron-phonon heat transfer in metal films. *Phys. Rev. B* **93**, 115405 (2016)
2. Nika, D.L., Balandin, A.A.: Two-dimensional phonon transport in graphene. *J. Phys. Condens. Matter* **24**, 233203 (2012)
3. Schuetz, M.J.A., et al.: Universal quantum transducers based on surface acoustic waves. *Phys. Rev. X* **5**, 031031 (2015)
4. Strocio, M.A., Dutta, M.: *Phonons in Nanostructures*. CUP, United Kingdom (2004)
5. Nika, D.L.: *Phonon Engineering in Graphene and Semiconductor nanostructures*. USM, Chisinau (2015)
6. Rose, J.L.: *Ultrasonic Guided Waves in Solid Media*. CUP, NY (2014)
7. Cheeke, J.D.N.: *Fundamentals and Applications of Ultrasonic Waves*. CRC, USA (2012)
8. Anghel, D.V., Cojocaru, S.: Heat exchange between electrons and phonons in nanosystems at sub-kelvin temperatures. *Eur. Phys. J. Web Conf.* **173**, 02002 (2018)
9. Anghel, D.V., Cojocaru, S.: Electron-phonon heat exchange in quasi-two-dimensional nanolayers. *Eur. Phys. J. B* **90**, 260 (2017)

Features of Radiative Recombination of Iron-Doped Gallium Antimonide

A. Mihalache

Abstract

We report on the results of the studies of the features of radiative recombination of iron-doped gallium antimonide at $T = 2$ K, in the absence of an external magnetic field. Specimens were prepared by a modified method of zone melting. The concentration of iron incorporated in the melt varied in the range of 0.001–3 (atomic percent). The studied specimens exhibited *p*-type conductivity. It was demonstrated that in gallium antimonide iron created a shallow acceptor level with the ionization energy of (22 ± 0.2) meV. In addition, the structure of the radiative recombination spectra was determined and the concentration of radiative centers was found out.

Keywords

GaSb • Photoluminescence

1 Introduction

Investigations of the behavior of the transition group elements (iron, manganese, nickel, chromium, etc.), used as doping agents in various semiconductor matrices, are quite topical as regards suggesting new theoretical models of structures of unusual doping centers and creating various microelectronic structures [1]. Impurities of transition metals of the iron family are known to be acceptors in the group AIIIBV compounds. At the same time, the impurities levels thus built can be either deep as in the case of GaAs [2], InP [3], GaP [4] or shallow as in the case of InSb, GaSb [5, 6]. The effects of impurities of transition metals on the properties of doped compounds are also different. Ambiguous behavior of these impurities makes it necessary to carry out a separate study of their roles in each particular material. That

A. Mihalache (✉)
Tiraspol State University, 5 Gh. Iablocikin str., Chisinau, Republic of Moldova
e-mail: alexei.mihalache@gmail.com

peculiar behavior has triggered intensive investigations aimed at fabricating new diluted magnetic semiconductors with spontaneous ferromagnetic ordering, that are very promising in contemporary spin microelectronics [7].

Some of the transition metal impurities in GaSb are insufficiently explored, for instance, manganese [8]. As to the radiative recombination of Fe-doped GaSb, to the best of the authors' knowledge, there is only one work [9] that deals with a narrow concentration range. The present paper offers the results of the investigations of the structure of spectra of radiative recombination of Fe-doped GaSb in a wide range of Fe concentrations—up to 3% (atomic percent). The spectra of radiative recombination were registered at $T = 2$ K, in the absence of an external field.

2 Experimental Results and Their Discussions

Specimens of GaSb doped by iron in various concentrations were prepared by a modified method of zone melting in the atmosphere of pure argon. The technology applied combined two processes: zone cleaning in the presence of an external electric field and growing of a single crystal. The velocity of a unidirectional zone was ~ 0.1 mm/h, the length of an ingot was ~ 18 – 22 cm and its diameter 6–8 mm. The concentration of the incorporated Fe varied in the range of 0.001–3 (atomic percent). For galvanomagnetic measurements, specimens of a standard shape were cut from different regions of an ingot. Galvanomagnetic measurements confirm relatively even distribution of impurities along the ingot length. All specimens analyzed by the authors of the present paper exhibited *p*-type conductivity. Studies of the temperature dependence of the specific resistance and of the Hall coefficient support the fact that Fe incorporated into the GaSb matrix is electrically active and causes the increase of the concentration of holes in specimens, which, depending on the percentage of Fe incorporation, varies in the range of 2.1017 – 8.1019 cm^{-3} .

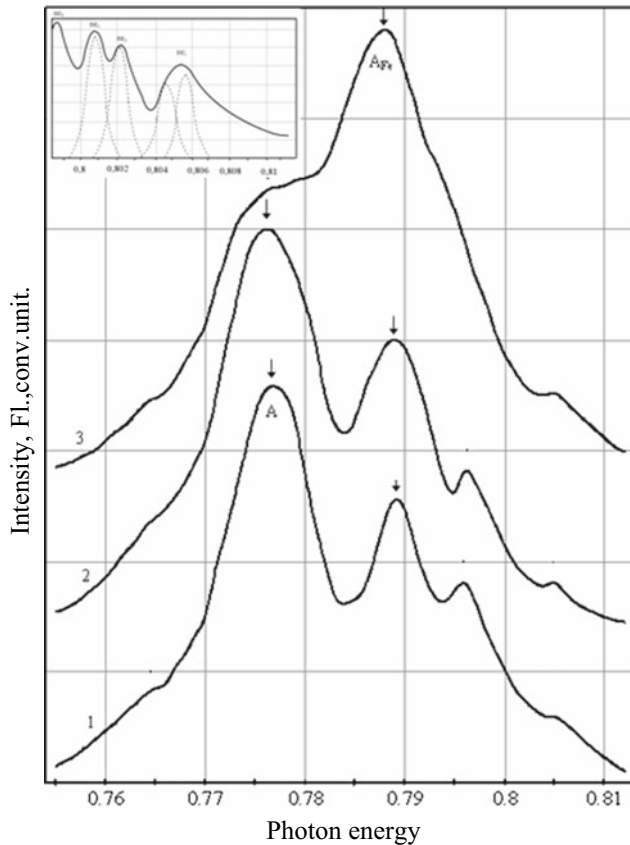


Fig. 1 Radiative spectra of Fe-doped GaSb at $T = 2$ K, $B = 0$. 1. GaSbFe, 0.000% (Fe), $N_A - N_D = 1.6 \times 10^{17} \text{ cm}^{-3}$. 2. GaSb(Fe), 1.00 % Fe, $N_A - N_D = 1.8 \times 10^{18} \text{ cm}^{-3}$. 3. GaSb(Fe), 3.00 % Fe, $N_A - N_D = 2.3 \times 10^{19} \text{ cm}^{-3}$

The analysis of the scattering of charge carriers according to Fe concentration [10] showed that the incorporation of Fe in the concentrations above those of the natural acceptors of GaSb ($\sim 10^{17} \text{ cm}^{-3}$) results in its uneven distribution in the specimens, in settling-out of iron as clusters (certain inclusions of the second phase) with geometrical nano-dimensions. The conclusion on the formation of clusters was complementary supported by the x-ray diffraction analysis. In order to specify the chemical structure of the incorporation of Fe in the main GaSb matrix additional investigations are necessary since so far there is no common point of view regarding that structure.

The excitation of luminescence of the specimens of Fe-doped GaSb was effected by circularly polarized light with the generation at the wavelengths of $1.52 \mu\text{m}$ (0.814 eV) or $1.15 \mu\text{m}$ (1.078 eV). In all of the experiments, the excitation density was not over 10 W cm^{-2} . At those excitation levels and lifetimes of non-equilibrium electrons, the concentrations of the non-equilibrium carriers always were of the several orders of magnitude less than the intrinsic carrier concentrations in the specimens under study. Circularly polarized light is known to excite, in the conduction zone, mostly electrons with unidirectional spin. If the electron recombination velocity is spin-independent, then, most

probably, in the recombination zone there will be the storage of spin-oriented carriers. It can occur even at such excitation intensities when the concentration of excess minority carriers (electrons in the case of p-GaSb) is still low in comparison with their equilibrium, which results in the polarization of radiative recombination. The registered luminescence spectra of GaSb doped with Fe in various concentrations are polarized. The degree of polarization of luminescence of GaSb at $T = 2$ K depends on Fe concentration. Polarization of photoluminescence in a transverse magnetic field allowed to measure the non-equilibrium carriers lifetimes. Under continuous excitation the Hanle effect can be used to measure very short lifetimes, i.e. those of $\sim 10^{-12}$ – 10^{-11} s [11].

In the present paper, the role of the acceptor iron impurity in the process of recombination of carriers has been studied, with the radiative recombination spectra near the edge of the forbidden band.

Photoluminescence spectra of the analyzed specimens are plotted in Fig. 1. The spectra have been registered at $T = 2$ K in the absence of an external magnetic field.

The depicted experimental results demonstrate that radiative recombination spectra at the given temperature have a complex structure and are subject to gradual modifications with increasing Fe concentration in the initial matrix. For comparison, Fig. 1 also shows the radiative recombination spectrum of the undoped GaSb measured at the same temperature, in the absence of a magnetic field. The procedure of identification of the structure of the spectrum of the undoped GaSb is described in [12]. Below we present an analysis of the radiative recombination spectrum of the undoped GaSb registered at $T = 2$ K, in the absence of a magnetic field. In Fig. 1, spectrum 1 was registered for a specimen of p-GaSb with $N_A - N_D = 2 \cdot 10^{16} \text{ cm}^{-3}$ ($E_g(2 \text{ K}) = 0.813 \text{ eV}$). The test results indicate that the radiative recombination spectrum of the undoped specimen has a number of clearly pronounced energy structures. Figure 1 shows as well a simple energy band denoted by the authors as A, with the energy max $(\hbar\omega_A)_{\text{max}} = 77 \pm 0.2 \text{ meV}$ and a complex band integrally denoted as B. Four to five features stand against the background of an energy band with the complex structure. Additional tests confirm that the energy band A registers donor-acceptor recombination's. Taking into account the literature data stating that the energy of the activation of donor levels in GaSb is 2–3 meV, the energy of the activation of acceptor levels was established by the authors of the present paper as being $E_i = 34 \pm 0.2 \text{ meV}$. This result is in conformity with our findings on the same specimen in terms of the Hall constant and electrical conductivity. Our concept of the nature of this radiative band is in accord with the literature interpretations [13]. As to the complex band B, we consider it being due to the disintegration of several exciton states. For the components of that complex band designations were borrowed from [13]. The

Alentsev-Fock method [14] was used to resolve the exciton band into components BE_1 , BE_2 , BE_3 , BE_4 . The energy maxima of exciton bands are given below:

$$\begin{aligned}(h\omega_1)_{\max} &= (805, 2 \pm 0, 2) \text{ meV} & (BE_1) \\(h\omega_2)_{\max} &= (802, \pm 0, 2) \text{ meV} & (BE_2) \\(h\omega_3)_{\max} &= (801, 1 \pm 0, 2) \text{ meV} & (BE_3) \\(h\omega_4)_{\max} &= (796, 3 \pm 0, 2) \text{ meV} & (BE_4)\end{aligned}$$

Excitons are bound to acceptor states. The complex structure of annihilation is in favor of the idea of a strongly defective gallium antimonide.

Spectrum 1 for the undoped specimen also reveals several features from the low-energy end of the radiative band A, denoted as C and D. In our opinion, those radiative bands are nothing else but phonon replica of exciton BE_4 .

Spectrum 2 in Fig. 1 depicts radiative recombination of Fe-doped GaSb at $T = 2$ K, in the absence of an external magnetic field. The concentration of the incorporated Fe is minimal—1.00% atomic percent. Spectrum 2 as well as Spectrum 1 of the radiative recombination of Fe-doped GaSb has a complex structure. The analysis of the former spectrum allowed to conclude the following. In the main, the general structure of spectrum 2 is analogous to the structure of the radiative spectrum of the undoped specimen: the energy state of band A is preserved, the radiation intensity does not change. However, there is the two-fold attenuation of the intensity of radiation of the block of bands identified as bound excitons, and a negligible shift in the high energy region of the exciton maxima BE_1 , BE_2 , и BE_3 . Between the exciton block B and the radiation band A (with the participation of intrinsic acceptors) there appears a new radiation band denoted by the authors of the present paper as AFe. The energy maximum of this new band is $(h\omega_{AFe})_{\max} = (788 \pm 0, 2) \text{ meV}$. The comparison of bands A and AFe demonstrates that although they have different intensity, their half-width is about the same and their dependence on the excitation intensity is really the same. These findings lead to the conclusion that those two radiative bands are of the same physical nature. The energy shift of the maximal of band AFe against the maximum of band A in the high energy region of $11 \pm 0.2 \text{ meV}$ determines the difference in the energy of ionization of the incorporated acceptor levels and the intrinsic acceptor level, the value of the latter was established by the authors of the present paper as $\varepsilon_i = 35 \pm 0.2 \text{ meV}$. From those values of ionization energy conditioned by Fe in acceptor levels we get $\varepsilon_i(\text{Fe}) = (22 \pm 0, 2) \text{ meV}$. It means that the radiative band under discussion here is due to the donor-acceptor recombination. In Fig. 1 spectra 1, 2, and 3 correspond to GaSb doped with Fe in different concentrations. Concentrations of Fe are: for spectrum 1 (0.000%, $N_A - N_D = 1.6 \times 10^{17} \text{ cm}^{-3}$), for spectrum 2 (1.00%, $N_A - N_D = 186 \times 10^{17} \text{ cm}^{-3}$), for spectrum 3

(3.00%, $N_A - N_D = 2.3 \times 10^{17} \text{ cm}^{-3}$). The analysis of the obtained results reveals that the higher the concentration of Fe incorporated in the melt, the higher the intensity of the radiative band AFe, the growth being almost proportional to Fe content in an active state. In addition, the structure of the exciton module is being modified, the intensity of bands BE_1 , BE_2 , BE_3 is getting lower. At the concentration of the incorporated Fe of 1%, all exciton bands are bound, and in the structure of the radiative spectrum, the dominant band is AFe, with a small shift in the high energy region, which is most probably related to the increase of NA-ND because of doping.

The lifetimes of non-equilibrium electrons in the specimens analyzed were established by the polarization properties of band AFe, through registration of the Hanle effects. Optical orientation of carriers, depolarization of luminescence in a transverse magnetic field. The determined lifetimes of minority carriers in GaSb doped with Fe in different concentrations are given in Table 1. These findings evidence that the higher the content of Fe in the main matrix, and the higher the concentration of acceptor states, the shorter are the lifetimes of minority carriers. The observed shortening of the lifetimes of non-equilibrium electrons is nearly inversely proportional to the increase of the concentration of holes, hence being caused by the increase of the concentration of Fe in the electrically active state. From the experiment one we obtained the lifetimes of non-equilibrium electrons and, using the formula $N_t = (\tau \cdot B)^{-1}$, we established the concentration of the recombined centers. In calculations of the coefficients of radiative recombination's, the authors used the value $B = 8 \times 10^{-10} \text{ cm}^3 \text{ s}^{-1}$, typical for hydrogen-like shallow centres [8]. The calculated values for the concentration of radiative centers N_t are presented in Table 1. As is evident in the Table, the concentration of radiative centers grows with the raise of concentration of Fe in the melt. Column 2 of the Table shows the data for NA-NB obtained from electrical measurements of the same specimens. There is a satisfactory agreement of the data on concentrations obtained by measurements at optical orientations and by those at electrical ones. Therefore, the effect of Fe in GaSb on the velocity of radiative recombination of carriers consists in the raise of concentration of shallow acceptor levels, and in accordance with [9], but unlike other compounds of group $A^{III}B^V$, does not lead to the creation of channels of a rapid nonradioactive recombination. Similar conclusions were drawn in [6] for GaSb doped with Mn, the difference being the following: when doping with Mn, at the increases of the concentration NA-ND (because of the higher Mn content in GaSb<Mn>), the concentration changes about 24 times, whereas the lifetime reduces eightfold. In GaSb<Fe>, the concentration changes about 130 times, whereas the lifetime reduces by 58 times. The findings under discussion refer only to the study of the energy structure of the

Table 1 Determined lifetimes of minority carriers in GaSb doped with Fe in different concentrations

Fe content in % atm	$N_A - N_D \text{ cm}^{-3}$	$\tau \text{ s}$	$N_t = (\tau \cdot B)^{-1} \text{ cm}^{-3}$	$\frac{N_t}{N_A - N_D}$	$\frac{N_t}{N_A - N_D} \cdot \%$
0	1.4×10^{17}	6.3×10^{-9}	1.9×10^{17}	1.35	135
0	1.6×10^{17}	5.8×10^{-9}	2.15×10^{17}	1.34	134
0.001	1.7×10^{17}	5.9×10^{-9}	2.11×10^{17}	1.24	124
0.005	1.9×10^{17}	6.0×10^{-9}	2.08×10^{17}	1.09	109
0.01	2.8×10^{17}	5.7×10^{-9}	2.19×10^{17}	0.78	78
0.1	1.1×10^{18}	8.2×10^{-10}	1.52×10^{18}	1.38	138
1.0	1.8×10^{18}	4.1×10^{-10}	3.04×10^{18}	1.68	168
2.0	2.1×10^{18}	3.8×10^{-10}	3.9×10^{18}	1.85	185
3.0	2.5×10^{18}	2.8×10^{-10}	3.1×10^{18}	1.48	148
3.0	2.3×10^{19}	1.6×10^{-10}	7.8×10^{18}	0.34	34
3.0	1.8×10^{19}	1.1×10^{-10}	1.14×10^{19}	0.63	63

incorporated impurity centers and their influence on the recombination of minority carriers. Thus attention was not attracted to the interaction of carriers and magnetic moments that were shown for the impurities of transition metals; besides, the effect of the clusters formed on the energy structure of the main matrix was not discussed either. Still, the issues not covered in the present paper are of interest and do deserve attention in further studies.

3 Conclusions

The results of the studies by the authors of the present paper could be specified as below:

1. An investigation was made on the effect of the incorporation of Fe on the structure of the spectra of radiative recombination of minority carries in GaSb.
2. The effect of the incorporation of Fe in GaSb on the recombination velocity of minority carries was shown to be an increase of concentration of shallow acceptor levels that, unlike other group AIIIBV compounds, does not result in the appearance of channels of rapid nonradioactive recombination.
3. The structure of the spectra of radiative recombination of the doped GaSb allowed the authors to establish the energy of the activation of the acceptor levels related to Fe as $(22 \pm 0.2) \text{ meV}$.

The higher the concentration of Fe incorporated in the main matrix, the shorter the lifetime of minority carriers, and the higher the intensity of the donor-acceptor radiative recombination with the participation of an acceptor level with F.

Conflict of Interest The authors declare that they have no conflict of interest.

References

1. Aguekian, V.F.: Phys. Solid State **44**(11), 1421 (2002). (in Russian)
2. Omelianovschii, E.M., Fistuli, V.I., Balagurov, A.A., Ivleva, V.S., Karashev, V.V., Melvitsckii, M.G.: Semiconductors, **9**, 576 (1975). (in Russian)
3. Ippolitova, G.K., Omelianovschii, G.M., Pavlov, N.M., Nashelischii A.Y., Jakobson, S.V.: The behavior of the Fe impurity in 1pR and the effect of covalency on the EPR spectrum of the Fe²⁺ ion in Td symmetry compounds. ShGP **11**(7), 1315–1320 (1977)
4. Andrianov, D.G., Grinshtein, P.M., Ippolitova, G.K., Omelianovschii, E.M., Suchkova, N.I., Fistuli, V.I.: Semiconductors **10**, 1173 (1976). (in Russian)
5. Vinogradova, K.I., Ivleva, V.S., Ilimenkov, G.I., Nasledov, D.N., Smeshannikova, Y.S., Tashkhodiev, T.K.: Semiconductors **6**, 1845 (1972). (in Russian)
6. Georgitse, E.I., Gutsulyak, L.M., Ivanov-Omschii, V.I., Pogoreletschy V.M., Titkov, A.N.: Мелкий акцепторный уровень марганца в антимониде галлия. J. Tech. Phys. Lett. **17**(17), 21 (1991). (in Russian)
7. Omelianovschii, E.M., Fistuli, V.I.: Impurities of Transition Metals in Semiconductors. Metallurgy, p. 192 (1983). (in Russian)
8. Plaza, J.L., Dieguez, E.: Experimental analysis of Mn segregation in Bridgman-grown gallium antimonide: dependency on the ampoule radius. Cryst. Res. Technol. **39**(5), 396 (2003)
9. Georgitse, E.I., Gutsulyak, L.M., Ivanov-Omskii, V.I., Masterov, V.F., Smirnov, V.A., Yuldashev, S.U.: Photoluminescence of manganese-doped gallium antimonide. Sov. Phys. Semicond. **25**, 1180 (1991)
10. Krukovskaya, L.P., Mironov, I.S., Titkov, A.N.: Shallow acceptor level of Fe in GaSb. Semiconductors, **12**(4) 689–692 (1978)
11. Aronov, A.G., Pikus, G.E., Titkov, A.N.: Spin relaxation of conduction electrons in p-type III-V compounds. JETP **57**(3), 1170 (1983)
12. Mihălache, A.: PL spectra of the Fe-doped Gallium antimonide. Book of abstracts. In: 10th International Balkan workshop on Applied Physics, p. 132 (2009)
13. Chidiey, T.R., Haywood, S.K., Hentiques, A.B., Masen, N.J., Nicolas, R.T., Walken, D.J.: Photoluminescence of GaSb grown by metal-organic vapour phase epitaxy. Semicond. Sci. Technol. **6** (6), 45 (1991)
14. Fock, M.V.: Proc. Phys. Inst. Acad. Sci. **59**, 3–24 (1972). (in Russian)

Spin Crossover in Iron(II) Complexes with Mixed Nitrogen-Sulfur Coordination: DFT Modeling

S. I. Klokishner and O. S. Reu

Abstract

The majority of known Fe^{II} spin crossover (SCO) complexes are based on a homogeneous octahedral nitrogen coordination of the metal ion. Currently a new type of compounds with mixed nitrogen-sulfur ligand surroundings of the iron(II) ions demonstrating spin transitions has attracted much attention. Despite the comprehensive experimental characterization the origin of SCO phenomena in these complexes has not been elucidated. In the present paper on the basis of DFT calculations we describe the course of the spin transformation in the γ -polymorph of the [Fe(bpte)(NCSe)₂] compound containing in the unit cell two different types of iron(II) ions which differ in the geometry of the {N₄S₂} ligand surroundings. To prove the adequacy of the suggested approach in the present paper the well known picture of SCO in the thoroughly characterized classic [Fe(ptz)₆](BF₄)₂ compound is also reproduced.

Keywords

Spin crossover • Iron(II) ion • Mixed nitrogen-sulfur surrounding • DFT calculations • Single point energy

consists of six nitrogen atoms. The mixed nitrogen-oxygen {N₄O₂} ligand surroundings of the SCO iron(III) ions is also known [4]. Recently a new trend in the field of SCO has been suggested and this is the study of spin transitions in compounds containing as a structural element Fe^{II} ions residing in the mixed {N₄S₂} environment [5, 6] which creates a weaker crystal field than that arising from the {N₆} coordination. Gradual increase of the temperature of the SCO transformation in iron(II) complexes [Fe(bpte)(NCE)₂] with the increase of the strength of the ancillary ligands E = NCS, NCSe⁻ and NCBH₃⁻ has been reported in [5]. Despite the vast experimental studies on the SCO transformation in iron(II) complexes with mixed {N₄S₂} ligand surroundings, the theoretical description of this problem has not been performed. The origin of the SCO phenomena in these complexes containing 4 nitrogen atoms creating a field of intermediate strength and 2 sulfur atoms giving a weaker field remains unclear. The goal of the present study is to understand the origin of SCO in iron(II) complexes with mixed {N₄S₂} ligand surroundings [5, 6]. In the present paper we demonstrate that an adequate description of the SCO phenomena in iron(II) ions with typical nitrogen {N₆} and mixed nitrogen-sulfur {N₄S₂} ligand surroundings of the iron(II) can be provided on the basis of single point DFT calculations.

1 Introduction

More than eighty years ago for iron(III) complexes the SCO phenomenon was discovered by Cambi and Szego [1, 2]. The phenomenon consists in the change of the ground state of the iron ion under action of the external stimuli such as temperature, pressure and light. Later on, the iron(II) SCO complexes have been reported [3]. In the majority of known SCO complexes the ligand surrounding of the metal ion

2 Computational Details

We examine the γ -polymorph of the [Fe(bpte)(NCSe)₂] compound [5, 6] and the classical [Fe(ptz)₆](BF₄)₂ compound [7]. The consideration of the latter compound is performed with the aim to prove that the suggested below approach correctly describes the earlier established picture of spin transformation that occurs in it. In the performed DFT calculations the iron(II) states with the spin values $s = 0, 1, 2$ are accounted for. For both compounds the calculations of the single point energies for the Fe^{II}-states with the above indicated spin values have been performed within the frames

S. I. Klokishner (✉) · O. S. Reu
Institute of Applied Physics, Academy Str. 5, Chişinău, Moldova
e-mail: klokishner@yahoo.com

of the density functional theory (DFT) using the program package ORCA 4.0.1.2 [8]. We settled on the calculation of the single point energies since they are associated to a multi-electron system under the potential created by a given arrangement of atoms and should reflect correctly the spin transformation which is accompanied by the change of the bond lengths with rising temperature. In the work the B3LYP functional [9] together with Grimme's dispersion correction [10] have been employed. The def2-TZVP basis together with the auxiliary SARC/J and def2-TZVP/C basis sets [11] have been used. To control the target precision of the energies and the wave functions for the compounds under examination the ORCA keyword "VeryTightSCF" was used, as a result the ground state energies were converged to 10^{-9} hartree.

In the calculations for the $[\text{Fe}(\text{ptz})_6](\text{BF}_4)_2$ compound the geometrical structure of the unit composed of the Fe^{II} ion and 106 surrounding atoms was taken from the experimental data published in [12–15]. For the γ -2 polymorph of the $[\text{Fe}(\text{bpte})(\text{NCSe})_2]$ compound [5, 6] we take into consideration that the unit cell contains 8 Fe^{II} ions of 2 types with the equal number of ions of each type which are referred further on as Fe1 and Fe2. The latter differ in the geometrical structure of the ligand surrounding consisting of 40 atoms and are expected to give a distinguished picture of the spin transformation.

Further on we demonstrate that the single point energies for iron(II) states with different spin values calculated with the aid of the variable temperature experimental structural data [5, 12–15] allow to reproduce the course of the spin transformation and to construct a transparent picture of this transformation in the above mentioned compounds.

3 Results and Discussion

First in the range of temperatures 10–295 K the single point energies $\varepsilon(s)$ of the thoroughly characterized $[\text{Fe}(\text{ptz})_6](\text{BF}_4)_2$ complex [7] are evaluated for spin values $s = 0, 1$ and 2 of the iron(II) ion in the N_6 surrounding. The obtained results presented in Fig. 1 show that at temperatures $T = 10$ K and 84 K the ground is the state of the complex corresponding to the spin $s = 0$ (*low-spin*(*ls*)-state) of the iron(II) ion, it is followed by the states with spin values $s = 1$ and 2 (*high-spin*(*hs*)-state) of this ion. At that the difference between the single point energies complying with the spin values $s = 0$ and $s = 1, 2$ remains practically unchanged at these temperatures. The minimal single point energy of the complex at 140 K corresponds to the spin value $s = 2$ of the Fe^{II} ion testifying the occurrence of SCO. The obtained result is in agreement with the experimental data on the magnetic susceptibility and Mössbauer spectra of the $[\text{Fe}(\text{ptz})_6](\text{BF}_4)_2$ compound [15] which show, respectively, an almost complete spin transition at 140 K. The

calculations also confirm that at temperatures higher than 140 K the iron(II) ion is in the state with $s = 2$. At the same time the single point energy of the complex corresponding to the spin value $s = 1$ changes insignificantly from 9978 to $10,000$ cm^{-1} in the temperature range 10 – 84 K, and it is in between the energies corresponding to spin values $s = 0$ and $s = 2$ of the iron(II) ion. Then this energy decreases up to 5067 cm^{-1} at 140 K and falls into the diapason 5711 – 5930 cm^{-1} in the temperature range 195 – 295 K, remaining in the whole temperature range higher than the single point energy of the complex with the Fe^{II} ion in the $s = 0$ state. From the calculations it follows that the spin transformation in the $[\text{Fe}(\text{ptz})_6](\text{BF}_4)_2$ complex occurs with the participation of states with $s = 0, 2$ confirming thus the commonly accepted picture of spin conversion in the $[\text{Fe}(\text{ptz})_6](\text{BF}_4)_2$ compound.

Since the performed calculations allow to reproduce correct the spin transformation in the $[\text{Fe}(\text{ptz})_6](\text{BF}_4)_2$ compound further the γ -polymorph of the $[\text{Fe}(\text{bpte})(\text{NCSe})_2]$ compound [5, 6] is examined in the same way. In Fig. 2 the single point energies for the Fe1 and Fe2 ions corresponding to $s = 0, 1, 2$ are presented in the ascending order for different temperatures. From Fig. 2 it is seen that both types of iron(II) ions in the γ -polymorph undergo SCO. Up to 180 K inclusive (Fig. 2a) the ground state of the Fe1-ion is diamagnetic. At the same time with temperature rise from 100 to 150 K the single point energies complying with spin values $s = 1$ and 2 of the Fe1-ion become lower, herewith the energies with $s = 0, 1$ and 2 are in the ascending order. At 180 K this order changes, and the single point energy of the Fe1 complex corresponding to the spin value $s = 2$ of the Fe^{II} ion is in between the energies complying with $s = 0$ and 1 . Finally, at 200 K the *hs*-state becomes the ground one thus testifying the occurrence of spin crossover in the Fe1

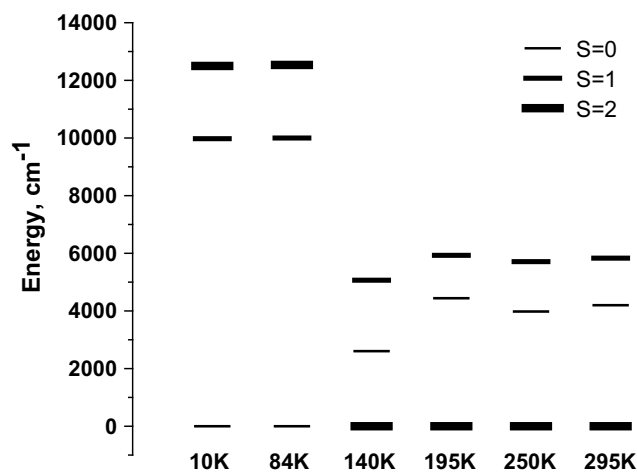


Fig. 1 Temperature dependence of the single point energies corresponding to spin values $s = 0, 1, 2$ of the iron(II) ion in the $[\text{Fe}(\text{ptz})_6](\text{BF}_4)_2$ compound

ion. Thus the DFT calculations show that the Fe1 ion changes its ground spin state in between 180 and 200 K. The *ls*-*hs* transition in the Fe2 ion occurs in a similar way but at a higher temperature as compared with that for the Fe1 ion (Fig. 2b). This temperature is in between 200 and 250 K. A more precise determination of the spin transition temperature for both ions will be possible if the structural data as a function of temperature are given with a smaller temperature step, especially for the Fe2 species. In spite of this the results presented in Fig. 2 together with the observed thermal variation of the *hs*-fraction [6] allow to restore the qualitative picture of spin transformation in the γ -polymorph of compound [Fe(bpte)(NCSe)₂] [6]. Up to 190 K the observed increase of the *hs*-fraction occurs on the account of the Fe1 ions for which the calculated difference between the single point energies of the complex corresponding to spin values $s = 0$ and 2 noticeably diminishes with rising temperature from 100 to 180 K as compared with that for the

Fe2 ion (Fig. 2b) and in between 180 and 200 K the *hs*-state is proved by the calculations to become the lowest one. In favor of this explanation is also the observed value 0.5 of the *hs* fraction at $T = 190$ K [6] which shows that only a half of ions in the unit cell has passed into the *hs*-state. For temperatures higher than 190 K the quite sharp growth of the *hs*-fraction is assured by the Fe2 ions. Actually already at 250 K the spin transition becomes complete because both type ions have passed to the *hs*-state (Fig. 2).

4 Conclusions

In the present paper the problem of SCO in iron(II) compounds has been examined within the framework of the DFT method. The suggested approach is based on the calculation of the single point energies as functions of temperature. The input for the task is represented by the variable temperature structural data. To be sure that the suggested approach gives reasonable results first the study of SCO in the well characterized [Fe(ptz)₆](BF₄)₂ compound has been performed, and a clear picture of spin transformation in this compound has been obtained which is in agreement with the experimental data [7]. Then the approach was applied to the explanation of the spin transformation in the γ -polymorph of the [Fe(bpte)(NCSe)₂] compound that contains in the unit cell two structurally different types of iron ions. For this polymorph it has been proved that both ions demonstrate spin crossover but at different temperatures. This assures the qualitative interpretation of the observed temperature transformation of the *hs*-fraction [6] in the compound. It should be also mentioned that in the framework of the suggested approach to the study of spin crossover the temperature dependence of the *hs*-state population can be restored for each compound with the aid of variable temperature structural data in the case if these data are known in a wide range of temperatures with a small temperature step.

Acknowledgements The financial support of the Science and Technology Center in Ukraine (STCU project N 6219) and of the Ministry of Education, Culture and Research of Moldova (project 15.817.02.06F) is highly appreciated.

Conflict of Interest The authors declare that they have no conflict of interest.

References

1. Cambi, L., Szego, L.: Über die magnetische Suszeptibilität der komplexen Verbindungen. Ber. Dtsch. Chem. Ges. **64**, 2591–2598 (1931). <https://doi.org/10.1002/cber.19310641002>
2. Cambi, L., Szego, L.: Über die magnetische Suszeptibilität der komplexen Verbindungen (II. Mitteil.). Ber. Dtsch. Chem. Ges. **66**, 656–661 (1933). <https://doi.org/10.1002/cber.19330660508>

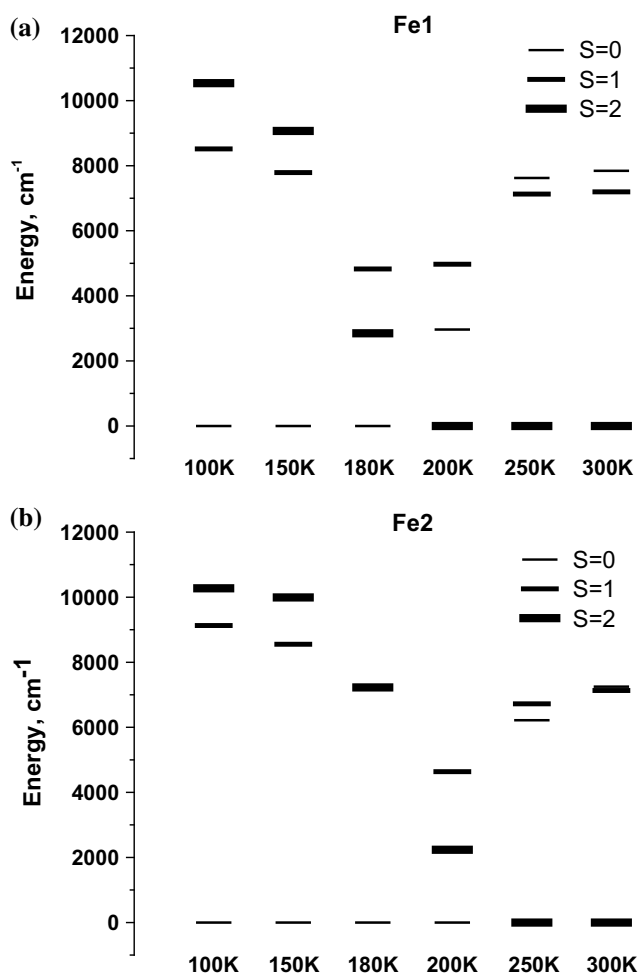


Fig. 2 Temperature dependence of the single point energies corresponding to spin values $S = 0, 1$ and 2 of the two iron(II) species in the γ polymorph of the [Fe(bpte)(NCSe)₂] compound: **a** Fe1—species, **b** Fe2—species

- Baker, W.A., Bobonich, H.M.: Magnetic properties of some high-spin complexes of iron(II). *Inorg. Chem.* **3**, 1184–1188 (1964). <https://doi.org/10.1021/ic50018a027>
- Boinnard, D., Bousseksou, A., Dworkin, A., et al.: Two-step spin conversion of $[\text{Fe}^{\text{II}}(5\text{-NO}_2\text{-sal-N}(1,4,7,10))]$: 292, 153, and 103 K X-ray crystal and molecular structure, infrared, magnetic, Moessbauer, calorimetric, and theoretical studies. *Inorg. Chem.* **33**, 271–281 (1994). <https://doi.org/10.1021/ic00080a015>
- Lennarson, A., Bond, A.D., Piligkos, S., McKenzie, J.: Four-site cooperative spin crossover in a mononuclear FeII complex. *Angew. Chem. Int. Ed.* **51**, 11049–11052 (2012). <https://doi.org/10.1002/anie.201204207>
- Arroyave, A., Lennartson, A., Dragulescu-Andrasi, A., Pedersen, K.S., et al.: Spin crossover in Fe(II) complexes with N_4S_2 coordination. *Inorg. Chem.* **55**, 5904–5913 (2016). <https://doi.org/10.1021/acs.inorgchem.6b00246>
- Jung, J., Schmitt, G., Wiehl, L., et al.: The cooperative spin transition in $[\text{Fe}_x\text{Zn}_{1-x}(\text{ptz})_6](\text{BF}_4)_2$: II. Structural properties and calculation of the elastic interaction. *Z. Phys. B* **100**, 523–534 (1996). <https://doi.org/10.1007/s002570050157>
- Neese, F.: The ORCA program system. *WIREs Comput. Mol. Sci.* **2**, 73–78 (2012)
- Becke, A.: A new mixing of Hartree-Fock and local density-functional theories. *J. Chem. Phys.* **98**, 1372–1377 (1993). <https://doi.org/10.1063/1.464304>
- Weigend, F., Ahlrichs, R.: Balanced basis sets of split valence, triple zeta valence and quadruple zeta valence quality for H to Rn: design and assessment of accuracy. *Phys. Chem. Chem. Phys.* **7**, 3297–3305 (2005). <https://doi.org/10.1039/B508541A>
- Pantazis, D., Neese, F.: All-electron scalar relativistic basis sets for the 6p elements. *Theor. Chem. Acc.* **131**, 1292 (2012)
- Kusz, J., Spiering, H., Gülich, Ph: The deformation tensor ε of the spin transition in the mixed crystal $[\text{Fe}_{0.46}\text{Zn}_{0.54}(\text{ptz})_6](\text{BF}_4)_2$. *J. Appl. Cryst.* **37**, 589–595 (2004). <https://doi.org/10.1107/S0021889804011720>
- Kusz, J., Zubko, M., Neder, R.B., Gülich, Ph: Structural phase transition to disorder lowtemperature phase in $[\text{Fe}(\text{ptz})_6](\text{BF}_4)_2$ spin-crossover compounds. *Acta Cryst. Sect. B* **B68**, 40–56 (2012). <https://doi.org/10.1107/S0108768111053298>
- Ozarowski, A., McGarvey, B.R.: EPR study of manganese(II) and copper(II) in single crystals of the spin-crossover complex $\text{Fe}(\text{PTZ})_6(\text{BF}_4)_2$. *Inorg. Chem.* **28**, 2262–2266 (1989). <https://doi.org/10.1021/ic00311a005>
- Wiehl, L.: Structures of hexakis(1-propyltetrazole)iron(II) bis(tetrafluoroborate), $[\text{Fe}(\text{CHN}_4\text{C}_3\text{H}_7)_6](\text{BF}_4)_2$, hexakis(1-methyltetrazole)iron(II) bis(tetrafluoroborate), $[\text{Fe}(\text{CHN}_4\text{CH}_3)_6](\text{BF}_4)_2$, and the analogous perchlorates. Their relation to spin crossover behaviour and comparison of Debye-Waller factors from structure determination and Mössbauer spectroscopy. *Acta Cryst. Sect. B* **B49**, 289–303 (1993). <https://doi.org/10.1107/S0108768192009042>

Change in Microstructure and Magnetic Properties of Transition Metal Nitride Thin Films by Substrate Temperature

M. Kamp, L. Voß, T. Bichel, M. Hicke, U. Schürmann, and L. Kienle

Abstract

The magnetic and mechanical properties of transition metal nitrides can be altered in many ways by their composition and microstructure, thus giving them excellent usability for spintronics and corrosion resistant coatings. The production of binary and ternary nitride thin films by reactive sputter deposition provides a wide variety of unique material combinations. This study shows the considerable influence of the substrate temperature on microstructure and magnetic properties for different nitride compounds (Fe–N, Ni–N, Fe–Ni–N, and Fe–Al–N). The substrate temperature is found to be a significant parameter which allows adjusting the phase formation and magnetic properties from soft ferromagnetic to superparamagnetic. Furthermore, the extent and incidence of texturing as well as the transition from poly- to monocrystalline thin films can be controlled.

Keywords

Nitrides • Thin film • Substrate temperature

1 Introduction

Transition metal nitrides are of great interest due to their electrical, mechanical and magnetic properties, which can be strongly influenced by the nitrogen content of the respective phase [1]. They are used in corrosion, optical coatings [2] and as diffusion barriers [3]. In addition, the binary iron-nitrogen compounds including metastable α' -Fe₁₆N₂, γ' -Fe₄N and ϵ -Fe₃N possess advantageous magnetic properties that have motivated research groups to conduct

M. Kamp · L. Voß · T. Bichel · M. Hicke · U. Schürmann
Synthesis and Real Structure, Institute for Materials Science,
Christian-Albrechts-Universität Kiel, Kiel, Germany

L. Kienle (✉)
Institute for Materials Science, Kaiserstraße 2, Kiel, Germany
e-mail: lk@tf.uni-kiel.de

experimental and theoretical studies for many years [4, 5]. The extension to ternary nitride thin films enables potential applications in data storage [6], spintronics and catalysis [7]. For the synthesis of transition metal nitrides, the nitridization of transition metals at elevated temperatures in ammonia and hydrogen atmosphere is frequently applied [5, 8]. Deposition of thin films by reactive magnetron sputtering allows an advanced film thickness control, by deposition power and time, without the use of highly reactive gases, but the deposition parameters have to be slightly adjusted especially for the synthesis of ternary transition metal nitrides by reactive co-sputtering. The microstructure of the film is mainly influenced by the substrate temperature (T_s) and substrate material, while the stoichiometry is ruled by the partial pressure of the reactive gas species [9, 10]. Higher T_s increases the grain size by enhanced (surface) diffusion processes, but for reactive sputtering of metastable transition metal nitrides, there is a threshold of the T_s at which a metallic film is formed [11]. Depending on the class of material, the change in T_s alone can also have a major influence on the composition and microstructure of the film, influenced by the temperature dependent atomic sticking coefficient. In this work, we present a systematic examination of the influence of T_s on the synthesis of binary Fe–N and Ni–N as well as ternary nitride thin films (Fe–Ni–N, Fe–Al–N).

2 Materials and Methods

The thin films are deposited in a homemade chamber by reactive magnetron sputtering with a mixture of Ar and N₂ gas (Linde 5.0). The magnetron (thin film consulting, IX2U-9A307-04) is mounted in an angle of 57° and a substrate distance of 100 mm is selected. The gas pressure is adjusted by MKS MF1 mass flow controllers, resulting in a sputtering pressure of 5.7×10^{-3} mbar. The base pressure of the chamber is 5.3×10^{-8} mbar. Fe–N and Ni–N are synthesized with a ratio of 7.5 and 80% N₂ in the sputter gas,

respectively. The samples are deposited on a carbon film (TEM grids, Plano GmbH), SrTiO₃ (001) or NaCl (001) substrates, which are dissolved in methanol to produce free-standing thin films. The electron diffraction patterns are recorded at an FEI Tecnai G² F30 STwin with an acceleration voltage of 300 kV and Cs = 1.2 mm. The magnetic characterizations are operated with a Lakeshore 7400 Series vibrating-sample magnetometer (VSM) with a maximum external field of 20 T.

3 Results and Discussion

Ni₃N shows a distorted hexagonal closed packed structure (hcp, space group *P*6₁22) of Ni atoms with N-atoms occupying octahedral cavities. This phase is deposited by magnetron sputtering with a layer thickness of 30 nm at different T_s . The main focus of our examinations, for these samples, is on differences in the microstructures, which was analyzed by electron diffraction. The diffraction patterns (Fig. 1a, b) show intensities on concentric rings, which can be clearly assigned to the Ni₃N phase. With increasing T_s , individual reflection intensity starts segregating on the rings, which indicates an increase of the grain size. At $T_s = 350$ °C (Fig. 1c), additional reflections appear that can be assigned to metallic Ni. Consequently, there is a threshold T_s above which the thin layers are metallic due to metastability of the transition metal nitride layer. On the basis of TEM bright field images (not shown), the average grain sizes were determined, which increase from 17 nm ($T_s = 25$ °C) to 27 nm ($T_s = 400$ °C). The grain sizes in Ni–N films can be successfully increased by the T_s , however, there is an intrinsic limitation due to the metallization of the films from 300 °C onwards. Corresponding limitations are expected for the Fe–N system at $T_s > 450$ °C.

Figure 1d, e shows electron diffraction patterns for Fe–N samples deposited at increasing T_s . By assigning the intensity on concentric rings to the resulting phases it becomes clear that T_s determines not only the microstructure but also the finally obtained iron nitride phases. At lower T_s , a mixture of Fe₃N (trigonal) and γ' -Fe₄N is obtained at N₂ partial pressure of 7.5%. γ' -Fe₄N crystalizes in a stable anti-perovskite structure (space group *Pm*-3 *m*). The iron atoms form a cubic fcc structure with N-atoms occupying octahedral cavities. The range of composition for ϵ -Fe_{3-x}N goes from $x = 0$ to 0.99. The crystal structure is based on nitrogen atoms occupying the octahedral sites in a hexagonal closed packed structure of Fe atoms (space group *P*6₃22). With increasing nitrogen content the symmetry is lowered to *P*312. A transformation to a single phase of hexagonal

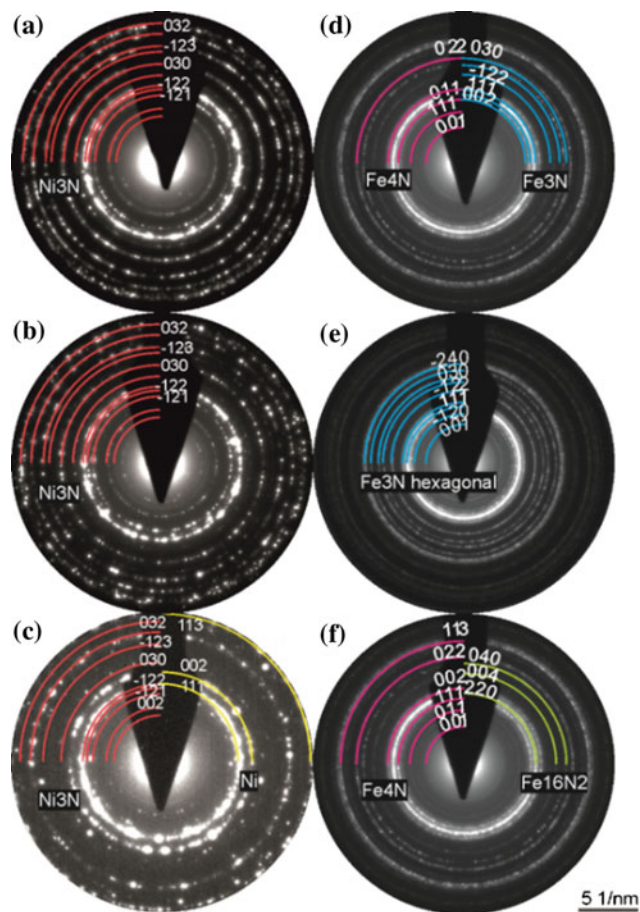


Fig. 1 Electron diffraction patterns of Ni–N thin films at different substrate temperatures, **a** 25 °C, **b** 300 °C and **c** 400 °C are shown and respective phases are indicated. Electron diffraction patterns of the Fe–N thin films at **d** 25 °C, **e** 350 °C and **f** 450 °C

ϵ -Fe₃N is obtained at 350 °C, while the grain sizes are slightly increased. A second transformation to Fe₁₆N₂ and γ' -Fe₄N occurs at 450 °C with almost constant grain sizes. Fe₁₆N₂ has a large unit cell with a complex bct structure that results from a distortion of the bcc α -Fe structure with *I*4/*mmm* space group. For the sample at 350 °C, the largest grain sizes are measured, that could be assigned to a single phase.

In addition to T_s , the surface energy can be changed during the deposition process by the substrate material itself. In the following, we have investigated the influence of NaCl and SrTiO₃ substrates on the film microstructure with equivalent sputter parameters to those specified for the carbon (TEM grid) substrate. By using monocrystalline substrates, the growth of epitaxial thin films can be achieved, whereby the properties can be decisively changed in their isotropy. The texturing of Ni₃N thin films, deposited on

NaCl (001) substrates is indicated by the electron diffraction patterns in Fig. 2a–c. Based on the non-uniform intensity distribution on the diffraction rings and the absence of some intensities, a texturing in [101] zone axis can be inferred, which enhances with increasing T_s . The absence of reflections [e.g. (−131)] in Fig. 2c underlines an increased texturing compared to Fig. 2a. The majority of the faceted grains ($T_s = 300$ °C) is aligned according to the texturing in [101] zone axis. A high-resolution TEM micrograph of a single grain is shown in Fig. 2d (center), with the corresponding FFT in [101] zone axis (2 d, bottom). Surprisingly, at 200 °C, multiple reproductions of the sample confirm that no texturing was present. The lack of texture at 200 °C could be due to an increase in the nucleation rate. The measured

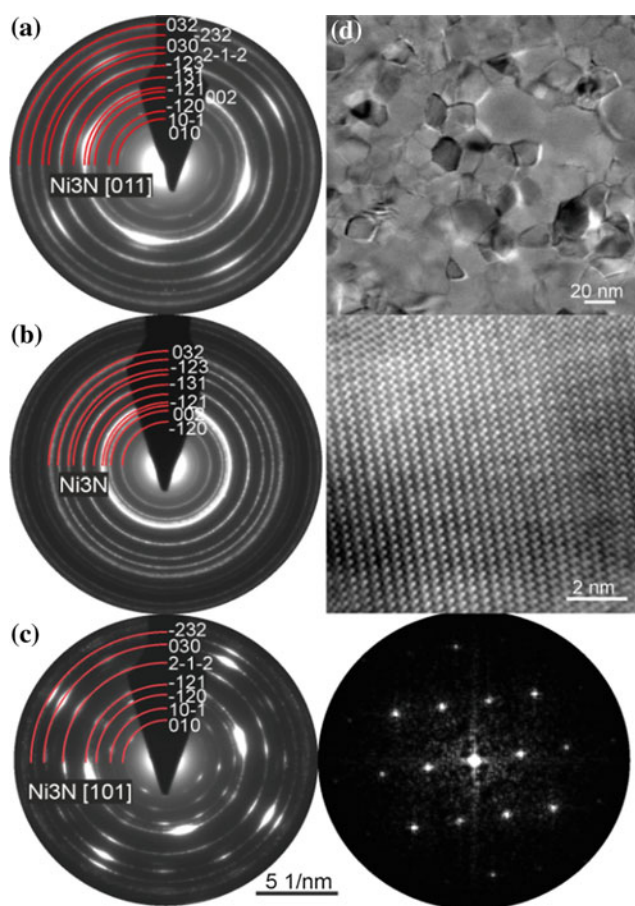


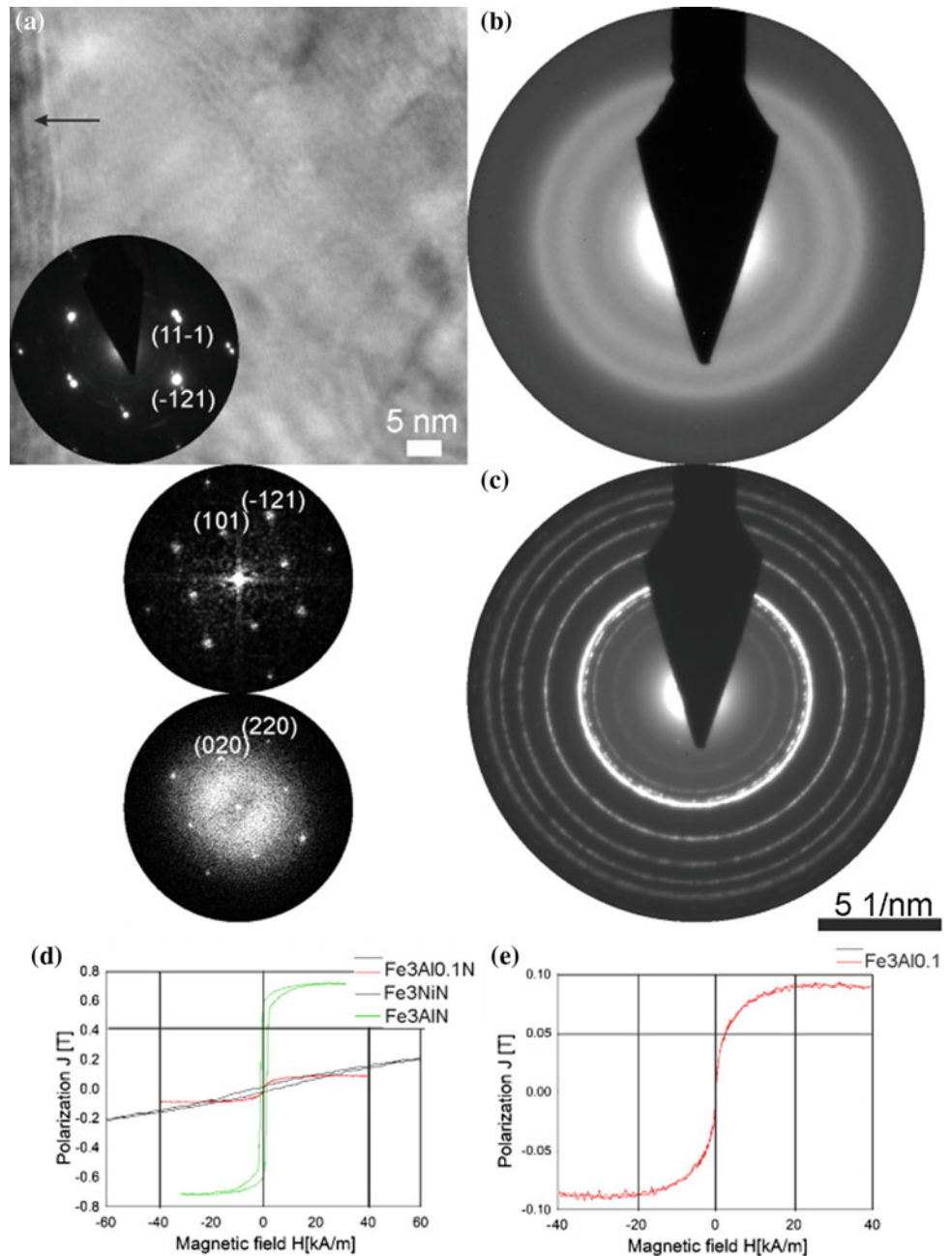
Fig. 2 Electron diffraction patterns of Ni_3N thin films deposited on NaCl substrates at **a** 25 °C, **b** 200 °C and **c** 300 °C. A [101] texture for **a** and **c** is observed due to the intensity distribution on concentric diffraction rings. The absence of reflections [e.g. (−131)] in (c) indicates increased texturing. **d** A TEM overview image of the sample at $T_s = 300$ °C (top). Center and bottom: a high-resolution TEM micrograph of a single grain and the corresponding Fast Fourier Transform, both for zone axis [101]

grain sizes are smallest for this sample supporting the increased nucleation rate, whereby the extremely significant influence of T_s becomes evident again.

Atiq et al. [12] synthesized single crystalline γ' - Fe_4N thin films on MgO substrates to analyze the impact of substrate material on the magnetic properties, furthermore, SrTiO_3 and NaCl substrates were investigated [13, 14]. In our study, we successfully demonstrated the deposition of single crystalline ϵ - Fe_3N on SrTiO_3 (001). The systematic variation of the deposition parameters allows the selective deposition of a ϵ - Fe_3N film with equal deposition parameters. A diffraction pattern of ϵ - Fe_3N [101] is given as an inset (Fig. 3a) and the orientation relationship is represented by the Fast Fourier Transformations (bottom), i.e., (−121) of ϵ - Fe_3N and (220) of SrTiO_3 [001] show the same orientation and comparable plane distances of 1.97 Å and 1.95 Å, respectively. The agreement of these distances is indicating an excellent match of the structures and can be a decisive factor for the deposition of epitaxial or monocrystalline layers.

The ϵ - Fe_3N phase is used as a starting material to investigate the microstructure and phase formation of ternary Fe_xMN ($M = \text{Al}, \text{Ni}$) materials by co-sputtering. This approach offers a wide range of possible changes in microstructures and properties. We adjusted the deposition parameters to extend a molar ratio of $M/\text{Fe} = 0.33$. The addition of Al results in a nanocrystalline microstructure with amorphous fractions (Fig. 3b, diffuse intensity distribution), while the addition of Ni preserves the microstructure, suggesting the substitution of Fe atoms by Ni atoms in the ϵ - Fe_3N structure (Fig. 3c). The drastic change of the magnetic properties is summarized in Fig. 3d (with a nominal composition of Fe_3NiN , Fe_3AlN , and $\text{Fe}_3\text{Al}_{0.1}\text{N}$). For both samples, saturation polarization and remanence are drastically reduced. The sample with Al shows no detectable remanence, indicating superparamagnetic properties. The precondition for the effect of superparamagnetism is given by the particle diameter in the nanometer regime. If the thermal energy is larger than the magnetic anisotropy energy of a single domain particle, its magnetization direction randomly switches. The result is the loss of spontaneous magnetization and remnant polarization. In addition, the exchange coupling between the particles must be prevented. The present non-ferromagnetic matrix (γ'' - FeN/β - AlN) can be responsible for this behavior. A possible microstructure that fits the electron diffraction pattern and the magnetic measurements may contain grains of ϵ - Fe_3N and γ' - Fe_4N in a matrix of γ'' - FeN/β - AlN , both are neither ferromagnetic or ferrimagnetic. This special microstructure was exclusively investigated for $T_s = 300$ °C, while marginal deviations from this temperature result in larger grain sizes with ferromagnetic properties.

Fig. 3 a Interface (arrow) of SrTiO₃ and Fe₃N thin film, the inset indicates an electron diffraction pattern of a single crystalline ϵ -Fe₃N phase in [101] zone axis orientation. The orientation relationship is represented by the Fast Fourier Transformations (bottom), (-121) of ϵ -Fe₃N and (220) of SrTiO₃ [001], show the same orientation. The electron diffraction patterns of Fe–Al–N and Fe–Ni–N are depicted in (b) and (c), respectively. Magnetic hysteresis loops are plotted in (d) and the superparamagnetic loop of Fe₃Al_{0.1}N is magnified in (e)



4 Conclusions

The deposition of crystalline nitride thin films requires a precise examination of the sputtering parameters. In this study, the influence of T_s and the associated shift of surface energy during the manufacturing process were investigated. Depending on the material system, this may cause microstructure as well as constituting phase changes. The grain size of Ni₃N films can be increased from 17 to 27 nm, a

change of the substrate resulted in a significant texturing of the film, surprisingly, the texturing is absent at intermediate temperature. For the Fe–N system, T_s triggered a change from γ' -Fe₄N and Fe₃N over ϵ -Fe₃N (hexagonal) to Fe₁₆N₂. By using a SrTiO₃ substrate a monocrystalline ϵ -Fe₃N film, with a defined orientation relationship, could be produced. By adding another substitutional element, massive influence can be exerted on the magnetic properties and the microstructure. The production of superparamagnetic Fe–Al–N thin films is indicated by electron diffraction and VSM measurements.

Acknowledgements We thank Christin Szillus for the sample preparation. We would also like to thank Prof. Dr. Andreas Leineweber for fruitful discussions.

Conflict of Interest The authors declare that they have no conflict of interest.

References

1. Vempaire, D., Miraglia, S., Pelletier, J., et al.: Structural and magnetic properties of Ni₃N synthesized by multipolar microwave plasma-assisted reactive sputtering. *J. Alloys Compd.* **2**, 225–229 (2009)
2. Gibson, J., Holiday, L.F., Allwood, D.A., et al.: Enhanced longitudinal magneto-optic Kerr effect contrast in nanomagnetic structures. *IEEE Trans. Magn.* **43**, 2740–2742 (2007)
3. Lingwal, V., Panwar, N.S.: Scanning magnetron-sputtered TiN coating as diffusion barrier for silicon devices. *J. Appl. Phys.* **97**, 104902 (2005)
4. Mosca, D.H., Dionisio, P.H., Schreiner, W.H., et al.: Compositional and magnetic properties of iron nitride thin films. *J. Appl. Phys.* **67**, 7514–7519 (1990)
5. Bartłomiej, W., Arabczyk, W.: Investigation of nitriding and reduction processes in a nanocrystalline iron–ammonia–hydrogen system at 350 C. *Phys. Chem. Chem. Phys.* **17**, 20185–20193 (2015)
6. Loloee, R.: Epitaxial Ni₃FeN thin films: a candidate for spintronic devices and magnetic sensors. *J. Appl. Phys.* **112**, 023902 (2012)
7. Gu, Y., Chen, S., Ren, J., et al.: Electronic structure tuning in Ni₃FeN/r-GO aerogel toward bifunctional electrocatalyst for overall water splitting. *ACS Nano* **12**, 245–253 (2018)
8. Leineweber, A., Lienert, F., Shang, S., et al.: Ni₃N compound layers produced by gaseous nitriding of nickel substrates; layer growth, macrostresses and intrinsic elastic anisotropy. *J. Mater. Res.* **27**, 1531–1541 (2012)
9. Wang, X., Zheng, W.T., Tian, H.W., et al.: Effect of substrate temperature and bias voltage on DC magnetron sputtered Fe–N thin films. *J. Magn. Magn. Mater.* **283**, 282–290 (2004)
10. Schwille, M., Oettel, M., Bartha, J.: Temperature dependence of the sticking coefficients of bis-diethyl aminosilane and trimethylaluminum in atomic layer deposition. *J. Vac. Sci. Technol. Vac. Surf. Films* **35**, 01B119 (2016)
11. Lindhal, E., Ottosson, M., Carlsson, J.: In situ study of nickel formation during decomposition of chemical vapor deposition Ni₃N films. *J. Vac. Sci. Technol. Vac. Surf. Films* **28**, 1203–1209 (2010)
12. Atiq, S., Ko, H., Siddiqi, S., et al.: Effect of epitaxy and lattice mismatch on saturation magnetization of γ' -Fe₄N thin films. *Appl. Phys. Lett.* **92**, 222507 (2008)
13. Nikolaev, K., Krivorotov, I., Dahlberg, E., et al.: Structural and magnetic properties of triode-sputtered epitaxial γ' -Fe₄N films deposited on SrTiO₃ (001) substrates. *Appl. Phys. Lett.* **82**, 4534–4536 (2003)
14. Na, Y., Wang, C., Xiang, J., et al.: Investigation of gamma'-Fe₄N thin films deposited on Si(100) and GaAs (100) substrates by facing target magnetron sputtering. *J. Cryst. Growth* **426**, 117–122 (2015)

Modeling of Charge Transfer Induced Spin Transition in a Linear {FeCoFe} Complex

S. M. Ostrovsky and S. I. Klokishner

Abstract

The magnetic behavior of the $\{[\text{FeTp}(\text{CN})_3]_2\text{Co}(\text{Meim})_4\} \cdot 6\text{H}_2\text{O}$ compound is examined. Since the observed charge transfer induced spin transition in this compound is accompanied by electronic density redistribution, the theoretical model includes the electron transfer between the Fe and Co ions and two types of cooperative interactions, namely, the electron-deformational and dipole-dipole interactions. It is demonstrated that at low temperatures the spin transformation in the compound under study is accompanied by the appearance of macroscopic polarization. The developed model gives a quite good explanation of the observed effective magnetic moment.

Keywords

Charge transfer induced spin transition (CTIST) • Macroscopic polarization • Electron transfer • Cooperative dipole-dipole interaction

1 Introduction

The study of compounds with tunable magnetic and optical properties is of great interest due to the possibility of their application in quantum electronics as optical and magnetic switches [1–7]. In these systems the change of the magnetic state under action of external stimuli (external electric and/or magnetic fields, temperature, pressure) manifests itself in the observed magnetic and spectroscopic characteristics. Recently the attention of researchers has been switched to a new type of compounds in which the significant change in the magnetic properties due to the intramolecular electron transfer is accompanied by polarization switching inside a

molecule. These systems manifesting a strong interconnection between their magnetic and polarization characteristics open the possibility for design of new switchable multifunctional materials.

The bimetallic neutral $\{[\text{FeTp}(\text{CN})_3]_2\text{Co}(\text{Meim})_4\}$ (Tp = hydrotris(pyrazol)borate, Meim = *N*-methylimidazole) compound was the first one showing both thermally and photoinduced electron transfer together with reversible polar-nonpolar transformation. The synthesis, crystal structure and magnetic behavior of this compound are presented elsewhere [8]. At high temperatures the trimeric complex consists of one high spin (*hs*) Co^{II} ion and two low spin (*ls*) Fe^{III} ions. With the temperature decrease the charge transfer converts Co^{II} into Co^{III} ions and parts of Fe^{III} into Fe^{II} ions, charge transfer occurs randomly on the two iron sites. Low temperature Mössbauer spectra demonstrate equal amount of Fe^{II} and Fe^{III} species confirming thus a complete charge transfer. All ions are in the *ls* configurations.

In the present contribution a theoretical model to the study of driven by temperature spin transition in trinuclear Fe–Co–Fe complexes is developed. Based on this model, the significant change in the magnetic and polarization properties of the $\{[\text{FeTp}(\text{CN})_3]_2\text{Co}(\text{Meim})_4\} \cdot 6\text{H}_2\text{O}$ compound is explained.

2 Model

Three electronic configurations of the linear Fe–Co–Fe trimer are regarded, namely, $\text{Fe}_{\text{ls}}^{\text{III}}-\text{Co}_{\text{ls}}^{\text{III}}-\text{Fe}_{\text{ls}}^{\text{II}}$, $\text{Fe}_{\text{ls}}^{\text{III}}-\text{Co}_{\text{ls}}^{\text{II}}-\text{Fe}_{\text{ls}}^{\text{III}}$ and $\text{Fe}_{\text{hs}}^{\text{III}}-\text{Co}_{\text{hs}}^{\text{II}}-\text{Fe}_{\text{ls}}^{\text{III}}$. The $\text{Co}_{\text{ls}}^{\text{III}}$ and $\text{Fe}_{\text{ls}}^{\text{II}}$ ions are diamagnetic, while the $\text{Co}_{\text{ls}}^{\text{II}}$ and $\text{Fe}_{\text{ls}}^{\text{III}}$ ions are regarded as pseudo-spins 1/2 due to strong Jahn-Teller effect and strong spin-orbital coupling, respectively. As for the $\text{Co}_{\text{hs}}^{\text{II}}$ ion, it is assumed that the nearest ligand surrounding of this ion is strongly distorted from the octahedral one, so this ion can be treated as a spin-only $s = 3/2$ system [9].

S. M. Ostrovsky · S. I. Klokishner (✉)
Institute of Applied Physics, Academy Str. 5,
Chişinău, Republic of Moldova
e-mail: klokishner@yahoo.com

The crystal Hamiltonian of the system under examination can be written as

$$\mathbf{H} = \mathbf{H}_0 + \mathbf{H}_{st} + \mathbf{V}_{dd} \quad (1)$$

where the first term represents the Hamiltonian of non-interacting clusters (crystal fields of the nearest ligands acting on the metal ions, intra-center Coulomb interactions, the electron transfer between the ls Fe and ls Co ions), the second one is the intermolecular electron-deformational interaction between trimeric clusters in the crystal and the last part is the intermolecular dipole-dipole interaction.

The joint effect of the crystal field of the nearest ligands and intra-center Coulomb interactions is accounted with the use of two Δ_i ($i = 1, 2$) parameters where Δ_1 and Δ_2 are the energies of the $\text{Fe}_{ls}^{\text{III}}-\text{Co}_{ls}^{\text{II}}-\text{Fe}_{ls}^{\text{III}}$ and $\text{Fe}_{ls}^{\text{III}}-\text{Co}_{hs}^{\text{II}}-\text{Fe}_{ls}^{\text{III}}$ configurations of trimer, respectively, counted from the energy of the $\text{Fe}_{ls}^{\text{III}}-\text{Co}_{ls}^{\text{III}}-\text{Fe}_{ls}^{\text{II}}$ configuration taken as an origin. The electron transfer between ls Fe and ls Co ions results in the non-diagonal matrix elements of \mathbf{H}_0 between the states of the $\text{Fe}_{ls}^{\text{III}}-\text{Co}_{ls}^{\text{III}}-\text{Fe}_{ls}^{\text{II}}$ and $\text{Fe}_{ls}^{\text{III}}-\text{Co}_{ls}^{\text{II}}-\text{Fe}_{ls}^{\text{III}}$ configurations.

The cooperative electron-deformational interaction in the crystal (\mathbf{H}_{st}) represents an infinite range interaction between the ions which undergo the spin transformation [10–12]. In the mean field approximation \mathbf{H}_{st} is decomposed into the sums of single-ion Hamiltonians [10]:

$$\mathbf{H}_{st} = -J\bar{\tau} \sum_n \tau_n \quad (2)$$

where $\bar{\tau} = \text{Tr}(\rho\tau_n)$ with ρ being the density operator and τ_n is a diagonal matrix that has a dimension of the whole basis of the problem under study:

$$\tau_n = \begin{pmatrix} I_0 & 0 & 0 \\ 0 & v_1/v_0 I_1 & 0 \\ 0 & 0 & v_2/v_0 I_2 \end{pmatrix} \quad (3)$$

In Eq. (3) v_0 , v_1 and v_2 are electron deformational coupling constants for $\text{Co}_{ls}^{\text{III}}$, $\text{Co}_{ls}^{\text{II}}$ and $\text{Co}_{hs}^{\text{II}}$ ions, respectively, and I_0 , I_1 and I_2 are the unit matrices that act in the corresponding configurations of the studied trimer (for details see [10]).

Finally, the intermolecular dipole-dipole interaction in the mean field approximation can be written as:

$$\mathbf{V}_{dd} = -L_{ZZ}\bar{d}^z \sum_n d_n^z \quad (4)$$

where $\bar{d}^z = \text{Tr}(\rho d_n^z)$ and d_n^z are diagonal matrices with matrix elements equal to d_0 , $-d_0$ for the states arising from configurations $\text{Fe}_{ls}^{\text{III}}-\text{Co}_{ls}^{\text{III}}-\text{Fe}_{ls}^{\text{II}}$, $\text{Fe}_{ls}^{\text{II}}-\text{Co}_{ls}^{\text{III}}-\text{Fe}_{ls}^{\text{III}}$, respectively. At the same time for both configurations $\text{Fe}_{ls}^{\text{III}}-\text{Co}_{ls}^{\text{II}}-\text{Fe}_{ls}^{\text{III}}$ and $\text{Fe}_{ls}^{\text{III}}-\text{Co}_{hs}^{\text{II}}-\text{Fe}_{ls}^{\text{III}}$ the matrix elements of the dipole moment are vanishing.

3 Analysis of the Experimental Data

The model presented above is applied for the description of the experimental magnetic behavior of the $\{[\text{FeTp}(\text{CN})_3]_2\text{Co}(\text{Meim})_4\} \cdot 6\text{H}_2\text{O}$ compound. To reduce the number of the independent parameters in the subsequent calculations it is set $v_1/v_0 = 1.2$ and $v_2/v_0 = 2.6$ [10] while for the electron transfer parameter the typical value of 300 cm^{-1} is accepted [13]. Figure 1 demonstrates the result of calculation of the effective magnetic moment (μ_{eff}) as a function of temperature. The values of the parameters used in the calculations are part of the Figure caption. The Landé factor for the $\text{Co}_{ls}^{\text{II}}$ ions was set equal to its usually accepted value 2, while for the $\text{Co}_{hs}^{\text{II}}$ and $\text{Fe}_{ls}^{\text{III}}$ ions these factors were determined on the base of the following considerations. For the examined abrupt spin transition accompanied by the hysteresis loop the Landé factors do not influence the behavior of the compound in the range of the spin transition temperature which is in between 221 and 230 K. In fact these factors for the Co and Fe ions affect the effective magnetic moment values at high and low temperatures and can be extracted using the experimental values of μ_{eff} in these temperature ranges. The magnitudes of the parameters Δ_1 , Δ_2 , $L_{ZZ}d_0^z$, and J are of the order of characteristic values for these parameters [10, 13]. From Fig. 1 it follows that the theoretical model describes quite well the observed curve for the effective magnetic moment in the range of low and high temperatures as well as in the range of the hysteresis loop wherein the charge transfer induced spin transition takes place and the system demonstrates bistability.

Figure 2 represents the thermal variation of the relative populations of different cluster configurations for the $\{[\text{FeTp}(\text{CN})_3]_2\text{Co}(\text{Meim})_4\} \cdot 6\text{H}_2\text{O}$ compound. It is seen that at low temperatures the majority of clusters is in the $\text{Fe}_{ls}^{\text{III}}-\text{Co}_{ls}^{\text{III}}-\text{Fe}_{ls}^{\text{II}}$ configuration, while at room temperature in

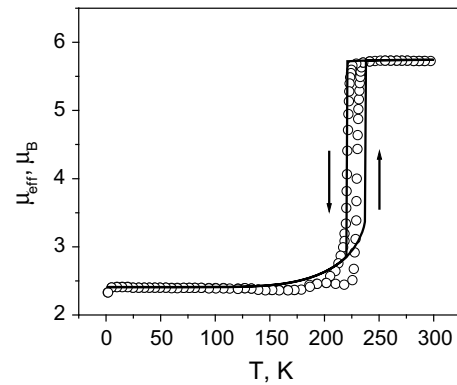


Fig. 1 Experimental μ_{eff} versus T dependence for $\{[\text{FeTp}(\text{CN})_3]_2\text{Co}(\text{Meim})_4\} \cdot 6\text{H}_2\text{O}$ (open circles [8]) and the theoretical curve calculated with $\Delta_1 = 1080 \text{ cm}^{-1}$, $\Delta_2 = 880 \text{ cm}^{-1}$, $J = 288 \text{ cm}^{-1}$, $L_{ZZ}d_0^z = 300 \text{ cm}^{-1}$, $g(\text{Co}_{hs}^{\text{II}}) = 2.8$, $g(\text{Fe}_{ls}^{\text{III}}) = 2.6$

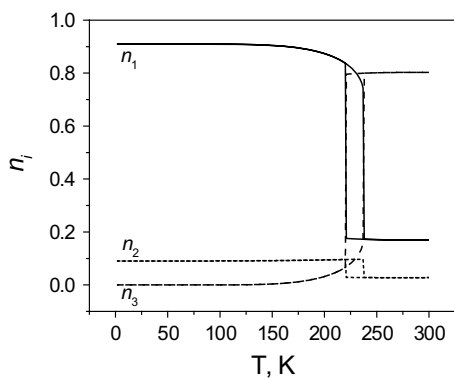


Fig. 2 Thermal variation of the populations of the $\text{Fe}_{\text{ls}}^{\text{III}}\text{-Co}_{\text{ls}}^{\text{III}}\text{-Fe}_{\text{ls}}^{\text{II}}$ (n_1 , solid curve), $\text{Fe}_{\text{ls}}^{\text{III}}\text{-Co}_{\text{ls}}^{\text{II}}\text{-Fe}_{\text{ls}}^{\text{III}}$ (n_2 , short dash curve) and $\text{Fe}_{\text{ls}}^{\text{III}}\text{-Co}_{\text{hs}}^{\text{II}}\text{-Fe}_{\text{ls}}^{\text{III}}$ (n_3 , dash curve) cluster configurations calculated with the same set of parameters as in Fig. 1

the compound under examination the number of clusters in the $\text{Fe}_{\text{ls}}^{\text{III}}\text{-Co}_{\text{hs}}^{\text{II}}\text{-Fe}_{\text{ls}}^{\text{III}}$ configuration dominates. The amount of trimers in the $\text{Fe}_{\text{ls}}^{\text{III}}\text{-Co}_{\text{ls}}^{\text{II}}\text{-Fe}_{\text{ls}}^{\text{III}}$ configuration is less than 10% at all temperatures. However, the inclusion of this configuration in the model reflects the real situation which takes place in the system under examination as well as in the systems demonstrating valence tautomerism [10, 14]. In fact the probability of charge transfer between the configurations $\text{Fe}_{\text{ls}}^{\text{III}}\text{-Co}_{\text{ls}}^{\text{III}}\text{-Fe}_{\text{ls}}^{\text{II}}$ and $\text{Fe}_{\text{ls}}^{\text{III}}\text{-Co}_{\text{hs}}^{\text{II}}\text{-Fe}_{\text{ls}}^{\text{III}}$ is much higher than that characterizing the transfer between the former configuration and the configuration $\text{Fe}_{\text{ls}}^{\text{III}}\text{-Co}_{\text{ls}}^{\text{II}}\text{-Fe}_{\text{ls}}^{\text{III}}$. Thus, the configuration $\text{Fe}_{\text{ls}}^{\text{III}}\text{-Co}_{\text{ls}}^{\text{II}}\text{-Fe}_{\text{ls}}^{\text{III}}$ represents the intermediate stage for the observed spin transition.

It is seen that the presented above model nicely describes the experimental observations on the magnetic behavior of the $\{[\text{FeTp}(\text{CN})_3]_2\text{Co}(\text{Meim})_4\} \cdot 6\text{H}_2\text{O}$ compound (Fig. 1). The calculations also demonstrate that the spin transition in this compound is accompanied by the appearance of macroscopic polarization which increases with temperature decrease.

4 Conclusions

A microscopic approach for the description of the charge transfer induced spin transition in the $\{[\text{FeTp}(\text{CN})_3]_2\text{Co}(\text{Meim})_4\} \cdot 6\text{H}_2\text{O}$ compound is presented. The spin transition is considered as a cooperative phenomenon that is driven by the interaction of electronic shells of the Co ions with the totally symmetric deformation of their local coordination environments that is extended over the crystal lattice via the

acoustic phonon field. The model also includes the electron transfer between the low spin Fe and Co ions that results in the redistribution of the electronic density inside the cluster leading thus to the cooperative dipole-dipole interaction.

Within the framework of the suggested model the experimental data on the variable temperature magnetic susceptibility were interpreted and the characteristic values of the parameters of the main interactions have been obtained from the comparison of the calculated and observed magnetic characteristics. It was demonstrated that the spin transition in the $\{[\text{FeTp}(\text{CN})_3]_2\text{Co}(\text{Meim})_4\} \cdot 6\text{H}_2\text{O}$ compound is also accompanied by the appearance of macroscopic polarization which is appreciable up to the temperature of the spin transition.

Acknowledgements The financial support of the Science and Technology Center in Ukraine (STCU project N 6219) and of the Ministry of Education, Culture and Research of Moldova (project 15.817.02.06F) is highly appreciated.

Conflict of Interest The authors declare that they have no conflict of interest.

References

1. Sanvito, S.: Molecular spintronics. *Chem. Soc. Rev.* **40**, 3336–3355 (2011)
2. Letard, J.-F., Guionneau, P., Goux-Capes, L.: Towards Spin Crossover Applications. *Top. Curr. Chem.* **235**, 221–249 (2004)
3. Kahn, O., Martinez, C.J.: Spin-transition polymers: from molecular materials TOWARD memory devices. *Science* **279**, 44–48 (1998)
4. Gamez, P., Sanchez Costa, J., Quesada, M., Aromi, G.: Iron spin-crossover compounds: from fundamental studies to practical applications. *Dalton Trans.*, 7845–7853 (2009)
5. Kahn, O., Launey, J.P.: Molecular bistability; an overview. *Chemtronics* **3**, 140–151 (1988)
6. Kahn, O., Krober, J., Jay, C.: Spin transition molecular materials for displays and data recording. *Adv. Mater.* **4**, 718–728 (1992)
7. Ruiz, E.: Charge transport properties of spin crossover systems. *Phys. Chem. Chem. Phys.* **16**, 14–22 (2014)
8. Liu, T., Dong, D.-P., Kanegawa, S., Kang, S., Sato, O., Shiota, Y., Yoshizawa, K., Hayami, S., Wu, S., He, C., Duan, C.-Y.: Reversible electron transfer in a linear Fe_2Co trinuclear complex induced by thermal treatment and photoirradiation. *Angew. Chem. Int. Ed.* **51**, 4367–4370 (2012)
9. Kahn, O.: *Molecular magnetism*. VCH Publishers, New York (1993)
10. Klokishner, S.: Cobalt valence tautomeric compounds: molecular and solid state properties. *Chem. Phys.* **269**, 411–440 (2001)
11. Klokishner, S.I., Varret, F., Linares, J.: Effect of hydrostatic pressure on phase transition in spin-crossover 1D-systems. *Chem. Phys.* **255**, 317–323 (2000)

12. Klokishner, S., Ostrovsky, S., Palii, A., Shatruk, M., Funck, K., Dunbar, K., Tsukerblat, B.: Vibronic model for cooperative spin-crossover in pentanuclear $[M^{III}(CN)_6]_2[M'^{II}(tmphen)_2]_3$ ($M/M' = Co/Fe, Fe/Fe$) Compounds. *J. Phys. Chem.* **115**, 21666–21677 (2011)
13. Roman, M., Reu, O., Klokishner, S.: Charge-transfer-induced spin transitions in crystals containing cyanide-bridged Co–Fe clusters: role of intra- and intercluster Interactions. *J. Phys. Chem. A* **116**, 9534–9544 (2012)
14. Ostrovsky, S., Palii, A., Klokishner, S., Shatruk, M., Funck, K., Achim, C., Dunbar, K.R., Tsukerblat, B.: Vibronic approach to the cooperative spin transitions in crystals based on cyano-bridged pentanuclear M_2Fe_3 ($M = Co, Os$) clusters. In: Atanasov, M., Daul, C., Tregenna-Piggott, P.L.W. (eds.) *Vibronic Interactions and the Jahn-Teller Effect: Theory and Applications*. *Progress in Theoretical Chemistry and Physics*, vol. 23, pp. 379–396. Springer (2012)

Mössbauer Effect in ^{57}Fe -Doped Gallium Antimonide

A. Mihalache

Abstract

The work offers for discussion the results of investigations of absorption spectra (gamma-ray nuclear resonance) of gallium antimonide doped with ^{57}Fe isotope in the concentration range of the atomic mass of 1–3%, within the temperature range of 4.2–300 K, in the absence of an external magnetic field. Also, a model of the impurity center of iron in gallium antimonide is described.

Keywords

GaSb • Nuclear magnetic resonance

1 Introduction

Gallium antimonide—GaSb, is a group A^{III}B^V semiconductor with a narrow energy band, small effective mass of electrons, and high mobility. GaSb can be the main material whose crystal lattice is suitable for fabricating optoelectronic devices in the range of 0.8–4.3 μm . Studies of GaSb have been progressing of late due to the growing demand in new compatible optoelectronic materials, in optic fibers of 2–4 μm . Information on the research and development of devices based on GaSb is available, for example, in Milnes and Polyakov [1], Dutta et al. [2].

The study of the behaviour of the dopants from the transition group, such as Fe, Ni, Cr, Mn, in gallium antimonide is topical and challenging. Still, physical properties of GaSb doped with elements from the transition group have not been thoroughly investigated yet.

As is known, in order to modify electrical and optical properties of specific devices it is necessary to dope the material used. This is achieved, as a rule, by diffusing the

element concerned in a semiconductor. The p-type GaSb is doped with ^{57}Fe by diffusion, because it is this isotope that is responsible for high mobility and solubility of GaSb. To control the doping with ^{57}Fe it is necessary to profoundly understand the mechanism of the diffusion of ^{57}Fe . No doubt the study of the diffusion of ^{57}Fe in GaSb is of interest in both theoretical and applied aspects.

Nowadays a variety of experimental technologies are used to study impurity atoms in semiconductors. Cutting-edge technologies of semiconductor materials make it possible to get samples that meet the requirements of practically every experimental method used in solid state physics. Most widely used are those to measure electrical conductivity, galvanomagnetic effects, photoconductivity, thermal and electrical conductivity, etc. All those methods, when used to study semiconductors, supply a lot of data on the impurity atoms in semiconductors. The methods mentioned may be called indirect methods, that is, the information obtained during the experiment concerns the charge carries but not the impurity atoms as such. The interpretation of these data, first of all, regarding the structure of the impurities centers and then the involvement, to a smaller or larger degree, of the arbitrary positions, should be very cautious and followed by the findings of direct methods.

Direct methods that can give direct information about the impurity atoms under investigation by the author of this article are: electronic paramagnetic resonance, nuclear magnetic resonance, nuclear quadrupole resonance, photoelectronic spectroscopy, perturbed angular correlation spectroscopy, etc. Among those is the Mössbauer spectroscopy, too. The role of the electronic paramagnetic resonance is well known, for example, when confirming the theory of the impurity centers in semiconductors. However those methods are not as universal as is the measurement of the electrical conductance or the Hall effect, that is, those methods mentioned above can be applicable to a limited number of semiconductor materials or impurities in them.

The features of the Mössbauer effect that allow it to compete with other direct methods are: (1) a possibility to

A. Mihalache (✉)
Tiraspol State University, 5 Gh. Iablocikin Str., Chişinău,
Republic of Moldova
e-mail: alexei.mihalache@gmail.com

obtain a number of parameters in a single experiment, which supplies direct information about impurity atoms and their surroundings; (2) an absolute selectivity of the isotope under study; (3) an insensibility to long-range rays.

In the past years, the literature in the field has accumulated a large volume of data on the impurities centers in semiconductors that became possible owing to the Mössbauer spectroscopy.

Figure 1 shows the schemes of the nuclear levels, revised and described by Mössbauer isotopes, and the schemes as the nuclear disintegration basis for these.

These schemes demonstrate the difference between the results with the absorption spectroscopy and those with the emission one, and they will be further used to illustrate the findings for certain impurities.

In both of those versions of spectroscopy there is a radioactive source that emits Mössbauer quanta when certain nuclei pass from the excited into the ground state, as well as the absorption that has the same nuclei in the ground state and can absorb radiation at a corresponding resonance frequency. More widely used is the version with the absorption, that is, the object studied is an absorber—a standard radiation source with a single emission line. The sensibility for this type of spectroscopy is up to 10^{18} at/cm³.

It is worth noting here that the emission spectroscopy allows to partially avoid one of the main bottlenecks of the Mössbauer effect—a limited number of isotopes. From the schemes of Mössbauer levels of ¹¹⁹Sn it is clear that the transition for ¹¹⁹Sn can be used for five different impurities: cadmium, indium, stannum, antimonium, tellurium Fig. 1. Nowadays, the Mössbauer effect has been found with over 40 isotopes. However in semiconductor physics only 15 isotopes could be used. It is necessary to underline here that the existing isotopes are of high importance as doping elements for many semiconductor materials.

In spite of all its advantages, emission spectroscopy has two heavy drawbacks. First, the information based on the emission spectra turned to be complicated—it refers to the parent atom according to its position in the crystal lattice, the formation of different types of associations with the lattice defects, and to the daughter atom, depending on the electronic state. Second, radioactive transformations preceding the Mössbauer transition, could change the initial position of the state of the charge of the parent atom, which leads to difficulties in treating the emission spectra [4].

The main parameters of the Mössbauer spectra that are used in the present work are: isomer shift δ (it allows to identify electronic states and the charge of the impurity atoms), quadrupole splitting Δ (it allows to determine the local symmetry of the impurity center and to draw conclusions concerning the formation of the associations of such a

center with other crystal defects), the width of the spectral line Γ (it contains the information on the weak hyperfine interactions).

2 Discussion of Experimental Results

Gallium antimonide doped with ⁵⁷Fe, under investigation in this article, was obtained in the following way: first, the synthesis of GaSb in evacuated fused quartz ampoules, with pure Ga and Sb as well as Fe dopants in predetermined concentrations was carried out. Then the container with the respective components was placed in an electric furnace (with the T kept at 9000 °C), connected to the mechanical vibrator at the frequency of 50 Hz. Under the experimental conditions mentioned above, the synthesis took 24 h; then the electric furnace with the container was left for cooling. The following step in the technological process was the homogenisation and the growth of single crystals in an installation for zone melting.

Interesting physical phenomena have been revealed while investigating more profoundly (a) the properties of gallium antimonide doped with transition elements, and (b) gamma-ray nuclear resonance—the Mössbauer effect—in the iron atoms diffused in GaSb. For instance, gallium antimonide doped with the isotope ⁵⁷Fe, enriched up to 99.99%, has been grown using the zone melting technique modified for the concentrations of 1–3% atomic mass.

Under investigation here were both p-type single crystals of GaSb with the charge carriers concentration of 4×10^{18} cm⁻³ and n-type single crystals of GaSb with the charge carriers concentration of 8×10^{16} cm⁻³. In order to get Mössbauer's spectra, absorbants from different zones of the ingot were prepared. The spectra were registered in the range from the room temperature to the temperature of liquid nitrogen. The estimations and the results of the spectra processing, as well as of the experimental data were carried out using the program WMOSS (solid lines) and are plotted in Figs. 2, 3 and 4.

Another object of study was the valence of the Fe impurity atoms arising from the ⁵⁷Co decay using Mössbauer's spectroscopy. The picture of the ⁵⁷Co radioactive decay is given in Fig. 2. Gamma-ray nuclear resonance spectra for GaSb doped with ⁵⁷Fe depend on the conductivity type and the concentration of charge carriers.

In p-type samples Mössbauer's spectra are in a form of a doublet, i.e. two specific peaks in a spectrum, with the quadrupole splitting $\Delta E_Q \approx 1.2$ mm s⁻¹ and the isomer shift $\delta \approx 0.5$ mm s⁻¹, whereas in n-type samples the quadrupole splitting is $\Delta E_Q \approx 0.5$ mm s⁻¹ and the isomer shift is $\delta \approx 0.4$ mm s⁻¹.

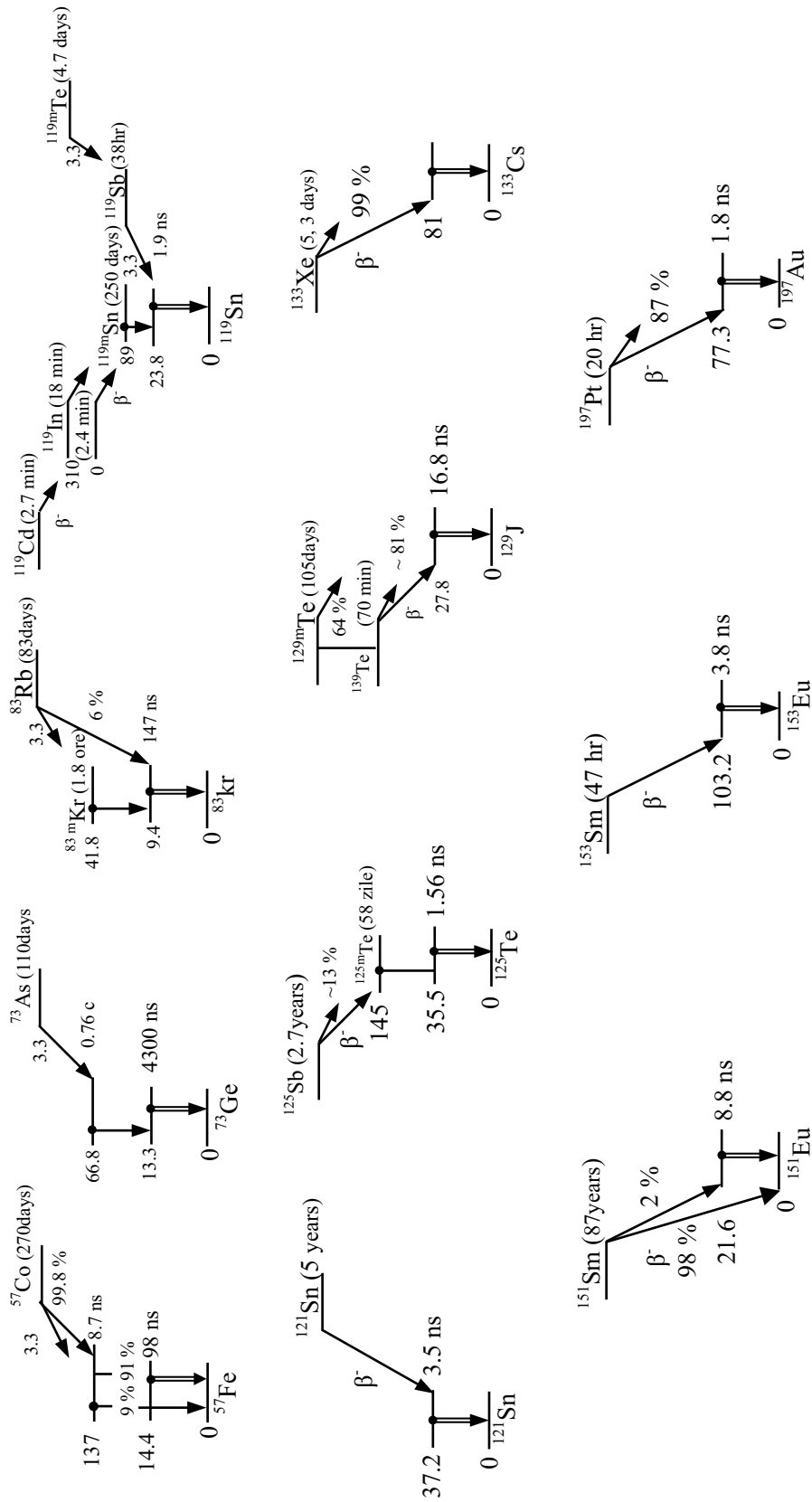


Fig. 1 Schemes of decay of radioactive nuclei, resulting in the formation of the Mössbauer levels ^{57}Fe , ^{73}Ge , ^{83}Kr , ^{121}Sb , ^{125}Te , ^{129}J , ^{133}Cs , ^{151}Eu și ^{197}Au [3]

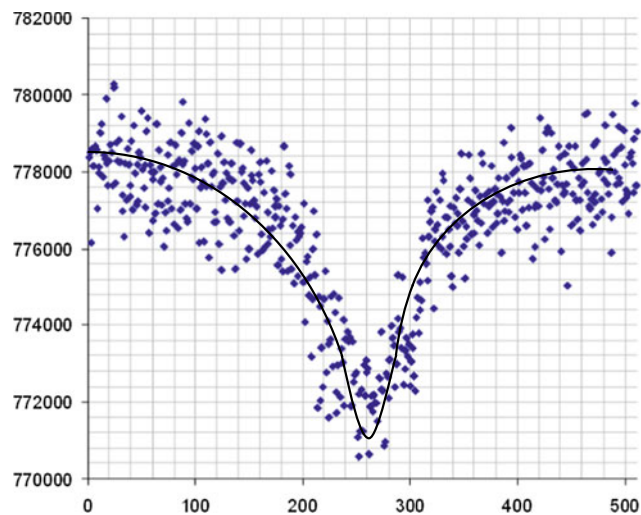


Fig. 2 Spectrum of Mössbauer spectroscopy of the ^{57}Fe , 1% atomic mass, in GaSb at $T = 300\text{ K}$

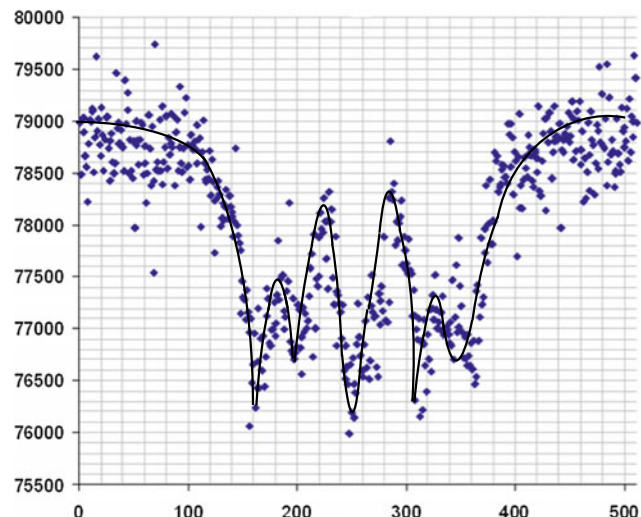


Fig. 4 Spectrum of Mössbauer spectroscopy of the ^{57}Fe , 3% atomic mass, in GaSb at $T = 5\text{ K}$

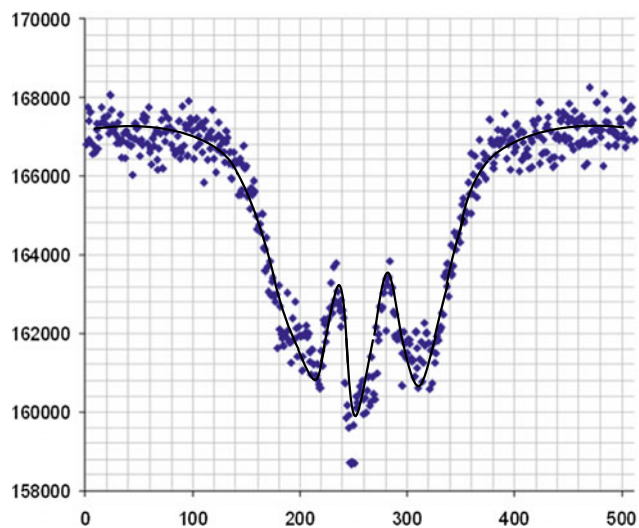


Fig. 3 Spectrum of Mössbauer spectroscopy of the ^{57}Fe , 3% atomic mass, in GaSb at $T = 300\text{ K}$

The authors in [5–7] have found a broad line in the gamma resonance (Mössbauer) spectra for GaSb. It is clearly seen there that for the Mössbauer impurity atoms, the parameters of those spectra have to be dependent, first of all, on the properties of the crystal lattice. From here, one could assume that in the same semiconductor, but in its different types and in different concentrations of the charge carriers, the Mössbauer spectra for the impurities of the electrically active atoms could be different relative to the parameters. Using Mössbauer's parameters, one can see that iron in the crystal lattice in AIIIBV substitutes the atoms of elements

for group III and has the configuration $3d^5$. As is known, elements from the Fe group in AIIIBV compounds should form acceptor levels [8]. In AIIIBV compounds with a broad energy band, GaSb being one of them, for the samples of the p-type, at $T < 295\text{ K}$, all impurity centers are not ionized, and those centers could be trivalent ions with the incomplete tetrahedral bonding arrangement, which leads to the appearance of the electric field gradient on ^{57}Fe nuclei as well as to a greater quadrupole splitting. With the rise of temperature, the impurity centers become ionised and hence can be formally described as the movement of holes from the impurity atoms. Thereby Fe atoms are complementing their bondings, thus reducing the quadrupole splitting. A process similar to ionisation of the impurities centers can be observed when inserting Fe atoms in the n-type samples. No doubt when the concentration of the charge carriers in the n-type samples is less than the concentration of the impurity atoms then the gamma-ray resonance (Mössbauer) spectrum should be composed of the overlapping of two types of spectra. Measuring the dependence of the quadrupole splitting temperature of the gamma-ray (Mössbauer) resonance of ^{57}Fe in GaSb allows to find out the nature of the impurity atoms as well as their energy levels.

The Mössbauer spectra for the samples of 1 and 3% concentrations were collected on a Model MS4 WRC spectrometer (SEE Co, Edina, MN), at the Centre "Physical Chemistry and Nanomaterials" of the Institute of Chemistry of the Academy of Sciences of Moldova. The conditions and facilities of the experiment were: the temperature range of 4.5–300 K, with the closed circuit; a system with refrigerated helium; and the temperature sensor of the model W106.

The source was a ^{57}Co (0.74 GBq) in Rh matrix; isomer shift refers to the metal α -Fe at 298 K. Experimental data were analysed using the program WMOSS (WEB Cercetare, Edina, MN).

3 Conclusions

As a result of the investigations it was found out that in GaSb doped with ^{57}Fe gamma-ray resonance spectra depend on the conductivity type and the concentration of charge carriers. Estimations of the temperature dependence of the quadrupole splitting of the gamma-ray resonance (Mössbauer) spectra allowed to determine the nature of the electrical activity of the Mössbauer impurity atoms and their energy levels. The data obtained allow to conclude that iron doped in gallium antimonide makes the latter to have the configuration of $3d^5$, to be a trivalent impurity, with a tetrahedral structure, thus broadening its bondings.

Conflict of Interest The authors declare that they have no conflict of interest.

References

1. Milnes, A.G., Polyakov, A.Y.: *Solid-State Electron.* **36**, 803 (1993)
2. Dutta, P.S., Bhat, H.L., Kumar, V.: The physics and technology of gallium antimonide: an emerging optoelectronic material. *J. Appl. Phys.* **81**(9), 5821–5870 (1997)
3. Nistriuk, I.V., Seregin, P.P.: Application of the Mössbauer emission spectroscopy in physics of semiconductors. Kishinev, 123 p (1982)
4. Seregin, P.P., Nasredinov, F.S., Vasilev, L.N.: *Phys. St. Sol.* **A45**(1), 11–45 (1978)
5. Beloserskii, G.N., Nemilov, Yu.A., Tomolov, S.B., Shvedchikov, A.V.: *Fizika tverdogo tela* **7**, 3607 (1965)
6. Beloserskii, G.N., Gusev I.A., Nemilov, Yu.A., Shvedchikov, A.V.: *Fizika tverdogo tela* **8**, 2112 (1966)
7. Basetsky, V.Ya., Veits, B.N., Grigalis, V.Ya., Lisin, Yu.D., Taksar, I.M.: *Fizika tverdogo tela* **10**, 2852 (1968)
8. Veisberg, I.: *Novel Semiconductor Materials*, p. 153. Metallurgizdat, Moscow (1964)

ZnO Nanometric Layers Used in Photovoltaic Cells

V. Botnariuc, L. Gorceac, A. Coval, B. Cinic, P. Gaugas, P. Chetrus, I. Lungu, and S. Raevschi

Abstract

The ZnO thin layers were grown on glass, InP and pInP-nCdS substrates from zinc acetate dissolved in water-acetic acid-methanol solution having a molarity of 0.2 M by using the spray method in the argon flow in the temperature range of (250–450) °C. The dependence of optical properties of ZnO layers on growth temperature have been investigated. The optical transmittance has values of 80–85% in the wavelength range of (200–1000) nm. The using of ZnO of the thickness of (60–80) nm as antireflective layers in nCdS-pInP structures allowed to increase the photovoltaic cell efficiency by 3%. The photosensitivity of the fabricated nZnO-pInP structures covers the wavelength region from 450 nm up to 1100 nm and allows the more efficient utilization of the incident light.

Keywords

Zinc oxide • Nanometric layers • Spraying • Transmittance • Photovoltaic cell

1 Introduction

A particular interest in zinc oxide (ZnO) is caused by the unique optical and electrophysical properties of this material. ZnO layers are chemically stable and do not react to the atmospheric instability and are used as transparent layers in the visible and infrared region of the spectrum as electrical contacts and buffer layers in solar cells and information

recording devices [1–3]. Zinc oxide ZnO is a semiconductor of the A_2B_6 group with a band gap of 3.37 eV at room temperature. Since the binding energy is close to 60 meV [4], which is several times higher than for GaN and the energy of biexciton formation is 15 meV [5] which is also higher than for GaN therefore ZnO is considered as promising material for excitonic devices. The zinc oxide layers doping allows to obtain layers with a relatively low resistivity of $2 \times 10^{-4} \Omega \text{ cm}$ [6, 7]. The zinc oxide layers possess high piezoelectric and electroluminescent characteristics and can be used as functional layers in acoustic devices [8, 9], ultraviolet and infrared radiation sources and detectors, and in linear optic elements [10–12]. The possibilities of this heated material allow the absorption of gases and thus their use as gas detecting sensors [13, 14].

For the deposition of ZnO thin layers different technologies were used, such as chemical vapor deposition (CVD) [15], magnetron spraying [16], sol-gel [17], laser evaporation [18], electrodeposition [19] and spray (pulverization) [20]. In this paper spray pyrolysis was used for ZnO layer deposition. An important advantage of this thin film deposition technology is that it is very economical, does not require costly installations and is accessible to the deposition of zinc oxide with properties that can be controlled by changing the technological regime of production. The prospect of the implementation of this technology consists in the simplicity of obtaining different compounds of semiconductor materials, their solid solutions, doping with impurities and fabrication of heterojunctions in a single technological cycle. These advantages make spraying as a perspective in nanotechnologies for the realization of new generations of devices in optoelectronics, photonics and the deposition of antireflective (AR) and anticorrosion coatings.

There are several papers proposing ZnO as AR coating for silicon and CIGS solar cells to improve the efficiency [21, 22] but, to best of our knowledge, no one yet reported use of ZnO as AR coating for InP/CdS solar cell. Therefore, the purpose of this paper is to investigate the optical properties dependencies of ZnO layers in function of the

V. Botnariuc (✉) · L. Gorceac · A. Coval · B. Cinic · P. Gaugas · P. Chetrus · I. Lungu · S. Raevschi
Department of Physics and Engineering, Moldova State University, 60, A. Mateevici Str., Chisinau, Republic of Moldova
e-mail: v_botnariuc@hotmail.com

L. Gorceac
e-mail: lgorceac@yahoo.com

deposition temperature and also, to study influence of ZnO as antireflective layer on photoelectrical parameters of nCdS/pInP structure.

2 Experiment

Zn acetate ($\text{Zn}(\text{CH}_3\text{COO})_2 \cdot 2(\text{H}_2\text{O})$) dissolved in water—acetic acid—methanol in a 25:10:65 ratio having the concentration of 0.2 M was used for to deposit ZnO layers.

The layer deposition facility described in [23–26] was used for fabrication of ZnO layers. The main components of this facility are: spraying system, electric furnace, substrate support, the system of support insertion into the furnace and the temperature control system. The equipment allows to fabricate ZnO layers having the area up to 80 cm^2 . The furnace temperature was maintained constant with an accuracy of $\pm 5 \text{ }^\circ\text{C}$. ZnO layers were grown in an argon atmosphere at 2 bar spray pressure. Glass plates were used as substrates being previously degreased in toluene, isopropyl alcohol, and then corroded in methanol +5%Br for 10 min, dried in isopropyl alcohol vapors, and then placed in the deposition chamber (electric furnace). Thereafter, the furnace temperature was raised to the needed for deposition value, the sprayer was connected to the carrier gas system, the zinc acetate solution is poured into the sprayer furnace and the deposition process is carried out. For a solution volume of 20 ml the deposition time was of 6 min. The heterojunction InP/CdS solar cells were fabricated by deposition of InP by HVPE on InP substrates with carrier concentration 10^{18} cm^{-3} and orientation [100] at $T_{\text{sub}} = 680 \text{ }^\circ\text{C}$ in hydrogen atmosphere. The CdS thin films were deposited by close space sublimation method at $T_{\text{sub}} = 650 \text{ }^\circ\text{C}$ in hydrogen atmosphere, also. Figure 1 show the schematic of the InP/CdS solar cell model proposed in this study. As contact ohmic was used Ag+5%Zn for InP, and In for CdS thin film, both deposited by thermal evaporation. Fortunately, refractive index of ZnO is very close to the ideal value required for antireflection (AR) coating of InP surface.

The optical transmittance of the ZnO layers in the wavelength range (200–1000) nm was measured by using

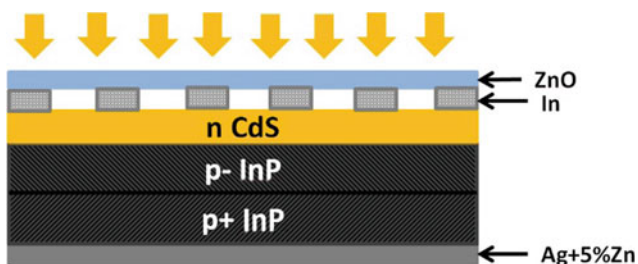


Fig. 1 The schematic of the InP/CdS solar cell with antireflective ZnO thin film

the Agilent Cary 60 spectrometer. The current-voltage characteristics were measured at Keithley 4200 Semiconductor characterization system at room temperature, 100 mW/cm^2 .

3 Results And Interpretation

The optical transmission spectral dependence of ZnO layers deposited within the temperature range of the glass support ($250\text{--}450$) $^\circ\text{C}$ at a constant volume of 20 ml is shown in Fig. 2. As we one see, the optical transmission has values (80–85)% within the wavelength range (300–1000) nm. For the layers obtained at all support temperatures, the same amount of the solution was sprayed. It was established that the spectral dependence of the optical transmittance was practically the same with the exception of the layers grown at temperatures of 400 and 450 $^\circ\text{C}$, whose crystalline structure is probably more qualitative.

In our proposed model, front region of the solar cell which is directly exposed to solar radiation is composed of n-type ZnO/CdS layers. Therefore, transparency of the ZnO layer for visible is very important. The nanometric ZnO anti-reflective layers deposited on nCdS-pInP structure frontal surface have been sprayed at 250 $^\circ\text{C}$ for not damage the grid of the generated charge carriers collection. The impact of ZnO thickness on open circuit voltage (U_{OC}), short circuit current (I_{SC}), fill factor (FF), and power conversion efficiency (η) of the ZnO/CdS/p⁻InP/p⁺InP solar cell are investigated. The photovoltaic parameters dependence on ZnO antireflective layer thickness of n CdS-pInP structure are given in Table 1. Thicknesses of (60–100) nm are the most favorable for increasing the photovoltaic cell efficiency (Fig. 3a, b).

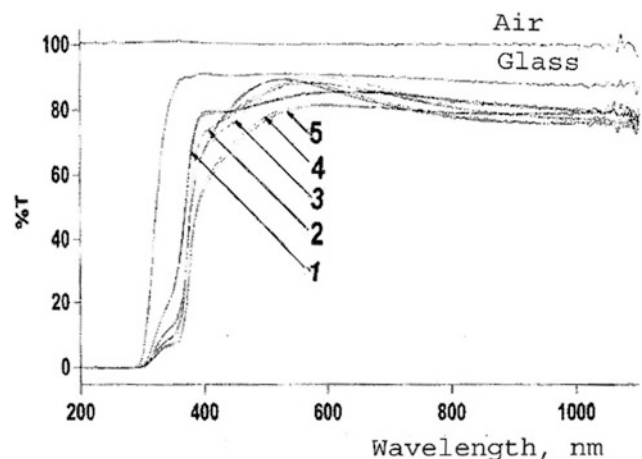


Fig. 2 The optical transmission spectral dependence of the ZnO layers obtained at different substrate temperatures. T ($^\circ\text{C}$): 1—250; 2—300; 3—350; 4—400; 5—450

Table 1 Photovoltaic parameters of the structure nCdS-pInP in dependence on the antireflective layer thickness

CF	d (nm)	J_{sc} (mA/cm ²)	U_{oc} (V)	FF (%)	η (%)	R_{ser} (Ω)
nCdS-pInP	0	18.33	0.73	64.75	8.56	5.2
	60	27.21	0.74	63.35	12.74	3.67
	120	25.36	0.74	61.51	11.54	4.33
	180	26.11	0.72	42.83	8.05	5.57
	300	23.96	0.72	34.7	5.98	11.88

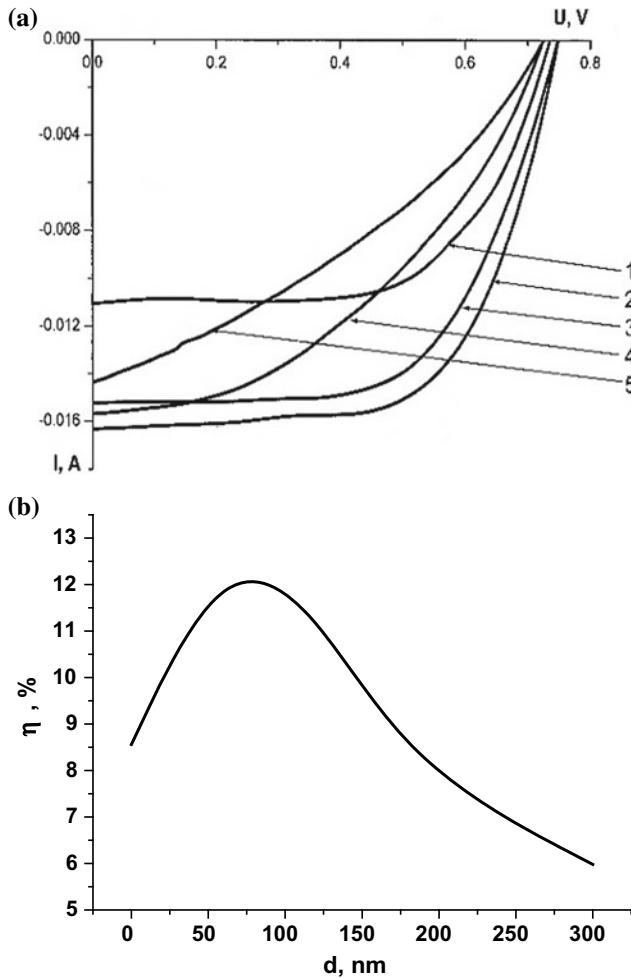


Fig. 3 a Load characteristics of the nCdS-pInP structure in dependence on the thickness d in nm of the ZnO antireflective layer (nm): 1—0; 2—60; 3—120; 4—180; 5—300. b Dependence of the photovoltaic structure efficiency on the thickness d of the ZnO antireflective layer

For these thicknesses of the antireflective layer, the photovoltaic cell efficiency increases by approximately 3%. At the thickness of antireflection layers higher than 100 nm, the short circuit current decreases along with the decrease of the filling factor FF (Fig. 4a). The decrease in short circuit current density and the fill factor is largely due to

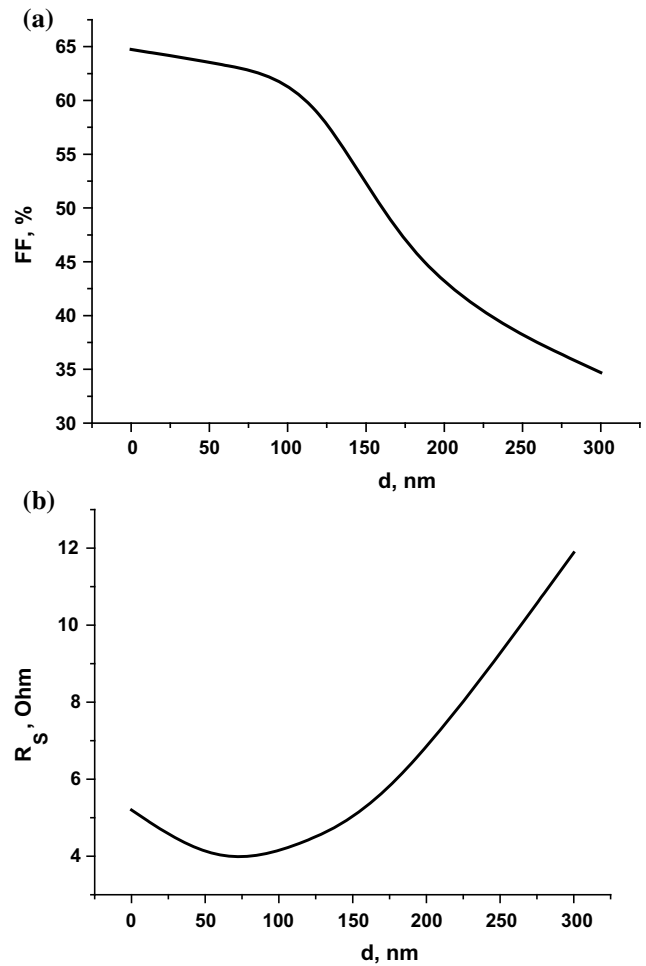


Fig. 4 Dependence of the fill factor (a) and of the series resistance (b) on the thickness of the antireflective layer

the increase in the structure series resistance (Fig. 4b). The increase in series resistance of the photovoltaic structure is related to the keeping of the photovoltaic structure at the temperature of 250° repeatedly.

For fabrication of the nZnO-pInP photovoltaic structure the nanometric ZnO layers having the thickness of 400 nm were deposited at 450 °C on the pInP substrate with crystallographic orientation (100) and charge carriers concentration of 10^{18} cm⁻³. The photosensitivity of the nZnO-pInP

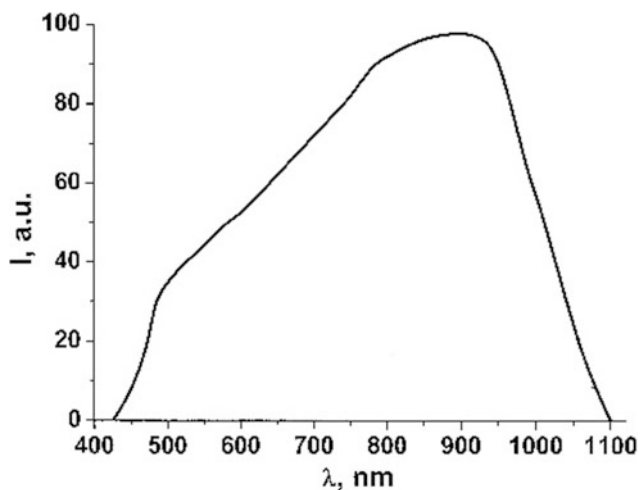


Fig. 5 Spectral dependence of nZnO-pInP structure photosensitivity

photovoltaic structure (Fig. 5) covers the wavelength region of (400–1100) nm similar to the ITO-pInP structure sensitivity values.

4 Conclusions

The nanometric ZnO layers were grown by spraying in the temperature range (250–450) °C by using zinc acetate as the precursor. In the range of wavelengths (300–1000) nm the optical transmission of the fabricated layers has values (80–85%). The ZnO layers grown at temperatures of 250 and 300 °C do not considerably change the series resistance of the structure. The efficiency of the nCdS-pInP photovoltaic cell is increasing by 3% due to the using of the ZnO as antireflective layer with a thickness of (60–100) nm. The J_{SC} reduces monotonically with increased ZnO thickness because of significant decrease in number of available photons in space charge region. The best efficiency for InP/CdS heterojunction solar cell was obtained for cell with 60 nm of ZnO.

Acknowledgements The authors would like to thank the Ministry of Education, Culture and Research of Republic of Moldova for supporting this research by funding the grant 15.817.02.34A.

Conflict of Interest The authors declare that they have no conflict of interest.

References

1. Granqvist, C.G.: *Solar Energy Mater. Solar Cells* **91**, 1529 (2007)
2. Ellmer, K., Clen, A., Rech, B.: *Transparent Conductivity Zinc Oxide. Basics and Applications in Thin Film Solar Cells*, vol. 9 (2008)
3. Look, D.C.: *Mater. Sci. Eng. B* **80**, 383 (2001)
4. Nahg, A., Remam, K., Rubenake, St.: *Solid State Commun.* **94**, 251 (1995)
5. Sulkar, M.N., Tuler, N.L.: *Adv. Ceram.* **7**, 71 (1984)
6. Lu, D.-S., Wu, C.-Y., Sheu, C.-S., Thai, F.-C., Li, C.-H.: *J. Appl. Phys.* **45**, 3531 (2005)
7. Кравченко, В.А., Лопав, Д.В., Пашенко, П.В., Пирогов, В.Г., Рахимов, А.Г., Суснин, Н.В., Трифонов, А.С.: *ЖТФ* **28**(8), 107 (2008)
8. Грузинцев, А.Н., Волов, В.К., Баргхоу, К., Бенаул, П.: *ФТП* **36**(6), 74 (2002)
9. Грузинцев, А.Н., Волков, В.К., Бергхоу, К., Бенаул, П.: *ФТП* **37**(3), 275 (2003)
10. Александров, А., Веселов, А.Г., Кирясова, О.А., Сердобинцев, А.А.: *Письма ЖТФ* **38**(18), 496 (2012)
11. Hung, N.L.: *J. Korean Phys. Soc.* **57**(6), 1784 (2010)
12. Dang, V.L., Fu, Y.Q., Lua, J.K., Flewitt, A.J., Milnc, W.L.: *Superlattices Microstruct.* **42**, 89 (2007)
13. Ataev, B.M., Bagamadova, A.M., Mamedova, Y.Y., Omaev, A.C., Ramadanov, M.R.: *J. Cryst. Growth* 198–199 (1999)
14. Song, D., Widenborg, P., Chin, W., Aberle, A.G.: *Solar Energy Mater. Solar Cells* **73**, 1 (2002)
15. Lee, J.H., Ko, K.H., Parc, B.O.: *J. Cryst. Growth* **247**, 119 (2003)
16. Singh, A.V., Cumar, M., Mehra, R.M., Vakamara, A., Ysihida, A.: *J. Indian Inst. Sci.* **52** (2001)
17. Yuosef, S., Combate, P., Podlecki, J., Asmar, R.A., Foucaran, A.: *Cryst. Growth Des.* **9**(2), 1008 (2009)
18. Combrero, J., Elmanount, A., Hartit, B., Mollar, M., Mari, B.: *Thin Solid Films* **451–452**, 198 (2004)
19. Ma, J.Y., Lee, F.S.C.: *J. Mater. Sci. Mater. Electron.* **11**, 35 (2000)
20. Ayouchi, F., Martin, D., Lenen, J., Ramos, R.: *J. Cryst. Growth* **247**, 497 (2003)
21. Hussain, B., et al.: *Solar Energy Mater. Solar Cells* **139**, 95–100 (2015)
22. Chant, E., Wongratanaphisan, D., Gardchareon, A., et al.: *Energy Procedia* **79**, 879–884 (2015)
23. Simașchevici, A., Șerban, D., Bruc, L., Coval, A., Gorceac, L., Monaco, E., Usatîi, Iu.: *Int. Sci. J. Altern. Energy Ecol. ISJAEET2* 3451–3454 (2006)
24. Kunar, N., Casturi, V., Bangera, V., Shivacunar, G.: T48, V.1050–1054 (2014)
25. Махнийт, В.П., Слетов, М.М., Хуснутдинов, С.В.: *Оптический журнал* **76**, 6 (2009)
26. Botnariuc, V., Gorceac, L., Pleșca, V., Rudi, A., Rudi, Iu., Simașchevichi, A., Șerban, D.: *Analele științifice ale Universității de Stat din Moldova, seria “Științe reale”*, pp. 61–69 (1997)

Resistivity Response to Stress and Strain of a Flexible Bi_2Te_3 Based Thermoelectric Material

L. O. Akinsinde, S. Scheitz, L. Zimoch, J. K. Sierck, L. Siebert, R. Adelung, U. Schürmann, M. A. Rübhausen, T. Dankwort, and L. Kienle

Abstract

Here we report about the synthesis of Bi_2Te_3 based flexible thermoelectric materials and the response of the electrical resistivity to tensile and compressive stress. As a template fiber spun polymers have been used onto which a thin composite film of graphene and Bi_2Te_3 nanoplates was deposited. The Bi_2Te_3 nanoplates were synthesized using the polyol method. Upon straining the material, the resistivity dropped which is attributed to the increased contact between the individual wires.

Keywords

Bi_2Te_3 • Flexible thermoelectric materials • Composite materials • Polyol process • Wet chemical method • Polymer fibers

1 Introduction

Bismuth Telluride (Bi_2Te_3), belonging to the chalcogenide-based thermoelectrics is well known for its high efficiency with respect to room temperature applications [1–3]. To obtain thermoelectric devices, conventional high temperature synthesis routes are used. Afterwards the material is ball milled to obtain powders, which in a consecutive step are sintered and compacted to obtain thermoelectric legs [4, 5]. Thus, the processing is technically costly and time consuming. An alternative synthesis route was found using wet chemical approaches. With the polyol method [6], it was

possible to grow nanoplates (nanoflakes) of various relevant thermoelectric materials [7, 8] including Bi_2Te_3 [9] at moderate temperatures. The obtained materials can be dried and sintered [10]. However, thermoelectric generators (TEGs) using sintered Bi_2Te_3 thermoelectric legs are brittle which limits the applicability of these generators. In recent years, flexible TEGs have been designed using e.g. Bi_2Te_3 suspensions, which were deposited on various types of flexible substrate materials [11, 12]. These types of thermoelectric materials have also attracted attention as self-powered pressure and temperature sensors [13].

In this contribution, we report about the synthesis of Bi_2Te_3 nanoplates and an infiltration method using these nanoplates to obtain flexible thermoelectric materials. As a template fiber spun polymers have been used. To enhance the conductivity and facilitate sticking of the Bi_2Te_3 nanoplates, graphene has been introduced. Furthermore, the response of the electrical resistivity to external stress and strain was investigated.

2 Experimental

The synthesis of stoichiometric single crystalline Bi_2Te_3 nanoplates was carried out via a simple wet chemical polyol method. The high-quality grade precursors used were purchased from Sigma Aldrich. To achieve an ideal stoichiometric Bi:Te ratio of 2:3 chemicals are weighted to 485 mg of $\text{Bi}(\text{NO}_3)_3 \cdot 5\text{H}_2\text{O}$ (98%, Sigma Aldrich), 0.5 g of polyvinylpyrrolidone (PVP) (30 K, Roth), 415 mg $\text{K}_2\text{TeO}_3 \cdot \text{H}_2\text{O}$ (97%, Alfa Aesar), 0.4 g NaOH (98%, Merck) and 50 ml of Ethylene glycol (EG) (>99.5%, Roth). The salts as well as the surfactants are dissolved in EG in a glass beaker on a hot plate set at a temperature of 65 °C while slightly stirring the mixture. The dissolved solution was then transferred via a long funnel into a three-neck round bottom flask connected to a water-cooled reflux. The flask remained closed during the entire synthesis with septum. The solution was stirred at 450 rpm with a Teflon bar and slowly heated

L. O. Akinsinde · S. Scheitz · M. A. Rübhausen
Center for Free Electron Laser Science (CFEL), Institute for Nanostructures and Solid State Physics (INF), University of Hamburg, Luruper Chaussee 149, 22761 Hamburg, Germany

L. Zimoch · J. K. Sierck · L. Siebert · R. Adelung · U. Schürmann · T. Dankwort (✉) · L. Kienle
Intitute for Materials Science, Kiel University, Kaiserstrasse 2, Kiel, Germany
e-mail: td@tf.uni-kiel.de

to allow the substance to mix homogeneously. This procedure further ensures proper nucleation of the seeds that later grow to form the nanoplates. After a duration of roughly 10 min, the solution reached the preset temperature of 180 °C and turned to a black color. The nanoplates were allowed to grow at 180 °C for 22 h. The solution was left to cool down to room temperature. Apparently, small black precipitates have formed. The isolation of the Bi_2Te_3 precipitates was achieved through centrifugation in acetone and isopropanol to remove the core-shell-like structures of the residual PVP as well as EG from the synthesis and then stored inside a vial. The Bi_2Te_3 nanoplates are dispersed in high purity isopropanol to avoid the agglomeration of the nanoplates.

In order to obtain a macroscopic flexible thermoelectric device, graphene-coated polymer composite fiber mesh was adopted and infiltrated with the Bi_2Te_3 nanoplates. The infiltration of the fiber mesh consisting of Polycaprolactone (PCL) template with Bi_2Te_3 nanoplates was achieved by dip-coating (soaking) simultaneously different fiber-meshes in 5 ml solution of Bi_2Te_3 and Isopropanol for 24 h as well as 48 h under ambient conditions.

The morphology, shape and degree of infiltration of the samples were investigated using a commercial field emission scanning electron microscopy (FE-SEM), Sigma from Zeiss Company, Germany.

Nanostructural investigation were performed using a transmission electron microscope (TEM), FEI Tecnai F30 G² STwin equipped with an 300 kV field emission gun.

A custom-build setup was used to validate the electrical response of each sample, which allows to apply stress and strain to the sample while simultaneously measure the resistivity changes. Therefore, a constant DC-voltage was applied, and the electrical conductivity measured. According to ohm's law the resistivity was calculated. Further, the applied stress was measured with a load cell.

3 Results and Discussion

Nanoplates of Bi_2Te_3 were synthesized by a reduction of a stoichiometric mixture in EG in the presence of PVP. PVP is very important due to its function as a capping agent as well as a trigger for crystal growth, i.e., it facilitates a uniform uniaxial growth [14–16]. More to this, PVP bonds to the polar basal planes of the crystal structure of Bi_2Te_3 and suppresses the growth dynamic of the crystals in the c-axis direction [16]. The thin PVP core-shell layer is determined to be in the range of 2–5 nm and is mostly not completely removed through centrifugation. A complete PVP removal is detrimental and might be achieved at the expense of the Bi_2Te_3 nanoplate being partly etched during the process. The transition between PVP- Bi_2Te_3 nanoplate is not readily determined.

To investigate the nanostructure of the Bi_2Te_3 nanoplates TEM was used. Figure 1 depicts representative nanoplates of Bi_2Te_3 . The different nanoplates extend over 3–5 micrometers, while their thickness is in the range of a few nanometers. Further, large particles are often decorated with smaller particles as also depicted in Fig. 1. The nanoplates were crystalline and exhibit rotational disordering [14, 15], thus the zone axis varies within a few nanometers and produces characteristic diffraction contrast (not shown here). This observation might be the result of a screw dislocation promoted growth [16].

Electron diffraction (ED) patterns in zone axis [001] exhibited additional reflections (not shown here), which indicates a lowering of the symmetry. Thus, it was concluded that due to slight variation in the stoichiometry a transition from $R\text{-}3m$ to $P\text{-}3m1$ crystal structure is observed.

The HRTEM micrograph and corresponding Fourier Transform (FFT) in Fig. 1 highlight rotational disorder resulting in weak satellite reflections (marked in yellow) in the FFT and pronounced Moiré contrast.

The chemical composition of the nanoplates was characterized using energy dispersive X-ray spectroscopy (EDX) in scanning TEM mode. It was observed, that the stoichiometry slightly deviates from the ideal ratio of Bi:Te = 2:3. In our system the ratio was found to be 1.8:3.2, thus this deviation presumably might be attributed to impurities in the system.

The obtained nanoplates were deposited on a graphene-coated PCL fiber mesh. FESEM images (Fig. 2), revealed a strong adhesion of the Bi_2Te_3 nanoplates on the coated fiber-meshes as seen in the long percolation network

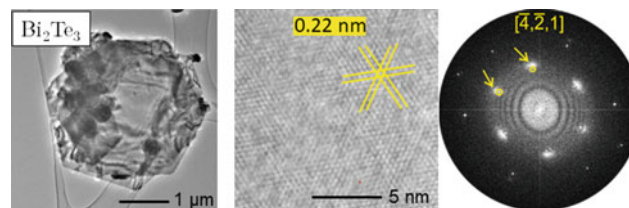


Fig. 1 Bright field image, HRTEM micrograph and corresponding FFT of a Bi_2Te_3 flake in zone axis $[-4\text{-}21]$. In the FFT satellite reflections are observed which can be attributed to rotational disorder

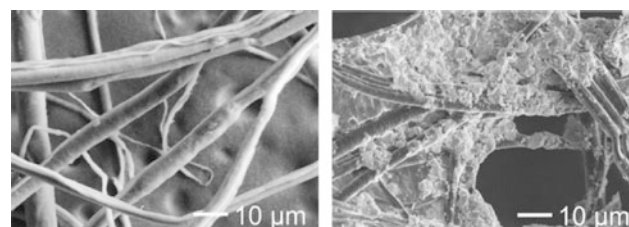


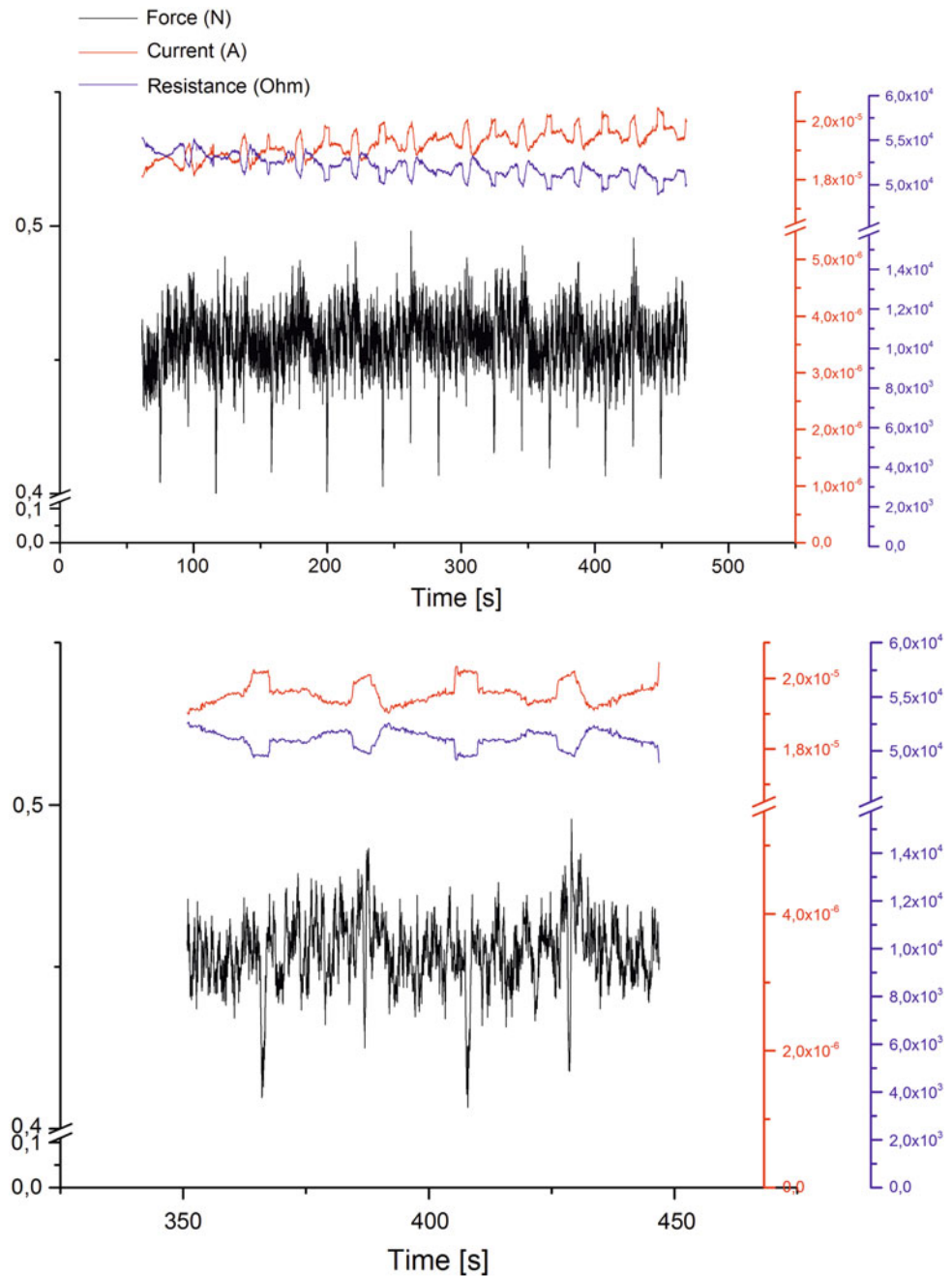
Fig. 2 FESEM micrographs of polymer fibers before and after coating with Bi_2Te_3 nanoplates

formed. Thus, strongly bonded Bi₂Te₃ nanoplates are part of a closed composite film. Also, smaller ‘plate-like’ structures are randomly dispersed on the surface of the fiber matrix. Overall, we assume that the weak van-der-Waals forces existing at different junctions and interfaces between Bi₂Te₃ nanoplates and the polymer fiber-mesh matrix is strongly responsible for the good adhesion. However, when no additional graphene was used the adhesion of Bi₂Te₃ nanoplates was significantly reduced, thus leading to only low coverage of the fiber-mesh (not shown here).

The mass weight as well as the dimensions of the graphene coated fiber-mesh was measured before and after dipping in Bi₂Te₃ suspension. The density of nanoplates deposited on the fiber-mesh matrix increases with the dwelling time. Lowest electrical resistivity was found for the samples with longest dwelling time.

The samples were folded, and tensile and compressive stress applied. Simultaneously, the resistivity was measured. A representative result of such measurement is depicted in Fig. 3.

Fig. 3 Change of current and resistance in dependence of mechanical loading. The upper graph represents several loading cycles while the lower graph represents an enlarged section highlighting the effect of resistivity changes upon applying tensile and compressive stress



Repeatedly compressive and tensile stress were applied to the sample applying. It is observed that a decrease in resistivity and, accordingly, an increase in electrical conductivity is observed for both cases (as seen in Fig. 3). This effect can be attributed to the re-orientation and increased overlapping of different wires/nanoplates due to the stress which is applied. With the tensile stress, it allows the coated nanoplatelets to create a junction through bonding of numerous nanoplatelets contacting each other thereby, increasing locally the conductivity whereas this effect is not strong or perhaps predominates during compressive stress. The overlapping of the nanoplatelets is predominant and we assume, the bonding of the nanoplatelets might not be too strong and responsible for the light drop in the resistivity. Supposedly, the tunneling barrier of the electron mobility is thus not completely overwhelmed. Furthermore, a memory effect is observed. With increasing number of load cycles, the resistivity further decreases leading to a remnant change in the resistivity in the unloaded state. The origin for this behavior might be again the result of different wires/nanoplates getting in contact irreversibly and forming new junctions. Thus, with an increased number of loading cycles an accumulation takes place, consequently leading to a remnant change in resistivity.

4 Conclusions

In this paper, we have highlighted the polyol wet chemical process as an effective simple chemical method to synthesize high quality and good grade nanoplates of Bi_2Te_3 that are single crystalline. The obtained nanoplates exhibit areal dimensions in the range of 3–5 μm and have a thickness of a few nanometers.

Furthermore, it was found that graphene coated PCL fiber spun polymers act as an ideal substrate for the deposition of Bi_2Te_3 nanoplates forming a long-range percolation network.

In the mechano-electrical transport measurement, tensile and compressive stress lead to a decrease in resistivity while after several cycles the material exhibited a remnant change in electrical conductivity.

These results highlight the potential of flexible thermoelectric materials to be used as pressure sensors while simultaneously being able to implement a power source or a temperature sensor.

Acknowledgements The authors like to thank the Land Schleswig-Holstein and Hamburg for financial support. Further, the authors like to thank the group of Prof. Oepen for the use of the SEM.

Conflict of Interest The authors declare that they have no conflict of interest.

References

1. Rowe, D.M.: *Thermoelectrics Handbook: Macro to Nano*. CRC Press (2005)
2. Eibl, O., Nielsch, K., Peranio, N., Völklein, F.: *Thermoelectric Bi_2Te_3 Nanomaterials*. John Wiley & Sons (2015)
3. Champness, C.H., Chiang, P.T., Parekh, P.: Influence of growth conditions and tellurium phase on the thermoelectric properties of bismuth telluride-type materials. *Can. J. Phys.* **43**, 653 (1965)
4. Böttner, H., Ebling, D.G., Jacquot, A., König, J., Kirste, L., Schmidt, J.: Phys. Structural and mechanical properties of spark plasma sintered n- and p-type bismuth telluride alloys. *Status Solidi RRL—Rapid Res. Lett.* **1**, 235 (2007)
5. Koenig, J., Winkler, M., Dankwort, T., Hansen, A.-L., Pernau, H.-F., Duppel, V., Jaegle, M., Bartholomé, K., Kienle, L., Bensch, W.: Thermoelectric efficiency of $(1-x)(\text{GeTe})_x(\text{Bi}_2\text{Se}_{0.2}\text{Te}_{2.8})$ and implementation into highly performing thermoelectric power generators. *Dalton Trans.* **44**, 2835 (2015)
6. Dong, H., Chen, Y.-C., Feldmann, C.: Polyol synthesis of nanoparticles: status and options regarding metals, oxides, chalcogenides, and non-metal elements. *Green Chem.* **17**, 4107 (2015)
7. Weller, D.P., Stevens, D.L., Kunkel, G.E., Ochs, A.M., Holder, C. F., Morelli, D.T., Anderson, M.E.: Thermoelectric performance of tetrahedrite synthesized by a modified polyol process. *Chem. Mater.* **29**, 1656 (2017)
8. Yang, L., Hng, H.H., Cheng, H., Sun, T., Ma, J.: Thermoelectric properties of p-type CoSb_3 nanocomposites with dispersed CoSb_3 nanoparticles. *Mater. Lett.* **62**, 2483 (2008)
9. Anderson, M.E., Bharadwaja, S.S.N., Schaak, R.E.: Modified polyol synthesis of bulk-scale nanostructured bismuth antimony telluride. *J. Mater. Chem.* **20**, 8362 (2010)
10. Soni, A., Yanyuan, Z., Ligen, Y., Aik, M.K.K., Dresselhaus, M.S., Xiong, Q.: Enhanced thermoelectric properties of solution grown $\text{Bi}_2\text{Te}_{(3-x)}\text{Se}_{(x)}$ nanoplatelet composites. *Nano Lett.* **12**, 1203 (2012)
11. Yadav, A., Pipe, K.P., Shtein, M.: Fiber-based flexible thermoelectric power generator. *J. Power Sources* **175**, 909 (2008)
12. Du, Y., Xu, J., Paul, B., Eklund, P.: Flexible thermoelectric materials and devices. *Appl. Mater. Today* **12**, 366 (2018)
13. Zhang, F., Zang, Y., Huang, D., Di, C., Zhu, D.: Flexible and self-powered temperature–pressure dual-parameter sensors using microstructure-frame-supported organic thermoelectric materials. *Nat. Commun.* **6**, 8356 (2015)
14. Eising, G., Niebuur, B.-J., Pauza, A., Kooi, B.J.: Competing crystal growth in Ge–Sb phase-change films. *Adv. Funct. Mater.* **24**, 1687 (2014)
15. Kolosov, V.Y., Thölen, A.R.: Transmission electron microscopy studies of the specific structure of crystals formed by phase transition in iron oxide amorphous films. *Acta Mater.* **48**, 1829 (2000)
16. Zhuang, A., Li, J.-J., Wang, Y.-C., Wen, X., Lin, Y., Xiang, B., Wang, X., Zeng, J.: Transmission electron microscopy studies of the specific structure of crystals formed by phase transition in iron oxide amorphous films. *Angew. Chem. Int. Ed.* **53**, 6425 (2014)

“True” Dose Rate Effect of the ELDRS Conversion Model

V. S. Pershenkov, A. S. Bakerenkov, V. A. Telets, V. V. Belyakov,
V. A. Felitsyn, and A. S. Rodin

Abstract

Modification of the ELDRS (Enhanced Low Dose Rate Sensitivity) conversion model is presented. The effect of the oxide trapped charge on the value of the oxide electric field and the yield of the oxide charge takes into account. It leads to dependence of the accumulation of radiation-induced oxide charge and interface traps on the dose rate. In enhancement version the ELDRS conversion model describes the low dose rate effect as “true” dose rate effect.

Keywords

ELDRS • Radiation hardness • Conversion model • Interface trap

1 Introduction

Bipolar devices demonstrate enhanced degradation during low dose rate (LDR) irradiation in comparison with irradiation at high dose rate (HDR) for the same total dose level [1]. The prediction of enhanced low dose rate sensitivity (ELDRS) effect in devices for long-term space mission using high dose rate laboratory testing is complicated due to ELDRS is “true” dose rate effect (TDRE) and not the time-dependent effect (TDE) often observed in CMOS. A true dose rate effect means that the degradation measured at the end of a low dose rate irradiation is greater than the degradation after irradiation at high dose rate followed by a high temperature anneal. A time-dependent effect means that the degradation at low dose rate and after high dose rate irradiation followed by a high temperature anneal is

essentially the same. For this reason test method “HDR irradiation + high temperature anneal”, often used for CMOS, cannot be used for bipolar devices. More often testing of bipolar devices is based on 10 mrad (Si)/s or high temperature irradiation [1].

In previous work [2] was shown that so-called the ELDRS conversion model [3, 4] may be used for the numerical estimation of device behavior during a hypothetical space mission during a dose rate variation corresponding to the 12-h orbit, an operation temperature variation from 268 K (−5 °C) to 328 K (+55 °C) and solar flare impact. The advantage of the conversion model in comparison with well-known models [1] connects with a possibility for numerical estimation of radiation degradation during long-term operation in space based on experimental extraction of the model fitting parameters during high dose rate test.

The conversion model does not obtain the wide recognition in world radiation community, may be for two reasons. First, it is based on not well known “hydrogen” model (H-model) of radiation-induced interface trap buildup [5, 6], but based on the conversion hydrogen-electron model (H-e model) [7, 8]. Second, according to the conversion model ELDRS is time-dependent effect. If first circumstance does not important, because our H-e model of the interface trap buildup does not contradict the popular H-e model but only expands it. The second circumstance has principal sense since conflicts with the numerous experimental data.

The goal of this work removes the contradiction between time-dependent nature of the ELDRS conversion model and experimental data concerning to reduction of the degradation after at high dose rate followed by a post irradiation anneal. We try to show that ELDRS conversion model describes “true” dose rate effect if the impact of the oxide charge on charge yield takes into account, because the value of the oxide charge depends on the dose rate.

In this work the hydrogen-electron model (H-e model) of radiation-induced interface trap buildup and the ELDRS conversion model are shortly described.

V. S. Pershenkov · A. S. Bakerenkov · V. A. Telets ·
V. V. Belyakov · V. A. Felitsyn · A. S. Rodin (✉)
National Research Nuclear University MEPhI (Moscow
Engineering Physics Institute), Kashirskoe Shosse, 31, Moscow,
Russian Federation
e-mail: ASRodin@mephi.ru

2 Hydrogen-Electron Model (H-e Model)

“Hydrogen” (H-model) is based on the assumption about the generation of hydrogen ions in the oxide bulk, which cracks the surface bounds reaching the Si/SiO₂ interface [5, 6]. The generation of interface traps can be attributed to the neutralization of positive charge by the electrons from the semiconductor substrate, i.e., the conversion of positive charge to interface traps [7]. Recently [8] it is experimentally was shown, that the most probable conversion mechanism includes the action of the hydrogen complexes, as well as substrate electrons. It is the hydrogen-electron model (H-e model), where the conversion process is an inherent component. The increasing of electron injection from substrate leads to increasing interface trap concentration on several times when hydrogen related species in oxide is fixed.

In Fig. 1 the experimental dependencies of the threshold voltage shift ΔV_{it} (caused by the interface-trap buildup) versus the annealing time for different four tests are presented. A maximum change of ΔV_{it} is observed in test 1 when both electrons and hydrogenous species are presented near the surface. In other cases, when there are no hydrogen species (test 3) or no electrons (test 2) or both near the interface (test 4), shift ΔV_{it} is essentially reduced. This experimental data confirms the hypothesis that the presence of hydrogen is sufficient for effective interface-trap buildup. According to the H-e model the interface trap buildup is connected with positive oxide trapped charge conversion due to interaction with substrate electrons and not with the action of hydrogen ions only. The H-e model is not in conflict with the most popular hydrogen model [5, 6], but it takes into account the contribution of substrate electrons to interface trap buildup process [7].

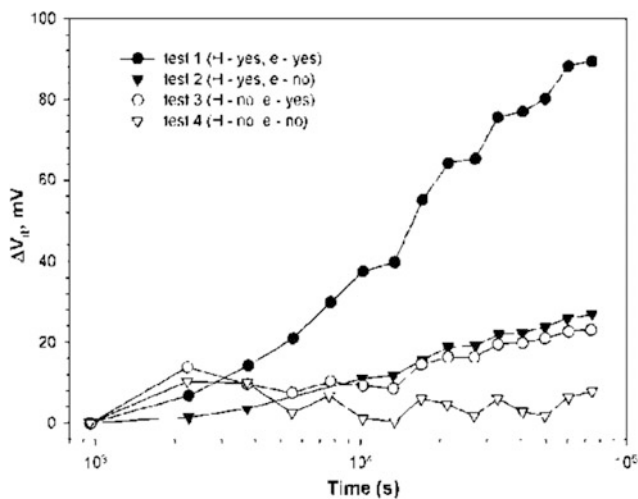


Fig. 1 The interface-trap component of the threshold voltage shift ΔV_{it} versus the annealing time in the hydrogen atmosphere (after Ref. [8])

3 ELDRS Conversion Model

In [3, 4] is supposed that interface trap buildup is connected with a conversion of rechargeable part of trapped positive charge located opposite the silicon forbidden gap [9]. Direct substrate electron tunneling to positive centers, located opposite the silicon forbidden gap, is impossible because the tunneling electron energy must be constant (according to basic principles of quantum mechanics). But tunneling to the thermally activated positive centers is still possible. The positive centers energy level can reach the silicon conduction band due to a thermally excited vibration of the lattice. An interaction of thermally excited rechargeable positive charge Q_{ot} and tunneling substrate electrons leads to interface trap buildup.

The probability of thermal excitation of the oxide trap energy level up to conduction band depends on the depth of its location opposite the silicon forbidden gap. Than close trap energy level to the middle of the forbidden gap than less the probability of the conversion process. In time scale, the shallow traps (near conduction level) are annealed first, after that the annealing front spreads to more deep energy levels.

It is supposed as in [3, 4] there are two types of oxide traps (Fig. 2): shallow traps with a short time of conversion responsible for the degradation at high dose rates (HDR), and deep traps that determine the excess base current at greater times of irradiation or LDR. The duration of HDR irradiation process is relatively short, that not enough to convert all radiation-induced positive charge to interface traps. Therefore at long-time LDR irradiation we can observe the increasing of the degradation.

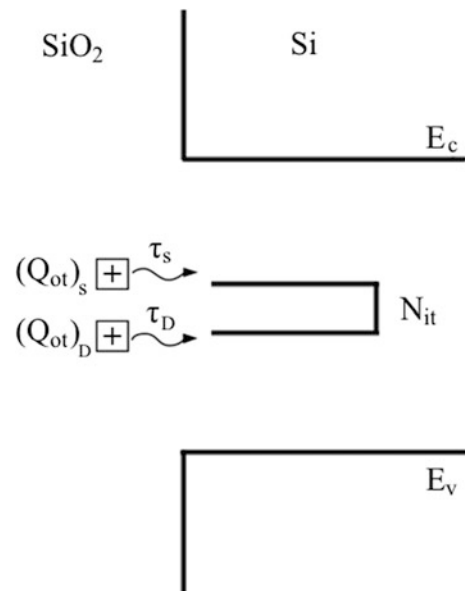


Fig. 2 Shallow $(Q_{ot})_s$ and deep $(Q_{ot})_D$ traps in oxide with conversion time τ_s and τ_D (after Ref. [4])

As was shown in [3, 4], the degradation of the base current as a function of the dose rate (for irradiation time essentially more than 1 s) can be written as [3, 4].

$$\Delta I_b = (K_D + K_S) \cdot D + P \cdot K_D \cdot \tau_D \left(e^{-D/P \cdot \tau_D} - 1 \right) \quad (1)$$

where K_S is the excess base current per unit dose at a high dose rate; K_D is the excess base current per unit dose at a low dose rate; P is a dose rate; τ_D is conversion time of the deep traps; and D is a total dose.

The conversion of oxide charge to interface traps is a thermally stimulated process. To consider the temperature effect on the base current degradation, a dependence of the deep traps conversion time on temperature is introduced. The temperature dependence of time constant τ_D can be described by the Arrhenius law:

$$\tau_D(T) = \tau_{D0} \exp\left(\frac{E_A}{kT}\right) \quad (2)$$

where T is the absolute temperature; E_A is the activation energy of deep oxide trap thermal excitation; k is the Boltzmann constant; τ_{D0} is a pre-exponential coefficient.

The model based on (1) and (2) has four effective fitting parameters: K_S ; K_D ; E_A and τ_{D0} .

The experimental extraction of effective parameters can be performed by the following steps [10]:

1. The constant K_S is estimated as the ratio of base current degradation to the specified total dose at high dose rate irradiation.
2. The pre-exponential constant τ_{D0} and activation energy E_A in (2) are derived from the data for two different temperatures of elevated temperature post-irradiation annealing.
3. The constant K_D is estimated from elevated temperature irradiation data. It is supposed that during elevated temperature irradiation all deep traps are converted to interface traps, as it is happened at low dose rate irradiation.

The extraction of four effective fitting parameters allows describe the behavior of the radiation-induced excess base current for arbitrary dose rate, total dose and temperature. The successful using this technique was demonstrated in [3, 4] for several types of ELDRS devices.

When reporting experiments on animals, authors should be asked to indicate whether the institutional and national guide for the care and use of laboratory animals was followed.

4 Physical Mechanism of True and Time Dependent Effect

We suppose that the accumulation and annealing of the positive oxide trapped charge Q_{ot} are described by the following equation:

$$\frac{dQ_{ot}}{dt} = K_{ot}P - \frac{Q_{ot}}{\tau_D} \quad (3)$$

where Q_{ot} is the oxide trapped charge; where K_{ot} is a coefficient characterizing the accumulation of trapped charge; P is the dose rate; τ_D is the conversion time of deep traps.

First term in the right-hand side of (3) represents the trapped charge accumulation in thick oxide by dispersion transport of radiation-induced holes. Second term in the right-hand side of (3) is responsible for the neutralization of deep trap charge by electrons from substrate.

The interface trap buildup N_{it} can be expressed as follows:

$$\frac{dN_{it}}{dt} = \frac{1}{q} \frac{Q_{ot}}{\tau_D}, \quad (4)$$

where q is the electronic charge.

The right-hand side of (4) represents the interface traps buildup through the conversion of trapped charge by the substrate electrons and radiation-induced electrons.

The relationship (1) follows from joint solution of (3) and (4). The parameters K_S and K_D in (1) depend on the coefficients K_{ot} characterizing the accumulation of the oxide trapped charge for shallow and deep traps. For ELDRS devices the main factor is an accumulation of the deep traps, which determines parameter K_D .

The accumulation of the oxide trapped charge is the strong function of an electric field in oxide. The effect of the electric field consists at separation of radiation induced electron-hole pairs and obstacle their initial recombination. At small electric field the electron-hole pairs do not separate, the recombination is great and the yield of the oxide trapped charge is small. The thick screening oxide above the passive transistor base region does not have any metallization, so the value of the oxide electric field is small and depends on the oxide trapped charge. Usually it is assumed that the initial build-in electric field in bipolar thick oxide is positive and equals several units of 10^5 V/cm [11]. An accumulation of the positive trapped charge in oxide near Si/SiO₂ interface leads to reducing of the oxide electric field. Using Gauss theorem, the value of reduction of the oxide electric field can

be estimated as $Q_{ot}/\varepsilon_{\text{SiO}_2}\varepsilon_0$ ($\varepsilon_{\text{SiO}_2}$ and ε_0 are the dielectric permittivity of oxide and vacuum). The charge yield for low and high dose rates is quite different. For LDR the value of the positive trapped charge is relatively small due to its conversion during long-time irradiation, as a result the reduction of the oxide electric field is small and the yield of the oxide trapped charge is relatively large. Since the duration of HDR irradiation is relatively short and time for the conversion is small, the value of the positive trapped non converted charge increases. It leads to decreasing of the oxide electric field and reduction of the total of the oxide charge yield. Therefore the reduction of the oxide electric field at LDR is less than in case of HDR. It leads to increasing the value of positive charge yield for LDR (more electric field relates less initial recombination) and increasing the value of interface traps due to converted the greater positive charge. The “true” effect connects with the dependence of coefficient K_D in (1) from the dose rate due to the different oxide charge yield at LDR and HDR irradiations. It means that the coefficient K_D in (1) is function of the dose rate. For this reason ELDRS is “true” dose rate effect because the accumulation of oxide charge and interface traps depends on the dose rate. Note that the ELDRS conversion model in form (1) has time-dependent nature for given dose rate.

The oxide charge yield is less for the high dose rate. Therefore HDR irradiation leads to an accumulation of the smaller oxide trapped charge in comparison with LDR irradiation. An high temperature annealing after HDR irradiation leads to the accumulation of the smaller value of interface traps due to conversion of the smaller positive charge. It means that the degradation measured at the end of a low dose rate irradiation is greater than the degradation after irradiation at high dose rate followed by a high temperature anneal (“true” dose rate effect).

The constant K_D is proportional to the coefficient characterizing the accumulation of trapped charge K_{ot} . According to the extraction technique the value K_D is estimated from elevated temperature irradiation data. As the main goal of the ELDRS conversion model is a prediction of the transistor parameter degradation for the extremely low dose rate in the space environment, the elevated temperature installs 100–120 °C when all radiation-induced deep oxide charges are converted to interface traps. It means that the ELDRS conversion model correct predicts the degradation for the small dose rate. The degradation at the high dose rate is estimated very easy during test laboratory experiment. Therefore the error at the description of the radiation degradation in the wide range of the dose rates using the ELDRS conversion model takes place only in the middle interval of the dose rates. But it has not any practical interest.

The correct description of the radiation degradation for any dose rate demands the extraction of the constant K_D for

the each dose rate. It can be done using elevated temperature irradiation in range 40–90 °C. The constants K_D are estimated from these experimental data correspond to not full conversion of the oxide trapped charge and in a first order describe the dependence K_D at the dose rate P . Using in (1) the value K_D as function of the dose rate P the ELDRS conversion model really describes the ELDRS as “true” dose rate effect.

5 Conclusions

The enhancement of early published ELDRS conversion model for the estimation of the radiation degradation of bipolar devices on the impact of low dose rate irradiation is fulfilled. The ELDRS conversion model is based on the hydrogen-electron model of radiation-induced interface trap buildup and assumption that there are the shallow and deep oxide trapped charges, which conversion are responsible for the degradation at high and low dose rates irradiation. The qualitative analysis is carried out concerning an effect of the oxide electric field on the oxide trap charge yield. With increasing the oxide charge the initial electric field reduces and the charge yield reduces too. This process connects with the value of the dose rate. The oxide charge yield is less for the high dose rate. It leads to dependence of the coefficient characterizing of the oxide deep trap accumulation on the dose rate. Therefore the degradation after irradiation at high dose rate followed by a high temperature anneal is less than the degradation measured at the end of a low dose rate irradiation. For this reason ELDRS is “true” dose rate effect because the accumulation of interface traps depends on the dose rate. The early published ELDRS conversion model does not take into account this circumstance. But early version of the ELDRS conversion model is correctly described the degradation on the very low dose rate (real space environment) because the extraction of model fitting parameters corresponds to the low dose rate. The correct description of the radiation degradation for the wide range of the dose rates demands the extraction of the fitting constants for the each dose rate what can be done using test elevated temperature irradiation in the wide temperature range.

Conflict of Interest The authors declare that they have no conflict of interest.

References

1. Pease, R.L., Schrimpf, R.D., Fleetwood, D.M.: ELDRS in bipolar linear circuits: a review. *IEEE Trans. Nucl. Sci.* **56**(4), 1894–1908 (2009). <https://doi.org/10.1109/TNS.2008.2011485>

2. Pershenkov, V.S., Bakerenkov, A.S., Telets, V.A., Belyakov, V. V., Shurenkov, V.V., Felitsyn, V.A., Rodin, A.S.: Study of ELDRS using the conversion model of the radiation-induced interface trap buildup. In: RADECS Workshop 2018 and The 2nd International Conference on Radiation Effects of Electronic Devices, Beijing, China, 16–18 May 2018
3. Pershenkov, V.S., Savchenkov, D.V., Bakerenkov, A.S., Ulimov, V.N., Nikiforov, A.Y., Chumakov, A.I., Romanenko, A.A.: The conversion model of low dose rate effect in bipolar transistors. In: RADECS Proceeding, 2009, pp 286–393. <https://doi.org/10.1109/radecs.2009.5994661>
4. Pershenkov, V.S., Savchenkov, D.V., Bakerenkov, A.S., Ulimov, V.N.: Conversion model of enhanced low dose rate sensitivity in bipolar ICs. *Russ. Microelectron.* **39**(2), 91–99 (2010). <https://doi.org/10.1109/23.903805>
5. McLean, F.B.: A framework for understanding radiation-induced interface states in MOS SiO₂ structures. *IEEE F Trans. Nucl. Sci.* **NS-27**(6), 1651–1657 (1980)
6. Oldham, T.R., McLean, F.B.: Total ionizing dose effects in MOS oxides and devices. *IEEE Trans. Nucl. Sci.* **50**(3), 483–499 (2003)
7. Lai, S.K.: Interface trap generation in silicon dioxide when electrons are captured by trapped holes. *J. Appl. Phys.* **54**, 2540–2546 (1983)
8. Sogoyan, A.V., Cherepko, S.V., Pershenkov, V.S.: The hydrogenic-electron model of accumulation of surface states on the oxide-semiconductor interface under the effects of ionizing radiation. *Russ. Microelectron.* **43**(2), 162–164 (2014)
9. Emelianov, V.V., Sogoyan, A.V., Meshurov, O.V., Ulimov, V.N., Pershenkov, V.S.: Modeling the field and thermal dependence of radiation-induced charge annealing in MOS devices. *IEEE Trans. Nucl. Sci.* **43**(6), 2572–2578 (1996)
10. Bakerenkov, A.S., Belyakov, V.V., Pershenkov, V.S., Romanenko, A.A., Savchenkov, D.V., Shurenkov, V.V.: Extracting the fitting parameters for the conversion model of enhanced low dose rate sensitivity in bipolar devices. *Russ. Microelectron.* **42**, 48–52 (2013)
11. Zebrev, G.I., Petrov, A.S., Useinov, R.G., Ikhsanov, R.S., Ulimov, V.N, Anashin, V.S., Elushov, I.V.: Simulation of bipolar transistors degradation at various dose rate and electrical modes for high dose conditions. RADECS-2013, session G, report PG-5

Modeling of the Valence Tautomeric Transformation in Heterometallic [Cr-Dhbq-Co] Molecules

M. A. Roman and S. I. Klokishner

Abstract

In the present communication we report a model that describes the valence tautomeric transformation in a crystal consisting of heterometallic [Cr-dhbq-Co] molecules. The model takes into account the states arising from two different configurations of the molecule, namely, $\text{Cr}^{3+}\text{-dhsq}^{3-}\text{-Co}^{3+}$ and $\text{Cr}^{3+}\text{-dhsq}^{2-}\text{-Co}^{2+}$, the Heisenberg exchange interaction between the dhsq^{3-} ligand and the Cr^{3+} ion as well as the cooperative electron-deformational and dipole-dipole interactions. The problem is solved in the mean field approximation. The main peculiarities of the valence tautomeric transformation are elucidated. It is demonstrated that the electron transfer ligand-Co is accompanied not only by the significant increase of the effective magnetic moment but also by the appreciable change in the microscopic polarization. The model provides quite a good description of the experimental data on the temperature dependence of the effective magnetic moment in the $[(\text{Cr}(\text{SS-cth}))(\text{Co}(\text{RR-cth}))(\mu\text{-dhbq})](\text{PF}_6)_3$ compound.

Keywords

Intramolecular and cooperative interactions • Mean field approximation • Effective magnetic moment

1 Introduction

One of the grand challenges of the present time is the development of molecular electronic devices. To tackle this problem chemists and physicists are working in this interdisciplinary field by addressing various new approaches. With this aim in mind the scientists focus on molecules exhibiting magnetic bistability since these systems are perspective for future applications in molecular electronics. Recently different classes of bistable molecules that manifest switching optical and magnetic properties under application of various external stimuli (temperature, pressure, light irradiation, electric field etc.) have got special attention. It is well documented that the most pronounced changes in the above mentioned characteristics are demonstrated by systems with labile electronic states such as spin crossover systems [1], molecules and crystals manifesting charge transfer induced spin transitions as well as valence tautomeric systems [2] etc. The latter ones are very perspective from the point of view of molecular electronics since in them the intramolecular electron transfer between the ligand and the metal ion is accompanied by appreciable changes in the magnetic and spectroscopic properties of a single molecule [3, 4]. Last time these systems have got a great deal of attention, and a significant development has been made in this area of research. At the moment, valence tautomeric systems can be found as mono-, di-, poly-nuclear complexes, chains, polymers etc. [3–10]. Meanwhile, the theoretical studies examining the valence tautomeric transformation are fewer as compared with the experimental ones. The main points discussed in the theoretical papers were the following ones. Firstly, early works were based on explaining valence-tautomeric transformation through thermodynamic calculations since the theorists determined that valence tautomerism is an entropy driven process [11–13]. A significant contribution to the interpretation of the changes in the optical, electronic and magnetic properties that accompany the valence tautomeric interconversion is given through DFT calculations [14–16].

In Memory of Alexandr Kuznetsov

M. A. Roman · S. I. Klokishner (✉)
 Institute of Applied Physics, Academy Str. 5, Chisinau, Republic of Moldova
 e-mail: klokishner@yahoo.com

The first microscopic model of valence tautomerism in a single molecule and in a crystal containing these molecules as a structural element has been suggested in [17]. The role of vibronic and electric dc field effects in the valence tautomeric transformation has been discussed in [18, 19]. Most of the theoretical studies are based on mononuclear Co-systems [14, 15, 17–19] and binuclear homometallic systems [20, 21]. Among the papers dealing with valence tautomerism those considering heterometallic binuclear systems [16, 22] should be also mentioned.

Recently in paper [22] a new synthetic and crystal engineering strategy has been applied to perform the selective synthesis of the binuclear [(Cr(SS-cth))(Co(RR-cth))(μ -d**hbq**)](PF₆)₃ ([CrCo]) complex which possesses a polar crystal structure. In this compound the intramolecular electron transfer between the ligand and cobalt ion induces pronounced changes in the polarizability and magnetic characteristics. However, the paper [22] contains only structural data and observed magnetic and spectroscopic characteristics.

In order to understand the processes responsible for the observed magnetic behavior in the heterometallic binuclear [CrCo] system demonstrating valence tautomeric transformation [22] accompanied by polarization changes in the present communication a theoretical model is suggested.

2 The Model

We examine a crystal consisting of molecules with each [CrCo] molecule containing a chromium ion, a cobalt ion and a ligand that bears an electron. The analysis of the magnetic susceptibility data and optical spectra of the compound [22] under examination shows that the ligand $dhsq^{3-}$ can transfer an electron to the Co ion. In this system the cobalt ion can be in the diamagnetic state ($ls-Co^{3+}$) or in the paramagnetic ones ($ls-Co^{2+}$, $hs-Co^{2+}$). The transfer of an electron from the ligand to the cobalt ion changes the state of the latter.

Further on we consider the following configurations of the molecule:

- I. $Cr^{3+}-dhsq^{3-}-ls-Co^{3+}$
- II. $Cr^{3+}-d**hbq**^{2-}-hs-Co^{2+}$

The configuration $Cr^{3+}-d**hbq**^{2-}-ls-Co^{2+}$ which is connected with configuration I by the spin allowed electron transfer is not included in consideration since the observed absorption spectra and the χT versus temperature plots [22] show that the energy of this configuration is much higher than that of configuration II and it does not manifest itself in the magnetic characteristics. The fact that the intermediate configuration lies higher than that containing the $hs-Co^{2+}$ ion

was confirmed by the examination of the valence tautomeric transformation in papers [17, 18].

In further consideration the following spin-coupling scheme is applied:

$$\begin{aligned} S_{aL} &= S_a + S_L \\ S &= S_{aL} + S_b \end{aligned} \quad (1)$$

where S is the full spin of the system, S_{aL} is the intermediate spin of the system, and S_a , S_b , S_L are the spins of the Cr-ion, the Co-ion and the ligands ($dhsq^{3-}$ or $d**hbq**^{2-}$), respectively. The spin value for the $dhsq^{3-}$ ligand is $1/2$, while the ligand in the $d**hbq**^{2-}$ state is diamagnetic [22]. In the states of configuration I, the values of the full spin S of the molecule are 1 and 2. In the case of configuration II, the full spin S of the molecule acquires the values 0, 1, 2, 3.

The total Hamiltonian of the system of interacting molecules looks as follows

$$H = H_e + H_{st} + V_{dd}, \quad (2)$$

here H_e is the Hamiltonian which includes the crystal field acting on the Co-ion and the Heisenberg exchange interaction $-2j_{ex}S_aS_L$ (j_{ex} —is the parameter of exchange interaction). Since the electron transfer from the ligand to the cobalt ion is accompanied by the deformation of the nearest cobalt surrounding that leads to the deformation of the soft inter-cluster space [17] in the crystal the cooperative electron-deformational interaction arises. The Hamiltonian of this interaction was deduced by the method suggested in [17, 23] and looks as follows

$$H_{st} = -\frac{J}{2N} \sum_{n,m} \tau^n \tau^m \quad (3)$$

J is the parameter characterizing the electron-deformational interaction. The diagonal matrices τ^n are of the dimension 56×56 , possess the non-vanishing matrix elements -1 and 1 which correspond to the states arising from configurations I and II, respectively. These matrices also take into account that the total degeneracy of states belonging to configuration I is equal to 8, while that for states of configuration II is 48. The indicated values 8 and 48 take into account that the states of configuration I are only degenerate on the spin values $S = 1$ and 2, while the degeneracy of states of configuration II is determined not only by the spins 0, 1, 2, 3, but also by the possibility to place three unpaired electrons in the orbitals of the $hs-Co^{2+}$ ion in three different ways.

The last term in (2)

$$V_{dd} = -\frac{1}{2} \sum_{n,m} K(n-m) d^n d^m \quad (4)$$

represents the dipole-dipole interaction, where d^n is the matrix of the operator of the n -th molecule dipole moment. This matrix is also diagonal and possesses the following non-vanishing matrix elements: d_0 and $-3d_0$, where $d_0 = eR$ is the dipole moment of the ligand in the states of configuration I, while $-3d_0$ denotes the dipole moment of states belonging to configuration II, in which the ligand is diamagnetic, while the Co^{2+} ion bears 3 unpaired electrons.

The problem is further solved in the mean field approximation in which the products $\tau^n \tau^m$ and $d^n d^m$ are replaced by:

$$\begin{aligned} \tau^n \tau^m &= \bar{\tau} \tau^m + \tau^n \bar{\tau} - \bar{\tau}^2 \\ d^n d^m &= \bar{d} d^m + d^n \bar{d} - \bar{d}^2 \end{aligned} \quad (5)$$

where the order parameters $\bar{\tau}$ and \bar{d} represent the mean value of the distortion and of the dipole moment, respectively, and are determined by the equations:

$$\begin{aligned} \bar{\tau} &= \frac{Tr \left(Exp \left(-\frac{\hat{H}}{kT} \right) \tau^n \right)}{Tr \left(Exp \left(-\frac{\hat{H}}{kT} \right) \right)} \\ \bar{d} &= \frac{Tr \left(Exp \left(-\frac{\hat{H}}{kT} \right) d^n \right)}{Tr \left(Exp \left(-\frac{\hat{H}}{kT} \right) \right)} \end{aligned} \quad (6)$$

where \hat{H} is the Hamiltonian of the system in the mean field approximation. The temperature behavior of the order parameters $\bar{\tau}$ and \bar{d} is determined by the competition of intra- and intercluster interactions.

3 Results

The effective magnetic moment was calculated using the following formula

$$\mu_{eff}^2 = g_s^2 \mu_B^2 \frac{\sum_i g_i S_i (S_i + 1) Exp \left(-\frac{\varepsilon_i(S_i)}{kT} \right)}{\sum_i g_i Exp \left(-\frac{\varepsilon_i(S_i)}{kT} \right)} \quad (7)$$

where g_i in (7) takes into account not only the spin degeneracy of the state with the energy ε_i , but also in the case of configuration II three possible different arrangements of the electrons placed in the lowest three orbitals of the h_s-Co^{2+} ion, ε_i are the eigenvalues of the total Hamiltonian in the molecular field approximation.

In Fig. 1 the calculated temperature dependence of the effective magnetic moment as a function of temperature [eq. (7)] is presented together with the experimental values for the [CrCo] system obtained in ref [22].

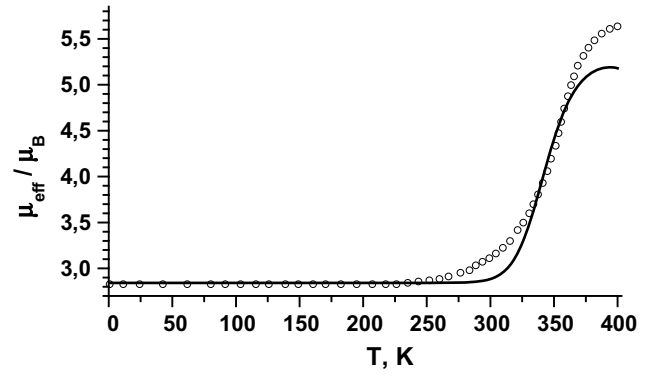


Fig. 1 Temperature dependence of the effective magnetic moment for the [CrCo] system. Circles represent the experimental data reported in reference [22], and the solid line is the theoretical curve calculated with the best fit parameters

Figure 1 shows a satisfactory agreement between the observed and calculated effective magnetic moment values, thus indicating that the presented model quite well describes the spin transformation which takes place in the [CrCo] compound. The agreement criterion is about 4%. The obtained best fit parameters for Δ , j_{ex} , Ld_0^2 and J are reasonable and of the same order as the known parameters for systems manifesting ligand-metal electron transfer [17]. As to the value of the parameter of exchange interaction ligand-metal it falls into the limits indicated in paper [24] for such type interactions. The results obtained also show the appreciable role of the dipole-dipole interaction which suppresses

$$\begin{aligned} j_{ex} &= -92 \text{ cm}^{-1}, \Delta = 1000 \text{ cm}^{-1}, J = 0.04 \text{ cm}^{-1}, Ld_0^2 \\ &= 300 \text{ cm}^{-1}. \end{aligned}$$

the ligand-metal electron transfer at temperatures up to 300 K and prevents the increase of the magnetic moment. In fact when the dipole ordering is destroyed the effective magnetic moment starts increasing that testifies that the “extra” electron of the ligand is transferred to the metal ion. The obtained characteristic energy of this interaction, $Ld_0^2 = 300 \text{ cm}^{-1}$ is in quite good agreement with the temperature at which this increase starts in the experiment.

4 Conclusions

In summary, we have analyzed the influence of different intrinsic parameters on valence tautomeric transformations in model crystals containing as a structural element $Co-Cr$ binuclear clusters. The following electronic processes and interactions were considered: (i) intramolecular magnetic exchange interactions; (ii) dipole-dipole interactions; (iii) intermolecular electron-deformational interactions. The

proposed model provides a reasonable explanation of the observed magnetic properties of the cluster *Co-Cr*.

Acknowledgements The financial support of the Science and Technology Center in Ukraine (STCU project N 6219) and of the Ministry of Education, Culture and Research of Moldova (project 15.817.02.06F) is highly appreciated.

Conflict of Interest The authors declare that they have no conflict of interest.

References

- Gütlich P, Goodwin H A (2004) Spin Crossover in Transition Metal Compounds I. Springer-Verlag, Berlin, Heidelberg
- Sato, O., Tao, J., Zhang, Y.-Z.: Control of magnetic properties through external stimuli. *Angew. Chem. Int. Ed.* **46**, 2152–2187 (2007)
- Pierpont, C.G., Buchanan, R.M.: Transition metal complexes of o-benzoquinone, o-semiquinone, and catecholate ligands. *Coord. Chem. Rev.* **38**, 45–87 (1981)
- Pierpont, C.G.: Studies on charge distribution and valence tautomerism in transition metal complexes of catecholate and semiquinonate ligands. *Coord. Chem. Rev.* **216–217**, 99–125 (2001)
- Dei, A., Gatteschi, D., Sangregorio, C., et al.: Quinonoid metal complexes: toward molecular switches. *Acc. Chem. Res.* **37**, 827–835 (2004)
- Glaser, T., Heidemeier, M., Fröhlich, R., et al.: Trinuclear nickel complexes with triplesalen ligands: simultaneous occurrence of mixed valence and valence tautomerism in the oxidized species. *Inorg. Chem.* **44**, 5467–5482 (2005)
- Sato, O.: Switchable molecular magnets. *Proc. Jpn. Acad. Ser B* **88**, 213–225 (2012)
- Tezgerevska, T., Alley, K.G., Boskovic, C.: Valence tautomerism in metal complexes: stimulated and reversible intramolecular electron transfer between metal centers and organic ligands. *Coord. Chem. Rev.* **268**, 23–40 (2014)
- Drath, O., Boskovic, C.: Switchable cobalt coordination polymers: Spin crossover and valence tautomerism. *Coord. Chem. Rev.* **375**, 256–266 (2017)
- Drath, O., Gable, R.W., Boskovic, C.: Structural investigation of one- and two-dimensional coordination polymers based on cobalt-bis(dioxolene) units and 1-hydroxy-1,2,4,5-tetrakis(pyridin-4-yl)cyclohexane. *Acta. Cryst.* **C74**, 734–741 (2018)
- Adams, D.M., Dei, A., Rheingold, A.L., et al.: Bistability in the [Co^{II}(semiquinonate)₂] to [Co^{III}(catecholate)(semiquinonate)] valence-tautomeric conversion. *J. Am. Chem. Soc.* **115**, 8221–8229 (1993)
- Jung, O.-S., Pierpont, C.G.: Bistability and low-energy electron transfer in cobalt complexes containing catecholate and semiquinone ligands. *Inorg. Chem.* **33**, 2227–2235 (1994)
- Caneschi, A., Cornia, A., Dei, A.: Valence tautomerism in a cobalt complex of a schiff base diquinone ligand. *Inorg. Chem.* **37**, 3419–3421 (1998)
- Sato, D., Shiota, Y., Juhász, G., et al.: Theoretical study of the mechanism of valence tautomerism in cobalt complexes. *J. Phys. Chem. A* **114**, 12928–12935 (2010)
- Tourón Touceda, P., Mosquera Vázquez, S., Lima, M., et al.: Transient infrared spectroscopy: a new approach to investigate valence tautomerism. *Phys. Chem. Chem. Phys.* **14**, 1038–1047 (2012)
- Minkin, V.I., Starikova, A.A., Starikov, A.G.: Quantum chemical modeling of magnetically bistable metal coordination compounds. Synchronization of spin crossover, valence tautomerism and charge transfer induced spin transition mechanisms. *Dalton Trans.* **45**, 12103–12113 (2016)
- Klokishner, S.: Cobalt valence tautomeric compounds: molecular and solid state properties. *Chem Phys.* **269**, 411–440 (2001)
- Klokishner, S.I., Reu, O.S.: Vibronic dynamic problem of valence tautomerism in cobalt compounds: magnetic and optical properties. *Polyhedron* **22**, 2401–2408 (2003)
- Reu, O., Ostrovsky, S., Decurtins, S., et al.: Electric field control of the valence-tautomeric transformation in cobalt complexes. *Eur. J. Inorg. Chem.* **2017**, 5356–5365 (2017)
- Minkin, V.I., Starikova, A.A., Starikov, A.G.: Valence tautomeric dinuclear adducts of Co(II) diketonates with redoxactive diquinones for the design of spin qubits: computational modeling. *Dalton Trans.* **44**, 1982–1991 (2015)
- Minkin, V.I., Starikova, A.A., Starikov, A.G.: Theoretical modeling of valence tautomeric dinuclear cobalt complexes. Adducts of Co^{II} diketonates with cyclic redox-active tetraone ligands. *Dalton Trans.* **44**, 17819–17828 (2015)
- Kanegawa, S., Shiota, Y., Kang, S., et al.: Directional electron transfer in crystals of [CrCo] dinuclear complexes achieved by chirality-assisted preparative method. *J. Am. Chem. Soc.* **138**(43), 14170–14173 (2016)
- Roman, M.A., Reu, O.S., Klokishner, S.I.: Charge-transfer-induced spin transitions in crystals containing cyanide-bridged co-Fe clusters: role of intra- and intercluster interactions. *J. Phys. Chem. A* **116**, 9534–9544 (2012)
- Ovcharenko, V.I., Gorelik, E.V., Fokin, S.V.: Ligand effects on the ferro- to antiferromagnetic exchange ratio in bis(o-semiquinonato)copper(II). *J. Am. Chem. Soc.* **129**, 10512–10521 (2007)

Fabrication and Application of TEM-Compatible Sample Grids for Ex Situ Electrical Probing

O. Gronenberg, N. Carstens, A. Vahl, F. Faupel, and L. Kienle

Abstract

Memristors are promising candidates for new memory technologies and are capable to mimic neural networks. The switching in memristive devices occurs typically in few nanometer thin oxide layers. The direct observation of the switching mechanism is crucial for better comprehension and improvements of memristors. Therefore, in situ experiments are conducted in a transmission electron microscope (TEM). However, electron beam irradiation can lead to a chemical modification of the active layers. Moreover, devices may show different performance due to the details of processing parameters. Thus, it is essential to characterize memristors electrically before microstructural analysis. In this work a TEM compatible grid is developed, which can be used for ex situ electrical probing and TEM investigations. Different techniques for the production, like shadowing and lithography are compared with their advantages and drawbacks.

Keywords

Memristor • TEM • Nanomaterials

1 Introduction

For the microstructural and chemical characterization of nanoscopic electronic devices TEM is the most suitable method. To prevent artefacts from the sample preparation it is best to do the investigation on working devices that

already follow the geometrical constraints of TEM. By this, it is possible to check the device before and after the TEM examination and proof that the observed features are part of the working device and no artefacts.

In the past, in situ switching experiments on memristors were conducted and highly cited works were published [1, 2]. However, our recent results have shown that the electron beam has a strong influence on the electrical characteristics, e.g., the beam can reversibly reduce memristive oxides [3] to form locally conducting filaments of suboxides or even metals. The re-oxidation is facilitated by the residual oxygen contaminating the TEM column. Moreover, the electron beam may charge electrically isolated particles, thus introducing artefacts in the electrical characterization. When scaling the production of memristive devices a second motivation for ex situ electrical characterization occurs. Recently, we demonstrated that devices prepared on wafer-scale may have variable electrical characteristics due to minute imperfections of the production process [4]. Consequently, it should be established as golden standard to characterize devices before and after TEM preparation in order to identify the intrinsic microstructural features establishing memristive switching.

The aim of this work is to fabricate a TEM grid which can be used to do ex situ switching experiments. Therefore, two separated electrodes are deposited on an electron-transparent membrane as depicted in Fig. 1.

Here, bimetallic clusters in a dielectric matrix were investigated using the novel grid design (cf. Figure 1 on the right site). In an electric field, the two metals in the clusters will electrochemically dissolve at different field strengths [2]. Accordingly, a depletion of the bimetallic cluster is observed. The decrease in content of the less noble metal stops when a conducting path has grown. This mechanism can act as a diffusive memristor when the conducting path is interrupted at lower field strength due to surface energy minimization.

We demonstrate how such a memristor can be characterized by ex situ TEM-experiments. In the first part the necessary preparation of TEM-sample-grids is described capable for ex situ electrical probing.

O. Gronenberg · L. Kienle (✉)
Synthesis and Real Structure, Institute for Materials Science,
CAU Kiel, Kaiserstraße 2, Kiel, Germany
e-mail: lk@tf.uni-kiel.de

O. Gronenberg
e-mail: og@tf.uni-kiel.de

N. Carstens · A. Vahl · F. Faupel
Nanocomposite Materials, Institute for Materials Science,
CAU Kiel, Kaiserstraße 2, Kiel, Germany

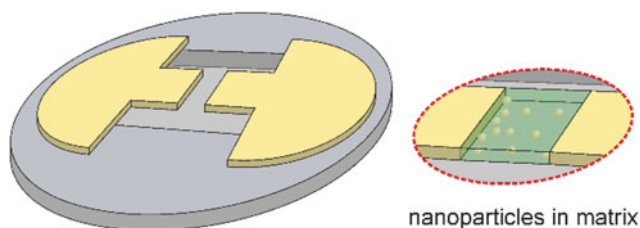


Fig. 1 Sketch of the structured electrodes on a TEM-grid

2 Preparation of Functional TEM-Grids

2.1 Materials and Possibilities

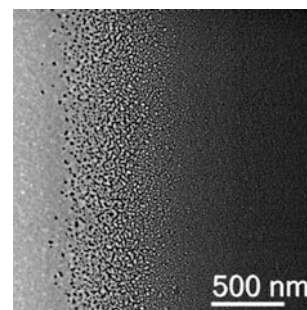
Inert and highly conductive electrodes are made of gold or platinum. The commercial TEM substrates are made from silicon with a 50 nm thick Si_3N_4 membrane. Si_3N_4 has the advantages of being chemically inert, one of the best insulators and thermally stable [5].

The separated electrodes can be fabricated in different ways, however all procedures are complicated by the tiny dimensions of the electrode's gap. For example a shadow mask during sputter-deposition can separate the deposited thin film. A thin foil or the edge of a razorblade clamped vertically above the sample-grid or a fiber can be used as shadow mask. On the other hand the electrodes can be structured by standard lithography techniques or more sophisticated by E-beam-lithography. Latter is necessary to fabricate electrodes with a distance below 1 μm what is unambiguous for the examination of nanoparticles. Furthermore, a Gas Injection Source can directly deposit separated electrodes on a sample-grid.

2.2 Shadow Mask

The simplest and fastest approach is to shadow a part of the sample-grid during the sputter-deposition by a mask. The mask needs to be attached to the fragile membrane with a drop of isopropanol. Furthermore, sputtering below the mask happens in the case of round masks like fibers. This sputtering below the mask results in a continuous transition from the compact gold film at the electrode sides via a percolating nanoparticle film to a nanoparticle island film. The size of the islands decreases continuously from 30 to 1 nm in direction of the center of the gap (cf. Fig. 2). This observed transition is probably the result of two phenomena: first the decreasing thin film thickness below the mask and second

Fig. 2 Scanning Transmission Electron (STEM) image of the edge of an electrode prepared with a glass fiber attached with isopropanol



the island-growth-mode of gold on Si_3N_4 [6]. In addition shadow-masks are quite thick (typically $>0.5 \mu\text{m}$) and not flexible in geometry. Accordingly, broad electrodes are deposited.

2.3 Lithography

A more sophisticated approach to structure the gold electrodes is lithography. Here, a resist is coated on the sample-grid followed by UV-illumination through a structured mask and development of the resist. By this, the resist is structured and gold below or on top can be etched or lifted off. This approach is much more time consuming and risky as a lot of working steps are necessary in which the fragile membrane can break. Furthermore, the grid can get contaminated by the resist or other used chemicals, thus inhibiting dedicated TEM analysis. The minimal feature-size is 1 μm in the case of photolithography. Using a focused electron beam in the case of E-beam-lithography the minimal feature-size is below 100 nm. Despite this approach is very time consuming it definitely provides advantages since no mask is necessary and the structured pattern can be freely designed. Electrodes produced by photo- and E-beam-lithography are shown in Figs. 3 and 4, respectively.

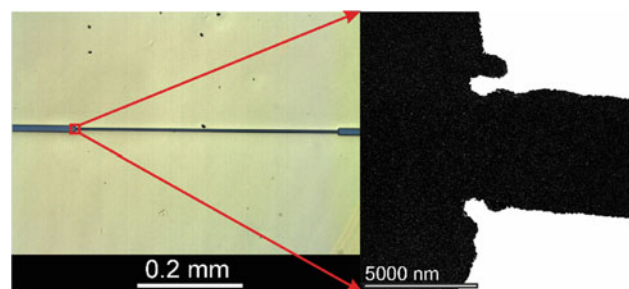


Fig. 3 Optical (left) and STEM (right) image of a grid prepared by photolithography and wet etching

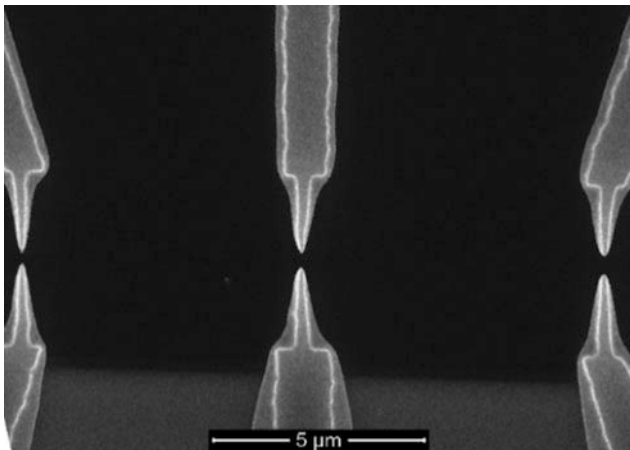
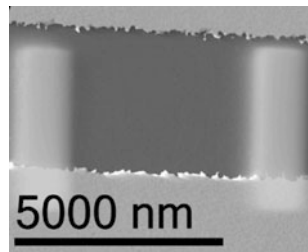


Fig. 4 SEM image of three electrodes structured with E-beam lithography

Fig. 5 STEM image of the edge of an electrode prepared with a glass fiber attached with isopropyl alcohol



2.4 Gas Injection Source (GIS)

As another technique to deposit electrodes on the sample-substrate a Gas Injection Source (GIS) was applied. A focused Ga-ion beam or an electron-beam decomposes a Pt precursor gas inside a vacuum chamber. By this, Pt is deposited in the defined areas. This technique is again time consuming and expensive. However, the possible electrode geometry is flexible and represents a one-step solution to deposit separated electrodes on a substrate. Two disadvantages deal with the minimum feature-size which is around ~ 400 nm and the contamination of the electrodes with mobile carbon species from the precursor. Figure 5 exemplifies two electrodes deposited with a GIS. Here, the blurred edges of the electrodes can be seen which stems from the gaseous precursor.

3 Example Measurement

3.1 Methods

Figure 6 shows an example measurement with a functionalized sample substrate fabricated by E-beam-lithography.

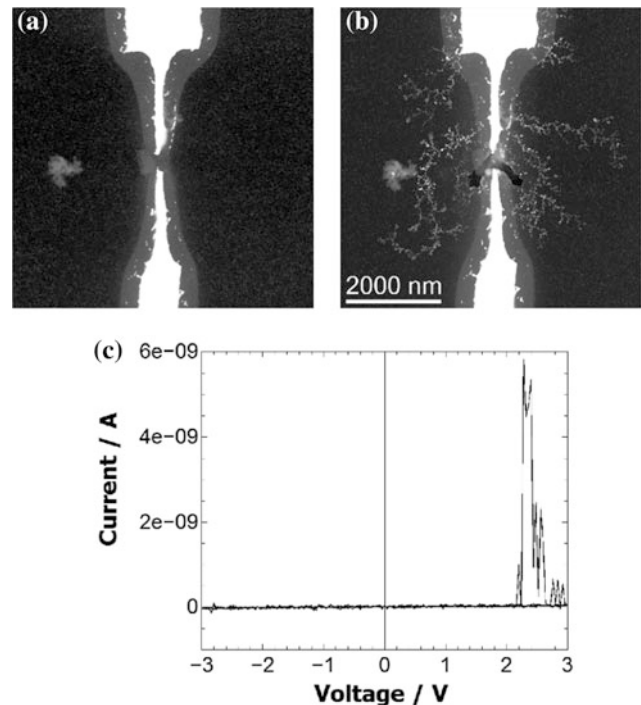


Fig. 6 **a** and **b** STEM images of two electrodes prepared by E-beam-lithography. Contrast and brightness was adjusted that both the gold electrodes and the bimetallic clusters are visible. **a** is the pristine state where AgPt-clusters and a SiN_x matrix is deposited on the grid. And **b** is the same region after electrical probing which is shown in graph (c)

12 nm AgPt-clusters were deposited with a Harberland-type cluster-source and these clusters were embedded in a 10 nm SiN_x matrix in the same vacuum-chamber by reactive sputtering. This deposition chamber is described elsewhere [7]. Electrical probing was done with a Keithley 2400 Source-Meter and needles on micro-positioners to contact the electrodes.

3.2 Results and Discussion

Figure 6a shows a STEM micrograph of this output state. Due to the Z-contrast the 50 nm-thick gold electrodes appear brightest. To this electrodes cyclic voltammetry between +3 V and -3 V was applied (cf. Fig. 5c). In the first cycle no current flows. However, in the second cycle at roughly 2.9 V the SiN_x matrix starts to breakdown. The TEM investigations after the electrical probing suggests that the breakdown is preceded (or accompanied) by massive dendritic silver migration. The dendritic silver structures can be clearly seen in Fig. 5b in light grey and the dielectric breakdown as the dark V-shaped area between the electrodes where the electric field was highest.

EDX-measurements show that the silver-content in the AgPt-clusters is drastically decreased after the electrical probing, whereas, the dendrites mainly consists of silver. This is an indirect proof that the silver in the AgPt-clusters is electrochemically released by the electric field leaving Pt-rich clusters behind.

The dielectric breakdown is likely to happen due to the mechanical stress stemming from the migrating silver and the Joule heating when a conducting path is grown. The Joule heating can be minimized by using thicker electrodes which act as bigger heat sinks.

4 Conclusions

We demonstrated that TEM sample substrates capable for ex situ electrical probing can be fabricated in different ways. With shadow masks during sputter-deposition a transition develops at the edge of the electrodes where percolating nanoparticles decrease in size to 1-nm-small nanoparticles. Lithography is suited best to fabricate sharp electrode edges. In ex situ measurements it was indirectly proven that bimetallic clusters deplete in the less noble metal which migrates in the electric field and builds up a conducting path.

Acknowledgements The authors acknowledge funding through the German Research Foundation (DFG) through the research unit FOR2093 (project B2) “Memristive devices for neuronal systems”. Further, the authors acknowledge helpful discussions and co-working with N. Carstens and A. Vahl.

Conflict of Interest The authors declare that they have no conflict of interest.

References

1. Strobel, J., Neelisetty, K.K., Chakravadhanula, V.S.K., Kienle, L.: Transmission electron microcopy on memristive devices: an overview. *Appl. Microsc.* **46**(4), 206–216 (2016). <https://doi.org/10.9729/AM.2016.46.4.206>
2. Yang, Y., Takahashi, Y., Tsurumaki-Fukuchi, A., Arita, M., Moors, M., Buckwell, M., Kenyon, A.J.: Probing electrochemistry at the nanoscale: in situ TEM and STM characterizations of conducting filaments in memristive devices. *J. Electroceram.* **39**(1–4), 73–93 (2017). <https://doi.org/10.1007/s10832-017-0069-y>
3. Neelisetty, K.K., Mu, X., Gutsch, S., Vahl, A., Molinari, A., von Seggern, F., Kübel, C.: Electron beam effects on oxide thin films—structure and electrical property correlations. *Microsc. Microanal.* 1–9 (2019). <https://doi.org/10.1017/s1431927619000175>
4. Cipo, J., Gauter, S., Georg, F., Zahari, F., Mussenbrock, T., Holger, K., Kohlstedt, H.: Diagnostic of a Process Plasma used for the Production of Memristive Devices. In: DPG Conference Munich 2019 (2019)
5. Nishi, Y., Doering, R. (eds.): *Handbook of Semiconductor Manufacturing Technology*. Marcel Dekker, New York (2000)
6. Ohring, M.: *Materials Science of Thin Films: Deposition and Structure*, 2nd edn. Academic Press, San Diego, CA (2002)
7. Vahl, A., Strobel, J., Reichstein, W., Polonskyi, O., Strunskus, T., Kienle, L., Faupel, F.: Single target sputter deposition of alloy nanoparticles with adjustable composition via a gas aggregation cluster source. *Nanotechnology* **28**(17), 175703 (2017). <https://doi.org/10.1088/1361-6528/aa66ef>

Refractive Index in the Region of Excitonic Resonances in TlGaSe₂ Crystals

A. V. Tiron

Abstract

The low-temperature transmission and wavelength modulated transmission spectra of TlGaSe₂ crystals with a thickness of 7, 5.7, 4.7 μm were measured. Refractive index was calculated from interference observed in transmission spectra. The spectral dependences of the normal dispersion n_a ($E \parallel a$) and n_b ($E \parallel b$) and $\Delta n = n_a$ ($E \parallel a$) - n_b ($E \parallel b$) on the long-wavelength and short-wave side of the ground states A, B and C of excitons are determined.

Keywords

Chalcogenide • Optical spectroscopy • Refractive index

1 Introduction

TlGaSe₂ crystals belong to the group of compounds of triple thallium chalcogenides with a pronounced layered structure. The TlGaSe₂ compound crystallizes in a monoclinic lattice [1, 2]. One of the features of these crystals is the strong anisotropy of physical characteristics, due to the specificity of their crystal structure [1–3]. In these crystals, optical spectra were studied in the region of the absorption edge, the effect of temperature, pressure on optical spectra [3]. In this paper, new data are obtained on the dispersion of the refractive index in the region of exciton resonances in TlGaSe₂ crystals.

A. V. Tiron (✉)

Department of Telecommunication, Technical University of Moldova, 168, Stefan cel Mare boulevard, Chisinau, Republic of Moldova
e-mail: andrei.tiron@scec.utm.md

2 Experimental Methods

The low-temperature spectra of TlGaSe₂ crystals were measured on a double Raman spectrometer DFS-32 and SDL-1 with a linear dispersion of 5 Å/mm and a relative aperture of 1:2. The detector was a photomultiplier operating in the photon counting mode. Optical systems are fully automated and provide data in the form of data files. The optical system makes it possible to record data with a spectral slit width of 0.02 Å (± 0.01 meV). The interference spectra of transmission and reflection are recorded with an accuracy of ± 0.2 meV. In the measurements, we used TlGaSe₂ cleaved crystals of various thickness attached to the cold loop of a closed helium cryostat LTS-22 C 330 optical cryogenic system.

3 Experimental Results and Discussion

According to the crystallographic data, the structure of TlGaSe₂ is described by the space group C_{2h}^6 . The primitive cell contains eight formula units. The basic motif of the structure is formed by tetrahedral polyhedra Ga₄Se₁₀ consisting of four GaSe₄ tetrahedra. The structure of TlGaSe₂ is referred to as pseudo tetragonal, since $a = b = 10.31$ Å, $c = 15.16$ Å, $\beta = 99.7^\circ$ [1–3].

In the transmittance spectra of TlGaSe₂ crystals with a thickness of 7 μm, modulated in a wavelength ($\Delta T/\Delta \lambda$), in the polarization $E \parallel a$ and $E \parallel b$ at 10 K, interference spectra are observed in the region of the ground states A of the excitons, Fig. 1A. Interference lines in modulated spectra thicken with increasing energy. This indicates an increase in the refractive index in the energy range 1.9–2.15 eV, because $n = 1/2d (v_a - v_b)$, where $v_a = 1/\lambda_a$ and $v_b = 1/\lambda_b$ and λ_a and λ_b are the wavelengths of the radial maxima or minima in the interference spectra. In the energy range $E > E$ ($n = 1$, A excitons), the distance between the interference lines decreases with increasing energy, which also indicates an increase in the refractive index. The refractive

index in the range 2.2–2.3 eV tends to saturation and again weakly increases in the region $E > 2.3$ eV. The change in the character of the spectral dependence in this region is due to the influence of the C exciton series.

Figure 1b shows the modulated transmittance spectra ($\Delta T/\Delta\lambda$) of TlGaSe₂ crystals 5.7 μm in thickness in the $E \parallel a$ polarization at 10 K in the energy range $E < E$ ($n = 1$, B exciton). In the spectra narrow interference lines are visible, the distance between which decreases as the energy approaches $n = 1$. In the energy range $E > E$ ($n = 1$, B exciton), the interference bands also condense down to 2.4 eV. From these spectra, the spectral dependence of the refractive index n is calculated. In the vicinity of the B exciton series, the refractive index increases as the energy approaches the resonance frequency of the exciton.

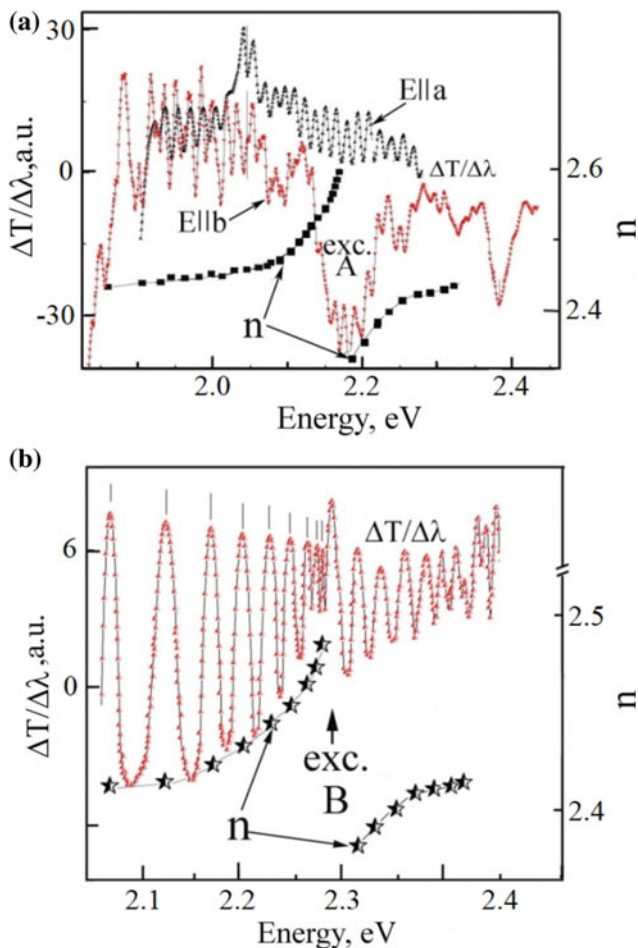


Fig. 1 Wavelength modulated transmittance spectra ($\Delta T/\Delta\lambda$) of TlGaSe₂ crystals with a thickness of 7 μm in $E \parallel a$, $E \parallel b$ polarization (a), crystals with thickness 5.7 μm in $E \parallel a$ polarization (b) at temperature of 10K and the spectral dependence of the refractive index n

Figure 2a shows the transmittance spectra (T) of TlGaSe₂ crystals 4.7 μm thick in $E \parallel b$ polarization at 10 K in the energy range $E < E$ ($n = 1$, C exciton). In the transmission spectra, narrow interference lines are visible, the distance between which varies in the range 4.5–5.5 \AA . In the high-energy region of the ground state C of the exciton series, narrow lines of interference enveloped by wider bands (1–4) also appear in the $\Delta T/\Delta\lambda$ spectra, Fig. 2b. From the interference spectra, the spectral dependence of the refractive index n is determined and the value of $\Delta n = n(E \parallel a) - n(E \parallel b)$ is determined, which varies within the limits $(0.4\text{--}0.6) \cdot 10^{-4}$, Fig. 2. The spectral dependences of the refractive indices presented in Fig. 2 correspond to the typical character of the normal dispersion in the region of the exciton resonances A, B, and C.

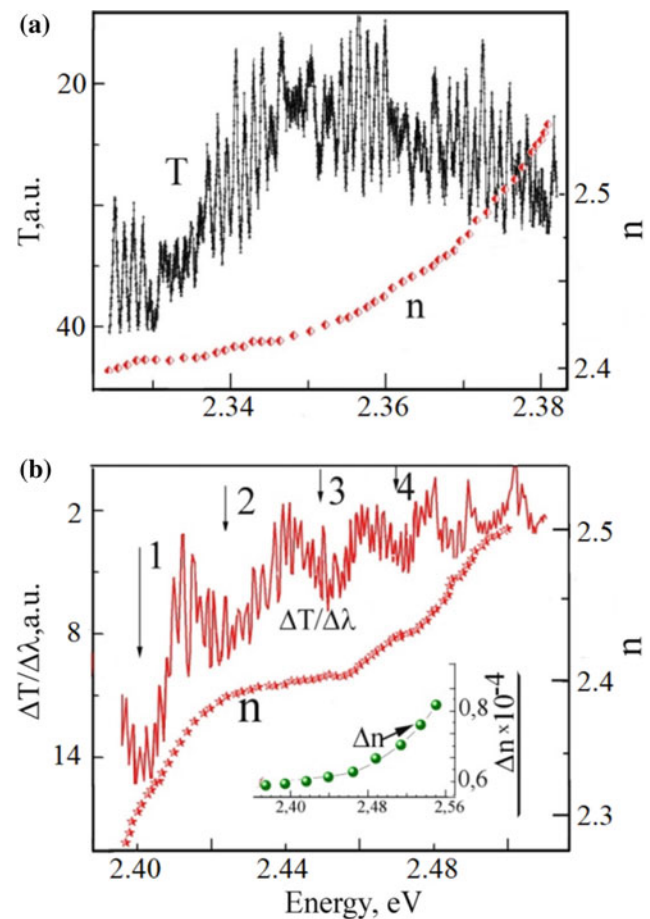


Fig. 2 a Transmission spectra (T) of TlGaSe₂ crystals with a thickness of 4.7 μm in $E \parallel b$ polarization at a temperature of 10 K in the energy range $E < E$ ($n = 1$, C-exciton) and the spectral dependence of the refractive index n . b spectral dependence $\Delta T/\Delta\lambda$ of the refractive index n for polarization $E \parallel b$ in the energy region $E > E$ ($n = 1$, C-exciton) and spectra $\Delta n = n(E \parallel a) - n(E \parallel b)$

4 Conclusions

Spectra of transmission interference in the region 1.8–2.56 eV are measured on thin TlGaSe₂ crystals. The spectral dependences of the normal dispersion (n) on the long-wavelength and short-wave side of the ground states A, B and C of excitons are determined. The anisotropy of the spectral dependence of the refractive indices n_a ($E \parallel a$) and n_b ($E \parallel b$) and $\Delta n = n_a$ ($E \parallel a$) – n_b ($E \parallel b$) in TlGaSe₂ crystals is investigated.

Conflict of Interest The authors declare that they have no conflict of interest.

References

1. Muller, D., Hahn, H.: Untersuchungen uber ternare Chalkogenide. XXIV Zur Struktur des TlGaSe₂. Zeitschrift für anorganische und allgemeine Chemie **432**, 258 (1978)
2. Range, K.J., Maheberd, G., Obenland, S.: High pressure phases of TlAlSe₂ and TlGaSe₂ with TlSe-type Structure. Zeitschrift für Naturforschung, **32a**, 1354 (1977)
3. Mustafaeva, S.N., Kerimova, E.M., Gasanov, N.Z.: Exciton characteristics of intercalated TlGaSe₂ single crystal. Semiconductors **32** (2), 145 (1998)

Optical Activity in Mn Doped As₂S₃ Glasses

V. V. Zalamai, A. V. Tiron, M. S. Iovu, and N. N. Syrbu

Abstract

Spectral dependences of transmittance (T) and wavelength modulated transmittance ($\Delta T/\Delta\lambda$) of As₂S₃ layers doped by manganese (Mn) of different concentrations (0–0.5%) were investigated at temperatures from 10 to 300 K. Photoluminescence bands at 1.762, 2.107 and 2.282 eV due to transition ${}^4A_{2g}({}^4F) \rightarrow {}^4E_g({}^2G)$, ${}^4T_{1g}({}^4G) \rightarrow {}^6A_{1g}({}^4F)$ and ${}^4T_{2g} \rightarrow {}^6A_{1g}$ of Mn ions, respectively were observed at argon laser excitation. On the luminescence spectra the absorption bands of electron transitions ${}^6A_{1g}({}^4F) \rightarrow {}^4T_{1g}({}^4G)$ were recognized. The magnitude of refractive index (n) of Mn (0.1 and 0.5%) ions doped As₂S₃ layers in low-energy range (1.6–1.9 eV) does not change at temperature decreasing from 300 to 10 K. The spectral dependences of refractive indices of As₂S₃ samples doped with Mn ions of different concentrations (0.1 and 0.5%) did not have any features.

Keywords

Chalcogenide glasses • Optical spectroscopy • Manganese doping • Refractive index • Interference spectra

1 Introduction

Chalcogenide glass-like materials attracts an attention of researchers and used as optoelectronics elements in the systems of analytical remote IR spectroscopy and as well as in telecommunications and nonlinear-optics [1]. The glasses activated by transition metal manganese were investigated as phosphors. Manganese ions incorporated in the glass matrix

V. V. Zalamai (✉) · A. V. Tiron · N. N. Syrbu
 Technical University of Moldova, 168 Stefan cel Mare Avenue,
 Chisinau, Republic of Moldova
 e-mail: victor.zalamai@cnstm.utm.md

M. S. Iovu
 Institute of Applied Physics, Chisinau, Republic of Moldova

lead to the changes in optical properties and photoluminescence (PL) of material. The self-to-shell emission of manganese ions (especially divalent ion) has a practical interest due to Mn²⁺ ions are the most effective electroluminescent impurity in glasses [1, 2].

The glass doping is an actual scientific problem with a wide practical application. The doped glass matrixes are available, are easy synthesized and have a relatively low cost. The glasses allow doping with impurities of high concentrations. The use of doped fluorescent glasses is not limited to the field of quantum electronics, where they can be used as elements of high-power lasers and various optical devices, as scintillators and dosimeters. In the fiber optics these glasses can be used as devices that allow optical signals manipulating in communication lines and as optical information storage devices.

In the present work optical properties, edge absorption (transmission), photoluminescence and spectral dependences of refractive indices of glassy As₂S₃ doped with manganese ions were studied. The changing of above-mentioned properties were investigated at temperature range 300–10 K and at different concentration of manganese impurity.

2 Experimental Methods

The bulk chalcogenide As₂S₃ glasses were made from initial elements of arsenic and sulfur (5N purity) by traditional melting method with quenching. The adding of transition metal impurity (Mn) into mixture of initial components was used for receiving of doped crystals. The synthesis process taken place in the quartz ampoules vacuumed to 10⁻⁴ to 10⁻⁵ Torr and deposited into the horizontal or vertical furnaces with vibrational and rotational mechanisms. Depending on glass composition the synthesis temperatures varied from 700 to 1100 °C and the synthesis duration was from 24 to 70 h. After the synthesis the ampoule with liquid compound was quickly cooled (hardening) in air, in cold water or in liquid nitrogen. The nominal concentration of

manganese ions was in the limits 0.01–0.5%. The color of received glasses varied from yellow-red (for undoped As_2S_3) to black (for As_2S_3 glass doped with Mn). Thin films of glasses with different thicknesses were made by vacuum deposition on glass substrates.

Absorption (transmission) and wavelength modulated transmission spectra were measured on MDR-2 spectrometer with linear dispersion 7 Å/mm and aperture 1:2. The low temperature spectra were measured in LTS-22 C 330 optical cryogenic system. Photoluminescence spectra were registered by double large-aperture spectrometer SDL-1 (aperture 1:2 and linear dispersion 7 Å/mm). The input and output slits of monochromators do not exceeded 70 μm i.e. the measurements resolution was ~0.5 meV.

3 Experimental Results and Discussions

It is known that intracenter emission from the rare-earth ions levels in materials (glasses), especially divalent manganese, is of practical interest because manganese ions are the most efficient electroluminescent impurity [3]. Especially successful is the use of manganese ions with other rare-earth elements. According Ref. [2] absorption bands of manganese ions are observed at 393, 400 and 413 nm and it can be attributed to next electron transitions ${}^6A_1({}^6S) \rightarrow {}^4T_2({}^4D)$, ${}^6A_1({}^6S) \rightarrow {}^4E({}^4G)$ and ${}^6A_1({}^6S) \rightarrow {}^4T_2({}^4G)$, respective. The absorption of Mn^{2+} ions in the region of 450–465 nm is absent, therefore for luminescent properties; ions of other rare-earth elements are introduced into the system, for example, Eu^{3+} with an absorption band at 465 nm (${}^7F_0 \rightarrow {}^5D_2$). The excitation of such system by light of wavelength range 450–465 nm is possible due to energy transfer from europium level 5D_2 to manganese level ${}^4T_2({}^4G)$. This indicates that there is an exchange of electrons between the levels of different rare-earth ions.

Figure 1 illustrates the spectral dependences of transmission of thin layers of undoped and doped by manganese chalcogenide glasses As_2S_3 near the fundamental absorption. The common property of edge absorption for all amorphous semiconductors is presence of the Urbach tail associated with localized states in the band gap. In chalcogenide glasses at photon energy decreasing the Urbach region transfers to the region of weak falling absorption or weak absorption tail [4]. Impurities incorporation into glass matrix orders glass structure in the region of valence and conduction bands edges and this leads to a decrease in the area blurring and to a shift of the edge absorption to the short-wavelength region. The introduced impurities energy levels affect in the region of high absorption coefficients.

The absorption coefficient changes in a wide interval from 10 to 10^4 cm^{-1} . A well pronounced interference in transmission (T) spectra is observed for thin samples in

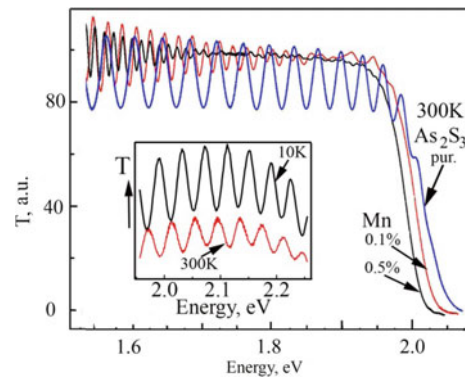


Fig. 1 Transmission (T) spectra of As_2S_3 glass layers of undoped ($d = 1.62 \mu\text{m}$) and doped by Mn ions of different concentrations (0.1–3.2 and 0.5–3.9 μm). Insert illustrates transmission interference spectra of As_2S_3 layer of $0.65 \mu\text{m}$ thickness with Mn 0.5% doping measured at temperatures 300 and 10 K

infrared region of absorption edge beginning. Figure 1 shows transmission spectra of chalcogenide As_2S_3 glasses doped by manganese ions (0.1–0.5%) in the region of high absorption coefficients. The high values of absorption were received on the thin vacuum deposited glass layers. In the high absorption coefficients the impurity incorporation leads to a shift of edge absorption toward lower energies. The insert of Fig. 1 shows the transmission interference spectra measured at 300 and 10 K for the same sample. These spectra demonstrate that the distance between maximums and minimums do not change at temperature changing from 300 to 10 K. The refractive index is calculated by equation $n = \frac{M}{2d \left(\frac{1}{\lambda_2} - \frac{1}{\lambda_1} \right)}$, where $M = 1$ for neighboring maximums (minimums) with λ_1 and λ_2 wavelength [5]. Taking into account that the interval between wavelength extremums (maximums or minimums) and the film thickness are unchanged with temperature, the refractive index does not change with temperature. The absorption edge shifts toward long-wavelength range with manganese concentration growth.

Figure 2 shows the spectral dependences of undoped and doped by manganese (0.1–0.5%) As_2S_3 films. The calculated refractive indices values are shown in Fig. 2 as points and its positions are corresponded with position of maximums and minimums. One can see this in the insert of Fig. 2. The spectral dependences of refractive index grow more drastically at achieving the absorption edge i.e. with energy increasing. The shifts of edge absorption (see Fig. 1) and spectral dependence of refractive index (see Fig. 2) take place with manganese concentration increasing. Simultaneously with manganese concentration growth the refractive index increases from 2.35 to 2.6. A weak band at energies 1.5–1.6 eV is recognized in refractive index spectra of samples doped with 0.5% manganese.

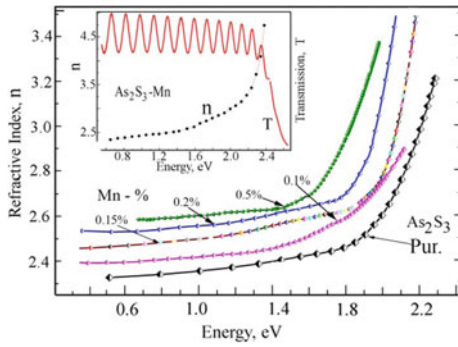


Fig. 2 Spectral dependences of refractive index (n) of undoped and doped by Mn of 0.1–0.5% concentrations As_2S_3 glasses. Insert shows the transmission spectrum of As_2S_3 film doped with 0.15% manganese and calculated from this spectrum refractive index

With temperature decreasing the edge absorption spectra are changes as one can see in the insert of Fig. 3. These spectra were measured for thin layers of As_2S_3 doped by 0.5% Mn. At low energies in these spectra the slope of the absorption curves changes with temperature. The slope of the curves becomes minimal at temperature 10 K. At energies $E < 2.3$ eV the absorption curve is shifted toward higher energies when temperature decreasing. The same behavior takes place and for the spectral dependences of refractive index. In the energy range $E > 2.3$ eV the absorption graphs tend to energy of 2.5 eV, Fig. 3. Absorption magnitude in this region is formed by the electron transitions between manganese ions levels.

The maximum $\times 2$ observed at energy 2.61 eV is more probably attributed to the absorption by electron transitions from levels ${}^6A_1(S) \rightarrow {}^4T_1(G)$ of Mn^{2+} ions (2.395 eV, [6]). Transitions ${}^4A_{2g}(^4F) \rightarrow {}^4T_{2g}(^4F)$ of Mn^{4+} ions (2.413 eV [7]) are also observed in the same spectral range. The maximum $\times 3$ (2.76 eV) is believed to be due to electronic transitions from the ${}^6A_1(S) \rightarrow {}^4T_2(G)$ Mn^{2+} ions

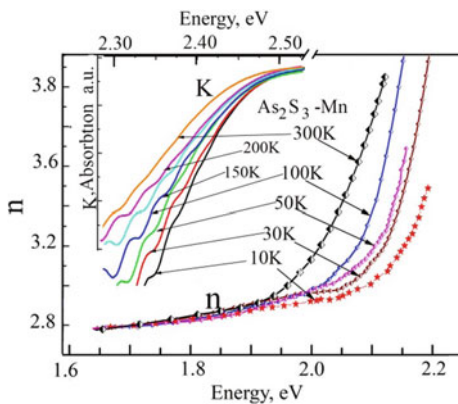


Fig. 3 Spectral dependences of absorption coefficient (K) and of refractive index (n) of As_2S_3 glass doped with Mn of 0.5% concentration measured at different temperatures

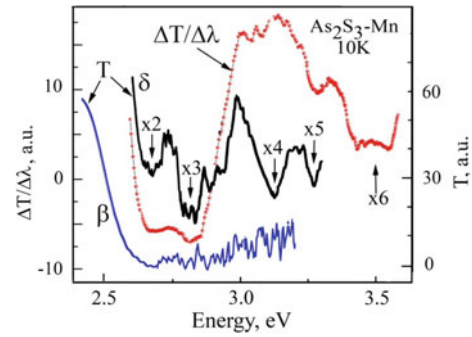


Fig. 4 Transmission (T) and of wavelength modulated transmission ($\Delta T/\Delta\lambda$) spectra of As_2S_3 layers ($d = 1.5 \mu\text{m}$, curve β) and nanolayers ($d = 350 \text{ nm}$, curve δ) doped with Mn of 0.5% concentration measured at 10 K

levels (2.799 eV, [6]) or ${}^4A_{2g}(^4F) \rightarrow {}^2T_{2g}(^2G)$ transitions of Mn^{4+} ions (2.761 eV [7]). According data of Ref. [8] the most intensive absorption band of manganese with maximum around 405 nm (3.06 eV) is a superposition of bands of the next energy transitions ${}^6A_1(^6S) \rightarrow {}^4T_2(^4D)$, ${}^6A_1(^6S) \rightarrow E(^4G)$ and ${}^6A_1(^6S) \rightarrow {}^4T_2(^4G)$. Observed absorption band $\times 4$ (3.15 eV, Fig. 4) is more probably associated with transitions ${}^6A_1(^6S) \rightarrow {}^4AE_2(^4D)$ of Mn^{2+} ions (3.141 eV [3]). The maximum $\times 5$ at energy 3.31 eV is due to the transitions ${}^4A_{2g}(^4F) \rightarrow {}^4T_{1g}(^4F)$ Mn^{4+} ions (3.308 eV) and $\times 6$ by transitions ${}^4A_{2g}(^4F) \rightarrow {}^4T_{1g}(^4F)$ (3.498 eV) [7].

A broad luminescence band at 2.282 eV is observed in As_2S_3 layers doped by manganese ions of 0.2 and 0.5% concentrations at excitation by 457.9 nm line of argon laser (see Fig. 5). A weak maximum at 2.107 eV is observed at long-wavelength side of the luminescence band. In the photoluminescence spectra for both manganese concentrations (0.2 and 0.5%) the dip is observed at energy 2.192 eV. The intensive luminescence maximum at 2.282 eV is attributed to electron transitions ${}^4T_{2g} \rightarrow {}^6A_{1g}$ of Mn^{2+} ions

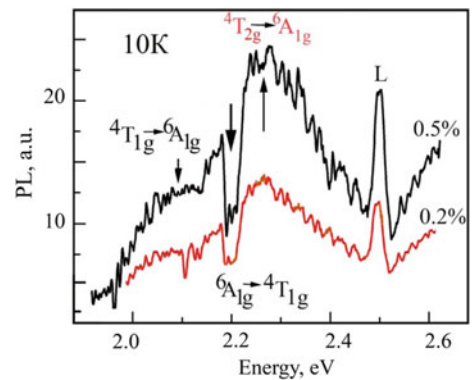


Fig. 5 Photoluminescence spectra of As_2S_3 layers doped with Mn of 0.2 and 0.5% concentrations measured at temperature 10 K and excited by 457.9 nm line of argon laser

(2.225 eV, [3]). It is possible that this maximum is also formed by electronic transitions ${}^4T_{2g}({}^4F) \rightarrow {}^4A_{2g}({}^4F)$ of manganese Mn^{4+} ions (2.413 eV, [7]). The maximum at an energy of 2.107 eV is most likely associated with the ${}^4T_{1g} \rightarrow {}^6A_{1g}$ transitions of manganese ions Mn^{2+} (2.225 eV, [7]). The dip in photoluminescence spectra (absorption band) at energy 2.192 eV is due to the absorption of energy by electron transitions between levels ${}^6A_{1g} \rightarrow {}^4T_{1g}$.

4 Conclusions

When photons with an energy range of 2.65–2.89 eV (argon laser lines) are absorbed, an excitation mechanism is realized, the transition of electrons from ${}^4A_{1g}({}^4F)$ to ${}^4T_{2g}({}^4G)$ levels (Mn^{2+} ions) or from ${}^4A_{2g}({}^4F)$ to ${}^4T_{2g}({}^4G)$ (Mn^{4+} ions). Charge carriers migrate nonradiatively between ion levels. The recombination of electrons from ${}^4T_{2g}({}^4G)$ to ${}^4A_{2g}({}^4F)$ or to ${}^6A_{1g}({}^4F)$ levels appears as a luminescence band at 2.282 eV. At energies of 2.127 eV, a weaker luminescence band associated with transitions ${}^4T_{1g}({}^4G) \rightarrow {}^6A_{1g}({}^4F)$ is observed. At energies of 2.192 eV, a narrow dip (absorption band) is detected on the contour of a wide band of luminescence spectra. This feature is associated with an absorption of emitted energy (photoluminescence) by electron transitions between levels ${}^6A_{1g}({}^4F) \rightarrow {}^4T_{1g}({}^4G)$.

Acknowledgements The authors acknowledge the support from the National Agency for Research and Development under the Grant #15.817.02.32A.

Conflict of Interest The authors declare that they have no conflict of interest.

References

1. Dianov, E.M., Petrov, M., Plotnichenko, V.G., Sysoev, V.K.: Estimation of the minimum possible optical loss in chalcogenide glasses. *Quantum Electron.* **9**(4), 798–807 (1982)
2. Aguekian, V.F.: Intracenter transitions of iron group ions in semiconductor matrices of II–VI type. *Phys. Solid State* **44**(11), 1921–1939 (2002)
3. Griscom, D.L., Griscom, R.E.: Paramagnetic resonance of Mn^{2+} in glasses and compounds of the lithium borate system. *J. Chem. Phys.* **47**, 2711–2722 (1967)
4. Sobotta H., Riede V.: Bestimmung der optischen Konstanten aus Reflexions- und Durchlässigkeitsmessungen im ferninfraroten Beispiel des n-GaAs. *Wiss Z Karl-Marx Univ. Leipzig, Math. Naturwiss. R. 20*, 147–156 (1971)
5. Mott N.F. and Davis E.A.: *Electronic processes in non-crystalline materials*, 437 pp. Clarendon Press, Oxford Univ. Press, Oxford (1971)
6. Menassa, P.E., Simkin, D.J.: Spectroscopic investigations of Mn^{2+} in sodium borosilicate glasses. *J. Lumin.* **35**, 223–233 (1986)
7. Srivastava A.M., Brik M.G., Camardello S.J., Comanzo H.A., and Garcia-Santamaria F.: Optical spectroscopy and crystal field studies of the Mn^{4+} Ion (3d3) in the Double Perovskite $NaLaMgTeO_6$. *Z. Naturforsch.* **69b**, 141–149 (2014). <https://doi.org/10.5560/znb.2014-3259>
8. Singh, V., Chakradhar, R.P.S., Rao, J.L., Kima, D.-K.: EPR and luminescence properties of combustion synthesized $LiAl_5O_8$: Mn phosphors. *Mater. Chem. Phys.* **110**, 43–51 (2008)

Electrical Properties of Thermal Annealed in Vacuum Spray Deposited Al-Doped ZnO Thin Films

T. Potlog, I. Lungu, S. Raevschi, V. Botnariuc, S. Robu, S. Worasawat, and H. Mimura

Abstract

Al-doped ZnO thin films have been prepared by spray pyrolysis, which facilitates the incorporation of a higher percentage of dopant atoms. The vacuum thermally annealed at 420 °C temperature thin films have been characterized by X-ray diffraction (XRD), optical spectroscopy. Electrical conductivity and the Hall effect are investigated in the temperature interval (77–300) K. X-ray analysis results reveal that all the films are polycrystalline with a hexagonal wurtzite structure with a preferential orientation according to the direction (002) plane. Different characters of the temperature dependence of conductivity are observed in the Al-doped ZnO films vacuum thermally annealed at 420 °C temperature. In all cases, the conductivity, mobility carriers and carriers' concentration of ZnO thin films obtained under Ar are higher than under O₂ atmosphere, unless they are not doped. of your paper no longer than 300 words.

Keywords

Spray pyrolysis • Al-doped ZnO thin films • XRD • Conductivity • Carriers concentration

1 Introduction

ZnO as a wide-bandgap semiconductor of the II–VI semiconductor group, with a direct band-gap of 3.2 eV at T = 300 K [1] is an attractive material for chemical threat detection, flame sensing, and ultraviolet environmental monitoring [2–6]. For the design and realization of

T. Potlog (✉) · I. Lungu · S. Raevschi · V. Botnariuc · S. Robu
Physics Department and Engineering, Moldova State University,
60, A. Mateevici str., Chisinau, Republic of Moldova
e-mail: tpotlog@gmail.com

S. Worasawat · H. Mimura
Research Institute of Electronics Shizuoka University Hamamatsu,
Hamamatsu, Japan

optoelectronic ZnO-based devices, one of the most significant issues is doping, which involves the heavy doping with trivalent elements (Al, Ga, In). Recently, the interest in study of ZnO thin films has increased considerably, because of their potential application for industrial application in photovoltaics. There are reviews on nanostructured photo electrodes for dye-sensitized solar cells (DSSCs) [7–9] and the use of III elements group-doped ZnO-based and ZnO nanostructures as contacts, light-trapping structures and anti-reflection coatings for well-established solar cell devices based on Si or inorganic thin films [10–15]. ZnO films and nanostructures have been used in OPV cells and photodetectors [16–21]. To the best of our knowledge, there is not enough systematic research in understanding the electrical properties of trivalent elements-doped ZnO thin films for further improvements in the performance of the optoelectronic devices. Therefore, in the present paper, we focus on the study to investigate in detail the effects of Al doping on the transport and optical properties of zinc oxide films.

2 Experimental Details

Al-doped ZnO thin films were deposited on glass substrates by spray pyrolysis technique from solution of zinc acetate (Zn(CH₃COO)₂·2(H₂O)) with a concentration of 0.2 M dissolved in acetic acid-methanol-water solution in the ratio 10:25:65. As the dopant source, aluminum nitrate was used. The concentration of Al was varied between 1 and 5% in the initial solution. A stable ZnO thin films were obtained by thermal annealing in vacuum at 420 °C. The structure of the films was investigated by X-ray diffraction (XRD) using a Bruker-AXS D8 Advance diffractometer (CuK_α radiation, 40 mA, 40 kV). The investigation of the *I*–*V* characteristic of the Au/ZnO indicates that the thermally evaporated gold electrode is a good ohmic contact to the ZnO thin film, which possesses *n*-type of conductivity. Electrical conductivity and Hall coefficient were measured by four-probe method in the Van der Paw configuration. The

measurements were performed under constant magnetic field induction (0.24 T) and stabilized direct current. Each sample was measured for three different values of current (50 μ A–2 mA). The transmittance and reflectance of the films were measured with a V-7100 UV-VIS Jasco Spectrophotometer in the wavelength range of 190–1200 nm.

3 Results and Discussion

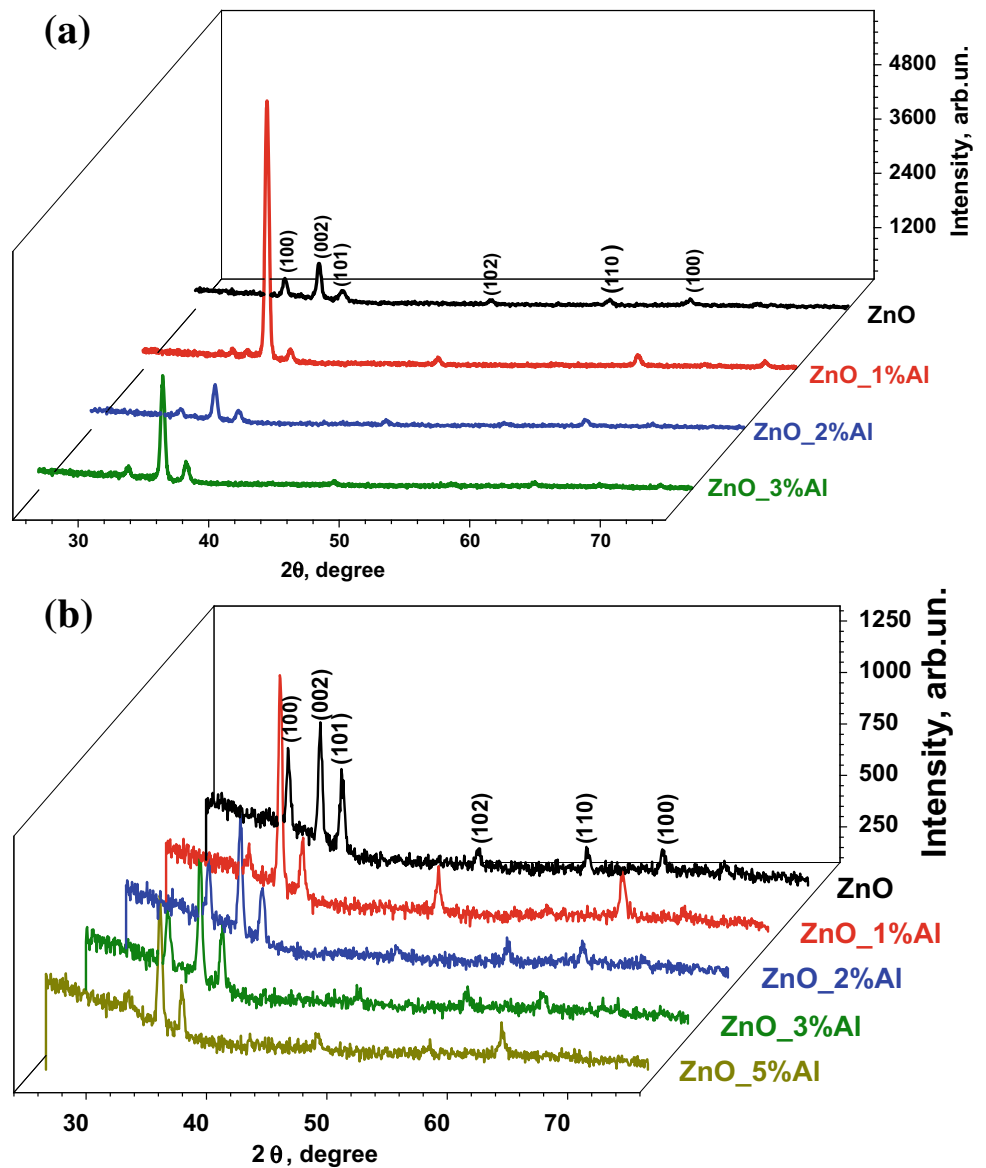
(A) Structural Analysis

The XRD patterns from all Al-doped films are shown in Fig. 1. The XRD results reveal in all cases the (002) orientation with small (100) and (101) peaks regardless of the

nature of synthesized atmosphere. The XRD patterns for the thermal annealed 1 at.% Al- and 2 at.% Al-doped ZnO thin films synthesized in O₂ atmosphere reveal a very lowest intensity peak situated at $2\theta = 32.95^\circ$ that corresponds to Al₂O₃ phase, oxidized from the Al in the ZnO films. The values of 2θ for the diffraction peaks are very close to that of the standard ZnO crystal [22]. The structural parameters show rather large variations by comparison with the values observed on undoped zinc oxide films. In the same way the full width at half maximum (FWHM) of (002) curves are significantly larger than the ones measured on undoped films, Al can be incorporated by substitution of Zn or in an interstitial position in the wurtzite ZnO lattice.

The values of the grains sizes indicate a small difference between them for all Al-doped ZnO films obtained in both atmospheres and decrease with the increases of the Al

Fig. 1 The XRD patterns from the vacuum annealed undoped and Al-doped ZnO thin films in O₂ (a) and Ar (b) atmospheres



concentration. The effects of incorporation of Al^{3+} ions on the structure, of Al-doped ZnO transparent conductive films were reported in [23, 24]. The shift of the (002) peak position towards higher values of 2θ compared to the peak position in the undoped film is observed in both types of atmospheres. Such shift to an increase in 2θ arises due the fact that the ionic radii of Zn^{2+} and Al^{3+} are 0.074 nm and 0.054 nm is different. It is found, that the lattice spacing between the (002) planes decreases with the increasing the Al concentration in the film. It means that the trivalent Al ions occupy divalent Zn sites, resulting in additional charge. Similar results have also been reported by publications [25, 26].

B. Optical Study

In order to find the band gap, it is necessary to verify which transmission mode is applicable to the films. For this purpose, the relation is used:

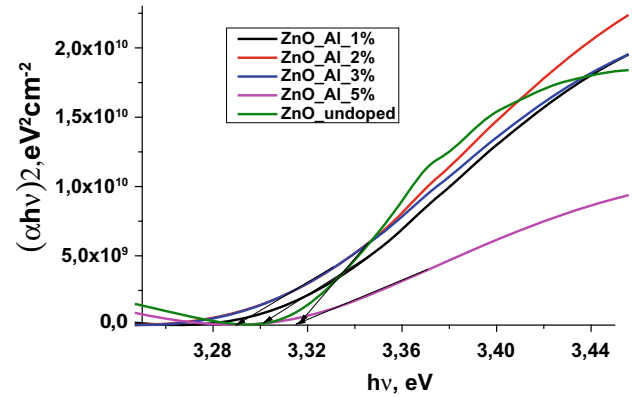
$$\alpha h\nu = A_z(h\nu - E_g)^n$$

where A is the absorption-edge width parameter, h is Planck's constant, E_g is the optical direct band-gap energy, ν is the frequency of incident radiation, and the value of n determines whether the transmission mode is allowed or forbidden. It is found that the values of n are about 0.54 for all samples. An ideal value is 0.5, which is referred to as the direct and allowed transition. Thus, the band-gap values were estimated using the $(\alpha h\nu)^2$ versus $(h\nu)$ plots by extrapolating the linear part of the absorption edge to the intersection with the energy axis as shown in Fig. 2a, b, article title for References

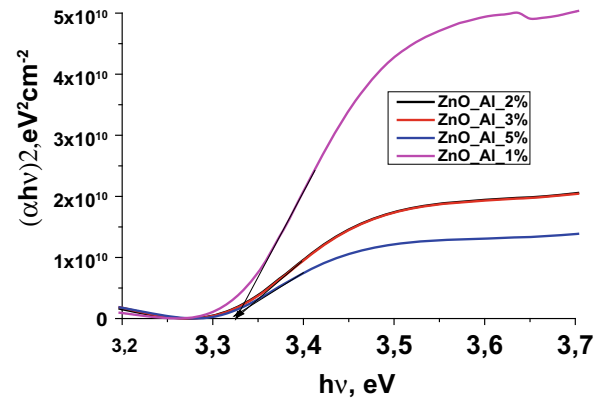
The values of band gap are presented in Table 1. As one can see, for the films grown in O_2 atmosphere, the bandgap value decreases with increasing Al concentration. A decrease in the bandgap from 3.32 eV for undoped to 3.29 eV for 3% Al-doped ZnO thin films obtained in O_2 atmosphere was observed. This variation may be due to the structural defects arisen at the time of film preparation, which could give rise to the allowed states near the conduction band in the energy bandgap. Another tendency is observed for films grown in Ar atmosphere. The value of band gap does not change with increasing the Al concentration in ZnO thin film.

C. Electrical Properties

Electrical conductivity and Hall coefficient were measured by four-probe method in the Van der Paw configuration. The measured values of the specific electrical resistivity, conductance, mobility and charge carrier concentration (at 295 K) for the all Al-doped ZnO thin films are summarized in Table 1. The average Hall mobility of undoped ZnO at room temperatures is smaller in comparison with Al-doped



(a) O_2 atmosphere



(b) Ar atmosphere

Fig. 2 Dependencies of $(\alpha h\nu)^2$ versus $h\nu$ of the vacuum annealed undoped and Al-doped ZnO thin films in O_2 (a) and Ar (b) atmospheres

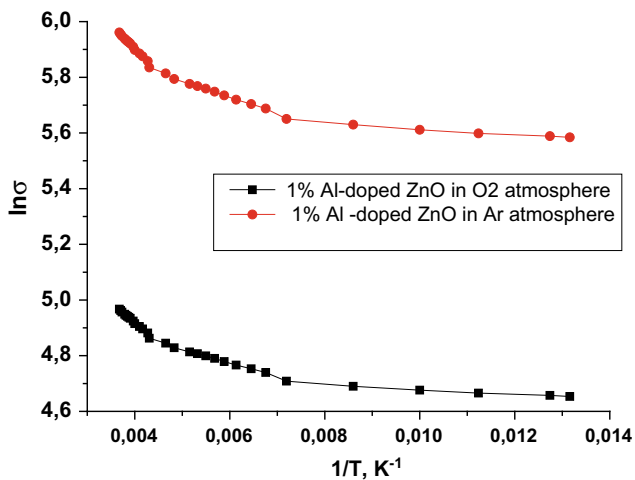
Table 1 Band gap values of Al-doped and vacuum thermal annealed ZnO thin films

Samples	E_g , eV	$d \pm 0.5$, nm
ZnO_Al_2%_Ar	3.32	302
ZnO_Al_3%_Ar	3.32	300
ZnO_Al_5%_Ar	3.31	298
ZnO_Al_1%_Ar	3.32	298
ZnO_Al_1%_O ₂	3.31	301
ZnO_Al_2%_O ₂	3.30	304
ZnO_Al_3%_O ₂	3.29	305
ZnO_Al_5%_O ₂	3.31	298
ZnO_O ₂ undoped	3.32	298

films and is very close to the values already reported in the literature by Major et al. [27]. For example, the electron mobility increased from $\sim 2.6 \text{ cm}^2\text{V}^{-1}\text{s}^{-1}$ for the undoped ZnO films obtained in O_2 atmosphere to $\sim 5.7 \text{ cm}^2\text{V}^{-1}\text{s}^{-1}$ for the ZnO films doped with $\sim 3.0\%$ Al (see Table 2). This increase in the mobility could be attributed to the suppression of the electron scattering due to the grain boundaries

Table 2 Electrical parameters of Al-doped ZnO films annealed in O₂ and Ar atmospheres

ZnO	ρ , Ω cm	σ , $(\Omega$ cm) ⁻¹	$n \times 10^{21}$ cm ⁻³	μ , cm ² /V s
3%Al_O ₂	0.0013	753	8.25	5.72
Undoped_O ₂	0.01	91	2.48	2.58
1%Al_O ₂	0.006	159	2.70	3.93
2%Al_O ₂	0.002	482	3.24	5.44
5%Al_O ₂	0.005	197	3.76	3.27
3%Al_Ar	0.025	222	4.79	2.79
2%Al_Ar	0.001	842.85	1.01	5.21
5%Al_Ar	0.002	581.72	2.8	1.45
1%Al_Ar	0.0007	1316	1.25	6.58
Undoped_Ar	0.181	5.504	0.11	3.33

**Fig. 3** The electrical conductivity as a function of the temperature of 1% Al-doped ZnO in O₂ and Ar atmospheres

present in the Al-doped ZnO thin films. The temperature dependence of conductivity (Fig. 3) of vacuum annealed 1% Al-doped ZnO films prepared in O₂ and Ar atmospheres in the temperature range from 300 to 77 K was studied and show the same behavior. The Arrhenius equation expresses the dependence of the rate constant over a wide range of temperatures in terms of only two parameters where σ_0 is the pre exponential factor; ΔE_a is the experimental activation energy by the following formula

$$\sigma = \sigma_0 \exp(-\Delta E_a/2kT)$$

From the slope of plots of $\ln(\sigma)$ versus $1/T$ for the 1% Al-doped ZnO synthesized in Ar the activation energy (ΔE_a) equals for the 1st, 2nd and 3rd regions with 14.4, 4.9 and 1.035 meV, respectively.

Table 2 Electrical parameters of Al-doped ZnO films annealed in O₂ and Ar atmospheres equals for the 1st, 2nd

and 3rd regions with 14.4, 4.9 and 1.035 meV, respectively. For the 1% Al-doped synthesized in O₂ for the 1st, 2nd and 3rd regions $\Delta E_a = 12.17$ meV, $\Delta E_a = 4.23$ meV and $\Delta E_a = 0.85$ meV. From the Arrhenius plots from Fig. 3 ΔE_a values show the lowering of the activation energy with decreasing the temperature. So the temperature dependence of σ is decided by the temperature dependences of μ as well as that of n . Since ZnO thin films have electron concentration higher than $\sim 1 \times 10^{19}$ cm⁻³ this indicate that the films are degenerate semiconductors. In general, the electrical conductivity of ZnO thin films increase with thermally annealing. The electrical conductivity of thin films is affected by the tunneling of the charge carriers through the barriers of the grain boundary and recrystallization of grains during the annealing treatment. The grain boundary model can be considered to explain the electrical conduction and charge transport in polycrystalline thin films, since this model is based on the flow of the majority and minority charge carriers, which might be either perpendicular or parallel to the grain boundaries [28]. In the first case, for flowing the current across a grain boundary, the transport of majority carriers has been slowed down by the potential barriers, the majority carrier mobility has been limited, whilst the minority carriers have been driven by the potential barriers towards recombination centers at the grain boundary, diminution the minority carrier diffusion lifetime and length. The size of these effects depends on many parameters; the density of interface states, the photogenerated carrier density, and the doping. While for the parallel case, the minority carriers will be affected by grain boundaries that lie parallel to the direction of current flow. In other wise, the majority carriers transporting parallel to the grain boundary are not affected (no barrier), but the minority carriers are continue trapped in the potential barrier and recombine [29].

4 Conclusions

Al-doped ZnO films synthesized by spray pyrolysis and thermally annealed in vacuum due to their good structural and electrical properties are promising candidates for use as transparent electrodes in solar cells. The output of this study displayed that the annealing temperature 420 °C in vacuum is the optimum condition for getting thin film with optimum characteristics, which can be suitable for the technology concerned. Based on the characterizations accomplished in this study result that the best conductor with a minimum resistivity of $7.5 \times 10^{-4} \Omega \text{ cm}$, was obtained for 1.0 at.% of Al-doped ZnO thin film synthesized in Ar atmosphere.

Acknowledgements The authors would like to thank the Ministry of Education, Culture and Research of Republic of Moldova for supporting this research by funding the grant 15.817.02.39A. In addition, authors extend their appreciation to the Research Institute of Electronic, Shizuoka University for co-funding this project.

Conflict of Interest The authors declare that they have no conflict of interest.

References

- Reynolds, D.C., Look, D.C., Jogai, B., Litton, C.W., Cantwell, G., Harsch, W.C.: Valence-band ordering in ZnO. *Phys. Rev. B* **60**, 2340 (1999)
- Ozgun, U., Alivov, Y.I., Liu, C., Teke, A., Reshchikov, M.A., Doan, S., Avrutin, V., Cho, S.-J., Morko, H.: A comprehensive review of ZnO materials and devices. *J. Appl. Phys.* **98**, 041301 (2005)
- Longxing, S., Yuan, Z., Quanlin, Z., Mingming, C., Xu, J., Wu, T., Xuchun, G., Bicai, P., Rong, X., Zikang, T.: Solar-blind wurtzite MgZnO alloy films stabilized by Be doping. *J. Phys. D* **46**, 245103 (2013)
- Hou, Y.N., Mei, Z.X., Liang, H.L., Ye, D.Q., Liang, S., Gu, C.Z., Du, X.L.: Comparative study of n-MgZnO/p-Si ultraviolet-B photodetector performance with different device structures. *Appl. Phys. Lett.* **98**, 263501 (2011)
- Ryu, Y.R., Lee, T.S., Lubguban, J.A., Corman, A.B., White, H.W., Leem, J.H., Han, M.S., Park, Y.S., Youn, C.J., Kim, W.J.: Wide-band gap oxide alloy: BeZnO. *Appl. Phys. Lett.* **88**, 052103 (2006)
- Bingqiang, C., Weiping, C., Yue, L., Fengqiang, S., Zhang, Lide: Ultraviolet-light-emitting ZnO nanosheets prepared by a chemical bath deposition method. *Nanotechnology* **16**, 1734 (2005)
- Zhang, Q.F., Dandeneau, C.S., Zhou, X.Y., Cao, G.Z.: ZnO nanostructures for dye-sensitized solar cells. *Adv. Mater.* **21**, 4087 (2009)
- Zhang, Q.F., Cao, G.Z.: Nanostructured photo-electrodes for dye-sensitized solar cells. *Nano Today* **6**, 91–109 (2011)
- Anta, J.A., Guillén, E., Tena-Zaera, R.: ZnO-based dye-sensitized solar cells. *J. Phys. Chem. C* **116**, 11413 (2012)
- Shashikant, D.S., Date, S.K., Alka, V.D., Amit, D., Pankaj, M., Kukreja, L.M., Adhi K.P.: Role of Al doping in structural, microstructural, electrical and optical characteristics of as-deposited and annealed ZnO thin films. *RSC Adv.* **5**, 24178 (2015)
- Boccard, M., Battaglia, C., Hänni, S., Söderström, K., Escarré, J., Nicolay, S., Meilaud, F., Despeisse, M., Ballif, C.: Multiscale transparent electrode architecture for efficient light management and carrier collection in solar cells. *Nano Lett.* **12**, 1344 (2012)
- Lai, K.C., Liu, C.C., Lu, C.H., Yeh, C.H., Houg, M.P.: Characterization of ZnO: Ga transparent contact electrodes for microcrystalline silicon thin film solar cells. *Sol. Energy Mater. Sol. Cells* **94**, 397 (2010)
- Wienke, J., Zanden, B.V.D., Tijssen, M., Zeman, M.: Performance of spray-deposited ZnO: In layers as front electrodes in thin-film silicon solar cells. *Sol. Energy Mater. Sol. Cells* **92**, 884 (2008)
- Park, H.K., Kang, J.W., Na, S.I., Kim, D.Y., Kim, H.K.: Characteristics of indium-free GZO/Ag/GZO and AZO/Ag/AZO multilayer electrode grown by dual target DC sputtering at room temperature for low-cost organic photovoltaics. *Sol. Energy Mater. Sol. Cells* **93**, 1994–2002 (2009)
- Gupta, A., Compaan, A.D.: All-sputtered 14% CdS/CdTe thin-film solar cell with ZnO: Al transparent conducting oxide. *Appl. Phys. Lett.* **85**, 684–686 (2004)
- Yip, H.L., Han, S.K., Baek, N.S., Ma, H., Jen, A.K.Y.: Polymer solar cells that use self-assembled-monolayer modified ZnO/Metals as cathodes. *Adv. Mater.* **20**, 2376–2378 (2008)
- Ibrahem, M.A., Wei, H.Y., Tsai, M.H., Ho, K.C., Shyue, J.J., Chu, C.W.: Solution-processed zinc oxide nanoparticles as interlayer materials for inverted organic solar cells. *Sol. Energy Mater. Sol. Cells* **108**, 156 (2013)
- Noori, K., Giustino, F.: Solar cells: ideal energy-level alignment at the ZnO/P3HT photovoltaic interface. *Adv. Funct. Mater.* **22**, 5089 (2012)
- Yip, H.L., Hau, S.K., Baek, N.S., Jen, A.K.Y.: Self-assembled monolayer modified ZnO/metal bilayer cathodes for polymer/fullerene bulk-heterojunction solar cells. *Appl. Phys. Lett.* **92**, 193313 (2008)
- Hsieh, C.H., Cheng, Y.J., Li, P.J., Chen, C.H., Dubosc, M., Liang, R.M., Hsu, C.S.: Highly efficient and stable inverted polymer solar cells integrated with a cross-linked fullerene material as an interlayer. *J. Am. Chem. Soc.* **132**, 4887 (2010)
- Sun, Y.M., Seo, J.H., Takacs, C.J., Seifert, J., Heeger, A.: J. Inverted polymer solar cells integrated with a low-temperature-annealed sol-gel-derived ZnO film as an electron transport layer. *Adv. Mater.* **23**, 1679 (2011)
- Look D. C.: Recent advances in ZnO materials and devices. *Mater. Sci. Eng., B* **80**, 381 (2001)
- Seeber, W.T., et al.: Transparent semiconducting ZnO: Al thin films prepared by spray pyrolysis. *Mater. Sci. Semicond. Process.* **2**, 45–55 (1998)
- Aoki, T., Hatanaka, Y., Look, D.C.: ZnO diode fabricated by excimer-laser doping. *Appl. Phys. Lett.* **76**, 3257 (2000)
- Mohammad, M.T., Hashim, A.A., Al-Maamory, M.H.: Highly conductive and transparent ZnO thin films prepared by spray pyrolysis technique. *Mat. Chem. Phys.* **99**, 382–387 (2006)
- Douayar, A., et al.: Investigation of the structural, optical and electrical properties of Nd-doped ZnO thin films deposited by spray pyrolysis. *Eur. Phys. J. Appl. Phys.* **61**, 10304 (2013)
- Major, S., Banerjee, A., Chopra, K.L.: Highly transparent and conducting indium-doped zinc oxide films by spray pyrolysis. *Thin Solid Films* **108**, 333–340 (1983)
- Patel, S.L., Chander, S., Purohit, A., Kannan, M.D., Dhaka, M.S.: Influence of NH₄Cl treatment on physical properties of CdTe thin films for absorber layer applications. *J. Phys. Chem. Solids* **123**, 216–222 (2018)
- Nelson, J.: *The Physics of Solar Cells*. Imperial College Press, UK, London (2002)

Growth of P-GaN on Silicon Substrates with ZnO Buffer Layers

S. Raevschi, L. Gorceac, V. Botnariuc, and T. Braniste

Abstract

GaN layers on Silicon with ZnO intermediate layer were synthesized by using the HVPE (Hydride Vapor Phase Epitaxy) method. ZnO layers were deposited from solutions of zinc compounds in ethanol or water in two steps. At the first step a ZnO nucleation layer was deposited from a solution of zinc acetate in ethanol, at the second step a ZnO precipitate was deposited from a solution of zinc nitrate and KOH in water by boiling. On the obtained structures the GaN nucleation layers were deposited at 500 °C for 15 min, then GaN layers were grown at 850–970 °C for 30 ± 5 min. Structures were studied by using the optical and SEM microscope and XRD method. The type of conductivity of the layers was determined by using the method of thermal electromotive force measurement (TEFM). The possibility of the electrical conductivity (EC) type changing from n- to p-type for the GaN layers deposited on silicon substrates with the use of intermediate ZnO layer deposited from solutions is demonstrated for the first time.

Keywords

GaN • ZnO • Si • HVPE • Termal electromotive force • Solution

1 Introduction

The development of the physical principles of fabrication of structures and devices based on III-N compounds is a current problem of modern electronics. The enhancement of the

device characteristics can be achieved by developing new methods of p-type materials fabrication, by improving the heteroepitaxial layers crystalline structure. Usually, at the p-GaN layers fabrication the vapors of II group elements (Mg, Zn, ...) (or metalorganic compounds) are introduced into the gaseous transport streams. The Mg is more preferable as the dopant, however, at high temperatures the given element reacts with the quartz, it can change the composition of the synthesis medium of the layers.

GaN epitaxial layers grown on Si (111) with nano metric AlN, AlGaIn intermediate layers, obtained by the HVPE method, have an electron concentration of $\sim 10^{19} \text{ cm}^{-3}$. The zinc doping from the vapor phase during the process of their fabrication changes the mechanisms of nucleation and growth. If the partial pressure of the zinc vapors in the gas stream exceeds 0.6 Torr the grown layers become polycrystalline, non-epitaxial, the surface morphology of the layers changes, the polarity of the EC on the surface becomes non-homogeneous.

Zinc oxide has several advantages and perspectives to be used as a buffer layer to obtain perfect GaN layers on silicon: firstly it is compatible with gallium nitride by crystalline structure, good crystalline lattice matching, close values of the thermal dilatation coefficient [1]; it is decomposing at high temperatures as a result zinc is becoming a potential p-type dopant in the later deposited GaN layer. Various methods are applied in the synthesis of ZnO layers: MOCVD, MOVPE, spray pyrolysis, pulsed laser evaporation [2, 3], etc. There are also quite effective methods of depositing ZnO layers of zinc compounds in solutions [4–6].

The purpose of the paper is to obtain layers of p-GaN on silicon substrates using the ZnO intermediate layers deposited from solutions of zinc compounds. The type of conductivity of the structures was determined by the method of the TEFM with a thermostatic probe.

S. Raevschi (✉) · L. Gorceac · V. Botnariuc
Institute of Research and Innovation, Moldova State University,
A. Mateevici 60, MD-2009, Chisinau, Republic of Moldova
e-mail: raevskis@mail.ru

T. Braniste
National Center for Materials Study and Testing, Technical
University of Moldova, Chisinau, Republic of Moldova

2 Experiment

The deposition of ZnO layers on Si was carried out in two steps. In the first step, nucleation layers were deposited using a solution of hydrated zinc acetate, $\text{Zn}(\text{CH}_3\text{COO}) \cdot 2\text{H}_2\text{O}$ (AcZn) in ethanol at a concentration of 0.6 M. The silicon substrates, directly after treatment, were installed in Petrie cup with the deposition surface on the top and covered with the AcZn-ethanol (96%) solution. Further they were left at room temperature until the liquid was evaporated, then were heat treated in air at 500 °C for 2 h. At the second stage, massive ZnO precipitates from zinc nitrate hexahydrate solutions, $\text{Zn}(\text{NO}_3)_2 \cdot 6\text{H}_2\text{O}$ and KOH in distilled water were deposited on the obtained structures according to the method developed in [2].

GaN layers were synthesized on ZnO/Si structures by the two-step HVPE method. At the first stage, the GaN nucleation layer was synthesized at 500 °C for 15 min and at the second stage GaN layer was grown at the substrate temperature of 850–970 °C for 30 ± 5 min. The pressure in the horizontal quartz reactor was higher than the atmospheric pressure by 70 mbar. Hydrogen purified by a palladium filter

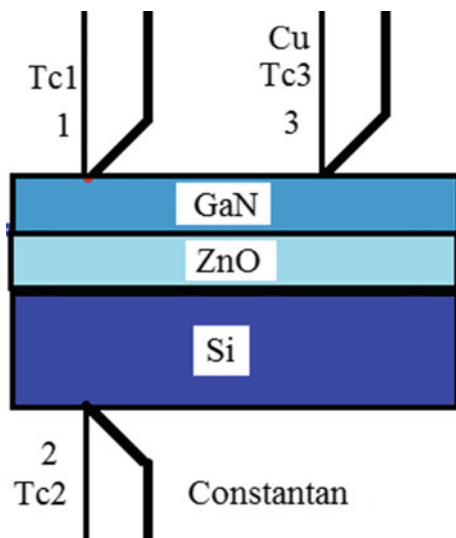


Fig. 1 The scheme of the device used to determine the EC type of the samples

Table 1 TEFM of samples

#	Sample	α_{12} , $\mu\text{V}/^\circ\text{C}$	α_{21} , $\mu\text{V}/^\circ\text{C}$
1	n-Si (100), 4.5 Ω cm	-790	-790
1z	ZnO/Si (100)	-440	-260
1g	GaN/ZnO/Si (100)	+190	+396
2	p-Si (111), 0.1 Ω cm	+458	+458
2z	ZnO/Si (111)	+470	+370
2g	GaN/ZnO/Si (111)	+128	+308
51	GaN/AlGaN/AlN/Si (111)	-115	-117

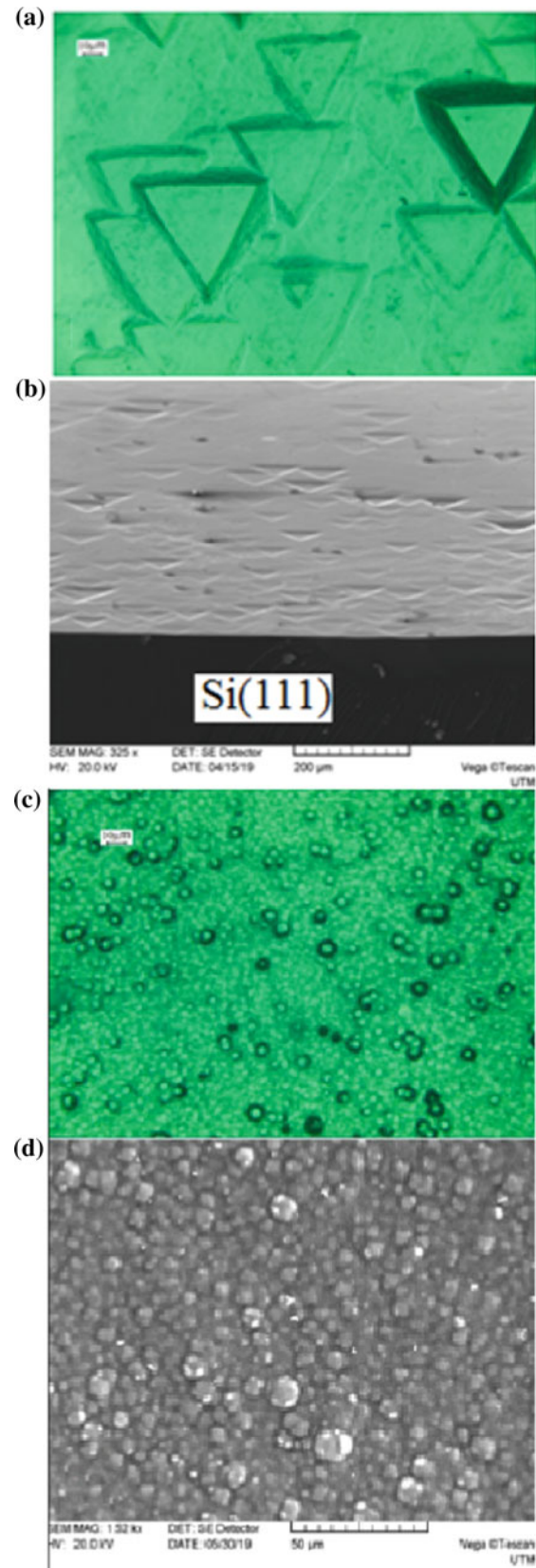


Fig. 2 The surface morphology of ZnO layers deposited on Si (111) (a, b), and Si (100) (c, d) studied with the optical microscope (a, c) and SEM (b, d)

was used as the transport gas. Ammonia, hydrogen chloride and gallium (5 N) were used as reagents. The consumption of hydrogen chloride was 0.02 slpm. The total hydrogen consumption was of 3.6 slpm and the ammonia consumption of 0.6 slpm. The thermal profile in the reactor was provided by a resistive electric heater. The Ga source temperature was constant of 850 °C. Si (111) and Si (100) wafers were used.

The determination of sample EC type was made by using the method of the TEMF measurements. The measurements were carried out by using of three thermocouples Cu-Constantan. The thermocouple (Tc) 2 was welded to the cold copper block. The temperature of the hot copper probe was measured with the thermocouple (Tc) 1. The surface signal was measured by using the probe 3 with the thermocouple (Tc) 3 as it is shown in Fig. 1. The temperature difference at the measurements was 10–15 °C. Measurements were carried out at room temperature.

The study of surface morphology was investigated by using the MMM 500 optical microscope and electronic VEGA TS 5130, SEM (Scanning Electron Microscope). XRD and GI-XRD studies were carried out by use of EMPYREAN diffractometer ($\text{Cu}_{K\alpha}$).

3 Results and Discussion

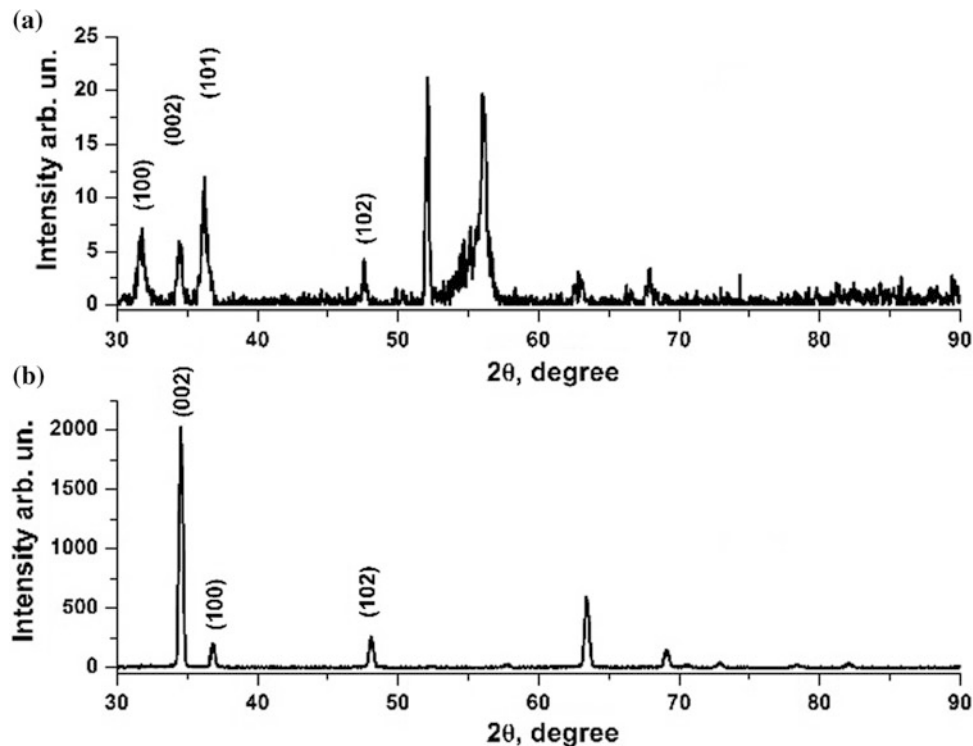
The images of the surface morphology of ZnO layers deposited on silicon are shown in Fig. 2. The morphology of the layers is determined by the silicon crystallographic plane on which ZnO layers are deposited. Structures of the

equilateral triangles which are evidence of plane (111), Fig. 2a, b are, probably, etching pits, occurring at the second stage of ZnO precipitate deposition in hot KOH solutions. ZnO layer is very thin, it is difficult to detect it from XRD measurement (Fig. 3). On the Si plane (100), Fig. 2c, d, a thicker ZnO precipitate was deposited. A homogeneous structure of hexagonal symmetry granules of different heights whose axis of symmetry is perpendicular to the surface of the substrate is obvious. SEM images of GaN layers grown on ZnO/Si structures are given in Fig. 4a, b.

The morphology of the layers also changes essentially depending on the crystallographic plane of the substrates. On the ZnO/Si (111) structures, the GaN layers exhibit a rather uniform, evenly contoured dispersed particle assembly. On the ZnO/Si structures (100), Fig. 4b, the GaN layer presents a non-coherent triangular peaks. The inclined hexagonal columns also appear.

The results of the TEMF measurements of the substrates as well as the ZnO/Si, GaN/ZnO/Si structures are presented in the Table 1. Measurements of α_{12} are carried out by using the hot probe 1 and α_{21} by using the hot probe 2. The initial Si substrates (100) have the n-type EC, the Si (111)-p-type. Their electrical resistivity values are shown in the Table. When depositing ZnO layers, the EC of the structures does not change the polarity, the TEMF values decrease, which can be attributed to the thermal annealing of the structures at 500 °C. The most pronounced conversion effect of the conductivity type occurs for GaN layers grown on ZnO/Si (100) structures. The p-GaN layers are also obtained on

Fig. 3 XRD diffraction pattern:
a ZnO/Si, b GaN/ZnO/Si



ZnO/Si (111) structures. Their TEMF values are lower that shows that the concentration of the holes in them is higher or the degree of EC compensation is lower. The conversion of the conductivity type also takes place in the GaN layers deposited at 850, 950, 970 °C. In the GaN/Si (100) layers grown at 950 and 970 °C the α_{13} values are +287 and +510 $\mu\text{V}/^\circ\text{C}$. For the GaN layers deposited on Si (111) under the same conditions the α_{13} values are lower. For com-

parison, we also present the results of the research of a GaN layer grown on Si (111) substrates with AlGaIn/AlN intermediate layers. The EC of this layer is n-type.

X-ray diffraction analysis has confirmed the formation ZnO and the GaN layers and one can observe in Fig. 3. The representative SEM pictures of GaN layers on Si and ZnO/Si are depicted in (Fig. 4).

4 Conclusion

ZnO layers on silicon substrates with n- and p-type EC were synthesized on the crystallographic planes (100) and (111) from of solution. It was established that ZnO precipitation adherence is more effective on the planes (100). On the obtained structures, GaN layers were grown by the HVPE method. The possibility of obtaining of p-GaN layers on silicon by using ZnO intermediate buffer layers deposited from solutions was shown.

Acknowledgements The authors acknowledge the support from Ministry of Education, Culture and Research of Moldova under the grant 15.817.02.34A. The authors would like to thank colleagues from CaRISMA (Regional Scientific and Educational Centre on Advanced Materials) of Moldova State University for carrying out X-Ray Diffraction analysis.

Conflict of Interest The authors declare that they have no conflict of interest.

References

1. Hanada, T.: Basic properties of ZnO, GaN, and related materials. In: Yao, T. (ed.) *Oxide and Nitride Semiconductors*. Advances in Materials Research (2009)
2. Umit, O., Daniel, H., Hadis, M.: *ZnO* devices and applications: a review of current status and future prospects. *Proc IEEE* (2010)
3. Kumari, N., Sanjaykumar, R., et. al.: Optical and structural properties of ZnO thin films prepared by spray pyrolysis for enhanced efficiency perovskite solar cell application. *Opt. Quantum Electron.* **50**(4), 180 (2018)
4. Плахова, Т.В., Баранов, А.Н., et al.: Влияние текстурированных затравок на морфологию и оптические свойства массивов наностержней ZnO синтезированных из раствора и газовой фазы. *Неорганические материалы* **48**(5), 549–556 (2012)
5. Ghorbani, H.R., Mehr, F.P., et al.: Synthesis of ZnO nanoparticles by precipitation method. *Orient J. Chem.* **31**(2) (2015)
6. Николаева, Н.С., Иванов, В.В., et al.: Синтез высокодисперсных форм оксида цинка: химическое осаждение и термоллиз. *J. Siberian Fed. Univ. Chem.* **2**, 153–173 (2010)

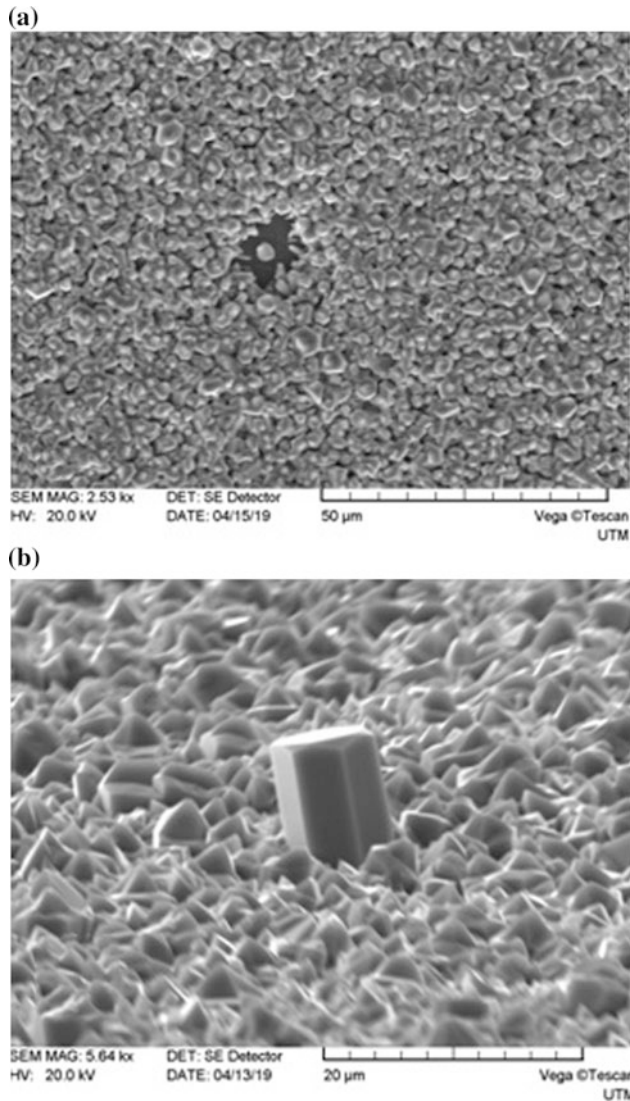


Fig. 4 SEM images of the surface of GaN layers synthesized on ZnO/Si (111) (a) and ZnO/Si (100) (b) structures

TEM and Electrochemical Investigation of Different Morphology Silicon Anodes

K. Saleem, U. Schürmann, S. Hansen, H. Cavers, R. Adelung, and L. Kienle

Abstract

The volumetric changes and the structural deterioration in Silicon anodes during successive electrochemical lithiation/delithiation cycles limits the utilization of Silicon (Si) anodes in Lithium-based batteries. However, using morphologically modified Si and suitable conducting additives can ensure better electrochemical performance and structural stability even after repeated electrochemical cycles. This research is aimed at comparing the electrochemical performance and solid electrolyte interface (SEI) of different Si anode geometries i.e. powdered Si and Si microwires after cycling. The SEI is analyzed using Transmission Electron Microscope (TEM) methods after cycling in the electrochemical half cell. Si microwires show relatively superior electrochemical performance compared to the powdered Si.

Keywords

TEM • Voltammetry • Battery materials • Powdered Si • Si microwires

1 Introduction

Lithium based batteries have been investigated around the globe because of their high energy density and lightweight. Graphite is a conventionally used anode material in the lithium ion batteries with approximately 340 mAhg^{-1} theoretical capacity. With the capacities more than 13 folds higher compared to carbon anode materials, Silicon (Si) could replace carbon as an anode material in battery applications [1, 2].

However, the utility of the Si is hindered by the mechanical failures due to large volumetric changes during early charging and dis-charging cycles [3, 4]. Moreover, the development of thin and stable Solid Electrolyte Interface (SEI) that protects the Si anode without hindering the Li-ion diffusion is also a challenge [5]. A fundamental understanding about the structural evolution in the Si anode materials during cycling is necessary to provide strategies to eliminate the anode failures and accompanied capacity fading for higher number of cycles [6]. Moreover, using appropriate binding materials to improve conductivity and suitable electrolyte can help achieve longer battery life while retaining high charge storage capacity [5, 7]. For the measurement of the electrochemical performance, cyclic voltammetry is a standard analytical tool to measure phase transformations [8]. The peaks appearing during the lithiation and delithiation cycles in the current-voltage (CV) curves are closely related to the structural and compositional changes occurring during the electrochemical cycles. During the cycling, the salt present in the electrolyte dissociates and reacts with the components and forms an interfacial layer composed of reduced products. The compounds of lithium i.e. Li_2O , Li_2CO_3 , LiF and polymer phases generally contribute in the Solid Electrolyte Interface (SEI) composition [9]. Moreover, due to lower viscosity and a higher dielectric constant, the salt dissociation and ionic diffusion rates are higher in EC based electrolytes compared to PC based electrolytes. Although a lot of research is being conducted presently, the formation of the SEI and its composition are not well understood both by experimental and theoretical viewpoint [10].

This paper deals with the electro-chemical characterization and TEM analysis of the powdered Si and Si microwire anodes and draws a brief comparison of their SEI composition and cycling performance. The study highlights the importance of the morphology of the Si anodes which determines the optimal charging/discharging conditions of the anodes. The TEM analysis was conducted to examine the distribution of elements and give an estimate about the thickness of the SEI layer in both type of anodes after cycling.

K. Saleem · U. Schürmann (✉) · L. Kienle
Synthesis and Real Structure, Institute for Materials Science,
CAU Kiel, Kaiserstraße 2, Kiel, Germany
e-mail: usc@tf.uni-kiel.de

S. Hansen · H. Cavers · R. Adelung
Functional Nanomaterials, Institute for Materials Science,
CAU Kiel, Kaiserstraße 2, Kiel, Germany

2 Materials and Method

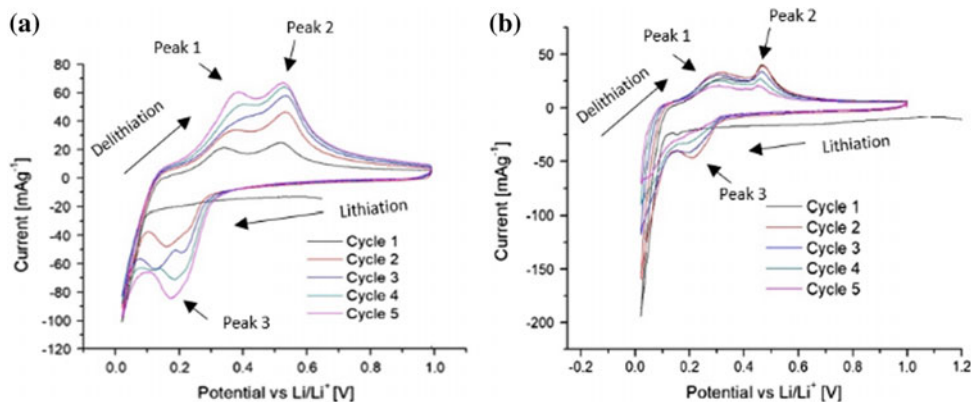
Powdered Si—In order to test the lithiation/delithiation performance of the powdered Si, paste electrodes were fabricated. The diameter of the spherical Si particles was around 70–80 μm . A mixture of Powdered Si, conductive carbon black (CB), carboxymethylcellulose (CMC) and water was pasted onto a copper foil current collector. The produced paste electrodes were then dried in the vacuum at around 70 $^{\circ}\text{C}$ for 5 h.

Si microwires—The Silicon wires are produced during electrochemical processes after various pre-structuring processes. Macropore etching allows a very defined geometry of the individual pore morphology. Subsequent chemical over-etching in a KOH solution results in the wires of 1 μm thickness and 60 μm length [11].

To be able to compare between powdered and microwire structures, the Si microwires were also embedded in a paste with CB and CMC. All of the CV curves are normalized to the amount of Si in order to compare the results efficiently.

The electrochemical characterization was performed in half cells which were prepared using metallic Li as counter electrode with an ether-based electrolyte composed of 0.7 M LiTFSi in 1,3 dioxolane, dimethylether in a volume ratio of 1:2 with the addition of LiNO_3 . This is a typical additive to support the self-oxidation mechanism of the LiTFSi salt at the lithium metal surface [12]. A potential scan was applied reversibly between 1 V and 20 mV at a scan rate of 0.1 mVs^{-1} for 5 cycles. The scan rate, electrochemical cycles, electrolyte and conductive additive were kept constant. The chemical composition of the SEI on the Si anodes was investigated using scanning TEM (STEM) in a FEI Tecnai F30 G² STwin equipped with an energy-dispersive X-ray (EDX) detector (Si/Li, EDAX). Li-containing samples were prepared in an inert atmosphere to prevent any oxygen contamination.

Fig. 1 Cyclic voltammetry of **a** Si microwires and **b** powdered Si anode materials cycled in the electrolyte for 5 cycles at a scan rate of 0.1 mVs^{-1}



3 Results and Discussion

The cyclic voltammetry of Si anodes was performed in order to compare their electrochemical performance. The incorporation and extraction of Li ions in Si anodes during lithiation/delithiation accompanied phase transformations. The peaks in the CV diagrams during lithiation and delithiation cycles indicate typical phase transformations in Li–Si anodes. Figure 1a and b represents typical voltammograms for powdered Si and Si microwires. In powdered Si the peak at 1.41 V marks the start of the SEI formation and thus reduction of the solvents. During the lithiation, as the lithium ions are incorporated in the Si anode, structural transformation takes place due to the formation of the Li_xSi_y alloy [2]. During the structural transformations the Si anode goes from crystalline to amorphous after cycling. The lithiation peak is marked as peak 3 and the delithiation peaks are marked as peak 1 and peak 2 in Fig. 1a, b. Due to the difference in morphology of the Si anodes there is a shift in

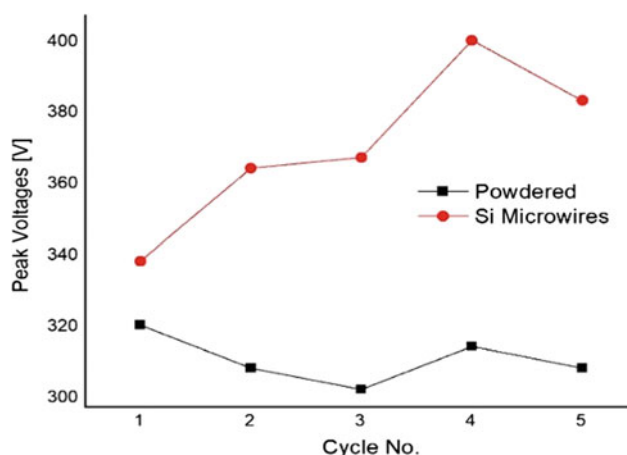


Fig. 2 Delithiation peaks potentials for powdered Si and Si microwires anode cycled in E1 electrolyte for 5 cycles at scan rate of 0.1 mVs^{-1}

the potential values of the peak 1 appearing in delithiation cycles. This shift is more clearly indicated in Fig. 2.

A clear shift in the delithiation peaks of Si microwires is noted compared to powdered Si. The figure shows almost a linear increase in the potential values in case of Si microwires compared to powdered Si. The increase in the delithiation voltage indicates the longer paths for the Li ions or the electrons in the case of Si microwires [2]. The peak

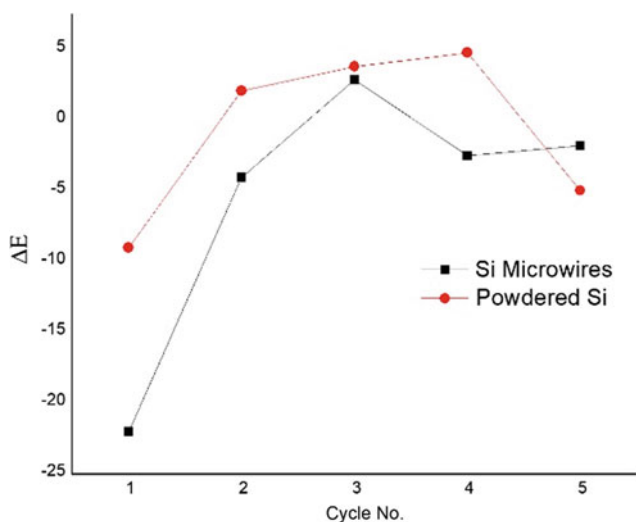


Fig. 3 Resultant ΔE representing the difference between the area under the lithiation and delithiation curves of powdered Si and Si microwires

voltages for the powdered Si on the other hand remains somewhat constant. A comparison between the areas under the lithiation and delithiation curves for powdered Si and Si microwires is shown in the Fig. 3a, b.

The area under the CV curve represents the amount of energy utilized for the lithiation and the amount of energy gained after delithiation during cycling. The difference (ΔE) between the areas under the lithiation and delithiation curves of powdered Si and Si microwires is shown in the Fig. 3. This difference, shown by the points for each cycle, indicates the irreversible losses in different cycles. The difference between the integrated areas indicate the higher number of irreversible losses in case of powdered Si compared to Si microwires.

The structural modifications of the powdered Si during cycling accompanied modifications of the solid electrolyte interface. The SEI layer is altered in terms of the (a) elements distribution and (b) thickness in both the morphologies. The TEM results of the compositional modifications after 5 cycles in powdered Si and Si microwires are shown in Figs. 4 and 5, respectively. The EDX elemental map was taken from the area marked in the High Angle Annular Dark Field (HAADF) image in both the figures and the SEI is marked in the images with arrows and dashed lines. The SEI layer comprises of fluorine, sulphur, oxygen and carbon which are contributing differently to the thickness of the SEI as shown in the figure. Fluorine is covering the Si anodes in both morphologies more uniformly compared to Sulphur and Oxygen. Additionally, the distribution of the elements in both the morphologies is similar since the

Fig. 4 STEM-EDX elemental mapping of powdered Si cycled in the electrolyte for 5 cycles at a scan rate of 0.1 mVs^{-1}

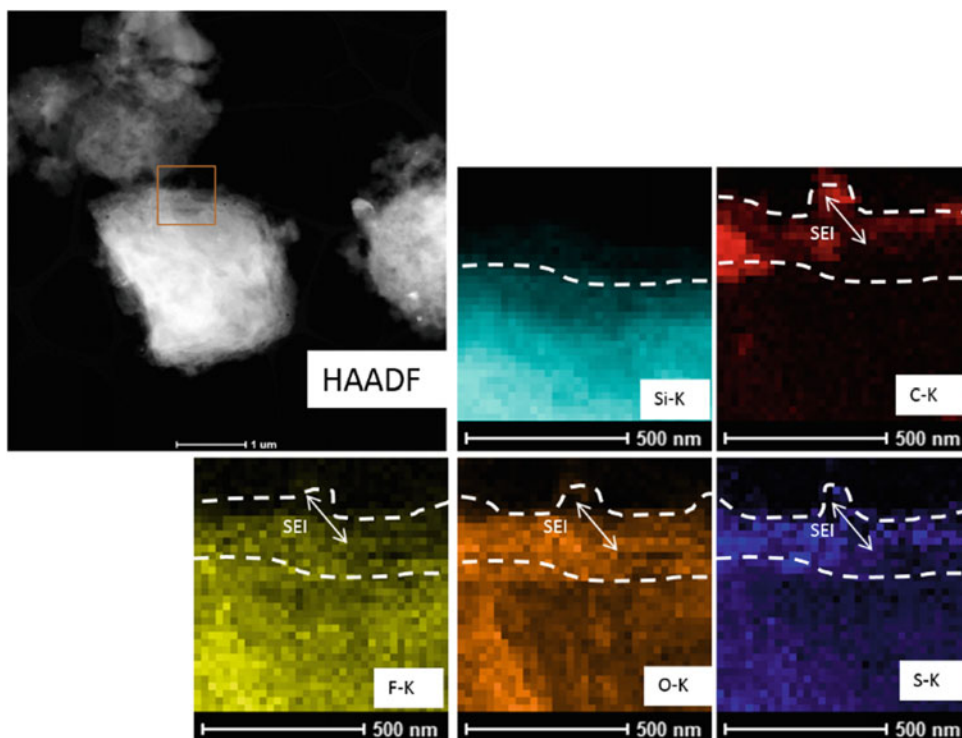
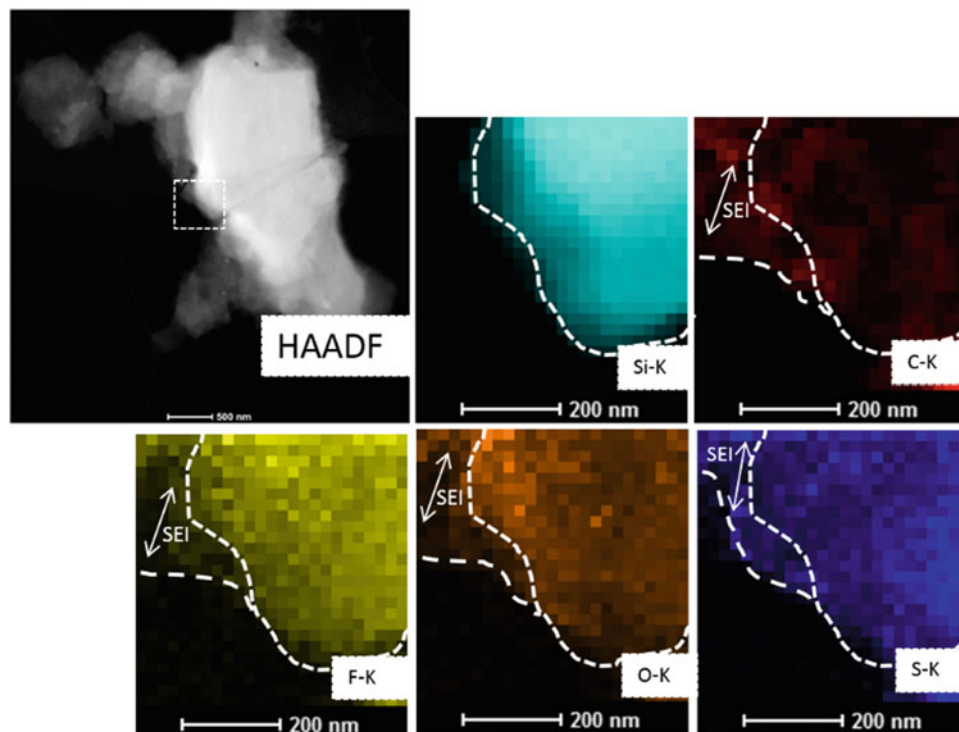


Fig. 5 STEM-EDX elemental mapping of Si microwires cycled in the electrolyte for 5 cycles at a scan rate of 0.1 mVs^{-1}



electrolyte and the parameters used in both the cases were same. Due to the lightweight of the lithium, it could not be resolved in the EDX elemental map.

4 Conclusions

Due to the difference in morphology, Si microwires have different electron and Li ion diffusion paths compared to powdered Si. Si microwires have compelling electrochemical performance because they provide short Li diffusion paths due to their narrow diameter combined with long continuous paths for electron transport down their length. They also have higher surface areas speeding the lithium insertion process.

Conflict of Interest The authors declare that they have no conflict of interest.

References

1. Fukata, N., Mitome, M., Bando, Y., Wu, W., Wang, Z.L.: Lithium ion battery anodes using Si-Fe based nanocomposite structures. *Nano Energy* **26**, 37–42 (2016)
2. Nöhren, S., Quiroga-González, E., Carstensen, J., Föll, H.: Electrochemical fabrication and characterization of silicon microwire anodes for Li Ion batteries. *J. Electrochem. Soc.* **163**(3), A373–A379 (2016)
3. Liu, X.H., et al.: In situ atomic-scale imaging of electrochemical lithiation in silicon. *Nat. Nanotechnol.* **7**(11), 749–756 (2012)
4. Yang, H., et al.: Orientation-dependent interfacial mobility governs the anisotropic swelling in lithiated silicon nanowires. *Nano Lett.* **12**(4), 1953–1958 (2012)
5. Zeng, P., Han, Y., Duan, X., Jia, G., Huang, L., Chen, Y.: A stable graphite electrode in superconcentrated LiTFSI-DME/DOL electrolyte and its application in lithium-sulfur full battery. *Mater. Res. Bull.* **95**, 61–70 (2017)
6. Haregewoin, A.M., Wotango, A.S., Hwang, B.-J.: Electrolyte additives for lithium ion battery electrodes: progress and perspectives. *Energy Environ. Sci.* **9**(6), 1955–1988 (2016)
7. Nguyen, C.C., Yoon, T., Seo, D.M., Guduru, P., Lucht, B.L.: Systematic investigation of binders for silicon anodes: interactions of binder with silicon particles and electrolytes and effects of binders on solid electrolyte interphase formation. *ACS Appl. Mater. Interfaces.* **8**(19), 12211–12220 (2016)
8. Wu, J., et al.: Multilayered silicon embedded porous carbon/graphene hybrid film as a high performance anode. *Carbon N. Y.* **84**(1), 434–443 (2015)
9. Jung, R., et al.: Consumption of fluoroethylene carbonate (FEC) on Si-C Composite electrodes for Li-Ion batteries. *J. Electrochem. Soc.* **163**(8), A1705–A1716 (2016)
10. Chen, Y., et al.: Chitosan as a functional additive for high-performance lithium-sulfur batteries. *J. Mater. Chem. A* **3**(29), 15235–15240 (2015)
11. Hansen, S., Quiroga-González, E., Carstensen, J., Föll, H.: Size-dependent cyclic voltammetry study of silicon microwire anodes for lithium ion batteries. *Electrochim. Acta* **217**, 283–291 (2016)
12. Varvara, S.: Enhancing the performance of lithium batteries through the development of improved electrolyte formulation, formation protocol and graphite surface modification (2017)

Adsorption of Lead Ions on Carbonaceous Sorbents of Nutshell Obtained from Secondary Raw Material

T. Marsagishvili, G. Tatishvili, N. Ananiashvili, N. Giorgadze, E. Tskhakaia, M. Gachechiladze, J. Metreveli, and M. Machavariani

Abstract

The sorption of Pb (II) ions from an aqueous solution of lead nitrate on carbon sorbents, obtained from waste based on cellulose-containing materials, was studied. Particularly, among studied carbons [hazel nutshell, walnut shell, sawdust, activated carbon (fraction size—40 μ)] material obtained from walnut shell shows the best adsorptive properties. The possibility of their use for the purification of drinking and waste waters contaminated with lead ions is established. The maximum amount of lead that can be bound by 1 g of sorbent is 154.0 mg/g, while 95% of metal ions are bound within 30–40 min.

Keywords

Sorption • Lead • Adsorption • Nutshell • Carbon

1 Introduction

Control of heavy metals content in natural waters is very important, because they are especially dangerous for human health. It must be mentioned, that metals often form water soluble complexes during chemical transformations in the medium. This complicates their removal by such well-known methods as coagulation, flotation, filtration, biochemical purification. However, the sorption method of water purification from heavy metals is the most effective way for neutralization of industrial wastewaters and for returning of pure water and precious metals to industry.

T. Marsagishvili (✉) · G. Tatishvili · N. Ananiashvili · N. Giorgadze · E. Tskhakaia · M. Gachechiladze · J. Metreveli · M. Machavariani
R. Agladze Institute of Inorganic Chemistry and Electrochemistry, Iv. Javakishvili Tbilisi State University, Mindeli str. #11, Tbilisi, Georgia
e-mail: tamaz.marsagishvili@gmail.com

M. Machavariani
e-mail: marinemachavariani@gmail.com

A problem of purification of drinking and waste waters is connected with their composition. In spite of the existence of general theoretical works in each particular instance it is necessary to select specific sorbent [1–15]. Therefore, creation of new cheap and effective adsorbents, especially on the basis of waste, is very important. Various sorbents were obtained from cellulose-contained waste by the help of worked out original technology [13, 14].

Lead is one of the most dangerous, environmentally toxic elements. Its accumulation in the environment is connected with the use of tetraethyl lead as an anti detonator, which is added to automotive fuel. Water contamination with lead is much higher in industrial regions. Lead accumulates in water in the form of ions or water-soluble complexes [1]. Removal of lead is realized by various methods, but the sorption method of water purification from lead is rather simple and effective method, which allows the neutralization of drinking and industrial wastewaters.

Maximum permissible concentration of lead ions in wastewaters is 1.0 mg/L, and in drinking water is 0.01 mg/L.

Search of new adsorbents in order to solve above mentioned problem in the world is very important. The analysis of literary data [2–15] has shown, that adsorbents, which were used for purification of drinking and wastewaters, oil products and organic solvents are characterized with high cost price and complicated regeneration technologies.

2 Materials and Methods

This work is devoted to the adsorption of lead from aqueous medium by new carbon materials—adsorbents obtained from wastes based on cellulose-containing materials, according to the technology developed by the authors of this article [13, 14].

The advantage of worked out technology is that during thermochemical conversion, cheap reagent is added to the raw materials, which ensures the low price of the obtained

carbonaceous material with high surface porosity. It must be noticed, that obtained sorbents are considerably cheaper and in contrast to other waste their reserves are constantly renewable, because of the growth of plants.

The possibility of use of obtained sorbents for the purification of drinking and waste water from lead ions is determined in this work.

Determination of the sorption activity of adsorbents with respect to lead ions (A_{Pb} , mg/g) was carried out at a temperature 20°–25 °C. A portion of the adsorbent (1.0 g) (three parallel experiments were carried out in one point) was stirred for 2 h with 100 ml of 0.01 M lead nitrate solution $Pb(NO_3)_2$, after which the solution was separated from the sorbent by filtration and the current (almost equilibrium) concentration of metal ions was detected in it (C_p , mg/L) (C_p was determined on atomic-absorptive spectrometer—ANALYST 200-1004 TAM (Pelkin-Elmer ICP-OES 3300XL, Perkin-Elmer, Billerica, MA, USA).

3 Results and Discussion

We have measured the chemical composition of samples on Scanning Electron Microscope (SEM and TESCAN). The results are shown on Table 1.

The adsorption capacity of carbonaceous materials from hazel nutshell, walnut shell, sawdust, activated carbon (fraction size—40 μ) obtained by the above-mentioned technology with respect to lead ions has been studied (Table 2).

The sorption capacity of sorbents (A_T) at each given moment of time was calculated by the formula [15]:

$$A = \frac{V_o(C_o - C)}{m}, \text{ (mg/g)} \quad (1)$$

Recovery ratio was calculated by the formula [15]:

$$\alpha = \frac{(C_o - C)}{C_o} \cdot 100\% \quad (2)$$

As it is obvious from the research, after two hours delay (practically, after 1 h delay equilibrium state is achieved) of adsorbents in solution of lead nitrate ($C_{(Pb)}^{++}{}_{init.} = 2.2$ g/L), material obtained from walnut shells shows the best adsorptive properties.

Dependence of lead ions sorption on walnut shells from delay time of sorbent in solution is studied. The results are given in Table 3 and Fig. 1.

From the above data it can be seen that equilibrium is established relatively quickly, after about 30–40 min. The maximum amount of lead that can be bound by 1 g of sorbent is 154.0 mg /g, while 95% of metal ions are bound within 30–40 min.

Studies of the dependence of lead ion sorption on mixing showed that it is almost not affected by mixing. This indicates that the external diffusion factor does not play a significant role in the process under study and proves that the process is determined by the internal diffusion of ions in the pores of the sorbent.

The removal of Pb(II) was maximal when the pH of water varied within 5.5–6.0.

Table 1 Chemical composition of the carbonaceous materials samples obtained from secondary raw materials (% averaged)

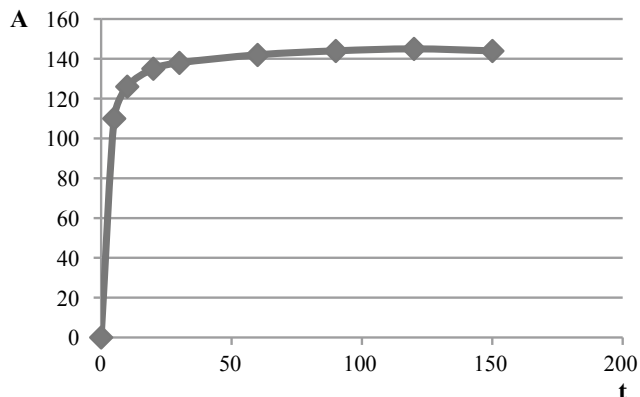
Sample	C	O	Ca	K	S	Fe	Ni	Cu
Hazelnutshell	85.1	10.7	2.07	0.6	0.2	0.5	0.4	0.2
Sawdust	94.6	4.3	0.5	0.1	–	–	0.2	–
Walnut shell	89.5	7.4	0.8	1.4	0.4	0.2	–	0.2
Activated carbon	89.6	8.69	0.7	0.4	–	0.1	–	0.4

Table 2 Equilibrium concentrations $C_{Pb^{++}}$ of adsorbents obtained from hazel nutshell, walnut shell, sawdust, activated carbon (fraction size—40 μ) after a two hours delay in solution (with stirring) and adsorption value (A , mg/g) of $Pb^{(II)}$ ions ($m_{sorb.} = 1$ g, $V_{sol.} = 100$ mL, $C_{(Pb)}^{++}{}_{init.} = 2.2$ g/L, $t = 20$ – 25 °C)

	Hazel nutshells	Walnut shells	Sawdust	Activated carbon
Average values of $C_{Pb^{++}}$ equilibrium concentration after adsorption $C_{av.}$ (g/L)	1.436	0.890	1.743	1.08
Average value of $Pb^{(II)}$ ion adsorption $A_{av.}$ (mg/g)	78.3	131.67	47.7	112.3
Recovery ratio of $Pb^{(II)}$ ions, %	35.5	60.0	21.5	51.3

Table 3 Dependence of adsorption value (A , mg/g) and recovery ratio (%) of $Pb^{(II)}$ ions on delay time of adsorbent in solution (with stirring) for the sample obtained from walnut shells (fraction size 40μ) ($m_{sorb.} = 1$ g, $V_{sol.} = 100$ mL, $C_{(Pb)_{init.}}^{++} = 2.2$ g/L, $t = 20-25$ °C)

Delay time in solution t (min)	5	10	20	30	60	90	120	150
Current concentration C (g/L)	1.0	0.84	0.75	0.72	0.68	0.66	0.65	0.66
Adsorption, A (mg/g)	120	136	145	148	152	154	155	154
Recovery ratio of $Pb^{(II)}$ ions (%) from solution (in comparison with $C_{(Pb)_{init.}}^{++}$)	52.6	61.8	65.9	67.3	69.0	70.0	70.45	70.0

**Fig. 1** Dependence of adsorption value (A , mg/g) on delay time (t , min) of adsorbent in solution

The influence of initial concentration of $Pb(II)$ on lead adsorption was studied.

The results of this influence are given in Table 4 (contact time of adsorbent with solution is fixed).

It turned out, that the higher the concentration of lead in the solution, the greater the adsorption of lead on the nutshell adsorbent.

For elementary analysis, you can recalculate some parameters, characterizing the process of adsorption. The calculation of the size of the surface of the adsorbent, which is required for the adsorption of lead ions on different sorbents is of interest. Let us estimate the surface occupied by the adsorbed particles of one gram equivalent of Pb ions.

As can be seen from Table 5, the size of the surfaces for the adsorption of one mole of different ions from the same type of solutions is not much different from each other. It

should be expected that this difference is related to the specificity of the electron orbitals of the adsorbable particles.

Table 6 shows the estimated data on what area on the surface S of the adsorbent is occupied by one adsorbed particle and also the distances R between the adsorbed particles.

4 Conclusion

1. It is established, that carbonaceous materials obtained from secondary raw materials by the original technology (thermal conversion) may be successfully used as sorbents because of their high BET surface area and porosity.
2. Among studied four samples (hazelnut shell, sawdust, walnut shell and active carbon) the best adsorption properties has hazelnut shell, as far as its BET surface area, micropore area and volume is larger in comparison to other samples.
3. The adsorption properties of carbonaceous materials obtained from various vegetable waste depend not only on chemical composition, but also on structure of the material.
4. Among studied carbons [adsorbents obtained from hazelnut shell, walnut shell, sawdust, activated carbon (fraction size— 40μ)] material obtained from walnut shell shows the best adsorptive properties against $Pb(II)$ ions.
5. The maximum amount of lead that can be bound by 1 g of sorbent is 154.0 mg/g, while 95% of metal ions are bound within 30–40 min.

Table 4 The influence of initial concentration of $Pb(II)$ on lead adsorption

Initial concentration of lead g/L	Contact time of adsorbent with solution, min	Lead concentration after contact, g/L	Recovery ratio of lead, %	Lead adsorption A , mg/g
2.22	10	0.82	62.2	138
2.07	10	1.12	45.9	95
0.93	10	0.71	23.7	22
0.50	10	0.39	21.0	10.5

Table 5 The size of the surfaces for the adsorption of one mole

Sorbent	BET Surface area, m ² g ⁻¹	Surface per one mole, m ² /M
Hazelnut shell	637.33	1.71 × 10 ⁶
Sawdust	492.95	2.14 × 10 ⁶
Walnut shell	499.0	0.67 × 10 ⁶
Activated carbon	708.7	1.31 × 10 ⁶

Table 6 Adsorption parameters for single particles

Sorbent	S, Surface per one adsorbed particle, m ²	R, Distance between nearest particles, A
Hazelnut shell	2.84 × 10 ⁻¹⁸	16.8
Sawdust	3.55 × 10 ⁻¹⁸	18.8
Walnut shell	1.11 × 10 ⁻¹⁸	10.5
Activated carbon	2.18 × 10 ⁻¹⁸	14.8

Conflict of Interest The authors declare that they have no conflict of interest.

References

- Moore, D., Ramamurti, S.: Heavy metals in natural waters. M.: Mir, 286 p (1987)
- Marsagishvili, T.A., Kirillov, S.A., Machavariani, M.N.: Some aspects of physical and chemical adsorption on surface of amorphous solid. In: Combined and Hybrid Adsorbents: Fundamentals and Applications, Kiev, Puscha-Voditsa, Ukraine 15–17 Sept 2005, p. 17
- Marsagishvili, T.A., Kirillov, S.A., Machavariani, M.N., Ananiashvili, N.Sh., et al.: Amorphous oxides of manganese as new sorbents of strontium ions. Chem. Ecol. **1**(23), 87–91(2007)
- Romanenko, K., Bogdanovich, N., et al.: Obtaining of activated carbons by pyrolysis hydrolytic lignin. For. J. **4**, 162 (2017). <https://cyberleninka.ru/article/v/poluchenie-aktivnyh-ugley-pirolizom-gidroliznogo-lignina>
- Marsagishvili, T., Ananiashvili, N., Metreveli, J., Kikabidze-Gachechiladze, M., Machavariani, M., Tatishvili, G., Tskhakaya, E., Khositashvili, R.: Applications of georgian zeolites for the extraction of useful components from natural and waste waters. Eur. Chem. Bull. **1**(3), 102–103 (2014). ISSN 2063–5346
- Zhilina, M.V., Karnozhitski, P.V.: The relevance of the study of carbonization process for obtaining of activated carbon with the aim of utilization of plant waste (2012)
- Cao, Y.: Activated carbon preparation and modification for adsorption. Ph.D. thesis, South Dakota State University (2017)
- Bezdenezhnikh, L., Alekseeva, T., et al.: New adsorbents from plant waste for adsorption purification of vegetable oil. Visnik KDPY imeni Mikhaila Ostrogradskogo. Issue 5/2007 (46) (2007)
- Ekpete, O., Marcus, A., Osi, V.: Preparation and characterization of activated carbon obtained from plantain (*Musa paradisiaca*) fruit stem. J. Chem. **2017**, Article ID 8635615, 6 pages (2017). <https://doi.org/10.1155/2017/8635615>
- Arjuman Banu, S., Nagarani, S., et al.: Preparation of low cost activated carbon adsorbents from natural sources. Int. J. Eng. Technol. Sci. Res. IJETSRS **3**(4) (2016). www.ijetsr.com. ISSN 2394 – 3386
- Ghaedia, M., Golestani, A., et al.: Application of activated carbon as adsorbents for efficient removal of methylene blue: kinetics and equilibrium study. J. Ind. Eng. Chem. **20**(4), 2317–2324 (2014)
- Moyo, M., Chikazaza, L., Chomunorwa, B., et al.: Adsorption batch studies on the removal of Pb(II) using Maize tassel based activated carbon. J. Chem. **2103**, Article ID 508934, 8 pages (2013) (Hindawi Publishing Corporation)
- United States Patent and Trademark Office, patent US 9,663,662 B1
- Method for obtaining sorbents from waste containing plastics and cellulose. Patent application, # AP 2019 15030. 25.03.2019 (Patent is under consideration)
- Smirnov, A.: Sorption purification of water. Leningrad “Khimia”, p. 188 (1982)

Structural and Photoluminescence Properties of Nanoparticles Formed by Laser Ablation of Porous Silicon in Ethanol and Liquid Nitrogen

A. V. Skobelkina, F. V. Kashaev, S. V. Zobotnov, A. V. Kolchin, T. P. Kaminskaya, D. E. Presnov, E. A. Sergeeva, M. Yu. Kirillin, L. A. Golovan, and P. K. Kashkarov

Abstract

Sequential use of electrochemical etching and picosecond laser ablation in ethanol and liquid nitrogen allows fabrication of silicon particles with size smaller than 100 nm and high level of crystallinity. Fabricated ensembles of nanoparticles exhibit effective photoluminescence with emission peaks located within biotissue optical transparency window, thus being promising as contrasting agents for bioimaging.

Keywords

Pulsed laser ablation • Silicon nanoparticles • Photoluminescence

1 Introduction

Silicon nanoparticles (Si-NPs) have high potential in different biomedical applications [1–4] owing to relatively high biocompatibility, biodegradability and low toxicity [3–6]. In particular, Si-NPs were demonstrated to serve as photoluminescence (PL) markers for bioimaging.

For efficient penetration into living tissue upon topical administration or transport within organism upon intravenous injection, the particles should have sizes smaller than 100 nm. Mechanical milling or ultrasound grinding techniques traditionally applied to porous or crystalline silicon do not allow to ensure the required size. Si-NPs with the desirable small size could be produced by colloidal synthesis or other similar chemical techniques. However, application of these techniques may result in numerous chemical impurities within nanoparticles that are undesirable for biomedical applications.

Pulsed laser ablation techniques in liquids or gases [7, 8] is an alternative way of “green synthesis” of chemically pure Si-NPs with the sizes ranging from 1 to 100 nm. However, relatively low product yield is a significant disadvantage of this technique. Moreover, this technique does not ensure efficient photoluminescence of the produced Si-NPs, especially if crystalline silicon targets are employed. The state-of-the-art technologies to produce photoluminescent Si-NPs are based on two-step approaches consisting in either mechanical milling of crystalline silicon followed by laser fragmentation in a liquid [7] or laser ablation in inert gas followed by ultrasound grinding [8].

In this paper, we propose a hybrid approach consisting in sequential application of electrochemical etching of initial silicon wafers with low doping level and laser ablation in ethanol or liquid nitrogen. As a result of electrochemical etching, microporous silicon films are formed. These structures exhibit effective photoluminescence in the red region [4] and reduced ablation threshold in comparison with unprocessed crystalline silicon [9]. Laser ablation allows to produce nanosized particles preserving, however, photoluminescence properties of the microporous silicon films.

This study presents a comprehensive analysis of the structural and photoluminescent properties of the fabricated Si-NPs by means of the atomic-force microscopy (AFM), scanning electron microscopy (SEM), Raman scattering, and photoluminescence spectroscopy techniques.

A. V. Skobelkina (✉) · F. V. Kashaev · S. V. Zobotnov · A. V. Kolchin · T. P. Kaminskaya · D. E. Presnov · E. A. Sergeeva · L. A. Golovan · P. K. Kashkarov
Faculty of Physics, Lomonosov Moscow State University, Leninskie Gory 1/2, Moscow, 119991, Russia
e-mail: snastya.19996@mail.ru

D. E. Presnov
Skobeltsyn Institute of Nuclear Physics, Lomonosov Moscow State University, Moscow, Russia

D. E. Presnov
Faculty of Physics, Quantum Technology Centre, Lomonosov Moscow State University, Moscow, Russia

E. A. Sergeeva · M. Yu. Kirillin
Institute of Applied Physics RAS, Nizhny Novgorod, Russia

2 Materials and Methods

The p-type monocrystalline silicon plates were chosen as an initial material with the (100) surface orientation and a specific resistivity value of 1–20 Ω cm to form the layers of microporous silicon by electrochemical etching. Solution of 47.5% hydrofluoric acid with ethanol in the 1:1 proportion was used for etching. The substrates of monocrystalline silicon were placed in pure hydrofluoric acid for a few seconds prior to etching in order to remove the natural oxide film from the surface. Etching was performed for 30 min with electric current density of 25 mA/cm².

After etching, the produced porous silicon film on initial wafer was placed into a cell (15 ml) filled with ethanol or liquid nitrogen and irradiated by picosecond pulsed laser (Nd:YAG laser EKSPLA PL2143A, 1064 nm, 34 ps, 10 mJ, 10 Hz) for 30 min [10]. Si-NPs suspensions were formed as a result of the picosecond laser ablation in a liquid.

To determine the size distribution of the ablated Si-NPs, AFM and SEM images were obtained using ND-MDT SolverPRO and Carl Zeiss Supra 40 microscopes, respectively. Raman spectra were measured using a Horiba Jobin Yvon HR 800 Raman microscope upon excitation with a He–Ne laser (632 nm). The photoluminescence spectra and kinetics were measured using a SpectraPro 2500i spectrograph upon excitation by the second harmonic (532 nm) of the Nd:YAG laser employed for ablation.

3 Results and Discussion

AFM-image analysis demonstrated that the proposed approach allows to fabricate Si-NPs with the size ranges of 5–100 nm and 7–60 nm for ablation in ethanol and liquid nitrogen, respectively. Relatively small sizes of the produced nanoparticles indicate low efficiency of agglomeration of the ablation products into nanoparticles in the used buffer environments. SEM inspection indicated that all types of fabricated Si-NPs have a smooth surface, without noticeable surface roughness, and a shape close to spherical (see, for example, Fig. 1a), which, in our opinion, should facilitate penetration of the particles into biological tissues with minimal mechanical damage.

Raman spectra of the formed Si-NPs were measured to estimate the level of the particle crystallinity by analysis of the integral intensities I_c and I_a of the lines for crystalline (520 cm⁻¹) and amorphous (480 cm⁻¹) silicon phases, respectively. A typical Raman spectrum of Si-NPs ensemble is presented in Fig. 1b.

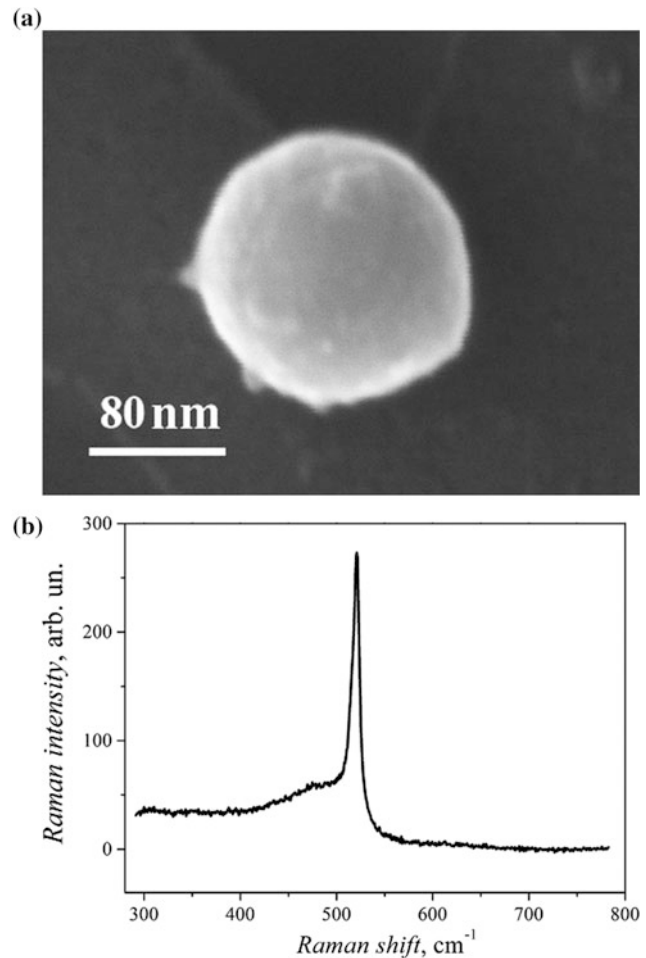


Fig. 1 SEM image (a) and Raman spectrum (b) of Si-NPs formed by laser ablation of microporous silicon in ethanol

To calculate the volume fraction f_a of amorphous silicon in a nanoparticle we applied a standard formula [11, 12]:

$$f_a = yI_a / (yI_a + I_c), \quad (1)$$

where y is the Raman scattering cross section ratio of the crystalline and amorphous phases. For relatively large Si-NPs without quantum confinement this value can be taken as 0.1 [12]. The volume fraction of the amorphous phase was revealed to be smaller than 13% for all studied Si-NPs.

The revealed relatively high level of crystallinity of the formed Si-NPs facilitates photoluminescence in the region of 600–900 nm (Fig. 2a) with maxima located at 720 and 746 nm for the Si-NPs ablated in ethanol and liquid nitrogen, respectively. Note, that the photoluminescence spectra are within the biotissue transparency window (700–1200 nm).

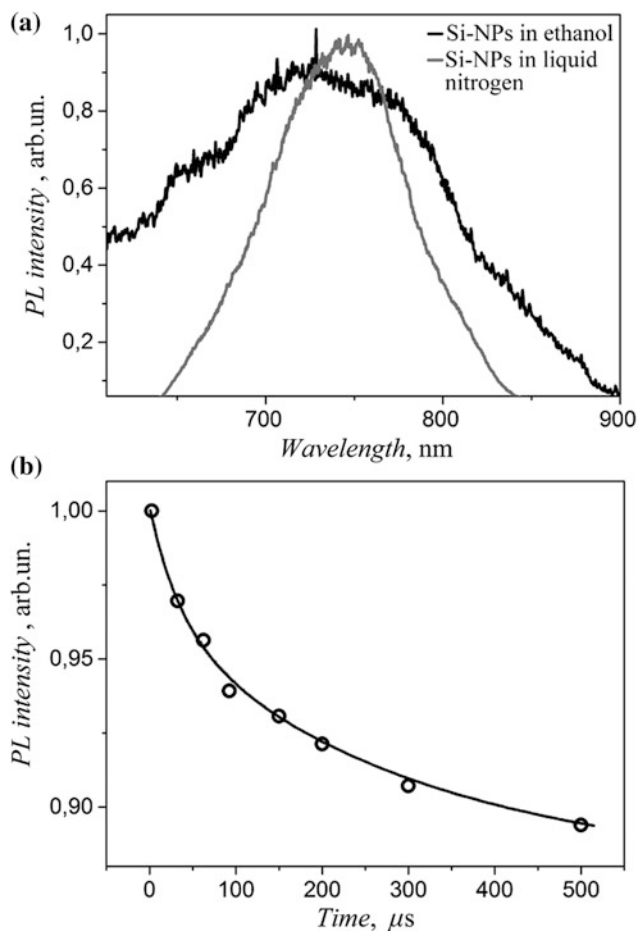


Fig. 2 PL spectra of Si-NPs formed by laser ablation of microporous silicon in ethanol and liquid nitrogen (a); PL kinetics of Si-NPs produced by laser ablation in ethanol (b)

A typical PL kinetics curve is shown in Fig. 2b. Experimental dependencies are accurately fitted by stretched exponential decay functions for all types of the studied nanoparticles. It is assumed that this approximation correlates with the presence of silicon nanocrystals with wide size distribution. The obtained values of PL lifetime and exponent stretching factor are $680 \pm 30 \mu\text{s}$ and 0.237 ± 0.012 , respectively, for the Si-NPs fabricated in ethanol and $28.0 \pm 1.4 \mu\text{s}$ and 0.34 ± 0.03 , respectively, for ablation in liquid nitrogen. It should be noted that the initial microporous silicon exhibits a faster PL decay in comparison with the Si-NPs: its PL lifetime and exponent stretching factor amount $5.5 \pm 0.3 \mu\text{s}$ and 0.368 ± 0.011 , respectively. Most likely, the observed tendency of significant increase of the PL lifetime after laser ablation originates from the

appearance of numerous defects in the formed nanocrystals as a result of the fabrication process and requires further study.

4 Conclusions

To conclude, in the present study the possibility of silicon nanoparticles formation as a result of sequential electrochemical etching and picosecond laser ablation in ethanol or liquid nitrogen was investigated. The proposed hybrid approach allows fabrication of Si-NPs with a size smaller than 100 nm and level of crystallinity higher than 87%.

The fabricated nanostructures exhibit effective photoluminescence with emission peaks in the red region and lifetimes of order of tens (ablation in liquid nitrogen) and hundreds (ablation in ethanol) μs . Since the emission peaks are within the biotissue transparency window (700–1200 nm), the fabricated Si-NPs have high potential as photoluminescent markers for bioimaging.

Acknowledgements This work was supported by the Russian Science Foundation (project № 19-12-00192).

Conflict of Interest The authors declare that they have no conflict of interest.

References

1. Stojanovic, V., Cunin, F., Durand, J.O., et al.: Potential of porous silicon nanoparticles as an emerging platform for cancer theranostics. *J. Mater. Chem. B* **4**, 7050–7059 (2016)
2. Yu, Kirillin M., Sergeeva, E.A., Agrba, P.D., et al.: Laser-ablated silicon nanoparticles: optical properties and perspectives in optical coherence tomography. *Laser Phys.* **251**, 075604 (2015)
3. Tolstik, E., Osminkina, L.A., Matthäus, C., et al.: Studies of silicon nanoparticles uptake and biodegradation in cancer cells by Raman spectroscopy. *Nanomedicine: NBM* **12**, 1931–1940 (2016)
4. Sviridov, A.P., Osminkina, L.A., Kharin, AYu., et al.: Cytotoxicity control of silicon nanoparticles by biopolymer coating and ultrasound irradiation for cancer theranostic applications. *Nanotechnology* **28**, 105102 (2017)
5. Ksenofontova, O.I., Vasin, A.V., Egorov, V.V., et al.: Porous silicon and its applications in biology and medicine. *Tech. Phys.* **59**, 66–77 (2014)
6. Park, J.-H., Gu, L., von Maltzahn, G., et al.: Biodegradable luminescent porous silicon nanoparticles for in vivo applications. *Nat. Mater.* **8**, 331–336 (2009)
7. Blandin, P., Maximova, K.A., Gongalsky, M.B., et al.: Femtosecond laser fragmentation from water-dispersed microcolloids: toward fast controllable growth of ultrapure Si-based nanomaterials for biological applications. *J. Mater. Chem. B* **1**, 2489–2495 (2013)

8. Gongalsky, M.B., Osminkina, L.A., Pereira, A., et al.: Laser-synthesized oxide-passivated bright Si quantum dots for bioimaging. *Sci. Rep.* **6**, 24732 (2016)
9. Golovan, L.A., Dzun, I.O., Dokukina, A.E., et al.: AFM investigation of nanoparticles formed on silicon surface by femtosecond laser pulses. *Bull. RAS Phys.* **73**(1), 39–41 (2019)
10. Perminov, P.A., Dzhun, I.O., Ezhov, A.A., et al.: Creation of silicon nanocrystals using the laser ablation in liquid. *Laser Phys.* **21**, 801–804 (2011)
11. Golubev, V.G., Yu, Davydov V., Medvedev, A.V., et al.: Raman scattering spectra and electrical conductivity of thin silicon films with a mixed amorphous-nanocrystalline phase composition: determination of the nanocrystalline volume fraction. *Phys. Solid State* **39**(8), 1197–1201 (1997)
12. Bustarret, E., Hachicha, M.A., Brunel, M.: Experimental determination of the nanocrystalline volume fraction in silicon thin films from Raman spectroscopy. *Appl. Phys. Lett.* **52**, 1675–1677 (1988)

Electrical and Photoelectrical Properties of $Zn_{1-x}Mg_xO$ Thin Films Obtained by Spin Coating and Aerosol Deposition Method

V. Morari, V. Postolache, G. Mihai, E. Rusu, Ed. Monaico, V. V. Ursachi, K. Nielsch, and I. M. Tiginyanu

Abstract

$Zn_{1-x}Mg_xO$ thin films were prepared by aerosol deposition and spin-coating method, using zinc acetate and magnesium acetate as precursors. The obtained films were investigated by scanning electron microscopy (SEM), electrical and photoelectrical characterization. SEM and energy dispersive x-ray (EDX) analysis has shown that the produced thin films are homogeneous in morphology and composition. The relaxation of photoconductivity under UV illumination was investigated in vacuum as a function of temperature. It was found that the thin films produced by spin-coating exhibit much higher photosensitivity and long duration relaxation of photoconductivity, in contrast to the films obtained by aerosol deposition. The investigation of photosensitivity in a wider spectral range demonstrated that the films are also sensitive to the visible and infrared irradiation.

Keywords

Semiconductors • $ZnMgO$ • SEM • I-V characterization • UV radiation

1 Introduction

Compound semiconductors are commonly used in many optoelectronic applications [1–4]. Modern light emitting diodes (LEDs), for the spectral range from ultraviolet (UV) to green light, are often made of III-N semiconductors such as InN, GaN, AlN and alloys [5–7]. However, the production of these materials is difficult and expensive. Furthermore, indium and gallium are very rare metals and the demand of these elements is rapidly growing. This situation stimulates the research for alternative solutions, such as II–VI group semiconductors, particularly ZnO [8], ZnMgO [9] and CdZnO, which show a great potential in replacing the nitrides. For the meantime, the growth of ZnMgO layers is difficult, because of low thermodynamic solubility of MgO in ZnO. However, recent works show a high improvement in growing techniques for ZnMgO layers and it makes possible to accurately investigate luminescence properties of this material. Finally, according to the recent research, ZnMgO shows high potential to become an extensively used material for production of optoelectronic devices, where wide band gap semiconductors are required. In this report we present results on the investigation of structural, electrical and photoelectrical properties of ternary ZnMgO layers grown by aerosol deposition and spin coating method [10, 11].

2 Technology of ZnMgo Thin Films Preparation

The spin-coating method (Fig. 1) is a procedure used to deposit thin films on Si, sapphire, quartz, glass and other substrates. Usually, a small amount of solution is placed at the center of a substrate rotating at a given speed (in this case of 2000 rpm), to spread the material over the entire surface of the substrate by the centrifugal force. The rotation takes 20 s, then the substrate is dried at 150 °C for 10 min. One

V. Morari (✉) · E. Rusu · V. V. Ursachi · I. M. Tiginyanu
Institute of Electronic Engineering and Nanotechnologies
“D. Ghitu”, Academy Street 3/3, Chisinau, Moldova
e-mail: vadimmorari2018@gmail.com

V. Postolache · Ed. Monaico · I. M. Tiginyanu
National Center for Materials Study and Testing, Technical
University of Moldova, Chisinau, Moldova

K. Nielsch
Leibniz Institute for Solid State and Materials Research (IFW
Dresden), Institute for Metallic Materials (IMW), Dresden,
Germany

G. Mihai
Center for Surface Science and NanoTechnology, University
Politehnica of Bucharest, Bucharest, Romania

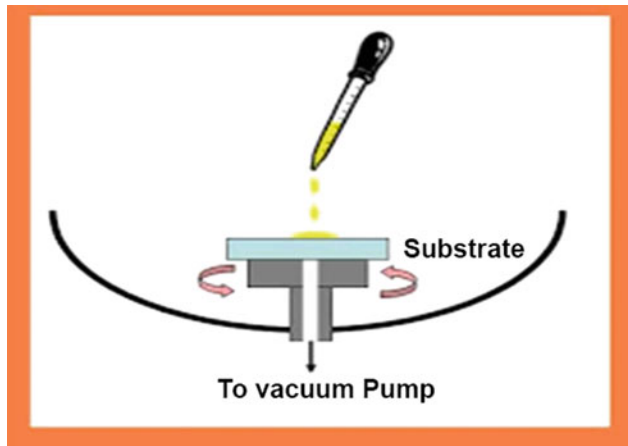


Fig. 1 Schematics of spin-coating method of spraying solutions by centrifugal force

should mention that the higher the spin speed, the thinner the film. The thickness of the film also depends on the viscosity and concentration of the solution, but also on the solvent used. The procedure is repeated until the desired film thickness is obtained. In our case, after depositing 10 layers, the sample was treated at 500 °C for one hour in air.

For the deposition of $Zn_{0.8}Mg_{0.2}O$ thin films by spin-coating, mixed solutions of $Zn(CH_3CO_2)_2$, $Mg(C_2H_3O_2)_2$, (0.35M) dissolved in 20 mL of 2-methoxyethanol + 0.5 mL of diethanolamine (DEA) were prepared in an ultrasonic bath for 30 min at a temperature of 50-60°C. Solutions with 0.2% concentration of Mg in ZnO were prepared with these two acetates.

The aerosol deposition method (Fig. 2) relies on spraying on a substrate a solution that contains precursors of the base material and, optionally, dopants. Therefore, the aerosol deposition technology requires a substrate, a heater to maintain the temperature of the substrate up to 600 °C, a sprayer, a gas flow (O_2 , N_2 , Ar), and also aerosols falling on the substrate. The aerosol is brought above the heated substrate, where the reaction of the precursors occurs at a given temperature, which ultimately produces the oxide deposited on the substrate.

The solutions of $Zn(CH_3CO_2)_2$, $Mg(C_2H_3O_2)_2$, (0.35 M) dissolved in 50 mL of C_2H_5OH were mixed in an ultrasonic bath for 30 min at a temperature of 50–60 °C for the aerosol deposition of $Zn_{0.8}Mg_{0.2}O$ thin films. Similarly to the films

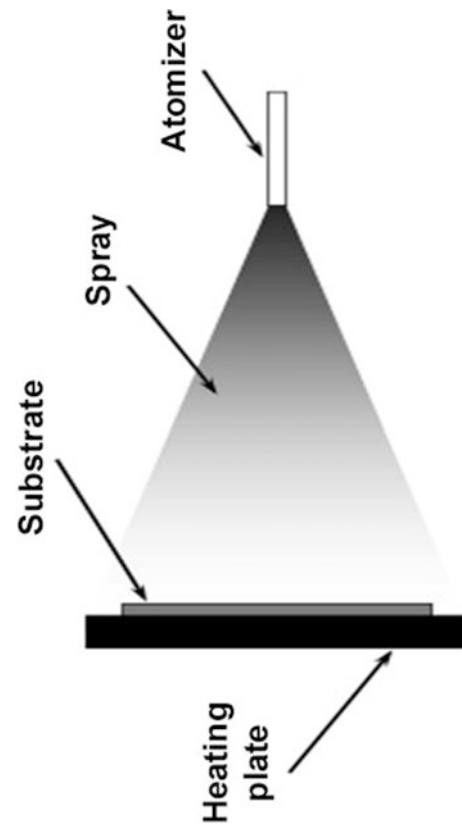


Fig. 2 Schematics of aerosol deposition method

deposited by spin-coating, solutions with 0.2% concentration of Mg in ZnO were prepared with these two acetates.

3 Study of Morphological Properties

$Zn_{1-x}Mg_xO$ Films with thicknesses between 50–100 nm and uniform morphology were prepared by aerosol deposition and spin-coating method at 500–550 °C on p-Si (100) substrates.

The morphology of $Zn_{0.8}Mg_{0.2}O$ thin films was studied with a Hitachi SU 8230 scanning electron microscope (SEM), using secondary electron images obtained at different magnifications: 10k, 40k, 60k. The SEM images of a $Zn_{0.8}Mg_{0.2}O$ film obtained by the aerosol deposition method are presented in Fig. 3.

Fig. 3 Top SEM view (a, b) and cross section (c) images of the p-Si/n- $Zn_{0.8}Mg_{0.2}O$ material obtained by the aerosol deposition method

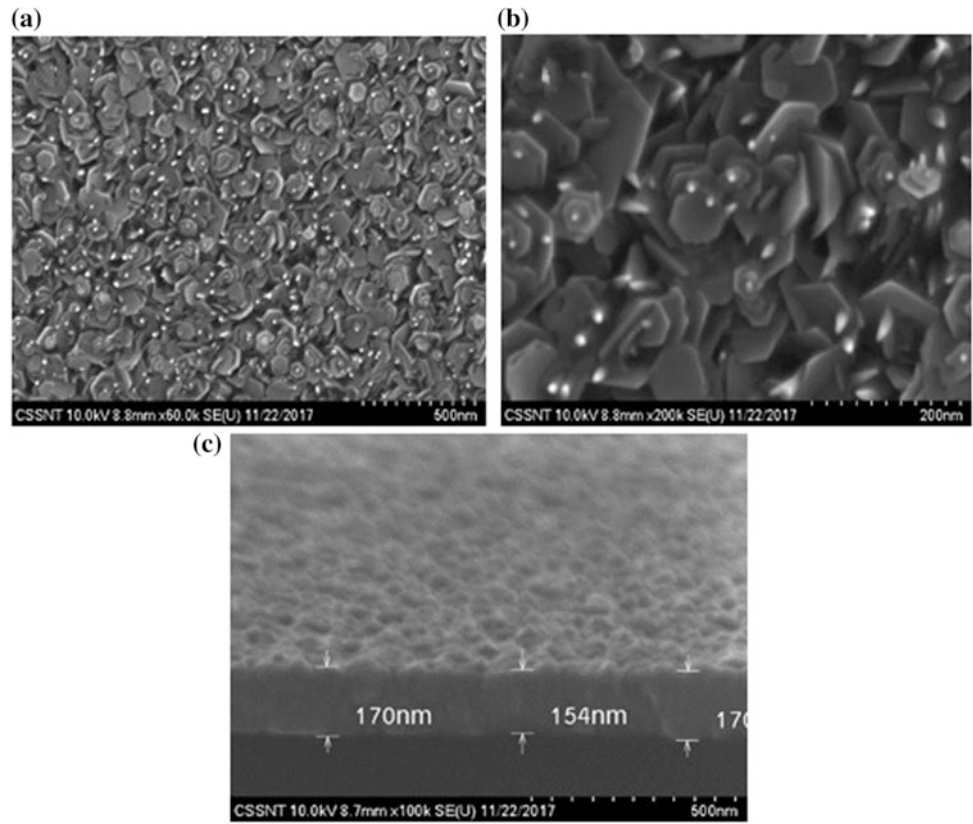


Fig. 4 Top SEM view (a, b) and cross section (c) images of the p-Si/n- $Zn_{0.8}Mg_{0.2}O$ material obtained by the spin-coating method

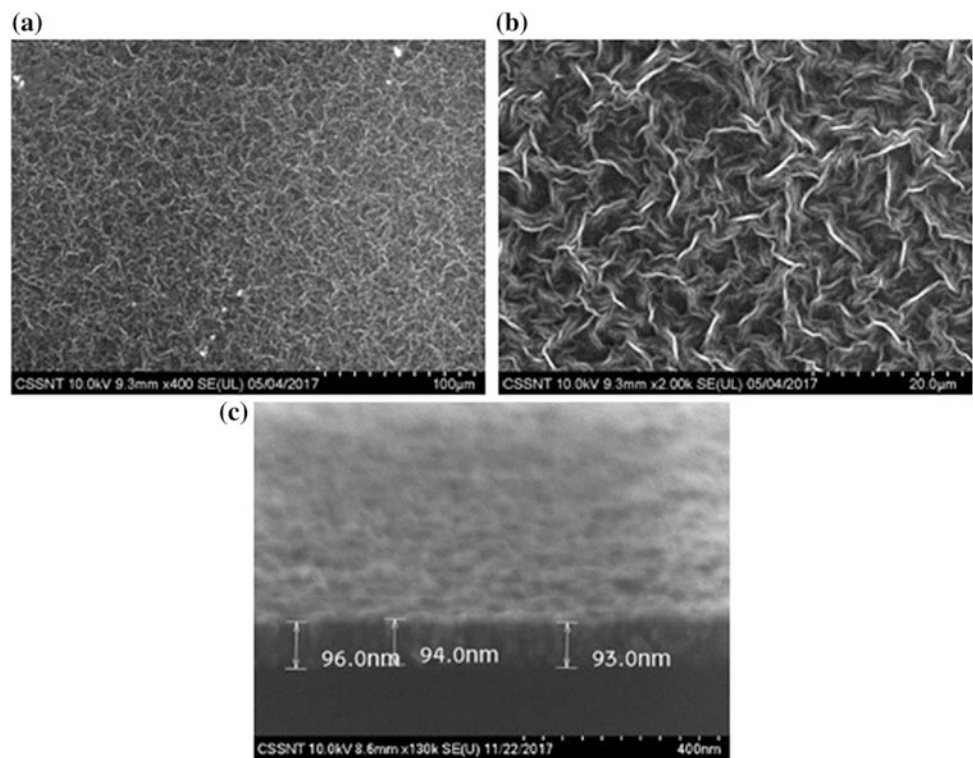


Figure 4 presents SEM images of a $Zn_{0.8}Mg_{0.2}O$ film obtained by the spin-coating method. One can see that the deposited film is planar.

4 Study of Electrical and Photoelectrical Properties

The measurements of current-voltage characteristics of n- $Zn_{0.8}Mg_{0.2}O$ /p-Si films prepared by aerosol deposition and spin-coating method were carried out with Pd contacts on the surface of the film. The films demonstrate photosensitivity under UV light irradiation, and the current increases proportionally to the excitation density. Figure 5 presents the current-voltage curves of the Pd/ $ZnMgO$ films at room temperature.

The I-V curves are symmetrical for both directions of the bias, and the characteristic measured in the dark is linear for the sample produced by aerosol deposition. Under UV light illumination (200–400 nm, 2.2 mW/cm²) the characteristic deviates from a linear one, and the sample demonstrates photosensitivity, which increases with increasing the bias. One can observe from Fig. 5 that the sample produced by spin-coating is much more sensitive, as compared to the one produced by aerosol deposition.

The relaxation of photocurrent measured under UV irradiation at 25 K demonstrates a fast response for samples

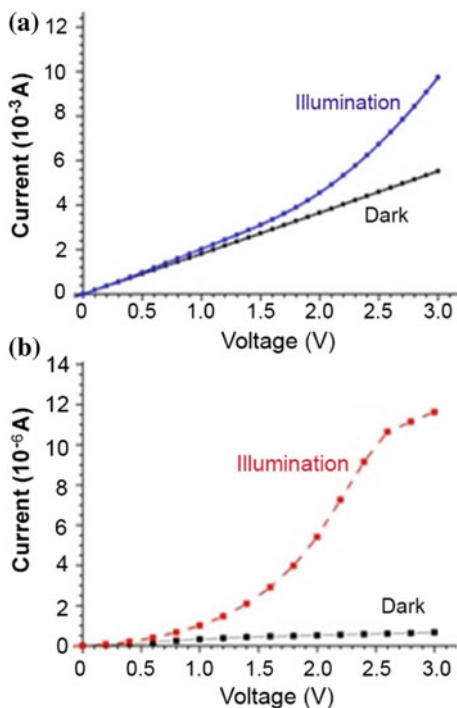


Fig. 5 The current-voltage characteristics in dark and under UV illumination for $Zn_{0.8}Mg_{0.2}O$ films deposited by aerosol (a) and spin-coating (b) methods

produced by both methods (aerosol deposition and spin-coating), without a long duration relaxation component. At 300 K there is a difference in the relaxation curves for samples produced by different methods. While the reaction of the photocurrent at UV irradiation is similar at low temperature (25 K) and room temperature (300 K) for samples produced by aerosol deposition (without a long duration relaxation component, the behavior is different for samples produced by spin-coating. The current built-up in samples produced by spin-coating demonstrates two components: a fast relaxation component, and slow one, with relaxation time of hundreds of seconds. Previously, long duration relaxation of photoconductivity was observed in highly doped and compensated semiconductors [12], porous semiconductors [13] and solid solutions [14]. In all of these cases, the phenomenon of long duration relaxation of

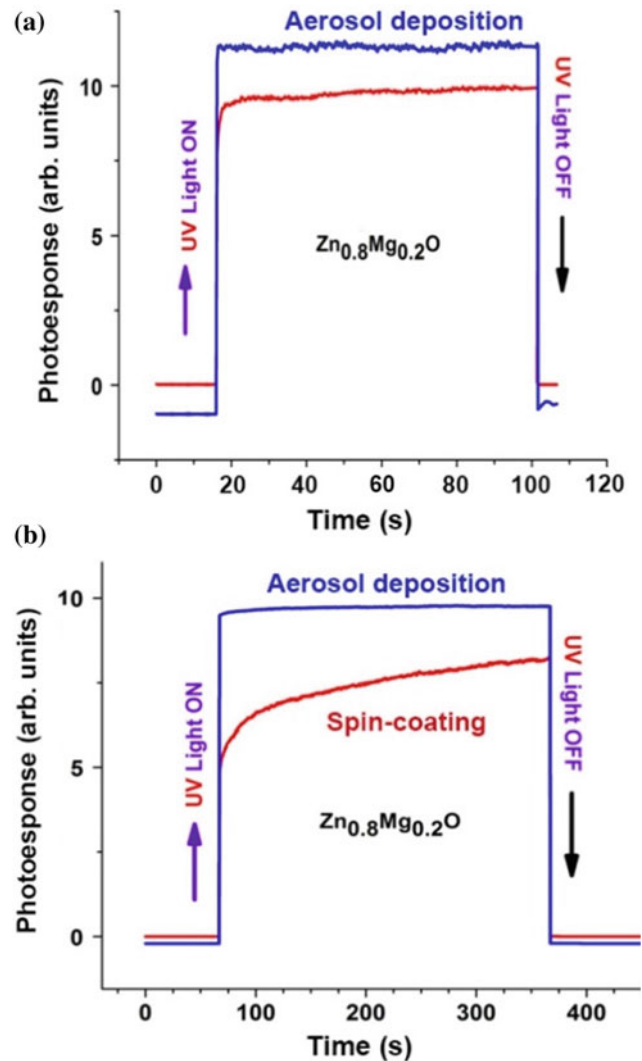


Fig. 6 The relaxation of photocurrent under UV irradiation measured in vacuum at 25 K (a), and 300 K (b) for films deposited by aerosol and spin-coating methods

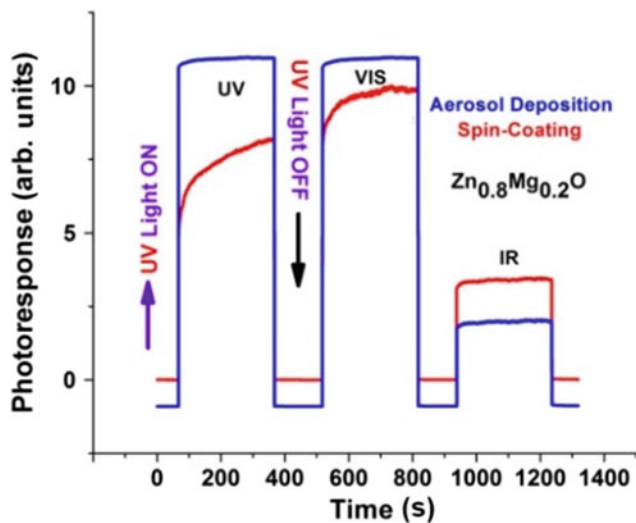


Fig. 7 The relaxation of photocurrent measured at 300 K in vacuum under irradiation with different wavelengths

photoconductivity and persistent photocurrent was explained by the random local-potential fluctuations, and formation of barriers for the relaxation of photoexcited carriers. The mechanisms of these fluctuations are different for the three systems. They are determined by the degree of conductivity compensation in the first case, by the degree of porosity in the second case, and by the local fluctuations of the solid solution composition in the third case. Since we deal with solid solutions, one can suggest that the long duration component of the relaxation of photoconductivity in our samples produced by spin-coating is due to the local fluctuations of the solid solution composition (Fig. 6).

The investigation of photoconductivity excited by irradiation from a wide spectral range (Fig. 7) shows that the samples produced by both the methods are sensitive in wide spectral range from UV to IR wavelengths. The sensitivity in the visible spectral range is comparable with that measured with the UV irradiation, while it is by a factor of 3–4 less for IR wavelengths.

5 Conclusions

The results of this study demonstrate preparation of $ZnMgO$ thin films with homogeneous morphology on Si substrates by aerosol deposition and spin-coating. The investigation of photoelectrical properties shows that the samples produced by aerosols deposition provide higher currents, while those prepared by spin-coating provide higher photosensitivity.

Acknowledgements This work was supported financially by the ANCD through grant no. 19.80013.50.07.02A/BL. V. Morari and E. Monaico thank to the Alexander von Humboldt Foundation for the research fellowships.

Conflict of Interest The authors declare that they have no conflict of interest.

References

- Sharma, A.K., et al.: Optical and structural properties of epitaxial $Mg_xZn_{1-x}O$ alloys. *Appl. Phys. Lett.* **75**(21), 27–33 (1999)
- Fan, M.-M., Liu, K.-W., Chen, X., Zhang, Z.-Z., Lia, B.-H., Shena, D.-Z.: A self-powered solar-blind ultraviolet photodetector based on a $Ag/ZnMgO/ZnO$ structure with fast response speed (2017). <https://doi.org/10.1039/c6ra28736k>
- Ohtomo, A., Kawasaki, M., Koida, T., Masubuchi, K., Koinuma, H., Sakurai, Y., Yoshida, Y., Yasuda, T., Segawa, Y.: $Mg_xZn_{1-x}O$ as a II–VI widegap semiconductor alloy. *Appl. Phys. Lett.* **72**(19), 24–66 (1998)
- Pan, C.J., Lin, K.F., Hsu, W.T., Hsieh, W.F.: Reducing exciton–longitudinal optical phonon coupling with increasing Mg incorporation in $MgZnO$ powders. *J. Appl. Phys.* **123**504, 102 (2007)
- Schubert, E.F., Cho, J., LEDs, U.V.: Electron-beam excitation. *Nat. Photonics* **4**, 735–736 (2010)
- Tsai, M.-C., Yen, S.-H., Kuo, Y.-K.: Deep-ultraviolet light-emitting diodes with gradually increased barrier thicknesses from n-layers to p-layers. *Appl. Phys. Lett.* **111**114, 98 (2011)
- Fujioka, A., et al.: Improvement in output power of 280-nm deep ultraviolet light-emitting diode by using $AlGaN$ multi quantum wells. *Appl. Phys. Express* **3**(4) (2010)
- Liang, S., Sheng, S., Liu, Y., Huo, Z., Lu, Y., Shen, H.: ZnO Schottky ultraviolet photodetectors. *J. Cryst. Growth* **225**, 110–113 (2001)
- Ni, P.-N., Shan, C.-X., Li, B.-H., Shen, D.-Z.: High Mg-content wurtzite $MgZnO$ alloys and their application in deep-ultraviolet light-emitters pumped by accelerated electrons. *Appl. Phys. Lett.* **032107**, 104 (2014)
- Morari, V., Curmei, N., Brincoveanu, O., Mesterca, R., Balan, D., Rusu, E., Prodana, M., Ursachi, V., Enachescu, M.: Prepararea și caracterizarea filmelor de $ZnSnO$ prin metoda aerosol. In: The 9th ICMCS & The 6th CFM, Publications by Technical University of Moldova, Chișinău, 19–21 Oct 2017, p. 482. ISBN 978-9975-4264-8-0
- Morari, V., Brincoveanu, O., Mesterca, R., Balan, D., Rusu, E., Zalamai, V., Prodana, M., Ursachi, V., Enachescu, M.: Synthesis of $Mg_1Zn_{1-x}O$ thin films by spin coating and aerosol deposition. In: The 9th ICMCS & The 6th CFM, Publications by Technical University of Moldova, Chișinău, 19–21 Oct 2017, p. 483. ISBN 978-9975-4264-8-0
- Шейнкман, М.К., Шит, А.Я.: Долговременные релаксации и остаточная проводимость в полупроводниках. *Физика и техника полупроводников* **10**(2), 209–233 (1976)
- Monaico, E., Postolache, V., Borodin, E., Ursaki, V., Lupan, O., Adelung, R., Nielsch, K., Tiginyanu, I.: Control of persistent photoconductivity in nanostructured InP through morphology design. *Semicond. Sci. Technol.* **30**, 035014 (7 pp) (2015)
- Jiangl, H.X., et al.: Persistent photoconductivity in II–VI and III–V semiconductor alloys and a novel infrared detector. *J. Appl. Phys.* **69**, 6701 (1991)

Peculiarities of Surface Relief Grating Formation in Nanomultilayer Structures Based on As_2S_3 -Se Chalcogenide Glasses

A. Meshalkin, O. Paiuk, E. Achimova, A. Stronski, V. Abaskin, A. Prisacar, G. Triduh, A. Korchovyj, and P. Oleksenko

Abstract

Chalcogenide glasses nanomultilayer structures based on As_2S_3 -Se were used for direct surface relief grating (SRG) formation by holographic recording. Grating recording process in As_2S_3 -Se nanomultilayer structure for different grating period and long recording time was performed. Simulated diffraction efficiency kinetics curves showed good agreement with the experimental results. Analyses of diffraction efficiency kinetics and AFM images of recorded SRG showed that grating period increasing led to the SRG depth increasing in linear way. It was revealed that SRG recording rate was characterized by non-linear behavior, while modulation depth remained approximately the same value for all gratings.

Keywords

Chalcogenide glasses • Nanomultilayer structures • Surface relief grating • Diffraction efficiency • Non-linear photoresponse

1 Introduction

Direct surface relief grating (SRG) recording in amorphous chalcogenide glasses (ChGs) has been extensively studied in recent years [1, 2]. The interest of this topic results from observation of the light-induced mass transport, firstly observed in thin films of azopolymers [3, 4], and further in chalcogenide glasses [5–7]. The effect of light induced surface deformation in ChG is intensively studied both experimentally and theoretically, however many details of the

process remain unclear. The first report of photo-induced mass transport observed in As_2S_3 revealed polarization dependence (vectorial) nature of this effect [8]. Later, vectorial SRG were formed in As-Se, As-S-Se, Ge-Se chalcogenide films and As_2S_3 -Se multilayer structures. Among ChGs thin films amorphous nanomultilayer structures (NML) are attractive because of the prominent photoinduced effects [9–11].

Two distinct mechanisms of SRG recording in ChGs thin films are distinguished depending on the polarization of writing beams: small scalar SRGs induced by photoinduced volume change, and giant vectorial SRGs induced by lateral mass transport [12]. Earlier [13] we have shown, that the diffraction efficiency (DE) of light-induced SRG recorded on NML structures strongly depends on polarization states of recording beams. Enhanced DE is obtained when the recording beams have orthogonal linear $\pm 45^\circ$ or circular LCP:RCP polarizations. The relationship between the depth of SRG and its period was studied in NML structures based on ChGs, where it was shown that grating period increasing led to the SRG depth increasing in linear way. In present studies we performed simulation of DE kinetics and we showed that calculated DE curves were in good agreement with the experimental results. Grating recording process in As_2S_3 -Se NML structure for different grating period and long recording time was performed. Such experiment turned out to be very interesting especially from the DE point of view and also from the efficiency of the surface relief grating formation. One cannot find in literature holographic grating experiments performed in ChGs for such set of grating periods and long recording time.

2 Materials and Methods

The experiments were performed on 1.7 μm thick As_2S_3 -Se NML structure deposited on rotated glass substrate by thermal evaporation from two isolated boats with bulk As_2S_3 and Se glasses. A thickness of each As_2S_3 nanolayer was 9

A. Meshalkin (✉) · E. Achimova · V. Abaskin · A. Prisacar · G. Triduh
Institute of Applied Physics, 5 Academiei str., Chisinau, Moldova
e-mail: alexei@asm.md

O. Paiuk · A. Stronski · A. Korchovyj · P. Oleksenko
V. Lashkaryov Institute of Semiconductor Physics, NAS
of Ukraine, 41 pr. Nauki, Kiev, Ukraine

and 6 nm of Se nanolayer correspondingly. More detailed description of deposition process can be found in paper [12]. The SRGs were formed using a holographic setup [11] with wave plates for obtaining the different states of polarizations. Edge of As_2S_3 -Se NML absorption light of DPSS laser operating at 532 nm was used. A beam splitter was used to obtain the two interfering beams and the angle between those beams was adjusted to provide the necessary spatial modulation periods. Series of holographic grating recording experiments were performed on studied NML structure. The experiments differed in period of the grating inscription: from 960 to 5000 nm (960, 1170, 1410, 1920, 3000 and 5000 nm), the rest of experimental conditions were unchanged. An optical intensity of 3.2 W/cm^2 was incident on the sample surface. Quarter wave retarders were used to obtain circular polarization configuration LCP:RCP. To monitor the dynamics of the formation of SRGs we used the evolution of diffraction efficiency (DE: the ratio of intensities of the transmitted first diffracted beam to the zero one before recording). A laser diode beam at wavelength 650 nm was used for DE monitoring. The surface relief structure of the gratings on As_2S_3 -Se NML structure was investigated by Nanoscope III atomic force microscope (AFM) after the holographic gratings were recorded.

3 Results and Discussion

Based on our previous studies we consider that the main process during polarization holographic recording in NML is surface relief formation. Surface relief gratings are interesting for large scale applications, since they can be reproduced relatively easy from a master. Gratings can be categorized as either thick or thin by comparing depth of surface modulation Δd and the wavelength λ with Δn and/or the average index of refraction n_{av} and the grating period Λ . While thick gratings show Bragg diffraction, thin gratings show Raman-Nath diffraction. In our experiments we consider surface relief gratings produced in chalcogenide glasses nanomultilayers ($n_{\text{eff}} = 2.50$) with a grating period compared to the incoming wavelength: $\Lambda = 960\text{--}5000 \text{ nm}$ and $\lambda = 650 \text{ nm}$, assuring that the gratings can be considered as thin. A sinusoidal profile leads to the well-known Raman-Nath expression and the diffraction efficiency of the m_{th} order η_m is given by: $\eta = J_m^2(\Delta\varphi/2)$, where J_m —is Bessel function of m order; $\Delta\varphi$ —is the maximum phase modulation of grating and it is equal to $\Delta\varphi = \frac{2\pi}{\lambda} \cdot (h \cdot (n - 1))$, where λ —wavelength, used for DE measurement; n —refractive index of grating material; h —SRG height.

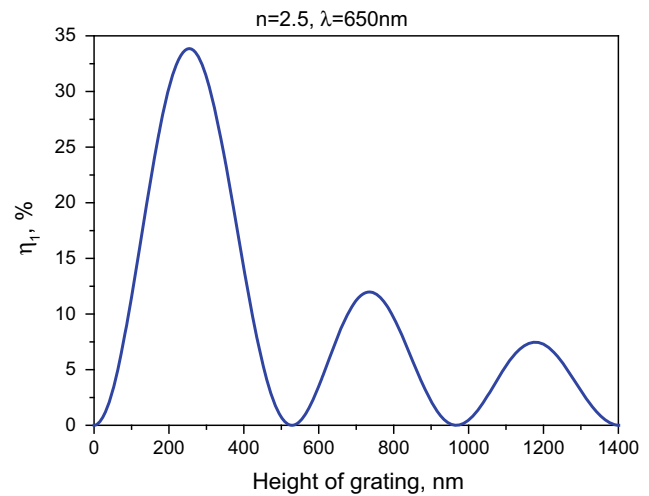


Fig. 1 The first order diffraction efficiency as a function of grating height

As the recording time increases during preparation of the gratings, the height of the corresponding grating also increases. This behavior corresponds to the dependence of the first order diffraction efficiency on the grating height, as shown in Fig. 1.

Here we assumed that the dynamics of surface relief grating formation in NML structure upon constant light illumination is linear. But in real recording the photoinduced surface relief formation can be described by the single-exponential functions of the form:

$$\Delta d = \Delta d_{\text{max}} [1 - \exp(-t/\tau)],$$

where τ is the characteristic grating formation time constant, and Δd_{max} is the maximum thickness modulation, for given experimental conditions.

This expression describes a natural tendency of reaching saturation of any material parameter for infinite exposure time.

In our experiment we have non-linear change of thickness modulation with saturation. In Fig. 2 non-linear thickness modulations with different time constant τ and corresponded first order diffraction efficiency kinetics are presented.

Having this in mind, by the analysis of diffraction efficiency kinetics the non-linear change of thickness modulation can be obtained.

In Fig. 3 the experimental first order diffraction efficiency of surface relief grating recorded in As_2S_3 -Se NML structure is shown.

AFM investigations showed high quality of the recorded surface relief's of gratings which had profiles close to the

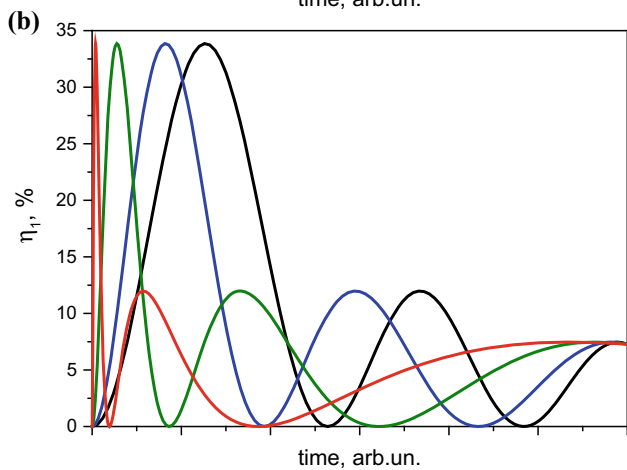
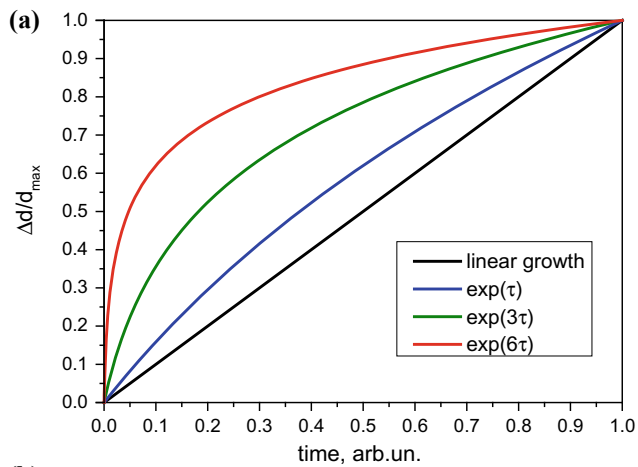


Fig. 2 Non-linear thickness modulations with different time constant τ (a) and corresponded first order diffraction efficiency kinetics (b)

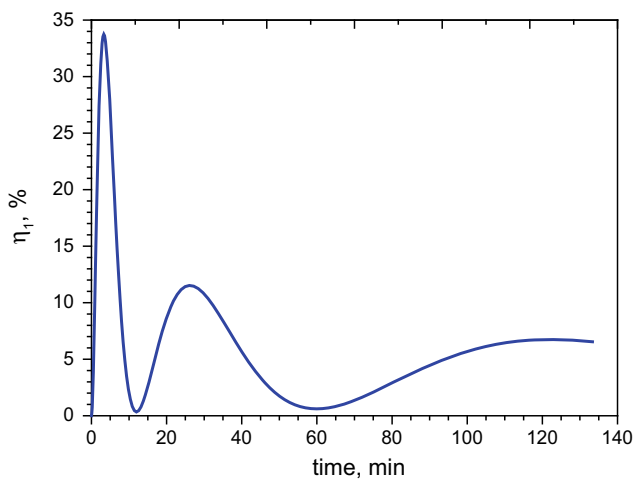


Fig. 3 Experimental first order diffraction efficiency of surface relief grating recorded in As_2S_3 -Se NML structure

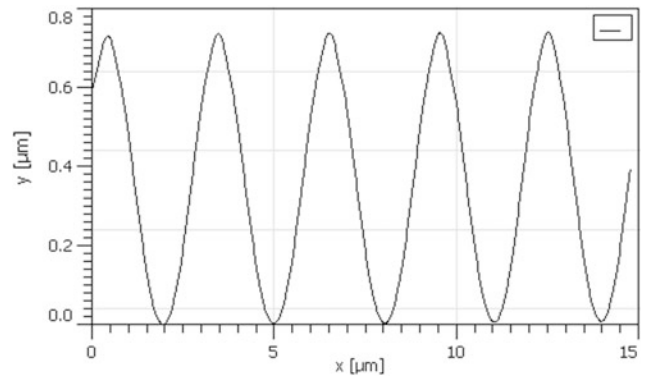


Fig. 4 Surface profile of recorded SRG with period 3000 nm

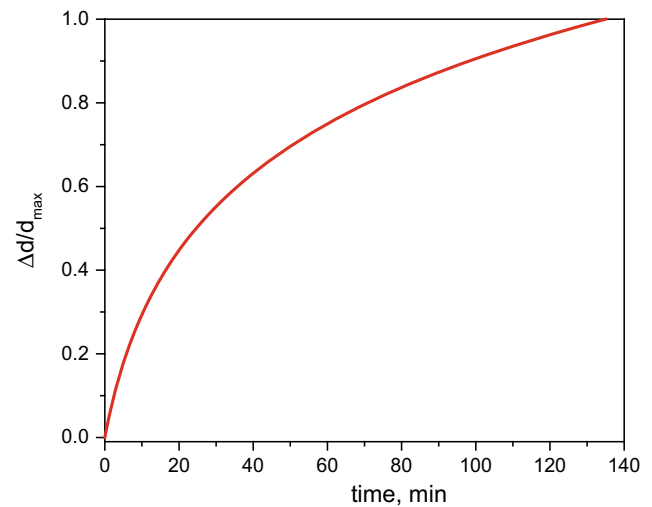


Fig. 5 The exponential change of thickness modulation

sinusoidal ones. Surface profile of recorded SRG with period 3000 nm is shown in Fig. 4.

This implies that the DE value depends on the SRG height and we can investigate the SRG formation by means of the changing of DE value during holographic recording.

The exponential change of thickness modulation was obtained by the analysis of diffraction efficiency kinetics shown in Fig. 5.

The result of the diffraction efficiency measurement for holographic recording of SRG in dependence of grating period is shown in Fig. 6.

The exposure time was chosen as time when saturation of DE was observed for grating with period 1170 nm. Saturation of DE reaches at saturation of the SRG height growth. For grating with 1170 nm period it was 34 min corresponded the exposure energy about 6.5 kJ/cm^2 . This exposure energy was used for all other periods of gratings. DE

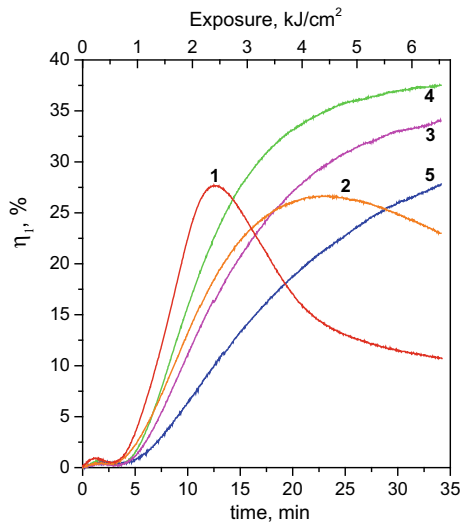


Fig. 6 The first order diffraction efficiency as a function of exposure time for gratings with period: 1—3000 nm; 2—1920 nm; 3—1410 nm; 4—1170 nm; 5—960 nm

kinetics of SRG recording using LCP:RCP polarization states of recording beams are shown in Fig. 2.

After grating recording experiments, performed for 960, 1170, 1410, 1920, and 3000 nm grating period, the surface profile and relief grating depth modulation Δd were directly measured by AFM. Surface profiles for each illumination time revealed the sinusoidal shape. These results and no observation of higher order harmonics in the diffraction signal confirm negligible role of the nonsinusoidal contribution in the proposed model. The AFM measurements enabled to calculate the modulation depth μ , determined as $\mu = h/\Lambda$, where h is SRG height and Λ is grating period (Fig. 7), in order to examine how it was changing with the grating period changing.

In assumption that SRG growth is linear in exposure time, recording rate is calculated as ratio (SRG height/recording time). The SRG height, modulation depth, recording rate and DE for different period of recorded gratings are presented in

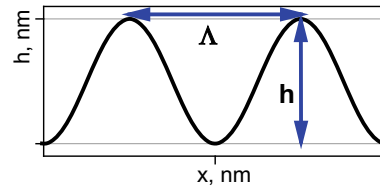


Fig. 7 Surface profile used to calculate the modulation depth μ , determined as $\mu = h/\Lambda$, where h is SRG height and Λ is grating period

Table 1. There is a good agreement between the amplitude of the SRG calculated from experimentally measured by AFM and the theoretical value obtained accordingly to the diffraction efficiency kinetics.

As it is seen from Table 1, increasing of period leads to SRG height increasing while exposure energy was equal. It means that SRG recording rate is much more for gratings with greater periods (from 6.1 nm/min for 960 nm period to 21.6 nm/min for 3000 nm period). Meanwhile the modulation depth was approximately the same for all gratings and averaged 0.22.

This theoretical estimation is in good agreement with the experimentally measured kinetics of DE.

4 Conclusions

Chalcogenide glasses nanomultilayer structures based on $\text{As}_2\text{S}_3\text{-Se}$ were used for direct surface relief grating formation by holographic recording. Grating recording process in $\text{As}_2\text{S}_3\text{-Se}$ nanomultilayer structure for different grating period and long recording time was performed. Simulated diffraction efficiency kinetics curves showed good agreement with the experimental results. Analyses of diffraction efficiency kinetics and AFM images of recorded SRG showed that grating period increasing led to the SRG depth increasing in linear way. It was revealed that SRG recording rate was characterized by non-linear behavior, while modulation depth remained approximately the same value for all gratings.

Table 1 SRG height, modulation depth, recording rate and DE of recorded gratings with different periods

Λ , nm	SRG height, nm	Modulation depth $\mu = h/\Lambda$	Recording rate, nm/min	η , %
3000	735	0.245	21.6	10.7
1920	450	0.234	13.2	23.0
1410	300	0.213	8.8	34.0
1170	250	0.214	7.3	37.5
960	207	0.216	6.1	27.8

Acknowledgements The research was supported by the bilateral Moldova-Ukraine project (17.80013.5007.03/Ua).

Conflict of Interest The authors declare that they have no conflict of interest.

References

1. Stronski, A., Revutska, L., Meshalkin, A., Paiuk, O., Achimova, E., et al.: Structural properties of Ag–As–S chalcogenide glasses in phase separation region and their application in holographic grating recording. *Opt. Mater.* **94**, 393–397 (2019)
2. Stronski, A.V., Vlček, M.: Photosensitive properties of chalcogenide vitreous semiconductors in diffractive and holographic technologies applications. *J. Optoelectron. Adv. Mater.* **4**, 699–704 (2002)
3. Achimova, E.: Direct surface relief formation in nanomultilayers based on chalcogenide glasses: A review. *Surf. Eng. Appl. Electrochem.* **52**, 456–468 (2016)
4. Trunov, M.L., Lytvyn, P.M., Yannopoulos, S.N., Szabo, I.A., et al.: Photoinduced mass-transport based holographic recording of surface relief gratings in amorphous selenium films. *Appl. Phys. Lett.* **99**, 051906 (2011)
5. Cazac, V., Meshalkin, A., Achimova, E., Abashkin, V., et al.: Surface relief and refractive index gratings patterned in chalcogenide glasses and studied by off-axis digital holography. *Appl. Opt.* **57**, 507–513 (2018)
6. Saliminia, A., Galstian, T.V., Villeneuve, A.: Optical field-induced mass transport in As_2S_3 chalcogenide glasses. *Phys. Rev. Lett.* **85**, 4112–4115 (2000)
7. Stronski, A., Achimova, E., Paiuk, O., Meshalkin, A., et al.: Optical and electron-beam recording of surface relief's using $Ge_5As_{37}S_{58}$ –Se nanomultilayers as registering media. *J. Nano Res.* **39**, 96–104 (2016)
8. Stronski, A., Achimova, E., Paiuk, O., Meshalkin, A., et al.: Direct magnetic relief recording using $As_{40}S_{60}$:Mn–Se nanocomposite multilayer structures. *Nanoscale Res. Lett.* **12**, 286 (2017)
9. Kokenyesi, S.: Amorphous chalcogenide nano-multilayers: research and development. *J. Optoelectron. Adv. Mater.* **8**, 2093–2096 (2006)
10. Meshalkin, A.: Reversible polarization recording in As_2S_3 –Se multilayer nanostructures. *Surf. Eng. Appl. Electrochem.* **54**, 407–414 (2018)
11. Achimova, E., Stronski, A., Abashkin, V., Meshalkin, A., Paiuk, O., Prisacar, A., Oleksenko, P., Triduh, G.: Direct surface relief formation on As_2S_3 –Se nanomultilayers in dependence on polarization states of recording beams. *Opt. Mater.* **47**, 566–572 (2015)
12. Stronski, A., Achimova, E., Paiuk, O., Abashkin, V., Meshalkin, A., Prisacar, A., Triduh, G., Lytvyn, O.: Surface relief formation in $Ge_5As_{37}S_{58}$ –Se nanomultilayers. *J. Non Cryst. Solids.* **409**, 43–48 (2015)
13. Achimova, E., Stronski, A., Abashkin, V., Meshalkin, A., Paiuk, O., Prisacar, A., Oleksenko, P., Triduh, G.: Direct surface relief formation on As_2S_3 –Se nanomultilayers in dependence on polarization states of recording beams. *Opt. Mater.* **47**, 566–572 (2015)

Near-Edge Optical Properties of Layered Tin Sulfide (Selenide) Crystals

V. V. Zalamai, A. V. Tiron, E. V. Rusu, E. V. Monaico, and N. N. Syrbu

Abstract

Absorption (K), reflection (R) and wavelength modulated transmission ($\Delta T/\Delta\lambda$) spectra in SnS, SnS₂ and SnSe crystals were investigated in temperature range from 300 to 10 K. Excitonic states were discovered in all investigated compounds. Parameters of observed excitons and character of electron transitions participating in absorption edge formation were determined. Optical anisotropy in interband gap minimum was investigated.

Keywords

Optical spectroscopy • Absorption spectra • Electron transitions • Direct transitions

1 Introduction

Layered crystals which including the tin sulfide and tin selenide compounds possess an attractive electronic and optical properties. The tin sulfide is A^{IV}B^{VI} compound and forms in several phases and has different stoichiometric composition from SnS to SnS₂ [1]. It has been established that tin sulfide (SnS) can crystallize in various phases: cubic phases of SnS (space groups *Fm-3 m* and *F-43 m*) [1], orthorhombic phases of α -SnS (space group *Pbnm*) and β -SnS (group *Cmcm*) [2], the hexagonal phases of SnS₂ (spatial groups *P3m1* and *P63/mmc*) and the orthorhombic phase Sn₂S₃ (space group *Pnma*) [1]. The low-temperature α -phase ($T < 870$ °C) and the high-temperature β -phase ($T > 870$ °C) are formed in orthorhombic crystal lattice. The available experimental data of tin sulfide parameters are

V. V. Zalamai (✉) · A. V. Tiron · E. V. Monaico · N. N. Syrbu
 Technical University of Moldova, 168 Stefan cel Mare Avenue,
 Chisinau, Republic of Moldova
 e-mail: victor.zalamai@cnstm.utm.md

E. V. Rusu
 Institute of Electronic Engineering and Nanotechnologies,
 Chisinau, Republic of Moldova

highly contradictory: the band gap ranges from 1.0 to 2.3 eV, and the absorption coefficient is of the order of 10^4 – 10^5 cm⁻¹ [3]. Information about the type and nature of electronic transitions responsible for the interband gap minimum are extremely contradictory and in fact unexplained [4].

Among the lead free tin chalcogenides the SnSe attract an attention due to thermoelectrical properties [5]. This layered semiconductor has orthorhombical lattice. Its band structure exhibits some “pudding mode” features. This leads to high electrical conductivity and Seebeck constant [5]. SnSe is suggested to use as solar energy convertor [6]. Despite this the optical properties of this material are studied insufficiently. It is well known that SnSe is anisotropic with respect to its optical, as well as thermoelectric, properties. The optical band gap is a different for single crystals and layers [7]. The recent experimental investigations on nanoparticles in colloidal solution shows that band gap of nanoparticles decreases with the grain size increasing and can be reaches to 1.2 eV [8]. And thus tin monoselenide can be used as solar cell [7].

The aim of this paper is to establish the nature of electronic transitions forming the interband gap minimum and the absorption coefficient in the band gap region.

2 Experimental Methods

The SnS and SnS₂ single crystals grown by gas transport method in ampoules were the ingots that were easily cleaved, which made it possible to obtain mirror surfaces of $\sim 5 \times 7$ mm and different thicknesses from 100 μ m to 3 mm. The surfaces of most plates were parallel to *b* axis.

The gas transport method was used for SnSe monocrystals growth. Received SnSe plates had a layered structure and sizes of $1.5 \times 0.8 \times 0.5$ cm. These plates were easily cleaved perpendicular to *a* axis for receiving of samples with thicknesses down to 100 μ m. These samples had a mirrored

face of 7×9 mm. The exfoliation by scotch type was used for thin layers receiving (3–20 μm).

Transmission, reflection and wavelength modulated transmission were studied by help of the MDR-2 spectrometer (luminosity 1:2 and linear dispersion $7 \text{ \AA}/\text{mm}$). The low temperature spectra of crystals deposited in closed helium LTS-22 C 330 optical cryogenic system were measured with resolution ~ 0.5 meV (entrance and exit slits of the spectrometer did not exceed 70μ). The morphology and chemical composition has been investigated by using Scanning Electron Microscopes (SEM) TESCAN Vega TS 5130 MM equipped with an Oxford Instruments INCA Energy EDX system operated at 20 kV.

3 Experimental Results and Discussions

A. SnS optical properties

The SnS crystals are convenient objects for measurements of optical transmission (absorption) spectra, since they are layered with a weak bond between the layers. A weak bond between the layers makes possible to obtain thin plates by the cleavage of different thicknesses.

Absorption spectra measured at temperature 10 K are shown in Fig. 1. The absorption coefficient of a_1 line (1.200 eV) in E||b polarization at 10 K exceeds 10^4 cm^{-1} . In the same polarization the maximum a_2 (1.52 eV) are observed and this maximum is weaker at similar energies in E⊥b polarization. Figure 1 shows reflection (R) spectra in both polarizations in region of a_1 maximum measured at temperature 300 K. One can see from figure that a_1 maximum presents only in E||b polarization.

We assume that transitions responsible for this feature are allowed in E||b polarization and are forbidden in E⊥b polarization. Weak features a_1^* and a_1^{**} at energies 1.300 eV

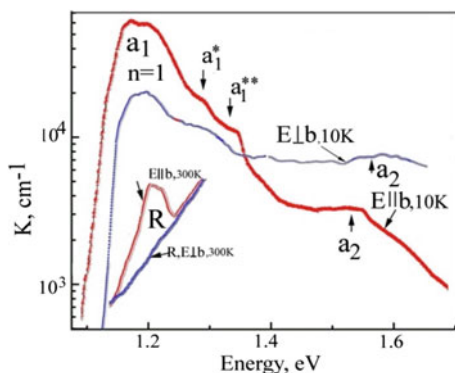


Fig. 1 Absorption (K) and reflection (R) spectra of SnS crystals

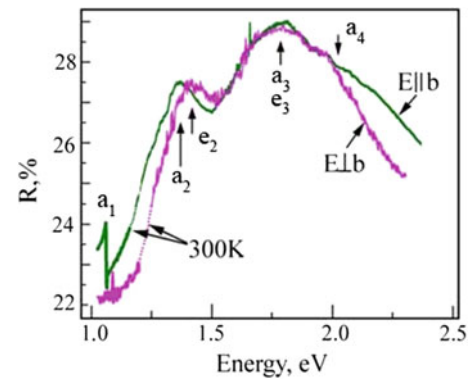


Fig. 2 Reflection spectra of SnS crystals measured in E||b and E⊥b polarizations at temperature of 300 K

and 1.321 eV are recognized in absorption spectra in E||b polarization measured at 10 K. Because these features are appeared both in reflection and absorption spectra we assume that these spectra are related to Frenkel excitonic states. Assuming that a_1 maximum is due to the ground state $n = 1$ of exciton and the weak features a_1^* and a_1^{**} are due to the excited states $n = 2$ and $n = 3$ of exciton. The Rydberg constant of exciton is estimated ($R = 150$ meV).

Maxima marked as a_1 (1.203 eV), a_2 (1.426 eV), a_3 (1.856 eV) and weak band a_4 (2.066 eV) are clearly recognized in reflection spectra measured in E||b polarization at temperature 300 K in energy interval 1–2.4 eV (see Fig. 2). At room temperature a_2 band has maxima at 1.364 eV in E||b polarization and band marked as e_2 is observed at higher energy (1.418 eV) in E⊥b polarization. Maxima a_3 and e_3 are discovered at the same energies (1.763 eV). At temperature decreasing all abovementioned maxima shifts toward higher energies a_1 (1.203 eV), a_2 (1.426 eV), e_2 (1.600 eV), a_3 , e_3 (1.856 eV) and a_4 (2.066 eV). The e_2 maximum has the most temperature shift coefficient, it observed in energies of 1.364 and 1.600 eV at 300 K and 10 K, respectively.

According to the theoretical calculations of the band structure [9], the observed exciton states are formed in Γ -Y direction of Brillouin zone, where the mass of holes is $m_{V1}^* = 2.6m_0$, and the effective mass of electrons in conduction band is $m_{C1}^* = 1.3m_0$. Excitonic states marked as a_2 are formed near point X in Γ -X direction and excitons marked as a_3 are in U point of Brillouin zone. These transitions (a_3 , e_3) are allowed in both polarizations and effective mass of holes in U point ($m_{V1}^* = 3.46m_0$) is higher than in Γ -Y point ($m_{V1}^* = 2.6m_0$).

B. SnS₂ optical properties

SnS₂ crystals cleaved along the plane of adhesion with mirror surfaces were used for optical transmission (absorption) spectra measurements.

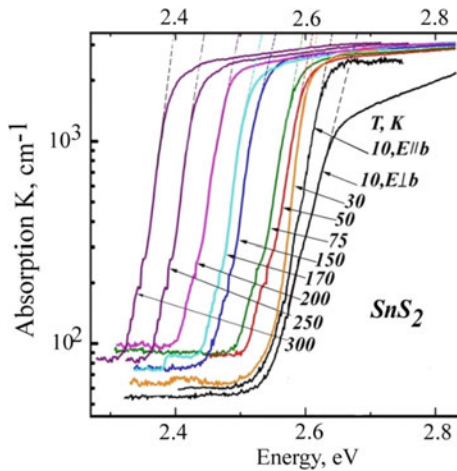


Fig. 3 Absorption spectra of SnS_2 crystals of measured at temperatures 300–10 K

Figure 3 illustrates absorption spectra for crystals with 0.5 mm thickness measured in unpolarized light at different temperatures as well as absorption spectra measured at 10 K in $E||b$ and $E\perp b$ polarizations. One can see from received data that absorption edge spectra are polarized at temperature 10 K. Edge absorption in $E||b$ polarization begins at lower energies than one in $E\perp b$ polarization. A difference of magnitudes of absorption coefficients for both polarizations in region of high absorption is observed, i.e. the absorption coefficient in $E\perp b$ polarization is less than in $E||b$ polarization. A temperature shift coefficient of edge absorption was estimated ($\beta = \Delta E/\Delta T = 8.275 \times 10^{-4}$ eV/K).

Absorption and wavelength modulated transmission spectra measured for the crystal of 830 μm in $E||b$ and $E\perp b$ polarizations are shown in Fig. 4. A feature marked as EI is observed clearly in absorption spectra of both polarizations. Minimal band gap determined from absorption and wavelength modulated transmission spectra is practically identical

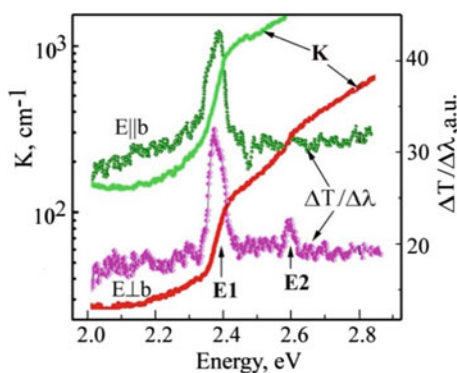


Fig. 4 Absorption (K) and wavelength modulated transmission ($\Delta T/\Delta\lambda$) spectra of SnS_2 crystals measured at temperature 10 K in $E||b$ and $E\perp b$ polarizations. Curves for $E\perp b$ polarization are shifted down on 200 cm^{-1} for clarity

and has magnitude of 2.403 eV in both polarizations. This value coincides with results of Ref. [10] (2.41 eV) and close to data from Ref. [11] (2.308 eV—indirect and 2.554 eV—direct). The character of electron transitions responsible for minimum band gap E_g is determined as indirect by all analyzed references, but magnitudes of band gaps are differ. This is due to the fact that thick crystals are required to determine the magnitude of indirect transitions, while most of the experimental measurements are performed on thin films. This indicates that the edge absorption and the EI feature are formed by indirect transitions. And $E2$ transitions in $E\perp b$ polarization are due to the direct forbidden transitions.

C. SnSe optical properties

Figure 5 shows edge absorption spectra of SnSe crystal of 467 μm thicknesses in unpolarized light (unp.) and $E||a$ and $E||c$ polarizations measured at temperature 300 K. One can see from the spectra that in $E||c$ polarization the transitions marked as A_I and in $E||a$ the transitions marked as B_I are observed. Such strong dependence of indirect transitions from light polarization and relatively high absorption coefficient ($\sim 6 \times 10^3 \text{ cm}^{-1}$) are unlikely. Believe that in $E||c$ polarization the edge absorption is formed by direct allowed transitions A_I and in $E||a$ polarization these transitions are forbidden.

According the data of Ref. [12] one can assume from the edge absorption that the absorption maximum A_I is due to indirect transitions and the minimal band gap at room temperature is equal to 1.091 eV. The B_I maximum is associated with direct transitions and the minimal direct interband gap at 300 K is amount of 1.360 eV. At the same time, a remarkable feature is that the absorption coefficient of the investigated crystals at indirect transitions is relatively high. This indicates that A_I feature is due to direct transitions allowed in $E||c$ and forbidden in $E||a$ polarization, respectively.

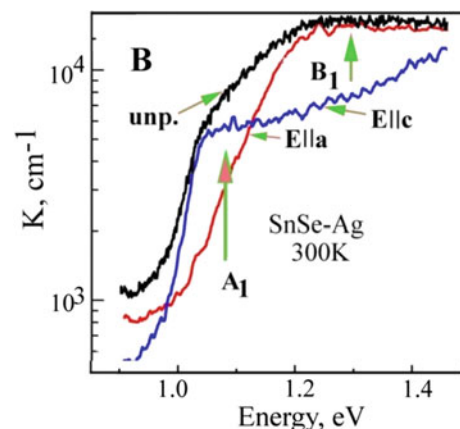


Fig. 5 Edge absorption of SnSe crystals in unpolarized light (unp.) and in polarization $E||a$ and $E||b$ measured at room temperature

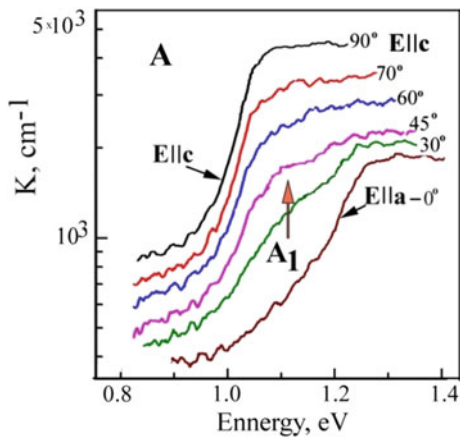


Fig. 6 Absorption spectra measured at room temperature in polarized light for SnSe crystal at sample rotation

In the absorption spectra in the region of A_1 transitions in the E||a polarization, the absorption band is practically not observed. The intensity of A_1 band changes at changing of angle between polarization direction of light waves and a axis of the crystal (see Fig. 6). The B_1 absorption band is not recognized in E||c polarization in this range. The B_1 absorption band is beginning observed when the polarization vector turning approximately on 30° from 90° (E||c) to 60° . The B_1 band has a maximum absorption ($\sim 10^4 \text{ cm}^{-1}$) at energy $\sim 1.3 \text{ eV}$ in the case of light wave orientation E||a.

4 Conclusions

Features of excitonic states (a_1 , $a_2(e_2)$ and $a_3(e_3)$) were discovered in absorption and reflection spectra at temperatures 10 K and 300 K in SnS crystals (phase with space group $Pnma$). Minimal energy interval due to excitonic states a_1 is formed in Γ -Y direction of Brillouin zone, where holes mass of top valence band ($m_{V1}^* = 2.6m_0$) and electron effective mass of bottom conduction band ($m_{C1}^* = 1.3m_0$) have been determined. The excitonic states $a_2(e_2)$ are formed near X point in Γ -X direction and excitons $a_3(e_3)$ are in U point of Brillouin zone. These transitions (a_3 , e_3) are allowed in both polarizations and effective mass of holes in U point ($m_{V1}^* = 2.46m_0$) is higher than in Γ -Y point ($m_{V1}^* = 2.6m_0$).

It was established by the investigation of absorption, reflection and wavelength modulated transmission spectra of hexagonal phase SnS₂ crystals (space group $P6_3/mmc$) in temperature interval 10–300 K that the minimal band gap is due to indirect transitions between points Γ and M ($E_g^{ind} = 2.403 \text{ eV}$). In E||b polarization the minimal direct energy interval ($E_g^{dir.allow.} = 2.623 \text{ eV}$) is formed by direct allowed transitions and in E||b polarization it is formed by

direct forbidden transitions ($E_g^{dir.forb.} = 2.698 \text{ eV}$) in Γ point of Brillouin zone.

By investigation of absorption spectra in temperature range 300–10 K it was established that the first minimal band gap A_1 (1.091 eV at 300 K) formed by direct allowed in E||c and forbidden in E||a polarization transitions. The next energy gap B_1 (1.316 eV) is formed by direct allowed in E||a and forbidden in E||c polarization transitions. The direct electron transitions occur in the excitonic bands. With decreasing of the temperature, the edge absorption is shifts toward higher energies. The temperature coefficient of edge absorption shift is $3.4 \times 10^{-3} \text{ eV/K}$.

Acknowledgements The authors acknowledge the support from the National Agency for Research and Development under the Grant #15.817.02.32A, #15.817.02.08A and #15.817.02.29A. E. Monaico acknowledges support from the Alexander von Humboldt Foundation. **Conflict of Interest** The authors declare that they have no conflict of interest.

References

1. Madelung, O.: Semiconductors: Data Handbook, p. 485. Springer, Berlin (2004)
2. Gao, Ch., Shen, H., Sun, L.: Preparation and properties of zinc blende and orthorhombic SnS films by chemical bath deposition. Appl. Surf. Sci. **257**, 6750–6755 (2011)
3. Shaposhnikov, V.L., Krivosheevq, A.V., Borisenko, V.E.: Electronic structure and optical properties of bi-dimensional SnS crystals. Dokl. Nats. Akad. Nauk Belarusi **60**(4), 50–55 (2016)
4. Ortiz, A., Alonso, J.C., Garcia, M., et al.: Tin sulphide films deposited by plasma-enhanced chemical vapour deposition. Semicond. Sci. Technol. **11**, 243–254 (1996)
5. Mathews, N.R.: Electrodeposited tin selenide thin films for photovoltaic applications. Sol. Energy **86**(4), 1010–1016 (2012)
6. Chung, K.M., Wamwangi, D., Woda, M., et al.: Investigation of SnSe, SnSe₂, and Sn₂Se₃ alloys for phase change memory applications. J. Appl. Phys. **103**, 083523–083529 (2008)
7. Boscher, N.D., Carmalt, C.J., Palgrave, R.G., et al.: Atmospheric pressure chemical vapour deposition of SnSe and SnSe₂ thin films on glass. Thin Solid Films **516**, 4750–4757 (2008)
8. Parvathi, M.M., Mohan A., Arivazhagan, V., Rajesh, S.: Preparation and characterization of vacuum evaporated SnSe and SnSe₂ multilayer thin films. In: AIP Conference Proceedings, vol. 1451, pp. 206–208 (2012)
9. Vidal, J., Lany, S., d’Avezac, M., et al.: Band-structure, optical properties, and defect physics of the photovoltaic semiconductor SnS. Appl. Phys. Lett. **100**, 032104 (2012)
10. Shi, C., Chen, Z., Shi, G., et al.: Influence of annealing on characteristics of tin disulfide thin films by vacuum thermal evaporation. Thin Solid Films **520**, 4898–4901 (2012)
11. Eads, C.N., Bandak, D., Neupane, M.R., et al.: Anisotropic attosecond charge carrier dynamics and layer decoupling in quasi-2D layered SnS₂. Nat. Commun. **8**, 1369 (2017)
12. Ivanova, A.G., Troyan, I.A., Chareev, D.A., et al.: Structural phase transitions and the equation of state in SnSe at high pressures up to 2 Mbar. J. Exp. Theor. Phys. **108**, 414–418 (2018)

Nanostructured Organic Crystals as Prospective Thermoelectric Materials for Infrared Sensors

I. I. Sanduleac, S. C. Andronic, and A. I. Casian

Abstract

In this paper we investigate the prospective of use of some nanostructured organic crystals as efficient thermoelectric material for infrared biosensors. Nowadays, the infrared sensors are widely implemented in thermal imaging system, night vision systems and different personal or clinical devices for health monitoring. A thermoelectric sensor consists of thermocouples of *n*-type and *p*-type materials with high electrical conductivity. The sensitivity of the sensor is determined mainly by the thermoelectric power factor of the material. Quasi-one dimensional organic crystals of tetrathiotetracene-iodide, TTT_2I_3 of *p*-type and tetrathiotetracene—tetracyanoquinodimethane, $\text{TTT}(\text{TCNQ})_2$ of *n*-type were proposed earlier as prospective materials with high thermoelectric power factor. In the following, the electrical conductivity, the Seebeck coefficient and the thermoelectric power factor of TTT_2I_3 crystals are calculated numerically as a function of temperature. The optimal values of charge carrier concentration in order to achieve a high thermoelectric power factor are determined.

Keywords

Thermal imaging • Thermoelectric sensor • Infrared radiation • Organic crystal • Thermoelectric power factor

1 Introduction

Every heated object, with a temperature above absolute zero, generates infrared radiation (IR), with a wavelength of 0.75–1000 μm . The intensity of radiation is a function of the

absolute temperature of the body. An infrared sensor is a light sensor that converts the incident IR radiation into electric signal. Depending on the detection mechanism, there are thermal and photon IR sensors. The last ones exhibit a good performance and a short response time. But with the increase of the ambient temperature, the noise in these sensors increases exponentially, and additional cooling systems are needed. Thermal sensors, in particular thermoelectric ones, have the advantage of a good response in a wide interval of wavelength, they can operate at room temperature without cooling, and the production technology is simple and inexpensive [1]. A thermoelectric IR sensor consists from several *p*–*n* pairs of different materials. The magnitude of the generated electric current is a function of the temperature difference and depends also on the material properties. The thermoelectric biosensors can be implemented in medicine [2], in particular as detectors of radiation in contactless thermometers for measurement of the human body temperature. A wide implementation of thermal imaging systems could ensure an efficient real-time monitoring of the health of passengers in airports, train stations and other agglomerated places to ensure security, as well as for everyday personal usage.

A thermoelectric sensor reliability is determined mainly by the thermoelectric power factor, $P = \sigma S^2$, where σ is the electrical conductivity of the material, and S is the Seebeck coefficient. For IR sensors, high values of P are needed. In ordinary thermoelectric materials, simultaneously increase of the electrical conductivity and Seebeck coefficient is contradictory. Quasi-one dimensional organic crystals have the advantage of a nanostructured compound, with more complicated internal structure and increased density of electronic states. It was shown that for such materials, σ and S are less interdependent and it is possible to enhance the TE properties by simple chemical techniques [3].

In the last years, very promising results were reported in inorganic thermoelectric materials: $P \sim 10.6 \text{ mW m}^{-1} \text{ K}^{-2}$ in $\text{Nb}_{1-x}\text{Ti}_x\text{FeSb}$ half-Heusler, $P \sim 4 \text{ mW m}^{-1} \text{ K}^{-2}$ in SnSe and $\text{Bi}_{0.5}\text{Sb}_{1.5}\text{Te}_3$ and $P \sim 3.6 \text{ mW m}^{-1} \text{ K}^{-2}$ in

I. I. Sanduleac (✉) · S. C. Andronic · A. I. Casian
 Department Electronics and Telecommunications, Technical
 University of Moldova, Av. Stefan cel Mare 168, 2004 Chisinau,
 Republic of Moldova
 e-mail: ionel.sanduleac@mt.utm.md

$\text{AgPb}_m\text{SbTe}_{2+m}$ have been reported [4]. In rough Si nano-wires $P \approx 3 \text{ mW m}^{-1} \text{ K}^{-2}$ were measured [5]. Recently, the compounds of $(\text{Bi}_2\text{Te}_3)_{0.15} + (\text{Sb}_2\text{Te}_3)_{0.85}$ and n -type full-Heusler Ba_2BiAu have been reported as a promising thermoelectric materials [6, 7]. In n -type and p -type PbTe/PbEuTE quantum wells, values of $P \approx 6 \text{ mW m}^{-1} \text{ K}^{-2}$ and $16 \text{ mW m}^{-1} \text{ K}^{-2}$, respectively, have been reported at room temperature [8].

An increased attention is paid in recent years for organic thermoelectric materials. Very good results have been reported in Hydrogel Polymer fibers [9]. High output power has been obtained with a polymeric device realized on the base of PS-PEDOT:PSS [10]. In blended polymers, a simultaneous enhancement of σ and S has been observed [11].

The p -type and n -type organic crystals of TTT_2I_3 and $\text{TTT}(\text{TCNQ})_2$ are proposed as efficient thermoelectric materials for IR sensor. Earlier, the thermoelectric properties of TTT_2I_3 crystals were calculated and modeled numerically as a function of the Fermi energy for different crystal parameters in order to obtain high power factor at room temperature. It was obtained that thermoelectric properties of the crystals can be significantly improved by accurate tuning of charge carrier concentration and further purification. The aim of this paper is to investigate the temperature dependences of the electrical conductivity, Seebeck coefficient and the thermoelectric power factor of TTT_2I_3 crystals.

2 The Physical Model of TTT_2I_3

The crystals of TTT_2I_3 are needle-shaped with a length of 3–6 mm. The internal structure consists of segregated planar stacks of TTT molecules and iodine ions (further defining the xy plane of a Cartesian coordinate system). Along the z direction, the molecules arrange in chains with an intermolecular distance of approx. 9 Å. The lattice constants are $b = 4.96 \text{ Å}$, $a = 18.35 \text{ Å}$ and $c = 18.46 \text{ Å}$ for x , y and z directions. Along the TTT chain, a narrow conduction band of $\sim 0.64 \text{ eV}$ is opening. Thus, the electrical conductivity of the whole crystal is of p -type, provided by holes. It has been calculated [12] that the electrical conductivity and the thermopower (Seebeck coefficient) depend strongly on the crystal purity and can be significantly enhanced by using more advanced synthesis methods.

In order to describe the charge transport along the TTT chains, a two-dimensional (2D) physical model was applied. Along the molecular chains, the band description to describe the charge transport is used. The small corrections due to the weak interchain interactions in the y direction and the scattering on point-like impurities and thermally activated defects are considered.

The Hamiltonian of the crystal has the form:

$$H = \sum_k E(k) a_k^+ a_k + \sum_q \hbar\omega_q b_q^+ b_q + \sum_{k,q} A(k, q) a_k^+ a_{k+q} (b_q + b_{-q}^+) + \left(I_i V_{0i} \sum_{l=1}^{N_i} e^{-iqr_l} + I_d V_{0d} e^{-E_0/k_B T} \sum_{j=1}^{N_d} e^{-iqr_j} \right) V^{-1} \sum_{k,q} a_k^+ a_{k+q}, \quad (1)$$

where the term

$$E(k) = -2w_1 [1 - \cos(k_x b)] - 2w_2 [1 - \cos(k_y a)] \quad (2)$$

describes the energy of carriers, in the nearest-neighbor and tight-binding electrons approximations. Here w_1 and w_2 are the transfer energies of a hole from the given molecule to the nearest one (the indices 1 and 2 indicate the x and y directions). Corresponding lattice constants are b and a , respectively). k_x and k_y are the projections of the quasi-wave vector \mathbf{k} . Due to the pronounced quasi-one dimensionality of the crystal, $w_2 \sim 0.01 w_1$. The energy is measured from the top of the conduction band.

At relatively low temperatures ($< 400 \text{ K}$), the conduction electron energy is relatively low and the scattering on optical phonons can be neglected. The acoustic phonons are considered:

$$\omega_q^2 = \omega_1^2 \sin^2(q_x b/2) + \omega_2^2 \sin^2(q_y a/2), \quad (3)$$

where ω_1 and ω_2 are limit frequencies, and q_x , q_y are the projections of the quasi-wave vector \mathbf{q} . From the condition of quasi one-dimensionality it results that $\omega_2 \ll \omega_1$.

The third term in the Hamiltonian (1) takes into account two main electron-phonon interactions: of the deformation potential type (with coupling constants—the derivatives of transfer energies with respect to the intermolecular distance w'_1 and w'_2) and of polaron type (the coupling constant is proportional to the mean polarizability of TTT molecules).

The last term in (1) describes the impurity and defect scattering processes. It takes into account the point-like, electrically neutral and randomly distributed impurities and thermally activated lattice defects (with the activation energy E_0). I_i and I_d are the energy of interaction of the electron with an impurity and with a defect within regions of volume V_{0i} and V_{0d} , respectively.

3 Transport Properties

The electric field and temperature gradient in an IR sensor are weak. The scattering of electrons on acoustic phonons can be considered as elastic. The kinetic equation is deduced by the method of two-particle temperature dependent retarded Green functions. It can be solved analytically and the electrical conductivity σ_{xx} , thermopower S_{xx} and the power

factor P_{xx} along the x direction of the conductive TTT wires can be obtained in the form:

$$\begin{aligned} \sigma_{xx} &= \sigma_0 R_0; S_{xx} = (k_0/e)(2w_1/k_0T)R_1/R_0; P_{xx} = \sigma_{xx} S_{xx}^2 \\ \sigma_0 &= 2e^2 M v_{s1}^2 w_1^3 r / \pi^2 \hbar a b (k_0 T)^2 w_1'^2 (T_0/T), \end{aligned} \quad (4)$$

where k_0 is the Boltzmann constant, e —elementary charge, M is the mass of TTT molecule, v_{s1} is the sound velocity along the TTT chains, r is the number of molecular chains per elementary cell. R_0 and R_1 are the transport integrals:

$$\begin{aligned} R_n &= \int_0^2 d\varepsilon \int_0^\pi d\eta [\varepsilon + d(1 - \cos \eta) - (1 + d)\varepsilon_F]^n \varepsilon(2 - \varepsilon) \\ &\times n_{e,\eta}(1 - n_{e,\eta}) [s_0 \sqrt{\varepsilon(2 - \varepsilon)} \text{cth}(s_0 T_0 \sqrt{\varepsilon(2 - \varepsilon)}/T) \\ &\times \gamma_1^2 (\varepsilon - \varepsilon_0)^2 + \frac{d^2}{8\varepsilon(2 - \varepsilon)} (1 + \gamma_2^2 + 2 \sin^2 \eta - 2\gamma_2 \cos \eta) \\ &+ D_0 + D_1 \exp(-E_a/k_0 T)]^{-1}, \text{ where } s_0 = \hbar v_{s1}/(a k_0 T_0). \end{aligned} \quad (5)$$

here γ_1 and γ_2 describe the ratio of amplitudes of the polaron-type interaction mechanism to the deformation potential one in the x and y directions:

$$\gamma_1 = 2e^2 \alpha_0 / (b^5 w_1'), \gamma_2 = 2e^2 \alpha_0 / (a^5 w_2') \quad (6)$$

$\varepsilon = E(\mathbf{k})/2w_1$ and ε_F are the dimensionless kinetic energy of a hole along chains and Fermi energy in units of $2w_1$, respectively. $n_{e,\eta}$ is the Fermi distribution function and $\eta = k_y a$ is the dimensionless quasi momentum. $\varepsilon_0 = (\gamma_1 - 1)/\gamma_1$ is the dimensionless resonance energy. The parameter $d = 0.015$ is the ratio of transfer energies $w_2 = d \cdot w_1$, D_0 describes the scattering on point-like impurities, D_1 —thermally activated lattice defects. In earlier investigations, the scattering parameter at room temperature was defined by one parameter D . By comparison of numerical calculation results with the experimentally reported ones, it was obtained that $D \sim 0.6$ for crystals grown from solution, and $D \sim 0.1$ for more pure crystals grown from gaseous phase. The integral from (5) takes into account also the influence of the thermal expansion on the parameter γ_1 .

4 Numerical Results

The electrical conductivity σ_{xx} , the Seebeck coefficient S_{xx} and the thermoelectric power factor P_{xx} have been calculated numerically after (4). The following parameters of the crystal were considered: $M = 6.5 \times 10^5 m_e$ (m_e is the mass of the free electron), $w_1 = 0.16$ eV, $w_1' = 0.26$ eVÅ⁻¹, $v_{s1} = 1.08 \times 10^3$ m/s, $\gamma_1 = 1.5$. The stoichiometric concentration of conducting holes in TTT₂I₃ crystals was estimated

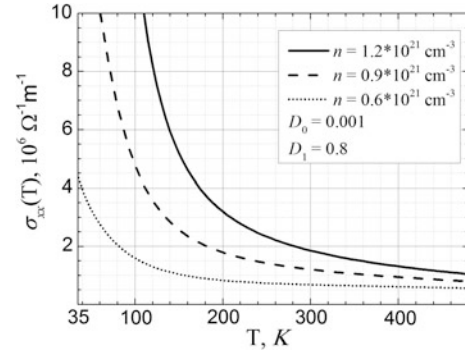


Fig. 1 Electrical conductivity in the direction of TTT chains as a function of temperature

to $n_h = 1.2 \times 10^{21} \text{ cm}^{-3}$. Three different values of holes concentration were considered: the stoichiometric one, $0.9 \times 10^{21} \text{ cm}^{-3}$ and $0.6 \times 10^{21} \text{ cm}^{-3}$, to which the dimensionless Fermi energies $\varepsilon_F = 0.35$, 0.2 and 0.1 correspond.

In Fig. 1 the electrical conductivity of the crystal as a function of absolute temperature is presented.

In stoichiometric crystals, grown from gaseous phase with $D \sim 0.1$, an electrical conductivity of $\sigma_{xx} \sim 10^6 \Omega^{-1} \text{ m}^{-1}$ was reported at room temperature [13]. From Fig. 1 it is observed that σ_{xx} increases rapidly with the decrease of the temperature. For temperatures below ~ 100 K, the fluctuations of lattice constants increase, leading to a smooth metal-dielectric transition of the Peierls type. This should lead to a rapid diminution of the electrical conductivity, which is not considered in the presented physical model. Therefore, the temperatures higher than 35 K are considered. However, the theory describes very well the experimentally reported behavior of the electrical conductivity for a temperature interval from 180 K up to ~ 400 K.

From Fig. 1 one observes that σ_{xx} decreases considerably with the decrease of n_h , especially at low temperatures.

In Fig. 2 the thermopower (Seebeck coefficient) as a function of the temperature is presented.

It is observed that S_{xx} grows when the temperature increases, achieving a maximum for smaller n . In the case of stoichiometric crystals, the physical model describes very well the behavior of the Seebeck coefficient for an interval of temperature $50 \text{ K} < T < 300 \text{ K}$, according with the experimentally reported data [14]. Experimentally it was reported $S_{xx} = 36 \mu\text{V/K}$ at room temperature for such crystals with $\sigma_{xx} = 10^5 \Omega^{-1} \text{ m}^{-1}$. Unfortunately, measurements for $T > 300 \text{ K}$ were not realized. From numerical calculations it is predicted that values of S_{xx} up to $\sim 140 \mu\text{V/K}$ could be obtained for a wide interval of T , if the concentration of holes is diminished by two times.

In Fig. 3 the thermoelectric power factor as a function of the temperature is presented.

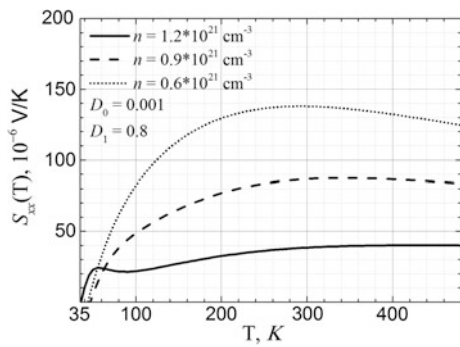


Fig. 2 Thermopower in the direction of TTT chains as a function of temperature

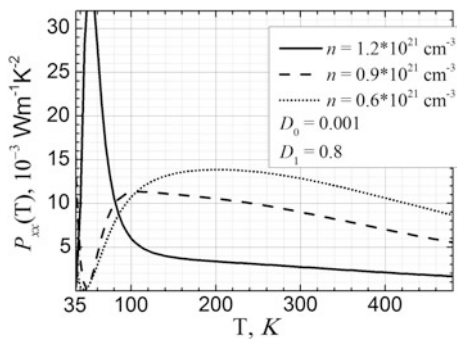


Fig. 3 Thermoelectric power factor along TTT chains as a function of temperature

From experimental data at room temperature, the crystal of TTT_2I_3 should exhibit a power factor $P_{xx} = \sigma_{xx} S_{xx}^2 = 0.13 \times 10^{-3} \text{ Wm}^{-1} \text{ K}^{-2}$. It was reported experimentally, that the electrical conductivity of crystals growth from gaseous phase could increase up to $10^6 \Omega^{-1} \text{ m}^{-1}$. In this case, the power factor is $\sim 10^{-3} \text{ Wm}^{-1} \text{ K}^{-2}$, a very prospective value. Such results are achievable, since the crystal admits non-stoichiometric compounds. Moreover, it was demonstrated that the thermoelectric properties can be significantly enhanced by accurate tuning of holes concentration and further purification of the crystal.

From Fig. 3 it is observed that with the increase of temperature, P_{xx} firstly increases, achieves a maximum, after that decreases. The position of this maximum depends on the charge carrier concentration and is displaced toward higher temperatures as the concentration is diminished. This is favorable for the enhancement of P_{xx} at room temperatures, since the maximum can be displaced by tuning the concentration of holes. For temperatures lower than $\sim 100 \text{ K}$, the numerical results have only qualitative meaning, since the physical model does not consider the metal-dielectric transition.

The numerical calculations are performed for crystals with a medium purity level, when the dimensionless scattering parameter is $D = 0.3$. In this case, values of $P_{xx} \sim 3$,

9 and $13 \times 10^{-3} \text{ Wm}^{-1} \text{ K}^{-2}$ are predicted for three different concentrations of holes, $n = 1.2, 0.9$ and $0.6 \times 10^{21} \text{ cm}^{-3}$ at room temperature. For higher temperatures, the power factor decreases because of the rapid diminution of the electrical conductivity (see Fig. 1). The decrease of charge carrier mobility is caused by the increasing intensity of scattering processes on thermally activated lattice defects. For instance, at $T = 400 \text{ K}$, $P_{xx} \sim 2, 7$ and $10 \times 10^{-3} \text{ Wm}^{-1} \text{ K}^{-2}$. It is observed (Fig. 3) that P_{xx} decreases more rapidly with the temperature increase for lower concentration of holes, because of the rapid decrement of the Seebeck coefficient (see Fig. 2). For comparison, in Bi_2Te_3 , $P \sim 4 \times 10^{-3} \text{ Wm}^{-1} \text{ K}^{-2}$.

5 Conclusions

The electrical conductivity, the thermopower and the thermoelectric power factor are modeled for nanostructured organic crystals of TTT_2I_3 as a function of temperature for different values of charge carrier concentrations. It is found that the crystal has prospective thermoelectric properties for a wide interval of temperatures, from $\sim 180 \text{ K}$ up to 450 K . In order to increase the power factor, some enhancement techniques are proposed, such as the carrier concentration tuning and the purification of the crystal. It was obtained the thermoelectric power factor could be enhanced for high temperatures if the hole concentration is diminished. Values of P_{xx} up to $13 \times 10^{-3} \text{ Wm}^{-1} \text{ K}^{-2}$ are predicted for crystals with holes concentration by two times lower than the stoichiometric one. In this case one could obtain a thermoelectric power factor of about 3 times higher than in Bi_2Te_3 .

Acknowledgement The authors acknowledge the support of the national projects 13/29.10.18F TC and 14.02.116F.

Conflict of Interest The authors declare that they have no conflict of interest.

References

1. Xu, D., Wang, Y., Xiong, B., et al.: MEMS-based thermoelectric infrared sensors: a review. *Front. Mech. Eng.* **12**, 557–566 (2017)
2. Ring, E., Ammer, K.: Infrared thermal imaging in medicine. *Physiol. Meas.* **33**, R33–R46 (2012). <https://doi.org/10.1088/0967-3334/33/3/R33>
3. Casian, A.: Violation of the Wiedemann-Franz law in quasi-one-dimensional organic crystals. *Phys. Rev. B* **81**, 155415–155420 (2000)
4. Ohta, H., Kim, S.W., Kaneki, et al.: High thermoelectric power factor of high-mobility 2D electron gas. *Adv. Sci.* **5**, 1700696 (2018). <https://doi.org/10.1002/advs.484>
5. Hochbaum, A.I., Chen, R.K., et al.: Enhanced thermoelectric performance of rough silicon nanowires. *Nature* **451**(7175), 163–167 (2008)

- Madavali, B., Kim, H., et al.: High thermoelectric figure of merit in *p*-type $(\text{Bi}_2\text{Te}_3)_x-(\text{Sb}_2\text{Te}_3)_{1-x}$ Alloys. *J. Electr. Mater.* **48**(1), 416–424 (2019). <https://doi.org/10.1007/s11664-018-6706-7>
- Park, J., Xia, Y., et al.: High *n*-type thermoelectric power factor and efficiency in Ba_2BiAu (2019). [arXiv:1804.09392v1](https://arxiv.org/abs/1804.09392v1) [cond-mat.mtrl-sci]
- Harman, T.C., Taylor, P.J., et al.: Quantum dot superlattice thermoelectric materials and devices. *Science* **297**, 2229–2232 (2002)
- Liu, J., Jia, Y., et al.: Highly conductive hydrogel polymer fibers toward promising wearable thermoelectric energy harvesting. *ACS Appl. Mater. Interfaces.* **10**(50), 44033–44040 (2018)
- Li, Z., Sun, H., et al.: A free-standing high-output power density thermoelectric device based on structure-ordered PEDOT:PSS. *Adv. Electron. Mater.* 1700496–1700450 (2018)
- Li, H., Plunkett, E., et al.: Dopant-dependent increase in seebeck coefficient and electrical conductivity in blended polymers with offset carrier energies. *Adv. Electron. Mater.* 1800618 (2019). <https://doi.org/10.1002/aelm.201800618>
- Sanduleac, I., Casian, A.: State of the art and new possibilities to increase the thermoelectric figure of merit of organic materials. *J. Thermoelectr.* **6**, 29–39 (2016)
- Hilti, B., Mayer, C.: Electrical properties of the organic metallic compound bis (Tetrathiotetracene)-Triiodide, $(\text{TTT})_2\text{I}_3$. *Helv. Chim. Acta* **61**(40), 501 (1978)
- Kaminskii, V.F., Khidekel, M.L., Lyubovskii, R.B., et al.: Metal-insulator phase transition in TTT_2I_3 affected by iodine concentration. *Phys. Stat. Sol. (a)* **44**, 77–82 (1977)

Effects of Green Silver Nanoparticles on CCl₄ Injured Albino Rats' Liver

Sh. Kazaryan, M. Petrosyan, L. Rshtuni, V. Dabaghyan,
and A. Hovhannisyanyan

Abstract

Nanoparticles green synthesis by plants and extracts is very cost-effective and can be used as an economic and environment friendly alternative in large-scale production. But the effect of these structures on the liver isn't fully investigated. In this study green silver nanoparticles (AgNPs) were synthesized by *O. araratum* 50% ethanol extract that has the highest antiradical activity. It was found that treatment by *O. araratum* extract leads to rats' liver structure normalization and normalization of liver injury markers' activity. Meanwhile, AgNPs at 20 mg/kg body weight dose leads to fibroblasts activation and fibrosis.

Keywords

Green silver nanoparticles • Extract • *Ocimum araratum* • Hepatotoxicity • Fatty liver

1 Introduction

According to 2016 WHO report liver diseases are among the ten most common causes of death [1]. Although the causes of liver pathologies are multifactorial, permanent sources of cellular stress (oxidative stress, apoptosis, LPS) play a crucial role in disease progression [2]. The danger of liver diseases consists in clinical manifestations at the late stages, when drug treatment is impossible.

In addition to NPs' potential use in medicine, they have been actively used in the production of various cosmetic means, packaging materials, textile, electrical devices, etc. Due to the increasing pace of nanotechnology development

and use of nanoparticles (NPs) in various fields, people contact with this type of materials becomes inescapable [3]. With such diverse and increasingly extensive use of NPs, the question of their safety for health is still relevant.

The aim of this work was to obtain green silver NP (AgNPs) and investigate their effects on albino Wistar rats' injured liver biochemical markers' activity.

2 Materials and Methods

2.1 Extracts Preparation and Detection of Antiradical Activity

O. araratum dry leaves after mechanical homogenization were exposed to ultrasound (Ultrasonic Homogenizer, Sonic-150W, MRC, Israel). 96, 70, 50, 25% ethanol and distilled water were used for extraction. After 24 h incubation extracts were centrifuged at 3000 rpm for 15 min (Jouan GR412, UK). Antiradical activity (ARA) was determined by free radical 2,2-diphenyl-1-picrylhydrazyl (DPPH) extinguishing detection at 517 nm using a UV/Vis spectrophotometer (JENWAY 6405 UK) [4].

2.2 Green Silver Nanoparticles Synthesis

Green silver nanoparticles (AgNPs) were obtained by adding an Ag⁺ salt solution to an *O. araratum* extract in volume ratio of 1:6. The size and shape of the NPs were investigated by SEM (SEMLEO-1430 VP, Carl Zeiss, Germany) [5].

2.3 Experimental Procedure

The study of toxic effects was leading on adult males of white outbred Wistar rats (200 ± 10 g). All manipulations with animals were carried out in accordance with Yerevan State Medical University's Ethical Committee Principles of

Sh. Kazaryan (✉) · M. Petrosyan · L. Rshtuni · A. Hovhannisyanyan
Russian-Armenian (Slavonic) University, 123 Hovsep Emin str.,
Yerevan, Armenia
e-mail: shushanik.kazaryan@rau.am

V. Dabaghyan
Yerevan State Medical University, Yerevan, Armenia

Laboratory Animal Care (Armenia) and Council of European Communities decision (2010/63/EU). Animals were divided into 4 experimental groups of 3 rats each, with intraperitoneal injection: group 1—control; group 2— CCl_4 (0.5 ml/kg); group 3—*O. araratum* 50% ethanol extract (0.017 mg/ml); group 4—AgNPs in *O. araratum* extract (20 mg/kg). Injections were performed twice a week for 2 months. In group 3 and 4, extract and NPs treatment was carried out after liver injury by CCl_4 for 2 months.

2.4 Histological Examination

Histological examination was held at “Armenia” hospital (Armenia, Yerevan). All animals were sacrificed by decapitation at the end of the experimental period. Liver was removed immediately and a portion of the tissue was instantly fixed in 10% formalin. Fixed tissues were embedded in paraffin wax and sections of 4 mm thickness were cut. Slides were stained with haematoxylin-eosin for histological examination [6].

2.5 Biochemical Analysis

Blood plasma biochemical analysis (AST, ALT, ALP, total protein, albumin, total cholesterol, HDL, LDL) was performed on a UV-VIS18 spectrophotometer (MRC, Israel) with commercial standard reagent kits (BioSystems, Spain).

2.6 Statistical Analysis

Statistical data processing was performed using the ANOVA program. Statistical significance was set at $p < 0.05$.

3 Results

3.1 Total Antiradical Activity of *O. araratum* Extracts

Extracts of various plants are used as reducing and stabilizing agent for AgNPs biosynthesis. Among all investigated extracts the highest ARA had *O. araratum* 50% ethanol extract ($\text{IC}_{50} = 0.26 \pm 0.04$ mg/ml), that was chosen for AgNPs synthesis (Fig. 1).

3.2 AgNPs Synthesis

AgNPs synthesis began in a few minutes. A black color appeared after addition of salt, indicating formation of

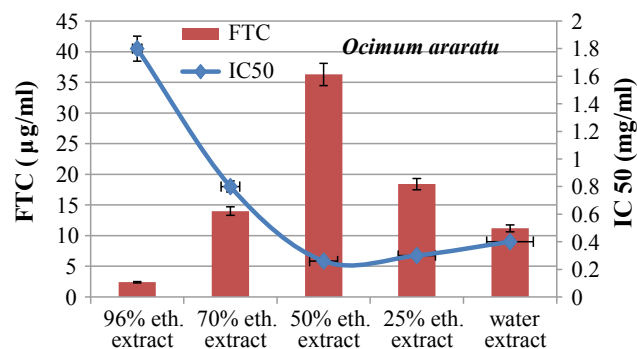


Fig. 1 IC_{50} and FTC (total flavonoids content) in different *O. araratum* extracts. *O. araratum* 50% extract shows the highest antiradical activity ($\text{IC}_{50} = 0.26 \pm 0.04$ mg/ml) and the highest amount of total flavonoids content (36.3 ± 0.8 µg/ml)

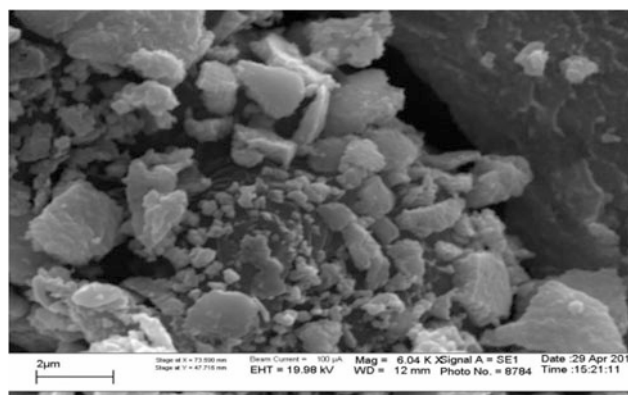


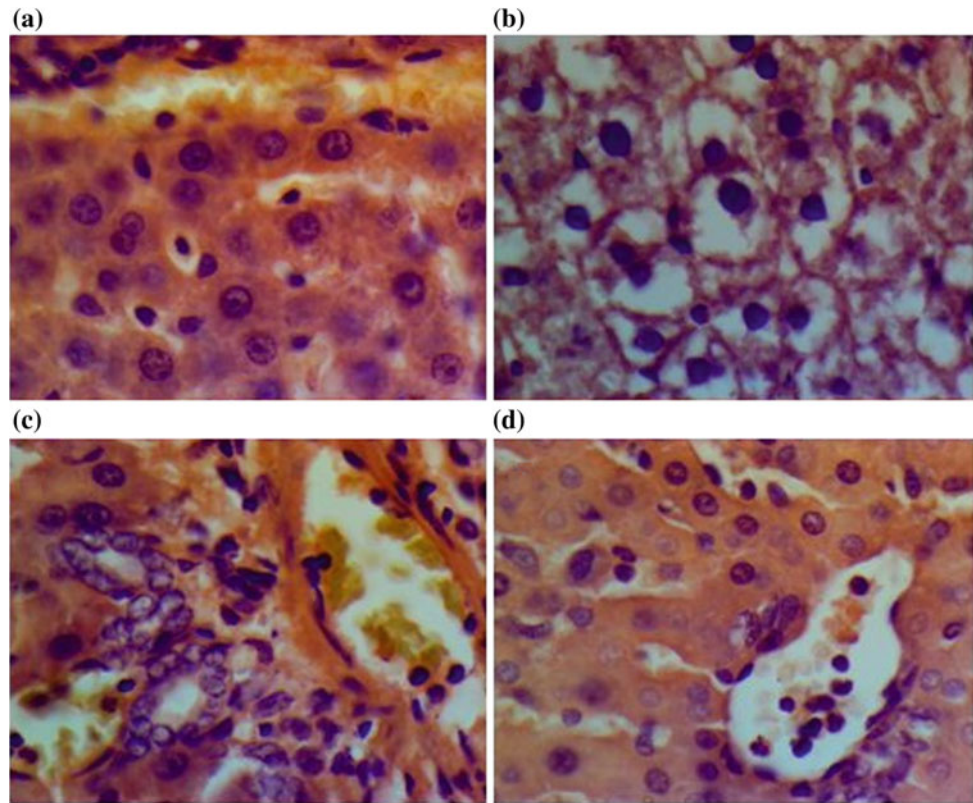
Fig. 2 SEM pictures of silver powder granulate deposited on a carbon strip

nanoparticles. Synthesis was completed after 24 h incubation. By this method silver NPs with diameter 6–18 nm were synthesized (Fig. 2).

3.3 Histological Examination

In control group, the liver sections exhibited the normal architecture of hepatic lobules. Each lobule is formed of cords of hepatocytes radiating from the central vein. Examination of group 2 animals' liver sections revealed the presence of centrilobular necrosis, hepatocytes' diffuse atrophy and fatty degeneration, what indicate fatty liver disease (Fig. 3b) [7]. Histological examination of group 3 rats' liver found a normal lobular structure (Fig. 3c). But large amount of neutrophils and lymphocytes were detected inside the lobules and around the triads; proliferation of bile capillaries was also detected. In group 4, areas of hepatocytes regeneration and false lobules were detected. Around triads among neutrophils and lymphocytes were found active fibroblasts (Fig. 3d).

Fig. 3 Liver histopathology (100×). Liver sections of: **a** control group rat liver; **b** treated by CCl₄; **c** treated by *O. araratum* extract; **d** treated by AgNPs' stabilized in *O. araratum* extract



3.4 Biochemical Analysis

As shown in Table 1, in group 2 toxic agent exposure leads to liver injury markers activity increase: more than 7 times for ALT, 5 times for AST and 8 times for ALP. At the same time, increasing in total cholesterol and all lipoprotein fractions is observed.

In the experimental group 3, the activities of ALT and ALP are reduced by 4.5 and 8 times in comparison with the control group. The activity of AST elevated relative to the control group, but it still remains within the reference values. *O. araratum* extract exposure leads to hypolipidemic effect that accompanied by all lipoprotein fractions descension. The extract leads to an increase in total protein content, but

albumin content decrease by 5.5 times relative to the control group.

In the experimental group 4, the activities of ALT, AST and ALP also reduced a few times in comparison with the group 2. There is also a hypolipidemic effect; however, unlike group 3, there is a decrease in total protein content and normalization of albumin values.

4 Discussions

The frequent use of nanoparticles in various areas of material production has led to the problem of finding a new, more profitable and safe method for their synthesis. NPs green

Table 1 Biochemical markers of experimental rats liver function

	Group 1	Group 2	Group 3	Group 4
ALT (U/L)	10.6 ± 0.10	76.6 ± 0.17	2.4 ± 0.02	2.9 ± 0.01
AST (U/L)	5.3 ± 0.13	15.9 ± 0.03	7.7 ± 0.01	2.9 ± 0.01
ALP (U/L)	14.7 ± 0.03	117.5 ± 0.15	1.8 ± 0.01	3.7 ± 0.01
Total cholesterol (mM/l)	2.9 ± 0.02	3.7 ± 0.001	1.40 ± 0.02	2.1 ± 0.01
HDL (mM/L)	0.8 ± 0.002	1.2 ± 0.01	0.6 ± 0.01	0.6 ± 0.01
LDL (mM/L)	2.1 ± 0.01	2.5 ± 0.03	0.7 ± 0.01	1.5 ± 0.02
Total protein (g/L)	36.7 ± 0.01	59.9 ± 0.02	61.9 ± 0.02	22.7 ± 0.02
Albumin (g/L)	16.9 ± 0.03	24.6 ± 0.03	3.1 ± 0.02	13.1 ± 0.03

synthesis by plants and extracts is very cost-effective and can be used as an economical and environment friendly alternative in large-scale production. In the method of green synthesis, extracts of various plants are used as reducing and stabilizing agents for AgNPs, what solves many problems of other methods. And, if the safety of the synthesis technique is proven, the determination of the effect of those structures on organs and systems hasn't been fully investigated yet [8].

To compare the effect of green AgNPs on the detoxification system of the body, the most convenient is the model of CCl₄ treatment, where a classic picture of liver injury is observed (Fig. 3). The mechanism of hepatotoxic effect is based on free radicals action, and those radicals are form from CCl₄ by cytochrome P450 liver enzymes [9]. At first, in the liver they are able to directly cause lipid and other structures peroxidation, what leading to hepatocytes necrosis. Secondly, they can covalently bind to hepatocytes' membrane proteins, inhibit lipid secretion and increase their synthesis. All this can lead to steatosis, fatty degeneration, fibrosis and cirrhosis. Thirdly, disturbance of intracellular Ca²⁺ homeostasis can also be the cause of hepatocytes necrosis [10]. The similar picture is observed from the group 2 histological (Fig. 3b) and biochemical (Table 1) assays results. However, *O. araratum* extract treatment leads to the normalization of liver structure and liver injury markers' activity (Fig. 3c, Table 1).

The results of our research correlate with literature data [11]. Meera et al. (2009) in vitro experiments showed that *Basil* extract has significant activity in the removal of superoxide and nitric oxide radicals [12]. Dasgupta et al. (2007) found that *O. basilicum* increases the activity of phase I and phase II drug-metabolizing enzymes, increases the activity of hepatic glutathione reductase, superoxide dismutase and catalase in the mice' liver [13]. The authors of those papers argue that basil extract's effects provided by a large amount of flavonoids and terpenoids, but in *O. araratum* 50% ethanol extract we found a large amount of rosmarinic acid (RA) [14].

RA is a secondary metabolite with strongly antiradical and hepatoprotective properties. The RA presence provides *O. araratum* extract manifested effects. According to Hasanein et al., RA at dose 50 mg/kg can leads to the formation of regeneration sites with preservation of apoptotic centers [15]. Given the fact that the content of RA in 50% *O. araratum* ethanol extract is about 10⁴ times less (5.43 µg/ml), it's not surprising that in the liver tissue hemorrhagic areas and areas of immune cells infiltration is found. However, *O. araratum* extract treatment (group 3) leads to the liver synthetic function decrease, what is a manifestation of the extract dose-dependent effect [16].

In studies of some authors, it is reported that liver is the main organ for AgNPs accumulation [17]. It was also shown that AgNPs reduce the ATP content in cells, cause mitochondria damage and increase the ROS production in a

dose-dependent manner. However, the biochemical results of our studies didn't reveal direct evidences of green AgNPs toxic effect on rats' liver. Moreover, the group 4 biochemical analyzes results can judge only about manifested hepatoprotective properties. AgNPs in addition to liver damage markers activity normalization also led to liver synthetic function activation. However, apparent at first glance hepatoprotective effect in group 4 is wrong, because histological analysis revealed the presence of active fibroblasts, which indicates the initial stage of liver fibrosis, that can't be detected by biochemical analyzes.

So it can be argued that green AgNPs with diameter 6–18 nm at 20 mg/kg body weight dose leads to the normalization of injured liver biochemical markers at the beginning, but also leads to fibroblasts activation and fibrosis.

Conflict of Interest The authors declare that they have no conflict of interest.

References

1. WHO, The top 10 causes of death at www.who.int
2. Piao, M., Kang, K., Lee, K., Choi, J., Choi, J., Hyun, J.: Silver nanoparticles induce oxidative cell damage in human liver cells through inhibition of reduced glutathione and induction of mitochondria-involved apoptosis. *Toxicol. Lett.* **201**, 92–100 (2011). <https://doi.org/10.1016/j.toxlet.2010.12.010>
3. Kulthong, K., Srisung, S., Boonpavanitchakul, K., Kangwansupamonkon, W., Maniratanachote, R.: Determination of silver nanoparticle release from antibacterial fabrics into artificial sweat. *Part Fibre Toxicol.* (2010). <https://doi.org/10.1186/1743-8977-7-8>
4. Vardapetyan, H., Tiratsuyan, S., Hovhannisyanyan, A.: Antioxidant and antibacterial activities of selected Armenian medical plants. *JEBAS* **2**(3), 300–307 (2014)
5. Tippayawat et al.: Green synthesis of silver nanoparticles in aloe vera plant extract prepared by a hydrothermal method and their synergistic antibacterial activity. *Peer J.* (2016). <https://doi.org/10.7717/peerj.2589>
6. Birgit, K., Him, Stephanie, et al.: Effects of silver nanoparticles on the liver and hepatocytes in vitro. *Toxicol. Sci.* **131**(2), 537–547 (2012). <https://doi.org/10.1093/toxsci/kfs306>
7. Van Herck, M., Vonghia, L., Francque, S.: Animal models of nonalcoholic fatty liver disease—a starter's guide. *Nutrients* **7**, 9(10) (2017). <https://doi.org/10.3390/nu9101072>
8. Stone, V., Johnston, H.: Development of in vitro systems for nanotoxicology: methodological considerations. *Crit. Rev. Toxicol.* **39**, 613–626 (2009)
9. Boll, M., Weber, L., et al.: Pathogenesis of carbon tetrachloride-induced hepatocyte injury. Bioactivation of CCl₄ by cytochrome P₄₅₀ and effects on lipid homeostasis. *Z Naturforsch* **56c**, 111–121 (2001)
10. Boll, M., Weber, D., et al.: Hepatocyte damage induced by carbon tetrachloride. Inhibited lipoprotein secretion and altered lipoprotein composition. *Z Naturforsch* **56c**, 283–290 (2001)
11. Hanan, A., Mohamed, A., et al.: Hepatoprotective effects of parsley, basil, and chicory aqueous extracts against dexamethasone-induced in experimental rats. *J. Intercult. Ethnopharmacol.* **5**, 65–71 (2016). <https://doi.org/10.5455/jjce.20160124113555>

12. Meera, R., Devi, P., Kameswari, B., Mahumita, B., Merlin, J.: Antioxidant and hepatoprotective activities of *Ocimum basilicum* Linn and *Trigonella foenum-graecum* Linn. Against H₂O₂ and CCl₄ induced hepatoyoxicity in goat liver. *Indian J. Exp. Biol.* **47**, 584–590 (2009)
13. Dasgupta, T., Rao, A., Yadava, P.: Chemomodulatory efficacy of basil leaf (*Ocimum basilicum*) on drug metabolizing and antioxidant enzymes, and on carcinogen-induced skin and fore stomach papilloma genesis. *Phytomedicine* **11**, 139–151 (2007)
14. Kazaryan, Sh: *Ocimum sanctum* and *Ocimum araratum* extracts antiradical properties and their action on human erythrocytes. *Vestnik RAU* **2**, 102–111 (2017)
15. Hasanein, P., Sharifi, M.: Effects of rosmarinic acid on acetaminophen-induced hepatotoxicity in male Wistar rats. *Pharm. Biol.* **55**(1), 1809–1816 (2017). <https://doi.org/10.1080/13880209.2017.1331248>
16. Muhammad, M., Naglaa, R., Nora, H.: Comparative effects of scorpion venom and aqueous basil (*Ocimum basilicum*) leaves extracts on CCl₄-induced toxicity in albino rats. *J. Liver* **5**, 3 (2016). <https://doi.org/10.4172/2167-0889.1000201>
17. Takenaka, S., Karg, E., Roth, C., Schulz, H., Ziesenis, A., Heinzmann, U., Schramel, P., Heyder, J.: Pulmonary and systemic distribution of inhaled ultrafine silver particles in rats. *Environ. Health Perspect.* **4**, 547–551 (2001). <https://doi.org/10.1289/ehp.01109s4547>

Luminescent Properties on ZnO:Cr Nanocrystals and Thin Layers

T. Goglidze, I. Dementiev, E. Goncarencu, N. Nedeoglo, T. Iurieva, and D. Nedeoglo

Abstract

Both undoped and chromium doped zinc oxide nanocrystal powders are obtained by chemical deposition and hydrothermal methods. ZnO and ZnO:Cr thin layers on the surface of ZnSe and ZnSe:Cr samples, respectively, are obtained by isovalent substitution of selenium by oxygen in the process of thermal treatment of the samples in air. Photoluminescence spectra of the ZnO and ZnO:Cr nanopowders and thin layers obtained by various techniques are investigated at room temperature. Cr doped ZnO powders obtained by chemical deposition and hydrothermal methods improves the powder quality, as evidenced exciton emission is more intensive. New emission bands are found in visible (615 nm, 625 nm) and infrared (925 nm, ~2000 nm) spectral ranges for ZnO:Cr nanopowders and thin films. The contribution of Cr impurity to the formation of emission bands is discussed.

Keywords

Photoluminescence • Zinc oxide • Chromium • Nanocrystal • Thin layer

1 Introduction

Wide-bandgap semiconductors are widely used for optoelectronic devices due to high optical transparency in visible range. Introduction of various impurities into these materials expands their application area. Zinc oxide is one of the

T. Goglidze · I. Dementiev · E. Goncarencu (✉) · N. Nedeoglo · T. Iurieva · D. Nedeoglo
Department of Physics and Engineering, State University of Moldova, A. Mateevici, 60, Chisinau, Moldova
e-mail: jjspace@rambler.ru

E. Goncarencu
National Institute of Laser, Plasma and Radiation Physics, Măgurele, Romania

materials with optical and radiative properties extensively investigated. Thus, manganese impurity (Mn) introduced into zinc oxide is responsible for new photoluminescence (PL) bands in visible range [1]. Doping of ZnO samples with chromium (Cr) ions quenches the ultraviolet (UV) PL band and forms a PL band in visible range [2, 3]. However, it is established that doping zinc oxide with chromium impurity is very hard in the process of chemical synthesis of the material.

In this paper, we have made a comparative analysis of radiative properties of ZnO and ZnO:Cr nanopowders and thin layers obtained by various techniques. The purpose of this analysis is the selection of the ZnO:Cr synthesis method that allows the most efficient doping of the samples with chromium impurity.

2 Experimental

ZnO and ZnO:Cr nanocrystal powders were synthesized by chemical deposition from water solutions and hydrothermal method. Identical equimolar (1:1) solutions of $\text{Zn}(\text{NO}_3)_2 \cdot 6\text{H}_2\text{O}$ zinc nitrate and $\text{C}_6(\text{NH}_3)_4$ hexa-methylenetetramine were used for both synthesis methods. Initially, impurity-free ZnO powders were synthesized. Then, Cr impurity was added to initial solution before starting the synthesis. As a dopant, CrCl_3 trivalent chromium chloride in amount of 50 mg per 300 ml of initial solution was used. It is worth mentioning that this chloride does not dissolve in water at room temperature and practically does not dissolve at higher temperatures. After completing the synthesis, a sediment of zinc oxide white powder and chromium (III) chloride microcrystals of the same violet color as before the synthesis was found at the bottom of reaction cell. A part of zinc oxide powder without chromium (III) chloride was used for fabrication of the samples to study luminescence.

A sediment obtained after hydrothermal synthesis also contained ZnO powder, as well as an unreacted impurity.

However, the impurity color was changed to green, which is characteristic for chromium oxide. Apparently, under the influence of higher temperature (~ 180 °C) in comparison with chemical deposition, chromium chloride was transformed to chromium oxide. Express-control of luminescent properties of the fabricated powders under laser excitation with 405 nm has shown that the emission color of undoped and doped powders differ. This gives reason to suppose that a number of Cr ions was incorporated into zinc oxide structure.

Polycrystalline ZnO layers on the surface of ZnSe samples and ZnO:Cr layers on the surface of ZnSe:Cr samples were obtained by isovalent substitution of selenium by oxygen in the process of annealing the samples at 830 K in air during 30 h. The initial ZnSe samples were grown from melt by zone melting technique. The doping of the samples was carried out in the process of the sample annealing in Zn + 3.2 at.% Cr melt at 1180 K during 100 h.

PL spectra of ZnO and ZnO:Cr nanopowders and thin layers were investigated in the wavelength range between 360 and 2500 nm at room temperature under laser excitation with 337, 473 and 532 nm. The spectra were registered using MDR-23 monochromator, FEU-100 photomultiplier and PbS-based detector.

3 Results and Discussion

Figure 1 shows visible-range PL spectra of undoped and Cr-doped ZnO samples registered under UV laser excitation ($\lambda_{exc} = 337$ nm).

The samples may be qualitatively separated into 2 groups: the weakly-doped samples (ZnO:Cr nanopowders, Fig. 1a, b) and highly-doped samples (ZnO:Cr layers fabricated on the surface of ZnSe:3.2 at.% Cr crystals, Fig. 1c). The exciton PL bands with maxima located between 381 and 392 nm are observed in the PL spectra of all the investigated samples. There are also wide PL bands in the long-wavelength region of visible spectrum. These bands in the range between 500 and 700 nm are usually associated with native defects of ZnO, such as V_O and V_{Zn} vacancies, Zn_O and Zn_i anti-structural defects, $Zn_i - V_{Zn}$ transitions. V_O and V_{Zn} vacancies in various charge states are considered to be the main defects responsible for the long-wavelength PL bands. The PL band near 490 nm is attributed to the transition of free electron to V_O level, while the PL band with maximum near 550 nm (Fig. 1a) is attributed to the transition of free electron to V_{Zn} level [4].

The edge PL band for ZnO thin films obtained by isovalent substitution is more intensive than that for ZnO powders obtained by chemical deposition (Fig. 1c, curve 1). This gives reason to suggest that ZnO films fabricated on the surface of ZnSe crystals have more perfect structure.

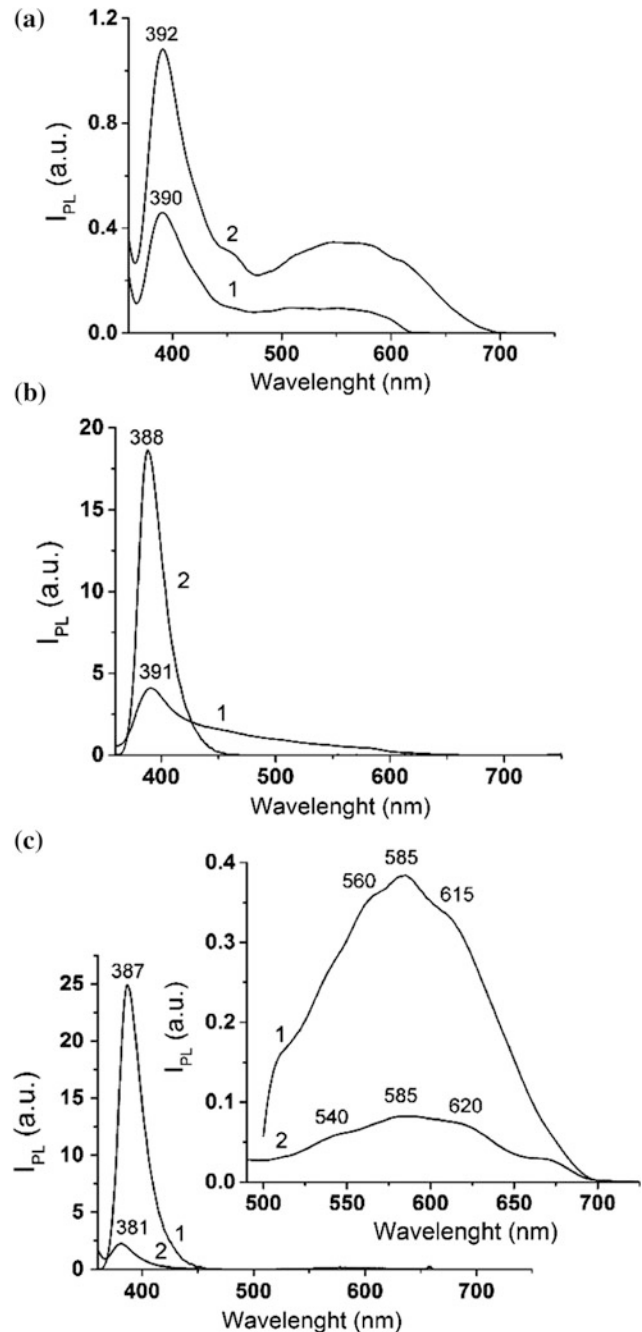


Fig. 1 PL spectra of ZnO (1) and ZnO:Cr (2) samples obtained by: **a** chemical deposition; **b** hydrothermal method; **c** isovalent substitution. $\lambda_{exc} = 337$ nm. $T = 300$ K

Doping of ZnO powders with Cr enhances the edge PL intensity (Fig. 1a, b). For the powders obtained by chemical deposition method, the long-wavelength PL also increases (Fig. 1a, curve 2), while for the powders obtained by hydrothermal method, it decreases (Fig. 1b, curve 2). These variations in the PL spectra seem to be caused by substitution of zinc vacancies by chromium ions.

At the same time, the formation of ZnO:Cr thin layers as a result of oxidation of ZnSe:Cr crystal surfaces leads to an opposite effect. Isovalent substitution of selenium atoms by oxygen atoms induces a sharp decrease in PL bands intensity both for edge and long-wavelength spectral ranges (Fig. 1c). It is likely caused by the fact that high concentration of Cr leads to increasing concentration of structural defects and increasing number of non-radiative recombination channels. Another probable explanation is the formation of $V_{Zn} + Cr$ complexes, which are characteristic for the samples saturated with oxygen [5].

Figure 2 shows normalized PL spectra of ZnO and ZnO:Cr Cr powders and thin layers in the long-wavelength visible range under laser excitation with 473 nm (Fig. 2a) and 532 nm (Fig. 2b). The PL spectra of both undoped and Cr-doped ZnO powders obtained by chemical deposition and hydrothermal method consist of a wide band with maximum at 530 nm under laser excitation with 473 nm. The doping of ZnO powders with Cr leads to decreasing intensity of this

PL band and to appearance of a feature on its long-wavelength wing near (615–620) nm. The PL spectra of undoped ZnO thin layers consist of the band with maximum at 590 nm and a feature near 615 nm (Fig. 2a). The formation of ZnO:Cr thin layers leads to a shift of the PL band towards long wavelengths due to increasing contribution of the emission at 615 nm.

The increase of excitation wavelength to 532 nm has no influence on the structure of the PL bands. For all undoped and Cr-doped samples, except for ZnO:Cr thin layers, PL maximum is localized at 580 nm (Fig. 2b). Similarly to the previous excitation energy, introduction of Cr into the samples decreases the PL band intensity and slightly broadens it towards long wavelengths. In the PL spectrum of ZnO:Cr thin layers, the PL band is localized at 625 nm (Fig. 2b).

Figure 3 shows infrared (IR) PL spectra of ZnO:Cr nanopowders and thin layers. For ZnO:Cr powders obtained by chemical deposition method, a wide PL band with maximum at 925 nm is observed. Intensity and spectral

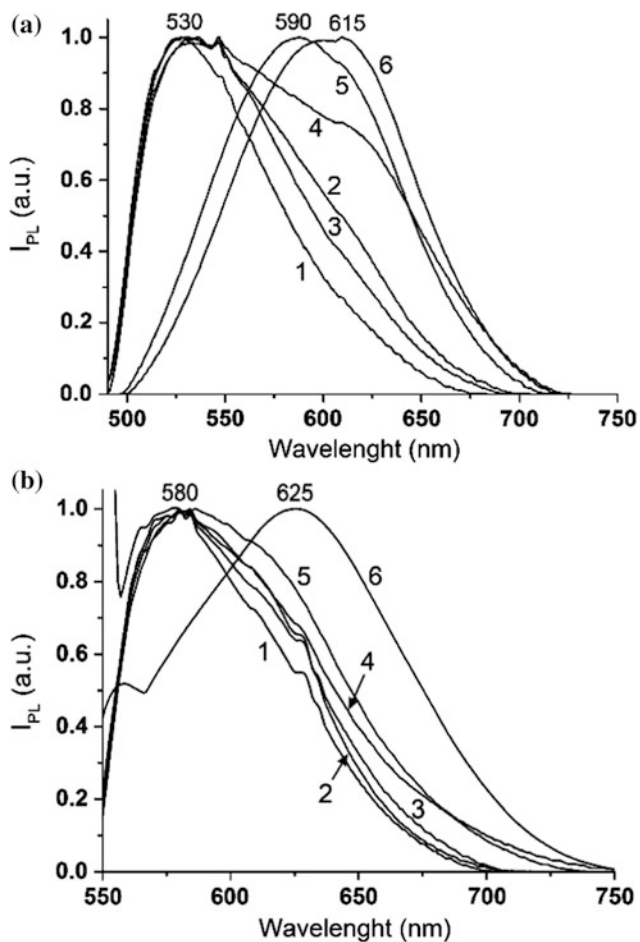


Fig. 2 Normalized visible PL spectra of ZnO (1, 3, 5) and ZnO:Cr (2, 4, 6) samples obtained by: 1, 2—chemical deposition; 3, 4—hydrothermal method; 5, 6—isovalent substitution. λ_{exc} , nm: 473 (a); 532 (b). $T = 300$ K

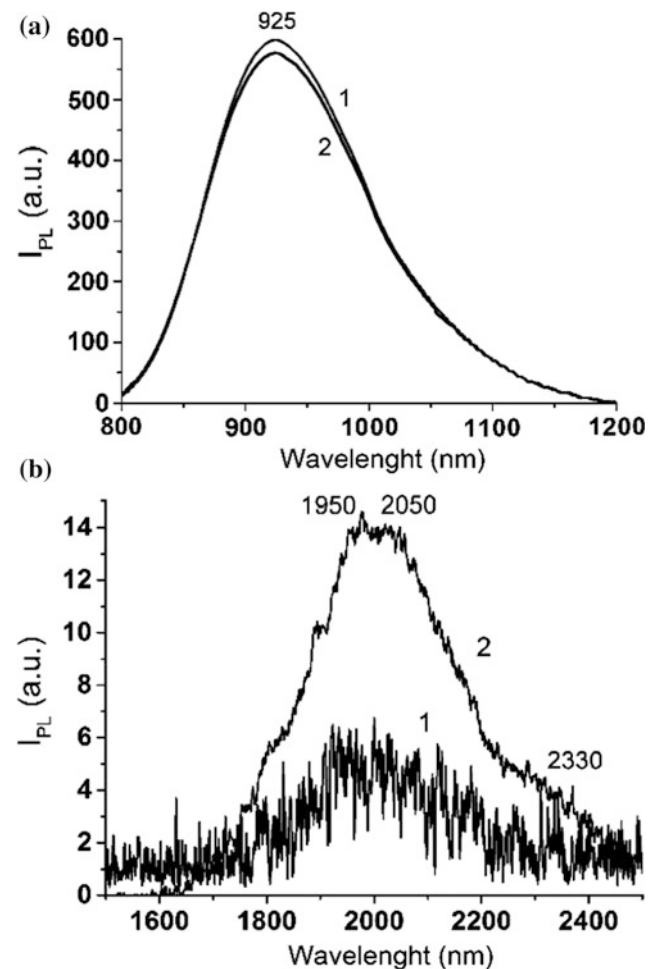


Fig. 3 IR PL spectra of ZnO:Cr samples obtained by chemical deposition (a) and isovalent substitution (b). λ_{exc} , nm: 473 (1); 532 (2). $T = 300$ K

position of the maximum of this band are independent on excitation wavelength (Fig. 3a). For ZnO:Cr thin layers obtained by isovalent substitution method, a PL band with maximum near 2000 nm is observed (Fig. 3b). Intensity of this PL band, which may be attributed to intracenter transitions within Cr^{2+} ions (${}^5\text{E} \rightarrow {}^3\text{T}_1$) [6], increases with increasing excitation wavelength.

4 Conclusions

The technology of ZnO nanopowder synthesis by chemical deposition and hydrothermal methods, as well as of the doping with Cr during the synthesis, is elaborated. The obtaining of ZnO and ZnO:Cr thin layers by isovalent substitution of selenium by oxygen in the process of high-temperature annealing of ZnSe and ZnSe:Cr samples in air is also demonstrated.

It is established that the PL intensity decreases in both edge and long-wavelength spectral ranges for Cr-doped ZnO thin layers, irrespective of excitation energy. The same behavior is observed for ZnO:Cr nanopowders at low-energy excitation ($\lambda_{\text{exc}} = 473$ nm, 532 nm), while under band-to-band excitation ($\lambda_{\text{exc}} = 337$ nm), PL intensity in visible range rapidly increases.

New emission bands in visible (615, 625 nm) and IR (925, ~ 2000 nm) spectral ranges are found in the PL spectra of ZnO:Cr samples at room temperature.

Acknowledgements This work is supported under the RM Project No. 15.817.02.27F.

Conflict of Interest The authors declare that they have no conflict of interest.

References

1. Smith, J., Jones, M. Jr, Houghton, L., et al.: Future of health (1999); Zhang, Y., Han, F., Dai, Q., Tang, J.: Magnetic properties and photovoltaic application of ZnO:Mn nanocrystals. *J. Colloid Interface Sci.* **517**, 194–203 (2018)
2. Torres-Torres, C., Garcia-Crus, M.L., Castaneda, L., et al.: Photoconductivity, photoluminescence and optical Kerr nonlinear effects in zinc oxide films containing chromium nanoclusters. *J. Lumin.* **132**, 1083–1088 (2012)
3. Singh, S., Kumar, E.S., Rao, M.S.R.: Microstructural, optical and electrical properties of Cr-doped ZnO. *Scripta Mater.* **58**, 866–869 (2008)
4. Rodnyi, P.A., Chernenko, K.A., Klimova, O.G., Gorokhova, E.I.: The annealing effect on green X-ray luminescence of zinc oxide powders. *St. Petersburg Polytech. Univ. J. Eng. Sci. Technol.* **182**, 21–30 (2013)
5. Wang, F.G., Pang, Zh, Lin, L.: Theoretical study of the magnetic interaction of Cr-doped ZnO with and without vacancies. *J. Magn. Mater.* **321**, 3067–3070 (2009)
6. Golibaba, G., Caraman, M., Evtodiev, I., Goncarencu, E., Nedeoglo, D., Nedeoglo, N.: Influence of annealing medium on photoluminescence and optical properties of ZnSe: Cr crystals. *J. Lumin.* **145**, 237–243 (2014)

Evaluation of Stimulatory, Antifungal and Thermo-Resistant Action of Aqueous Dispersions of Nanoparticles on Seeds of Parental Forms and Reciprocal Hybrids of Winter Wheat

S. N. Maslobrod, G. A. Lupashku, S. I. Gavzer, A. I. Gore, and Yu. A. Mirgorod

Abstract

For the first time in the crop technology, the effect of aqueous dispersions of nanoparticles was investigated on seeds of parental forms and their reciprocal hybrids, making it possible to effectively use this factor in plant breeding and genetic practice. The received data can be used to select optimal pairs for crossing and obtain new promising hybrids. It was shown the stimulatory, anti-fungal and thermo-resistant action (increase of resistance to pathogenic fungus) of water dispersed solutions of silver and copper nano-particles on seeds of winter triticale. The antifungal effect of the nanofactor is more effective than of the potassium permanganate. In terms of seed germination energy and sprout length of winter wheat (parent varieties and their reciprocal hybrids) we revealed the stimulatory and antifungal action of aqueous dispersions of silver, copper, bismuth, and zinc oxide nanoparticles on the seeds. The maternal effect is revealed—the primary influence of the maternal form on the physiological parameters of the hybrid.

Keywords

Water dispersed solutions • Nanoparticles • Seed germination energy • Antifungal effect • Sprout length • Reciprocal hybrids • Parent varieties

1 Introduction

Aqueous dispersions containing nanoparticles of various substances have bactericidal and fungicidal effects on a plant object (Ling and Yatts 2005; Zhu et al. 2008; Yatts and Ling 2007; Morgalev et al. 2010; Glushchenko et al. 2006).

They also function as trace elements of the mineral nutrition of plants of prolonged action, increasing the adaptive potential of the plant organism. Nanoparticles are electrically neutral, which allows them to be evenly distributed in the film former and develop a thin layer to envelop the seeds. This provides reliable seed protection from pathogens. Oxidizing gradually in the soil, nanoparticles create unfavorable conditions for pathogenic microorganisms and at the same time are used by plants as trace elements in the process of growth (Zhu et al. 2008; Yatts and Ling 2007; Morgalev et al. 2010; Glushchenko et al. 2006; Panichkin and Raikova 2009; Raikova 2004).

Nanopowders have extremely huge specific surface area (of the order of several hundred square meters per 1 g), therefore, they can be effectively used in micro-doses. Thus, for the pre-sowing treatment of 1 ton of seeds is used only few milligrams of nanopowder (Ling and Yatts 2005), which at the same time ensures ecological safety of both the environment and the bioproduct. Herewith, the toxicity of metal nanopowders is 10–40 times less than the toxicity of salts of the same metals (Glushchenko et al. 2006).

We began intense research on nanotechnology in crop production in 2014 (Maslobrod et al. 2014). The task was to study the effect of aqueous dispersions (AD) of nanoparticles (NP) of various metals and their oxides on seed germination of parental forms (varieties) and reciprocal hybrids of tomato and wheat, as well as on the resistance of these seeds to pathogenic fungi and low temperature (Maslobrod et al. 2017). The data of such studies can be taken into account when selecting parental pairs for crossing in order to obtain productive and environmentally sustainable hybrids. This publication reflects the

S. N. Maslobrod (✉) · G. A. Lupashku · S. I. Gavzer · A. I. Gore
Institute of Genetics, Physiology and Plant Protection of ASM, 20,
Padurii str., Chisinau, Moldova
e-mail: maslobrod37@mail.ru

Yu.A. Mirgorod
Southwest State University, Kursk, Russia

results of ongoing research in this direction using both other types of nanoparticles and genotypes.

2 Materials and Methods

Experiments were conducted in the Laboratory of Applied Genetics of the Kursk South-West State University (Russia) where the nanoparticles were obtained and characterized in detail (Mirgorod et al. 2012, 2013, 2018) (Fig. 1). Seeds of winter triticale (variety *Ingen93*) were used for conducting the methodological experiment. As parental forms, in the main experiments, we took seeds of winter wheat (variety): (1) *Odessa 267* and *Nikonika*, (2) *Accent* and *Select*, (3) *Basarabianka* and *M/M3* and their reciprocal hybrids. Seeds were soaked in AD of NPAg, NPCu, NPBi and NPZnO (concentration and exposure are presented in the results of the study). The seeds were treated with *Helminthosporium avenae* fungus (the main pathogen for cereal seeds) (Methods 1982). Fungus exposure is within 18 h. For comparison, we used 1% potassium permanganate solution (KMnO_4) in the methodological experiment, with a 1 h exposure. When evaluating the thermo-resistant effect of the nanofactor, the seeds were subjected to low temperatures ($+4\text{ }^\circ\text{C}$) during 12 h. After the treatment, the seeds were germinated in distilled water in *Petri* dishes at the temperature of $20 + 25\text{ }^\circ\text{C}$. We used 200–300 seeds in each embodiment. The following signs were taken into consideration: seed germination energy SGE (number of germinated seeds on the 2nd day), length of the sprout root LR (on the 3rd day), length of the seedling LS (on the 7th day).

3 Results and Discussions

3.1 Methodological Experiment

The aim of this experiment was to compare the antifungal effects induced by potassium permanganate solution

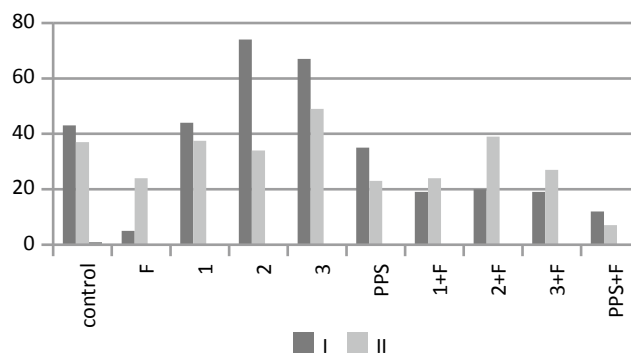


Fig. 2 Germination of triticale seeds (variety *Ingen 93*) under the action of nanoparticles aqueous dispersions of silver (I), of copper (II), *Helminthosporium avenae* fungus (F), potassium permanganate (PPS) (the arithmetic mean error does not exceed 10%) 1,2,3—concentrations of NPAg [I], respectively, 8×10^{-6} mol/l, 16×10^{-7} mol/l, 32×10^{-8} mol/l; of NPCu (II)— 8×10^{-6} mg/l, 16×10^{-7} mg/l, 32×10^{-8} mg/l

(PPS) and aqueous dispersions at three different concentrations of NPAg and NPCu. The criterion for assessing the effect was the operational parameter *seed germination energy* (Fig. 2). When using AD of NPAg, stimulation was obtained by 72% and 56% at NP concentration respectively 16×10^{-7} mol/l and 32×10^{-8} mol/l. The antifungal effect was observed from both the nanofactor and PPS. The nanofactor turned out to be more effective than PPS: the *fungus+NPAg* variant was 4 times more effective than the *fungus* variant, and the *fungus+PPS* variant was 2.4 times more efficient. In general, the antifungal effect was 1.7 times higher than that of PPS. When using AD of NPCu, the concentrations were calculated in mg/l. Stimulation was obtained at the concentration of 32×10^{-8} mg/l and it increased by 32%. The antifungal effect was obtained at the NP concentration of 32×10^{-8} mg/l, exceeding the *fungus* variant by 1.6 times. The PPS increased the negative effect of the fungus by 3.4 times. In further experiments, AD of NPBi, NPCu, NPZnO were used at stimulative concentrations: 10^{-7} mg/l, and AD of NPAg at 10^{-7} mol/l concentration.

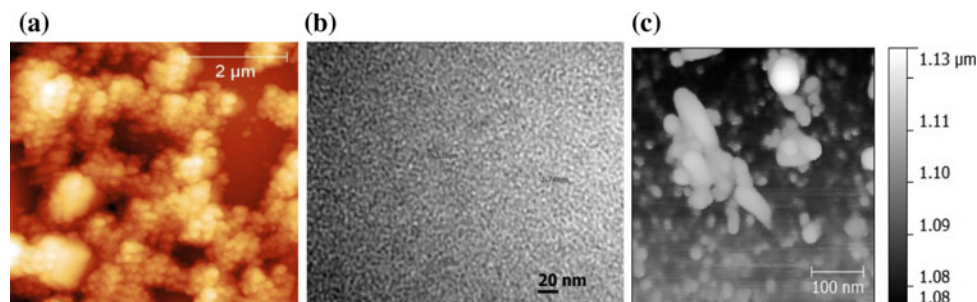


Fig. 1 General view of nanoparticles of copper (a), silver (b) and bismuth (c) used in our research. Images were developed by Mirgorod et al. (2012, 2013, 2018) and reprinted here with permission of the author

3.2 Evaluation of the Stimulatory, Antifungal and Thermo-Resistant Action of Aqueous Dispersions of Nanoparticles on Seeds of Parental Forms and Winter Wheat Hybrids

As can be seen in Table 1, AD of NPBi, by the seed germination energy (SGE) parameter, has a significant stimulatory effect on all the genotypes—the parent forms *Odessa267* and *Nikonika* and their reciprocal hybrids: the excess of SGE is by 1.75, by 1.53, by 1.36 and by 1.69 times. Here there is revealed a predominant influence of the maternal form on the SGE of the hybrid.

Aqueous dispersion of NPZnO also has a stimulating effect on the three genotypes (in the same parental forms and hybrids, the excess of SGE was by 1.20, by 1.57, by 1.44 and by 1.03 times). The maternal effect is again observed (Table 1). With the same genotypes, the stimulating and antifungal action of the nanofactor (AD of NPAg) was tested by a different parameter—the length of the seedling sprout (Table 1). The stimulation effect was obtained only with *Nikonika* seeds. The antifungal effect was observed with *Nikonika*, *Odessa267-x-Nikonika* and *Nikonika-x-Odessa267*, excess of the NPAg + *Fungus* variant over the *Fungus* variant being respectively by 1.06, by 1.06 and by 1.16 times).

With the seeds of winter wheat of other genotypes: *Accent*, *Select*, *Accent-x-Select*, *Select-x-Accent*, the

stimulating and antifungal effect was tested by the length of the germ (Table 2). Here, the stimulation is observed with the AD of NPAg on *Accent-x-Select* seeds (by 5%) and with the AD of NPCu on *Select* seeds (by 9%). The antifungal effect was not found.

3.3 Evaluation of the Thermo-Resistant Effect of Aqueous Dispersions with Nanoparticles on Seeds of Parental Forms and Hybrids of Winter Wheat

We observed a significant stimulation of the seed germination energy in the study aimed to assess the thermo-resistant effect of the nanofactor on the seeds of the parent forms pair *Basarabianka* and *M/M3* and their reciprocal hybrids (Table 3): (1) *Basarabianka*—only in the aqueous dispersion of the mixture of nanoparticles variant (by 12%), (2) *M/M3*—in all variants of the nanofactor: aqueous dispersions of NPBi, NPCu, NPZnO and of the mixture of nanoparticles (maximum stimulation was observed in the latter variant—by 64%), (3) *Basarabyanka-x-hybrid M/M3*—in all variants of the nanofactor (up to 33%), (4) for the hybrid—practically in all variants with the nanofactor (up to 17%).

As can be seen, aqueous dispersions of nanoparticles of three types—bismuth, copper, and zinc oxide, as well as of the mixture of these nanoparticles have increased seeds thermal resistance, i.e. the resistance of *M/M3* seeds and two

Table 1 Seed and seedling parameters of parent wheat forms and reciprocal hybrids after treating the seeds with nanoparticles aqueous dispersions and fungus

Variant	Odessa 267	Nikonika	Odessa267-x-Nikonika	Nikonika-x-Odessa 267
Control	33.5 ± 3.25	30.0 ± 3.83	40.0 ± 3.07	27.5 ± 4.78
ADNPBi	58.5 ± 3.40**	46.0 ± 0.82*	54.5 ± 4.03*	46.5 ± 1.26*
Control	55.0 ± 3.00	38.5 ± 2.50	44.5 ± 4.37	59.5 ± 4.57
ADNPZnO	66.5 ± 2.06*	60.5 ± 4.71*	64.0 ± 3.91*	61.0 ± 6.13
Control	97.6 ± 1.18	91.5 ± 1.09	104.0 ± 1.40	112.3 ± 1.08
ADNPAg	100.0 ± 1.65	99.9 ± 1.18***	99.1 ± 1.18**	110.1 ± 1.17
Fungus	97.6 ± 1.12	90.4 ± 1.20	97.3 ± 1.31	95.9 ± 1.15
ADNPAg + Fungus	90.3 ± 1.11	95.6 ± 1.19**	103.6 ± 1.09**	111.1 ± 1.22***

*, **, *** - differences are significant compared with the control at a confidence level, respectively 0.95, 0.99, 0.999

Table 2 Sprout length of parent wheat varieties and reciprocal hybrids when treating the seeds with nanoparticles aqueous dispersions and fungus, mm

Variant	Accent	Select	Accent-x-Select	Select-x-Accent
Control	81.1 ± 1.27	75.6 ± 1.30	84.4 ± 1.20	84.8 ± 1.08
ADNPAg	81.7 ± 1.06	74.4 ± 1.09	89.0 ± 1.42**	84.0 ± 1.02
ADNPCu	79.6 ± 1.24	82.7 ± 1.11***	85.3 ± 1.45	86.7 ± 1.21
Fungus	76.8 ± 1.28	76.8 ± 1.47	84.2 ± 1.11	84.5 ± 1.25
ADNPAg + Fungus	78.7 ± 1.12	74.2 ± 1.18	80.8 ± 1.10	85.3 ± 1.21
ADNPCu + Fungus	74.2 ± 1.15	74.3 ± 1.19	82.7 ± 1.22	81.6 ± 1.32

*, **, *** - differences are significant compared with the control at a confidence level, respectively 0.95, 0.99, 0.999

Table 3 Seed germination energy of parental forms and reciprocal winter wheat hybrids treated with nanoparticles aqueous dispersions subjected to subsequent action of a temperature of +4 °C, in %

Nanoparticle aqueous dispersions	Basarabianka	M/M3	Basarabianka-x-M/M3	M/M3-x-Basarabianka
Control	48.7 ± 2.40	33.3 ± 3.71	42.7 ± 1.20	34.7 ± 2.68
ADNPBi	54.7 ± 1.76	48.0 ± 1.00**	56.7 ± 4.09*	58.0 ± 4.58**
ADNPCu	50.0 ± 2.31	44.7 ± 3.28*	54.7 ± 3.96**	46.7 ± 0.83**
ADNPZnO	54.0 ± 1.52	47.3 ± 3.17*	56.7 ± 2.33***	41.3 ± 1.77
AD Σ NP	61.0 ± 3.27*	54.0 ± 2.54***	48.7 ± 1.67*	46.7 ± 3.84*

*, **, *** - differences are significant compared with the control at a confidence level, respectively 0.95, 0.99, 0.999

Table 4 Length of coleoptiles seedlings of parental forms and reciprocal hybrids of winter wheat, after seeds treating with water dispersions of nanoparticles and subjected to subsequent temperature of +4 °C, mm

Nanoparticle aqueous dispersions	Basarabianka	M/M3	Basarabianka-x-M/M3	M/M3-x-Basarabianka
Control	23.6 ± 0.88	19.7 ± 0.91	19.7 ± 0.94	20.0 ± 0.98
ADNPBi	30.6 ± 0.96***	29.7 ± 0.91***	25.7 ± 1.48*	23.9 ± 1.07*
ADNPCu	23.4 ± 0.87	21.7 ± 1.02	29.5 ± 1.12***	26.7 ± 0.81***
ADNPZnO	25.6 ± 0.87	20.4 ± 0.80	27.9 ± 0.92***	29.2 ± 0.88***
AD Σ NP	25.9 ± 1.00	23.1 ± 1.07*	21.8 ± 0.64	26.3 ± 0.91***

*, **, *** - differences are significant compared with the control at a confidence level, respectively 0.95, 0.99, 0.999

Table 5 Plant mass factors of winter triticale (variety *Ingen-93*) grown in field conditions after pre-sowing seed treatment with nanoparticle aqueous dispersions of Ag

Variant	Number of shoots (%)	Length of the main stem (cm)	Number of stems (pcs.)	Weight of 1000 grain (g)	Yield from a plot (g)
Control	65.9 ± 1.2	95.6 ± 1.03	2.05 ± 0.21	51.5	1551 ± 40
Test	75.4 ± 2.0**	96.3 ± 1.23	2.21 ± 0.20	50.5	2426 ± 45**

*, **, *** - differences are significant compared with the control at a confidence level, respectively 0.95, 0.99, 0.999

reciprocal hybrids to low positive temperature, causing more active germination compared with the control. The predominant influence on one of the parental forms of the hybrid was not found.

For the same objects, the following results were obtained by the *coleoptiles length* parameter (Table 4): (1) aqueous dispersions of NPBi caused significant stimulation in all genotypes (up to 50% in *M/M3*), which generally coincides with the data on the *seed germination energy* parameter, (2) with the hybrids it was observed a stimulation in all variants of AD of NP (with a maximum for NPCu (by 50%) and NPZnO (by 46%). Here, aqueous dispersions of all types of nanoparticles cause a more pronounced increase in the thermo-resistance level in hybrids.

3.4 Effect of Pre-sowing Treatment of Triticale Seeds with Water Dispersion of Silver Nanoparticles on the Productivity of Plants in Field Conditions

A small-plot experiment was carried out (accounting plot being of 4 m²) in three replications, on the IGPPP field site in order to check the effectiveness of pre-sowing seed

treatment (using winter triticale *Ingen93* variety as an example) with water dispersion of silver nanoparticles at a concentration of 10⁻⁷ mol/l. The same concentration turned out to be simulative in laboratory conditions. The increase in plant productivity (yield from a plot) by 56% (Table 5) was revealed. This growth was caused, in our opinion, by the increase of the following plant mass factors: (1) number of seedlings, (2) length of the main stem and (3) number of productive stems of the plant grown from a single grain.

4 Conclusions

1. For the first time in the crop technology, the effect of aqueous dispersions of nanoparticles was investigated on seeds of parental forms and their reciprocal hybrids, making it possible to effectively use this factor in plant breeding and genetic practice. The received data can be used to select optimal pairs for crossing and obtain new promising hybrids.

2. The research has revealed changes of *seed germination* parameters in winter triticale seeds (*Ingen 93* variety). Aqueous dispersions of silver and copper nanoparticles produce stimulative and antifungal effects increasing seed resistance to the pathogenic fungus. The antifungal action of the nanofactor is more pronounced than of the potassium permanganate solution.
3. Stimulative and antifungal action on seeds of aqueous dispersions of silver, copper, bismuth and zinc oxide nanoparticles was detected by the parameters: *seed germination energy* and *sprout length*. The study was carried out on winter wheat (parent varieties *Odessa267* and *Nikonia*, *Accent* and *Select* and their reciprocal hybrids). The effect depends on the genotype of the seed. The maternal effect is revealed—the predominant influence of the maternal form on physiological parameters of the hybrid.
4. After treating the seeds with water dispersions of nanoparticles of bismuth, copper, zinc oxide and a mixture of these nanoparticles, increase of seeds thermal stability is revealed. Winter wheat seeds (parent varieties *Basarabianka* and *M/M3* and their reciprocal hybrids) showed an increase in *seed germination energy* and length of coleoptiles, being exposed to low temperature (+4 °C).
5. In a small-plot experiment in field conditions, an increase by 56% in the productivity of triticale plants (variety *Ingen93*) was obtained as a result of pre-sowing treatment of seeds with water dispersions of silver nanoparticles.

Conflict of Interest The authors declare that they have no conflict of interest.

References

Glushchenko, N.N., Bogoslovskaya, O.A., Olkhovskaya, I.P.: Comparative toxicity of salts and metal nanoparticles and peculiarity of

- their biological action. Materials of the International Scientific and Practical Conference “Nanotechnology and Information Technology—Technology of the XXI century. Moscow, Russia, pp. 93–95 (2006)
- Ling, Y., Yatts, D.: Particle surface characteristics may play an important role in phytotoxicity of alumina nanoparticles. *Toxicol. Lett.* **158**, 122–132 (2005)
- Maslobrod, S.N., Mirgorod, Yu.A., Lupashku, G.A., et al.: Effect of water dispersions of NPBi and NPZnO and weak electromagnetic fields on the viability of parental forms and reciprocal hybrids of winter wheat. *Phys. Technol. Nanomater. Struct. Kursk*, pp. 8–13 (2017)
- Maslobrod, S.N., Mirgorod, YuA, Borodina, V.G., Borshch, N.A.: Influence of aqueous disperse systems with copper and silver nanoparticles on seed germination. *Electr. Process. Mater.* **50**(4), 103–112 (2014)
- Methods of experimental mycology. Kiev: Naukova Dumka. (1982), 550 p
- Mirgorod, Yu.A., Borodina, V.G.: Preparation and bactericidal properties of silver nanoparticles in aqueous tea leaf extract. *Inorg. Mat.* **49**(10), 980–983 (2013)
- Mirgorod, Yu.A., Borsch, N.A., Chekadanov, S.A., Abakumov, P.V., Kondrya, E.P.: Obtaining and characterizing bismuth nanoparticles for optical fibers. In: The 6th International Conference Telecommunications, Electronics and Informatics. Chisinau, Moldova, pp. 219–220 (2018)
- Mirgorod, YuA, Borshch, N.A., Borodina, V.G., Yurkov, GYu.: Production and characterization of cotton fabric modified by copper nanoparticles. *Chem. Ind.* **89**(6), 310–316 (2012)
- Morgalev, YuN, Khoch, N.S., Morgaleva, T.G., et al.: Biotesting of nanomaterials: about the possibility of translocation of nanoparticles into food networks. *Russian Nanotechnol.* **5**(11–12), 131–135 (2010)
- Panichkin, L.A., Raikova, A.P.: The use of metal nanopowders for pre-sowing seed treatment of agricultural products cultures. *News of the Timiryazev Agricultural Academy*, vol. 1, pp. 59–65 (2009)
- Raikova, A.P.: Environmentally friendly flax cultivation technology. In: Materials of the International Scientific-Practical Conference, Vologda, Russia, pp. 15–20 (2004)
- Yatts, D., Ling, Y.: Nanoparticles could have a negative effect on plant growth. *Nanotechn. News* **3**, 86–92 (2007)
- Zhu, H., Han, J., Xiao, J.Q., Jin, Y.: Uptake, translocation and accumulation of manufactured iron oxide nanoparticles by pumpkin plants. *J. Environ. Monit.* **10**, 713–717 (2008)

Photocatalytic Degradation of Methylene Blue with Composite Nanocrystalline TiO₂+ Diatomite

T. Ya. Datsko, V. I. Zelentsov, and D. P. Dvornikov

Abstract

In this study photocatalytic activity of the prepared nano-sized TiO₂-based composite was tested by decolorisation/degradation of Methylene blue (MB) as a model pollutant under UV illumination. The composite was synthesized by a modified heterogeneous hydrolysis method in the presence of diatomite suspension by using TiCl₄ as titania precursor. The photocatalyst was found to be very active for the photocatalytic decomposition of MB in aqueous solution. The percent decolorization in 60 min was 98% with initial MB concentration 53 mg/L. The photocatalytic activity was correlated with physico-chemical properties of the synthesized materials. There is a synergistic effect of grafting titanium dioxide onto the surface of diatomite: the photocatalytic activity of TiO₂ dispersed on the diatomite surface was found to be much higher than of the bulk titania mainly due to the high surface area and uniform distribution of TiO₂ on clay mineral avoiding aggregation.

Keywords

Diatomite • Nanocrystalline TiO₂ • Photocatalytic degradation • Methylene blue

1 Introduction

In recent decades water becomes not only an economic, but also an increasingly important social goods. Drinking water is an important resource for supporting economic and social development. However, the intensification of human activity

has led to the exposure of the aquatic environment to chemical, microbial and biological pollutants, as well as micropollutants: liquid effluents containing toxic substances are waste products from various chemical industrial processes, as well as domestic or agricultural origin.

Now new, economic, more effective methods for pollution control and prevention are required for environmental protection and waste disposal.

Photocatalytic degradation of pollutant molecules from water and environment is an interesting technology due to its low energy, minimum cost and less chemicals used. Currently available chemical and photochemical technology permits the conversion of organic pollutants with a wide range of chemical structures into substances less toxic and/or more readily biodegradable by employing chemical oxidizing agents in the presence of an appropriate catalyst and/or ultraviolet light to oxidize or degrade the pollutant of interest. These technologies known as advanced oxidation processes (AOP) or advanced oxidation technologies (AOT), have been widely studied for the degradation of diverse types of industrial wastewaters [1]. These processes are particularly interesting for the treatment of effluents containing highly toxic organic compounds, for which biological processes may not be applicable. The production of powerful oxidizing agents, such as the hydroxyl radical, is the main objective of most AOP. The hydroxyl radical reacts rapidly and non-selectively with organic compounds by hydrogen abstraction, by addition to unsaturated bonds and aromatic rings, or by electron transfer.

Heterogeneous photocatalysis using semiconductors such as titanium dioxide can be more interesting than conventional methods for removing organic species in the environment. Because the process gradually breaks down the contaminant molecule, no residue of the original material remains and therefore no sludge requiring disposal to landfill is produced. The catalyst itself is unchanged during the process and no consumable chemicals are required. These results in considerable savings and a simpler operation of the equipment involved. Additionally, because the contaminant

T. Ya. Datsko (✉) · V. I. Zelentsov
Institute of Applied Physics, 5, Academiei str., Chisinau,
Republic of Moldova
e-mail: datsko.tatiana@yandex.ru

D. P. Dvornikov
Institute of Electronic Engineering and Nanotechnologies
D. Ghitu, Chisinau, Moldova

is attracted strongly to the surface of the catalyst, the process will continue to work at very low concentrations allowing sub part-per-million consents to be achieved. Taken together, these advantages mean that the process results in considerable savings in the water production cost and keeping the environment clean [2].

Research and development in the area of photocatalysis today is mainly concerned with the topic of active macroscopic surfaces. Initially, the particle surfaces of the photocatalysts themselves suspended in water have been investigated and in the past decades titanium dioxide (TiO_2) has emerged as the most widely used photocatalyst. The experiments showed that TiO_2 under UV-illumination is able to mineralize nearly every organic compound dissolved in water and, consequently, water purification was proposed as a potential application [3].

Recently, TiO_2 which is one of the common photocatalysts has been the most widely investigated due to its low cost, chemical stable and high efficiency properties [4].

Laboratory studies on photocatalysis are typically performed using nano-sized catalyst suspended in the reactor. In these designs the catalyst is evenly dispersed in the solution as it passes through the reactor. The uniform catalyst distribution provides very high surface area to volume ratios with low mass transfer limitations.

However, from the standpoint of large-scale practical application and commercial benefits, titania nanoparticles (TNPs) show disadvantages, which may result in a low photocatalytic efficiency and high cost. For example: strong tendency to aggregate, difficult to be recovered from the solution after treatment and low adsorption capacity. To overcome these drawbacks, recently many researchers are focused on immobilizing TNPs on supports having large surface area and excellent adsorption capacity. This approach may enhance the TNPs distribution in suspension which enables to adsorb and concentrate the target substances. Furthermore, the substances can easily diffuse from the adsorption site to the photocatalytic surface.

Recently, porous non-metal minerals have been taken into account as supports of TiO_2 -based photocatalysts, such as perlite, zeolite and others due to their low costs [5–9].

The support must meet the following requirements: high surface areas, good thermal resistance and mechanical stability, inexpensive, conformable to reactor configuration, and suitable for coating process. The porous materials are involved the adsorption of pollutants on the surface sites, then the photocatalytic degradation of pollutants is improved, simultaneously [10].

From this viewpoint diatomite is one of the most suitable supports for titania nanoparticles covering due to its unique physico-chemical properties.

Diatomite (or diatomaceous earth) are mineral deposits of diatomaceous algae, which accumulated starting from the Miocene. Amorphous silica, a constituent of the diatom frustule, is the main component of diatomite, although variable quantities of other materials (metal oxides, clays, salts (mainly carbonates) and organic matter) may also be present. Diatomite is abundant in many areas of the world and has unique physical characteristics, such as high permeability and porosity (35–65%), small particle size, low thermal conductivity and density and high surface area [11–15].

Thus, a combination of diatomite and nano-sized titanium oxide yields a photocatalyst with a high specific surface and photocatalytic activity [16–20].

This study presents the photocatalytic properties of composite photocatalyst (DDT) based on TiO_2 nanoparticles, immobilized on a porous mineral sorbent as a substrate—diatomite on the example of photodegradation of the generally accepted model organic pollutant—methylene blue (MB) dye.

2 Experimental

2.1 Materials and Chemicals

The diatomite used in the study was supplied from the deposits of Vyshkautsy village in the Orgeev region in Moldova after appropriate cleaning (purification), whose main composition is SiO_2 79.20%, Al_2O_3 5.07%, and Fe_2O_3 2.40%. Other minerals containing—about 3%. Its medium particle size is 7.8 μm , specific surface area 36.45 m^2/g .

Titanium (IV) chloride (TiCl_4 , 99.9%), hydrochloric acid (HCl, 38%) ammonia (NH_4OH , 25%) were purchased from Sigma Aldrich.

2.2 Preparation of TiO_2 /Diatomite Composite

The photocatalyst was prepared via heterogeneous hydrolysis of TiCl_4 as a precursor of TiO_2 in the presence of diatomite at room temperature and normal pressure. The obtained product was further washed, dried and calcined at 450 °C for anatase phase development.

2.3 Material Characterization

Crystal structure, chemical composition and adsorption-structure properties (specific surface area, adsorption pore volume) in nanocomposite and its components were determined with XRD, XPS and EDX analyses and low temperature adsorption of nitrogen. The specific surface area and

adsorption pore volume have been calculated by BET method from nitrogen adsorption—desorption isotherms.

The crystallite size of nano TiO₂ particles was estimated by applying the Debye–Scherer equation [21].

3 Results and Discussion

3.1 Photocatalytic Activity of DDT

MB photodegradation experiments were carried out in a batch mode under UV illumination in a standard reaction flask, volume of 250 mL composed of a medium pressure mercury lamp, 125 W, dominant wavelength 365 nm. The reaction flask was continuously magnetically stirred and tempered to (20 ± 3) °C. For the analysis, 5 mL samples were withdrawn from the illuminated suspensions in certain intervals. After centrifugation of samples at 2500 rpm analysis of solutions on the MB content was carried out by determining the absorbance at the characteristic wavelength of 665 nm using a dual-beam spectrophotometer KFK-2.

In Fig. 1 there are results of dye adsorption without exposure to UV irradiation and when the suspension of DDT + MB is irradiated with UV light.

The data in Fig. 1 show the high activity of the photocatalyst during the decolorizing of the dye. Without mentioning that the adsorption process is a transfer of a substance from one phase (liquid) to another (solid surface) without changing its structure, while photodegradation is accompanied by the mineralization of the organic compound to simple non-toxic compounds, usually water, carbon dioxide and etc. The almost complete degradation took place for dye concentrations 126 mg/L in 250 min. It is worth mentioning that the dye does not occur in such concentrations in the wastewater and the decomposition rate will be

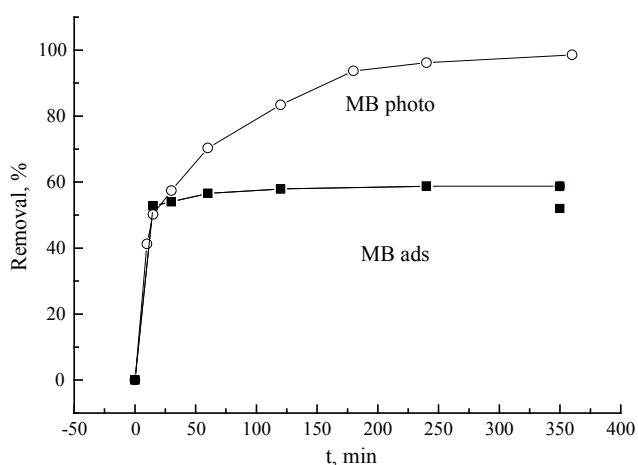


Fig. 1 The MB removal degree by adsorption and through photodegradation on DDT composite. $C_{in} = 126$ mg/L

much higher at an initial concentration of 10 mg/L, and complete decolorization occurs in seconds.

3.2 Effect of Initial Concentration of Dye

The initial concentration of MB influenced the UV light absorption of TiO₂ catalyst. It could be seen from Fig. 2 that MB was degraded slowly at a high concentration. It was noted that the degradation rate of MB solution decreased with the concentration increasing.

As the MB concentration increased, some of the UV light photons were absorbed by the substantial amount of MB molecules. The quantity of effective photons which was absorbed by the surface of catalyst was reduced. The quantity of excited TiO₂ electrons produced by effective photons decreased, making the generating holes lessened. So fewer and fewer holes entered the MB solution and reacted with adsorbed hydroxide ions to produce hydroxyl radicals, the main oxidizing species responsible for the photooxidation of organic compounds [1–4].

3.3 Effect of pH Value of the Solution on the Photo-Degradation

The pH of solution was an important influencing factor for the photocatalytic reaction. Figure 3 shows the effect of pH on TiO₂/diatomite photocatalytic reaction.

The results showed that too high or too low pH were all not suitable for the reaction, the optimum pH was 6.2–6.5. The charge property of diatomite was negative due to the ionization of silicon hydroxyl. When the pH was high, the dye molecule was difficult to contact the diatomite because of repulsive interaction. The decolorizing rate was low in

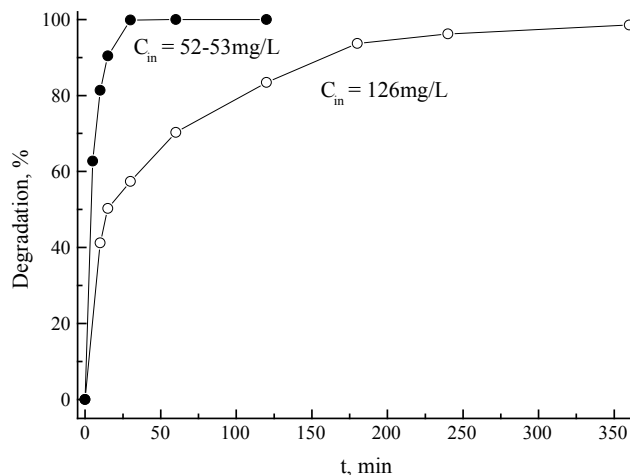


Fig. 2 The effect of initial MB concentration on dye photodegradation rate. pH=6.8, t=20 °C

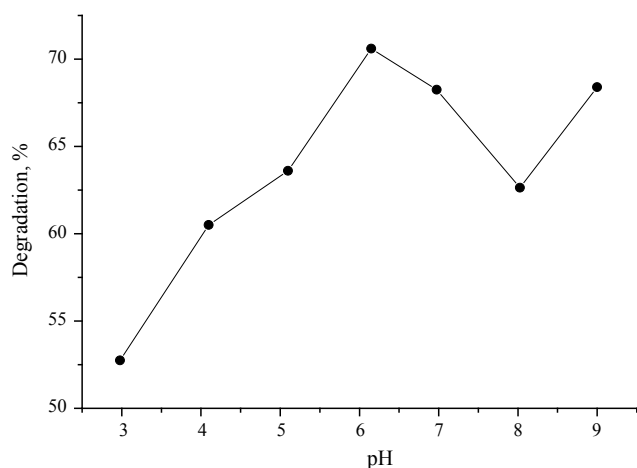


Fig. 3 The dependence of MB degradation on solution pH. $C_{in} = 126$ mg/L

alkaline environment. In strong acidic environment the decolorizing rate was also low, because too many dye molecules adsorbed on the surface of diatomite, O_2 , H_2O , OH^- cannot contact with TiO_2 to produce radicals.

3.4 Effect of DDT Doze on the Photo-Degradation of MB

The effect of catalyst amount on the MB removal was investigated by varying the initial catalyst dosage (0, 1–3.5 g/L) at MB initial concentration of 142 mg/L. The results were shown in Fig. 4.

It was observed that the removal of MB without of catalyst was almost negligible. When the amount of catalyst

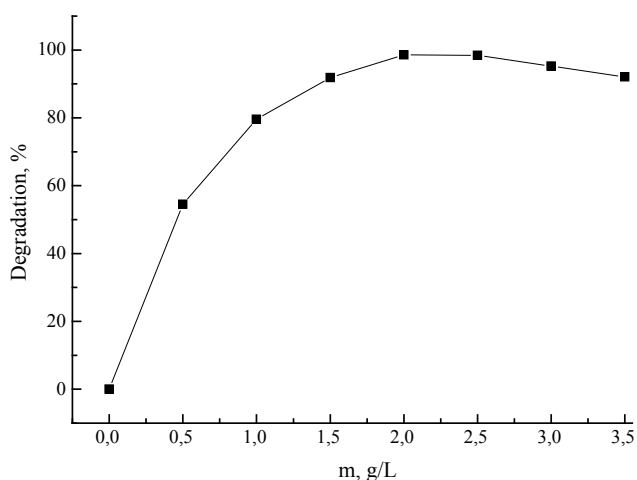


Fig. 4 The effect of DDT dosage on the MB degradation degree. $C_{in} = 142$ mg/L, pH=6.8, $t=20$ °C

increases to 2 g/L, the removal efficiency of MB increases. This trend can be explained by increasing the reaction sites available for MB adsorption and degradation. However, an increase on the catalyst loading to 2.5 g/L and more resulted in a decrease in the degradation ratio.

It can be ascribed to a steric effect: the greater the content of DDT in the suspension, the less active centers are available for UV radiation. Following these observations, it was decided to keep the amount of DDT catalyst TiO_2 at the value of 2 g/L in subsequent photocatalytic degradation experiments.

4 Conclusions

The composite photocatalyst DDT on the base of nanocrystalline TiO_2 and diatomite as carrier has proved its high activity on the photocatalytic degradation of model organic pollutant—methylene blue dye.

The rate of dye destruction depends on initial MB concentration, solution pH and photocatalyst loading.

It was found that at the DDT doze 2 g/L, pH = 6.5–7.0 and the initial MB concentration 53 mg/L under UV irradiation complete MB degradation takes place in 5 min.

Conflict of Interest The authors declare that they have no conflict of interest.

References

1. Sobczyński, A., Dobosz, A.: Water purification by photocatalysis on semiconductors. *Polish J. Env. Stud.* **10**(4), 195–205 (2001)
2. Lee, S.-K., Mills, A.: Detoxification of water by semiconductor photocatalysis. *J. Ind. Eng. Chem.* **10**, 173–187 (2004)
3. Lachheb, H., Puzenat, E., Houas, A., et al.: Photocatalytic degradation of various types of dyes (Alizarin S, Crocein Orange G, Methyl Red, Congo Red, Methylene Blue) in water by UV-irradiated titania. *Appl. Cat. B: Environ.* **39**, 75–90 (2002)
4. Šíma, J., Hasal, P.: Photocatalytic degradation of textile dyes in a TiO_2 /UV system. *Chem. Eng. Trans.* **32**, 79–84 (2013)
5. Song, H., Jiang, H., Liu, X., Meng, G.: Nano TiO_2 deposited on crude mineral and the photoactivity to the degradation of chloroform. *Am. J. Env. Sci.* **2**(2), 60–65 (2006)
6. Rossetto, E., Petkowicz, D.I., dos Santos, J.H.Z., et al.: Bentonites impregnated with TiO_2 for photodegradation of methylene blue. *Appl. Clay Sci.* **48**, 602–606 (2010)
7. De Witte, K., Meynen, V., Mertens, M., et al.: Multi-step loading of titania on mesoporous silica: influence of the morphology and the porosity on the catalytic degradation of aqueous pollutants and VOCs. *Appl. Cat. B: Environ.* **84**, 125–132 (2008)
8. Pucher, P., Benmami, M., Azouani, R., et al.: Nano- TiO_2 sols immobilized on porous silica as new efficient photocatalyst. *Appl. Cat. A: General* **332**(2), 297–303 (2007)
9. Zhang, G.K., Ding, X.M., He, F.S., et al.: Low-temperature synthesis and photocatalytic activity of TiO_2 pillared montmorillonite. *Langmuir* **24**(3), 1026–1030 (2008)

10. Wang, B., Zhang, G., Sun, Z., Zheng, S.: Synthesis of natural porous minerals supported TiO₂ nanoparticles and their photocatalytic performance towards Rhodamine B degradation. *Powder Technol.* **262**, 1–8 (2014)
11. Korunic, Z.: Diatomaceous earths, a group of natural insecticides. *J. Stored Prod. Res.* **34**, 87–97 (1998)
12. Ilija, I.K., Stamatakis, M.G., Perraki, ThS: Mineralogy and technical properties of clayey diatomites from north and central Greece. *Cent. Eur. J. Geosci.* **1**(4), 393–403 (2009)
13. Mohamedbaker, H., Burkitbaev, M.: Elaboration and characterization of natural diatomite in Aktyubinsk Kazakhstan. *Open Miner. J.* **3**, 12–16 (2009)
14. Bakr, H.E.G.M.: Diatomite: its characterization, modifications and applications. *Asian. J. Mater. Sci.* **2**(3), 121–136 (2010)
15. Goren, R., Baykara, T., Marsoglu, M.: Effects of purification and heat treatment on pore structure and composition of diatomite. *Br. Ceramic. Trans.* **101**, 177–180 (2002)
16. Sun, Z., Bai, C., Zheng, S., et al.: A comparative study of different porous amorphous silica minerals supported TiO₂ catalysts. *Appl. Catal. A: General* **458**, 103–110 (2013)
17. Jia, Y., Hana, W., Guoxing, X., Weishen, Y.: Layer-by-layer assembly of TiO₂ colloids onto diatomite to build hierarchical porous materials. *J. Colloid Interface Sci.* **323**, 326–331 (2008)
18. Yu, C.L., Kang, Y., Zhao, W.: Preparation of nano-TiO₂ immobilized onto diatomite micro-particles. *Nanotech. Prec. Eng.* **6**(4), 254–260 (2008)
19. Wang, B., Condi de Godoi, F., Sun, Z., et al.: Synthesis, characterization and activity of an immobilized photocatalyst: natural porous diatomite supported titania nanoparticles. *J. Colloid Interface Sci.* **438**, 204–211 (2015)
20. Toster, J., Harnagea, C., Iyer, K.S., et al.: Controlling anatase coating of diatom frustules by varying the binding layer. *CrystEngComm* **14**, 3446–3450 (2012)
21. Дацко, Т.Я., Зеленцов, В.И.: Композит нано-TiO₂. диатомит: синтез, структура и термостойкость. *ЭОМ* **3**, 1–14 (2019)

Micromechanical Properties and Plastic Deformation Features of the $\text{Pb}_{1-x}\text{Yb}_x\text{Te}$ Ternary Semiconductors

D. Z. Grabco, V. Z. Nicorici, Z. A. Barbos, D. Topal, and O. A. Shikimaka

Abstract

In this paper, the effect of ytterbium (Yb) impurity on the microstructure, the specificity of plastic deformation and the strength properties of PbTe crystals has been studied. The researches have been conducted on a PMT-3 microhardness tester using loads in the range (50–1000) mN. For all applied loads, the $\text{Pb}_{1-x}\text{Yb}_x\text{Te}$ ($x = 0.0025; 0.0075$ and 0.01 at.%) single crystals showed pronounced plasticity and very low hardness values ($H = 0.35\text{--}0.39$ GPa), which is characteristic of compounds containing lead. It was suggested that the deformation of $\text{Pb}_{1-x}\text{Yb}_x\text{Te}$ crystals under microindentation occurs by a dislocation mechanism with some contribution of the structure compaction in the bulk beneath the indentations.

Keywords

$\text{Pb}_{1-x}\text{Yb}_x\text{Te}$ single crystals • Microhardness • Microstructure • Deformation specificity

1 Introduction

Alloys based on the lead telluride, doped with rare earth elements, in particular, ytterbium (Yb), are promising semiconductor materials. Binary PbTe compounds and solid solutions based on them have a narrow band gap and possess of a number of important physical properties, such as, the ability to create a “continuous” matrix of infrared images, the use of a new method of reading information from such a matrix, high radiation resistance. Such unique physical properties of the lead chalcogenides allow them to be widely used as basic elements of sensitive IR photodetectors, in

thermoelectric devices, lasers and strain gages and can significantly increase the capabilities of the devices derived from them [1].

Lead chalcogenides crystallize into a cubic lattice of the NaCl type. The unit cell is a face-centered cube with a coordination number of 6 and a lattice constant of 6.462 Å. It was found that doping of $\text{A}^{\text{IV}}\text{B}^{\text{VI}}$ semiconductors with ytterbium leads to their unusual physical properties [2]. For example, the deep level of ytterbium, in dependence on the alloy composition, can be located both in the band gap and in the valence band, near its ceiling.

At the same time, it was shown that the use of rare-earth elements, in particular ytterbium, as an impurity in semiconductor compounds of the $\text{A}^{\text{IV}}\text{B}^{\text{VI}}$ group leads to a change in stoichiometry and improvement of their crystalline structure [2].

In turn, the state of the crystal structure is inseparably linked with the mechanical properties of the material, which have a great influence on the parameters and reliability of the manufactured semiconductor devices. However, the effect of ytterbium impurity on the strength and plastic properties of the lead chalcogenides is very little studied today [3, 4] and requires further research to use this compound for fabrication of the new semiconductor devices. With this in mind, the task of the paper was to investigate the microstructure, microhardness and plasticity of the $\text{Pb}_{1-x}\text{Yb}_x\text{Te}$ ternary semiconductors and evaluate the mechanism of plastic deformation under microindentation.

2 Experimental

The $\text{Pb}_{1-x}\text{Yb}_x\text{Te}$ single crystals with a variable composition of the rare-earth element Yb ($x = 0.0025, 0.0075,$ and 0.01 at.%) were grown by the vertical Bridgman method. The type of conductivity has been determined using a thermal sound and it was showed that crystals with ytterbium content $x = 0.0025$ had *p*-type conductivity over the entire length of the ingot, and crystals with Yb $x = 0.0075$ and 0.01 had

D. Z. Grabco (✉) · Z. A. Barbos · D. Topal · O. A. Shikimaka
Institute of Applied Physics, 5, Academy str., Chisinau, Republic of Moldova
e-mail: grabco@mail.ru; grabco@phys.asm.md

V. Z. Nicorici · D. Topal
State University of Moldova, Chisinau, Republic of Moldova

p-type conductivity at the beginning of the ingot which then changed to *n*-type. Considering that Yb impurity is distributed unevenly along the ingot, only samples from the initial sections of the ingot were selected for the study.

The microhardness was studied by the quasistatic method using the PMT-3 microhardness tester equipped with a Vickers indenter. Five loads ($P = 50, 100, 200, 500$ and 1000 mN) were applied on the indenter for the microhardness evaluation. At each load 10 imprints were plotted, then the average value was taken to calculate the hardness. The microstructure of the surface of samples and the relief in the indentation neighborhood were studied by the optical microscopy method using XJL-101 and Amplival instruments with digital monitoring and an MII-4 microinterferometer.

3 Results and Discussion

First, we consider the microstructure of the surface of the crystals under study. Figures 1, 2 and 3 shows the surface of the studied $\text{Pb}_{1-x}\text{Yb}_x\text{Te}$ ternary compounds containing different concentrations of ytterbium. Attention is drawn to the substantial increase and complication of defects on the surface of samples as the ytterbium concentration increases. On the surface of $\text{Pb}_{1-x}\text{Yb}_x\text{Te}$ crystals ($x = 0.0025$) there are visible areas of the clean surface between which zones with randomly arranged defects of different types are located, from dark points of a few microns to threadlike defects ranging in length from a few microns to tens and even hundreds of microns (Fig. 1).

The transfer to the $\text{Pb}_{1-x}\text{Yb}_x\text{Te}$ structure ($x = 0.0075$) dramatically changes the surface morphology. Here the number of elongated rod-shaped defects significantly increases (Fig. 2a). The length of these defects varies from several tens to hundreds of micrometers, their thickness is about $(10\text{--}30)$ μm .

Point and filamentary defects, similar to those shown in Fig. 1, for this ytterbium concentration, are clearly visible with a larger magnification in Fig. 2b. Also in Fig. 2b, dark rounded outlines, arranged in rows, are visible. The size of them is about $(20\text{--}50)$ μm . As will be shown below by the method of interference, such defects impart a large waviness of the crystal surface (Fig. 4b).

The general background of the surface on $\text{Pb}_{1-x}\text{Yb}_x\text{Te}$ crystals ($x = 0.01$) somewhat resembles the appearance of the surface of $\text{Pb}_{1-x}\text{Yb}_x\text{Te}$ crystals ($x = 0.0025$), this is especially evident with a larger magnification (Fig. 3b). However, along with this, new defects appeared on the crystal, and namely, rounded and elongated, curved defects of black color, the nature of which is not yet clear.

On the one hand, they can be precipitates of undissolved ytterbium, on the other hand, they can be pores due to

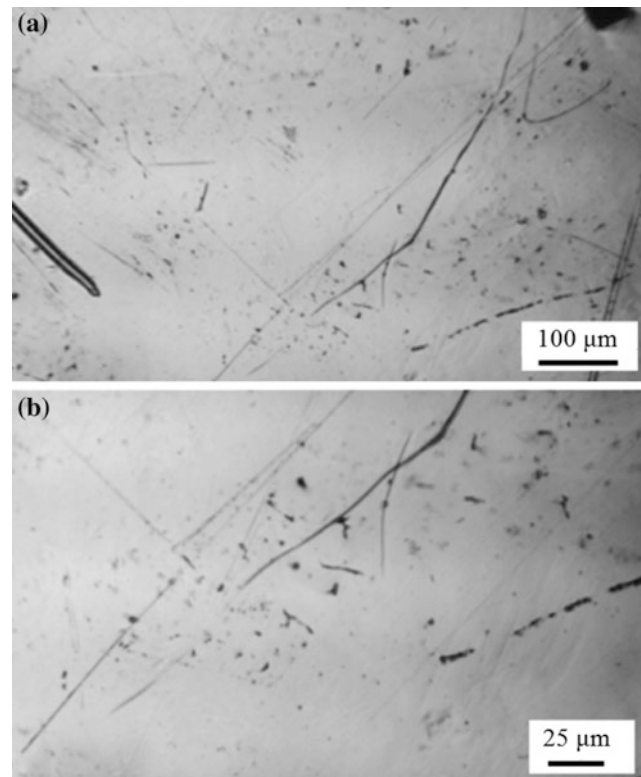


Fig. 1 The microstructure of the $\text{Pb}_{1-x}\text{Yb}_x\text{Te}$ single crystal surface area, ($x = 0.0025$) at two magnifications of the microscope: **a** a small magnification; **b** a big magnification

imperfect structures. The size of these defects varies within $(10\text{--}100)$ μm . More they will be studied in the future.

Interferograms in Fig. 4 demonstrate how the various types of defects presented in Figs. 1, 2 and 3 contribute to the change in the surface relief. It is seen that the smallest curvature of the surface is introduced by point and filamentary defects (Fig. 4a).

The darkest rounded contours make the greatest bend (Fig. 4b). The rounded and elongated curved black defects give a strong but local curving surface. The bending of the strips shows that these defects are located below the surface level (Fig. 4c). Naturally, all types of identified defects to some extent affect the electrophysical properties of the crystals under study and should be taken into account when developing the technology of their growth in order to obtain highly perfect compounds for their successful practical application.

The inhomogeneity of the microstructure of the samples and its complication with an increase in the content of ytterbium also affected the microhardness values. As shown by microindentation tests, all samples showed low hardness values, which is characteristic of compounds containing lead [3, 4]. The dependence of the microhardness on the load for all the investigated crystals is shown in the Fig. 5.

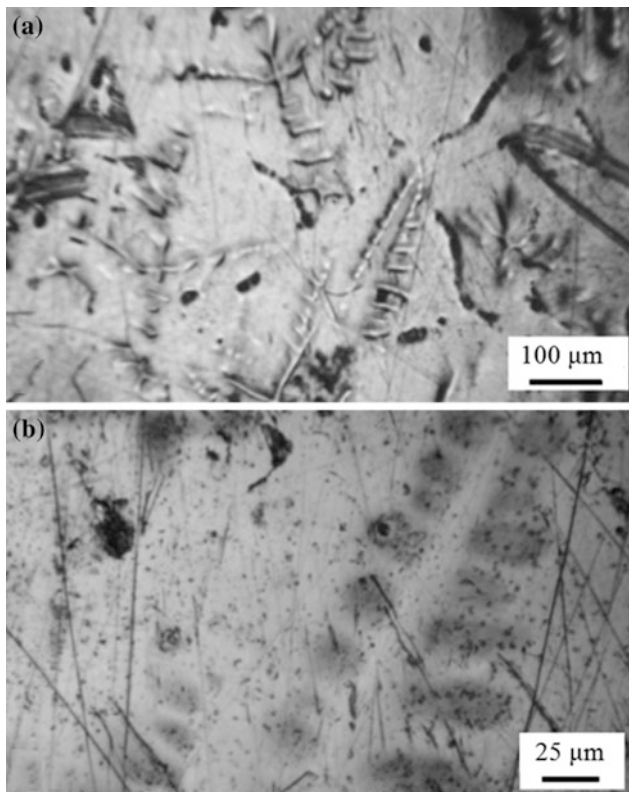


Fig. 2 The microstructure of the $\text{Pb}_{1-x}\text{Yb}_x\text{Te}$ single crystal surface area, ($x = 0.0075$) at two magnifications of the microscope: **a** small magnification; **b** a big magnification

From figure it follows that the dependences $H(P)$ have shown a non-monotonic course. Three branches can be seen on the curves: (i) an increasing section in the region of small loads for curves 2 and 3 (50–100 mN); for curve 1, this part may manifest itself in the load region $P < 50$ mN; (ii) drop-down section in the field of medium loads (100–500 mN) for curves 2, 3 and in the field (50–100 mN) for curve 1; (iii) the section of saturation in the field of large loads (500–1000 mN).

In order to understand what caused the non-monotonous behavior of the $H(P)$ curves and which is the mechanism of deformation of the studied crystals during indentation, the surface relief in the vicinity of the imprints made with different loads was studied. It was shown that at all loads, the $\text{Pb}_{1-x}\text{Yb}_x\text{Te}$ single crystals showed pronounced plasticity and the absence of any signs of brittle fracture.

As an example, indentations and interference patterns around them are shown below. Two loads on the indenter were selected for the $\text{Pb}_{1-x}\text{Yb}_x\text{Te}$ single crystals with different Yb contents: 0.0025 (Fig. 6); 0.0075 (Fig. 7); 0.01 (Fig. 8).

As you can see, the indentations in Figs. 6 and 8 are almost undistorted square. A noticeable deviation from the square shape is noted on the indentations of Fig. 7, which is

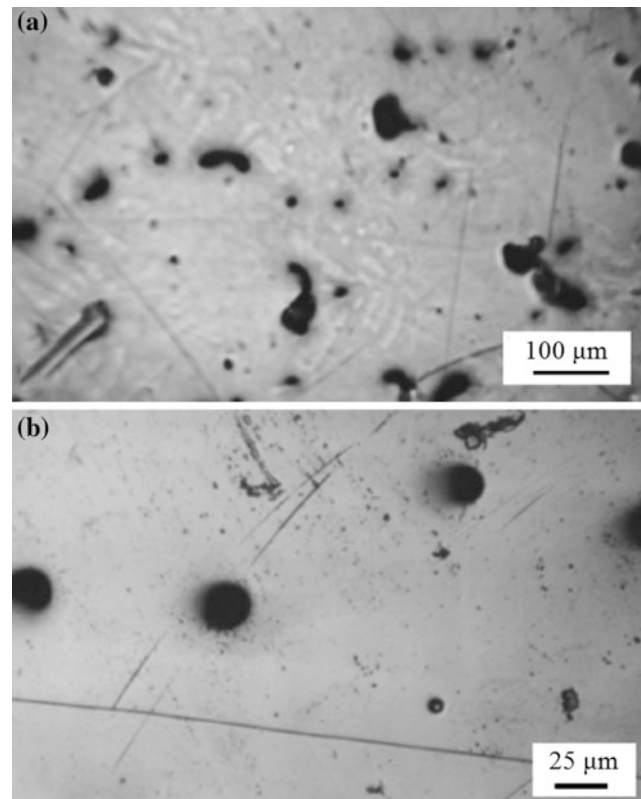


Fig. 3 The microstructure of the $\text{Pb}_{1-x}\text{Yb}_x\text{Te}$ single crystal surface area, ($x = 0.01$) at two magnifications of the microscope: **a** small magnification; **b** a big magnification

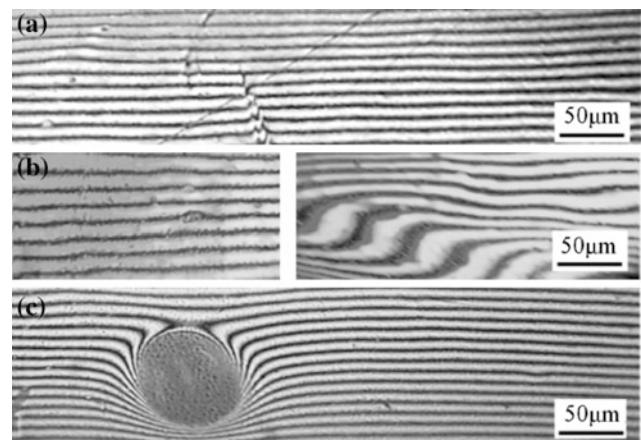


Fig. 4 Interferograms of the surface of $\text{Pb}_{1-x}\text{Yb}_x\text{Te}$ single crystals with different content of Yb, at. %: **a** 0.0025; **b** 0.0075; **c** 0.01

associated with the wave-like surface relief on a crystal with $x = 0.0075$, which was recorded in the above images (Figs. 2 and 4b), and not caused by the specificity of deformation of the indentations.

Thus, the obtained results show that the features of the course of microhardness-load curves can be defined by

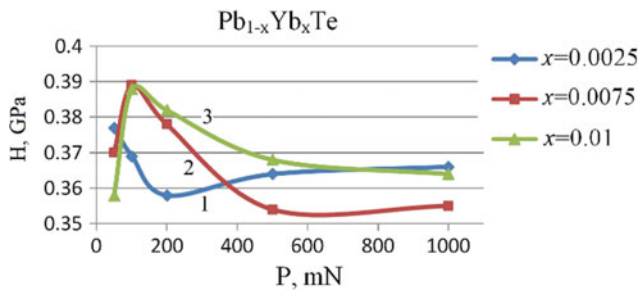


Fig. 5 Dependence of microhardness on the load on $\text{Pb}_{1-x}\text{Yb}_x\text{Te}$ single crystals with different content of Yb, at. %: 1—0.0025; 2—0.0075; 3—0.01

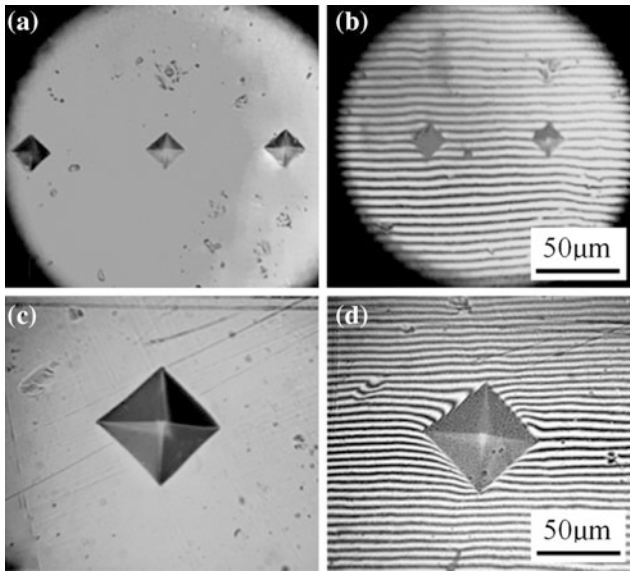


Fig. 6 $\text{Pb}_{1-x}\text{Yb}_x\text{Te}$, $x = 0.0025$. Shape of indentations (a, c) and interferogram of the surface around them (b, d); a, b $P = 50$ mN; c, d $P = 500$ mN

following factors. In the initial parts of the $H(P)$ curves, the lower microhardness on the $\text{Pb}_{1-x}\text{Yb}_x\text{Te}$ sample, $x = 0.0025$, is due to the perfect crystal structure and the lightweight process of the slip of dislocations.

In the area of high loads, its hardness is equal to the hardness of the $\text{Pb}_{1-x}\text{Yb}_x\text{Te}$ sample, $x = 0.01$, in which large local defects are formed, resulting in the remaining structure cleared and approached the structure of the crystal with a low impurity content.

The wave-like relief of the surface of $\text{Pb}_{1-x}\text{Yb}_x\text{Te}$ crystal, $x = 0.0075$, was the cause of the curvature of the shape of indentations with an increase in their size, and as a result, a decrease in hardness compared to the other two crystals.

As regards the mechanism of plastic deformation during the formation of an indentation, one can say the following. The square shape of the indentations is due to the crystal

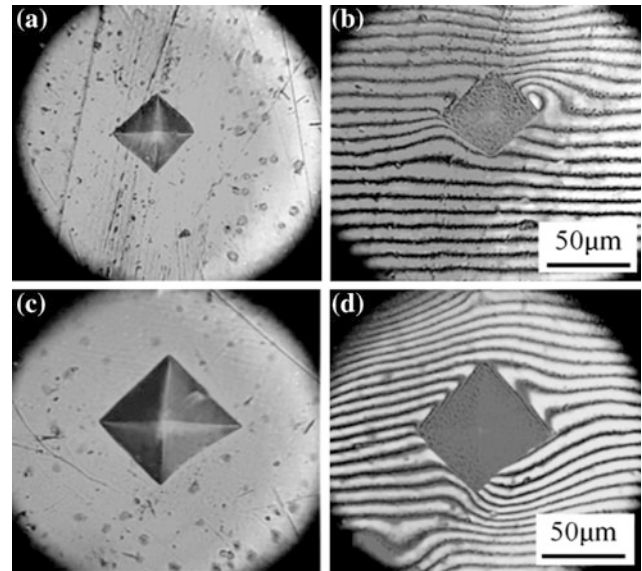


Fig. 7 $\text{Pb}_{1-x}\text{Yb}_x\text{Te}$, $x = 0.0075$. Shape of indentations (a, c) and interferogram of the surface around them (b, d); a, b $P = 200$ mN; c, d $P = 500$ mN

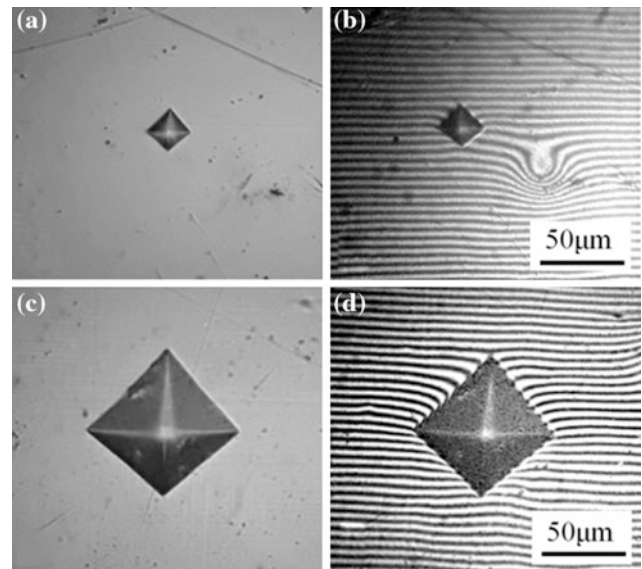


Fig. 8 $\text{Pb}_{1-x}\text{Yb}_x\text{Te}$, $x = 0.01$. Shape of indentations (a, c) and interferogram of the surface around them (b, d); a, b $P = 50$ mN; c, d $P = 500$ mN

structure of the NaCl type, which has low anisotropic properties and characteristic sliding elements.

From Figs. 6d and 8d it can be seen that around the indentations the material is slightly raised in the form of pile-ups (otherwise, hillocks), which descend slightly as it approaches the indentation creating small sink-ins. The occurrence of pile-ups should be due to the dislocation mechanism of deformation. However, the magnitude of this

pile-up is not so large as to compensate for the amount of material removed from the indentation.

Therefore, it should be assumed that only a certain fraction of the transferred material forms plastic pile-up around the indentation. The other part may be due to compaction of the structure *in the bulk beneath* the indentation. This assumption is based on the previously obtained results in the indentation of a large number of ionic, ionic-covalent and covalent crystals, including galena single crystals (PbS) [5–8].

4 Conclusions

In this paper, the microstructure, the specificity of plastic deformation and the strength properties of $\text{Pb}_{1-x}\text{Yb}_x\text{Te}$ single crystals with different ytterbium contents were studied. In a wide range of loads, the samples showed pronounced plasticity and low microhardness values ($H = 0.35\text{--}0.39$ GPa), which is characteristic of compounds containing lead. The opinion was expressed that the deformation of $\text{Pb}_{1-x}\text{Yb}_x\text{Te}$ crystals by the microindentation method proceeds by a dislocation mechanism with some contribution to the compaction of the structure in the bulk beneath the indentation.

Acknowledgements This work was supported by the Research Project of the Institute of Applied Physics of RM (Project no. **15.817.02.06A**).

Conflict of Interest The authors declare that they have no conflict of interest.

References

1. Волков, Б.А., Рябова, Л.И., Хохлов, Д.Р.: Примеси с переменной валентностью в твердых растворах на основе теллурида свинца. УФН, т. 172, 8, 875–906 (2002)
2. Чернова, Н.А.: Примесные состояния иттербия в сплавах на основе теллурида свинца/Диссертация на соискание ученой степени кандидата физ.-мат. наук. М., МГУ (2001). <http://www.disser-cat.com/content/primesnye-sostoyaniya-itterbiya-d-splavakh-na-osnove-tellurida-svintsa>
3. Nicorici, V., Grabco, D., Barbos, Z. et al.: Micromechanical properties of the $\text{Pb}_{1-x}\text{Yb}_x\text{Te}$ ternary semiconductors. In: Abstracts of 9th International Conference MSCMP-2018, Chisinau, Moldova, 163 (2018)
4. Грабко, Д., Барбос, З., Попа, М., Никорич, В.: Электрофизические свойства кристаллов $\text{Pb}_{1-x}\text{Yb}_x\text{Te}$. Rezumat al Conf. Stiint. "Integrare prin cercetare si inovare", Chisinau, Moldova, pp. 286–288 (2018)
5. Chaudhri, M.M.: Dislocations and Indentations. Nabarro, F.R.N., Hirth, J.P. (eds.), pp. 450–550. Cavewnsish Laboratory, UK (2004)
6. Боярская, Ю.С., Мелентьев, И.И., Грабко, Д.З.: О природе анизотропии твердости на грани (001) монокристаллов PbS и CaF_2 . Физика 2, 84–88 (1971)
7. Боярская, Ю.С., Грабко, Д.З., Кац, М.С.: Физика процессов микроиндентирования, ред. р. 294с. М. Вальковская, Кишинев, Штиинца (1986)
8. Grabco, D., Shikimaka, O., Harea, E.: Translation-rotation plasticity as basic mechanism of plastic deformation in macro-, micro- and nanoindentation processes. J. Phys. D: Appl. Phys. **41**(9), 074016 (2008)

Quantum Interferences with Equidistant Three-Level Quantum Wells

V. Ceban and M. A. Macovei

Abstract

A three-level ladder-type equidistant quantum-well with perpendicular transition dipoles, tuned in resonance with an optical cavity have been investigated in the good cavity limit. Under the laser pumping, a quantum interference phenomena occurs. This phenomenon is controlled via the laser intensities and phases and may be tuned in order to destructively interfere. The cavity mean photon number vanishes under these conditions.

Keywords

Quantum interferences • Quantum-wells

1 Introduction

Various effects in quantum optics are originating from the quantum interference phenomena [1]. The nature of this kind of phenomena is related to a broad palette of various cases of quantum superposition. Fundamental phenomena as gain without inversion have been reported to occur with three-level atomic systems [2] and electromagnetically induced transparency have been observed in [3]. The possibility to control how a system interferes gives an additional degree of freedom in the manipulation of this phenomenon. One method of control is to explore the phase dependency of the interfering system. For example, a mechanism of manipulation of collective fluorescence of a pumped collective sample of three-level emitters via quantum interferences have been proposed in [4]. The phase difference of the two pumping lasers have influenced the decrease and even lead to the cancelation of the sample's fluorescent emission. The phase dependency of the spontaneous emission of a four-level emitter can be tuned in order to cancel the atomic

decay, as reported in [5]. Vacuum induced quantum interferences can be controlled via the phase difference of the pumping lasers [6].

In this paper, one investigates the case when a three-level equidistant ladder-type emitter is placed in an optical cavity. Quantum-wells are particularly good candidates for this type of emitters as they can be engineered as equidistant three-level emitters [7, 8], a condition which is difficult to achieve with real atoms. The emitter is pumped via two lasers with different phases. Each laser is applied resonantly to one of the two quantum-well transitions. Under the laser driving, the energetic levels of the quantum-well are subject to the dynamical Stark splitting effect [9]. Various transitions with different transition frequencies appear among the split energy levels.

As the quantum-well architecture has equidistant energy levels and orthogonal transition dipoles, the optical cavity couples to both of the emitter transitions in the good cavity limit. As under the laser pumping the quantum-well is prepared in a superposition of states, the cavity indistinguishably interacts with the upper and the lower transitions. These indistinguishable amplitudes of the cavity interaction with the different quantum-well transitions lead to the interference effect. In order to solve the system dynamics, one was able to significantly reduce the complexity of the quantum dynamics without losing much of generality of the problem by tuning the cavity in resonance with the degenerate transition frequency of the quantum-well.

As the interaction amplitudes may be influenced by the laser intensities and phases, one is able to achieve strong destructive quantum interferences. Therefore, the cavity field may be emptied for a well-chosen laser phase difference as the laser phases are transferred to the interactional amplitudes. In this case, the pumped QW spontaneously decays in all directions except the cavity. Furthermore, this behavior of the interfering quantum-well-cavity system is associated with a quantum switch, where the income laser signals may switch the cavity field on and off by varying their phase difference (Fig. 1).

V. Ceban (✉) · M. A. Macovei
Institute of Applied Physics, 5, Academiei str., Chişinău, Moldova
e-mail: victor.ceban@phys.asm.md

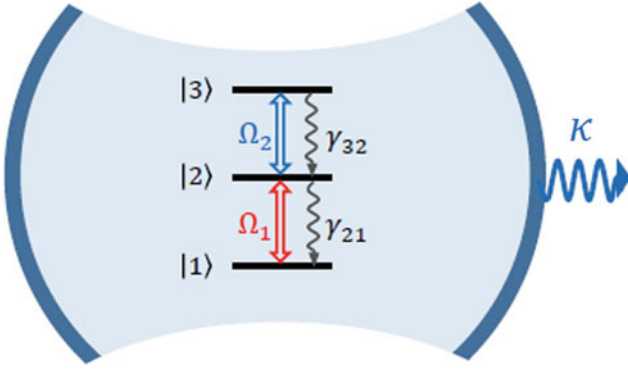


Fig. 1 The schematic of the model

2 The Model

The QW is described by its bare-states $|i\rangle, i = \{1, 2, 3\}$ and their corresponding eigen energies $\hbar\omega_i$. The quantum well free Hamiltonian is expressed as a summation performed over all the three atomic eigen energies. The atomic operators of the three-level emitter are defined as $S_{ij} = |i\rangle\langle j|, \{i, j\} = \{1, 2, 3\}$ and obey the commutation rule $[S_{\alpha\beta}, S_{\alpha'\beta'}] = \delta_{\beta\beta'}S_{\alpha\alpha'} - \delta_{\alpha'\alpha}S_{\beta'\beta}$.

The most energetic level $|3\rangle$ may spontaneously decay to the intermediate level $|2\rangle$ with a emission rate γ_{32} , while the last one decays to the ground level $|1\rangle$ with a rate γ_{21} .

The laser pumping of the QW is obtained by applying different lasers for each atomic transition. The laser driving the lower transition is described by its frequency ω_{L1} and phase ϕ_1 , while the laser applied on the upper transition is given by ω_{L2} and ϕ_2 . The quantum-well pumping is described via semi-classic interactions given by the Rabi frequencies Ω_1 and Ω_2 for the lower and upper transitions, respectively. The corresponding interaction Hamiltonian is given by semi-classical interaction terms, adapted for each of the atomic transition.

The cavity-quantum-well interaction is also expressed via two separate Hamiltonian terms, one for each of the transitions. The two corresponding terms are described by a fully quantum treatment given by the interaction part of the Jaynes-Cummings model [10]. The two terms are described by the coupling constants g_1 and g_2 . The first coupling constant represents the quantum interaction of the optical resonator with the lower transition, while the second one—with the upper transition.

The quantized cavity field is defined by its frequency ω_c and the bosonic creation operator a^\dagger and annihilation operator a . The bosonic operators commute as $[a, a^\dagger] = 1$. The optical cavity is dumped by an environmental electromagnetic vacuum reservoir at a leaking rate κ .

The system Hamiltonian is defined as:

$$\begin{aligned}
 H = & \hbar\omega_c a^\dagger a + \sum_{i=1}^3 \hbar\omega_i S_{ii} \\
 & + \hbar\Omega_1 \left(S_{12} e^{i(\omega_{L1}t + \phi_1)} + S_{21} e^{-i(\omega_{L1}t + \phi_1)} \right) \\
 & + \hbar\Omega_2 \left(S_{23} e^{i(\omega_{L2}t + \phi_2)} + S_{32} e^{-i(\omega_{L2}t + \phi_2)} \right) \\
 & + i\hbar g_1 (a^\dagger S_{12} - S_{21} a) \\
 & + i\hbar g_2 (a^\dagger S_{23} - S_{32} a),
 \end{aligned} \quad (1)$$

where the first two terms describe the single-mode free cavity field and the quantum-well free Hamiltonians. As mentioned previously, the external laser fields and the cavity field interact with both transitions of the quantum-well and every interaction is defined via separate terms according to each transition. Thus, the next two terms of the Hamiltonian represent the interaction of the quantized cavity with the atom whereas the last two terms describe the laser-atom semi-classical interaction.

The system's quantum dynamics is given by the master equation for the density operator ρ as:

$$\dot{\rho} = -\frac{i}{\hbar} [H, \rho] + \frac{\kappa}{2} \mathcal{L}(a) + \frac{\gamma_{32}}{2} \mathcal{L}(S_{23}) + \frac{\gamma_{21}}{2} \mathcal{L}(S_{12}), \quad (2)$$

where, on the right-hand side of the equation, the first term represents the coherent part based on the von-Neumann equation, while the other terms describe the damping phenomena. The second term of the equation represents the cavity photon leaking term, which appears due to the interaction of the optical resonator with the environmental electromagnetic vacuum. The last two terms represent the spontaneous emission of the two excited states, with two different rates corresponding to each of the transitions of the quantum-well. In the case of a multi-level atomic structure, as in our case, the reservoir theory may be applied to each transition separately. Therefore, the spontaneous decay dynamics will be defined by separate damping terms adapted for each of the possible decay transitions.

The damping effects are expressed by the Liouville super-operator \mathcal{L} , which acts on a given system operator σ as $\mathcal{L}(\sigma) = 2\sigma\rho\sigma^\dagger - \sigma^\dagger\sigma\rho - \rho\sigma^\dagger\sigma$.

A direct implementation of the system Hamiltonian of Eq. (1) into the master equation of Eq. (2) does not allow one to accurately solve it without adopting drastic approximations to the system dynamics. A set of various transformations shall be applied to the system dynamics in order to obtain a solvable master equation, without losing much of the generality of the problem.

A first step consists in setting the pumping laser frequencies in resonance with the two transitions of the equidistant three-level emitter, i.e., $\omega_{L1} = \omega_2 - \omega_1$ and

$\omega_{L2} = \omega_3 - \omega_2$. As the transition frequencies of the quantum-well are equal, one may further note $\omega_{L1} = \omega_{L2} = \omega_L$. This allows the free quantum-well Hamiltonian term to vanish when one goes in the frame rotating with ω_L .

Next, one transfers the phase term from the laser-quantum-well interaction terms to the cavity-quantum-well interaction terms by applying the phase-dependent exponential terms to the atomic operators. This allows one to bring the Hamiltonian term to an easy diagonalizable form of the quantum-well-lasers subsystem terms.

$$H = \hbar(\omega_c - \omega_L)a^\dagger a + \hbar\Omega_1(S_{12} + S_{21}) + \hbar\Omega_2(S_{23} + S_{32}) + i\hbar g_1(a^\dagger S_{12}e^{-i\phi_1} - e^{i\phi_1}S_{21}a) + i\hbar g_2(a^\dagger S_{23}e^{-i\phi_2} - e^{i\phi_2}S_{32}a) \quad (3)$$

Within this form, one adopts the semi-classical dressed-state transformation according to the dynamical Stark splitting effect of the quantum well under the laser pumping [9]. The new Hermitian base is defined considering the pumped quantum-well subsystem eigenfunctions obtained after the diagonalization of the Hamiltonian part corresponding to this sub-system. The new atomic wavefunction basis vectors, i.e., the dressed-states, are defined as:

$$\begin{aligned} |1\rangle &= -\frac{1}{\sqrt{2}}\cos\theta|-\rangle - \sin\theta|0\rangle + \frac{1}{\sqrt{2}}\cos\theta|+\rangle, \\ |2\rangle &= \frac{1}{\sqrt{2}}|-\rangle + \frac{1}{\sqrt{2}}|+\rangle, \\ |3\rangle &= -\frac{1}{\sqrt{2}}\sin\theta|-\rangle + \cos\theta|0\rangle + \frac{1}{\sqrt{2}}\sin\theta|+\rangle, \end{aligned} \quad (4)$$

Here, the angle θ is defined as $\theta = \tan^{-1}(\Omega_2/\Omega_1)$ and the generalized Rabi frequency is given as $\Omega = \sqrt{\Omega_1^2 + \Omega_2^2}$.

Within the dressed-state basis, the interaction picture allows one to distinguish the cavity-emitter interaction terms according to the dynamic Stark splitting which occurs under the laser pumping of the two transitions. By tuning the optical cavity with one of the possible transitions one is able to apply a secular approximation to the system Hamiltonian. This approximation is valid as long as $\frac{\Omega_1}{\Omega} \ll 1$ and $\frac{\Omega_2}{\Omega} \ll 1$.

In this study one tunes the optical cavity in resonance with the emitter's bare-state degenerate transition frequency, i.e., $\omega_c = \omega_2 - \omega_1 = \omega_3 - \omega_2$. As the two lasers are set in resonance with the emitter, the cavity frequency may be defined as $\omega_c = \omega_L$.

The resonant Hamiltonian term within the dressed-state basis and within the interaction picture, is given as:

$$H = i|g\rangle\langle g|(a^\dagger e^{i\Psi} - e^{-i\Psi}a)R_z, \quad (5)$$

where

$$g = \frac{1}{2}(g_2 \sin\theta e^{-i\phi_2} + g_1 \cos\theta e^{-i\phi_1}) \quad (6)$$

and $\Psi = \arg(g)$. Note that the new set of atomic dressed-state operators is defined as $R_{ij} = |i\rangle\langle j|$, $\{i, j\} = \{-, 0, +\}$, $R_z = R_{++} - R_{--}$ and obey similar commutation relations as the bare-state operators.

Within the dressed-state basis, the master equation is defined as:

$$\begin{aligned} \dot{\rho} &= -\frac{i}{\hbar}[H, \rho] + \frac{\kappa}{2}\mathcal{L}(a) + \frac{\gamma_{32}\cos^2\theta}{4}(\mathcal{L}(R_{-0}) + \mathcal{L}(R_{+0})) \\ &+ \frac{\gamma_{32}\sin^2\theta + \gamma_{21}\cos^2\theta}{8}(\mathcal{L}(R_z) + \mathcal{L}(R_{+-}) + \mathcal{L}(R_{-+})) \\ &+ \frac{\gamma_{21}\sin^2\theta}{4}(\mathcal{L}(R_{0-}) + \mathcal{L}(R_{0+})). \end{aligned} \quad (7)$$

Here, a secular approximation was performed in the spontaneous emission terms by neglecting the time-dependent rapidly oscillating terms. This approximation is valid as long as $\frac{\gamma_{32}}{\Omega} \ll 1$ and $\frac{\gamma_{21}}{\Omega} \ll 1$.

The master equation of Eq. (7) using the resonant Hamiltonian expression of Eq. (5), is solved by building the equation of motion of the parameters of interest. In this study, the quantum interference phenomena are observed by investigating the steady-state behavior of the cavity mean photon number given as $n = a^\dagger a$. Its equation of motion is found from a system of coupled linear differential equations given as:

$$\begin{aligned} \frac{\partial \langle a^\dagger a \rangle}{\partial t} &= |g|\langle a^\dagger R_z \rangle + \langle a R_z \rangle - \kappa \langle a^\dagger a \rangle, \\ \frac{\partial \langle a^\dagger R_z \rangle}{\partial t} &= |g|\langle R_z^2 \rangle - \left(\frac{\kappa}{2} + 2\gamma_a + \gamma_d\right)\langle a^\dagger R_z \rangle, \\ \frac{\partial \langle a R_z \rangle}{\partial t} &= |g|\langle R_z^2 \rangle - \left(\frac{\kappa}{2} + 2\gamma_a + \gamma_d\right)\langle a R_z \rangle, \\ \frac{\partial \langle R_z^2 \rangle}{\partial t} &= -(2\gamma_c + \gamma_d)\langle R_z^2 \rangle + 2\gamma_c. \end{aligned} \quad (8)$$

where $\gamma_a = (\gamma_{32}\sin^2\theta + \gamma_{21}\cos^2\theta)/4$, $\gamma_b = (\gamma_{21} + \gamma_{32} - 3\gamma_{32}\cos^2\theta)/4$, $\gamma_c = \gamma_{32}\cos^2\theta/2$ and $\gamma_d = \gamma_{21}\sin^2\theta/2$.

Within the steady-state regime, the system of equation is solved and the analytic expression of the cavity mean photon number is given as:

$$\langle n \rangle = \langle a^\dagger a \rangle = \frac{4|g|^2\gamma_c}{\kappa\left(\frac{\kappa}{2} + 2\gamma_a + \gamma_d\right)(2\gamma_c + \gamma_d)}. \quad (9)$$

3 Results and Discussions

When the cavity is set in resonance with the bare-state transition, an effective coupling among the emitter and the cavity appears. The destructive nature of these interferences is expressed in the analytical form of the effective coupling constant g of Eq. (6), when one interaction amplitude cancels the other. This condition is achieved when the amplitudes are equal, i.e., $g_1/g_2 = \Omega_2/\Omega_1$ and interfere destructively, i.e., $\phi_2 = \phi_1 + (2m+1)\pi, m \in \mathbb{Z}$. This condition is verified in Fig. 2, where one shows the cavity mean photon number n as function of Rabi frequencies ratio Ω_2/Ω_1 and laser phase ϕ_2 , while keeping the phase of the laser pumping the lower transition at a fixed value of $\phi_1 = 0$. The other system parameters are $\gamma_{32} = \gamma_{21} = \gamma$, $g_1/\gamma = 4$, $g_2/\gamma = 2$ and $\kappa/\gamma = 10^{-3}$.

The two deeps in the surface of n corresponds well to the previously mentioned interference condition with $g_1/g_2 = \Omega_2/\Omega_1 = 2$ and $\phi_2 = \phi_1 + \pi$ or $\phi_2 = \phi_1 + 3\pi$. In this particular points, one observes an effective decoupling of the quantum well from the optical cavity. The cavity is empty, although the atom is pumped and spontaneously emits photons in all other directions except the cavity.

The currently investigated system allows one to switch the cavity field on and off via a change in the input laser parameters. This particularity of the system can be used for a potential application for quantum network circuit elements [11]. While on-chip quantum circuits allow a good integration of semiconductor artificial-atoms-based systems [12].

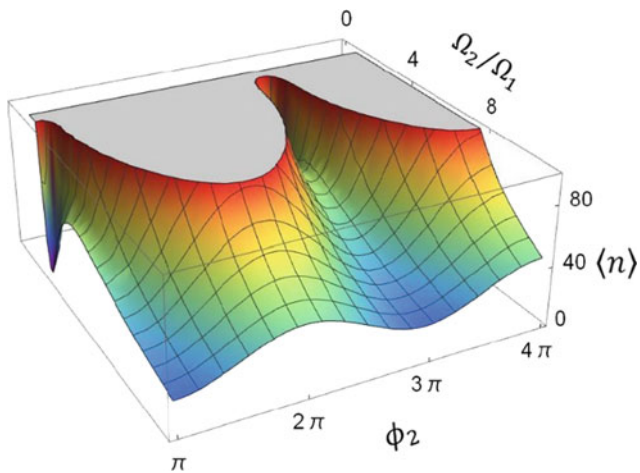


Fig. 2 The cavity mean photon number n as functions of the laser phase ϕ_2 and Rabi frequencies ratio Ω_2/Ω_1

4 Conclusions

We have investigated a system made of a pumped three-level ladder-type equidistant quantum-well interacting with an optical cavity. When the cavity is tuned in resonance with the degenerate transition frequency of the quantum-well, quantum interference occurs. The intensities and the phase difference of the pumping lasers are used to destructively tune the quantum interference phenomena. When the two indistinguishable interaction amplitudes are tuned to be equal and dephased by half period, the cavity field vanishes. An empty cavity field is obtained in a steady-state regime, although the atom is continuously pumped.

Previously, one has reported that the field cancellation may be achieved by tuning the cavity in resonance with the external sidebands [13] and that this type of interferences can be also controlled via the phase difference of the pumping lasers [14]. In this study, the field cancellation is obtained for the cavity tuned in resonance with the free emitter transition frequency, which does not depend on the ac-Stark splitting. Therefore, one does not have to re-tune the cavity when varying the laser intensities. Here, the laser parameters are used only to tune the interferences destructively by choosing a suitable intensity ratio and phase difference.

Conflict of Interest The authors declare that they have no conflict of interest.

References

1. Scully, M.O., Zubairy, M.S.: Quantum Optics. Cambridge University Press, Cambridge (1997)
2. Kocharovskaya, O.A., Khanin Ya, I.: Coherent amplification of an ultrashort pulse in a three level medium without a population inversion. Sov. Phys. JETP Lett. **48**, 630 (1988)
3. Boller, K.-J., Imamoglu, A., Harris, S.E.: Observation of electromagnetically induced transparency. Phys. Rev. Lett. **66**, 2954 (1991)
4. Macovei, M., Evers, J., Keitel, C.H.: Phase control of collective quantum dynamics. Phys. Rev. Lett. **91**, 233601 (2003)
5. Paspalakis, E., Knight, P.L.: Phase control of spontaneous emission. Phys. Rev. Lett. **81**, 293 (1997)
6. Macovei, M.A.: Enhancing superfluorescence via decay interference. J. Phys. B: At. Mol. Opt. Phys. **40**, 387 (2007)
7. Sadeghi, S.M., Leffer, S.R., Meyer, J.: Quantum interferences and gain processes in optically-driven n-doped quantum wells with Ξ configurations. Opt. Commun. **151**, 173 (1998)
8. Rosencher, E., Bois, Ph: Model system for optical nonlinearities: asymmetric quantum wells. Phys. Rev. B **44**, 11315 (1991)

9. Dynes, J.F., Frogley, M.D., Beck, M., Faist, J., Phillips, C.C.: ac Stark splitting and quantum interference with intersubband transitions in quantum wells. *Phys. Rev. Lett.* **94**, 157403 (2005)
10. Jaynes, E.T., Cummings, F.W.: Comparison of quantum and semiclassical radiation theories with application to the beam maser. *Proc. IEEE* **51**, 89109 (1963)
11. Kimble, H.J.: The quantum internet. *Nature* **453**, 1023 (2008)
12. Houck, A.A., Türeci, H.E., Koch, J.: On-chip quantum simulation with superconducting circuits. *Nat. Phys.* **8**, 292 (2012)
13. Ceban, V., Macovei, M.A.: Cavity quantum interferences with three-level atoms. *J. Opt. Soc. Am. B* **33**, 942 (2016)
14. Ceban, V.: Phase-dependent quantum interferences with three-level artificial atoms. *Rom. J. Phys.* **62**, 207 (2017)

Luminescence Properties of a Novel Eu³⁺ Dinuclear Coordination Compound

V. I. Verlan, I. P. Culeac, O. Bordian, V. E. Zubareva, I. Bulhac, M. S. Iovu, M. Enachescu, N. A. Siminel, and V. V. Nedelea

Abstract

The paper presents experimental results on a novel Eu³⁺ dinuclear coordination compound [Eu(μ₂-OC₂H₅)(NO)₃(phen)]₂·phen with high emission quantum yield. The complex has been characterized by photoluminescence (PL) spectroscopy. The absolute PL quantum yield, and the sensitization efficiency were determined to be 49.2% and 78.7% respectively.

Keywords

European complex • Dinuclear compound • Luminescence • Quantum yield

1 Introduction

Eu³⁺ based coordination complexes present interest for a large number of applications in optoelectronics, biochemistry, medicine, etc. [1–5]. The goal of research described in this report was synthesis and characterisation of a novel Eu³⁺ dinuclear coordination compound bis[(μ₂-etoxi)(benzoyl trifluoroacetato)(nitrate)(1,10-phenantroline)europium(III)] 1,10-phenantroline, hereafter [Eu(μ₂-OC₂H₅)(NO)₃(phen)]₂·phen, with high emission quantum yield. Potential application of the new dinuclear complexes refers to optoelectronics, medicine, biology, biochemistry, etc.

V. I. Verlan · I. P. Culeac (✉) · O. Bordian · M. S. Iovu · N. A. Siminel · V. V. Nedelea
Institute of Applied Physics, No 5 Academiei Str., 2028 Chisinau, Republic of Moldova
e-mail: ion.culeac@gmail.com

V. E. Zubareva · I. Bulhac
Institute of Chemistry, Chisinau, Republic of Moldova

M. Enachescu
University Politehnica Bucharest, Bucharest, Romania

2 Methods for Characterisation of the Complex

The dinuclear complex [Eu(μ₂-OC₂H₅)(NO)₃(phen)]₂·phen have been synthesized as described elsewhere [6, 7]. The molecular structure of the complex is illustrated in Fig. 1. Samples were characterized by PL spectroscopy. PL emission spectra were recorded using different excitation sources with a MDR-23 single emission monochromator. A pulsed nitrogen laser at 337 nm with repetition rate 10–100 Hz and the pulse width 10 ns was used for excitation of Eu³⁺ ions in the charge transfer band. Another excitation light source was a Thorlabs LD at 405 nm. The emitted PL signal was detected with a Hamamatsu phomultiplier module H8259-01 with a counting unit C8855-01 connected to a PC. Fluorescence measurements were performed in a photon counting mode. The spectral resolution for PL spectra measurements was as low as 0.125 nm. For both the PL spectra and the quantum yield measurements the emission spectra were corrected for the instrument spectral sensitivity.

PL intensity time decay was recorded using nitrogen pulsed laser at the repetition rate 10 Hz. The PMT module Hamamatsu H8259-01 with the pulse-counter C8855-01 provides time-resolved measurements with the time resolution 50 ns, which was sufficient for registration of the Eu³⁺ complex PL relaxation in the range 50 μs–10 ms.

Measurement of the photoluminescent quantum yield was performed using the absolute method of integration sphere [8–10]. The integration sphere was 150 mm in diameter, and the inner spherical cavity wall was coated with MgO by burning magnesium ribbon in an O₂ stream.

The quantum yield Q (the quantum efficiency) is commonly defined as the ratio of the number of emitted photons N_{em} to the number of absorbed photons N_{abs} [1, 8]:

$$Q = N_{em}/N_{abs} \quad (1)$$

Figure 2 illustrates experimental approach for measuring the absolute quantum yield. Firstly, the excitation spectrum

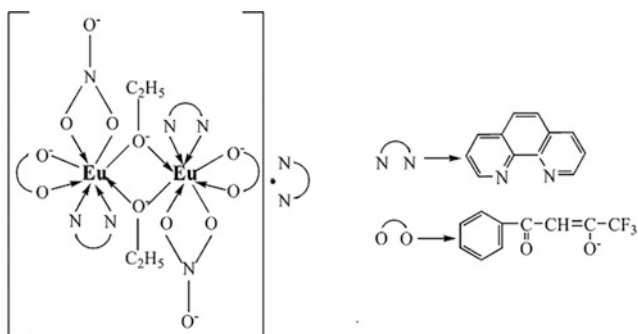


Fig. 1 Illustration of the molecular structure of the dinuclear complex $[\text{Eu}(\mu_2\text{-OC}_2\text{H}_5)(\text{btfa})(\text{NO})_3(\text{phen})]_2 \cdot \text{phen}$

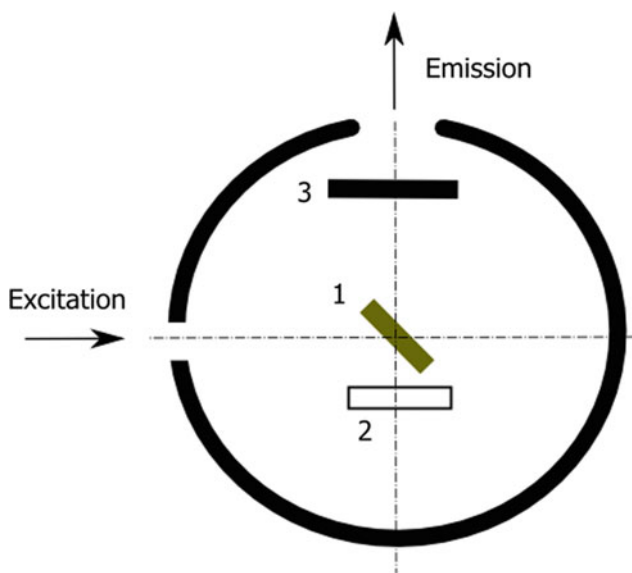


Fig. 2 Schematic illustration of sample in the integrating sphere: 1—sample under direct laser excitation; 2—sample under diffuse laser excitation; 3—baffle

is registered when the substrate without the sample is placed under direct excitation beam in the sample holder. The total area under this spectrum (S_0) is proportional to the number of excitation photons minus those absorbed in the substrate. In the next step we registered the excitation spectrum when the measured sample itself (the substrate with PL compound) is placed under excitation beam in the sample holder. The total area under this spectrum (S_1) is proportional to the number of excitation photons minus those absorbed in the substrate and the compound (Fig. 3).

The PL emission spectrum was registered with the probe (substrate with the sample powder) under excitation beam placed in the sample holder. The total area under this spectrum (S_2), is proportional to the number of emission photons under direct and diffuse excitation. Next, the PL spectrum was registered when the probe is excited only by

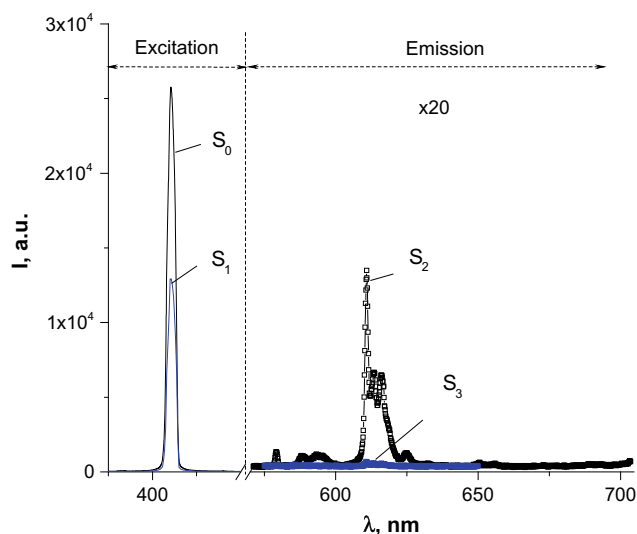


Fig. 3 Illustration of the excitation and emission spectra registered for determination of the quantum yield

indirect excitation light, diffusively reflected from the integrating sphere walls (S_3). The quantum yield was determined as follows [8, 10]:

$$Q = (S_2 - S_3)/(S_0 - S_1) \quad (2)$$

3 Photoluminescence Spectra and Discussion

PL emission spectra of the dinuclear complex $[\text{Eu}(\mu_2\text{-OC}_2\text{H}_5)(\text{NO})_3(\text{phen})]_2 \cdot \text{phen}$, registered at 300 K under excitation of the diode laser beam 405 nm in powder samples and in solution of dimethylformamide are represented in Fig. 4. Upon UV excitation the Eu^{3+} complex exhibits the well-known characteristic transition bands ${}^5\text{D}_0 \rightarrow {}^7\text{F}_j$ ($j = 0, 1, 3, 4$) with typical narrow band features. The complex shows strong emission bands in solid state, and less intense bands are registered in the solution sample (Fig. 4).

The transition ${}^5\text{D}_0 \rightarrow {}^7\text{F}_2$ (electric-dipole transition) at around 611 nm is the most prominent one. The other bands corresponding to ${}^7\text{F}_j$ ($j = 0-4$) are not very intense. Among these bands the most remarkable in the luminescence spectrum of the complex $[\text{Eu}(\mu_2\text{-OC}_2\text{H}_5)(\text{btfa})(\text{NO})_3(\text{phen})]_2 \cdot \text{phen}$ is the band at 580 nm, corresponding to the transition ${}^5\text{D}_0 \rightarrow {}^7\text{F}_0$ with very small line width. For example, for the PL spectrum represented in Fig. 5 the full width at half maximum (FWHM) equals 32 cm^{-1} . The ${}^5\text{D}_0 \rightarrow {}^7\text{F}_0$ transition is strictly forbidden by the selection rules and usually can be observed only in low-symmetry complexes [11, 12].

The ${}^5\text{D}_0 \rightarrow {}^7\text{F}_0$ peak appears narrow in the powder sample (32 cm^{-1}) and a little bit wider (45 cm^{-1}) in the solution

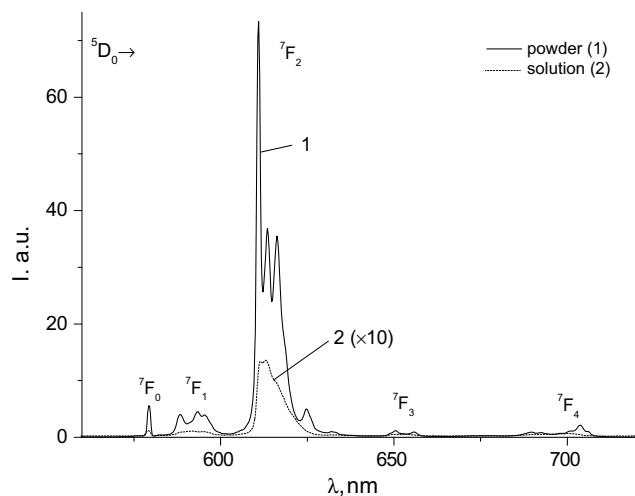


Fig. 4 PL spectra of the powder sample (1) and dimethylformamide solution sample (2) for $[\text{Eu}(\mu_2\text{-OC}_2\text{H}_5)(\text{NO})_3(\text{phen})]_2\cdot\text{phen}$ complex at 300 K under excitation 405 nm

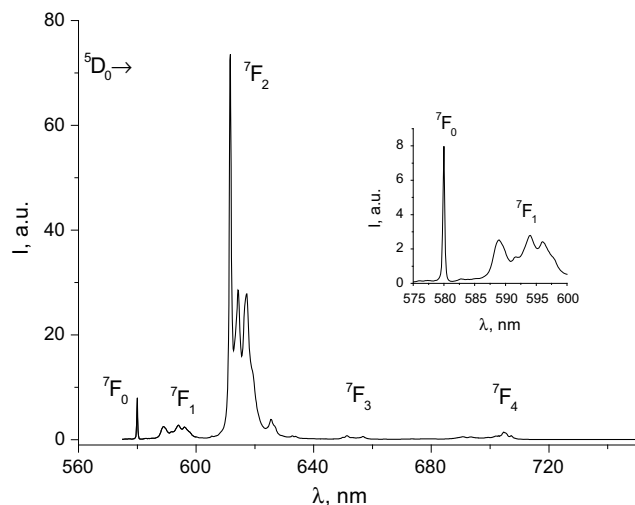


Fig. 5 PL spectrum of the powder sample of the complex $[\text{Eu}(\mu_2\text{-OC}_2\text{H}_5)(\text{NO})_3(\text{phen})]_2\cdot\text{phen}$ at 300 K under excitation 405 nm. The integrated intensity ratio $I_2(^5\text{D}_0 \rightarrow ^7\text{F}_2)/I_1(^5\text{D}_0 \rightarrow ^7\text{F}_1)$ is 9.02

sample (Fig. 4). The wider width of the peak in the solution sample suggests a higher degree of freedom for the complex molecules in the dimethylformamide solution compared to solid state sample.

The emission spectrum of the complex registered in the powder sample exhibits a slightly different degree of splitting compared to the complex dissolved in the solution of the dimethylformamide (Figs. 5 and 6). This difference in splitting degree suggests different degree of distortion of the crystal field in different media.

The ratio of integrated intensities of the $^5\text{D}_0 \rightarrow ^7\text{F}_2$ and $^5\text{D}_0 \rightarrow ^7\text{F}_1$ bands $I_2(^5\text{D}_0 \rightarrow ^7\text{F}_2)/I_1(^5\text{D}_0 \rightarrow ^7\text{F}_1)$ is commonly

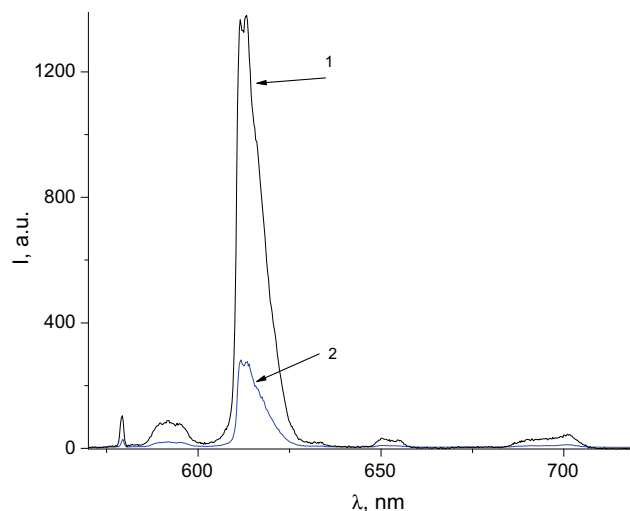


Fig. 6 PL spectra of the dimethylformamide solution sample $[\text{Eu}(\mu_2\text{-OC}_2\text{H}_5)(\text{NO})_3(\text{phen})]_2\cdot\text{phen}$ under excitation 405 nm (1), and 337 nm (2) at 300 K. The integrated intensity ratio $I_2(^5\text{D}_0 \rightarrow ^7\text{F}_2)/I_1(^5\text{D}_0 \rightarrow ^7\text{F}_1)$ is 14.4 for (1) and 13.5 for (2) spectrum

accepted as an indicator of Eu³⁺ site symmetry, as far as it is dependent on the type and coordination of the ligands around the Eu³⁺ ion [11–14]. In this context sometime the parameter called effective site symmetry ($\text{ESS} = I_1/I_2$) is used, which describes not exactly the site symmetry of the ions in the crystal structure, but rather the response of the Eu³⁺ ions to the average crystal field [15, 16].

In the case of powder sample of the complex $[\text{Eu}(\mu_2\text{-OC}_2\text{H}_5)(\text{NO})_3(\text{phen})]_2\cdot\text{phen}$ the integrated intensity ratio $I_2(^5\text{D}_0 \rightarrow ^7\text{F}_2)/I_1(^5\text{D}_0 \rightarrow ^7\text{F}_1)$ is 9.02 (Fig. 5), while in the dimethylformamide solution sample the ratio is *ca.* 14 (Fig. 6). As it was shown elsewhere [15, 17] the higher the ratio $I_2(^5\text{D}_0 \rightarrow ^7\text{F}_2)/I_1(^5\text{D}_0 \rightarrow ^7\text{F}_1)$, the lower the effective site symmetry.

The PL emission band in the range 585–600 nm is attributed to the $^5\text{D}_0 \rightarrow ^7\text{F}_1$ transition which is a magnetic dipole transition, and it reflects the crystal-field splitting of the $^7\text{F}_1$ level (Fig. 5, the inset). Commonly in the case of single Eu³⁺ site the total removal of crystal field degeneracies results in three sublevels for $^7\text{F}_1$. In the case of dinuclear complex $[\text{Eu}(\mu_2\text{-OC}_2\text{H}_5)(\text{NO})_3(\text{phen})]_2\cdot\text{phen}$ we can distinguish $^7\text{F}_1$ splitting into 4 components, which can be related to the dinuclear nature of the complex. Indeed, PL measurements, carried out at low temperatures [18], show PL spectra splitting into multiple lines, that points to existence of two distinct, although chemically very similar, emitting Eu³⁺ centers in the dinuclear complex $[\text{Eu}(\mu_2\text{-OC}_2\text{H}_5)(\text{btfa})(\text{NO})_3(\text{phen})]_2\cdot\text{phen}$.

The PL decay curves of the complex were registered for $^5\text{D}_0 \rightarrow ^7\text{F}_2$ transition both in solid state and dimethylformamide solution. Temporal characteristics of the PL exhibit

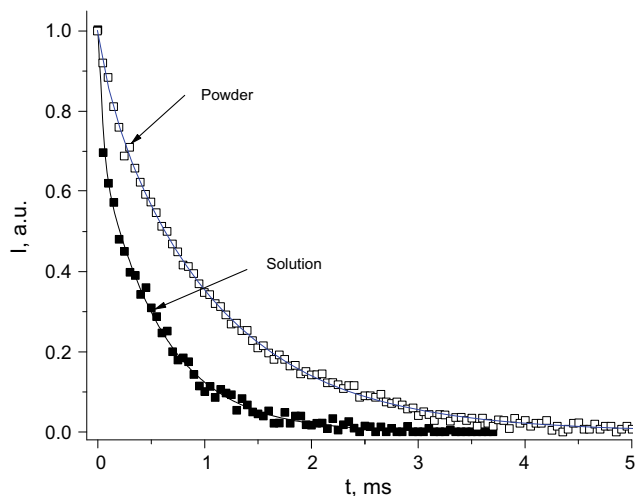


Fig. 7 PL decay profiles for powder and solution sample of $[\text{Eu}(\mu_2\text{-OC}_2\text{H}_5)(\text{btfa})(\text{NO}_3)(\text{phen})]_2\cdot\text{phen}$ complex at 300 K registered at 611 nm under pulsed excitation 337 nm

a bi-exponential decay; both for the powder sample, as well as for the dimethylformamide solution sample (Fig. 7). Both of the decay curves can be fitted by two-exponential function:

$$I(t) = A_1 \exp(-t/\tau_1) + A_2 \exp(-t/\tau_2) \quad (3)$$

where A_1 and A_2 are pre-exponential factors, and τ_1 and τ_2 are the time constants.

The lifetime constants for Eu^{3+} obtained from the plot in Fig. 7 are respectively $\tau_1 = 1.08$ ms and $\tau_2 = 0.13$ ms for the powder sample; while the time constants measured in dimethylformamide solution of the complex are a bit lower and equals $\tau_1 = 0.57$ ms and $\tau_2 = 0.28$ ms. The lifetime decrease can be related to the higher degree of freedom for the complex molecules in the dimethylformamide solution compared to solid state sample. The absolute quantum yield of PL measured in powder samples by the integration sphere was found to be 49.2%. The intrinsic quantum yield and the sensitization efficiency were determined as described in [14] and found to be 62.5% and 78.7% respectively.

4 Conclusions

A new dinuclear complex $[\text{Eu}(\mu_2\text{-OC}_2\text{H}_5)(\text{NO}_3)(\text{phen})]_2\cdot\text{phen}$ has been synthesized and characterized by PL spectroscopy. PL emission spectra exhibit characteristic emission lines attributed to the transitions ${}^5\text{D}_0 \rightarrow {}^7\text{F}_j$ ($j = 0-4$). Both

the emission spectra as well as PL kinetics suggest the presence of two sites of the Eu^{3+} ion. The absolute PL quantum yield, and the sensitization efficiency were determined to be 49.2%, and 78.7% respectively. The new dinuclear complex appears attractive for application in optoelectronics, medicine, biochemistry, etc.

Conflict of Interest The authors declare that they have no conflict of interest.

References

- Hanninen, P., Harma, H. (eds.): Lanthanide luminescence. Photo-physical, analytical and biological aspects. In: Wolfbeis, O.S. (Series ed.), Springer Series on Fluorescence, Methods and Applications, vol. 7. Springer-Verlag, Berlin Heidelberg (2011)
- Lakowicz, J.R.: Principles of Fluorescence Spectroscopy, 2nd edn. Kluwer Academic Plenum Publishers, New York, Boston, Dordrecht, London (1999)
- Blasse, G., Grabmaier, B.C.: Luminescent Materials. Springer (1994)
- Eliseeva, V., Bunzli, J.-C.G.: Lanthanide luminescence for functional materials and bio-sciences. Chem. Soc. Rev. **39**, 189–227 (2010)
- Demchenko, A.P.: Introduction to Fluorescence Sensing, 2nd edn. Springer International Publishing Switzerland (2015). ISBN 978-3-319-20779-7 ISBN 978-3-319-20780-3 (eBook), <https://doi.org/10.1007/978-3-319-20780-3>
- Bordian, O., Verlan, V., Culeac, I., Iovu, M., Bulhac, I., Zubarev, V., Enachescu, M.: Cerere de brevet de invenție, Nr deposit a2018 0063 din data 2018.08.17
- Bordian, O., Verlan, V., Culeac, I., Iovu, M., Bulhac, I., Zubarev, V.: Synthesis, absorption and photoluminescence properties of the new coordination compound $\text{Eu}(\text{DBM})_3(\text{Ph}_3\text{PO})_1\text{H}_2\text{O}$. In: Vladescu, M., Tamas, R., Cristea, I. (eds.), Advanced Topics in Optoelectronics, Microelectronics, and Nanotechnologies IX, Proc. of SPIE vol. 10977, 109771E ©2018 SPIE CCC code: 0277-786X/18/\$18, <https://doi.org/10.1117/12.2323761>
- Obtaining Absolute Quantum Yields Using an Integrating Sphere, Application Note FP-0008, Application Library: <http://www.jascoinc.com/applications>
- Rurack, K.: Fluorescence Quantum Yields: Methods of Determination and Standards. In: Springer Ser. Fluoresc., vol. 5, pp. 101–145 (2008). Springer, Berlin Heidelberg Published online: 11 March 2008. https://doi.org/10.1007/4243_2008_019
- <http://www.otsukael.com/product/detail/productid/9/category1id/3/category2id/8/category3id/10>
- Binnemans, K.: Review: Interpretation of europium(III) spectra. Coord. Chem. Rev. **295**, 1–45 (2015)
- Binnemans, K., Van Deun, R., Gorller-Walrand, C., Collinson, S.R., Martin, F., Bruce, D.W., Wickleder, C.: Spectroscopic behaviour of lanthanide(III) coordination compounds with Schiff base ligands. Phys. Chem. Chem. Phys. **2**, 3753–3757. <https://doi.org/10.1039/b003379k>
- Jean, C.G.: Bünzli and Georges Olivier Pradervand, The $\text{Eu}(\text{III})$ ion as luminescent probe: Laser spectroscopic investigation of the

- metal ion sites in an 18crown6 complex. *J. Chem. Phys.* **85**, 2489 (1986). <https://doi.org/10.1063/1.451057>
14. Bunzli, J.-C.G., Eliseeva, S.V.: Basics of Lanthanide Photo-physics. In: Hanninen, P., Harma, H. (eds.), *Lanthanide Luminescence: Photophysical, Analytical and Biological Aspects*, Springer Ser Fluoresc. Springer-Verlag, Berlin Heidelberg (2010). https://doi.org/10.1007/4243_2010_3
 15. Banski, M., Podhorodecki, A., Misiewicz, J.: Influence of sol-gel matrices on the optical excitation of europium ions. *Mater. Scie. Poland* **28**(1) (2010)
 16. Zhao, Z., Zenga, Q.G., Zhanga, Z.M., Ding, Z.J.: *J. Lumin.* **122**, 862 (2007)
 17. Bunzli, J.C., Choppin, G.R. (eds.): *Lanthanide Probes in Life, Chemical and Earth Sciences: Theory and Practice*. Elsevier, Amsterdam-Oxford-New York-Tokyo (1989)
 18. Culeac, I.P., Verlan, V.I., Bordian, O., Zubareva, V.E., Bulhac, I.F., Iovu, M.S., Enachescu, M., Siminel, N.A., Siminel, A.V.: Synthesis and Characterisation of Novel Photoluminescent Eu(III) Dinuclear Coordination Compound (to be published)

Me-ZnP₂ Diodes Sensible to Optical Gyration

A. V. Dorogan, S. I. Beril, I. G. Stamov, and N. N. Syrbu

Abstract

Spatial dispersion in ZnP₂-D₄⁸ has been studied. The spectral dependences of the refractive index $n^c(E|c, k|a)$, $n^a(E|a, k|c)$ and $n^b(E|b, k|c)$ had been determined. It was shown that the dispersion is positive $n^c(E|c, k|a)$, $n^a(E|a, k|c) > n^b(E|b, k|c)$ in $\lambda > \lambda_0$ region, the dispersion is negative $n^c(E|c, k|a)$ at $\lambda < \lambda_0$, and $\Delta n = n^c - n^b = 0$ at $\lambda = \lambda_0$. The LIV characteristics of Me-ZnP₂-D₄⁸ diodes had been studied at different temperatures, the temperature dependences of the “imperfection” factor δ for different Schottky barriers. Capacitance voltage characteristics of Me-ZnP₂-D₄⁸ photodiodes obtained by electrochemical deposition of metal and by thermo-chemical spraying in vacuum had been studied. The influence of birefringence and gyration on spectral characteristics of *p-n* photodiodes and Schottky diodes had been revealed. The ability of controlling photodiodes’ characteristics was obtained using the gyration particularities in ZnP₂-D₄⁸ crystals.

Keywords

Schottky diodes • Optical gyration • Anisotropy

1 Introduction

Zinc diphosphide—is a wide gap semiconductor material of A²B⁵ group, which possesses the anisotropy of optical properties with natural gyrotropy [1–5]. Devices of quantum electronics and nonlinear optics had been elaborated basing

A. V. Dorogan (✉) · N. N. Syrbu
 Laboratory of Micro-Optoelectronics, Technical University of
 Moldova, 168 Stefan cel Mare Bvd, MD2004 Chisinau, Republic
 of Moldova
 e-mail: andrei.dorogan@srco.utm.md

S. I. Beril · I. G. Stamov
 T.G. Shevchenko State University of Pridnestrovie, Tiraspol,
 Republic of Moldova

on ZnP₂ crystals, which operating principle is based on gyrotropy and nonlinear crystal polarizability [4, 5]. The values of nonlinear polarizability and gyrotropy of ZnP₂ are higher than those for other crystals [1–5]. The low thermal conductivity of ZnP₂ crystals (10 W/m K) is used to create laser beam deflectors with thermally induced gradient of the refractive index [4, 5].

The developed photoresists based on ZnP₂ possess a low relaxation time constant and are suitable for registering impulse radiation flows of 1×10^{-9} s duration. Photoelectric emitters and photodiodes, electric switches and Zener diodes had been developed based on ZnP₂ single crystals [1–5]. ZnP₂ crystals change the optical activity with temperature change, while maintaining the linear dependence of the rotational ability of polarization plane on the temperature (temperature sensors) [4, 5].

The birefringent properties on perfect, high-quality ZnP₂ crystals, LIV, capacitance-voltage characteristics, and photovoltaic characteristics of *p-n*-ZnP₂ structures, (*n-p*-ZnP₂) are studied in this paper, including the characteristics of Me-ZnP₂ diodes and ZnP₂-D₄⁸, ZnP₂-C_{2h}⁵ heterojunctions. A comparison of the characteristics of the device structures obtained by electrochemical deposition of metal and metal thermo-chemical spraying in vacuum on the surface of the crystals has been made. The influence of the gyration phenomenon on the characteristics of *p-n* photodiodes and Me-ZnP₂ photodiodes was examined.

2 Experimental Method

The process of growing single crystals of zinc diphosphide from Zn and P precursors occurred in two stages. The first step was the synthesis conducted in a quartz ampoule placed in a pressure container (≈ 40 atm.). 300–500 g of substance were synthesized simultaneously. The synthesized compound is sublimed in vacuum to obtain single crystals in the second step. The maximum dimensions of ZnP₂ ingots obtained from the gas phase reached $10 \times 10 \times 20$ mm.

The single crystals had been cleaved perpendicular to the C axis. The measurements were carried out on single crystals obtained in plates form or prisms grown along the C axis and having a not treated mirror surface. Schottky diodes, p - n junctions had also been obtained on the cleaved not polished surface. Optical transmission spectra in crossed polarizers were measured with MDR-2 and JASCO-670 spectrometers. Low-temperature measurements were made using LTS-32C330 Workhorse-type optical cryostat.

3 Experimental Results and Discussions

A characteristic feature of $\text{ZnP}_2\text{-D}_4^8$ crystals is the dispersion of the refractive indices n_o and n_e at the absorption edge (birefringence), which is associated with the peculiarities of the band structure. The selection rules of electronic transitions determine the nature (allowed, prohibited) of these electronic transitions. This will determine the value of absorption and dielectric constant in the respective polarizations, and hence the sign of birefringence. These features lead to the rapid growth of one of the refractive indices as approaching to the fundamental absorption edge. This determines the anisotropy of the interband absorption edge of the crystal in the respective polarizations. The intersection of the dispersion curves (isotropic point— IP) from the long wavelength side of the absorption edge is observed in ZnP_2 crystals.

The existence of two types of waves in the crystal—ordinary and extraordinary, for which there are two refractive indices n_o and n_e , is determined by the crystal's dielectric tensor $\varepsilon(\omega, k)$, which depends on the frequency ω , and the wave vector K .

Figure 1 shows the interference spectra of the transmission of $\text{ZnP}_2\text{-D}_4^8$ crystals with $470 \pm 2 \mu\text{m}$ thickness at polarizations Elb , Ela and Elc at 300 K. The transmission spectra at polarization Elb are stretched in the interference pattern on the wavelength scale for clarity. The curves for the Ela and Elc polarizations intersect approximately at 610–620 nm wavelength values. Simultaneously, it should be noted that the crystals' transmittance at Elb polarization is somewhat larger than at other polarizations.

The edge absorption is also polarized, and it is due to direct allowed transitions in the region of high absorption coefficients. The bandgap at $E_{\perp c}$ polarization is less than at Elc polarization. The zones' splitting value is 42 meV at 9 K [2, 3].

The transmittance spectra of $\text{ZnP}_2\text{-D}_4^8$ crystals are measured at room temperature in the Ela and Elb polarizations for undoped samples ($z1$) in the 560–1800 nm region, Fig. 2. The crystals had approximately the same thickness ($d = 245 \pm 5 \mu\text{m}$) and natural chipped surfaces.

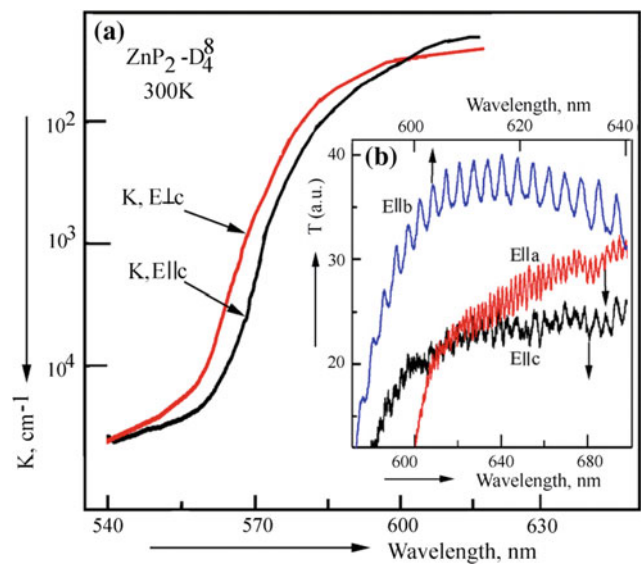


Fig. 1 a Edge absorption spectra; b transmittance interference of $\text{ZnP}_2\text{-D}_4^8$ crystals at Elb , Ela and Elc polarizations at 300 K

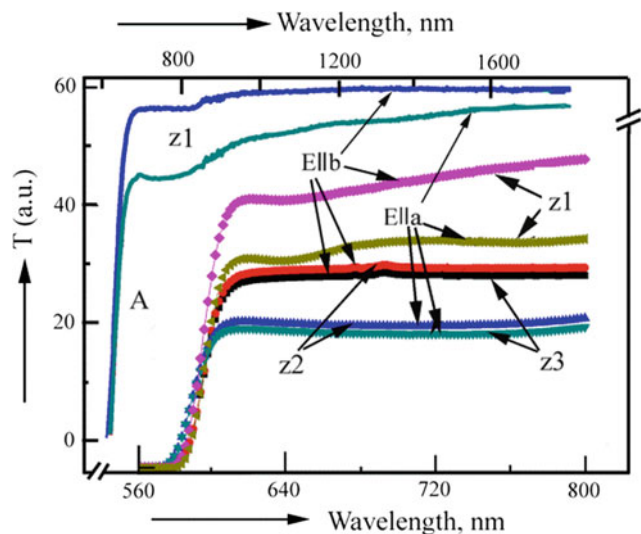


Fig. 2 A Transmittance spectra of $\text{ZnP}_2\text{-D}_4^8$ crystals at Ela and Elb polarizations for undoped samples ($z1$) and antimony-doped 1% ($z2$) and 1.5% ($z3$)

The value of the transmittance coefficient for the Elb polarization is a bit more than for the Ela polarization and in undoped crystals ($z1$) and antimony-doped 1% ($z2$) and 1.5% ($z3$), Fig. 2. The spectral dependence of the refractive indices for Ela , Elb and Elc ($z1$) polarizations and for the Ela and Elb polarizations in samples doped with antimony 1% ($z2$) and 1.5% ($z3$) are calculated from the reflectance spectra using the Kramers-Kronig method, Fig. 3.

Transmittance maximum is observed at this wavelength in the crystals' transmission spectra placed between crossed

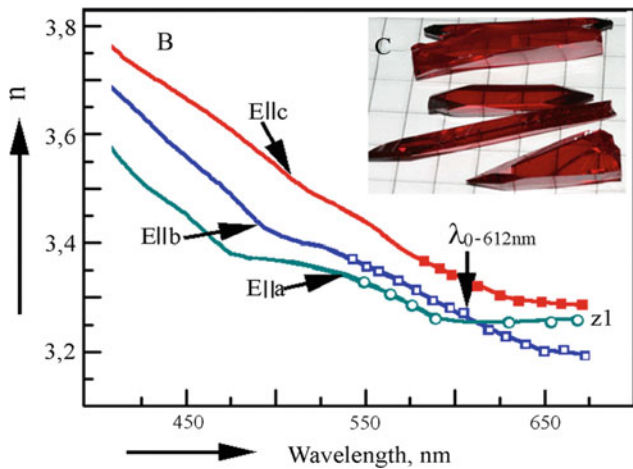


Fig. 3 The spectral dependences of the refractive index obtained from the Kramers-Kronig calculations for the *E||c*, *k||a*, *E||a*, *k||c* and *E||b*, *k||c* polarizations for undoped crystals (*z1*)

polarizers (Fig. 4a). λ_0 wavelength is shifted to shorter wavelengths region in accordance with the temperature coefficient of the offset absorption edges at $E\perp c$ and $E\parallel c$ polarizations and 9 K. The difference of refractive indices difference $\Delta n = n^a - n^b$, $\Delta n = n^c - n^a$, $\Delta n = n^c - n^b$ are positive values in the short-wavelength region of λ_0 . These values are negative in the long-wavelength region of λ_0 , Fig. 4a. This crystal is a phase plate in which two light waves propagate at different speeds.

Rotation of the polarization plane of light waves is observed in case of the propagation of light waves along the *C* axis of ZnP₂ crystals. ZnP₂-D₄⁸ crystals possess a natural optical activity. The optical activity is observed along the *C* axis of the uniaxial ZnP₂-D₄⁸ crystal.

The value of the rotation ability for left and right rotating planes of light's polarization increases near the fundamental absorption edge. The characteristics of the optical activity are practically identical in the left and right rotating ZnP₂ crystals, obtained in different technological regimes (Fig. 4b).

The electromotive force (EMF) of Me-ZnP₂ diodes created on fractured surfaces of undoped crystals, which possess a natural gyrotropy can have a positive or negative value at *E||a* polarization change with *E||b*. The transmittance spectra of doped crystals (T_b) are more intense in the area of $\lambda > 612$ nm ($\lambda > \lambda_0$) at *E||b* polarization than at *E||a* polarization (T_a). The light waves penetrate to a shallower depth at *E||a* polarization, i.e. create a photo-EMF J_{ph}^a in the active region of the upper diode (conventionally has a positive direction). The wave polarization corresponds to *E||b* case if turning the polarization plane of the incident waves at 90°. The transmittance coefficient T_b is higher at this polarization than at *E||a*. The waves penetrate the spatial charge region of the lower photodiode creating a photo-EMF in this area. If

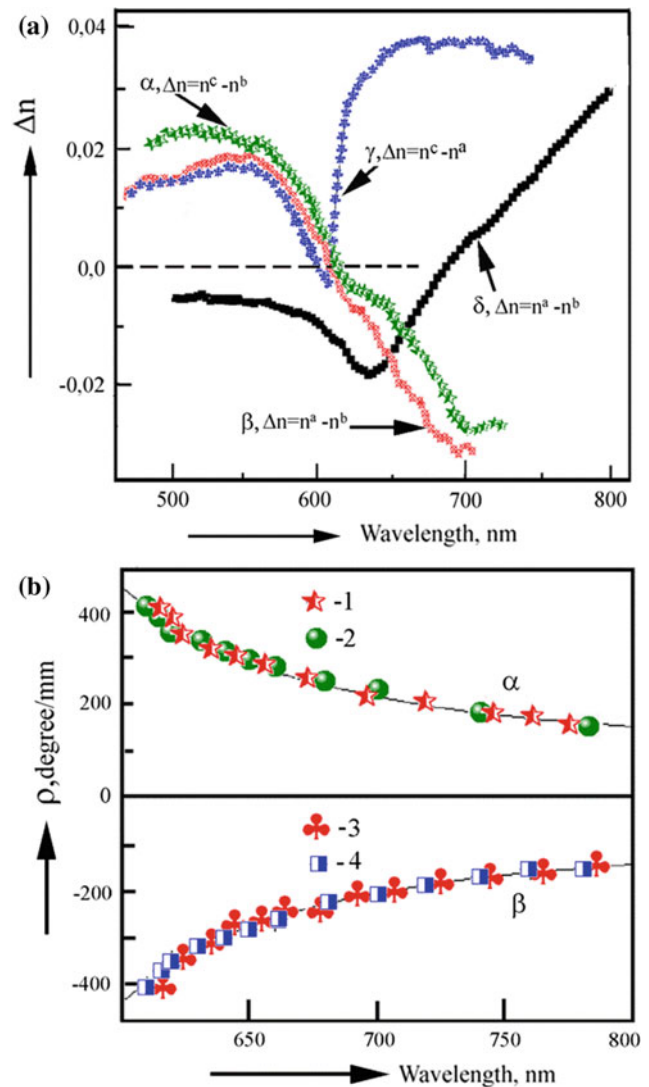


Fig. 4 a The spectral dependence of the refractive index difference $\Delta n = n^a - n^b$, $\Delta n = n^c - n^a$ and $\Delta n = n^c - n^b$ of ZnP₂ crystals, where n^a , n^b , n^c refractive indices for *E||a*, *E||b*, *E||c* polarizations, respectively (α , β , γ -undoped crystals, δ -doped crystals 1.5% Sb), **b** the spectral characteristics of the rotation capacity of four undoped ZnP₂ crystals, obtained under different processing conditions

the thickness of the crystal corresponds and provides the plane rotation of the light waves at 90°, the photo-EMF will fit the polarized waves at *E||b*. The EMF J_{ph}^b has an opposite direction comparing to the photocurrent direction J_{ph}^a (conditionally negative value). The spectral characteristics of the photoconductivity in the short- and long-wavelength region of λ_0 (612 nm) are shown in Fig. 5.

The gyration of the polarization vector of light waves occurs in case of light waves propagation along the *C* axis of the crystal. The light is absorbed in the spatial charge region of the lower diode for the wavelength range $\lambda > \lambda_0$, generating a photo-EMF and in the upper diode generating an opposite sign photo-EMF of in the short-wavelength region

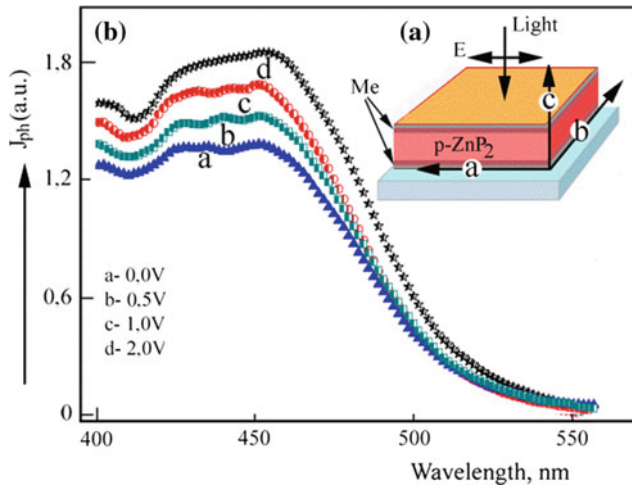


Fig. 5 **a** Me-*n-p*-ZnP₂-D₄⁸-Me (Me-Au, Ni, In) structure obtained on the fractured surfaces of the crystal with a 270 μm; **b** spectral response of photosensitivity in $\lambda < \lambda_0$ region

($\lambda < \lambda_0$). The spectral response curve crosses the zero axis of EMF approximately at a λ_0 (612 nm) wavelength. The value of the photosensitivity in the maximum of In-ZnP₂ structures is higher than for Ni-ZnP₂ and Au-ZnP₂ structures for the same conditions, Fig. 5b. The crystal's thickness affects the spectral characteristics of the diodes, which determines the angle of the polarization plane of light waves that reach the lower photodiode.

The transmittance coefficient T is described by an expression $T = \sin^2(\rho d)$, where ρ is the value of the specific rotation at λ_0 wavelength and at the same time is the interaction constant. The transmittance coefficient may be represented as:

$$T = \frac{\sin^2(\pi/\lambda) \left[(\delta n^2 + \Delta n^2)^{0.5} d \right]}{1 + (\Delta n/\delta n)^2}, \quad (1)$$

where $\Delta n = n_e - n_o$ —is the linear birefringence of the crystal; $\delta n = \lambda\rho/\pi$ —circular birefringence; d —thickness of the crystal element. From this expression it follows that the optimum thickness of the crystal that corresponds to the transmittance maximum is $d = \pi/2\rho_o$, where $\rho_o = \rho(\lambda_o)$.

The spectral characteristic of photosensitivity has an intense peak at a 650–760 nm wavelength value and crosses the axis of wavelengths at 600–615 nm energy with decreasing wavelength, and has a negative value of the EMF at 450–500 nm wavelength. This characterization of photosensitivity is due to competing mechanism of EMF arising in a structure with oppositely connected photodiodes. The light waves penetrate deeper and create a photo-EMF in the positive charge region (PCR) of the lower In-ZnP₂ photodiode, which has conditionally a positive value in the

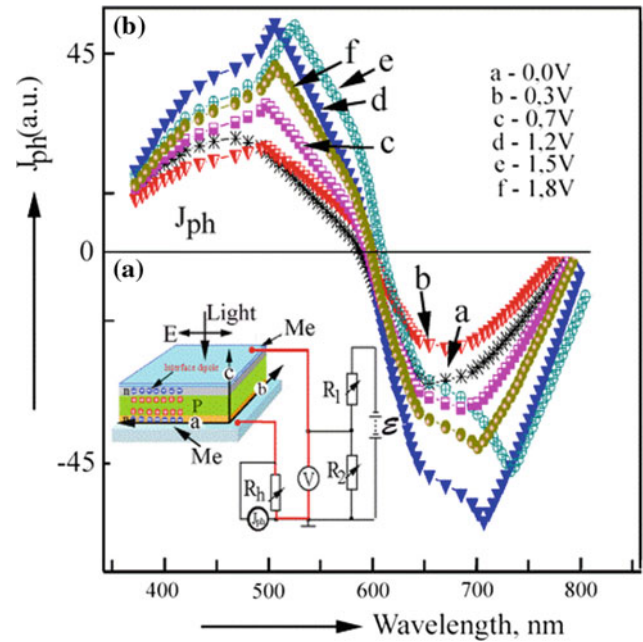


Fig. 6 **a** The structure of Me-*n-p*-ZnP₂-*p-n*-Me photodiode; **b**—the spectral distribution of the photo response (J_{ph}) at Elc polarization, under different applied voltages

long-wavelength region of the isotropic point (λ_0) (curve J_{ph} , Fig. 6). The absorption coefficient increases as the wavelength decreases and the photo-EMF is generated by direct transitions. This leads to the excitation of charge carriers in PCR of the upper *n-p* (ZnP₂) diode, which possesses negative photovoltage.

4 Conclusions

The spectral dependences of the refractive indices $n^c(Elc, k|a)$, $n^a(El|a, k|c)$ and $n^b(El|b, k|c)$ in ZnP₂-D₄⁸ crystals intersect at a wavelength $\lambda_0 = 612$ nm. The crystals are isotropic at λ_0 wavelength and, in case of crossed polarizers, have a maximum bandwidth. The refractive indices $n^c(Elc, k|a)$ and $n^a(El|a, k|c)$ are higher in the λ_0 wavelength region, than the refractive indices at $n^b(El|b, k|c)$ polarization, the dispersion is positive. Inverse relationship was observed in the long-wavelength region, the dispersion is negative. $\Delta n = n^c - n^b = 0$ at $\lambda_0 = 612$ nm wavelength.

The birefringence and gyration phenomenon affect the spectral characteristics of the p-n photodiodes and Schottky diodes. The possibility of controlling the characteristics of photodiodes using the gyration features in ZnP₂-D₄⁸ crystals was obtained.

Conflict of Interest The authors declare that they have no conflict of interest.

References

1. Syrbu, N.N., Stamov, I.G., Kamertsel, A.I.: Sov. Phys. Semicond. **26**, 7,665, Original Russian Text published in Fizica i Tekhnica Poluprovodnikov, **26** (1992), pp. 1191–1224 (1992)
2. Bodnari, I.V., Osipova, M.A., Rud, V.Yu., Rud, Yu.V., Bairamov, B.Kh.: J. Appl. Spectro. **77**(1), 146–151 (2010)
3. Stamov, I.G., Tkacenco, D.V.: Semiconductors, **42**(6), 662 (2008), Original Russian Text, published in “Fizica I Tekhnica Poluprovodnikov”, **42**(6), 679–685 (2008)
4. Patscun, I.I., Sliukhina, I.A.: Semiconductor Physics, Quantum Electronics and Optoelectronics **7**, 31–35 (2005)
5. Stamov, I.G., Syrbu, N.N., Dorogan, A.V.: Phys. B **412**, 130–137 (2013)

Applications of Chalcogenides as Electron Transport Layers and Doping Materials in Perovskite Solar Cells

M. E. Popa

Abstract

The work contains the experimental results obtained by applying of ZnS and ZnSe thin films in perovskite solar cells. The techniques of preparing and researching the electrical properties of the obtained devices have been described in details.

Keywords

ZnS • ZnSe • Perovskite • Solar cells • Open circuit voltage • Short circuit current • Electron

1 Introduction

Recently, organic/inorganic hybrid perovskite materials of the type ABX_3 ($A = CH_3NH_3$ or $HC(NH_2)_2$, $B = Pb$ or Sn , $X = I, Br$ or Cl) have been of great interest due to their promising applications in solar cells as a light harvesting element and light absorption element with wide absorption spectrum and high excitonic diffusion length. Perovskite solar cells (PSC) can reduce the production costs and get a power conversion efficiency significantly higher compared with standard silicon cells and other cells with thin layers [1–10].

The purpose of this paper is to present the obtained results in the use of ZnS and ZnSe thin films as electron transport layer and dopant in perovskite ($CH_3NH_3PbI_3$) solar cells.

2 Experimental Details

The thin layer of indium tin oxide (ITO) was deposited by engraving on Corning 7059 glass that was later cleaned by ultrasonic detergent, deionized water, acetone, methanol and isopropanol for the function of electrode that collects holes.

The PEDOT-PSS (poly (3,4-ethylenedioxythiophene)-poly (styrene sulfonate)) layer, which has the function of the hole transport layer, was deposited on ITO. This is, usually, deposited from a solution (80 μ l) by the spin-coating method at a rotational speed of 3000 rpm for 60 s followed by heat treatment in the air for 10 min at the temperature of 1500 °C. The time of the treatment is measured by the phone chronometer.

The solution of perovskite $CH_3NH_3PbI_3$ (methylammonium lead iodide) was used for the preparation of bulk heterojunction. The perovskite layer is deposited from the solution (80 μ l) by the two-stage spin coating process: after depositing for 23 s the layer is rotated at 1000 rpm, followed by a second deposition for 30 s at a speed of 4000 rpm. At the 13th second 150 μ l of toluene is dripped.

For the function of electron transport layer a ZnS (or ZnSe) layer with an evaporation mass of about 32 mg of ZnS (or ZnSe powder) is deposited at the temperature of the glass substrate $T_{sub} = 300$ K by vacuum thermal evaporation. The vacuum pressure is about 72×10^{-4} torr, and the electrical current through the evaporator is approximately 50 A. The Ag electrodes are deposited analogously by thermal evaporation in quasi-closed volume.

A layer deposited from 60 μ l solution of PCBM = PC61BM (fullerene derivate [6,6]-phenyl-C61-butyric acid methylester) doped with ZnS or ZnSe was used as the transport electron layer in another type of solar cell. The layer was deposited through dynamic dispensing (in g-box) spin-coating in the argon chamber at a rotation speed of 1000 rpm for 40 s. It was found that the most successful solar cell was at the concentration of 1.4 mg of ZnSe in one

M. E. Popa (✉)

Department of Physical and Engineering Sciences, Alecu Russo
Balti State University, Pushkin street 40, Balti, Republic of
Moldova

e-mail: miheugpopa@yahoo.com

ml of PC61BM. The other layers were deposited as in the previous cells.

Two layers of electron transport layer type have been deposited in the third variant of solar cells: the first layer of ZnS (or ZnSe) was deposited by vacuum thermal evaporation under the same conditions as in the first variant of solar cells; the second layer of PC₆₁BM was deposited through dynamic dispense (in g-box) spin-coating in the argon chamber at a rotation speed of 1000 rpm for 40 s. The other layers were deposited as in the previous cells.

In the fourth variant of solar cells, the bulk heterojunction layer is obtained from ZnS or ZnSe-doped perovskite (CH₃NH₃PbI₃) solution. The deposition was carried out similarly as in depositing perovskite without impurities. It was found that the most successful solar cell of this kind was obtained for the concentration of 1.6 mg of ZnSe in one ml of CH₃NH₃PbI₃. The other layers have been deposited as in previous devices.

The current density-voltage curves of the devices were measured in a N₂ filled glove box using simulated AM1.5G sun light which was calibrated to 100 mW/cm² using a NREL traceable Si photodiode (PV Measurements Inc.) and a Keithley 2400 source measurement unit controlled by a PC. The photovoltaic parameters of the multijunction solar cells were investigated at 300 K. The surface morphology of the solar cells was observed using the scanning electron microscope (SEM) type VEGA3 TESCAN and HITACHI S-3000 N.

3 Discussions

Figure 1a presents the cascade structure and the energy diagram of a solar cell with inverted planar architecture in which ZnSe plays the role of electron transport layer, and the PEDOT: PSS layer plays the role of hole transport layer. Figure 1b presents a photo of the samples, made before the deposition of silver electrodes.

In Fig. 2 we can see the current density—voltage curves of the most representative solar ITO/PEDOT:PSS/CH₃NH₃PbI₃/ZnSe/Ag cell at forward scanning (at voltage increase) and reverse scanning (at voltage decrease).

We notice that curve hysteresis is almost similar, and the values of photovoltaic parameters are insignificantly changed. At forward scanning we obtain an open circuit voltage $V_{oc} = 0.677$ V, the short-circuit current $J_{sc} = -8.627$ mA/cm², the fill factor $FF = 40.315\%$ and the power conversion efficiency $PCE = 2.379\%$. At reverse scanning we get slightly higher values ($V_{oc} = 0.687$ V, $J_{sc} = -9.266$ mA/cm², $FF = 40.758\%$, $PCE = 2.565\%$) (Table 1).

The paper has demonstrated the use of various structures of ZnS and ZnSe as an electron transport layer or as a dopant in perovskite solar cells with inverse planar architecture. The

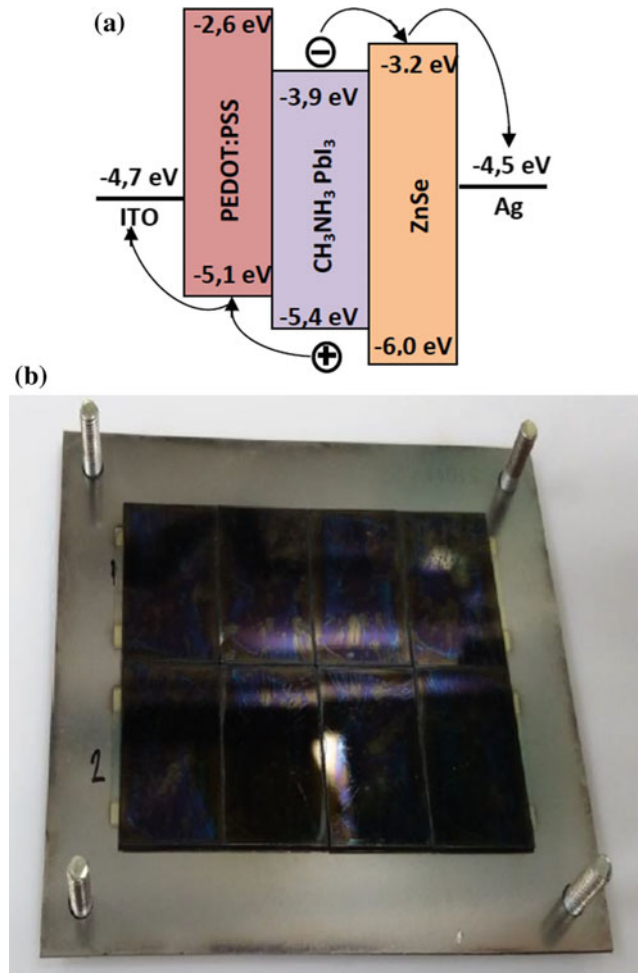


Fig. 1 The energy diagram (a) and photo (b) of ITO/PEDOT:PSS/CH₃NH₃PbI₃/ZnSe/Ag thin cells

advantages of these cells would be their preparation at low temperatures by two relatively cheap methods: spin-coating and thermal evaporation. Table 1 presents the best values of the photovoltaic parameters of eight types of perovskite solar cells.

4 Conclusions

The displacement of the conduction band at the interface between the perovskites and the electron transport layer layers proved to be successful for the reduction of energy losses for the transport and collection of loads and for the reduction of recombination of load carriers.

We believe that the successful use of ZnS or ZnSe thin films (and ZnS or ZnSe-doped solutions) in perovskite-based solar cells can extend to several inorganic semiconductor materials, including n-type semiconductors (CdSe, ZnS, In₂S₃ etc.).

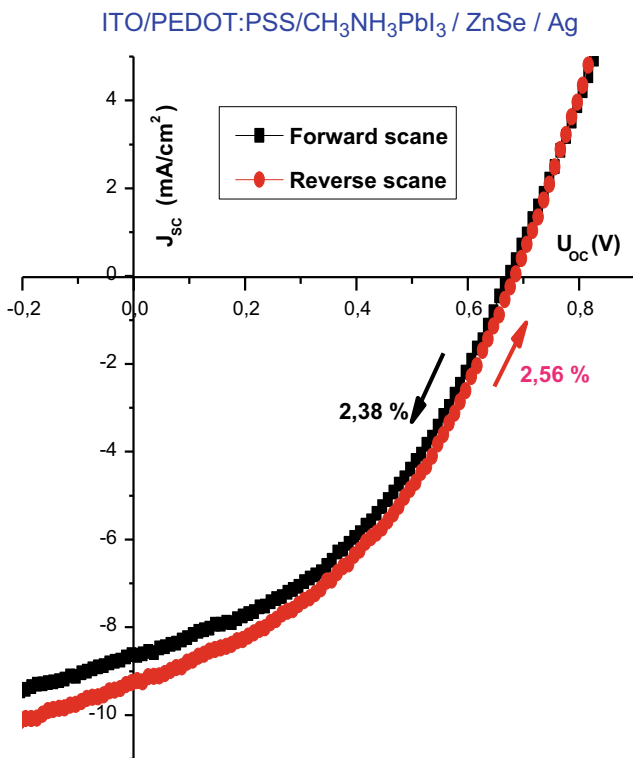


Fig. 2 Current density—voltage characteristics of perovskite solar cells with ZnSe as electron transport layer

Table 1 Photovoltaic parameters of perovskite solar cells

Type of device	U_{oc} (V)	J_{sc} (mA/cm ²)	FF (%)	PCE (%)
ITO/PEDOT:PSS/CH ₃ NH ₃ PbI ₃ /ZnS/Ag	0.570	-6.350	44.790	1.640
ITO/PEDOT:PSS/CH ₃ NH ₃ PbI ₃ /ZnSe/Ag	0.687	-9.266	40.758	2.565
ITO/PEDOT:PSS/CH ₃ NH ₃ PbI ₃ /PC ₆₁ BM:ZnSe/Ag	0.727	-10.131	48.518	3.572
ITO/PEDOT:PSS/CH ₃ NH ₃ PbI ₃ /PC ₆₁ BM:ZnS/Ag	0.940	-7.390	57.460	3.980
ITO/PEDOT:PSS/CH ₃ NH ₃ PbI ₃ /ZnS/PC ₆₁ BM/Ag	0.820	-13.510	52.170	5.760
ITO/PEDOT:PSS/CH ₃ NH ₃ PbI ₃ /ZnSe/PC ₆₁ BM/Ag	0.927	-13.207	54.157	6.628
ITO/PEDOT:PSS/CH ₃ NH ₃ PbI ₃ /ZnS/PC ₆₁ BM/Ag	0.947	-14.292	65.878	8.916
ITO/PEDOT:PSS/CH ₃ NH ₃ PbI ₃ /ZnSe/PC ₆₁ BM/Ag	0.947	-15.521	61.556	9.047

From the point of view of toxicity, ZnS and ZnSe is, undoubtedly, a better candidate than CdS or CdSe, which makes it more suitable for incorporation into such solar cells.

The use of ZnS and ZnSe thin films in various perovskite structures represents a scientific novelty in the field.

Conflict of Interest The author declare that he have not of conflict of interest.

References

1. Im, J.H., Lee, Ch.R., Lee, J.W., Park, S.W., Park, N.G.: 6.5% efficient perovskite quantum-dot-sensitized solar cell. *Nanoscale* **3**, 4088 (2011)
2. Lee, M.M., Teuscher, J., Miyasaka, T., Murakami, T.N., Snaith, H.J.: Efficient Hybrid Solar Cells Based on Meso-Superstructured Organometal Halide Perovskites. *Science Express, Supplementary*

- Materials, www.sciencemag.org/cgi/content/full/science.1228604/DC1, Published online 4.X.2012
- Jeng, J.Y., Chiang, Y.F., Lee, M.H., Peng, S.R., Guo, T.F., Chen, P., Wen, T.C.: CH₃NH₃PbI₃ perovskite/ fullerene planar-heterojunction hybrid solar cells. *Adv. Mater.* (2013)
 - Conings, B., Baeten, L., De Dobbelaere, C., D'Haen, J., Manca, J., Boyen, H.G.: Perovskite-based hybrid solar cells exceeding 10% efficiency with high reproducibility using a thin film sandwich approach. *Adv. Mater.* (2013)
 - Stranks, S.D., Eperon, G.E., Grancini, G., Menelaou, C., Alcocer, M.J.P., Leijtens, T., Herz, L.M., Petrozza, A., Snaith, H.J.: Electron-hole diffusion lengths exceeding 1 micrometer in an organometal trihalide perovskite absorber. *Science* **341**, 342 (2013)
 - Yin, W.J., Shi, T., Yan, Y.: Unique properties of halide perovskites as possible origins of the superior solar cell performance. *Adv. Mater.* (2014). www.advmat.de
 - Lin, Q., Armin, A., Chandra, R., Nagiri, R., Burn, P.L., Meredith, P.: Electro-optics of perovskite solar cells. *Nat. Photonics*. Published online: 1 Dec 2014
 - Jeon, N.J., Noh, J.H., Kim, Y.Ch., Yang, W.S., Ryu, S., Seok, S.I.: Solvent engineering for high-performance inorganic-organic hybrid perovskite solar cells. *Nat. Mater.* Published online: 6 July 2014
 - Yin, W.J., Shi, T., Yan, Y.: Superior photovoltaic properties of lead Halide Perovskites: insights from first-principles theory. *J. Phys. Chem. C*. Publication Date (Web): 6 Feb 2015
 - Milichko, V.A., Shalin, A.S., Mukhin, I.S., Kovrov, A.E., Krasilin, A.A., Vinogradov, A.V., Belov, P.A., Simovskii, C.R.: Solar photovoltaics: current state and trends **59**, 727–772 (2016)

Applications of Chalcogenides as Hole Transport Layers and Dopants in Perovskite Solar Cells

M. E. Popa

Abstract

In the work are presented the experimental results obtained by applying ZnTe as a hole transport layer and as a dopant in perovskite solar cells with inverted planar architecture.

Keywords

Solar cells • ZnTe • Perovskite • Hole • Fill factor • Power conversion efficiency

1 Introduction

Last years have seen unprecedented growth of interest in perovskite solar cells based on organic—inorganic halides due to their distinct combination of high efficiency and easy preparation [1–3]. Impressive progress has been made in improving photovoltaic performance. The use of thin absorbent layers in solar energy conversion devices will lead to the real possibility of a durable and inexpensive replacement of solid silicon based devices.

This work pursues the following purposes:

1. to present the results obtained by using ZnTe thin films as a hole transport layer in perovskite solar cells;
2. to present the results obtained by using ZnTe powder as a dopant in solar cells.

2 Experimental Details

Lower contacts of solar cell were prepared from indium tin oxide (ITO) deposited by engraving on Corning 7059 glass. Subsequently, the thin layer of ZnTe which fulfilled hole transport layer function was deposited by thermal evaporation in vacuum. To measure the thickness of ZnSe thin films the interference microscope MII-4 (Linnik type) was used. For preparation of the bulk heterojunction layer, the methylammonium lead iodide ($\text{MAPbI}_3 = \text{CH}_3\text{NH}_3\text{PbI}_3$) solution was used. As the transport electron layer, the PCBM = PC_{61}BM (fullerene derivative [6,6]-phenyl-C₆₁-butyric acid methyl ester) layer was used.

The second type of solar cells is different from the first type owing to the fact that as a hole transport layer in it was used film formed from the PEDOT-PSS solution (poly (3,4-ethylenedioxythiophene) poly (styrene sulfonate)) doped with ZnTe powder.

In the third variant of solar cells were deposited two layers with hole transport layer function. The first layer of ZnTe was obtained by thermal evaporation in quasi-closed volume under the same conditions as in the first variant of solar cells. The second layer of PEDOT-PSS was deposited by the spin-coating method.

In the fourth variant of solar cells the bulk heterojunction layer was obtained by doping of the perovskite solution $\text{CH}_3\text{NH}_3\text{PbI}_3$ with the ZnTe powder. The obtained solution and the other layers were deposited analogously to the first variant of solar cells.

Current density-voltage experimental dependencies of devices were measured in a N_2 filled glove box using simulated AM1.5G sun light which was calibrated to 100 mW/cm^2 using an NREL traceable Si photodiode (PV Measurements Inc.) and a Keithley 2400 source measurement unit controlled by a PC. The photovoltaic parameters of the multijunction solar cells were investigated at 300 K.

M. E. Popa (✉)

Department of Physical and Engineering Sciences, Alecu Russo
Balti State University, Pushkin street 40, Balti, Republic of
Moldova

e-mail: miheugpopa@yahoo.com

3 Discussions

In Fig. 1 are presented the most representative curves of ZnTe—based of perovskite solar cells and all dependencies J-U were analyzed according to the layer thickness of ZnTe deposited on ITO. In Table 1 are presented photovoltaic parameters of the respective solar cells.

ITO/ZnTe/MAPbI₃/PC₆₁BM/Ag structure: For layer thickness of about $d = 20$ nm the ZTa1 functional curve was obtained with the following characteristics: open circuit voltage (V_{oc}) of about 0.44 V, a short-circuit current (J_{sc}) of about 6.24 mA/cm^2 and a fill factor (FF) of 59.48%, corresponding to a power conversion efficiency (PCE) of 1.66%. For the thickness layer of about $d = 33$ nm (ZTa2 device) curve hysteresis has increased up to the value of short-circuit

current about 9.98 mA/cm^2 , and open circuit voltage decreased to 0.39 V. If the layer thickness increases up to $d = 48$ nm (ZTa3 device), the hysteresis of the J-U characteristic obtains the shape of the initial curve (device ZTa1).

ITO/PEDOT-PSS:ZnTe/MAPbI₃/PC₆₁BM/Ag structure: For devices with the concentration $n = 1.2 \text{ mg/ml}$, the experimental curve ZTb1 was obtained with the following characteristics: open circuit voltage (V_{oc}) of about 0.58 V, a short-circuit current (J_{sc}) of about 5.64 mA/cm^2 and a fill factor (FF) of 43.94%, corresponding to a power conversion efficiency (PCE) of 1.43%. By increasing the concentration of ZnTe to $n = 1.8 \text{ mg/ml}$ we notice that the hysteresis of the curves is continuously increasing reaching up to a short-circuit current of about 9.27 mA/cm^2 and an open circuit voltage of about 0.69 V, corresponding to a maximum PCE

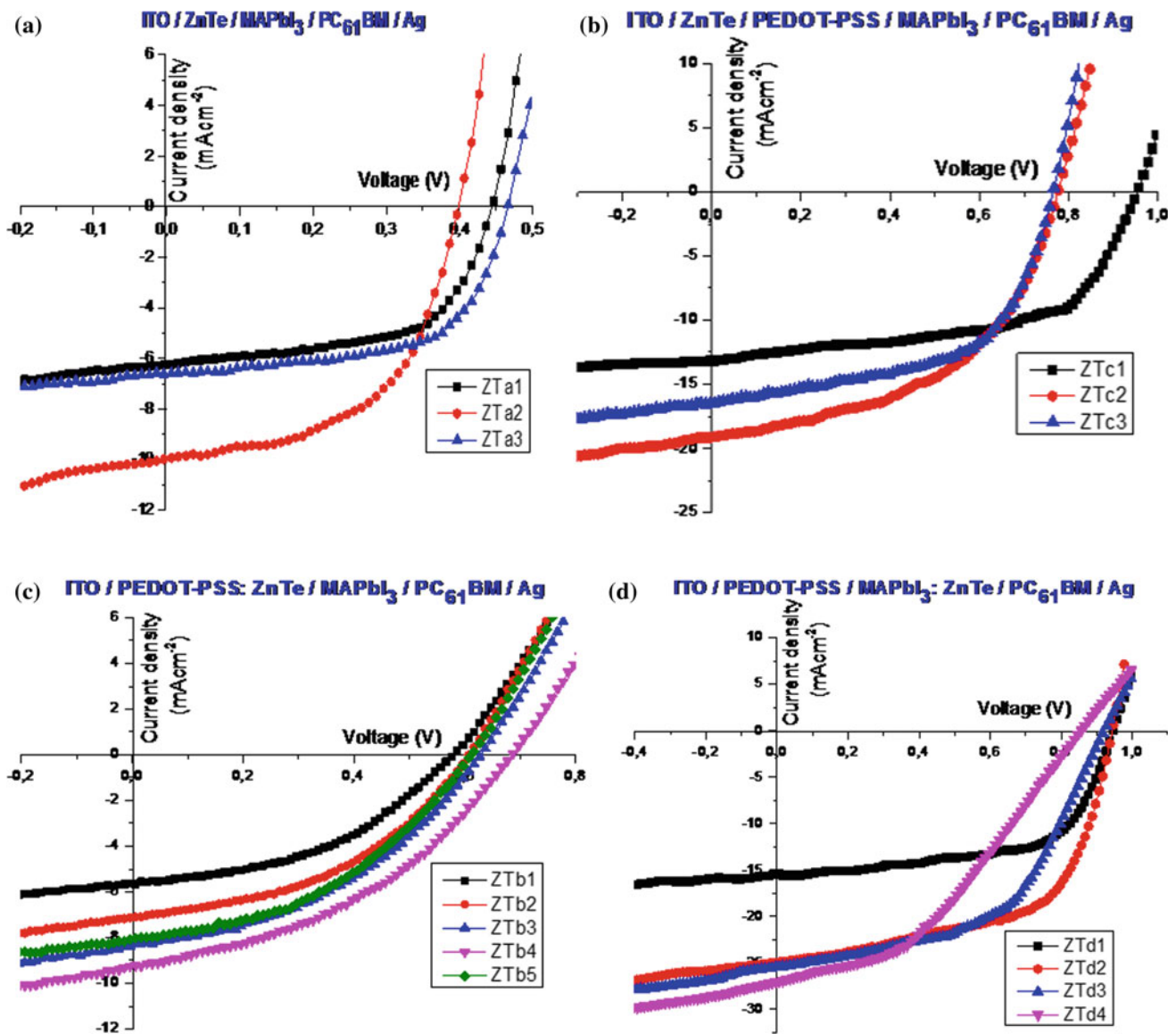


Fig. 1 ZnTe—based perovskite solar cells

Table 1 Photovoltaic parameters of ZnTe-based thin solar cells

Devices	d_{ZnTe} (nm)	U_{oc} (V)	J_{sc} (mA/cm ²)	FF (%)	PCE (%)
ZTa1	20	0.44	-6.24	59.48	1.66
ZTa2	33	0.39	-9.98	54.19	2.14
ZTa3	48	0.46	-6.62	61.14	1.88
Devices	n (mg/ml)	U_{oc} (V)	J_{sc} (mA/cm ²)	FF (%)	PCE (%)
ZTb1	1.2	0.58	-5.64	43.94	1.43
ZTb2	1.4	0.60	-7.14	43.32	1.88
ZTb3	1.6	0.63	-8.40	40.94	2.15
ZTb4	1.8	0.69	-9.27	40.31	2.56
ZTb5	2.0	0.62	-8.10	41.50	2.07
Devices	d_{ZnTe} (nm)	U_{oc} (V)	J_{sc} (mA/cm ²)	FF (%)	PCE (%)
ZTc1	20	0.94	-12.73	59.87	7.14
ZTc2	33	0.78	-19.16	49.71	7.40
ZTc3	48	0.77	-16.52	56.38	7.14
Devices	n (mg/ml)	U_{oc} (V)	J_{sc} (mA/cm ²)	FF (%)	PCE (%)
ZTd1	1.2	0.95	-15.52	61.56	9.05
ZTd2	1.4	0.95	-24.97	58.53	13.84
ZTd3	1.6	0.92	-25.97	51.92	12.36
ZTd4	1.8	0.86	-27.04	39.36	9.12

value of 2.56%. If the concentration of ZnTe in PEDOP:PSS increases more than 1.8 mg/ml, the energy efficiency of solar cells decreases continuously. The hysteresis with the concentration $n = 2.0$ mg/ml is lower than in the previous cell, and energy efficiency decreases to 2.07%.

ITO/ZnTe/PEDOT:PSS/MAPbI₃/PC₆₁BM/Ag structure: For the device with ZnTe layer with a thickness $d = 20$ nm, the ZTc1 functional dependence was obtained with the following characteristics: $V_{\text{oc}} = 0.94$ V, $J_{\text{sc}} = 12.73$ mA/cm², FF = 59.87% and PCE = 7.14%. For the device with a ZnTe thickness of about $d = 33$ nm (ZTc2 device) the short circuit current value increased significantly to about 19.16 mA/cm² and the open circuit voltage decreased to 0.78 V. If the thickness of the layer reaches the value $d = 48$ nm (ZTa3 device), the hysteresis decreases and the J-U characteristic moves upward, perpendicular to the current density axis. The respective devices showed a PCE > 7%, which for ZnTe as the electron transport layer in perovskite solar cells is a breakthrough in solar photovoltaics.

ITO/PEDOT:PSS/MAPbI₃: ZnTe/PC₆₁BM/Ag structure: For a device with the concentration $n = 1.2$ mg/ml the ZTd1 curve has been obtained with the following characteristics: open circuit voltage (V_{oc}) of about 0.95 V, a

short-circuit current (J_{sc}) of about 15.52 mA/cm² and a fill factor (FF) of 61.56%, corresponding to a power conversion efficiency (PCE) of 9.05%. By increasing the concentration of ZnTe to $n = 1.4$ mg/ml we notice that the open circuit voltage practically remains constant and the hysteresis of the J-U curve increases to a short-circuit current value of about 24.97 mA/cm², corresponding to the maximum value of PCE = 13.84%. If the concentration of ZnTe in CH₃NH₃PbI₃ increases more than at device ZTd2, the energy efficiency of solar cells decreases continuously as it decreases the V_{oc} and FF values.

4 Conclusions

We believe that the successful use of ZnTe thin films (and ZnTe-doped solutions) in perovskite-based solar cells can extend to several inorganic semiconductor materials, including n-type semiconductors (CdSe, ZnS, In₂S₃ etc.).

The use of ZnTe thin films in various perovskite structures represents a scientific novelty in the field.

Conflict of Interest The author declare that he have not of conflict of interest.

References

1. Stranks, S.D., Eperon, G.E., Grancini, G., Menelaou, C., Alcocer, M.J.P., Leijtens, T., Herz, L.M., Petrozza, A., Snaith, H.J.: Electron-hole diffusion lengths exceeding 1 micrometer in an organometal trihalide perovskite absorber. *Science* **341**, 342 (2013)
2. Yin, W.J., Shi, T., Yan, Y.: Unique properties of halide perovskites as possible origins of the superior solar cell performance. *Adv. Mater.* (2014)
3. Yin, W.J., Shi, T., Yan, Y.: Superior photovoltaic properties of lead halide perovskites: insights from first-principles theory. *J. Phys. Chem. C*. Publication Date (Web): 6 Feb 2015

The Influence of the External Magnetic Field on the Electronic Density of States of Quasi-1D System in the Mixed Phase of Superconductivity and Spin Density Wave

M. E. Palistrant, I. D. Cebotari, and S. A. Palistrant

Abstract

A method for calculating the electronic density of states in the mixed phase: superconductivity (SC) and the magnetic state of the spin-density wave (SDW) is proposed. The main mechanism for the appearance of this phase is considered the doping of the system and allowance for the lattice structure (Umklapp processes). The effect of an external magnetic field and the possibility of increasing the superconducting transition temperature T_c are analyzed.

Keywords

Superconductivity • Spin density wave • Electronic density of state • Umklapp processes • Green functions

1 Introduction

Numerous experimental studies of the properties of modern high-temperature materials demonstrate a surprising property: magnetism accompanies superconductivity; superconductivity (SC) arises either against the background of a state of a spin density wave (SDW), or after the suppression of magnetism because of doping. Modern high-temperature materials contain a number of features in the electronic energy spectrum, namely: it is multi-band system (several energy bands are present on the Fermi surface). Herewith a certain number of these bands characterize each compound, which can only be electronic, only of the hole-type or alternate between the two in different ratios. This situation requires a separate approach, when considering compounds

from the class of ferropnictides and ferrochalcogenides; different ideas are emerging about the mechanism of the appearance of superconductivity in these systems (reviews of the works refer to [1–3]). At present an agreement has been reached that in systems in which there are electron bands on the Fermi surface (the FeAs plane is responsible for superconductivity) the main mechanism of interaction in the appearance of superconductivity are the spin fluctuations. In other compounds with a basic superconducting plane FeSe, such a mechanism cannot be realized due to the lack of “nesting” in the electronic energy spectrum and the absence of a magnetic exchange interaction. In this case [3], the cause of high-temperature superconductivity is the numerous interband electron-electron interactions in a rarefied BCS type system [4]. It is interesting to note that in modern high-temperature superconductors phase transitions are observed, for example, the commensurate-incommensurate state of a spin density wave. As a result, in such materials occur the displacement of dielectric gap relative to the Fermi level and transition to a gapless magnetic system.

Another approach related to the role of the Fermi surface is given in [5, 6], which is based on the accounting of the changes of parameters (when doping) such as the change in the difference in the areas of the cavities of the Fermi surface of the bands under consideration and of the deviations from ellipticity.

As in the above-mentioned our works and in [5, 6], the appearance of superconductivity near the temperature of the magnetic transition is essential for the appearance of a mixed phase of the (SC + SDW). As already noted, the thermodynamic properties of this state are studied both in quasi-1D and two-dimensional cases. Of undoubted interest are the kinetic properties of such systems. In the study of kinetic characteristics, an important step is to determine the electronic density of states in the “mixed” phase of two long-range orderings: superconductivity and the spin-density wave state. This paper is devoted to this problem.

M. E. Palistrant · I. D. Cebotari (✉) · S. A. Palistrant
Institute of Applied Physics, Academiei, 5, Chisinau,
Republic of Moldova
e-mail: chebotar.irina@gmail.com

2 Hamiltonian of the System and Main Definitions

In the mean-field approximation, the Hamiltonian of the system under consideration has the form

$$\mathcal{H} = \mathcal{H}_0 + \mathcal{H}_{BCS} + \mathcal{H}_{SDW} + \mathcal{H}_{H_0}, \quad (1)$$

where

$$\mathcal{H}_0 = \sum_{\vec{k}\alpha} \left[\left(\varepsilon(\vec{k}) - \mu \right) a_{\vec{k}\alpha}^+ a_{\vec{k}\alpha}^- \right],$$

$$\mathcal{H}_{BCS} = \Delta \sum_{\vec{k}} \left(a_{\vec{k}\uparrow}^+ a_{-\vec{k}\downarrow}^+ + h.c. \right) \quad (2)$$

$$\mathcal{H}_{SDW} = -M \sum_{\vec{k}, \alpha, \beta} (\sigma^i)_{\alpha\beta} \left(a_{\vec{k}\alpha}^+ a_{\vec{k}+\vec{Q}, \beta}^- + h.c. \right),$$

$$\mathcal{H}_{H_0} = - \sum_{\vec{k}, \alpha, \beta} H_0 (\sigma^z)_{\alpha\beta} a_{\vec{k}\alpha}^+ a_{\vec{k}\beta}^-$$

Expression (1) contains the terms responsible for superconductivity, magnetism, and for the interaction of electrons with an external magnetic field. We chose representation in which for $i = z$ we have a parallel magnetic field ($\vec{H}_0 \parallel \vec{M}$) and for $i = x$ —perpendicular ($\vec{H}_0 \perp \vec{M}$), $\vec{\sigma}$ is the Pauli matrix:

$$\sigma^x = \begin{pmatrix} 0 & 1 \\ -1 & 0 \end{pmatrix}; \quad \sigma^z = \begin{pmatrix} 1 & 0 \\ 0 & -1 \end{pmatrix} \quad (3)$$

In expression (2), $a_{\vec{k}\alpha}^+$ and $a_{\vec{k}\alpha}^-$ are the creation and annihilation operators of electron with momentum \vec{k} and spin $\alpha = \uparrow, \downarrow$, μ is deviation from the middle filling of the energy band. The values Δ and M are the superconducting and magnetic order parameters:

$$\Delta = VT \sum_{\vec{k}, \omega_n} F_{-\vec{k}\vec{k}}^{\uparrow\downarrow}(\omega_n),$$

$$M = \frac{1}{2} IT \sum_{\vec{k}, \omega_n, \alpha} \alpha G_{\vec{k}-\vec{Q}, \vec{k}}^{\alpha\alpha}(\omega_n), \quad (4)$$

$$\omega_n = (2n + 1)\pi T, \quad n = 0, \pm 1, \pm 2, \pm 3, \dots$$

Here V and I are the BCS- and exchange interaction constants; F and $G^{\alpha\alpha}$ is the Fourier representation of the temperature Green's functions (normal and anomalous), ω_n is Matsubara frequency.

We consider a quasi-1D system with the dispersion law

$$\varepsilon(k) = -W \cos kd, \quad (5)$$

where W is the half-width of the energy band, d is the lattice parameter. With the middle filling of the energy band $\mu = 0$

and the external magnetic field $H_0 = 0$, the “nesting” condition is satisfied:

$$\varepsilon(k) = -\varepsilon(k + Q_0). \quad (6)$$

Herewith the quasi-1D system is in the magnetic state of the SDW with the wave vector $Q_0 = \pi/d$. The deviation from the middle filling of the energy band $\mu \neq 0$, as well as the inclusion of an external magnetic field \vec{H}_0 violate the “nesting” condition, as a result, there are phase transitions of the commensurable-incommensurable state of the SDW, an order parameter arises that determines this incommensurability. Herewith the dielectric gap shifts with respect to the Fermi surface, and the magnetic system goes to a gapless state: free carriers appear on the Fermi surface and, as a result, coexistence of superconductivity and magnetism is possible.

Such a mechanism for the appearance of superconductivity against the background of magnetism has been studied, for example, in our works [3, 7, 8]. In these papers, thermodynamic properties of doped systems of reduced dimensionality are mostly analyzed. A further stage of the investigation consists in a more detailed study of the effect of an external magnetic field on the thermodynamic properties of the systems under consideration, as well as the study of the effect of the lattice structure (the Umklapp process) on the kinetic characteristics of the mixed state (SC + SDW). The first step to solve this problem is to calculate the density of electronic states. We start from the mean-field approximation. This approach is possible if we consider a three-dimensional system in which the motion of electrons is one-dimensional. The three-dimensionality of the system cancels the existing fluctuations, which makes it possible to apply the mean-field theory (the justification see in the above our works). We use the method of Green's functions [9]. In the Hamiltonian (1), the order parameters of the magnetic (M) and superconducting (Δ) orderings are determined by the relation (5), where ω_n is the Matsubara frequency. Applying the method of temperature Green's functions [9] based on the Hamiltonian (1) we obtain for the introduced Green's functions in the case of a parallel magnetic field $\vec{H}_0 \parallel \vec{M}$ following expressions:

$$G_{kk}^{\uparrow\downarrow}(\omega_n) = -\frac{D_1(\omega_n)}{D_{H_0}(\omega_n)},$$

$$F_{-kk}^{\uparrow\downarrow} = \frac{\Delta \left\{ -(i\omega_n + H_0)^2 + \varepsilon_2^2 + \Delta^2 + M^2 \right\}}{D_{H_0}(\omega_n)}, \quad (7)$$

$$G_{\vec{k}-\vec{Q}, \vec{k}}^{\sigma\sigma}(\omega_n) = \sigma \frac{M [M^2 - \Delta^2 + (i\omega_n + H_0 + \varepsilon_1)(i\omega_n + H_0 + \varepsilon_2)]}{D_{H_0}(\omega_n)},$$

where

$$D_1 = \left[-(i\omega_n + H_0)^2 + \varepsilon_2^2 + \Delta^2 \right] + M^2(i\omega_n + H_0 - \varepsilon_2),$$

$$D_{H_0}(\omega_n) = (i\omega_n + H_0)^4 - (i\omega_n + H_0)^2(\varepsilon_1^2 + \varepsilon_2^2 + 2M^2 + 2\Delta^2) + \varepsilon_1^2\varepsilon_2^2 - 2M^2\varepsilon_1\varepsilon_2 + \Delta^2(\varepsilon_1^2 + \varepsilon_2^2) + (M^2 - \Delta^2)^2.$$

Substituting the necessary Green's functions (7) into the expressions (4), we obtain a system of equations for the order parameters Δ and M . One can solve this system numerically for given values of the parameters μ and H_0 . First we should choose a one-dimensional or two-dimensional cosine law of dispersion and go from summation over \vec{k} to integration with respect to energy, taking into account the transition of the system to the incommensurate state of the SDW (for example, refer to [3, 7, 8]). Below we present a method for taking into account the Umklapp processes associated with a change in the wave vector of a spin density wave $Q \neq 2k_F$ of a quasi-1D system.

3 The Calculation of the Electronic Density of States

The relation determines the density of electronic states with allowance for Umklapp processes and in the presence of an external magnetic field $H_0 \parallel M$

$$N^\dagger(\omega) = N_N^\dagger(\omega) + N_u^\dagger(\omega), \quad (8)$$

where $N_N^\dagger(\omega)$ is determined by the normal processes and $N_u^\dagger(\omega)$ by the Umklapp processes in the magnetic field H_0 chosen in the direction \vec{M} .

The contribution to the electronic density of state from the normal processes is determined by the following equation

$$N_N^\dagger(\omega) = \frac{1}{\pi} \sum_{q < k < Q_0} \text{Im} G_{kk}^{\dagger\dagger}(z) \Big|_{z=\omega-i\delta} \quad (9)$$

The domain of sum in this formula is determined by the conditions $|\vec{k}| < Q_0$ and $|\vec{k} - \vec{Q}| < Q_0$.

The account of Umklapp processes reduces to additional summation over the domain $-Q_0 < k < q$, that is

$$N_u^\dagger(\omega) = \frac{1}{2\pi^2} \int_{-Q_0}^q dk \text{Im} G_{kk}^{\dagger\dagger}(z) \Big|_{z=\omega-i\delta} \quad (10)$$

Next, we substitute the expression of necessary Green function from (7) in (9) and (10) and use the cosine law (5), representing ε_1 and ε_2 as

$$\varepsilon_1 = \varepsilon_{k-\frac{q}{2}} \cos \frac{qd}{2} - \mu_-$$

$$= \varepsilon - \mu_-$$

$$\text{and } \varepsilon_2 = - \left[\varepsilon_{k-\frac{q}{2}} \cos \frac{qd}{2} + \mu_- \right] = -(\varepsilon + \mu_-).$$

$$\mu_{\pm} = \mu \pm \eta, \quad \eta = W \sin \left(\frac{qd}{2} \right).$$

We consider small deviations of the wave vector of the spin density wave from $2k_F$ ($\frac{q}{2k_F} \ll 1$); therefore, we will assume $\sin(qd/2) \approx qd/2$ and $\cos(qd/2) \approx 1$.

After performing the integration in (9) and (10), for the total electronic density of states we obtain

$$\frac{N(\omega)}{N_0} = \text{Re} \{ I(\omega, H_0, \mu_-) + I(\omega, H_0, \mu_+) \}, \quad (11)$$

where

$$N_0 = 4\pi dW \cos \frac{\pi d}{2},$$

$$I(\omega, H_0, \mu_{\pm}) = \frac{C}{B} [F_1 - F_2] - [\omega + H_0 + \mu_{\pm}] [F_1 + F_2],$$

$$C = C(\omega, H_0, \mu_{\pm}) = -2\mu(\omega + H_0)(\omega + H_0 + \mu) + 2\mu_{\pm}^2,$$

$$B = B(\omega, H_0, \mu_{\pm}) = -2 \text{sign}(\omega + H_0)^2 [\mu_{\pm}^2(\omega + H_0) + M^2\Delta^2 - \mu_{\pm}^2\Delta^2]^{1/2},$$

$$F_1 = F_1(\omega, H_0, \mu_{\pm}) = -\text{sign} \left[\omega + H_0 - \frac{\mu_{\pm}(\omega + H_0)}{\sqrt{\mu_{\pm}^2(\omega + H_0)^2 + M^2\Delta^2 - \mu_{\pm}^2\Delta^2}} \right] \cdot \left[(\omega + H_0)^2 + \mu_{\pm}^2 - M^2 - \Delta^2 + B \right]^{-1/2},$$

$$F_2 = F_2(\omega, H_0, \mu_{\pm}) = -\text{sign} \left[\omega + H_0 + \frac{\mu_{\pm}(\omega + H_0)}{\sqrt{\mu_{\pm}^2(\omega + H_0)^2 + M^2\Delta^2 - \mu_{\pm}^2\Delta^2}} \right] \cdot \left[(\omega + H_0)^2 + \mu_{\pm}^2 - M^2 - \Delta^2 + B \right]^{-1/2}.$$

4 Numerical Calculation and Discussion of Results

The expressions (11) determine the electronic density of states in the mixed phase (SC + SDW) for a given value of the external magnetic field H_0 and the deviation from the

middle filling of the energy band μ in the phase of coexistence of the SC and the incommensurate state of SDW due to the external magnetic field H_0 and the deviation of vector of a spin density wave from $2k_F$.

No parameters of the theory μ , η , T , H_0 , M , Δ are independent. They are in complex dependence on each other, which is defined by the system of Eqs. (4). The problem becomes simpler, if we consider the nucleation of weak superconductivity against the background of the SDW. In this case, we pass to the limiting transition $\Delta \ll M$.

As a result, we obtain

$$\frac{N(\omega)}{N_0} = \text{Re} \left\{ \frac{|\omega + H_0 + \mu_-|}{\sqrt{(\omega + H_0 + \mu_-)^2 - M^2}} + \frac{|\omega + H_0 + \mu_+|}{\sqrt{(\omega + H_0 + \mu_+)^2 - M^2}} \right\}, \quad (12)$$

It follows that $N(\omega) \neq 0$, if $|\omega + H_0 + \mu_-|, |\omega + H_0 + \mu_+| > M$.

In Fig. 1 the dependence of density of electronic states on the Matsubara frequency for this case is presented. It is assumed that the system is in a weak magnetic field, such that the energy of interaction of electrons with a system of spins is of the order of $0.2 T_{s0}$ (here T_{s0} —is the temperature of magnetic transition in absence of superconductivity at $\mu = 0$). In this case, the η and μ weakly depend on the magnetic field. In this regard, we can use the values of these parameters calculated for a quasi-1D system in the absence of a magnetic field [7]. Figure 1 shows that parameter η contributes to the increase of the electronic density of state in some regions of ω/T_{s0} .

Now let us consider some limiting cases:

1. $H_0 = 0$, $\eta = 0$. The system is in a dielectric state (in the commensurate state of the SDW, the “nesting” condition is satisfied (6)).
2. $H_0 = 0$, $\eta \neq 0$

For $\mu = \mu_c$ the system goes to the phase of the incommensurate state of the spin density wave with the incommensurability parameter η . In the domain $\mu > \mu_c$ an ambiguous correspondence arises between the temperature of the magnetic transition T_M and μ , i.e. the state of the SDW becomes unstable. The phase transition to the incommensurate state of the SDW, taking into account the Umklapp processes, contributes to the stabilization of the state by transition to a semi-metallic state ($Q \neq 2k_F$, $\eta \neq 0$). There is the possibility of the appearance of superconductivity.

The inclusion of an external magnetic field makes a definite contribution to the value of η and, consequently, in a definite range of values of the magnetic field accelerates the transition to the above-mentioned metallic state, and, consequently, gives an increase in the superconducting

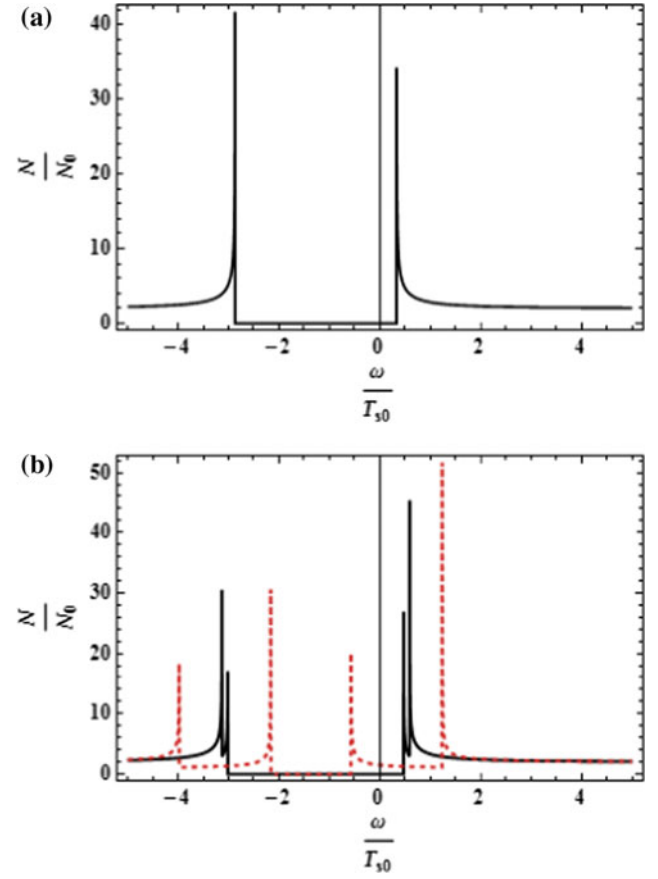


Fig. 1 The electronic density of state $N(\omega)/N_0$ at $H_0 = 0.2T_{s0}$ **a** $\mu = 1.072T_{s0}$, $\eta = 0$, $M = 1.6T_{s0}$; **b** $\mu = 1.17T_{s0}$, $\eta = 0.904T_{s0}$, $M = 1.7T_{s0}$ (dashed curve), $\mu = 1.073T_{s0}$, $\eta = 0.059T_{s0}$, $M = 1.8T_{s0}$ (thin curve)

transition temperature. The same situation occurs when charge density wave and superconductivity arise in the system (for example, refer to [10]). Consequently, in strongly anisotropic systems with a variable density of charge carriers in the phase of coexistence of superconductivity and spin density wave, as well as superconductivity and charge density wave, the temperature of the superconducting transition may increase with increasing external magnetic field.

5 Conclusions

Using the method of Green’s function, we determined the electronic density of states of a quasi-1D system in the “mixed phase” of coexistence of SC and the incommensurate state of the SDW in the presence of an external magnetic field. Herewith we took into account the influence of the Umklapp processes (lattice structure). Under the assumption of the generation of weak superconductivity against the background of the SDW, we analyzed various

limiting cases. As a result, we discussed the possibility of realizing the mixed phase of the incommensurate state of SDW with superconductivity. We have shown that the inclusion of an external magnetic field of a certain range promotes an increase in the electronic density of states and an increase in the temperature of the superconducting transition. This is an unusual and surprising picture, illustrating the favorable effect of an external magnetic field on superconductivity.

Conflict of Interest The authors declare that they have no conflict of interest.

References

1. Chubukov, A., Hirschfeld, P.J.: Iron-based superconductors, seven years later. *Phys. Today* **68**(6), 46–52 (2015)
2. Sadovskii, M.V.: High-temperature superconductivity in monolayers FeSe. *Phys. Usp* **59**, 947–967; *Usp Fiz Nauk* **186**, 1035–1057 (2016)
3. Palistrant, M.E.: Magnetism and superconductivity in a quasi-2D anisotropic system doped with charge carriers. *JETP* **123**, 86–97; *Zh. Exp. Teor. Fiz.* **150**, 97–110 (2016)
4. Kochorbe, F.G., Palistrant, M.E.: Thermodynamic properties of two-band superconductors with low carrier density. *Theor. Math Phys.* **96**, 1083–1091; *Teor. Mat. Fiz.* **96**, 459–472; *Zh. Exp. Teor. Fiz.* **104**:3084–3102; *JETP* **77**, 442–452 (1993)
5. Vorontsov, A.B., Vavilov, M.G., Chubukov, A.V.: Superconductivity and spin-density waves in multiband metals. *Phys. Rev. B* **81** (17), 174538; arXiv: 1003.2389 (2010)
6. Kuzmanovski, D., Levchenko, A., et al.: Effect of spin-density wave fluctuations on the specific heat jump in iron pnictides at the superconducting transition. *Phys. Rev. B* **89**(14), 144503 (2014)
7. Moskalenko, V.A., Kon L.Z., Palistrant M.E.: Low-temperature properties of metals with features of the band spectrum, Stiinta, Kishinev (in Russian) (1989)
8. Moskalenko, V.A., Kon, L.Z., Palistrant, M.E.: Theory of Many-Band Superconductivity. Editura tehnica, Bucuresti (2008). (in Romanian)
9. Abrikosov, A.A., Gorkov, L.P., Dzyaloshinski, I.E.: Methods of Quantum Field Theory in Statistical Physics. Gos. Izd. fiz. mat. literatury, Moscow (1962). (in Russian)
10. Vackalyuk, V.M., Palistrant, M.E., Padure, I.V.: Thermodynamic and magnetic properties of quasi-one-dimensional systems in the coexistence phase of the charge-density wave and superconductivity. *J. Phys. Condens. Matter* **2**, 2699–2711 (1990)

Elastic Coupling at Epitaxial Multiferroic Interfaces: In Situ X-Ray Studies of Electric Field Induced Strain

C. T. Koops, S. B. Hrkac, M. Abes, P. Jordt, J. Stettner, A. Petraru, H. Kohlstedt, V. Hrkac, N. Wolff, L. Kienle, O. H. Seeck, G. Nisbet, O. M. Magnussen, and B. M. Murphy

Abstract

The elastic coupling in multiferroic materials and even more so in magnetoelectric composites plays an important role for the properties and function. In this study, the electrically induced strain at the epitaxial interface of $0.72\text{Pb}(\text{Mn}_{1/3}\text{Nb}_{2/3})\text{O}_3\text{--}0.28\text{PbTiO}_3\text{--}\text{CoFe}_2\text{O}_4$, a magnetoelectric composite, is characterized by in situ X-ray scattering experiment and transmission electron microscopy study. For the measured range all strain induced lattice changes are reversible ruling out plastic deformation. The surprisingly non-perfect elastic coupling of $87 \pm 7\%$ in this epitaxial system can be explained by the presence of planar defects in the CFO film.

Keywords

Magnetoelectric composites • Strain coupling • XRD • TEM

1 Introduction

Multiferroic materials combine different interesting properties, such as magnetic polarization and elastic deformation [1]. Magnetoelectric (ME) materials are of great interest as magnetic field sensors or in electrically switchable memory structures [2]. In particular ME composites present exciting opportunities because as compared to single-phase ME materials, they have very high ME coefficients at room temperature [3]. The possibility to tailor specific components with a strong ME response, makes them excellent candidates for technological applications such as magnetic field sensors [4]. ME composites consist of a magnetostrictive (MS) and a piezoelectric (PE) component. An applied electric field induces strain in the PE phase, the strain is then transferred via the interface into the MS phase and changes the magnetization or vice versa [5]. Hence, the elastic coupling at the interface is of central importance. To date, detailed structural investigations of the field dependent strain near these interfaces are very rare and recent simulations of the ME coefficient result systematically in values that are too high [6].

Strain engineering in epitaxial films of ferroic oxides has been investigated intensively in the last years [7]. It was shown that with increasing film thickness dislocations are introduced, leading to inhomogeneous strain distributions and the degradation of strain-induced properties. In contrast we discuss the reduction of epitaxial strain in the elastic regime and its influence on the interface coupling in ME composites based on X-ray scattering and transmission electron microscopy (TEM) [8]. As PE component lead based ferroelectric materials with a perovskite structure are ideal because of their extremely high PE coefficient [9]. Domain engineered single crystals of the relaxor material $\text{Pb}(\text{Mn}_{1/3}\text{Nb}_{2/3})\text{O}_3$ (PMN) and ferroelectric PbTiO_3 (PT) exhibit a morphotropic phase boundary (MPB) between the rhombohedral and the tetragonal phase. For $0.71\text{PMN}\text{--}0.29\text{PT}$ a large d_{33} piezoelectric coefficient of $1540 \text{ pC} = N$ is reported [10]. As MS material an epitaxial ferroic

C. T. Koops · S. B. Hrkac · M. Abes · P. Jordt · J. Stettner · O. M. Magnussen · B. M. Murphy (✉)
Institute of Experimental and Applied Physics, Kiel University,
19 Leibnizstr., Kiel, Germany
e-mail: murphy@physik.uni-kiel.de

A. Petraru · H. Kohlstedt
Nanoelectronics, Technical Faculty, Kiel University, Kiel,
Germany

V. Hrkac · N. Wolff · L. Kienle
Institute of Material Sciences, Kiel University, Kiel, Germany

O. H. Seeck
Photon Science, DESY, Hamburg, Germany

G. Nisbet
Diamond Light Source, Harwell Science and Innovation Campus,
Didcot, UK

O. M. Magnussen · B. M. Murphy
Ruprecht Haensel Laboratory, Kiel University, Kiel, Germany

oxide CoFe_2O_4 (CFO). CFO has been shown to grow epitaxially on PMN-PT substrates [11] and has a high saturation magnetostriction (-6×10^{-4}) [12] along the [100] direction.

2 Experimental Setup

We use 0.72PMN-0.28PT (001) single crystalline substrates of $10 \times 10 \text{ mm}^2$ from SINOCERA polished chemo-mechanically (Crystec GmbH, Berlin) down to a thickness of 0.3 mm to achieve a flat interface with low roughness. The long edges are parallel to the [100] and [010] direction respectively. Afterwards, an epitaxial CFO layer of 200 nm thickness is grown on top of the polished (001) surface via pulsed laser deposition (PLD). The high quality of both the PMN-PT substrate and the epitaxially grown CFO layer were verified using a combination of X-ray and TEM methods (see Fig. 1). This CFO layer thickness allows X-ray grazing incidence diffraction (GID) investigations. The corresponding interface structure is shown in Fig. 2b. The lattice parameter of the cubic spinel structure of the CFO is 8.391 \AA and is therefore 4.2% larger than twice the lattice parameter of the PMN-PT substrate (4.027 \AA), allowing epitaxial growth. These epitaxial conditions and the stoichiometric composition of Fe and Co are confirmed by TEM/EDX (see Fig. 1c) measurements. A gold electrode is deposited on the back of the substrate allowing a uniform electric field up to 17 kV cm^{-1} to be applied along the [001] crystal direction for the largest piezoelectric response of the substrate [13] (see Fig. 2a). The large electromechanical response in PMN-PT substrates is attributed to the polarization rotation mechanism induced by the applied electric field involving structural phase transformations [14]. Using

high resolution GID and bulk X-ray diffraction, the electrically induced strain in a single crystalline PMN-PT substrate and its transfer to epitaxially grown CFO layers is studied [15]. Here, the field induced in-plane and out-of-plane strain were obtained for both the PMN-PT substrate and the CFO layer on top by monitoring the corresponding Bragg reflections.

To investigate the electric field induced strain behavior in situ GID investigations were carried out at the Diamond Light Source and at PETRA III. Here, we show GID data measured using a 6-circle-diffractometer at a photon energy of 25.06 keV with the scattering geometry shown in Fig. 2a. To vary the penetration depth we chose the incidence angles α of 1.26, 1.55 or 2.42 times the critical angle ($\alpha_c = 0.103^\circ$) of the CFO layer, to measure the CFO(400) and PMN-PT (200) reflections and consequently the field dependent deformation of both materials in parallel. The use of a 1-D Mythen detector (DECTRIS) gives access to a wide range of exit angles β and consequently several penetration depths at every incidence angle. The beam size was set to $50 \times 100 \mu\text{m}^2$ (Hor. \times Vert.). The probed volume as defined by Dosch [16] can be calculated from the incidence angle α and the angle β . In addition, complementary X-ray diffraction measurements of the out-of-plane PMN-PT(002) and CFO(004) reflections were performed at a rotating anode lab-source with a photon energy of 8.048 keV equipped with a Ge(111) double crystal monochromator.

For real structure studies transmission electron microscopy (TEM) was applied using a FEI Tecnai F30 G² STwin which is operated at 300 kV. The spherical aberration coefficient of the microscope is given by $C_s = 1.2 \text{ mm}$. A specimen was prepared as cross-section thin lamellae via focused ion beam (FIB) milling using a lift-out method with

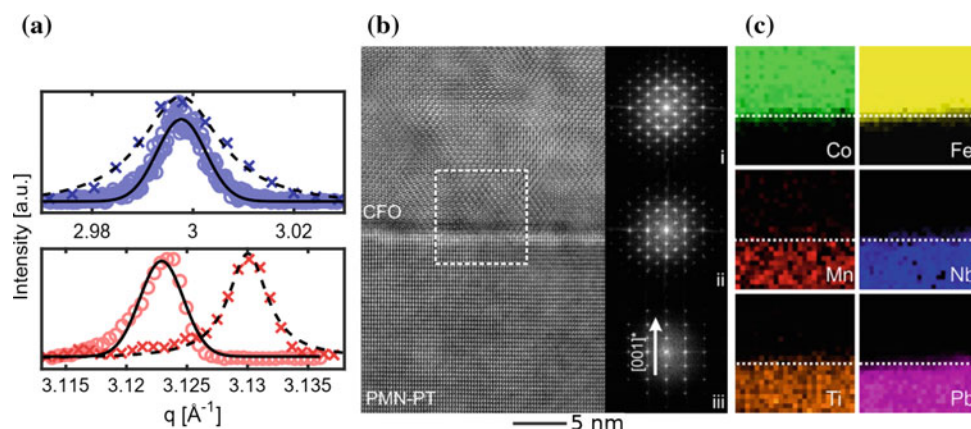


Fig. 1 X-ray and TEM measurements showing the high quality within the short- and long-range order of crystalline CFO/PMN-PT. **a** Out-of-plane (o) and in-plane (x) reflections of CFO(004) & CFO (400) (upper panel) and PMNPT(002) & PMN-PT(200) (lower panel). The out-of-plane peaks were fitted with Gaussian (—), the in-plane peaks with Lorentzian (— —) functions. **b**, **c** TEM study of the

CFO/PMN-PT interface. **b** HRTEM micrograph with associated FFTs for (b-i) the CFO layer, (b-ii) the interface region and (b-iii) the PMN-PT layer. **c** STEM-EDX measurement of the chemical composition at the interface region. The elemental maps were recorded inside the squared region in (b)

a FEI Helios Nanolab system. High resolution (HR)TEM micrographs and its corresponding Fast Fourier Transforms (FFTs) were evaluated with the analysis software Digital Micrograph 3.6.1 (Gatan, Inc.) (DM) and CRISP (Calidris). For the contrast enhancement of HRTEM micrographs the HRTEM filter plug-in for DM was applied [17].

3 Results and Discussion

Figure 2 shows the GID measured CFO(400) (c) and PMN-PT(200) (d) reflections for electric fields of 16.7 and 1.7 kV cm⁻¹. These in-plane peaks were fitted with two Lorentzian curves, as multiple close-by crystalline domains emerge due to domain reorientation by in situ applying external forces [18]. The out-of-plane reflections CFO(004) and PMNPT(002) (see Fig. 1) were fitted with Gaussian peaks because of the limiting lower resolution of the laboratory source. The lattice parameter can be calculated from the position of the peaks as a function of the electric field. During the increase of the applied electric field a nonlinearity can be observed at the coercive field. Hence, we saturated the sample with high fields first and focus on the behavior for decreasing field, so that it can be described with a constant PE coefficient [19]. The field dependent peak shift

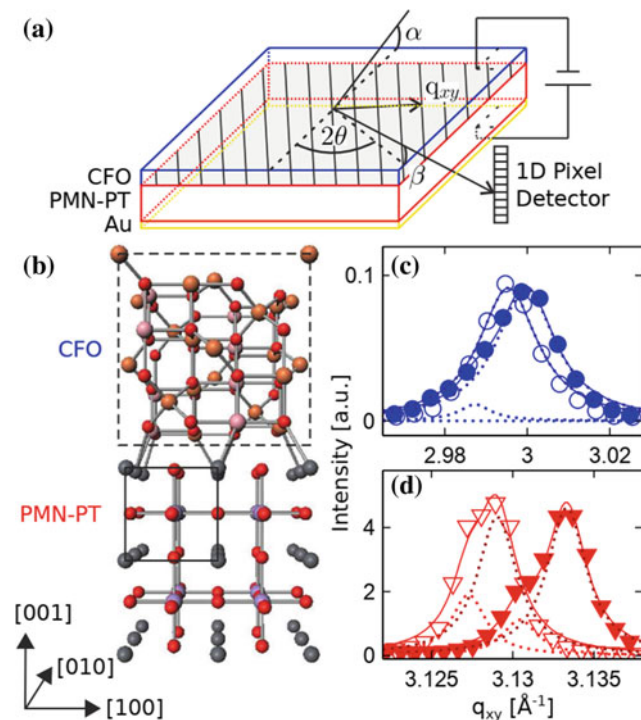


Fig. 2 **a** Scattering geometry. **b** Atomic interface structure. The lattice parameter of the CFO unit cell (dashed box) is more than twice as large as the PMNPT lattice parameter (solid box). In-plane reflections at $1.55 \times \alpha_c$ of **c** CFO(400) and **d** PMN-PT(200) for 1.7 kV cm⁻¹ (open symbols) and 16.7 kV cm⁻¹ (solid symbols)

in both materials is clearly visible, although the peak width of the CFO layer is significantly larger than the width of the PMN-PT peak. An influence of the field onto the peak width cannot be seen. Taking into account the large footprint due to the GID geometry which means that the X-ray data are averaged along the whole surface of the sample we conclude that the constant peak width for different electric fields verifies the homogeneous deformation of the crystal lattice. Consequently, the electric field within the sample is homogeneous, too.

The upper panel in Fig. 3a shows the out-of-plane deformation for both materials as a function of the decreasing electric field. The lower panel shows the compressive strain perpendicular to the field measured in GID geometry, revealing a significantly reduced strain in the CFO layer compared with the substrate. The field was repeatedly cycled and demonstrated a fully reversible behavior, see Fig. 3b. The lattice mismatch of 4.2% results in a compressive deformation of the CFO layer. Thus, the reduced strain in the CFO layer cannot be explained by mismatch relaxation.

The PE coefficient $d_{[100]} = \Delta\epsilon/\Delta E$ was determined by linear fits to the data with $d_{[100]}^{PMN-PT} = -998 \pm 21$ pm V⁻¹

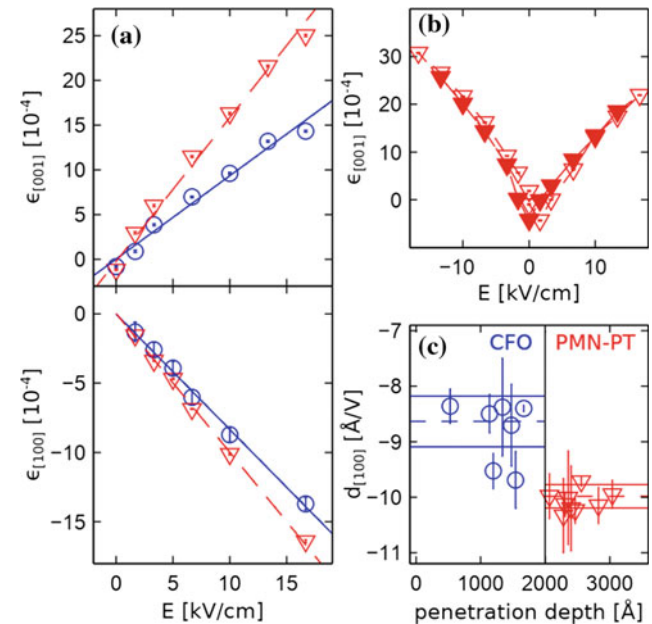


Fig. 3 **a** Strain as a function of decreasing electric field in the PMN-PT substrate (triangles) and the CFO film (circles). The data corresponds to out-of-plane strain $\epsilon_{[001]}$ (upper panel) and in-plane strain $\epsilon_{[100]}$ (lower panel). The corresponding linear fits are shown as dashed or solid lines, respectively. **b** Induced strain $\epsilon_{[100]}$ as a function of the applied electric field from the PMN-PT(002) reflection. The reversibility proves the elastic behavior of the PMN-PT substrate. The displacement because of the ferroelectric hysteresis is visible. **c** $d_{[100]}$ as a function of the penetration depth. The stepwise change at the interface indicates imperfect elastic coupling

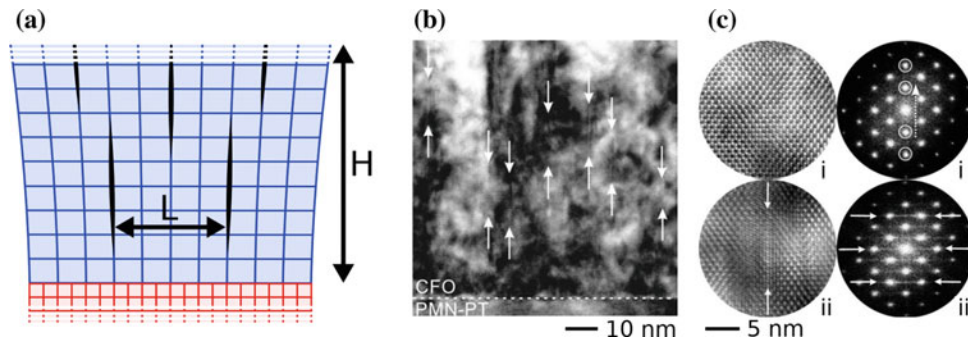


Fig. 4 **a** Schematic of strained multiferroic composite. The macroscopically induced tensile strain in the piezoelectric induces a deformation within the magnetostrictive layer into an intracolumnar component with a width of L quantifiable via X-ray diffraction and an intercolumnar component, responsible for creating additional volume between the columnar domains of the magnetostrictive layer visible as planar defects in **(b, c)** HRTEM measurements. **b** HRTEM micrograph

from the interface of CFO and PMN-PT along the $[110]$ zone axis. **b** Magnified view of two regions: (i) without and (ii) with the presence of planar defects. **c** Corresponding FFTs of the micrographs of **(b)**. The solid arrows mark selected planar defects in the real and reciprocal space. The dashed arrow **(c-i)** marks the growing direction along $[100]$ and the Bragg intensities marked with white circles **(c-i)** correlate with the (002) planes of CFO

for PMN-PT and $d_{[100]}^{CFO} = -863 \pm 46 \text{ pm V}^{-1}$ for CFO. Figure 3c shows the piezoelectric coefficient as a function of the depth. No systematic relaxation of $d_{[100]}$ with increasing depth is found, suggesting a homogeneous deformation of the film. At the interface the in-plane PE coefficient changes abruptly, indicating that the transfer of the strain at the interface is non perfect. The resulting strain coupling at the interface is $c_{[100]} = 87 \pm 7\%$. A similar non-perfect coupling is observed for the out-of-plane strain $\epsilon_{[001]}$ (see Fig. 3a, upper panel). The out-of-plane changes in the lattice parameter of the CFO films depend of course also on the elastic properties of the CFO films (Poisson ratio). These values can be directly compared to the data from the GID experiment, because of the homogeneous film deformation. The resulting PE constants are $d_{[100]}^{PMN-PT} = 1663 \pm 80 \text{ pm V}^{-1}$ for PMN-PT and $d_{[100]}^{CFO} = 1000 \pm 40 \text{ pm V}^{-1}$ for CFO. The strain coupling between the out-of-plane coefficients $d_{[001]}$ is calculated to be $c_{[001]} = 60 \pm 6\%$, which is clearly lower than the in-plane coupling from the GID experiment. This result is expected, as c_{001} is a product property of the PE coefficients of PMN-PT, the Poisson ratio of the CFO layer and the in-plane coupling.

The Poisson ratio of the CFO layer can be calculated directly from the in-plane and out-of-plane strain. For decreasing field, in the case of an intrinsic piezoelectric response the averaged piezoelectric deformation is symmetric [13]. For an epitaxial film subjected to biaxial stress, the apparent Poisson ratio ν^* is given by $\nu^* = -\epsilon_{[001]}/\epsilon_{[100]} = 2\nu/(1 - \nu) = 1.2 \pm 0.1$, where $\epsilon_{[001]}$ and $\epsilon_{[100]}$ are the strains measured in bulk and GID geometry respectively and ν is the Poisson ratio. One can calculate then the Poisson ratio for our CFO films $\nu = \nu^*/(\nu^* + 2) = 0.37 \pm 0.02$. Our results show that the 2000 \AA film under electrically induced strain behaves exactly like bulk CFO.

The surprising non-unity in-plane coupling c_{100} cannot be explained by a model assuming homogeneous materials since inelastic effects can be excluded because of the high reversibility of the strain behaviour in the applied field. However, by considering a second elastic component contributing to the strain relaxation apart from the lattice deformation of the CFO crystallites this behaviour can be explained. We attribute this second elastic component to a columnar structure induced by the presence of planar defects in our films, as suggested by the HRTEM micrographs from the interface. These defects are propagating parallel to the $[001]$ growth direction within the CFO layer. We can regard the volumes between two adjacent planar defects as small incoherently diffracting domains. The averaged size of these domains can be roughly estimated using Scherrer's equation from the broadening of the measured CFO (100) XRD peaks. The result indicates a columnar growth separated by planar defects with an in-plane size of $330 \pm 40 \text{ \AA}$. Hence, the columnar structure of CFO exhibits microscopic boundaries where epitaxial defects occur. This morphology is also confirmed by TEM investigations showing the planar defects in the CFO layer. The common interface between the PMN-PT and the CFO layers is depicted in the HRTEM micrographs of Fig. 4. Within the CFO layers planar defects can be detected propagating parallel to the growth direction $[001]$ as indicated by arrows in Fig. 4a, b. As a further effect of the defects, diffuse intensity streaks are observable within the corresponding Fourier transform extended perpendicular to the growth direction, cf. Fig. 4c. Additionally, an elongation of the Bragg intensities is found, compare Fig. 4c-i with Fig. 4c-ii. A theoretical model that reveals a relation between stress and macroscopic strain in nanocrystalline materials has been developed by Weissmüller et al. [20]. These considerations result in an effective Young's modulus $Y_{eff} = Y_0(1 - \frac{2}{15}kY_0\alpha)$, with the bulk modulus Y_0 , volume

specific domain boundary area $\alpha = A/V$ and a scalar slip compliance parameter k [20] which describes the statistical averaged displacement at the grain boundaries for a given tension. In our case, the ratio of the effective Y_{eff} and the bulk modulus Y_0 is given by the ratio of the piezoelectric constant of PMN-PT (d_{100}^{PMN-PT}) and the d_{100}^{CFO} coefficient of the CFO layer. If we assume a Young modulus of a bulk CFO crystal of 146.56 GPa calculated from experimentally determined elastic coefficients [21] and an in-plane columnar domain size of 330 ± 40 Å, the resulting slip compliance parameter is 55 ± 30 pm GPa⁻¹. The value is of the same order of magnitude, as for Pd [20] and corresponds to a realistic root-mean-square displacement at the boundaries of just a few picometers.

4 Conclusions

In summary, our direct high resolution X-ray studies of field-induced strain demonstrate that even for structurally well-defined epitaxial systems the coupling at ME interfaces is imperfect. The homogeneous deformation occurs directly at the interface, which can be explained by the presence of planar defects in the CFO layer. These results indicate that the defects have an important influence on the efficiency of the elastic coupling at multiferroic interfaces and hence, on the magnitude of multiferroic effects. Similar and even stronger strain relaxation is expected in composites for technological applications, which often are non-epitaxial the grain boundaries may accommodate a large amount of mechanical strain. Consequently, multiferroic effects may be significantly improved by controlled grain-engineering and simulations may reach a new level of accuracy contributing to future developments in magnetic sensor technologies.

Acknowledgements We acknowledge the financial support provided via SFB855, PAK902 & SFB1261 (Deutsche Forschungsgemeinschaft) and the ERA.Net RUS project NANO-C (STProjects-133). We thank DESY and the Diamond Light Source for access and the staff of P08 and I16 for the support during the experiments.

Conflict of Interest The authors declare that they have no conflict of interest.

References

1. Eerenstein, W., Mathur, N.D., Scott, J.F.: *Nature* **442**, 759 (2006)
2. Bibes, M., Barthélémy, A.: *Nat. Mater.* **7**, 425 (2008)
3. Eerenstein, W., Wiora, M., Prieto, J.L., Scott, J.F., Mathur, N.D.: *Nat. Mater.* **6**, 348 (2007)
4. Röbisch, V., Salzer, S., Urs, N., Reermann, J., Yarar, E., Piorra, A., Kirchhof, C., Lage, E., Höft, M., Schmidt, G., et al.: *J. Mater. Res.* **32**, 1009 (2017)
5. Sahoo, S., Polisetty, S., Duan, C.-G., Jaswal, S.S., Tsymbal, E.Y., Binek, C.: *Phys. Rev. B* **76**, 092108 (2007)
6. Liverts, E., Grosz, A., Zadov, B., Bichurin, M.I., Pukinskiy, Y.J., Priya, S., Viehland, D., Paperno, E.: *J. Appl. Phys.* **109**, 07D703 (2011)
7. Zhu, M., Nan, T., Peng, B., Zhang, Y., Zhou, Z., Yang, X., Ren, W., Sun, N., Liu, M.: *IEEE Trans. Magn.* **53**, 1 (2017)
8. Zheng, R., Wang, Y., Liu, Y., Gao, G., Fei, L., Jiang, Y., Chan, H., Li, X., Luo, H., Li, X.: *Mater. Chem. Phys.* **133**, 42 (2012)
9. Bellaiche, L., Vanderbilt, D.: *Phys. Rev. Lett.* **83**, 1347 (1999)
10. Zhang, S.J., Lee, S.M., Kim, D.H., Lee, H.Y., Shrout, T.R.: *J. Am. Ceram. Soc.* **91**, 683 (2008)
11. Wang, Z., Viswan, R., Hu, B., Li, J., Harris, V., Viehland, D.: *J. Appl. Phys.* **111**, 034108 (2012)
12. Bozorth, R.M., Tilden, E.F., Williams, A.J.: *Phys. Rev.* **99**, 1788 (1955)
13. Zhang, R., Jiang, B., Cao, W.: *J. Appl. Phys.* **90**, 3471 (2001)
14. Bai, F., Wang, N., Li, J., Viehland, D., Gehring, P., Xu, G., Shirane, G.: *J. Appl. Phys.* **96**, 1620 (2004)
15. Abes, M., Koops, C.T., Hrkac, S.B., Greve, H., Quandt, E., Collins, S.P., Murphy, B.M., Magnussen, O.M.: *Appl. Phys. Lett.* **102**, 011601 (2013)
16. Dosch, H.: *Critical Phenomena at Surfaces and Interfaces—Evanescent X-Ray and Neutron Scattering*, Springer Tracts in Modern Physics, vol. 126. Springer (1992)
17. Kilaas, R.: *J. Microsc.* **190**, 45 (1998)
18. Abes, M., Koops, C., Hrkac, S., McCord, J., Urs, N., Wolff, N., Kienle, L., Ren, W., Bouchenoire, L., Murphy, B., Magnussen, O.M.: *Phys. Rev. B* **93**, 195427 (2016)
19. Dörr, K., Nilani-Zeneli, O., Herklotz, A., Rata, A.D., Boldyreva, K., Kim, J.-W., Dekker, M.C., Nenkov, K., Schultz, L., Reibold, M.: *Eur. Phys. J. B* **71**, 361 (2009)
20. Weissmüller, J., Markmann, J., Grewer, M., Birringer, R.: *Acta Mater.* **59**, 4366 (2011)
21. Fritsch, D., Ederer, C.: *Phys. Rev. B* **82**, 104117 (2010)

Investigation of the Electrochemical Properties of Lithium–Sulfur Cells with Sulfur Electrodes Based on Carbon Inverted Opals

N. S. Sukhinina, E. V. Karaseva, V. M. Masalov, E. V. Kuzmina, A. A. Zhokhov, V. S. Kolosnitsyn, and G. A. Emelchenko

Abstract

Carbon structures with an inverted opal lattice was synthesized. Comparative studies of the electrochemical properties of lithium–sulfur cells with sulfur electrodes based on the samples and other carbon materials have been carried out. The synthesized material showed a good stability when cycling in the range of more than 300 cycles. That says about the prospects for the use of such structures in lithium–sulfur batteries.

Keywords

Inverted opals • Carbon structures • Lithium–sulfur cells • Electrochemical properties

1 Introduction

Recently, the use of carbon materials in promising lithium–sulfur batteries has been actively investigated. Such batteries have a higher theoretical specific charge energy compared to lithium-ion batteries. But along with this, lithium–sulfur batteries also have a number of drawbacks: low conductivity, interaction with electrolyte, which leads to a short battery life time [1]. To eliminate these drawbacks, when fabricating the electrodes, the addition of carbon materials is used. Thus, in [2], the authors demonstrated that the cathode based on the nanostructured sulfur-mesoporous carbon composite can overcome the limitations associated with poor conductivity in the cell and solubility of lithium

polysulfides, and show high capacity (up to 1320 mAh/g) with good cycling efficiency. Different forms of carbon (graphite, carbon black, activated carbons, glass carbon, nanotubes, and other carbon structures) used in lithium–sulfur batteries are characterized by different conductivity and specific surface area. Therefore, during the synthesis of the carbon component of the electrodes, it is important to choose carbon precursors and production methods that would ensure the formation of carbon forms with high indices of these properties. Promising precursors from the point of view of electrical conductivity are graphitizing materials, i.e. those materials in the process of carbonization of which carbon is formed with a graphite-like structure. The method of chemical activation is effectively applied to obtain structures with high surface area. It is usually carried out at low temperatures ($\sim 400\text{--}800\text{ }^{\circ}\text{C}$) with the use of dehydrating agents (phosphoric acid, potassium hydroxide, sodium hydroxide), requiring subsequent washing of residual reagents [3, 4]. Among the methods for the synthesis of carbon materials, the template method stands out for its ability to control and manage the porous structure of the material [5]. Chemical activation of carbon contributes mainly to the formation of micropores (less than 2 nm), but larger pores are required to ensure the accessibility of pore space and increase the rate of electrolyte penetration into the internal structure of the developed electrode surface. The combination of the template method of carbon material synthesis with its subsequent chemical activation will allow the controlled formation of structures containing both micro- and meso- and macropores.

This paper presents the results of studies on the synthesis, the structure of carbon inverted opals and the electrochemical properties of lithium–sulfur cells with sulfur electrodes based on them in comparison with the electrochemical parameters of lithium–sulfur cells with electrodes based on carbon materials produced in industry.

N. S. Sukhinina (✉) · V. M. Masalov · A. A. Zhokhov · G. A. Emelchenko
Institute of Solid State Physics Russian Academy of Sciences (ISSP RAS), 2 Academician Ossipyan str., Chernogolovka, Moscow District, Russia
e-mail: suhinina@issp.ac.ru

E. V. Karaseva · E. V. Kuzmina · V. S. Kolosnitsyn
Ufa Institute of Chemistry UFRC RAS, Ufa, Republic of Bashkortostan, Russia

2 Experimental

2.1 Synthesis of Carbon Material C-IOP-160-8

Carbon nanostructures with an inverted opal lattice were obtained by the template method. Opal matrices composed of spherical particles of amorphous silicon dioxide 160 nm in diameter were used as a template. Monodisperse spheres of amorphous SiO₂ were synthesized by combined method, including the production of seed particles by heterogeneous hydrolysis of tetraethoxysilane (TEOS) using L-arginine as a catalyst [6] followed by their further growth by the modified Stöber-Fink-Bohn method in aqueous alcoholic solution in the presence of ammonium hydroxide [7, 8]. Anthracene, which belongs to the graphitizing materials, was used as an organic carbon precursor [9]. The process of filling the pore space of the matrix with anthracene and carbonization were carried out in an autoclave, followed by etching the template and activation using potassium hydroxide. The synthesis is described in detail in [10].

2.2 Characterization of the Obtained Materials

The material was characterized by scanning electron microscopy (SEM) and transmission electron microscopy (TEM). The porosity of the sample was measured by the method of adsorption-desorption of nitrogen (77 K) (Quantachrome QuadraWin).

To research the possibility of using carbon inverted opals C-IOP-160-8 as the carbon component of sulfur electrodes, electrochemical properties of lithium–sulfur cells with sulfur electrodes based on them were studied. Also for comparison, electrodes based on carbon black Ketjenblack EC-600JD (Akzo Nobel Polymer Chemicals LLC) and graphene GLNP-0350 (provided by Graphene Lab) were investigated. Sulfur electrodes were made of the following composition: 70%—S, 10%—C, 20%—polyethylene oxide ($M_r = 4 \times 10^6$, PEO). The sulfur content in the electrode was Qs 2.0–2.2 mAh/cm², which is equivalent to 1.2–1.3 mg of sulfur per 1 cm². The separator was 1 layer of Celgard®3501 microporous polypropylene with a diameter of $d = 2.85$ cm and an area of $A = 6.38$ cm². 1M LiSO₃CF₃ in sulfolane in the amount of 4 μl/mAh(S) was used as the electrolyte, and lithium foil about 120 μm thick ($d = 2.55$ cm, $A = 5.10$ cm²) was used as a negative electrode.

Lithium–sulfur cells were cycled using battery testers developed by the authors [11] in the potential range of 1.5–2.8 V at a temperature of +30 °C; the charge current density was 0.1 mA/cm², the discharge current density was 0.2 mA/cm².

3 Results and Discussion

Figure 1 shows the results of electron microscopic measurements with a high resolution of a carbon inverted opal-like nanostructure C-IOP-160-8.

Morphologically, the structure looks like an ordered carbon frame, filling the interglobular space around the spherical voids, from which SiO₂ nanoparticles were removed (Fig. 1a). The carbon frame is a graphite-like structure with a significant proportion of multi-graphene layers (up to 10 layers, Fig. 1b).

The results of the study of the porous system of carbon inverted opals by the method of gas adsorption-desorption (N₂) are shown in Fig. 2. The specific surface area of the samples was 238 m²/g (BET-method), the pore volume was 0.30 cm³/g. Of these, 67% of the area and 22% of the pore volume are formed by micropores (up to 2 nm). From the pore diameter distribution (Fig. 2b), it can be seen that the main contribution to the pore volume is made by mesopores (from 2 to 50 nm).

Before conducting studies of the electrochemical properties of carbon materials the content of acidic and basic groups on the surface of carbon materials was determined by acid-base titration with potentiometric indication of the end point of titration. The data obtained are presented in Table 1.

It can be seen that the carbon black Ketjenblack EC600-JD contains the basic groups on its surface, and the surface of the carbon inverted opals C-IOP-160-8 have the acid groups. Graphene GLNP-0350 contains neither acid nor basic groups.

Figure 3 shows the discharge curves of the first cycle (a), which is most indicative for lithium–sulfur cells, and the charge-discharge curves of the second cycle (b). The discharge capacity on the first cycle (Fig. 3a) for lithium–sulfur cells with sulfur electrodes based on Ketjenblack EC-600JD was 1292 mAh/g(S), based on inverted carbon opals C-IOP-160-8 was 350 mAh/g(S) and based on graphene GLNP-0350 was 247 mAh/g(S).

It can be seen that carbon material influences the speed and the depth of electrochemical reduction of both sulfur (high-voltage platform) and poly-lithium sulphides (Li₂S_n; low-voltage platform), as evidenced by differences in the values of potentials and capacitance on the discharge curves (Fig. 3a). It is seen (Fig. 3b) that the speed and depth of the electrochemical oxidation of lithium polysulfides (charging curves) are also determined by the type of carbon material in the composition of sulfur electrodes. The speed and depth of electrochemical oxidation of lithium polysulfides in lithium–sulfur cells with sulfur electrodes based on carbon inverted opals C-IOP-160-8 is less than with sulfur electrodes based on carbon black Ketjenblack EC-600JD, but more than that with sulfur electrodes based on graphene

Fig. 1 Image of sample C-IOP-160-8 in SEM (a) and PEM (b) modes

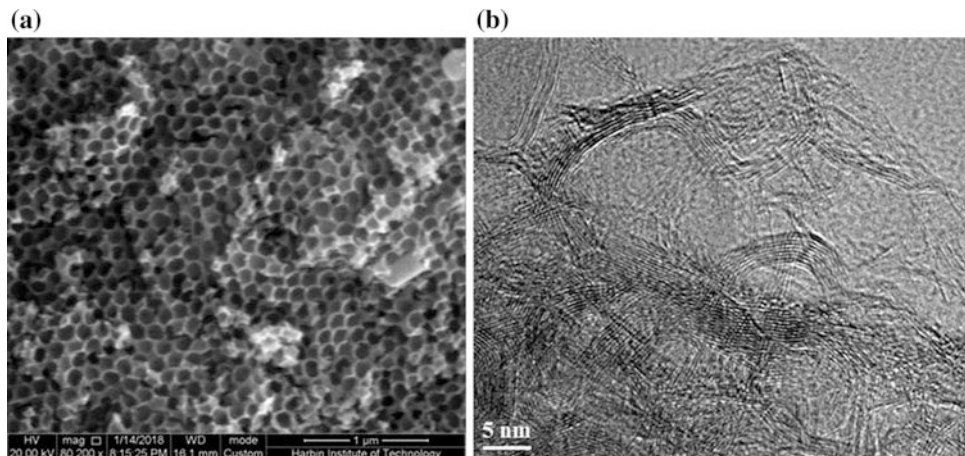


Fig. 2 Characterization of the C-IOP-160-8 porous system: a the nitrogen adsorption-desorption isotherms (77 K) and b the pore-size distribution and distribution of volumes accumulated in these pores

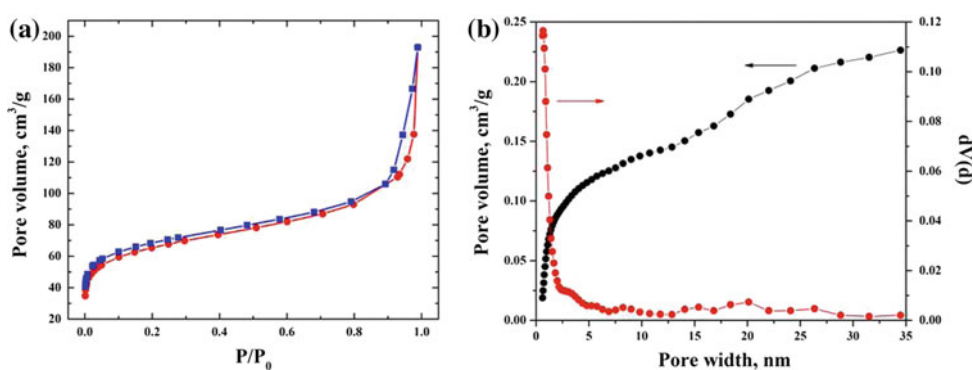


Table 1 The content of acidic and basic groups on the surface of carbon materials and the value of their specific surface

Carbon materials	C _{OH⁻} , mmol/g	C _{H⁺} , mmol/g	S _{BET} , m ² /g
GLNP-0350	–	–	80 ^a
C-IOP-160-8	–	0.049 ± 0.002	237
Ketjenblack EC-600JD	0.11 ± 0.01	–	1306 ^b

^aData provided by Graphene Lab

^bData were taken from passport (SAFETY DATA SHEET) provided by the supplier company

Fig. 3 Charge-discharge curves of lithium-sulfur cells with sulfur electrodes based on various carbon materials: a 1st cycle and b 2nd cycle

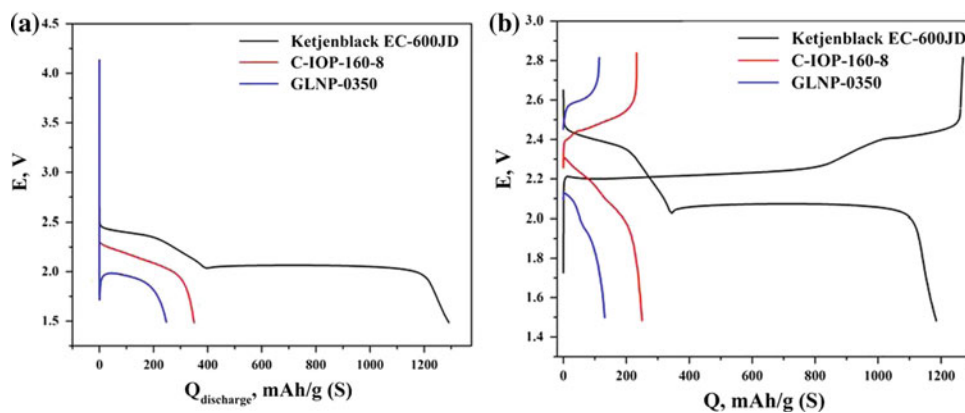
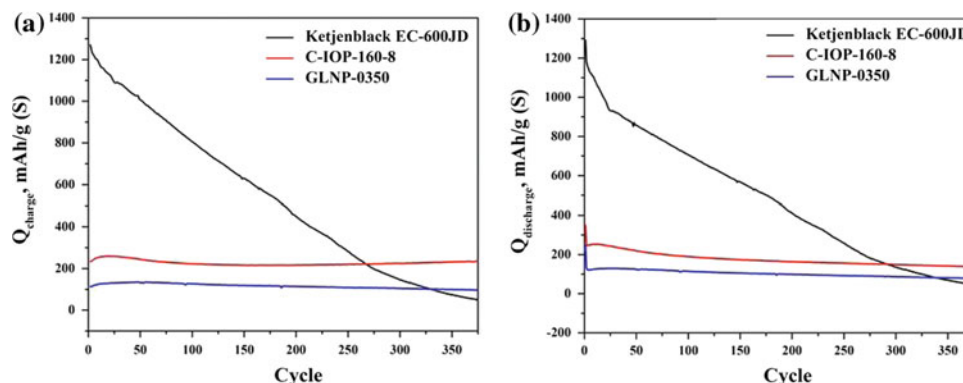


Table 2 Specific discharge capacity of lithium–sulfur cells with sulfur electrodes based on carbon materials

Carbon materials	Specific discharge capacity, mAh/g(S)				
	1st cycle	2nd cycle	10th cycle	50th cycle	100th cycle
GLNP-0350	247	131	126	122	115
C-IOP-160-8	350	250	252	219	189
Ketjenblack EC-600JD	1292	1185	1089	857	707

Fig. 4 The charging (a) and discharging (b) capacitances change of lithium–sulfur cells with sulfur electrodes based on various carbon materials during the cycling process



GLNP-0350. Carbon black has a significantly higher specific surface area compared with C-IOP-160-8 and graphene (Table 1), which apparently determines the higher capacities of this material (Table 2).

Figure 4 demonstrates graphs of charging (a) and discharging (b) capacitances of lithium–sulfur cells with sulfur electrodes based on various carbon materials during cycling. It can be seen that the capacity of carbon black after 300 cycles becomes equal to that of C-IOP-160-8 and further continues to decline at a faster rate than for C-IOP-160-8 and graphene. This data gives reason to believe that if we will increase the specific surface area of the carbon inverted opals, it is possible to achieve higher capacitances of lithium–sulfur cells with electrodes based on them, while having saved a good stability during recharging.

EC-600JD, but more so than with electrodes based on graphene GLNP-0350. Herewith the sample showed a good stability during cycling in the range of more than 300 cycles. This suggests that an increase of the specific surface area of our material will lead to higher values of specific capacities, while maintaining high stability during multiple recharging.

Acknowledgements This work was partially supported by ISSP RAS—Russian Government contracts and the RFBR grants No. 16-29-06164 and No. 16-29-06190 ofi-m. The authors are grateful to E. N. Kabachkov for assistance in measuring the sorption isotherms of the samples and Prof. J. Wang (Harbin Engineering University, P.R. China) for assistance in electron microscopic investigations.

Conflict of Interest The authors declare that they have no conflict of interest.

4 Conclusions

The carbon structures with the inverted opal lattice were synthesized using the template method. Anthracene as a graphitizable material was used as carbon precursor. The specific surface area of the samples was 238 m²/g, the pore volume was 0.30 cm³/g. It has been established that the main contribution to the specific surface area is made by micropores (~67%). The test of carbon inverted opals C-IOP-160-8 as a carbon component of sulfur electrodes showed that the speed and depth of the electrochemical oxidation of lithium polysulfides in lithium–sulfur cells with sulfur electrodes based on C-IOP-160-8 is less than that with sulfur electrodes based on carbon black Ketjenblack

References

- Zhang, S.S.: Liquid electrolyte lithium/sulfur battery: fundamental chemistry, problems, and solutions. *J. Power Sour.* **231**, 153–162 (2013). <https://doi.org/10.1016/j.jpowsour.2012.12.102>
- Ji, X., Lee, K.T., Nazar, L.F.: A highly ordered nanostructured carbon-sulphur cathode for lithium-sulphur batteries. *Nat. Mater.* **8**, 500–506 (2009). <https://doi.org/10.1038/NMAT2460>
- Lozano-Castello, D., Lillo-Rodenas, M.A., Cazorla-Amoros, D., et al.: Preparation of activated carbons from Spanish anthracite: I. Activation by KOH. *Carbon* **39**(5), 741–749 (2001). [https://doi.org/10.1016/S0008-6223\(00\)00185-8](https://doi.org/10.1016/S0008-6223(00)00185-8)
- Romero-Anaya, A.J., Lillo-Rodenas, M.A., Salinas-Martinez de Lecea, C., et al.: Hydrothermal and conventional H₃PO₄ activation of two natural bio-fibers. *Carbon* **50**(9), 3158–3169 (2012). <https://doi.org/10.1016/j.carbon.2011.10.031>
- Marsh, H., Reinoso, F.R.: *Activated Carbon*, p. 536. Elsevier Ltd., UK (2006)

6. Masalov, V.M., Sukhinina, N.S., Emel'chenko, G.A.: Synthesis of monodisperse silica nanoparticles via heterogeneous tetraethoxysilane hydrolysis using L-arginine as a catalyst. *Inorg. Mat.* **54**(2), 156–162 (2018). <https://doi.org/10.1134/s0020168518020103>
7. Stöber, W., Fink, A., Bohn, E.: Controlled growth of monodisperse silica spheres in the micron size range. *Thin Solid Films* **26**(1), 62–69 (1968)
8. Masalov, V.M., Sukhinina, N.S., Emel'chenko, G.A.: Colloidal particles of silicon dioxide for the formation of opal like structures. *Phys. Solid State.* **53**(6), 1135–1139 (2011). <https://doi.org/10.1134/s1063783411060229>
9. Harris, P.J.F., Burian, A., Duber, S.: High-resolution electron microscopy of a microporous carbon. *Phil. Mag. Lett.* **80**(6), 381–386 (2000). <https://doi.org/10.1080/095008300403512>
10. Sukhinina, N.S., Masalov, V.M., Zhokhov, A.A., et al.: Synthesis and modification of carbon inverse opal nanostructures based on anthracene and their electrochemical characteristics. *Nanotech. Russ.* **12**(11–12), 635–642 (2017). <https://doi.org/10.1134/S199507801706012X>
11. Mochalov, S.E., Antipin, A.V., Nurgaliev, A.R., et al.: Multichannel potentiostat-galvanostat for battery and electrochemical cells cycling. *Elektrokhim. Energ.* **15**(1), 45–50 (2015)

Peierls Structural Transition in Organic Crystals of TTT_2I_3 with Intermediate Carrier Concentration

S. C. Andronic, I. I. Sanduleac, and A. I. Casian

Abstract

The Peierls structural transition in the nanostructured tetrathiotetracene-iodide crystal with intermediate carrier concentration is studied in 2D approximation. In the frame of the physical model, two the most important electron-phonon interactions are considered: of the deformation potential type and of the polaron type. The interaction of carriers with the structural defects is also taken into account. The renormalized phonon spectrum is calculated in the random phase approximation. The method of retarded temperature dependent Green function is applied. It is shown that the transition is of Peierls type and strongly depends on iodine concentration.

Keywords

Quasi-one-dimensional organic materials • Metal-insulator transition • Peierls critical temperature • Renormalized phonons • Interchain interaction

1 Introduction

Our recent research has been devoted to studying the Peierls transition in quasi-one-dimensional organic crystals (Q1D). These materials manifest unusual properties [1–3]. Organic nanomaterials have large potential applications in electronics, sensing, energy harnessing and quantum-scale systems [4]. Quasi-one-dimensional organic crystals, also, may have very prospect thermoelectric applications [5, 6]. Among the most studied Q1D organic crystals are those of the tetrathiofulvalinium tetracyanoquinodimethane (TTF-

TCNQ)—of *n*-type, tetrathiotetracene—tetracyanoquinodimethane ($\text{TTT}(\text{TCNQ})_2$) of *n*-type and tetrathiotetracene—iodide (TTT_2I_3) of *p*-type. These crystals with rather high electrical conductivity near room temperature, at low temperature showed a transition into a dielectric state. Such transition has firstly observed in the Q1D charge transfer compound TTF-TCNQ [7, 8] and was the first experimental confirmation of the structural transition, predicted earlier by Peierls [9] in 1D conductors.

This phenomenon has been studied by many authors (see [10–14] and references therein). According to Peierls, at some lowered temperatures, the one-dimensional metallic crystal with a half filled conduction band has to pass in a dielectric state with a dimerized crystal lattice. This temperature is called the Peierls critical temperature.

However, the Peierls structural transition in crystals of TTT_2I_3 , was not studied neither theoretically, nor experimentally, by other authors.

In [15] we have investigated the Peierls transition in a 2D physical model for a $\text{TTT}_2\text{I}_{3.1}$ crystal.

In [16] the 3D approximation was analyzed for the same crystal. It has been established that Peierls transition begins at $T \sim 35$ K in TTT chains. Due to interchain interaction the transition is finished at $T \sim 9.8$ K, as it is observed experimentally.

In [17] the Peierls transition in the TTT_2I_3 crystals with the lowest value of carrier concentration was studied. The Peierls transition begins at $T = 90$ K. At this temperature, the electrical conductivity achieves a maximum. With the lowering temperature, the electrical conductivity decreases. Due to interchain interaction the transition is finished at $T = 20$ K.

In this paper, we will study the behavior of Peierls transition in the TTT_2I_3 crystals with the intermediate value of carrier concentration in 2D approximation. We will analyze the Peierls structural transition for the curve presented in Fig. 1. The dimensionless Fermi momentum in this case is $k_F = 0.508 \pi/2$. The Peierls critical temperature is determined too.

S. C. Andronic (✉) · I. I. Sanduleac · A. I. Casian
Department of Physics, Technical University of Moldova, Stefan cel Mare bd, 168, Chisinau, Republic of Moldova
e-mail: silvia.andronic@mt.utm.md

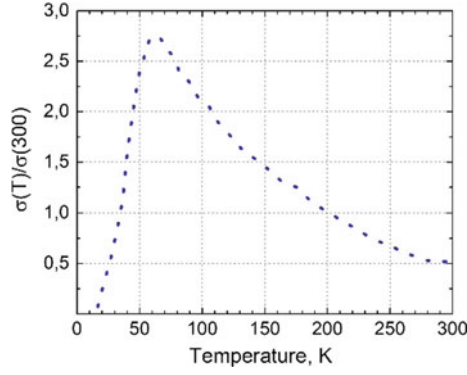


Fig. 1 Temperature dependence of electrical conductivity of $\text{TTT}_2\text{I}_{3+\delta}$ crystal, $\delta = 0.06$. Max – 62 K, $\sigma \rightarrow 0$ at 12 K [18]

2 The Physical Model of the Crystal

The crystal of TTT_2I_3 is a charge transfer compound. The orthorhombic crystal structure consists of segregated chains or stacks of plane TTT molecules and of iodine chains. The compound is of mixed valence. Two molecules of TTT give one electron to iodine chain formed of I_3^- ions that play the role of acceptors. Only TTT chains are conductive and the carriers are holes. The electrons on iodine ions are in a rather localized states and do not participate in the transport. The lattice constants are $a = 18.40 \text{ \AA}$, $b = 4.96 \text{ \AA}$ and $c = 18.32 \text{ \AA}$, which demonstrates a very pronounced crystal quasi-one-dimensionality. The highly conducting direction is along \mathbf{b} .

The physical model of the crystal was described in more detail in [15]. The Hamiltonian of the 2D crystal model in the tight binding and nearest neighbor approximations has the form:

$$H = \sum_{\mathbf{k}} \varepsilon(\mathbf{k}) a_{\mathbf{k}}^+ a_{\mathbf{k}} + \sum_{\mathbf{q}} \hbar \omega_{\mathbf{q}} b_{\mathbf{q}}^+ b_{\mathbf{q}} + \sum_{\mathbf{k}, \mathbf{q}} A(\mathbf{k}, \mathbf{q}) a_{\mathbf{k}}^+ a_{\mathbf{k}+\mathbf{q}} (b_{\mathbf{q}} + b_{-\mathbf{q}}^+) \quad (1)$$

In Eq. (1) the first term is the energy operator of free holes in the periodic field of the lattice.

The hole energy is measured from the top of band and it is presented in the form:

$$\varepsilon(\mathbf{k}) = -2w_1(1 - \cos k_x b) - 2w_2(1 - \cos k_y a) \quad (2)$$

where w_1 and w_2 are the transfer energies of a hole from one molecule to the nearest one along the chain (x direction) and in perpendicular (y direction).

In Eq. (1) $a_{\mathbf{k}}^+$, $a_{\mathbf{k}}$ are the creation and annihilation operators of the hole with a 2D quasi-wave vector \mathbf{k} and projections (k_x, k_y) ; $b_{\mathbf{q}}^+$, $b_{\mathbf{q}}$ are creation and annihilation operators of an acoustic phonon with 2D wave vector \mathbf{q} and frequency $\omega_{\mathbf{q}}$.

The second term in the Expression (1) is the energy operator of longitudinal acoustic phonons,

$$\omega_{\mathbf{q}}^2 = \omega_1^2 \sin^2(q_x b/2) + \omega_2^2 \sin^2(q_y a/2) \quad (3)$$

where ω_1 and ω_2 are the limit frequencies in the x and y directions.

The third term represents the electron-phonon interactions. In the frame of the crystal model, two the most important electron-phonon interaction mechanisms are considered: of the deformation potential type and of the polaron type. The coupling constants of the first interaction are proportional to the derivatives w'_1 and w'_2 of w_1 and w_2 , with respect to the intermolecular distances. The coupling constant of second interaction is proportional to the average polarizability of the molecule α_0 . This interaction is important for crystals composed of large molecules as TTT, so as α_0 is roughly proportional to the volume of molecule. The ratio of amplitudes of polaron-type interaction to the deformation potential one in the x and y directions is described by parameters γ_1 and γ_2 .

$$\gamma_1 = 2e^2 \alpha_0 / b^5 w'_1, \gamma_2 = 2e^2 \alpha_0 / a^5 w'_2 \quad (4)$$

The square module of matrix element $A(\mathbf{k}, \mathbf{q})$ from Eq. (1) can be written in the form:

$$\begin{aligned} |A(\mathbf{k}, \mathbf{q})|^2 &= 2\hbar w_1^2 / (NM\omega_{\mathbf{q}}) \\ &\times \{ [\sin(k_x b) - \sin(k_x - q_x, b) - \gamma_1 \sin(q_x b)]^2 \\ &+ d_1^2 [\sin(k_y a) - \sin(k_y - q_y, a) - \gamma_2 \sin(q_y a)]^2 \}. \end{aligned} \quad (5)$$

Here, M is the mass of the molecule, N is the number of molecules in the basic region of the crystal, $d_1 = w_2/w_1 = w'_2/w'_1$.

To explain the behavior of the electrical conductivity from the Fig. 1, it is necessary to take into account also the dynamical interaction of carriers with the defects. The static interaction will give contribution to the renormalization of hole spectrum. The defects in TTT_2I_3 crystals are created due to different coefficients of dilatation of TTT and iodine chains.

The Hamiltonian of this interaction H_{def} is presented in the form:

$$H_{def} = \sum_{\mathbf{k}, \mathbf{q}} \sum_{n=1}^{N_d} B(q_x) \exp(-iq_x x_n) a_{\mathbf{k}}^+ a_{\mathbf{k}-\mathbf{q}} (b_{\mathbf{q}} + b_{-\mathbf{q}}^-) \quad (6)$$

Here $B(q_x)$ is the matrix element of a hole interaction with a defect and it is presented in the form:

$$B(q_x) = \sqrt{\hbar / (2NM\omega_{\mathbf{q}})} \cdot I(q_x) \quad (7)$$

where $I(q_x)$ is the Fourier transformation of the derivative with respect to intermolecular distance from the energy of interaction of a carrier with a defect, x_n numbers the defects,

which are considered linear along x -direction of TTT chains and distributed randomly.

$$I(q_x) = D(\sin(bq_x))^2 \quad (8)$$

where D is a parameter that determines the intensity of hole interaction with a defect. It has the same meaning as w'_1 in (5) and is measured in $\text{eV} \text{ \AA}^{-1}$.

The renormalized phonon spectrum, $\Omega(\mathbf{q})$ is determined by the pole of the Green function and is obtained from the transcendent dispersion equation

$$\Omega(\mathbf{q}) = \omega_{\mathbf{q}}[1 - \bar{\Pi}(\mathbf{q}, \Omega)]^{1/2} \quad (9)$$

where the principal value of the dimensionless polarization operator takes the form:

$$\text{Re}\bar{\Pi}(\mathbf{q}, \Omega) = -\frac{4}{\hbar\omega_{\mathbf{q}}} \sum_{\mathbf{k}} \frac{[|A(\mathbf{k}, -\mathbf{q})|^2 + |B(q_x)|^2](n_{\mathbf{k}} - n_{\mathbf{k}+\mathbf{q}})}{\varepsilon(\mathbf{k}) - \varepsilon(\mathbf{k} + \mathbf{q}) + \hbar\Omega} \quad (10)$$

Here $n_{\mathbf{k}}$ is the Fermi distribution function. The Eq. (9) can be solved only numerically.

3 Results and Discussion

Computer modeling for the 2D physical model of the crystal are performed for the following parameters [19]: the dimensionless Fermi momentum $k_F = 0.508 \pi/2$, $M = 6.5 \times 10^5 m_e$ (m_e is the mass of the free electron), $w_1 = 0.16 \text{ eV}$, $w'_1 = 0.26 \text{ eV} \text{ \AA}^{-1}$, $d_1 = 0.015$, $\gamma_1 = 1.7$, γ_2 is determined from the relation: $\gamma_2 = \gamma_1 b^5 / a^5 d_1$. The sound velocity along TTT chains was estimated by comparison of the calculated results for the electrical conductivity of TTT_2I_3 crystals [19] with the reported ones [20], $v_{s1} = 1.5 \times 10^5 \text{ cm/s}$. For v_{s2} in transversal direction (in a direction) we have taken $1.35 \times 10^5 \text{ cm/s}$.

In Figs. 2 and 3, in the same graphs, the dependences for initial phonon frequency $\omega(q_x)$ and the dependences of renormalized phonon frequencies $\Omega(q_x)$ as functions of q_x for different temperatures and different values of q_y are presented. One can observe that the values of $\Omega(q_x)$ are diminished in comparison with those of $\omega(q_x)$ in the absence of electron-phonon interaction. This means that the electron-phonon interaction and structural defects diminish the values of lattice elastic constants. Also, it is seen that with a decrease of temperature T the curves change their form, and in dependencies $\Omega(q_x)$ a minimum appears. This minimum becomes more pronounced at lower temperatures.

In Fig. 2 it is presented the renormalized phonon spectrum $\Omega(q_x)$ as function of q_x , when $q_y = 0$, the dimensionless Fermi momentum $k_F = 0.508 \pi/2$ and $D = 1.062 \text{ eV} \text{ \AA}^{-1}$.

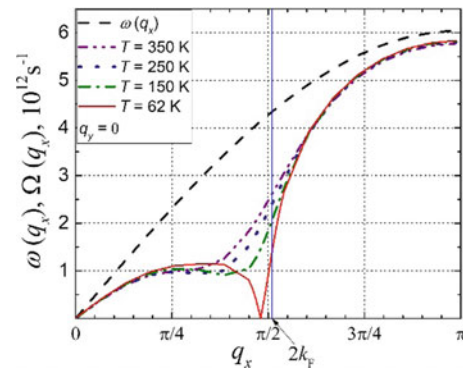


Fig. 2 Renormalized phonon spectrum $\Omega(q_x)$ for $\gamma_1 = 1.7$ and different temperatures. The dashed line is for the spectrum of free phonons. $k_F = 0.508 \pi/2$, $D = 1.062 \text{ eV} \text{ \AA}^{-1}$

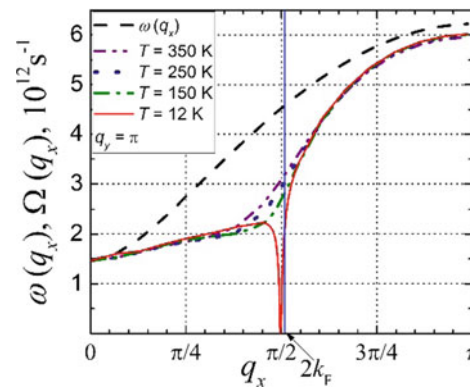


Fig. 3 Renormalized phonon spectrum $\Omega(q_x)$ for $\gamma_1 = 1.7$ and different temperatures. The dashed line is for the spectrum of free phonons. $k_F = 0.508 \pi/2$, $D = 0.987 \text{ eV} \text{ \AA}^{-1}$

Parameter D determines the intensity of hole interaction with a defect. In this case the interaction between TTT chains is neglected. The Peierls transition begins at $T = 62 \text{ K}$.

Figure 3 shows the case when the interaction between TTT chains is taken into account ($q_y = \pi$), $D = 0.987 \text{ eV} \text{ \AA}^{-1}$ and $k_F = 0.508 \pi/2$. In this case the transition is finished at $T = 12 \text{ K}$. It was observed that parameter D decrease, or the hole interaction with a defect is smaller in this case. As it is seen from Fig. 1, the electrical conductivity is strongly reduced, and achieves zero at $T \sim 12 \text{ K}$. Thus, the metal—dielectric transition in TTT_2I_3 crystals with intermediate carrier concentration is of Peierls type.

4 Conclusions

The behavior of Peierls structural transition in organic crystals of TTT_2I_3 (tetrathiotetracene iodide) with intermediate value of carrier concentration was investigated. The 2D physical model is considered. Two the most important electron-phonon interaction mechanisms are considered: the

first mechanism is of the deformation potential type and the second one is of the polaron type. The ratios of amplitudes of second electron-phonon interaction to the first one along chains and in transversal direction are noted by γ_1 and γ_2 , respectively. The dynamical interaction of carriers with the defects is also taken into account. The renormalized phonon spectrum is calculated in the random phase approximation. The method of retarded temperature dependent Green function is applied. The numerical calculations for renormalized phonon spectrum, $\Omega(q_x)$ as function of q_x , for different temperatures are presented in two cases: (1) when the interaction between transversal chains is neglected ($q_y = 0$) and (2) when the interaction between the adjacent chains are considered ($q_y \neq 0$). It is shown that the Peierls transition temperature strongly depends on iodine concentration. It has been established that when $k_F = 0.508 \pi/2$ and the hole concentration achieves an intermediate value, the Peierls transition begins at $T \sim 62$ K in TTT chains and reduces considerably the electrical conductivity. Due to interchain interaction the transition is finished at $T \sim 12$ K.

Acknowledgements The authors acknowledge the support of the national projects 13/29.10.18F TC and 14.02.116F.

Conflict of Interest The authors declare that they have no conflict of interest.

References

- Jerome, D.: Organic superconductors: when correlations and magnetism walk in. *J. Supercond. Novel Mag.*, **25**, 633–655 (2012)
- Pouget, J.P.: Bond and charge ordering in low-dimensional organic conductors. *Phys. B* **407**, 1762–1770 (2012)
- Sun, X., Zhang, L., Di, C., Wen, Y., Guo, Y., Zhao, Y., Yu, G., Liu, Y.: *Adv. Mater.* **23**, 3128–3133 (2011)
- Torres, T., Bottari, G. (eds.): *Organic Nanomaterials: Synthesis, Characterization, and Device Applications*. Wiley, Hoboken (2013)
- Casian, A., Pflaum, J., Sanduleac, I.: Prospects of low dimensional organic materials for thermoelectric applications. *J. Thermoelectr.* **1**, 16 (2015)
- Harada, K., Sumino, M., Adachi, C., Tanaka, S., Miyazaki, K.: Improved thermoelectric performance of organic thin-film elements utilizing a bilayer structure of pentacene and 2,3,5,6-tetrafluoro-7,7,8,8-tetracyanoquinodimethane (F4-TCNQ). *Appl. Phys. Lett.* **96**, 253304 (2010)
- Ferraris, J., Cowan, D.O., Walatka, W., Perlstein, J.H.: Electron transfer in a new highly conducting donor-acceptor complex. *J. Am. Chem. Soc.* **95**, 948–949 (1973). <https://doi.org/10.1021/ja00784a066>
- Coleman, L.B., Cohen, M.J., Sandman, D.J., Yamagishi, F.G., Garito, A.F., Heeger, A.J.: Superconducting fluctuations and the Peierls instability in an organic solid. *Solid State Commun.* **12**, 1125–1132 (1973)
- Peierls, R.: *Quantum Theory of Solids*. Oxford University Press, London (1955)
- Jerome, D.: Organic conductors: from charge density wave TTF-TCNQ to superconducting (TMTSF)₂PF₆. *Chem. Rev.* **104**, 5565–5592 (2004). <https://doi.org/10.1021/cr030652g>
- Pouget, J.P.: The Peierls instability and charge density wave in one-dimensional electronic conductors. *C R Phys.* **17**, 332–356 (2016). <https://doi.org/10.1016/j.crhy.2015.11.008>
- Streltsov, S.V., Khomskii, D.I.: Orbital-dependent singlet dimers and orbital-selective Peierls transitions in transition-metal compounds. *Phys. Rev. B* **89**, Article ID: 161112 (2014). <https://doi.org/10.1103/physrevb.89.161112>
- Chernenkaya, A., et al.: Nature of the empty states and signature of the charge density wave instability and upper Peierls transition of TTF-TCNQ by temperature-dependent NEXAFS spectroscopy. *Eur. Phys. J. B* **88**, 13 (2015). <https://doi.org/10.1140/epjb/e2014-50481-9>
- Bulaevskii, L.N.: Peierls structure transition in quasi-one-dimensional crystals. *Sov. Phys. Usp.* **18**, 131 (1975). <https://doi.org/10.1070/PU1975v018n02ABEH001950>
- Andronic, S., Casian, A.: Metal-insulator transition of Peierls type in quasi-one-dimensional crystals of TTT₂I₃. *Adv. Mater. Phys. Chem.* **7**, 212–222 (2017). <https://doi.org/10.4236/amc.2017.75017>
- Andronic, S., Balmus, I., Casian, A.: Metal-insulator transition of Peierls type in TTT₂I₃ crystals in 3D approximation. *ICMCS* **2017**, 539–542 (2017)
- Andronic, S., Casian, A.: Peierls structural transition in organic crystals of TTT₂I₃ type in 2D approximation. *MJPS*, 5 p (2019)
- Shchegolev, I.F., Yagubskii, E.B.: Extended linear chain compounds. In: Miller, I.S., (ed.), vol. 2, pp. 385. Plenum Press, New York (1982)
- Casian, A., Sanduleac, I.: Thermoelectric properties of tetrathio-tetracene iodide crystals: modeling and experiment. *J. Electron. Mater.* **43**(10), 3740–3745 (2014)
- Hilti, B., Mayer, C.W.: Electrical properties of the organic metallic compound bis (tetrathiotetracene)-triiodide, (TTT)₂-I₃. *Helv. Chim. Acta* **61**, 501 (1978)

GaN-Based 2D and 3D Architectures for Electronic Applications

Vladimir Ciobanu

Abstract

In this paper we demonstrate the fabrication of electronic devices based on GaN nanostructures. For fabrication of 2D and 3D GaN nanostructures, Surface Charge Lithography (SCL) and Hydride Vapor Phase Epitaxy (HVPE) techniques were used. A memristor device based on GaN ultrathin membranes with the thickness of 15 nm obtained by SCL was elaborated. For GaN microtetrapods growth, the HVPE method was used, where ZnO microtetrapods were used as sacrificial template. Because of the high temperature in the reactor and presence of hydrogen gas, ZnO is decomposed, resulting in the formation of ultra-porous hollow GaN microtetrapods. A hydrostatic pressure sensor based on GaN hollow microtetrapods with the wall thickness of 80 nm covering the pressure interval up to 40 atm was fabricated and characterized.

Keywords

GaN microtetrapods • Ultrathin membrane • Pressure sensor • Memristor • Artificial synapses

1 Introduction

At present, GaN is considered the second most important semiconductor after Silicon, because of its remarkable optical properties, thermal and chemical stability and capability to work at high powers and high frequencies [1]. GaN is known to possess piezoelectric and piezoresistive properties which open a wide range of applications in piezoelectronic, SAW sensors, MEMS/NEMS, nanogenerators, etc. [2–5].

V. Ciobanu (✉)

National Center for Materials Study and Testing, Technical University of Moldova, 168 Stefan cel Mare av., Chisinau, Moldova
e-mail: vladimir.ciobanu@cnstm.utm.md

Memristors represent nonlinear circuit elements displaying a pinched hysteretic behavior of the current when the voltage is applied from negative to positive values [6]. The resistance of the memristor depends on the history of the applied voltage. Its resistance can be programmed and subsequently remains stored. Since the memristor remembers its previous state when the applied voltage is turned off, it is strongly related to non-volatile memories [7]. Memristors have attractive features like requirement of less energy to operate, are faster than similar known devices and can store at least twice as much data in the same area. Memristors could also be used in neuromorphic systems in order to mimic the synapses [8].

Pressure detection technologies utilize physical properties of materials such as inertial mass variation [9], optical properties of semiconductor materials [10], piezoelectric or piezoresistive effects, acoustic emission (AE) wave [11].

Pressure sensors find a wide range of applications like power switches, aerospace, weight scales, keyboards, touchscreens, submarines. In order to use them for aerospace applications, they need to withstand radiation, aggressive chemicals and vacuum. Besides, they should be robust under strongest accelerations and vibrations.

2 Results And Discussions

2.1 Memristors

The GaN memristive device was fabricated using surface charge lithography (SCL). The SCL is based on ion beam-writing of surface negative charge followed by photoelectrochemical (PEC) etching of the GaN layer. The ultrathin GaN membrane array was fabricated on the same MOCVD grown GaN layer by treating some regions with 0.5 keV Ar⁺ ions at the dose of 10¹¹ cm⁻² [12]. The ohmic contacts were made by depositing Ti/Au on as-grown GaN via photo-lithographically defined windows. Figure 1 illustrates SEM images of the GaN membrane which is sustained

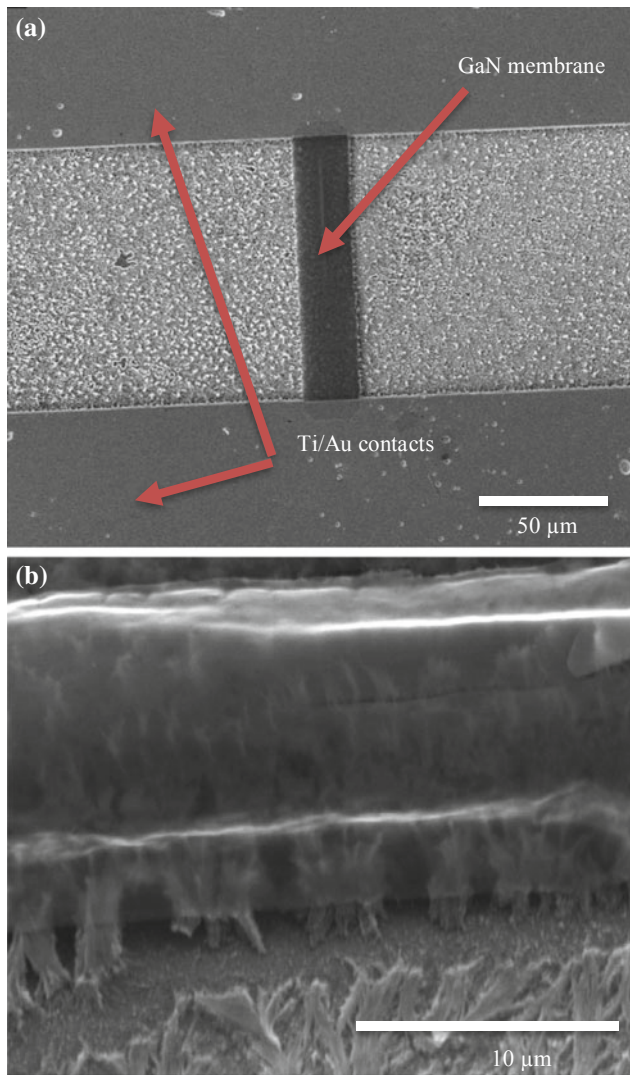


Fig. 1 SEM image of a GaN ultrathin membrane **a** connected to two terminals; **b** image taken at 45°

by a network of pillars formed by nanowires that represent threading dislocations.

The SEM image from Fig. 2b taken at 45°, demonstrates that the membrane is very flexible and stays suspended on insulating GaN nanowires.

The electrical measurements were performed inside a Faraday cage, in the dark using a Keithley 4200 SCS equipment with low noise amplifiers at the output. The current–voltage dependences at consecutive sweeps are represented in Fig. 2. The voltage is swept first from 0 up to +8 V and then backwards, from +8 to 0 V. This procedure is repeated several times, the successive sweeps being marked on Fig. 2 as sweeps 1, 2, 3, and 4. It can be seen that the GaN membrane array behaves like a memristor because the I–V dependence in the range 0 to +8 V is strongly nonlinear and has a pinched hysteric shape. Moreover, at consecutive sweeps the initial pinched hysteresis is shifted towards

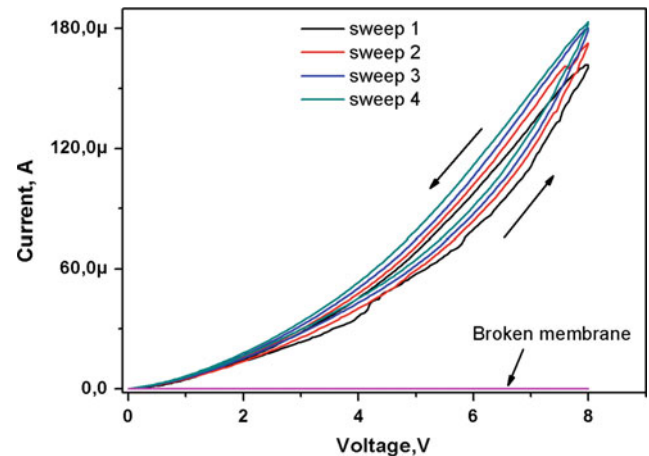


Fig. 2 Current–voltage dependence of the memristor device based on GaN membrane at consecutive sweeps

higher currents but preserves its shape, illustrating clearly another property of the memristor: memory, i.e. dependence on the previous state [13].

The increase of current at consecutive voltage sweeps was also observed in other materials and was explained by trap-controlled space charge limited current mechanism. According to this mechanism, negatively charged traps generate electric field with the same orientation as the applied field [14]. In the GaN membrane the negatively charged deep traps are formed during the irradiation with Ar^+ ions.

In order to demonstrate the conductance path through the membrane during electrical measurements, the membrane was intentionally broken. In this case, the resistance increases up to few $\text{G}\Omega$, as it is illustrated in Fig. 2, suggesting that the substrate has no influence to the memristive effect.

2.2 Pressure Sensors

The aero-GaN, also called Aerogalnite used in this work was grown by HVPE method, which means the deposition of a thin GaN layer on a sacrificial template composed of ZnO microtetrapods. ZnO microtetrapods were obtained by Flame Transport Synthesis approach [15]. For the grown process, a four-temperature-zone-heated horizontal reactor was used. Metallic gallium, ammonia (NH_3) gas, hydrogen chloride (HCl) gas, and hydrogen (H_2) being used as source materials and carrier gases. At the beginning the temperature was kept at 600 °C for 10 min to initiate nucleation of GaN on the surface of ZnO microtetrapods, and then increased up to 850 °C for 20 min to produce GaN layers. At the growth temperature of 850 °C, along with GaN deposition, simultaneous gradual decomposition and removal of the

underneath ZnO template occurs. Finally, hollow GaN microtetrapods with wall thickness of 80 nm are obtained.

The fabricated aero-GaN pressure sensor is very simple and thus robust, consisting only of aero-GaN represented in Fig. 3, as a pressure transducer layer, silver metallic contacts and a battery or a low-voltage DC source.

In Fig. 4, the dependence of conductivity on applied pressure is illustrated. A nonlinear dependence can be observed with pressure increasing. This behaviour can be interpreted as the contact resistance variation between interconnected microtetrapods but also because of the intrinsic resistivity variation of the material. The sensitivity given by

$$S = (\Delta G/G_0)/\Delta P, \quad (1)$$

where

$$G_0 = G(P_0 = 1 \text{ atm}) \quad (2)$$

is nonlinear and varies from $16.2 \times 10^{-3} \text{ kPa}^{-1}$ at 5 atm to $6.2 \times 10^{-3} \text{ kPa}^{-1}$ at 40 atm [16].

In order to prove the elasticity of the material and robustness of the sensor, a single tetrapod bending test in situ SEM using a calibrated AFM cantilever was done. In

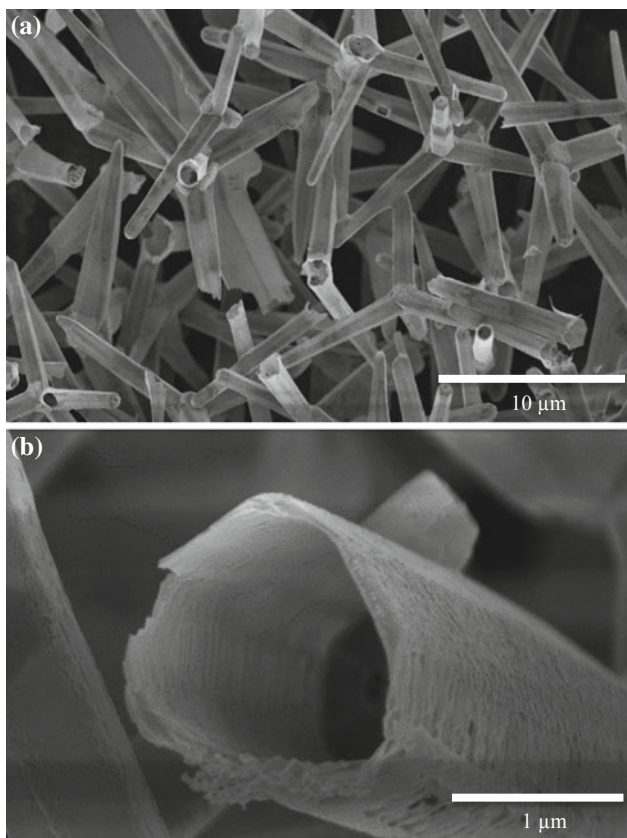


Fig. 3 SEM images at **a** low and **b** high magnification of GaN aero-tetrapods

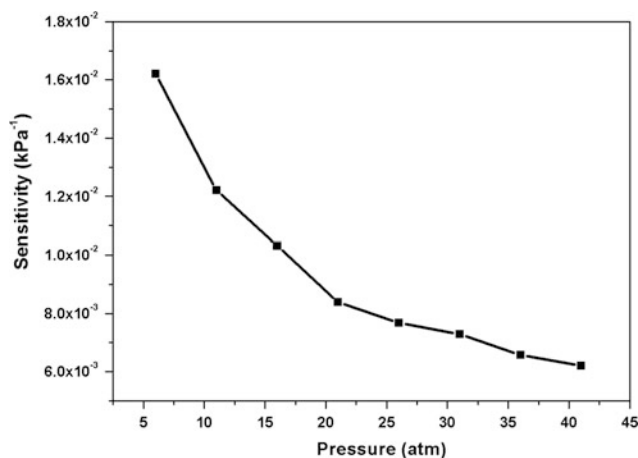


Fig. 4 Sensitivity dependence on pressure up to 40 atm

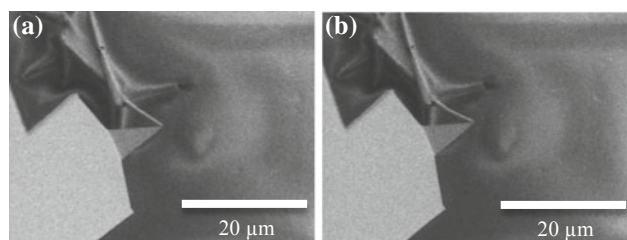


Fig. 5 SEM images of a single tetrapod during the bending test: **a** initial, **b** after applying a lateral force on an arm

Fig. 5 are represented two SEM images of a tetrapod in the initial form and after the lateral force on an arm was applied.

A lateral bending of the tetrapod arm of about $0.6 \mu\text{m}$ from the initial position is shown. The arm stays stable at bending for more than $1 \mu\text{m}$ and after that it breaks.

3 Conclusions

In this work a memristor device based on GaN ultrathin membranes and a pressure sensor consisting of interconnected GaN microtetrapods were experimentally demonstrated. The memristor based on GaN membrane is a high-power device compared to other memristors reported in the literature. The sensitivity of the pressure sensor reported here varies from $16.2 \times 10^{-3} \text{ kPa}^{-1}$ at 5 atm to $6.2 \times 10^{-3} \text{ kPa}^{-1}$ at 40 atm. The sensitivity and high current response in the mA range makes this kind of sensors feasible for portable electronic equipment.

Acknowledgements The author acknowledges the support from the Ministry of Education, Culture and Research of the Republic of Moldova under the Grant # 15.817.02.29A. Further, the author acknowledges for helpful discussions and co-working with Prof. Mircea Dragoman's group from IMT Bucharest and Prof. Ion Tighineanu's group from NCMST.

Conflict of Interest “The authors declare that they have no conflict of interest”.

References

- Rajan, S., Jena, D.: Gallium nitride electronics. *Semicond. Sci. Technol.* **28**(7) (2013). <https://doi.org/10.1088/0268-1242/28/7/070301>
- Kang, M.S., Lee, C.H., Park, J.B., Yoo, H., Yi, G.C.: Gallium nitride nanostructures for light-emitting diode applications. *Nano Energy* **1**, 391–400 (2012). <https://doi.org/10.1016/J.NANOEN.2012.03.005>
- Wang, X., Peng, W., Yu, R., Zou, H., Dai, Y., Zi, Y., Wu, C., Li, S., Wang, Z.L.: Simultaneously enhancing light emission and suppressing efficiency droop in GaN microwire-based ultraviolet light-emitting diode by the piezo-phototronic effect. *Nano Lett.* **17**, 3718–3724 (2017). <https://doi.org/10.1021/acs.nanolett.7b01004>
- Peng, M., Liu, Y., Yu, A., Zhang, Y., Liu, C., Liu, J., Wu, W., Zhang, K., Shi, X., Kou, J., Zhai, J., Wang, Z.L.: Flexible self-powered GaN ultraviolet photoswitch with piezo-phototronic effect enhanced on/off ratio. *ACS Nano* **10**, 1572–1579 (2016). <https://doi.org/10.1021/acs.nano.5b07217>
- Wang, X., Yu, R., Peng, W., Wu, W., Li, S., Wang, Z.L.: Temperature dependence of the piezotronic and piezophototronic effects in a-axis GaN nanobelts. *Adv. Mater.* **27**, 8067–8074 (2015). <https://doi.org/10.1002/adma.201504534>
- Chua, L.: If it's pinched it's a memristor. In: Tetzlaff, R. (ed.) *Memristors and Memristive Systems*, pp. 17–90. Springer, New York (2014)
- Xia, Q.: Memristor device engineering and CMOS integration for reconfigurable logic applications. In: Tetzlaff, R. (ed.) *Memristors and Memristive Systems*, pp. 195–221. Springer, New York (2014)
- Jo, S.H., Chang, T., Ebong, I., Bhadviya, B.B., Mazumder, P., Lu, W.: Nanoscale memristor device as synapse in neuromorphic systems. *Nano Lett.* **10**, 1297–1301 (2010)
- Zhua, R., Songlin, C., Henggao, D., Yangb, Y.J., Su, Y.: A micromachined gas inertial sensor based on thermal expansion. *Sens. Actuators, A* **212**, 173–180 (2014)
- Hazarika, D., Pegu, D.S.: Micro-controller based air pressure monitoring instrumentation system using optical fibers as sensor. *Opt. Fiber Technol.* **19**(2), 83–87 (2013)
- Fua, Y.Q., Luob, J.K., Dub, X., Flewittb, A.J., Markxa, G., Waltond, A., Milneb, W.: Recent developments on ZnO films for acoustic wave based bio-sensing and microfluidic applications: a review. *Sens. Actuators* **143**, 13 (2010)
- Tiginyanu, I., Popa, V., Stevens-Kalceff, M.A.: *Mater. Lett.* **65**, 360–362 (2011)
- Dragoman, M., Tiginyanu, I., Dragoman, D., Braniste, T., Ciobanu, V.: Memristive GaN ultrathin suspended membrane array. *Nanotechnology* **27**, 295204 (2016)
- Obreja, A.C., Cristea, D., Mihalache, I., Radoi, A., Gavrilă, R., Comanescu, F., Kusko, C.: Charge transport and memristive properties of graphene quantum dots embedded in poly (3-hexylthiophene) matrix *Appl. Phys. Lett.* **105**, 083303 (2014)
- Mishra, Y.K., Kaps, S., Schuchardt, A., Paulowicz, I., Jin, X., Gedamu, D., Freitag, S., Claus, M., Wille, S., Kovalev, A., Gorb, S.N., Adelung, R.: *Part. Part. Syst. Charact.* **30**, 775 (2013)
- Dragoman, M., Ciobanu, V., Shree, S., Dragoman, D., Braniste, T., Raevschi, S., Dinescu, A., Sarua, A., Mishra, Y.K., Pugno, N., Adelung, R., Tiginyanu, I.: Sensing up to 40 atm using pressure-sensitive aero-GaN. *PSS RRL*, 1900012 (2019). <https://doi.org/10.1002/pssr.201900012>

The Structure and Chemical Composition of Ga₂O₃ Oxide Prepared by Annealing of Ga₂Se₃ Crystals

V. Sprincean, E. Vatavu, L. Dmitroglu, D. Untila, I. Caraman, and M. Caraman

Abstract

The chemical composition and structure of Ga₂O₃ obtained by thermal treatment (TT) in air of β-Ga₂Se₃ crystals were studied using the X-ray diffraction (XRD) method, Raman spectroscopy, EDX, and SEM. The surface of the Ga₂Se₃ crystal air annealed at 770 K is covered by β-Ga₂O₃ layer of microcrystallites and as well as by β-Ga₂Se₃ crystallites. The oxygen is non-homogeneously distributed on the surface of the 770 K annealed sample. The sample obtained by TT at 1150 K consists of nanolamella, nanotowers, and nanobars of β-Ga₂O₃, their size being estimated to 10–200 nm.

Keywords

Ga₂Se₃ • Ga₂O₃ • XRD • SEM • EDX

1 Introduction

$A_2^{III}B_3^{VI}$ compounds, particularly Ga₂Se₃, are of high interest due to possible applications in optoelectronic devices [1, 2]. Ga₂Se₃ belong to the class of semiconductors with their own structural defects, in which one third of the cationic nodes are vacant [3]. The arrangement of these vacancies influences the anisotropy of the optical and luminescence properties and at the same time increases the thermal and radiation stability of the electronic devices based on this compound [4, 5]. Being of high sensitivity in the visible spectral region, Ga₂Se₃ semiconductor, with a direct bandgap of $E_g = 2.0$ eV, is a promising semiconductor for PV and luminescent devices for both VIS and IR [6, 7]. Recent

studies indicate the possibility to use this compound as an intermediate layer in $A^{III}B^V$ and $A_2^{III}B_3^{VI}$ semiconductor structures [8, 9].

Highly important properties are revealed in Ga₂Se₃ – Ga₂O₃ structure. Gallium oxide β-Ga₂O₃, being a wide bandgap ($E_g = 4.8$ eV), semiconductor can be successfully used to prepare radiation sources in the violet-blue spectral region, transparent optical electrodes for photovoltaics, and as a high-temperature gas sensor [10]. Based on nanoformations (nanofires, nanoribbons, nanospheres) of β-Ga₂O₃, photodetectors for the UV region and solar-blind photodetectors with sensitivity of ~ 0.19 A/W have been prepared [11]. Nanostructures of β-Ga₂O₃ can be obtained by various methods, including laser ablation, electric arc discharge, CVD, etc. [12, 13].

In this paper, the elementary composition, crystalline structure and surface morphology of the β-Ga₂O₃ layer obtained by air TT Ga₂Se₃ crystals is studied.

2 Materials and Methods

Ga₂Se₃ was synthesized from elemental components Ga (5 N) and Se (5 N) taken in stoichiometric amounts. The synthesis was carried out in a furnace with two thermal sectors, fixed at an angle of 30° to the horizon. The quartz ampoules with an inner diameter of ~ 15 mm and a length of ~ 200 mm containing material (Ga and Se with a total mass of 20 g) were placed in the furnace so that the primary material was in the second sector (1/3 of the ampoule length) at 1370 K. The temperature in the other sector was maintained at 870 K for 6 h, after which the temperature in both sectors was 1370 K. After two hours the ampoule is move into first sector, and the furnace was moved to its vertical position. The solidification temperature of Ga₂Se₃ determined from the FeSe-Ga₂Se₃ phase diagram is equal to 1278 K [14]. The temperature in the second sector decreased to 770 K in 3 h; a temperature gradient of $\sim 80^\circ/\text{cm}$ exists inbetween zones 1 and 2. For to obtain Ga₂Se₃ single

V. Sprincean (✉) · E. Vatavu · L. Dmitroglu · D. Untila · M. Caraman
Moldova State University, 60 A.Mateevici, Chisinau, Republic of Moldova
e-mail: sprincean@gmail.com

I. Caraman
University of Bacau, Bacau, Romania

crystals, the synthesized material was passed through the temperature gradient zone at a rate of ~ 1 mm/h. The pieces of Ga_2Se_3 (with a weight of 3–5 g) were cleaved from the Ga_2Se_3 ingot and air TT at 770 K for 1 h, and at 1150 K for 30 min. As a result, the surface of the Ga_2Se_3 crystals was covered by a white porous layer.

The structure, elemental composition and surface morphology of the obtained samples were studied by X-ray diffraction (XRD), Raman spectroscopy, electron beam scanning microscopy and EDX spectroscopy.

XRD patterns have been recorded by use of Empyrean diffractometer (CuK_α $\lambda = 1.540598$ Å).

Raman spectra at room temperature have been recorded by WITec alpha 300R spectrometer, having a ± 3 cm^{-1} resolution.

Surface morphology and elemental composition studies have been done by use of Zeiss Ultra Plus SEM, having an EDX attachment and used for accelerating voltages of 5.0–20.0 kV.

3 Results and Discussion

Figure 1 gives the XRD patterns of initial, source Ga_2Se_3 material used for $\beta\text{-Ga}_2\text{O}_3$ oxide preparation (Fig. 1a) and the patterns for 770 and 1150 K air TT Ga_2Se_3 material (Fig. 1b and c) respectively.

The peaks at 28.11° , 28.41° , 47.25° , 55.77° , 69.11° , 75.91° , 85.00° and 88.01° , correspond to (200), (002), (331), (260), (243), (513), (0110) and (446) planes according to PDF nr. 76-2310 C (monoclinic lattice of $\beta\text{-Ga}_2\text{Se}_3$ having the parameters $a = 6.660$ Å, $b = 11.65$ Å, $c = 6.649$ Å and $\beta = 108.84^\circ$).

$\beta\text{-Ga}_2\text{Se}_3$ TT 770 K results in formation on its surface of a white thin layer. As one can see from Fig. 1a, b, a weak trace of $\beta\text{-Ga}_2\text{O}_3$ is found along with $\beta\text{-Ga}_2\text{Se}_3$. The XRD pattern of the sample annealed at 1150 K (Fig. 1c) consists of peaks positioned at 30.03° , 30.40° , 31.62° , 33.40° , 35.11° , 38.30° , 64.63° which correspond to (401), (110), (002), ($\bar{1}11$), (111), ($\bar{3}11$), ($21\bar{7}$) planes of $\beta\text{-Ga}_2\text{O}_3$ (monoclinic lattice $a = 12.23$ Å, $b = 3.04$ Å, $c = 5.800$ Å and $\beta = 103.7^\circ$)—PDF 43-1012.

To be underlined that the same results were obtained for Ga_2Se_3 thin polycrystalline layers deposited on TiN substrate [8], from Ga_2Se_3 nanopowders [15] and Bridgman grown monocrystals Ga_2Se_3 [16].

By comparing the XRD patterns (Fig. 1), one can conclude that by air thermal treatment at 1150 K for 30 min a $\beta\text{-Ga}_2\text{O}_3\text{-Ga}_2\text{Se}_3$ composite is formed. It has been observed that starting with 970 K, an intense sulfur emission take place. The structural transformation of Ga_2Se_3 along with

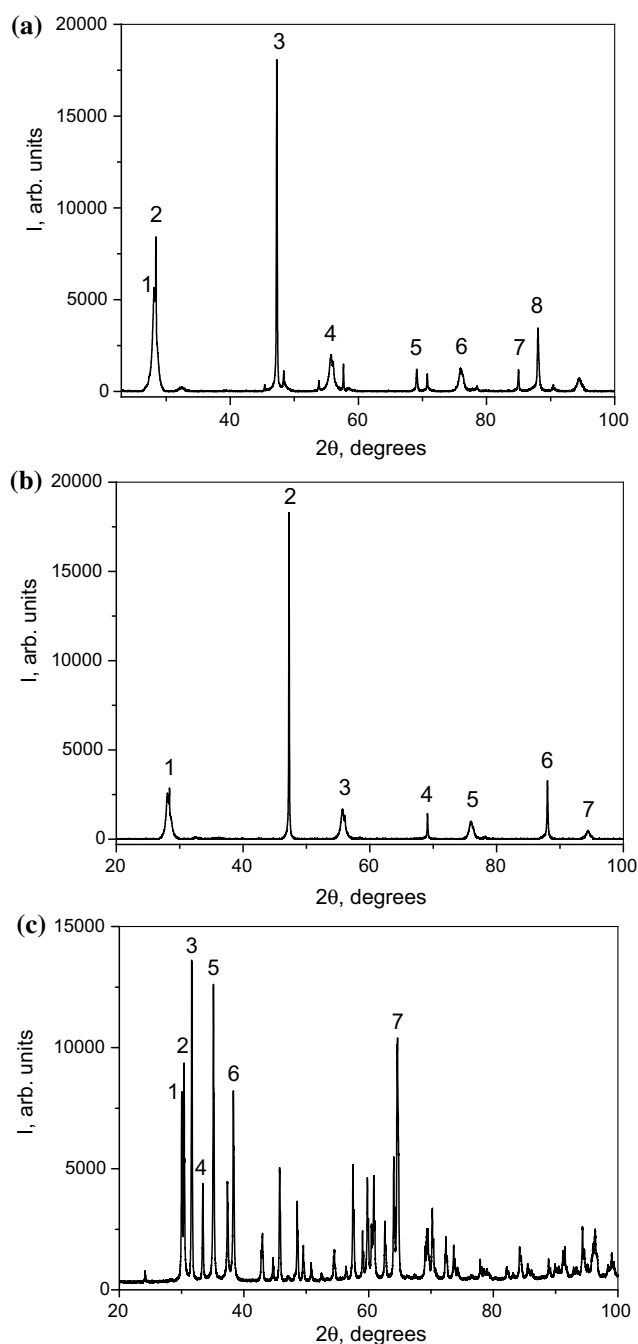
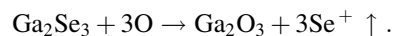


Fig. 1 XRD pattern of initial Ga_2Se_3 compound (a), air annealed Ga_2Se_3 at 770 K (b) and 1150 K (c)

Ga_2O_3 oxide formation takes place according to the reaction [17]:



In [18], Ga_2O_3 nanoribbons and nanowires were prepared by oxidizing of metallic gallium in water vapors ambient at 970 K for 30 min. The dynamics of the formation of

Table 1 Elemental composition of the surface of β -Ga₂O₃ layer

Chemical element	Composition of the material, at. %		
	I	II	III
Ga K	18.23	15.97	1.24
Se L	2.85	2.57	2.02
O K	78.92	81.46	84.85
C K	–	–	11.89
Totals	100	100	100

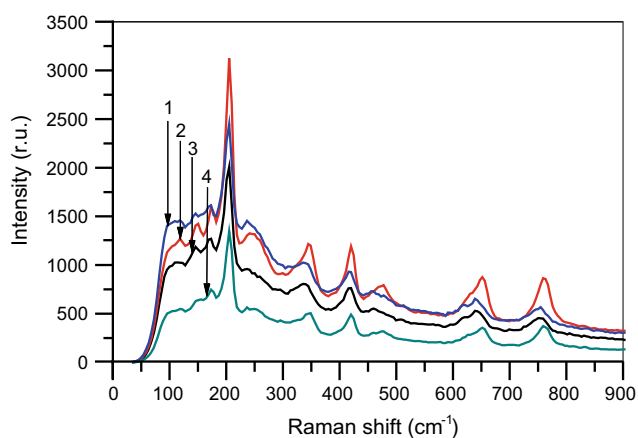
different types of β -Ga₂O₃ nanostructures by oxidation of the metallic gallium in the oxygen-argon atmosphere in the temperature range 1145–1270 K were studied in [19].

At low temperatures, micrometric nanoplates of β -Ga₂O₃ dimensions were obtained, while at higher temperatures these are transforming into nanowires and nanoribbons. Up to 10 μ m long nanowires of β -Ga₂O₃, were obtained by thermal oxidation of GaSe plates in air-Ar ambient at high temperatures (\sim 1200 K) [20].

The chemical composition of material obtained by TT of Ga₂Se₃ polycrystals at 770 K for 60 min in the atmosphere was determined from measurements of EDX spectra. The composition of the surface of the material is given in Table 1.

As can be seen from Table 1, the concentration of Ga₂Se₃ in β -Ga₂O₃ vary as 3.5–3.7%.

The traces of Ga₂Se₃ are found in the Raman spectra as well (low intensity satellite lines) (Fig. 2). TT 770 K reveals that the β -Ga₂O₃ oxide is formed, a result confirmed by XRD measurements and Raman spectra. The concentration of β -Ga₂O₃ on the surface of the sample is about 31–45%, so the EDX measurements point at an excess of molecular oxygen of 51–58% (O₂), which, the most probably, was trapped in Ga₂O₃ nanoformations at high TT temperatures.

**Fig. 2** The Raman spectra of the β -Ga₂O₃ layer formed during air oxidation at 1150 K for 30 min of Ga₂Se₃

Also, as it was demonstrated in [10], Ga₂O₃ is a good gas adsorber especially at high temperatures.

Figure 2 shows the micro-Raman spectra room temperature in different places on the surface of the sample obtained by TT of the Ga₂Se₃ crystal at 1150 K. As can be seen from these spectra, in the wavelength range from 109 to 759 cm⁻¹, ten Raman vibrational bands are revealed. The wavenumbers and corresponding peak assignment as well as symmetry modes are included in Table 2.

These vibrational bands are attributed to symmetrical pair vibrations (A_g), with except of the ones in the 141–146 cm⁻¹ range, which are attributed to asymmetrical pair vibrations (B_g). The data given in Fig. 2 and Table 2, are in good agreement with the Raman data for β -Ga₂O₃ crystallites of different sizes [21–23]. To be underlined, that the wavenumbers for the Raman vibrational bands differ by 3–5 cm⁻¹ depending on the paper, which probably is related by the structure and type of the nanoformations and β -Ga₂O₃ preparation technology β -Ga₂O₃. 3–5 cm⁻¹ shift of the Raman peak positions one can find in [24] for β -Ga₂O₃ nanowires and nanopowders, TT at 1173 K and 1223 K. A even bigger shift of Raman bands as a result of TT for β -Ga₂O₃ nanowires one can find in [23].

As can be seen from Fig. 2, next to the main Raman bands, low intensity peaks, shifted by 10–15 cm⁻¹ to lower wavenumber values are present (wavenumber region less than 300 cm⁻¹). The Raman spectra of β -Ga₂Se₃ in the range from 90 to 300 cm⁻¹ consists of bands with wave numbers of 90, 106, 121, 155, 198, 220, 240, 250, 280, and 300 cm⁻¹ [25]. Some wavenumbers, as shown in Fig. 2, might be attributed to low-intensity Raman peaks adjacent to wavenumbers of 118, 146, and 237 cm⁻¹, pointing at the presence of low quantity β -Ga₂Se₃ crystals in β -Ga₂O₃. Wide and elongated contours towards small energies of the Raman bands with wave numbers of 345, 420, 652, and 759 cm⁻¹ (Fig. 2) can be determined by the presence of different β -Ga₂O₃ nanoformations.

SEM images are given in Fig. 3 (a and b) of the surface and cleavage of Ga₂Se₃ ingot prepared by use of Ga (5 N) and Se (5 N) as described in previous section. After synthesis, the melt was cooled slowly to form an ingot composed of crystalline blocks with medium size hundreds of micrometers (Fig. 3b).

It is known that the Ga₂Se₃ compound sublimates at temperatures, bigger than 770 K. As can be seen from Fig. 3a, the condensate forms on the surface of the ingot isolated zones with areas ranging from several tens to several thousand μ m². As a result of TT at 770 K in air for 1 h, the surface of the polycrystalline Ga₂Se₃ is covered by a dense layer consisting of nanowires of β -Ga₂O₃ (Fig. 4a). As can be seen from Fig. 3b, there are some cracks in-between the Ga₂Se₃ crystals' blocks, allowing atmospheric oxygen to

Table 2 The Raman vibrational modes of β -Ga₂O₃ monoclinic lattice (nanowires and nanoribbons)

1		2		3		4	
$\tilde{\nu}$, cm ⁻¹	<i>I</i> , u. a.	$\tilde{\nu}$, cm ⁻¹	<i>I</i> , u. a.	$\tilde{\nu}$, cm ⁻¹	<i>I</i> , u. a.	$\tilde{\nu}$, cm ⁻¹	<i>I</i> , u. a.
118	1459.4	118	1270.6	118	1025.0	108	548.9
146	1530.0	150	1424.0	146	1187.2	141	639.6
173	1613.3	173	1597.2	173	1270.2	181	747.7
205	2447.8	205	3124.6	205	2007.2	205	1345.5
237	1453.8	241	1325.3	237	959.4	252	565.1
340	1019.1	345	1216.0	340	805.8	345	500.1
420	927.4	420	1191.9	420	762.9	420	490.3
460	731.2	478	794.3	460	553.1	478	319.3
639	653.6	652	876.6	639	529.1	652	355.4
755	567.6	759	865.9	755	452.6	759	373.7

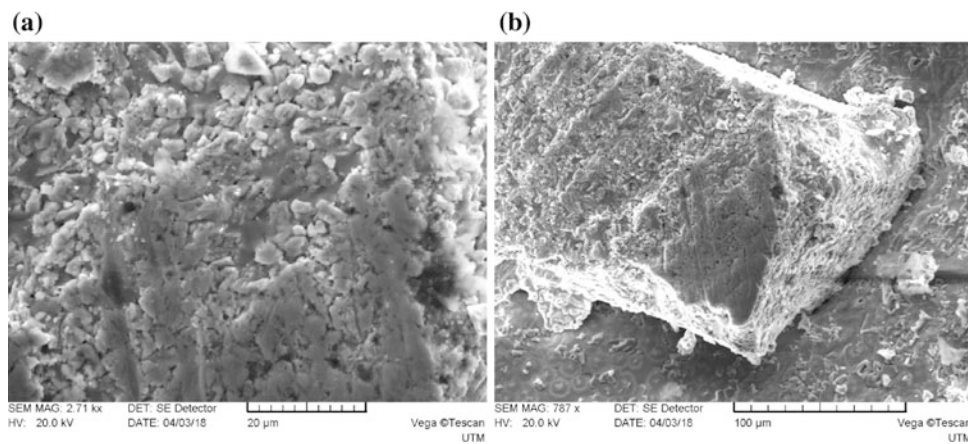


Fig. 3 SEM image of the surface (a) and cleavage (b) of the Ga₂Se₃ ingot

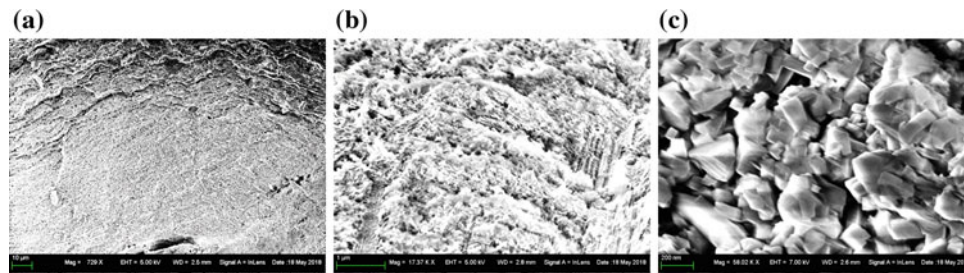


Fig. 4 SEM images of Ga₂O₃ layer formed as a result of TT at 770 K (a and b) and 1150 K (c) of Ga₂Se₃ crystals. **a** Top surface of the sample; **b** cross-section of the bulk β -Ga₂O₃; **c** surface of the sample prepared by TT at 1150 K

form microgranules which are nonhomogenously distributed β -Ga₂O₃.

Figure 4b gives a clear view of the cleavage of the sample. As a result of TT at 770 K polycrystalline blocks of β -Ga₂Se₃ have been completely transformed in a porous β -Ga₂O₃. When the TT temperature is increased from 770 K to 1150 K, the surface of the polycrystalline β -Ga₂Se₃ is covered with a white layer (Fig. 4c). Surface

inhomogeneities (cracks etc.) (Fig. 4c) may be caused by the polycrystalline structure of the β -Ga₂Se₃ sample and different formation rates of the β -Ga₂O₃ layer on it. Analogue nanoforms were obtained by transporting of Ga-vapor in an oxygen-argon ambient at a temperature of 1148 K [19]. The type of nanoforms changes from microcrystals of different shapes and sizes at 1148 K to nanowires and nanoribbons at 1248 K.

4 Conclusions

The Ga₂O₃ nanoparticles have been prepared by thermal treatment of Ga₂Se₃ poly and monocrystalline compound at 770–1150 K. The material obtained at 770 K consists of crystals of β-Ga₂O₃ with Ga₂Se₃ inclusions.

Raman spectra contain 10 vibrational modes out of 15 possible related to GaO₆ and GaO₄.

At 1150 K TT in air ambient, material consists of nanoforms (nanoribbons, nanotowers, nanopyramids) with dimensions of 10–200 nm, nonhomogeneously distributed on the surface.

Conflict of Interest The authors declare that they have no conflict of interest.

References

- Okamoto, T., Konagai, M., Kojima, N., et al.: Anomalous anisotropy in the absorption coefficient of vacancy-ordered Ga₂Se₃. *J. Electron. Mater.* **22**, 229–232 (1993)
- Khanfar, H.K., Qasrawi, A.F., Zakarneh, Y.A., et al.: Design and applications of Yb/Ga₂Se₃/C Schottky barriers. *IEEE Sens. J.* **17**, 4429–4434 (2017)
- Dai, Z.R., Ohuchi, F.S.: Vacancy ordering of Ga₂Se₃ at GaSe/GaAs(100) interface. *Appl. Phys. Lett.* **73**, 966–968 (1998)
- Okamoto, T., Kojima, N., Yamada, A., et al.: Optical anisotropy of vacancy-ordered Ga₂Se₃ grown by molecular beam epitaxy. *Jpn. J. Appl. Phys.* **31**, L143 (1992)
- Nakayama, T., Ishikawa, M.: Bonding and optical anisotropy of vacancy-ordered Ga₂Se₃. *J. Phys. Soc. Jpn.* **66**, 3887–3892 (1997)
- Мушинский, В.П., Караман, М.И.: Оптические свойства халькогенидов галлия и индия. Кишинев, Штиинца (1973)
- Abdal-Rahman, M., El Shaikh, H.A.: Photoelectric properties of Ga₂Se₃ single crystals. *J. Phys. D Appl. Phys.* **29**, 889 (1996)
- George, K., (Kees) de Groot, C.H., Gurnani, C., et al. (2013). Low pressure chemical vapour deposition of crystalline Ga₂Te₃ and Ga₂Se₃ thin films from single source precursors using telluroether and selenoether complexes. *Phys Procedia* **46**, 142–148
- Teraguchi, N., Kato, F., Konagai, M., et al.: Growth of III-VI compound semiconductors by metalorganic molecular beam epitaxy. *Jpn. J. Appl. Phys.* **28**, L2134 (1989)
- Baban, C., Toyoda, Y., Ogita, M.: Oxygen sensor based on Ga₂O₃ films operating at high temperature. *JOAM* **7**, 891–896 (2005)
- Cui, S., Mei, Z., Zhang, Y., et al.: Room-temperature fabricated amorphous Ga₂O₃ high-response-speed solar-blind photodetector on rigid and flexible substrates. *Adv. Opt. Mat.* **5**, 1700454 (2017)
- Xiang, X., Cao, C.-B., Guo, Y.-J., et al.: A simple method to synthesize gallium oxide nanosheets and nanobelts. *Chem. Phys. Lett.* **378**, 660–664 (2003)
- Lee, J.-S., Park, K., Nahm, S., et al.: Ga₂O₃ nanomaterials synthesized from ball-milled GaN powders. *J. Cryst. Growth* **244**, 287–295 (2002)
- Мамедов, Ф.М.: Уточнение фазовых диаграмм систем FeSe-Ga₂Se₃ и Ga₂Se₃-In₂Se₃. *Азерб хим журнал* **3**, 46–49 (2018)
- Kristl, M., Gyergyek, S., Srt, N., et al.: Mechanochemical route for the preparation of nanosized aluminum and gallium sulfide and selenide. *Mater. Manuf. Process* **31**, 1608–1612 (2016)
- Guler, I., Isik, M., Gasanly, N.M., et al.: Structural and optical properties of Ga₂Se₃ crystals by spectroscopic ellipsometry. *J. Electron. Mater.* **48**, 2418–2422 (2019)
- Balitskii, O.A., Savchyn, V.P., Savchyn, P.V.: Thermal oxidation of indium and gallium sulphides. *Phys. B Condens. Matter* **355**, 365–369 (2005)
- Li, J., Chen, X., Qiao, Z., et al.: Large-scale synthesis of single-crystalline β-Ga₂O₃ nanoribbons, nanosheets and nanowires. *J. Phys.: Condens. Matter* **13**, L937 (2001)
- Chen, Z., Wang, X., Saito, K., et al.: The impact of growth temperature on the structural and optical properties of catalyst-free β-Ga₂O₃ nanostructures. *Mater Res Express* **3**, 025003 (2016)
- Filippo, E., Siciliano, M., Genga, A., et al.: Single crystalline β-Ga₂O₃ nanowires synthesized by thermal oxidation of GaSe layer. *Mater. Res. Bull.* **48**, 1741–1744 (2013)
- Dohy, D., Lucazeau, G., Revcolevschi, A.: Raman spectra and valence force field of single-crystalline β-Ga₂O₃. *J. Solid State Chem.* **45**, 180–192 (1982)
- Filippo, E., Tepore, M., Baldassarre, F., et al.: Synthesis of β-Ga₂O₃ microstructures with efficient photocatalytic activity by annealing of GaSe single crystal. *Appl. Surf. Sci.* **338**, 69–74 (2015)
- Jung, W.-S.: Synthesis and characterization of GaN powder by the cyanonitridation of gallium oxide powder. *Ceram. Int.* **38**, 5741–5746 (2012)
- Kumar, S., Tessarek, C., Christiansen, S., et al.: A comparative study of β-Ga₂O₃ nanowires grown on different substrates using CVD technique. *J. Alloy. Compd.* **587**, 812–818 (2014)
- Takumi, M., Koshio, Y., Nagata, K.: X-Ray, Raman and photoluminescence study of vacancy ordered β-Ga₂Se₃ under high pressure. *Phys. Stat. Sol. b* **211**, 123–129 (1999)

The Use of Metal Oxide Semiconductors for THz Spectroscopy of Biological Applications

H. L. Hartnagel and V. P. Sirkeli

Abstract

Terahertz (THz) waves refer to the electromagnetic radiation in the frequency range from 0.1 to 10 THz, which corresponds to the wavelengths from 3 mm to 30 μm , respectively. This spectral region, called also as “T-gap”, is important for many practical applications, including THz imaging, chemical and biological sensing, high-speed telecommunication, security and medical applications. THz waves have low photon energies (~ 4.1 meV for 1 THz), which is about 1 million times weaker than the energy of X-ray photons. They do neither ignite any explosive materials at typical power levels nor cause any harmful ionization in biological tissues. The terahertz radiation is strongly attenuated by water and is very sensitive to water content. Unique THz absorption spectra caused by intermolecular vibrations in this spectral region have been found in different biological materials and tissues. Thus, Terahertz spectroscopy provides a powerful tool for characterization of a great many bio molecules and tissues. All these applications require relatively high power terahertz sources with milliwatt-level output power, which could operate at room temperature. Despite great progress, made in the last few years of design, fabrication and demonstration, THz devices based on GaAs/AlGaAs materials, there are some limits of bandgap engineering due to the relatively low (0.72 eV for GaAs/AlAs) conduction band offset, and most terahertz sources with one milliwatt-power like quantum cascade lasers (QCLs) require cryogenic cooling

down to less than 200 K. To overcome the issue the new material systems such as metal oxide materials are considered as promising for room-temperature THz sources. The interest in terahertz imaging and spectroscopy of biologically related applications is increasing more and more within the last few years. This paper provides a review and current status of using metal oxide materials for THz spectroscopy, and recent advances in terahertz spectroscopy techniques in biological and medical applications.

Keywords

Terahertz radiation • Metal oxides • Semiconductors • Quantum cascade structures • Biological tissue

1 Introduction

Terahertz (THz) waves refer to the electromagnetic radiation in the frequency range from 0.1 to 10 THz, which corresponds to the wavelengths from 3 mm to 30 μm , respectively [1]. This spectral region, called also “T-gap”, is important for many practical applications, including THz imaging, chemical and biological sensing, high-speed telecommunication, security and medical applications. Moreover, the THz spectral region covers intermolecular vibrations of biological molecules and low frequency crystalline lattice vibrations of chemical materials, including drugs, explosives and related compounds (ERCs) such as TNT, RDX, HMX, PETN and other explosive materials [2]. THz waves have low photon energies (~ 4.1 meV for 1 THz), which is about 1 million times weaker than the energy of X-ray photons, they neither ignite any explosive materials at typical power levels nor cause any harmful ionization in biological tissues [3, 4]. Thus, THz waves can be considered as a safe method for investigation of biological materials and which can be used in medicine for THz imaging and for other applications.

H. L. Hartnagel · V. P. Sirkeli (✉)

Institute of Microwave Engineering and Photonics, Technische Universität Darmstadt, Merckstrasse 25, Darmstadt, 64283, Germany
e-mail: sirkeli@imp.tu-darmstadt.de

H. L. Hartnagel

e-mail: hartnagel@imp.tu-darmstadt.de

V. P. Sirkeli

Department of Applied Physics and Computer Science, Moldova State University, Chisinau, Moldova

Despite the great progress made in the last few years in the design, fabrication and demonstration THz devices based on GaAs/AlGaAs materials, there are some limits of band-gap engineering due to the relatively low conduction band offset (CBO) (0.72 eV for GaAs/AlAs). This in particular means, THz generation cannot be obtained at room temperatures, as required for the many applications envisaged. It is therefore important to consider other compound semiconductors.

A good number of years ago, I wrote a book on transparent semiconductors [5]. Here a number of metal oxides such as Indium Tin Oxide (generally known as ITO) were important. They were widely used in important engineering projects like aircraft windows and large glass structures in architectural buildings. Since then, new material combinations appeared, such as Ga- and Al-oxides and in particular ZnO/ZnMgO. The latter ones are suitable for room-temperature THz sources [6]. Below we review the recent progress and current status of metal oxides-based terahertz sources and the perspective for THz spectroscopy of biological applications.

2 THz Spectroscopy of Biological Applications

In the last two decades THz spectroscopy has been widely used to probe and characterize various biomolecules because most low-frequency biomolecular motions, including vibration and rotation of the molecular skeletons, lie in the same frequency range as THz radiation. Therefore, various molecules can be clearly identified and characterized according to their spectral fingerprints. Moreover, THz spectroscopy has demonstrated unique advantages for detecting the coupling between molecules and their hydration shells when compared with conventional UV-Vis spectroscopy, X-ray crystallography, or nuclear magnetic resonance spectroscopy [7].

2.1 Nucleic Acids

Nucleic acids are crucial biological macromolecules, which are composed of nucleotide linear polymers linked by phospholipid bonds. THz spectrum of nucleic acids can reflect their intermolecular collective vibrations, the lattice vibrations and the configuration characteristics of nucleic acid molecules. In 2000, Markelz et al. [8] for the first time used THz-TDS technology for spectroscopy of nucleic acids and found that DNA, bovine serum protein and collagen showed different absorption characteristics in the THz frequencies. In 2015, Tang et al. [9] reported on the point

mutation of DNA molecules in aqueous solution through THz spectroscopy for the first time. The results showed that the four samples had characteristic absorption peaks at 1.29 THz, 1.97 THz, 2.20 THz, 2.32 THz and 2.47 THz respectively. These absorption peaks are related to the base of the mutation, and hybridized DNA membranes have a higher refractive index than denatured DNA membranes [10]. This research confirms the wide perspectives of THz spectroscopy for detecting the mutation of gene points.

2.2 Amino Acids and Peptides

The 20 naturally-occurring amino acids have an absorption characteristic in the 1–15 THz range. Kutteru et al. reported THz absorption spectra of solid phase peptides at 77 and 298 K, and proved that the structure information of a short peptide chain in the range of the 1–15 THz band was highly consistent with the measured spectral information [11]. It was observed that as the temperature decreased, the absorption peak of the peptide chain became sharp. It is established that with an increase in the number of amino acids the peptide absorption lines became complicated, the density and uniqueness of different absorption peaks predicted the correlation between THz spectrum and the sequence structure. Yamamoto et al. used THz-TDS to study the absorption coefficient and refractive index of glycine, l-alanine and its corresponding polypeptides in 7–55 cm^{-1} (0.21–1.65 THz) frequency bands [12]. For the first time, polyglycine was observed showing peaks at 45.5 cm^{-1} (1.365 THz) and it was induced by the interaction of the chain while poly-l-alanine was not found.

2.3 Proteins

Proteins are the irreplaceable constituents of all cells and tissues of the human body, and many important physiological processes of the body are also related to its activities. Ogawa et al. performed THz spectroscopy on label-free protein attached to polydifluoroethylene films. Experiments measured chain mildew THz signal observation and the combination of biotin avidin protein [13]. The results showed that the limit of streptomycin avidin protein was 27 ng/mm in 1.5 THz. It is revealed that pH has a significant effect on the THz absorption of β -lactoglobulin (β LG). It may help to study the water activity in close proximity to the fibrils [14]. Protein-induced solvation kinetics can be accurately identified by THz spectroscopy to accurately determine the hydrated shell of a protein [7]. It was found that the main effect is the collective water hydrogen bond kinetics near the protein [15].

2.4 Cancer Detection

The early detection of cancer is one of the most important issues in medical diagnosis because it provides a possibility to treat cancer before it grows too large and spreads to other organs [16–18]. To achieve early cancer detection many techniques have been suggested, including optical techniques. Among these techniques, terahertz spectroscopy shows a high sensitivity for chemical and structural changes in biological molecules without causing ionization, due to its low photon energy [19–22]. Carcinogenesis involves the structural and chemical and alteration of biomolecules in cells. Aberrant methylation of DNA is a well-known carcinogenic mechanism. Terahertz waves can directly observe changes in DNA because the characteristic energies lie in the same spectral region. The authors of Ref. [23] reported on terahertz molecular resonance fingerprints of DNA methylation in cancer DNA. They measured the THz absorption coefficients of nucleoside samples and defined THz resonance fingerprints based on the chemical changes caused by DNA methylation. They detected THz molecular resonance fingerprints caused by the methylation of cancer DNA extracted from living cell lines and quantified them to distinguish cancer types. Two major absorption peaks (1.29 and 1.74 THz) for methylation were identified between 0.4 and 2.0 THz by comparing two nucleoside samples, 2'-deoxycytidine (2'-dC) and 5-methylcytidine (5-mC), as well as chemical analogues. They also found the same resonance peaks at 1.67 THz in genomic DNA from various types of cancer (PC3, A431, A549, MCF-7 and SNU-1 cell lines). Thus, it was established that the methylation signal of cancer DNA in the THz range can be used to distinguish between normal and cancer DNA.

3 THz Sources Based on Zinc Oxide Materials

3.1 ZnO-Based THz QCLs

GaAl-THz-QCLs can produce milliwatt-level output power, but they require cryogenic cooling down to less than 200 K [1]. The first demonstration of THz QCLs (4.4 THz at 50 K) has been reported by Köhler et al. in 2002 [24]. The maximum operation temperature of 200 K was reported by Fathololoumi et al. in 2012 [25] for 3.22 THz $\text{Al}_{0.15}\text{Ga}_{0.85}\text{As}/\text{GaAs}$ THz QCLs in pulse mode operation. For design and fabrication of high-performance room-temperature THz QCLs, a II–VI wide bandgap material system like ZnMgO/ZnO has several advantages in comparison to the AlGaAs/GaAs such as higher value of LO-phonon energy (72 meV for ZnO vs. 36 meV for GaAs) and higher conduction band offset (CBO) values (~ 2.38 eV for ZnO/MgO vs. 0.72 eV for GaAs/AlAs) [5, 26–29]. It is

well known that ZnO-based materials have spontaneous and piezoelectric polarizations, which play an important role regarding optical properties and resulting built-in electric field in c-plane ZnO-based heterostructures. To overcome this problem it was suggested to use non-polar m-plane grown heterostructures. Recently, Bajo et al. [28] reported on successful fabrication m-plane ZnMgO/ZnO multi-quantum wells with low defects density and investigated intersubband absorption in such structures.

Sirkeli et al. [29] numerically investigated ZnMgO/ZnO THz QCL devices with different design schemes with diagonal laser transitions, employing resonant-tunneling and intra-well depopulation of lower laser state mechanisms. As reference, we chose the design of ZnMgO/ZnO THz QCL suggested by Bellotti et al. [6]. It is established that among all of the investigated devices, at room temperature the best value of optical gain of 300 cm^{-1} @ 4.96 THz is given by the ZnMgO/ZnO THz QCL with a 2-well design scheme and variable barrier heights. This value is significantly higher than the performance of the other devices: 60 cm^{-1} @ 3.13 THz for ZnMgO/ZnO THz QCL with a 2-well design scheme and fixed barrier heights, and 1.4 @ 7.13 THz for ZnMgO/ZnO THz QCL with a 3-well design scheme and fixed barrier heights [5]. The higher laser performance of ZnMgO/ZnO THz QCLs compared with AlGaAs/GaAs is attributed to the higher LO-phonon energy in ZnO (72 meV for ZnO vs. 36 meV for GaAs). The approach of THz QCL devices with 2-well design scheme employing alternating variable barrier heights leads to further enhancement of optical gain: the barriers with lower heights enhance electron injection in the active region, while the barriers with higher heights limit escaping of injected carriers from the quantum well and also reduce thermally activated carrier leakages via higher-energy parasitic levels [26].

3.2 ZnO-Based THz RTDs

Among electronic devices, resonant tunneling diodes (RTDs) are other promising candidates for terahertz wave generation at room temperature. In the last decade, significant progress has been made in the design and fabrication of THz RTDs based on AlGaAs/GaAs, InGaAs/AlAs, InGaAs/InAs and AlGaN/GaN material systems. In 2016 Maekawa et al. [30] reported on the achievement of a large increase in oscillation frequency up to 1.92 THz in InGaAs-based RTDs. A maximum output power of 0.61 mW at 620 GHz, 20–30 μW at 1 THz, and 0.4 μW at 1.92 THz was obtained for InGaAs-based RTD structures with slot antenna and two-array configuration and was reported in Ref. [30]. Increasing the output power of RTD devices at THz frequencies and increasing the operation frequency are crucial tasks. To solve these, II–VI

compounds like ZnO/ZnMgO are considered as promising materials for high-power THz RTDs.

Sirkeli et al. [31] reported on a numerical study of the quantum transport in the non-polar m-plane ZnO/ZnMgO RTDs with double and triple quantum barriers. The investigated THz RTD devices consist of one (two) ZnO quantum wells and two (three) Zn_{0.85}Mg_{0.15}O quantum barriers. The electronic quantum transport in ZnO-based RTDs were investigated numerically within single band effective mass approximation using nextnano.MSB solver software [32]. Devices with different designs were investigated: structure A is an RTD with single ZnO quantum well and two symmetrical ZnMgO quantum barriers with (Mg: $x = 0.15$), structure B is an RTD with two ZnO quantum wells and triple symmetrical ZnMgO quantum barriers (Mg: $x = 0.15$), and structure C is an RTD with two ZnO quantum wells and triple quantum barriers with variable heights (Mg: $x = 0.10/0.20/0.10$). The room-temperature current density-voltage characteristics of these RTD devices were investigated. For all the investigated RTD devices the j - V dependences exhibit the region with a negative differential resistance. It could be seen, that among all structures, the better one is structure C, which has a maximum value of current density PVR ratio. Using the small-signal equivalent circuit model for a RTD device [27] the authors have estimated cut-off frequency and maximum of output power at room temperature for the RTD devices with structures A, B and C, which are equal to: 240 μ W @ 1 THz, 194 μ W @ 1 THz and 912 μ W @ 1 THz, respectively. These values are about 6–30 times higher than the maximum output power of terahertz emission from the best InGaAs-based RTDs reported by Maekawa et al. [30].

4 Conclusions

This review concerns the recent progress of THz spectroscopy of biological molecules and tissues as well as applications of metal oxide materials for the use in terahertz devices. We show that non-polar m-plane ZnO/ZnMgO-based quantum structures are promising for the fabrication of THz RTD and QCL devices operating at room temperatures with the emitting frequencies from 1 THz up to 4.96 THz and terahertz output power up to 1 mW, and which could be used for THz spectroscopy of biomedical applications. From the review of recent papers we can conclude that THz spectroscopy macromolecular detection has made remarkable progress. In addition, it shows great potential for clinical applications, such as

label-free pathogen identification. However, some challenges must be overcome, because the strong absorption of water throughout the THz frequency range has been a huge obstacle to biological detection. The THz signal of water is stronger than that of biomolecules, thus impairing accurate detection.

Conflict of Interest The authors declare that they have no conflict of interest.

References

1. Belkin, M.A., Capasso, F.: *Phys. Scr.* **90**, 118002 (2015)
2. Leahy-Hoppa, M.R., Fitch, M.J., Zheng, X., Hayden, L.M., Osiander, R.: *Chem. Phys. Lett.* **434**, 227–230 (2007)
3. Scarfi, M.R., Roman, M., et al.: *J. Biol. Phys.* **29**, 171–177 (2003)
4. Clothier, R.H., Bourne, N.: *J. Biol. Phys.* **29**, 179–185 (2003)
5. Hartnagel, H.L., Dawar, A.W., Jain, A.K., Jagadish, C.: *Semiconducting Transparent Thin Films*. Institute of Physics Publishing, Bristol (1995)
6. Bellotti, E., Driscoll, K., Moustakas, T.D., Paiella, R.: *J. Appl. Phys.* **105**, 113103 (2009)
7. Born, B., et al.: *Faraday Discuss.* **141**, 161–173 (2009). <https://doi.org/10.1039/B804734K>
8. Markelz, A., Whitmire, S., Hillebrecht, J., Birge, R.: *Phys. Med. Biol.* **47**, 3797 (2002)
9. Tang, M., Huang, Q., Wei, D., et al.: *J. Biomed. Opt.* **20**, 095009 (2015)
10. Brucherseifer, M., Nagel, M., Bolivar, P.H., Kurz, H.: *Mater. Sci. Forum* **77**, 4049–4051 (2000)
11. Kutteruf, M.R., Brown, C.M., et al.: *Chem. Phys. Lett.* **375**, 337–343 (2003)
12. Kohji, Y., Keisuke, T., Hiroaki, S., Atsuo, T., Hidetoshi, M.: *Biophys. J.* **89**, L22–L24 (2005)
13. Ogawa, Y., Hayashi, S., Oikawa, M., Otani, C., Kawase, K.: *Opt. Express* **16**, 22083–22089 (2008)
14. Png, G.M., Falconer, R.J., Abbott, D.: *IEEE Trans Terahertz Sci Technol* **6**, 45–53 (2016)
15. Xu, Y., Bäumer, A., Meister, K., et al.: *Chem. Phys. Lett.* **647**, 1–6 (2016)
16. Moffat, B.A., et al.: *PNAS* **102**, 5524–5529 (2005)
17. Weissleder, R.: *Science* **321**, 1168–1171 (2006)
18. Zhang, Z., et al.: *Cancer Res.* **64**, 5882–5890 (2004)
19. Yamamoto, K., Kabir, H., Tominaga, K.: *J Opt Soc Am B* **22**, 2417–2426 (2005)
20. Plusquellic, D.F., Siegrist, K., Heilweil, E.J., Esenturk, O.: *Chem Phys Chem* **8**, 2412–2431 (2007)
21. Markelz, A.G.: *IEEE J Sel Top Quant* **14**, 180–190 (2008)
22. Arora, A., et al.: *Analyst* **137**, 575–579 (2012)
23. Cheon, H., et al.: *Sci Rep* **6**, 37103 (2016). <https://doi.org/10.1038/srep37103>
24. Köhler, R., Tredicucci, A., et al.: *Nature* **417**, 156–159 (2002)
25. Fatholouloumi, S., Dupont, E., et al.: *Opt. Express* **20**, 3866–3876 (2012)
26. Sirkeli, V.P., Yilmazoglu, O., Küppers, F., Hartnagel, H.L.: *Phys Status Solidi. (RRL) Rapid Res. Lett.* **11**, 1600423 (2017). <https://doi.org/10.1002/pssr.201600423>

27. Sirkeli, V.P., Yilmazoglu, O., Ong, D.S., Preu, S., Küppers, F., Hartnagel, H.L.: *IEEE Trans. Electron Devices* **64**, 3482–3488 (2017). <https://doi.org/10.1109/TED.2017.2718541>
28. Bajo, M.M., Tamayo-Arriola, J., et al.: *Proceedings of SPIE* **10105**, 101050O (2017). <https://doi.org/10.1117/12.2252056>
29. Sirkeli, V.P., Hartnagel, H.L.: *Opto-Electron. Rev.* **27**, 119–122 (2019). <https://doi.org/10.1016/j.opelre.2019.04.002>
30. Maekawa, T., Kanaya, H., Suzuki, S., Asada, M.: *Appl. Phys. Express* **9**, 024101 (2016)
31. Sirkeli, V.P., Vatavu, S., Yilmazoglu, O., Preu, S., Hartnagel, H.L.: In: *Proceedings of the 44th International Conference on Infrared, Millimeter and Terahertz Waves, IRMMW-THz 2019, Paris, France, (2019)* (in press)
32. Greck, P., Birner, S., Huber, B., Vogl, P.: *Opt. Express* **23**, 6587–6600 (2015)



ZnO-Based Quantum Structures for Terahertz Sources

V. P. Sirkeli, H. L. Hartnagel, O. Yilmazoglu, and S. Preu

Abstract

In this paper we report on the numerical study of the terahertz devices based on metal oxide semiconductors and its application in biology and medicine. We also report on the recent progress of the theoretical and experimental studies of ZnO-based THz quantum cascade lasers (QCLs) and resonant tunneling diodes (RTDs). We show that ZnO-based semiconductor compounds are promising materials for fabrication terahertz sources operating up to room temperature due to their unique properties such as large bandgap and conduction band offset (CBO) energy, high LO-phonon energy, and high resistant to the high breakdown electric field. Moreover, it was established that the ZnO-based terahertz sources can cover the spectral region of 5–12 THz, which is very important for THz imaging and detection of explosive materials, and which could be not covered by conventional GaAs-based terahertz devices. In terms of the reported significant progress in growth of non-polar m-plane ZnO-based heterostructures and devices with low density defects, it is open a wide perspective towards design and fabrication of non-polar m-plane ZnO-based high power terahertz sources with capabilities of operation at room temperature.

Keywords

Terahertz radiation • Metal oxides • Semiconductors • Quantum cascade structures • Resonant tunneling diode

1 Introduction

Terahertz (THz) waves refer to the electromagnetic radiation in the frequency range from 0.1 to 10 THz, which corresponds to the wavelengths from 3 to 30 μm , respectively [1]. This spectral region, called also as “T-gap”, is important for many practical applications, including THz imaging, chemical and biological sensing, high-speed telecommunication, security and medicine applications [1–6]. Moreover, THz spectral region covers intermolecular vibrations of biological molecules and low frequency crystalline lattice vibrations of chemical materials, including drugs, explosive and related compounds (ERCs) such as TNT, RDX, HMX, PETN and other explosive materials [2–4]. Transmitted and reflectance THz spectra of these materials contain specific THz absorption peaks (finger-prints), which characterize vibration modes of these materials and provide information which could be used for identification of the ERC, and which is not available in the other regions of the electromagnetic spectrum. Leahy-Hoppa et al. [2] are investigated the THz absorption spectra of many explosives and found that the THz absorption peaks (finger-prints) of these explosives are located in the terahertz frequency range of 0.8–6.0 THz. For security applications it is very important to find a reliable, fast, contact-less, and non-destructive method to detect explosive materials such as TNT, RDX, HMX, and PETN. THz waves have low photon energies (~ 4.1 meV for 1 THz), which is about 1 million times weaker than the energy of X-ray photons, and do neither ignite any explosive materials at typical power levels nor cause any harmful ionization in biological tissues [5, 6]. Thus, THz waves can be considered as a safe method for investigation of biological materials and which can be used in medicine for THz imaging and for other applications.

Despite the great progress in the last few years of design, fabrication and demonstration THz devices based on GaAs/AlGaAs materials, there are some limits of bandgap engineering due to the relatively low (0.72 eV for

V. P. Sirkeli (✉) · H. L. Hartnagel · O. Yilmazoglu · S. Preu
Institute for Microwave Engineering and Photonics, Technische
Universität Darmstadt, Merckstrasse 25, Darmstadt, Germany
e-mail: sirkeli@imp.tu-darmstadt.de

V. P. Sirkeli
Department of Applied Physics and Computer Science, Moldova
State University, A. Mateevici str. 60, Chisinau, Moldova

GaAs/AlAs) conduction band offset (CBO). To overcome the issue the new material systems such as ZnO/ZnMgO are considered as promising for room-temperature THz sources.

Below we report the results of numerical study of room-temperature ZnO-based terahertz sources.

2 THz Sources Based on Zinc Oxide Materials

2.1 ZnO-Based THz QCLs

THz QCLs can produce milliwatt-level output power, but they require cryogenic cooling down to less than 200 K [1]. The first demonstration of THz QCLs (4.4 THz at 50 K) has been reported by Köhler et al. in 2002 [7]. The most reported THz QCL devices are based on the AlGaAs/GaAs material system. The maximum operation temperature of 200 K was reported by Fathololoumi et al. in 2012 [8] for 3.22 THz $\text{Al}_{0.15}\text{Ga}_{0.85}\text{As}/\text{GaAs}$ THz QCLs in pulse mode operation based on a 4 well diagonal design scheme with longitudinal-optical phonon (LO-phonon) depopulation of the lower laser state. To overcome the problem of low-temperature operation of the THz QCLs several approaches have been suggested such as QCLs with a tall quantum barrier, QCLs with variable barrier heights and others. Also other material systems have been considered and studied such as InGaAs/GaAs, AlGaIn/GaN, InGaN/GaN, ZnMgCdSe/ZnCdSe, ZnMgSe/ZnSe, ZnMgO/ZnO, SiGe/Si [1, 7–11]. For design and fabrication of high-performance room-temperature THz QCLs, a II–VI wide bandgap material system like ZnMgO/ZnO has several advantages in comparison to the AlGaAs/GaAs such as higher value of LO-phonon energy (72 meV for ZnO vs. 36 meV for GaAs) and higher conduction band offset (CBO) values (~ 2.38 eV for ZnO/MgO vs. 0.72 eV for GaAs/AlAs) [9]. It is well known that ZnO-based materials have spontaneous and piezoelectric polarizations, which play an important role regarding optical properties and resulting built-in electric field in c-plane ZnO-based heterostructures. To overcome this problem it was suggested to use non-polar m-plane grown heterostructures. Recently, Bajo et al. [12] reported on successful fabrication m-plane ZnMgO/ZnO multi-quantum wells with low defects density and investigated intersubband absorption in such structures.

Sirkeli et al. [13, 14] numerically investigated ZnMgO/ZnO THz QCL devices with different design schemes with diagonal laser transitions, employing resonant-tunneling and intra-well depopulation of lower laser state mechanisms. As reference, it was chosen the design of ZnMgO/ZnO THz QCL suggested by Bellotti et al. [9]. This THz QCL device consists of three ZnO quantum wells and $\text{Zn}_{0.85}\text{Mg}_{0.15}\text{O}$ quantum barriers. The layer thicknesses of one cascade of such a THz QCL starting from the injector barrier in nm is: 3.0/3.1/2.5/2.4/3.4/5.5, where the

underlined quantum well is homogeneously n-type doped with a concentration of $3 \times 10^{16} \text{ cm}^{-3}$. The suggested approach for high-power room-temperature ZnMgO/ZnO THz QCLs is based on a 2-well design scheme employing the fixed and variable barrier heights and a delta-doped injector well of $1 \times 10^{18} \text{ cm}^{-3}$. The layer thicknesses of one cascade of such structures starting from injector well in nm are equal to 2.7/6.0/2.6/4.0 and 2.7/6.0/1.5/4.0, respectively. The THz QCL with fixed barriers consist of $\text{Zn}_{0.85}\text{Mg}_{0.15}\text{O}$ quantum barriers, while devices based on a design with variable barrier heights consist of $\text{Zn}_{0.80}\text{Mg}_{0.20}\text{O}$ and $\text{Zn}_{0.70}\text{Mg}_{0.30}\text{O}$ quantum barriers. For comparison, it was also simulated the best experimental $\text{Al}_{0.15}\text{Ga}_{0.85}\text{As}/\text{GaAs}$ THz QCL based on a 3-well design scheme with fixed barriers [8]. The layer thicknesses of one cascade of this THz QCL starting from the injector barrier in nm is: 4.3/8.9/2.46/8.15/4.1/16, where the last quantum well is homogeneously n-type doped with a concentration of $6 \times 10^{16} \text{ cm}^{-3}$. The dependences of the optical gain of THz laser emission as function of temperature for AlGaAs/GaAs and ZnMgO/ZnO THz QCLs with different design schemes are shown in Fig. 1.

It can be seen from Fig. 1 that optical gain of all devices decreased with increasing temperature. The calculated maximum operating temperature of AlGaAs/GaAs-based THz QCL is about 200 K, which is in good agreement with experiment [8].

The calculated radiation frequency of this device at 200 K is 3.50 THz, slightly higher than the experimental value of 3.22 THz. Thus, these results confirm the validity of the used model and software. As can be seen from Fig. 2, among all devices, at room temperature the best value of optical gain of 300 cm^{-1} @ 4.96 THz is given by the ZnMgO/ZnO

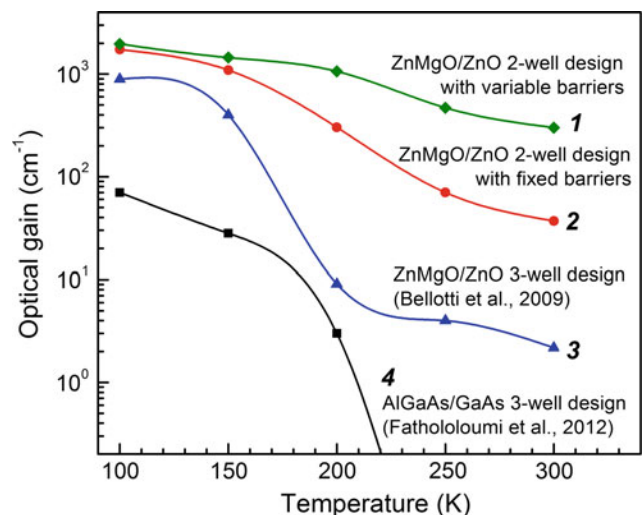


Fig. 1 Calculated optical gain of terahertz laser emission for four THz QCL devices with different designs as function of temperature

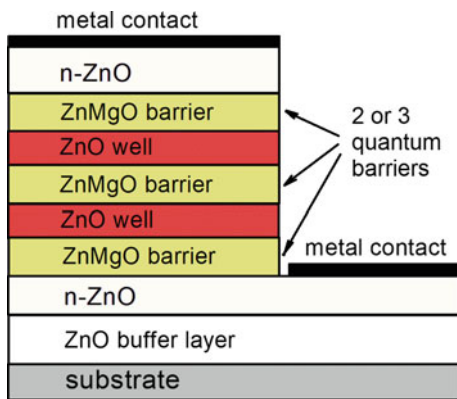


Fig. 2 Schematic structure of non-polar m-plane ZnO/ZnMgO RTDs with double and triple quantum barriers

THz QCL with a 2-well design scheme and variable barrier heights. This value is significantly higher than the performance of the other devices: 60 cm^{-1} @ 3.13 THz for ZnMgO/ZnO THz QCL with a 2-well design scheme and fixed barrier heights, and 1.4 @ 7.13 THz for ZnMgO/ZnO THz QCL with a 3-well design scheme and fixed barrier heights [9]. The higher laser performance of ZnMgO/ZnO THz QCLs compared with AlGaAs/GaAs is attributed to the higher LO-phonon energy in ZnO (72 meV for ZnO vs. 36 meV for GaAs). The approach of THz QCL devices with 2-well design scheme employing alternating variable barrier heights leads to further enhancement of optical gain: the barriers with lower heights enhance electron injection in the active region, while the barriers with higher heights limit escaping of injected carriers from the quantum well and also reduce thermally activated carrier leakages via higher-energy parasitic levels [10]. Moreover, by varying and optimizing constituent layer widths and barrier heights, the optical gain and radiation frequency of ZnMgO/ZnO THz devices at room temperature can be tailored from 108 cm^{-1} @ 2.18 THz (for a device with $\text{Zn}_{0.90}\text{Mg}_{0.10}\text{O}$ and $\text{Zn}_{0.80}\text{Mg}_{0.20}\text{O}$ quantum barriers and layer thicknesses of one cascade in nm of 2.7/6.2/1.5/11.9) to 300 cm^{-1} @ 4.96 THz (for a device with $\text{Zn}_{0.80}\text{Mg}_{0.20}\text{O}$ and $\text{Zn}_{0.70}\text{Mg}_{0.30}\text{O}$ quantum barriers described above and shown in Fig. 1) [13, 14].

2.2 ZnO-Based THz RTDs

Among electronic devices, resonant tunneling diodes (RTDs) is another promising as the candidate for terahertz wave generation and amplification, for signal detection and frequency mixing, all at room temperature. In the last decade, significant progress has been made in the design and fabrication of THz RTDs based on AlGaAs/GaAs, InGaAs/AlAs, InGaAs/InAs and AlGaN/GaN material

systems. In 2016 Maekawa et al. [15] published the achievement of a large increase in oscillation frequency up to 1.92 THz in InGaAs-based RTDs by reducing the conduction loss. A maximum output power of 0.61 mW at 620 GHz, 20–30 μW at 1 THz, and 0.4 μW at 1.92 THz was obtained for InGaAs-based RTD structures with slot antenna and two-array configuration and reported in Ref. [15]. Increasing the output power of RTD devices at THz frequencies and increasing the operation frequency are crucial tasks. To solve these, II–VI compounds like ZnO/ZnMgO are considered as promising materials for high-power THz RTDs.

Sirkeli et al. [16] reported on a numerical study of the quantum transport in the non-polar m-plane ZnO/ZnMgO RTDs with double and triple quantum barriers. They show that by optimizing the design structure of RTDs, the constituent layer material, its width and doping level, the mW-level output power of terahertz emission from these devices could be achieved at room temperature. The schematic structure of investigated non-polar m-plane ZnO-based THz RTDs with double and triple quantum barriers is shown in Fig. 2.

The investigated THz RTD devices consist of one (two) ZnO quantum wells and two (three) $\text{Zn}_{0.85}\text{Mg}_{0.15}\text{O}$ quantum barriers. The constituent layer thicknesses of such RTD devices with 2 and 3 quantum barriers starting from the emitter in nm are: 10/3/3.5/3/10 and 10/2.7/6/1.5/4/2.7/10, respectively. In order to enhance quantum transport in the investigated RTDs the emitter and collector were n-doped with concentration varied from 10^{16} to 10^{19} cm^{-3} . The electronic quantum transport of non-polar m-plane ZnO-based RTDs were investigated numerically within single band effective mass approximation using nextnano. MSB solver software [10, 11, 17, 18]. The material parameters were taken from [9, 12, 14, 19–21] and the cross section area of all investigated RTDs is $1.0 \times 1.0 \mu\text{m}^2$.

To improve output power performance of ZnO-based THz RTDs it was investigated the devices with different designs: structure A is a RTD with single ZnO quantum well and two symmetrical ZnMgO quantum barriers with (Mg: $x = 0.15$), structure B is a RTD with two ZnO quantum wells and triple symmetrical ZnMgO quantum barriers (Mg: $x = 0.15$), and structure C is a RTD with two ZnO quantum wells and triple quantum barriers with variable heights (Mg: $x = 0.10/0.20/0.10$). The thicknesses of constituent layers of investigated RTD devices starting from the emitter region in nm are: 10/3/3.5/3/10, 10/2.7/6/2.6/4/2.7/10 and 10/2.7/6/1.5/4/2.7/10 for structures A, B and C, respectively. The room-temperature current density-voltage characteristics of these RTD devices is shown in Fig. 3.

As could be seen from Fig. 3, for the all investigated RTD devices the j - V dependences exhibit the region with a

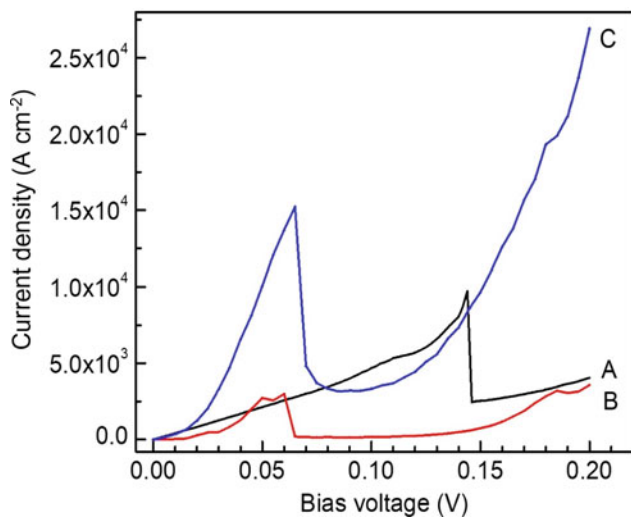


Fig. 3 Current density-voltage characteristics for the non-polar m-plane ZnO/ZnMgO RTDs with different designs. $T = 300$ K

negative differential resistance. It could be seen, that among all structures, the better one is structure C, which has a maximum value of current density PVR ratio.

Using the small-signal equivalent circuit model for a RTD device [11] the authors have estimated the maximum intrinsic frequency of oscillation (cut-off frequency) and maximum of output power at room temperature for the RTD devices with structures A, B and C, which are equal to: $240 \mu\text{W} @ 1 \text{ THz}$, $194 \mu\text{W} @ 1 \text{ THz}$ and $912 \mu\text{W} @ 1 \text{ THz}$, respectively. These values are about 6–30 times higher than the maximum output power of terahertz emission from the best InGaAs-based RTDs reported by Maekawa et al. [15].

3 Conclusions

In this paper we show that non-polar m-plane that ZnO/ZnMgO-based quantum structures are promising for fabrication THz RTD and QCL devices operating at room temperatures with the emitting frequencies from 1 THz up to 4.96 THz and output power up to 1 mW, and which could be used in various type of security and biomedical applications.

Acknowledgements V. P. S. gratefully acknowledges financial support from the Alexander von Humboldt Foundation. This work was partly supported under RM institutional project No. 15.817.02.34A. The authors also would like to acknowledge Dr. Stefan Birner and Nextnano GmbH Company for the providing nextnano.MSB code.

Conflict of Interest The authors declare that they have no conflict of interest.

References

1. Belkin, M.A., Capasso, F.: New frontiers in quantum cascade lasers: high performance room temperature terahertz sources. *Phys. Scr.* **90**, 118002 (2015)
2. Leahy-Hoppa, M.R., Fitch, M.J., et al.: Wideband terahertz spectroscopy of explosives. *Chem. Phys. Lett.* **434**, 227–230 (2007)
3. Liu, H.B., Zhong, H., et al.: Terahertz spectroscopy and imaging for defense and security applications. *Proc. IEEE* **95**, 1514–1527 (2007)
4. Choi, K., Hong, T., et al.: Reflection terahertz time-domain spectroscopy of RDX and HMX explosives. *J. Appl. Phys.* **115**, 023105 (2014)
5. Scarfi, M.R., Roman, M., et al.: THz exposure of whole blood for the study of biological effects on human lymphocytes. *J. Biol. Phys.* **29**, 171–177 (2003)
6. Clothier, R.H., Bourne, N.: Effects of THz exposure on human primary keratinocyte differentiation and viability. *J. Biol. Phys.* **29**, 179–185 (2003)
7. Köhler, R., Tredicucci, A., et al.: Terahertz semiconductor-heterostructure laser. *Nature* **417**, 156–159 (2002)
8. Fatholouloumi, S., Dupont, E., et al.: Terahertz quantum cascade lasers operating up to ~ 200 K with optimized oscillator strength and improved injection tunneling. *Opt. Express* **20**, 3866–3876 (2012)
9. Bellotti, E., Driscoll, K., Moustakas, T.D., Paiella, R.: Monte Carlo simulation of terahertz quantum cascade laser structures based on wide-bandgap semiconductors. *J. Appl. Phys.* **105**, 113103 (2009)
10. Sirkeli, V.P., Yilmazoglu, O., Küppers, F., Hartnagel, H.L.: Room-temperature terahertz emission from ZnSe-based quantum cascade structures: a simulation study. *Phys. Status Solidi (RRL)—Rapid Res. Lett.* **11**, 1600423 (2017). <https://doi.org/10.1002/pssr.201600423>
11. Sirkeli, V.P., Yilmazoglu, O., Ong, D.S., Preu, S., Küppers, F., Hartnagel, H.L.: Resonant tunneling and quantum cascading for optimum room-temperature generation of THz signals. *IEEE Trans. Electron Devices* **64**, 3482–3488 (2017). <https://doi.org/10.1109/TED.2017.2718541>
12. Bajo, M.M., Tamayo-Arriola, J., et al.: Intersubband absorption in m-plane ZnO/ZnMgO MQWs. *Proc. SPIE* **10105**, 1010500 (2017). <https://doi.org/10.1117/12.2252056>
13. Sirkeli, V.P., Yilmazoglu, O., Küppers, F., Hartnagel, H.L.: 2.08 THz and 4.96 THz room-temperature quantum cascade lasers based on non-polar M-plane ZnMgO/ZnO. In: Proceedings of the 43rd International Conference on Infrared, Millimeter and Terahertz Waves, IRMMW-THz 2018, Nagoya, Japan, 2018, pp. 1–2 (2018). <https://doi.org/10.1109/irmmw-thz.2018.8510344>
14. Sirkeli, V.P., Hartnagel, H.L.: ZnO-based terahertz quantum cascade lasers. *Opto-Electron. Rev.* **27**, 119–122 (2019). <https://doi.org/10.1016/j.opelre.2019.04.002>
15. Maekawa, T., Kanaya, H., Suzuki, S., Asada, M.: Oscillation up to 1.92 THz in resonant tunneling diode by reduced conduction loss. *Appl. Phys. Express* **9**, 024101 (2016)
16. Sirkeli, V.P., Vatavu, S., Yilmazoglu, O., Preu, S., Hartnagel, H.L.: Negative differential resistance in ZnO-based resonant tunneling diodes. In: Proceedings of the 44th International Conference on Infrared, Millimeter and Terahertz Waves, IRMMW-THz 2019, Paris, France, 2019 (in press)

17. Greck, P., Birner, S., Huber, B., Vogl, P.: Efficient method for the calculation of dissipative quantum transport in quantum cascade lasers. *Opt. Express* **23**, 6587–6600 (2015)
18. Web site of Nextnano GmbH Company at <http://www.nextnano.de>
19. Sirkeli, V.P., Yilmazoglu, O., Küppers, F., Hartnagel, H.L.: Effect of p-NiO and n-ZnSe interlayers on the efficiency of p-GaN/n-ZnO light-emitting diode structures. *Semicond. Sci. Technol.* **30**, 065005 (2015). <https://doi.org/10.1088/0268-1242/30/6/065005>
20. Sirkeli, V.P., Yilmazoglu, O., Küppers, F., Hartnagel, H.L.: Effect of p-NiO interlayer on internal quantum efficiency of p-GaN/n-ZnO light-emitting devices. *J. Nanoelectron. Optoelectron.* **9**, 811–818 (2014). <https://doi.org/10.1166/jno.2014.1687>
21. Adachi, S.: *Properties of Semiconductor Alloys: Group—IV, III—V and II—VI Semiconductors*. Wiley, Berlin (2009)

Surface Modification of PVDF Copolymer Nanofiber by Chitosan/Ag(NP)/Nanosilica Composite

M. Nasir, R. I. Sugatri, and D. M. Agustini

Abstract

PVDF copolymer nanofiber showed good chemical, mechanical and high hydrophobicity properties. PVDF copolymer nanofiber can be modified and functionalized by introducing hydrophilic and antibacterial materials such as chitosan composite. In this work, PVDF copolymer nanofiber with an average diameter 427.00 nm was modified by dip-coating process by using mixture of chitosan/Ag(NP)/nanosilica. Chitosan/Ag(NP)/nanosilica/PVDF copolymer nanofiber composite was successfully synthesized after analysis and confirmed by using ATR-FTIR spectroscopy, scanning electron microscopy (SEM), water contact angle and water spreading time analysis. SEM analysis showed the diameter of chitosan/Ag(NP)/nanosilica/PVDF copolymer nanofiber has an average diameter 443.50 nm. Post dip coating, it was found the specific vibration band peak IR spectrum which identify the presence of chitosan, SiO₂, and the shifting band peak which was caused by interaction between chitosan and Ag⁰ in nanofiber composite. Chitosan/Ag(NP)/nanosilica/PVDF copolymer nanofiber composite with different content of nanosilica have lower water contact angle than pristine PVDF copolymer nanofiber. Water contact angle of PVDF copolymer nanofiber, chitosan/Ag(NP)/nanosilica (0.05%)/PVDF copolymer nanofiber and chitosan/Ag(NP)/nanosilica (0.20%)/PVDF copolymer nanofiber were 108°, 60° and 77°, respectively. Water spreading time analysis showed that modified PVDF copolymer has faster water spreading time than pristine PVDF copolymer nanofiber. It meant

modification of PVDF copolymer nanofiber by chitosan/Ag(NP)/nanosilica gave hydrophilic and antibacterial properties to nanofiber.

Keywords

Chitosan/Ag(NP)/nanosilica/PVDF copolymer nanofiber • Chitosan • Ag(NP) • Nanosilica • Dip coating

1 Introduction

Poly(vinylidene fluoride) (PVDF) nanofibers are potential materials that can be used for some applications such as antibacterial [1], polymer electrolyte [2], separation performance and fouling control [3], filtration [4], and separation water/oil [5] due to their good electrolyte and high ionic conductivity [2], excellent resistance towards harsh chemicals [4] and hydrophobicity properties [5].

For the some cases, hydrophobicity of PVDF nanofibers restrict their applications. Some researcher modified PVDF membranes to decrease the hydrophobicity. Various methods were used for enhancing hydrophilicity of PVDF namely blending hydrophilic polymers or/and inorganic nanoparticles and surface modification of existing membranes [6]. Obaid et al. [7] blended dispersion of SiO₂ nanoparticles with polymer solution to adjust hydrophobicity of PVDF membranes. In certain concentrations, the presence of SiO₂ is able to decrease hydrophobicity of PVDF nanofiber. Sheikh et al. [4] decreased hydrophobicity of PVDF nanofiber by PVA solution using hydrothermal approach. The results showed coating method PVA to PVDF nanofibers increase their diameters and affect in improving surface wettability. In other hands, Boributh et al. [8] modified PVDF membrane by chitosan solution for reducing protein fouling. The results indicated that modified membranes have

M. Nasir (✉) · R. I. Sugatri
 Research Unit for Clean Technology, Indonesian Institute of Sciences (LIPI), Jalan Cisitua Sangkuriang, Bandung, West Java, Indonesia
 e-mail: mnasir71@yahoo.com; muhammad.nasir@lipi.go.id

D. M. Agustini
 Department of Chemistry, Jenderal Achmad Yani University (UNJANI), Cimahi, West Java, Indonesia

higher hydrophilicity than unmodified membrane. Chanchai, et al. [9] coated PVDF membrane with chitosan by dip coating method. They reported modified membrane provided better protection against wetness of membrane and also increased water flux of PVDF membrane. Besides, to enhance antibacterial activities of PVDF nanofiber, Yuan et al. [1] spun PVDF which was blended with silver nanoparticles using electrospinning process. Higher silver content enhances the antibacterial ability of the nanofiber composite.

In this work, we modified PVDF copolymer nanofiber by composite solution using dip coating method. The composite solution contains chitosan, Ag(NP), and nanosilica where the Ag(NP) was synthesized by the presence of chitosan and nanosilica using microwave-assisted reflux. This composite is expected can control surface properties of PVDF copolymer nanofibers to improve their function.

2 Eksperimental Section

2.1 Materials

PVDF copolymer nanofiber with diameter average of 427.00 nm which was synthesized by electrospinning method (polyvinylidene fluoride co-hexafluoro propylene with concentration 24% (w/v) in N,N-dimethylacetamide solution with parameters 0.004 mL/min, 13 cm, 22 kV). Chitosan (Mw = 39 kDa, 87% deacetylation) was extracted from crab shell of *Portunus pelagicus* by Rhazi et al. [10] method. Glacial acetic acid technique. Silver nitrate and tri-sodium citrate dehydrate were purchased by Merck. Nanosilica was synthesized by sol-gel method: ammonia solution 25%, N-cetyl-N,N,N-Trimethyl-Amonium Bromide (CTAB) and tetraethyl ortosilicate 98% (TEOS) that were purchased by Merck.

2.2 Preparation of Chitosan/Ag(NP)/Nanosilica Solution

AgNO₃ 1 mM was added to C₆H₅O₇Na₃ 1% with ratio 10:1 (v/v) than was stirred until homogeneous. Chitosan 1.5% (w/v) was dissolved in acetic acid 2% (v/v). Subsequently, chitosan solution mixed with AgNO₃ solution using ratio 2:1 (v/v). Furthermore, nanosilica was added to chitosan/Ag (NP) solution with various concentrations 0.20, 0.10, 0.05% (w/v). The composite solutions were heated by microwave-assisted reflux at low power condition (300 W) for 5 min.

2.3 Preparation of Coating PVDF Copolymer Nanofiber

PVDF copolymer nanofiber was immersed in chitosan/Ag (NP) and chitosan/Ag(NP)/nanosilica, respectively, for 2 h and dried at room temperature.

2.4 Characterization

PVDF copolymer nanofibers before and after coated by dip coating method were characterized using Attenuated Total Reflectance-Fourier Transform Infrared Spectroscopy (ATR-FTIR) Shimadzu IR Prestige 21, Scanning Electron Microscopy (SEM) tipe JOEL-JSM-6510LV and calculated water contact angle by equation:

$$\frac{\theta}{2} = \tan^{-1} \left(\frac{h}{d} \right) \quad (1)$$

θ = contact angle, d = diameter, h = height of water droplet.

3 Result and Discussion

3.1 Synthesis of Chitosan/Ag(NP)/Nanosilica Solution

Chitosan/Ag(NP)/nanosilica composite solution was synthesized by microwave-assisted reflux. This method can result a faster reaction and produce higher concentration of silver nanoparticles than conventional heating [11]. In this work, we used silver nitrate as a precursor, tri-sodium citrate and chitosan as reductor and stabilizer, respectively, and nanosilica as modifier in composite solution.

Chitosan has been dissolved in acetic acid 2% (v/v) than added to AgNO₃/na-citrate solution which causes bonding between Ag⁺ and chitosan by electrostatic interaction. Electron-rich oxygen atoms of the hydroxyl group and glucosidic of chitosan interact with electropositive transition metal cations. Ag⁺ oxidizes hydroxyl group of chitosan to carbonyl group and finally reduce to Ag⁰ [12]. Besides, the presence chitosan in synthesis of composite is expected to prevent agglomeration of Ag(NP) since the nanoparticles were covered by chitosan [13]. In this work, we used sodium citrate to enhance formation of Ag⁰. Nanosilica was added to the solution to add nanosilica properties which are well known has high stability, low toxic, resistance in high temperature, and good mechanical [14]. The forming of Ag⁰

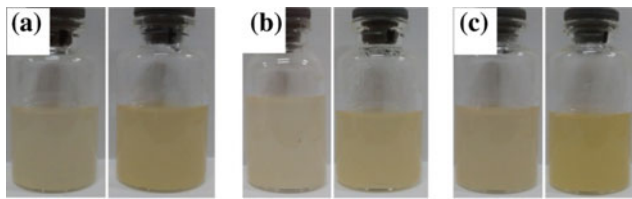


Fig. 1 Chitosan/Ag(NP)/nanosilica solution with variation of nanosilica **a** 0.20%, **b** 0.10%, and **c** 0.05% (w/v)

causes changing color in chitosan/Ag(NP)/nanosilica composite solution from pale yellow into yellow (Fig. 1).

3.2 Morphology

PVDF copolymer nanofibers were successfully coated by chitosan/Ag(NP)/nanosilica composite solution by dip coating method. Hydrophilic modifiers exist on PVDF membrane surface via physical interaction but not covalent bonding [6]. The morphology of modified and unmodified PVDF copolymer nanofiber were showed at Fig. 2. The glossy thin layer reveals on the surface of nanofiber (b–d) compared with unmodified nanofiber (a).

Based on SEM image, Fig. 3, coated PVDF copolymer nanofiber using dip coating method results in increasing diameter of the nanofiber. The unmodified PVDF copolymer nanofiber has a diameter average of 427.00 nm and after coating with chitosan/Ag(NP)/nanosilica (0.20%) composite is 443.50 nm.

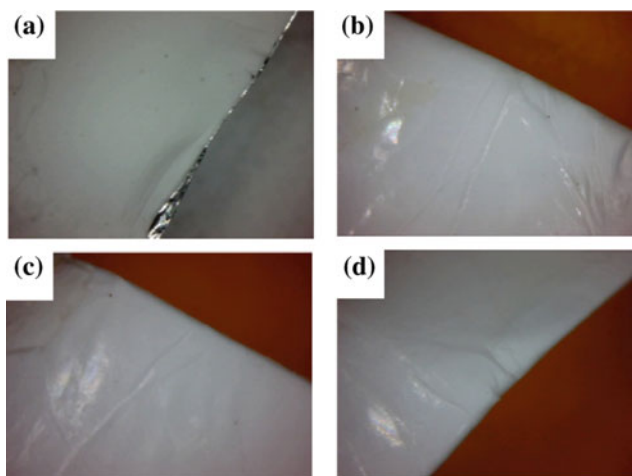


Fig. 2 Morphology of modification of **a** PVDF copolymer nanofiber, coated by **b** chitosan/Ag(NP), **c** chitosan/Ag(NP)/nanosilica (0.05%), and **d** chitosan/Ag(NP)/nanosilica (0.20%)

3.3 Spectrum Analysis of ATR-FTIR

IR spectrum of unmodified and modified PVDF copolymer nanofibers were showed at Fig. 4. PVDF copolymer spectrum has band at 1411.89 cm^{-1} due to the CH_2 stretching, 1330.88 and 1089.78 cm^{-1} show CF_2 symmetry stretching [15, 16], 839.03 due to the CH_2 [4, 17], and 524.64 cm^{-1} shows CF_2 bending [17]. The presence of Ag(NP) and nanosilica in chitosan layer gives effect on shifting OH band to higher wavenumber which was caused by the interaction between chitosan with Ag(NP) [13] and nanosilica.

In chitosan spectrum, 1600.92 cm^{-1} shows NH bending of NH_2 and 1462.04 cm^{-1} shows CH bending of CH_2OH . Post dip coating of PVDF copolymer nanofiber with chitosan/Ag (NP) causes increasing intensity sharply and widely at 1560.41 cm^{-1} which shows NH bending of NH_2 and 1411.89 cm^{-1} shows $-\text{CH}_2$. The increasing was caused by hydrogen bonding between $-\text{CF}_2$ with N–H and C–H of chitosan. The shifting 1560.41 cm^{-1} of chitosan/Ag (NP)/PVDF copolymer nanofiber composite into 1600.92 cm^{-1} of chitosan/Ag(NP)/nanosilica (0.20%)/PVDF copolymer nanofiber composite show the presence of interaction between $-\text{NH}_2$ of chitosan with OH of nanosilica. In PVDF copolymer nanofiber coated by chitosan/Ag(NP)/nanosilica (0.20%) composite form sharp intensity at 2351.23 cm^{-1} which shows vibration of Si–C stretching and intensity at 1091.71 , 1037.70 , 995.27 , 954.76 , and 921.97 cm^{-1} show Si–O stretching.

3.4 Water Contact Angle

Surface modification of PVDF copolymer nanofiber using chitosan which has hydrophilicity properties [8] gives effect on decreasing hydrophobicity of PVDF copolymer nanofiber. Unmodified PVDF copolymer nanofiber has water contact angle 108° and after coated by chitosan/Ag(NP), the water contact angle decreases into 55° . The contact angle can be controlled by the addition of nanosilica 0.05% and 0.20% (w/v) into 60° and 77° , respectively. Amount of nanosilica affects the amount of aggregate which is deposited on surface nanofiber. It gives effect on decreasing free surface energy and increasing water contact angle [5, 18] (Fig. 5).

When the water droplet hits the surface nanofiber, a spread occurs gradually and is characterized by an increase in the contact diameter coupled with significant deformation of the free surface [19]. The correlation of water contact angle towards time was shown at Fig. 6. The presence of nanosilica restrains droplet to spread slower than nanofibers that coated by chitosan/Ag(NP) and faster than unmodified nanofiber.

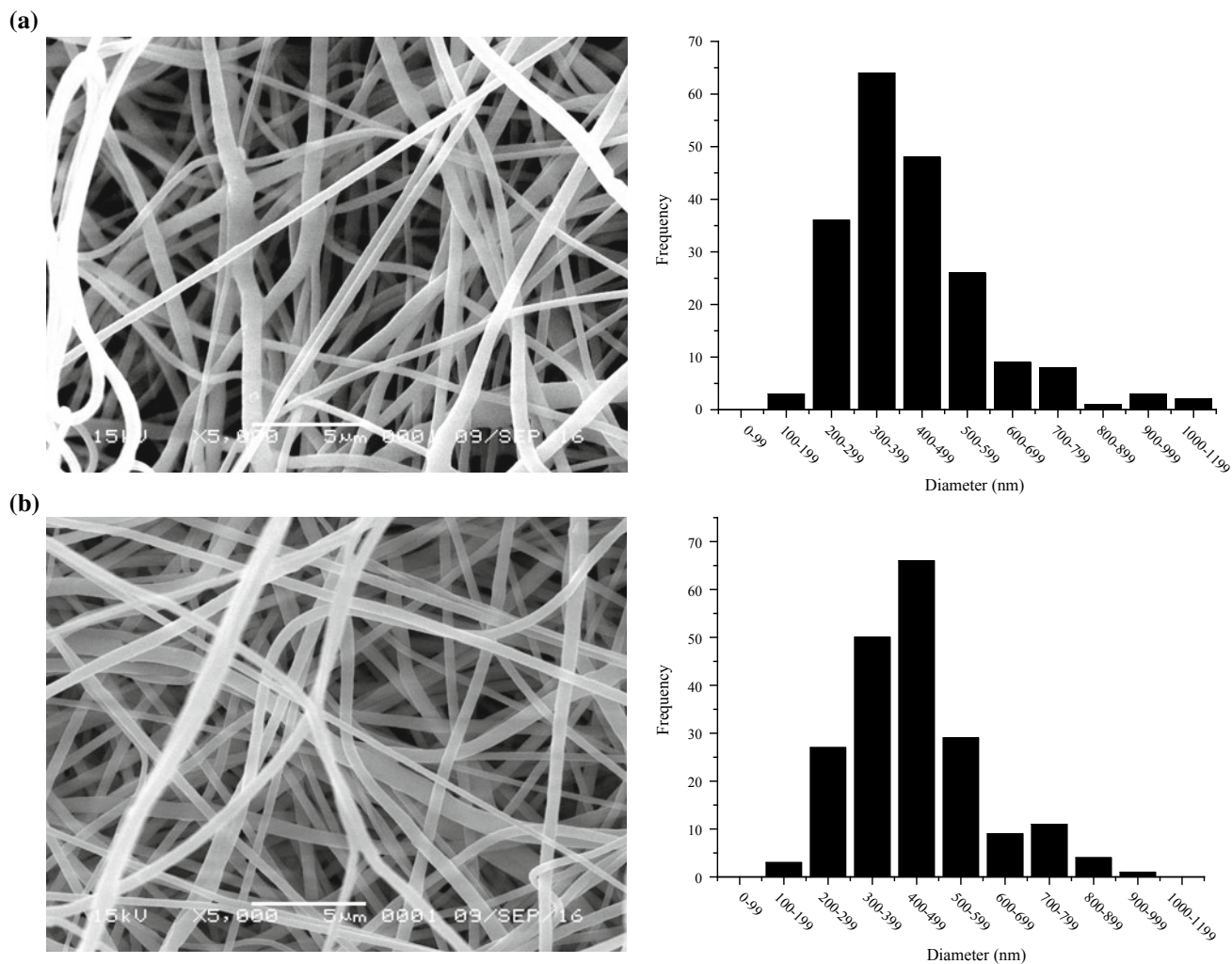


Fig. 3 SEM Image of PVDF copolymer nanofiber and distribution of diameter **a** before and **b** after dip coating with chitosan/Ag(NP)/nanosilica (0.20%)

4 Conclusions

PVDF copolymer nanofiber was successfully coated by chitosan/Ag(NP)/nanosilica composite solution. Their presence can control surface properties of PVDF copolymer nanofiber through water contact angle analysis and the spreading time. The water contact angle of PVDF copolymer nanofiber is 108° which showed hydrophobicity of nanofiber and de-creases into 60° and 77° after coated by chitosan/Ag

(NP)/nanosilica with the concentration of nanosilica 0.05 and 0.20% (w/v), respectively. The result is also confirmed by IR spectrum before and after dip coating. Some bands which identify the presence of chitosan, SiO_2 and the shifting band caused by an interaction between chitosan and Ag^0 revealed in the IR spectrum. In addition, diameter average of coated nanofiber is wider at 427.00 nm for chitosan/Ag(NP)/nanosilica (0.20%)/PVDF copolymer nanofiber compared with un-modified PVDF copolymer nanofiber at 443.50 nm.

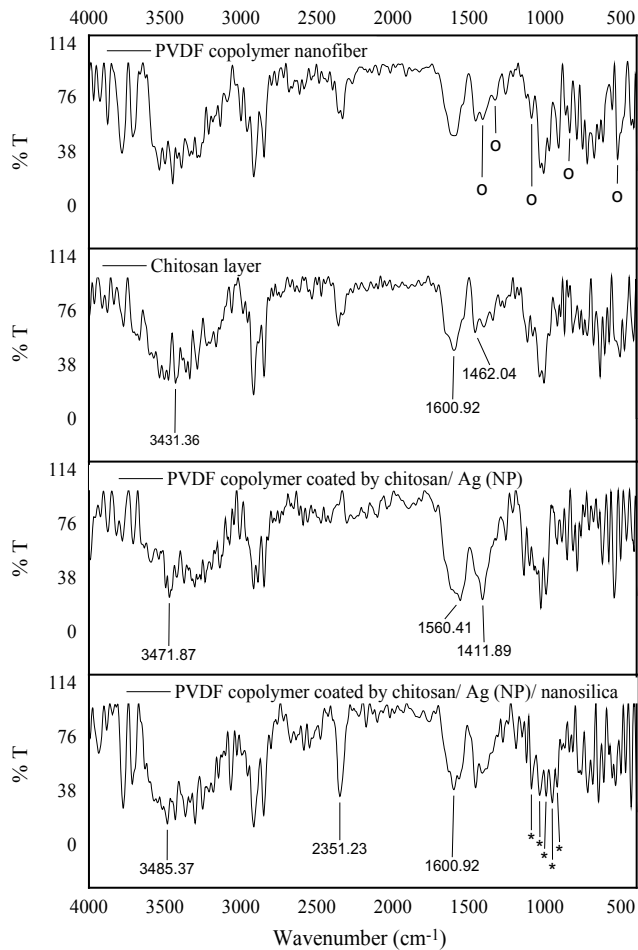


Fig. 4 IR spectrum of PVDF copolymer nanofiber before and after dip coating with chitosan/Ag(NP)/nanosilica (0.20%) ($^{\circ}$ typical band of PVDF copolymer and * typical band of Si-O)

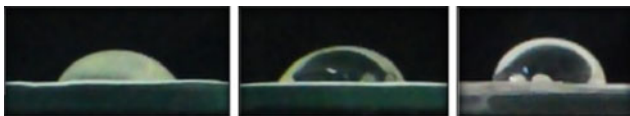


Fig. 5 Water contact angle of PVDF copolymer nanofiber coated by **a** chitosan/Ag(NP), **b** chitosan/Ag(NP)/nanosilica (0.05%), **c** chitosan/Ag(NP)/nanosilica (0.20%)

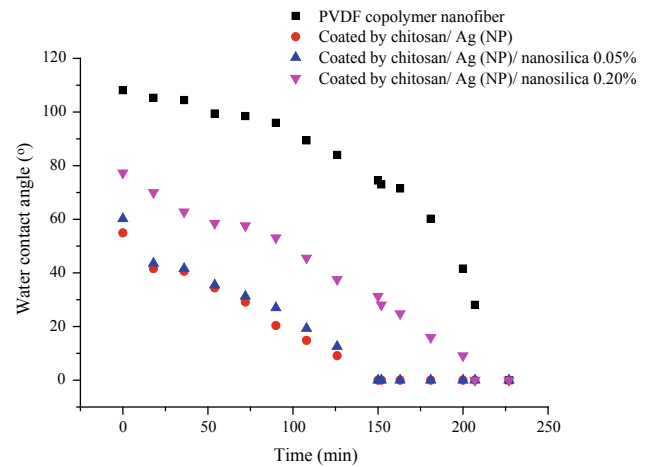


Fig. 6 Correlation graphic of water contact angle towards time of chitosan/Ag(NP)/nanosilica/PVDF copolymer nanofiber

Acknowledgements The author (MN) thank to Indonesian Institute of Sciences and Ministry of Research, Technology and Higher Education for Research Funding.

Conflict of Interest We declare there is no conflict of interest in this research.

References

1. Yuan, J., Geng, J., Xing, Z., Shen, J., Kang, I.K., Byun, H.: Electrospinning of antibacterial poly(vinylidene fluoride) nanofibers containing silver nanoparticles. *J. Appl. Polym. Sci.* **116**, 668–672 (2010)
2. Sethupathy, M., Sethuraman, V., Manisankar, P.: Preparation of PVDF/SiO₂ composite nanofiber membrane using electrospinning for polymer electrolyte analysis. *Soft Nanosci. Lett.* **3**, 37–43 (2013)
3. Fontananova, E., Bahattab, M.A., Aljlil, S.A., Alowairdy, M., Rinaldi, G., Vuono, D., Nagy, J.B., Drioli, E., Profio, G.: From hydrophobic to hydrophilic polyvinylidene fluoride (PVDF) membranes by gaining new insights into material's properties. *RSC* (2015). <https://doi.org/10.1039/C5RA08388E>
4. Sheikh, F.A., Zargar, M.A., Tamboli, A.H., Kim, H.: A super hydrophilic modification of Poly(vinylidene fluoride) (PVDF) nanofibers: By in situ hydrothermal approach. *Appl. Surf. Sci.* **365**, 417–425 (2016)

5. Peng, L., Lei, W., Yu, P., Luo, Y.: Polyvinylidene fluoride (PVDF)/hydrophobic nano-silica (H-SiO₂) coated superhydrophobic porous materials for water/oil separation. *RSC Adv.* **6**, 10365–10371 (2016)
6. Kang, G.D., Cao, Y.M.: Application and modification of poly (vinylidene fluoride) (PVDF) membranes—a review. *J. Membr. Sci.* **463**, 145–165 (2014)
7. Obaid, M., Ghouri, Z.K., Fadali, O.A., Khalil, K.A., Almajid, A. A., Barakat, N.A.M.: Amorphous SiO₂ NP-incorporated poly (vinylidene fluoride) electrospun nanofiber membrane for high flux forward osmosis desalination. *Appl. Mater. Interfaces* (2015). <https://doi.org/10.1021/acsami.5b09945>
8. Boributh, S., Chanachai, A., Jiratananon, R.: Modification of PVDF membrane by chitosan solution for reducing protein fouling. *J. Membr. Sci.* **342**, 97–104 (2009)
9. Chanachai, A., Meksup, K., Jiratananon, R.: Coating of hydrophobic hollow fiber PVDF membrane with chitosan for protection against wetting and flavor loss in osmotic distillation process. *Sep. Purif. Technol.* **72**, 217–224 (2010)
10. Rhazi, M., Desbrieres, A., Tolaimate, A., Alagui, A., Vottero, P.: Investigation of different natural sources of chitin: influence of the source and deacetylation process on the physicochemical characteristics of chitosan. *Polym. Int.* **49**, 337–344 (2000)
11. Prabhu, S., Poulouse, E.K.: Silver nanoparticles: mechanism of antimicrobial action, synthesis, medical applications, and toxicity effects. *Int. Nano Lett.* **2**, 1–10 (2012)
12. Abdelgawad, A.M., Hudson, S.M., Rojas, O.J.: Antimicrobial wound dressing nanofiber mats from multicomponent (chitosan/silver-NPs/polyvinyl alcohol) systems. *Carbohydr. Polym.* **100**, 166–178 (2014)
13. Govindan, S., Nivethan, E.A.K., Saravan, R., Narayanan, V., Stephen, A.: Synthesis and characterization of chitosan-silver nanocomposite. *Appl. Nanosci.* (2012). <https://doi.org/10.1007/s13204-012-0109-5>
14. Gorji, B., Ghasri, M.R.A., Fazaeli, R., Niksirat, N.: Synthesis and characterizations of silica nanoparticles by a new sol-gel method. *J. Appl. Chem. Res.* **6**, 22–26 (2012)
15. Attaollahi, N., Ahmad, A., Hamzah, H., Rahman, M.Y.A., Mohamed, N.S.: Preparation and characterization of PVDF-HFP/MG49 based polymer blend electrolyte. *Int. J. Electrochem. Sci.* **7**, 6693–6703 (2012)
16. Sivakumar, P., Gunasekaran, M., Sasikumar, M., Jagadeesan, A.: PVDF-HFP based porous polymer electrolyte for lithium battery applications. *Int. J. Sci. Res.*, 22–25 (2013). ISSN (Online): 2319-7064
17. Nasir, M., Matsumoto, H., Danno, T., Minagawa, M., Irisawa, T., Shioya, M., Tanioka, A.: Control of diameter, morphology, and structure of PVDF nanofiber fabricated by electrospray deposition. *J. Polym. Sci., Part B: Polym. Phys.* **44**, 779–786 (2006)
18. Conradi, M., Intihar, G., Zorko, M.: Mechanical and wetting properties of nanosilica/epoxy-coated stainless steel. *Mater. Technol.* **49**, 613–618 (2015)
19. Vadillo, D.C., Soucemarianadin, A., Delattre, C., Roux, D.C.D.: Dynamic contact angle effects onto the maximum drop impact spreading on solid surfaces. *Phys. Fluids* **21**, 122002 1–122002 8 (2009)



Recent Progress in GaN-Based Devices for Terahertz Technology

V. P. Sirkeli, I. M. Tiginyanu, and H. L. Hartnagel

Abstract

This paper reviews the crystal growth, basic properties, and principle of operation of III-nitride based terahertz devices. We provide a brief history and current status of crystal growth of polar and non-polar GaN-based heterostructures and its properties. The role of spontaneous and piezoelectric polarization in polar III-nitride structures and its impact on performance of terahertz devices is discussed in detail. We show that GaN-based semiconductor compounds are promising materials for fabrication terahertz sources operating up to room temperature due to their unique properties such as large bandgap and conduction band offset (CBO) energy, high LO-phonon energy, and high resistant to the high breakdown electric field. Moreover, it was established that the GaN-based terahertz sources can cover the spectral region of 5–12 THz, which is very important for THz imaging and detection of explosive materials, and which could be not covered by conventional GaAs-based terahertz devices. In terms of the reported significant progress in growth of non-polar m-plane GaN-based heterostructures and devices with low density defects, it is open a wide perspective towards design and fabrication of non-polar m-plane GaN-based high power terahertz sources with capabilities of operation at room temperature.

Keywords

GaN • Terahertz • Quantum-cascade lasers • Tunneling diodes • Gunn diodes

1 Introduction

Terahertz (THz) waves refer to the electromagnetic radiation in the frequency range from 0.1 to 10 THz, which corresponds to the wavelengths from 3 mm to 30 μm , respectively [1]. This spectral region, called also as “T-gap”, is important for many practical applications, including THz imaging, chemical and biological sensing, high-speed telecommunication, heterodyne receiver for astronomy, security and other applications [1, 2]. Moreover, THz spectral region covers intermolecular vibrations of biological molecules and low frequency crystalline lattice vibrations of chemical materials, including drugs, explosive and related compounds (ERCs) such as TNT, RDX, HMX, PETN and other explosive materials [2, 3]. Transmitted and reflectance THz spectra of these materials contain specific THz absorption peaks (finger-prints), which characterize vibration modes of these materials and provide information which could be used for identification of the ERC, and which is not available in the other regions of the electromagnetic spectrum. Leahy-Hoppa et al. [3] are investigated the THz absorption spectra of many explosives and found that the THz absorption peaks (finger-prints) of these explosives are located in the terahertz frequency range of 0.8–6.0 THz. For security applications it is very important to find a reliable, fast, contact-less, and non-destructive method to detect explosive materials such as TNT, RDX, HMX, and PETN.

THz waves have low photon energies (~ 4.1 meV for 1 THz), which is about 1 million times weaker than the energy of X-ray photons, and do neither ignite any explosive materials at typical power levels nor cause any harmful ionization in biological tissues [4]. Thus, THz waves can be considered as a safe method for investigation of biological

V. P. Sirkeli (✉) · H. L. Hartnagel
Institute for Microwave Engineering and Photonics, Technische
Universität Darmstadt, Darmstadt, Germany
e-mail: sirkeli@imp.tu-darmstadt.de

V. P. Sirkeli
Department of Applied Physics and Computer Science, Moldova
State University, A. Mateevici, 60, MD-2009 Chisinau, Moldova

I. M. Tiginyanu
National Center for Materials Study and Testing, Technical
University of Moldova, Chisinau, Moldova

materials and which can be used in medicine for THz imaging and for other applications.

2 Growth, Crystal Structure and Basic Properties of III-Nitrides

THz III-Nitride materials, which include binary compounds InN, GaN, AlN and their alloys, have been investigated last several decades and are among the most important semiconductor materials for photonics, opto-electronics, high-power and high frequency electronics. These materials have a direct bandgap and their bandgap energy covers broad spectral range from the near infrared to deep ultraviolet: $E_g = 0.7$ eV for InN, $E_g = 3.4$ eV for GaN, and $E_g = 6.2$ eV for AlN [5–7]. III-nitride materials can be doped n- and p-types using Si(Ge) or Mg impurities [6–8], respectively, and can be also grown heteroepitaxially on different foreign substrates, including sapphire, SiC and Si. Contrary to other III-V compounds like InP and GaAs, which have the zinc blende structure, III-nitride binary semiconductors have the wurtzite structure [9].

Wurtzite crystal structure consists of two hexagonal close packed lattices, displaced towards the direction perpendicular to the hexagonal base (c-direction) by $\pm 3c/8$, where c is the lattice parameter [9]. Also, the III-nitrides can be crystallized in the rock-salt [10] and meta-stable zinc blende crystal structures [11]. The wurtzite crystal structures lack of inversion symmetry along the c-direction, which is referred to as a crystallographic polarity. In GaN the c-direction is the polar direction. GaN films can be grown along c-direction in two different polarities: “Ga-polar” ([0001] direction) and “N-polar” ([0001 $\bar{1}$] direction). The polarity is the bulk property of GaN, which results in different chemical and physical properties.

For the first time GaN was synthesized by Juza and Hahn in 1938 [12]. In 1969 Marushka and Tietjen [13] grown large area thin film GaN on sapphire substrates using the hydride vapor phase epitaxy (HVPE). One of major issues of III-nitride semiconductor materials is the lack of the substrates for homoepitaxial growth of thin films. The most GaN-based devices are grown heteroepitaxially on different foreign substrates including sapphire, silicon carbide and silicon. Due to the lattice mismatch between foreign substrates and III-nitrides a nucleation buffer layer is needed. To overcome this issue and reduce the dislocations density in the grown films several research groups suggested to use the nitridation of the sapphire, or to use the AlN and GaN low temperature buffer layers [14] grown by the molecular beam epitaxy (MBE) or the metal organic chemical vapor deposition (MOCVD) methods.

3 GaN-Based THz Quantum Cascade Lasers

Among different types of terahertz sources, the quantum cascade lasers (QCLs) at THz frequencies offer technology platform for the high power generation of THz radiation at room temperature. The QCL was originally proposed by Kazarinov and Sirius in 1971 [15] and was first demonstrated by Faist et al. [16] in the mid-infrared region (70 THz) in 1994 and Köhler et al. [17] in the terahertz region (4.4 THz) in 2002. In general, QCL makes use of electron transitions between subbands formed by multiple strongly coupled quantum wells. By adjusting the widths of the quantum wells/barriers, the emission frequency and performance of the laser can be tailored, adding additional flexibility in the laser design. The QCL operates on optical transitions not between different electronic bands but on intersubband (ISB) transitions of a semiconductor structure. For practical applications of any lasers, one of the key desired characteristics is room-temperature operation. Mid-IR QCLs with CW room-temperature operations have been demonstrated in spectral region from 4.5 to 10 μm [18]. However, THz QCLs have not yet satisfied this requirement. The cryogenic cooling is required, which is the main obstacle towards making THz QCL a compact radiation source. The most successful material system for THz QCL is GaAs/AlGaAs heterostructure grown on GaAs substrate. The present GaAs/AlGaAs-based THz QCLs have covered the spectral range 1–5 THz, and maximum operating temperature is about 200 K at a radiation frequency of 3.2 THz [19]. With regard to output power, a single state-of-art THz QCL could provide 1 W peak power in pulsed mode [20] and over 130 mW in continuous wave (CW) [21] at 10 K heat-sink temperature. Therefore, the main challenge in this field is to achieve room-temperature THz QCLs, which can enable practical applications of THz technology.

The relatively small LO-phonon energy is an obvious obstacle for further temperature improvement. Among II–VI and III–V semiconductor compounds, GaN/AlGaN seems to be a promising candidate for room temperature THz QCL thanks to its much larger LO-phonon energy (92 meV) [5]. The standard III–V semiconductors like GaAs cannot be operated in the 5–12 THz frequency range because of their Reststrahlen band, i.e. the spectral region where the material is completely opaque due to the absorption by optical phonons. This is not the case for GaN because of the three-fold larger energy of the optical phonons. Thus, GaN offers prospects for THz quantum cascade devices, which can operate in a much broader spectral range, in particular in the 5–12 THz, which cannot be covered by other III–V semiconductors.

Bellotti et al. [5] theoretically established that the GaN/AlGaIn-based THz QCLs could operate up to room temperature. The design of nitride-based THz QCL devices operating at room temperature is more complex than conventional GaAs/AlGaAs devices due to the spontaneous and piezoelectric polarizations in III-Nitride materials and the lattice mismatch. To overcome this issue, Shishehchi et al. [22] suggested to use of III-Nitride lattice-matched structures for THz QCLs. They reported on numerical simulation study of lattice-matched GaN/InAlGaIn-based THz QCLs using an ensemble Monte Carlo method. The QCL structure consists of GaN quantum well and $\text{Al}_{0.318}\text{In}_{0.0707}\text{Ga}_{0.6113}\text{N}$ barriers. This GaN/ $\text{Al}_{0.318}\text{In}_{0.0707}\text{Ga}_{0.6113}\text{N}$ structure is lattice matched compared to the GaN/ $\text{Al}_{0.15}\text{Ga}_{0.85}\text{N}$ structures from Ref. [5] that is not lattice matched. The authors [22] calculated the fractional population inversion versus temperature for four different QCL structures GaN/AlGaIn, GaN/ $\text{Al}_{0.318}\text{In}_{0.0707}\text{Ga}_{0.6113}$, GaAs/AlGaAs and ZnO/MgZnO and they found that the lattice-matched GaN/InAlGaIn THz QCL structure has the highest population inversion. It was also established that the degradation of population inversion versus temperature in the III-nitride THz QCLs is much less compared to the GaAs/AlGaAs and ZnO/MgZnO QCL structures.

Terashima et al. [23] reported on successful fabrication of GaN-based THz QCLs employing two-well design scheme with a pure 3-level laser system. They used a radio-frequency molecular beam epitaxy (RF-MBE) technique to grow GaN/AlGaIn THz QCL devices. The contact layers were grown on a high-quality c-plane AlGaIn/AlN templates. To achieve the population inversion condition, the 6 nm thick GaN wells were doped by Si with concentration of $5 \times 10^{17} \text{ cm}^{-3}$. The frequency spectrum of this GaN-based QCL in pulse mode (with 200 ns pulse width) was recorded at 5.6 K and the peak frequency of 5.47 THz was observed in the laser spectrum of this device.

4 GaN-Based THz Resonant Tunneling Diodes

In the last decade, significant progress has been made in the design and fabrication of THz RTDs based on AlGaAs/GaAs, InGaAs/AlAs, InGaAs/InAs and AlGaIn/GaN material systems. In 2012 Feiginov et al. [24] reported on experimental fabrication of RTDs based on InGaAs/InAs/InGaAs with heavily doped collectors where they achieved a maximum operating frequency of 1.1 THz. In 2016 Maekawa et al. [25] reported on the achievement of a large increase in oscillation frequency up to 1.92 THz in

InGaAs-based RTDs by reducing the conduction loss. A maximum output power of 0.61 mW at 620 GHz, 20–30 μW at 1 THz, and 0.4 μW at 1.92 THz were obtained for InGaAs-based RTD structures with slot antenna and two-array configuration and reported in Refs. [25]. To enhance frequency performance of THz RTDs several approaches have been suggested, including the design schemes with step-graded emitter [25], with variable barrier heights and RTDs with double-well triple barriers [26, 27]. Thus, increasing the output power of RTD devices at THz frequencies and increasing the operation frequency are crucial tasks. To solve these, GaN-based compounds are explored as materials for high-power terahertz emitter devices due to the higher CBO (1.57 eV for GaN/AlN vs. 0.72 for GaAs/AlAs) [5].

In the last two decades resonant tunneling transport has been extensively studied in the GaN/AlGaIn double-barrier structures [28, 29]. In the first reports [28] it was found that the current-voltage characteristics of GaN-based RTD structures have a strong hysteresis and it rapidly degrade upon repeated voltage scans. This behavior of current-voltage dependences of the GaN-based RTDs is generally attributed to filling of traps related to threading dislocations. In later papers [29] it was reported on stable and repeatable NDR feature in the current-voltage dependence of GaN-based RTD, which was grown under conditions minimizing the formation of strain-induced defects. Also, the sequential tunneling transport in a simple GaN/AlGaIn quantum cascade structures has been investigated, and it was found that current-voltage characteristics of such structures have a highly nonlinear behavior [30]. Moreover, in paper [31] it was found that experimental turn-on voltages are well reproduced by simulation results. Also authors [32] reported on the observation of electroluminescence peak at near 10 THz, which is related to the photon-assisted tunneling process in the active QWs. Terashima et al. [31] reported on more significantly stronger emission at 1.4 THz, which was observed in the GaN-based quantum cascade structures and attributed to the intersubband (ISB) transitions in QCL structures. In recent paper, Encomendero et al. [32] reported on the room-temperature generation of microwave oscillations from GaN/AlN RTDs, which exhibit record-high current densities up to 220 kA/cm^2 with an output power of 3 μW . The RTD devices were grown by molecular beam epitaxy (MBE) method on freestanding GaN substrates with nominal dislocation densities $< 5 \times 10^4 \text{ cm}^{-2}$. The active of the RTDs consists of two 2 nm-thick AlN barriers and a 1.75 nm-wide GaN quantum well, which confines the resonant states. The authors found that the fundamental

oscillation frequency of such RTDs is ~ 0.94 GHz with output power of $3 \mu\text{W}$, which is limited by the RC of the external biasing circuit. Using the small-signal equivalent circuit model of RTD devices [26], the authors estimated a maximum oscillation frequency $f_{\text{max}} \sim 0.2$ THz. This value of the maximum oscillation frequency is within the same order of magnitude as the values of f_{max} obtained from GaAs/AIAs and InGaAs/AIAs RTD devices [24, 25]. Moreover, reducing the series resistance with improved ohmic contacts and by further optimization of the doping level and collector space width, the capacitance of the GaN-based RTD devices could be significantly reduced [33], and thus achieving the oscillation frequency with $f_{\text{max}} \sim 1$ THz.

5 GaN-Based THz Gunn Diodes

Gunn diodes represent another type of semiconductor structures, which are conventionally used for generation of high-frequency microwave signals due to the presence of negative differential resistance (NDR) feature in current-voltage characteristics of such devices. GaAs and InP are conventional semiconductor materials used for fabrication of Gunn diodes. GaAs has an energy-relaxation time of 10 ps and exhibits sharp suppression in output power of microwave emission with frequencies higher than 100 GHz. In contrast to GaAs, GaN has a shorter energy relaxation time among III-V semiconductors and exhibits the NDR effect in the threshold fields above 80 kV/cm [34]. GaN-based Gunn diodes have a higher electron velocity and reduced time constants compared to conventional GaAs-based Gunn diodes. Therefore, GaN-based Gunn diodes can generate microwaves with THz frequencies.

The first GaN-based Gunn diodes were fabricated by researchers from the University of Michigan in 2000 [35]. They used a $3 \mu\text{m}$ thick GaN active layer with an electron concentration of $1 \times 10^{17} \text{ cm}^{-3}$ sandwiched between anode and cathode, which have been made of $0.1 \mu\text{m}$ thick GaN layer n-type doped with concentration of $1 \times 10^{19} \text{ cm}^{-3}$. The diameter of fabricated Gunn diode was $50 \mu\text{m}$ and the output power of GaN-based Gunn diodes was up to four times higher than that of GaAs-based devices. The NDR relaxation frequency was estimated to be ~ 1 THz for GaN-based devices for inter-valley transfer-based NDR, and ~ 4 THz for the inflection-based NDR devices [35]. These values of microwaves frequencies are about one order of magnitude higher than that for GaAs-based NDR devices ($f_{\text{NDR}} \sim 100$ GHz for GaAs-based NDR devices) [35].

In 2016 Wang et al. [36] proposed a GaN-based planar Gunn diode. On the interface of GaN/AlGaIn heterostructures a two-dimensional degenerated (2DEG) electron gas is formed with high electron concentration, which is beneficial

for the fast formation of the dipole domain layer. This results in enhancing the microwave frequency output power.

6 Conclusions

In this paper, we have provided a comprehensive review of the recent progress and current status of terahertz sources based on III-nitride semiconductor compounds. It was established that GaN-based semiconductor compounds are promising materials for the fabrication of terahertz sources operating up to room temperature due to their unique properties such as large bandgap and CBO energies, high LO-phonon energy, and high breakdown electric field. Moreover, the GaN-based terahertz sources can cover the spectral region of 5–12 THz, which is very important for THz imaging and detection of explosive materials, and which could be not covered by conventional GaAs-based terahertz devices. This paper includes a review of theoretical and experimental study of GaN-based THz QCLs, RTDs and Gunn diodes. Recent papers report on significant progress in growth of non-polar m-plane GaN-based heterostructures and devices with low density of defects and solving one of the main issues of polar c-plane grown nitride materials—the presence of spontaneous and piezoelectric polarizations in such structures. Thus, a wide perspective is open to design and fabricate non-polar m-plane GaN-based high power terahertz sources, and to achieve room temperature operation.

Acknowledgements V.P.S. gratefully acknowledges financial support from the Alexander von Humboldt Foundation. This work was partly supported under RM institutional project No. 15.817.02.34A.

Conflict of Interest The authors declare that they have no conflict of interest.

References

1. Williams, B.S.: *Nat. Photonics* **1**, 517–525 (2007)
2. Sirkeli, V.P., et al.: *Sens. Lett.* **16**, 1–7 (2018). <https://doi.org/10.1166/sl.2018.3919>
3. Leahy-Hoppa, M.R., et al.: *Chem. Phys. Lett.* **434**, 227–230 (2007)
4. Scarfi, M.R., et al.: *J. Biol. Phys.* **29**, 171–177 (2003)
5. Bellotti, E., et al.: *J. Appl. Phys.* **105**, 113103 (2009)
6. Sirkeli, V.P., et al.: *J. Nanoelectron Optoelectron* **9**, 811–818 (2014). <https://doi.org/10.1166/jno.2014.1687>
7. Sirkeli, V.P., et al.: *Semicond. Sci. Technol.* **30**, 065005 (2015). <https://doi.org/10.1088/0268-1242/30/6/065005>
8. Sirkeli, V.P., et al.: *J. Phys. D: Appl. Phys.* **50**, 035108 (2017). <https://doi.org/10.1088/1361-6463/50/3/035108%23>
9. Morkoc, H.: *Gallium Nitride (GaN) I. Semiconductors and Semimetals*. In: Pankove, J.L., Moustakas, T.D., vol. 50, ch 8. Academic, San Diego (1998)
10. Xia, Q., et al.: *J. Appl. Phys.* **73**, 8198 (1993)
11. Lei, T., et al.: *J. Appl. Phys.* **71**, 4933 (1992)

12. Juza, R., et al.: *Anorg. Allgem Chem.* **234**, 282 (1938)
13. Maruska, H.P., Tietjen, J.J.: *Appl. Phys. Lett.* **15**, 367 (1969)
14. Mikroulis, S., et al.: *Appl. Phys. Lett.* **80**, 2886 (2002)
15. Kazarinov, R.F., Suris, R.A.: *Fiz Tekh Poluprovod* **5**, 797–800 (1971)
16. Faist, J., et al.: *Science* **264**, 553–556 (1994)
17. Köhler, R., et al.: *Nature* **417**, 156–159 (2002)
18. Yao, Y., et al.: *Nat. Photon* **6**, 432–439 (2012)
19. Fatholoulumi, S., et al.: *Opt. Express* **20**, 3331–3339 (2012)
20. Li, L., et al.: *Electron. Lett.* **50**, 309–311 (2014)
21. Williams, B.S.: *Electron. Lett.* **42**, 89–91 (2006)
22. Shishehchi, S., et al.: *Proc. SPIE* **8980**, 89800T (2014)
23. Terashima, W., et al.: *Proc. SPIE* **9483**, 948304 (2015)
24. Feiginov, M., et al.: *Proc. SPIE* **8496**, 84960A (2012)
25. Maekawa, T., et al.: *Appl. Phys. Express* **9**, 024101 (2016)
26. Sirkeli, V.P., et al.: *IEEE Trans. Electron. Devices* **64**, 3482–3488 (2017). <https://doi.org/10.1109/TED.2017.2718541%23>
27. Sirkeli, V.P., et al.: *Phys. Status Solidi RRL* **11**, 1600423 (2017). <https://doi.org/10.1002/pssr.201600423>
28. Kikuchi, A., et al.: *Appl. Phys. Lett.* **81**, 1729–1731 (2002)
29. Li, D., et al.: *Appl. Phys. Lett.* **100**, 252105 (2012)
30. Sudradjat, F., et al.: *J. Appl. Phys.* **108**, 103704 (2010)
31. Terashima, W., Hirayama, H.: *Phys. Status Solidi C* **8**, 2302 (2011)
32. Encomendero, J., et al.: *Appl. Phys. Lett.* **112**, 103101 (2018)
33. Kanaya, H., et al.: *J. Infrared Millim Terahertz Waves* **35**, 425–431 (2014)
34. Krishnamurthy, S., et al.: *Appl. Phys. Lett.* **71**, 1999–2001 (1997)
35. Alekseev, E., et al.: *IEEE MTT-S Int microwave symp digest (Cat. No. 00CH37017)*. **3**, 1905–1908 (2000)
36. Wang, Y., et al.: *Phys. Status Solidi C* **13**, 382–385 (2016)

Silanized Citric Acid Capped Magnetic Nanoparticles and Influence on Chlorophylls

L. Popescu, L. Sacarescu, M. Grigoras, C. Morosanu, D. Creanga, D. Dorohoi, and C. Stan

Abstract

Two step synthesis of cobalt ferrite nanoparticles capped with citric acid and coated with silica was carried out. Citric acid coated magnetic grains were synthesized by chemical co-precipitation starting from iron and cobalt salt solutions in stoichiometric ratio. Adapted sol-gel method was applied to yield the silica/citrate/cobalt ferrite nanocomposites. Microstructural and magnetic properties were evidenced by TEM, XRD and VSM. Nanotoxicity tests were done on maize plants during their early ontogenetic stages. Quantum mechanical characterization was performed with specialized software to evidence chlorophylls molecular properties for discussing their diminished contents in the green tissues of young seedlings supplied with magnetic nanocomposites.

Keywords

$\text{Co}_{0.5}\text{Fe}_{2.5}\text{O}_4$ • Co-precipitation • Sol-gel • Nanotoxicity • Photosynthetic pigments

1 Introduction

Magnetic nanoparticles (MNPs) and nanocomposites for life science applications [1–3] are widely studied due to specific properties given by high surface to volume ratio, allowing

L. Popescu · C. Morosanu · D. Creanga (✉) · D. Dorohoi
Physics Faculty, Alexandru Ioan Cuza University,
11, Blvd. Carol I, Iasi, Romania
e-mail: dorina.emilia.creanga@gmail.com

L. Sacarescu
P. Poni Institute of Macromolecular Chemistry, Iasi, Romania

M. Grigoras
National Institute of Research, Development for Technical
Physics, Iasi, Romania

C. Stan
Faculty of Applied Sciences, University Politehnica of Bucharest,
Bucharest, Romania

large interface with surrounding media. Especially cobalt ferrite MNPs are used in experimental medicine for tumor hyperthermia due both to their superparamagnetic and ferromagnetic features [4, 5]. Various synthesis methods were developed, the chemical co-precipitation still remaining a convenient one by versatility, low toxicity and low cost yielding. Since after medical uses (drug delivery, contrast agent in magnetic resonance imaging and local radiotherapy) the MNPs are eliminated through body physiological pathways and reach the biosphere components, their nanotoxicity issues are also analyzed [6]. We present $\text{Co}_{0.5}\text{Fe}_{2.5}\text{O}_4$ MNPs capped with citrate and silica coated, tested for their nanotoxicity on the seedlings of maize.

2 Experimental

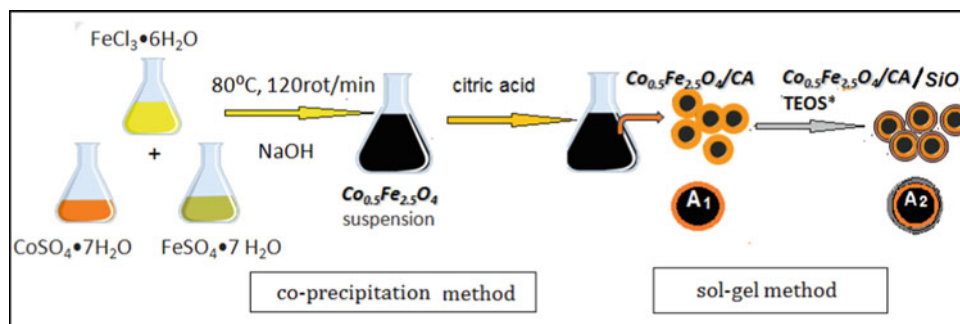
A. Two step synthesis protocol

The first synthesis step: in the first step we used iron and cobalt salts from Sigma: $\text{FeCl}_3 \times 7\text{H}_2\text{O}$, $\text{CoSO}_4 \times 4\text{H}_2\text{O}$ and $\text{FeSO}_4 \times 7\text{H}_2\text{O}$ without additional purification and sodium hydroxide, NaOH and citric acid ($\text{C}_6\text{H}_8\text{O}_7$). To prepare metal salt solutions, in their stoichiometry, we used deionized water (18.2 M Ω , Barnstead UltraPure). According to modified Massart's method [7], all solutions (Table 1) were heated on electrical source under magnetic stirring; then their mixture was further stirred also at over 90 °C to homogenize before hot solution of sodium hydroxide (1.7 M) was poured drop by drop to trigger chemical reactions that resulted in cobalt ferrite particles ($\text{Co}_{0.5}\text{Fe}_{2.5}\text{O}_4$) precipitation.

The brownish black precipitate was washed with deionized water to remove all impurities. Over the wet filtrated powder, 1.7 g citric acid in 3.5 ml deionized water was added and let to interact for one hour under mechanical stirring on water bath (1200 rpm) at over 90 °C temperature. The extracted nanoparticles were further washed with deionized water to eliminate citric acid excess; this way the

Table 1 The reagents used for the synthesis of doped ferrite nanocores

Sample	x	FeCl ₃	CoSO ₄	FeSO ₄	NaOH
Fe ₃ O ₄	0	3.62 g, 134 mM	–	1.86 g, 67 mM	3.4 g, 1.7 M
Co _{0.5} Fe _{2.5} O ₄	0.5	3.62 g, 134 mM	0.94 g, 67 mM	0.93 g, 67 mM	3.4 g, 1.7 M

Fig. 1 Scheme of magnetic nanocomposite synthesis with chemical co-precipitation and sol-gel method

sample A1 was obtained as a stable nanoparticle suspension at pH of about 5 (Fig. 1).

The second step: TEOS (tetraorthosilicate, (Si(OC₂H₅)₄) from Merck and 1-propanol from Sigma were used to coat with amorphous silica the A1 MNPs. We applied sol-gel method [8, 9] by three-hour TEOS hydrolysis at room temperature. Nanocomposites separated by centrifugation (3500 rpm) were washed up to pH of about 6 with deionized water. The final waxy magnetic material was dried under vacuum for 6 h at 90 °C and moderately thermally treated at 165 °C for 3 h to complete [10] the formation of silica/citrate/cobalt ferrite nanocomposites A2 (Fig. 1).

Biological material was consistent with uniform genophond maize caryopses (from single mother plant); they were washed with 3% hydrogen peroxide and let to germinate in IncuCell room at 22.0 ± 0.1 °C on watered porous paper in adequate Petri dishes. After germination, daily supply with diluted A1 and respectively A2 suspension in aqueous suspensions (20, 40, 60, 80 and 100 µl/l) was carried out for almost two weeks.

B. Investigation methods

(i) Transmission Electron Microscope (TEM) model Hitachi High-Tech HT7700 was utilized to record images and measure physical diameter; (ii) X-ray Diffraction (XRD) analysis with Shimadzu LabX XRD-6000 diffractometer (Cu-K α radiation at $\lambda = 1.5406 \text{ \AA}$) was carried out in Bragg Brentano arrangement for checking crystalline structure of ferrophase; (iii) Magnetic properties analysis (with Vibrating Sample Magnetometry (VSM)) was performed using MicroMag model 2900/3900 at room temperature in order to evidence magnetization capacity of nanoparticles up to 2000 Oe and to estimate magnetic diameter of MNP; (iv) Shimadzu spectrophotometer type

Pharma Spec 1600, provided with 1 cm quartz cells was used to record UV-Vis electronic absorption spectra of photosynthetic pigments in acetone extract (85% acetone in deionized water) and the contents of chlorophyll A, chlorophyll B and total carotenes were estimated with quasi-empirical formula widely accepted in literature [10].

Quantum-mechanical simulation of chlorophylls optimized molecular structures and properties with HyperChem 8.0 (PM3-Parameter Method 3, based on parametrization by optimization of one-center electron repulsion integrals) was done as well as with Spartan14 (DFT-Density Functional Theory, with basic set B3-LYP/6-31G*).

Statistics. Each assay of photosynthetic pigments was repeated three times with different aliquots from maize seedling green tissue. Average values and standard deviation were used for graphical interpretation.

3 Results and Discussion

A. Characterization of A1 and A2 samples

Analysis of TEM recordings has evidenced mainly round but also irregular shape structures with nanometric size (Table 2). Mean diameter value of citrate/cobalt ferrite nanoparticles was around 10 nm while around 12 nm mean value was found for the silica coated nanocomposites (Table 1)—in accord with [11]; rare largest particles had 45 (for A1) and respectively 50 nm (for A2) (Fig. 2).

Good crystallinity was evidenced by XRD, in both samples, with all characteristic peaks of inverse spinel structure in total accord with JCPDS data (card number #022–1086) and with no noticeable differences between A1 and A2. Using Scherrer's formula the average crystallite size was estimated from highest intensity peak, (311), resulting in about 8 nm and respectively 10 nm values (Table 1).

Table 2 Microstructural and magnetic properties

Sample	D_{TEM} (nm)	D_{311} (nm)	M_s (emu/g)
A1	10.4	8.3	65.0
A2	12.3	9.8	42.3

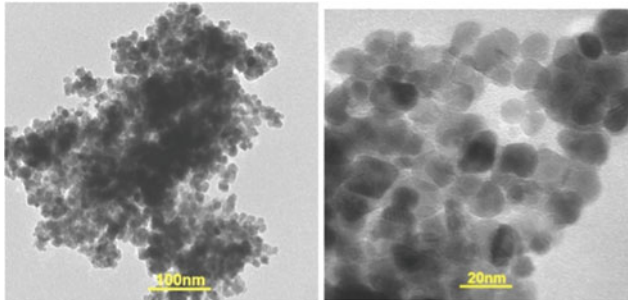


Fig. 2 A1 nanoparticles (left) and A2 nanocomposites (right)

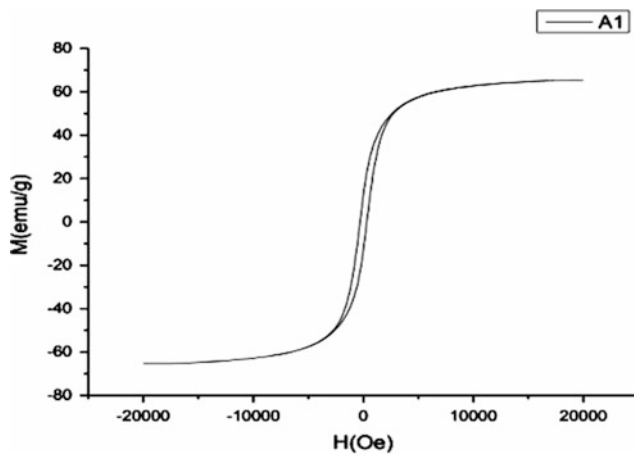


Fig. 3 Magnetization curve for A1 sample; M-specific magnetization, H-magnetic field intensity

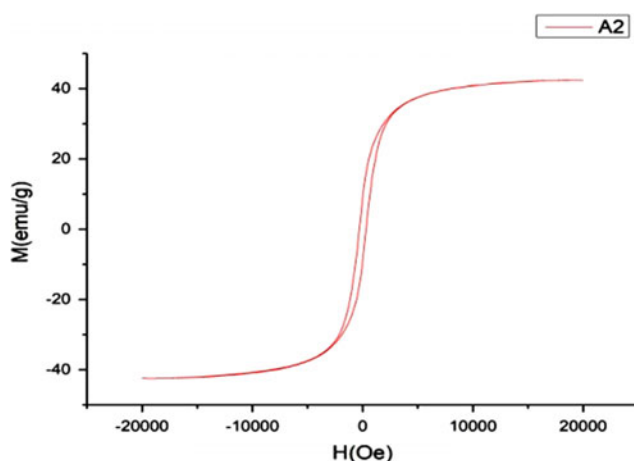


Fig. 4 Magnetization curve for A2 sample; M-specific magnetization, H-magnetic field intensity

Higher saturation value of specific magnetization (superparamagnetism) was evidenced by VSM investigation (Table 2, Figs. 3 and 4) for A1 nanopowder (65 emu/g) compared to A2 (about 42 emu/g) where most possibly a dilution effect has resulted because of silica layer contribution.

Coercivity was revealed for both A1 and A2 since some ferrimagnetic larger particles could coexist with dominant superparamagnetic ones [12–14]; similar values resulted for both A1 and A2 (of about 100 Oe).

B. Study on the cobalt ferrite toxicity in young plantlets

Production of cobalt ferrites for biomedical applications and also for technical purposes means finally the release of most part of used MNPs in the water, air and soil, affecting plants, beneficial microorganisms and animal organisms. We explored the MNPs effects in maize seedlings grown in laboratory as shown above. As can be seen (Fig. 5) there was general diminution—even for citrate-capping control there was about 11% decrease (standard deviation of about 9%); the presence of MNPs amplifies the effect especially for higher concentrations (80 and 100 μ l/l) recording about 25% for highest A1 suspension concentration (100 μ l/l).

The effect of silica/citrate/magnetic nanocomposite A2 (data not shown) has led to the chlorophyll and carotenoid pigment levels lowered with about the same amount as previously in the case of A1. This could suggest that the biophysical and biochemical mechanisms involved in the observed experimental data are not much dependent on the silica coating shell. It is more probable that iron and cobalt catalytic action affected cell metabolic chain for photosynthetic pigment production or/and the already synthesized molecules of pigments. Those metal ions could be released

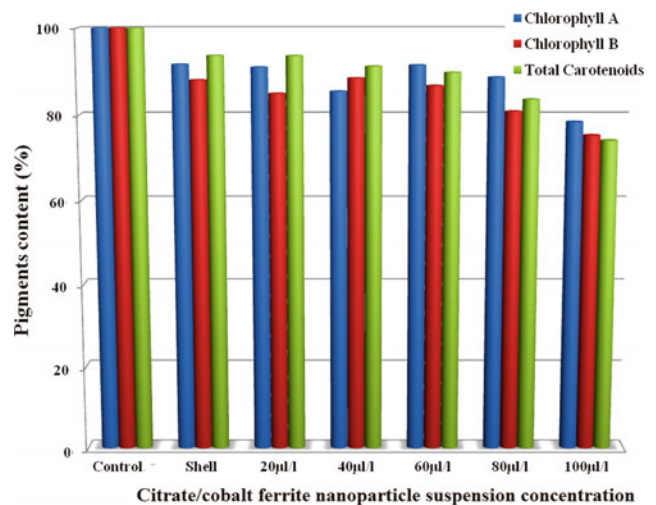


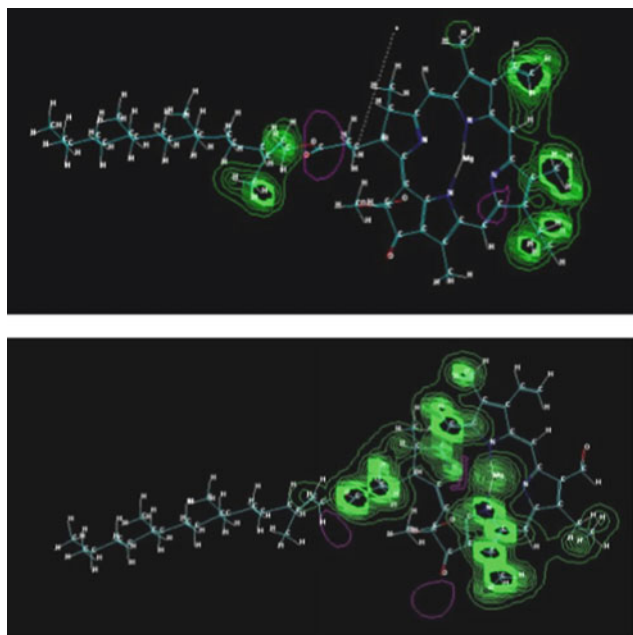
Fig. 5 Photosynthetic pigments in maize supplied with A1;” shell”—the sample corresponding to citric acid level in 100 μ l/l A1 concentration

Table 3 Some data from quantum mechanical modeling

Parameter	Chlorophyll A	Chlorophyll B
Total energy (kcal/mol)	-225300.0	-231350.0
Dipole moment (D)	6.242	3.292
E_{HOMO} (eV)	-7.5839	-7.7564
E_{LUMO} (eV)	-1.9042	-2.0033

following particle digestion into the cells where the smallest of them could be internalized through endocytosis. Iron and cobalt ions could trigger Fenton reactions that yield reactive oxygen species disturbing the vegetal cell biochemical balance, including that of chlorophyll A and B synthesis [6]. Theoretical approach by quantum mechanical simulation evidenced similar values for both chlorophylls (Table 3) for total energy and the energies of frontier orbitals (HOMO-Highest Occupied Molecular Orbital, LUMO-Lowest Unoccupied Molecular Orbital) involved in electronic absorption transitions that are related to UV-Vis spectra. Also they are the most likely to be involved in chemical reactivity, determining the chemical stability of the molecule, and the interaction with other molecular species. The about 2 times larger dipole moment of chlorophyll A (Table 3) could represent an argument for its better interaction with metal cations as well as with citrate and even silanol from capping and coating shells of magnetic cores.

However in Fig. 6 the electric charge maps indicating several molecular sites available for direct interaction with metal cations, seem to indicate, qualitatively, higher charge

**Fig. 6** Electric charge (in green) maps in chlorophyll A (up) and chlorophyll B (down)

densities for chlorophyll B. Thus both chlorophylls could be affected by metal cations probably by different dominant mechanisms. We mention that values of dipole moments and frontier orbitals calculated with PM3/Hyperchem are concordant with those provided by DFT/Spartan and with other authors' results [15].

4 Conclusions

Magnetic nanoparticles and nanocomposites based on $\text{Co}_{0.5}\text{Fe}_{2.5}\text{O}_4$ were successfully prepared by adapted co-precipitation method and respectively sol-gel technique. Dominant superparamagnetism was revealed by magnetization saturation (65 emu/g and respectively 42 emu/g) related to most frequent values of physical diameter of about 10 nm and respectively 12 nm.

Coercive field of about 100 Oe in both cases was given by small fraction of larger particles with ferromagnetic features.

Moderate nanotoxicity in maize seedlings was found at the level of photosynthetic pigments. Further study will be dedicated to oxidative stress assessing following supply with magnetic nanostructures.

Acknowledgements Part of this study was supported by JINR-RO projects 2019.

Conflict of Interest The authors declare no conflict of interests.

References

- Ito, A., Shinkai, M., Honda, H., et al.: Medical application of functionalized magnetic nanoparticles. *J. Biosci. Bioeng.* **100**(1), 1–11 (2005)
- Bedanta, S., Barman, A., Kleemann, W., et al.: Magnetic nanoparticles: a subject for both fundamental research and applications. *J. Nanomater* **2013**, 952540 (2011)
- Akbarzadeh, A., Samiei, M., Davaran, S.: Magnetic nanoparticles: preparation, physical properties, and applications in biomedicine. *Nanoscale Res. Lett.* **7**, 144–157 (2012)
- Dai, Q., Lam, M., Swanson, S., et al.: Monodisperse cobalt ferrite nanomagnets with uniform silica coatings. *Langmuir* **26**(22), 17546–17551 (2010)
- Amiri, S., Shokrollahi, H.: The role of cobalt ferrite magnetic nanoparticles in medical science. *Mater. Sci. Eng., C* **33**(1), 1–8 (2014)
- López-Luna, J., Camacho-Martínez, M.M., Solís-Domínguez, F.A., et al.: Toxicity assessment of cobalt ferrite nanoparticles on wheat plants. *J. Toxicol. Environ. Health A* **81**(14), 604–619 (2018)
- Massart, R.: Preparation of aqueous magnetic liquids in alkaline and acidic media. *IEEE Trans. Magn.* **17**, 1247–1248 (1981)
- Lu, Y., Yin, Y., Mayers, B.T., Xia, Y.: Modifying the surface properties of superparamagnetic iron oxide nanoparticles through a sol-gel approach. *Nano Lett.* **2**, 183–186 (2002)
- Puscasu, E., Sacarescu, L., Lupu, N., et al.: Iron oxide silica nanocomposites yielded by chemical route and sol-gel method. *J. Sol-Gel. Sci. Technol.* **79**, 457–465 (2016)

10. Lichtenthaler, H.K., Wellburn, A.R.: Determinations of total carotenoids and chlorophylls *a* and *b* of leaf extracts in different solvents. *Biochem. Soc. Trans.* **11**(5), 591–592 (1983)
11. Puscasu, E., Sacarescu, L., Popescu, et al.: Study on the effect of some surface phenomena on the properties of citrate capped cobalt doped ferrites. *Appl. Surf. Sci.* **483**, 1182–1191 (2019)
12. Zi, Z., Sun, Y., Zhu, X., Yang, Z., Dai, J., Song, W.: Synthesis and magnetic properties of CoFe_2O_4 ferrite nanoparticles. *J. Magn. Mater.* **321**(9), 1251–1255 (2009)
13. Ortega, D., García, R., Marín, R., et al.: Maghemite–silica nanocomposites: sol–gel processing enhancement of the magneto-optical response. *Nanotechnol* **19**(47), 475706 (2008)
14. Calero-DelC, V.L., Rinaldi, C.: Synthesis and magnetic characterization of cobalt-substituted ferrite ($\text{Co}_x\text{Fe}_{3-x}\text{O}_4$) nanoparticles. *J. Magn. Mater.* **314**(1), 60–67 (2007)
15. Hedayatifar, L., Irani, E., Mazarei, M., et al.: Optical absorption and electronic spectra of chlorophylls *a* and *b*. *RSC Adv* **6**, 109778 (2016)

Enhancement in Conductivity and Photoresponse of Ga Doped ZnO Nanofibers

M. N. Martyshov, A. S. Ilin, V. B. Platonov, P. A. Forsh, and P. K. Kashkarov

Abstract

Nanofibers ZnO and ZnO:Ga with a diameter of 100–250 nm were obtained by electrospinning. Introduction of Ga impurity at a concentration of 1 at. % leads to a significant increase in the conductivity of ZnO nanofibers. It is found that the temperature dependences of the conductivity of ZnO and ZnO:Ga films consist of two activation regions with different activation energies. Under the influence of UV radiation on the samples there is a long-term increase and decrease in conductivity associated with the processes of adsorption and desorption of oxygen molecules. It is shown that the Ga-doped ZnO sample has greater photoconductivity and photoresponse to UV radiation compared to pure ZnO.

Keywords

Zinc oxide • Electrical properties • Photoconductivity • Nanofibers • Electrospinning

1 Introduction

Zinc oxide (ZnO) is an important semiconductor material with a number of unique properties. Various nanomaterials based on zinc oxide are used to create solar cells, supercapacitors, UV photodetectors, photodiodes, etc. [1]. Due to its large specific surface area and high stability, nanostructured zinc oxide is also used as a sensitive layer of resistive type gas sensors [2]. The mechanism of resistive gas sensors is

based on the change in the conductivity of the sensitive layer when molecules of the detected gas appear in the environment. The sensing properties of the material are largely determined by its morphology and methods of production. One of the promising methods of obtaining nanostructures based on ZnO with a large specific surface area is electrospinning [3]. This method is based on the pulling of ultrathin fibers from the liquid medium under the strong electric field and allows to obtain fibers with a diameter of about several hundred nanometers. Nanostructures usually have a significantly reduced conductivity than bulk ones. Zinc oxide is an n-type semiconductor, so its conductivity decreases when exposed to oxidizing gases such as NO₂, CO, CO₂ and O₃. A low initial conductivity can lead to a decrease in the sensor gas response. Therefore, there is a problem of doping this material in order to increase its conductivity. Various metals, such as Co, Ga, Ag are used for doping zinc oxide [4, 5]. It is necessary to study in detail the effect of doping impurities on the electrical properties of the material. In addition, sensors based on nanostructured metal oxides can operate in conditions of illumination by UV radiation [6] or visible light [7]. Therefore, it is also important to study the photoelectrical properties of these materials and their changes as a result of doping. In this paper, the electrical and photoelectrical properties of nanostructured films of pure zinc oxide and zinc oxide doped with gallium obtained by electrospinning are compared.

2 Database and Methods

ZnO and ZnO:Ga samples studied in the work were obtained by electrospinning. To prepare the precursor solution in 5 ml of 2-methoxyethanol 200 mg of zinc acetate was added and mixed by a magnetic stirrer at 40 °C until completely dissolved (solution A). In 5 ml of isopropanol 900 mg of polyvinylpyrrolidone was added and actively stirred by a magnetic stirrer at 40 °C until completely dissolved (solution B). Then the solution A slowly (drop by drop) was

M. N. Martyshov · A. S. Ilin (✉) · P. K. Kashkarov
Physics Department, Lomonosov Moscow State University,
Leninskie Gory, Moscow, Russia
e-mail: as.ilin@physics.msu.ru

V. B. Platonov
Chemistry Department, Lomonosov Moscow State University,
Moscow, Russia

P. A. Forsh · P. K. Kashkarov
National Research Centre, Kurchatov Institute, Moscow, Russia

poured to the solution B with simultaneous stirring. The resulting solution was further mixed for an hour. To obtain gallium doped ZnO together with zinc acetate, gallium nitrate was introduced at a concentration of 1 at. %.

Further, the resulting precursor solution was placed in a medical syringe. Then the syringe was fixed in the syringe plunger BYZ-810, with which the solution was delivered at a speed of 1 ml/h to a metal needle of caliber G21 with an internal diameter of 510 μm . At a distance of 125 mm from the needle was a collector made in the form of a stainless wire frame. The voltage between the needle and the collector was maintained at the level of 10–11 kV using high voltage source Plazon IVNR-50/5.

The material obtained in the electrospinning process was heated for 5 h to a temperature of 550 $^{\circ}\text{C}$ with a heating rate of 1 $^{\circ}\text{C}/\text{min}$. As a result of the annealing, zinc oxide powder was obtained, which retained the fibrous structure. The synthesized powders were mixed with a binder (α -terpineol solution in ethanol) and deposited as a paste to the glass substrate. Then the glass substrate with the deposited film was dried at 30 $^{\circ}\text{C}$ for 24 h and annealed at 550 $^{\circ}\text{C}$ for 5 h.

The structural properties of the obtained films were investigated by scanning electron microscopy (Carl Zeiss NVision 40 electron microscope) and X-ray diffraction (DRON-3 diffractometer). To study the electrical properties of the obtained ZnO and ZnO:Ga Samples, gold contacts with a size of $2 \times 3 \text{ mm}^2$ and a distance between them of 150 μm were deposited on the surface of the films. The conductivity of the films was studied in the temperature range of 30–150 $^{\circ}\text{C}$ using the Keithley 6487 picoammeter. In experiments on the study of photoelectrical properties, the samples were illuminated by a UV led with a wavelength $\lambda = 385 \text{ nm}$. The intensity of radiation incident on the sample was $5 \text{ mW}/\text{cm}^2$.

3 Results

Figure 1 shows microphotographs of ZnO samples obtained with a scanning electron microscope. The figures show that the samples consist of long fibers with a diameter of 100–250 nm. As a result of thermal annealing of the samples, nanocrystals are formed inside the fibers of ZnO. The data obtained by the SEM and XRD methods show that the fibers are composed of ZnO nanocrystals with an average size of 30–50 nm. There are no noticeable differences in the structure of pure ZnO and ZnO:Ga samples.

Temperature dependences of the dark conductivity (σ_d) of ZnO and ZnO:Ga films measured in the temperature range of 30–150 $^{\circ}\text{C}$ are shown in Fig. 2. Doping of zinc oxide with gallium at a concentration of 1 at. % leads to an increase in conductivity by more than an order of magnitude in the entire region of temperatures. The obtained temperature

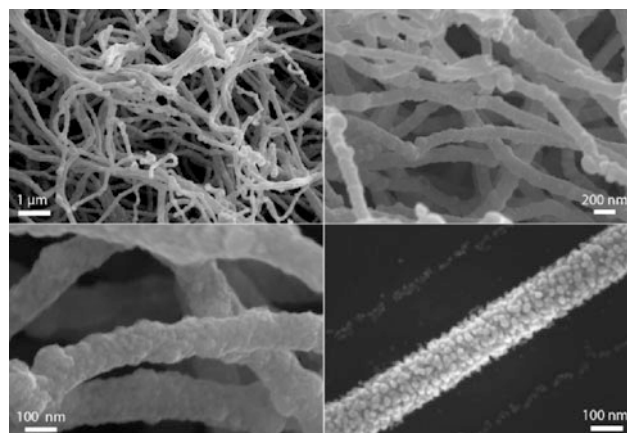


Fig. 1 SEM images of ZnO nanofibers

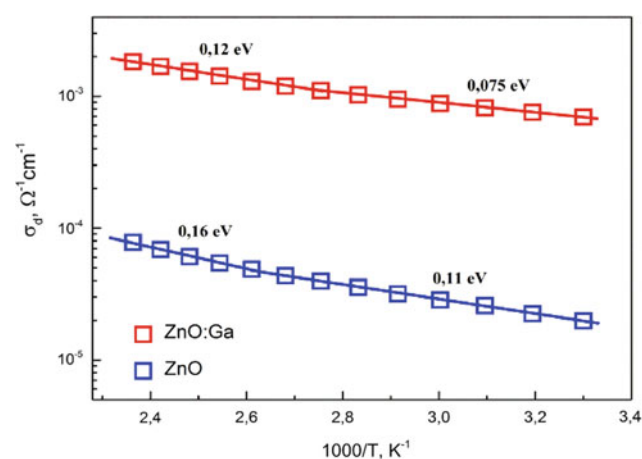


Fig. 2 Temperature dependences of conductivity of ZnO and ZnO:Ga nanofibers thick films

dependences of conductivity are thermally activated and can be expressed by the equation:

$$\sigma_d = \sigma_{d0} e^{-\frac{E_A}{kT}} \quad (1)$$

where σ_{d0} is a pre-exponential factor weakly dependent on temperature, k is the Boltzmann's constant, and E_A is the activation energy. The figure shows that the temperature dependences of conductivity for each sample have two areas with different activation energies. These dependences were approximated by Eq. (1) and as a result the activation energy values for these areas were obtained. Values of 0.11 and 0.16 eV were obtained for the pure ZnO sample and 0.075 and 0.12 eV for the ZnO:Ga sample.

A change in the activation energy may indicate a change in the conduction mechanism. In particular, in nanocrystalline metal oxides at low temperatures, a transition to hopping conductivity described by the Mott law can occur [8]. However, in our case the measurements were carried out

at relatively high temperatures. In addition, the change in the activation energy of the conductivity is not so significant. Therefore, a change in the conductivity mechanism in our case is unlikely.

In nanostructured ZnO, the band gap varies in the range of 3.1–3.3 eV [9]. Therefore, such small values of activation energy, which were obtained in the experiment, indicate that activation occurs from donor levels located close to the conduction band. The presence of two areas with different activation energies may be associated with the existence of two donor levels in the band gap of ZnO, from which electrons are activated into the conduction band [10, 11]. Firstly at relatively low temperatures, the activation of electrons occurs from a level closer to the conduction band. When the temperature rises, this donor level is getting empty, and activation occurs from another level lying closer to the middle of the band gap. The activation energy thus increases, as observed in the experiment. In addition, since the change in activation energy occurs near the temperature of 100 °C, this effect can also be associated with the desorption of water molecules from the surface of the material. It is known that water molecules adsorbed on the surface reduce the conductivity of ZnO [12]. At temperatures above 100 °C, the desorption rate of water molecules increases sharply, which can lead to an increase in activation energy.

To study the photoelectric properties, the obtained samples ZnO and ZnO:Ga were illuminated by UV light with a wavelength $\lambda = 385$ nm. Figure 3 shows dynamic response of samples conductivity measured in air at room temperature. Illumination was carried out for 30 min, and then also for 30 min the samples were in the dark. As can be seen from the figure, the increase and decrease of conductivity are slow.

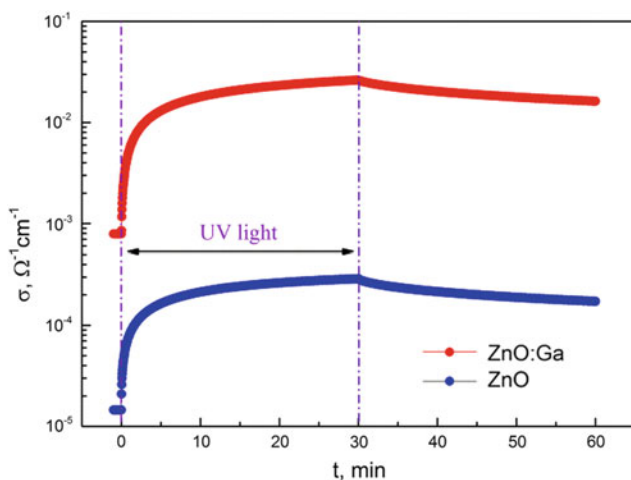
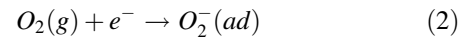
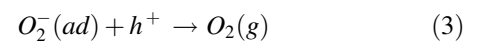


Fig. 3 Dynamic response of ZnO and ZnO:Ga films conductivity under UV light illumination

Such long-term processes of increase and decrease of conductivity under the influence of radiation are often observed in ZnO and other metal oxides with a large surface area and are usually associated with adsorption and desorption of oxygen molecules [13, 14]. Oxygen molecules adsorbed on the surface of ZnO fibers capture free electrons:



where $O_2(g)$ и $O_2^-(ad)$ designate oxygen in the free and adsorbed state, respectively. The capture of electrons leads to the fact that the surface of the fibers is charged negatively and as a result a depleted surface layer is formed. This leads to a decrease in the conductivity of the material. Oxygen desorption occurs as a result of recombination of a trapped electron with a hole formed under the influence of UV light:



Thus, under the influence of UV light, the oxygen molecules trapped on the surface of the ZnO fibers are desorbed. The result is a decrease in the thickness of the depleted layer on the surface of the fibers and increase the conductivity of the material. After the illumination is turned off, the oxygen molecules need a long time to be adsorbed on the surface again and restore the initial value of conductivity.

The photoconductivity (σ_{ph}) values of the material were calculated using the formula:

$$\sigma_{ph} = \sigma_{ill} - \sigma_d \quad (4)$$

where σ_{ill} is the conductivity of samples as illumination with UV light is turning on for 30 min. Table 1 shows the values of dark conductivity, photoconductivity, and photoresponse of ZnO and ZnO:Ga samples. Photoresponse was calculated as the ratio of photoconductivity and dark conductivity.

As can be seen from the table, doping of ZnO nanofibers with gallium leads to a significant increase of dark conductivity and photoconductivity. In addition, the photoresponse of the films also increases, which may be important for production of photodetectors using ZnO nanofibers.

4 Conclusions

In this work, the electrical and photoelectrical properties of ZnO and ZnO:Ga nanofiber films are investigated. The samples were obtained by electrospinning and consisted of fibers with a diameter of 100–250 nm. The temperature dependences of the conductivity of the samples are thermally activated with two activation energies. The change in the activation energy of conductivity can be due to the presence of two donor levels in the band gap of a semiconductor, as

Table 1 Dark conductivity, photoconductivity, and photoresponse of ZnO and ZnO:Ga samples at room temperature

Sample	$\sigma_d, \Omega^{-1}\text{cm}^{-1}$	$\sigma_{ph}, \Omega^{-1}\text{cm}^{-1}$	σ_{ph}/σ_d
ZnO	1.5×10^{-5}	2.7×10^{-4}	18
ZnO + Ga	7.9×10^{-4}	2.5×10^{-2}	32

well as the interaction of the material with water molecules from the air. However, additional research is needed to clarify this effect. The long-term increase and decrease in conductivity were observed when the films were illuminated with UV light, which is apparently associated with the processes of adsorption and desorption of oxygen molecules from the surface of nanofibers. It is shown that the introduction of Ga impurity in the amount of 1 at. % significantly increases the conductivity, photoconductivity and photoresponse of ZnO. The results obtained can be useful for production of gas sensors and photoelectric devices based on ZnO nanofibers.

Acknowledgements The reported study was funded by RFBR according to the research project № 18-32-20101.

Conflict of Interest The authors declare that they have no conflict of interest.

References

- Rong, P., Ren, S., Yu, Q.: Fabrications and applications of ZnO nanomaterials in flexible functional devices—a review. *Crit. Rev. Anal. Chem.* **49**, 336–349 (2019). <https://doi.org/10.1080/10408347.2018.1531691>
- Kumar, R., Al-Dossary, O., et al.: Zinc oxide nanostructures for NO₂ gas–sensor applications: A review. *Nano-Micro Lett.* **7**(2), 97–120 (2015). <https://doi.org/10.1007/s40820-014-0023-3>
- Platonov, V., Romyantseva, M., et al.: Nanofibers of semiconductor oxides as sensitive materials for detection of gaseous products formed in low-temperature pyrolysis of polyvinyl chloride. *Russ. J. Appl. Chem.* **91**(3), 447–453 (2018). <https://doi.org/10.1134/s1070427218030175>
- Lupan, O., Cretu, V., Postica, V., et al.: Silver-doped zinc oxide single nanowire multifunctional nanosensor with a significant enhancement in response. *Sens. Actuators B Chem.* **223**, 893–903 (2016). <https://doi.org/10.1016/j.snb.2015.10.002>
- Bhosle, V., Tiwari, A., Narayan, J.: Electrical properties of transparent and conducting Ga doped ZnO. *J. Appl. Phys.* **100**, 033713 (2006). <https://doi.org/10.1063/1.2218466>
- Ilin, A., Martyshev, M., Forsh, E., et al.: UV effect on NO₂ sensing properties of nanocrystalline In₂O₃. *Sens. Actuators B Chem.* **231**, 491–496 (2016). <https://doi.org/10.1016/j.snb.2016.03.051>
- Ilin, A., Ikim, I., Forsh, P., et al.: Green light activated hydrogen sensing of nanocrystalline composite ZnO-In₂O₃ films at room temperature. *Sci. Rep. UK* **7**(1), 12204 (2017). <https://doi.org/10.1038/s41598-017-12547-5>
- Vladimirova, S., Krivetskiy, V., Romyantseva, M., et al.: Co₃O₄ as p-type material for CO sensing in humid air. *Sensors* **17**(10), 2216 (2017). <https://doi.org/10.3390/s17102216>
- Arif, A., Belahssen, O., Gareh, S., et al.: The calculation of band gap energy in zinc oxide films. *J. Semicond.* **36**(1), 013001 (2015). <https://doi.org/10.1088/1674-4926/36/1/013001>
- Naveen, C., Dinesha, M., Jayanna, H.: Effect of fuel to oxidant molar ratio on structural and DC electrical conductivity of ZnO nanoparticles prepared by simple solution combustion method. *J. Mater. Sci. Technol.* **29**(10), 898–902 (2013). <https://doi.org/10.1016/j.jmst.2013.07.011>
- Belysheva, T., Ikim, M., Ilin, A., et al.: Features of the electrical and photoelectrical properties of nanocrystalline indium and zinc oxide films. *Russ. J. Phys. Chem. B* **10**(5), 810–815 (2016). <https://doi.org/10.1134/S1990793116050171>
- Jacobs, C., Maksov, A., Muckey, E., et al.: UV-activated ZnO films on a flexible substrate for room temperature O₂ and H₂O sensing. *Sci. Rep.* **7**, 6053 (2017). <https://doi.org/10.1038/s41598-017-05265-5>
- Forsh, E., Martyshev, M., Forsh, P., et al.: Transient photoconductivity in nanocrystalline indium oxide. *J. Nanoelectron Optoelectron.* **9**, 124–127 (2014). <https://doi.org/10.1166/jno.2014.1541>
- Bao, J., Shalish, I., Su, Zh, et al.: Photoinduced oxygen release and persistent photoconductivity in ZnO nanowires. *Nanoscale Res. Lett.* **6**, 404 (2011). <https://doi.org/10.1186/1556-276X-6-404>

Luminescence of β -Ga₂O₃ Nanoforms Obtained by Oxidation of GaSe Doped with Eu

V. Sprincean, D. Untila, A. Chirita, I. Evtodiev, and I. Caraman

Abstract

The GaSe single crystals were doped with Eu in the process of their synthesis and growth. The oxide of β -Ga₂O₃ doped with Eu in the form of massive nanowires was obtained by thermal treatment (TT) in the atmosphere of GaSe single crystals doped with 1.0 and 3.0 at.% of Eu. The crystalline structure, surface morphology and photoluminescence spectra of GaSe:Eu and β -Ga₂O₃:Eu single crystals were studied. The Photoluminescence (FL) spectrum of GaSe doped with 1.0 at.% of Eu at room temperature is formed as a result of transitions of $^5D_0 \rightarrow ^7F_1$ to Eu³⁺ ion and as a result of radiation annihilation of $n = 1$ excitons in GaSe. The FL spectra of Ga₂O₃:Eu was interpreted on the basis of the energy level diagram of electrons in Eu³⁺ ion.

Keywords

Thermal treatment • Nanowires • Crystalline structure surface • Gallium selenide • Gallium oxide

1 Introduction

The β -Ga₂O₃ is a n-type wide-band-gap semiconductor. The direct width of the band-gap at room temperature is 4.5–4.9 eV [1, 2]. This material is chemically and thermally stable at room temperature. Electric conductivity, through

electrons, is determined by the presence of oxygen vacancies. The concentration of the electrons depends on the technology of obtaining of Ga₂O₃. Nanoforms (nanowires, nanoribbons, nanotubes) with wide-band-gap are perspective materials for functional photo-electronics in the UV spectrum [3, 4]. As it was shown in the paper [4] the photo-sensitivity spectrum of photodetectors based on the thin layer structures of β -Ga₂O₃ obtained onto the substrate of Al₂O₃ covers the wavelength range of 220–280 nm. By doping the n-formations of β -Ga₂O₃ with Mn and rare earths elements (Er, Eu) the materials for radiation sources in visible and near IR spectrum were obtained [5, 6]. Photoluminescence spectrum of β -Ga₂O₃ single crystals doped with rare earths elements (in particular with Eu³⁺ and Er³⁺) contain intensive emission lines in the wavelength range of 540–560, 650–670 and 1450–1600 nm [7]. The CL spectra of compound Ga₂O₃ doped with Mn and thermal treated at 1300 °C predominate by the band intensity with the maximum centered at \sim 590 nm, while the peak band of CL for samples obtained by thermal treatment at 1500 °C is placed in the green spectrum (\sim 500 nm).

In this work the chemical composition, surface morphology and photoluminescence of β -GaSe single crystals and the β -Ga₂O₃:Eu nanoforms, obtained by TT in the atmosphere of GaSe single crystals doped with 3.0% of Eu, were studied.

2 Materials and Methods

The GaSe compound was synthesized from the Ga (5N) and Se (5N) elemental components in a two-furnace furnace. Temperatures in these areas could be adjusted over a wide range of temperatures—from room temperature to 1300 K. As a doping material, the EuSe was synthesized. Components, taken in stoichiometric quantities with a total mass of 20 g with 1 and 3 at.% of Eu, were placed in quartz ampoules with internal diameter 12–14 mm. After evacuation of the atmosphere to 5×10^{-5} Torr and sealing the

V. Sprincean (✉) · A. Chirita
Faculty of Physics and Engineering, Moldova State University,
60 A.Mateevici str., Chisinau, Republic of Moldova
e-mail: sprincean@gmail.com

D. Untila · I. Evtodiev
Institute of Electronic Engineering and Nanotechnologies
“D. Ghitu”, Chisinau, Republic of Moldova

I. Caraman
Department of Environmental Engineering and Mechanical
Engineering, University of Bacau, Bacau, Romania

ampoules they were placed in the first furnace area. The furnace was fixed at an angle of $20\text{--}30^\circ$ to the horizon. The temperature in that area was raised slowly (for 8 h) to a temperature of 1300 K, after which during 12 h the temperature in the second zone also rose to 1300 K. The synthesis process lasted ~ 24 h, after which the furnace was moved vertically. The temperature in the second zone was reduced to a temperature of 1170 K and the melt was passed through a temperature gradient of 30°cm^{-1} from the first thermal zone in the second area. The crystallized material was cooled at a rate of $\sim 100^\circ \text{C/h}$ to room temperature. The ingots, composed of single crystal blocks, were obtained. The ingots could be split into plates with smooth surfaces (observed microscopic with $1/900$ magnification) in red. To obtain the nano and microforms of $\beta\text{-Ga}_2\text{O}_3\text{:Eu}$ the plates of GaSe:Eu with thickness of 0.5–1.0 mm were thermal treated at 1100 K in the atmosphere for 3–12 h. Originally, the obtained material is covered with a white coat of the parallel surfaces at the C_6 axis of the GaSe:Eu plates. After 12 h of thermal treatment at the same temperature, GaSe plates with a thickness of 100–300 μm turn into a white porous material.

The crystalline structure of the obtained materials was studied by the XRD method using the Rigaku Ultima IV installation with CuK_α $\lambda = 1.54060 \text{ \AA}$. The morphology of the surface of GaSe:Eu single crystals and $\beta\text{-Ga}_2\text{O}_3\text{:Eu}$ oxide was analyzed using SEM images obtained with a help of SEM ZEISS ULTRA PLUS electronic microscope. Photoluminescence (FL) spectra at 80–300 K were obtained using the MDR-2 monochromator supplemented with 600 and 1200 mm^{-1} diffraction gratings. The signal was measured using the photomultiplier detector with photocathode (Na_2K) Cs + Sb. Photoluminescence was excited by He–Ne laser with the wavelength of 337.4 nm and power of 20 mW.

3 Results and Discussion

In Fig. 1 (a, b, c, d) are presented the XRD diagrams of non-doped and doped (with 1.0 and 3.0 at.% of Eu)

GaSe compound, as well as the material obtained by TT at 1100 K in the atmosphere during the 6 h of GaSe:Eu polycrystals.

The 2θ angles corresponding to the X-ray diffraction lines are included in Table 1.

The identification of the diffraction peaks using the PDF 01-078-1927 and 01-070-2524 cards was done. As shown in the Table 1, the peaks from the plane system with the Miller indexes (002), (004), (008) and (0012) are present in the studied samples. These peaks correspond to the diffraction from atomic planes perpendicular to the C_6 axis in $\varepsilon\text{-GaSe}$

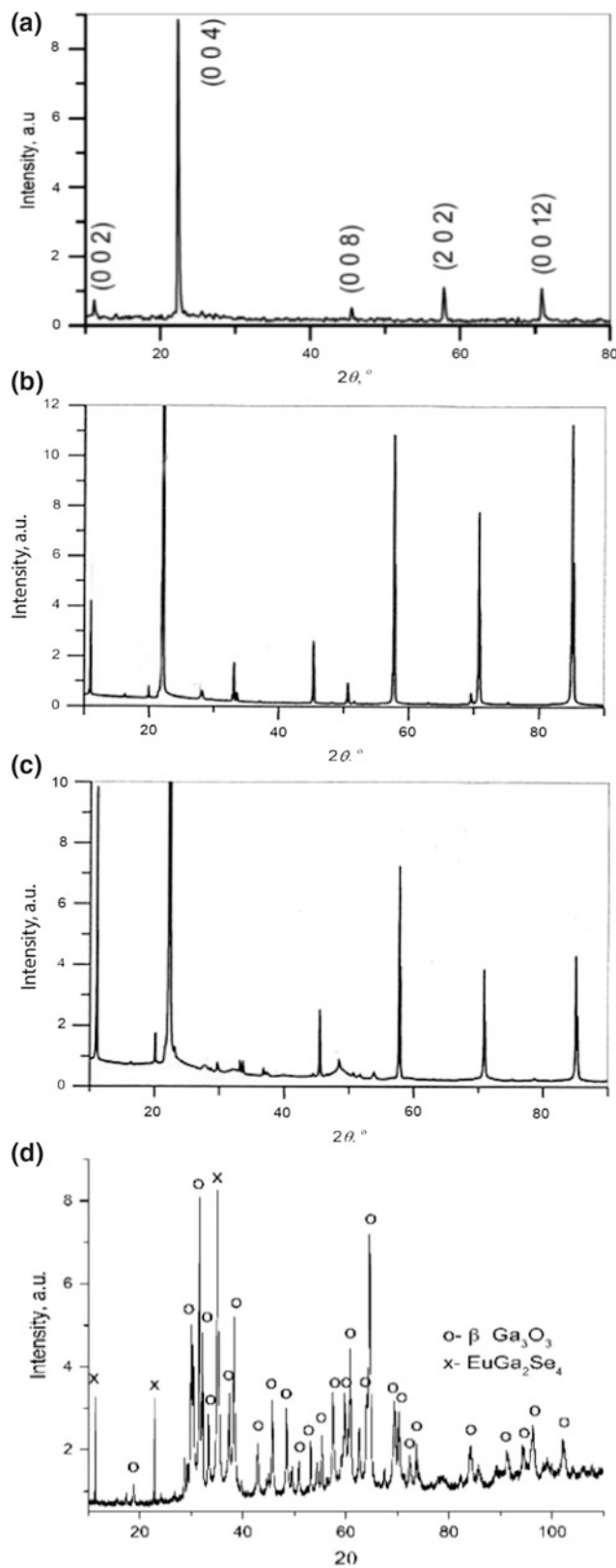


Fig. 1 XRD diagrams of the GaSe compound. **a** Non-doped, **b** doped with 1.0 at.% of Eu. **c** Doped with 3.0 at.% of Eu. **d** $\text{Ga}_2\text{O}_3\text{:Eu}$

Table 1 Identifying of XRD diagrams

Nr	20°			DS		
	0	1%	3%	Compound	Card-PDF	(hkl)
1	11.11	11.12	11.12	GaSe	01-078-1927	(0 0 2)
2	22.23	22.30	22.70	GaSe	-//-	(0 0 4)
3	-	32.86	33.80	EuGa ₂ Se ₄	01-070-2524	(0 4 4)
4	45.32	45.48	45.58	GaSe	01-078-1927	(0 0 8)
5	-	51.66	51.78	EuGa ₂ Se ₄	01-070-2524	(6 10 2)
6	57.92	57.94	57.92	GaSe	-//-	(2 0 2)
7	71.02	71.06	71.04	GaSe	01-078-1927	(0 0 12)

crystals. The parameters of the hexagonal crystalline grid are: $a = 0.3755$, $c = 1.5995$ nm. At the same time, there are two diffraction lines, which according to the card PDF 01-070-2524 card, are identified as diffraction from atomic planes with epy Miller indices (044) and (6102) of EuGa₂Se₄ crystals with parameters: $a = 2$, 1579 , $b = 2.1336$ nm, $c = 1.2736$ nm and $\alpha = \beta = \gamma = 90^\circ$. As shown in Fig. 1 (b, c and d) the intensity of the XRD lines, which correspond to the phase of EuGa₂Se₄, increases with the increase of the Eu concentration from 1.0 to 3 at.%, which can be explained by the low solubility of Eu in the GaSe compound.

The XRD diagram of the studied material, obtained by thermal treatment of GaSe plates doped with 3.0 at.% of Eu in the atmosphere at 1100 K for 12 h, is presented in Fig. 1d. The identification of the XRD lines using the PDF-43-1012 card was done. According to obtained results, the analyzed material is composed of gallium oxide crystals of β -Ga₂O₃ type with a monoclinic crystalline structure with the following parameters: $a = 1.223$ nm, $b = 0.304$ nm, $c = 0.580$ nm and $\beta = 103.7^\circ$, the space group— $c2/m$. At the same time, the XRD diagram in the 2θ angles from 10 to 90° also shows three XRD lines at 2θ angles equal to 11.34° , 22.84° and 32.18° , which can be obtained as a result of X-ray diffraction with a wavelength of 0.154060 nm from the atomic planes of the EuGa₂Se₄ orthorhombic crystal system. From the comparison of the XRD diagrams, presented in Fig. 1 (a, b, c and d), it can be seen that EuGa₂Se₄ crystals formed in Ga₂Se₄:Eu are stable at thermal treatment in the atmosphere at high temperatures (~ 1100 K).

The SEM image of the surface of β -Ga₂O₃ layer, formed by atmospheric oxidation of the GaSe plate doped with 3 at.% of Eu, is shown in Fig. 2. As can be seen from Fig. 2, the surface of the sample is covered with a dense layer of nanowires of oxide, with the growth direction perpendicular to the surface (0001) of the GaSe:Eu single crystal. The average length of nanowires is ~ 2 μ m. At the same time the unitary nanowires with the length of 4–5 μ m and higher are observed. It can be seen, that defects on the GaSe surface (deformations and dislocations) influence the length and direction of growth of β -Ga₂O₃:Eu nanowires.

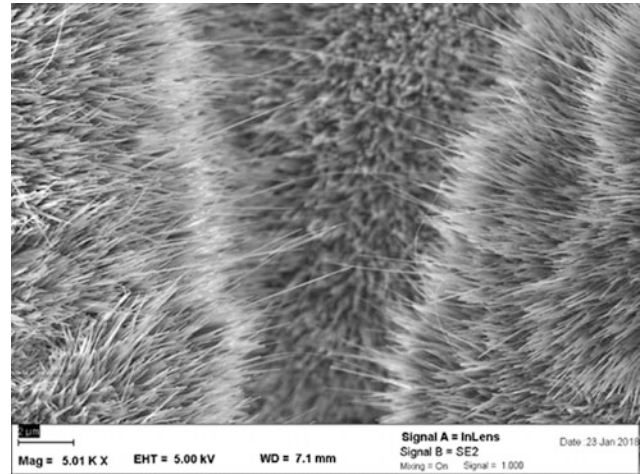


Fig. 2 The SEM image of the surface of the Ga₂O₃ oxide layer, formed by oxidation at 1100 K in the atmosphere of β -GaSe plate doped with 3 at.% of Eu with a thickness of ~ 330 μ m

The direct bandgap width in GaSe crystals at 293 K and 80 K is equal to 2.00 eV and 2.118 eV respectively [8]. The FL spectrum of the ϵ -GaSe single crystals is composed of the direct exciton emission band at $n = 1$ at 80 K with a maximum of 2.098 eV, and a band of D-A in the range of 670–800 nm.

The FL spectra at room temperature of GaSe crystals, non-doped and doped with 0.1, 0.5, and 1 at.% of Eu are shown in Fig. 3. As shown in Fig. 3b, the FL at room temperature of GaSe crystals contain a single band with a maximum centered at 626 nm (1.98 eV). The difference between the maximum of FL (1.98 eV) and the bandgap width (2.00 eV) is ~ 20 meV, which coincides with the excitement energy of the direct excitons in the state $n = 1$ [5]. Therefore, we can admit that the photoluminescence of undoped GaSe crystals at the room temperature of luminescence decay of excitons in state $n = 1$. The FL Spectrum of GaSe crystals doped with 1.0 at.% of Eu contains two bands: one in the region of the maximum absorption band edge and a low intensity band in the wavelength range of 700–950 nm. As can be seen from Fig. 3 (1), the peak of the

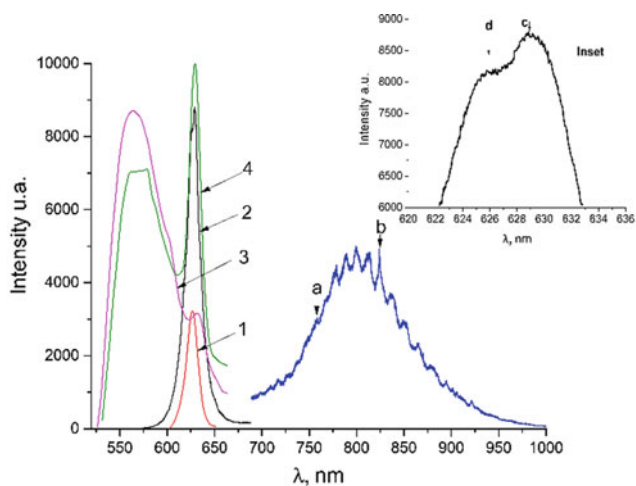


Fig. 3 The FL spectra at room temperature of non-doped GaSe crystals (curve 1), doped with 0.1 at.% of Eu (curve 2), doped with 0.5 at.% of Eu (curve 3), doped with 1.0 at.% of Eu (curve 4) and the contour of the top of FL stripline (insert)

photoluminescence band is divided into two components with maxima of 1.990 eV and 2.003 eV. The energy between levels 5D_0 și 7F_2 in the Eu^{3+} ion is equal to 2.025 eV [9]. We can consider that the margin band FL is formed as a result of luminescence decay of the excitons in state $n = 1$ in GaSe and the emission band $^5D_0 \rightarrow ^7F_2$ in the Eu^{3+} ion.

The FL spectrum with a maximum width at 1.54 eV has a contour characteristic of the D-A bands with the emission of the longitudinal optical phonons (LO) [10]. The average energy interval between two consecutive peaks is ~ 23 meV, less than 3 meV representing the thermal energy at room temperature and less than 8 meV, which is the energy of the longitudinal optical phonons in GaSe [11].

FL spectra of GaSe crystals doped with 0.5 and 1.0 at.% of Eu Fig. 3 (curves 3 and 4) along with the 626 nm band contains a broad band in the 520–610 nm range. FL in this spectral range is obtained as a result of the merging of eight emission bands into the Eu^{3+} ion, with the wavelengths centered at 537 nm ($^5D_2 \rightarrow ^7F_4$), 539 nm ($^5D_1 \rightarrow ^7F_1$), 559 nm ($^5D_1 \rightarrow ^7F_2$), 569 nm ($^5D_2 \rightarrow ^7F_3$), 576 nm ($^5D_0 \rightarrow ^7F_0$), 586 nm ($^5D_1 \rightarrow ^7F_3$), 588 nm ($^5D_0 \rightarrow ^7F_1$), 606 nm ($^5D_2 \rightarrow ^7F_6$) [10].

The FL spectra (at room temperature) of materials, obtained by thermal treatment of GaSe single crystals doped with 1.0 and 3.0 at.% of Eu at 1100 K in the atmosphere, are shown in Fig. 4. In these FL spectra is a dominant band with a maximum centered wavelength of 614 nm (2.02 eV). This band, as is shown in work [12], is identified as a radiant transition between the excited energy level 5D_0 and the fundamental level 7F_2 of the Eu^{3+} .

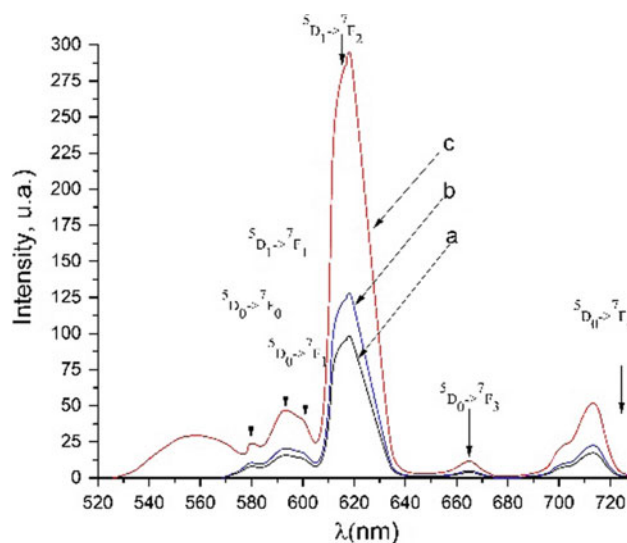


Fig. 4 Photoluminescence at temperature 293 K (curve a) and 80 K (curves b, c) of the $\text{Ga}_2\text{O}_3:\text{Eu}$ oxide obtained by oxidation by TT in the atmosphere at 1100 K of the GaSe crystals doped with 1 at.% of Eu (curve b) and 3.0 at.% of Eu (curve c)

According to the energy level diagram of the Eu^{3+} ion [10], the FL bands with the maximum centered at wavelengths 579, 599, 655, and 703 nm can be interpreted as transitions $^5D_0 \rightarrow ^7F_0$, $^5D_0 \rightarrow ^7F_1$, $^5D_0 \rightarrow ^7F_3$ and $^5D_0 \rightarrow ^7F_4$ in Eu^{3+} ion from $\beta\text{-Ga}_2\text{O}_3$ nanowires. As is shown in Fig. 4, with the increase of the dopant concentration from 1.0 to 3.0 at.% an increase in the intensity of the FL bands of the Eu^{3+} ion in the $\beta\text{-Ga}_2\text{O}_3$ nanowires. In the FL spectrum (at a temperature of 80 K) of $\beta\text{-Ga}_2\text{O}_3$ oxide doped with Eu, which was obtained by the thermal treatment of the GaSe₂ plates doped with 3.0 at.% of Eu. (curve 3), along with the room temperature bands, the photoluminescence band (curve “a”, Fig. 4) with maximum centered at wavelength of 555 nm (2.23 eV) is presented. The photoluminescence in this range was observed in the Na_2O_3 nanowires massive obtained by the CVD method and thermal treated at 1000 °C [13].

4 Conclusion

The thermal treatment of the $\beta\text{-GaSe}$ single crystals doped with 1 and 3 at.% of Eu, a compound material is formed from nanowires on $\beta\text{-Ga}_2\text{O}_3:\text{Eu}^{3+}$ oxide. The emission spectra in the green-red range at room temperature and 80 K are composed of 5 bands. These bands are obtained as a result of electron transitions from the excited state 5D_0 to the fundamental states 7F_1 , 7F_2 , 7F_3 , 7F_4 .

Europium, as a dopant material in the $\epsilon\text{-GaSe}$ hexagonal single crystals, forms the luminescence centers with emitting

bands in the green-red spectrum. An increase the concentration of Eu from 1 to 3 at.%, as well as a decrease of the temperature, leads to the formation of new PL bands, which are located in the area of the fundamental absorption of GaSe compound.

Conflict of Interest The authors declare that they have no conflict of interest.

References

1. Zhengwei, C., et al.: Band alignment of Ga₂O₃/Si heterojunction interface measured by X-ray photoelectron spectroscopy. *Appl. Phys. Lett.* **109**, 102106 (2016)
2. Giriya, K., Thirumalairajan, S., Mangalaraj, D.: Morphology controllable synthesis of parallelly arranged single-crystalline β -Ga₂O₃ nanorods for photocatalytic and antimicrobial activities. *Chem. Eng. J.* **236**, 181–190 (2014)
3. Kong, W.Y., et al.: Graphene- β -Ga₂O₃ heterojunction for highly sensitive deep UV photodetector application. *Adv. Mater.* **28**, 10725–10731 (2016)
4. Huang, L., et al.: Comparison study of β -Ga₂O₃ photodetectors grown on sapphire at different oxygen pressures. *IEEE Photonics J.* **9**, 1–8 (2017)
5. Shujuan, C., et al.: Room temperature fabricated amorphous Ga₂O₃ high response speed solar blind photodetector on rigid and flexible substrates. *Adv. Opt. Mater.* **5**, 1700454 (2017)
6. Zervos, M., et al.: Sn doped β -Ga₂O₃ and β -Ga₂S₃ nanowires with red emission for solar energy spectral shifting. *J. Appl. Phys.* **118**, 194302 (2015)
7. Biljan, T., Gajović, A., Meić, Z.: Visible and NIR luminescence of nanocrystalline β -Ga₂O₃: Er³⁺ prepared by solution combustion synthesis. *J. Lumin.* **128**, 377–382 (2008)
8. Williams, F.: Donor acceptor pairs in semiconductors. *Phys. Status Solidi B* **25**, 493–512 (1968)
9. Capozzi, V., Montagna, M.: Optical spectroscopy of extrinsic recombinations in gallium selenide. *Phys. Rev. B* **40**, 3182 (1989)
10. Shyama, P.S.: Europium. Springer-Verlag, New York (1967)
11. Yoshida, H., Nakashima, S., Mitsuishi, A.: Phonon Raman spectra of layer compound GaSe. *Phys. Status Solidi B* **59**, 655–666
12. Chen, Z., et al.: Low temperature growth of europium doped Ga₂O₃ luminescent films. *J. Cryst. Growth* **430**, 28–33 (2015)
13. Li, Y., et al.: Efficient assembly of bridged β -Ga₂O₃ nanowires for solar-blind photodetection. *Adv. Funct. Mater.* **20**, 3972–3978 (2010)

Sensorial and Local Reflectivity Properties of the Columnar ZnO:Eu Films

C. Lupan, A. Schütt, A. Bîrnaz, M. Hoppe, and R. Adelung

Abstract

In this work, we report on sensorial properties dependent on the operating temperature for Eu-doped ZnO columnar samples. The films demonstrated sensorial properties to volatile compounds, namely for 2-propanol. The results have been explained by increased basic properties of ZnO after doping with ions of Eu, that lead to catalyzing of dehydrogenation processes of molecules, and higher response. Local reflectivity maps of the sensor samples with a very high spatial resolution were recorded by using a specially modified measurement set-up, which had been originally designed for the electrical characterization of photovoltaic solar cells. The variation of the local reflectivity of the active sensor area is caused by different film properties that are most probably the result of the deposition process and/or handling. In the future, a systematic analysis and correlation of the performance data of various sensor samples with such reflectivity maps may lead to a better understanding and improvement of the film deposition process and thus to finally better sensors.

Keywords

ZnO:Eu • Columnarfilms • 2-propanol • Reflectivity • Gas sensor

1 Introduction

Volatile organic compounds, such as 2-propanol, are found in a variety of consumer products and may yield harmful or toxic products for humans, that can cause health problems [1]. Zinc oxide with large bandgap (3.37 eV at room temperature) is an attractive material for doping with rare-earth elements, like Ce, Er, La, Eu, etc. [2–5]. Rare-earth elements are known for their ability to donate valence electron pairs and to increase basic properties of zinc oxide [2, 6]. Chemical synthesis from the solution method represents an advantage, because it allows efficient doping with ions of different metals, including rare-earth elements, by adding salts in the complex solution of zinc oxide [7, 8]. Among all rare-earth elements, europium has attracted attention for its excellent optical properties [2–5]. Also, there will be shown sensorial properties of vapors of 2-propanol of samples at an operating temperature of 300 °C.

The solar cell local characterization technique (CELLO) was originally designed for the local electrical characterization of photovoltaic solar cells. Light intensity modulated laser beams are scanned across the sample solar cell via a piezo-electric mirror and the small signal response of the laser light is recorded. The set-up combines a four probe set-up and a lock-in measurement for a very sensitive current and voltage measurement. Recently, the set-up has been modified to measure local reflectivity maps with a very high local resolution and any sample like e.g. also porous silicon foils for Li-ion batteries [9, 10]. Four different laser wavelengths (401, 658, 830, and 934 nm) are applicable for the reflectivity maps. The maximum sample size is 15 × 15 cm. The circular laser focus size is around 80 μm and allows maps with a very high local resolution.

C. Lupan (✉) · A. Bîrnaz
Department of Microelectronics and Biomedical Engineering,
Technical University of Moldova, 168 Stefan cel Mare Av.,
Chisinau, Republic of Moldova
e-mail: cristian.lupan@mib.utm.md

A. Schütt (✉) · M. Hoppe · R. Adelung
Funtional Nanomaterials, Institute for Materials Science,
Kiel University, Kiel, Germany
e-mail: asc@tf.uni-kiel.de

2 Experimental

Columnar films of Eu-doped ZnO were deposited on glass substrate using chemical synthesis from the solution method [7, 8]. For doping with ions of Eu, EuCl_3 was added to the solution. After using this method of deposition, the films were thermal treated in air at different temperatures.

The morphology and thickness of the films (about 1.3–1.5 μm) were measured by a scanning electron microscope (ZEISS). The sensorial properties were measured using a “home-made” set-up, which was described in [1, 7, 8].

For the reflectivity measurement a commercially available CELLO-system has been modified. The reflectivity was measured by placing the samples on the measurement chuck and the reflectivity measurement is conducted as described in detail in [8]. In short, the lasers are scanned across the sample and the reflected light is collected by a separate mini-solar module (detector). The space around sample and detector is covered with reflecting material similar to an integrating sphere. The sample is placed next to an object of known-reflectivity that is used in the final map for calibrating. The sample is placed on a chuck that is temperature controlled to 25 °C.

3 Results and Discussion

Figure 1 shows SEM images of columnar films of Eu-doped ZnO. The films are formed of grains, which are well-packed on the glass substrate. There are no clusters or islands observed of Eu-doped ZnO grains. The grain diameter is about 200–400 nm, which is comparable to columnar films of ZnO:Fe and ZnO:Sn, deposited with the same method, reported before [7, 8]. The advantages of interconnected grains for sensor applications were discussed before in previous works and can increase gas response [7, 8, 11].

The final calibrated reflectivity maps are presented in Figs. 2, 3, 4 and 5. In Fig. 2 the gold contacts of the sample are highlighted as well as the active area. The variation of the reflectivity in the active area ranges from 8.4% for the blue map to 9.6% for the IR map.

The observed reflectivity variation in the active area is most probably caused by inhomogeneous deposition

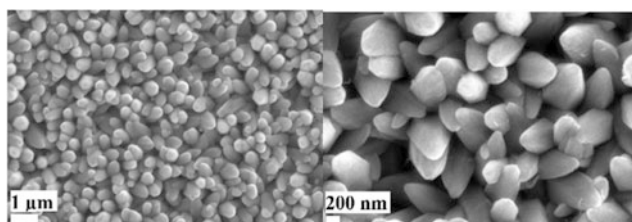


Fig. 1 SEM images of columnar of Eu-doped ZnO films

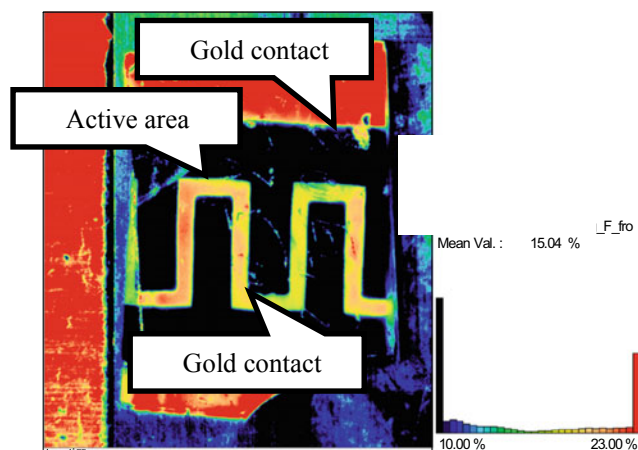


Fig. 2 Blue (401 nm) laser reflectivity map from the sample. The active area shows a reflectivity variation of 8.4% (maximum reflectivity of 22.4%, minimum 14%)

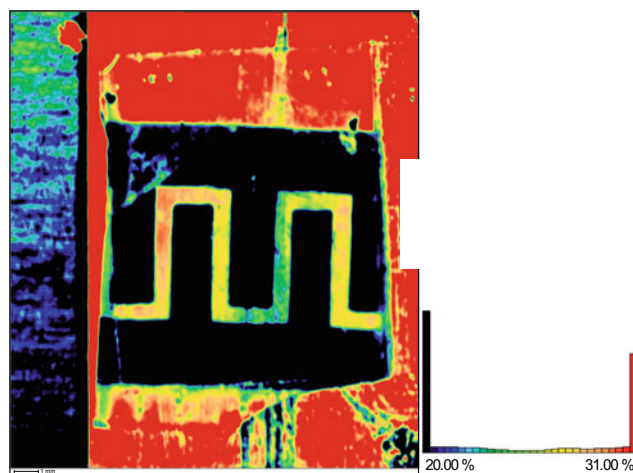


Fig. 3 RED (658 nm) laser reflectivity map of Eu-doped ZnO sensor structure. The active area shows a reflectivity variation of 9.3% (maximum reflectivity of 29.6%, minimum 20.3%)

conditions or deterioration of the active material during experiments thus resulting in inhomogeneous film properties. The reflectivity variation can be for example caused by a different surface roughness or a change in the chemical composition as demonstrated in [10]. It has been seen on other samples that the visible color of the active area change over time at ambient conditions at room temperature. That color change is then also visible as a change in the reflectivity map that in this case could indicate that a chemical composition change had happened.

The scratch-like shape of the high reflective active area in Fig. 2 on the left indicates that this reflectivity variation may be caused by a different surface roughness, possibly caused by handling or scratching of the sample.

In the future, the comparison of the sensor performance with the film properties from reflectivity measurements of

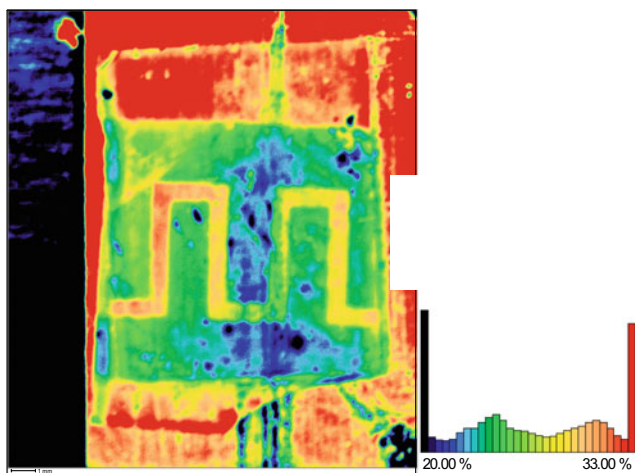


Fig. 4 IR (830 nm) laser reflectivity map of the same sample. The active area shows a reflectivity variation of 9.6% (maximum reflectivity of 31.4%, minimum 21.8%)

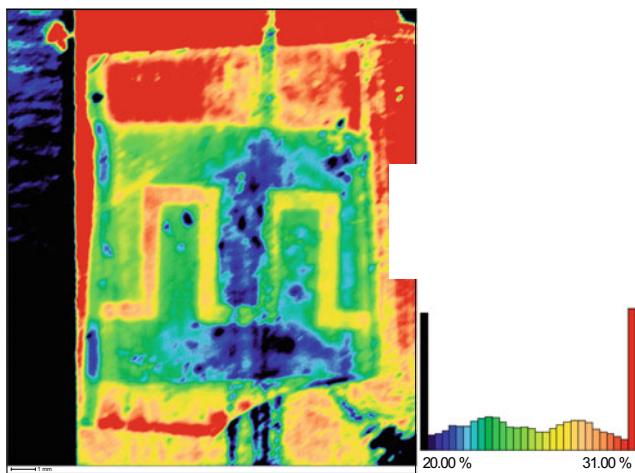


Fig. 5 SIR (934 nm) laser reflectivity map from the sample. The active area shows a reflectivity variation of 8.5% (maximum reflectivity of 29.8%, minimum 21.3%)

various samples may be a very promising tool to identify better deposition parameters in order to improve the sensor properties even further. Promising further measurements are reflectivity measurements with various sample temperatures; the range of the temperature control is roughly 15–50 °C. These measurements may reveal different thermal behavior that varies locally. Another promising set of experiments are reflectivity measurement under changing halogen lamps bias light conditions.

Figure 6 shows the current-voltage characteristics of Eu-doped ZnO film based sensors at different operating temperatures. As can be observed, the current increases from room temperature (RT) until 200 °C, and then it decreases. At all operating temperatures sample exhibits linear Ohmic characteristics.

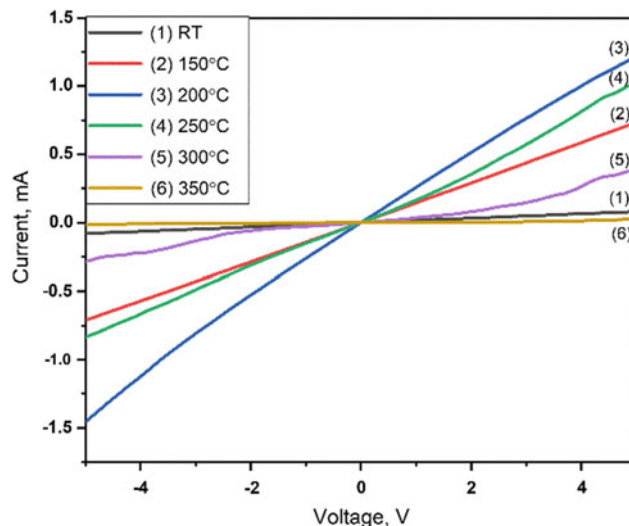


Fig. 6 Current-voltage characteristics of Eu-doped ZnO film based sensor structure at different operating temperatures

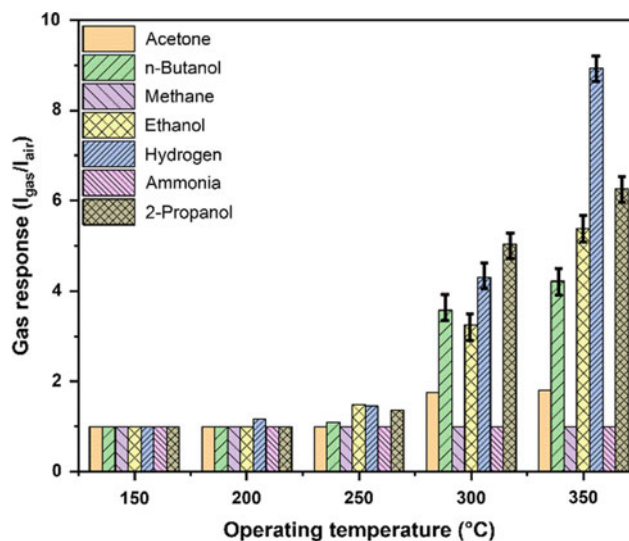


Fig. 7 Gas response of Eu-doped ZnO film based sensor structure to 100 ppm of different gases at different operating temperatures

Figure 7 shows the gas response to 100 ppm to a series of gases at different operating temperatures. It has been observed that the gas response increases with the temperature of sensor operation, obtaining highest response at 350 °C of ~9 for hydrogen gas. A low selectivity at all operating temperatures was observed.

The gas response (S) was calculated using $S = I_{gas}/I_{air}$, where I_{gas} is current when gas was introduced into the test chamber, and I_{air} the current through the sample at the exposure in air. The measurements were carried out at operating temperature of 300 °C at 100 ppm of 2-propanol

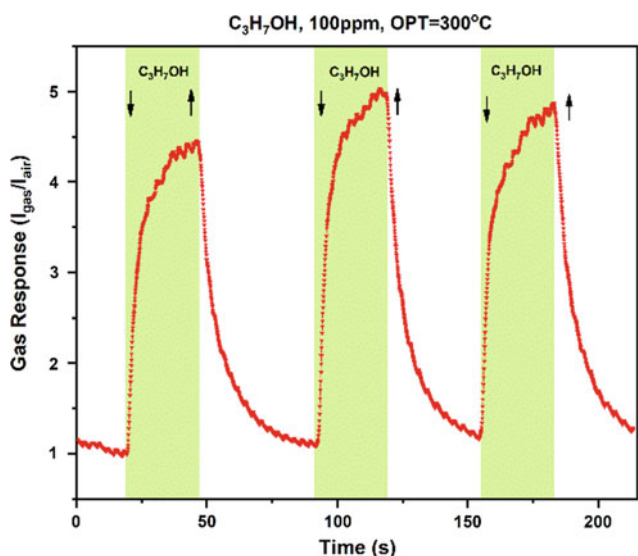
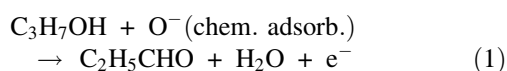


Fig. 8 Dynamic response at an operating temperature of 300 °C of Eu-doped ZnO film based sensor structure to 100 ppm of 2-propanol

(C₃H₇OH). The dynamic response is presented in the Fig. 8, obtaining a value of ~5 for 2-propanol, with a response time of around 10 s and recovery time of 30 s. The results for 2-propanol can be explained by increased basic properties after incorporating Eu³⁺ ions instead of Zn²⁺ [12], that leads to a higher grade of dehydrogenation of volatile compound molecules, thus leading to a higher gas response [13–16].

The increase in the current when gas is introduced into test chamber is related to oxidation of 2-propanol through dehydrogenation to acetaldehyde in the presence of chemisorbed oxygen species such as O⁻ and O⁻². Additional electrons are released back to the conduction band as expressed in the following reaction [14]:



From the reaction it is clear that a release of electrons to ZnO:Eu, which is an *n*-type material, leads to an increase in current. For further improvement of this proposed mechanism additional adjustments to the parameters are required.

4 Conclusions

In this work it was reported that columnar films of ZnO:Eu with high crystallinity can be obtained by using chemical synthesis from the solution method. SEM images showed that the films are consisting of well-packed columnar grains and are partially interconnected. The measurement of the gas response revealed a potential for producing gas sensors for 2-propanol by adjusting synthesis parameters and concentration control of Eu ions in columnar films of ZnO:Eu.

In this work high resolution reflectivity maps of ZnO:Eu sensor samples at four different wavelengths were recorded and analyzed for the first time. The results reveal reflectivity variations in the active area that are most probably caused by the film deposition process and/or due to handling during sensing measurements. The reflectivity maps are a powerful tool for local characterization of such samples. In the future, the correlation of further reflectivity maps with sensor performance data might become a very promising new tool for the optimization of the sensor production process leading to better performing sensors.

Acknowledgements C. Lupan and A. Bîmaz acknowledge the Faculty of Engineering, Kiel University, Kiel, Germany for an invited internship positions in 2018–2019. This research was partly supported by the project Institutional inst-15.817.02.29A funded by the Government of the Republic of Moldova and by the Technical University of Moldova.

Conflict of Interest The authors declare that they have no conflict of interest.

References

- Hoppe, M., Ababii, N., Postica, V., Lupan, O., Polonskyi, O., Schütt, F., Kaps, S., Sukhodub, L.F., Sontea, V., Strunskus, Th, Faupel, F., Adelung, R.: (CuO-Cu₂O)/ZnO: Al heterojunctions for volatile organic compound detection. *Sens. Actuators B: Chem.* **255**, 1362–1375 (2018)
- Stănoiu, A., Simion, C.E., Somăcescu, S.: NO₂ sensing mechanism of ZnO–Eu₂O₃ binary oxide under humid air conditions. *Sens. Actuators B: Chem.* **186**, 687–694 (2013)
- Lupan, O., Pauporté, T., Viana, B., Aschehoug, P., Ahmadi, M., Cuenya, B.R., Rudzevich, Y., Lin, Y., Chow, L.: Eu-doped ZnO nanowire arrays grown by electrodeposition. *Appl. Surf. Sci.* **282**, 782–788 (2013)
- Ahmed, S.M., Szymanski, P., El-Nadi, L.M., El-Sayed, M.A.: Energy-transfer efficiency in Eu-doped ZnO thin films: the effects of oxidative annealing on the dynamics and the intermediate defect states. *ACS Appl. Mater. Interfaces.* **6**, 1765–1772 (2014)
- Geburt, S., Lorke, M., da Rosa, A.L., Frauenheim, T., Röder, R., Voss, T., Kaiser, U., Heimbrot, W., Ronning, C.: Intense intrashell luminescence of Eu-doped single ZnO nanowires at room temperature by implantation created Eu–O_i complexes. *Nano Lett.* **14**, 4523–4528 (2014)
- Chi Tsang, S., Bulpitt, C.: Rare earth oxide sensors for ethanol analysis. *Sens. Actuators B: Chem.* **52**, 226–235 (1998)
- Postica, V., Hölken, I., Schneider, V., Kaidas, V., Polonskyi, O., Cretu, V., Tiginyanu, I., Faupel, F., Adelung, R., Lupan, O.: Multifunctional device based on ZnO: Fe nanostructured films with enhanced UV and ultra-fast ethanol vapour sensing. *Mater. Sci. Semicond. Process.* **49**, 20–33 (2016)
- Shishiyanu, S.T., Shishiyanu, T.S., Lupan, O.I.: Sensing characteristics of tin-doped ZnO thin films as NO₂ gas sensor. *Sens. Actuators B: Chem.* **107**, 379–386 (2005)
- Schütt, A., Wahl, S., Meyer, S., Hirsch, J., Lausch, D.: Fast large area reflectivity scans of wafers and solar cells with high spatial resolution. *Energy Procedia* **124**, 166 (2017)
- Hansen, S., Schütt, A., Carstensen, J., Adelung, R.: Local transmittance measurements as large area diagnostic tool for the

- optimization of porous Si foils for Li-Ion battery anodes. *J. Electrochem. Soc.* **163**, A3036 (2016)
11. Xu, X.-Y., Yan, B.: Eu(III)-functionalized ZnO@MOF heterostructures: integration of pre-concentration and efficient charge transfer for the fabrication of a ppb-level sensing platform for volatile aldehyde gases in vehicles. *J. Mater. Chem. A* **5**, 2215–2223 (2017)
 12. Allred, A.: Electronegativity values from thermochemical data. *J. Inorg. Nucl. Chem.* **17**, 215–221 (1961)
 13. Jinkawa, T., Sakai, G., Tamaki, J., Miura, N., Yamazoe, N.: Relationship between ethanol gas sensitivity and surface catalytic property of tin oxide sensors modified with acidic or basic oxides. *J. Mol. Catal. A: Chem.* **155**, 193–200 (2000)
 14. Hullavarad, Nilima V., Hullavarad, Shiva S.: Direct-vapor-phase grown IrO₂ micronanostructures for ethanol, acetone, and propanol gas sensor. *IEEE Trans. Nanotechnol.* **9**(5), 625–629 (2010)
 15. Siebert, L., Lupan, O., Mirabelli, M., Ababii, N., Terasa, M.-I., Kaps, S., Cretu, V., Vahl, A., Faupel, F., Adelung, R.: 3D-Printed chemiresistive sensor array on nanowire CuO/Cu₂O/Cu heterojunction nets. *ACS Appl. Mater. Interfaces.* **11**, 25508–25515 (2019)
 16. Lupan, O., Braniste, T., Deng, M., Ghimpu, L., Paulowicz, I., Mishra, Y.K., Kienle, L., Adelung, R., Tiginyanu, I.: Rapid switching and ultra-responsive nanosensors based on individual shell-core Ga₂O₃/GaN:O_x@SnO₂ nanobelt with nanocrystalline shell in mixed phases. *Sens. Actuators, B: Chem.* **221**, 544–555 (2015)

Effects of Heat Treatment on Palladium-Doped Zinc Oxide on Sensory Selectivity

N. Magariu

Abstract

In this paper I investigated the sensor response based on palladium-doped zinc oxide. How did the hydrogen and ethanol response change to a simple sensor that was not treated quickly and a heat treatment at 650 °C.

Keywords

Zinc oxide • Heat treatment • Gas sensor

1 Introduction

Zinc oxide is a *n*-type semiconductor with a bandgap 3.1–3.3 eV [1, 2]. However, different impurities such as titanium oxide, palladium [3], cadmium, europium, silver, iron, titanium oxide and other materials are used to modify the forbidden strip. All these changes are made to develop gas sensors that will be incorporated into various portable gas detection devices such as ammonia, methane, ethanol, hydrogen, ethanol and other gases. In this paper, sensible sensors were subjected to hydrogen and ethanol testing, in a small operating temperature range, from 150 to 225 °C.

2 Experimental

One of the most effective and inexpensive methods for making oxide based semiconductors, including zinc oxide, is the synthesis method of chemical solutions. This is a simple method which also involves doping with impurities such as palladium, silver and other impurities during the production of zinc oxide. Substrate glass on which the zinc oxide was deposited was pre-cleaned, then sensitized in

SnCl₂·2H₂O/HCl solution. To form the complex solution as starting reagents zinc sulfate is used as a cationic precursor and sodium hydroxide. All solutions of chemical reagents were of analytical purity without any further purification. The ZnSO₄ solution was gradually added to the NaOH solution which was continuously mixed with a magnetic stirrer until the solution became transparent. Doping is accomplished by introducing palladium ions into the complex solution. The surface of the glass substrate was cleaned by successive washing in acids with decontamination in distilled water. The cleaning method is widely described in the previous works [4–6]. After SCS chemical deposition of the films, rinse in deionized water and dry in a hot air stream at ~150 °C for 1 min. Fast post-growth thermal treatment is mandatory for SCS materials to improve structural, chemical and optical properties, and to diversify the scope of nanomaterials. In this paper, palladium-doped zinc oxide of the same concentration will be investigated, except that a sensor has been thermally treated at 650 °C. A layer of titanium oxide was deposited on both sensors. A nanoparticle of Ag and Pt was deposited at the sensor treated beside the titanium oxide. Both sensors were tested on hydrogen and ethanol, starting at 150 °C and finishing at 225 °C. The results obtained are shown in Fig. 1.

The following relationship was used to determine the value of the sensor response on the studied gas:

$$R = \frac{I_{gas}}{I_{air}} \quad (1)$$

Figure 1a shows the response of the palladium doped zinc oxide sensor which has been treated. It is noted that the sensor is a hydrogen selector at 175 and 200 °C and at 225 °C it also responds to ethanol, but the response to hydrogen is one higher. It is noticed that with the gradual increase of the temperature the response value increases.

Figure 1b shows the sensor response based on palladium-doped zinc oxide not subjected to thermal treatment. As with the sensor that has been treated, the hydrogen response begins to occur at 175 °C where the I_{gas}/I_{air} ratio is

N. Magariu (✉)

Department of Microelectronics and Biomedical Engineering,
Technical University of Moldova, 168 Stefan cel Mare, 2004
Chisinau, Republic of Moldova
e-mail: nicolae.magariu@mib.utm.md

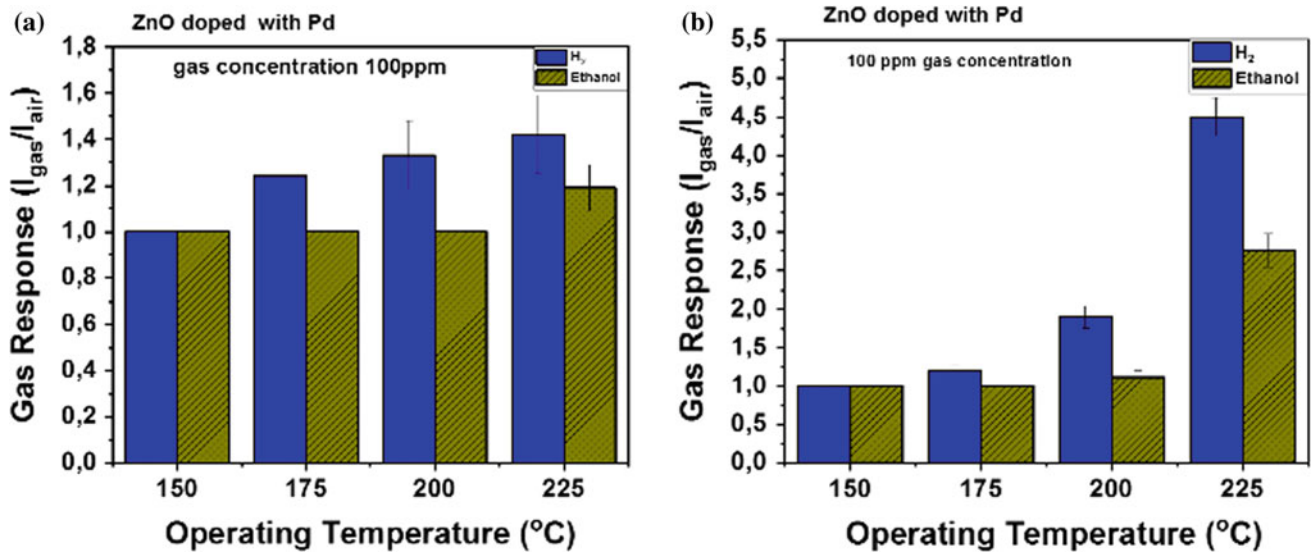


Fig. 1 The response obtained at different operating temperatures after applying the hydrogen and ethanol gases of the TiO₂/ZnO nano-heterostructures: **a** treated and **b** untreated

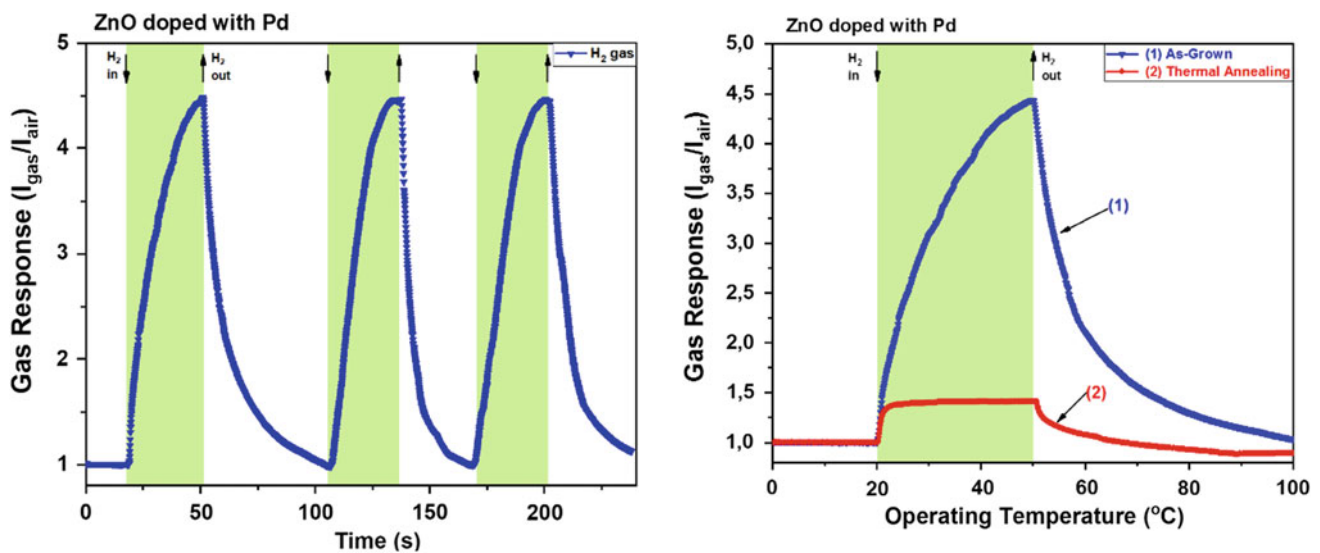


Fig. 2 Dynamic response to hydrogen at 225 °C

1.2. As temperature increases, there is a much higher increase compared to the sample treated at 650 °C. At 200 °C the ratio of 1.9 was obtained, we have an improvement of the result by 0.7 only when raising the temperature by 25 °C. By increasing the temperature by only 25–225 °C, the $I_{\text{gas}}/I_{\text{air}}$ 4.5 ratio was obtained. So within a range of 50 °C the response from 1.2 to 175 °C to 4.5 at 225 °C improved. Because the best result was determined at 225 °C at hydrogen we checked the dynamic response at that temperature. The result is shown in Fig. 2.

Fig. 3 Hydrogen response to zinc oxide gas sensing structures doped with palladium impurities: untreated (1) and treated (2)

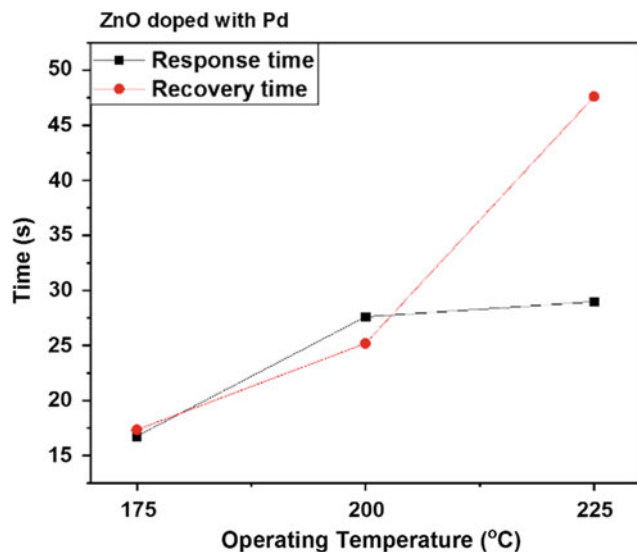
We notice that after applying the gas we obtain the same response and approximately the same response and recovery times.

To show the difference between the response to the same temperature of the treated and untreated sensor, we analyze Fig. 3.

From the given figure we can see that the zinc oxide based on the untreated zinc oxide has a higher response than the treated one, we can state that the $I_{\text{gas}}/I_{\text{air}}$ response value is 1.4 at the treated sensor and the untreated sensor is 4.5.

Table 1 Indication of response and recovery times of the sensor based on untreated zinc oxide

Operating temperature (°C)	Response time (s)	Recovery time (s)
150	–	–
175	16.77	17.34
200	27.61	25.19
225	28.98	47.62

**Fig. 4** Response and recovery times to operating temperature

Because the best response is to the untreated sensor, we calculate the response and recovery time. The response time is 90% of the maximum response. We will show the values obtained in Table 1.

Based on the results obtained, we build Fig. 4.

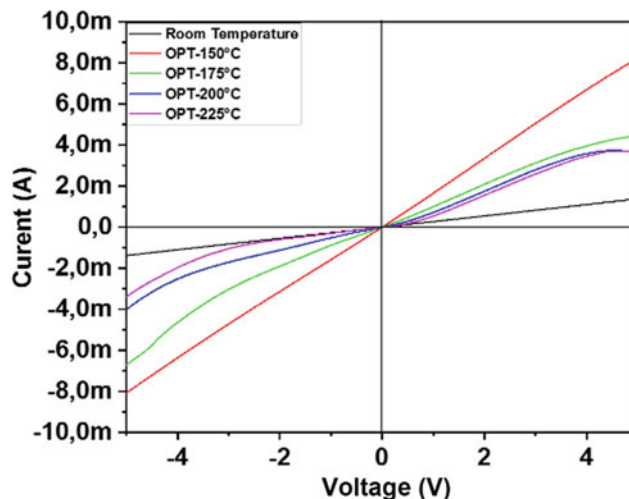
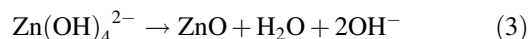
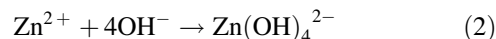
From Fig. 4 we can see that the reaction times at 200 and 225 °C are practically the same, the difference is 1.37 s.

To see how the current-voltage characteristics change for each temperature, look at Fig. 5.

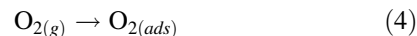
Figure 5 shows the current-voltage characteristic of the untreated sensor at different operating temperatures. From this we can mention that the operating characteristic of the 150 °C is linear and the temperature increases the formation of the Schottky contacts [7]. The best highlight is at 225 °C. We notice that the behavior of the sensor changes also in a small operating temperature range.

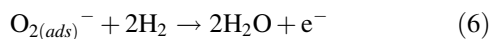
Hydrogen Gas-Sensing Mechanism

The gaseous reaction of zinc oxide is dependent, the type of defects and impurities. Thus, surface phenomena have an important role to play in understanding the gas detection mechanism for n-type semiconductors. Chemical equations for zinc oxide production can be described using the following relation:

**Fig. 5** Current voltage characteristic of the untreated film at different operating temperatures

This can be found from Eqs. 2 and 3, that during the hydrothermal reaction an intermediate product of zinc hydroxide is formed and decomposes into many small nuclei of ZnO, which further develop into nanodules. By adding Pd in the zinc oxide component, an increase in the active surface for interaction with hydrogen. The Pd–ZnO referral mechanism can be assigned 2 factors [8]: The first is the interaction of the palladium particles with hydrogen molecules, which leads to the formation of PdH_x [9] to obtain a lower function (Φ) than pure Pd nanoparticles and to further accelerate the free electrons in the Pd transfer to the p-n heterojunction. The second factor can be described as follows: the oxygen molecules absorbed on the ZnO conduction band are ionized to single-negative oxygen ions by capturing free electrons on the surface of ZnO. Reactions can be described in the following way [8]:





The reaction has occurred between the Pd particles with hydrogen, which will lead to increased conductivity and will reduce the working function, resulting in the diminution of the height of the Schottky potential barrier. In this way, the electric charge will be easily transferred to the p-n heterojunction.

On the one hand, when the sensor is exposed to hydrogen, the active reaction of the negative ions with oxygen can reduce the width of the depletion layer through which the electron travels from the high Fermi level to the low level, showing a decrease in sensor resistance. On the other hand, when hydrogen comes out of the sensor surface, the width of the depletion layer will recover and will increase resistance. Thus modulation of p-n heterojunction plays an important role in improving the hydrogen detection properties of Pd doped zinc oxide [8].

3 Conclusions

In this paper, Pd-based gas sensors were investigated with the same concentration of Pd. It has been observed that the best response is to hydrogen at the sensor which has not been thermally treated. Both sensors began to respond to an operating temperature of 175 °C. And at 225 °C the untreated sensor had a response that was determined using the $I_{\text{gas}}/I_{\text{air}} = 4.5$ ratio. It has been observed that the response times at temperatures of 200 and 225 °C are approximately equal.

Acknowledgements Magariu Nicolae, thanks to Mr. Professor dr.hab. Lupan Oleg for active support and guidance. The research was partly

funded by the Technical University of Moldova and the institutional project inst-15.817.02.29A.

References

1. Srikant, V., Clarke, D.R.: On the optical band gap of zinc oxide. *J. Appl. Phys.* **83**(10), 5447–5451 (1998)
2. Ortega, J.J., Aguilar-Frutos, M.A., Alarco'n, G., Falcony, C., Me'ndez-García, V.H., Araiza, J.J.: Band gap engineering of indium zinc oxide by nitrogen incorporation. *Mater. Sci. Eng. B* **187**, 83–88 (2014)
3. Lupan, O., Postica, V., Hoppe M., Wolff, N., Polonskyi, O., Pauporté, T., Viana, B., Majérus, O., Kienle, L., Faupel, F., Adelung, R.: PdO/PdO₂ functionalized ZnO : Pd films for loweroperating temperature H₂ gas sensing. *Nanoscale* **10**, 14107–14127
4. Xu, C.K., Liu, Y.K., Xu, G.D., Wang, G.H.: Preparation and characterization of CuO nanorods by thermal decomposition of Cu₂O₄ precursor. *Mater Res Bull* **37**, 2365–2372 (2002)
5. Lupan, O., Cretu, V., Postica, V., Polonskyi, O., Ababii, N., Schütt, F., Kaidas, V., Faupel, F., Adelung, R.: Non-planar nanoscale p-p heterojunctions formation in ZnxCu_{1-x}O_y nanocrystals by mixed phases for enhanced sensors. *Sens Actuators B Chem* **230**, 832–843 (2016)
6. Lupan, O., Chow, L., Shishiyanu, S., Monaico, E., Shishiyanu, T., Şontea, V., Roldan, Cuenya B., Naitabdi, A., Park, S., Schulte, A.: Nanostructured zinc oxide films synthesized by successive chemical solution deposition for gas sensor applications. *Mater. Res. Bull.* **44**, 63–69 (2009)
7. Siebert, L., Lupan, O., Mirabelli, M., Ababii, N., Terasa, M.-I., Kaps, S., Cretu, V., Vahl, A., Faupel, F., Adelung, R.: 3D-printed chemiresistive sensor array on nanowires CuO/Cu₂O/Cu heterojunction net. *ACS Appl. Mater. Interfaces* (2019)
8. Yan'e, S., Dongzhi, Z., Hongyan, C., Yong, Z.: Fabrication of palladium–zinc oxide–reduced graphene oxide hybrid for hydrogen gas detection at low working temperature. *J. Mater. Sci. Mater. Electron* <https://doi.org/10.1007/s10854-016-5710-z>
9. Phan, D.T., Chung, G.S.: Reliability of hydrogen sensing based on bimetallic Ni–Pd/graphene composites. *Int. J. Hydrogen Energy* **39**, 20294–20304 (2014)

Mechanical and Wetting Properties of Three-Dimensional Flexible Tetrapodal ZnO Networks ALD-Coated with Al₂O₃

A. Gapeeva, M. T. Bodduluri, S. Kaps, F. Rasch, B. Wagner, R. Adelung, and O. Lupan

Abstract

Nano- and microscale tetrapodal shaped ZnO particles (T-ZnO) are considered to be truly multi-functional and have a tremendous potential for a large variety of applications ranging from gas/vapor sensors to biomedical implants. In this approach highly porous interconnected networks were formed from T-ZnO particles produced by the versatile flame transport synthesis (FTS) at Kiel University and coated by Al₂O₃ with different film thicknesses by atomic layer deposition (ALD) technique. Presence of Al₂O₃ inside the network was confirmed by the energy-dispersive X-ray spectroscopy (EDX). Compression tests showed that with increasing Al₂O₃ coating thickness mechanical properties were significantly improved, e.g. the Young's modulus of networks with a T-ZnO density of 0.5 g/cm³ was raised from 1.0 ± 0.3 MPa (pure T-ZnO) to 1.80 ± 0.2 MPa when coated with 60 nm Al₂O₃, whereby the elastic limit (yield strength) was increased by a factor of two as well. Contact angle (CA) measurements revealed that switching of wetting properties from super hydrophilic (water droplet is rapidly sucked into the network) to super hydrophobic (water droplet lies on the surface with CA = 142° ± 2°) is possible depending on the hydration state of Al₂O₃. The successful combination of T-ZnO and Al₂O₃ can further broaden the application range of T-ZnO particles, e.g. for humidity detection as well as in the field of bio-electronic devices.

Keywords

Tetrapodal zinc oxide • Aluminium oxide • Atomic layer deposition • Flexible ceramics • Wettability switching

1 Introduction

ZnO is a direct wide gap metal oxide semiconductor and belongs to the ceramic class. Tetrapodal shaped ZnO (T-ZnO) particles (Fig. 1) attracted large attention due to their flexibility and light weight compared to the bulk form which results from the high aspect ratio (length/diameter) of T-ZnO arms and therefore large surface-to-volume ratio of the network [1]. Pure T-ZnO as well as alloyed T-ZnO networks have already been successfully integrated in various nanosensors, e.g. for gas and vapor detection [2–4]. Moreover, T-ZnO particles can be used as filler particles or scaffolds for creating novel composite materials and as a sacrificial template for production of porous 3D microstructures from other materials [5–7]. Combining unique properties of T-ZnO with aluminium oxide, which is a well-proven biocompatible ceramic [8] with excellent insulating properties may provide a large span of new applications, such as, for example, a protective coating in order to prevent electrical leakage for devices intended for implantation [9]. Thereby atomic layer deposition (ALD) is a method of choice for coating complex 3D structures like a T-ZnO network.

2 Materials and Methods

2.1 Sample Preparation

T-ZnO particles were synthesized by the FTS process [3] in a furnace (ROHDE GmbH) at 900 °C with a growth time of 20 min. Particles were then uniaxially compressed inside a

A. Gapeeva (✉) · S. Kaps · F. Rasch · R. Adelung · O. Lupan
Functional Nanomaterials, Institute for Materials Science, Kiel University, Kaiserstr. 2, Kiel, 24143, Germany
e-mail: ang@tf.uni-kiel.de

M. T. Bodduluri · B. Wagner
Materials and Processes for Nanosystem Technologies, Institute for Materials Science, Kiel University, Kiel, Germany

O. Lupan
Department of Microelectronics and Biomedical Engineering, Technical University of Moldova, Chisinau, Republic of Moldova

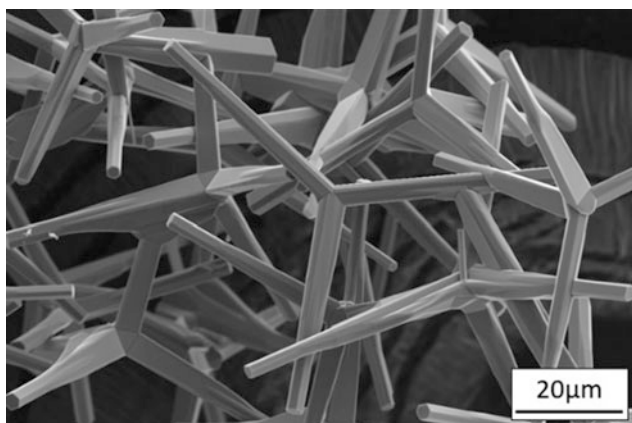


Fig. 1 SEM image of T-ZnO particles produced by the FTS process at Kiel University

cylindrical metal mold to form templates of 3 mm height and 6 mm diameter. By varying the amount of T-ZnO particles, templates with three different densities (0.3 , 0.4 and 0.5 g/cm^3) were produced and then sintered at $1150 \text{ }^\circ\text{C}$ for 5 h in a furnace (Nabertherm GmbH) in order to achieve an interconnected network.

Al_2O_3 deposition was carried out using the Picosun's R-200 series thermal ALD system. In this study, two film thicknesses (25 nm and 60 nm) of Al_2O_3 were realized by depositing alternating precursor pulses of trimethylaluminum (TMA) and H_2O at the chamber temperature of $300 \text{ }^\circ\text{C}$. The measured growth is 0.11 nm/cycle . PicoflowTM diffusion enhancer mode was employed in order to enable conformal 3D coating of T-ZnO particles.

2.2 SEM/EDX

To verify the presence of the Al_2O_3 inside the networks, T-ZnO/ Al_2O_3 samples were cut in the middle and investigated by means of SEM/EDX. Studies were conducted with the ZEISS ULTRA PLUS microscope with the GEMINI column (Carl Zeiss Microscopy GmbH, Jena, Germany) equipped with a EDX analysis system from Oxford Instruments. Measurements were performed at accelerating voltage of 20 kV.

2.3 Compression Tests

Mechanical tests of pure T-ZnO as well as T-ZnO/ Al_2O_3 samples were performed. Compression test setup and the corresponding software used for this work were developed at the Institute for Material Science, Kiel University. The samples were compressed using a rate of 0.05 mm/s speed. A typical stress-strain curve for a pure T-ZnO network is

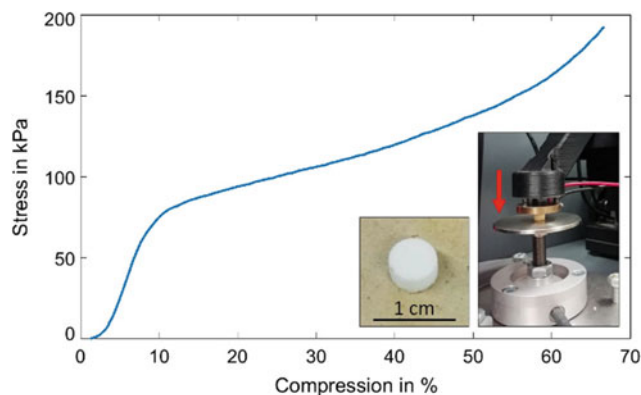


Fig. 2 Exemplary stress-strain curve of a sintered T-ZnO network with a density of 0.5 g/cm^3 . In the inset a typical T-ZnO sample and its arrangement during the compression test are shown

shown in Fig. 2, whereby same characteristics were observed for coated networks. A small non-linear region at the beginning of the compression curve is due to the initial contact establishment between a sample, which doesn't have a perfectly flat surface, and the pressure plate [10]. After a whole sample surface is in contact, a linear region of elastic deformation can be observed. For a proper comparison of compression curves, the beginning of the linear region was shifted to 0% compression using a MATLAB[®] routine for all curves. Since the yield point is not clearly distinguishable from the graph, the yield strength was calculated at 0.2% plastic strain. Because no rupture occurred during the compression test, the stress at 50% compression was calculated from the fitted curve for the evaluation of the compression strength. For each variation three samples were tested. Measurement errors of the compression setup are $\Delta t = 10^{-4} \text{ s}$ and $\Delta F = 10^{-5} \text{ N}$ and are insignificant for the measured values range.

2.4 Contact Angle (CA) Measurements

Wetting properties of the samples were evaluated by the sessile drop technique using a custom-made setup. For the experiments distilled water and a drop volume of $3 \mu\text{l}$ were used. For each material variation five measurements were conducted in order to obtain an average value. The samples were investigated before and after drying for 2 h in a vacuum furnace (Heraeus Instruments GmbH) at $50 \text{ }^\circ\text{C}$.

3 Results and Discussion

3.1 SEM/EDX

Investigation of T-ZnO/ Al_2O_3 samples by means of SEM revealed a smooth uniform surface of coated tetrapods,

Fig. 3 SEM micrograph of a T-ZnO/Al₂O₃ sample with 60 nm Al₂O₃ and a corresponding EDX element map

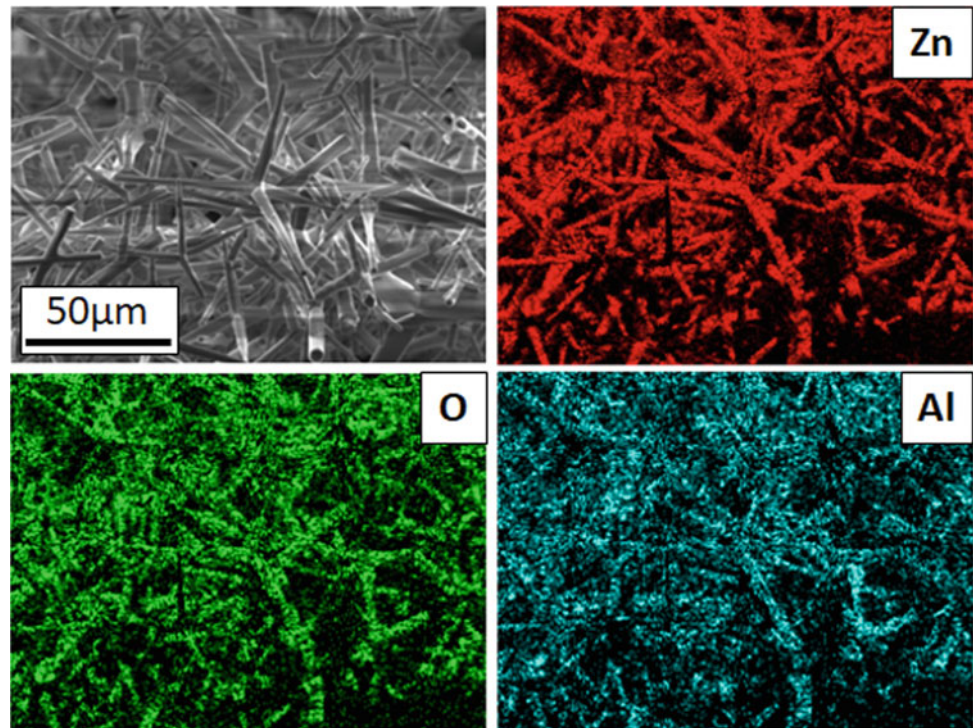


Table 1 Element composition of T-ZnO/Al₂O₃ samples from EDX analysis

Al ₂ O ₃ thickness (nm)	Composition (wt.%)		
	Zn	O	Al
60	64.3	24.9	10.8
25	72.4	22.1	5.5

which is typical for a Al₂O₃ film deposited by ALD [11]. The presence of Al₂O₃ coating on top of the T-ZnO particles was confirmed by the EDX-analysis. For the sample with 60 nm Al₂O₃ (Fig. 3) 10.8 wt.% of Al was detected while for the sample with 25 nm Al₂O₃ the amount of detected Al was decreased to 5.5 wt.%. The exact sample composition is given in Table 1.

3.2 Compression Tests

Evaluation of mechanical properties of T-ZnO/Al₂O₃ samples showed an overall performance improvement of networks with increasing Al₂O₃ film thickness.

While the Young's modulus for pure T-ZnO networks amounted to 0.4 ± 0.1 MPa, 0.7 ± 0.1 MPa and 1.0 ± 0.3 MPa for T-ZnO densities of 0.3 g/cm^3 , 0.4 g/cm^3 and 0.5 g/cm^3 respectively, networks coated with 25 nm and 60 nm Al₂O₃ revealed values which were up to two times higher (Fig. 4). The highest value (1.8 ± 0.2 MPa) was

obtained for T-ZnO/Al₂O₃ samples with 0.5 g/cm^3 T-ZnO density and 60 nm coating.

Coated networks exhibited a significant increase in the yield strength compared to uncoated networks as can be seen from Fig. 5. Yield point of pure T-ZnO samples ($\rho_{\text{T-ZnO}} = 0.3\text{--}0.5 \text{ g/cm}^3$) was increased from 18 ± 2 kPa, 33 ± 6 kPa and 65 ± 4 kPa to 24 ± 2 kPa, 69 ± 13 kPa and 101 ± 1 kPa respectively when coated with 25 nm Al₂O₃. In

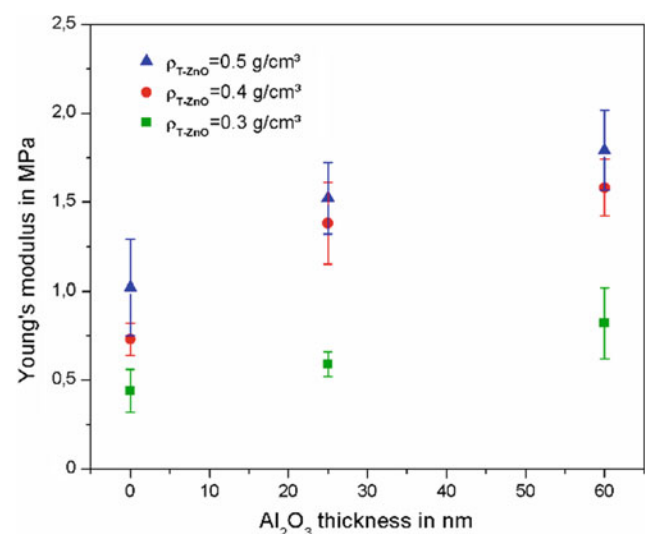


Fig. 4 Young's modulus as a function of Al₂O₃ coating thickness on T-ZnO

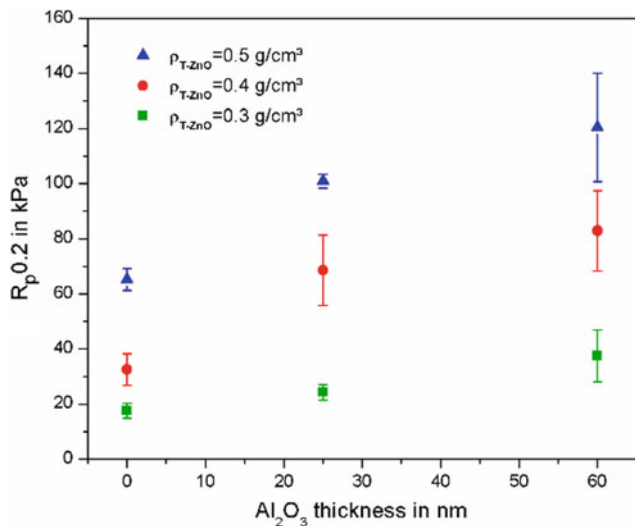


Fig. 5 Yield strength as a function of Al₂O₃ coating thickness on T-ZnO

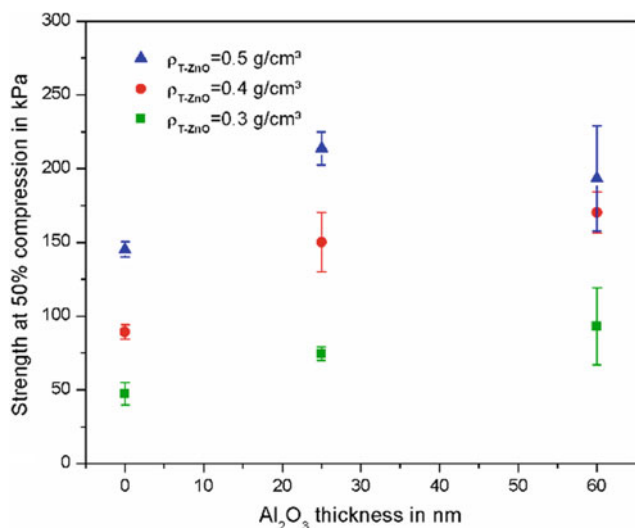


Fig. 6 Compressive strength at 50% load as a function of Al₂O₃ coating thickness on T-ZnO

case of a 60 nm coating, the yield strength was approx. twice that of corresponding uncoated networks of the same density.

Calculation of compressive strength values at 50% load showed as well that a thin Al₂O₃ coating contributes to a mechanical stability of the network (Fig. 6). Even though the difference between 25 and 60 nm coatings is less pronounced, an overall increase of compressive strength in comparison to pure T-ZnO networks can be stated.

Obtained results for mechanical performance of 3D networks are highly important for technological applications where flexible ceramics are desirable.

3.3 Contact Angle (CA) Measurements

Water droplets placed on T-ZnO/Al₂O₃ samples were observed to sink into the network independent on the Al₂O₃ coating thickness, which indicates a hydrophilic state of the surface. However, after drying inside a vacuum oven for 2 h, samples revealed a super hydrophobic (water-repellent) behavior, where the droplet stayed on the surface and the measured CA amounted to $142^\circ \pm 2^\circ$.

For comparison, a 60 nm Al₂O₃ film was deposited on a MenzelTM microscope glass slide. CA measurements conducted on this sample revealed an average CA of $66^\circ \pm 3^\circ$, which clearly lies within the hydrophilic range. After a heat-treatment under vacuum, the wetting state of the surface switched from hydrophilic to hydrophobic ($92^\circ \pm 1^\circ$). The difference in wettability states before and after the treatment in the vacuum oven can be attributed to a difference in the hydration state of the Al₂O₃ surface [12].

From results which are summarized in Table 2 and shown in Fig. 7, it can be concluded that due to a high roughness of

Table 2 Contact angle measurements of a 60 nm Al₂O₃ film on a rough (T-ZnO) and a smooth (glass slide) surfaces before and after a heat treatment under vacuum

Substrate for Al ₂ O ₃ coating	Contact angle (CA)	
	Before	After
T-ZnO	Droplet sucked into the template	$142^\circ \pm 2^\circ$
Glass slide	$66^\circ \pm 3^\circ$	$92^\circ \pm 1^\circ$

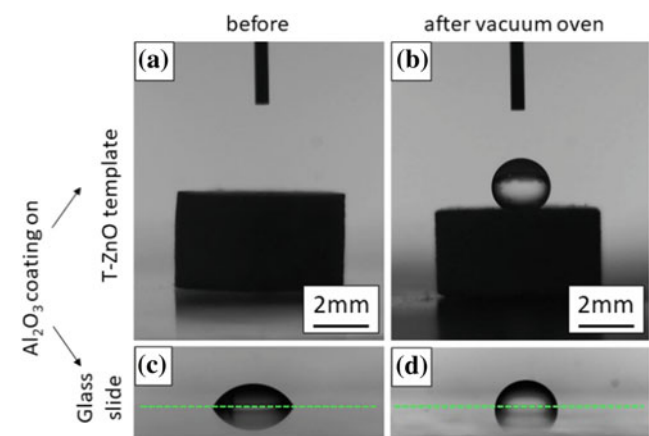


Fig. 7 Contact angle measurements before and after a heat treatment under vacuum: **a, b** T-ZnO/Al₂O₃ samples: before treatment the droplet is sucked into the network while after treatment the droplet stays on the surface. **c, d** Al₂O₃ coating on a MenzelTM microscope glass slide (green line indicates a glass slide surface): before treatment the surface shows a hydrophilic and after treatment a hydrophobic behavior

the surface given by the T-ZnO geometry, the initial wettability state of Al₂O₃ is enhanced, which is a well-known phenomenon [13, 14]. Therefore, the enhancement of wetting properties of Al₂O₃ leads to either super hydrophilic or super hydrophobic behavior depending on the hydration state.

4 Conclusion

Nanometer thin films of Al₂O₃ (25 and 60 nm) were successfully deposited on T-ZnO networks of three different densities (0.3, 0.4, 0.5 g/cm³) by ALD technique. The presence of a conformal Al₂O₃ film inside the networks was confirmed by SEM/EDX analysis. Compression tests revealed that a Al₂O₃ coating improves the mechanical performance of the network to a great extent. High roughness given by the tetrapodal shape of ZnO particles constituting the networks allows a switching of wettability properties depending on the hydration state of a Al₂O₃ film.

Conflict of Interest The authors declare that they have no conflict of interest.

References

- Paulowicz, I., Hrkac, V., Kaps, S., Cretu, V., Lupan, O., Braniste, T., Duppel, V., Tiginyanu, I., Kienle, L., Adelung, R., Mishra, Y. K.: Three-dimensional SnO₂ nanowire networks for multifunctional applications: from high-temperature stretchable ceramics to ultrasensitive sensors. *Adv. Electr. Mater.* **1**(8), art. no. 1500081 (2015)
- Paulowicz, I., Postica, V., Lupan, O., Wolff, N., Shree, S., Cojocar, A., Deng, M., Mishra, Y.K., Tiginyanu, I., Kienle, L., Adelung, R.: Zinc oxide nanotetrapods with four different arm morphologies for versatile nanosensors. *Sens. Actuators, B Chem.* **262**, 425–435 (2018)
- Mishra, Y.K., Modi, G., Cretu, V., Postica, V., Lupan, O., Reimer, T., Paulowicz, I., Hrkac, V., Benecke, W., Kienle, L., Adelung, R.: Direct growth of freestanding ZnO tetrapod networks for multifunctional applications in photocatalysis, UV photodetection, and gas sensing. *ACS Appl. Mater. Interfaces* **7**(26), 14303–14316 (2015)
- Lupan, O., Postica, V., Gröttrup, J., Mishra, A.K., De Leeuw, N. H., Carreira, J.F.C., Rodrigues, J., Ben Sedrine, N., Correia, M.R., Monteiro, T., Cretu, V., Tiginyanu, I., Smazna, D., Mishra, Y.K., Adelung, R.: Hybridization of zinc oxide tetrapods for selective gas sensing applications. *ACS Appl. Mater. Interfaces* **9**(4), 4084–4099 (2017)
- Taale, M., Schütt, F., Zheng, K., Mishra, Y.K., Boccaccini, A.R., Adelung, R., Selhuber-Unkel, C.: Bioactive carbon-based hybrid 3D scaffolds for osteoblast growth. *ACS Appl. Mater. Interfaces.* **21**(6), 43874–43886 (2018)
- Qiu, H., Hölken, I., Gapeeva, A., Filiz, V., Adelung, R., Baum, M.: Development and characterization of mechanically durable silicone-polythiourethane composites modified with tetrapodal shaped ZnO particles for the potential application as fouling-release coating in the marine sector. *Materials (Basel)* **11** (12) (2018)
- Mishra, Y.K., Adelung, R.: ZnO tetrapod materials for functional applications. *Mater. Today* **21**(6), 631–651 (2018)
- Al-Sanabani, F.A., Madfa, A.A., Al-Qudaimi, N.H.: Alumina ceramic for dental applications: a review article. *Am. J. Mater. Res.* **1**(1), 26–34 (2014)
- Schulman, J.H., Lucisano, J.Y., Shah, R., Byers, S.M.P.: Alumina insulation for coating implantable components and other micro-miniature devices. U.S. Patent 6,844,023 B2 (2005)
- Gröttrup, J., Paulowicz, I., Schuchardt, A., Kaidas, V., Kaps, S., Lupan, O., Adelung, R., Mishra, Y.K.: Three-dimensional flexible ceramics based on interconnected network of highly porous pure and metal alloyed ZnO tetrapods. *Ceram. Int.* **42**(7), 8664–8676 (2016)
- Elam, J.W., George, S.M.: Growth of ZnO/Al₂O₃ alloy films using atomic layer deposition techniques. *Chem. Mater.* **15**(4), 1020–1028 (2003)
- Nahar, R.K., Khanna, V.K., Khokle, W.S.: On the origin of the humidity-sensitive electrical properties of porous aluminium oxide (sensor application). *J. Phys. D Appl. Phys.* **17**(10), 2087–2095 (1984)
- Wenzel, R.N.: Resistance of solid surfaces to wetting by water. *Ind. Eng. Chem.* **28**(8), 988–994 (1936)
- Cassie, A.B.D., Baxter, S.: Wettability of porous surfaces. *Trans. Faraday Soc.* **40**, 546–551 (1944)

Polarization Holographic Recording on Photosensitive Polymers

E. Achimova, V. Abaskin, A. Meshalkin, A. Prisacar, L. Loghina, M. Vlcek, and A. Yakovleva

Abstract

In this paper we report on direct holographic recording of surface relief gratings in carbazole-based polymers. Evolution of the transmittance spectrum and diffraction efficiency upon irradiation with 532 nm laser light demonstrated the photo-induced surface patterning of gratings.

Keywords

Azopolymer • Chalcogenide quantum dots • Holographic recording • Surface relief grating • Diffraction efficiency

1 Introduction

Hybrid organic/inorganic materials represent a multidisciplinary area where both academic and application driven research has exploded in the last two decades [1]. Functional hybrid nanocomposites are characterized by versatility in morphological, chemical, and physical properties. They are thus serious candidates for applications, such as optics, photonics, functional and protective coatings, sensing, and biomaterials. The number of articles on applications of hybrid nanocomposites (HN) in holographic recording has been significantly increasing and many are dedicated to the incorporation of quantum dots (QD) of different sizes and composition in conventional photosensitive materials [2].

Since the first observation of surface relief grating (SRG) formation in azobenzene containing photosensitive polymer films in 1995 [3], a wide variety of novel and highly efficient azobenzene containing photosensitive polymers

have been synthesized. The driving mechanism SRG formation is the cyclic photo-isomerization of the azobenzene molecules that undergo reversible transition from trans- to cis-conformation. The photoinduced patterns of surface deformations are determined by the state of the incident light polarization and the light intensity distribution [4].

A surface relief, which is due to a photoinduced mass movement of the azopolymer, is produced by an interference pattern of light. Azo dyes are optical materials that allow us to manipulate their optical characteristics through photoisomerization and following chemical and physical processes initiated by absorption of polarized light. It is possible to form variable patterns of optical constant by irradiating interfering light beams that lead to birefringence, density modulation and surface relief grating. Their properties depend on characteristics of the illumination (intensity, wavelength, polarization, periodicity of the interference pattern) and the parameters of polymers such as molecular structure and weight, matrix type and modes of incorporation (guest–host, side-chained and so on), the substituent of the azobenzene ring and their concentration within the film thickness.

The first azopolymer-inorganic material HN “azopolymer—porous glass” in which the photoinduced anisotropy has been studied was reported by Reshetnyak et al. [5]. Different functional composite materials were fabricated in the past few years by combining azo-benzene derivatives with inorganics [6] including azobenzene/noble metal (Ag or Au) composites, and these composites showed novel properties. For example, Zhou et al. [7] doped silver NP in polymer containing azo group and methyl methacrylate to find that at certain wavelengths (namely 442 nm) there is a considerable increase in the value of the photoinduced transmittance.

SRG formation can be controlled during the recording by measuring the kinetics of diffraction efficiency (DE). The DE measurement probes photo-induced amplitude and phase gratings in the film during holographic irradiation. The analyses of these phenomena indicate that photoinduced organization of molecules plays an important role in the formation of phase topography.

E. Achimova (✉) · V. Abaskin · A. Meshalkin · A. Prisacar
Institute of Applied Physics, Academiei Street, 5, Chisinau,
Moldova
e-mail: achimova@phys.asm.md

L. Loghina · M. Vlcek · A. Yakovleva
Pardubice University, Pardubice, Czech Republic

The main purpose of this work consists in the study of new photosensitive QD-doped azopolymers for one step relief formation of gratings by using polarization holography. As soon as this technique was reported, a procedure for post-modification of polymer chains of epoxypropyl carbazole-containing oligomer was suggested. In fact, the end- group of oligomer can be transformed into amine substituted azopolymers. New photosensitive azopolymer based on carbazole-containing oligomer with azo dye Disperse Orange 3 (PEPC-*co*-DO) and doped Cd_{0.2}Zn_{0.8}Se QDs was synthesized. Semiconductor ternary Cd_{0.2}Zn_{0.8}Se QDs was synthesized according to modified procedure described earlier [8]. In this work optical and holographic recording properties of the films deposited on glass substrates were studied. Holographic grating formation in interference patterns were investigated by in situ DE measurement. We studied the photosensitive properties of the PEPC-*co*-DO with and without Cd_{0.2}Zn_{0.8}Se QDs in dependence on polarization states of recording beams.

2 Materials and Methods

All chemicals were purchased from Sigma-Aldrich and used without further purification. Solvents were procured from Fisher Scientific and used for purification of QDs and for spin coating. Air- and/or moisture-sensitive chemicals were handled in Ar atmosphere, syntheses of QDs were carried out with a standard Schlenk line under an inert atmosphere. Synthesis of ternary Cd_{0.2}Zn_{0.8}Se QDs was performed in organic disperse medium in non-coordinating solvent 1-octadecene at 280 °C. As a selenium source was taken trioctylphosphine selenide. Purified QDs were characterized by all known methods, including transmission electron microscopy (TEM) and optical measurements.

According to TEM measurements (Fig. 1) average size of synthesized Cd_{0.2}Zn_{0.8}Se QDs is 3.5 nm. Furthermore,

uniformity of prepared QDs was confirmed by photoluminescence (PL) and absorbance spectra (Fig. 2).

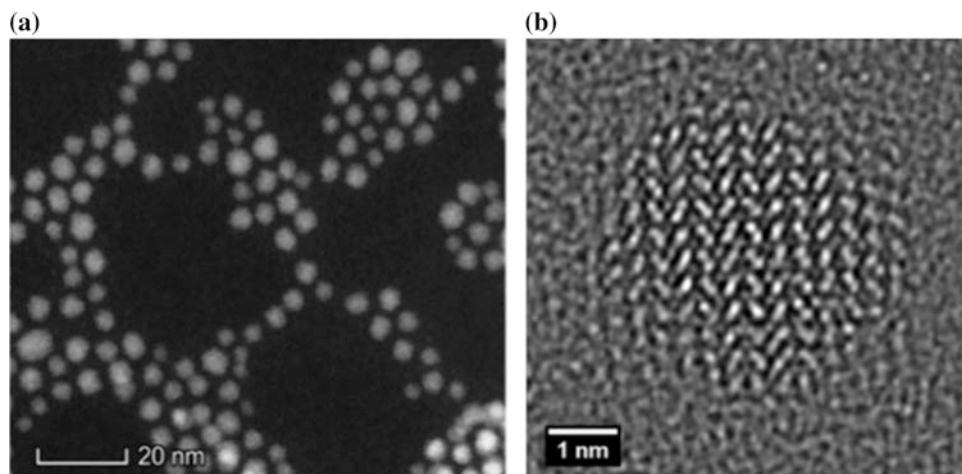
The wide excitation band with a maximum of 445 nm, the position of the first exciton maximum, and the emission band with a maximum wavelength of 523 nm correlate with the absorption maximum of the azo dye DO ($\lambda_{\text{max}} = 443$ nm) (Fig. 2).

To obtain a copolymer of PEPC-*co*-DO, DO (0.3 g) and PEPC (1.0 g) the chemicals were boiled in 8 ml of toluene for 6 h. After cooling to room temperature, the resulting mixture was filtered. The transparent filtrate without dilution was used for coating films by spin-coater. To develop HN the Cd_{0.2}Zn_{0.8}Se QDs (5 wt.%) were added to the carbazole-containing oligomer PEPC-*co*-DO. Thin azopolymer films were obtained in equal conditions by spin-coating of initial and diluted solution under 500 rpm for 30 s and dried (1 h at 60 °C). The thicknesses of dried films were measured by high-precision interference microscopy.

An interferometric method of holographic recording was used to record gratings on the HN like described in [9]. The SRG formation experiments were performed using different polarization states of recording beams (Fig. 3). The period of the grating $d = \lambda / (2 \sin \alpha)$, where λ is the wavelength of laser beam, α is the angle between the incidence laser beams. CW DPSS single mode laser operated at wavelength $\lambda = 532$ nm and averaged spot power density from 150 up to 350 mW/cm² on the sample was used for recording. The intensity ratio 1:1 of the recording beams was used in order to achieve maximum interference fringes contrast. Two symmetrical angled laser beams respecting to the sample surface normal recorded the holographic gratings with various periods (Λ). The angle between the two interfering beams in this experiment has been chosen like that the period of grating was 5.0 μm . The image of recorded grating is on the inset on Fig. 3.

We distinguish between two forms of recording: scalar process (intensity holography), resulting in intensity gratings

Fig. 1 TEM in dark field (a) and high-resolution HR-TEM (b) images of Cd_{0.2}Zn_{0.8}Se QDs prepared in organic disperse medium



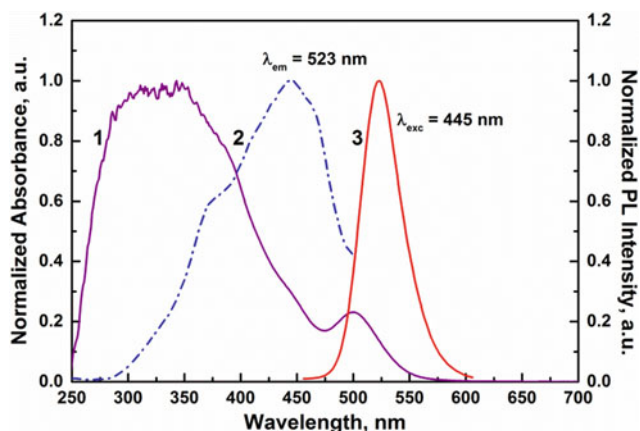


Fig. 2 Optical properties of $\text{Cd}_{0.2}\text{Zn}_{0.8}\text{Se}$ QDs prepared in organic disperse medium: absorbance (1); excitation at $\lambda_{\text{exc}} = 523$ nm (2); emission at $\lambda_{\text{em}} = 445$ nm (3)

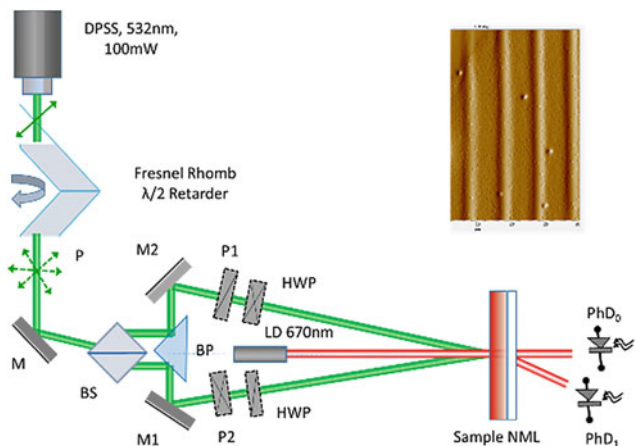


Fig. 3 Optical arrangement for holographic grating recording with real-time measurement of diffraction efficiency by photodiodes. CW DPSS laser ($\lambda = 532$ nm, power = 100 mW), M, M1, M2—mirrors; BP—right-angle prism with Al coating; BS—beam splitter; LD—laser diode ($\lambda = 650$ nm) for monitoring of the recording process; P1, P2—polarization plates; HWP—halfwave plates; PhD₀, PhD₁—photodetectors

and polarization holography (with a periodic variation of the polarization); resulting in polarization gratings recording. So the spatial modulation period means the intensity modulation period.

The interference pattern of two coherent waves with two parallel linear polarizations (SS, PP) has a largest periodically modulated intensity when the contrast of an interference pattern is close to 1, but a polarization state is no spatial modulation in the direction of the resultant electrical vector. In case of orthogonal linear $\pm 45^\circ$ and circular RL polarizations, the interference pattern has a small modulated intensity and is uniform over the entire exposed area. However, these polarizations ($\pm 45^\circ$ and RL) produce the

largest periodically modulation in the resultant electrical field direction on the film surface. Very small DE and surface relief modulation were obtained for SP polarization states. For this configuration, there is no component of resultant electric vector of light along the grating vector direction.

The quarter wave plates were mounted on rotation mounts. The phase shift experiments were performed by angular adjustment the quarter wave plates in each optical path, therefore, we can change the state of polarization of both recording beams. The two interfering beams independently pass through phase turning quarter wave plates to provide a control over the polarization state of the writing beams. Interfering beams with PP, SS, LR or $\pm 45^\circ$ polarization combinations were used for SRG recording.

In our work during the holographic recording, the linear polarized laser (P-polarization) at wavelength of 650 nm was directed to the sample at normal incidence to serve as the probe beam. The zero-order and first-order diffraction intensities of sample were monitored in situ to diagnose the kinetics of grating formation. First-order of DE η is defined $\eta = \frac{I_1}{2I_1 + I_0} * 100\%$, where I_1 is the light intensity diffracted in first diffraction order, I_0 is light intensity in zero-order diffraction. I_1 and I_0 intensities were measured with two silicon photodiodes equipped with amplifiers. Since this wavelength is outside the absorption region, only a phase holographic recording was considered by DE measurement. The higher diffraction intensity implies the larger phase modulation of recorded grating.

After the completion of recording the grating, the Atomic Force Microscopy (AFM) was employed to measure the surface relief of recorded structures.

3 Results and Discussion

The dependence of DE on recording time for all of the studied polarization configurations is shown in Fig. 4. Holographic recording was performed on PEPC-co-DO with $\text{Cd}_{0.2}\text{Zn}_{0.8}\text{Se}$ QDs film where the concentration of azo dye 30 wt%. As it can be seen in the Fig. 4, the DE strongly depends on the polarization configuration. The best performance is reached at LR and $\pm 45^\circ$ polarization configurations. For all polarization configurations, the diffraction efficiency versus time has increased and eventually reached a relatively steady state during the exposure.

This can result in a periodic modulation of the refractive index as well as periodic modulation of film thickness. The phase delay amplitude of such type of grating can be written as $\Delta\varphi = \frac{2\pi}{\lambda \cos \alpha} \cdot (h \cdot (n - 1) + d \cdot \Delta n)$, where λ is the probe wavelength, h —amplitude of surface modulation, n is the average refractive index of azopolymer, d is film thickness,

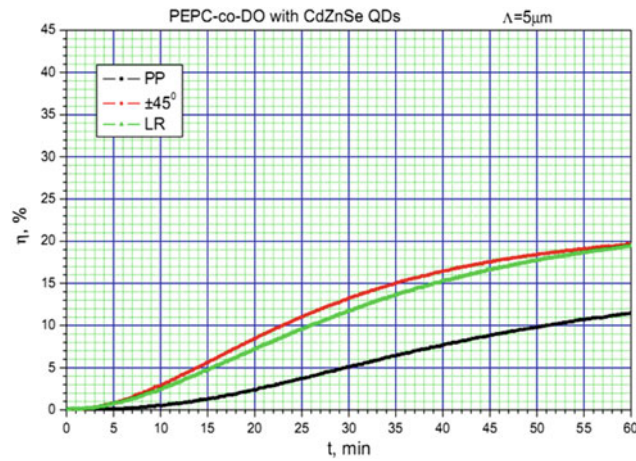


Fig. 4 The dependence of diffraction efficiency in transmission mode on recording time for the all studied polarization configurations using PEPC-*co*-DO with Cd_{0.2}Zn_{0.8}Se QDs film and the concentration of azodye 30 wt.%

Fig. 5 The AFM images and profiles of gratings recorded on PEPC-*co*-DO for: **a** PP; **b** LR; **c** ±45° polarization configurations

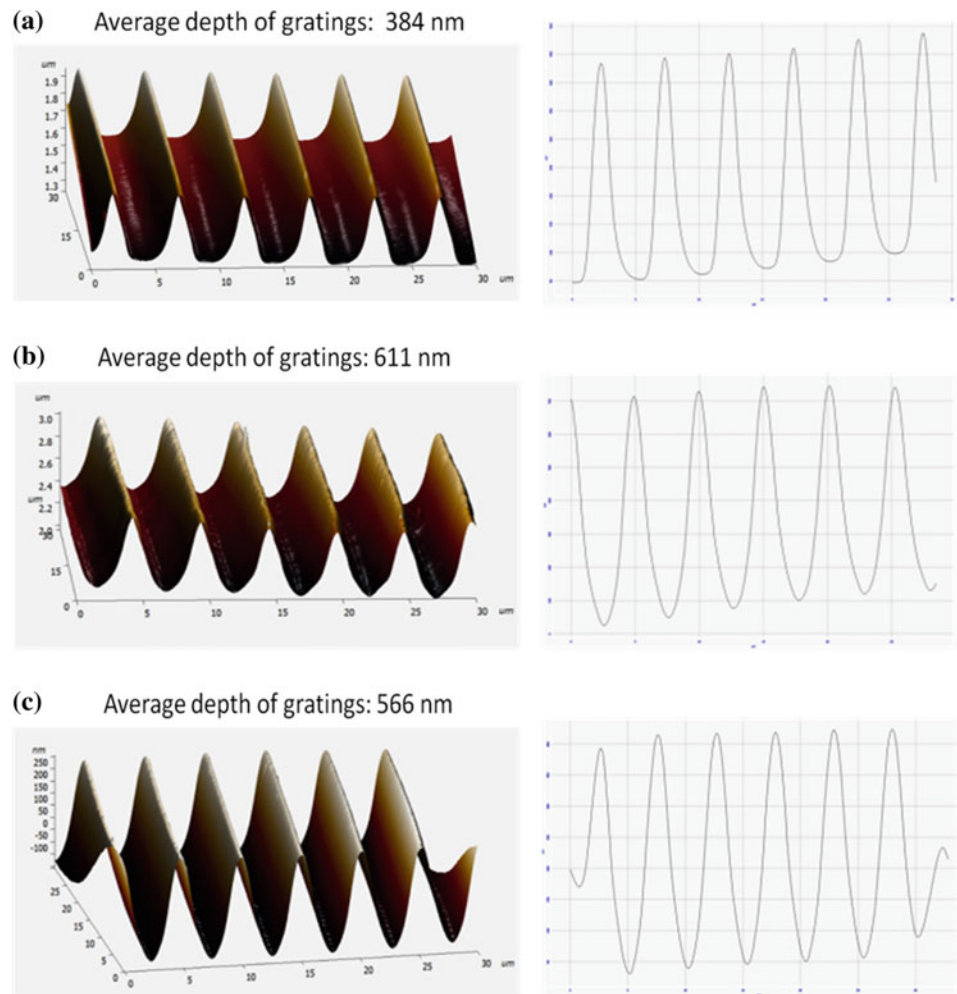
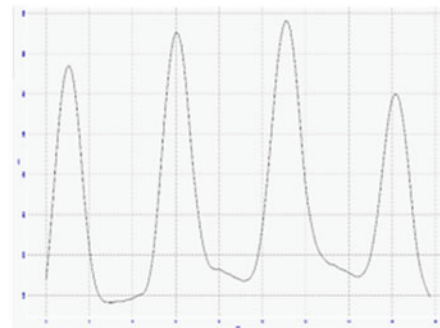
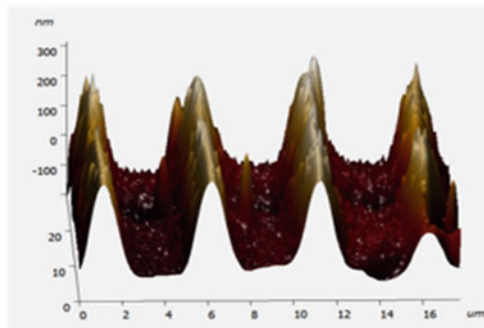
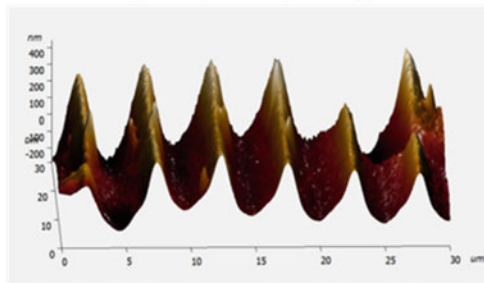


Fig. 6 The AFM images and profiles of gratings recorded on PEPC-*co*-DO with Cd_{0.2}Zn_{0.8}Se QDs for: **a** PP; **b** LR; **c** ±45° polarization configurations

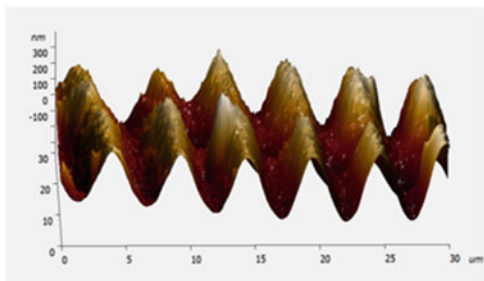
(a) Average depth of gratings: 312 nm



(b) Average depth of gratings: 391 nm



(c) Average depth of gratings: 345 nm



and Δn is the maximum change in the refractive index, α is a angle of diffraction for the probe wavelength.

The diffraction efficiency in this readout scheme can results from both the anisotropic grating formed in the volume of the layer, and the surface relief grating induced on the surface of the film. The amplitude grating due to absorption coefficient changes $\Delta\alpha$ is out of readout wavelength $\lambda = 650$ nm and hence the DE was not affected by light absorption modulation.

Diffraction gratings made by two-beam interference that leads to a sinusoidal profile of intensity/polarization in the film with the modulation direction being parallel to the film surface. Using a probe beam at normal incidence, the first-order diffraction efficiency of thin sinusoidal diffraction grating is given by $\eta = J_1^2\left(\frac{\Delta\varphi}{2}\right)$, where J_1 is a Bessel function of the first kind, $\Delta\varphi$ represents the peak-to-peak amplitude of phase delay in grating. According to the

equation, the largest possible diffraction efficiency into one of the +1 and -1 diffraction orders is the maximum value of J_1^2 and is equal 33.8%.

The AFM images of recorded surface grating on PEPC-*co*-DO and PEPC-*co*-DO with Cd_{0.2}Zn_{0.8}Se QDs thin films are presented in Figs. 5 and 6.

From comparison the gratings presented in Figs. 5 and 6, we can see that difference between amplitude (PP) and phase grating is more evidence for PEPC-*co*-DO with Cd_{0.2}Zn_{0.8}Se QDs thin films than for PEPC-*co*-DO thin films. Although the magnitude of DE is high for pure azopolymer.

4 Conclusions

In conclusion, we have shown that a holographic grating with high diffraction efficiency can be made in PEPC-*co*-DO with Cd_{0.2}Zn_{0.8}Se QDs films by two-beam polarization

interference. Thus, we have shown that synthesized PEPC-co-DO with $\text{Cd}_{0.2}\text{Zn}_{0.8}\text{Se}$ QDs films can be applied for using as a recording media for SRG formation with high DE.

Conflict of Interest The authors declare that they have no conflict of interest.

References

1. Sanchez, C., Belleville, P., Popall, M., Nicole, L.: Applications of advanced hybrid organic-inorganic nano-materials: from laboratory to market. *Chem. Soc. Rev.* **40**, 696–753 (2011)
2. Moothanchery, M., Naydenova, I., Mintova, S., Toal, V.: Nanozeolites doped photopolymer layers with reduced shrinkage. *Opt. Express* **19**, 25786–25791 (2011)
3. Rochon, P., Batalla, E., Natansohn, A.: Optically induced surface gratings on azoaromatic polymer films. *Appl. Phys. Lett.* **66**, 136–138 (1995). <https://doi.org/10.1063/1.113541>
4. Meshalkin, A., Robu, S., Achimova, E., Prisacar, A., Shepel, D., Abashkin, V., Triduh, G.: Direct photoinduced surface relief formation in carbazole-based azopolymer using polarization holographic recording. *J. Optoelectron. Adv. M.* **18**, 763–768 (2016)
5. Reshetnyak, V., Shanskii, L., Yaroshchuk, O., et al.: Photoorientation of polymer fragments in a system azopolymer-microporous glass. *Mol. Cryst. Liq. Cryst.* **329**, 447–456 (1999)
6. Li, X., Chon, J.W.M., Evans, R.A., Gu, M.: Two-photon energy transfer enhanced three-dimensional optical memory in quantum-dot and azo-dye doped polymers. *Appl. Phys. Lett.* **92**, 063309 (2008)
7. Zhou, J., Yang, J., Sun, Y., et al.: Effect of silver nanoparticles on photo-induced reorientation of azo groups in polymer films. *Thin Solid Films* **515**, 7242–7246 (2007)
8. Slang, S., Loghina, L., Palka, K., Vlcek, M.: Exposure enhanced photoluminescence of $\text{CdS}_{0.9}\text{Se}_{0.1}$ quantum dots embedded in spin-coated $\text{Ge}_{25}\text{S}_{75}$ thin films. *RSC Adv.* **7**, 53830–53838 (2017)
9. Achimova, E.: Polarization holography for direct surface grating patterning on chalcogenide nanomultilayers. *J. Physics Conf. Series* **1096**, 012133 (2019)

QDs Doped Azopolymer for Direct Holographic Recording

C. Loşmanskii, E. Achimova, V. Abaskin, A. Meshalkin, A. Prisacar, L. Loghina, M. Vlcek, and A. Yakovleva

Abstract

This paper describes a direct holographic recording of surface relief gratings in QD doped carbazole-based polymers. The evolution of the transmittance spectrum and diffraction efficiency upon irradiation with 473 nm polarized laser light demonstrated the photo-induced surface patterning of gratings.

Keywords

Azopolymer • Chalcogenide quantum dots • Holographic recording • Surface relief grating • Diffraction efficiency

1 Introduction

Nanocomposites are promising materials for various applications, such as photonics, biomedicine, surface engineering, and they have an academic interest. The doping of polymer matrices by organic and inorganic compounds can carry out, which leads to a change in the properties of the polymer. The polymer matrix doped with nanoparticles acquires new properties due to changes such parameters as the absorption coefficient, refractive index, photoconductivity, sensitivity to light, mechanical and others [1].

One of the most important properties of photosensitive polymer films containing azo dyes, discovered in 1995, is the formation of surface gratings under the light influence [2]. The mechanism of gratings formation is based on the photoisomerization of the azobenzene molecule with a reversible change in conformation from *trans*- to *cis*-.

Isomerization is accompanied by a large photo-induced molecular motion, which is able to significantly affect the physical and chemical properties of the materials in which they are incorporated. Moreover, the deformation of the surface relief with the subsequent formation of the grating depends on both the states of polarization and the distribution of the intensity of the incident light beams [3]. The process of recording of the surface grating on the azopolymer film in the place, where the interference pattern is formed, is accompanied by the mass transfer of the polymeric material. This phenomenon allows to fabricate a surface relief grating (SRG) by a simple one-step process, without development process. One of the important properties of azo dyes is the ability to affect the optical properties of materials through exposure to the material of polarized light. Thus, azopolymer films are materials that allow obtaining of the different form of surface relief under a modulated light irradiation. The properties of azopolymer films depend on the parameters of the incident light, such as radiation power, wavelength, polarization, and period of the recorded grating. In addition, the properties of the polymer depend on itself, i.e. polymer structure, molecular weight, type of polymer (main chain or side chain), and from functional groups in substituted aromatic azobenzene rings.

The interest in QD doped organic materials appeared due to the manifestation of improved optical, electrical and mechanical properties. Moreover, the literature data give examples of azo polymers doping with nanoparticles that leads to an increase in the diffraction efficiency by up to 100% [4].

In this paper, it is examined the optical properties of the azopolymer doped by quantum dots and the direct holographic recording on this media. The polymeric matrix of poly-epoxypropylcarbazole was modified with azo-dye Disperse Orange 3 to which quantum dots of the composition $Cd_{0.2}Zn_{0.8}Se$ were added. This composition was synthesized according to the procedure proposed previously [5]. The formation of surface gratings during the direct holographic recording was studied by registration of the

C. Loşmanskii (✉) · E. Achimova · V. Abaskin · A. Meshalkin · A. Prisacar
Institute of Applied Physics, Academiei Street,
5, Chisinau, Moldova
e-mail: constantinlindemann@yahoo.com

L. Loghina · M. Vlcek · A. Yakovleva
Pardubice University, Pardubice, Czech Republic

diffraction efficiency during the recording process. The transmission and reflection spectra of azopolymer films containing quantum dots and without them were also measured.

2 Materials and Methods

All reagents and precursors were purchased from Sigma Aldrich and used without further purification. The solvent used in the reaction was purchased from Fisher Scientific and was used to clean the quantum dots and spin-coating the films. Reagents sensitive to air or moisture were cleaned and the synthesis itself was carried out in an inert atmosphere of argon in the standard Schlenk line.

The preparation of the ternary compound $\text{Cd}_{0.2}\text{Zn}_{0.8}\text{Se}$ was carried out in an organic solvent 1-octadecene at a synthesis temperature of 280 °C. Selenium trioctylphosphine was selected as the source of selenium. The resulting quantum dots have been described by known methods, such as optical measurements and electron transmission microscopy. The average size of quantum dots is 3.5 nm. The homogeneity of the obtained quantum dots is confirmed by the luminescence and absorption spectra.

The PEPC-co-DO copolymer was synthesized in a reflux by mixing DO3 azo dye (0.3 g) and polyepoxypropylcarbazole (1.0 g), followed by boiling in toluene for 6 h. After cooling, the solution was filtered. Transparent films were obtained on a glass substrate by spin-coating. In order to obtain PEPC-co-DO films with $\text{Cd}_{0.2}\text{Zn}_{0.8}\text{Se}$ content, a solution of quantum dots $\text{Cd}_{0.2}\text{Zn}_{0.8}\text{Se}$ was mixed with a concentration of 5% to a PEPC-co-DO solution. The application of films by the spin-coating method was carried out at a speed of 500 rpm for 30 s, followed by drying at a temperature of 60 °C for 1 h. The thickness of the obtained films was measured by high-resolution interference microscopy. Also, optical properties of QD doped PEPC-co-DO film was studied from transmittance and reflectance spectra.

As described in Ref. [6], in order to record gratings on the azopolymer, it was used an interferometric method of holographic recording. The surface relief grating formation experiments were performed using different polarization states of recording beams (Fig. 1). The period of the grating can be calculated as $d = \lambda / (2 \sin \alpha)$, where λ is the wavelength of laser beam, α is the angle between the incidence laser beams. CW DPSS single mode laser operated at wavelength $\lambda = 532 \text{ nm}$ and spot power density from 150 up to 350 mW/cm^2 on the sample was used for recording. In order to achieve the maximum interference fringes contrast, it was used the intensity ratio 1:1 of the recording beams. Two symmetrical angled laser beams superpose on the

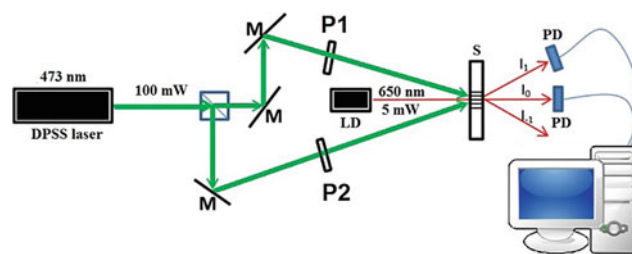


Fig. 1 Setup for holographic grating recording with real-time measurement of diffraction efficiency by photodiodes. CW DPSS laser ($\lambda = 473 \text{ nm}$, $P_{\text{out}} = 100 \text{ mW}$), M—mirrors; LD—laser diode ($\lambda = 650 \text{ nm}$) for monitoring of the recording process; P1, P2—polarization plates; S—photosensitive material; PD—photodetectors

sample surface and the holographic gratings with various periods (Λ) are recorded. The grating period that appeared between two interfering beams in this experiment was 5.0 μm . The setup for holographic grating recording with real-time measurement of diffraction efficiency can be seen in Fig. 1.

Once the interference pattern contrast is approximately 1, the interference pattern of two coherent beams has a largest periodical modulated intensity having two parallel linear polarizations, SS or PP. On the contrary, in the direction of the resultant electrical vector, a polarization state has not a spatial modulation. A constant intensity has the interference pattern, but a polarization state is periodically modulated in case of orthogonal linear polarizations SP. The interference pattern has a small modulated intensity and is even over the entire exposed area, when orthogonal linear $\pm 45^\circ$ and circular RL polarizations. On the other hand, in the resultant electrical field direction on the film surface, these polarizations ($\pm 45^\circ$ and RL) produce the largest periodical modulation. There were obtained very small DE and surface relief modulation for SP polarization states. For this formation, there is no component of resultant electric vector of light along the grating vector direction.

Polarizers were mounted on rotation mounts. This allowed modifying polarizations of two incident beams. Interfering beams with PP, SS or LR polarization combinations were used for surface relief gratings recording.

During the holographic recording, in order to serve as the probe beam, the linear polarized laser (P-polarization) at wavelength of 650 nm was positioned to the sample at a normal incidence. For diagnosing the kinetics of gratings formation, the zero-order and first-order diffraction intensities of sample were monitored in situ. It is determined the first-order of DE η as $\eta = \frac{I_1}{2I_1 + I_0} * 100\%$, where I_1 is the light intensity diffracted in the first diffraction order and I_0 is light intensity in zero-order diffraction. Two silicon photodiodes equipped with amplifiers measured I_1 and I_0 intensities. Only

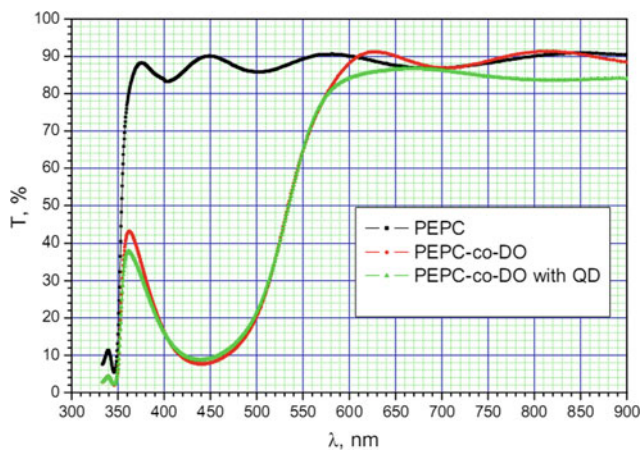


Fig. 2 Transmittance spectra of PEPC, PEPC-co-DO and PEPC-co-DO with QD thin films

a holographic recording phase was considered by DE measurement, because this wavelength is outside the absorption region (Fig. 2). The larger phase modulation of recorded grating is suggested by the higher diffraction intensity.

3 Results and Discussion

Figure 3 presents the spectra of absorbance for the samples with 0% and 10 wt.% concentration of the doped $\text{Cd}_{0.2}\text{Zn}_{0.8}\text{Se}$ QD. The spectra indicate that the addition of QD does not shift the peak of absorbance and its maximum is at 450 nm. It is also seen that doping even 10% of QD does not give raise to scattering outside the absorbance band (beyond 700 nm) i.e. there is no increase of the absorbance coefficient. This is also confirmed by the visual observation

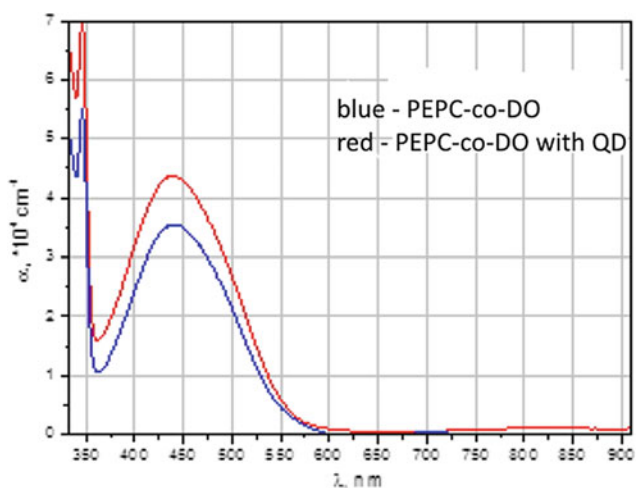


Fig. 3 Absorption coefficient spectra of PEPC-co-DO and PEPC-co-DO with QD thin films

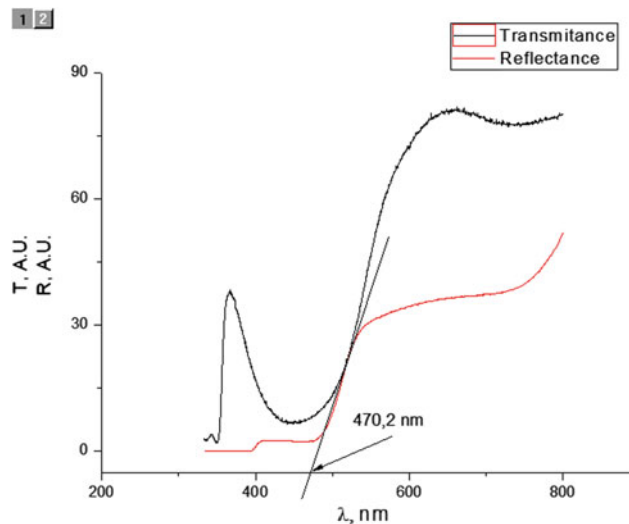


Fig. 4 Transmittance and reflectance spectra of PEPC-co-DO thin film, doped with QD

of the films—they are with good optical quality and high transparency.

The absorption spectra for PEPC-co-DO and PEPC-co-DO doped with QDs indicate an increased absorption in the sample that contains QDs. Also from the transmission and reflection spectra, the absorption edge of the doped azopolymer was determined (Fig. 4). The absorption edge from the transmission spectrum corresponds to the absorption maximum of the reflection spectrum, having a maximum at $\lambda = 470.2$ nm, which is close to the laser wavelength of a holographic recording setup.

The diffraction efficiency in the readout scheme can result from both, the anisotropic grating formed in the volume of the layer, and the surface relief grating induced on the surface of the film. The amplitude grating due to absorption coefficient changes, $\Delta\alpha$ is out of readout wavelength $\lambda = 650$ nm and hence, the DE was not affected by light absorption modulation.

In Fig. 5, it is shown the dependence of DE on time for RCP:LCP (LR) of the studied polarization configurations for PEPC-co-DO (P10 D3) films with concentration of azo dye 30 wt.% as a base matrix with $\text{Cd}_{0.2}\text{Zn}_{0.8}\text{Se}$ and Ag QDs.

For a PEPC-co-DO azopolymer without quantum dots and with $\text{Cd}_{0.2}\text{Zn}_{0.8}\text{Se}$, a maximum diffraction efficiency of about 1.4% was recorded in RCP:LCP polarization of the incident beams. The DE of azopolymer with Ag has lower value which may be explained by noncoincidence of absorption band of azopolymer and Ag QD.

DE strongly depends on the polarization configuration which can be seen in Fig. 6. While on the azopolymer films with a PEPC-co-DO composition doped with QDs, the maximum diffraction efficiency is observed in the circular polarization of the beams (LCP:RCP, Fig. 6).

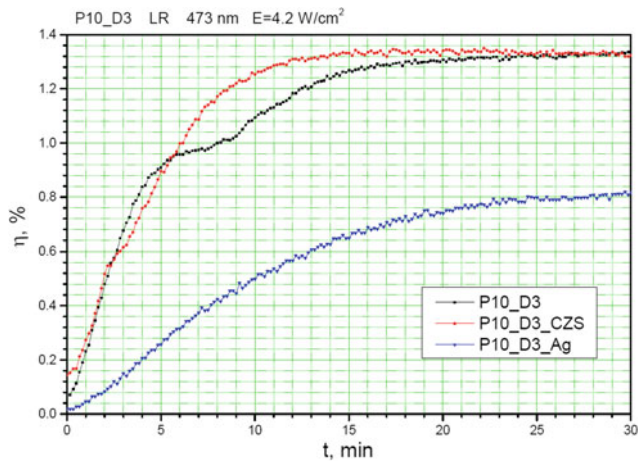


Fig. 5 The dependence of diffraction efficiency in transmission mode on recording time for RCP:LCP studied polarization configurations using PEPC-*co*-DO with Cd_{0.2}Zn_{0.8}Se QDs film and PEPC-*co*-DO with Ag QDs (the concentration of azodye 30 wt.%)

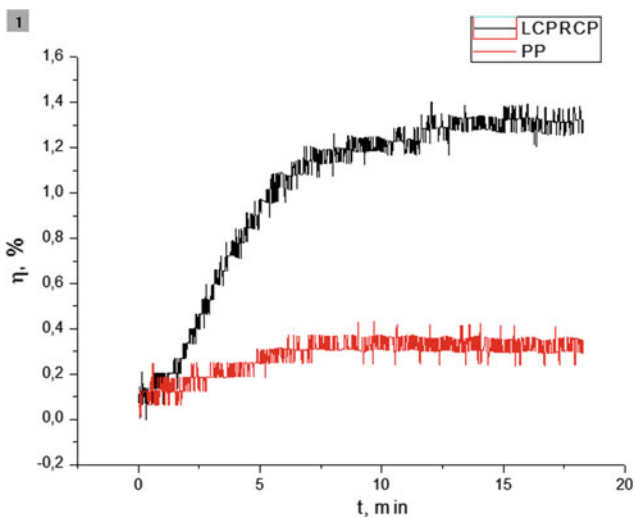


Fig. 6 The dependence of diffraction efficiency in transmission mode on recording time for PP and RCP:LCP studied polarization configurations using PEPC-*co*-DO with Cd_{0.2}Zn_{0.8}Se QDs film and the concentration of azodye 30 wt.%

The diffraction efficiency of the gratings was recorded on azopolymer films doped with QDs, 1.5% for RCP: LCP and 0.35% for PP polarization.

4 Conclusions

In conclusion, we have shown that a holographic grating can be recorded on PEPC-*co*-DO with Cd_{0.2}Zn_{0.8}Se and Ag QDs films by two-beam polarization interference. We also showed that azopolymer doped with quantum dots leads to change its properties. In the case of PEPC-*co*-DO with Cd_{0.2}Zn_{0.8}Se QD, the maximum diffraction efficiency was obtained for RCP:LCP. The synthesized films PEPC-*co*-DO with Cd_{0.2}Zn_{0.8}Se and Ag QDs can be applied for using a recording media for surface relief gratings formation.

Conflict of Interest The authors declare that they have no conflict of interest.

References

1. Aziz, S.B., Abdullah, O.G., Hussein, A.M., et al.: J. Mater. Sci. Mater. Electron. **28**, 7473 (2017). <https://doi.org/10.1007/s10854-017-6437-1>
2. Zhao, Y., Ikeda, T.: Smart Light-Responsive Materials: Azobenzene-Containing Polymers and Liquid Crystals. Wiley, Hoboken (2009)
3. Coelho, P., Sousa, C., Castro, M.C., Fonseca, A., Raposo, M.: Fast thermal cis–trans isomerization of heterocyclic azo dyes in PMMA polymers. Opt. Mater. **35**, 1167–1172 (2013). <https://doi.org/10.1016/j.optmat.2013.01.007>
4. Nazarova, D., Nedelchev, L. & Mintova, S.: Birefringence improvement in azopolymer doped with MFI zeolite nanoparticles. Optofluidics Microfluidics Nanofluidics **1**(1) (2014). <https://doi.org/10.2478/optof-2014-0005>
5. Slang, S., Loghina, L., Palka, K., Vlcek, M.: Exposure enhanced photoluminescence of CdS_{0.9}Se_{0.1} quantum dots embedded in spin-coated Ge₂₅S₇₅ thin films. RSC Adv. **7**, 53830–53838 (2017)
6. Loşmanskii, C., Achimova, E., Abaşkin, V., Mesalchin, A.: Polarized holographic recording of superimposed diffractive grating on azopolymers. In: Abstracts of the 6th International Conference on “Telecommunications, Electronics and Informatics”, Chisinau, Moldova, 24–27 May 2018

Radiative Recombination of Bound Excitons in MoSe₂:I₂ Layered Crystals

N. Siminel, V. Nedelea, K. Sushkevich, A. Siminel, A. Micu, and L. Kulyuk

Abstract

The steady-state and time-resolved photoluminescence (PL) of excitons bound on intercalated iodine molecules was studied for the first time in MoSe₂:I₂ layered single crystals. Along with narrow exciton spectral lines located near the energy of the MoSe₂ indirect bandgap in the region of 0.98–1.06 eV, an IR broadband radiation centered at 0.78 eV and caused by the recombination of photoexcited carriers through the intrinsic lattice defects were found. To describe the temperature dependences of the intensity of steady-state PL, as well as its temporal characteristics, a kinetic model was proposed that takes into account the radiative and non-radiative recombination channels present in this quasi-two-dimensional semiconductor.

Keywords

Transition metal dichalcogenides • Molybdenum diselenide • Layered crystals • Intercalation • Luminescence • Bound excitons

1 Introduction

The layered quasi-two-dimensional transition metal dichalcogenides (TMDs) (e.g. WS₂, WSe₂, MoS₂, MoSe₂) are of great interest due to their attractive electronic, optical, mechanical, chemical and thermal properties [1–3]. The bulk TMDs materials has an indirect band gap in the near IR spectral region [3], whereas a single layer film is a direct gap

semiconductor [3–5], that is an advantage compared to graphene, being a convenient material for digital electronics, solar-energy conversion and optoelectronic two-dimensional devices.

TMDs are a class of layered materials with formula MX₂, where M is a transition metal (e.g. Mo, W, Re, V, etc.) and X is chalcogen (S, Se or Te). The crystalline structure of these materials consists of weakly coupled X-M-X sandwich hexagonally arranged layers where a layer of M atoms is constrained between two layers X [3]. The adjacent layers are attracted by the van der Waals interaction, which allows the formation of the allotropic crystal. For example in the case of MoS₂, or MoSe₂ there are three crystal modifications —1T, 2H and 3R [6, 7], where the number refers to the number of monolayers stacked in a unit cell, and the letter indicates cell symmetry: triangular, hexagonal and rhombohedral respectively. The polytype 2H-MoSe₂ crystallizes in the P6₃/mmc (*D*_{6h}⁴) space group. Similar to all TMDs, the bulk 2H-MoSe₂ is characterized by an indirect forbidden bandgap which constitutes $E_g = 1.10$ eV [8].

Due to the layered framework, the electronic characteristics of the TMDs can be substantially altered by intercalating various chemical species between layers [9, 10]. In particular, the iodine, bromine or chlorine molecules, that usually are used as transport agents during the halogen vapor transport, can also be treated as intercalants [11–13].

In this work, for the first time the results of an experimental study of the PL of bound excitons in 2H-MoSe₂:I₂ single crystals is presented. Temperature dependencies of the steady-state emission spectra and of the luminescence decay time were investigated. In order to describe the observed experimental results a kinetic model and a single configuration coordinate diagram for the states involved in the recombination processes of photo-excited carriers in 2H-MoS₂:I₂ are proposed.

N. Siminel (✉) · V. Nedelea · K. Sushkevich · A. Siminel · A. Micu · L. Kulyuk
Institute of Applied Physics, Academiei Street 5, Chisinau, 2028, Republic of Moldova
e-mail: siminel.n@gmail.com

V. Nedelea · K. Sushkevich
Moldova State University, Mateevici Street 60, Chisinau, 2009, Republic of Moldova

2 Experimental Results

The 2H-MoSe₂ single crystals were grown by means of chemical vapor transport using iodine as a transport agent. The investigated samples were a several millimeters in diameter and a few tens of micrometers thick.

The PL measurements in the temperature range $T = 11\text{--}120$ K were performed with a grating monochromator using a standard lock-in technique, or broadband oscilloscope and IR photomultipliers. The steady-state luminescence was excited using a CW semiconductor laser operating at the wavelength $\lambda_{L1} = 447$ nm (2.77 eV). The time-resolved PL (resolution ~ 10 ns) was excited with a Q-switched YAG: Nd laser ($\lambda_{L2} = 532$ nm (2.33 eV), pulse duration ~ 2 ns).

Figure 1 illustrates the typical PL spectrum of the MoSe₂: I₂ at temperature $T = 11$ K. The spectrum is composed of two characteristic parts. In the short-wavelength excitonic region (1.05–0.98 eV), as in the case of other TMDs single crystals grown by the gas transportation method [11, 12], at low temperatures one can observe at least two zero-phonon lines followed by their phonon replicas. This emission is due to the recombination of excitons bound to the electron-attractive neutral centers, formed by diatomic halogen molecules embedded in the van der Waals gap [12–14]. The broadband IR spectrum centered at 0.78 eV with a half-width of approximately 0.12 eV, by analogy with similar spectra inherent to MoS₂, WS₂ and WSe₂ compounds, can be attributed to the radiative recombination via a deep levels caused by the intrinsic defects of the crystalline structure of MoSe₂—vacancies of selenium [15].

The temperature evolution of the narrow lines emission spectrum is shown in Fig. 2. At low temperatures, two lines, labelled as A and B, dominate the spectra. They are separated

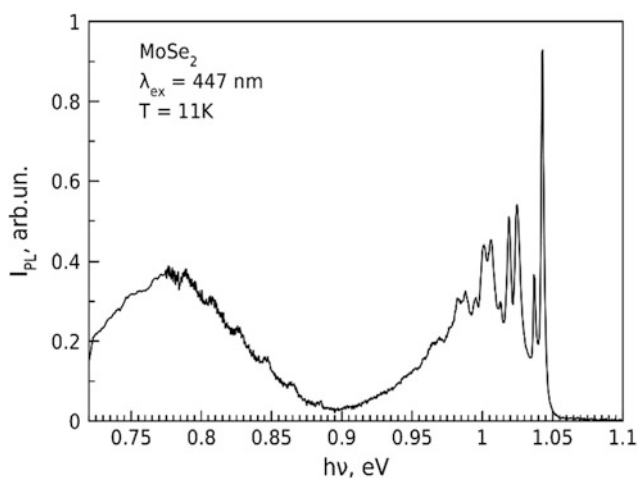


Fig. 1 Photoluminescence spectrum of 2H-MoSe₂ at $T = 11$ K. Two distinct regions can be observed: the exciton region and the broadband region. The broadband contains luminescence interference peaks

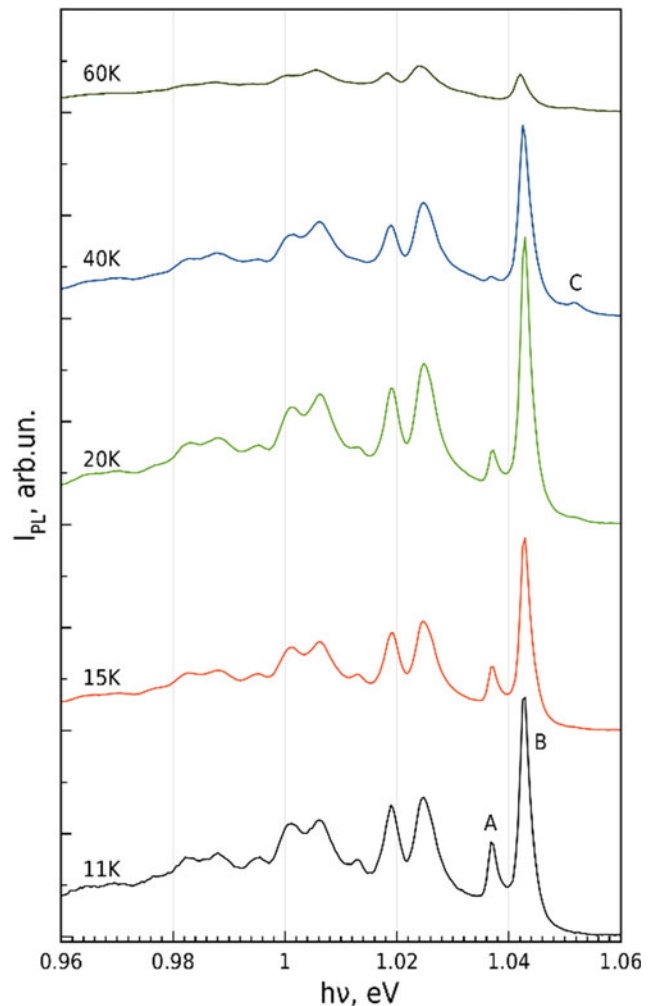


Fig. 2 Bound-exciton emission spectra of 2H-MoSe₂ at different temperatures

by $\Delta_{AB} = 6$ meV and located at $E_A = 1.037$ eV and $E_B = 1.043$ eV. The lower energy part of the spectrum is characterized by their phonon replicas. With the increase of temperature, the intensities of A and B lines are redistributed in favor of the line B (Fig. 2). The intensity of that peak increases up to 30 K. At the same time, the third line C ($E_C = 1.336$ eV) arises, however its contribution is quite small.

The increase of temperature above 50 K leads to rapid quenching of bound-excitons luminescence. Similarly, the IR broadband emission intensity (Fig. 1) gradually diminishes with the rise of temperature and at $T > 60$ K the thermal quenching occurs.

Analysis of the spectrum in the region of phonon repetitions of the excitonic lines, suggests the presence of phonons with the following energies: $E_{ph1} = 18$ meV, $E_{ph2} = 24$ meV and $E_{ph3} = 30$ meV. These energies differ from the frequencies measured by IR and Raman spectroscopy [6], and can be attributed to the local modes

induced by the intercalated halogen in the crystalline structure [11].

The PL decay time curves for the short-wave excitonic region (1.043 eV) and IR broadband (0.78 eV) at different temperatures were analyzed. As a general trend, the photoluminescence starts to decay faster at higher temperatures. Each decay curve is fitted by exponential decay models to evaluate PL lifetimes τ_R . A significant difference in τ_R was observed for two spectral regions of 2H-MoSe₂. At low temperature ($T = 11$ K) the lifetime of the PL at short-wavelength excitonic region is equal to $\tau_R^x = 260$ μ s and at long-wave broadband $\tau_R^{BB} = 850$ μ s.

The increase of temperature above 50 K leads to rapid quenching of bound-excitons luminescence. Similarly, the IR broadband emission intensity (Fig. 1) gradually diminishes with the rise of temperature and at $T > 60$ K a thermal quenching occurs.

The PL decay time curves for the short-wave excitonic region (1.043 eV) and IR broadband (0.78 eV) at different temperatures were analyzed. As a general trend, the photoluminescence starts to decay faster at higher temperatures. Each decay curve is fitted by exponential decay models to evaluate PL lifetimes τ_R . A significant difference in τ_R was observed for two spectral regions of 2H-MoSe₂. At low temperature ($T = 11$ K) lifetime of the PL at short-wavelength excitonic region constitutes $\tau_R^x = 260$ μ s = 260 μ s and at long-wavelength broadband – $\tau_R^{BB} = 850$ μ s.

3 Discussion

The temperature dependence of the steady-state PL intensity of the A, B and C spectral lines can be described by means of excitonic recombination kinetic model similar to that was proposed for description of the narrow line emission due to excitons bound on the isoelectronic impurity of nitrogen in GaP:N [16]. In our case the role of isoelectronic trap plays the iodine molecule I₂, intercalated between the layers. For the case of low-level excitation the following equations describe the kinetic behaviour of the carrier concentration in the material:

$$\frac{dN_{T1}^x}{dt} = p \cdot v_{th} \cdot \sigma_{px} (N_{T1}^e - N_{T1}^x) - \frac{N_{T1}^x}{\tau_{Rx}} - \frac{N_{T1}^x}{\tau_{xp}} \quad (1)$$

$$\frac{dp}{dt} = G - p \cdot v_{th} \cdot \sigma_{px} (N_{T1} - N_{T1}^x) - p \cdot v_{th} \cdot \sigma_{ps} \cdot N_D \quad (2)$$

$$\frac{dN_{T1}^e}{dt} = \frac{n}{\tau_{nT1}} - (N_{T1}^e - N_{T1}^x) \left(\frac{1}{\tau_{T1n}} \right) - N_{T1}^x \left(\frac{1}{\tau_{xR}} + \frac{1}{\tau_{xn}} + \frac{1}{\tau_{xN}} \right) \quad (3)$$

$$\frac{dn}{dt} = G - n \left(\frac{1}{\tau_{nT1}} + \frac{1}{\tau_{nT2}} \right) \quad (4)$$

$$\frac{dN_{T2}^e}{dt} = \frac{n}{\tau_{T2n}} - (N_{T2} - N_{T2}^e) \left(\frac{1}{\tau_{T2n}} + \frac{1}{\tau_{N2}} \right) \quad (5)$$

where n (p) is the concentration of free-electron (hole), τ_{px} —exciton hole capture time, τ_{T2n} —deep level capture time, σ_{px} —hole capture cross-section by T_1 traps, formed by intercalated molecules, N_{T1} —concentration of these traps, N_{T2} —concentration of deep levels, N_{T1}^x —concentration of traps with a bound exciton, $N_{T1,T2}^e$ —electron occupied traps and deep levels, τ_R^x —bound exciton radiative recombination time, N_D —concentration of deep centers, σ_{ps} —hole shunt-path capture cross-section by deep centers, v_{th} —thermal velocity and G —excitation rate.

In the case of steady-state conditions, all derivatives in the system of Eqs. (1)–(6) are equal to zero and the numeric solution of the system results in the expression for quantum efficiency of the bound excitons luminescence in the following form:

$$\eta_R^x(T) = \frac{N_{T1}^x(T)}{\tau_R^x(T)} \cdot \frac{1}{G} \quad (6)$$

The experimental temperature dependences of PL integral intensity and of decay time τ_R^x of bound excitons emission in MoSe₂:I₂ is shown in Fig. 3. The theoretically calculated quantum efficiency $\eta_R^x(T)$ as a function of temperature is also presented in Fig. 3.

The agreement between experiment and excitonic recombination kinetic model is reasonable. It is obvious that below 25 K the discrepancy reaches its highest value. That can be caused by overlapped A and B excitonic lines in low temperature PL spectra, which does not allow correct measurements of $I_{A,B}(T)$. In addition to the lifetime temperature dependence parameters used in the model, the following values were introduced: $G = 10^{20}$ cm⁻³/s, $N_{T1} = 10^{19}$ cm⁻³, $E_h = 0.02$ eV, $E_{T1} = 0.1$ eV. At this excitation rate G and low temperature the value of N_{T1}^x was calculated as 7.5×10^{14} cm⁻³.

The very fast radiative-less recombination, described by the lifetime τ_N^x (the excitonic annihilation processes) can be

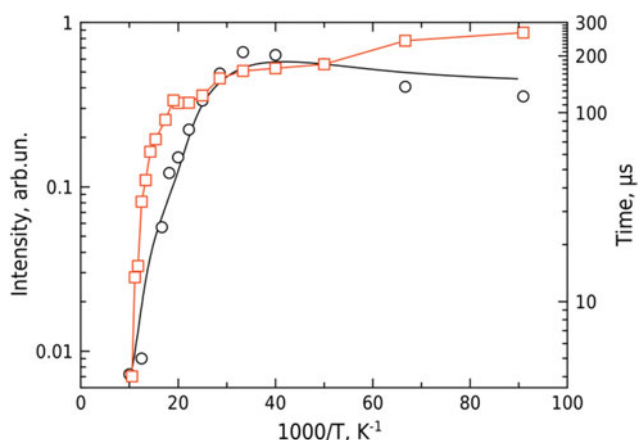


Fig. 3 Measured temperature dependence of the PL integral intensity and decay time of bound excitons PL of MoSe₂: black circles—steady-state luminescence intensity; black line—theoretical calculation of quantum efficiency of excitonic luminescence; red squares—decay times

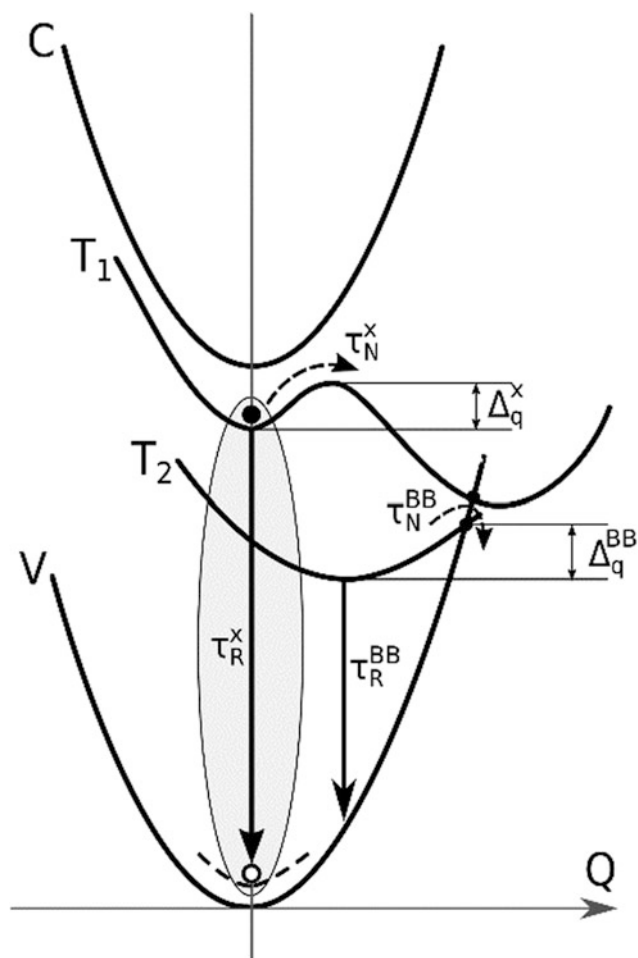


Fig. 4 Single-configuration coordinate diagram describing the recombination processes of bound excitons in MoSe₂:I₂ compounds

explained using the single configuration coordinate diagram shown on Fig. 4. The nonradiative recombination transition represented by the curved arrow describes the luminescence thermal quenching with activation energy E_{qx} that can occur due to the extrinsic self-trapping of the electron component of the bound exciton [17]. Such a process assumes the coexistence of two types of states of the impurity center [17, 18]. The first state, characterized by a weak electron–phonon coupling, provides the formation of the bound excitons; the second one (self-trapped state) is deeper, it shows a large lattice relaxation and plays the role of an intermediate state. The quenching of the broad-band emission is due to the multi-phonon nonradiative transitions with the life-time τ_N^{BB} over the energy barrier Δ_q^{BB} .

4 Conclusion

The luminescent properties (steady-state and time-resolved) of 2H-MoSe₂:I₂ single crystal were investigated. The PL spectra consist of two separate spectral regions — the short wavelength, with narrow spectral lines, and the long wavelength broadband. The first is related to the radiative recombination of excitons bound to the neutral centers formed by iodine molecules. The latter is attributed to the recombination radiative channel via a deep level due to the chalcogen vacancies in the crystalline structure of the 2H-MoSe₂. The temperature dependence of the steady-state PL intensity has been described using a kinetic model, taking into account both channels of radiative recombination as well as the radiativeless transitions which lead to the efficient PL quenching at $T > 50$ K. The fast thermal quenching of the excitonic emission is explained by the occurring of the self-trapping process of the bound excitons.

The proposed kinetic model is in good agreement with the observed characteristics of the steady-state and time-resolved luminescence.

For the areas of future research, it is interesting to extend the bound excitons luminescence study to MoSe₂:I₂ monolayers.

Conflict of Interest The authors declare that they have no conflict of interest.

References

1. Wang, Q.H., Kalantar-Zadeh, K., Kis, A., Coleman, J.N., Strano, M.S.: Electronics and optoelectronics of two-dimensional transition metal dichalcogenides. *Nat. Nanotechnol.* **7**, 699–712 (2012). <https://doi.org/10.1038/nnano.2012.193>
2. Kalantar-zadeh, K., Ou, J.Z., Daeneke, T., Strano, M.S., Pumera, M., Gras, S.L.: Two-dimensional transition metal dichalcogenides

- in biosystems. *Adv. Func. Mater.* **25**, 5086–5099 (2015). <https://doi.org/10.1002/adfm.201500891>
- Kolobov Alexander, V., Junji, T.: *Two-Dimensional Transition-Metal Dichalcogenides*, vol. 239. Springer Series in Materials Science, Berlin (2016)
 - Mak, K.F., Lee, C., Hone, J., Shan, J. Heinz, T.F.: Atomically thin MoS₂: a new direct-gap semiconductor. *Phys. Rev. Lett.* **105**(1–4), 136805. <https://doi.org/10.1103/physrevlett.105.136805> (2010)
 - Tongay, S., et al.: Thermally driven crossover from indirect toward direct bandgap in 2D semiconductors: MoSe₂ versus MoS₂. *Nano Lett.* **12**, 5576–5580 (2012). <https://doi.org/10.1021/nl302584w>
 - Lu, X., et al.: Rapid and nondestructive identification of polytypism and stacking sequences in few-layer molybdenum diselenide by Raman Spectroscopy. *Adv. Mater.* **27**, 4502–4508 (2015). <https://doi.org/10.1002/adma.201501086>
 - Gupta, U., et al.: Characterization of few-layer 1T-MoSe₂ and its superior performance in the visible-light induced hydrogen evolution reaction. *APL Mater.* **2**(1–8), 092802 (2014). <https://doi.org/10.1063/1.4892976>
 - Böker, T., et al.: Band structure of MoS₂, MoSe₂, and α -MoTe₂: angle-resolved photoelectron spectroscopy and ab initio calculations. *Phys. Rev. B* **64**, 235305 (2001). <https://doi.org/10.1103/PhysRevB.64.235305>
 - Friend, R.H., Yoffe, A.D.: Electronic properties of intercalation complexes of the transition metal dichalcogenides. *Adv. Phys.* **36**, 2 (1987). <https://doi.org/10.1080/00018738700101951>
 - Benavente, E., Santa Ana, M.A., Mendizábal, F., González, G.: Intercalation chemistry of molybdenum disulphide. *Coord. Chem. Rev.* **224**, 87–109 (2002). [https://doi.org/10.1016/s0010-8545\(01\)00392-7](https://doi.org/10.1016/s0010-8545(01)00392-7)
 - Kulyuk, L., Bucher, E., Charron, L., Fortin, E., Nateprov, A., Schenker, O.: Bound exciton luminescence of the intercalated tungsten dichalcogenide layer compounds. *Nonlinear Opt. (Mlc) Sect. B* **29**, 501–506 (2002). <https://doi.org/10.1080/1058726021000045234>
 - Kulyuk, L., Charron, L., Fortin, E.: Radiative properties of MoS₂ layered crystals. *Phys. Rev. B* **68**(1–5), 075314 (2003). <https://doi.org/10.1103/physrevb.68075314>
 - Kulyuk, L., Dumcehnko, D., Bucher, E., Friemelt, K., Schenker, O., Charron, L., Fortin, E., Dumouchel, T.: Excitonic luminescence of the Br₂-intercalated layered semiconductors 2H – WS₂. *Phys. Rev. B* **72**(1–7), 075336 (2005). <https://doi.org/10.1103/physrevb.72.075336>
 - Anghel, S., et al.: Site-selective luminescence spectroscopy of bound excitons and local band structure of chlorine intercalated 2H- and 3R-MoS₂ polytypes. *J. Lumin.* **177**, 331–336 (2016). <https://doi.org/10.1016/j.jlumin.2016.05.017>
 - Dumchenko, D., Gherman, C., Kulyuk, L., Fortin, E., Bucher, E.: Intercalated halogen molecules as radiative centers in transition metal dichalcogenides layered crystals. *Thin Solid Films* **495**, 82–85 (2006). <https://doi.org/10.1016/j.tsf.2005.08.225>
 - Dapkus, P.D., Hackett Jr., W.H., Lorimer, O.G., Bachrach, R.Z.: Kinetics of recombination in nitrogen-doped GaP. *J. Appl. Phys.* **45**, 4920–4927 (1974). <https://doi.org/10.1063/1.1663155>
 - Stavola, M., Levinson, M., Benton, J.L., Kimerling, L.C.: Extrinsic self-trapping and negative U in semiconductors: a metastable center in InP. *Phys. Rev. B* **30**, 832–836 (1984). <https://doi.org/10.1103/PhysRevB.30.832>
 - Piekara, U., Langer, J.M., Krukowska-Fulde, B.: Shallow versus deep In donors in CdF₂ crystals. *Sol. State Comm.* **23**, 583–587 (1977). [https://doi.org/10.1016/0038-1098\(77\)90655-x](https://doi.org/10.1016/0038-1098(77)90655-x)

Acetone Sensing Properties of Nanostructured Copper Oxide Films on Glass Substrate

V. Cretu, N. Ababii, V. Postica, N. Magariu, M. Hoppe, V. Verjbitki, V. Sontea, R. Adelung, and O. Lupan

Abstract

Copper oxide nanostructured films were synthesized via a chemical synthesis (SCS) method and annealed in low vacuum. The morphological properties were investigated using scanning electron microscopy (SEM). The elaborated sensor structures based on CuO/Cu₂O films were tested to 100 ppm of acetone vapor. It was observed that by applying different temperatures for rapid thermal annealing the surface morphology of the films can be modified, as well as the composition of the films, which leads to the changes in gas response value for the tested gases. The possibility of controlling the sensitivity of the sensors by changing the RTA treatment temperature and the operating temperature was demonstrated.

Keywords

CuO • Nanostructured films • SCS • Chemical synthesis • Metal oxides • Acetone sensors

1 Introduction

Nowadays, the increasing popularity is gained by non-invasive diagnostic methods. One example of the non-invasive method consists in analyzing the expired air from the human lungs. This method can be implemented using simple portable devices based on gas sensors. Detection of acetone vapor in human-expired air is a marker that can be used for the preventive diagnosis of diabetes [1–3].

Acetone is also used in various industrial applications and the detection of acetone vapor is of major importance in the detection of industrial gas leakage and the environmental protection. As gas sensing materials for detection of acetone vapor were investigated a series of materials such as polymers [4], composited based on carbon nanotubes [5], and different types of semiconducting oxides [6, 7]. The complexity of the synthesis, along with the high cost of production limits the applications of these materials. At the nanoscale, physicochemical properties are closely dependent on surface morphology [8, 9]. Thermal treatment by various methods is the simplest method of modifying the surface structure and phase of the material [10].

The rapid thermal treatment (RTA) applied for Cu₂O films leads to formation of nanoscale heterojunctions of CuO/Cu₂O [10].

Copper oxides, namely CuO and Cu₂O are materials with *p*-type electrical conductivity. The mixed phase of CuO/Cu₂O, due to specific mechanism [10, 11] is of high interest for gas sensing applications.

Also, gas sensing properties of copper oxide nano- and microstructures are highly influenced by different factors such as the presence or not of pores, the size of crystallites, and crystallographic orientation [12]. In the literature, there are presented several techniques for the synthesis of CuO nanostructures, including chemical solutions [13], thermal decomposition [14], thermal oxidation [15], etc.

In this paper we studied the gas sensing properties of the sensor structures based on CuO/Cu₂O nanostructured films to 100 ppm acetone vapor, in dependence of post-deposition temperature of rapid thermal annealing (RTA) in vacuum.

2 Experimental

2.1 Synthesis of CuO/Cu₂O Nanostructured Films via a Chemical Synthesis Method

The nanostructured films of cuprite (Cu₂O) were grown on glass substrates with dimensions of 76 mm × 25 mm × 1

V. Cretu (✉) · N. Ababii · V. Postica · N. Magariu · V. Verjbitki · V. Sontea · O. Lupan
Department of Microelectronics and Biomedical Engineering,
Technical University of Moldova, Bd. Ștefan cel Mare, 168,
Chisinau, Republic of Moldova
e-mail: vasilii.cretu@mib.utm.md

M. Hoppe · R. Adelung · O. Lupan
Kiel University, Kiel, Germany

mm, using the synthesis from chemical solutions (SCS) developed by Lupan [10, 16–18]. The surface cleaning of substrates was performed by dipping in different acids and with decontamination in distilled water. The synthesis method and RTA procedure and ramps are described in detail in our previous works [10, 16–18]. The complex solution is formed of copper thiosulfate, as a cationic precursor, where is added 1 M of copper sulphate pentahydrate ($\text{CuSO}_4 \cdot 5\text{H}_2\text{O}$) and 1 M of sodium thiosulfate pentahydrate ($\text{Na}_2\text{S}_2\text{O}_3 \cdot 5\text{H}_2\text{O}$). More details on synthesis of Cu_2O nanostructured films using the SCS method is presented in previous work [10].

In order to control the thickness of the deposited film, a preliminary plot is used, according to which the substrate passes through a fixed number of SCS cycles. After the chemical deposition of the Cu_2O nanostructured films, rinsing in deionized water and drying in a hot air stream ($\sim 150^\circ\text{C}$) during 1 min is performed.

To modify surface morphology of nanostructured films, the rapid thermal annealing (RTA) in vacuum is used during 60 s at different temperatures. The expressed data will be presented depending on the temperature of the rapid thermal annealing.

In this paper, we studied the gas sensing properties of sensor structures based on nanostructured $\text{CuO}/\text{Cu}_2\text{O}$ films to 100 ppm of acetone vapor. The different temperatures of RTA treatment were investigated, at 400, 450, 525, 575, 600, 625 and 725 $^\circ\text{C}$ in vacuum (10^{-5} bar).

2.2 Characterization

For the electrical measurements of the samples, the two-point method was used. Aluminum contacts in the shape of a meander with a contact distance of 1 mm were used. The aluminum deposition was performed in high vacuum with pre-heating of glass substrate at temperature of 200 $^\circ\text{C}$ in the installation VUP-4. The value of the current, depending on the introduction of gas in test chamber, is determined using the Keithley 2400 source meter. Surface morphology was investigated using the scanning electron microscope (SEM, Zeiss, 7 kV, 10 μA).

3 Results

3.1 Morphological Characterization

The surface morphology and thickness of nanostructured films obtained using a SCS method is directly dependent on the duration of substrate maintenance in solutions and the number of cycles [13].

In previous works [10], the optimal thickness of films was determined to be about 0.8 μm , determined by the number of substrate dipping. Surface morphology is changed by RTA treatment at different temperatures (525, 575, 600 and 625 $^\circ\text{C}$) during 60 s in vacuum.

Figure 1 shows SEM images of $\text{Cu}_2\text{O}/\text{CuO}$ samples treated RTA during 60 s at temperature of 450 $^\circ\text{C}$ (a), and 525 $^\circ\text{C}$ (b) with the scale of 1 μm . From these images the columnar growth of the micro- and nanogranules on the surface of the copper oxide film with the diameter of the 0.5–1.5 μm . In Fig. 1a is presented the nanostructured $\text{Cu}_2\text{O}/\text{CuO}$ film with the scale of 1 μm , from this picture we can see that the surface morphology is composed of micro- and nanogranules formed from nanocrystalline particles penetrated between them.

In Fig. 1b it can be observed that nanocrystallites are structured and interpenetrate with each other. The nanocrystallites observed from Fig. 1a fuse together to form a smooth micro-nanogranule surface structure, keeping columnar growth with the same size of micro-nano granules of 0.5–1.5 μm . Both in Fig. 1a, b it can be observed that nanogranules have an irregular shape with the island structure. In the case RTA 525 $^\circ\text{C}$ treatment it can be observed a relief of the columnar granules raised to the formation of the island structure. In the case of RTA 450 $^\circ\text{C}$ treatment micro- and nanogranules have a less pronounced and stronger form intercalate without forming the island surface and the nanocrystals are more highlighted.

In Fig. 2 are presented SEM images of the $\text{Cu}_2\text{O}/\text{CuO}$ samples treated RTA in vacuum at 625 $^\circ\text{C}$ (a) and 725 $^\circ\text{C}$ (b) with a scale of 1 μm and 2 μm , respectively. In Fig. 2a it is noticed that the surface of the film has an irregular structure. The nanocrystallites interconnect in an amorphous film, but at the lower level it is observed the highlighting of the individual nanocrystalline. While in Fig. 2b the individual nanocrystals are much weaker, the films obviously have a more amorphous structure both at the surface and at the lower level.

3.2 Gas Sensing Properties

The gas response of the samples was studied to 100 ppm of acetone vapor at different temperatures in order to determine the optimal operating temperature. The sensibility of the samples was calculated using the equation [15]:

$$S \approx \left(\frac{R_{\text{gas}} - R_{\text{air}}}{R_{\text{air}}} \right) * 100 \quad (1)$$

where R_{air} and R_{gas} is the resistance of sensor structures under exposure in air and after introduction of gas in test chamber.

Fig. 1 SEM images of nanostructured $\text{Cu}_2\text{O}/\text{CuO}$ films grown using SCS method and treated RTA at **a** 450 °C and **b** 525 °C in vacuum

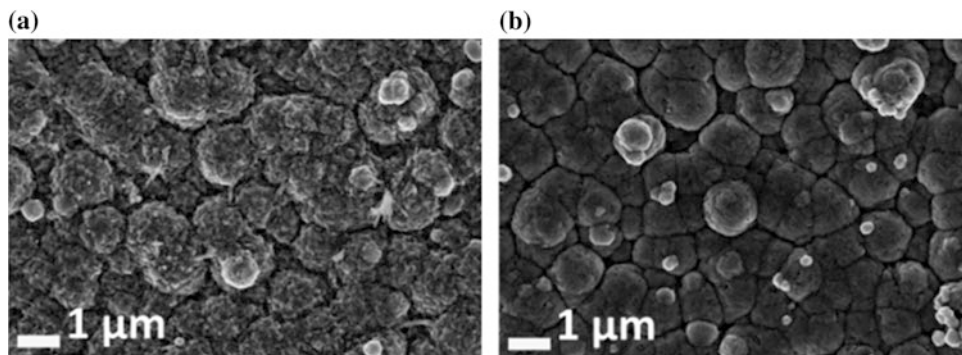
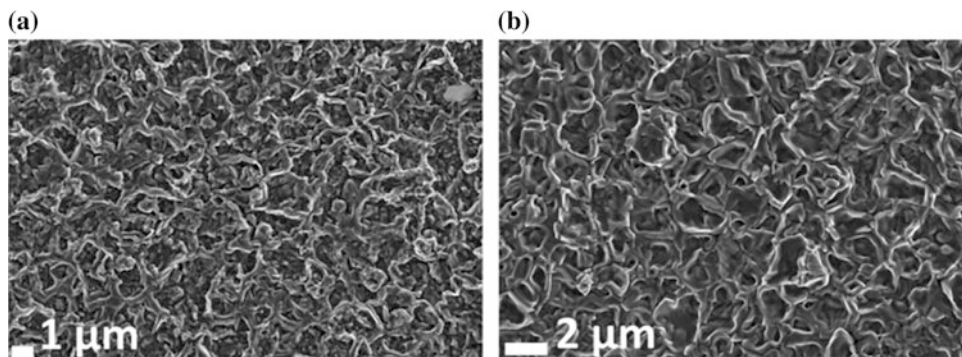


Fig. 2 SEM images of the nanostructured copper oxide films grown using a SCS method and treated RTA in vacuum at **a** 625 °C and **b** 725 °C



In Fig. 3 is presented the comparison of the gas response values to 100 ppm of acetone vapor for samples treated RTA at 525, 575, 600 and 625 °C during 60 s, and at operating temperature from 250 to 400 °C. It was observed that up to temperature of 250 °C the samples do not show the response to acetone vapor. The highest gas response to acetone vapor was observed for sample treated RTA at 625 °C with a response of about 40% at operating temperature of 300 °C. At the same time, the sample treated RTA at 575 °C shows a response of 30% at 250 °C.

These two samples show the highest values of response to the 100 ppm of acetone vapor. At the same time, samples treated RTA at 450 and 725 °C did not respond to acetone vapor.

The dependence of the acetone vapor response on the RTA treatment temperature and the operating temperature applied on the sample is evident. By analyzing Fig. 3 we can state that for the detection of 100 ppm of acetone vapor the most optimal sample is the nanostructured film treated RTA at 625 °C at an operating temperature of 300 °C.

In Fig. 4 is presented the gas response of nanostructured copper oxide films treated RTA in vacuum at different temperatures (from 525 to 625 °C) versus operating temperature (from 250 to 400 °C with a step of 50 °C) to 100 ppm of acetone vapor. Thus, from the presented figure we can state that the optimal response was observed for the films at an operating temperature of 300 °C with the approximate value of the 40% response. By the increase of

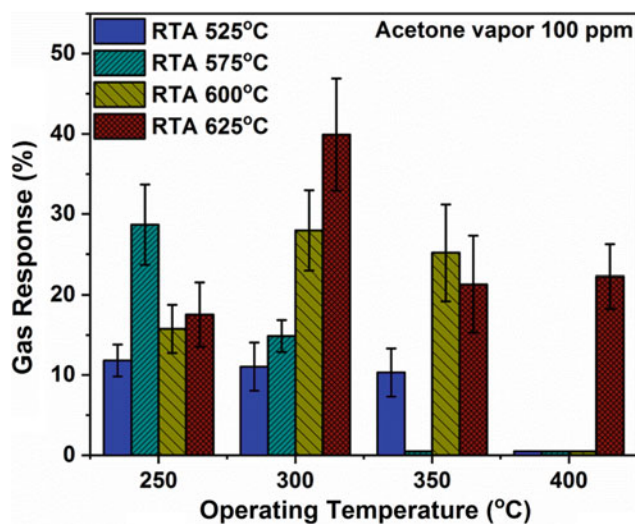


Fig. 3 The gas response of nanostructured copper oxide films with mixed phases treated RTA in vacuum at different temperatures to 100 ppm of acetone vapor versus operating temperature

the operating temperature, it is noticed that the value of the response to acetone vapor is decreasing.

Figure 5 shows the current-voltage characteristics of nanostructured films treated RTA at 625 °C at different operating temperatures. From this figure (in insertion) we notice that at room temperature the contacts are Ohmic and at the operating temperature of 250 °C the current-voltage

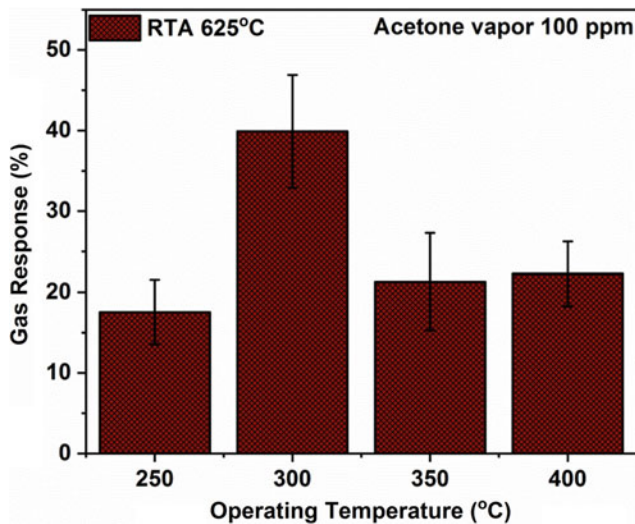


Fig. 4 The gas response of nanostructured CuO/Cu₂O films treated RTA at 625 °C to 100 ppm of acetone vapor versus operating temperature

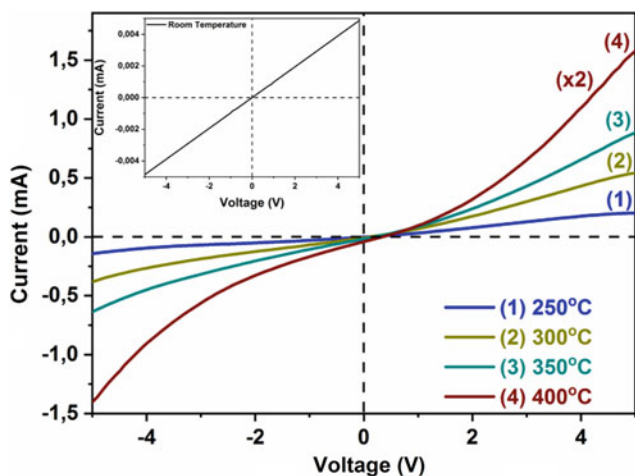


Fig. 5 Current-voltage characteristics of a nanostructured films treated RTA in vacuum at 625 °C at different operating temperatures

characteristics have a shape close to the shape of the Schottky double contacts [19].

In Fig. 6 the dynamic response of the nanostructured films treated RTA at 625 °C to 100 ppm of acetone vapor is presented. Two consecutive pulses of 100 ppm of acetone vapor were applied on the surface of sensor, showing in both cases a response of 40%. The response time was calculated to be 5.68 s from gas response of 0% to the gas response of 36% (i.e. 90% from total response). The partial recovery time was calculated to be 17 s from the maximal value down to 12% of response. After the recovery value of 12%, the recovery is much slower and the total recovery has an indefinite duration of 60 s.

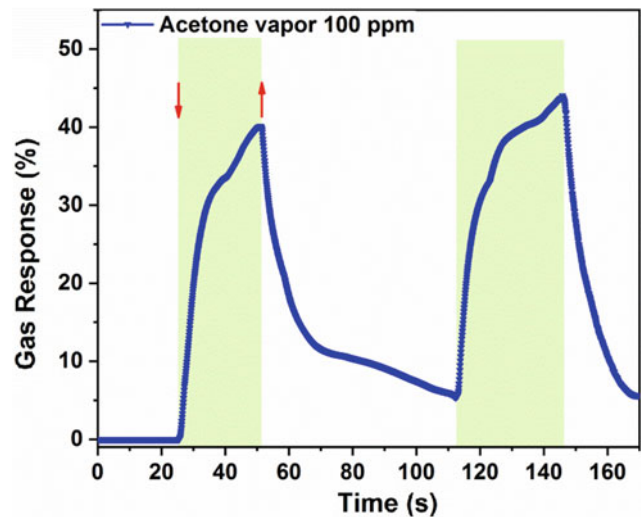
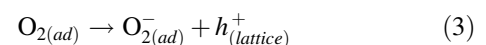


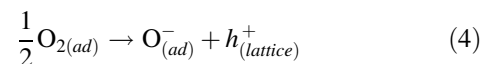
Fig. 6 The dynamic response of the nanostructured films treated RTA in vacuum at 625 °C to 100 ppm of acetone vapor

4 Proposed Mechanism

The reaction to gases at the surface of copper oxide is closely related to the type of defects and surface impurities [20]. Accordingly, a very important role in the gas detection mechanism for *p*-type semiconductors plays the surface phenomena. Thus, surface adsorption of oxygen can take place which can be ionized in several forms, namely molecular form O_2^- and atomic form O^- or O^{2-} . At temperatures lower than 200 °C, the predominant species at the surface are oxygen molecules O_2^- [21]:



While at temperatures higher than 200 °C the predominant species at the surface are atomic species O^- or O^{2-} [21]:



The ionosorbed oxygen at the surface generates holes and captures free electrons from the valence band, resulting in increased concentration of the holes at the surface resulting in decreasing of resistance. Thus, an hole accumulated layer is formed at the surface (HAL). The thickness of hole accumulated layer is proportional with Debye length (λ_D). The current flow takes place through the hole accumulation layer while the inner layers of the oxide have a high resistance. The copper oxide film consists of interconnected nanocrystals, so the gas detection mechanism influences the variation of the barrier potential between nanocrystallites,

the electrical conductivity of the sensor is modulated according to the equation [21, 22]:

$$G_p \approx \exp\left(\frac{qV_s}{2kT}\right) \quad (5)$$

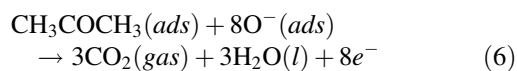
In the case of samples treated RTA, the nanostructured films are composed of mixed phase of copper oxide, namely CuO and Cu₂O [16].

Therefore, the nanoscale Cu₂O/CuO heterojunctions play an important role in gas sensing mechanism [16], which is based on combination of mechanism of core-shell structures and double-layer structures [23–25].

The valence band of Cu₂O is positioned at a level lower than in the case of CuO [26] which leads to the formation of a stream of holes from Cu₂O to CuO, and due to adsorbed surface oxygen the hole accumulation layer (HAL) extends to the interface [27, 28]. In previous work [16] the dependence of the gas response on the thickness of the surface-formed CuO film was investigated. In turn, the thickness of this film is slightly dependent on the temperature of RTA treatment. Thus, we can assume that at lower RTA temperatures the CuO film does not form on the whole surface, and at higher RTA treatment temperatures the surface-formed CuO film is thicker than the HAL region, and only the CuO phase participate to the gas sensing process [16].

Thus, we can assume that the highest value response will be when the thickness of the CuO layer will be comparable to the thickness of the HAL.

If the sensor structure is exposed to an atmosphere containing acetone vapor, the interaction of atomic oxygen with acetone vapor molecules at the surface of nano-crystalline layer will take place. As a result, acetone molecules are oxidized to molecules of CO₂ and H₂O with the release of electrons this can be represented by the following reaction [29]:



Thus, an acetone molecule interacts with eight adsorbed oxygen ions, eight electrons donated by the acetone molecules interact with eight holes donated by the copper oxide, and as a result the reduction of the HAL region and corresponding increase in sensor resistance.

An effective method for controlling of the gas sensing properties of semiconductor oxide films is the modification of the surface morphology which results in a change in the response value for both *n*-type and *p*-type conductivity [30].

Copper oxide particles with a relatively smaller diameter allow to improve the gas sensing properties of the nanostructured films [31, 32]. Also, the smaller particle diameter

forms a higher surface/volume ratio, which allows a larger amount of oxygen species to be adsorbed on the surface to increase the gas response value of the nanostructured film [30]. Thermal post-deposition treatment at different temperatures allows to form different appropriate surface morphologies and to modify the gas sensitivity and selectivity properties of the investigated films.

5 Conclusions

In this paper, the research nanostructured films of CuO/Cu₂O to acetone vapor with the concentration of 100 ppm is presented. The possibility of controlling the sensitivity of the sensors by changing the RTA temperature and operating temperature has been demonstrated. It has been determined that for the detection of 100 ppm acetone vapor, the optimal temperature of the rapid heat treatment is 625 °C for 60 s. The obtained nanostructured film shows the response value of about 40% at an operating temperature of 300 °C. With the response time of 5.68 s and with partial recovery within 17 s.

Acknowledgements The research presented in this work was supported financially by the young researchers Project no 17 TC (19.80012.50.04A) from 24 May 2019 funded by the Government of the Republic of Moldova and by the Technical University of Moldova (T.U.M.).

Conflict of Interest The authors declare that they have no conflict of interest.

References

- Cheng, L., Ma, S.Y., Li, X.B., Luo, J., Li, W.Q., Li, F.M., Mao, Y. Z., Wang, T.T., Li, Y.F.: Highly sensitive acetone sensors based on Y-doped SnO₂ prismatic hollow nanofibers synthesized by electrospinning. *Sens. Actuators B* **200**, 181 (2014)
- Xiao, T., Wang, X.-Y., Zhao, Z.-H., Li, L., Zhang, L., Yao, H.-C., Wang, J.-S., Li, Z.-J.: Highly sensitive and selective acetone sensor based on C-doped WO₃ for potential diagnosis of diabetes mellitus. *Sens. Actuators B* **199**, 210 (2014)
- Wang, Z.N., Wang, C.J., Lathan, P.: Breath acetone analysis of diabetic dogs using a cavity ringdown breath analyzer. *IEEE Sens. J.* **14**, 1117 (2014)
- Do, J.-S., Wang, S.-H.: On the sensitivity of conductimetric acetone gas sensor based on polypyrrole and polyaniline conducting polymers. *Sens. Actuators B* **185**, 39 (2013)
- Ding, M., Sorescu, D.C., Star, A.: Photoinduced charge transfer and acetone sensitivity of single walled carbon nanotube–titanium dioxide hybrids. *J. Am. Chem. Soc.* **135**, 9015 (2013)
- Khandekar, M.S., Tarwal, N.L., Mulla, I.S., Suryavanshi, S.S.: Nanocrystalline Ce doped CoFe₂O₄ as an acetone gas sensor. *Ceram. Int.* **40**, 447 (2014)
- Jiao, W.-L., Zhang, L.: Preparation and gas sensing properties for acetone of amorphous Ag modified NiFe₂O₄ sensor. *Trans. Nonferrous Met. Soc. China* **22**, 1127 (2012)

8. Murray, C.B., Norris, D.J., Bawendi, M.G.: Synthesis and characterization of nearly monodisperse CdE (E = S, Se, Te) semiconductor nanocrystallites. *J. Am. Chem. Soc.* **115**, 8706 (1993)
9. Alivisatos, A.P.: Semiconductor clusters, nanocrystals, and quantum dots. *Science* **271**, 933 (1996)
10. Lupan, O., Cretu, V., Postica, V., Ababii, N., Polonskyi, O., Kaidas, V., Schutt, F., Mishra, Y., Monaico, E., Tiginyanu, I., Sontea, V., Strunskus, Th, Faupel, F., Adelung, R.: Enhanced ethanol vapour sensing performances of copper oxide nanocrystals with mixed phases. *Sens. Actuators B Chem.* **224**, 434–448 (2015)
11. Siebert, L., Lupan, O., Mirabelli, M., Ababii, N., Terasa, M.-I., Kaps, S., Cretu, V., Vahl, A., Faupel, F., Adelung, R.: 3D-printed chemiresistive sensor array on nanowires CuO/Cu₂O/Cu heterojunction net. *ACS Appl. Mater. Interfaces* **11**(28), 25508–25515 (2019)
12. Choi, Y., Kim, D., Hong, S., Hong, K.S.: H₂ and C₂H₅OH sensing characteristics of mesoporous p-type CuO films prepared via a novel precursor-based ink solution route. *Sens. Actuators B* **178**, 395–403 (2013)
13. Shishiyanu, S.T., Shishiyanu, T.S., Lupan, O.I.: Novel NO₂ gas sensor based on cuprous oxide thin films. *Sens. Actuators B Chem.* **113**(1), 468–476 (2006)
14. Debbichi, L., Marco de Lucas, M.C., Pierson, J.F., Krüger, P.: Vibrational Properties of CuO and Cu₄O₃ from first-principles calculations, and Raman and infrared spectroscopy. *J. Phys. Chem. C* **116**, 10232–10237 (2012)
15. Xu, C.K., Liu, Y.K., Xu, G.D., Wang, G.H.: Preparation and characterization of CuO nanorods by thermal decomposition of CuC₂O₄ precursor. *Mater. Res. Bull.* **37**, 2365–2372 (2002)
16. Lupan, O., Cretu, V., Postica, V., Polonskyi, O., Ababii, N., Schütt, F., Kaidas, V., Faupel, F., Adelung, R.: Non-planar nanoscale p–p heterojunctions formation in Zn_xCu_{1-x}O_y Nanocrystals by mixed phases for enhanced sensors. *Sens. Actuators B Chem.* **230**, 832–843 (2016)
17. Lupan, O., Chow, L., Shishiyanu, S., Monaico, E., Shishiyanu, T., Şontea, V., Roldan, Cuenya B., Naitabdi, A., Park, S., Schulte, A.: Nanostructured zinc oxide films synthesized by successive chemical solution deposition for gas sensor applications. *Mater. Res. Bull.* **44**, 63–69 (2009)
18. Lupan, O., Shishiyanu, S., Shishiyanu, T.: Nitrogen oxides and ammonia sensing characteristics of SILAR deposited ZnO thin film. *Superlattices Microstruct.* **42**, 375–378 (2007)
19. Kobayashi, M., Kinoshita, A., Saraswat, K., Philip Wong, H.-S., Nishi, Y.: Fermi level depinning in metal/Ge Schottky junction for metal source/drain Ge metaloxide-semiconductor field-effect-transistor application. *J. Appl. Phys.* **105**, 023702 (2009)
20. Cretu, V., Postica, V., Mishra, A.K., Hoppe, M., Tiginyanu, I., Mishra, Y.K., Chow, L., De Leeuw, N.H., Adelung, R., Lupan, O.: Synthesis, characterization and DFT studies of zinc-doped copper oxide nanocrystals for gas sensing applications. *J. Mater. Chem. A* **4**(7), 6527–6539 (2016)
21. Hübner, M., Simion, C.E., Tomescu-Stănoiu, A., Pokhrel, S., Bârsan, N., Weimar, U.: Influence of humidity on CO sensing with p-type CuO thick film gas sensors. *Sens. Actuators B Chem.* **153**, 347–353 (2011)
22. Zhang, J., Liu, J., Peng, Q., Wang, X., Li, Y.: Nearly monodisperse Cu₂O and CuO nanospheres: preparation and applications for sensitive gas sensors. *Chem. Mater.* **18**(4), 867–871 (2006)
23. Katoch, A., Choi, S.-W., Sun, G.-J., Kim, S.S.: An approach to detecting a reducing gas by radial modulation of electron-depleted shells in core–shell nanofibers. *J. Mater. Chem. A* **1**(43), 13588 (2013)
24. Choi, S.-W., Katoch, A., Sun, G.-J., Kim, J.-H., Kim, S.-H., Kim, S.S.: Dual functional sensing mechanism in SnO₂–ZnO core-shell nanowires. *ACS Appl. Mater. Interfaces* **6**(11), 8281–8287 (2014)
25. Kim, J.-H., Katoch, A., Kim, S.S.: Optimum shell thickness and underlying sensing mechanism in p–n CuO–ZnO core–shell nanowires. *Sens. Actuators B Chem.* **222**, 249–256 (2016)
26. Huang, Q., Kang, F., Liu, H., Li, Q., Xiao, X.: Highly aligned Cu₂O/CuO/TiO₂ core/shell nanowire arrays as photocathodes for water photoelectrolysis. *J. Mater. Chem. A* **1**(7), 2418–2425 (2013)
27. Sharma, B.L., Purohit, R.K.: *Semiconductor Heterojunctions*. Elsevier (2013)
28. Oldham, W.G., Milnes, A.G.: Interface states in abrupt semiconductor heterojunctions. *Solid-State Electron.* **7**(2), 153–165 (1964)
29. Qin, L., Xu, J., Dong, X., Pan, Q., Cheng, Z., Xiang, Q., Li, F.: The template-free synthesis of square-shaped SnO₂ nanowires: the temperature effect and acetone gas sensors. *Nanotechnology* **19**(18), 185705 (2008)
30. Yamazoe, N.: New approaches for improving semiconductor gas sensors. *Sens. Actuators B Chem.* **5**(1–4), 7–19 (1991)
31. Zoolfakar, A., Ahmad, M., Rani, R., Ou, J., Balendhran, S., Zhuiykov, S., Latham, K., Wlodarski, W., Kalantar-Zadeh, K.: Nanostructured copper oxides as ethanol vapour sensors. *Sens. Actuators B Chem.* **185**, 620–627 (2013)
32. Lupan, O., Postica, V., Ababii, N., Hoppe, M., Cretu, V., Tiginyanu, I., Sontea, V., Pauporte, Th, Viana, B., Adelung, R.: Influence of CuO nanostructures morphology on hydrogen gas sensing performances. *Microelectron. Eng.* **164**, 63–70 (2016)

Influence of the Growth Temperature on the Properties of the Transparent and Conductive NiO Thin Films Obtained by RF Magnetron Sputtering

L. Ghimpu, V. Suman, and D. Rusnac

Abstract

Transparent and conductive nickel oxide (NiO) thin films were deposited on the glass supports by magnetron pulverization (RF). The NiO thin films were investigated by X-ray diffraction (XRD), scanning electron microscopy (SEM), SEM equipped with X-ray detector-analyzer (EDX), UV-VIS spectroscopy and Hall measurements. XRD revealed that the NiO thin films obtained at different substrate temperatures are textured and possess a cubic crystalline structure. SEM analysis indicates the formation of the crystallites with a granular structure. The EDX spectra of the NiO thin films highlighted the presence of Ni and O as elementary components. With the increase of the substrate temperature from 50 to 450 °C Hall measurements show a decrease of the resistivity of the NiO thin layers due to the increase of the concentration and mobility of the free carriers.

Keywords

RF magnetron pulverization • NiO thin films • XRD diffraction • EDX analysis • UV spectroscopy • Electrical properties

1 Introduction

Presently, nanomaterials are involved in a variety of applications in many domains. The nickel oxide as the semiconductor becomes a remarkable subject in new research

L. Ghimpu (✉) · V. Suman
Institute of Electronic Engineering and Nanotechnologies,
Academy of Sciences of Moldova, 3/3 Academiei str., Chisinau,
Republic of Moldova
e-mail: lidia.ghimpu@gmail.com

D. Rusnac
Department of Physics and Engineering, Moldova State
University, Chisinau, Republic of Moldova

space due to its quantitative impact, quantity of dimension effect, surface effect, and at the same time macroscopic quantum effect. Nanocrystalline NiO is supposed to possess more improved properties in comparison with the micrometric dimensions. Nickel oxide is a semiconductor with the p-type conductivity and is widely used as a conductive transparent layer [1]. The width of the forbidden band of the nickel oxide at $T = 300$ K varies between 3, 6 and 4 eV [2]. NiO is an oxide material that is produced easily and possesses a cubic crystalline structure. NiO thin films have an excellent chemical stability, as well as optical, electrical and magnetic properties, and have been employed as an anti-ferromagnetic material [3]. Also, NiO p-type transparent conducting films were used as material for electrochromic display devices [4] and a part of functional sensor layers in chemical sensors [1]. Besides, (002), (111)-oriented NiO films was used as buffer layers that are deposited on oxide films with other orientations, such as c-axis-oriented perovskite type ferromagnetic films and superconducting films [5–11]. NiO films have been obtained using various techniques, including spray pyrolysis [12, 13], electron beam evaporation [14], pulsed laser deposition [15], plasma-enhanced chemical vapor deposition [16] and reactive sputtering [17]. In this paper, NiO films with a thickness of approximately 200 nm were grown on glass substrates by reactive radio-frequency (RF) magnetron sputtering under various substrate temperature. The effect of substrate temperature on the microstructure, composition, optical and electrical properties of the films are described, and is discussed as follows.

2 Experiment

Transparent and conductive NiO thin films were obtained on glass supports through RF magnetron pulverization from the metallic target of Ni in a constant stream of argon and oxygen directed by an electronic flux-meter. The working power of the magnetron was 190 W. The values of the rate

of Ar and O were 60 ml/min and 5 ml/min, respectively. A set of NiO samples in the temperature range from 50 to 450 °C were obtained. The temperature was monitored by the electronic temperature control device with the accuracy of ± 1 °C, other essential parameters of preparation being the same. The thickness of the obtained layers being of 200 nm, monitored by the electronic thickness control device with the precision of 0.1 nm. In this paper the physical properties of these films are investigated.

3 Results and Discussion

3.1 Optical Properties

In Fig. 1. the transmittance spectra of NiO thin films deposited at different substrate temperature from 50 to 450 °C.

The transmittance for the deposited layer at the substrate temperature 50 °C does not exceed 40%. With the increase of the substrate temperature of preparation, the probability of the Ni-non-oxidized re-evaporation from the surface of the support increases that in its turn causes the increase of the transmittance of the layers. The films prepared at $T_{\text{sup}} > 100$ °C were characterized by a high-transmittance coefficient throughout the visible domain of spectrum. We observed that the value of the optical forbidden band gap of NiO thin films presented in Fig. 2 increases from 3.76 to 3.9 eV as the temperature of the support increases to 400 °C.

3.2 Electrical Properties

In Fig. 3. are presented the dependences of mobility, resistivity and concentration of free carriers on the temperature of

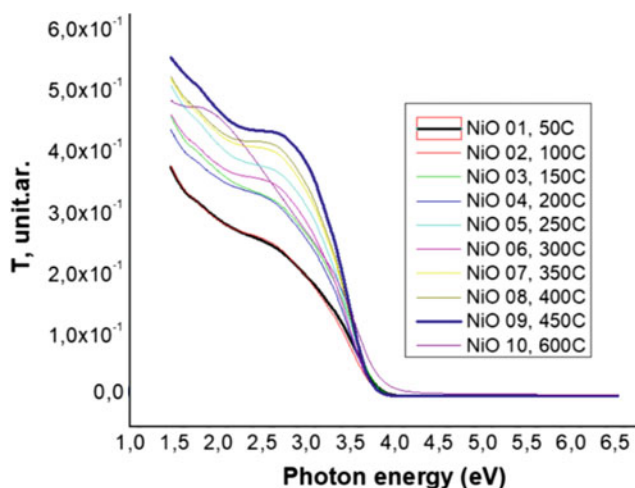


Fig. 1 Transmission spectra of NiO thin layers at different substrate temperatures

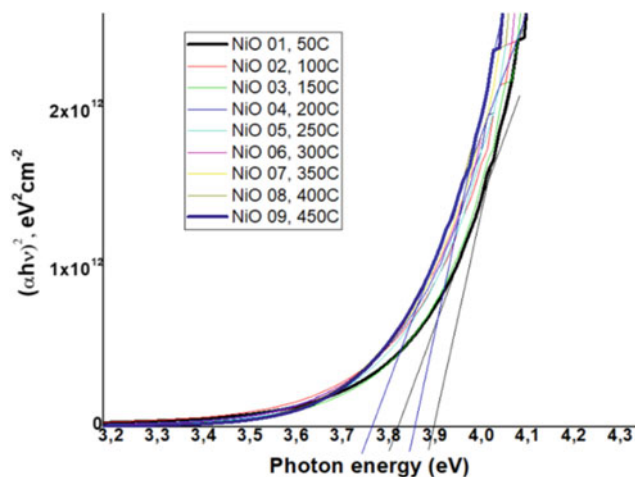


Fig. 2 Dependencies $(\alpha h\nu)^2 = f(h\nu)$ of NiO thin films at different substrate temperatures

growth of the NiO thin layers. The study of the electrical resistivity of the NiO thin layers with the thickness of 200 nm demonstrated that the dependence of the resistivity in function on the temperature of growth is non-monotonic.

The minimum value of the specific resistance is reached at a substrate temperature of 350 °C, then slightly increases. Investigation on Hall parameters demonstrated that the mobility of the carrier's increases monotonously with the increase of the substrate temperature, and the concentration of the free carriers has a maximum at the temperature of the support of 290 °C. This nature of the temperature-dependence of the concentration of the free carriers in the thin layers of NiO is also due to the fact that the nickel oxide contains its own acceptor defects in the volume and on the surface of the crystallites. The known experimental and theoretical data confirm the fact that oxygen vacancies play an important role in the conductivity of the transparent and conductive NiO layers [18]. Increase of the Hall mobility at the temperatures above 200 °C is also due to a decrease of the potential barrier for the free carriers at the boundaries of crystallites due to the intensification of the thermal diffusion of oxygen from the surface of the granules during the growth of the layer in a high vacuum.

3.3 Structure and Composition of the Films

The X-ray diffraction (XRD) diffractogram of the NiO thin layer obtained at $T_{\text{sub}} = 100$ °C are presented in Fig. 4.

It is observed that the X-ray diffraction spectrum indicates the specific peaks of the nickel oxide. The position of the peaks for the angle 2θ are: 31,6983; 35,5307; 66,2136 having as crystalline plans (002), (101) and (004) for NiO. X-ray studies highlighted the fact that the layers obtained at

Fig. 3 Temperature -dependence of mobility (1), resistivity (2), concentration of free carriers (3) of the NiO thin layers

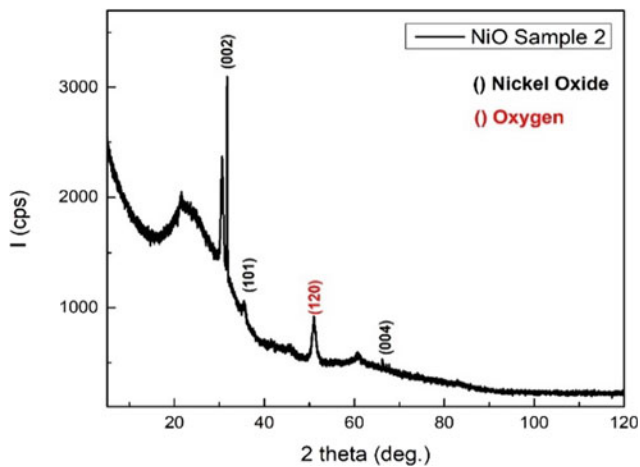
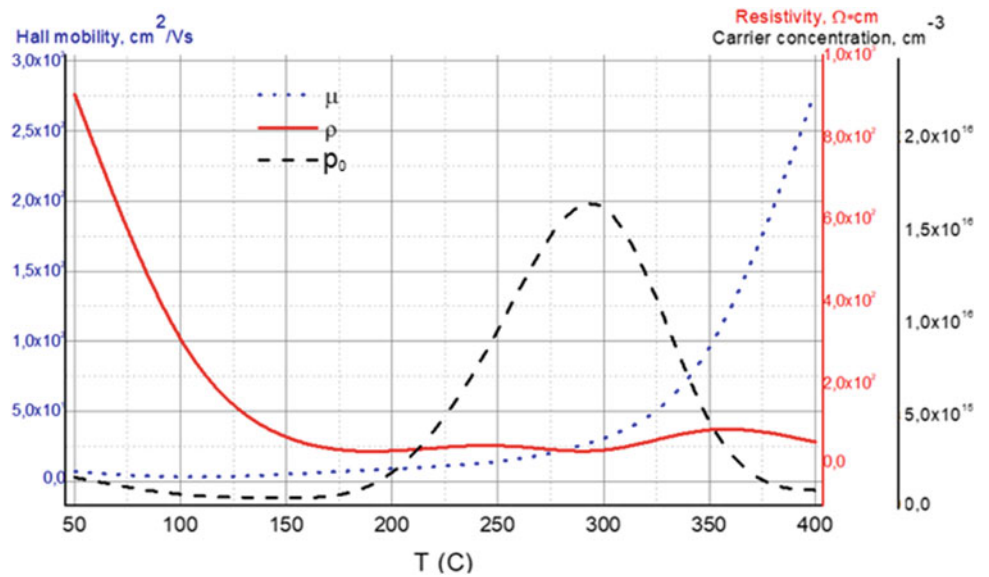


Fig. 4 XRD pattern of the NiO thin layer obtained at $T_{sub} = 100\text{ }^{\circ}\text{C}$

different temperatures of the support are textured and possess a cubic crystalline structure.

The XRD data demonstrate that the samples are monophase and do not contain other distinct impurities in the diffraction peaks. The grain sizes of the granules of the nanoparticles of NiO were using the well-known formula:

$$D = \frac{k\lambda}{\cos \theta}$$

where k —is constant most often cited in the literature as having a value of about 0.9, λ —is the X-ray wavelength and θ_{hkl} is the Bragg angle.

The diameter of the grains estimated according to the Debye-Sherrer formula is 27 nm for $T_{sup} = 100\text{ }^{\circ}\text{C}$.

The morphological studies and composition of the surface of the analysis of the of NiO thin layers were investigated using the SEM and EDX images presented in Fig. 5a, b.

From the SEM analysis we conclude the formation of the crystallites with a granular structure, the EDX spectrum for the thin layers of NiO presented in Fig. 5b highlighted the presence of Ni and O as elementary components of the pulverized material. Moreover, there are no other peaks of other chemical elements except the observed Ni and O.

4 Conclusions

Nanostructured transparent and conductive p -type NiO thin films were prepared successfully by RF sputtering from Ni metal target. The XRD analysis of the NiO thin layers highlighted a high crystalline structure with a preferential crystalline orientation in the plane (002). The optical transparency of the of NiO layers for $T > 100\text{ }^{\circ}\text{C}$ exceeds 80% throughout the interval of the visible spectrum. The concentration of the free carriers reached the value of $2.12 \times 10^{16}\text{ cm}^{-3}$ at a $300\text{ }^{\circ}\text{C}$ substrate temperature. The increase of the temperature of the support from 50 to $450\text{ }^{\circ}\text{C}$ leads to a decrease of the resistivity of the NiO layers due to the increase of the concentration and mobility of the free carriers. The increase of the carrier's concentration is due to the formation of some acceptor centers (oxygen vacancies)

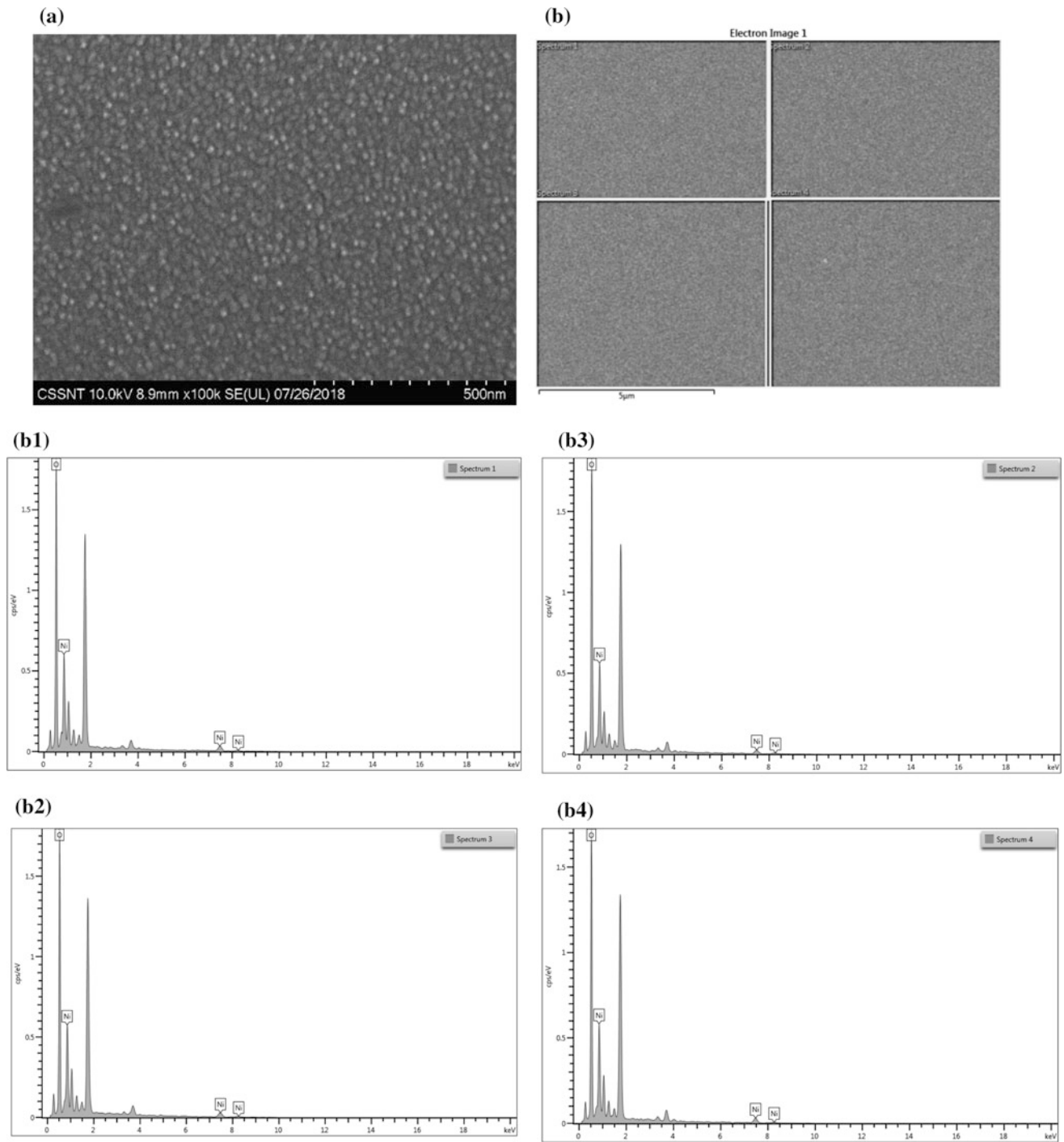


Fig. 5 a SEM image of NiO thin film deposited at $T_{\text{sub}} = 200$ °C, b EDX of NiO thin film deposited at $T_{\text{sub}} = 200$ °C

with the increase of the temperature of the support. An increase of the concentration of the free carriers leads to a significant increase of the difference in the values of band gap due to the Burstein-Moss effect. The increase of the Hall mobility correlates with the results of the structural studies that highlights the increase of the size of crystallites with the increase of the temperature of the support.

Acknowledgements The authors thank the Ministry of Education, Culture and Research of Republic of Moldova for funding the Institutional Grant 15.817.02.08A.

Conflict of Interest The authors declare that they have no conflict of interest.

References

1. Sato, H., Minami, T., Tokata, S., Yamada, T.: *Thin Solid Films* **236**, 27–31 (1993)
2. Adler, D., Feinlib, J.: *Phys. Rev. B* **2**, 3112 (1970)
3. Chen, H.-L., Lu, Y.-M., Wu, J.-Y., Hwang, W.S.: *Mater Trans* **46** (11), 2530–2535 (2005)
4. Fujii, E., Tomozawa, A., Torii, H., Takayama, R.: *Jpn. J. Appl. Phys.* **35**, L328–L330 (1996)
5. Kitao, M., Izawa, K., Urabe, K., Komatsu, T., Kuwano, S., Yamada, S.: *Jpn. J. Appl. Phys.* **33**, 6656–6662 (1994)
6. Kumagai, H., Matsumoto, M., Toyoda, K., Obara, M.: *J. Mater. Sci. Lett.* **15**, 1081–1083 (1996)
7. Yang, J., Shi, D.Q., Park, C., Song, K.J., Ko, R.K., Liu, H.Z., Gu, H.W.: *Physica C* **412–414**, 844–847 (2004)
8. Maeda, T., Kim, S.B., Suga, T., Kurosaki, H., Toyotaka, Y., Yamada, Y., Watanabe, T., Matsumoto, K., Hirabayashi, I.: *Phys C* **357–360**, 1042–1045 (2001)
9. Lee, S.S., Hwang, D.G., Park, C.M., Rhee, J.R. (1997) *J. Appl. Phys.* 815298–53008; Puspharajah, P., Radhakrishna, S., Arof, A. K.: *J. Mater. Sci.* **32**, 3001–3006 (1997)
10. Wang, S.Y., Wang, W., Wang, W.Z., Du, Y.W.: *Mater. Sci. Eng.* **B90**, 133–137 (2002)
11. Agrawal, A., Habibi, H.R., Agrawal, R.K., Cronin, J.P., Roberts, D.M., R'Sue, C.P., Lampert, C.M.: *Thin Solid Film* **221**, 239–253 (1992)
12. Tanaka, M., Mukai, M., Fujimori, Y., Kondoh, M., Tasaka, Y., Babaand, H., Usami, S.: *Thin Solid Films* **281–282**, 453–456 (1996)
13. Fujii, E., Tomozawa, A., Fujii, S., Torii, H., Hattori, M., Takayama, R.: *Jpn. J. Appl. Phys.* **32**, L1448–L1450 (1993)
14. Patel, K.J., Desai, M.S., Panchal, C.J., Rehani, B.: *J. Nano-Electron. Phys.* **1**, 376–382 (2011)
15. Franta, D., Negulescu, B., Thomas, L., Dahoo, P.R., Guyot, M., Ohlidal, I., Mistrik, J., Yamaguchi, T.: *J. Appl. Surf. Sci.* **244**(1–4), 426–430 (2005)
16. Fujii, E., Tomozawa, A., Torii, H., Takayama, R.: *Jpn. J. Appl. Phys.* **35**, 328–330 (1996)
17. Xiao, Z.H., Xia, X.F., Xu, S.J., Luo, Y.P., Zhong, W., Ou, H., Jiang, E.S.: *ICADME Proceeding 5th International Conference on Advanced Design and Manufacturing Engineering*, pp. 827–832 (2015)
18. Samuelraj Visuvasam, A., Dineshababu, N.K.: *IJARTET* **3**(13), 234 (2016)

Part II

Plasmonics and Metamaterials

Active Spectral Absorption Control in a Tunable Liquid Crystal/Metamaterial Structure by Polarization Plane Rotation

A. Bărar, O. Dănilă, D. Mănăilă-Maximean, and V. A. Loiko

Abstract

We present theoretical studies conducted on the newly-introduced controllable metamaterial—liquid crystal system. Our model consists of a standard metamaterial single cell split ring resonator array with dimensions tailored to match a desired frequency in the infrared frequency regime, with an added liquid crystal layer, in order to control the refractive index surrounding the resonator array. We show that this type of system can show controllable spectral absorption in the desired range, making them suitable for a range of optical applications.

Keywords

Metamaterial • Split ring resonator • Liquid crystal

1 Introduction

Metamaterial structures [1–3] are a relatively new and interesting approach to achieve complete control of the electromagnetic field, by means of periodicity, geometrical design and electromagnetic properties of the structure [4, 5]. Although metamaterials were theoretically envisioned [6] and studied [7–10] since more than fifty years ago, it was only recently that this field was able to become relevant for applications in the optical regime. Most notably, microwave and optical cloaks [11–13], together with perfect optical

meta-lenses [14, 15] were distinct highlights in the re-establishment of the field in the general scientific attention. Specifically, magnetic field enhancers known as split-ring resonators (SRR-s) are able to provide a significant increase in the magnetic field around a certain resonance frequency. Owing to their geometric design, SRRs are considered single-frequency nano-LC resonators, in which the electrical charge excited by the electromagnetic field oscillates at a single fixed frequency. In this configuration, due to the left handedness of the metamaterial (both electric permittivity and magnetic permeability are negative), negative refraction has been observed [15]. However, due to the fact that physical considerations regarding negative electric and magnetic susceptibilities indicate the array should be constructed out of metals, real metamaterial systems exhibit a strong Ohmic loss due to the formation of currents in the metal layers. Also, dilation of the metamaterial structure through heat conversion is one of the strongest parasitic effects appearing in such systems, due to a reconfiguration of the geometrical layout of the unit cell. A possible bypass of this disadvantage may be constituted by the newly-developed all-dielectric metamaterials [16], that manage to exhibit left handedness without the expense of ohmic loss that generally appears in metals. Another disadvantage is the fixed resonance frequency at which the metamaterial structure operates, which may be limiting for certain broadband applications. This limitation may be overcome by constructing mechanically actuated structures [17], which can produce tunable inductances and/or capacitances in the SRR structure. While this resolves the issue of the fixed resonance frequency, the spectral tuning range is typically low when compared to the range needed by applications. Moreover, this approach does not solve deviations from the ideal transversal electric (TE) or transversal magnetic (TM) propagation modes, which are usually assumed in theory but difficult to control in real systems.

To compensate for both geometric and polarization tuning, we theoretically investigate a new double SRR model, on which a layer of liquid crystal molecules are deposited. Tuning of both the resonance frequency and input

A. Bărar

Department of Electronic Technology and Reliability, University Politehnica of Bucharest, Bucharest, Romania
e-mail: ana.d.barar@gmail.com

O. Dănilă (✉) · D. Mănăilă-Maximean

Physics Department, University Politehnica of Bucharest, 313 Splaiul Independenței, District 6, 060082 Bucharest, Romania
e-mail: octaviandanila2013@yahoo.com

V. A. Loiko

Stepanov Institute of Physics, National Academy of Sciences of Belarus, Minsk, Belarus

polarization control can be executed by rotating the liquid crystal molecule using an external electric field of considerably lower frequency (Hz regime). Moreover, the use of liquid crystal composites, such as polymer dispersed liquid crystals (PDLCs), together with electric or magnetic response enhancers, which have been extensively studied [18–20], does not perturb the effective behaviour of the layer, only contributing to the establishment of an effective refractive index. Also, the alignment of the liquid crystal molecule on the metamaterial surface can be either planar, homeotropic or hybrid, with the precaution that practical implementation of the liquid crystal-SRR structure takes into account the appropriate direction for applying the control voltage. The effective refractive index of the liquid crystal in the proximity of the SRR structure introduces both a different refractive index mismatch, and in some cases a damping coefficient, which induces a change in the absorption peaks, while the optical anisotropy of the molecules resolves the TE or TM conditions on the desired propagation direction.

2 Model Design Considerations

2.1 Model Description

The envisioned model consists of a modified ‘W’-shaped single-cell split ring resonator having the dimensions indicated in Fig. 1. The SRR structure has its dimensions in the hundred nanometer range, far smaller than the operating wavelength range, taken in the near and middle infrared

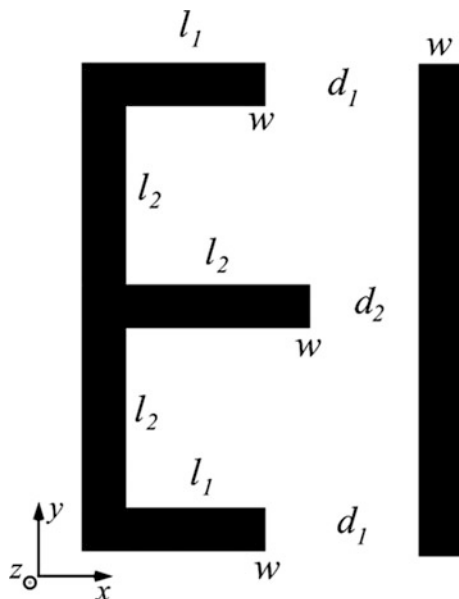


Fig. 1 Layout of the SRR metamaterial structure

spectrum, from 1 to 3 μm . The detailed dimensions are given in Table 1. Due to its absorptive nature, metal, namely gold was used to create the metamaterial structure. The gold layer thickness was chosen at 200 nm. The chosen substrate was a polyimide-derived material, based on practical advantages such as a relatively small skin depth and a relatively high mechanical adherence to the gold substrate.

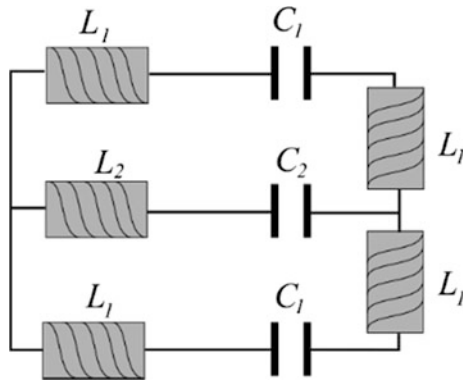
All geometrical considerations (cell dimensions, SRR geometry and thickness and layer thickness were created in close correlation with the technological possibilities such as electron beam lithography (EBL). Due to its modified nature, the SRR can be described based on a modified transmission line LC resonator model, with the values of the inductances and capacitances given by both material properties and SRR geometry. The transmission line model describing the model is presented in Fig. 2, with a vacuum resonance frequency $f_0 = \frac{1}{2\pi\sqrt{L_e C_e}} \simeq 2.1 \text{ THz}$, where L_e and C_e are the equivalent inductance and capacitance of the resonant structure. We also assumed both a 20 μm layer of air, to establish a reference in the spectral behavior, and a layer of liquid crystal having the same thickness, to observe the deviations from the reference. The substrate thickness was chosen ten times larger than the skin depth of the radiation taken at the maximum frequency, in order to ensure that no transmission occurs. Regarding the liquid crystal layer, the thickness was chosen at 20 μm , which is a typical thickness for liquid crystal sample cells [21, 22]. With this model, simulations were performed in the absence and presence of the liquid crystal layer, to be detailed in the following section.

2.2 Simulation Description

To highlight the spectral and polarization behavior of the metamaterial-liquid crystal cell, we performed simulations for the full electric and magnetic field of a polarized plane electromagnetic wave having a frequency around the computed value. As a rule of thumb, we have assumed the electric field component only in the Ox direction for the metamaterial-air reference cell, with a nominal value. Based on this, the boundary conditions were chosen as Perfect Electric Conductor (PEC) on the Ox axis and Perfect Magnetic Conductor (PMC) on the Oy axis. The boundary condition of the 200 nm air-to-metamaterial interface was chosen as Transition Electric and Magnetic, and the full absorption and propagation parameters of the media were considered (electric permittivity, magnetic permeability and electric conductivity). To further ensure that there will be no transmission on the back of the substrate, an Impedance Matching (IM) boundary condition was imposed on the backside of the substrate. To characterize the anisotropic nature of the liquid crystal layer, we used the effective

Table 1 Geometric values used in the construction of the SRR

Geometry	Value (nm)
l_1	300
l_2	400
w	100
d_1	200
d_2	100

**Fig. 2** Equivalent electric circuit of the SRR

medium approach, in which we have specified both an effective isotropic refractive index for the medium and an effective polarization rotation angle for the input electric field. Due to this rotation, in the case of liquid crystal-metamaterial cell system, the PEC and PMC conditions applied to the lateral boundaries were modified accordingly. In the simulation, we used one of the most commonly-used liquid crystals, namely the 5CB in its nematic phase. Note that according to our prior discussion, any liquid crystal or liquid crystal composite can be used for investigation. The input power of the incident wave was low enough to maintain the system in the linear regime, and the Joule effect was low enough to not induce a nematic-to-isotropic phase transition.

The material properties describing the metamaterial structure have been used throughout the study, and have been centralized in Table 2.

Table 2 Material properties for the SRR system

Material	Electromagnetic property	Value (unit)
Air	Refractive index	1
Polymide	Relative permittivity	$2.88 - j \cdot 0.01$ (F/m)
Polymide	Relative permeability	1 (H/m)
Gold	Relative permittivity	1 (H/m)
Gold	Relative permeability	1 (H/m)
Gold	Conductivity	4.09×10^7 (S/m)
5CB	Refractive index	1.5112

3 Results and Discussions

3.1 Reference Cell Results

For the air-metamaterial system, we have obtained a complete resonance at a wavelength of around $1.9 \mu\text{m}$, with an estimated bandwidth of approximately 120 nm , between 1.87 and $2.02 \mu\text{m}$. The result is shown in Fig. 3. The bandwidth estimation was taken for values of the absorption coefficient exceeding the 0.9 threshold. Moreover, the electric and magnetic field profiles at the maximum absorption peak have been plotted. It can be seen from the 2D graphs that the electric field is highly concentrated in the capacitor exhibiting the shortest plate distance, as is expected, while the magnetic field is concentrated at the middle of the ‘W’ shaped SRR. The normalized values of both fields exceed unity by far, which is in complete accordance with a resonance oscillation, but the validation of the SRR comes from the normalized magnetic field values, which exceed a factor of 400 in the maximum region.

3.2 Liquid Crystal—Metamaterial Results

When introducing the liquid crystal layer, although the two-dimensional electric and magnetic profiles do not suffer a change, however, a significant change in the absorption spectra can be observed as the input polarization plane is rotated at a certain angle. Also, within the same spectral region, the refractive index of the liquid crystal changes the absorption coefficient at the extremities of the spectral

Fig. 3 Air-metamaterial SRR results: **a** electric and **b** magnetic field amplitudes taken at resonance peak; **c** absorption coefficient

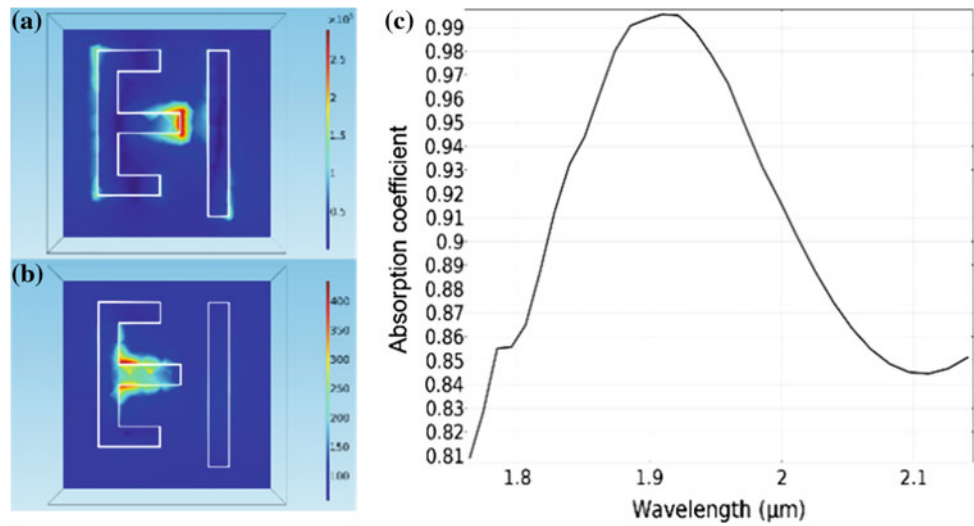
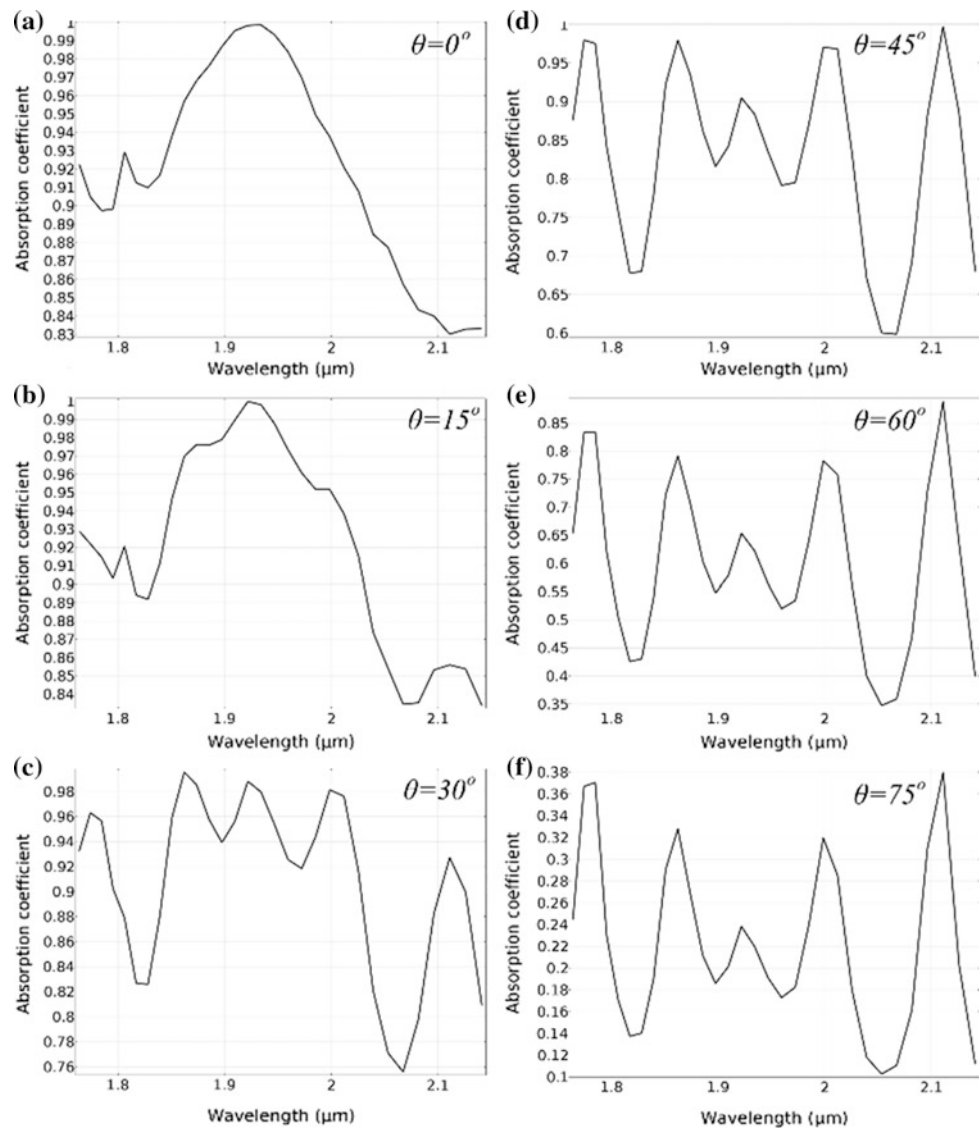


Fig. 4 Liquid crystal-metamaterial SRR structure for a 5CB liquid crystal that rotates the input polarization plane at **a** 0; **b** 15; **c** 30; **d** 45; **e** 60 and **f** 75  with respect to the Ox axis



interval by approximately 2%. Upon increasing the polarization angle, the central absorption peak starts to decrease, and two sideband peaks start to dominate. However, as the polarization plane becomes increasingly parallel to the Oy axis, the net absorption values start to decrease. This is an expected behavior, as the electric field is established parallel to the capacitor plates and therefore does not contribute to the resonant behavior of the system. Due to the fact that the liquid crystal can be actively controlled, the structure can be efficiently used as a controlled absorption filter, with a series of potential applications in infrared optics (Fig. 4).

4 Conclusions

In this paper, we have theoretically investigated the controllability of the absorption properties of a liquid crystal—metamaterial compound system. The absorption spectrum for a reference air—metamaterial were first determined, and the absorption band was extracted from the simulation. After adding the liquid crystal layer, the optical properties of the compound system change in terms of effective refractive index and input polarization plane, resulting in the increase in absorption on the sidebands surrounding the central band, together with a decrease of the absorption coefficient in the central band. We thus show that active control of the spectral absorption properties can be achieved with various liquid crystal media.

Acknowledgements The authors thank the Romanian Academy for support in the frame of the Joint Research Project: Romanian Academy—National Academy of Sciences in Belarus, 2019, and the Belarusian Foundation for Fundamental Research (BRFFR), project F18PA-003.

Conflict of Interest The authors declare that they have no conflict of interest.

References

- Cai, W., Shalaev, V.: *Optical Metamaterials*. Springer, New York (2010)
- Pendry, J.B., Holden, A.J., Robbins, D.J., Stewart, W.J.: Magnetism from conductors and enhanced nonlinear phenomena. *IEEE Trans. Microw. Theory Tech.* **47**, 2075–2084 (1999)
- Eleftheriades, G.V., Balmain, K.G. (ed.): *Negative-refraction metamaterials*. IEEE Press, Wiley Interscience (2005)
- Smith, D.R., Padilla, W.J., Vier, D.C., Nemat-Nasser, S.C., Schultz, S.: Composite medium with simultaneously negative permeability and permittivity. *Phys. Rev. Lett.* **84**, 4184–4187 (2000). <https://doi.org/10.1103/PhysRevLett.84.4184>
- Shelby, R.A., Smith, D.R., Schultz, S.: Experimental verification of a negative index of refraction. *Science* **292**, 77–79 (2001). <https://doi.org/10.1126/science.1058847>
- Veselago, V.G.: Electrodynamics of materials with negative index of refraction. *UFN J.* **173**(7), 790–794 (1968). <https://doi.org/10.3367/UFNr.0173.200307m.0790>
- Ritchie, R.H.: Plasma losses by fast electrons. *Phys. Rev.* **106**, 874–881 (1957)
- Iyer, A.K., Kremer, P.C., Eleftheriades, G.V.: Experimental and theoretical verification of focusing in a large periodically loaded transmission line negative refractive index metamaterial. *Opt. Express* **11**, 696–708 (2003)
- Grbic, A., Eleftheriades, G.V.: Experimental verification of backward-wave radiation from a negative refractive index metamaterial. *J. Appl. Phys.* **92**, 5930–5935 (2002)
- Pendry, J.B., Holden, A.J., Stewart, W.J., Youngs, I.: Extremely low frequency plasmons in metallic microstructures. *Phys. Rev. Lett.* **76**, 4773–4776 (1996)
- Alu, A., Engheta, N.: Achieving transparency with plasmonic and metamaterial coatings. *Phys. Rev. E* **72**, 016623 (2005)
- Schurig, D., et al.: Metamaterial electromagnetic cloak at microwave frequencies. *Science* **314**, 977–980 (2006)
- Cai, W., Chettiar, U.K., Kildishev, A.V., Shalaev, V.: Optical cloaking with metamaterials. *Nat. Photon.* **1**, 224–227 (2007). <https://doi.org/10.1038/nphoton.2007.28>
- Grover, B., Rubin, N.A., Balthasar, J.P., Devlin, R.C., Capasso, F.: High-efficiency chiral meta-lens. *Sci. Rep.* **8**, 7240 (2018). <https://doi.org/10.1038/s41598-018-25675-3>
- Pendry, J.B.: Negative refraction makes a perfect lens. *Phys. Rev. Lett.* **85**, 3966 (2000). <https://doi.org/10.1103/PhysRevLett.85.3966>
- Jahani, S., Jacob, Z.: All-dielectric metamaterials. *Nat. Nanotech.* **11**, 23–26 (2016). <https://doi.org/10.1038/nnano.2015.304>
- Walia, S., et al.: Flexible metasurfaces and metamaterials: a review of materials and fabrication processes at micro- and nano-scales. *Appl. Phys. Rev.* **2**, 011303 (2015). <https://doi.org/10.1063/1.4913751>
- Rosu, C., Manaila Maximean, D., Kundu, S., Almeida, P.L., Danila, O.: Perspectives on the electrically induced properties of nematic liquid crystal/copolymer particles composite. *J. Electrostat.* **69**, 623–630 (2011). <https://doi.org/10.1016/j.elstat.2011.08.009>
- Manaila Maximean, D., Danila, O., Stefanescu, B., Bena, R., Rosu, C., Donescu, D., Eugeniu, V.: Study of a new composite: polymer-magnetite particles/lyotropic liquid crystal. In: 3rd International Conference on Nontechnologies and Biomedical Engineering. Springer IFMBE Proceedings, vol. 55, pp. 226–229 (2015). https://doi.org/10.1007/979-981-287-736-9_56
- Manaila Maximean, D., Danila, O., Almeida, P.L., Ganea, C.P.: Electrical properties of a liquid crystal dispersed in an electrospun cellulose acetate network. *Beilstein J. Nanotech.* **9**, 155–163 (2018)
- Loiko, N.A., Miskevich, A.A., Loiko, V.A.: Method for describing the angular distribution of optical radiation scattered by a monolayer of ordered spherical particles (normal illumination). *J. Exp. Theor. Phys.* **126**(2), 159–173 (2018). <https://doi.org/10.1134/S1063776118020139>
- Loiko, N.A., Miskevich, A.A., Loiko, V.A.: Incoherent component of light scattered by a monolayer of spherical particles: analysis of angular distribution and absorption of light. *J. Opt. Soc. Am. A* **35**(1), 108–118 (2018). <https://doi.org/10.1034/JOSAA.35.000108>

Spectral Investigation of Surface Plasmon Resonance Bands of Silver Nanoparticles Capped with Gallic Acid

L. Popescu, G. Ababei, D. Babusca, D. Creanga,
C. A. Benchea, N. Lupu, and L. Oprica

Abstract

The study of silver nanoparticles fabricated more and more for textile industry, cosmetics, pharmaceuticals and other utilizations has led to the diversification of synthesis protocols. First we present single pot reaction of silver nitrate with gallic acid, rather newly used as reducer, with focus on the influence of reaction parameters on the Surface Resonance Plasmon bands of resulted silver nanoparticles. Four experimental variants of chemical reduction were conducted at room and at 60 °C, at 7.5 pH and at 10.5 pH. Secondly, two phase photochemical reduction with gallic acid using UV exposure was carried out. The Surface Plasmon Resonance spectral band of silver nanoparticle suspensions was rather broad indicating dimensional polydispersion, while symmetrical shape and maximum position suggested dominant spherical nanosized particles. The study of aged samples yielded by one pot reduction revealed higher stability for alkali samples. In the case of photochemical synthesis, submicron particles in not stable suspension were revealed. To support spectrophotometric experimental data, Transmission Electron Microscopy imaging was done, revealing tens of nm particles in the case of chemical reduction but considerably larger particles, over 100 nm in the case of photochemical synthesis. The results discussion was based on the influence of reaction conditions (temperature, pH, UV exposure) on the silver particle spectral properties and also on the capping molecular shell.

Keywords

Silver nanoparticles • Surface plasmon resonance • Chemical reduction • UV-C exposure

1 Introduction

The phenomenon of Surface Plasmon Resonance (SPR) can be seen as the luminescent emission, confined at the surface of noble metal nanostructures exposed to visible light; it is known as non-radiative electromagnetic waves propagating along illuminated objects that result from collective electron oscillations after incident light absorption. This is why these oscillations are very sensitive to any change of the interface metal-environment (metal-air, metal-surfactant molecular shell, [1]). The evidence of this phenomenon could be easily obtained by UV-Vis spectroscopy, since specific band recording could give information on the dependence on the particle size of SPR band maximum position, on the bands shape symmetry/asymmetry dependence on the particle shape, or on the band width dependence on particle size polydispersity. Although traditional chemical syntheses use sodium salts (citrate, borohydride) as silver ion reducer [2], we present the results of two synthesis methods of silver nanoparticles using gallic acid, relatively new considered reducer, by adapting literature protocol [3], the investigation being based on the features and behavior of SPR band as well as on electron microscopy imaging.

2 Experimental

2.1 Materials and Methods

Silver nitrate (AgNO_3), gallic acid ($\text{C}_6\text{H}_2(\text{OH})_3\text{COOH}$) and sodium hydroxide (NaOH) were purchased from Sigma Aldrich and used without additional purification. Deionized water was provided by Barnstead UltraPure, with 18.2 M Ω .

L. Popescu · D. Babusca · D. Creanga (✉) · C. A. Benchea
Physics Faculty, Alexandru Ioan Cuza University, 11, Blvd. Carol
I, Iasi, Romania
e-mail: dorina.emilia.creanga@gmail.com

G. Ababei · N. Lupu
National Institute of Research and Development for Technical
Physics, Iasi, Romania

L. Oprica
Biology Faculty, Alexandru Ioan Cuza University, Iasi, Romania

UV-Vis monitoring was carried out on SPR band of silver nanoparticles (AgNP) with Shimadzu PharmaSpec 1700 device equipped with quartz 1 cm cells and provided with data acquisition and analysis specialized soft. Transmission Electron Microscopy (TEM) was applied to visualize AgNP with model Hitachi High-Tech HT7700 device and to measure particle physical diameter. Quantum-mechanical modeling was accomplished with PM3 (Parametric Method 3 based on parametrization by optimization of one-center electron repulsion integrals) implemented in Hyperchem 8.0 soft package and DFT (Differential Functional Theory) using algorithms with basic function set B3LYP/6-31G*.

2.2 AgNP Prepared by Reduction with Gallic Acid at High Temperature and at Room Temperature

Silver nitrate was dissolved in deionized water to result in 10^{-3} M solution that was heated at about 60 °C while 0.01 g of gallic acid dissolved in 10 ml of deionized water was also heated at over 60 °C. In 100 ml silver nitrate stock solution, the gallic acid solution was poured continuously under magnetic stirring and keeping temperature at about 60 °C for 30 min until the color changed indicated nanoparticles formation. To control reaction medium alkalinity, 1 M NaOH was added drop by drop to adjust the pH to neutral or alkali range (measured with pH indicator paper); this way two sample variants were prepared: Ag1 with 7.5 pH and respectively Ag2 with 10.5 pH. The samples Ag3, with 7.5 pH, and Ag4 with 10.5 pH, were yielded by mixing the same solutions as above, also under magnetic stirring for the same time duration, but with no heating over the room temperature. All suspensions appeared as ivory turbid fluids in ambient room conditions.

2.3 AgNP Photochemical Synthesis with Gallic Acid

The first step consisted in preparing the two stock solutions resulted by solving 0.0169 g of silver nitrate in 100 ml deionized water and by solving 0.01 g of gallic acid in 10 ml deionized water at room temperature. The two solutions were carefully mixed and exposed for half an hour to UV radiation (UV-C 30 W sterilization lamp emitting in the range 100–280 nm at 25 cm over the sample, consisting in 10 ml volume of the prepared mixture put in a 3 cm diameter vessel). In the second step the UV irradiated sample was transferred for heating on a hot plate to about 60 °C under vigorous magnetic stirring until silver nanoparticle formation has led to changing of color and transparency as above, then the reaction vessel was removed from the heat source and let to cool down (sample Ag 5). This protocol is new, an

adaptation of that described in [3], where UV exposure and heating were carried out simultaneously.

3 Results and Discussion

In Fig. 1 the samples yielded according to Sect. 2.2 and 2.3 (containing colloidal gallic acid/AgNPs) are presented by means of the SPR bands. For one pot chemical reduction,

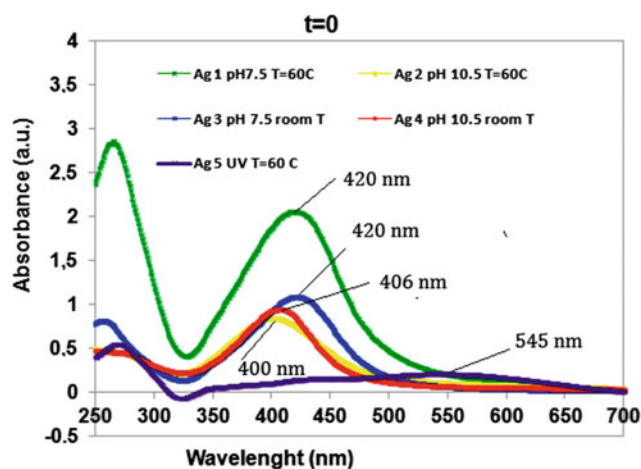


Fig. 1 The influence of synthesis conditions on the SPR band of fresh suspensions of gallic acid/AgNPs. pH adjusted at about 7.5 led to identical band maximum positions (at 420 nm) for both synthesis temperatures, but for 60 °C the band intensity is higher. Alkali pH of about 10.5 resulted in SPR band blue shift: for higher temperature the band shift is higher (400 nm) than for room temperature (406 nm). UV exposure induced the formation of much larger band, red shifted (545 nm)

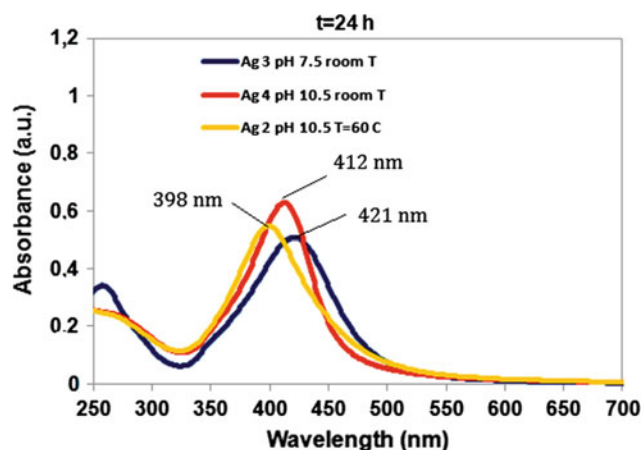


Fig. 2 The SPR bands of 24 h aged suspensions of gallic acid/AgNPs synthesized by one pot chemical reduction. Compared to fresh samples, for all aged ones the intensities are smaller, especially for 7.5 pH, where the band maximum position was just 1 nm red shifted (421 nm); for alkali samples, blue shift of SPR band maximum was seen for 60 °C (398 nm) while red shift was found for the same pH of 10.5 at room temperature (412 nm)

Fig. 3 **a** TEM image of smallest silver nanoparticles synthesized by one pot chemical reduction (two examples are marked: 13.3 and 11.6 nm diameter). **b** Polydispersed silver nanoparticles no larger than 25 nm in one pot chemical reduction. **c** Irregular shape silver particle aggregates up to 50 nm diameter among generally smaller round nanoparticles for one pot chemical synthesis

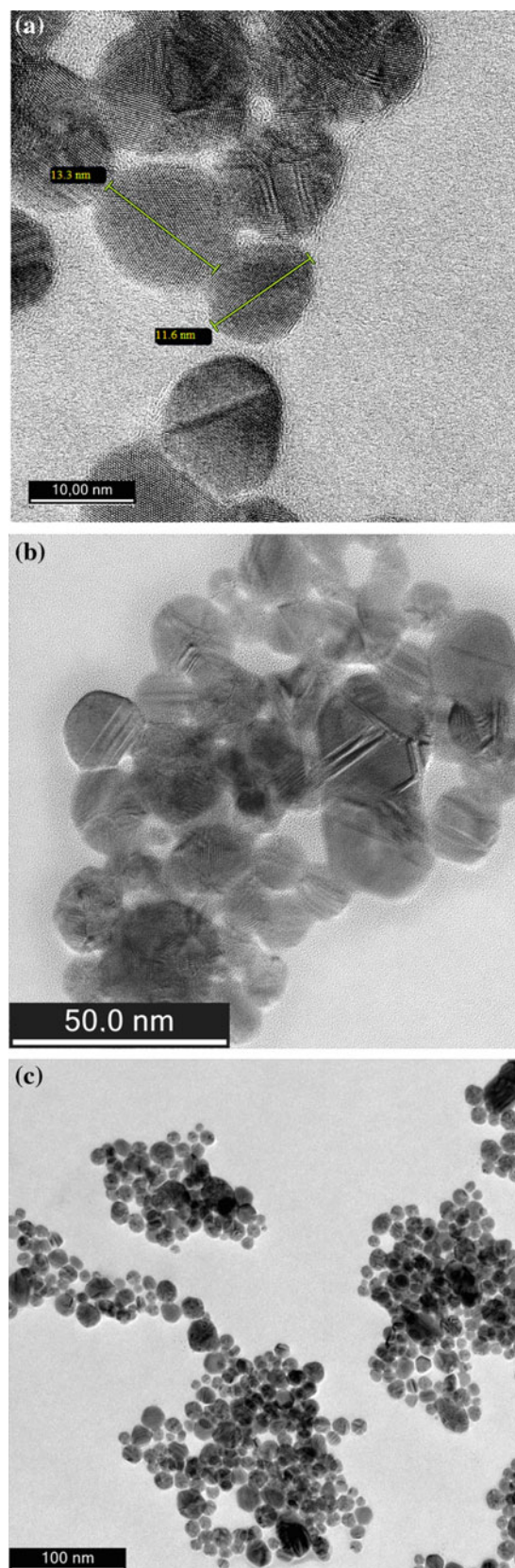
band maximum was at: 400 nm, 406 nm and 420 nm. Rather symmetrical shape and large width indicates mostly quasi-round particles with polydispersity [2–4]. In freshly prepared samples at 60 °C the maximum position of SPR band depends on final pH (Fig. 1), being at 420 nm for 7.5 pH (Ag1), with 2.048 intensity; for 10.5 pH (Ag 2), SPR maximum was at 400 nm and the intensity was of 0.839. It seems that the reduction reaction efficacy was highest in Ag1 sample. For almost neutral pH, of 7.5, the sample Ag3 prepared at room temperature has SPR maximum position also at 420 nm as in the case of 60 °C but lower intensity (of 1.078); it seems that neutral pH led to the similar SPR band positions not depending on the temperature.

At 10.5 pH, (Ag4, the room temperature synthesis) SPR band was blue shifted to 406 nm with 0.94 intensity denoting generally smaller AgNPs than for 7.5 pH, in Ag3.

Totally distinct aspect was seen for Ag5 sample that exhibited very broad band (maximum at 450 nm) and very low intensity (0.204). It seems that UV exposure carried out before heating, in contrast with literature [3] favors most dramatic polydispersity and the larger particles.

According to literature [3] gallic acid is decomposed by UV rays and the silver metallic cores are coated with decomposition reaction product, thus SPR emission interacts differently with new coating shell and particle size is expected to be affected. After 24 h of keeping samples in refrigerator, new spectra were recorded; unexpectedly Ag1 became dark opaque—unsuitable for UV-Vis investigation. Also Ag5 presented inhomogeneous aspect with high turbidity that impeded us to record its spectrum.

The remaining samples stayed stable in refrigerator for one month. New SPR analysis was accomplished in 24 h aged samples (Fig. 2) observing that all SPR bands maximum intensities were diminished under 0.5. This could mean that certain amount of larger colloidal gallic acid/AgNPs that were present at the initial time or were formed during storage time, have precipitated from suspensions with possible release of gallic acid. Indeed in 24 h aged Ag2 sample the SPR maximum slightly shifted to blue (398 nm); it seems that relatively higher concentration of gallic acid could cause SPR band blue shift [5] which suggests that: (i) in the applied synthesis protocol the reaction is not complete and not all gallic acid was consumed initially or (ii) the precipitated AgNPs in the aged Ag2, with SPR band intensity diminished to 0.547, have released part of



molecular shell when have associated in higher precipitant systems.

The SPR band position in aged Ag3, prepared at room temperature, at pH of 7.5, seems to remain almost the same (at 421 nm in Fig. 2 compared to 420 nm in Fig. 1). But it is the less intense SPR band (intensity of 0.508) meaning that particle precipitation was favored by relatively lower pH. In aged Ag4 sample, the red shift of SPR band was noticed, at 412 nm, together with band intensity decrease at 0.627. Searching for alternative evidence of microstructural differences, we present TEM images of freshly prepared samples. There were two types of particles provided by TEM: for all gallic acid/AgNP samples yielded by chemical reduction we found very similar diameters of mostly round grains, but also rare prolonged, larger ones; for the photochemical synthesis, larger, polyhedral structures were revealed among smaller AgNPs similar to those corresponding to chemical reduction. In Fig. 3a–c we present as example the AgNPs from Ag2 sample prepared at 60 °C and alkali pH. Fig. 3a emphasizes couple of smallest AgNPs, with 12–13 nm diameter. Most AgNPs in Fig. 3b have less than 25 nm diameter values, polydispersity being also noticeable. In Fig. 3c, larger nanosystems with prolonged shape seem to be nanoparticle aggregates, with rare frequency, among individually dispersed nanoparticles.

Figure 4 presents the nanosystems from Ag 5, prepared by photochemical synthesis. TEM analysis has shown polyhedral particles with submicron size having actually diameters of several hundreds of nm which could be favored by UV action on gallic acid, that absorbs strongly in the UV

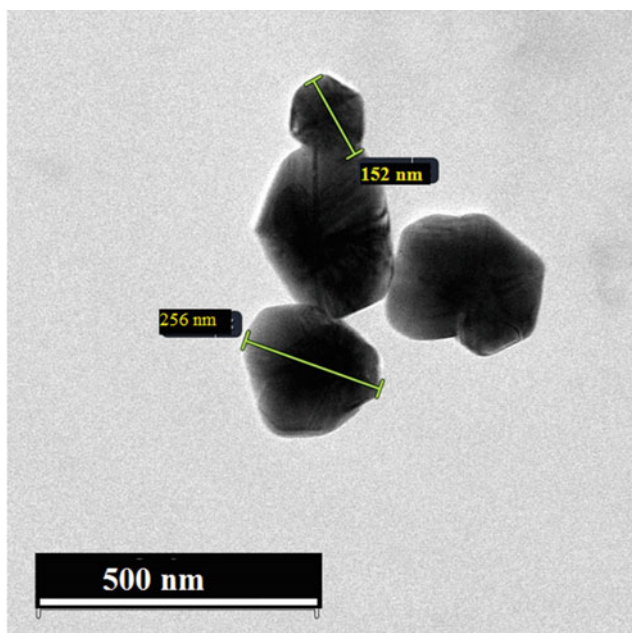


Fig. 4 Polyhedral nanosystems of AgNPs, of several hundreds of nm (two examples: 152 and 256 nm) for photochemical synthesis

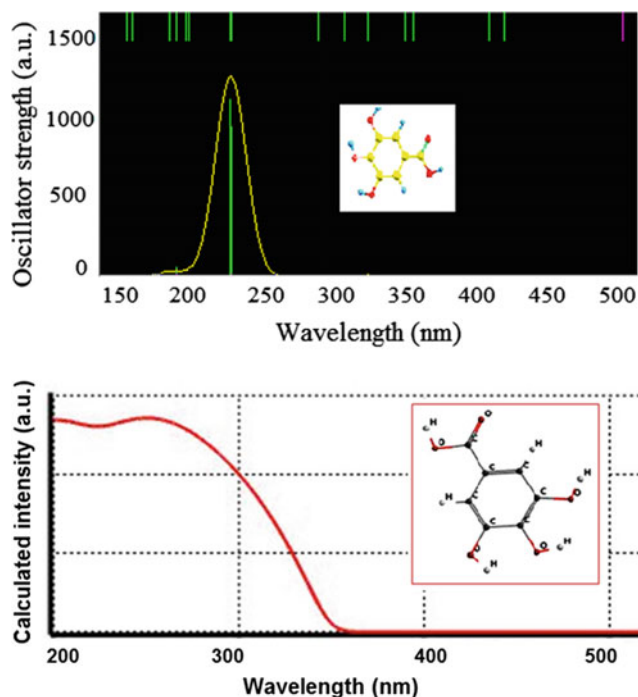


Fig. 5 UV-Vis electronic absorption spectrum of gallic acid: (PM3/Hyperchem (up); DFT/Spartan (down))

range, as confirmed also by quantum–mechanical modeling of its electronic absorption spectrum; following UV radiation absorption it could be chemically changed, thus silver nanocores could be capped with the product of gallic acid photolysis.

In Fig. 5 the simulated UV-Vis electronic absorption spectrum of gallic acid optimized structure is presented (with PM3/Hyperchem and DFT/Spartan).

In Fig. 5 (up) the maximum absorption of UV-C radiation (at 225 nm) was revealed as continuous envelope together with progressively lower intensity spectral lines in UV-B, UV-A and visible range; this being concordant with experimental spectra [6]. It is remarkable that gallic acid absorption is negligible at wavelengths larger than 400 nm. In Fig. 5 (down) similar position of gallic acid band maximum with no sharp peak is suggested but no noticeable absorption in the visible range. Our microstructural investigation results with TEM are concordant with [3] where similar but not identical photochemical synthesis was used.

4 Conclusions

Silver nanoparticle synthesis was conducted by different protocols using gallic acid, recently considered in such technologies: conventional chemical reduction and modified photochemical synthesis that was developed by us. For one pot chemical reduction, in 24 h aged samples, SPR have red

shifted maxima (room temperature, alkali pH) or blue shifted (60 °C, alkali pH). TEM results revealed only nanometric structures (12–13 nm diameter) for all samples yielded by chemical synthesis, while for adapted photochemical synthesis, large, polyhedral submicron particles (over 100 nm) have characterized the silver nanosystems. In the next research step the optimization of photochemical method is needed to get large nanoparticles but stable suspensions; also further optimization of pH and temperature levels is planned to get most stable samples by chemical reduction.

Acknowledgements This study was supported by JINR-RO projects 2019.

Conflict of Interest The authors declare no conflict of interests.

References

1. Willets, K.A., Van Duyne, R.P.: Localized surface plasmon resonance spectroscopy and sensing. *Annu. Rev. Phys. Chem.* **58**, 267–297 (2007)
2. Lee, S.H., Jun, B.-H.: Silver nanoparticles: synthesis and applications for nanomedicine. *Int J Mol Sci* **20**(4), 865 (2019)
3. Martinez, G.A., Nino, N., Martinez, F., et al.: Synthesis and antibacterial activity of silver nanoparticles with different sizes. *J. Nanopart. Res.* **10**, 1343–1348 (2008)
4. García-Barrasa, J., López-de-Luzuriaga, J.M., Monge, M.: Silver nanoparticles: synthesis through chemical methods in solution and biomedical applications. *Cent. Eur. J. Chem.* **9**(1), 7–19 (2011)
5. Shi, S.: Using surfactant-based colloidal systems to promote photoinduced synthesis of silver nanoparticles. Thesis, Rouen University (2012)
6. Jancovivova, V., Ceppan, M., Havlinova, B., et al.: Interaction of iron gall inks. *Chem. Pap.* **61**(5), 391–397 (2017)

Part III

Bio-micro/nano Technologies and Devices

Cathodoluminescent UV Sources for Biomedical Applications

D. I. Ozol, E. P. Sheshin, M. I. Danilkin, and N. Yu. Vereschagina

Abstract

Ultraviolet radiation is widely used in biomedical practice. In some areas, its use is limited by the lack of sufficiently cheap sources of the desired spectrum and power. The prototypes of mercury-free cathodoluminescent UV-radiation sources are manufactured. They use field emission cathodes on the basis of carbon fiber. These sources exhibit various UV spectra depending on the phosphors used. New types of UV-emitting cathode-ray-tube phosphors are suggested.

Keywords

UV light source • Ultraviolet radiation • Disinfection • Germicidal range • Cathodoluminescence

1 Introduction

In recent decades the field of application of ultraviolet (UV) light sources has been rapidly expanding. UV radiation has a wide variety of biological responses starting from well-known short-term effects like sunburn. That is why UV sources are used for multiple purposes in medicine and industry, especially for disinfection of air, water, and surfaces [1, 2] in medical centers, in the food and pharmaceutical industries, veterinary, greenhouses, for disinfection of drinking, circulated, and waste water. UV radiation exerts much more effective action on viruses than chlorine. Therefore, application of UV radiation for preparation of drinking water allows one to solve the problem of

elimination of hepatitis A virus that sometimes cannot be solved when a traditional method of chlorination is used. The most efficient for disinfection is the UV radiation within a so-called germicidal range where the mercury gas discharge lamps of low and medium pressure are nowadays most widely used.

In the agricultural sector such fields of application of UV radiation can be mentioned as plant lighting and plant disease prevention.

In medicine the following areas where UV light sources are used can be named: sterilization (including medical equipment) predominantly with UV-radiation with wavelengths within 200–300 nm; curing of skin diseases—psoriasis [3], vitiligo [4], and many other common and uncommon dermatoses—predominantly using narrow-band sources for wavelengths within 300–360 nm, and UV-curing in dentistry using wavelengths of 300–400 nm.

There are other fields for biomedical application of UV-radiation, and later we can expect the appearance of new ones. In several fields application of UV radiation is limited since there are no sufficiently cheap, compact, and ecologically acceptable sources for the necessary spectral range and power.

The wavelength dependences of the biological responses differ significantly depending on the targeted molecules (their absorption spectra), their localization (transmission to the target depth), and the photochemical reactions involved (especially their quantum yield). Therefore, each application has its own optimal UV spectrum.

Nowadays in conventional UV technologies mercury vapor-filled lamps produce germicidal UV radiation with fixed emission patterns dictated by the inherent properties of mercury atoms. Most of the devices designed for phototherapy in UV-A and UV-B range known as cost-effective treatment are table-top projectors, booths or chamber-type devices (solaria) that rely upon tubular fluorescent or mercury bulbs as UV sources.

Research related to novel UV radiation sources is topical due to several reasons. First, nowadays a strong tendency

D. I. Ozol (✉)

Moscow Institute of Physics and Technology, 9 Institutskiy per., Dolgoprudny, Russian Federation
e-mail: ozol.mipt@gmail.com

E. P. Sheshin · M. I. Danilkin · N. Yu. Vereschagina
P.N. Lebedev Physical Institute of the Russian Academy of Sciences, Moscow, Russian Federation

exists to eliminate mercury-containing sources, both in industry and especially in household usage as potentially ecologically dangerous [5]. This leads to an aspiration to develop mercury-free UV light sources. Second, the UV radiation sources with improved spectral characteristics and stability are needed for many purposes including medical treatments.

Among such sources excimer lamps and UV light-emitting diodes (UV-LEDs) can be named. Recently a new kind of lamps has been developed – cathodoluminescent UV light sources, especially with field emission cathodes.

UV-LEDs exhibit excellent characteristics in the wave range within 370–400 nm. However, they dramatically deteriorate for wavelengths less than 370 nm [6, 7]. At this state of development UV-LEDs suffer from low output powers and high initial degradation. The reasons for the initial degradation are not completely understood [7]. In the wave range most interesting for disinfection and other biomedical applications (250–350 nm) the wall-plug efficiency does not usually exceed 1%, the service life amounts to several hundreds of hours, the power of a single source is small (milliwatts), but the costs are very high. This state of the art will obviously remain the same within at least the nearest decade [7]. We even can consider this 2016 forecast to be too optimistic. Nowadays, typical measured efficiencies of UV-LEDs in the germicidal range amount to $\sim 0.5\%$, and the best of them exhibit the output power less than 10 mW. This means, the efficiencies have to become approximately 50–90 times greater to economically compete with the modern low-pressure mercury UV lamps [8]. Consequently, the sources of sufficiently powerful UV-radiation (greater than 1 W) will not only be expensive, but due to their low efficiency they will need a special cooling. LEDs are very sensitive to overheating (their efficiency and service life drastically drop), this limits the development of compact sources.

Cathode-ray UV radiation sources represent one of the possible alternative solutions. The electron-beam excitation of a luminophore is well-known in cathode-ray tubes (CRTs) having a long application history in TV sets. Since the CRTs' spectrum depends only on the type of the phosphor used, it is possible to create sources of UV radiation [9–14] by replacing in such devices the CRT phosphor with a UV-emitting one. Many types of UV-band luminophores are already known with the efficiency of cathodoluminescence up to 9% [15] and even 20%. The theoretical limit is 30–40% for phosphors emitting in the visible spectral range [16, 17] and up to 40–50% for deep-UV emitting phosphors [18, 19]. These sources switch on quickly and can work in pulse regime.

2 Experiment

We have developed several prototypes of cathodoluminescent UV sources of various spectra with field emission cathodes on the basis of carbon fiber.

The lamp (Figs. 1 and 2) with triode scheme comprises cathode (1), modulator (2), and anode (3).

The use of novel field emission cathodes (also known as cold cathodes) instead of thermocathodes used in television CRTs allows decreasing the power consumption of the device and increases its service life.



Fig. 1 Finger-type cathodoluminescent UV lamp (switched on)

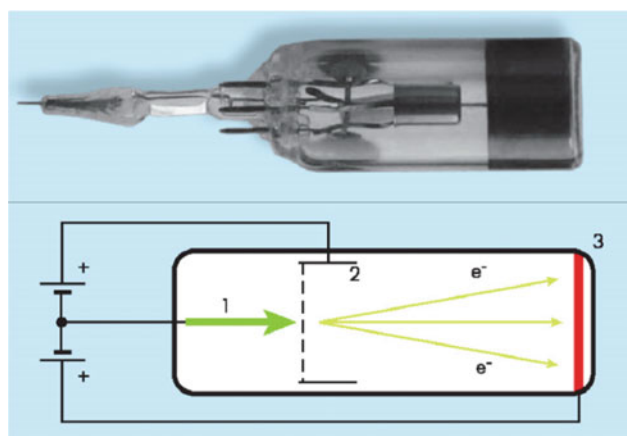


Fig. 2 Image and schematic view of a finger-type lamp with triode design. (1) Cathode, (2) control electrode (modulator), (3) luminescent anode

Carbon fiber based field emission cathodes for cathode-ray light sources have been already proposed and investigated [20, 21]. The cathode is manufactured of specifically treated carbon fiber. Field emission cathodes on the basis of carbon fiber exhibit long service life (not less

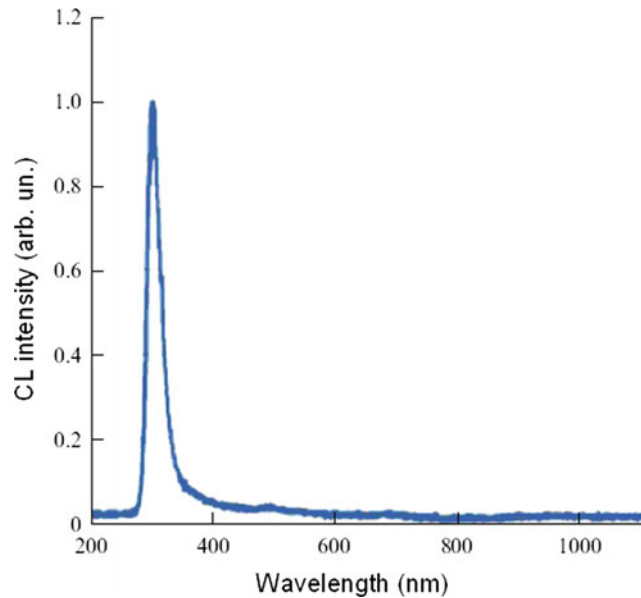


Fig. 3 An example of narrowband cathodoluminescent spectrum of $Y_2O_3:Gd$ ($U = 15$ kV, $I = 0.3$ mA)

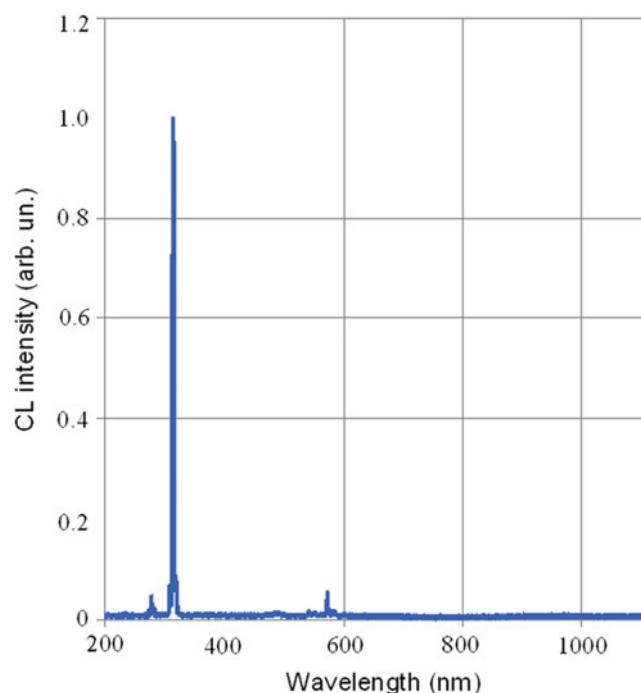


Fig. 4 Cathodoluminescent spectrum of $ZnAl_2O_4$ luminophore ($U = 15$ kV, $I = 0.3$ mA)

than 10,000 h of continuous operation without marked changes of their parameters). The emission spectrum of cathodoluminescent lamps depends on the phosphor used (see, for example, Figs. 3 and 4). The CRT phosphor must be resistant to heat and prolonged exposure to electron beams.

Phosphor is the most important component in the development of cathodoluminescent UV radiation sources. Nowadays, there are no special commercially available UV cathodoluminescent phosphors for UV-B and UV-C spectral ranges. Since many phosphors can be named that can be excited by UV radiation in UV-B and UV-C ranges, and under the electron beam irradiation they emit light in the same ranges (with very slight difference), the majority of them cannot be used as good cathodoluminophores. Their energy efficiency, resistance to the electron beam irradiation, and the saturation current value are questionable. For example, $Y_2O_3:Gd$ (Fig. 3) exhibits low energy efficiency (1–2%); well-known [10] zink aluminate (Fig. 4) is not adequately stable. Its electronic band gap and chemical structure change over time, and its spectrum significantly shifts even during the storage without any irradiation.

Lithium tetraborate $Li_2B_4O_7$ (LTB) based phosphors are promising as UV cathodoluminophores [14]. Cu and Ag are the most promising impurities in LTB for obtaining practically applicable UV luminophores. The CL spectra of these two phosphors are shown in Fig. 5. The luminescence

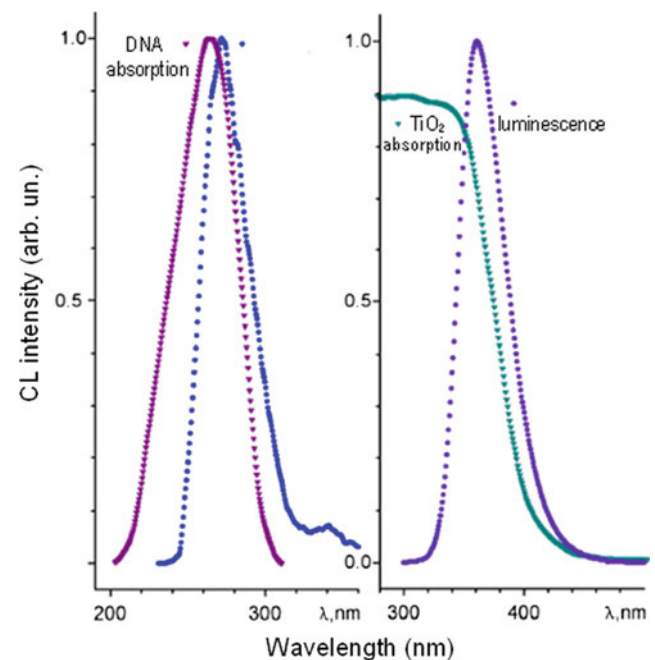


Fig. 5 Cathodoluminescence spectra of two types of LTB based phosphors (doped with Ag and Cu) applicable for disinfection purposes and their overlapping with the DNA absorption spectrum and TiO_2 fundamental absorption edge



Fig. 6 Image of CL lamp using LTB phosphor

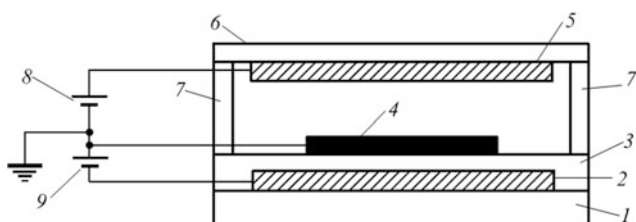


Fig. 7 Flat UV-module. (1) Cathode substrate, (2) control electrode, (3) insulation layer, (4) emitting layer, (5) phosphor, (6) transparent substrate, (7) support element, (8) anode power supply, (9) control electrode power supply

spectrum of LTB:Ag overlaps with the DNA destruction spectrum, while the luminescence spectrum of LTB:Cu overlaps with the spectrum of photocatalytic activity of TiO_2 . Our further investigations revealed some other effective dopants that improve the light yield. So, employing the same basic phosphor we can obtain materials with radiation in various spectral ranges that is very advantageous from the technological point of view.

Field emission UV lamps can be made with different shapes, not only a finger-type one (Fig. 6). The schemes of the field emission flat and tubular lamps are shown in Figs. 7, 8 and 9. Other form-factors are possible, too.

3 Conclusions

Prototypes of cathodoluminescent UV radiation sources with field emission cathodes on the basis of carbon fiber are manufactured. The use of non-heated field emission cathodes allows decreasing the power consumption of the device and its long service life. A new type of LTB-based UV-emitting cathode-ray-tube phosphors is proposed, which are very promising for cathodoluminescent UV light sources. In particular, LTB doped with Ag is suitable for direct disinfection in the range near 270 nm; LTB doped with Cu can be used in photocatalytic units.

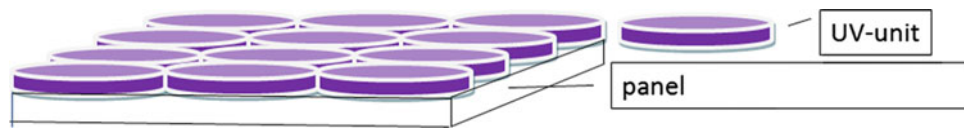


Fig. 8 Planar UV lamp consisting of a set of UV modules placed on a single electrical panel

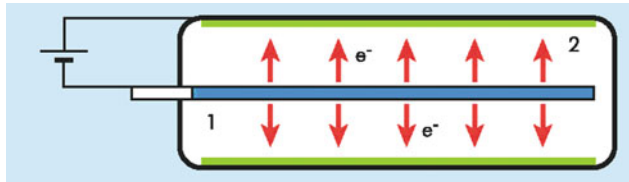


Fig. 9 Schematic view of a tubular cathodoluminescent radiation source. (1) Central part with a cathode structure, (2) cylindrical anode with a phosphor coating

Conflict of Interest The authors declare that they have no conflict of interest.

References

- Kowalski, W.: *Ultraviolet Germicidal Irradiation Handbook: UVGI for Air and Surface Disinfection*. Springer, Heidelberg (2010)
- Mehta, D., Lim, H.W.: Ultraviolet B phototherapy for psoriasis: review of practical guidelines. *Am. J. Clin. Dermatol.* **17**(2), 125–133 (2016)
- Zhang, P., Wu, M.X.: A clinical review of phototherapy for psoriasis. *Lasers Med. Sci.* **33**(1), 173–180 (2018)
- Scherschun, L., Kim, J.J., Lim, H.W.: Narrow-band ultraviolet B is a useful and well-tolerated treatment for vitiligo. *J. Am. Acad. Dermatol.* **44**(6), 999–1003 (2001)
- Minamata Convention on Mercury at <http://www.mercuryconvention.org/>
- Muramoto, Y., Kimura, M., Nouda, S.: Development and future of ultraviolet light-emitting diodes: UV-LED will replace the UV lamp. *Semicond. Sci. Technol.* **29**(8), 084004 (2014)
- Kneissl, M., Rass, J.: *III-Nitride ultraviolet emitters*. Springer, Cham (2016)
- Beck, S.E., Ryu, H., Boczek, L.A., et al.: Evaluating UV-C LED disinfection performance and investigating potential dual-wavelength synergy. *Water Res.* **109**, 207–216 (2017)
- Watanabe, K., Taniguchi, T., Niiyama, T., et al.: Far-ultraviolet plane-emission handheld device based on hexagonal boron nitride. *Nat. Photonics* **3**(10), 591–594 (2009)
- Ishinaga, T., Iguchi, T., Kominami, H., et al.: Luminescent property and mechanism of ZnAl_2O_4 ultraviolet emitting phosphor. *Phys. Status Solidi C* **12**(6), 797–800 (2015)
- Lee, D., Song, S.H.: Ultra-thin ultraviolet cathodoluminescent device based on exfoliated hexagonal boron nitride. *RSC Adv.* **7**(13), 7831–7835 (2017). <https://doi.org/10.1039/c6ra27279g>
- Yoo, S.T., Hong, J.H., Kang, J.S., Park, K.C.: Deep-ultraviolet light source with a carbon nanotube cold-cathode electron beam. *J. Vac. Sci. Technol. B* **36**(2), 02C103 (2018)
- Hamamatsu Photonics. UVCL (Ultra Violet Cathode emitting Light source) at <http://www.hamamatsu.com/us/en/product/category/1001/3068/index.html>
- Vereschagina, N.Y., Danilkin, M.I., Kazaryan, M.A., et al.: Cathodoluminescent UV-radiation sources. In: *Proceedings of the SPIE, 10614, International Conference on Atomic and Molecular Pulsed Lasers XIII, 106141F* (2018). <https://doi.org/10.1117/12.2303579>
- Broxtermann, M., Den Engelsen, D., Fern, G.R., et al.: Cathodoluminescence and photoluminescence of $\text{YPO}_4:\text{Pr}^{3+}$, $\text{Y}_2\text{SiO}_5:\text{Pr}^{3+}$, $\text{YBO}_3:\text{Pr}^{3+}$, and $\text{YPO}_4:\text{Bi}^{3+}$. *ECS J. Solid State Sci. Technol.* **6**(4), R47–R52 (2017)
- Levshin, V.L., Ya, Arapova E., Popov, Y.M., et al.: Investigations of the cathodoluminescence of zinc sulfide and certain other luminophores. *Trudy FIAN* **23**, 64–135 (1963)
- Ozol, D.I.: On the limits of the cathodoluminescence energy efficiency of phosphors. In: *IVESC Proceedings, 10th International Vacuum Electron Sources Conference*, pp. 1–2. St. Petersburg, Russia, 2016 (2014). <https://doi.org/10.1109/ivesc.2014.6892049>
- Aluker, E., Lusic, D., Chernov, S.: *Electronic Excitations and Radioluminescence of Alkali Halide Crystals*. Zinatne, Riga (1979)
- Ozol, D.I.: Cascade luminescence as a way to increase the energy efficiency of cathodoluminophores. In: *IVNC Proceedings, 29th International Vacuum Nanoelectronics Conference*, pp. 1–2. Vancouver, Canada (2016). <https://doi.org/10.1109/ivnc.2016.7551487>
- Baturin, A.S., Yeskin, I.N., Trufanov, A.I., et al.: Electron gun with field emission cathode of carbon fiber bundle. *J. Vac. Sci. Technol. B* **21**(1), 354–357 (2003)
- Egorov, N., Sheshin, E.: *Field Emission Electronics*. Springer, Cham (2017)

European Terahertz Technology for Environmental Monitoring and Bio-friendly Imaging

O. Cojocari, M. Hoefle, D. Mopro-Melgar, I. Oprea, and M. Rickes

Abstract

Main properties of Terahertz Waves are analyzed in view of potential applications for radio astronomy and bio-friendly imaging applications. A short overview of European State-Of-The-Art Technology is provided.

Keywords

Terahertz-technology • Frequency multipliers • mm/sub-mm wave receivers • Transceivers

1 Introduction

Frequency band between 100 GHz and 10 THz is so-called Terahertz (THz) band and it lies between microwave (MW) and infrared (IR) regions of the Electromagnetic (EM) spectrum. This region of the EM-spectrum is also traditionally called “THz-gap” because it still remains not fully exploited. That is because particular transit times limit maximal operation frequency of traditional microelectronic devices usually below 100 GHz, whereas quantum energy levels severely limit room-temperature operation of photonic devices at frequencies below 10 THz. Figure 1 gives an overview of the EM-spectrum and related applications and employed technologies.

Nevertheless, THz region of the EM-spectrum is an extremely interesting region because it offers unique opportunities employing spectroscopy and imaging for a large variety of applications like are radio astronomy, scientific instrumentation, medical diagnostic, high-speed data communication, security, but also non-destructive quality control in industrial production and pharmacology.

Among several classification criteria, passive and active detection/imaging shall be addressed in this contribution

O. Cojocari (✉) · M. Hoefle · D. Mopro-Melgar · I. Oprea · M. Rickes
ACST GmbH, Josef-Bautz-Straße 15, Hanau, Germany
e-mail: oleg.cojocari@acst.de

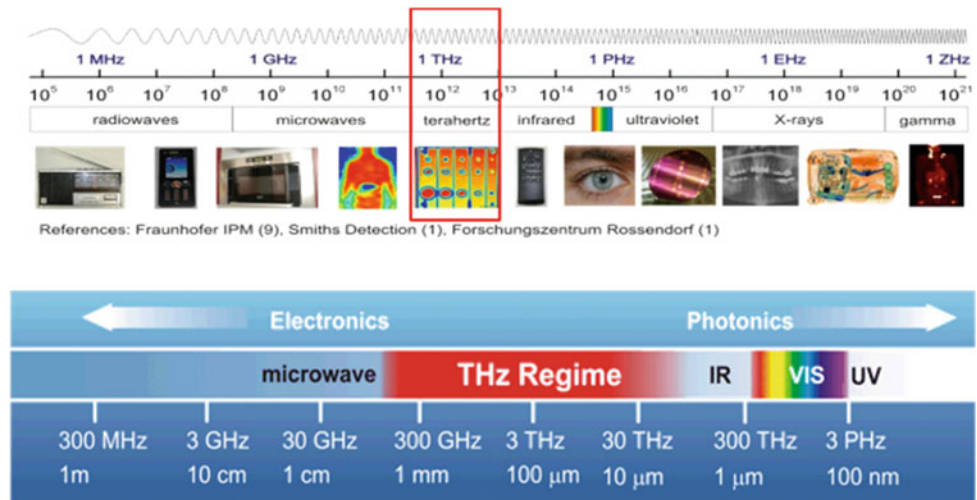
considering European state-of-the-Art THz-technology. For overview and overall understanding, properties of THz waves and potential applications are also shortly overviewed here.

2 Properties of THz Waves and Applications

There three main properties of THz waves, which suggest large potential for applications in different areas:

1. **Penetration of THz waves through most of dielectric materials.** This property is widely used for remote detection and imaging applications. Just like microwaves, THz waves can be used for imaging radars but with better spatial resolution because of significantly shorter wavelength. On the other hand, penetration of THz waves through many materials can be compared with penetration of X-Rays but with radical difference that THz-irradiation is not ionizing, and therefore, not hazardous for biological tissue. This property can be largely used for security imaging of live organisms and medical diagnostic but also in situ quality control in industrial production and pharmacology.
2. **“Spectral Finger Print”.** In fact, atoms and/or molecules of any physical material have particular resonances in EM-spectrum, which are unique and can be compared to “finger print”. This property can be used for remote identification of different materials, their composition, pressure and temperature. Many of these “finger prints” become evident within THz spectrum. Therefore, THz spectroscopy is widely used in Radio-astronomy for investigation of surrounding us universe. Moreover, this property can effectively be used for scientific applications like is plasma diagnostic but also for security application and medical diagnostic.
3. **Frequency bandwidth.** Either due to lumped or distributed elements of electrical circuitry like are resistance, capacitance and inductances, operation of microelectronic

Fig. 1 Overview of the EM-spectrum



devices and systems are usually limited in frequency to a specific bandwidth. This bandwidth usually defines the system performance. The larger frequency bandwidth is, the better performance is achievable and additional functions may be feasible. Bandwidth is usually limited relatively to center/carrier frequency. That means, higher carrier frequency automatically implies larger absolute frequency band at same relative bandwidth.

Due to higher carrier frequency, operation at THz frequencies offers extreme large absolute bandwidths. This is extremely beneficial, for instance, for high bit rate data transmission. Since the bit-rate is directly proportional to available absolute bandwidth, this is a direct figure-of-merit of a data-transmission system. Another application is imaging using FMCW-radar. The larger bandwidth and the higher center frequency is the better special resolution can be obtained.

3 Passive Receiver Technology for Space THz-Applications

Passive receivers are mandatory when detection/Imaging should be performed from very large distances and/or illumination of the target with appropriate waves is not allowed by some application-related conditions. One of the most representative application for passive detection/imaging/spectroscopy is Radio-Astronomy.

The surrounding Earth universe is full of THz radiation. In fact, huge volume of information about planets, stars and Galaxies just go past the Earth, remaining undetected and unrecognized by People. National Aero-Space Agency (NASA) in the USA and European Space Agency (ESA) are traditionally main promoters for THz receiver technology in USA and Europe, respectively.

When it comes to absolute performance and high reliability for mm&sub-mm wave receiver systems at room temperature, the choice today is Schottky diodes. One of the most recent and most significant space missions of ESA is ESA/EUMETSAT MetOp-SG mission (Meteorological Operational Satellite—Second Generation). All front-end receivers from 89 GHz to 664 GHz are equipped with European Schottky technology. Related instruments are the Microwave Sounder (MWS), Microwave Imager (MWI), and Ice Cloud Imager (ICI). Out of 8 types of Schottky diodes used in high-frequency channels of these instruments, 6 types are provided by ACST GmbH (see Table 1). In fact, ACST diodes are suitable for all these channels, but due to ESA policy, alternative diodes were selected where they sufficiently perform. Noticeable is the fact, that ACST diodes are the ONLY European solution for high-power LO-sources for heterodyne receivers, for frequency mixers above 325 GHz, and for zero-bias diodes within 89 GHz Direct Detection Radiometer. These facts and numbers place ACST in a leading position as European supplier of Schottky diodes for space THz applications.

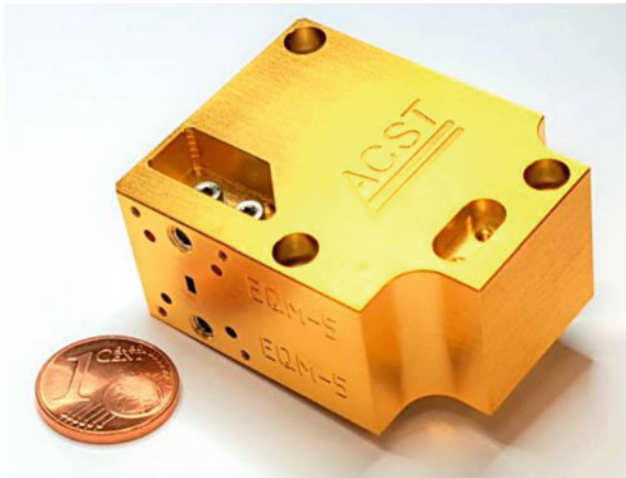
3.1 Direct Detection Receivers (DDR)

Direct detection offers opportunity for reduced mass, volume and power consumption with the absence of medium power local oscillator sources. The front-end receiver at 89 GHz for MWS and MWI instruments is designed around the ACST 89 GHz Schottky detector (Fig. 2) [1] based on ACST film-diode technology.

Excellent EQM (Engineering Qualification Model) detector performance has been demonstrated in 2017/18 with low noise, high RF voltage responsivity and high linearity. Until late 2019, all diode wafer and assembly process

Table 1 Frequency channels of the three instruments on board of ESA MetOp-SG space mission and their population with ACST Schottky diodes

Instrument	Frequency channels (GHz)												
	18,9	23,10	31,6	54	89	118,9	165,7	183,5	229	243	325	448	664
Microwave Imager (MWI)	x	x	x	x	x	x	x	x					
Microwave sounder (MWS)		x	x	x	x		x	x	x				
Ice-Cloud Imager (ICI)								x		x	x	x	x

**Fig. 2** ACST 89 GHz EQM Schottky detector for MetOp-SG MWS/MWI instruments

qualifications are going to be finished, followed by PFM production, assembly and testing at ACST. Responsible for the 89 GHz receiver is DA-Design in Finland and instrument prime are England, French, and Spanish divisions of AIRBUS Defense&Space. Figure 3 shows the EQM version after black painting with the ACST detector in the centre.

**Fig. 3** DA-design 89 GHz EQM receiver with integrated ACST detector in the centre

For future missions, the rapid progress made on low noise MMIC technology allows to consider the DDR architecture for an increasing number of radiometric bands.

3.2 Heterodyne Receivers

Higher frequency channels in MetOp-SG are designed with heterodyne receiver topology, with amplifier multiplier chains (AMC) in the local oscillator path and subharmonic mixers for signal down-conversion. ACST supports with multiple discrete diodes and integrated structures for modules up to the ICI 664 GHz channel. ACST high-power varactor diodes allow for power up-conversion up to 332 GHz and provide enough LO-power for highest heterodyne receiver at 664 GHz. Varistor diodes and integrated structures, also based on ACST film-diode technology, lead to high performance mixer designs at frequencies above 325 GHz. For lower frequency mixers and lower power frequency multipliers Schottky diodes from a British company “Teratech Components LTD” are selected.

4 Active THz Detection/Imaging

Active Detection differs from Passive one by availability of power transmitter, just like a flash for a good quality photograph under insufficient illumination, or a simple bright-lighting source for video recording. The difference is, that this lighting source should be in an appropriate THz frequency range of EM-spectrum. This approach relaxes requirements to the receiver/detector and offers opportunity for considerable increase of sensibility and Signal-to-Noise-Ratio (SNR) of detected signal.

Availability of THz power is always an issue when reasonable volume, weight, and costs are mandatory for particular applications. For instance, there is available Gyrotron technology, capable of generating mm-wave power levels in the range of kW. However, gyrotron sources are bulky, expensive and extremely power-hungry, which is not acceptable for many “real-life” applications. Free-electron

lasers and Synchrotron Light Sources are able for even more power levels but are even worse from practical point of view.

Relatively high power, in the range maybe of 1 W, is desired for many applications at mm/sub-mm waves, including active imaging, high bit-rate data transmission, and inferior chains for LO-sources in THz heterodyne receivers. Moreover, most of “real-live” applications impose severe requirements to THz sources like compactness, reliability, and price. Many R&D groups worldwide address these requirements but the current state-of-the-art devices still do not fulfil all requirements.

Recent advance in MMIC technology allows power amplification up to 1 W at frequencies up to about 100 GHz [1]. However, there is no demonstration of such power levels above W-Band. This directly indicates a demand for high-efficient power up-conversion above W-Band. The most practicable approach nowadays to up-convert power above 100 GHz is frequency multiplication approach based on Schottky diodes. There are few European suppliers for THz sources, like are Radiometric Physics GmbH (RPG) in Germany and Farran Technology LTD in Ireland.

However, power-handling capability of multiplier modules is still a severe limiting factor. For instance, state-of-the-art MM-Wave doubles perform about 25–30% efficiency, but their maximum input power-handling capability is usually limited in the range of 200 mW [2]. This limitation basically defines maximal achievable output power from a single chip (not power combined) of about 50–60 mW.

The limiting factor for high output power of frequency multipliers is twofold. On one hand, this is limited

electrically, basically due to breakdown voltage of Schottky varactors and series resistance. On another hand, power-handling capability is thermally limited by inferior heat dissipation approaches.

The breakdown voltage of ACST varactor diodes is highest-possible for any particular doping concentration, and is close to theoretical limit.

On another hand, CVD-diamond is known to be one of the best thermal conductive dielectrics in the nature. ACST has recently modified their Film-Diode process for fabrication of high-breakdown varactor diodes on transferred Diamond substrate [2]. These diodes integrate a CVD-diamond (Chemical Vapour Deposition) substrate to improve thermal performance and prevent overheating of the anodes (see Fig. 4). This technology allows a very efficient heat dissipation from hot area of the diode structure and allows to increase power-handling capability by several times in comparison to traditional diodes on GaAs-substrate.

The combination of the two aspects, high breakdown voltage and high power-dissipation in ACST varactor diodes offers represent a break-through technology considering power-handling capability and conversion efficiency of mm-wave frequency multipliers, which is key-factor for achieving high-power THz-sources.

4.1 High-Power Multipliers

The single chip 135–160 GHz doubler (D150 in Fig. 4) is able to handle up to 600 mW input power and provide more than 180 mW output power [3]. The single chip 270–320 GHz doubler (D300 in Fig. 4) is able to handle up to

Fig. 4 Development of high-power varactor array on diamond-substrate at ACST GmbH

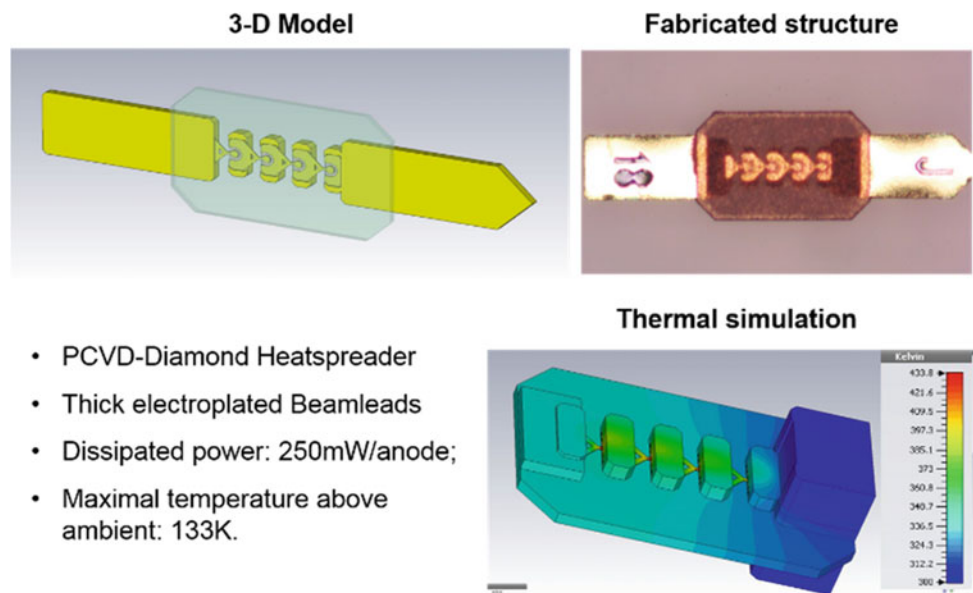
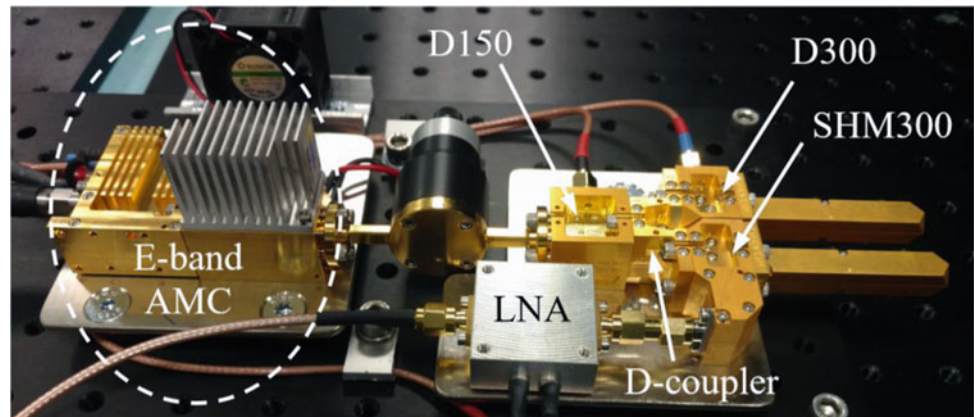


Fig. 5 ACST heterodyne 275–305 GHz transceiver system



140 mW input power and provide more than 40 mW output power. These results have been obtained without using power-combining techniques and are the proof of concept of discrete diamond diodes for high power applications. This technology opens the possibility to drastically reduce receiver complexity for space missions and on-ground applications.

4.2 300 GHz Transceiver System

Based on the new high power varactor technology, heterodyne 275–305 GHz transceiver systems (Fig. 5) are designed for frequency modulated continuous wave radar applications. The transmitter part of the transceiver consists of the two high power single-chip doublers at 150 GHz and 300 GHz (D150 and D300 in Fig. 4). The receiver part of the transceiver consists of a subharmonic 300 GHz mixer (SHM300 in Fig. 4) based on ACST film-diode technology. Most of the available power at 150 GHz is used to pump the 300 GHz doubler (D-coupler in Fig. 4) and a smaller part is used as local oscillator for the 300 GHz mixer considering a directional coupler between the 150 GHz and the 300 GHz doublers. The transceiver is able to provide more than 10 dBm transmitted power between 275 and 305 GHz and the receiver introduces less than 10 dB noise figure to the received signal.

5 Conclusions

THz-technology has considerably advanced within last decades. If in 2000th all THz technology was mainly relying on USA R&D institutes, nowadays European companies become strategic partners on this fast developing technology area. In particular, recent developments at of ACST GmbH, located in Germany, defines technology state-of-the-art for THz-receiver technology for space applications but also for industrial quality control and biomedical imaging applications.

Conflict of Interest The authors declare that they have no conflict of interest.

References

1. Hoefle, M., Rickes, M., Oprea, I., Cojocari, O.: Qualification of direct detection technology for ESA MetOp-SG space mission. In: 28th International Symposium on Space THz Technology ISSTT (2017)
2. Cojocari, O., Oprea, I., Gibson, H., Walber, A.: SubMM-wave multipliers by film-diode technology. In: 46th European Microwave Conference (EuMC) (2016)
3. Moro-Melgar, D., Cojocari, O., Oprea, I., Rickes, M., Hoefle, M.: Single-chip 135–160 GHz doubler with more than 150 mW output power based on discrete Schottky diodes. In: 29th International Symposium on Space THz Technology ISSTT (2018)

Synthesis and Characterization of Self-assembled Submicron Particles Based on Biotinylated N-palmitoyl Chitosan

V. Balan, C. I. Moise, and L. Verestiuc

Abstract

Self-assembled particles based on amphiphilic chitosan derivatives represent a promising research area, as remarkable properties of these polymeric structures can significantly improve their biological behaviour of the drug delivery systems. In the same time, biotin has been proposed as an active targeting molecule in anti-tumoral formulations. In this paper, self-assembled submicron particles based on biotinylated N-palmitoyl chitosan and loaded with a chemotherapeutic agent (Paclitaxel) have been prepared by dialysis method combined with ultrasonication. The composition of the particles has been confirmed by FT-IR Spectroscopy. Paclitaxel loaded particles exhibited narrow size distribution, negative charge, a pH-dependent release profile of drug and redispersion ability in simulated body fluids, features which can be useful in drug delivery applications.

Keywords

Self-assembled particles • Biotin • Chitosan • Chemotherapeutic agent • Drug delivery applications

1 Introduction

Biopolymers and especially chitosan are often used to design microparticulate systems, due to its significant properties: biocompatibility biodegradability, mucoadhesivity, anti-tumoral activity [1, 2]. Also, the presence of the reactive groups ($-\text{NH}_2$ and $-\text{OH}$) allows several chemical modifications intended to obtain new derivatives with improved features. A particular interest for the development of controlled release systems for hydrophobic drugs (i.e. Paclitaxel)

exhibits amphiphilic N-acyl derivatives of chitosan, such as N-palmitoyl chitosan [3, 4] due to their ability to self-assemble in biological media. Paclitaxel is a cytotoxic drug used to treat various types of cancer, especially breast, ovarian, lung or cervical cancer.

In the same time, active targeting has been proposed as a solution to direct the drug delivery systems to tumoral cells [5, 6]. Recent studies revealed that overexpression of biotin receptors on the surface of tumoral cells, especially breast cancer cells can modulate the uptake of biotinylated systems through a receptor-mediated endocytosis mechanism [7].

In this context, this paper presents the preparation and characterization of self-assembled particles based on biotinylated N-palmitoyl chitosan and Paclitaxel and evaluates the ability of these systems to be used as drug delivery systems in cancer therapy.

2 Materials and Methods

2.1 Materials

Biotinylated N-palmitoyl chitosan (codified BPCs) was synthesized through the reaction of N-palmitoyl chitosan with biotin, according to our previous report [8]. Paclitaxel (PTX) isolated from fungi (*Taxus brevifolia* and *Taxus yunnanensis*) and solvents were purchased from Sigma-Aldrich and used as received.

2.2 Methods

2.2.1 Synthesis of Self-assembled Particles

Self-assembled particles based on biotinylated N-palmitoyl chitosan and loaded with chemotherapeutic agent—Paclitaxel, denoted as BPCs-PTX were prepared by dialysis combined with ultrasonication method [9]. Briefly, 5 mL of PTX solution (0.1% in ethanol) were dropped into 50 mL of

V. Balan (✉) · C. I. Moise · L. Verestiuc
Faculty of Medical Bioengineering, Grigore T. Popa University of Medicine and Pharmacy, 9-13 Kogalniceanu Street, Iasi, Romania
e-mail: balanvera@yahoo.com; balan.vera@umfiiasi.ro

BPCs solution (0.1% in 0.1 M AcOH) with ultrasonication (Bandelin Sonopuls HD 2200, Germany) at an output power of 50 W for 5 min, under ice temperature condition. Following this, the mixture was dialyzed against phosphate buffer saline solution, pH = 7.4, 0.1 M, ultrasonicated for 2 min and then purified by dialysis with distilled water and finally freeze-dried. Likewise, free-drug self-assembled particles have been prepared in the absence of drug (BPCs-NP).

2.2.2 Self-assembled Particles Characterization

Zeta potential and hydrodynamic mean diameter of self-assembled particles were determined by Dynamic Light Scattering (DLS) measurements in water, at 25 °C using a Malvern Zetasizer NanoS (Malvern Instruments, UK). A Fourier Transform Infrared (FT-IR) spectrophotometer, model Vertex 70 (Brüker) was used to record the FT-IR spectra of all samples. FT-IR spectra were recorded on 500–4000 cm^{-1} domain, with a resolution of 4 cm^{-1} . Redispersion ability of the particles has been tested in injectable fluids (NaCl 0.9% and glucose 20%).

2.2.3 In Vitro Drug Release Studies

In vitro drug release studies were performed in two simulated biological media (phosphate buffer saline—pH 7.4 and acetate buffer saline—pH 5.5) at 37 °C, for 48 h. A weighed amount of particles was redispersed in buffer solutions and transferred into a dialysis bag (molecular weight cut-off 12 400 Da) that have been placed in preheated PBS (total volume: 25 mL). The release study was performed in an incubator shaker, at 37 °C. At selected time intervals, the

solution outside of the dialysis bag was removed ($n = 3$) for UV–Vis analysis at 227 nm (UV-1700 PharmaSpec, Shimadzu) and replaced with fresh buffer solution.

3 Results and Discussions

3.1 Preparation of Self-assembled Particles

Biotinylated N-palmitoyl chitosan (BPCs), obtained through the reaction of N-palmitoyl chitosan (PCs) with biotin, in the presence of 1-ethyl-3-(3-dimethyl aminopropyl) carbodiimide hydrochloride (EDAC) and N-hydroxysuccinimide (NHS) have been self-assembled by dialysis combined with ultrasonication method. In Fig. 1 is depicted a schematic diagram of self-assembled particles (denoted as BPCs-PTX) preparation.

The self-assembly of chitosan amphiphiles is a bottom-up process, that imply a combined effect of hydrophobic interactions, hydrogen bonds and van der Waals forces, well promoted by ultrasonication, without the addition of any additives [10].

3.2 Characterization of Self-assembled Particles

3.2.1 FT-IR Spectroscopy

Self-assembled particles were investigated by FT-IR spectroscopy (Fig. 2). FT-IR spectrum of the polymer (BPCs) showed characteristic bands for the structure of chitosan,

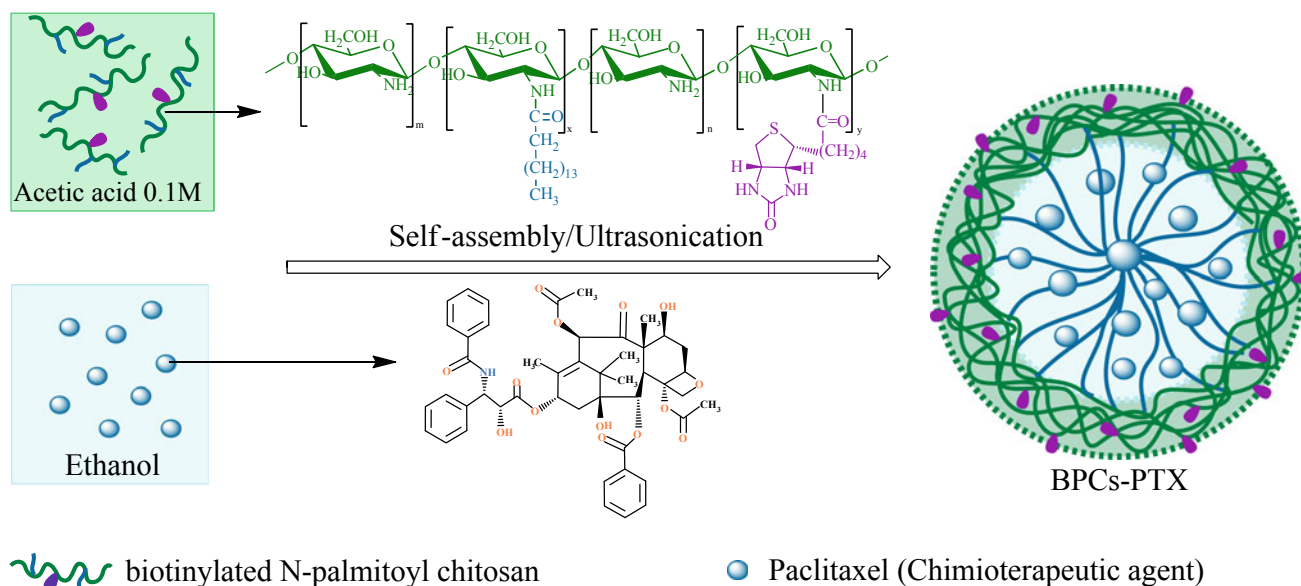
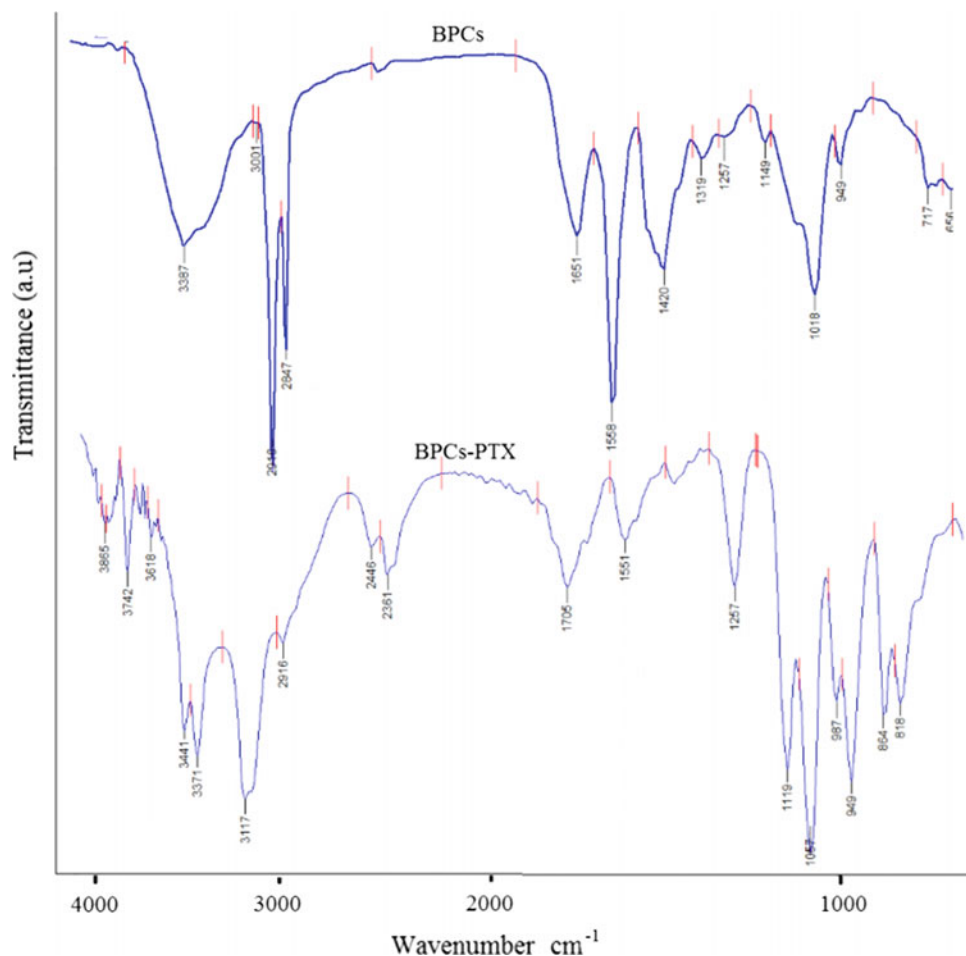


Fig. 1 Schematic diagram of BPCs-PTX synthesis

Fig. 2 FT-IR spectra of BPCs and BPCs-PTX



biotin and palmitoyl—at 3387 cm^{-1} corresponding to the imidazole ring and to the stretching vibrations of the amino and hydroxyl groups, while the bands at 2919 cm^{-1} and 2847 cm^{-1} can be attributed to the symmetrical and asymmetric deformation vibrations of the methylene group of the palmitoyl chain.

Likewise, the signals at 1651 cm^{-1} and 1558 cm^{-1} are also present, being representative for primary and secondary amide (C=O), meanwhile the bands at 1319 cm^{-1} and 1257 cm^{-1} can be assigned to the skeletal vibrations of the fragments (C–C). The band at 1018 cm^{-1} is the representative for the vibration of the C–O–C group while the vibration at 1420 cm^{-1} is characteristic of C–N stretching.

In the FT-IR spectrum of drug-loaded particles (BPCs-PTX) it was observed that drugs bands overlap generally over those of the polymeric structure due to the fact that Paclitaxel spectra exhibited common bands at the 3376 cm^{-1} , 1695 cm^{-1} (regions of the OH, N–H and C=O groups) and also in the $2913\text{--}2855\text{ cm}^{-1}$ (area of CH_2 stretching) [11]. In addition, a difference in the region of 3390 cm^{-1} can be observed, indicating the formation of hydrogen bonds between the polymer and the drug and also hydrophobic interactions.

3.2.2 Size and Surface Charge of Self-assembled Particles

Self-assembled particles obtained were analyzed in terms of size, polydispersity index, the surface charge and conductivity in water (1) and respectively in various injectable media, namely glucose 20% (2) and NaCl 0.9% (3) in order to study their redispersion ability. The results are detailed in Table 1 and Fig. 3.

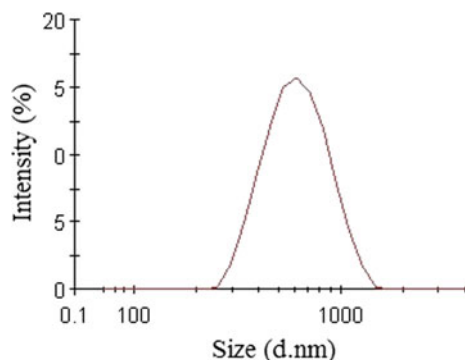
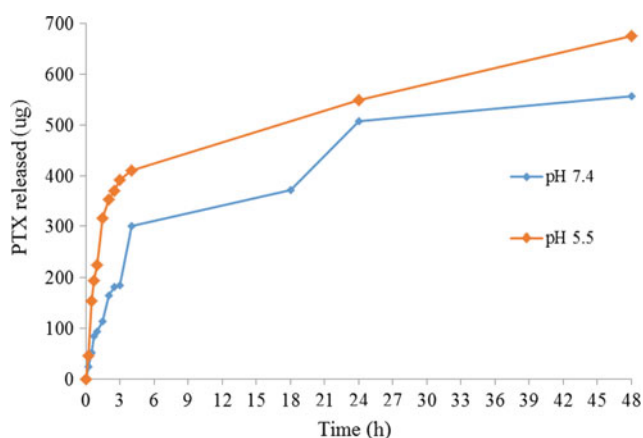
Analysing the results it can be observed that particles size in water is around 600 nm, meanwhile the other media induce an aggregation of the particles. Zeta potential of the particles in water registered a negative value determined by the presence of biotin on the surface.

3.3 In Vitro Drug Release Study

In order to evaluate the potential of self-assembled submicron particles prepared to be used as drug delivery systems, in vitro release tests were performed in PBS that mimic normal cells media (pH = 7.4) but also in PBS that simulate cancer cells media (pH = 5.5). As shown in Fig. 4, the

Table 1 Particles characteristics

No.	Z av (d nm)	Size (d nm)/I (%)	PdI	ZP (mV)	Cond. (mS/cm)
1	645	885.8 (90.3)	0.72	-4.86	1.68
2	3433	5287 (73.4)	0.89	8.27	0.297
3	1632	861.2 (92.7)	0.77	0.205	16

**Fig. 3** Average size of BPCS-PTX in water (1)**Fig. 4** In vitro drug release

particles exhibited a biphasic drug release pattern: an initial fast release in the first 3 h, followed by a second phase corresponding to a constant release up to 48 h. Noteworthy to mention, a more pronounced drug release within acidic media as a result of the higher polymer swelling and degradation, this feature being important because tumoral tissue exhibit similar interstitial acidity values.

4 Conclusions

This study proposes a method to obtain self-assembled particles based on biotinylated N-palmitoyl chitosan and loaded with a chemotherapeutic agent—Paclitaxel through

dialysis method combined with ultrasonication. The obtained systems exhibited submicron size and negative zeta potential. FT-IR Spectroscopy confirmed the structure of the particles. In vitro release studies have shown the ability of the particles to release the drug for a period of 48 h and a more pronounced drug release within acidic media, characteristics that sustain future experiments aiming to assess the suitability of self-assembled particles as drug delivery system.

Acknowledgements This work was supported by a grant of Grigore T. Popa University of Medicine and Pharmacy, no. 27499/2018.

Conflict of Interest The authors declare that they have no conflict of interest.

References

- Liu, M., Zhong, X., Yang, Z.: Chitosan functionalized nanochitosan for enhanced oral absorption of cyclosporine A. *Sci. Rep.* **7**, 41322 (2017)
- Soares, P.I.P., Isabel, A., Carvalho, J., Ferreira, I.M.M., Novo, C. M.M., Paulo, J.: Chitosan-based nanoparticles as drug delivery systems for doxorubicin: optimization and modelling. *Carbohydr. Polym.* **147**, 304–312 (2016)
- Balan, V., Dodi, G., Tudorachi, N., Ponta, O., Simon, V., Butnaru, M., Verestiuc, L.: Doxorubicin-loaded magnetic microcapsules based on N-palmitoyl chitosan and magnetite: synthesis and characterization. *Chem. Eng. J.* **279**, 188–197 (2015)
- Larsson, M., Huang, W.C., Hsiao, M.H., Wang, Y.J., Nydén, M., Chiou, S.H., Liu, D.M.: Biomedical applications and colloidal properties of amphiphilically modified chitosan hybrids. *Prog. Polym. Sci.* **38**, 1307–1328 (2013)
- Chen, H., Xie, L.Q., Qin, J., et al.: Surface modification of PLGA nanoparticles with biotinylated chitosan for the sustained in vitro release and the enhanced cytotoxicity of epirubicin. *Colloids Surf. B: Biointerfaces* **138**, 1–9 (2016)
- Chen, H., Nan, W., Wei, X., et al.: Toxicity, pharmacokinetics, and in vivo efficacy of biotinylated chitosan surface-modified PLGA nanoparticles for tumor therapy. *Artif. Cells Nanomed. Biotechnol.* **45**, 1115–1122 (2017)
- Bu, L., Gan, L.C., Guo, X.Q., Chen, F.Z., Song, Q., Zhao, Q., Guo, X.J., Hou, S.X., Yao, Q.: Transresveratrol loaded chitosan nanoparticles modified with biotin and avidin to target hepatic carcinoma. *Int. J. Pharm.* **452**, 355–362 (2013)
- Balan, V., Redinciuc, V., Tudorachi, N., Verestiuc, L.: Biotinylated N-palmitoyl chitosan for design of drug loaded self-assembled nanocarriers. *Eur. Polym. J.* **81**, 284–294 (2016)

9. Kim, D.G., Jeong, Y.I., Choi, C., Roh, S.H., Kang, S.K., Jang, M. K., Nah, J.W.: Retinol encapsulated low molecular water-soluble chitosan nanoparticles. *Int. J. Pharm.* **319**, 130–138 (2006)
10. Liu, Y., Cheng, X.J., Dang, Q.F., Ma, F.K., Chen, X.G., Park, H. J., Kim, B.K.: Preparation and evaluation of oleoyl-carboxymethyl-chitosan (OCMCS) nanoparticles as oral protein carriers. *J. Mater. Sci. Mater. Med.* **23**, 375–384 (2012)
11. Kathiravan, et al.: Infrared spectral analysis of Taxol produced by different species of *Pestalotiopsis*. *J. Anal. Bioanal. Tech.* **5**(4), 1–9 (2014)

Part IV

Biomaterials for Medical Applications

A Novel Nanocomposite (SR/HA/-nZnO) Material for Medical Application

H. Sh. Majdi, A. N. Saud, and M. H. Al-Mamoori

Abstract

A novel biocomposite material SR/HA/ZnO for maxillofacial prosthetics and jawbone. In this work, hydroxyapatite synthesized by sol-gel technique. $\text{Ca}(\text{NO}_3)_2 \cdot 4\text{H}_2\text{O}$ and $(\text{NH}_4)_2\text{HPO}_4$ used as precursors, and nano ZnO was prepared and modify the surface using Oleic acid to get uniform distribution Within the matrix and reduce nanoparticles agglomeration ZnO. Silicone rubber composites were prepared as a second part by using HA as to increase the biocompatibility, mechanical properties of SR, and to get antibacterial nanocomposites ZnO modified were used. The mechanical properties as a property of tensile strength, elastic modulus, elongation, hardness, compressibility, and antibacterial were examined after the addition of HA and ZnO to silicon rubber. The results show the ability to prepare n-ZnO and HA used to enhance the mechanical properties also acts as antimicrobial media for the biocomposite that can be used for prosthetics and jawbone.

Keywords

Silicon rubber • Hydroxyapatite • n-ZnO • Maxillofacial prosthetics • Jawbone

1 Introduction

In recent years, there has been an increasing interest in materials applications in medical areas. A nanocomposite is termed when at least one of the phases within the composite has a Nano-scale [1]. Nanocomposites in medical applications must have special and important properties. For

H. Sh. Majdi · A. N. Saud (✉) · M. H. Al-Mamoori
Biomedical Engineering Department, Al-Mustaqbal University
College, 40st, Babylon, Iraq
e-mail: amir.saud92@gmail.com

A. N. Saud
Material Engineering, University of Babylo, Babylon, Iraq

example, medical nanocomposites must not be harmful to living tissue, not-having the potential to cause cancer, corrosion-resistant, and has low poisoning [2]. Silicone rubber (SR) has been used in the clinic as an implant for a long time. It is well known that SR is of good biocompatibility and physiological physics. It's very viable property promises great convenience in clinical applications. However, SR is not able to detach organically from an apparatus due to its inertia. In several cases, inflammation and a strong-body reaction after the implant [3]. In addition, the prosthetic materials produced by maxilographs are very easy [4]. Consequently, an SR-based prosthesis can be permanently damaged. There are three types of silicone rubber compounds: high-temperature vulcanization (HTV) silicone rubber, room temperature vulcanization (RTV) silicone rubber, and liquid silicone rubber (LSR). In recent years, many attempts have been made to improve the biocompatibility and biological properties of RS [3, 5–8]. One of these methods is by adding hydroxyapatite to the SR. Hydroxyapatite (HA) can form a bond with the tissues and excellent biocompatibility, but despite the biocompatibility, it is very brittle [8]. Based on the fact that the extension of the reinforcement increases with the decrease of the particle size of the filler [9], we propose the use of n-ZnO and hydroxyapatite as a filler and to get antibacterial to form SR-HA-nZnO composites this study, we developed a novel biocomposite SR-HA-nZnO in which the dispersion state of n-ZnO and HA particles is homogeneous, which is better to give a good mechanical property and antibacterial to the silicon rubber.

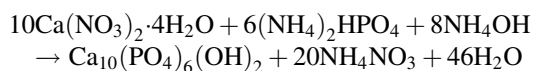
2 Experimental

In this section will give details about the materials and procedures used to prepare hydroxyapatite (HA), n-ZnO, and the biocomposite obtained by adding different weight percentage of HA, and n-ZnO to silicon rubber.

Materials	Chemical formula	Purity	Prepare
Calcium nitrate tetrahydrate (CN)	Ca(NO ₃) ₂ ·4H ₂ O	99	HA
Di-ammonium hydrogen phosphate (DAP)	(NH ₄) ₂ HPO ₄	~ 99	
Ammonium hydroxide solution	NH ₄ OH	24–30 w/w	
Oleic acid	C ₁₈ H ₃₄ O ₂	99.6	n-ZnO
Oxalic acid	HOOC-COOH·2H ₂ O	99.6	
Zinc acetate	C ₄ H ₆ O ₄ Zn·2H ₂ O	...	
O-xylene	C ₆ H ₄ (CH ₃) ₂	...	
Toluene	C ₆ H ₅ -CH ₃	...	

2.1 Preparation Hydroxyapatite Powder

First, prepare 1 M of Ca(NO₃)₂·4H₂O and 0.67 M of (NH₄)₂HPO₄ be dissolved in 500 ml of distilled water in separate beakers using magnetic stirrer for about 30 min. Then, CN aqueous solution was rapidly added into the DAP solution at 75 °C under stirring. Then NH₄OH solution with the concentration of 1 mol/l was added to the mixture system dropwise until the pH value of the mixture rose up to 10. The reaction system was further stirred at 70 °C for 2 h and aged at ambient temperature for 4 h, the suspension filtered and washed by ethanol and distilled water then, washed with distilled water and ethanol three times and filtered. Finally, dried at 85 °C and hydroxyapatite obtained according to the equation.



2.2 Preparation of N-ZnO Powder

First, prepare 0.06 M of C₄H₆O₄Zn·2H₂O by dissolving in 300 ml ethanol, and 0.1 M of HOOC-COOH·2H₂O be dissolved in 200 ml of ethanol in separate beakers using magnetic stirrer at a temperature of 50 °C for 30 min. Then adding C₄H₆O₄Zn·2H₂O to HOOC-COOH·2H₂O under constant mixing at 120 °C for 12 h. The suspension was filtered and drying at 100 °C to remove any humidity from powder, and then calcination at 600 °C with low heating rate to prevent the rapid growth of particle. The surface modification of nano fillers was achieved by the introduction of reactive groups to the filler surface to get perfect homogeneity of nano ZnO with silicone rubber. A typical process was achieved by using Oleic acid for the surface modification of ZnO nanoparticles. Typically, (10 ml) was dissolved in 300 ml o-xylene to form an oleic acid solution. Then, recently prepared n-ZnO particles were added to the above solution and allowed the reaction to perform at 50 °C under stirring for 1 h. Finally, the particles were separated by centrifuge at 15,000 rpm for 15 min and washed three times with toluene, to remove the un-reacted coupling agents and then dried. The flask was covered by para film and standing for 1 days. Then the modified n-ZnO particles become ready to use.

2.3 Preparation of Nanocomposite Material

The masterbatch is prepared by mixing the silicon rubber which properties are shown in Table 1, with the prepared HA and n-ZnO. First silicon rubber mixed with different ratio of (0, 5, 20)% HA particles for 15 min until having a homogenous mixture. Then n-ZnO was add in different ratio (0, 1, 5)% to the previous mixture and repeat mixing for 1 min. Lubricated the molds for mechanical tests, then pour

Table 1 The experimental data

Sample No.	Cons. of HA %	Cons. of n-ZnO %	Tensile strength	Tear	Elongation	Hardness
1	0	0	2.03	1.74	365	34.3
2	0	1	3.78	5.02	353	32.1
3	0	5	4.55	8.13	280	36.8
4	5	0	2.91	2.21	273	38.3
5	5	1	5.32	7.35	235	39.2
6	5	5	13.22	12.14	221	41.3
7	20	0	4.89	3.37	216	44.1
8	20	1	9.04	10.01	178	45.6
9	20	5	17.43	15.42	125	47.2

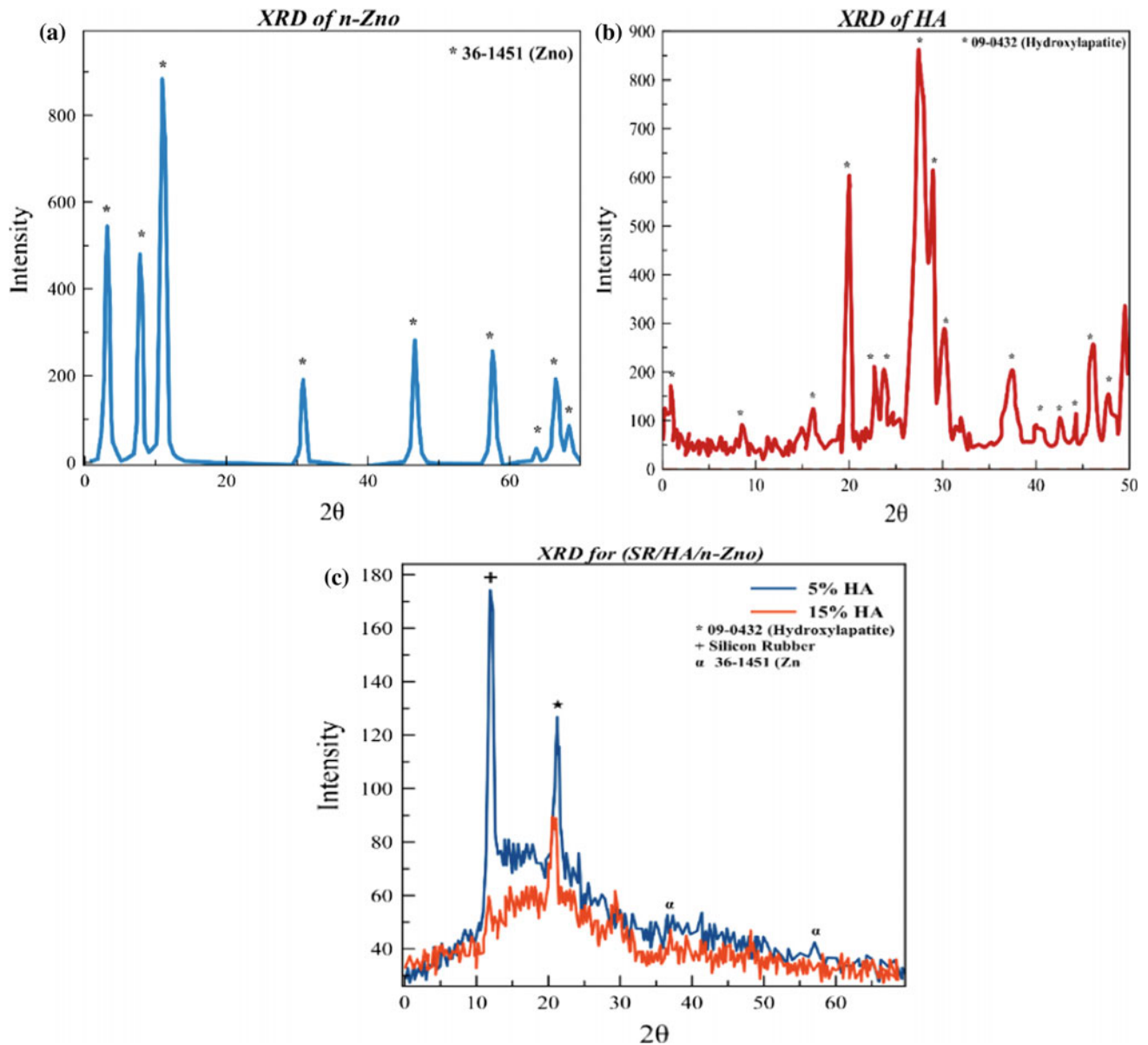


Fig. 1 XRD spectrum of **a** n-ZnO prepared, **b** HA, and **c** SR/HA/n-ZnO

the silicone rubber composites in those molds. After that leaving the molds at room temperature for 24 h. Afterward, the specimen was cutting for tensile strength and percentage of elongation with dimension accordance with ASTM-D412. Also, it was cutting for with diameter 45 mm for testing Shore A Durometer hardness in accordance with ASTM D2240.

3 Results and Discussion

3.1 XRD Diffraction

Figure 1a show the XRD of the synthesized n-ZnO a diffracted angle (30–70°), a crystalline peak appeared which indicates the crystalline structure ($2\theta = 36^\circ$). The result

shows broad peaks at ($2\theta = 31.9, 34.5, 36.3, 56.7,$ and 62.9) that deal with ZnO structure after comparison with the standard XRD card (JCPDS, card No. 36-1451). Crystallite size is calculated using the Scherrer equation

$$(CS = 0.9\lambda \beta \cos \theta) \quad (1)$$

where CS is the crystallite size, λ is the wavelength of X-rays used (1.54060 \AA), β is the full width at half maximum (FWHM) and θ is the angle of diffraction. The crystallite size of prepared nanopowder is found to be around 29–33 nm, which is in the order of nanosize that is close to that obtained from [10].

Figure 1b shows the XRD patterns of HA powder obtained by sol-gel technique and it shows high purity and diffracted at an angle ($10\text{--}50^\circ$). The patterns showed that all peaks were pure hexagonal Hydroxyapatite $\text{Ca}_{10}(\text{PO}_4)_6(\text{OH})_2$ after comparison with the standard XRD card (JCPDS, card No. 03-0717). The intensity of the broad peaks for the prepared HA is an indication of being a nanoparticle, this because of reality that nanomaterials are short-range materials. These results can be attributed to the successful manufacturing of the nano-HA powder high purity by the sol-gel method.

The XRD patterns of the composite samples are shown in Fig. 1c. The figures showed a difference in the peak intensity of both polymer and HA powder with increasing HA content in the matrix. Furthermore, it showed to be the effect of HA addition on the XRD chart of the pure matrix in apparent clear peaks of HA. Moreover, it can be observed that the intensity of the polymer peaks decreased while the intensity of HA peaks increased with increasing the HA content.

3.2 FTIR Spectrum

The FTIR spectrum of crystalline ZnO is shown in Fig. 2a in which indicated to these several transmission bands. FTIR spectrum of ZnO nanoparticles showed a broad peak at 3419 cm^{-1} due to the stretching vibrations of the ($-\text{OH}$) group on the surface of ZnO nanoparticles the results converge with [11, 12], and a high-intensity broadband around 559.79 cm^{-1} due to the vibration mode of zinc and oxygen bond. Generally, all the metals and its oxide, give the FTIR peaks at lower wavenumber ranging from 400 to 800 cm^{-1} and this approximately compatible with [13]. FTIR indicated that coupling agents have been successfully grafted onto the surface of ZnO nanoparticles caused slight changes in the intensities producing a new transmission band at 1500 cm^{-1} .

Figure 2b shows the FTIR test of HA. The broadband at 3437 and 1610 cm^{-1} were attributable to adsorb water, while sharp peak at 3572 cm^{-1} was attributable to stretching vibration of lattice $-\text{OH}$ ions and a medium sharp peak at 632 cm^{-1} assigned to the O–H deformation mode. The characteristic bands for PO_4^{3-} appear at $570, 601, 960, 1049$ and 1089 cm^{-1} . The result shows that the powders of hydroxyapatite free from carbonate groups.

3.3 SEM Result

Figure 3c shows SEM of ZnO modified nanoparticles (MN). The results showed that highly agglomeration is observed by this examination in Fig. 3a, b because ZnO nanoparticles

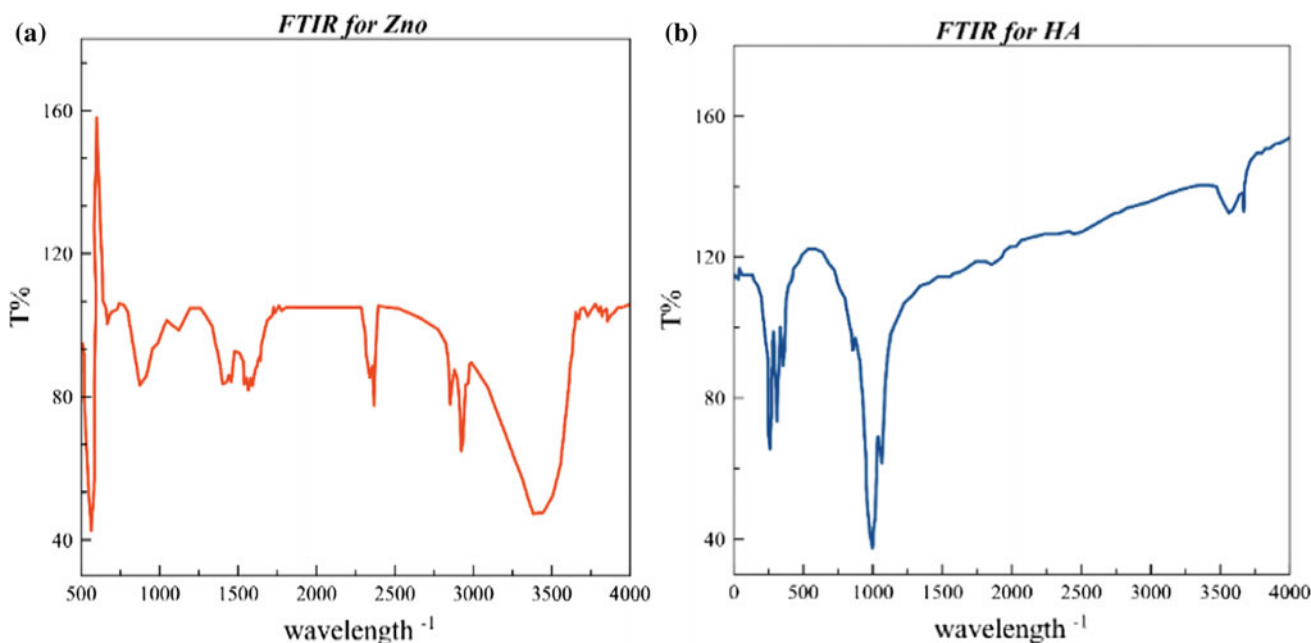
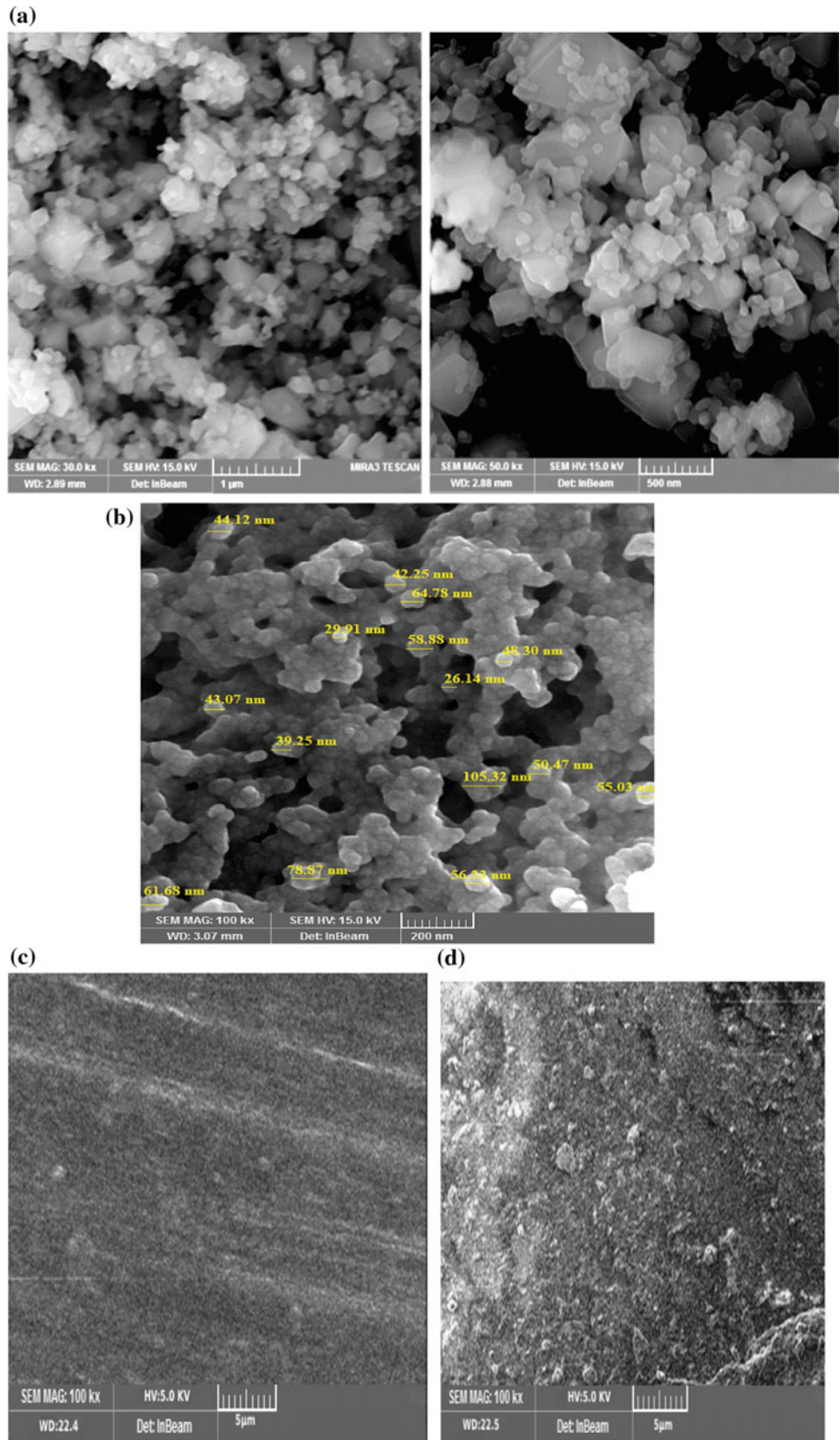


Fig. 2 FTIR spectrum of a n-Zno, b HA

Fig. 3 SEM of **a** HA powder (left and right), **b** n-Zno, **c** SR, and **d** SR/HA/(15%)/n-ZnO(1%)



with high surface energy tend to clump together in large particles which are disappearing in Fig. 3c that is the modification case. It was found that the surface of modified ZnO nanoparticles by coupling agent has reduced the agglomeration by reducing the energy of the surface, which is reflected in the homogeneous dispersion after modification [14]. Figure 3e show SEM images of a pure matrix, 15% HA-resin and 1% ZnO resin composites. The structure presented in Fig. 3e showed some irregular distribution of additive within the matrix. This distribution can be attributed to the high surface area resulting from using nano-sized particles.

Figure 4a show the tensile strength of the composite rubber silicon with different ratio of N-ZnO and HA. Its show that addition of modified n-ZnO still has high mechanical properties such behavior can explain that n-ZnO will increase the contact surface area between rubber chains thus will give a rigid structure with better tensile strength (4.55 MPa). Also, it is clear that the tensile strength increased with increasing of HA. The HA powder as a filler could improve the tensile strength of the compound due to their high mechanical properties.

3.4 Mechanical Properties

It is interesting to observe that particle size of addition effect on the mechanical properties. Figure 4b show the tear of the composite (SR-HA-ZnO). This property is related to the tensile property, so that, tear-resistance increases with the addition of n-ZnO and HA. For the same reason as previously mentioned in the case of the tensile property that the particles will uniformly distribute between rubber chains and increase the mechanical bond between them. This leads to better tear resistance.

In the case of increasing the ratio of n-ZnO, tensile strength and tear resistance decreases. This is due to the irregular distribution of n-ZnO in silicon rubber matrix and aggregate between chains [15]. Figure 4c shows hardness property increases with different ratio of both HA and n-ZnO because the addition will acts as a filler that it strengthens the recipe and makes it resistant to the applied forces. The filler can physically be entrapped in the rubber and share in the load-bearing process in the matrix which leads to higher hardness which is considered to be due to the overall effect of crosslinking of the polymer network, polymer-filler

Fig. 4 The mechanical properties of composite (SR/HA/n-ZnO)

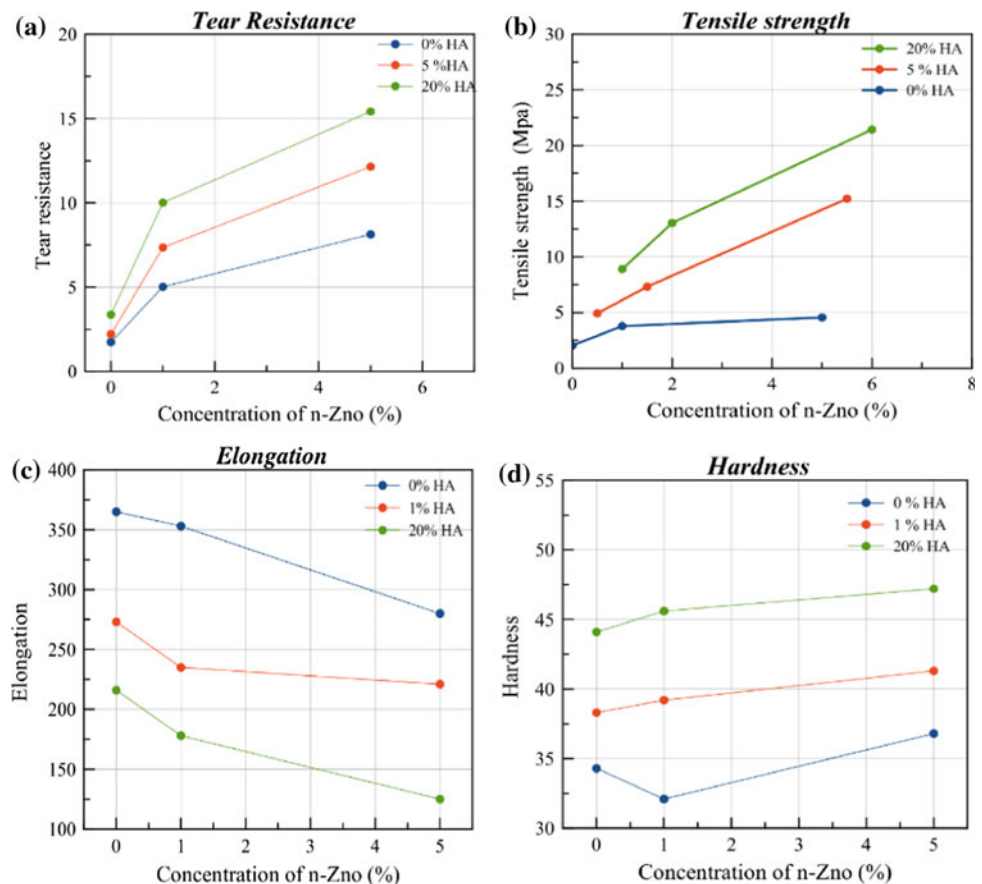
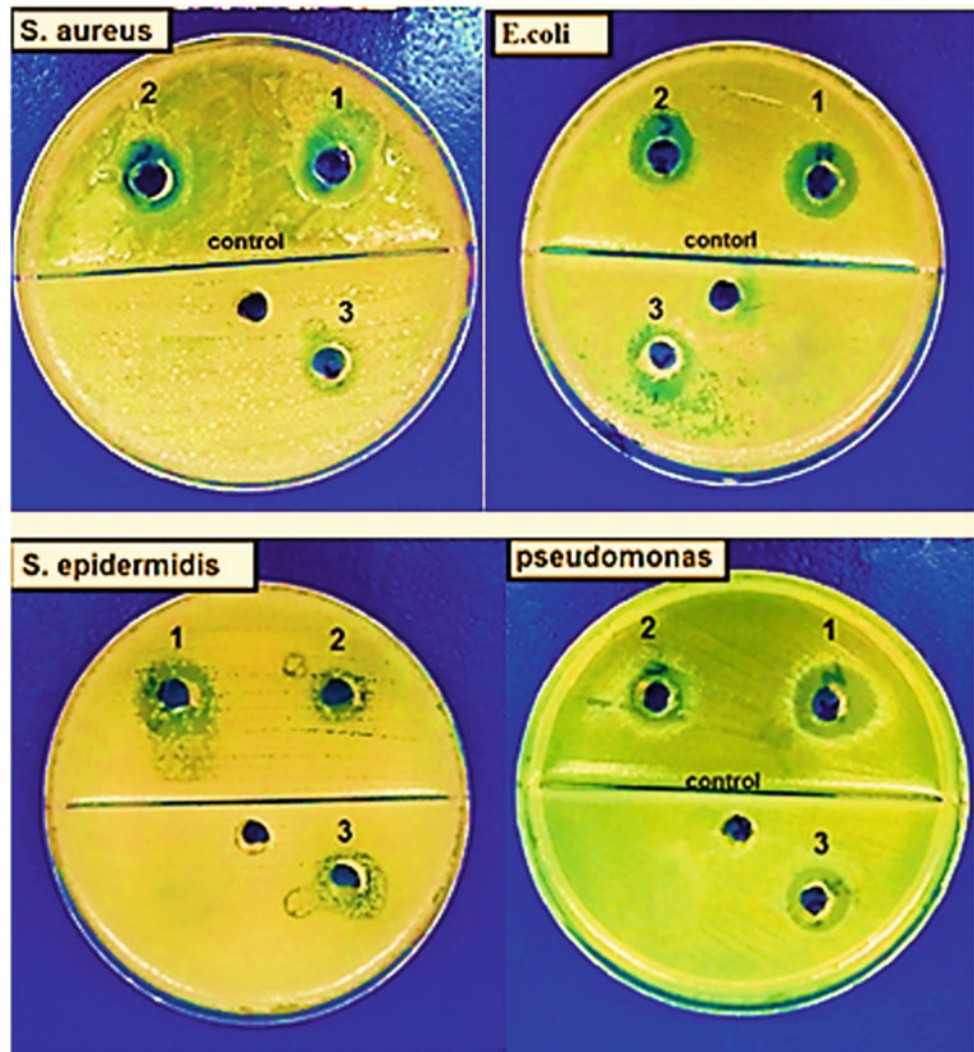


Fig. 5 Agar well diffusion test for composite, which no. (1 = 0, 2 = 1, 3 = 5) wt%



interactions which may be physical and chemical and formation of occluded rubber give high hardness value [16]. Figure 4d show the elongation result. It was noted that for both of the HA and n-ZnO have the same behavior. The elongation property decreases with the addition of HA and n-ZnO, this because the rubber is highly stretching so that when the very fine particles fill the spaces, it will restrict the movement of chains due to the diffusion of very fine n-ZnO and HA particles through the silicon rubber chains which are responsible for riveting the rubber chain and then decrease elongation [15]. All the mechanical result of composite (SR/HA/n-ZnO) shown in Fig. 4a–d.

3.5 Antibacterial Tests

Antibacterial activity test of ZnO, against a different type of bacteria (*Escherichia coli*, *Staphylococcus aureus*, and

Pseudomonas aeruginosa) and fungi (*Candida albicans*), was done by Agar Well Diffusion method [17]. Using a sterile plastic pipette, four holes were punched in each of the culture plates with a diameter of (6) mm. One of the holes was punched in the center of the plate where 50 μ l of silicon rubber was added as control; 50 μ l of the composite solution was added as a test tube in the other hole at the Muller-Hinton agar plate. One-hour pre diffusion time was allowed, after which the plates were incubated at 37 $^{\circ}$ C for 18 h. The zones of inhibition were then measured in millimeter after four weeks. In comparison with control silicon rubber. The result showed that inhibition zone for (SR/ZnO) increase with increasing ZnO concentration as shown in Fig. 5, where the efficacy against the bacteria was calculated by calculating the diameter of the inhibition zone in (mm), as shown in Table 2, this behavior depends on the mechanism of killing the bacteria by n-ZnO particle, it can be explain as the following: Due to direct contact of nanoparticles with

Table 2 Antibacterial activity for composite

Type of bacteria	The concentration of n-ZnO (%)		
	0	1	5
<i>S. epidermidis</i>	11.8	12.2	14.9
<i>E. coli</i>	11	13.3	15.2
<i>Pseudomonas</i>	6.3	8.8	11.8
<i>S. aureus</i>	13.5	15.4	18.2

cell walls, destruction of bacterial cells [18–20], or release of Zn ions as antibodies [21, 22] or the formation of effective oxygen ions [23].

It demonstrates the generation of high-efficiency aggregates such as OH^- , H_2O_2 , and O_2^{-2} as following. If zinc oxide has an electron-gap pair (eh+). The energy gap in zinc oxide divides the H_2O particles into OH and H+. Thus, oxygen molecules are split into free radicals (O^{-2}), which in turn interact with H^+ to create roots (HO_2^\bullet), which collide with the electrons that produce hydrogen peroxide (HO_2). They then interact with hydrogen ions to produce H_2O_2 molecules that led to generate cell membrane penetration and kill bacteria.

4 Conclusion

A novel biocomposite material from Silicon rubber, hydroxyapatite, and n-ZnO for maxillofacial prosthetics and jawbone. In this work, hydroxyapatite synthesized by sol-gel technique. $\text{Ca}(\text{NO}_3)_2 \cdot 4\text{H}_2\text{O}$ and $(\text{NH}_4)_2\text{HPO}_4$ used as precursors, and nano ZnO was prepared and modify the surface using Oleic acid to get uniform distribution within the matrix and reduce nanoparticles agglomeration ZnO. Silicone rubber composites were prepared as a second part by using HA as to increase the biocompatibility and mechanical properties of SR, and to get antibacterial nanocomposites ZnO modified were used. The results show the ability of additive (HA and n-ZnO) to enhance the mechanical properties: tensile strength, tear, and hardness of the biocomposite. Also, n-ZnO show a good ability to increase the antimicrobial activity for the biocomposite.

Conflict of Interest The authors declare that they have no conflict of interest.

References

- Kutějová, L., Vilčáková, J., Moučka, R., Natalia, E., Babayan, V.: A solvent dispersion method for the preparation of silicone composites filled with carbon nanotubes. *Chem. Listy* **108**, s78–s85 (2014)
- Smith, A.L., Winefordner, J.D., Kolthoff, I.M. (eds.): *The Analytical Chemistry of Silicones*, vol. 112. Wiley (1991)
- Abbasi, F., Mirzadeh, H., Katbab, A.A.: Modification of polysiloxane polymers for biomedical applications: a review. *Polym. Int.* **50**(12), 1279–1287 (2001)
- Erlich, Mark A., Parhiscar, Afshin: Nasal dorsal augmentation with silicone implants. *Facial Plast. Surg.* **19**(04), 325–330 (2003)
- Abbasi, F., Mirzadeh, H., Katbab, A.A.: Bulk and surface modification of silicone rubber for biomedical applications. *Polym. Int.* **51**(10), 882–888 (2002)
- Aziz, T., Waters, M., Jagger, R.: Surface modification of an experimental silicone rubber maxillofacial material to improve wettability. *J. Dent.* **31**(3), 213–216 (2003)
- Furuzono, T., Sonoda, K., Tanaka, J.: A hydroxyapatite coating covalently linked onto a silicone implant material. *J. Biomed. Mater. Res.* **56**(1), 9–16 (2001)
- Mou, S.S., Tu, M., Tang, S.Q., Zhou, C.R.: Effect of hydroxyapatite on the blood compatibility of silicone rubber composite materials. *Cailiao Kexue yu Gongcheng (Mater. Sci. Eng.) (China)* **21**, 162–164 (2003)
- Bokobza, L.: Elastomeric composites. I. Silicone composites. *J. Appl. Polym. Sci.* **93**(5), 2095–2104 (2004)
- Kahn, M.L., Monge, M., Colliere, V., Senocq, F., Maisonnat, A., Chaudret, B.: Size- and shape-control of crystalline zinc oxide nanoparticles: a new organometallic synthetic method. *Adv. Funct. Mater.* **15**(3), 458–468 (2005)
- Ao, W., Li, J., Yang, H., Zeng, X., Ma, X.: Mechanochemical synthesis of zinc oxide nanocrystalline. *Powder Technol.* **168**(3), 148–151 (2006)
- Talam, S., Karumuri, S.R., Gunnam, N.: Synthesis, characterization, and spectroscopic properties of ZnO nanoparticles. *ISRN Nanotechnol.* **2012** (2012)
- Silverstein, R.M., Webster, F.X., Kiemle, D.J.: *Proton NMR spectrometry. Spectrometric Identification of Organic Compounds*, 7th ed., p. 142. Wiley, New York, NY, USA (2005)
- Yeo, S.Y., Lee, H.J., Jeong, S.H.: Preparation of nanocomposite fibers for permanent antibacterial effect. *J. Mater. Sci.* **38**(10), 2143–2147 (2003)
- Ahmad, A., Mohd, D.H., Abdullah, I.: Mechanical properties of filled NR/LLDPE blends. *Iranian Polym. J. (Engl. Ed.)* **13**(3) (2004)
- Hanim, H., Zarina, R., Ahmad Fuad, M.Y., Mohd. Ishak, Z.A., Hassan, A.: The effect of calcium carbonate nanofiller on the mechanical properties and crystallisation behaviour of polypropylene. *Malays. Polym. J.* **31**(1), 38–49 (2008)
- Irobi, O.N., Moo-Young, M., Anderson, W.A., Daramola, S.O.: Antimicrobial activity of bark extracts of *Bridelia ferruginea* (Euphorbiaceae). *J. Ethnopharmacol.* **43**, 185–190 (1994)
- Lee, W.-I., Young, R.-L.: Defects and degradation in ZnO varistor. *Appl. Phys. Lett.* **69**, 526–528 (1996)
- Koughia, C., Kasap, S., Capper, P.: Doping aspects of Zn-based wide-band-gap semiconductors. *Springer Handbook of Electronic and Photonic Materials*, pp. 843–854 (2007)
- Fan, Zhiyong, Lu, J.G.: Zinc oxide nanostructures: synthesis and properties. *J. Nanosci. Nanotechnol.* **5**, 1561–1573 (2005)

21. Padmavathy, N., Vijayaraghavan, R.: Enhanced bioactivity of ZnO nanoparticles—an antimicrobial study. *Sci. Technol. Adv. Mater.* **9**, 35004 (2008)
22. Song, Z., Kelf, T.A., Sanchez, W.H., Roberts, M.S., Rička, J., Frenz, M., Zvyagin, A.V.: Characterization of optical properties of ZnO nanoparticles for quantitative imaging of transdermal transport. *Biomed. Opt. Express* **2**, 3321–3333 (2011)
23. Özgüra, Ü., Alivov, Ya. I., Liu, C., Tekeb, A., Reshchikov, M.A.: A comprehensive review of ZnO materials and devices. *J. Appl. Phys.* **98**, 41301 (2005)

Influence of MW Irradiation on the Hydroxyapatite/Chitosan Composite Structure and Drug Release Kinetics

L. B. Sukhodub, M. O. Kumeda, and L. F. Sukhodub

Abstract

Biocomposite material based on hydroxyapatite (HA) and chitosan (CS) in form of beads was synthesized using microwave irradiation (MW) of different power and investigated by methods of XRD and HPLC. MW reduces the time of HA formation to 20 min without affecting its structure. Liquid absorption and liquid retention for the synthesized at maximum MW power HA-CS-MW800 sample is 27%, while for the control HA-CS 5%. HPLC showed significant differences in the release kinetics of the hydrophilic Chlorhexidine (CHX) and hydrophobic benzocaine (BZ) and proved the composite ability to prolonged drug release to 336 h for CHX and 384 h for BZ. The HA-CS-MW800 demonstrates the highest release rate for CHX and the lowest one for BZ. From HA-CS-MW800 sample in the first 2 h is released the smallest amount of BZ (about 32%), compared to 45% for others. The effect of MW contributes to the specific location of binding sites in composite and access of drug molecules to these sites.

Keywords

Hydroxyapatite • Chitosan • Microwave irradiation • Drug release

1 Introduction

For bone engineering good biocompatibility, osteoconductivity and porosity of biomaterials are crucial criteria. HA is biologically active, has osteoconductive properties, causes rapid bone formation and integration with host tissue [1]. As components of one composite biomaterial, HA and CS complement each other, providing material for the bone

tissue regeneration with elasticity and mechanical strength. In addition, the properties of both components allow the composite material to be used in delivery systems for drugs, growth factors or other bioactive elements [2]. CS is a natural polymer that is often used in bone engineering due to its biocompatibility and its ability to biodegrade [3].

Functional hydroxyl and amine groups on the CS polymer chains make it possible to chemically change the CS structure with the formation of modifications that allow binding of CS macromolecules to the metals, target ligands, proteins or drugs. Due to the cationic nature, CS possesses mucoadhesive properties which are useful for the improvement of drugs bioavailability [4]. Under acidic conditions, it exhibits viscosity, chelating and polyelectrolyte properties [5]. CS is used in prolonged drug delivery systems, where a longer in vivo residence time of a drug's dosage is essential for enhanced biosafety [6]. CS polymer molecules may act as a physical barrier to the release of the drug or as a way to slow down the degradation of rapidly degradable materials with drug content [7]. The duration of the drug release process is affected by the content of surfactants in the composite, the molecular weight of CS and cross-linking degree of its macromolecules [8]. CS antimicrobial effect is a function of its intrinsic properties, such as an excess of positive charge, hydrophobicity, chelate effect, and physical stability of the CS polymer [9]. But in the case of inflammatory processes, the effect of CS is insufficient and it is necessary to additionally use antimicrobial and anesthetic drugs. Among them, there is CHX, a water-soluble local antimicrobial agent [10]. Because of its positive charge, the CHX molecules react with the microbial surface of the cells, destroying the integrity of the cell membrane that leads to the bacterial cell death. BZ is a water-insoluble local anesthetic of the etheric type. Poorly soluble in aqueous fluid, BZ tends to remain at the site of use and is poorly absorbed into the systemic circulation.

The purpose of this work was to study the effect of microwave radiation (MW) during synthesis on the properties of the HA/CS composite as a system of prolonged

L. B. Sukhodub (✉) · M. O. Kumeda · L. F. Sukhodub
Laboratory Bionanocomposite, Sumy State University, 2,
Rymyskogo-Korsakova Street, Sumy, Ukraine
e-mail: l.sukhodub@gmail.com

release of various drugs—hydrophilic CHX and BZ. It was also important to study and compare the pharmacokinetics of drugs release from the HA/CS beads.

2 Materials and Methods

2.1 Materials

The following chemicals were used for synthesis: biomedical grade chitosan (M.M. 100–300 kDa, 85% degree of the deacetylation, Acros organics, USA); calcium chloride (CaCl_2), 85% orthophosphoric acid (H_3PO_4), Sodium hydroxide (NaOH) were of analytical grade and supplied by Merck; commercially available pharmaceutical BZ and 0.05% CHX.

2.2 Preparation of the Composite Materials

2.2.1 Preparation of CS-HA Gel

To 100 ml of 0.1 M CaCl_2 , 10 M NaOH was added to reach pH = 12. To the above solution drop by drop was added 100 ml of 0.06 M H_3PO_4 containing 0.4 g of chitosan (M. M. 150 kDa). The resulting mixture was divided into 4 samples, three of which were exposed to domestic microwave at different irradiation power of 300, 600 and 800 W for 5 min. After cooling and centrifugation, a CS-HA gel with a moisture of 90 wt.% was obtained. The samples were named HA-CS-MW300, HA-CS-MW600, HA-CS-MW800. The fourth control sample CS-HA was synthesized by method, which included heating to 80 °C and aging for 24 h without MW influence.

2.2.2 Preparation of the HA-CS Beads

3% solution of CS (M.M. 300 kDa) in 1% acetic acid was prepared and added to HA-CS gel at a weight ratio of 1:1, and mixtures were sonicated for 5 min, followed by dripping into 1% sodium tripolyphosphate (TPP) solution for cross-linking during 24 h. The formed beads were thoroughly washed and dried at room temperature.

2.2.3 Preparation of the Drug Loaded HA-CS Beads

The pharmaceutical BZ solution with concentration 12 mg/ml and 0.05% CHX were used as a model drugs. The experimental beads were saturated with BZ and CHX for 4 h followed by drying at 37 °C. BZ is a hydrophobic molecule (M.m 165.189 g/mol) poorly soluble in water, CHX (M.m 505.4 g/mol) is well soluble in water.

2.3 Investigation Methods

2.3.1 XRD Analysis

The X-ray diffraction studies of the sample crystallographic structure were performed on the diffractometer DRON-3. $\text{CuK}\alpha$ -radiation (wavelength 0.154 nm) with θ 2 θ Bragg-Brentano geometry (2 θ is the Bragg angle) was used. Identification of the crystal phases was performed using the JCPDS (Joint Committee on Powder Diffraction Standards) card catalog.

2.3.2 Swelling and Liquid Retention Ability Measurement

The swelling behaviour was quantified by measuring the changes in sample weight as a function of sample immersion time in phosphate-buffered saline (PBS) [9] for 2 h at different pH, namely 4.52, 6.49 and 7.3. The swelling ratio (S_w) was calculated using the following equation [11]:

$$S_w = (W_t - W_o)/W_o \quad (1)$$

where W_o is the initial sample weight, and W_t is the final weight of the swollen sample.

To measure the liquid retention ability, the wet beads were transferred to centrifuge tubes with filter paper at the bottom, centrifuged at 600 rpm for 5 m and weighed immediately (W'_t). The percentage of liquid retention (E_r) were calculated using following equation [12]

$$E_r = (W'_t - W_o)/W_o * 100\% \quad (2)$$

2.3.3 HPLC Analysis

The BZ and CHX loaded experimental beads with mass of 0.15 g each sample were placed into 6.0 ml of PBS (pH = 7.4) and incubated at 37 °C with continues shaking at 80 rpm. The rate of drug release from composites was determined by taking of 600 μl aliquots of PBS from each experimental tube in 1, 2, 3 h and than daily until complete release of the drug. The drug release was studied using high-performance liquid chromatography (HPLC; Agilent Technologies 1200, detector with UV-Vis Abs, detection at $\lambda = 280$ nm, column C18 (Zorbax SB-C18 4.6 \times 150 mm, 5 μm)).

The next mobile phase was used for the BZ release determination: 10% of methanol; 90% of glacial acetic acid (10%, v/v) and for CHX release determination: 0.05 M potassium hydrogen phosphate buffer with 0.2% triethylamine (pH = 3.1 at 210 °C)—68%; acetonitrile—32%.

Isostatic treatment was applied at a rate of eluent elution 2 ml/min and temperature of analytical column 40 °C. UV detection was performed at 239 nm.

3 Results and Discussion

3.1 XRD Analysis

XRD patterns of the experimental samples, dried at 37 °C and sintered at 600 °C are shown in Fig. 1. It is revealed that HA is formed just after MW irradiation. In obtained composites HA corresponds to JCPDS 00-046-0905, but some peaks in the XRD patterns for sintered at 600 °C samples are slightly shifted to lower angle side compared to stoichiometric HA.

The average crystallites size from the (002), (310) peaks estimated by Sherrer equation [13] was 12–13 nm for dried at 37 °C samples and increased up to 28 nm after sintering at 600 °C. It is noteworthy, that with increase of the MW from 300 to 800 W, the crystallite size decreased from 28 to 23 nm, respectively.

3.2 Swelling and Water Retention Ability Studies

The uptake or release of water molecules is very important in the size changes of the polymer containing biomaterials.

CS contains primary amino groups that may be protonated by acids. Carboxyl and amino groups are capable of gaining charge and are responsible for strong interactions with polar water molecules and the ability of the system to swell. In the group of investigated samples (Fig. 2) the highest swelling degree was observed in the case of sample

HA-CS-MW800, and least one for the sample synthesized without MW influence. The lowest swelling ability for all experimental samples was observed in PBS at pH 6.49. In this case the amino groups are mainly unprotonated, whereas carboxyl groups are undissociated. With the increase or decrease of the pH value of the solution, the swelling capacity of the composites increased. As the pH value decreases up 4.6, protonation of the amino groups occurs, so the swelling capacity of the hydrogel increases. The same mechanism occurs with increasing pH up to 7.3, that is ionization of carboxylic groups and formation of highly polar structures can be observed.

Water absorption and water retention ability of the experimental samples were additionally evaluated after 30 days of their being in PBS at 37 °C under continuous shaking. The beads saved shape stability and the degree of swelling remained practically the same as after 2 h staying in PBS. The greatest difference between water absorption and water retention was observed for the HA-CS-MW800 sample, while for the control HA-CS this difference was the smallest. It is obvious that under MW influence a specific surface is formed which has a greater ability to adsorb and desorb the liquid.

3.3 HPLC Analysis

During the chemical reactions that occurred in the synthesis of HA-CS gel and beads formation, the number of functional groups of CS, which are responsible for interactions with

Fig. 1 XRD pattern of the HA-CS, HA-CS-MW300, HA-CS-MW600, HA-CS-MW800, sintered at 600 °C

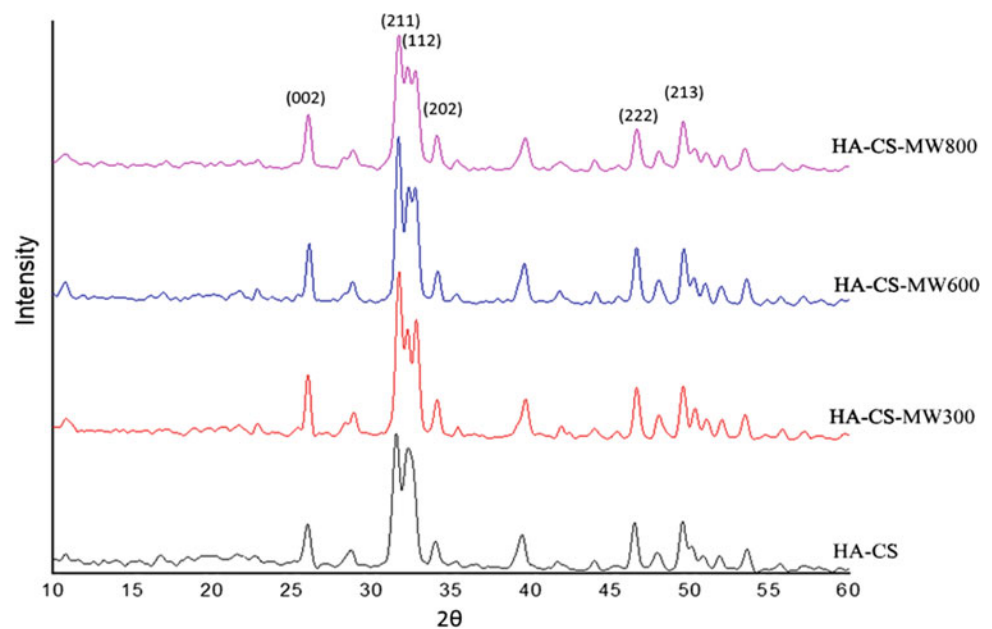
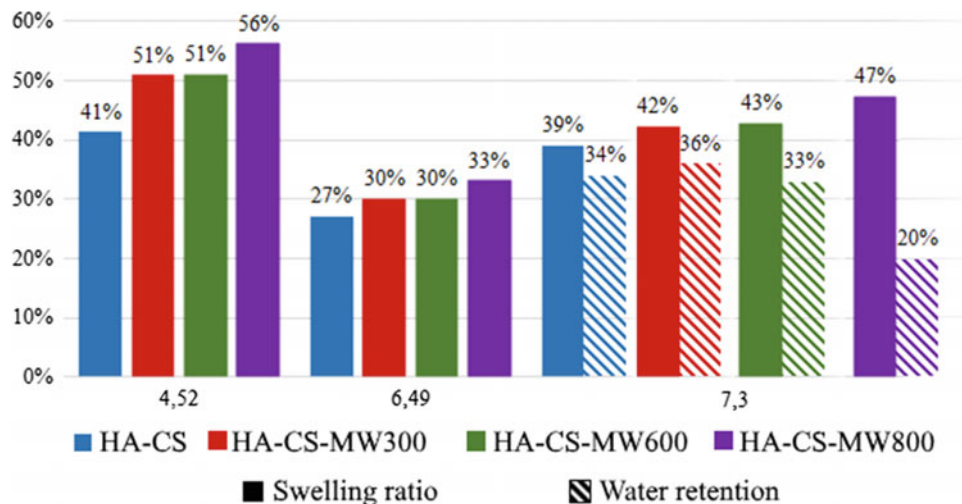


Fig. 2 Swelling ratio of HA-CS, HA-CS-MW300, HA-CS-MW600, HA-CS-MW800 samples at PBS pH value of 4.52; 6.49; 7.3 and water retention of samples that were in PBS at pH 7.3



polar water molecules or drug solutions, decreases. Nevertheless, not all groups underwent crosslinking reactions. Immobilization of the drug into the composite structure, occurred due to the electrostatic forces and the binding to the chitosan chain.

The pharmacokinetic release profiles depend on the many factors (physicochemical properties of CS, particles size, pH), but sometimes a suitable CS cross-linker may result in better drug release profile even for CS with a low degree of deacetylation [14]. In experiment conditions was used TPP as cross-linker for CS macromolecules. The kinetics of CHX and BZ release from the experimental samples is presented in Figs. 3 and 4.

It should be noted that the samples kept a high degree of shape stability throughout the study period. Thus, the pharmacokinetics of the release was determined mainly by the adsorption of the drug to the surface of the material and

the possibility of its diffusion. Particular attention is paid to the HA-CS-MW800 sample. The results have shown that the release of hydrophilic CHX from this sample occurs at a higher rate (100% for 336 h) than the BZ release (100% for 384 h). In addition, the CHX release kinetics for HA-CS-MW800 is almost the same as for the control HA-CS, and the CHX release rate in the first 72 h is the highest among the studied samples. Another tendency is observed for hydrophobic BZ. There is the lowest drug release rate for HA-CS-MW800 and highest for the control HA-CS. In the first 2 h the smallest amount of BZ (about 32%) is released from HA-CS-MW800 sample, which is a positive moment. For other samples, drug release in the first hours is about 45%.

In addition, the HA-CS-MW800 shows the most prolonged release time (384 h) compared to other experimental specimens (288 h). Obviously, this fact is the result of

Fig. 3 Chlorhexidine release from experimental samples during 336 h

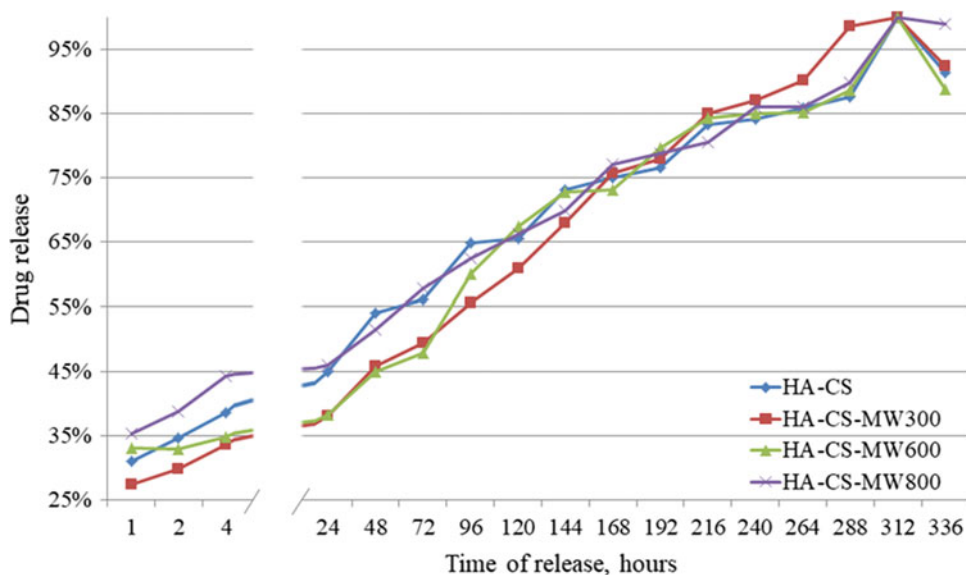
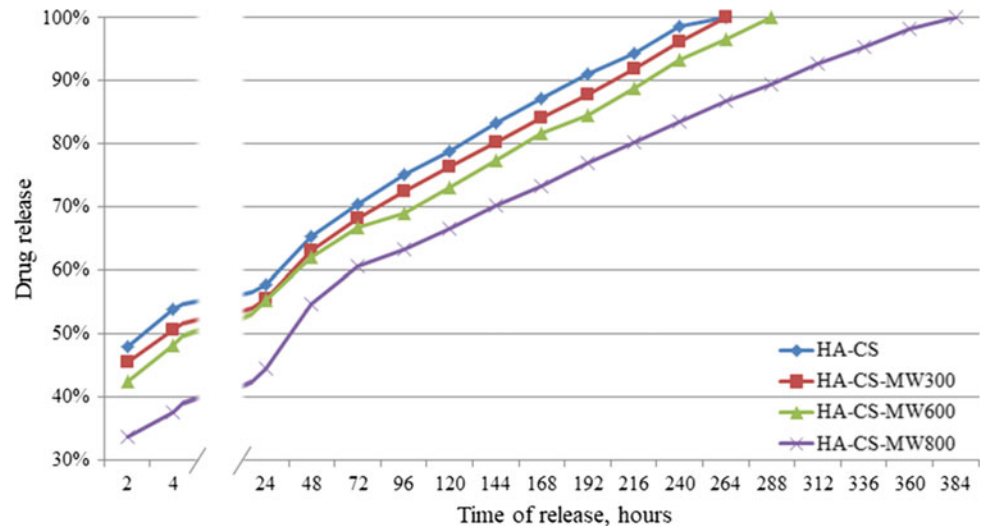


Fig. 4 Benzocaine release from experimental samples during 384 h



hydrophobic interactions between BZ and material components, and the effect of MW contributes to the specific location of binding sites and access of BZ molecules to these sites.

4 Conclusions

Biocomposite material based on HA and CS in form of beads was synthesized using MW of different power and investigated by methods of XRD and HPLC. MW reduces the time of HA formation without affecting its structure. Swelling study demonstrates the greatest difference between liquid absorption and liquid retention for the synthesized at maximum MW power HA-CS-MW800 sample, while for the control HA-CS this difference was the smallest. HPLC showed significant differences in the release kinetics of the of hydrophilic CHX and hydrophobic BZ and proved the composite ability to prolonged drug release to 336 h for CHX and 384 h for BZ. The HA-CS-MW800 demonstrates the highest release rate for hydrophilic CHX and the lowest for hydrophobic BZ. In the first 2 h the smallest amount of BZ (about 32%) is released from HA-CS-MW800 sample, while for other samples drug release in the first hours is about 45%. The effect of MW contributes to the specific location of binding sites in composite and access of drug molecules to these sites. Formed under MW influence nanoparticles surface has a greater ability to adsorb and desorb the liquid.

Conflict of Interest The authors declare that they have no conflict of interest.

References

- Melo, M.A.S., Cheng, L., Weir, M.D., Hsia, R.-C., Rodrigues, L. K.A., Xu, H.H.K.: Novel dental adhesive containing antibacterial agents and calcium phosphate nanoparticles. *J. Biomed. Mater. Res. B Appl. Biomater.* **101B**(4), 620–629 (2012)
- Sukhodub, L.F., Dyadyura, K.: Design and fabrication of polymer-ceramic nanocomposites materials for bone tissue engineering. *J. Nano- Electron. Phys.* **10**(6), 06003 (2018)
- Jain, A., Duvvuri, L.S., Farah, S., Beyth, N., Domb, A.J., Khan, W.: Antimicrobial polymers. *Adv. Healthc. Mater.* **3**(12), 1969–1985 (2014)
- Casettari, L., Illum, L.: Chitosan in nasal delivery systems for therapeutic drugs. *J. Control. Release* **190**, 189–200 (2014). <https://doi.org/10.1016/j.jconrel.2014.05.003>
- Katarina, R.K., Takayanagi, T., Oshima, M., Motomizu, S.: Synthesis of a chitosan-based chelating resin and its application to the selective concentration and ultratrace determination of silver in environmental water samples. *Anal. Chim. Acta* **558**(1–2), 246–253 (2006). <https://doi.org/10.1016/j.aca.2005.11.010>
- Park, J., Kim, Y., Choi, S., Koh, H., Lee, S.-H., Kim, J.-M., Chung, J.: Drosophila porin/VDAC affects mitochondrial morphology. *PLoS ONE* **5**(10), e13151 (2010). <https://doi.org/10.1371/journal.pone.0013151>
- Beenken, K.E., Mrak, L.N., Zielinska, A.K., Atwood, D.N., Loughran, A.J., Griffin, L.M., Smeltzer, M.S.: Impact of the functional status of saeRS on in vivo phenotypes of *Staphylococcus aureus* sarA mutants. *Mol. Microbiol.* **92**(6), 1299–1312 (2014). <https://doi.org/10.1111/mmi.12629>
- Harris, M., Alexander, C., Wells, C.M., Bumgardner, J.D., Carpenter, D.P., Jennings, J.A.: Chitosan for the delivery of antibiotics. *Chitosan Based Biomater.* **2**, 147–173 (2017). <https://doi.org/10.1016/b978-0-08-100228-5.00006-7>
- Sukhodub, L.: Metal ions doped chitosan nanoparticles. *J. Nano-Electron. Phys.* **6** (2014)
- Neiders, M.E., Weiss, L.: The effects of chlorhexidine on cell detachment in vitro. *Arch. Oral Biol.* **17**(6), 961–967 (1972). [https://doi.org/10.1016/0003-9969\(72\)90119-7](https://doi.org/10.1016/0003-9969(72)90119-7)

11. Han, Y., Zeng, Q., Li, H., Chang, J.: The calcium silicate/alginate composite: preparation and evaluation of its behavior as bioactive injectable hydrogels. *Acta Biomater.* **9**(11), 9107–9117 (2013). <https://doi.org/10.1016/j.actbio.2013.06.022>
12. Venkatesan, J., Qian, Z.-J., Ryu, B., Ashok Kumar, N., Kim, S.-K.: Preparation and characterization of carbon nanotube-grafted-chitosan – natural hydroxyapatite composite for bone tissue engineering. *Carbohydr. Polym.* **83**(2), 569–577 (2011). <https://doi.org/10.1016/j.carbpol.2010.08.019>
13. Klug, H.P., Alexander, L.E.: *X-ray Diffraction Procedures for Polycrystalline and Amorphous Materials*. Wiley, New York (1974)
14. Oliveira, P.M., Matos, B.N., Pereira, P.A.T., Gratieri, T., Faccioli, L.H., Cunha-Filho, M.S.S., Gelfuso, G.M.: Microparticles prepared with 50–190 kDa chitosan as promising non-toxic carriers for pulmonary delivery of isoniazid. *Carbohydr. Polym.* **174**, 421–431 (2017). <https://doi.org/10.1016/j.carbpol.2017.06.090>

Improvement of the Antibacterial Activity of Benzylpenicillin in Combination with Green Silver Nanoparticles Against *Staphylococcus aureus*

S. Ohanyan, H. Grabski, L. Rshtuni, S. Tiratsuyan, and A. Hovhannisyan

Abstract

The antibiotic resistance crisis is one of the most pressing public health issues worldwide. Nanoparticles (NPs) can offer a promising solution, since they have antibacterial properties, and can act as carriers for antibiotics and natural antimicrobial compounds. The purpose of this work was to study the antibacterial activity of silver nanoparticles, which are obtained by “green synthesis” from *Ocimum araratum* extract, against *Staphylococcus aureus* bacteria, as well as to study their combined action with antibiotic benzylpenicillin. The results show that the antibacterial effect of silver nanoparticles is higher than that of nanoparticles stabilized by the extract on the growth of *S. aureus*. It has been shown that benzylpenicillin can interact with the allosteric site of penicillin-binding protein 2a. It has also been shown that “green” AgNPs, which include phytocompounds of the extract of *O. araratum* can enhance the antibacterial effect of benzylpenicillin synergistically.

Keywords

Green silver nanoparticles • *Staphylococcus aureus* MDC5233 • Benzylpenicillin • Antibacterial effect • Penicillin-binding protein 2a

1 Introduction

Infectious diseases remain one of the leading causes of death worldwide. World Health Organization (WHO) expressed serious concern about the continued development of multidrug resistance among bacteria. The lack of new

antimicrobials is associated with an increase in antibiotic resistance. This led to the creation of new initiatives around the globe to develop new and more effective antimicrobial compounds, as well as new delivery and targeting strategies.

There are many strategies to counter bacteria and biofilms. One of them is nanotechnology, which is a set of technological methods, dealing with manipulations on the scale of individual atoms and molecules, with size tolerance less than 100 nm. The distinctive functionality of NPs is achieved by their ultra-small dimensions and huge surface-to-volume ratio. This is a key competitive advantage compared with traditional methods of treating infections caused by intracellular pathogens and MDR strains [1, 2]. Numerous experimental data show that NPs, in particular silver (AgNPs), are capable of destroying bacterial membranes and can inhibit biofilm formation. This reduces the survival of the microorganism [3–5]. AgNPs are considered as the most effective nanomaterial against bacteria [6]. AgNP is known to exert antimicrobial properties, which decreases inflammation and modulate cytokine expression, generate reactive oxygen species (ROS), induce intracellular effects (interaction with DNA and/or proteins), thereby providing a new therapeutic way to fight bacteria [7]. β -Lactam antibiotics acylate enzymes that participate in the biosynthesis of peptidoglycan cell wall. The primary mechanism of resistance of *Staphylococcus aureus* is an enzyme, called penicillin-binding protein 2a (PBP2a). PBP2a is a transpeptidase that catalyzes cell-wall crosslinking. It discriminates against β -lactam antibiotics via an allosteric site, distal from the active site, which realigns the conformation of key residues for catalysis [8]. The aim of this work was to study the mechanisms of the antibacterial activities of silver nanoparticles obtained by “green synthesis” from basil extracts, as well as to study their action in combination with benzylpenicillin (BP) against the growth of gram-positive *S. aureus* and molecular docking simulation of the interaction of BP with PBP2a.

S. Ohanyan · H. Grabski · L. Rshtuni · S. Tiratsuyan · A. Hovhannisyan (✉)

Department Medical Biochemistry and Biotechnology,
Russian-Armenian University, Hovsep Emin 123 Street, Yerevan,
Armenia
e-mail: ashkhen.hovhannisyan@rau.am

2 Methods and Materials

2.1 Characterization of Nanoparticles

Plant extract of *Ocimum araratum* was added to the silver nitrate solution. The transition of Ag^{+1} to Ag^0 was confirmed by the alteration of the color of the solution from colorless to brown. SEM (SEMLEO-1430 VP, Carl Zeiss, Germany) was used for the detection of the forms and types of NPs. The UV–vis absorption spectra were recorded using a spectrophotometer from 200 to 700 nm after mixing for 0, 2 and 24 h relative to deionized water. The results indicate that AgNPs were formed during the “green” synthesis.

2.2 Bacterial Strain, Cultivation Conditions and Determination of Growth

The bacteria *S. aureus* MDC5233, a natural lysogenic strain from the collection of the Department of Microbiology and Biotechnology of the YSU, was cultivated in peptone medium in thermostat at 37 °C for 18–20 h. The antibacterial activity of nanoparticles was studied using disc-diffusion method on agar [9]. The monitoring of the optical density of the suspension was carried out using a spectrophotometer. The optical density of the bacterial suspension with a concentration of 1.5×10^8 under visual control complies with a turbidity standard of 0.5 based on the McFarland criteria. Inhibition zones (pixel²) with/without core diameter were calculated using “Image Repair” software package [10].

2.3 Determination of Colony-Forming Activity by Serial Dilution

Serial dilution method was used for the determination of the colony-forming unit (CFU), which allows to quantify the sensitivity of the selected microbe to antibacterial drugs and determine the minimum inhibitory concentration (MIC) of the drug. After inoculation, the plates were left at room temperature for drying, then turned over and incubated at 35 °C for 24 h, then the grown colonies were counted. Spectral analysis of the complexation of silver NPs and BP was performed using UV/Vis spectrophotometer at a wavelength of 200–700 nm (Fig. 1).

2.4 Molecular Modeling of Benzylpenicillin with PBP2a Protein

At the current moment there are two crystallic structures where the ligands interact with the allosteric binding site of

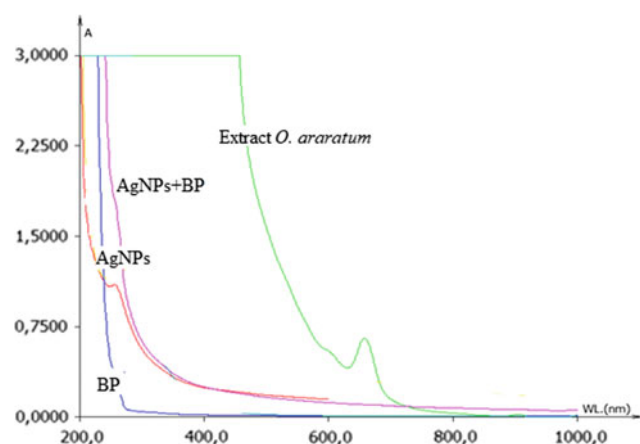


Fig. 1 Spectral analysis of the *O. araratum* extract (green); AgNPs (red); BP (blue); BP + NPs (crimson)

PBP2a: The crystal structure ceftaroline acyl-PBP2a from MRSA with non-covalently bound ceftaroline and muramic acid at allosteric site [PDB ID: 3ZFZ] and crystal structure of PBP2a from MRSA in complex with quinazolinone ligand [PDB ID: 4CJN] were used for structure alignment. It has been shown that these ligands have very strong antibacterial properties. The two structures were aligned with an RMSD of 0.7 Å.

The protein structure [PDB ID: 4CJN] was used as the basis for molecular docking studies, because of the better resolution. The protein structure was cleaned from ions, water molecules and ligands, then the structure was minimized and the steric clashes were solved using Chiron [11]. Chiron minimizes the number of nonphysical atomic interactions (clashes) in the protein structure, which then can be used for molecular docking. The molecular structure of BP was taken from PubChem [12]. Molecular docking was performed using Autodock Vina [13]. Vina relies on the parameter exhaustiveness for thorough conformational sampling. Exhaustiveness value 24 was chosen for more consistent results based on the recommendation of the program creators [14]. For each ligand 10 docking simulations were performed with different random seeds.

The box size was chosen based on radius of gyration (Rg) of the molecules [15], where the optimal box size ($2.857 \cdot \text{Rg}$) was calculated. The Rg of the molecules was calculated using MDTraj [16]. The Rg of ceftaroline was used for the calculation of the box size ($16.05 \times 16.05 \times 16.05$), because its size is bigger than quinazolinone and BP. This allows to cover the binding site more properly. The center of the box coordinates was calculated by averaging the center of mass coordinates of the binding modes of ceftaroline and quinazolinone. The final coordinates of the box center are X: 16.128, Y: 27.391, Z: 25.055.

The hydrophobic and hydrogen interactions were analyzed with LigPlot⁺ [17].

2.5 Statistical Analysis of Results

The statistical analysis of the material was carried out using the integrated standard statistical methods of the Microsoft Excel program: the calculation of the mean values, standard deviations, standard mean errors. The experiments have been repeated 4–6 times with 2–3 series of experiments in each, where $p < 0.05$.

3 Results

3.1 Effect of Silver Nanoparticles Without Extract and Stabilized by *O. araratum* Extract on the Growth of *S. aureus* Using the Disk-Diffusion Method

Disk diffusion was used to investigate the effect of 50% ethanol extract of *O. araratum* and silver nanoparticles (AgNPs). AgNPs in the extract stabilized the growth of *S. aureus* bacteria (Fig. 2). Studies of the antibacterial activity of the *O. araratum* extract showed that it does not possess antibacterial properties. Inhibition was observed when AgNPs were added at all concentrations (0.125–1 mg/ml). The lysis area zones were 153,007–162,129 pixel² (Fig. 1), while the zones of inhibition of the stabilized NPs are smaller compared to silver NPs only (Fig. 2).

3.2 Effects of AgNPs Dispersed in Peptone and Stabilized in the Extract on the Growth of *S. aureus* Colonies

The results show that the antibacterial effect of nanoparticles dispersed in peptone is higher than that of nanoparticles stabilized by the extract on the growth of *S. aureus*. This can be explained by the fact that *O. araratum* extract contains antioxidants and membrane-protective components, and since the formation of ROS is one of the mechanisms of action of nanoparticles, the extract can neutralize the destructive effect of the latter.

When studying the effect of silver nanoparticles dispersed in peptone and stabilized in the extract on the formation of *S. aureus* microcolonies, the opposite effect is observed. Stabilized NPs almost completely suppresses the colony formation of *S. aureus* at all concentrations. At low concentrations, the activity of the stabilized NPs is 163–188 times higher than NPs without the extract (Fig. 3).

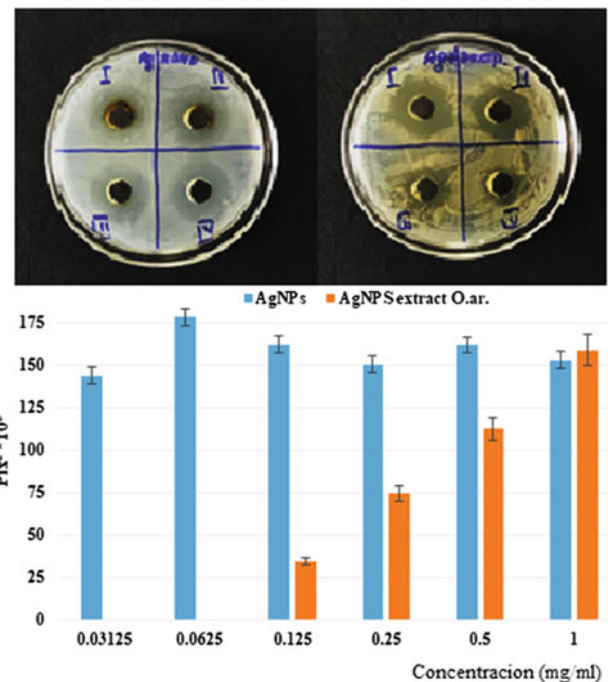


Fig. 2 Lysis area zones and values (pix²) of *S. aureus* bacteria after adding AgNPs and AgNPs stabilized in the extract (I—1 mg/ml; II—0.5 mg/ml; III—0.25 mg/ml; IV—0.125 mg/ml AgNPs) $p < 0.05$

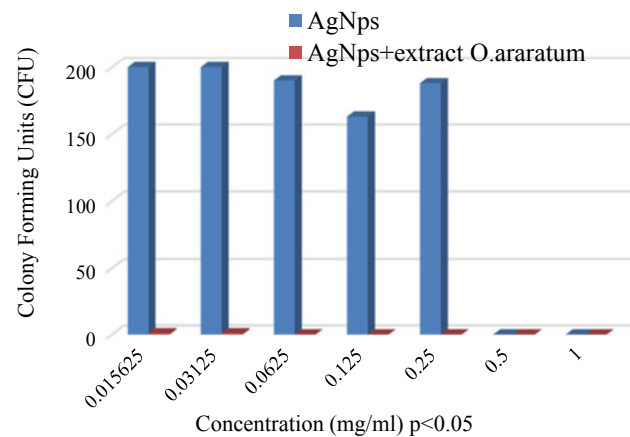


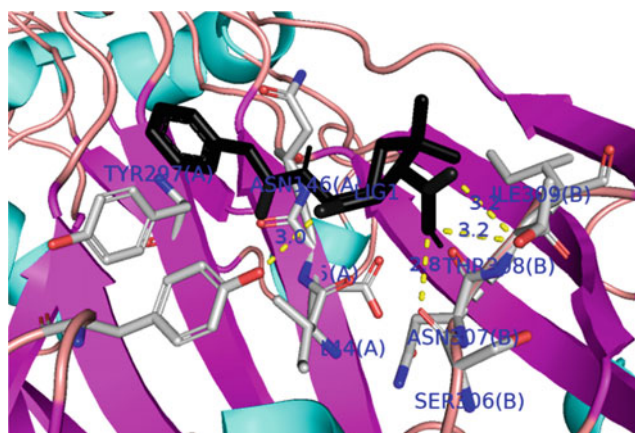
Fig. 3 The effect of AgNPs without extract and stabilized in *O. araratum* on colony forming units (CFU) of *S. aureus* MDC5233, $p < 0.05$

3.3 Study of the Effect of Benzylpenicillin Separately and in Combination with AgNPs on the Growth of *S. aureus* Using the Disk-Diffusion Method

We have tested the joint effect of nanoparticles and the β -lactam antibiotic BP on bacterial growth using the disk diffusion method. *S. aureus* growth was totally inhibited at all concentrations in the presence of BP in complex with AgNPs.

Table 1 Binding affinities of ligands to the allosteric site of PBP2A

Ligand	Kcal/mol	Hydrophobic interactions	Hydrogen bonds
Ceftaroline	-6.2	Ile144, Glu145, Asn146, Asp275, Tyr297, Ser306, Asn307, Thr308, Ile309	Tyr105 Asp295
Quinazoline	-6.9	Tyr105, Ile144, Asn146, Lys273, Glu294, Asp275, Tyr297, Gly296, Asn307, Ile309	
Benzylpenicillin	-6.5	Ile144, Glu145, Asn146, Tyr297, Asn307, Ile309,	Tyr105, Ser306, Thre308

**Fig. 4** Interaction of BP with the allosteric site of PBP2A

3.4 The Effect of Benzylpenicillin With/Without AgNPs on the Growth of *S. aureus* Colonies

AgNPs and BP form a complex (Fig. 1). The complexes completely suppressed the growth of the formation of microcolonies of *S. aureus* at all concentrations. The action of the complex is two orders of magnitude higher than the action of BP. Our experiments have shown that AgNPs can enhance the antibacterial effect of antibiotics synergistically, while the concentration of silver NPs does not cause hemolysis of erythrocytes of healthy donors (RBC test, data not shown).

3.5 Molecular Docking of Benzylpenicillin with PBP2A

The molecular docking results indicate the BP has higher binding affinity than ceftaroline and lower than quinazoline (Table 1). Both of them are known for their antibacterial properties.

The results also indicate that BP forms 3 hydrogen bonds with key residues important for allosteric changes (Table 1, Fig. 4).

This could explain the molecular mechanism of the interaction of BP and that “green” AgNPs, which include

phytocompounds of the extract of *O. araratum*, such as rosmarinic acid, flavonoids and terpenoids, can enhance the antibacterial effect of BP synergistically.

4 Conclusions

Based on the obtained data, it is obvious that the combination of traditional lactam antibiotics with NPs may be one of the promising approaches in the fight against bacterial resistance. However, the use of nanoparticles is still a problem for therapy, and much more research is needed to overcome it.

Conflict of Interest The authors declare that they have no conflict of interest.

References

- Hemeg, H.: Nanomaterials for alternative antibacterial therapy. *Int. J. Nanomed.* **10**(12), 8211–8225 (2017). <https://doi.org/10.2147/ijn.s132163-329>
- Slavin, Y., Asnis, J., et al.: Metal nanoparticles: understanding the mechanisms behind antibacterial activity. *J. Nanobiotechnol.* **15**, 65 (2017). <https://doi.org/10.1186/s12951-017-0308-z>
- Falagas, M., Kasiakou, S., et al.: Colistin: the revival of polymyxins for the management of multidrug-resistant gram-negative bacterial infections. *Clin. Infect. Dis.* **40**(9), 1333–1341 (2005). <https://doi.org/10.1086/429323>
- Peulen, T.-O., Wilkinson, K.: Diffusion of nanoparticles in a biofilm. *Environ. Sci. Technol.* **45**(8), 3367–3373 (2011). <https://doi.org/10.1021/es103450g>
- Li, P., Pu, X., et al.: FocVell influences asexual production, filamentous growth, biofilm formation, and virulence in *Fusarium oxysporum* f. sp. *cucumerinum*. *Front. Plant. Sci.* **6**, 312 (2015). <https://doi.org/10.3389/fpls.2015.00312>
- Isiaku, A., Sabri, M., et al.: Biofilm is associated with chronic streptococcal meningoenkephalitis in fish. *Microb. Pathog.* **102**, 59–68 (2017). <https://doi.org/10.1016/j.micpath.2016.10.029>
- Fehaid, A., Taniguchi, A.: Silver nanoparticles reduce the apoptosis induced by tumor necrosis factor- α . *Sci. Technol. Adv. Mater.* **19**(1), 526–534 (2018). <https://doi.org/10.1080/14686996.2018.1487761>
- Mahasenani, K., Molina, R., et al.: Conformational dynamics in penicillin-binding protein 2a of methicillin-resistant *Staphylococcus aureus*, allosteric communication network and enablement of catalysis. *J. Am. Chem. Soc.* **139**(5), 2102–2110 (2017). <https://doi.org/10.1021/jacs.6b12565>

9. Bauer, A.: Antibiotic susceptibility testing by a standardized single disk method. *Am. J. Clin. Pathol.* **45**(1), 493–496 (1966). https://doi.org/10.1093/ajcp/45.4_ts.493
10. Vardapetyan, H., et al.: Antioxidant and antibacterial activities of selected Armenian medicinal plants. *JEBAS* **2**(3), 300–307 (2014)
11. Ramachandran, S., Kota, P., et al.: Automated minimization of steric clashes in protein structures. *Proteins* **79**(1), 261–270 (2010). <https://doi.org/10.1002/prot.22879>
12. Kim, S., Thiessen, P., et al.: PubChem Substance and Compound databases. *Nucleic Acids Res.* **44**(D1), D1202–D1213 (2015). <https://doi.org/10.1093/nar/gkv951>
13. Trott, O., Olson, A.: AutoDock Vina: improving the speed and accuracy of docking with a new scoring function, efficient optimization, and multithreading. *J. Comput. Chem.* **31**(2), 455–461 (2009). <https://doi.org/10.1002/jcc.21334>
14. Forli, S., Huey, R., et al.: Computational protein–ligand docking and virtual drug screening with the AutoDock suite. *Nat. Protoc.* **11**(5), 905–919 (2016). <https://doi.org/10.1038/nprot.2016.051>
15. Feinstein, W., Brylinski, M.: Calculating an optimal box size for ligand docking and virtual screening against experimental and predicted binding pockets. *J. Cheminform.* **7**(1) (2015). <https://doi.org/10.1186/s13321-015-0067-5>
16. McGibbon, R., Beauchamp, K., et al.: MDTraj: a modern open library for the analysis of molecular dynamics trajectories. *Biophys. J.* **109**(8), 1528–1532 (2015)
17. Laskowski, R., Swindells, M.: LigPlot+: multiple ligand–protein interaction diagrams for drug discovery. *J. Chem. Inf. Model.* **51**(10), 2778–2786 (2011). <https://doi.org/10.1021/ci200227u>

Functionalization of Flavonoids (Quercetin) to Chitosan Matrix and Determination of Antioxidant Activity of Obtained Bio-composites

M. Gonta, E. Sirbu, S. Robu, A. Gonta, and L. Mocanu

Abstract

In recent years, particular attention has been paid to antioxidant systems functionalized with natural organic polymers such as starch, dextran and especially chitosan. Chitosan is a polysaccharide with very good functional properties, which is obtained from natural sources and has a range of applications. The most significant improvement of chitosan macro-molecules is focused on the functionalization of natural biologically active compounds from the flavonoid group such as quercetin and others in its polymeric structure. Within the given paper, new compounds of chitosan were synthesized with quercetin natural antioxidant. The antioxidant activity of modified chitosan was determined and changes in the chemical structure of chitosan and quercetin were established.

Keywords

Quercetin • Chitosan • Functionalization • Antioxidant • DPPH

1 Introduction

Chitosan is a versatile compound due to its functionalization with various bioactive compounds, allows the introduction of the desired properties and the widening of its application field. Functionalization of different biologically active compounds occurs due to its reactive groups ($-\text{NH}_2$ or $-\text{OH}$) [1].

The advantages of using chitosan are: this polymer can be obtained from by-products of the marine extraction industry, this compound is obtained from renewable sources, is

non-toxic and biodegradable. Thus, as a natural renewable source, chitosan exhibits unique properties such as biocompatibility, biodegradability, low toxicity and antibacterial properties [2, 3].

The most significant improvement of chitosan macromolecules is focused on the functionalization of natural biologically active compounds from the flavonoid group such as quercetin and others in its polymeric structure. Quercetin, 3,3',5,5'-tetrahydroxyflavone is one of the most abundant flavonoids found in human food. It has been shown to possess a range of biological activities that are considered to have important human health benefits including antioxidant activity, free radical capture activity, anticancer activity and antiviral activity [4, 5].

The authors Torres, et al., studied functionalization of quercetin by oxidation with chloroperoxidase, firstly, which resulted a brown product, characteristic of o-quinones, which is generated by oxidases. O-quinones produced by the oxidation of flavonoids may subsequently be subjected to non-enzymatic reactions [5, 6].

An innovative method of grafting flavonoids in the chitosan macromolecule is the free radical mediated method [6, 7].

Among the various systems of free radical initiators, the most used pair is ascorbic acid and hydrogen peroxide. These were first used for the synthesis of catechin grafted chitosan. The mechanism of action of the reaction is as follows: initially the hydroxyl radical OH^\bullet is generated, due to the reaction between ascorbic acid and hydrogen peroxide. Subsequently the generated radical is involved in the grafting process by removing the hydrogen atom from the polymer macromolecule, with the formation of chitosan macroradicals. The catechin molecules, which are in close, become macroradical acceptors of chitosan and thus inducing catechin grafting to chitosan is formed [8–11].

In connection with the above, the authors of this paper come with an original method, which consists of grafting quercetin into chitosan macromolecules with the help of

M. Gonta (✉) · E. Sirbu · S. Robu · L. Mocanu
Moldova State University, Chisinau, Republic of Moldova
e-mail: mvgonta@yahoo.com

A. Gonta
Institute of Chemistry, Academy of Science of Moldova, Chisinau,
Republic of Moldova

ethyl chloroformate and investigating the antioxidant properties of the obtained polymeric products

2 Materials and Methods

2.1 Materials

Quercetin (Sigma-aldrich), industrial chitosan with relatively high molecular weight (172 kDa), dimethylformamide (DMF), acetic acid (cp), triethylamine (TEA), ethyl chloroformate (CFE), di-phenylpicrylphenylhydroxylate (DPPH), methanol (Sigma Aldrich).

Several physico-chemical analysis methods have been used in the synthesis of quercetin-grafted chitosan as: IR analysis, UV-VIS spectroscopy and others.

2.2 Functionalization of Quercetin on Chitosan

1 g of chitosan is mixed with 30 ml of dimethylformamide under magnetic stirrer. As a result, an emulsion is formed according to the scheme (Fig. 1). Moreover, triethylamine was added dropwise as an equimolar amount of (0.0062 mol/0.86 ml), then ethyl chloroformate (0.0062 mol/0.61 ml) and the solution of quercetin in 10 ml DMF (0.0062 mol/1.87 g) under ice bath condition and continuous stirring. The mixture was stirred at room temperature for 3 h. Thereafter, the liquid is separated from the precipitate and concentrated by evaporation to 1/3 of the initial volume, then purified by sedimentation in hexane. The functionalization of chitosan with ethyl chloroformate increase the chemical reactivity of the amine group to the hydroxyl group of the quercetin compound follows by the scheme below (Fig. 1).

The obtained product called analogue polymer is soluble in DMF. After sedimentation in water and drying, it is subjected to subsequent analysis

2.3 Determination of Antioxidant Activities

The antioxidant activity of chitosan functionalized with quercetin was determined using the DPPH free radical method. A DPPH solution of 1×10^{-4} M concentration was prepared and the concentration of the assay was varied between 1×10^{-4} M to 3.5×10^{-5} M. To check the antioxidant activity were introduced into a 1 cm cuvette 2 ml of methanolic DPPH solution is added, and the same amount of solution of inhibitor compound with the corresponding concentration; absorbance was determined at time intervals: 0, 1, 3, 5, 10, 20, 30 min in correlation to the blank 70% methanol; the DPPH kinetic curves were plotted.

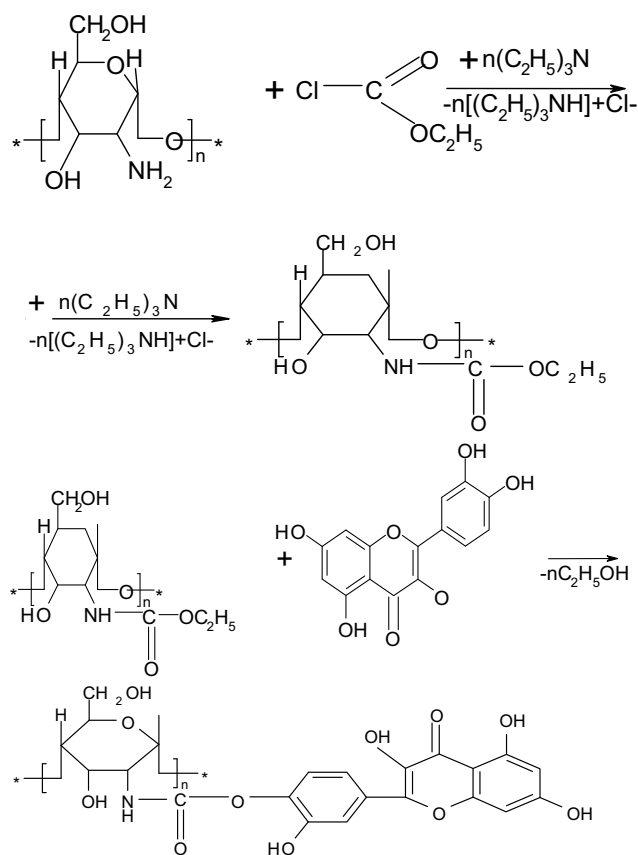


Fig. 1 Reaction stages of grafting quercetin to chitosan

3 Results and Discussions

3.1 Antioxidant Activities

The influence of chitosan functionalized with Que on DPPH consumption was studied, measuring the variation in the absorbance of the mixture. Upon interaction of the DPPH functionalized compound, rapid change of color of the DPPH solution from purple to yellow-brown was observed. Based on the obtained data, DPPH's kinetic curves were plotted. Subsequently, the concentration of DPPH (%) in solution was calculated, and the data were entered in Fig. 2. After this, the antioxidant activity of the functionalized complex was determined; EC50 which represents the amount of antioxidant required to reduce the DPPH concentration by 50% was determined. Subsequently, DPPH equilibrium concentrations (%) were calculated in all modeled systems, the $[Antiox.]/[DPPH]$ molar ratio and Wech dependence $(DPPH) = f [Inh.]/[DPPH]$ were analyzed (Table 1).

From the obtained experimental results, EC50 for Que-grafted chitosan was calculated (Fig. 2). Its value is 0.71. The obtained complex formed between chitosan with

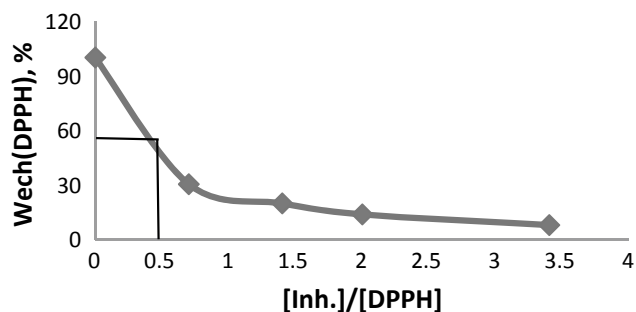


Fig. 2 EC50 molar ratio [Antiox.]/[DPPH]

Table 1 Percentage of consumed DPPH calculated after interaction with functionalized chitosan

Nr. Comp.	% of consumed DPPH
1	69.7
2	80.31
3	86.36
4	92.2

quercetin, was washed with DMF and used for subsequent syntheses.

To compare the antioxidant activity of quercetin to the functionalized chitosan activity, the antioxidant activity of quercetin was studied by the DPPH method. Therefore, the content of the radical quenched was determined at the same time intervals, and the dependence [DPPH] was plotted against time (Fig. 3).

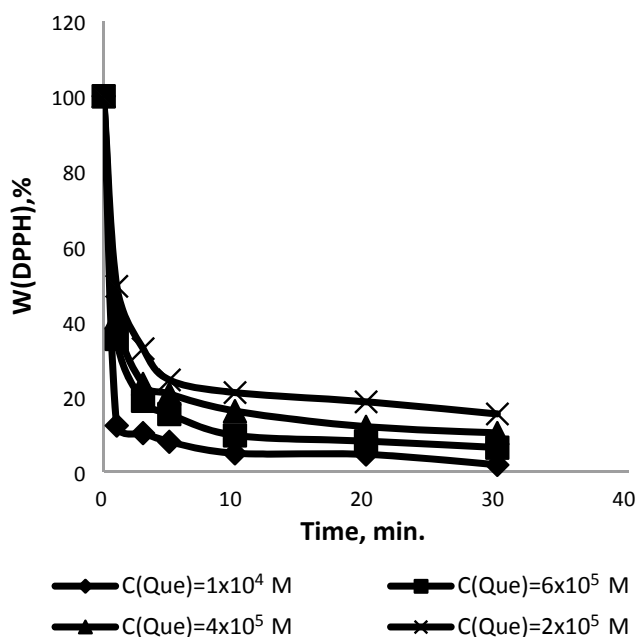


Fig. 3 Variation of DPPH concentration based on quercetin concentration

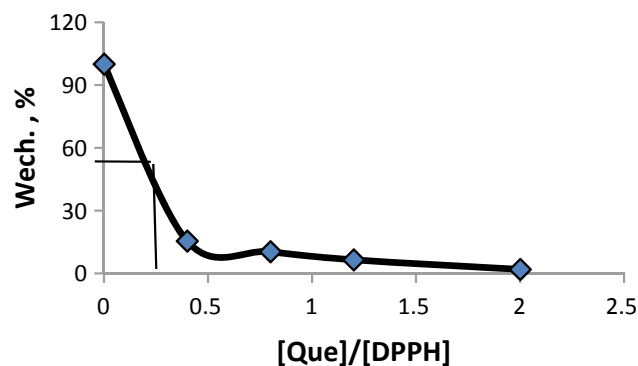


Fig. 4 [DPPH] dependence, % of the initially molar ratio quercetin: DPPH

Table 2 Percentage of DPPH consumed in the quercetin reaction

Nr. Comp.	% of consumed DPPH	Concentration of quercetin (M)
1	84.62	2×10^{-5}
2	89.67	4×10^{-5}
3	93.54	6×10^{-5}
4	98.15	1×10^{-5}

Calculating W (%) of DPPH according to the initial quercetin: DPPH molar ratio, the EC50 was determined by the graphical method which is equal to 0.21 (Fig. 4).

It has been established according to the obtained data and the calculations made that the antioxidant activity of quercetin has been preserved in the chemical reactions that took place during the process of operation (Table 2).

Significant antiradical activity was attested in the quercetin functionalized chitosan complex. The compound 4 obtained after functionalization has an antiradical power of 0.71, which is due to the fact that it contains less quercetin.

3.2 Determination of Prolongation Effect and Maximum Amount of Quercetin Grafted to Chitosan

To determine the amount of quercetin functionalized to the initial polymer macromolecule, the quercetin calibration curve was constructed at different concentrations at optical density = 290 nm. Under the same conditions, the absorbance of the DMF quercetin solution after precipitation was measured, then calculating the amount of quercetin grafted to chitosan ($37.7 \mu\text{g}$ quercetin/mg chitosan).

Moreover, investigation of the effect of prolongation of quercetin-functionalized polymers was performed by the semipermeable membrane dialysis method, which is recommended in the pharmaceutical practice. At the first stage, the semipermeable quercetin solution was passed, and in the second stage, the polymer-complex solution.

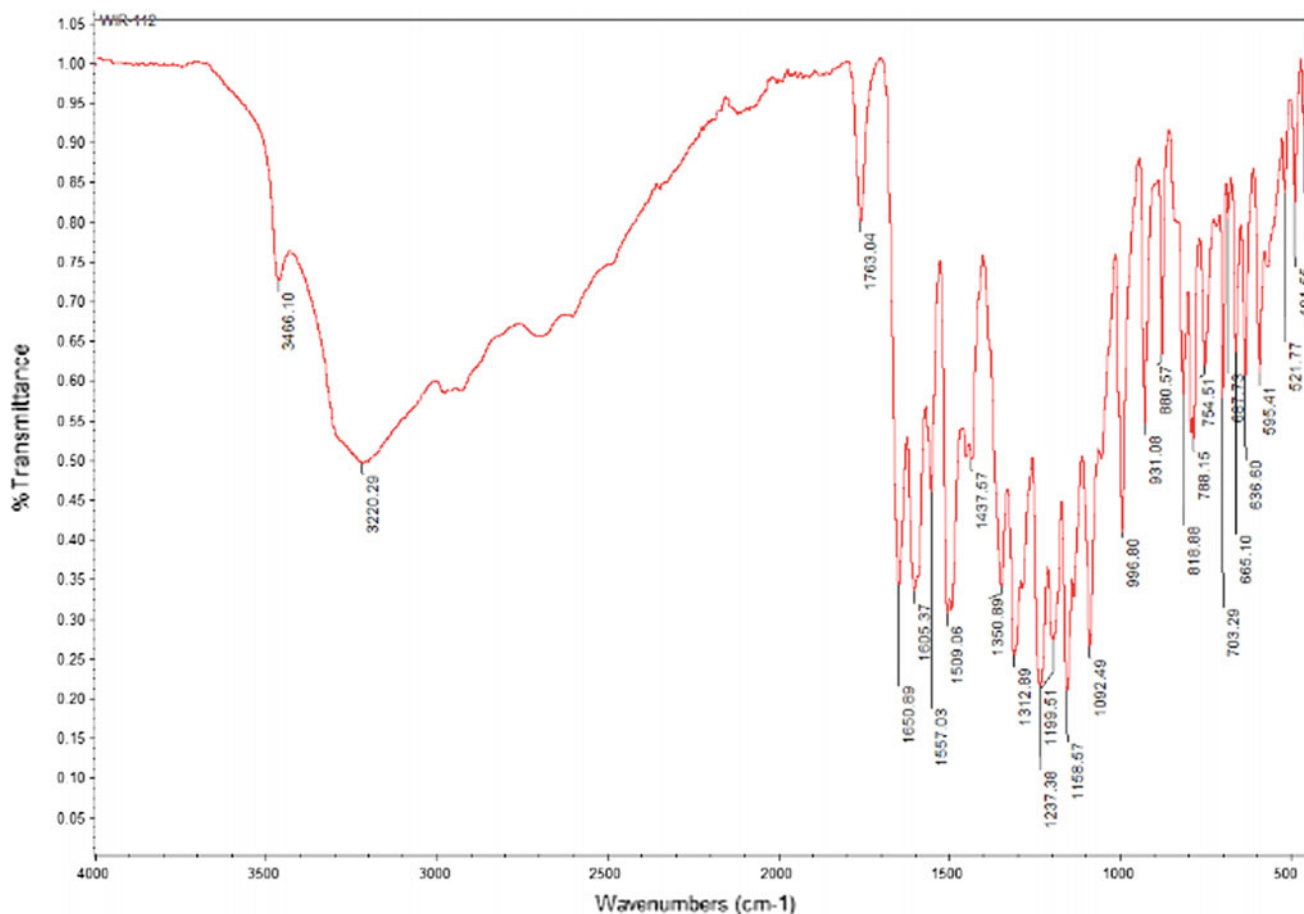


Fig. 5 FTIR spectra of chitosan-quercetin complex

The essence of this method consists in passing the solution of quercetin and complex polymer through the membrane into DMF solution in a dialysis time, thus investigating the quercetin time, then the quercetin-functionalized polymers by detecting the increase of the amplitude of a band of UV absorption.

By means of the dialysis method of quercetin solutions and quercetin-functionalized polymer solution, it was demonstrated that the polymeric material probably after the dissociation passes the semi-permeable membrane 6–8 times slower than quercetin, so quercetin functionalization of chitosan conferred to quercetin prolongation effect.

3.3 Physico-Chemical Characterization (FTIR)

Comparative analysis of IR spectra of the obtained compounds confirm the structure of the functionalized polymer, IR spectroscopy of the obtained compounds and of the starting substances are presented below.

Analyzing the obtained IR spectra, we deduced that the reaction occurred with the supposed changes of the functional groups.

In the spectra of the obtained compounds (Fig. 5) we observe characteristic bands of free polyphenol and chitosan described in Table 3. The appearance of stretching vibration of ester moiety at 1763 cm^{-1} confirms that reaction of quercetin with modified chitosan took place. Moreover band 3465 cm^{-1} confirms the occurrence of secondary NH group.

4 Conclusions

The quercetin functionalization was performed using a chemical coupling method. The chemical structure of the obtained compound was confirmed by IR and UV-vis spectroscopy. The antioxidant activity of chitosan functionalized with quercetin with the help of DPPH was tested. It has been established that the compound obtained has anti-radical activity comparable to quercetin antiradical activity.

Table 3 FTIR characteristic bands of free chitosan and quercetin

Characteristic bands	Wavelength (cm ⁻¹)
Quercetin	– C = C stretching 1450–1600 – OH groups of the Phenolic bending (1200–1350) – C = O (1725 and 1605)
Chitosan	– 1650 amide I – 1562 amide II – 1374 N-acetyl residue

The amount of quercetin grafted to the chitosan polymer was calculated, its value being 37.7 µg/mg. It has been established that the quercetin-chitosan polymer possesses a prolongation effect due to the longer passage time of the solution through the semipermeable membrane.

Acknowledgements Authors are grateful for the financial support accorded by the Science and Technology Center in Ukraine (STCU grant Nr.6377).

Conflict of Interest The authors declare that there is no conflict of interest regarding the publication of this paper.

References

- Aljawish, A., Chevalot, I., Jasniewski, J., Scher, J., Muniglia, L.: Enzymatic synthesis of chitosan derivatives and their potential applications. *J. Mol. Catal. B Enzym.* **112**, 25–39 (2015)
- Taguri, T., Tanaka, T., Kouno, I.: Antimicrobial activity of 10 different plant polyphenols against bacteria causing food-borne disease. *Biological and Pharmaceutical Bulltin.* **27**, 1965–1969 (2004)
- Ruiz, G.A.M., Corrales, H.F.Z.: Chitosan, chitosan derivatives and their biomedical applications. *Intech* 88–106 (2017)
- Chen, J., Zhu, Z., Hang, K., Yang, X.: Relationship between structure and activity of eight natural flavonoids against oxidation. *J East China Norm Univ* **1**, 90–95 (2001)
- Torres, E., Marín, V., Aburto, J., Beltrán, H.I., Shirai, K., Villanueva, S., Sandoval, G.: Enzymatic modification of chitosan with quercetin and its application as antioxidant edible films. *Applied biocemistry and Microbiology.* **48**, 151–158 (2012)
- Hu, Qiaobin, Luo, Yangchao: Polyphenol-chitosan conjugates: synthesis, characterization, and applications. *Carbohyd. Polym.* **151**, 624–639 (2016)
- Schreiber, S.B., Bozell, J.J., Hayes, D.G., Zivanovic, S.: Introduction of primary antioxidant activity to chitosan for application as a multifunctional food packaging material. *Food Hydrocolloids* **33**, 207–214 (2013)
- Leopoldini, M., Russo, N., Toscano, M.: The molecular basis of working mechanism of natural polyphenolic antioxidants. *Food Chem.* **125**, 288–306 (2011)
- Quideau, S., Deffieux, D., Douat-Casassus, C., Pouységu, L.: Plant polyphenols: chemical properties, biological activities, and synthesis. *Angew. Chem. Int. Ed.* **50**, 586–621 (2011)
- Kean, T., Thanou, M.: Biodegradation, biodistribution and toxicity of chitosan. *Adv. Drug Deliv. Rev.* **62**, 3–11 (2010)
- Liu, J., Pu, H., Liu, S., Kan, J., Jin, C.: Synthesis, characterization, bioactivity and potential application of phenolic acid grafted chitosan: a review. *Carbohydrate Polymers* 174:999–1017 (2017)

Molecular Docking of Compounds Modulating Amyloid Peptide Aggregation Schemes

S. Ginosyan, Y. Hambardzumyan, T. Mkrtychyan, H. Grabski, and S. Tiratsuyan

Abstract

Alzheimer's disease is characterized by the formation of plaques in the brain, which are commonly composed of amyloid peptides as a result of aspartyl protease β -secretase expression. This work is dedicated to in silico studies of the interaction of artemisinin, dihydroartemisinin, dihydroartemisinin dimer with amyloid 12A β_{9-40} peptide and β -secretase. The comparison was made with curcumin, which is in phase II of clinical trials. It has been shown that all ligands, similarly to curcumin, bind to the specific amino acids of the peptide that are responsible for the formation and the growth of the fibril with high affinity. Moreover, dihydroartemisinin and dihydroartemisinin dimer bind to amino acids that are responsible for the stabilization of formed fibril. All studied ligands interact with the critical amino acids of the catalytic center of β -secretase, while dihydroartemisinin dimer can also bind to Arg235, which is characteristic of peptide inhibitors of β -secretase. Dihydroartemisinin dimer has a higher binding affinity compared to other ligands. Thus, the selected compounds can be considered as possible candidates for the treatment of Alzheimer's disease.

Keywords

Amyloid peptide • β -secretase • Artemisinins • Curcumin • Molecular docking

S. Ginosyan (✉) · Y. Hambardzumyan · H. Grabski
Department of Medical Biochemistry and Biotechnology, Institute of Biomedicine and Pharmacy, Russian-Armenian University, 123 Hovsep Emin Str, Yerevan, Armenia
e-mail: siranush.ginosian@student.rau.am

T. Mkrtychyan · S. Tiratsuyan
Department of Bioengineering, Bioinformatics and Molecular Biology, Institute of Biomedicine and Pharmacy, Russian-Armenian University, Yerevan, Armenia

S. Tiratsuyan
Department of Biophysics, Faculty of Biology, Yerevan State University, Yerevan, Armenia

1 Introduction

Alzheimer's disease (AD) is the most common age-related disease, a multifactorial neurodegenerative disease. The multi-factor nature of AD requires new drug development strategies. Many small molecules and bioproducts have been developed for the treatment of asthma in recent decades. However, there are still no drugs that would be effective against the disease [1]. Pathological signs of AD are the presence of amyloid aggregates in neurofibrils. According to the amyloid hypothesis, transmembrane aspartic protease, β -secretase (BACE1), is a promising molecular target for the development of drugs against Alzheimer's disease. This protease triggers the formation of amyloid β (A β), which is involved in the development of Alzheimer's disease [2]. A series of peptide inhibitors have been identified and strong non-peptide inhibitors of BACE1 have been developed. Some of them showed effective inhibition of BACE1 in cultured cells and a significant reduction of A β production in vivo [3]. One of the modern approaches to search for possible drugs is the study of the interaction of plant metabolites with β -amyloid and BACE1 using molecular modeling methods. Artemisinins, secondary metabolites of the medicinal plant *Artemisia annua* have antioxidant, anti-inflammatory, anti-amyloidogenic, neuroprotective and cognitive-stimulating effects [4].

In this paper molecular docking of the interaction of artemisinin (ART), dihydroartemisinin (DHA) and dihydroartemisinin dimer (DDHA) with peptide 12A β_{9-40} and BACE1 was conducted. Comparative analysis was performed with curcumin (CUR), which is currently undergoing phase II clinical trials.

2 Materials and Methods

The 3D chemical structures of CUR [CID: 969516], ART [CID: 68827], DHA [CID: 456410], DDHA [CID: 44564070] were obtained from PubChem database [5]. The 3D structures of 12A β_{9-40} and BACE1 were obtained from RCSB PDB [6]. The PDB codes are 2LMN and 2WJO for 12A β_{9-40} and BACE1, respectively. Autodock Tools and Autodock Vina were used for molecular docking [7]. The exhaustiveness value of 128 was used for the blind docking for 12A β_{9-40} and BACE1 with the grid box size describing the entire surface of the targets. For local docking the grid box size was 16 × 16 × 16 [8] and exhaustiveness set to 24 [9]. PyMOL was used for data visualization [10], Ligplot+—for analysis of hydrogen bonds and hydrophobic interactions [11].

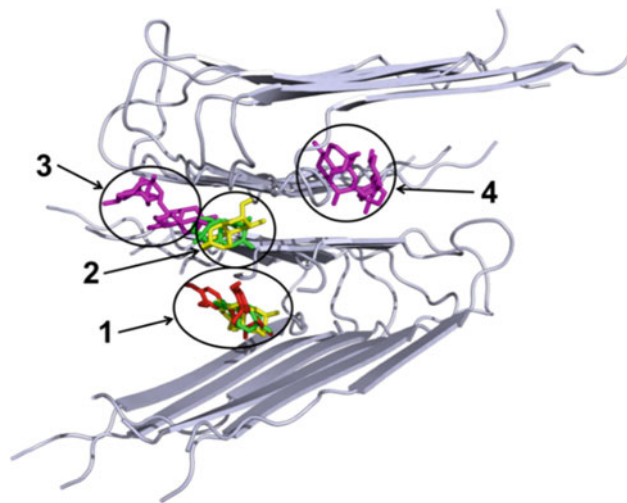


Fig. 1 Docking of 12A β_{9-40} with CUR (red), ART (green), DHA (blue) and DDHA (magenta). The numbers identified as 1, 2, 3 and 4 binding sites, respectively

3 Results

3.1 Docking Analysis for Ligands with 12A β_{9-40}

The PDB structure of 12A β_{9-40} was obtained by NMR and contains 10 models [12]. Blind docking with 4 ligands was performed for the determination of the model that has the highest binding affinity (ΔG_b). Average binding affinities of ligands with 10 models of peptide 12A β_{9-40} from the results of the docking analysis are shown in Table 1.

On this basis the 6th model of 12A β_{9-40} was chosen, because it exhibited relative high binding affinities for all ligands. The results of the docking analysis of ligands with 12A β_{9-40} showed that CUR interacts with one binding site, while ART, DHA, DDHA interact with two. There are 4 binding sites, where all ligands interact with 12A β_{9-40} : ART, CUR and DHA interact with the first site, ART and DHA interact with the second site and DDHA interacts with the third and the fourth sites (Fig. 1).

We performed local docking with these binding sites of 12A β_{9-40} for the determination of the best ligand

conformations. Docking analysis of CUR with the 6th model of 12A β_{9-40} ($\Delta G_b = -8.1$ kcal/mol) revealed 2 hydrogen bonds with Val18 of chain B and Gly37 of chain E and hydrophobic interactions with Gly38 (D), Gy38 (E), Gly38 (C), Leu17 (A) Leu17 (B), Leu17 (C), Phe19 (B), Val36 (E), Val36 (D), Val36 (C). The number of contacts for CUR with the 6th model of 12A β_{9-40} is 18 (Fig. 2a). In the case of DHA and ART many hydrophobic interactions were formed and ΔG_b equal to -8.3 and -8.2 kcal/mol. The number of contacts for DHA and ART is 17 and 18 (Fig. 2b and c).

In the second site ART, with ΔG_b equal to -7.4 kcal/mol, forms a hydrogen bond with Val40 (E) and hydrophobically interacts with Asp27 (J), Val39 (D), Val39 (E), Val40 (D), Gly38 (D), Gly38 (E), Gly29 (K), Gly29 (L) and Ile31 (K). The number of contacts of ART with 12A β_{9-40} is 14 (Fig. 3a). Docking analysis for DHA with 12A β_{9-40} ($\Delta G_b = -7.1$ kcal/mol) revealed 2 hydrogen bonds with Asn27

Table 1 The average values of ΔG_b (kcal/mol) CUR, ART, DHA, DDHA with 10 models of peptide 12A β_{9-40}

	CUR	ART	DHA	DDHA
1	-7.4 ± 0.4	-7.2 ± 0.33	-7.2 ± 0.29	-9 ± 0.54
2	-7.3 ± 0.39	-6.9 ± 0.16	-6.99 ± 0.28	-8.8 ± 0.49
3	-7.98 ± 0.34	-6.8 ± 0.35	-6.8 ± 0.28	-8.7 ± 0.22
4	-4.4 ± 0.23	-4.6 ± 0.32	-4.5 ± 0.16	-6.3 ± 0.33
5	-7.8 ± 0.38	-6.9 ± 0.296	-6.97 ± 0.25	-8.7 ± 0.33
6	-7.8 ± 0.24	-7 ± 0.38	-7.2 ± 0.37	-9.1 ± 0.25
7	-7.8 ± 0.38	-6.9 ± 0.31	-7 ± 0.36	-8.9 ± 0.3
8	-7.2 ± 0.24	-6.9 ± 0.22	-7 ± 0.34	-8.96 ± 0.47
9	-8.2 ± 0.85	-6.6 ± 0.3	-6.5 ± 0.289	-8.9 ± 0.22
10	-6.9 ± 0.28	-7.1 ± 0.39	-7.1 ± 0.26	-9.1 ± 0.42

Fig. 2 Analysis of hydrophobic interactions and hydrogen bonds of $12A\beta_{9-40}$ with CUR (a), DHA (b) and ART (c)

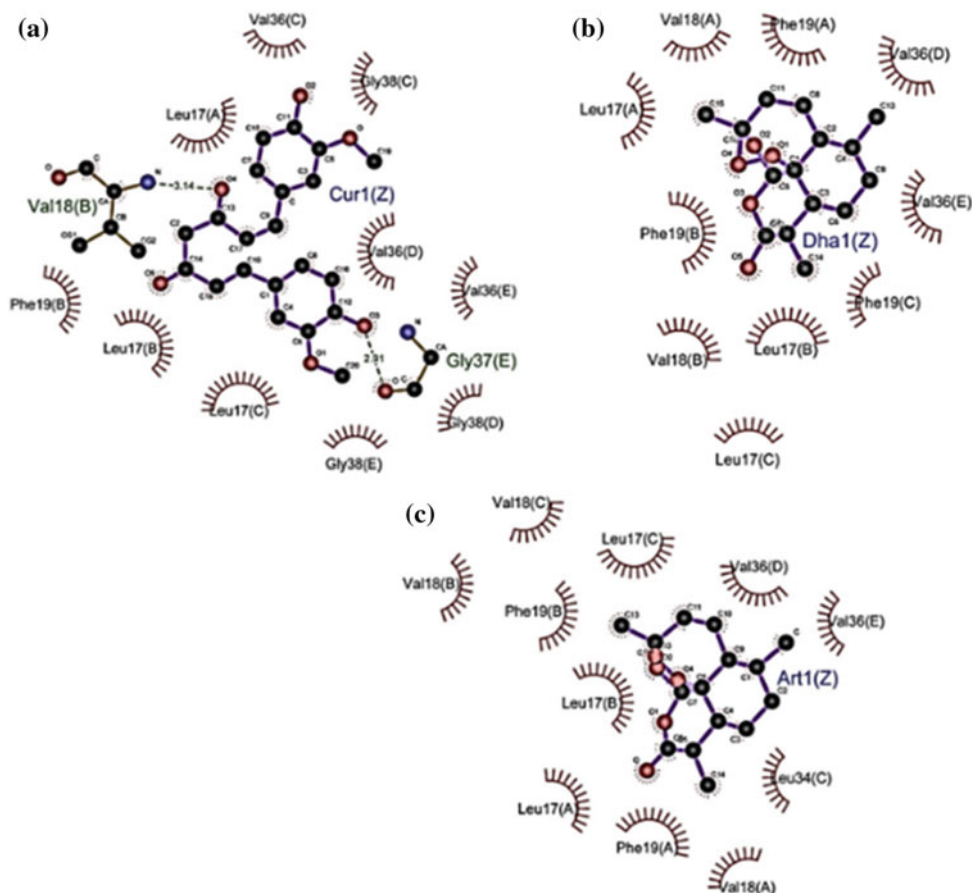
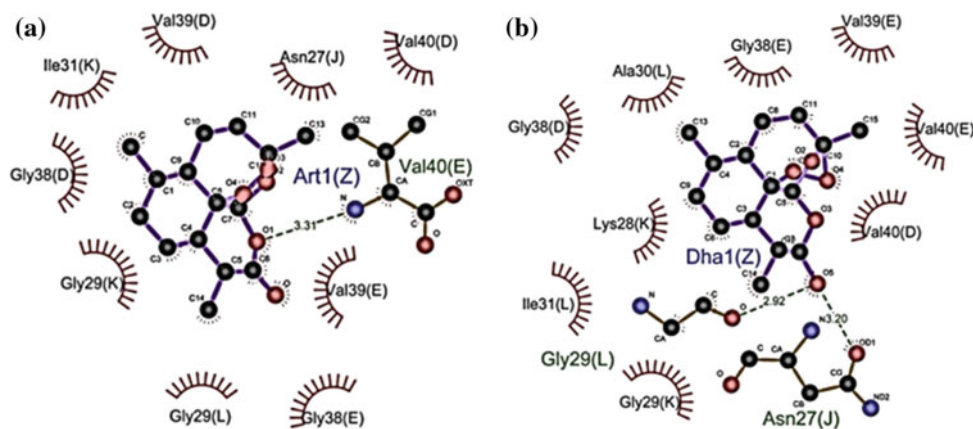


Fig. 3 Analysis of hydrophobic interactions and hydrogen bonds of $12A\beta_{9-40}$ with ART (a) and DHA (b)



(J) and Gly29 (L), and hydrophobic interactions with Gly29 (K), Ile31 (L), Lys28 (K), Val39 (E), Val40 (D), Val40 (E), Gly38 (D), Gly38 (E), Ala30 (L). The number of DHA contact with $12A\beta_{9-40}$ was 11 (Fig. 3b).

Dihydroartemisinin dimer binds to the 3rd and the 4th sites with binding energies equal to -9.5 and -9.2 kcal/mol, respectively. In the 3rd site DDHA forms one hydrogen bond with Val40 (D) and many strong hydrophobic interactions. The number of contacts is 18. In the 4th site only

strong hydrophobic interactions were revealed for DDHA, with the number of contact equal to 19 (Fig. 4).

3.2 Docking Analysis for CUR, ART, DHA and DDHA with BACE1

We carried out blind docking analysis for CUR, ART, DHA and DDHA with BACE1. It has been shown, that all ligands

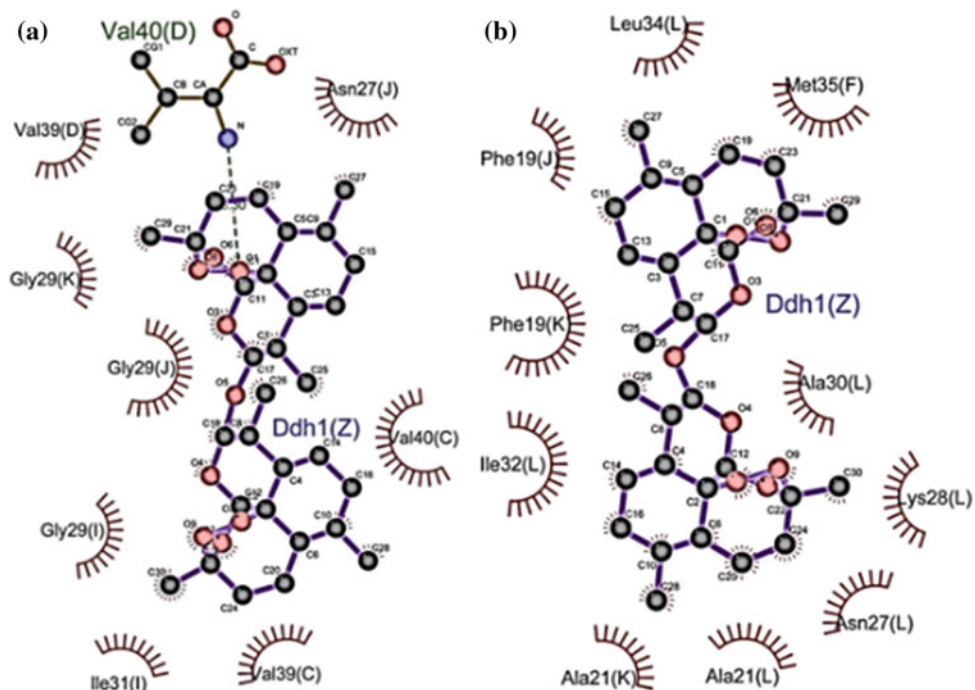


Fig. 4 Analysis of hydrophobic interactions and hydrogen bonds of 12A β_{9-40} with DDHA of 3rd (a) and 4th (b) binding sites

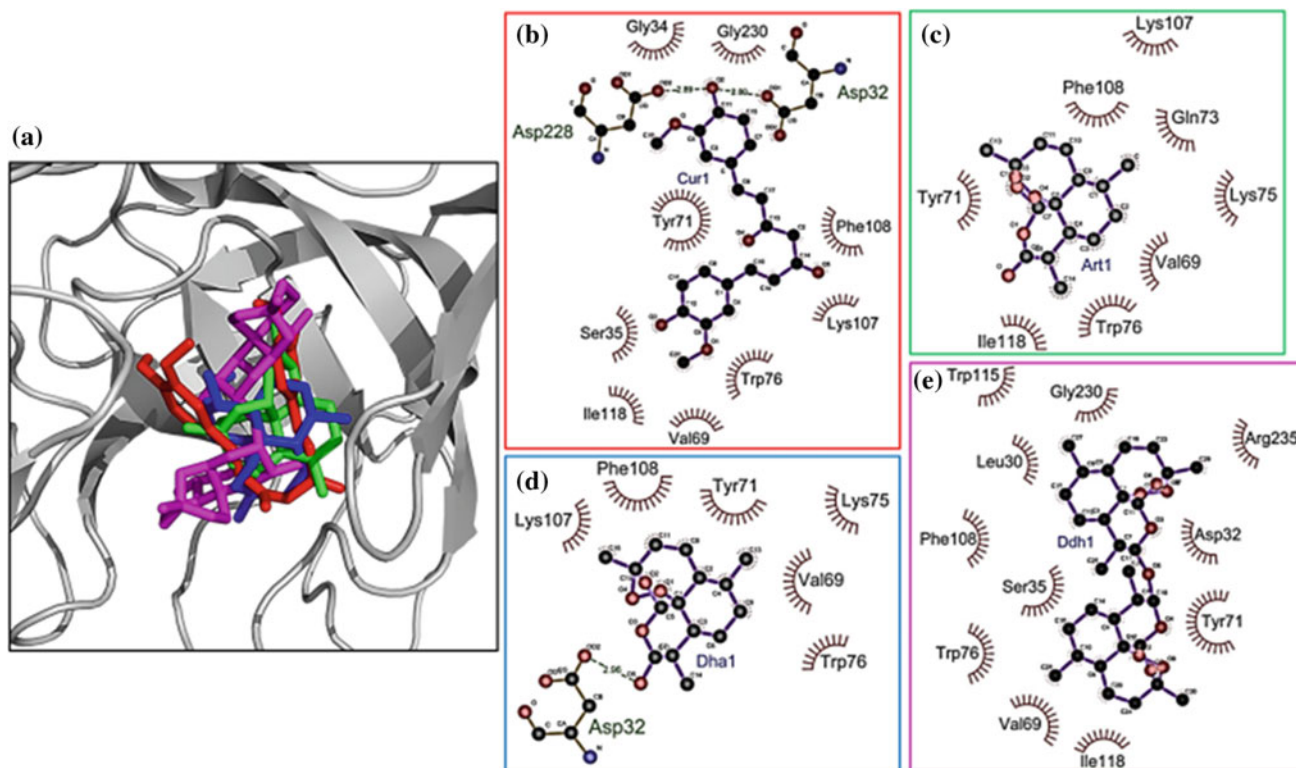


Fig. 5 Docking (a) of BACE1 with CUR (red), ART (green), DHA (blue) and DDHA (magenta). Analysis of hydrophobic interactions and hydrogen bonds of BACE1 with CUR (b), ART (c), DHA (d) and DDHA (e)

bind to one site, which is the catalytic center [2]. Local docking for all ligands with BACE1 was performed (Fig. 5a). The results of docking showed that CUR forms hydrogen bonds with Asp32 and Asp228 and a lot of hydro-phobic interactions. The number of contact is 19, and the binding energy is -7.3 kcal/mol (Fig. 5b).

Artemisinin hydrophobically interacts with Lys107, Phe108, Gln73, Tyr71, Lys75, Val69, Trp76 and Ile118 of BACE1 (Fig. 5c). The binding energy is equal to -7.9 kcal/mol, the number of contacts is 10. Dihydroartemisinin forms hydrogen bond with Asp32 and interacts hydrophobically with Lys107, Phe108, Tyr71, Lys75, Val69 and Trp76. The number of contacts is 10, and the interaction energy was -7.5 kcal/mol (Fig. 5d). Dihydroartemisinin dimer interacts hydrophobically with Trp115, Gly230, Leu30, Arg235, Phe108, Asp32, Ser35, Tyr71, Trp76, Val69, Ile118 with binding energy -10.5 kcal/mol. The number of contacts is 23 (Fig. 5e). Note that of all the ligands we studied, only DDHA interacts with the Arg235 side chain.

4 Discussion

In vivo and in vitro investigations revealed that artemisinins showed neuroprotective action during AD pathology, inhibiting the activity of NF- κ B and the activation of NALP3 inflammation [13]. It is noteworthy that artemisinins can be considered as therapeutic agents for the treatment of central nervous system diseases, affecting the inflammatory process [4]. It is known that CUR and ART interfere with A β aggregation [4, 14]. On the other hand, as our experiments show, they are also closely associated with the fibrils [15] and BACE1. Hence, we can conclude that inhibition of the formation of fibrils is mediated by the direct binding mechanism, i.e. binding to fibrils modulates the ability to aggregate. Amino acid residues Leu17-Ala21 and Gly37-Ala42, located in β_1 and β_2 are involved in the formation and further growth of fibrils [16]. We have shown that in the first binding site, ART and DHA bind to amino acid residues from β_1 and CUR to both β_1 and β_2 . In the second site, ART and DHA bind to amino acid residues from β_2 . In the case of DDHA, it binds with amino acids from β_2 in the third site, and in the fourth site from β_1 . Amino acids Lys28 and Asp23 in the area of rotation between β_1 and β_2 participate in the stabilization of the formed fibrils due to creation of a salt bridge with a bound water layer [17]. Of all the ligands, only DHA from the second site and DDHA from the fourth site interact hydrophobically with Lys28.

All of the studied ligands interact with the active center of BACE1 with a high binding affinity and, regardless of their chemical structure, interact with Val69, Tyr71, Trp76, and Phe108. The active site of β -secretase consists of Asp32 and

Asp228, which are conservative in eukaryotic aspartic proteinases [2]. Of all the ligands, only CUR, DHA, DDHA are bound to either Asp32 or Asp228. Moreover, CUR forms a hydrogen bond with both Asp32 and Asp228. It is known that the conservative water molecule (W2) forms three hydrogen bonds with Tyr71, Asn37 and Ser35 residues. This leads to the formation of a continuous chain of hydrogen-bound Trp76-Tyr71-W2-Ser35-Asp32 residues [18]. As it was noted above, all ligands interact with Tyr71 and Trp76, while CUR, DHA, DDHA also interact with Asp32 and CUR, DDHA with Ser35. The proximity of the OH of the Ser35 group to the carboxyl group of Asp32 was observed in all the β -secretase enzyme crystal structures in complex with inhibitors [19]. There is a mechanism that, during the initial stages of catalysis, promotes the release of proton from the carboxyl group of Asp32 and the adoption of the proton after the cleavage of the substrate, i.e. Ser35 assists in the adoption of protons and the release of Asp32 during the catalytic cycle [18]. Curcumin and DDHA interact with the amino acid residues of the entire continuous chain, thus likely compete for the catalytic activity of BACE1. The interaction with Asp32 and Ser35 will additionally break the chain that promotes the cleavage of the substrate. Dihydroartemisinin dimer also interacts with Arg235, which is typical for strong peptide inhibitors of BACE1 [3]. The quantum-chemical interaction between the inhibitors and the arginine 235 side chain of the active site of BACE1 plays a crucial role for the inhibition mechanism. This probably contributes to enhanced interaction compared to non-peptide inhibitors, which may be important for the development and optimization of drug design.

5 Conclusions

All ligands interact directly with 12A β_{9-40} and BACE1. Artemisinin, DHA and DDHA in similar manner to CUR can suspend the formation and growth of 12A β_{9-40} fibrils, while DHA and DDHA can destabilize the already formed amyloid. Only DDHA interacts with the Arg235 side chain of BACE1. It has similar interaction mechanisms of peptidomimetics. All studied ligands interact with the active center showing a high binding affinity, which can be arranged in the following descending order: DDHA (-10.5 kcal/mol) > ART (-7.9 kcal/mol) > DHA (-7.5 kcal/mol) > CUR (-7.3 kcal/mol).

Acknowledgements We are grateful for the financial support to the Ministry of Education and Science of the Republic of Armenia (grant № 10-2/I-1).

Conflict of Interest The authors declare that they have no conflict of interest.

References

1. Alzheimer's association: 2018 alzheimer's disease facts and figures. *Alzheimer's dement* **14**, 367–429 (2018)
2. Venugopal, C., et al.: Beta-secretase: structure, function, and evolution. *CNS Neurol Disord Drug Targets (Formerly Curr Drug Targets CNS Neurol Disord)* **7**, 278–294 (2008)
3. Discovery of BACE1 inhibitors for the treatment of Alzheimer's disease. In: *Quantitative structure-activity relationship*, IntechOpen
4. Shi, Z. et al.: Resolving neuroinflammation, the therapeutic potential of the anti-malaria drug family of artemisinin. *Pharmacol Res.* (2018)
5. Bolton, E.E., et al.: PubChem: integrated platform of small molecules and biological activities. *Annu. Rep. Comput. Chem.* **4**, 217–241 (2008)
6. Berman, H.M., et al.: The protein data bank. *Nucleic Acids Res.* **28**, 235–242 (2000)
7. Trott, O., Olson, A.J.: AutoDock Vina: improving the speed and accuracy of docking with a new scoring function, efficient optimization, and multithreading. *J. Comput. Chem.* **31**, 455–461 (2010)
8. Feinstein, W.P., Brylinski, M.: Calculating an optimal box size for ligand docking and virtual screening against experimental and predicted binding pockets. *J. Cheminform.* **7**, 18 (2015)
9. Forli, S., et al.: Computational protein–ligand docking and virtual drug screening with the AutoDock suite. *Nat. Protoc.* **11**, 905 (2016)
10. DeLano, W.L.: Pymol: an open-source molecular graphics tool. *CCP4 Newsletter On Protein Crystallography* **40**, 82–92 (2002)
11. Wallace, A.C., et al.: LIGPLOT: a program to generate schematic diagrams of protein-ligand interactions. *Protein Eng. Des. Sel.* **8**, 127–134 (1995)
12. Paravastu, A.K., et al.: Molecular structural basis for polymorphism in Alzheimer's β -amyloid fibrils. *PNAS* **105**, 18349–18354 (2008)
13. Shi, J.Q., et al.: Antimalarial drug artemisinin extenuates amyloidogenesis and neuroinflammation in APP^{swe}/PS1^{dE9} transgenic mice via inhibition of nuclear factor- κ B and NLRP3 inflammasome activation. *CNS Neurosci. Ther.* **19**, 262–268 (2013)
14. Yang, F., et al.: Curcumin inhibits formation of amyloid β oligomers and fibrils, binds plaques, and reduces amyloid in vivo. *J. Biol. Chem.* **280**, 5892–5901 (2005)
15. Hambarzumyan, Y.R., et al.: Assessment of the therapeutic potential of anti-malarial drugs as β -amyloid inhibitors using molecular modeling methods. *Biol. J. Armen.* In press (2019)
16. Han, W., Schulten, K.: Fibril elongation by A β 17–42: kinetic network analysis of hybrid-resolution molecular dynamics simulations. *J. Am. Chem. Soc.* **136**, 12450–12460 (2014)
17. Kundaikar, H.S., Degani, M.S.: Insights into the Interaction mechanism of ligands with A β 42 based on molecular dynamics simulations and mechanics: implications of role of common binding site in drug design for alzheimer's disease. *Chem. Biol. Drug Des.* **86**, 805–812 (2015)
18. Mishra, S., Caffisch, A.: Dynamics in the active site of β -secretase: a network analysis of atomistic simulations. *Biochem.* **50**, 9328–9339 (2011)
19. Liu, S., et al.: Exploring the binding of BACE-1 inhibitors using comparative binding energy analysis (COMBINE). *BMC Struct. Biol.* **12**, 21 (2012)

Use of the Auto Osteomatrix Forte Graft in Total Tympanomastoid Dissection

I. Ababii, S. Vetrician, V. Smetanca, and L. Danilov

Abstract

The study aim is to evaluate the efficacy of meatotympanoplasty with the use of the auto osteomatrix forte graft (AOMF) associated with temporal fascia and mastoid obliteration with pediculated musculoperiosteal flap in patients after total tympanomastoid dissection (ETMT) in comparison to patients after revision surgery of the eardrum cavity. Materials and methods: The prospective cohort study which included 2 batches of patients, 58 patients with ETMT and reconstruction by means of the elaborated method, and 59 patients with revision surgery of the eardrum cavity and reconstruction by means of the elaborated method. The patient batches were similar according to age, gender and living environment. Results: 12 months postoperatively, in all patients of both study groups was determined: significant decrease of complaints, ameliorated anatomical outcomes (small, clean and dry eardrum cavity), eradication of the eardrum cavity pathology, improvement of the auditory functional results (statistically significant increase in the perception of voice on whispering and speech, airway and bone conduction), improvement of the vestibular function and life quality. Conclusions: Meatotympanoplasty with the use of the auto osteomatrix forte autograft when associated with the temporal fascia and the mastoid dislocation with pediculated musculoperiosteal flap is a feasible and safe technique for pathology eradication involving the eardrum cavity. The use of the autologous bone for reconstruction is effective for the stability of the external auditory canal and for the tympanic membrane. It preserves and/or restores hearing, and has a lot of advantages: is immediately available in primary and revision surgeries, is economical, does not cause inflammation processes in the body, contributes to the growth of

the new bone, reduces the risk of infection, resorption and subsequent degradation and improves life quality.

Keywords

Mastoidectomy • Reconstruction • Obliteration • Osteomatrix

1 Introduction

A canal wall down tympanomastoidectomy is a very effective technique for eradication of advanced chronic otitis media or cholesteatomas. The advantages of canal wall down mastoidectomy include excellent exposure for disease eradication and postoperative monitoring, and low rates of residual and recurrent disease. However, the disadvantages of canal wall down mastoidectomy include cavity problems, such as continuous ear drainage, accumulation of keratin debris, frequent vertigo attacks following temperature or pressure changes, and difficulty in fitting a hearing aid [1, 2].

In order to eliminate open cavity problems, reducing the mastoid cavity volume and/or covering the denuded area is a critical factor to prevent granulation tissue and accelerate epithelialization [3, 4]. Clinical studies have shown that the most common free graft used to cover mastoid cavity is temporalis fascia [5]. Despite its acknowledged application, fascia grafts are inadequate in size to cover all areas of the mastoid cavity. In addition, random flaps are the most common soft tissue flaps used for mastoid obliteration. Overall, the procedure of choice for mastoid obliteration is a controversial issue among otolaryngologists. Therefore, otolaryngologists need to acquaint themselves with various mastoid obliteration options to facilitate the healing process in a variety of clinical situations [6].

The study aim is to evaluate the efficacy of meatotympanoplasty with the use of the auto osteomatrix forte graft (AOMF) associated with temporal fascia and mastoid obliteration with pediculated musculoperiosteal flap in

I. Ababii · S. Vetrician · V. Smetanca (✉) · L. Danilov
Department of Otorhinolaryngology, State University of Medicine and Pharmacy “Nicolae Testemitanu”, bd. Ștefan cel Mare și Sfânt, 165, Chisinau, Republic of Moldova
e-mail: Smetanca_vova@mail.ru

patients after total tympanomastoid dissection (ETMT) in comparison to patients after revision surgery of the eardrum cavity.

2 Materials and Methods

To determine the effectiveness of the use of autogenous bone grafts with AOMF osteoinductive properties in reconstruction surgery after ETMT the prospective cohort study was conducted which included 2 batches of patients:

- Group of patients with ETMT and reconstruction by means of the elaborated method included 58 patients: 28 (48.3%) women and 30 (51.7%) men with mean age of 41.83 ± 1.2 years from 24 up to 60 years old—the baseline lot (LB);
- Group of patients with revision surgery of the eardrum cavity and reconstruction by means of the elaborated method constituted 59 patients: 30 (50.8%) women and 29 (49.2%) men with mean age of 40.44 ± 1.3 years (from 18 up to 61 years old)—control group (LM).

From the study were excluded: patients with malignant ear cancer, patients with congenital disorders, patients that were not fully investigated preoperatively or postoperatively according to the study protocol, patients that did not attend the medical check-ups on the schedule, patients that refused to participate in the study or abandoned it.

All patients were treated at the Department of Otorhinolaryngology of the Republican Clinical Hospital in Chisinau, during 2005–2014.

We applied meatotympanoplasty with the use of autologous matrix graft associated with temporal fascia and mastoid obstruction with pediculated musculoperiosteal flap. The first variant is used in patients that were not previously operated by OMCS. Firstly the mastoid plane is opened within the limits of the Chipault triangle. The rectangular bone fragment with the dimensions of 1.5×2.5 cm and the thickness of 1 cm is cut from the cortical layer. After that typical ETMT is performed. When EAC postero-superior wall is removed, 2 fine crests are cut into their upper and lower sides. EAC plastic surgery of the skin is not performed. The postoperative cavity is treated with Mirocel or with mesh gauzes with antibacterial ointment. The plaque remains opened during 3–5 days (time required to prepare the OMF autograft from the bone fragment of the cortical layer, extemporary prepared). Daily, on the post-operative cavity are performed measures for rehabilitation and removal of pathological secretions with microscopic revision. The reconstruction stage is performed on the 4th up to 6th day (depending on the preparation of the OMF

autograft). The prepared autografts have sufficient elasticity and strength to provide the shape and position required to model the EAC posterior wall. In addition, it offers the possibility of bonding the fascicular graft to reconstruct the eardrum. On the margins of OMF grafts, longitudinal incisions of 1.5–2 mm are made. After attaching the fascicular graft, the EAC postero-superior wall is reconstructed. The bonding of OMF grafts is achieved by using the upper and lower ridges prepared during the rehabilitation stage. In the mastoid cavity is introduced a 5 mm diameter polycarbonate perforated drainage tube and the mastoid cavity is obliterated by placing the pediculated musculoperiosteal flap taken from the retroauricular area. EAC is swabbed with Mirocel or treated with mesh gauzes with antibacterial ointment. Plaque is sutured layer by layer.

The second variant is used in patients with ETMT antecedents and with MUO. Until the revision of the eardrum cavity, a bone fragment from the cortical layer is cut to prepare the OMF autograft. After revision, the mastoid cavity is swabbed with Mirocel or treated with mesh gauzes with antibacterial ointment. The plaque remains opened during 3–5 days (the time required to prepare the OMF autograft). Daily, on the postoperative cavity are performed procedures for rehabilitation and removal of pathological secretions with microscopic revision. The reconstruction stage is performed on 4th up to 6th day (depending on the preparation of the OMF autograft). The bonding of the OMF graft and mastoid obliteration is similar to the first variant.

Plaque is sutured layer by layer. EAC is treated swabbed with Mirocel or mesh gauzes with antibacterial ointment. To achieve the study objectives, patients underwent a complex clinical and paraclinical examination program according to pre-established research designs (at the onset of the study and in dynamics at 1, 6 and 12 months postoperatively).

Patient examination protocol included: (1) history of the disease taking into consideration the duration and severity of the symptoms (otorrhea, hearing loss, tinnitus, dizziness, otalgia, cephalalgia) and previous surgical procedures, (2) otomicroscopic and/or otoendoscopic examination, (3) complete audiological evaluation (audiometry, instrumental audiometry with diapason, Liminal pure-tone audiometry, acoustic impedancemetry), (4) vestibular function test, (5) temporal bone imaging examination by high resolution computerized tomography, life quality assessment by applying the Chronic Ear Survey.

Primary data processing was performed with the help of “Statistical Package for the Social Sciences” program, version 20.0 for Windows (SPSS, Inc., Chicago, IL, 2011) using descriptive and inferential statistics. The X^2 method was used with Yates correlation or Fisher’s exact method to compare discrete variables, unifactorial variance analysis with the application of post hoc analysis test, the difference

between the mean values in the study batches, correlation analysis to determine the relationship between variables, power and direction.

3 Results

Comparative examination of patients from LB and LM groups did not reveal significant statistic differences according to: age (40.44 ± 1.3 years and 41.83 ± 1.2 years, respectively; $p > 0.05$), gender (50.8 and 48.3% women, $p > 0.05$; 49.2 and 51.7% men, $p > 0.05$), living environment (52.5 and 56.9% rural area, $p > 0.05$; 47.5 and 43.1% urban area, $p > 0.05$).

During the preoperative examination, patients from LB group frequently complained of headaches (94.8 and 78.0%, $p < 0.05$), otalgia (94.8 and 78.0%, $p < 0.05$) and tinnitus, 1 and 90.8%, $p < 0.01$). Patients' general state of moderate severity constituted 71.2% in LM patients and 81.0% in LB patients ($p > 0.05$).

Hearing test revealed reduced and similar incidence of EAC narrowing in patients from both study groups: 8.5% of LM patients and 6.9% of LB patients ($p > 0.05$). Although pathological eliminations were identified in all patients in both groups, in LB patients were revealed frequent statistically significant pathological eliminations with fetid odor (49.2 and 100.0%, $p < 0.001$), and in LM—odorless pathological eliminations without fetid odor (50.8 and 0%, $p < 0.001$).

During the objective exam, the postero-superior wall was absent statistically significantly more frequently in LM patients (100.0 and 0%, $p < 0.001$) was normal (0 and 89.7%, $p < 0.001$) and protruded (0 10.3%, $p < 0.05$) more frequently in LB, the evoidation cavity was recorded only in

LM patients. The tympanic membrane (TM) was presented with perforation and localization in par sensing and pars flaccida in all patients from both study groups. Granulations were present in all patients from both study groups. Polyps (22.0 and 43.1%, $p < 0.05$) and cholesteatoma (39.0 and 100.0%, $p < 0.001$) presented statistically significant incidence in LB patients.

One month postoperatively, the majority of complaints in patients from both study groups were significantly reduced. Although, all patients complained of hearing loss in both study groups, patients from LB group complained of more pronounced statistically significant hearing loss (86.4 and 98.3%, $p < 0.05$), and patients from LM group complained more frequently of moderate hearing loss (13.6 and 1.7%, $p < 0.05$). The general condition was similar in patients from both study groups.

Hearing test revealed statistically significantly higher incidence of moderate otorrhea (22.0 and 54.4%, $p < 0.001$) and mild otorrhea (67.8 and 40.4%, $p < 0.01$) was more rare

in LB patients. The objective examination revealed normal postero-superior wall incidence. Perforated and absent integral MT was similar. Cholesteatoma, granulations and adhesions were not found in patients from both study groups. The evoidation cavity was closed without pathologies in all patients from both study groups.

Six months postoperatively, the complaints frequency continued to reduce, and their incidence was the same in both study groups. The objective examination did not reveal statistically significant differences in the frequency and characteristics of pathological eliminations, postero-superior wall, MT, and pathology of the cavity was not found in patients in both study groups. The hearing test showed statistically significantly higher improvement in LB patients.

Although 12 months postoperatively, hypoacusis was reported in all patients from both subgroups of study, insignificant hearing loss was more common in patients from LB group (11.9 and 41.4%, $p < 0.001$), acute hypoacusis (22.0 and 0%, $p < 0.001$)—was statistically significantly more frequent in LM patients. The general condition was satisfactory in the majority of patients from both study groups.

The hearing test did not reveal a narrowing of the EAC and did not reveal statistically significant differences in the incidence and characteristics of the otorrhea and the MT state. The condition of the cavity was shown to be closed and without pathological changes in all patients from both study groups.

4 Discussion

The management of open mastoid cavity has two options: conservative and revision surgery with correction (surgery for elimination of mastoidectomy adverse effects) [7]. The procedure for the revision surgery of the evoidation cavity includes the complete elimination of the disease and methods for the prevention of recurrent diseases. It also includes the reconstruction of EAC posterior wall with meatoplasty, mastoid obliteration procedures, reconstruction of the tympanic membrane (tympanoplasty), reconstruction of the ossicular chain (ossiculoplasty), and meatoplasty [8].

Mercke suggested an innovative procedure in which the EAC posterior wall is temporarily removed, in order to avoid the disadvantages and combine certain features of CWD mastoidectomy. This procedure facilitated the complete removal of the impairment. Subsequently, it is followed by the reconstruction using autologous grafts (bone, cartilage) or alloplastic grafts (HA cement, ionomeric glass cement, titanium plates). This technique, called the canal wall reconstruction, with a single step for the removal of cholesteatoma and reconstruction of the EAC wall, had long acceptable results [9, 10].

Many techniques and materials for grafting (autologous, allogeneic, heterologous or synthetic biocompatible) have been used in the reconstruction of the posterior wall of EAC and mastoid obliteration, but none of these proved to be ideal for obliteration. Patient's tissues are considered to be selective materials in reconstruction [11–13].

In our study the dynamic evaluation found more significant improvement in LB patients in comparison to LM patients. These results coincide with the specialized literature data. Kronenberg and co-authors reported the results of a retrospective case study of 49 consecutive patients (31 children and 18 adults) with the reconstruction of the EAC posterior wall with autologous bone paste and obliteration of the mastoid cavity with tympanomeatal flap. After an average 28 months follow-up, 30 primary operated patients achieved impermeable ears in 85.7% of cases, dry ears in 90% of cases, intact MT in 93.3% of cases, and recurrent cholesteatoma in 10.0% of cases, compared to 64.7, 73.7, 73.7 and 15.8%, respectively, in 19 patients with secondary intervention for the revision of the cavity [14].

A significant complaints reduction (headache, otalgia, nausea, dizziness, and general weakness) was determined in patients from both study groups, 1 month postoperatively.

Although all patients had hearing loss in both groups, there was statistically significant increase of mild and moderate hypoacusis and statistically significant reduction of acute hypoacusis. However, the modification rate was higher in patients from LB group. Tinnitus and otorrhea were significantly statistically reduced after 6 months postoperatively.

Although at the objective structured primary examination the general condition was more severe, the improvement rate was higher in LB patients.

The examination of the evoidation cavity found, 1 month postoperatively, a closed cavity in all patients from both study groups. One month postoperatively almost all pathologies of evoidation cavity were eradicated, in all patients from both study groups. Exception presented desquamation of the epidermis and mucositis that significantly statistically decreased 1 month and 6 months postoperatively and completely disappeared after 12 months postoperatively in patients from LM group.

Patients from both study groups showed a statistically significant increase of voice perception on whistling and speech and duration of airway and bone conductions. But the growth rate was also higher in LB group.

Subjective examination using the Likert—CES scale found a statistically significant life quality improvement. Statistically significantly increased the subscale score of activity limitation/restriction, symptom subscale score, medical resource utilization subscale score, and total score.

However, the rate of life quality improvement was higher in LM patients.

Our preliminary results indicate good overall results for the stability of the external auditory canal and MT, the preservation and/or improvement of hearing and cholesteatoma.

In order to overcome the problem of oversized mastoid cavity, reconstruction of the EAC posterior wall with immediate mastoid obliteration or revision intervention is performed. Several autologous materials (cartilage, bone paste, local pediculated flaps of soft tissue) or synthetic biocompatible (bone cement, HA granules, bioactive glass) have been used to reduce the size of the cavity. The use of the autologous bone contributes to the creation of the new bone, reduces the risk of infection, resorption and subsequent degradation. It contributes to bone graft survival and a lower risk of subsequent repair of the reconstruction compared to heterologous materials. The use of the autologous cortical bone to reconstruct the posterior wall of the EAC has advantages: it is autologous, immediately available and economical, does not develop an inflammatory reaction to a foreign body and improves the life quality.

5 Conclusions

1. Dynamic assessment found a more significant improvement of complaints and general condition of patients after ETMT and reconstruction by the elaborated method, in comparison to patients with revision surgery of the evoidation and reconstruction cavity by the elaborated method.
2. Improvement of anatomical outcomes (low, clean and dry cavity) and functional outcomes (auditory function, vestibular function and life quality) was statistically significantly earlier, more stable and with higher rate in patients from the control group.
3. Use of the autologous bone for the reconstruction of the EAC posterior wall has advantages. It is an autologist; is immediately available in both primary surgery and revision surgery; is economical; does not develop inflammatory response to the body; contributes to new bone creation; reduces the risk of infections, resorption and subsequent degradation; contributes to the survival of the graft, restores the almost normal anatomy of EAC; improves the life quality.

Conflict of Interest The authors declare that they have no conflict of interest.

References

1. Palva, T.: Operative technique in mastoid obliteration. *Acta Otolaryngol.* **75**(4), 289–290 (1973)
2. Sade, J., Weinberg, J., Berco, E., Brown, M., Halevy, A.: The marsupialized (radical) mastoid. *J. Laryngol Otol.* **96**(10), 869–875 (1982)
3. Harris, A., Mettias, B., Lesser, T.: Pooled analysis of the evidence for open cavity, combined approach and reconstruction of the mastoid cavity in primary cholesteatoma surgery. *J. Laryngol. Otol.* **130**, 235–241 (2016)
4. Harun, A., Clark, J., Semenov, Y.R., Francis, H.W.: The role of obliteration in the achievement of a dry mastoid bowl. *Otol. Neurotol.* **36**, 1510–1517 (2015)
5. Shojaku, H., Takakura, H., Okabe, M., Fujisaka, M., Watanabe, Y., Nikaido, T.: Effect of hyperdry amniotic membrane patches attached over the bony surface of mastoid cavities in canal wall down tympanoplasty. *Laryngoscope* **121**, 1953–1957 (2011)
6. Yung, M., Bennett, A.: Use of mastoid obliteration techniques in cholesteatoma. *Curr. Opin. Otolaryngol. Head Neck. Surg.* **21**, 455–460 (2013)
7. Black, B.: Mastoidectomy elimination. *Laryngoscope* **105**(12 Pt 2 Suppl 76), 1–30 (1995)
8. Nadol, J.B.: Revision mastoidectomy. *Otolaryngol. Clin. North Am.* **39**(4), 723–740 (2006)
9. Roux, A., Bakhos, D., Lescanne, E., et al.: Canal wall reconstruction in cholesteatoma surgeries: rate of residual. *Eur. Arch. Otorhinolaryngol.* **272**(10), 2791–2797 (2015)
10. Mobashir, M.K., Basha, W.M., Mohamed, A.E., et al.: Posterior canal wall reposition for management of cholesteatoma: technique and results. *Auris. Nasus. Larynx* **45**(2), 254–260 (2018)
11. Roberson, J.B., Mason, T.P., Stidham, K.R.: Mastoid obliteration: autogenous cranial bone pate reconstruction. *Otol. Neurotol.* **24**(2), 132–140 (2003)
12. Leatherman, B.D., Dornhoffer, J.L.: The use of demineralized bone matrix for mastoid cavity obliteration. *Otol. Neurotol.* **25**(1), 22–26 (2004)
13. Sayed, R.H.: One-stage reconstruction in management of extensive cholesteatoma. *IFOS Int. Congr. Series.* **1240**, 121–131 (2003)
14. Kronenberg, J., Shapira, Y., Migirov, L.: Mastoidectomy reconstruction of the posterior wall and obliteration (MAPRO): preliminary resu.lts. *Acta Otolaryngol.* **132**(4), 400–403 (2012)

Composite Metamaterials for Biological Decontamination of Fluids

N. A. Enaki, M. Turcan, S. Bazgan, E. Starodub, T. Paslari, A. Nistreanu, C. Ristoscu, and I. N. Mihailescu

Abstract

The dependence of the contact surface of contaminated fluids with metamaterial, formed from various dimension quartz bubbles is proposed. As a simple mathematical model is proposed to packing the space between the relative big spheres with the smaller one with dimensions $d_1/10$, $d_1/10^2, \dots, d_1/10^n$. Here d_1 is the diameter of packing the biggest spheres in the system. It is established that this contact surface increase in such metamaterial and becomes proportional to the surface of the smallest spheres proposed in the model. In order to confirm these results experimentally, we propose a series of experiments with yeast fungus dissolved in the water. The systems of metamaterial like fiber optics, a system of quartz bubbles and composite granulated quartz material were proposed in order to demonstrate this effect. The qualitative correspondence between the experimental results and a theoretical model is obtained.

Keywords

Metamaterial • Decontamination • Evanescent zone

1 Introduction

The increasing the popularity of metamaterials and their applications in decontamination of fluids and implant treatments opens the new possibilities to use together with the decontamination and adhesion of implant surface to the

organic tissue. Taking into consideration the increasing of decontamination surface of the metamaterials like photonic crystals and photonic crystal fiber [1, 2] we propose to use this optical system not only in the decontamination of fluids but on the improving of implant possibilities too. In order to treat the surface infection formed on the region between the implant and cellular tissue in the process of poor adhesion, we propose to use these optical systems in the controlling and managing of modern therapeutic implants. Such metamaterials like photonic crystals each can be deposited on the implant surface and can be used as a dispersion of UV radiation on the large surface to treat the infection on the surface between the implant and adhesion tissue. The adherence of implant to the human tissue may be accompanied to the growth of cells between the elements of the bubble structure of the implant surface [1, 2]. Here may appear a possibility to restore the peripheral neural system in order to feel and to control the surface of the implant by the brain through a neural network.

Below we have modified our conception in the improving of efficient decontamination of trans-lucid fluids using UVC (ultraviolet C) and metamaterials. In order to improve the penetration of the UVC radiation inside the liquids we first proposed to minimize the elements of quasi-periodical dispersion structures in order to achieve the increase of the volume of the evanescent zone of the free space between the elements of metamaterial. The observation demonstrates that the increase of the reflection from contact between the elements of metamaterials practically becomes an obstacle in the deep penetration of radiation inside the metamaterial [2]. To solve this problem we proposed to use the combined metamaterials consisted of big and small elements in optical contact inside the same contaminated fluid. The big elements permit the UVC radiation to penetrate large distance inside the contaminated liquid. The small elements introduced in the free space between the big elements permit the good diffusion and dispersion of radiation in large volume. This method was confirmed using the crushed quartz crystals.

N. A. Enaki (✉) · M. Turcan · S. Bazgan · E. Starodub · T. Paslari · A. Nistreanu

Quantum Optics and Kinetic Processes Laboratory, Institute of Applied Physics, Academiei str. 5, Chisinau, Republic of Moldova
e-mail: enache_nicolae@yahoo.com; enakinicolae@yahoo.com

C. Ristoscu · I. N. Mihailescu
Laser-Surface-Plasma Interactions Laboratory, National Institute for Lasers, Plasma and Radiation Physics (INFLPR), Magurele, Romania

This paper is constructed in the following way. In Section Firstly we give the theoretical approach to the problem of decontamination proposing the new composite metamaterial which consists of big and small granules. Section 3 contains some experimental results obtained with quartz elements with different dimensions and geometry in the packing structure. Some correspondence between the theoretical prediction and experimental results is observed.

2 Packing Method

For this, we revised all packing structures formed by the balls packing method. We are interested in the remain free space between the big balls. This space may be expressed through the atomic packing density in each meta-material cell, $V_F = V(1 - \rho)$, where the cell density, ρ , depends on the packing structure of metamaterial. For example, in the hexagonal lattice arrangement (see Fig. 1) This density is equal to $\rho = \pi/(3\sqrt{3}) = 0.6086$ which is larger than tetrahedral lattice packing (see Fig. 2), $\rho = \pi\sqrt{3}/16 = 0.3401$. The free volume in the above example is so that in tetragonal packing, we have more free space than in hexagonal one.

Following this example, we want to find the efficient decontamination volume which is proportional to the contact surface of the contaminated liquid with such packing balls.

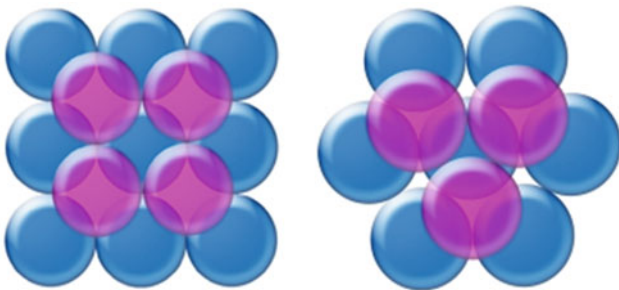


Fig. 1 The hexagonal lattice arrangement of the quartz spheres

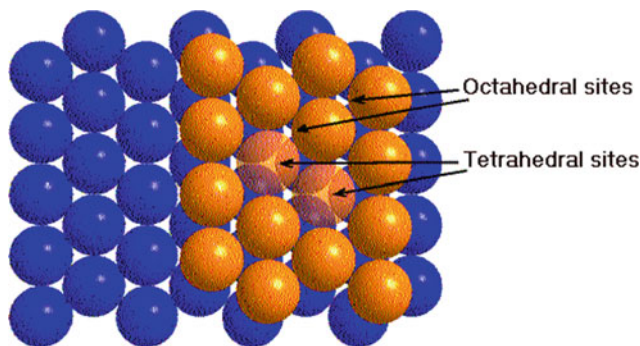


Fig. 2 The tetrahedral lattice packing

Taking into consideration that the penetration deeps, D , on the free space between the balls are estimated equal to half of the wavelength, $D \sim \lambda/2$, we can find this effective volume $V_u = A\lambda/2$. Let us demonstrate that this volume is smaller than the free volume between the balls, V_f . According to the relation between the surface of the ball and its diameter, d , we find the dependence between the total surface number of balls and their diameter, $A = \pi d^2 N$. Representing the number of the balls in the “i” direction of the box with volume, $V = L_x L_y L_z$, by $N_i = L_i/d$, $i = x, y, z$ it is easy to find that number of spheres in the box $N = N_x N_y N_z$ is proportional to the volume $N \sim V/d^3$. Now the decontamination efficient volume around the ensemble of packing balls is proportional to the penetration deeps D and inverse proportional to the diameter of the balls, $V_u \sim V\lambda/(2d)$. Only for the small diameter of the balls $d \sim \lambda$ it can achieve the free volume between the balls described by the free volume V_f . The idea to use the small balls is not so agreeable in decontamination of fluids. First of all, in this case, increases the friction and resistance of flow liquid between the balls with the decreasing of the dimensions and second it connected with multiple reflections of UVC radiation on the contact surfaces between the small balls.

Let us propose one packing procedure with the packing structures formed from the big and small balls. In this situation, of course, we must found the resonances between the gallery modes of the waves in two balls with different diameters as this is represented in Fig. 3 by spheres “1” and “2”. Not so larger estimations show us that for the ball diameters $d \gg \lambda$ practically these resonances exists for the aleatory dimensions of the spheres.

$$A_n = S_1 + S_2 + S_3 + \dots + S_n. \quad (1)$$

We fill up the free space between the elements of metamaterial with other small elements. We observe that the total surface of “i”-species of balls $S_i = 4\pi V_f/d_i$, where $V_{if} = V(1-\rho)^{(i-1)}$ is the free volume remain free volume after the introducing the spheres with the dimension d_{i-1} . Here the diameter d_i of “i” type of spheres is connected with the diameter of the first big sphere by the relation $d_i = K^{-(i-1)} d_1$, here K is ordered parameter (K may be 5, 10, 100 and so one). If we introduce the “n” type of spheres in the contaminated liquid we obtain the following expression for the total surface.

In other words, introducing in the expression (1) for the total surface of balls with diameters, d_1, d_2, \dots, d_n , we obtain the new relation for contact surface of the composite ensemble formed from “n” species of balls

$$A_n = 4\pi V/d_1 + 4\pi V(1-\rho)/d_2 + 4\pi V(1-\rho)^2/d_3 + 4\pi V(1-\rho)^3/d_3 + 4\pi V(1-\rho)^{n-1}/d_n. \quad (2)$$

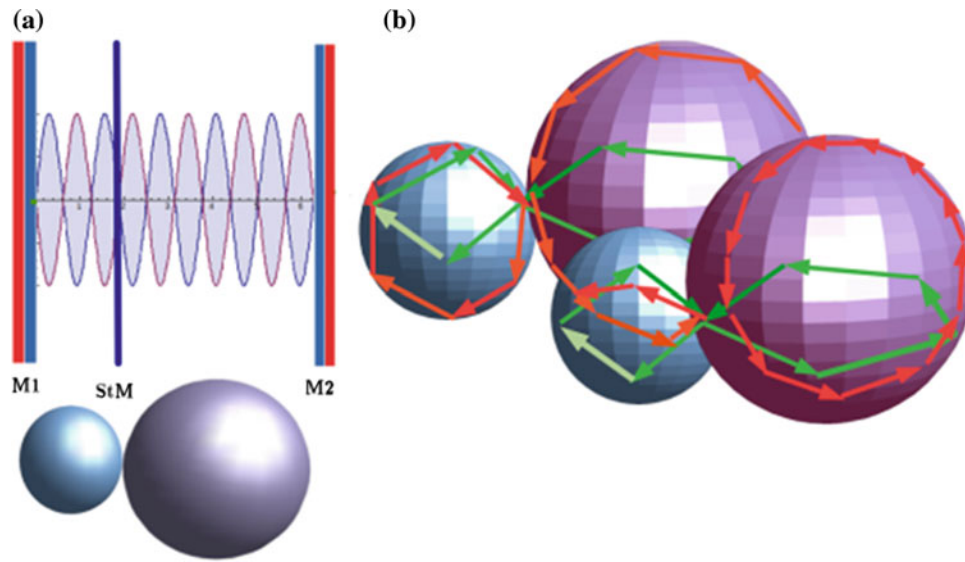


Fig. 3 The resonances between the gallery modes of the waves in two balls with different dimensions. **a** describes the possible resonances between two Fabry-Pérot interferometers connected through the semitransparent mirror, StM. Here M1 and M2 are the lateral mirrors.

b describes the similar resonances between the two spherical resonators. The green and red wave paths describe the propagation of two gallery waves

In this situation, let us take the big spheres (diameter about $d_1 \sim 2\text{--}3\text{ mm}$) and filled up space between them with the quartz microspheres with diameter 10 times smaller ($d_2 \sim 0.2\text{--}0.3\text{ mm}$) as this is represented in Fig. 4a. After that, it is possible to fill up again space between d_2 -spheres by other granules with the diameter 10 times less than d_2 ($d_3 \sim 0.02\text{--}0.03\text{ mm}$). If we 10-times increase the dimensions between the blue spheres of Fig. 4a after filling this space with violet balls the situation looks like in Fig. 4b.

We can observe that after introducing of the diameter of the spheres, $d_i = 10^{-(i+1)} d_1$, in the above expressions (1) and (2), it is obtained the geometric sum with the ration $q = 10(1 - \rho)$

$$A_n = \frac{4\pi V}{d_1} \frac{1 - q^n}{1 - q} \quad (3)$$

In the above assumptions, we observe that the last term of the expression (2) gives the main contribution

$$A_n = \frac{4\pi V}{d_1} q^{(n-1)} = \frac{4\pi V}{d_1} 10^{(n-1)} (1 - \rho)^{(n-1)}. \quad (4)$$

For ration $q \gg 1$ we obtain that the main contribution in total surface sum (3) gives the surface of smallest spheres described by the expression (4). This expression demonstrates that the total area drastically increases with decreasing of the sphere diameter, $d_n = 10^{-(n-1)} d_1$, of the last type of metamaterial introduced into the contaminated liquid in comparison with traditional one.

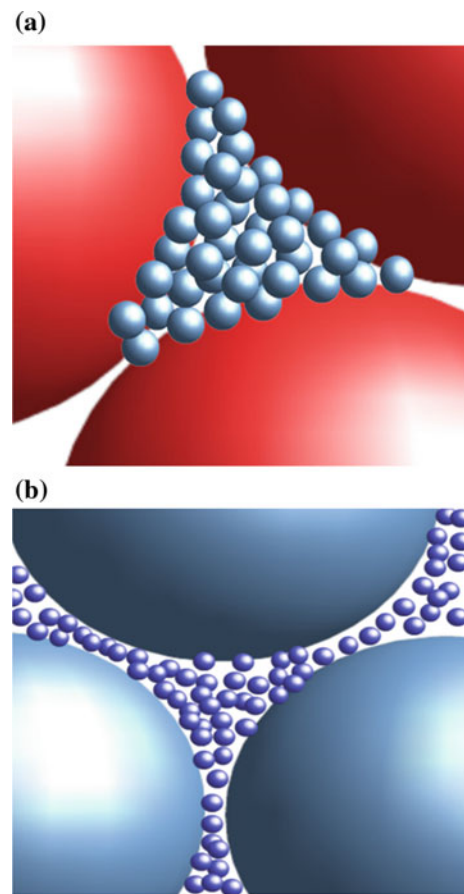


Fig. 4 **a** The space between the big spheres with diameter d_1 . **b** In the “ n ” phase of constraint of the free space between the spheres, it is proposed to continue the filling procedure with the spheres with the diameter $d_1/10$ filled up by the spheres with diameter $d_1/10$

3 Statistical Estimation of Number of Colonia Antil and After Decontamination

Two experiments were proposed to explain the concept examined above. The first experiment consists of a 2.7 cm diameter quartz tube and is filled up with 1 mm diameter quartz fiber. The decontamination volume is smaller than the free volume. It is formed by the surface of all fibers, together with the surface of the quartz tube, s , multiplied by the radiation penetration depth D , $V_u = (A + s)D$. The estimation demonstrates that for the free volume between three fibers of length 100 cm and a diameter of 0.1 cm can easily calculate. It is equal to the difference between the area of the equilateral triangle (like in Fig. 4) and the three circle segments which are at the 60-degree angle to the length of the fibers $v_f = L(\sqrt{3} - \pi/2)r^2 = 0.16 r^2 L$. The efficiency of decontamination rate of the volume situated between these fibers of big cylinder may be calculated in the two ways. The first method corresponds to the calculation of the effective volume between three fibers. This corresponds to the volume is equal to the length of the three arc portions multiplied by the radiation penetration depth, $D \sim \lambda/2$, in the liquid: $v_u = rDL$. It is not difficult to observe that ratio, $Ef = v_u/v_f \sim \lambda/r$, is quite small for wavelength $\lambda \sim 250\text{--}280$ nm and describes the contact efficiency. The second method may be used as an integral estimation. The free volume, V_f is the difference between the total volume of the big cylinder ($V = \pi R^2 L$, $R \sim 1\text{--}2$ cm, $L \sim 100$ cm) and the volume of packed fibers in it, $\pi N r^2 L$, we can find the free volume $V_f = \pi (R^2 - N r^2) L$. The contact efficiency is $Ef = V_u/V_f \sim \lambda/r$, where V_u was defined in the last section.

Experimentally observations have shown that a big part of liquid flows is well decontaminated during the time $t = 10$ min. The decontamination can be stimulated and by the attenuation effect in which the velocity of flow fungus near the surface of the fibers during the non-laminar flow. In this case, due to different velocities between the layers of liquid, the fungus suspensions with high density may

achieve the decontamination zone of the free space between the fibers. This may be another decontamination mechanism in which it is taken into consideration the attenuation and deposition of high-density fungus suspensions in the water during the acceleration. As it is shown Fig. 6 dimensions become smaller than the initial one and many of them were destroyed (about 70–80% of the fungus colonials) in comparison with the non-decontaminated liquids represented in Fig. 5.

In order to demonstrate that filling up the space between the elements of metamaterial play an important role, it is proposed another experiment. In this case, the big space between the quartz granules is filled up by small one so that the volume of radiation non-penetrated free space decreases. This reduction of the space between the elements of metamaterial demonstrates that decontamination rate increases. This is in accordance with the theoretical prediction proposed in the section before. In experimental situation represented in Fig. 6, the mixture of the granulated quartz material with large dispersion in the mean value of the granule dimension (from 0.01 to 0.5 cm) demonstrate the big decontamination rate in comparison with fiber system represented in Fig. 7.

The simple explanation of this effect consists in the fact that the size of the granules allows the radiation to be directed to the center of the tube with a diameter of about 2.3 cm.

The role of the small granules in the optical contact with the large one scattered the standing waves in the non-penetrating free space between the large granules. This cannot be decontaminated with metamaterial of other dimensions.

Thus, the volume of decontamination increases substantially as in the theory proposed above. According to the estimated data, for the same amount of liquid and the same amount of fungus, the above-mentioned composite decontaminates with a much better rate at the same time of exposure of the liquid to UV radiation.

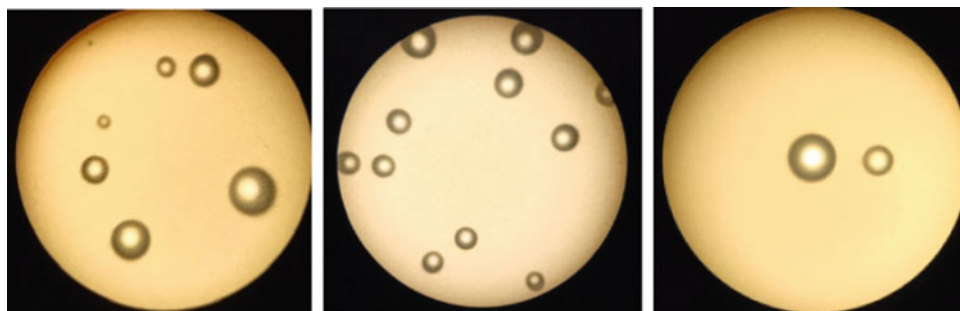


Fig. 5 The yeast fungus before going through the decontamination system. The mediation on the number of colonies observed on the 10 experiments was about 5 per figure



Fig. 6 The yeast fungus after it has gone through the decontamination system filled with quartz fibers during 10 min. The number of colonies after the mediation on 10 experiments was 1.5

Fig. 7 The yeast fungus after it has gone through the decontamination system filled with mixture of the granulated quartz



From the experiments observed there is a noticeable substantial decrease in the radius of fungus colonies and its number. In composite granulated metamaterial, it is observed the higher decontamination rate under the same exposure time and the same concentration of fungus colonies used in the fiber system.

4 Conclusions

The proposed method opens a new opportunity in the construction and development of UVC equipment for decontamination using optical resonances between granules with various dimensions. The combination of small and large elements of metamaterial opens the new possibility of establishing the optical connection between the big elements and pathogens from the fluid through the small granules of the proposed composites. The resonance penetration of radiation from one granule to another with smaller order can be used in the transmission of UV radiation to bimolecular tissue of living cells, in which the

exact channelization of radiation in the small regions of phototransformation reactions in many cases is not so well understood.

Acknowledgements This paper is supported by the projects: No. 15.817.02.07F, for young scientists No. 18.80012.50.33A and NATO EAP SFPP 984890.

Conflict of Interest The authors declare that they have no conflict of interest.

References

1. Enaki, N.A., Bazgan, S., Ciobanu, N., Turcan, M., Paslari, T., Ristoscu, C., Vaseaseasta, A., Mihailescu, I.: Improvement in ultraviolet based decontamination rate using metamaterials. *Appl. Surface Sci.* **417**, 40–47 (2017)
2. Enaki, N.A., Profir, A., Ciobanu, N., Bazgan, S., Nistreanu, A., Turcan, M., Starodub, E., Paslari, T., Ristoscu, C., Badiceanu, M., Mihailescu, I.N.: Optical metamaterials for decontamination of translucent liquids and gases. *J. Phys. D: Appl. Phys.* **51**(38), 385101-1–385101-11 (2018)

Study of a Customized Implant in Cranio-Maxillofacial Surgery

C. Miron-Borzan, H. Chezan, C. Buciuman, and E. Sabau

Abstract

Latest developments in engineering are increasingly applicable in medicine. The use of Additive Manufacturing (AM) methods in the customized surgery can improve the patients' life quality. The customized implants are created in the pre-surgical stage, on the basis of the medical data acquired by computer-assisted-tomography or nuclear magnetic resonance using three-dimensional virtual models and CAD/CAM techniques. The paper presents the required steps for manufacturing a customized cranial implant. During this study, a cranial defect was reconstructed using a personalized cranioplasty plate produced by AM methods. The surgery was successful and the patient feels well, has an improved physical aspect after implantation.

Keywords

Customized implant • Additive manufacturing • Tridimensional model • Maxillofacial surgery

1 Introduction

Through the advantages that offer, the selective laser sintering technology is a viable solution for manufacturing of customized implants using biocompatible materials as an alternative to the current situation found in the healthcare system, concerning medical devices used in various prosthesis for bone areas affected by trauma, malformations and tumors. Customized implants have the advantage of reduced surgery time, improved cosmetic results, faster postoperative recovery and lower overall costs.

A cranial bone defect can occur from trauma, infection, and tumor surgery and result in aesthetic and functional

deficiencies [1–3]. Calvarial reconstruction should provide biomechanical stability, cerebral protection, and restoration of the cranial contour [4].

Customized cranioplasty implantation has many advantages, such as a shorter operative time, its positive effects on the healing process, less invasive surgery, improved cosmetic results, faster recuperation, and lower costs owing to a shorter operative time [5, 6].

Posttraumatic skeletal defects benefit from the use of three-dimensional models in order to accurately assess their dimensions and morphology, thus facilitating the reconstruction planning.

In the scientific literature there are many studies regarding the cranioplasty and the materials that can be used for it. In surgery, a biocompatible material is a synthetic or natural material used to replace part of a living system or to function in intimate contact with living tissue. Biocompatible materials are intended to interface with biological systems to evaluate, treat, augment or replace any tissue, organ or function of the body.

According to the specialists, the ideal material used for cranioplasty would be: radiolucent, resistant to infections, not conductive of heat or cold, resistant to biomechanical processes, malleable to fit defects with complete closure, inexpensive, and ready to use [7]. There are many materials used in manufacturing of a cranial implant ranging from autogenic tissue to metallic or acrylic alloplastic. Besides natural materials such as autograft, allograft, or xenograft, varieties of artificial materials such as titanium, poly (methyl methacrylate) (PMMA), polyether ether ketone (PEEK), and hydroxyapatite (HA) have been developed [8].

The CT or RMN investigations, provides high resolution images of internal structures of the human body and based on this data, a physical model can be created, which will be very helpful in preparation of a complex surgery.

The physical model simplifies the communication between surgical team members, between the radiologist and surgeon, between doctor and patient. These models allow the measurement and simulation of the intra-operative situation.

C. Miron-Borzan (✉) · H. Chezan · C. Buciuman · E. Sabau
Technical University of Cluj-Napoca, Bdul Muncii no 103-105,
Cluj-Napoca, Romania
e-mail: cristina.borzan@tcm.utcluj.ro

Using Additive Manufacturing and an indirect method, the achieving of prosthesis is much easier by the manufacturing of an accurate physical model for an existing structure. That model can be used as a negative, or as a master model for manufacturing a customized implant from biocompatible materials (with the help of silicone rubber molds). These applications have an increased impact on traumatology, in the field of genetic malformations, in oncological pathology or reparative plastic surgery.

There are 2 ways of obtaining a customized implant: direct method (when the final biocompatible implant is directly manufactured) and indirect method (when during the additive manufacturing process is not used a biocompatible material and is required a mold in which will be casted the biocompatible material).

The paper describes the manufacturing steps for the indirect method of obtaining a customized cranial implant.

2 Experimental Part

The input data for manufacturing this customized implant were achieved from Oral and Maxillofacial Surgery Clinique, where a team of surgeons analyzed the complexity of the bone lesions. The patient had multiple fractures of the parietal bone and the natural welding of the bones could be very dangerous and also could lead to multiple defects of the

patient's physiognomy. The surgeons concluded that the optimal solution is a customized implant (Fig. 1).

In order to obtain the customized implant, the patient was investigated through Computer Tomography and 2D data as DICOM unprocessed files were obtained. Radiation beam thickness was 3.3 mm and the distance between two successive sections of the scan was 2 mm.

Some images from CT are shown in Fig. 2.

Data imported as unprocessed DICOM files were segmented, filtered and reconstructed three-dimensional, for obtaining the virtual model of the soft tissues and patient skull. With the help of MIMICS software, the tridimensional virtual model of the patient skull was obtained. Using MAGICS software, was extracted the damaged area and by comparison with the mirror image and in this way the virtual model of the cranial implant was obtained. A manual adjustment was made to fit in the damaged area (Fig. 3).

The virtual model was imported into the computer of Sinterstation 2000 Machine and using the Selective Laser Sintering technology, the physical model was manufactured from PA6 powder.

In case of Selective Laser Sintering (SLS), layers of 0.05–0.3 mm thickness are obtained by thermal binding of small particles that are agglomerated together by the action of a laser source whose wavelength depends of the powder adopted. CAD software is commonly used to decompose a 3D drawing into a sequence of thin layer whose shape is

Fig. 1 Affected area before surgery



Fig. 2 Computer-tomographic images of affected area

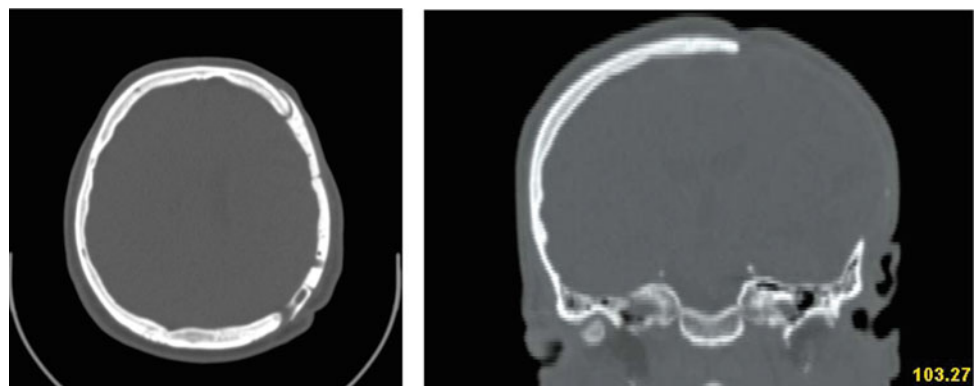


Fig. 3 Virtual three-dimensional reconstruction of the patient's skull

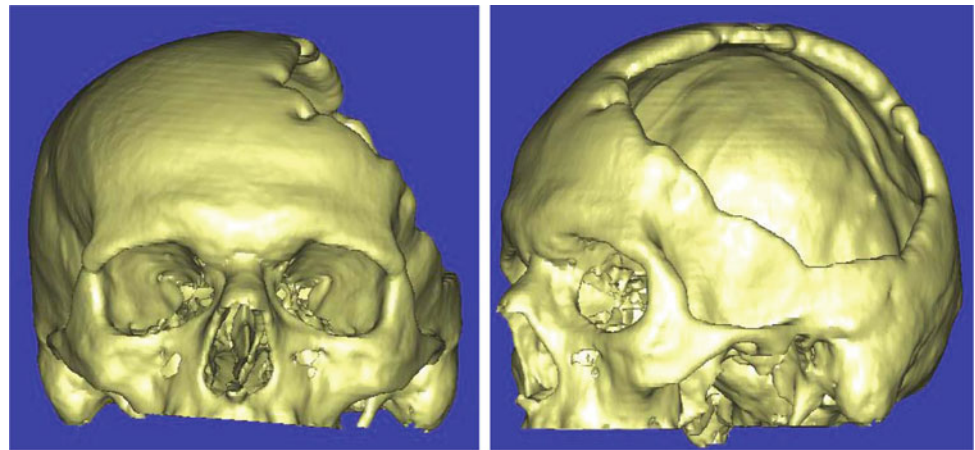
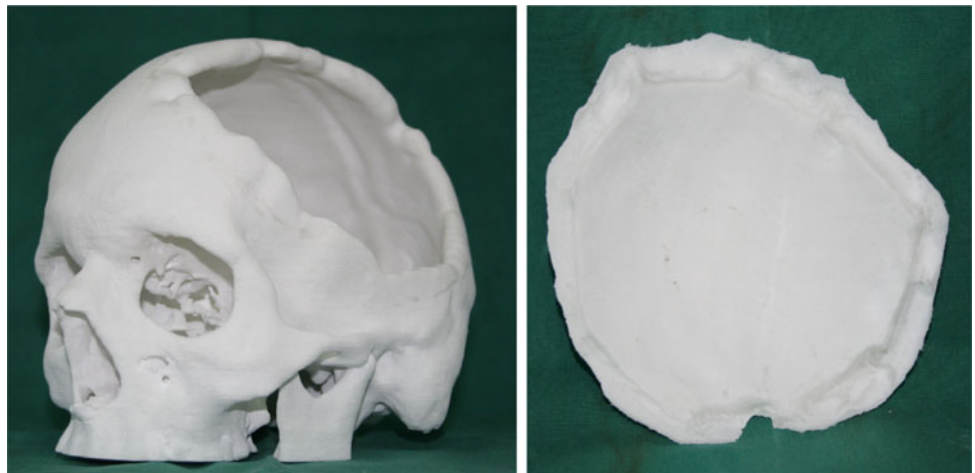


Fig. 4 PA6 physical model of the patient's skull and implant



used to set the working area of the laser beam. After a layer is sintered at a predefined focal length, new uncured powder is levelled on a platform whose vertical adjustment allows re-focusing of the laser beam [9]. After repeating this process, the physical model was obtained Fig. 4.

The working parameters for manufacturing the physical model for the cranial implant are presented in Table 1.

The polyamide, PA6 has good mechanical properties, but is not biocompatible with the human body. So, another step was required in order to obtain the final implant: manufacturing of a silicone rubber mold in which can be casted a biocompatible material.

Achieving the silicone rubber mold required in its turn, more phases. First of all, the physical model (master model) was checked, cleaned and on its surfaces was applied chemical substances to prevent sticking of the silicone. A green colored Release Agent was used. The dried process of the model took 2 h, at room temperature (Fig. 5).

In the next phase, a shaped-box, using MDF as a building material (wood with glossy surface) was manufactured, in which the master model could fit and the silicone rubber (CS) in a liquid state could be casted. For economic reasons this box was made with approximately 20–25 mm larger than the size of the model.

Table 1 Used parameters for the SLS manufacturing process

Parameters	Values
Temperature	183 [°C]
Laser power	5 [W]
The thickness of the deposited powder	0.1 [mm]

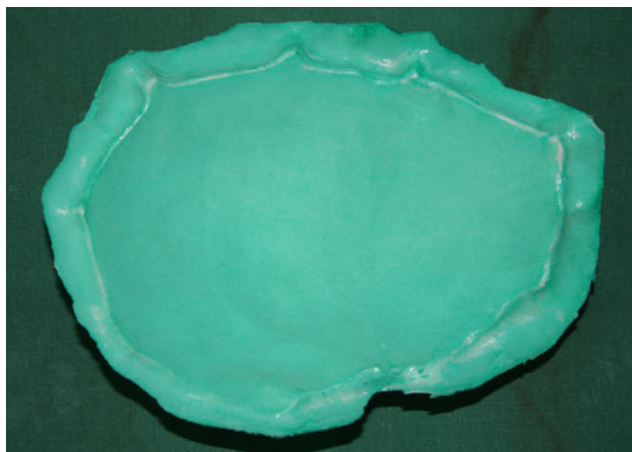


Fig. 5 The master model with release agent

The master model was suspended into the box and the silicone rubber mixture was prepared using 2 components: “ESSIL 291 RESIN” and catalyst “ESSIL 291 CATALYSEUR”—for hardening. The ratio of silicone and catalyst was 10:1.

The mixture was introduced into a vacuum chamber (MCP-001 Machine PLC) for degassing, where it stayed until most of the air bubbles gone and after, the mixture was casted in the box over the model (approximately 5 cm over the model).

The box with silicone rubber was introduced again into the vacuum chamber to remove air bubbles accumulated at casting process, around the master model. The box was introduced into a polymerization oven, for 2 h, at 50 °C temperature, for solidification of the silicone rubber block. After the silicone rubber block was removed from the box and the block was cut and the master model was extracted, remaining the silicone rubber mold with the shape of the cranial implant (Fig. 6).



Fig. 6 The silicone rubber mold



Fig. 7 Final implant forming

For the final implant, Simplex Bone Cement material, based on Poly methyl methacrylate, was used. This material is biocompatible with the human body and has mechanical properties close to the bone properties.

Bone cement was made by mixing two components: a poly methyl methacrylate-based powder, as initiator and a liquid monomer (stabilizing and inhibiting). The mixture was casted after into the silicone rubber mold (Fig. 7) and after the block was pressed in order that the material to fill all the parts of the mold.

After full polymerization (Fig. 8), the final implant was finished for fitting into the damaged area and drilled in order to obtain some holes with the role of draining the surgery area (Fig. 9).

The dimensions and the shape of the obtained implant from Bone Cement was checked, sterilized and after that,



Fig. 8 Bone cement cranial implant



Fig. 9 Final implant

Fig. 10 Patient aspect after 1 month from the surgery



was implanted into the patient's body. The surgery gone well and one month after the surgery, the aspect of the patient was improved Fig. 10.

3 Conclusions

Each human body has different anatomy. By mixing the Medical Imagistic with Additive Manufacturing techniques appeared the possibility of applications in medical field, obtaining the customization of the implants.

In this paper were presented the steps for achieving an implant for cranioplasty, following the indirect method and using a mold.

The CT data were used in order to obtain the virtual model, which was transformed into physical model using Selective Laser Sintering method. For this model, a silicone rubber mold was achieved, in which was casted Bone Cement material to obtain the final implant. The obtained part is biocompatible, respects all the characteristics of the

damaged area and after, sterilization was implanted into the patient's body. After 1 month of implantation, the physical aspect of the patient was improved and no problems or reject reactions appeared.

The paper highlighted the advantages of the customized implant by reducing the operative time, improved cosmetic results, faster postoperative recovery, and lower overall costs.

Conflict of Interest The authors declare that they have no conflict of interest.

References

1. Durand, J.L., Renier, D., Marchac, D.: The history of cranioplasty. *Ann. Chir. Plast. Esthet.* **42**, 75–83 (1997)
2. Dujovny, M., Aviles, A., Agner, C.L., et al.: Cranioplasty: cosmetic orthoerapeutic? *Surg. Neurol.* **47**, 238–241 (1997)
3. Dujovny, M., Agner, C., Aviles, A.: Syndrome of the trephined: theory and facts. *Crit. Rev. Neurosurg* **9**, 271–278 (1999)

4. Hyung, R.C., Tae, S.R., et al.: Skull reconstruction with custom made three dimensional titanium implant. *Arch. Craniofac. Surg.* **16** (1), 11–16 (2014)
5. Dean, D., Min, K.J., Bond, A.: Computer aided design of large format prefabricated cranial plates. *J. Craniofac. Surg.* **14**:819 (2203)
6. van Putten, M.C., Jr, Yamada S.: Alloplastic cranial implants made from computed tomographic scan-generated casts. *J. Prosthet. Dent.* **68**, 103 (1992)
7. Shah, A.M., Jung, H.L., et al.: Materials used in cranioplasty: a history and analysis. *Neurosurg. Focus* **36**(4), E19 (2014)
8. Yu, Q.S., Chen, L., et al.: Skull repair materials applied in cranioplasty: history and progress. *Transl. Neurosci. Clin.* **3**(1), 48–57 (2017)
9. Franco, A., Lanzetta, M., Romoli, L.: Experimental analysis of selective laser sintering of polyamide powders: an energy perspective. *J. Clean. Prod.* **18**, 1722–1730 (2010)

Hydrogels Based on Collagen and Dextran for Bioartificial Tissues

Maria Butnaru, A. M. Lucaci, B. P. Cosman, and L. Verestiuc

Abstract

Hydrogels are crosslinked polymeric networks with a large number of hydrophilic domains. They can expand in numerous solvents and aqueous environments without dissolving owing to the chemical or physical bonds formed between polymer chains. During the past decades, hydrogels have been designed using synthetic or natural polymers like proteins or polysaccharides for biomedical applications such as tissue engineering. Due to its biocompatibility and its structure, most commonly used in tissue engineering is collagen, the most abundant structural protein of the extracellular matrix, which is predominantly found in fibrous connective tissues. In the present study to obtain hydrogels alongside collagen was used also dextran, a polysaccharide derived from glucose condensation. The crosslinking was made under the influence of riboflavin, which is a water-soluble vitamin that plays an important role in the production of energy in the body. In addition, the hydrogels have been exposed to physical treatments like UV radiation and lyophilization. The hydrogels were characterized using FT-IR spectroscopy and to highlight the hydrogels porous was used microscopy in phase contrast and fluorescence microscopy. The cytocompatibility tests (MTT) indicated normal values for the cells viability in the presence of hydrogels. For detection of living cells the hydrogels a treatment with calcein AM solution was used and for detection of living cell nuclei was used the DAPI solutions.

Keywords

Tissue engineering • Collagen • Dextran • Riboflavin • Crosslinking

1 Introduction

Tissue engineering is a modern field of the regenerative medicine which integrates all the technologies using live cells or biomaterials (synthetic or natural) with the purpose of promote the quality of human life by obtaining tissues and bioartificial organs, outside the body, in vitro. Natural polymers, specifically collagens and polysaccharides, are frequently used for hydrogel preparation because of their biocompatibility and chemical structure. Hydrogels consist of a water swollen network of crosslinked polymer chains that can have a wide range of physical and biological properties depending on the composition of the polymer and the nature of the crosslinks [1, 2].

Until now, biocompatible and biodegradable hydrogels have been designed using polysaccharides and functionalized polysaccharides for biomedical applications such as tissue engineering. Due to the advantage of biocompatibility and biodegradability, the natural polymers such as collagen and dextran have been studied as the potential matrix for tissue engineering applications [3–7].

Collagen is the most abundant structural protein of the extra cellular matrix (ECM), showing good attachment/adhesion to different kinds of cells and has been studied for several biomedical applications. Is one of the most used polymers in biomaterials field, due to its excellent properties in biocompatibility, biodegradability, with well-established structure, biologic profile, and in vivo response [1, 8].

Dextran is a nontoxic, hydrophilic bacterial polysaccharide that is broadly applicable in the biomedical field owing to its biocompatibility and biodegradability. It is mainly composed of linear α -1,6-linked d-glucopyranose residues with allow percentage of α -1,2-, α -1,3- and α -1,4-linked side chains [9].

Dextran is present in the extracellular matrix (ECM) and shows superior properties of interaction with human body tissues. It is known that dextran promotes adhesion between proteins and cells. It is commonly used to decrease vascular

M. Butnaru (✉) · A. M. Lucaci · B. P. Cosman · L. Verestiuc
Faculty of Medical Bioengineering, University of Medicine and Pharmacy, 9-13, Kogalniceanu, Iasi, Romania
e-mail: maria.butnaru@umfiasi.ro; maributnaru@yahoo.com

thrombosis, reduce inflammatory response and prevent ischemia–reperfusion injury in organ transplantation in which dextran acts as a mild reactive oxygen species scavenger and reduces platelet activation in excess. Dextran has volume expansive properties and therefore its inclusion can improve blood flow [10, 11].

A new trend in the crosslinking of the hydrogels takes in consideration biological active molecules, like riboflavin, an essential water-soluble vitamin with unique biological and physicochemical properties [12, 13].

The objective of this study was to develop a new method for obtaining hydrogels based on collagen and dextran, made by crosslinking with riboflavin. The future objectives of the study are related to increasing the biocompatibility of hydrogels and the population of these materials with cells through the encapsulation process.

2 Materials and Methods

2.1 Materials

The hydrogels were obtained by using 1% collagen solution (with initial pH = 2, which was adjusted to pH = 6 by the addition of NaOH 1M) and 1% dextran solution. Initial collagen solution was kindly donated by Lohmann & Rauscher GmbH & Co. KG, Germany, and Dextran sulfate sodium salt from *Leuconostoc* spp. from Sigma-Aldrich (average Mw >500,000). The riboflavin as crosslinking agent was purchased from Sigma-Aldrich and used at a concentration of 1% in bidistilled water.

2.2 Methods

For the crosslinking reaction the following compositions of hydrogels were chosen: 100% collagen; 75% collagen-25% dextran; 50% collagen-50% dextran. The final volume of each hydrogel composition was 1500 μ l and was made in the wells of 6 well-culture plates for cell cultures. Thus, after mixing collagen and dextran in the desired ratio, a 120 μ l of riboflavin solution was added to each composition, followed by 15 min exposure to UV radiation in the aim to achieve the crosslinking. The wavelength of UV radiation was 365 nm and distance between hydrogel solution and UV source was 100 mm.

The culture plate with the three crosslinked hydrogel compositions was frozen at $-19\text{ }^{\circ}\text{C}$ overnight then dried using freeze-drying method to obtain a porous structure (Labconco Ltd freeze-dryer). Successive washes of the lyophilized hydrogels were carried out with 70% ethyl alcohol to remove traces of riboflavin. The bacterial decontamination of the hydrogels was proceed in 70%

aqueous sterile ethyl alcohol solution, followed by washing with bidistilled water and swelling for 48 h in saline phosphate buffer (HBSS).

Dried porous supports were characterized using FT-IR spectroscopy and phase contrast microscopy.

The biocompatibility of the collagen/dextran hydrogels crosslinked with riboflavin was analyzed through MTT cytotoxicity evaluation and capacity to be populated by living cells.

The MTT assay based on 3-(4,5-dimethylthiazol-2-yl)-2,5-diphenyltetrazolium bromide was performed by the direct contact technique. The MTT reagent being pale yellow in solution can be reduced through oxidative reaction of living cells to dark blue formazan. Thus, the amount of the formazan in the cell culture is directly proportional to the cell viability rate [14].

The MTT assay was performed in 12-well culture plates seeded with 3×10^4 cells/well primary fibroblasts from *Albino rabbit* dermis. One small piece of the hydrogels, about 6 mm diameter, was put on the bottom of each culture well, over which the cell suspension was added. The cells and hydrogels were incubated for 72 h then MTT reaction

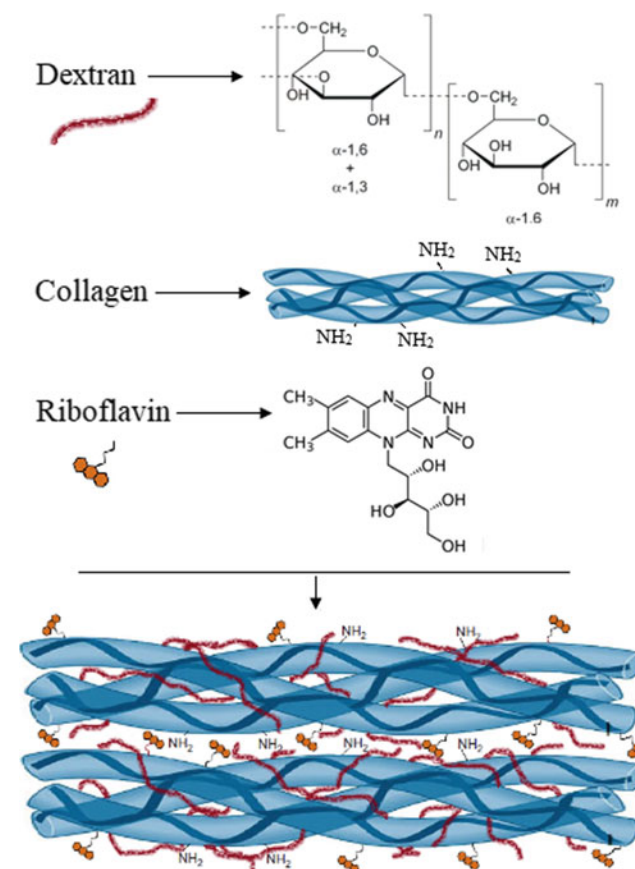
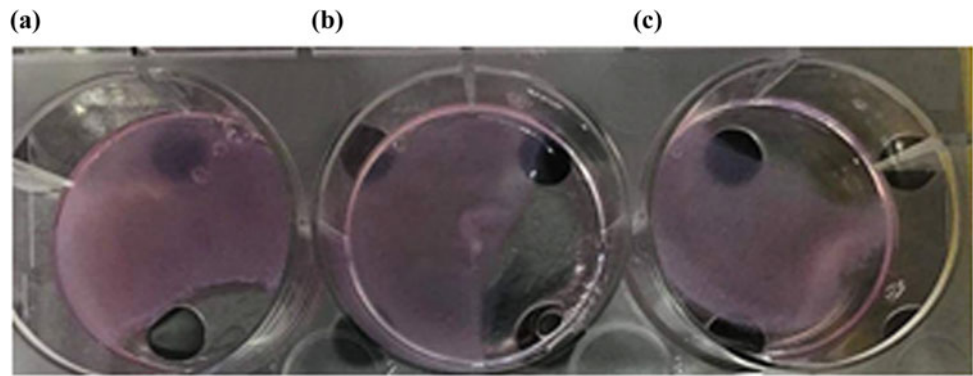


Fig. 1 Reaction scheme for obtaining hydrogels based on collagen and dextran crosslinked with riboflavin

Fig. 2 Samples from 3 compositions of hydrogels (a 100% collagen; b 75% collagen-25% dextran; c 50% collagen-50% dextran)



was performed using 1 ml of 0.25 mg/ml MTT solution. The absorbance of the formazan solution was measured using Tecan plate-reader spectrophotometer at the 570 nm wavelength. The cell viability was calculated as percent of formazan absorbance in the cell cultures incubated with the hydrogels, compared to controls (cultures without hydrogels). The experiment of each hydrogel was performed in triplicate.

The capacity of the hydrogels to be populated with living cell was performed after MTT test. The cells were seeded on the hydrogel surface as was described for MTT test. A vital staining with green fluorescence was performed to highlight the cells on the materials. Therefore, a Calcein AM solution (Sigma-Aldrich) in a concentration of 2 μ l/ml of HBBS (without phenol red) was used. The staining was carried out in the dark condition, for 30 min.

The living cells were observed and analyzed after 72 h, using Leica DMIL optical microscope in fluorescence mode, at excitation/extinction wavelength of 455/530 nm. The presence of the cell in the hydrogel structure was analyzed as well by DAPI staining of the cell nuclei, using broadly used method. The blue fluorescent cell nuclei were analyzed using

Leica DMIL optical microscope in fluorescence mode, at excitation/extinction wavelength of 358/461 nm.

3 Results and Discussions

Hydrogels based on collagen and dextran were obtained by crosslinking with riboflavin (Figs. 1 and 2).

The FT = IR result as for crosslinked hydrogels are presented in Fig. 3.

Collagen-specific absorption bands occur at the following wavelengths: valency vibrations of $-\text{OH}$ —3317 cm^{-1} , valence vibrations of $-\text{C}-\text{H}$ from $-\text{CH}_2-$ 2982 cm^{-1} ; Amide I—1643 cm^{-1} ; Amide II 1551 cm^{-1} ; Amide III—1234 cm^{-1} ; Amide IV—795 cm^{-1} . The collagen stretch bands overlap with OH bands of dextran. As the dextran concentration increases, the amide band intensity decreases.

The microscopic analysis of the porous structure of hydrogels is showed in images A, B and C from Fig. 4.

The images from the Fig. 4 show the evenly distributed porous structure with large and interconnected pores. Each pore exceeds the size of 100 μm . This structure reveals an

Fig. 3 Structural analysis FT-IR of hydrogels (1—100% collagen; 2—75% collagen-25% dextran; 3—50% collagen-50% dextran)

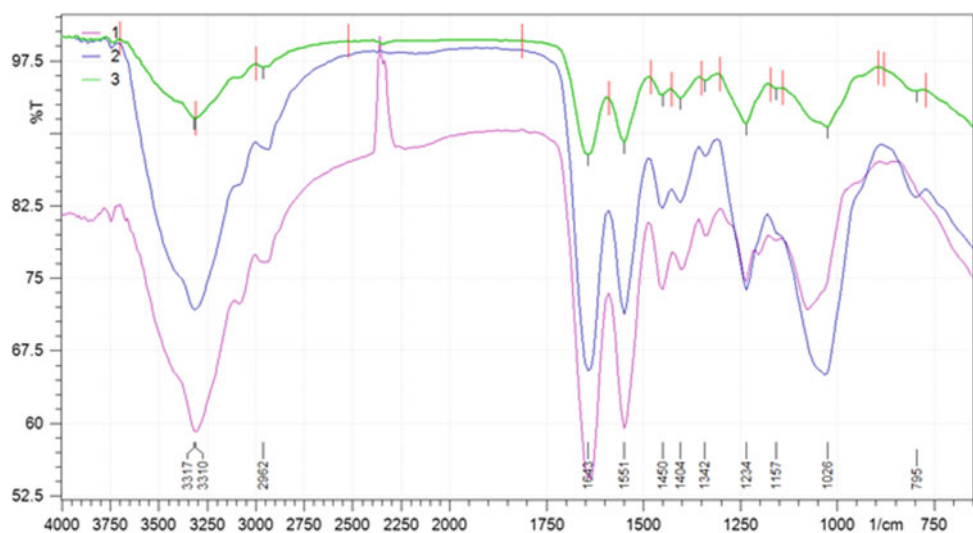


Fig. 4 Microscopic images of hydrogels (a 100% collagen; b 75% collagen-25% dextran; c 50% collagen-50% dextran)

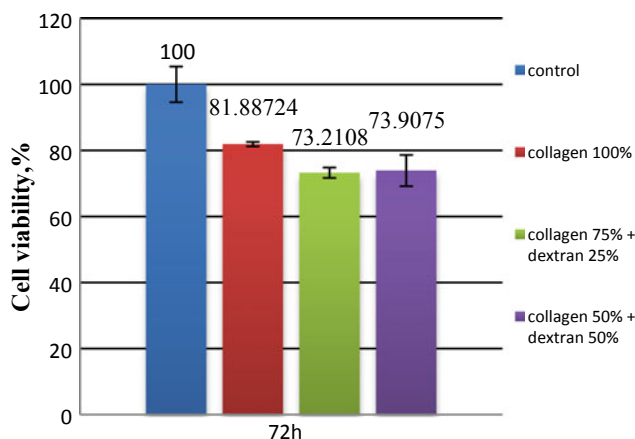
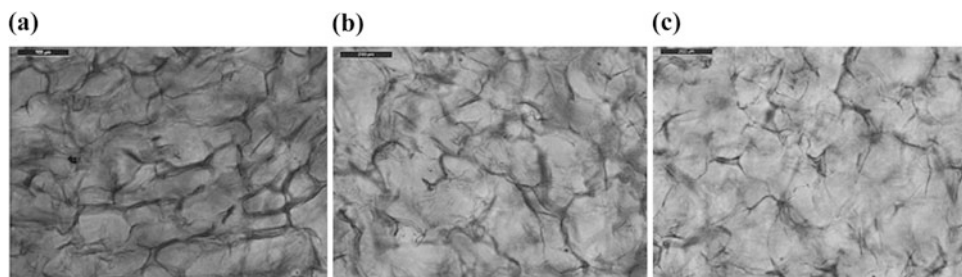
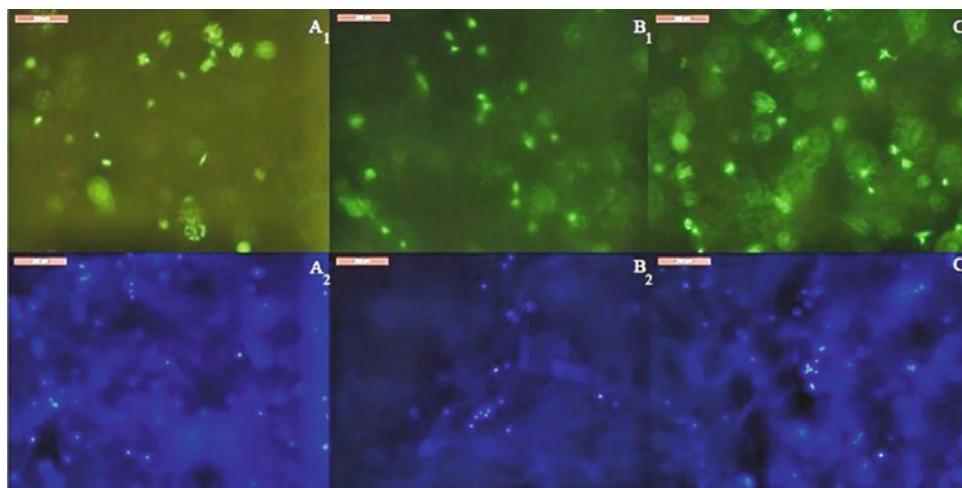


Fig. 5 Cells viability test results at 72 h

architecture with a potentially capacity to be populated with cells.

The MTT assay, which was performed as direct contact with cells, proved an acceptable cytocompatibility of the hydrogels. Cells viability after 72 h of contact with materials was 81–82% for collagen 100%; 73% for 75% collagen-25% dextran; and 73–74% for 50% collagen-50% dextran. It can be concluded that the collagen component increase the cytocompatibility of the hydrogels (Fig. 5).

Fig. 6 Optical fluorescence microscopic images for hydrogels with the following compositions: a 100% collagen, b 75% collagen-25% dextran; c 50% collagen-50% dextran



The differences were observed between control and analyzed hydrogels that could be explained by the technical errors which are often occurs in the direct contact MTT tests. This supposition is based on the capacity of the hydrogels to be populated with cells, which was proved through Calcein AM and DAPI staining and shown in the Fig. 6.

Thus, A₁, B₁, and C₁ represent the microscopic analysis of the hydrogels treated with calcein AM solution for the detection of living cells, and the images A₂, B₂, C₂ represent the microscopic analysis of the hydrogels stained with the DAPI solution for the detection of cell nuclei. From the images it can be seen that cells are present in the hydrogel pores. The cells are evenly distributed in the each type of hydrogel. The nuclei with a normal shape and no fragmentation were found by DAPI staining.

4 Conclusions

The preliminary study showed that hydrogels based on collagen and dextran crosslinked with riboflavin have potential for tissue engineering applications. These hydrogels are translucent in biological media, are non-cytotoxic and allow cell adhesion inside of their porous structure. The future objectives of the study are related to reveals the potential benefits of the presence of the dextran in the

hydrogel structure for a longer cell growth inside the material and possibility to use the reticulation technique for cells encapsulation.

The initiative of this project was to improve the materials used in surgery through the availability of financially accessible and highly efficient products.

Tissue engineering and, implicitly, regenerative medicine provide through the bioartificial tissues a new chance for patients who have suffered various traumas. The possibilities offered by these hydrogels are many, besides being used to replace a certain affected portion of an organ, these materials can also be used as dressings to heal burns or wounds difficult to heal, diagnostic devices, contact lenses and patches applicable to the skin for controlled drug delivery.

Conflict of Interest The authors declare that they have no conflict of interest.

References

1. Geckil, H., Xu, F., Zhang, X., Moon, S., Demirci, U.: Engineering hydrogels as extracellular matrix mimics. *Nanomedicine* **5**, 469–484 (2010)
2. Ferreira, L.S., Gerecht, S., et al.: Bioactive hydrogel scaffolds for controllable vascular differentiation of human embryonic stem cells. *Biomater* **28**(17), 2706–2717 (2007)
3. Punnida, N., Akimasa, M., et al.: Controlling the degradation of an oxidized dextran-based hydrogel independent of the mechanical properties. *Carbohydr. Polym.* **2014**, 131–141 (2018)
4. Chen, Y.M., Sun, L., et al.: Self-healing and photoluminescent carboxymethyl cellulose-based hydrogels. *Eur. Polym. J.* **94**, 501–510 (2017)
5. Geng, X., Mo, X., Fan, L., Yin, A., Fang, J.: Hierarchically designed injectable hydrogel from oxidized dextran, amino gelatin and 4-arm poly(ethylene glycol)-acrylate for tissue engineering application. *J. Mater. Chem.* **22**, 25130–25139 (2012)
6. Lisman, A., Butruk, B., Wasiak, I., Ciach, T.: Dextran/Albumin hydrogel sealant for Dacron(R) vascular prosthesis. *J. Biomater. Appl.* **28**, 1386–1396 (2014)
7. Zhang, X., Yang, Y., Yao, J., Shao, Z., Chen, X.: Strong collagen hydrogels by oxidized dextran modification. *ACS Sustain. Chem. Eng.* **2**(5), 1318–1324 (2014)
8. Caliari, S.R., Burdick, J.A.: A practical guide to hydrogels for cell culture. *Nat. Meth.* **13**, 405–414 (2016)
9. Bachelder, E.M., Beaudette, T.T., Broaders, K.E.: Acetal-derivatized dextran: an acid-responsive biodegradable material for therapeutic applications. *J. Am. Chem. Soc.* **13**, 10494–10495 (2008)
10. Robless, P., Okonko, D., et al.: Dextran reduces in vitro platelet aggregation in peripheral arterial disease. *Platelets* **15**(4), 215–222 (2004)
11. Dubniks M, Persson J, Grande PO (2019) Comparison of the plasma volume expanding effects of 6% dextran 70, 5%albumin, and 6% HES 130/0.4 after hemorrhage in the guinea pig. *J. Trauma* **67**(6), 1200–1204
12. Tirella, A., Ahluwalia, A.: Riboflavin and collagen: new crosslinking methods to tailor the stiffness of hydrogels. *Seria Științele Vietii* **26**(2), 243–249 (2016)
13. Beztsinna, N., Sole, M., Taib, N., Bestel, I.: Bioengineered riboflavin in nanotechnology. *Biomaterials* **80**, 121–133 (2016)
14. Malich, G., Markovic, B., Winder, C.: The sensitivity and specificity of the MTS tetrazolium assay for detecting the in vitro cytotoxicity of 20 chemicals using human cell lines. *Toxicology* **124**, 179–192 (1997)

Part V

Biomimetics and Sensors

Microelectronic Pyroelectric Measuring Transducers

Andriy O. Semenov, S. V. Baraban, O. V. Osadchuk, O. O. Semenova, K. O. Koval, and A. Yu. Savytskyi

Abstract

The basic pyroelectric structures and circuits of measuring transducers on their basis are given. The prospect of the use of thin pyroelectric films for the development and design of microelectronic pyroelectric measuring transducers based on transistor structures with negative differential resistance is shown.

Keywords

Measuring transducer • Transistor structure • Negative differential resistance • Frequency • Pyroelectric capacitor • Active inductive element

1 Introduction

The use of advances in modern technology has led to significant success in the creation of various control and control devices [1]. However, the reception of high metrological characteristics of the equipment is often achieved by increasing its complexity, size, mass and value. To further substantially improve the quality of controls it is necessary to use new physical phenomena, search for new principles for implementing devices characterized by multifunctionality, low power consumption, stability characteristics, high sensitivity, high performance and reliability [2].

A. O. Semenov (✉) · S. V. Baraban · O. V. Osadchuk · O. O. Semenova · K. O. Koval · A. Yu. Savytskyi
Faculty for Infocommunications, Radioelectronics and Nanosystems, Vinnytsia National Technical University, 95 Khmelnytske Shose, Vinnytsia, Ukraine
e-mail: semenov.a.o@vntu.edu.ua

2 Analysis of Microelectronic Pyroelectric Measuring Transducers

From the analysis of the article [1] follows that the perspective direction in the development of frequency measuring transducers is the creation of integral active structures with the use of thin films of pyroelectric materials. From the invention [3] we use a thermosensitive capacitor, that performs its functional purpose in the scheme [4]. We propose to turn this capacitor into a MOS-BJT structure for the construction of the frequency measuring transducer (Fig. 1) [5].

Frequency measuring transducer (Fig. 1) works as follows. The power of incident radiation changes the capacitive component of complete resistance at the electrodes drain—collector the field transistor VT_1 and the bipolar transistor VT_2 , that causes a change in the resonant frequency of the oscillatory circuit, which is reflected at the output frequency of the signal device.

As a result of the simulation, the graph of the frequency dependence of the measurement transducer on the change in capacitance of the pyrocapacitor is shown on Fig. 2.

Now it is necessary to find the dependence of the frequency of generation of the Microelectronic measuring transducer on temperature changes. This dependence was found and the result is presented on Fig. 3. As can be seen from Fig. 3, the graph is clearly followed by a peak—this is the Curie temperature for pyroelectric material of the investigated structure.

We perform the combination of the graphs of Figs. 2 and 3 according to the capacitance values. Thus, we obtain the transformation function of the microelectronic measuring transducer based on a pyroelectric capacitor. On Fig. 4 it is shown the transformation function the temperature region to the Curie point, and on Fig. 5 it is shown the transformation function in the temperature range after the Curie point of a pyroelectric capacitor.

From the transformation function of the microelectronic measuring transducer based on a pyroelectric capacitor

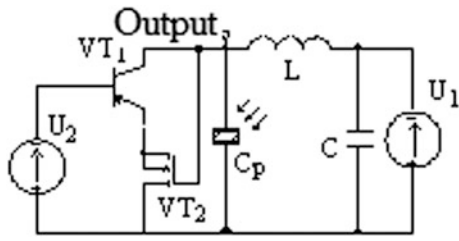


Fig. 1 Microelectronic measuring transducer based on a pyroelectric capacitor [5]

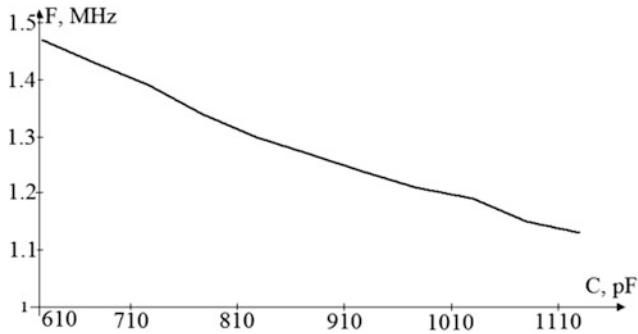


Fig. 2 The dependence of the generation frequency of the measuring transducer on the capacitance of the pyroelectric capacitor

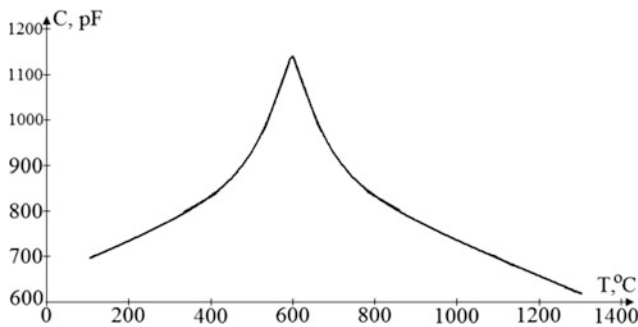


Fig. 3 The dependence of the capacity of the pyro-capacitor on temperature

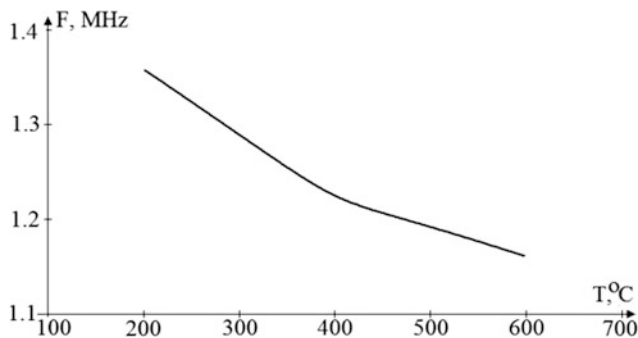


Fig. 4 The transformation function of measuring transducer based on a pyroelectric capacitor in the temperature range below the Curie point

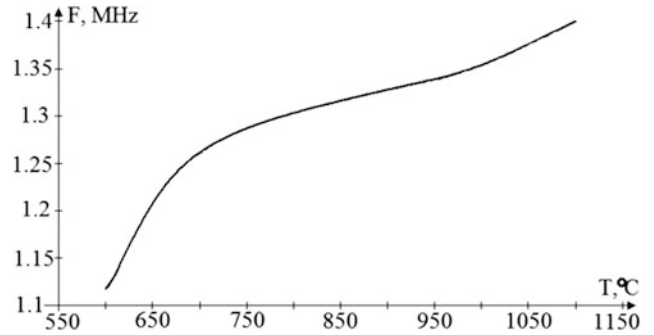


Fig. 5 The transformation function of the microelectronic measuring transducer in the region of high temperatures

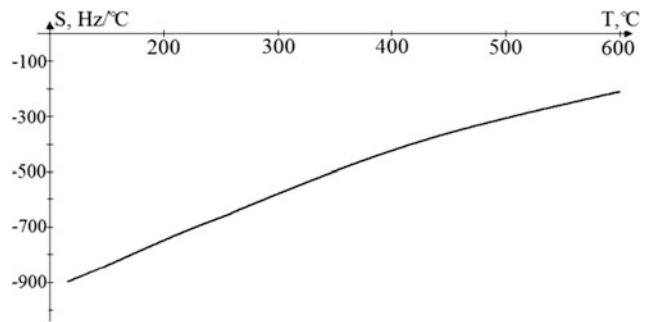


Fig. 6 The sensitivity function of the microelectronic measuring transducer based on a pyroelectric capacitor

(Fig. 5) by differentiating the temperature we find the sensitivity function of the developed scheme of the device. On Fig. 6 it is shown the graph of the dependence of the sensitivity function of the measuring transducer on temperature.

As can be seen from the graph on Fig. 6 when the temperature varies from 100 to 600 °C, the sensitivity of the microelectronic measuring transducer based on a pyroelectric capacitor varies from 200 to 900 Hz/°C. To increase the measurement sensitivity of this circuit (Fig. 1), it is proposed to use the inductive nature of the complete resistance of a bipolar transistor with an RC-scheme, that can be easily performed as an integral circuit [6]. Consequently, the scheme of the such measurement transducer with the active inductive element is shown on Fig. 7.

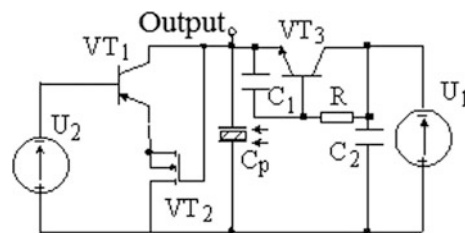


Fig. 7 Microelectronic measuring transducer with active inductive element

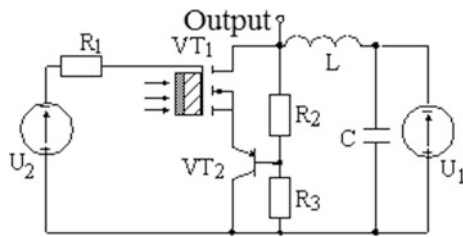


Fig. 8 Microelectronic measuring transducer based on a pyroelectric transistor

Other schemes of measuring transducers are possible, if we use the structure of a metal-pyroelectric-semiconductor [7]. About the possibility of constructing and using as heat sensors pyroelectric field-effect transistors was known in the 60-years of the last century [7]. However, their practical implementation with the entry into production became possible only in the 90-years of the last century with the development of relevant technologies [8]. In our scheme of a transistor generator we use a field-effect pyroelectric transistor [7], the technology of which, description of work and characteristics can be found in [8]. Then the measuring circuit of the frequency device will look like on Fig. 8.

The power of the optical radiation acting on the pyrotechnic VT_1 will change the voltage value existing on the field-effect transistor gate VT_1 gate-source electrodes and change the value of the capacitance of the oscillatory circuit formed by the sequential inclusion of a complete resistance with a capacitive character on the drain-collector electrodes of the field-effect pyroelectric transistor VT_1 and the bipolar transistor VT_2 and the inductive resistance of the passive inductance L , that will change the resonance frequency of the oscillatory circuit. The transformation function of the microelectronic measuring transducer based on a pyroelectric transistor is shown on Fig. 9.

As can be seen from the graph on Fig. 9 change in frequency of generation of the microelectronic measuring

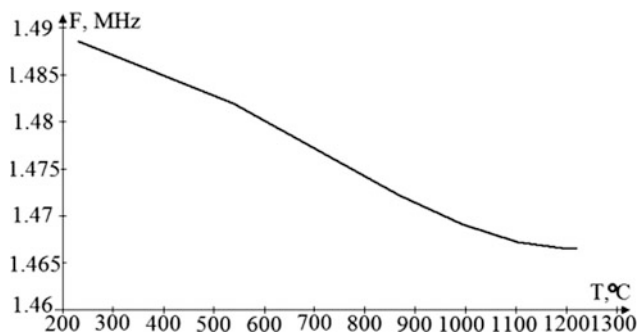


Fig. 9 The transformation function of the microelectronic measuring transducer based on a pyroelectric transistor

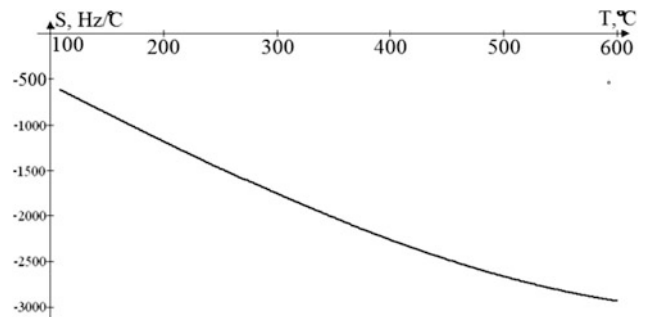


Fig. 10 The sensitivity function of the microelectronic measuring transducer based on a pyroelectric transistor

transducer based on a pyroelectric transistor on the temperature is 250 kHz on 1000 °C at the nonlinear transformation function of the device.

From the transformation function of the microelectronic measuring transducer based on a pyroelectric transistor (Fig. 8) by differentiating the temperature we find the sensitivity function of the developed scheme of the device. On Fig. 10 it is shown the graph of the dependence of the sensitivity function of the measuring transducer on temperature.

As can be seen from the graph on Fig. 10 when the temperature varies from 100 to 600 °C, the sensitivity of the microelectronic measuring transducer based on a pyroelectric transistor varies from 500 to 3000 Hz/°C.

Since the data structures of the measuring transducers are fully compatible with modern integral technology [8], it is possible to obtain the structure of the metal-pyroelectric-semiconductor structure and in the Bipolar-MOS structures (Fig. 11) [9]. By evaporation of the source materials in a vacuum ($P = 10^{-6}$ Pa) over the channel of the field-effect transistor and the base of the bipolar transistor, a thin layer of the pyroelectric film precipitates and crystallizes. After the technological process of metallization, a layer of metal is formed over the film, which acts as a squirt of radiation, the thermal effect of which will affect the formation of the pyroelectric effect in the film. Instead of a metal layer, an optically transparent semiconductor, for example polysilicon, can be used. In addition, transistors such as polysilicon-ferroelectric-semiconductor already exist [10] and are widely used in microelectronics [9]. On Fig. 11 is a device for measuring the temperature on the basis of the Bipolar-MOS transistor pyroelectric structure. The transistor structure with negative differential resistance in this device acts as a sensitive element, that allows to increase the accuracy and sensitivity of power of the optical radiation measurement compared with a device containing a pyroelectric transistor as a sensitive element [9].

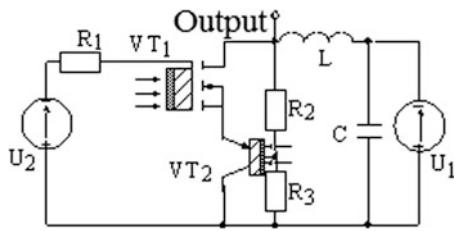


Fig. 11 Microelectronic measuring transducer based on pyroelectric bipolar-MOS transistor structure

On Fig. 12 is a schematic diagram of a measuring transducer with a pyroelectric Bipolar-MOS transistor structure and a pyroelectric capacitor. The parallel connection to the pyroelectric transistor structure (Fig. 12) of the pyroelectric capacitor makes it possible to increase the sensitivity and accuracy of the power of the optical radiation measurement, since the capacitance of the oscillatory circuit formed by the sequential inclusion of a complete resistance with a capacitive character on the electrodes of the drain-collector of the field-effect transistor VT_1 and the bipolar transistor VT_2 and the inductive resistance of the passive inductance L , will change from the effect of the power of the optical radiation.

To increase the measurement sensitivity of these circuits (Figs. 8 and 11), it is proposed to use the inductive nature of the complete resistance of a bipolar transistor with an RC-scheme, that is easily performed as an integral circuit [6]. Consequently, the circuits of the measuring transducers with active inductive elements are shown on Fig. 13. The oscillating circuit in the circuits of such transducers is formed by a parallel connection of complete resistance with a capacitive character on the drain-collector electrodes of the field-effect transistor VT_1 and the bipolar transistor VT_2 and a complete resistance with an inductive character on the electrodes of the emitter-collector of the bipolar transistor VT_3 .

It is possible to increase the accuracy and sensitivity of measuring the power of the optical radiation of the developed measuring transducers by using the pyroelectric

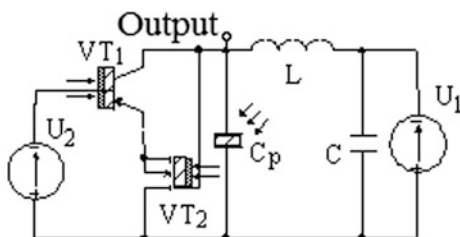


Fig. 12 Microelectronic measuring transducer based on pyroelectric bipolar-MOS transistor structure and capacitor

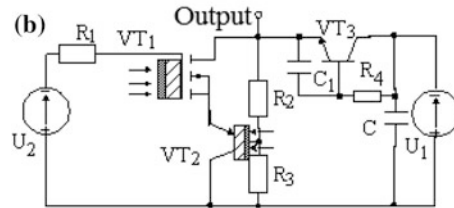
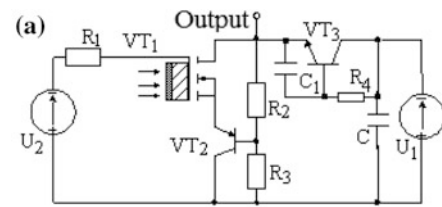


Fig. 13 Microelectronic measuring transducers with active inductive element: **a** based on a pyroelectric transistor, **b** based on a pyroelectric transistors structure

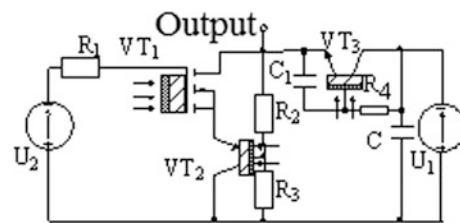


Fig. 14 Microelectronic measuring transducer with active inductive element

transistor as an active inductive element [11]. On Fig. 14 it is shown the scheme of the measuring transducer.

3 Conclusions

An overview of modern microelectronic pyroelectric measuring transducers was conducted, it was established that it is promising to use thin pyroelectric films and bipolar, field and bipolar-field transistor structures with a negative differential resistance to measure the power of optical radiation.

On the basis of the obtained results, it is planned in the future to develop mathematical models of microelectronic pyroelectric transistor structures with negative differential resistance, which will allow to detect the change of active and reactive components of complete resistance from the power of optical radiation, and also allow to investigate its influence on active and reactive components of complete resistance.

Conflict of Interest The authors declare that they have no conflict of interest.

References

1. Ponomarev, S.V., Mishchenko, S.V., Divin, A.G.: Teoreticheskie i prakticheskie aspekty teplofizicheskikh izmereniy (Theoretical and practical aspects of thermophysical measurements). Publishing House Tamb. State Tech. University, Tambov, Russia (2006)
2. Osadchuk, A.V., Semenov, A.A., Baraban, S.V., et al.: Noncontact infrared thermometer based on a self-oscillating lambda type system for measuring human body's temperature. In: 2013 23rd International Crimean Conference "Microwave & Telecommunication Technology", pp 1069–1070. Sevastopol, Ukraine, 8–14 Sept 2013
3. Mantese, J.V.: Pyroelectric Sensor. US patent 0108385, G01J5/00, 17 March 2007
4. Miller, R.C., Wu, S.Y.: Pyroelectric-field effect electromagnetic radiation detector. US patent 4024560, H01L29/78, 17 March 1977
5. Osadchuk, V.S., et al.: Mikroelektronnyi peretvoriuvach temperatury na osnovi piroelektrychnoho kondensatora (Microelectronic temperature transducer based on a pyroelectric capacitor). Visnyk of Vinnytsia Politechnical Institute **2**, 103–108 (2010)
6. Osadchuk, V.S.: Induktivnyy effekt v poluprovodnikoviyh priborah (Inductive effect in semiconductor devices). High school, Kyiv (1987)
7. Munich, W.H.: Field Effect Transistor with a Ferroelectric Control Gate Layer. US patent for invention No 3426255, H01L11/14, stated 01 Jul 1965, published 29 Jun 1966
8. Araujo, C.P.: Science and technology of integrated ferroelectrics. In: Selected Papers from Eleven Years of the Proceedings of the International Symposium on Integrated Ferroelectrics. Gordon and Breach Science Publishers (2000)
9. Osadchuk, V.S., et al.: Rozrobka radiovymiriuvalnykh mikroelektronnykh peretvoriuvachiv temperatury na osnovi struktury metal-sehnetoelektryk-napivprovodnyk (Development of radio-measuring microelectronic temperature transducers based on metal-ferroelectric-semiconductor structure). Visnyk of Vinnytsia Politechnical Institute **3**, 94–97 (2008)
10. Grimes, C.A., et al.: Encyclopedia of Sensors, vol. 10. American Scientific Publishers (2006)
11. Semenov, A.O., et al.: Statistical express control of the peak values of the differential-thermal analysis of solid materials. Solid State Phenom. **291**, 28–41 (2019). <https://doi.org/10.4028/www.scientific.net/ssp.291.28>

Ionizing Radiation Dose Sensor Based on *n*-channel MOSFET

B. I. Podlepetsky, V. S. Pershenkov, V. V. Belyakov, A. S. Bakerenkov, V. Felitsyn, and A. S. Rodin

Abstract

We investigated the radiation sensitivity of dose-metrical sensors based on *n*-channel MOSFETs taking into account the effects of temperature and electrical modes. There were measured the output voltages V being equal to the gate voltage V_G of MOSFET-based dosimeter as function of the radiation doses at const values of the drain current I_D and the drain—source voltage V_D (conversion functions), as well as the $(I_D - V_G)$ characteristics before, during and after irradiations at different temperatures. It was shown how the conversion functions and the radiation sensitivities are depending on the temperature and electrical modes. It is found that the conversion functions $V(D)$ have two characteristic regions for low and high doses (with negative and with positive radiation sensitivities). To interpret experimental data there were proposed the models of conversion function and its components taking into account the separate contributions of charges in the dielectric and in SiO₂–Si interface.

Keywords

Ionizing dose sensors • MOSFET • Temperature • Electrical modes • Radiation sensitivity

1 Introduction

The need for instruments to measure radiation parameters is constantly growing. This is primarily due to developments of nuclear physics and energy. In addition, radiation measurement tools have been used in biology, medicine, space exploration, archaeology, geology and human radiation

safety systems. To create small-size dosimeters there are presented very promising MOSFETs, which except the small size have a good compatibility with integrated circuits elements. Such transistors are widely used in medicine (radiology, radio diagnostics and radiation therapy) and space exploration (in radiation monitoring systems on board space objects). In this case, discrete or integrated sensors based on both *p*-channel and *n*-channel MOSFETs can be used in dosimeters. The characteristics of some dosimeters based on MOSFETs were presented in works [1–16]. We have previously researched *n*-channel MOSFET as the dose-metric sensor at room temperature [17]. However, radiation changes of effective charges $\Delta Q_i(D)$ and $\Delta Q_s(D)$ at different temperatures T and electrical modes remain unexplored issues.

The motivations of this work are to investigate of the influence temperatures in ranges from -50 °C to 125 °C on the total ionizing dose (TID) effects in *n*-channel MOSFETs at different electrical modes, and to propose models taking into account the separate contributions of Q_i and Q_s to radiation sensitivity.

2 Experimental

2.1 The Structure of Sensors and Circuitries

MOSFETs with *n*-channel and Al-SiO₂-Si structure were fabricated by means of conventional *n*-MOS-technology. The chip photo and the structure fragment of MOSFE with its designations are demonstrated in Fig. 1.

The circuit of MOSFET-dosimeter demonstrated in Fig. 2. In this circuitry the voltage V is equal to the gate voltage V_G . The simplified structure of the measuring system is shown in Fig. 2b. The temperatures $T \pm 2$ °C were supported by thermoelectrical module (Peltier element), using the temperature control circuitry with reference temperature sensor as thermo-resistor 703-103-BB-A00.

B. I. Podlepetsky (✉) · V. S. Pershenkov · V. V. Belyakov · A. S. Bakerenkov · V. Felitsyn · A. S. Rodin
Micro- and Nanoelectronics Department, National Research Nuclear University MPEPhI (Moscow Engineering Physics Institute), Street: 31, Kashirskoe shosse, Moscow, Russia
e-mail: bipod45@gmail.com

Fig. 1 a MOSFET's chip photo (1—source pad; 2—gate pad; 3—drain pad); b The structure fragment of MOSFET with designations of its parameters

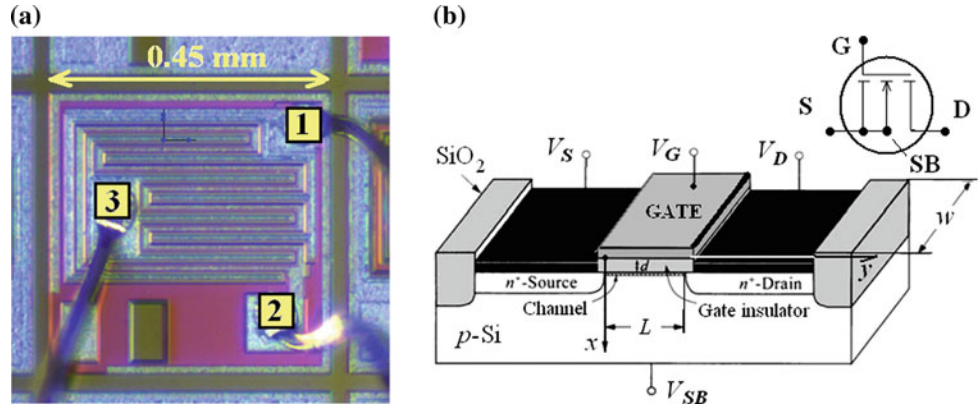
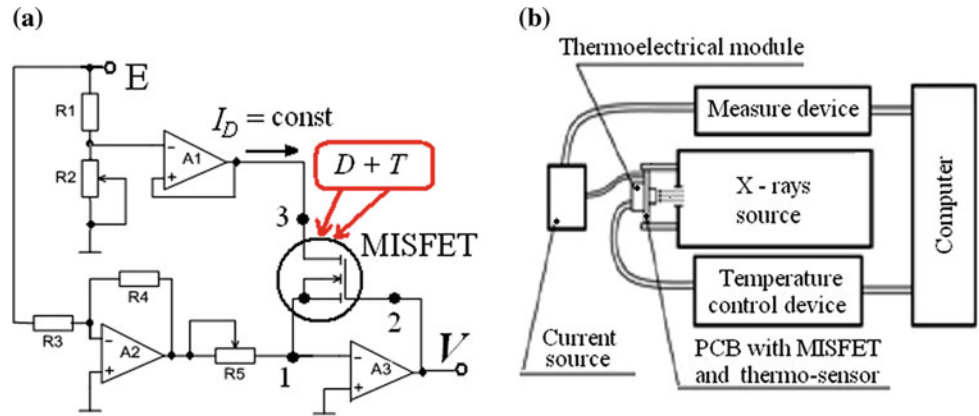


Fig. 2 The experimental schemes: a The circuit of MOSFET based dosimeter (1—source; 2—gate; 3—drain); b The structure of measuring system



2.2 The Experimental Results

Experimental conversion functions $V(D)$ of four different sensors at various drain currents I_D and room temperature T are presented in Fig. 3. Average experimental conversion functions $V(D)$ at constant currents I_D and different temperatures T are presented in Fig. 4. The example of $(I_D - V_G)$ characteristics (CVC) before and after irradiations is

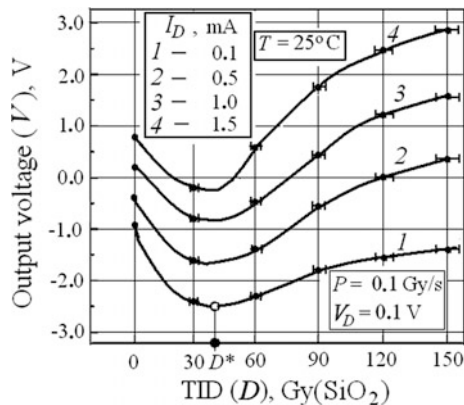


Fig. 3 Conversion functions $V(D)$ at different currents I_D and $T = 25^\circ\text{C}$. D^* is dose of local extremum

illustrated in Fig. 5. It is found that the conversion functions $V(D, T, I_D)$ of n -channel MOSFETs have two characteristic regions for low and high doses (with negative and with positive radiation sensitivities S_D being equal to dV/dD).

3 The Interpretation and Processing of Experimental Data

3.1 Modeling of Radiation-Temperature-Electrical Effects

To interpret the experimental results there were proposed the models of conversion function and CVC. The conversion function $V(D, T)$ of the any TID sensors is generally represented as

$$V(D, T) = V_0(T) + \Delta V(D, T) \tag{1}$$

where the initial value V_0 of the output voltage V (at $D = 0$), and the voltage change $\Delta V(D)$ determines the sensor sensitivity to ΔD . There are differential S_D and integral S radiation dose sensitivities:

$$S_D = dV/dD \text{ and } S = \Delta V/\Delta D \tag{2}$$

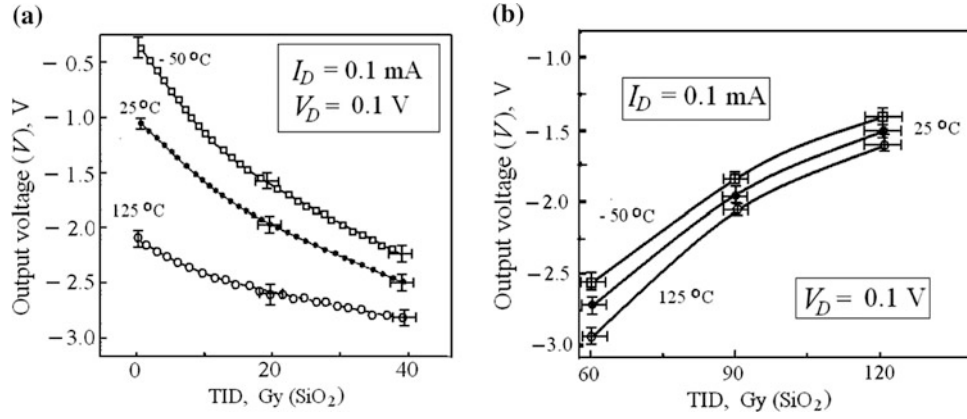


Fig. 4 Conversion functions at different temperatures T : **a** for low and **b** for high total ionizing doses D

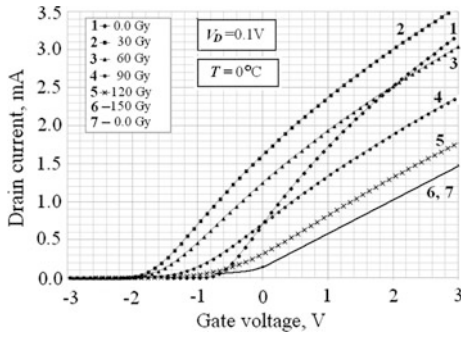


Fig. 5 The $I_D - V_G$ characteristics of the same sensor for different TID at constant temperature 0°C

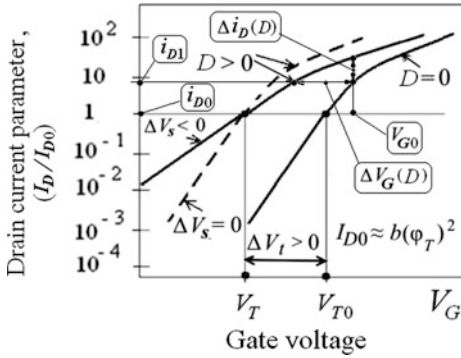


Fig. 6 Typical deformations of CVC under the action of ionizing radiation taking into account the contributions $\Delta V_i(D)$ and $\Delta V_s(D)$. The values Δi_D and ΔV_G are shifts of the operating points

To interpret results the following 3-components' model of the voltage $V(D, T, I_D)$ was used:

$$V(D, T, I_D) = V_0(T, I_D) - \Delta V_i(D, T, I_D) - \Delta V_s(D, T, I_D) \quad (3)$$

where

$$\begin{aligned} V_i(D, T, I_D) &= \Delta Q_i / C_0 = DV_{iM} [1 - \exp(-k_1 D)] > 0; \\ \Delta V_s(D, T, I_D) &= \Delta Q_s / C_0 = DV_{sM} [1 - \exp(-k_2 D)] < 0; \\ DV_{sM} &= (\gamma_M - \gamma_0) \cdot (\varphi_{s0} - \varphi_s) < 0, \\ \Delta V_i(T, I_D) &= (\Delta Q_{0M} + k_0 U) / C_0; \quad \text{at } U = (V_G - V_T) > 0. \end{aligned}$$

The value of $V_0(T)$ depends on temperature, electrical mode (by surface potential φ_s), structural and technological parameters of MOSFET and is theoretically for ideal transistor defined as

$$V_0 = \varphi_{ms} + \varphi_s(I_D) + a \{ \varphi_s(I_D) + \varphi_T \exp[(\varphi_s(I_D) - 2\varphi_{s0}) / \varphi_T] \}^{0.5} \quad (4)$$

where φ_{ms} and φ_s are of the Al-Si work functions difference and the surface potentials; a is equal $(2q \cdot \epsilon_s \epsilon_0 N_A)^{0.5} / C_0$; φ_T is thermal potential (kT/q); φ_{s0} is $\varphi_T \ln(N_A/n_i)$; N_A and n_i are concentrations of acceptors and intrinsic carriers; drain current I_D (Fig. 6).

To estimate the separate contributions of $Q_i(T, D)$ and $Q_s(T, D)$ being equal to $(C_0 \times \Delta V_i)$ and $(C_0 \times \Delta V_s)$ respectively, we measured CVCs and calculated values of ΔV_i and ΔV_s as in our works [17–19]:

The 3-component model of CVC was used for the dimensionless values of current $i_D = (I_D/I_{D0})$:

- (1) $i_D = \exp\{U / [(c + \gamma) \cdot \varphi_T]\}$ at $U = (V_G - V_T) < 0$ and $i_D < i_{D0} = 1$;
- (2) $i_D = [1 + 0,5(U/\varphi_T)^2] / n$ at $0 \leq U/n \leq V_D$ and $i_D \in [1; i_{D1}]$;
- (3) $i_D = V_D \cdot (U - 0,5nV_D) / (\varphi_T)^2$ at $0 < V_D < U/n$ and $i_D > i_{D1}$;
 $I_{D0} = b \cdot (\varphi_T)^2 \cdot [1 - \exp(-V_D/\varphi_T)] \approx b \cdot (\varphi_T)^2 \approx 5 \mu\text{A}$
 (at $V_D = 0.1 \text{ V}$ and $T = 25^\circ\text{C}$); $i_{D1} = 0,5(nV_D/\varphi_T)^2 \approx 9$ (at $V_D = 0.1 \text{ V}$ and $T = 25^\circ\text{C}$).

Table 1 Average values (dispersion <12%) of parameters of MOSFETs and models at $I_D = 0.1$ mA

T (°C)	V_0 (V)	ΔV_{iM} (V)	ΔV_{sM} (V)	$k_1, 10^{-2} \text{ Gy}^{-1}$	$k_2, 10^{-2} \text{ Gy}^{-1}$	$-S_{DM1}$ (mV/Gy)
-50	-0.67	2.6	3.8	2.4	0.22	51.7
0	-0.78	2.5	4.2	2.5	0.26	51.0
25	-0.87	2.5	4.4	2.7	0.30	53.3
50	-0.92	2.5	4.5	2.8	0.40	53.1
70	-1.12	2.5	4.6	2.9	0.43	53.0
125	-1.32	2.4	4.9	3.1	0.51	48.5

The radiation sensitivity determined as

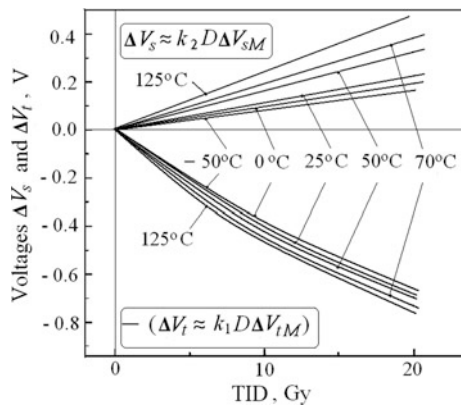
$$S_D = dV/dD = k_2 \Delta V_{sM} \cdot \exp(-k_2 D) - k_1 \Delta V_{iM} \cdot \exp(-k_1 D);$$

$$S_{DM1} = k_2 \Delta V_{sM} - k_1 \Delta V_{iM}; S_{DM2} = \max\{S_D\} \text{ at } D > D^* \quad (4)$$

3.2 Experimental Data of Model Parameters

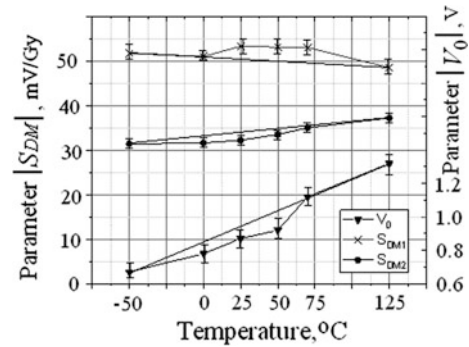
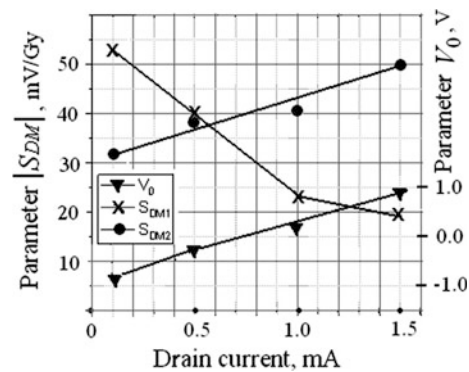
It was found that radiation sensitivity; model parameters ΔV_{iM} , ΔV_{sM} , k_0 , k_1 and k_2 depend on temperature T and drain current I_D . The average values of parameters of model components at $I_D = 0.1$ mA are presented in Table 1. Calculated dose dependences of model components $\Delta V_i(D, T)$ and $\Delta V_s(D, T)$ for low doses are shown in Fig. 7.

It was found that as the temperature increases, the voltage V_0 , parameters ΔV_{iM} and k_0 decrease, and the parameters ΔV_{sM} , k_1 and k_2 increase. Linear approximation of a parameter Y on the temperature T in the range from T_1 to T_2 can be represented as $Y(T) = Y(T_1) \times [1 + 0.01 \alpha_Y (T - T_1)]$, where α_Y is equal to $100\% \times [Y(T_2) - Y(T_1)] / [Y(T_1) (T_2 - T_1)]$, %/K. The average temperature coefficient of initial output voltage α_0 being equal to $[\Delta V_0 / (|V_0| \cdot \Delta T)] \times 100\%$ is (-0.47%/K), where values of $\Delta V_0 = V_0$

**Fig. 7** Calculated dose dependences of model components $\Delta V_i(D, T)$ and $\Delta V_s(D, T)$ at different temperatures

(398 K) – V_0 (223 K) = -0.55 V. Temperature dependences of values of initial voltage and sensitivities at low and high doses are shown in Fig. 8.

With the increase of operating drain current I_D the radiation sensitivity at high doses is increasing, and at low doses it slightly decreases. The absolute values maximum sensitivities and initial voltage as a function of the drain current I_D are illustrated in Fig. 9.

**Fig. 8** Temperature dependences of absolute values of initial voltage and sensitivities at low and high doses**Fig. 9** The absolute values maximum sensitivities and initial voltage versus the drain current

4 Discussion

Analysis of the results of the study of the effect of temperature in the range from 50 to 125 °C on the radiation sensitivity of *n*-channel MOSFET, as well as the influence of operating currents I_D at room temperature allows us to draw the following conclusions. The conversion function $V(D)$ is non-monotonic and has local extremum, which divides it into two parts—with positive and negative radiation sensitivities, in which there are areas of low and high doses. This kind of conversion function is a feature of *n*-channel MOSFETs. The temperature affects components of the conversion function in different ways. As the temperature increases, the parameter V_0 and the absolute values of radiation sensitivity in the low-dose region decrease, and the radiation sensitivity in the high-dose region increases. Herewith the initial voltage V_0 has the greatest temperature sensitivity, while parameters of the radiation sensitivity depend on the temperature slightly. The average value of maximum radiation sensitivity is about 50 mV/Gy. The average temperature coefficients of maximum sensitivities for low doses is about (−0.02%/K) and for high doses is 0.1%/K. The average temperature coefficient of initial voltage V_0 is (−0.47%/K). The temperature change of V_0 , considered as the error of the zero, must be taken into account in the calibration of the dosimeter. The operating drain current I_D effects on the initial voltage V_0 and the radiation sensitivity of MOSFET. If the operating current increases, that the parameter V_0 and the radiation sensitivity in the high-dose region increase, and the radiation sensitivity in the low-dose region decreases. When the drain current changes from 0.1 to 1.5 mA, the initial voltage increases from (−0.9 V) to 0.8 V. These changes must be taken into account to set the operating current and calibration of the dosimeter. With the increase of operating current the maximum radiation sensitivity for low doses decreases from 53 to 19 mV/Gy, and the maximum sensitivity for high doses increases from 32 to 50 mV/Gy. On the basis of the proposed models, the effect of drain current on changes on the components of the conversion function are explained by the dependence surface potential φ_s on current I_D , which increases monotonically and reaches saturation at a current of about 3 mA. The optimal operating currents can be considered for the region of low doses of 0.1 mA current, and for the region of high doses of 2 mA current.

5 Conclusions

It was shown how the conversion functions and the radiation sensitivities are depending on the temperature and electrical modes, and that the conversion functions have two characteristic regions with negative and with positive radiation sensitivities.

Acknowledgements This research was funded by the Ministry of Education and Science of the Russian Federation; (project № 2.1.2/11280), and was supported by the MEPhI Academic Excellence Project (contract No. 02.a03.21.0005, 27.08.2013). Authors acknowledge support from the MEPhI Academic Excellence Project (Contract No. 02.a 03.21.0005).

Conflict of Interest The authors declare that they have no conflict of interest.

References

- Holmes-Siedle, A.: The space charge dosimeter—general principles a new method of radiation dosimetry. *Nucl. Instrum. Methods* **121**, 169–179 (1974)
- Carvajal, M., Escobedo, P., Jimenez-Melguizo, M., et al.: A compact dosimetric system for MOSFETs based on passive NFC tag and smartphone. *Sens. Actuators, A* **267**, 82–89 (2017)
- Moreno, D., Hughes, R., Jenkins, M., et al.: A simple ionizing radiation spectrometer/dosimeter based on radiation sensing field effect transistors (RadFETs). SAND97-0255C, Sandia National Laboratories, Albuquerque, NM, pp. 26–28 (1997)
- Rosenfeld, A., Lerch, M., Kron, T., et al.: Feasibility study of online high spatial resolution MOSFET dosimetry in static and pulsed x-ray radiation fields. *IEEE Trans. Nucl. Sci.* **48**, 2061–2067 (2001)
- Ramaseshan, R., Kohli, K., Zhang, T., et al.: Performance characteristics of a micro MOSFET as an in vivo dosimeter in radiation therapy. *Phys. Med. Biol.* **49**, 4031–4048 (2004)
- Cheung, T., Butson, M.: MOSFET dosimetry in-vivo at superficial and orthovoltage x-ray energies. *Australas. Phys. Eng. Sci. Med.* **26**, 82–84 (2003)
- Cheung, T., Butson, M.: Energy dependence corrections to MOSFET dosimetric sensitivity. *Australas. Phys. Eng. Sci. Med.* **32**, 16–20 (2009). <https://doi.org/10.1007/BF03178623>
- Martinez-Garcia, M., Simancas, F., Palma, A., et al.: General purpose MOSFETs for the dosimetry of electron beams used in intra-operative radiotherapy. *Sens. Actuators, A* **210**, 175 (2014). <https://doi.org/10.1016/j.sna.2014.02.019>
- Wang, Y., Xiang, Z.-Q., Hu H.-F., et al.: Feasibility study of semifloating gate transistor gamma-ray dosimeter. *IEEE Electron Device Lett.* **36**(2), 99–101 (2014)
- Martinez-Garcia, M., Palma, A., Lallena-Arquillo, M., et al.: Accuracy improvement of MOSFET dosimeters in case of variation in thermal parameters. *IEEE Trans. Nucl. Sci.* **62**(2), 487–493 (2015)
- Pejovic, M.: P-channel MOSFET as a sensor and dosimeter of ionizing radiation. *Facta Universitatis, Series: Electron. Energetics* **29**(4), 509–541 (2016)
- Bakerenkov, A., Podlepetsky, B., Felitsyn, V., et al.: Digital total ionizing dose sensor based on the commercial MOSFET. [Datchiki i Sistemi (In Russian)] **2**, 31–36 (2018)
- Collins, D., Sah, C.: Effects of X-rays on characteristics of MOS structures. *Appl. Phys. Lett.* **8**, 124–128 (1966)
- Mitchell, J.: Radiation-induced space-charge buildup in MOS structures. *IEEE Trans. Electron Devices* **ED 14**, 764–774 (1967)
- Podlepetsky, B.: Total ionizing dose effects in hydrogen sensors based on MISFET. *IEEE Trans. Nucl. Sci.* **63**(4), 2095–2105 (2016). <https://doi.org/10.1109/TNS.2016.2557080>
- Podlepetsky, B., Sukhoroslova, Yu.: Influence of electrical modes on sensitivity of MISFET ionizing radiation dose sensors. *Proc. Eng.* **168**, 741–744 (2016)

17. Podlepetsky, B., Bakerenkov, A., Sukhoroslova, Yu.: Radiation sensitivity modeling technique of sensors' MIS-transistor elements. *Autom. Remote Control* **79**, 180–189 (2018)
18. Podlepetsky, B., Pershenkov, V., Bakerenkov, A., et al.: Effect of temperature and electrical modes on radiation sensitivity of MISFET dose sensors. In: *Proceedings 2018*, vol. 2, p. 954 (2018). <https://doi.org/10.3390/proceedings2130954>
19. Bakerenkov, A.: An automatic equipment for measure of electrical characteristics of nanoelectronic devices. *Adv. Mater. Res.* **1083**, 211–216 (2015)

Conductance and Photoconductance of Indium Oxide-Zinc Oxide Composites in the Hydrogen-Containing Atmosphere

Alexander S. Ilin, P. A. Forsh, M. I. Ikim, A. V. Koroleva, M. N. Martyshov, L. I. Trakhtenberg, and P. K. Kashkarov

Abstract

Photovoltaic properties of composites based on nanocrystalline indium and zinc oxides, promising as sensitive elements of gas sensors, were investigated. It is shown that under visible light the conductivity of composites changes with the change of hydrogen concentration in the environment even at room temperature, which allows the use of composites to detect hydrogen without heating. The curves of the kinetics of photoconductivity of the composites are studied and possible mechanisms of photoconductivity are analyzed. The mechanism of the sensor response of composites under illumination is proposed. The mechanism considers the illumination turns the composite into nonequilibrium state and the photoconductivity change in the H_2 atmosphere is linked with alteration of nonequilibrium charge carriers recombination rate.

Keywords

Zinc oxide • Indium oxide • Metal oxide composite • Photoconductivity • Resistive gas sensor

1 Introduction

Metal oxides In_2O_3 , ZnO and SnO_2 can be used as a sensitive material of gas sensors for various gases, as their conductivity varies greatly when placed in a chamber with a small concentration of a certain gas [1, 2]. To increase the selectivity and sensitivity to a certain gas, it is possible to use composites based on mixtures of different metal oxides instead of using the original single metal oxides [1, 3, 4]. So, the use of a composite based on indium and zinc oxides increases the sensitivity of the sensor to hydrogen [3].

In resistive gas sensors, the sensitive layer is maintained at high temperature. Operating at high temperature leads to the explosiveness of sensor, so investigations to reduce of sensor operating temperature are actual. Some resistive gas sensors can operate at room temperature under ultraviolet illumination (UV) [2, 5, 6]. However UV light emitting diodes (LEDs) have lower efficiency and are much more expensive than visible LEDs. Therefore the utilizing of visible LEDs for the sensor response activation is more effective from a practical point of view.

Much less attention is paid to the effects of visible illumination and effects of illumination on response to oxidizing species are investigated mainly. Number of researches studying the photo-activation of the sensor response to reducing gases is much smaller, and there is no definitive interpretation of the observed processes

This work was aimed at determining the mechanism of sensor response of metal oxide resistive gas sensor (based on In_2O_3 and ZnO) under visible illumination.

2 Materials and Methods

Nanocrystalline composite films were synthesized from commercial nanopowders In_2O_3 (99.5%, BDH/Merck Ltd) and ZnO (99.9%, Sigma–Aldrich Chemical Co). The average nanocrystal size of the oxides in the original powder is

A. S. Ilin (✉) · P. A. Forsh · A. V. Koroleva · M. N. Martyshov · P. K. Kashkarov
Physics Department, Lomonosov Moscow State University, Leninskie Gory, Moscow, Russia
e-mail: as.ilin@physics.msu.ru

P. A. Forsh · P. K. Kashkarov
National Research Centre “Kurchatov Institute”, Moscow, Russia

M. I. Ikim · L. I. Trakhtenberg
N.N. Semenov Federal Research Center for Chemical Physics, Russian Academy of Sciences, Moscow, Russia

L. I. Trakhtenberg
Chemistry Department, Lomonosov Moscow State University, Moscow, Russia

50–80 nm. Nanocrystalline composite films were prepared using aqueous suspensions of nanopowders. The suspension was screen printed on a dielectric alumina substrate equipped with platinum contacts and a heater. The resulting layer was heated during 3 h at 120 °C and then annealed in air, the temperature was gradually raising up to 550 °C and was kept at this value until a constant resistance value of the resulting nanocomposite film was obtained.

Illumination of the samples was performed by green LED with a maximum intensity at 525 nm. The intensity of light incident on the sample was 5 mW/cm². For sensing experiments the samples were placed in chamber with mounted LED and pure air or air containing 1000 ppm of hydrogen flowed through the chamber. The sensor response S was determined as:

$$S = \frac{\sigma(H_2)}{\sigma(\text{air})} \quad (1)$$

where $\sigma(H_2)$ and $\sigma(\text{air})$ —conductivity of sample in the hydrogen atmosphere and in pure atmosphere, respectively.

3 Results

At room temperature the dark conductivity of the composites does not change when the hydrogen content changes in the chamber. On the contrary, the conductivity of the light changes when the hydrogen concentration changes. Figure 1a shows the sensor response to H₂ for composites with different portion of zinc oxide under green illumination. It is seen that the response changes non-monotonically with the increase of zinc oxide in the composite. The composites with a mass fraction of ZnO 65% show the highest value of the sensor response under illumination among the studied composites.

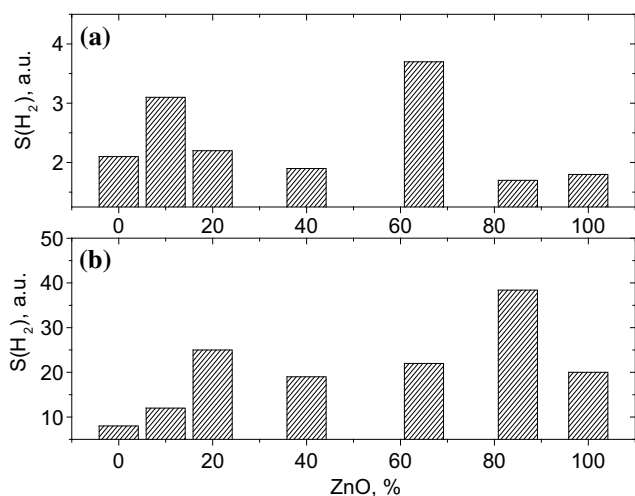


Fig. 1 Sensor response of In₂O₃-ZnO composites to 1000 ppm H₂ at room temperature under illumination (a) and at 400 °C (b)

When the composites are heated, their dark conductivity depend on the hydrogen content in the atmosphere. The existing of a sensor response under heating can be caused by various mechanisms. First, when heated on the surface of indium oxide (and composites) may appear chemisorbed oxygen atoms O⁻ in addition to chemisorbed molecules O₂⁻, which are existed at room temperature. Secondly, at high temperature hydrogen molecules can dissociate on the surface of the oxide into atoms and interact with chemisorbed oxygen species both in atomic and molecular form. In addition, an increase of temperature can accelerate the reaction of hydrogen with chemisorbed oxygen species and lead to a faster response and recovery [7].

The sensor response of In₂O₃/ZnO composites in the dark at 400 °C also changes non-monotonically with alteration of ZnO fraction in the composite. The sensor responses of composites in the dark at 400 °C are shown in Fig. 1b. At 400 °C the response of composites is much higher than under illumination. It can be seen that the response of In₂O₃/ZnO composites is higher than the response of source oxides In₂O₃ and ZnO. It is possible to distinguish 2 composites, the response of which is greater than the response of other composites—it is composites with a content of ZnO 20% and 85%. It should be noted that content of composites, that have maximum response under heating and illumination, distinguish (compare Fig. 1a, b). As already mentioned, under illumination the composites with a content of ZnO 65% show the maximum response. Those composites, which show the highest response during heating (20% ZnO and 85% ZnO), have low response under illumination.

In literature the increase in sensitivity of composites sometimes explains by the formation of new chemical compounds in the composite [1]. The IR spectra of the manufactured composites were investigated to study this explanation. Absorption bands assigned to vibrations of the In-O bond occur at 410, 536, 563, and 598 cm⁻¹ in the IR spectrum of indium oxide (Fig. 2). Absorption bands attributed to the vibrations of the Zn-O bond were observed at 408, 453, 484, 500 cm⁻¹ in the IR spectrum of zinc oxide. The obtained results are in accordance with the results received earlier by other authors [8, 9]. The spectrum of zinc oxide is shifted relative to the spectrum of indium oxide to the region of smaller wavenumbers (Fig. 2).

Absorption bands corresponding to vibrations of the In-O and Zn-O bonds are observed in the IR spectra of the composites. In particular, absorption bands assigned to In-O vibrations at 410, 536, 563, 598 cm⁻¹, absorption bands corresponding to the vibrations of the Zn-O bond at 408 and 460 cm⁻¹ take place in the IR spectrum of the 10% ZnO/90% In₂O₃ composite. Thus, evidences of the formation of new chemical compounds in the manufactured composites were not detected.

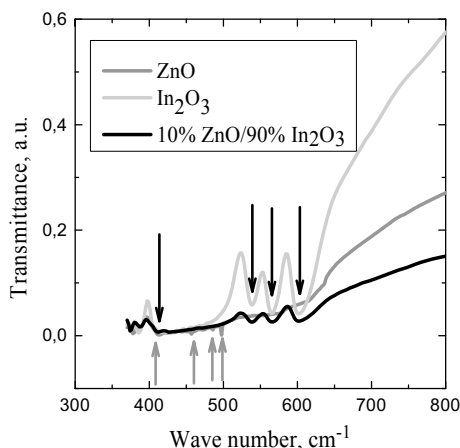


Fig. 2 FT-IR spectra of ZnO, In₂O₃ and composite 10% ZnO. The absorption bands corresponding to the vibrations of the In-O and Zn-O bonds in the spectra are shown by black and grey arrows correspondingly

The fact that under illumination and during the heating of the different composites show the highest response to H₂, can confirm that under the illumination the mechanism of the sensor response is completely different than at heating. The dynamic photoconductivity of composites was studied to clarify the mechanism of sensor response.

The kinetic of photoconductivity increase of ZnO-In₂O₃ composite film containing 65 wt% ZnO is presented in Fig. 3. The similar dependences have been obtained for other samples. The relaxation of photoconductivity is continued for a long time, that is inherent for nanocrystalline metal oxide [10]. The photoconductivity kinetic for all samples can be approximated by exponential dependence

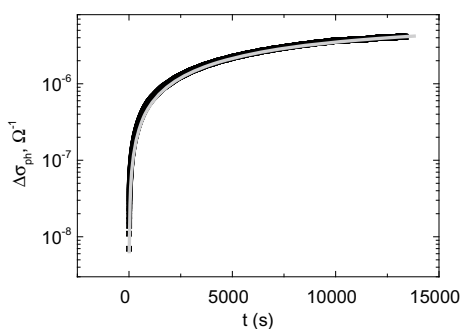


Fig. 3 Transient photoconductivity of ZnO-In₂O₃ composite containing 65 wt% ZnO (black points). The grey line is approximation of photoconductance increase Eq. (1). The approximated parameters $\sigma_{ph} = 5.67 \times 10^{-6} \Omega^{-1}$ and $\tau = 10,200$ s

$$\Delta\sigma_{ph}(t) = \sigma_{ph}(1 - e^{-t/\tau}) \tag{2}$$

where, according to [11] σ_{ph} —stationary photoconductivity and τ —relaxation time of photoconductivity. Excitation of nonequilibrium carriers under illumination should be monopolar from either localized states in the band gap or surface states, as the energy of green light photons is smaller than band gap values of ZnO and In₂O₃.

In Fig. 4 on the X-axis the relaxation time of the photoconductivity for composites is postponed, and on the Y-axis—the sensor response of composites to H₂ under illumination is postponed. Values for pure oxides are not shown in the Fig. 4. There is a good correlation between the relaxation time of the photoconductivity and the sensor response. The linear correlation coefficient between relaxation time and sensor response is slightly less than 0.99. This fact confirms the assumption that changes of photoconductivity in hydrogen atmosphere in the composites ZnO-In₂O₃ are determined by the recombination.

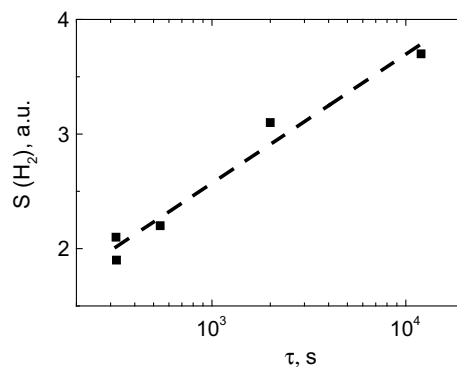


Fig. 4 Relaxation time of photoconductivity and response of composites to H₂ under illumination for ZnO-In₂O₃ composites (black points)

The following explanation of observed correlation may be proposed. The relaxation time of photoconductivity in the composites of ZnO-In₂O₃ is determined by various processes. First, the recombination centers in ZnO and In₂O₃ have different nature and different parameters of the carriers' capture. The concentration change of one kind of centers leads to more significant change in the photoconductivity relaxation time than the concentration change of other centers does. Second, there is a spatial separation of electrons and holes in the ZnO-In₂O₃ composites. In the energy diagram of heterojunction ZnO-In₂O₃ ZnO is a potential well for electrons, and In₂O₃—potential well for holes [12].

The separation of charges increases the relaxation time of photoconductivity, especially this effect should be noticeable for composites with approximately same content of In_2O_3 and ZnO .

It can be assumed that the recombination rate of nonequilibrium electrons is relatively small for the $\text{ZnO-In}_2\text{O}_3$ composites with large values of τ before gas injection. Since the hydrogen concentration in the atmosphere with H_2 is the same for all samples, the change in the recombination centers concentration is assumed to be the same. The last in turn affects the recombination rate. The recombination rate change should be more significant in relative units for samples with initially low recombination rate and ratio of photoconductivity in atmosphere of hydrogen to initial photoconductivity in pure air for these samples should be greater. It explains the observed correlation between sensor response and photoconductivity relaxation time.

4 Conclusions

The opportunity of H_2 detecting at room temperature by nanocrystalline indium and zinc oxides (and composites on their base) is shown. Detection is produced by observation of magnitude alteration of conductivity at illumination (it is shown on illumination by light with wavelength 525 nm). It is found that sensitivity of $\text{ZnO-In}_2\text{O}_3$ composite to H_2 is larger than sensitivity of source oxides and nonmonotonically depends on the oxides' content. The maximum sensitivity to H_2 is observed for the nanocomposite films based on 65 wt% ZnO and 35 wt% In_2O_3 . At the same time at 400 °C the composite with another content of components shows the largest response. The formation of new chemical compounds in the composite was not found out. So the new chemical compound can't explain the elevated sensor response.

As there are many reasons to confirm that the mechanism of sensor response changes at illumination, we proposed the new mechanism of nanocrystalline $\text{ZnO-In}_2\text{O}_3$ sensor sensitivity to H_2 under illumination. The mechanism considers the illumination turns the composite into nonequilibrium state. In this regard the photoconductivity of the $\text{ZnO-In}_2\text{O}_3$ composite change in the H_2 atmosphere is largely determined by recombination processes. The recombination processes determine the photoconductivity relaxation time which in turn determines the photoconductivity of the composite. It is shown that the photoconductivity relaxation time is linked with the response of the $\text{ZnO-In}_2\text{O}_3$ composites to H_2 . The possible recombination mechanisms of non-equilibrium charge carriers in the studied structures are

discussed. The proposed mechanism links the response of the $\text{ZnO-In}_2\text{O}_3$ composites to H_2 under illumination with change of the nonequilibrium charge carriers recombination rate.

Acknowledgements The reported study was funded by RFBR according to the research projects № 18-32-00741 mol_a and № 19-07-00251 A.

Conflict of Interest The authors declare that they have no conflict of interest.

References

- Korotcenkov, G. (ed.): Chemical Sensors: Simulation and Modeling Vol 2: Conductometric-Type Sensors. Momentum Press (2012). <https://doi.org/10.5643/9781606503140>
- Ilyin, A.S., Fantina, N.P., Martyshov, M.N., et al.: Voltage effect on the sensitivity of nanocrystalline indium oxide to nitrogen dioxide under ultraviolet irradiation. *Tech. Phys. Lett.* **41**, 252–254 (2015). <https://doi.org/10.1134/S1063785015030074>
- Trakhtenberg, L.I., Gerasimov, G.N., Gromov, V.F., et al.: Conductivity and sensing properties of $\text{In}_2\text{O}_3 + \text{ZnO}$ mixed nanostructured films: Effect of composition and temperature. *Sens. Actuators B Chem.* **187**, 514–521 (2013). <https://doi.org/10.1016/j.snb.2013.03.017>
- Ilin, A.S., Ikim, M.I., Forsh, P.A., et al.: Green light activated hydrogen sensing of nanocrystalline composite $\text{ZnO-In}_2\text{O}_3$ films at room temperature. *Sci. Rep.* **7**, 12204 (2017). <https://doi.org/10.1038/s41598-017-12547-5>
- Ilin, A., Martyshov, M., Forsh, E., et al.: UV effect on NO_2 sensing properties of nanocrystalline In_2O_3 . *Sens. Actuators B: Chem.* **231**, 491–496 (2016). <https://doi.org/10.1016/j.snb.2016.03.051>
- Wang, C.Y., Cimalla, V., Kups, T., et al.: Photoreduction and oxidation behavior of In_2O_3 nanoparticles by metal organic chemical vapor deposition. *J. Appl. Phys.* **102**, 044310 (2007). <https://doi.org/10.1063/1.2770831>
- Meloro, J., Perroy, R., Careas, S.: Metal Oxide Nanomaterials for Chemical Sensors (ed. Carpenter, M.A., Mathur, S., Kolmakov, A.). Springer, New York (2013)
- Rey, J.F.Q., Plivelic, T.S., Rocha, R.A., et al.: Synthesis of In_2O_3 nanoparticles by thermal decomposition of a citrate gel precursor. *J. Nanopart. Res.* **7**, 203–208 (2005). <https://doi.org/10.1007/s11051-004-7899-7>
- Nandi, A., Majumder, R., Nag, P., et al.: Precursor dependent tailoring of morphology and bandgap of zinc oxide nanostructures. *J. Mater. Sci.: Mater. Electron.* **28**, 10885–10892 (2017). <https://doi.org/10.1007/s10854-017-6867-9>
- Forsh, E.A., Ilyin, A.S., Martyshov, M.N., et al.: Relaxation of photoconductivity in nanocrystalline indium oxide. *Nanotechnol. Russ.* **9**, 618–622 (2014). <https://doi.org/10.1134/S1995078014060093>
- Ryvkin, S.M.: Photoelectric Effects in Semiconductors. Springer, Heidelberg (1964)
- Wang, Z., Huang, B., Dai, Y., et al.: Highly photocatalytic $\text{ZnO/In}_2\text{O}_3$ heteronanostructures synthesized by a coprecipitation method. *J. Phys. Chem. C* **113**, 4612–4617 (2009). <https://doi.org/10.1021/jp8107683>

Part VI

Biomedical Instrumentation

Visual Control of Human Locomotion

H. N. Rozorinov, N. I. Chichikalo, E. H. Arkhiereieva, and E. Yu. Larina

Abstract

An objective method for instrumental assessment of the state of the human locomotion system in real time has been proposed. A universal method of studying human motor functions based on the principles of technical vision has been developed. Using the visualization of the projection of the three-dimensional location of the sensors on the profile, frontal and horizontal planes allows to assess the current state of the spine and can be widely used in clinical practice.

Keywords

Virtual design • Locomotion • Human spine • Computer vision

1 Introduction

The rapid development and implementation of intelligent systems, the functioning of which is based on obtaining information on the basis of visual observation of an object, allowed not only to inspect industrial goods, but also a human body [1].

The aim of the work is to develop a system for monitoring the state of the human locomotion system using sensors located on the spine, processing of static and dynamic data at fixed intervals.

2 Main Part

Considering the extremely small deformations of the cervical spine, we place the sensors only on the thoracic and lumbar sections (Fig. 1).

Of course, to obtain a comprehensive picture, it is necessary that the sensors are located on each spinal bone (vertebra). However, it is necessary and sufficient to have three sensors. A sensor is a device that measures coordinates in three-dimensional space relative to some reference system, which can be specified using triangulation or any other methods. In any case, information is taken from the sensors, which represents the numerical values of the coordinates. Further, these data enter the information processing system on three subchannels, in each of which an array of homonymous coordinates of the sensors is transmitted.

These subchannels are grouped in pairs, thereby forming the projections of the three-dimensional arrangement of the sensors on the profile, frontal and horizontal planes, respectively. It is convenient to present the results in the form of graphs that are updated at set intervals.

To analyze the results we consider some functional modules.

The most important of these is the formula node containing the program in the language G [2]. This program performs averaging of sensor readings (Fig. 2).

Here $N_{\max} = 0 \dots 30$ —is the number of sensors that can be placed on a person; *count* is the current number of averaging cycles, which is incremented when moving to a new averaging cycle; *arr_x* [30], *arr_y* [30], *arr_z* [30] are arrays of current coordinate values that come from the sensors and are used in the adder accumulator cycle; *mean_x* [30], *mean_y*[30], *mean_z*[30]—are the mean values of the *x*, *y* and *z* coordinates of the sensors at the current stage of averaging.

In cycle 1, the sums of coordinates are accumulated for each sensor located on the spine, separately for each coordinate.

H. N. Rozorinov (✉) · N. I. Chichikalo · E. H. Arkhiereieva · E. Yu. Larina
National Technical University of Ukraine “Igor Sikorsky Kyiv Polytechnic Institute”, Peremogy Ave., 37, Kiev, Ukraine
e-mail: grozoryn@gmail.com

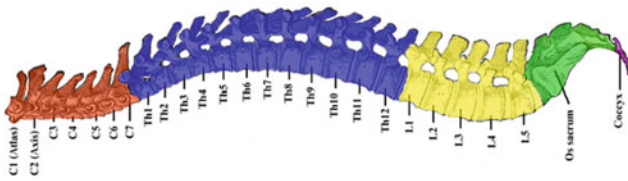


Fig. 1 Human spine

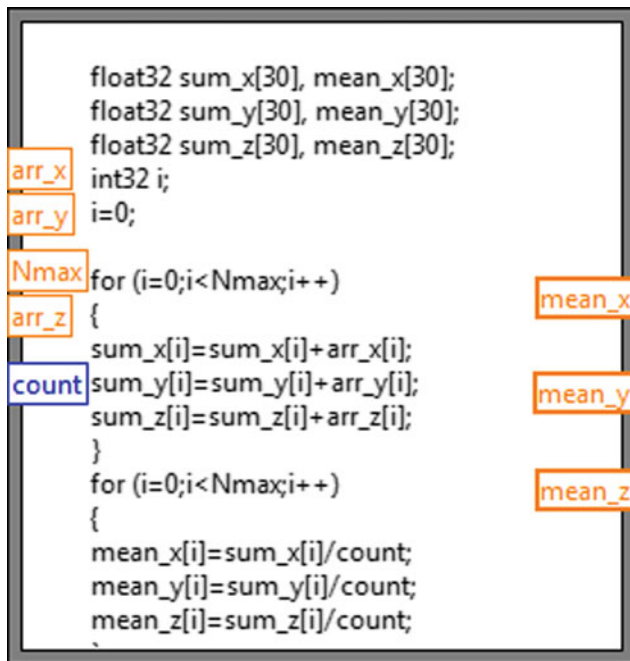


Fig. 2 Formula node that implements the averaging of sensor readings

In cycle 2, the average values of coordinates are calculated at each step of the system operation. The results of calculations are derived from the formular block in the form of arrays and are used for plotting graphs. In a real system, data comes from sensors, and the model uses pseudo-random data generators (Fig. 3).

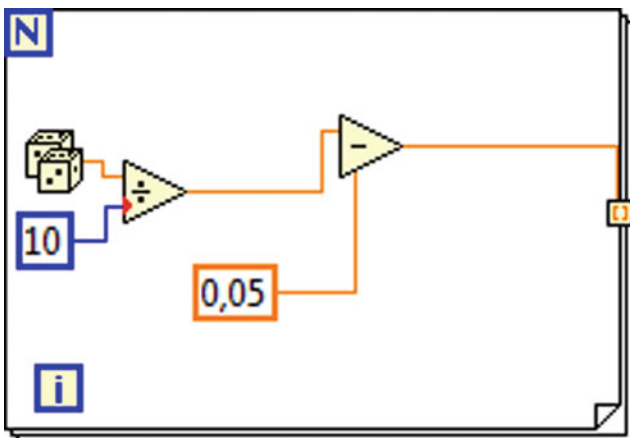


Fig. 3 Block of sensors readings generation

Formular node calculates the average values of the coordinates of each of the sensors, which allows to see a picture of the deviation of the spine from the norm. After processing, the data is transferred to plotters of the front, horizontal and profile surfaces (Fig. 4).

Let us denote $x_i(t)$ as the value of the coordinate x of i sensor at the moment of time t . Accordingly, the values of the coordinates y and z are denoted as $y_i(t)$ and $z_i(t)$. Then the average values of the coordinates of each sensor during the observation period T are defined as:

$$\bar{x}_i = \lim_{T \rightarrow \infty} \frac{1}{T} \int_0^T x_i(t) dt, \quad (1)$$

$$\bar{y}_i = \lim_{T \rightarrow \infty} \frac{1}{T} \int_0^T y_i(t) dt, \quad (2)$$

$$\bar{z}_i = \lim_{T \rightarrow \infty} \frac{1}{T} \int_0^T z_i(t) dt. \quad (3)$$

The discrete equivalents of these formulas are:

$$\bar{x}_i = \frac{\sum_{k=1}^N x_i(k)}{N}, \quad (4)$$

$$\bar{y}_i = \frac{\sum_{k=1}^N y_i(k)}{N}, \quad (5)$$

$$\bar{z}_i = \frac{\sum_{k=1}^N z_i(k)}{N}. \quad (6)$$

To determine the coordinates of the vertebrae is also convenient to use the principles of computer vision [3]. Wherein there are at least two options for determining the coordinates of the sensors: from a photo (Fig. 5, 6 and 7) and from a video image in real time.

Analyzing the block diagrams of tools for identifying sensors in a photo and in real time it can be noted that they differ only in initial blocks. In the case of a photo, functions are used to open and select an image type, and in the case of video, functions are used to search for a video capture device and start recording.

The blocks presented in the program require the IMAQdx and Vision libraries. They can be downloaded from the official website of National Instruments.

After installing the necessary libraries, a new section *Vision and Motion* appears in the functions menu. With it, the work is carried out with a machine vision system (Fig. 8).

In the *Vision and Motion* functions section, the NI-IMAQ and NI-IMAQdx subsections contain blocks for working

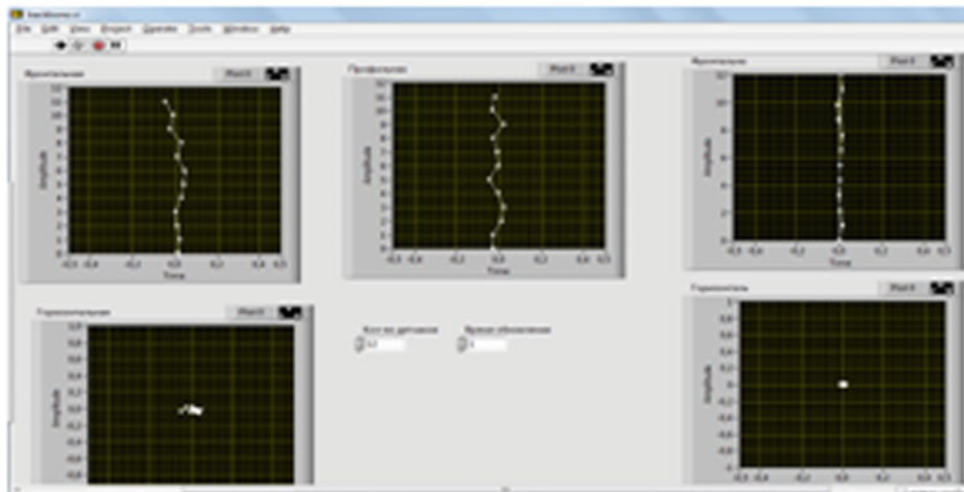


Fig. 4 Deviation of spine from a norm



Fig. 5 Photo of the patient

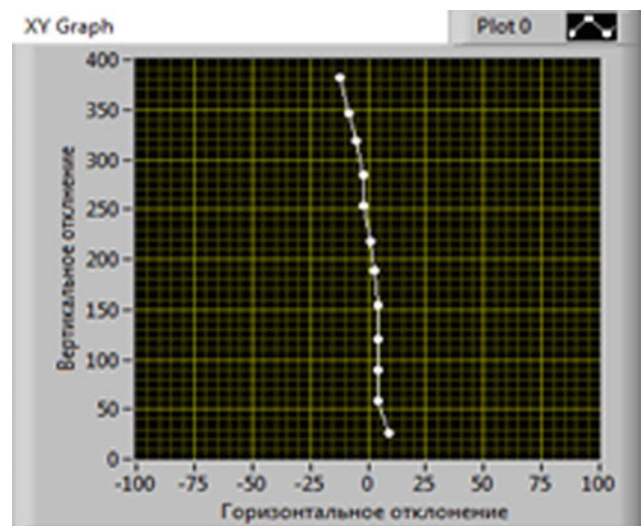


Fig. 7 Spine model

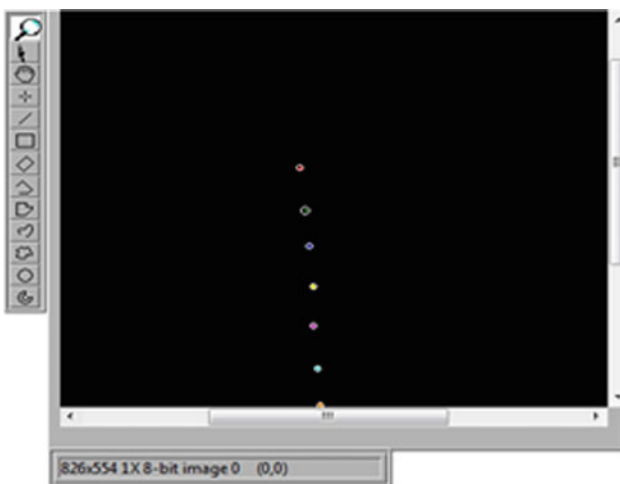


Fig. 6 Photo after processing

with cameras and capturing an image (choosing a camera, opening a video device, preparing cyclic buffers, starting recording, stop recording, closing a video device). IMAQ and NI-IMAQdx are almost identical in functionality, but NI-IMAQdx is a newer version of the IMAQ library.

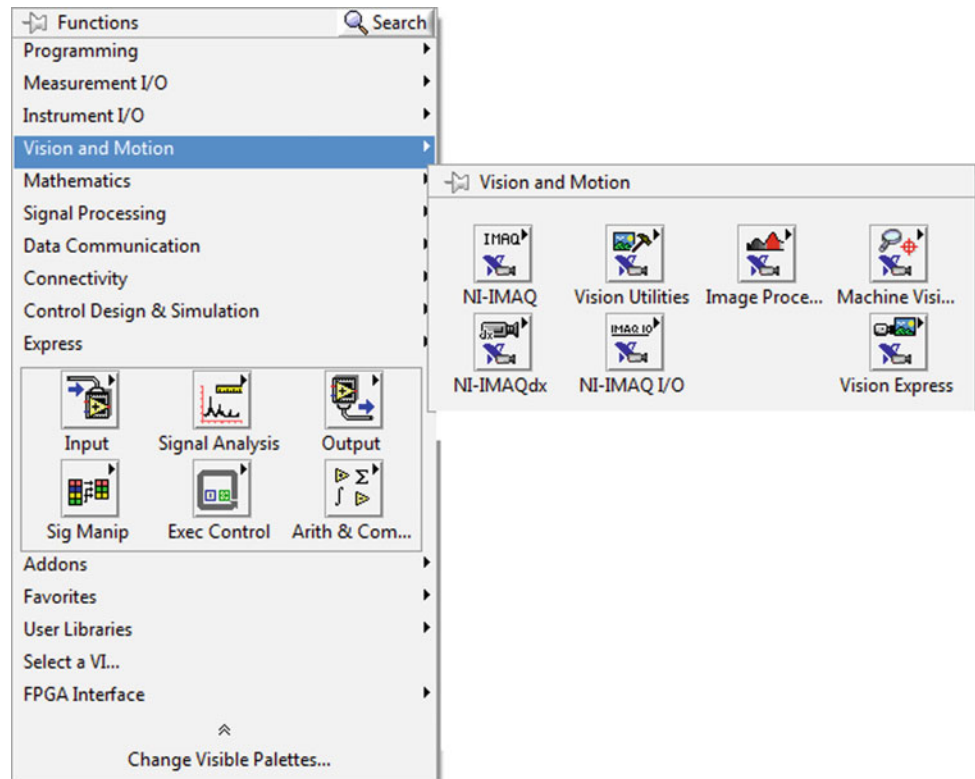
Subsections *Image Processing*, *Machine Vision*, *Vision Utilities* are responsible for digital image processing and the use of technical vision as a mathematical apparatus.

The operation of the system in real time is based on determining the coordinates of the so-called visual sensors.

A visual sensor is any object that differs in its optical or geometrical properties from other background objects present in the image.

This may be an object that differs in color, brightness, radiation intensity, and shape. Such objects can be

Fig. 8 Library of *Vision and Motion* in LabView



distinguished using a chain of successive transformations. When using visual sensors based on color, it is desirable that the color of the sensor does not match the color of the background objects in the image. Otherwise, this may complicate their selection from the rest of the mass of objects. In this work, we used red color visual sensors (Fig. 9).

Image analysis using the machine vision system is performed in stages [4]:

1. Image binarization using a threshold device. Image pixels that satisfy threshold conditions turn red, otherwise—black. This stage is perhaps the most important of all, since it is necessary to select such values of the range of RGB colors that would ensure the removal of as many background objects as possible. In the optimal case, only visual sensors with red color remain on the output image, and all other objects are black (Fig. 10).
2. Search for circles on a binary image and determination of their coordinates. After a binary image is obtained, it is



Fig. 9 Back of a man with visual sensors applied

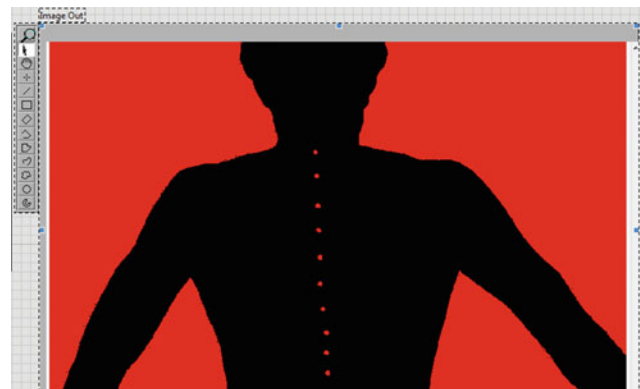


Fig. 10 Binary image obtained after threshold

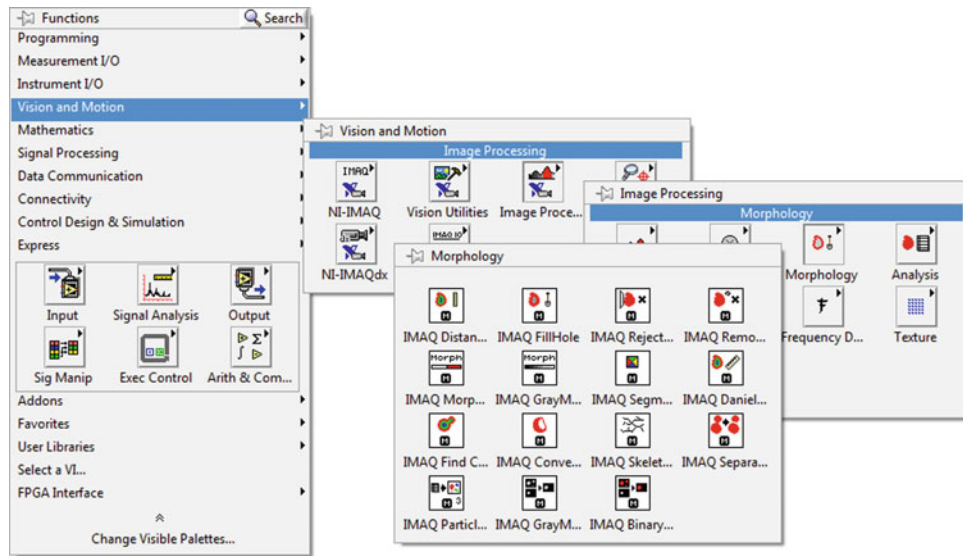


Fig. 11 Location of the circle determination block

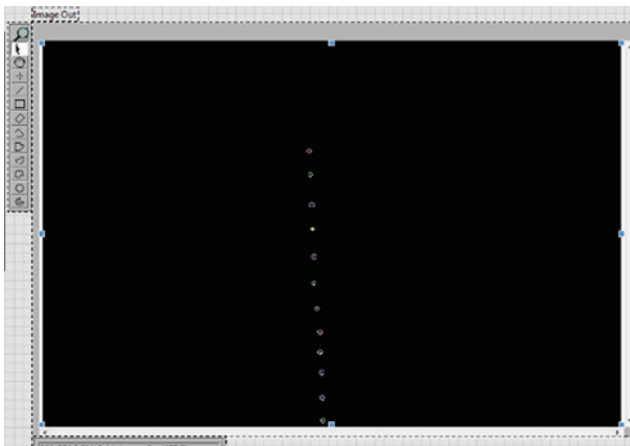


Fig. 12 The result of the function of the search for circles

possible to search for elementary geometric objects with a relative definition of their coordinates. In the *Morphology* catalog of the *Image Processing* sub-section there is an *IMAQ Find Circle* function that is responsible for determining the circles in the image (Fig. 11).

The result of the search for circles is shown in Fig. 12.

3. Based on the obtained coordinates, a numerical model is constructed, which can be subjected to further statistical analysis (Fig. 13).

To find the actual size of the image by photo, the principles of geometric optics or comparison with scaling objects must be used. We single out several functional modules that are included in cyclic structures.

For example, the camera randomly set so that its optical not coincide with the frontal plane axis of the spine. In this

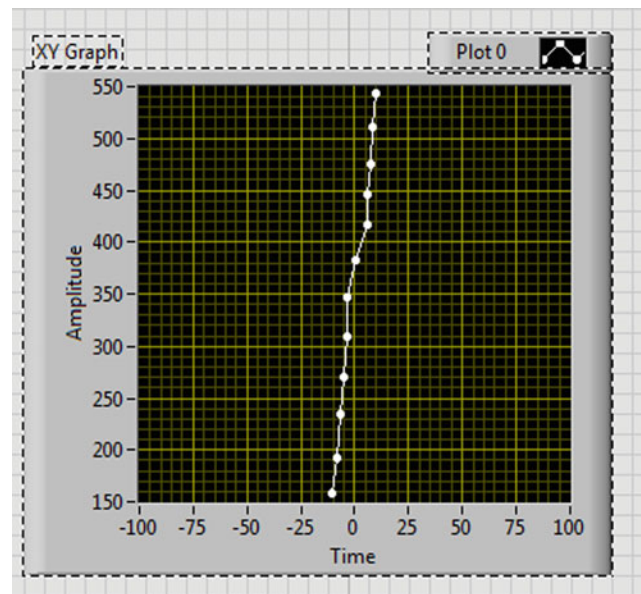


Fig. 13 Model of the spine based on sensor readings

case, the readings of the virtual instrument may be shifted to the right or left by some constant. This block calculates the average value of the coordinates of all sensors and then shifts the resulting values to this coordinate, thereby restoring symmetry relatively to zero. The shift process is the process of subtracting the average of the coordinates from the coordinates of each sensor. This allows us to obtain the value of the location of each sensor and the distance between the sensors in pixels. The physician should receive this information in the metric system, in units of distance. Geometric optics formulas allow us to set the size of the

object according to the size of the image in pixels. To do this, we need to know: the focal length of the camera, the distance from the camera to the object, the linear size of the pixel of the camera.

This recalculation provides a definition of the linear dimensions of objects relative to the bottom edge of the photo. To determine the coordinates of objects relative to the level of the floor, it is necessary to add to the coordinate a height value to which the bottom edge of the photo corresponds.

3 Conclusion

1. A virtual device has been created that allows real-time monitoring of the human locomotive system, and a calculator unit allows detecting abnormal deviations and its violations in the early stages.
2. Within the framework of the concept of machine vision, a system has been created that allows one to obtain relative coordinates of visual sensors.
3. The obtained information can be used for subsequent statistical processing.

Conflict of Interest The authors declare that they have no conflict of interest.

References

1. Ларин В.Ю. Концепции профессионального проектирования приборов и систем/учебник. Книга 1./В. Ю. Ларин, Е. Ю. Ларина, Я. А. Савицкая, Г.Н. Розоринов, Н.И. Чичикало, Е. Е. Федоров. – К.: Кафедра, 2016. – 468 с
2. Федосов В.П. Цифровая обработка сигналов в LabVIEW. Под ред. В.П. Федосова/В.П. Федосов, А.К. Нестеренко. – М.: ДМК Пресс, 2007. – 456 с
3. Lyons, R.G.: Understanding Digital Signal Processing, 3rd edn. Pearson Education, Inc., 564 p (2011)
4. Коберниченко В.Г. Основы цифровой обработки сигналов: учеб. пособие, Урал. федер. ун-т. – Екатеринбург: Изд-во Урал. ун-та, 2018. – 150 с

Method for Performance Evaluation of Electrostimulation of the Lower Esophageal Sphincter

V. Sontea, S. Ungureanu, N. Sipitco, D. Fosa, and V. Vidiborschii

Abstract

Recognized world experience could confirm, that gastroesophageal reflux disease (GERD) is one of the most common gastroenterological diseases. In many cases conservative treatment is not efficient, that could lead to severe complications. Existing options like antireflux laparoscopic surgery in recent years were supplemented with direct tone modulation of lower esophageal sphincter (LES) with implantable electrical stimulator. Having experience in development of wireless powered LES electrostimulators (WPLES), authors elaborated simple and inexpensive method of assessing the effectiveness of LES stimulating devices during tests on laboratory animals.

Keywords

GERD • LES • Wireless implantable electrostimulator

1 Introduction

Existing data confirm effectiveness of direct modulation of the lower esophageal sphincter (LES) pressure with implantable electrostimulators [1–3].

Because of generally big size, such devices usually are implanted subcutaneously in the abdominal wall and associated with terminals, fixed to the esophagus during a laparoscopic surgery.

Existing disadvantages, such as need of general anesthesia to 3 h, hospital stay up to 5 days after procedure,

significant level of complications (up to 22%) and battery life time up to 7–8 years, leads to looking for alternatives with more benefits, such as wireless powered LES electrostimulator (WPLES) [4, 5]. This type of could receive energy from an electric and/or magnetic field and may be significantly smaller measured, resulting improves quality, safety and simplicity of use.

Having good results of development of WPLES devices authors for many times were looking for simple method of assessing the effectiveness of manufactured prototype at stage of animal tests [6–9]. Existing and generally used in medical practice multi-channel esophageal manometry requires very expensive equipment (fragile and heavy) and costly disposables.

We have developed and tested own technique of prototype assessing, consisted of 3 different methods.

2 Materials and Methods

2.1 Object for Performance Evaluation

Experimental prototype of a programmable micro-stimulator of the lower esophageal sphincter with wireless powering [6–9]. This prototype was manufactured and prepared for evaluation of the clinical efficacy of various operating modes during trials on laboratory animals.

Animal tests were performed on 15.10.2018 in *Centrul de chirurgie experimentală “Pius Brânzeu”, P-ța Eftimie Murgu Nr. 2, 300041 Timisoara, Romania*, specially equipped for surgical operations on laboratory animals.

2.2 Equipment Used

Digital oscilloscope Siglent SHS810 (0–100 MHz, 0–600 V measuring range, 3% accuracy), self-manufactured “Implant activity checker” adaptor for evaluation of electrical activity and *in vivo* temperature, self manufactured test bench “High

V. Sontea · V. Vidiborschii (✉)
 Technical University of Moldova, Bld. Ștefan cel Mare și Sfint
 168, Chișinău, Republic of Moldova
 e-mail: vidiborschii@yahoo.com

S. Ungureanu · N. Sipitco · D. Fosa
 State University of Medicine and Pharmacy „Nicolae
 Testemitanu“, Chișinău, Republic of Moldova

resolution LES pressure manometry analyzer (HiLESPMA)” for evaluation of LES pressure modulation via 24-bit digital pressure logging, PC (notebook) with specialized software.

2.3 Procedure for Testing of WPLES Prototype

Performance evaluation of WPLES implantable prototype was performed after surgery procedure of implantation, with electrodes placement of external esophagus wall of a laboratory animal (pig, about 15 kg weights). Registration of implant activity with above mentioned equipment was assessed using 3 different methods:

1. Indirect electrical activity evaluation;
2. Comparative temperature measurements with esophageal probe versus internal prototype sensor;
3. Digital 24-bit resolution (0.01 mmHg) measuring of LES pressure.

All above mentioned methods were used to evaluate effectiveness of every mode of operation, programmed in prototype—totally 5 different modes, listed in Table 1.

Selectable stimulation current was in range 2–6 mA for each mode. Control of working mode and output current of prototype was performed with a custom made mobile application installed on an Android-based smartphone. Both stimulation control and telemetry data (communication signal power, temperature, device version) were transmitted wirelessly via Bluetooth BLE.

2.4 Evaluation of Electrical Activity and Temperature

For estimation of the electrical activity and temperature a self manufactured esophageal catheter probe was used. Having 3 stainless electrical leads (1-2-3 sequence, 40 mm interval) and embedded NTC thermocouple, it was connected to digital scope meter using the “Implant activity checker” device. This test bench was build with digital thermometer module installed, internally connected to NTC thermocouple in catheter’s end. See connection schematics below (Fig. 1):

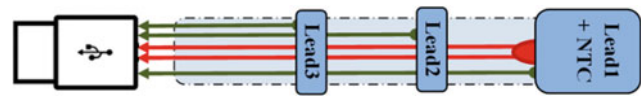


Fig. 1 Schematic view of custom made esophageal catheter

During trials catheter probe was installed by placing of its sensitive end in esophagus of a laboratory animal, in the projection of implanted prototype electrodes. By its other end probe was connected to the “Implant activity checker” test bench, which had a test pin for every of 3 leads of the probe. Scope meter could be connected to any pair of 3 leads, depending of relative position of implanted stimulators and esophageal catheter probe.

During the tests, various operating modes of the prototype were sequentially launched with simultaneous recording of electrical signals using the Siglent’s SHS810 oscilloscope.

In same time was possible to compare the probe temperature data with the temperature transmitted by the implanted prototype, measured by 12-bit ($\pm 0.0625\text{ }^{\circ}\text{C}$) digital temperature sensor—see Fig. 2:

Although this method of electrical activity evaluation is not allowing recording exact amplitude way form of electric stimulation, it could display almost the same pulse timing picture of running stimulation current.

In same time temperature display could be used as telemetry for implantable device or for debugging purposes.

It is recommended to ensure processing of calibration of both temperature sensors before using, using for example, a warm water bath.

2.5 Evaluation LES Pressure Alteration

To explore the effectiveness of modulating the tone of the lower esophageal sphincter (LES), a standard Sengstaken-Blakemore three-lumen esophageal obturating catheter was used (Fig. 3).

Cather was installed according to the standard method with the placing of esophageal balloon in LES projection. Output tubing port of esophageal balloon was connected to the HiLESPMA (High Resolution LES Pressure Manometry Analyzer), see Fig. 4.

Table 1 Stimulation modes for prototype

Stimulation mode	Pulse width	Pulse frequency	Stimulation duration (s)
Nr.1	220 μs	20 Hz	10
Nr.2	100 μs	10 Hz	10
Nr.3	300 μs	40 Hz	10
Nr.4	220 μs	20 Hz	60
Nr.5	375 ms	6 pulses/min	60

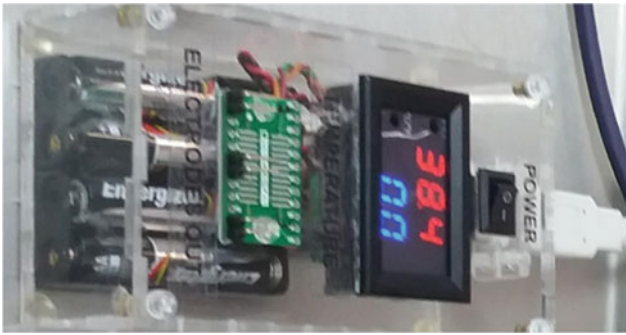


Fig. 2 Photo of “Implant activity checker” device



Fig. 3 Sengstaken-Blakemore esophageal catheter

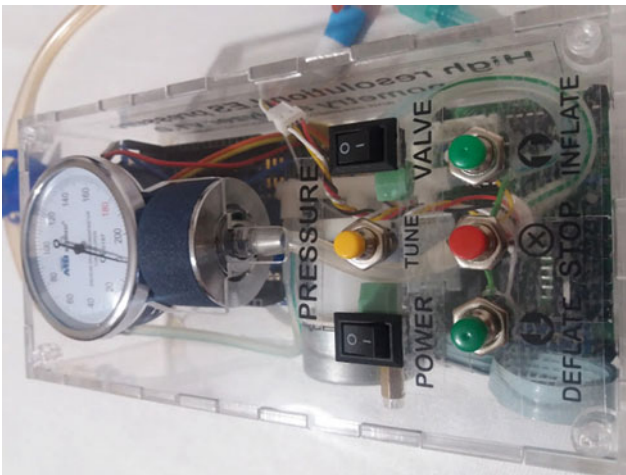


Fig. 4 “High Resolution LES Pressure Manometry Analyzer” test bench

This test bench has several components inside:

- low speed air pump, powered by stepper motor;
- stepper motor driver with start/stop/speed buttons;
- air pressure release valve;
- dial pressure indicator 0–200 mmHg;
- 0–300 mmHg, 24-bit pressure sensor, gage type;
- Honeywell SEK002 evaluation module.

During animal test esophageal balloon of Sengstaken-Blakemore catheter was pre-inflated with a HiLESPMA’s microcompressor to ~ 50 mmHg pressure, after that were started electro stimulation of implanted prototype, resulting muscle tone modulation of LES sphincter (LES) and respectively pressure of esophageal balloon of catheter. Pressure changes were noticed by moving of pressure dial gauge arrow and registered with digital pressure sensor output, received by PC with running software (Honeywell SEK002 Sensor Evaluation Kit v4.0.0.5). See below screenshot of working SW (Fig. 5).

With data rate up to 200 samples/sec is possible to register even smallest pressure changes, like changes from respiration (regular small peaks on image above) or body position change. In our case was used software averaging of data flow to 10 samples/sec to minimize noises.

Performed tests showed, that positive modulation of the LES tone was up to +8.78 mmHg above the background fluctuations, that is very good result.

Usually normal pressure of the lower esophageal sphincter in a healthy human is ~ 20 mmHg, while at pathology less than 10 mmHg.

3 Discussion

Proposed technique of performance evaluation of electrostimulation of the lower esophageal sphincter (LES) is an affordable and inexpensive alternative to multichannel manometry of the esophagus. Our research confirms that even single-channel pressure data received from pre-inflated Sengstaken-Blakemore esophageal obturating catheter could be sufficiently informative for confirmation of effective LES stimulation. The main idea is using of high resolution digital pressure sensor with high speed data recording for successful registration of the slightest pressure fluctuations.

In same time evaluation of electrical activity and temperature could be used for debugging purposes and telemetry checking of running prototype.

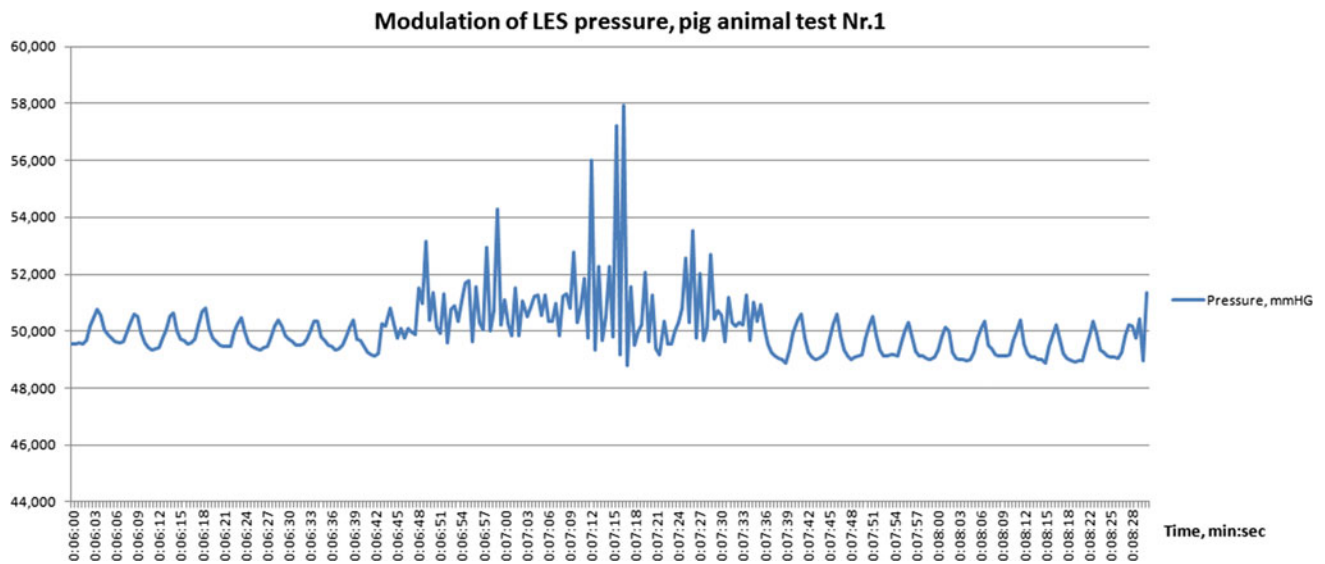


Fig. 5 LES pressure modulation during work of prototype

Conflict of Interest The authors declare that they have no conflict of interest.

References

- Hoppo, T., Rodríguez, L., Soffer, E., Crowell, M.D., Jobe, B.A.: Long-term results of electrical stimulation of the lower esophageal sphincter for treatment of proximal GERD. *Surg. Endosc.* 22 Jul 2014
- Siersema, P.D., Bredenoord, A.J., Conchillo, J.M., et al.: Electrical Stimulation Therapy (EST) of the Lower Esophageal Sphincter (LES) for refractory Gerd and two year results of an international multicenter trial. *Gastroenterology*. **152**(5), Supplement 1, S470
- Vakil, N., et al.: The Montreal definition and classification of gastroesophageal reflux disease: a global evidence-based consensus. *Am. J. Gastroenterol.* **101**(8), 1900–1920 (2006)
- U.S. Food and Drug Administration (FDA)- H990014 Summary of Safety and Probable Benefit, Enterra Therapy System 2015. https://www.accessdata.fda.gov/cdrh_docs/pdf/h990014b.pdf
- Medtronic Inc., Enterra Therapy Fact Sheet (2003). <http://www.medtronic.com/downloadablefiles/Gastro-EnterraFactSheet.pdf>
- Ungureanu, S., Sipitco, N., Vidiborschii, V., Fosa, D.: Clinical study of the lower esophageal sphincter electrical stimulation. *Glob. J. Res. Anal.* **7**(1), 423–426 January-2018, ISSN No 2277 – 8160, <https://doi.org/10.15373/22778160>
- Ungureanu, S., Sontea, V., Sipitco, N., Fosa, D., Vidiborschii, V.: Long distance wireless powered implantable electrostimulator. In: Ist International Scientific and Practical Conference “Information Systems and Technologies in Medicine” ISM-2018, 28–30 Nov 2018, Kharkiv, Ukraine
- Ungureanu, S.N., Lepadatu, K.I., Sipitco, N.I., Vidiborschi, V.L., Gladun, N.V., Balica, I.M.: Influence of electrical stimulation on the function of lower esophageal sphincter in patients with gastroesophageal reflux disease. *Exp. Clin. Gastroenterol.* **128**(4), 51–55 (2016)
- Vidiborschii, V.: Efficiency of the les implantable stimulator in animal tests. In: Technical Scientific Conference of Students, Master Students and PhD Students (with international participation), 26–29 March 2019

Profile Forming of Infrared Cabin User's Biomedical Indicators

M. M. Mezhennaya, A. V. Vorobey, V. Y. Drapeza,
A. N. Osipov, S. K. Dick, and M. X.-M. Thostov

Abstract

The construction and methodology of a infrared cabin developed by the authors for activation of human body functional reserves are described in the article. A device is equipped with a system of human physiological parameter monitoring. The results of thermal load level produced by the infrared cabin on the human cardiovascular system are presented.

Keywords

Infrared radiation • Infrared cabin • Monitoring of biomedical parameters

1 Introduction

In modern medicine, infrared (IR) therapy is widely used for the treatment of skin diseases (acne, eczema, atopic dermatitis, allergic skin rash), surgical diseases (trophic ulcers, bedsores, burns), diseases of the locomotor apparatus (sprain, calcaneal spur, bruises and injuries of joints, dislocations, arthroses and arthritises, miozita, sports injuries), pathologies of ENT organs (rhinitis, plays the dandy, tonsillitis, otitis, laryngitis). The modern level of technologies development allows to improve medical equipment. Therefore, the development of medical and diagnostic complexes with a management function of exposure parameters proceeding from physiological characteristics of a bioobject is perspective.

An Infrared (IR) therapy can be performed either by means of warming up of a human in the infrared cabin (sauna) or by local radiation of parts of human body by infrared radiators. The first direction is especially essential in

treatment and rehabilitation: by means of the exposure on the whole human body an activation of metabolic processes, an acceleration of the metabolism in tissue, removal of toxins at the expense of the strengthened sweating are reached.

The majority of modern IR cabins implements a long-wave exposure on human body, thus causing a temperature increase of the upper skin layers, while for a deep tissue warming up they recommend to use short-wave sources of IR radiation. It is also necessary to note that the existing IR cabins have no control system of physiological parameters of a human, not allowing to coordinate a heat strain with an individual functional user state. Overheating of an organism can cause a sudden increase of temperature indicators, pressure, pulse thus imposing restrictions for use of the infrared saunas in case of heart failure, stenocardia, increased arterial blood pressure.

For the purpose of elimination of the above described shortcomings authors have developed an energy efficient mobile infrared cabin for the low-intensive exposure of IR radiation, mainly by a short-wave infrared range, on human body [1]. The device is equipped with a monitoring system of biomedical parameter and parameters of a thermal mode inside the cabin. This monitoring system is a capacious and convenient form to provide information in the course of a IR-therapy.

In order to control the safety and assessment of efficiency of the physico-therapeutic procedure a profile forming of user's biomedical indicators are being carried out during a IR-therapy session.

2 Device Description

The infrared cabin design (Fig. 1) and an automatic control algorithm of operational modes are presented [1–3].

The IR cabin represents a rectangular camera with an entrance door and can be located both in horizontal, and in vertical positions. The most convenient option is the horizontal location. A flap lid is designed for entrance in the

M. M. Mezhennaya (✉) · A. V. Vorobey · V. Y. Drapeza ·
A. N. Osipov · S. K. Dick · M. X.-M. Thostov
Belarusian State University of Informatics and Radioelectronics,
P.Brovky 6, Minsk, 220013, Republic of Belarus
e-mail: mezhennaya@bsuir.by

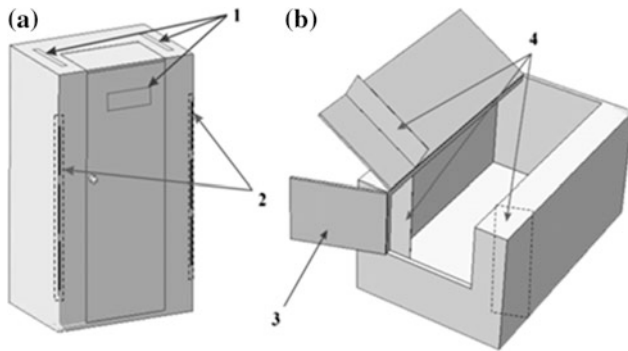


Fig. 1 IR cabin design: vertical location (a), horizontal location (b): 1—ventilating windows, 2—IR radiators, 3—a flap cover, 4—protective reflectors, reflecting IR radiation

horizontally located cabin. Additional air flow is provided by the ventilating windows. Protection against undesirable user's head overheating is realized through the protective reflectors, reflecting IR radiation.

As IR radiators halogen quartz lamps with a maximum emission spectrum in the near infrared range were used (to warm up deep-lying human body tissues) [4, 5].

The device skeleton diagram is provided in Fig. 2 [2].

The IR cabin consists of sensors for registration of user's physiological indicators, thermal mode sensors, an analog-to-digital converter, a transmission data unit, a data reception block, a control panel, an input data device, an information display device, IR radiators, a power supply block of IR radiators..

3 Profile Forming of User's Biomedical Indicators of Infrared Cabin

The infrared therapy methodics with the help of the developed device was resulted in user's location in in the horizontally located infrared cabin. A session time was 20 min. During the procedure directly inside the IR cabin the registration of body temperature in three points was being carried out (on forehead, in armpit, in an abdominal zone), upper and lower blood pressure, user's pulse. After the IR-therapy completion an examinee was left in the IR cabin within 20 min. At this time the registration of body temperature, pulse, upper and lower arterial blood pressure was being carried out (for assessment of the recovery nature of physiological indicators after the completion of a therapeutic session). In its turn before and after the IR-procedure the user's weight had been registered. The air registration inside the IR cabin had also been carried out in two points (in examinee's abdominal and head zone) in dependence on time.

In the software program Excel environment in real time the obtained data were processed and the graphics of the registration of body temperature, pulse, upper and lower pressure were formed—a profile of user's biomedical indicators of the infrared cabin.

8 examinees took part in the studies (7 men, 1 woman, age from 19 to 24 years).

Figures 3, 4, 5 and 6 an example of the resulting temperature indicators, pulse figures, upper and lower pressure of examinee No. 7 is shown.

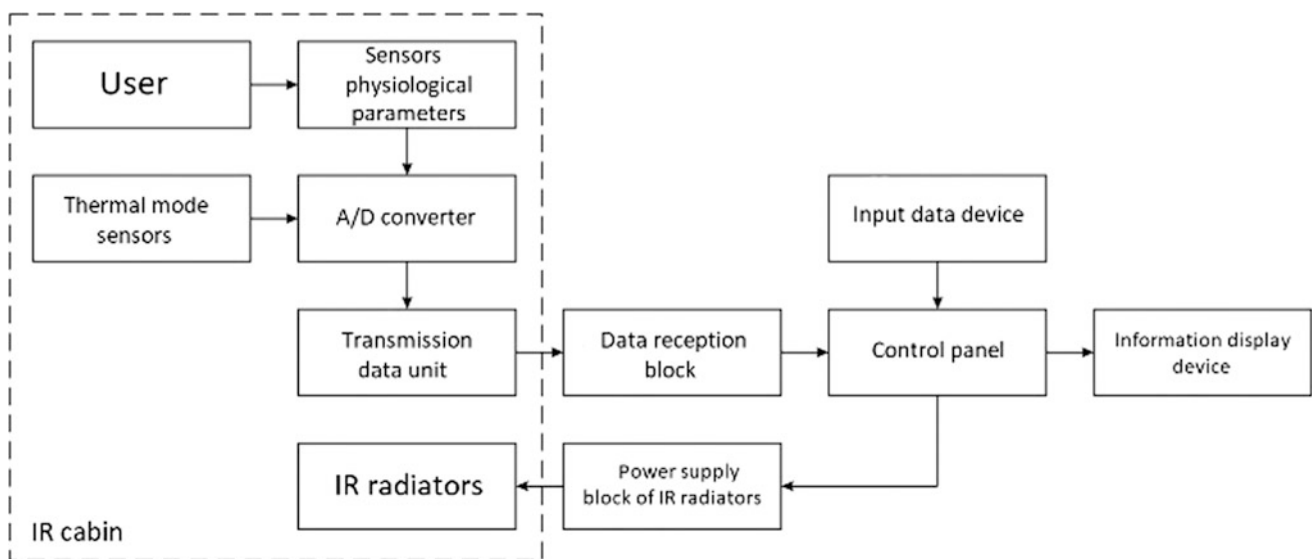


Fig. 2 Infrared cabin design skeleton diagram with automatic control of exposure parameters

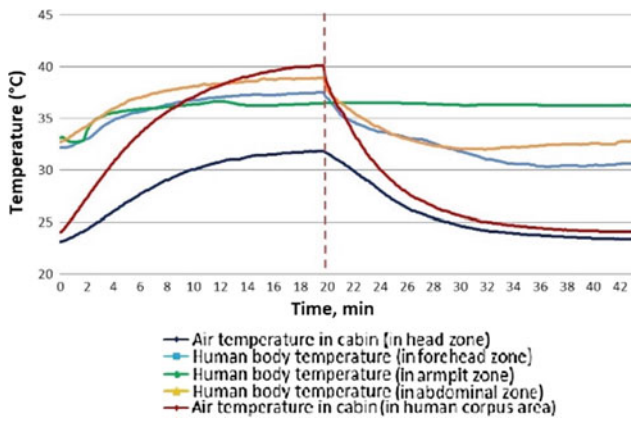


Fig. 3 Dependence of examinee's body temperature and also air temperature in IR cabin depending on time

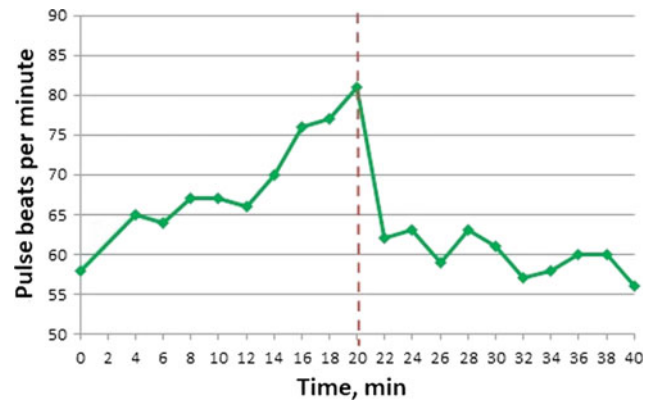


Fig. 6 Dependence of relative change of examinee's pulse at different times

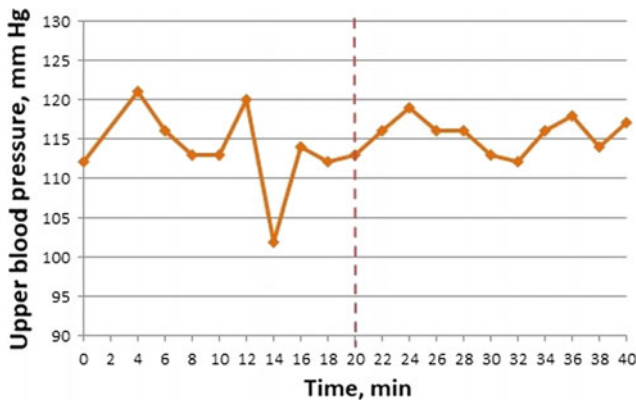


Fig. 4 Dependence of relative change of examinee's upper blood pressure at different times

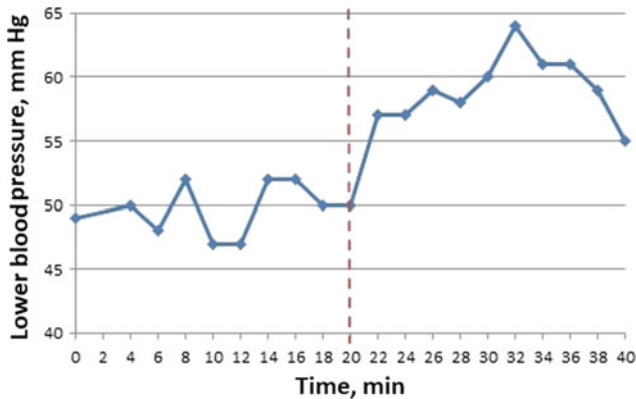


Fig. 5 Dependence of relative change of examinee's lower blood pressure at different times

In Fig. 3 a dependence graphic of examinee's body temperature and also the air temperature in the IR cabin is provided in dependence on time.

The temperature numbers, which are located in three points of examinee's body, are graphically placed between the air temperature curves in the head and abdominal zones, have been increasing during the 20-min IR procedure, and have returned to the original numbers after turning off the IR emitters.

On average after 10 min since the turn on of the infrared cabin the air temperature inside the cabin (in the human corpus area) reaches 37–38 °C. The cabin is being heated; starting from this period the increased heating of examinee's body begins.

After 20 min since the turn on of the infrared cabin the air temperature inside the cabin in the human corpus area reaches 40–42 °C. During this period, the examinee's body temperature in the abdominal zone makes up 38.0–38.8 °C, in the armpit zone—36.4–37.3 °C. The body temperature increase to 38.5 °C imitates a natural organism reaction on infectious processes. At the same time the activation of defense mechanisms and the suppression of pathogenic bacteria and viruses development also happens. After 20 min since the turn on of the infrared cabin the air temperature inside the cabin in the head zone reaches 31–32 °C (due to the protective reflectors on the head level), thus providing head protection from undesirable overheating. During this period, examinee's body temperature in the forehead zone makes up 36.0–37.5 °C.

For dynamics assessment of physiological indicators in order to form the profile relative changes of the upper and lower pressure, pulse at different times were calculated (Figs. 4, 5 and 6). As initial level a number was taken into account that had been recorded before the procedure was started.

After the procedure completion was carried out an analysis of the obtained data that revealed the following regularities.

The upper blood pressure is reduced on average by 1.6 ± 5.19 mm Hg within the 20-min time interval spent in the infrared cabin. Furthermore, it is possible to highlight an examinees' group with a lowering tendency of the upper blood pressure, and an examinees' group with an increasing tendency of the upper blood pressure, finally saying of the allocation of the hypertensive and hypotensive among the population.

The lower blood pressure is reduced on average by $0.7 \div 1.95$ mm Hg within the 20-min time interval spent in the infrared cabin. Furthermore, in the highlighted by the upper pressure (see above) examinees' groups a similar lowering and increasing tendency of blood pressure is observed.

The pulse increases on average by $11.1 \div 6.97$ beats per minute within the 20-min time interval spent in the infrared cabin. The weight was decreased by 160 grams during the procedure.

Figures 7, 8, 9 and 10 the resulting temperature numbers, the pulse, upper and lower pressure numbers, of all the examinees are also listed. Figure 7 shows a graph of dependence of examinees' body temperature as well as the air temperature in the infrared cabin, in dependence on time.

The temperature numbers, which are located at three points of examinee's body, have been increasing during the 20-min IR procedure, and have returned to the original numbers after turning off the IR emitters.

On average after 10 min since the turn on of the infrared cabin the air temperature inside the cabin (in the human corpus zone) reaches 37.5–38.5 °C.

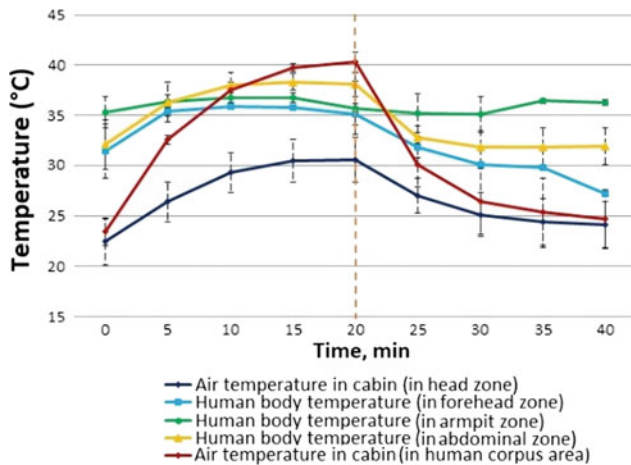


Fig. 7 Dependence of examinees' body temperature as well as air temperature in infrared cabin at different times

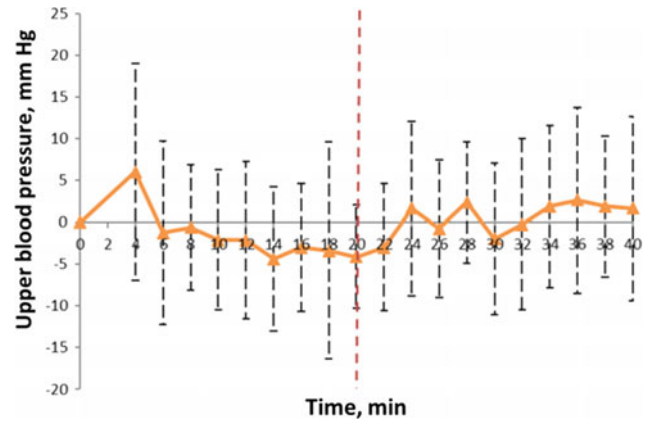


Fig. 8 Dependence of relative change of examinees' upper blood pressure at different times

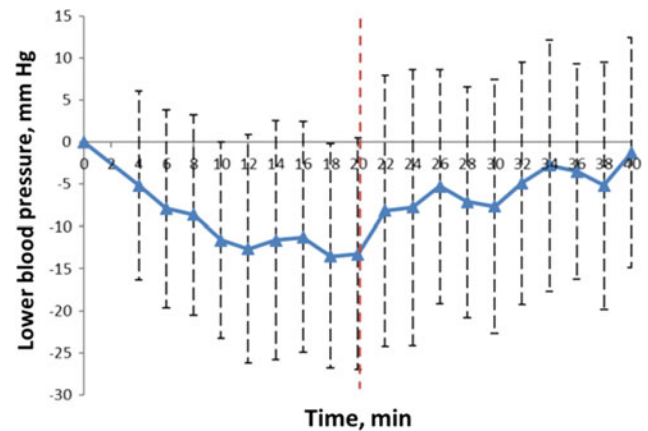


Fig. 9 Dependence of relative change of examinees' lower blood pressure at different times

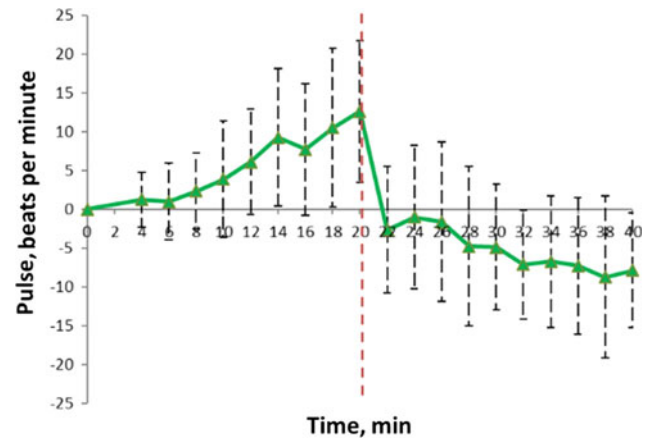


Fig. 10 Dependence of relative change of examinees' pulse at different times

After 20 min since the turn on of the infrared cabin the air temperature inside the cabin in the human corpus zone reaches 40–41.5 °C. Furthermore, the human body temperature in the abdominal zone makes up 38.0–38.5 °C, in the armpit zone—36 to 37 °C.

After 20 min since the turn on of the infrared cabin the air temperature inside the cabin in the head zone reaches 30.5–31.5 °C. Furthermore, the human body temperature in the forehead zone makes up 35.0–37.5 °C.

For profile formation and dynamics assessment of physiological indicators relative changes of the upper and lower pressure, pulse at different times were calculated (Figs. 8, 9 and 10).

After having analyzed the pulse, upper and lower arterial blood pressure data, were identified the following regularities.

The upper blood pressure is being reduced on average by 4.13 ± 6.15 mm Hg within the 20-min time interval of the IR procedure.

The lower blood pressure is being reduced on average by $13.25 \div 13.75$ mm Hg. within the 20-min time interval of the IR procedure.

The pulse is being increased on average by $12.63 \div 9.16$ beats per minute within the 20-min time interval of the IR procedure.

The weight is being decreased by $368 \div 342$ g within the 20-min time interval of the IR procedure.

4 Conclusions

The results performed by the authors of the experiment allow to draw a conclusion about the heat load minimization on the user when conducting the IR therapy by means of the developed device, compared to the same IR cabins [1–3]: the air temperature inside the infrared cabin does not exceed 42 °C in the user's corpus zone and makes up 31–32 °C in the head zone; also at the same time the maximum human body surface tissues temperature makes up 38.8 °C (in the abdominal zone), for pressure numbers, there is the decreasing tendency not increasing.

A positive physiological effect is achieved through the use of sources of near infrared radiation as well as the cabin design features, allowing to reduce the air temperature upon

safety of the heating efficiency. The presence of the protective reflectors and ventilation valves protects the user's head from undesirable overheating. In the end, all that allows to extend the scope of application of such devices by eliminating restrictions on its usage for people with cardiac insufficiency, stenocardia, increased blood pressure.

The profile forming of user's biomedical indicators provides the safety and efficacy of the infrared therapy procedure, as well as a possibility of an individual approach to a thermal load formation on the user during a session.

The authors plan to use the obtained information for matching heat load intensity with user's individual functional state throughout the whole session of the infrared therapy by means of automatic power control of the IR emitters on the basis of monitoring of user's physiological parameters. Also in the future the application of the developed by the authors IR cabin is planned for a multisession (10 sessions) 30-min therapy.

Conflict of Interest The authors declare that they have no conflict of interest.

References

- Osipov, A.N., Thostov, T.M.-H., Mezhenaya, M.M., Kulchitsky, V.A., Davydov, M.V., Kotov, D.A., Stetukevich, N.I., Shevtsov, V. F., Davydova, N.S., Drapeza, V.Y.: Infrared Cabin with a Biotechnical Feedback, vol. 1, No. 120., pp. S169–S170. Official Bulletin/National Center of Intellectual Property, IPC A61H33/06, Pat. 11587 Republic of Belarus
- Mezhenaya, M.M., Osipov, A.N., Drapeza, V.Y., Thostov, M. M.-H., Davydova, N.S., Davydov, M.V.: Algorithm of automatic control of operation modes of the infrared cabin on the results of monitoring physiological parameters of the user. In: Collection of Scientific Papers of the XI International Scientific-Technical Conference "Medelektronika—2018. Means of Medical Electronics and New Medical Technologies", pp. S71–S74. Mn.: BSUIR (2018)
- Drapeza, V.Y., Vorobey, A.V., Stasishina, A.M., Rozum, G.A., Davydov, M.V.: Study of the dynamics of physiological parameters of the user during therapy infrared cabin. In: In: Bogush, V.A., et al. (eds.) Scientific Journal "Reports BSUIR", vol. 7, No. 117, pp. S123–S127. Mn.: BSUIR (2018)
- Издательство: J. Biomed. Opt. 12(4), SPIE—International Society for Optical Engineering (2007). ISSN 10833668
- Ulashchik, V.S.: General Physical Therapy, p. S512. I.V. Book House, Lukomsky, Minsk (2008)

The Algorithms Modernization of Temperature and Gas Control Systems of Ion Mobility Spectrometer

Y. R. Shaltaeva, A. V. Golovin, V. K. Vasilyev, E. A. Gromov, M. A. Matusko, E. K. Malkin, I. A. Ivanov, V. V. Belyakov, and V. S. Pershenkov

Abstract

New algorithms were developed to control the drift region heaters and the gas pumps of ion mobility spectrometer. The efficiency of substances detection was increased. Control algorithm block heaters can improve the accuracy of temperature stabilization in terms of the significant events of the time constants of thermal circuits and high heat capacity elements of the drift region. The improved control algorithm of a block of gas pumps minimizes the duration of the transition process when changing the predetermined level of the engine speed over a wide range. The study and optimization of control algorithms for heaters of the drift region and the gas pump ion mobility spectrometry.

Keywords

Ion mobility spectrometry • Ions • Detection of explosives • Trace detection • Bipolar mode and design

1 Introduction

Ion mobility spectrometry is a rapidly developing method for the analysis of various chemicals in many industries [1]. Interest in ion mobility spectrometry arose with the appearance of the first experimental facilities in the 70 s. However, later on, the initial enthusiasm decreased, as many reactions and behavior of ions at that time were poorly explained. The method revived in the 90 s when progress in

understanding the methods of ion mobility spectrometry coincided with technical progress in the field of spectroscopic data processing with the help of computers. Portable computers that appeared on the mass market contributed to the creation of fundamentally new compact devices that quickly found application in law enforcement agencies and armed forces of different states.

The essence of the method is as follows. Ion mobility spectrometers are widely used for express detection of explosives, narcotics, and poisonous substances. The principle of ion mobility spectrometry is based on the measurement of the time of passage by the ion of a certain distance in a drift chamber in a gas medium at a constant electric field [2] and a given temperature. The peculiarity of the ion mobility spectrometer design is high values of constant time of heat circuits and high heat capacity of drift area elements, which are under high voltage, which limits the possibility of their heating [3] and temperature measurement. At the same time, operational characteristics require that the device has a stable temperature [4], because this determines the accuracy of the determination of mobility, and as a consequence, the identification of the substance under study.

Ion mobility spectrometer is a sophisticated measuring device that takes and analyzes the gas sample from the ambient air. In the operation of the device, it is necessary to change and quickly stabilize the gas flows [5] in a wide range because of the concentration of pump.

This article considers the algorithms of control of the heating system and the control system of gas pumps of the current (classical) variant of the ion mobility spectrometer. The used system of stabilization allows changing the characteristics in the range of $\pm 2\%$ of the stabilization value. This has a negative impact on the accuracy of detection since ion mobility depends on temperature, as well as on detection thresholds since the height of the peaks depends on the concentration of matter in the ionization chamber, determined by the flow through the chamber. Ways to improve the stabilization system are suggested to improve the efficiency and accuracy of the detection of substances.

Y. R. Shaltaeva (✉) · A. V. Golovin · V. K. Vasilyev · E. A. Gromov · M. A. Matusko · E. K. Malkin · I. A. Ivanov · V. V. Belyakov · V. S. Pershenkov
Institute of Nanoengineering in Electronics, Spintronics and Photonics, National Research Nuclear University MEPhI (Moscow Engineering Physics Institute), 31 Kashirskoe shosse, Moscow, Russia
e-mail: shaltaeva@yandex.ru

2 The Algorithm for Stabilizing the Temperature of the Drift Camera

In the classic version of the device [6] temperature stabilization was carried out according to the following algorithm: the controller periodically interrogated the temperature sensors and decided to turn on or off a specific heater based on the results of this analysis. The drift chamber temperature stabilization accuracy was $\pm 3\text{ }^{\circ}\text{C}$ at $100\text{ }^{\circ}\text{C}$. Temperature maintenance accuracy limitations were related to the significant influence of the heat front propagation time from the heater to the temperature sensor and the use of a pulse control algorithm. The thermodynamic processes are in practice simulated as transient processes in the electrical circuit. The electrical circuit, which is a model of a drift chamber, is shown in Fig. 1. The thermal resistance of a drift chamber cell is determined by the thermal conductivity of the electrical insulation. To simulate the heat flow, a heat circuit current source is used.

The result of the new algorithm of temperature stabilization is shown in Fig. 2. These parameters of the control system microcontroller were obtained with the help of the program “STM-studio.”

The microcontroller memory stores the values of the current heating power (green line), maximum (red line), and minimum (blue line) limits.

The temperature graph is analyzed to find the points where the derivative is equal to zero. In the above points (overheating) it turns out that the power is higher than necessary and the maximum limit starts to shift downwards. Conversely, in the lower points (underheating), the power is below the required power, and the minimum boundary shifts upwards. In the process of temperature stabilization, the

algorithm consistently brings together the levels of maximum and minimum limits, which ensures the convergence of temperature values in a relatively narrow range. Besides, the value of the derivative (temperature change rate) is taken into account, and the speed of boundary approximation depends on it. Soon the temperature stabilizes, the process becomes equilibrium; the power takes on values from the nominal range (Fig. 3).

To measure the speed of the gas pumps, the winding changeover signal (Fig. 4) is measured during rotation. In the classic version of the device, the raw signal was analyzed. The absolute minimum (blue line) and the average value (red line) were searched. Then the reference level (violet line) was calculated. This algorithm has several drawbacks associated with the fact that the duration of the signal ejection when switching windings may be short enough and not be registered at the current sample of ADC (analog-to-digital converter). Also, a large RAM buffer in the control microcontroller is required to store the graphics with sufficient resolution.

To solve this problem, the signal integration (green line) is used, and the global minima and maxima on the periodic structure are analyzed, which allows the precise determination of the rotation period.

In the classic version of the device, a simple algorithm was used to stabilize the rotation speed: the actual value of the rotation speed was measured, and the power supplied increased or decreased depending on its value. In the operation of the device, it is necessary to change and quickly stabilize the gas flows in a wide range. A new algorithm for stabilizing the speed of gas pump engines allows you to quickly set the desired level of gas flows. The microcontroller periodically calibrates the actual engine speed and the corresponding voltage level for each pump (Fig. 5).

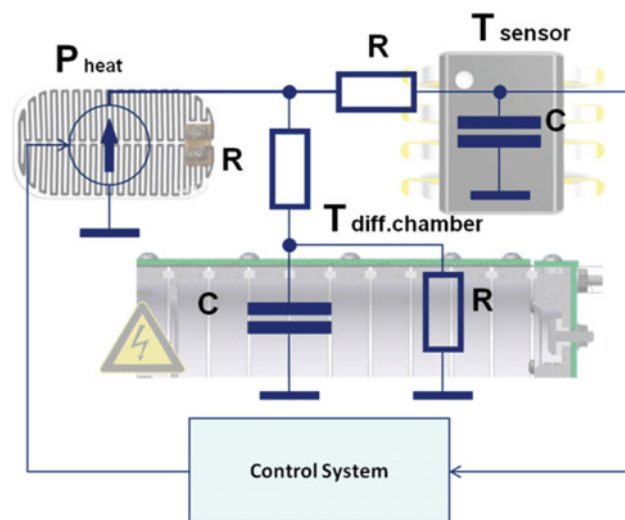


Fig. 1 Thermal circuit of the drift chamber heating

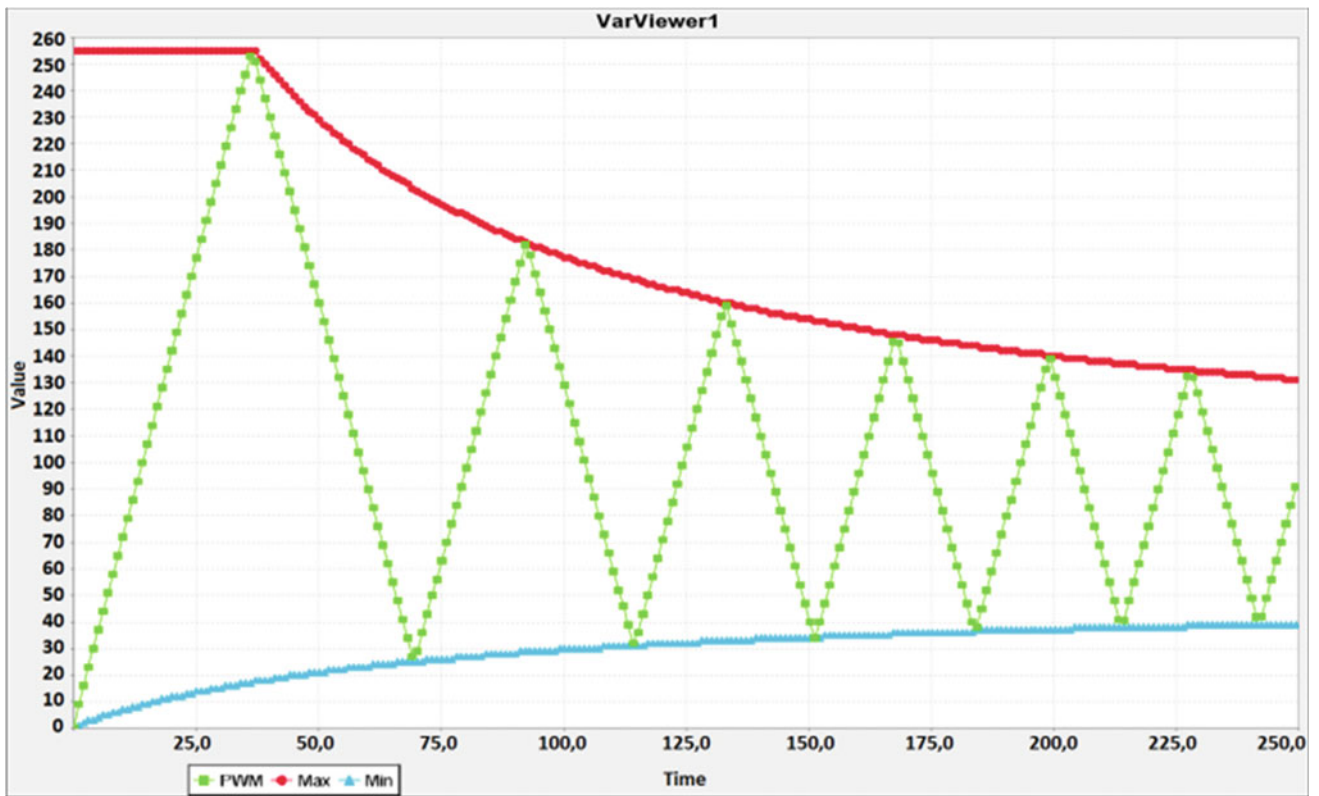


Fig. 2 Power control schedules

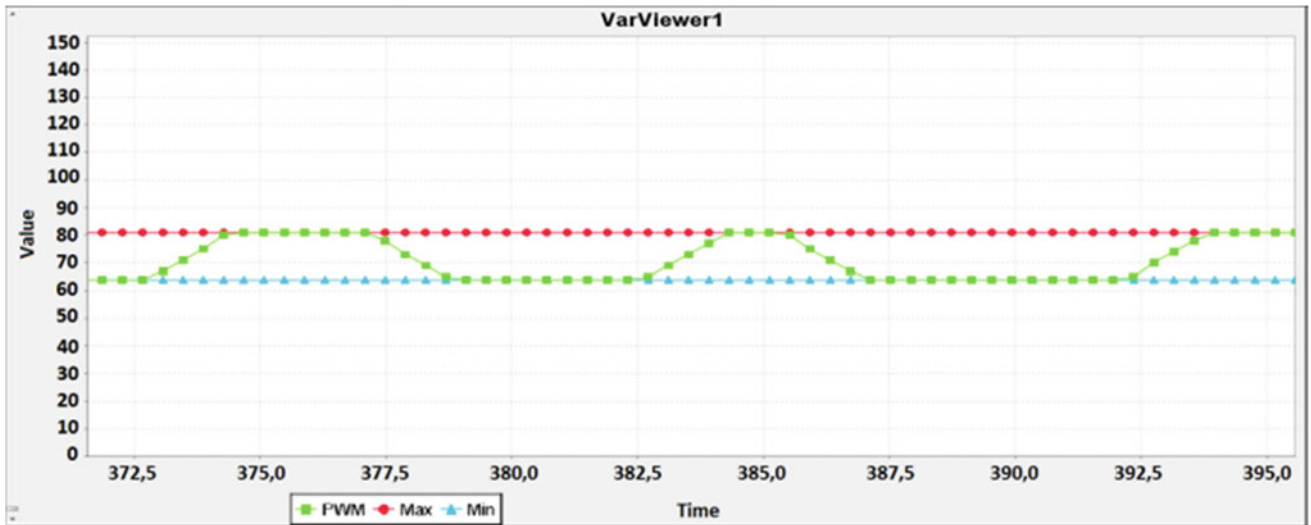


Fig. 3 Gas pump speed stabilization algorithm

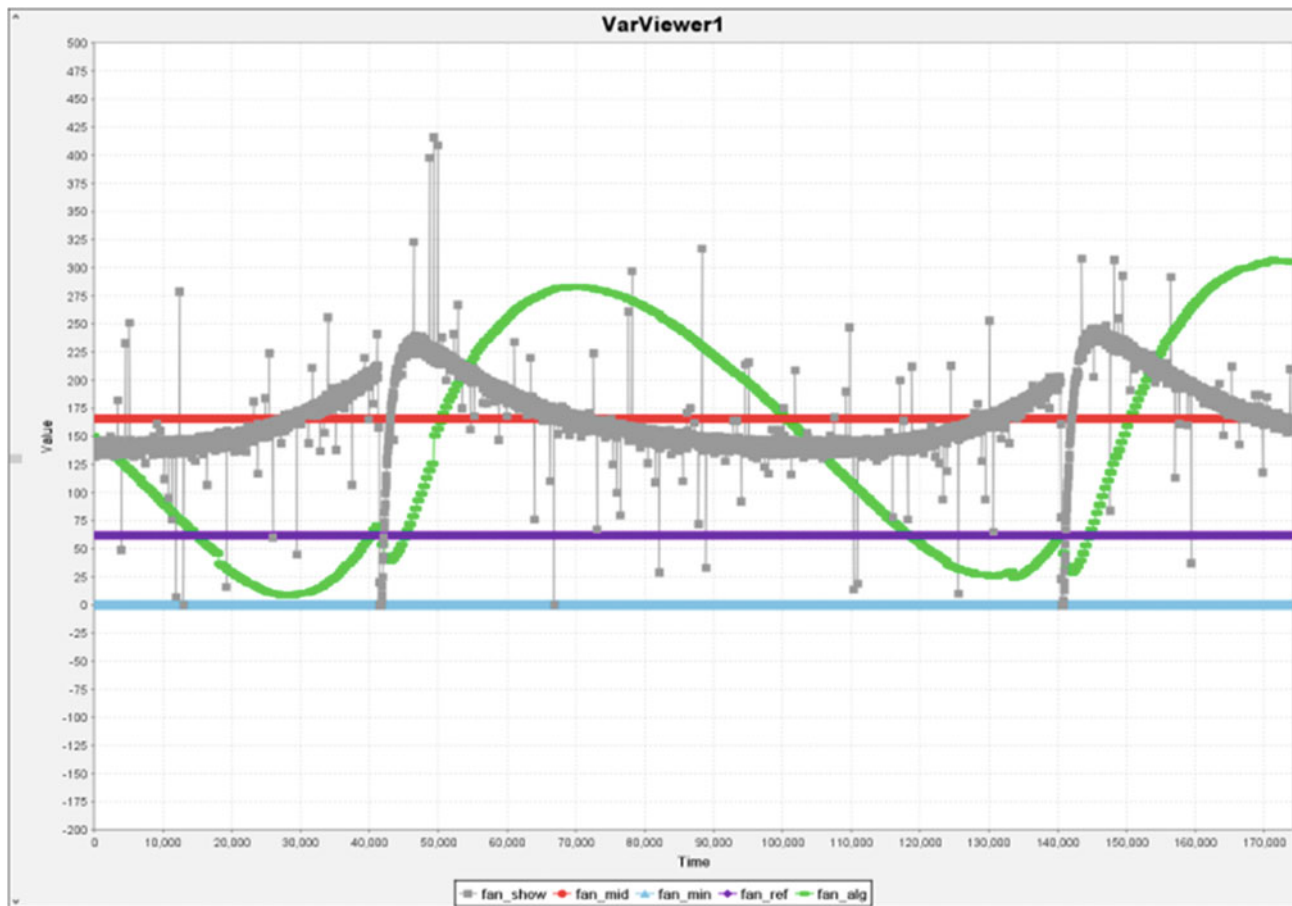


Fig. 4 Gas pump winding switching signal

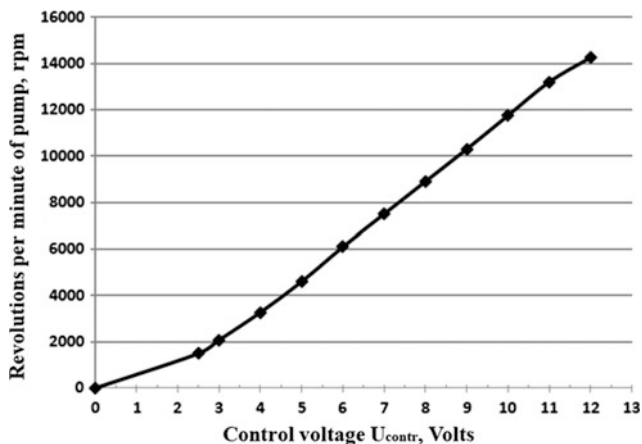


Fig. 5 The dependence of the speed of rotation on the control voltage

This allows you to create a calibration table stored in the RAM memory of the microcontroller, which can be used for pre-installation. The values of the table can be adjusted during operation. This method allows you to stabilize the speed in (2... 3) seconds. Previously (in a classic device) this required about 10 s.

3 Conclusions

As a result of this work, the accuracy of temperature stabilization of the drift area of the ion mobility spectrometer was increased from ± 3 to ± 0.2 °C. The fan speed stabilization time is (2...3) s, which previously required about 10 s.

The control system of the ion mobility spectrometer and the developed algorithms of work have improved a number of parameters of the device and have allowed raising the efficiency of detection of substances.

Conflict of Interest The authors declare that they have no conflict of interest.

References

1. Eiceman G.A., Karpas Z.: Ion Mobility Spectrometry, 2nd edn. CRC Press (2005)
2. Eiceman, G.A., Vandiver, V.J., Chen, T., Rico-Martinez, G.: Electrical parameters in drift tubes for ion mobility spectrometry. *Anal. Instrum*, **18**, 227–242 (1989)

3. Hill, C.A., Thomas, C.L.P.: A pulsed corona discharge switchable high resolution ion mobility spectrometer-mass spectrometer. *Analyst* **128**, 55–60 (2003)
4. Viitanen, A.K., Mattila, T., Mäkelä, J.M., Marjamäki, M., Anttalainen, O., Keskinen, J.: Experimental study of the effect of temperature on ion cluster formation using ion mobility spectrometry. *Atmos. Res.* **90**(2–4), 115–124 (2008)
5. Golovin, A.V., Makarova, N.V., Poturuy, A.A., Belyakov, V.V. Prospects for the use of security air flow to prevent ion-molecule reactions in the ionization and drift zone in classical IMS. In: IOP Conference Series: Materials Science and Engineering, vol. 151, Issue 1 (2016)
6. Vasilyev, V., Pershenkov, V., Belyakov, V.A.O.: Ion mobility spectrometer for rapid simultaneous detection of positive and negative ions. In: IFMBE Proceedings, vol. 55, pp. 515–519 (2016)

An Optimal Path Planning Proposal for Motion Robots with Specific Constraints Applicable in Biomedical Engineering

C. Corciovă, M. Turnea, A. Gheorghită, and D. Arotăriței

Abstract

Optimal path planning for motion robots is an interesting research subject with many applications in various domains including biomedical applications when a mobile robot can distribute medication for patients. A fuzzy environment with object approximated by ellipses is a common situation in terrain applications when a mobile robot must find an optimal route. In some situations, e.g. biomedical applications, some additional constraint related to medical instrumentation impose to find some pathway where a mobile robot must be at an equal distance between the objects in order to have a good balance between possible electrical influences or specific requirements. The results show a feasible solution that can be implemented for predefined routes which must go among a marked set of objects, left and right parts of the mobile robot.

Keywords

Optimal path planning for motion robots • Genetic algorithms with constraints • Biomedical engineering • Computational geometry

1 Introduction

The general problem for motion planning path of a mobile robot is to find an optimal or suboptimal path from a source (start point) to a destination (end point) through a workspace that has obstacles in stationary or moving form. Sometime, additionally constraints can be imposed to trajectory of the

mobile robot, which made the problem more difficult in order to obtain an optimal path.

An optimal path planning for a defined complex cost spaces is proposed by [1]. Two algorithms (T-RRT* and AT-RRT) based on RRT (sampling-based algorithms for path planning) were propose for a framework populated with rectangular-shaped obstacles having as objective the maximization of clearance [1] The algorithms are proved to be asymptotically optimal by Devaurs et al. [1].

A complex algorithm based on higher geometry (λ -geometry) maze routing algorithm is proposed by Jan et al. [2]. The obstacles can be stationary or moving and the mobile robot must find an optimal path with no collision at a constant speed and instantaneous acceleration [2]. A survey about optimal path planning using approaches based on RRT* (Rapidly-exploring Random Tree Star) algorithm in presented in [3].

A generation of path based on growth-based topology optimized (in an explicit form) is proposed by Li et al. [4]. The model is inspired by heat conduction: feasible regions are domains through the heat transfer occur, objects are modeled as thermal insulators, and the start-end is the pair heat source-heat sink [4]. One of the most common constraints is the minimum of the path length between the start point and the goal point. An algorithm for search of near shortest path for mobile robot (NSPMR) is proposed by Nguyen and Le [5]. The algorithm is based on minimization of energy consumption [5].

Evolutionary algorithms and related techniques proved to be a very good solution as an alternative for classical methods and algorithms in many technical (and not only) problems. A multi objective genetic algorithm (GA) was proposed by Xue and Sun [6]. The path is represented by a successive pair of xy points, and the objectives are: and path smoothness, path length and path safety [6].

A multi objective approach based on evolutionary computation of non-Darwinian-type and learnable evolution model (LEM) is proposed by Moradi [7]. A bee's pollen optimization algorithm (BPO) was used for optimal path

C. Corciovă · M. Turnea · A. Gheorghită (✉) · D. Arotăriței
Biomedical Sciences Department, University of Medicine and Pharmacy “Grigore T. Popa”, Universitatii no 16, Iasi, Romania
e-mail: andughe@gmail.com

C. Corciovă
e-mail: calin.corciova@bioinginerie.ro

planning with Pareto solutions in [8]. There are also mixed approaches. In [9], the authors proposed a mixed algorithm, Q-table for path learning initialized with flower pollination algorithm.

Sometime, the algorithm for path optimization can be very sophisticated. Recently a membrane evolutionary artificial potential field was proposed by Orozco-Rosas et al. [10]. This is a hybrid approach that combines three methods: membrane computing evolutionary computation and artificial potential field approach [11]. There are few approaches that can be seen as a path finding with constraint, which is the path, should be at an equal distance from fixed objects modeled by circles [12] and rectangles [13]. Practically it is about fuzzy Voronoi diagrams but the assertions for crisp cases [14–16] can be applicable to motion path planning for a mobile robot.

As application of nonlinear programming (NLP), GAs [17] were extended to GA with constraints, inequality constraints and/or equality constraints [18]. There are various methods to deal with constrains, and among of the most used are: penalty method (static, dynamic, varying) applied to objective function, removing of infeasible individuals, starting with a selected feasible population, dominance concepts, infeasible individuals repairing, preservation of feasibility, and hybrid methods [18]. Depending of application, the results can better for an algorithm that the other algorithm applied to same problem.

2 Material and Method

A common case for a biomedical engineering problem but not only is to find an optimal path for a mobile robot in a predefined space populated with obstacles or objects keeping an equal distance from them between left and right object. In 2D space, the objects can be approximated by slanted ellipses (the circles are treated as degenerated ellipse with both major and minor axes equal) (Fig. 1).

All the calculus is in computational geometry. Let's be an ellipse of center $C(c_x, c_y)$, rotated angle θ , the major semi-axis a and minor semi-axis b . The equation of general parametric is given by:

$$\frac{[(x - c_x) \cdot \cos \theta + (y - c_y) \cdot \sin \theta]^2}{a^2} + \dots + \frac{[(x - c_x) \cdot \sin \theta - (y - c_y) \cdot \cos \theta]^2}{b^2} = 1 \quad (1)$$

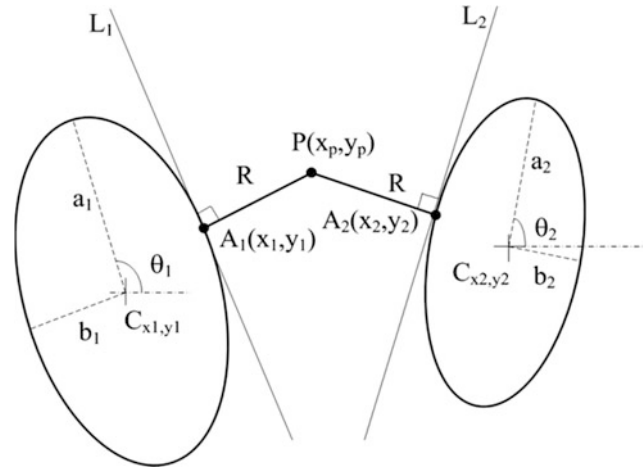


Fig. 1 The construction of geometrical point P at equal distance from two ellipses E_1 and E_2

In a more convenient form:

$$f(x, y) = \frac{[(x - c_x) \cdot \cos \theta + (y - c_y) \cdot \sin \theta]^2}{a^2} + \dots + \frac{[(x - c_x) \cdot \sin \theta - (y - c_y) \cdot \cos \theta]^2}{b^2} - 1 \quad (2)$$

The equation above is obtained from a standard ellipse with center in $O(0,0)$, major semi-axis a on x axis and minor semi-axis b on axis y by rotation with θ angle counter clock wise and translation in a new center $C(c_x, c_y)$. It is known that the rotation and translation keep distances, so the slanted ellipse will keep the same (a, b) parameters.

By differentiating Eq. (2) the slope m of tangent in a point $A(x,y)$ is given by $\partial f / \partial x = 0$:

$$m = -\left(\frac{x}{a^2} \cos \theta - \frac{y}{b^2} \sin \theta\right) / \left(\frac{x}{a^2} \sin \theta - \frac{y}{b^2} \cos \theta\right) \quad (3)$$

The slope of the normal at $A(x, y)$ is given by $m' = -1/m$.

The general form of NLP is formulated as follow:

$$\text{find } X \text{ which optimize } F(X) \quad (4)$$

$$\text{Subject to } g_j(X) \leq 0, j = 1, \dots, m \quad (5)$$

$$h_k(X) = 0, k = 1, \dots, p \quad (6)$$

where X is a n dimensional vector of solutions, $X = (x_1, x_2, \dots, x_n)$, m is the number of inequality constraints and p is the the number of equality constraints. F is denoted the feasible space and S is denoted the entire space.

x_p	y_p	x_1	y_1	x_2	y_2
-------	-------	-------	-------	-------	-------

Fig. 2 The chromosome for a pair of ellipses (E_1, E_2)

In order that the point P to be at equal distance from both two ellipses E_1 and E_2 , the segments $\overline{PA_1} = \overline{PA_2}$, the slopes of line L_1 (tangent to ellipse E_1) must be normal on slope given by a line passing through points P and R, that is $m_{p1} = (y_p - y_1)/(x_p - x_1)$. The same assertions are made for the other ellipse E_2 and the points P and A_2 .

For GA with constraints, a method based on starting with a feasible population modified is proposed. The space-state search is split in a no uniform grid and the trajectory space is located in rectangles with feasible points located inside each rectangle. The chromosome for a pair of ellipses (E_1, E_2) has the form as in Fig. 2 and the optimal path has the for from Fig. 3.

The bounds are set for all the pairs (x_p, y_p) , (x_1, y_1) and (x_2, y_2) . The setting for a grid is showed by geometrical approach in Fig. 4. The oy axis is equally spaced meanwhile the ox axis in limited by bound. The initial population is set as close as possible to feasible solution. The method applied there is practically the “starting with a selected feasible population”. The Darwinian elitism is applied and the rest of operations as in classic Gas: selection (tournament), crossover (one split point) and mutation. The best offspring will survive for next generation and the iterations will continue until stop condition is fulfilled. The maximum numbers of generations or precision for fitness function are usually the stop conditions.

The fitness condition is $\overline{PA_1} = \overline{PA_2} = R$, translated in minimization of a function toward zero (Eq. 4):

$$f_{fitness} = [((x_p - x_1)^2 + (y_p - y_1)^2)^2 - ((x_p - x_1)^2 + \dots + (y_p - y_1)^2)^2] \quad (7)$$

The lower bound (LB_{x_p}, LB_{y_p}) and the upper bound (UB_{x_p}, UB_{y_p}) are functions of type g_j (Eq. 5). The points A_i (x_i, y_i), $i = 1, 2$ are initially set to be between limits of values taken by ellipse. The points A_i must satisfy also equality conditions (to be on ellipse), that is conditions h_k (Eq. 6).

$$h_1 = \frac{[(x_1 - c_{x1}) \cdot \cos \theta_1 + (y_1 - c_{y1}) \cdot \sin \theta_1]^2}{a_1^2} + \dots - \frac{[(x_1 - c_{x1}) \cdot \sin \theta_1 - (y_1 - c_{y1}) \cdot \cos \theta_1]^2}{b_1^2} - 1 \quad (8)$$

$$h_2 = \frac{[(x_2 - c_{x2}) \cdot \cos \theta_2 + (y_2 - c_{y2}) \cdot \sin \theta_2]^2}{a_2^2} + \dots - \frac{[(x_2 - c_{x2}) \cdot \sin \theta_2 - (y_2 - c_{y2}) \cdot \cos \theta_2]^2}{b_2^2} - 1 \quad (9)$$

The equality conditions are included in fitness function by additive operator.

The final trajectory is made by connection of all the points found, one-point P for each feasible F_i domain. The higher is the granularity, the higher is the precision of the trajectory. A higher granularity involves more computational effort so it is preferable to have a tradeoff between the number of feasible domains and the computational effort.

3 Results and Discussion

A grid with $ng = 20$ feasible regions has used for a map with $ne = 10$ ellipses. There are intersection points of curves that describes optimal path situated at equal distances from ellipses, e.g. between E_1 and E_2 , the line with star mark and between E_1 and E_2 , the line with square mark (Fig. 5). In order to find the intersection of paths, each path is approximated by a polynomial of degree seven, with coefficients determines by the best fit for the given points in the LMS (Least Mean Square) approach. The solution is given numerically as by intersection of these two curves given by two polynomials. There will be a single point, selected from all the solution by constrain to be close to a Voronoi point between the three centers of ellipses. There could be other simple solutions also.

For each F_i region, a population with $n = 50$ individuals are selected and six variables must be found ($x_p, y_p, x_1, y_1, x_2, y_2$). The GA with constrains as described in precedent section is applied. The probability of crossover is $p_c = 0.35$, and the probability of mutation is set to $p_m = 0.01$. The selection is based on tournament model and the crossover is made at a single point.

x_{p1}	y_{p1}	*	x_{p2}	y_{p2}	*	...	x_{pq}	y_{pq}	*
----------	----------	---	----------	----------	---	-----	----------	----------	---

Fig. 3 The vector of optimal trajectory. The marker * is for delimitation of points

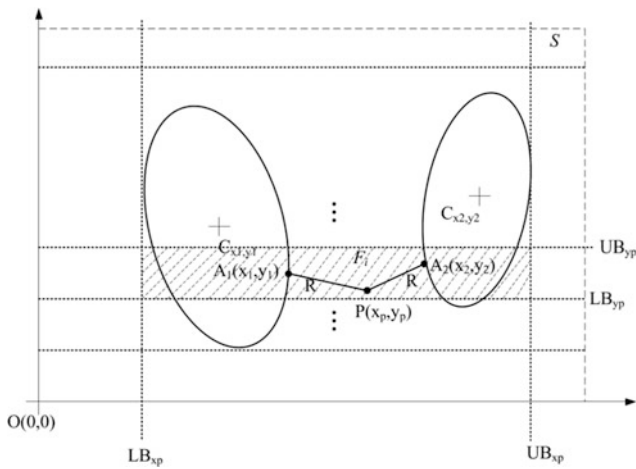


Fig. 4 The grid selection for F_i feasible area in “starting with a selected feasible population”

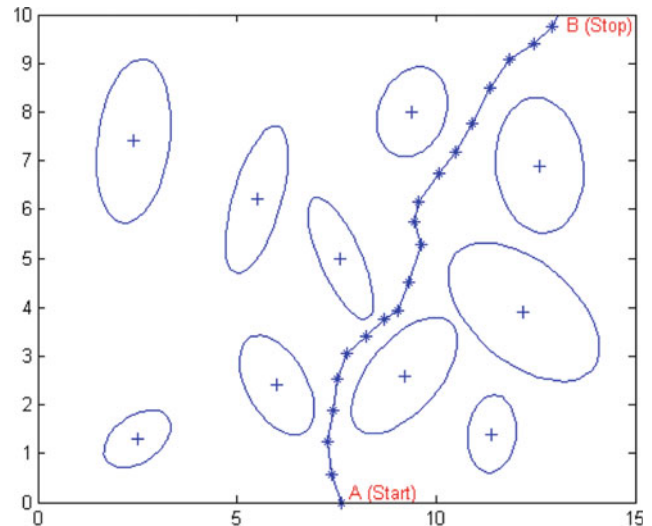


Fig. 6 Optimal path with constraints

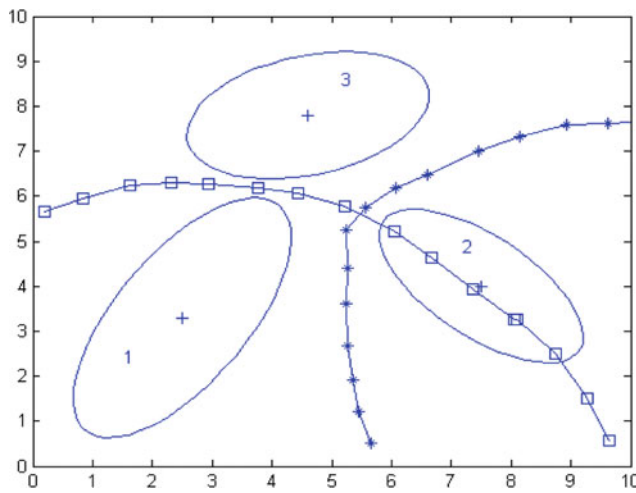


Fig. 5 Intersection of two optimal paths

The start point (A) and the stop point (B) are marked initially along with a path among objects, as pair of ellipses, e.g. $V = ((E_1 - E_2), (E_2, E_3))$.

It is known that the convergence of the solution depend on the initial set. The generation of initial points is made using a uniform probability of distribution. If the population doesn't converge satisfactory, a common approach is to start the algorithm with a new population.

The results for optimal path with constraints are given in Fig. 6. The convergence of the algorithm for the point number three from A (Start) to B (Stop) is given in Fig. 7. The tolerance error become lower that 0.5×10^{-7} after maximum 57 generations, that is a good result.

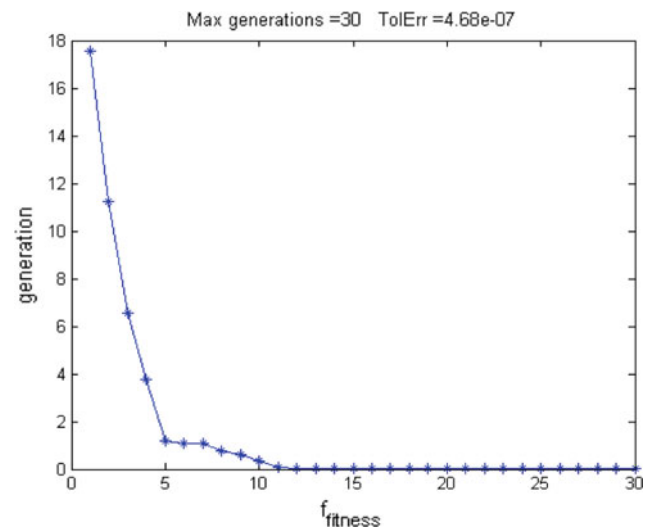


Fig. 7 The convergence og GA with constraints for F_3 feasible region

4 Conclusions

A new application of GA with constraints has been proposed for optimal path with constraints in a framework populated with objects modeled by 2D ellipses.

The results showed a solution numerically feasible; the trajectory is easy to be implemented in a tabular for a mobile robot. The path that are the trajectory of the mobile robot can calculate interpolated points for next step at desired precision of stem using linear-piecewise approximation.

Conflict of Interest The authors declare that they have no conflict of interest.

References

1. Devaurs, D., Simeon, T., Cortés, J.: Optimal path planning in complex cost spaces with sampling-based algorithms. *IEEE Trans. Autom. Sci. Eng. Inst. Electr. Electron. Eng.* **13**(2), 415–424 (2016)
2. Jan, G.E., Chang, K.Y., Parberry, I.: Optimal path planning for mobile robot navigation. *IEEE/ASME Trans. Mechatron.* **31**(4), 451–460 (2008)
3. Noreen, I., Khan, A., Habib, Z.: Optimal path planning using RRT* based approaches: a survey and future directions. *Int. J. Adv. Comput. Sci. Appl. (IJACSA)* **7**(10), 97–107
4. Li, B., Liu, H., Su, W.: Topology optimization techniques for mobile robot path planning. *Appl. Soft Comput.* (2019). <https://doi.org/10.1016/j.asoc.2019.02.044>
5. Nguyen, H.T., Le, H.X.: Path planning and obstacle avoidance approaches for mobile robot. *Int. J. Comput. Sci. Issues (IJCSI)* **13**(4), 1–10 (2016)
6. Xue, Y., Sun, J.-Q.: Solving the path planning problem in mobile robotics with the multi-objective evolutionary algorithm. *Appl. Sci.* **8**(9), 1425 (2018)
7. Moradi, B.: Multi-objective mobile robot path planning problem through learnable evolution model. *J. Exp. Theor. Artif. Intell.* **31**(2), 325–348 (2019)
8. Dao, T.-K., Pan, J.-S., Pan, T.-S., Nguyen, T.-T.: Optimal path planning for motion robots based on bees pollen optimization algorithm. *J. Inf. Telecommun.* **1**(4), 1–16 (2017)
9. Low, E.S., Ong, P.: Solving the optimal path planning of a mobile robot using improved Q-learning. *Robot. Auton. Syst.* **115**, 143–161 (2019)
10. Orozco-Rosas, U., Montiel, O., Sepúlveda, R.: Mobile robot path planning using membrane evolutionary artificial potential field. *Appl. Soft Comput. J.* **77**, 236–251 (2019)
11. Khatib, O.: Real-time obstacle avoidance for manipulators and mobile robots. In: *Proceedings: IEEE International Conference on Robotics and Automation*, vol. 2, pp. 500–505 (1985)
12. Jooyandeh, M., Mohades, A., Mirzakah, M.: Uncertain Voronoi diagram. *Inf. Process. Lett.* **109**, 709–712 (2019)
13. Arotaritei, D., Ionescu, F.: Fuzzy Voronoi diagram for disjoint fuzzy numbers of dimension two. *J. Intell. Fuzzy Syst.: Appl. Eng. Technol.* **26**(3), 1253–1262 (2014)
14. Jin, L., Kim, D., Mu, L., Kim, D.S., Hu, S.M.: A sweepline algorithm for Euclidean Voronoi diagram of circles. *Comput. Aided Des.* **41**, 260–272 (2006)
15. Karavelas M, Yvinec M.: Voronoi diagram of convex objects in the plane. In: *Proceedings of European Symposium on Algorithms, LNCS*, pp. 337–348 (2003)
16. Yap, C.K.: An $O(n \log n)$ algorithm for the Voronoi diagram of a set of simple curve segments. *Discrete Comput. Geom.* **2**, 365–393 (1987)
17. Michalewicz Z (1996) *Genetic Algorithms + Data Structures = Evolution Programs*. Springer
18. Ponsich, A., Azzaro-Pantel, C., Domenech, S., Pibouleau, L.: Constraint handling strategies in genetic algorithms application to optimal batch plant design. *Chem. Eng. Process.* **47**(3), 420–424 (2008)

Intelligent System for Monitoring Vital Signs at Patient's Home

R. Fuior, D. Andrițoi, C. Luca, and C. Corciovă

Abstract

The primary concern in present healthcare systems is increasingly shifting towards chronic diseases. This presents itself with the difficulty to monitor and follow-up a demanding number of patients. Technology development allows to significantly improving the quality of life. The aim of this project is to monitor a number of vital functions while making it accessible for the patients and the care takers. The vital functions of interest were: heart's electrical activity, heart rate, oxygen saturation levels in peripheral blood, arterial blood pressure, temperature and galvanic skin response. In addition, there is the possibility of geo-tracking. The system uses a Healthy Pi board for data acquisition using the Linux operating system. The ECG module is based on an operational amplifier with multiple filtering levels so as to acquire a series of signals corresponding to a physiological graph in one lead which are sent to an Atmega microcontroller. They are forwarded towards the Raspberry Pi platform which compiles and shows it on the attached display. Signal calibration was done using a simulator for ECG testing for physiological and pathological heart conditions (ventricular fibrillation, heart stroke). The pulse-oximetry module determines the oxygen saturation levels in blood, but also helps monitor/compare the peripheral values (upper limbs) of pulse against heart rate according to the ECG. The advantages of this system consist of: efficient, quick data acquisition and storage, remote real time monitoring, friendly user interface, possibility of geo-tracking, accessibility for the patients and care takers.

Keywords

Vital signs • Software • Microcontroller • Calibration
• Heart rate • Arterial blood pressure

R. Fuior · D. Andrițoi · C. Luca · C. Corciovă (✉)
Biomedical Sciences Department, University of Medicine and
Pharmacy “Grigore T. Popa”, Universitatii No. 16, Iasi, Romania
e-mail: calin.corciova@bioinginerie.ro

1 Introduction

According to the latest research, it has been found that a significant number of people die on a monthly basis due to neglect of health. This is due to the constraint of time and the ignoring of health through the increased volume of daily activity [1].

The objective of this project is related to the continuous development of technology and the need for regular health check-ups, which is recommended to be done monthly or quarterly for people with chronic pathologies. It is also obvious that the evolution of technology improves the quality of life [2].

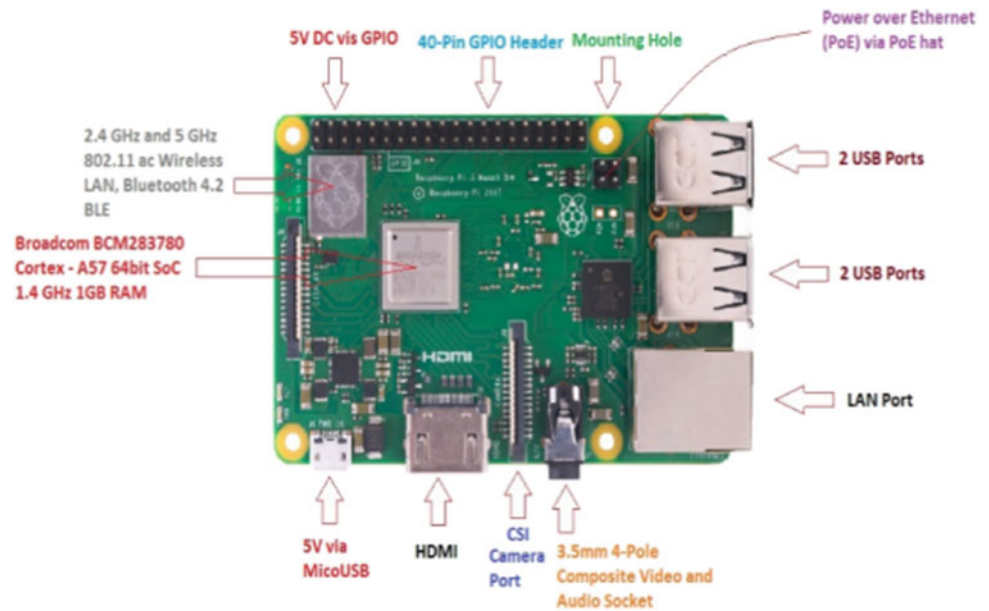
The current project aims to provide healthcare through a complex system of vital function monitoring at home and remotely using the Internet and transmitting it to a specialized data acquisition center [3].

The Healthy Pi based healthcare system offers a solution for measuring body parameters such as ECG, GSR, blood pressure, temperature and pulse. It also detects body condition and patient location. The software application for the patient and doctors contains a very simple graphical interface for reading all the parameters on the mobile phone or anywhere in the world by using internet connectivity [4].

2 Material and Method

Raspberry Pi 3 is a 64-bit quad-core processor at 1.4 GHz, a 2.5 and 5 GHz dual-mode dual-speed processor for much higher data transfer rates for both internet and between other devices. It also has a Bluetooth module to connect to the mobile phone. It feeds at a voltage of 5 V with an approximate consumption of 2.5 A and has 40 digital ports to connect different sensors. Featuring a powerful 4-core processor, it also has 4 USB ports, an audio output, a LAN port, an audio output jack, and an HDMI port that supports up to 1080p resolution (Fig. 1).

Fig. 1 Raspberry Pi—functional diagram



Raspberry Pi runs with the Linux-based operating systems. It is preinstalled with the bootable Linux system to test the platform's functionality, with a high-capacity optional processor; a version of Windows can also be installed if you want to install certain applications that cannot run on Linux.

The ATmega2560 microcontroller on the Arduino Mega design plate has a 5 V operating voltage, but with a voltage stabilizer it can power up to 12 V. It has 54 input and output pins (external connections), 15 pins of PWM (Pulse-Width Modulation), which we can buy/transfer, but also 16 analog pins. It also has 4 UART pins that are generally used to display information on the display. The flash memory is 256 KB, of which 8 KB occupy the boot loader with a 16 MHz operating frequency.

The ECG signal acquisition and amplification part is made by Spark Fun's AD8232. It functions as an operational amplifier that measures the electrical activity of the heart and produces an analog signal at the output. It also contains filters for smoothing and *noise* attenuation that may appear during the measure. AD8232 is designed to extract and amplify low-value biopotentials. [5, 6]

AD8232 I used pins: LO+, LO-, OUTPUT, 3.3 V and GND, the SDN pin will be used to further optimize the device. The exits to the electrodes will be through the ports RL, LA, RA. In the right hand the electrode will be connected to the RA port, the electrode at the LA port is connected to the left hand, and at the RA the left electrode's electrode (Fig. 2) [7].

Fig. 2 Operational amplifier AD8232

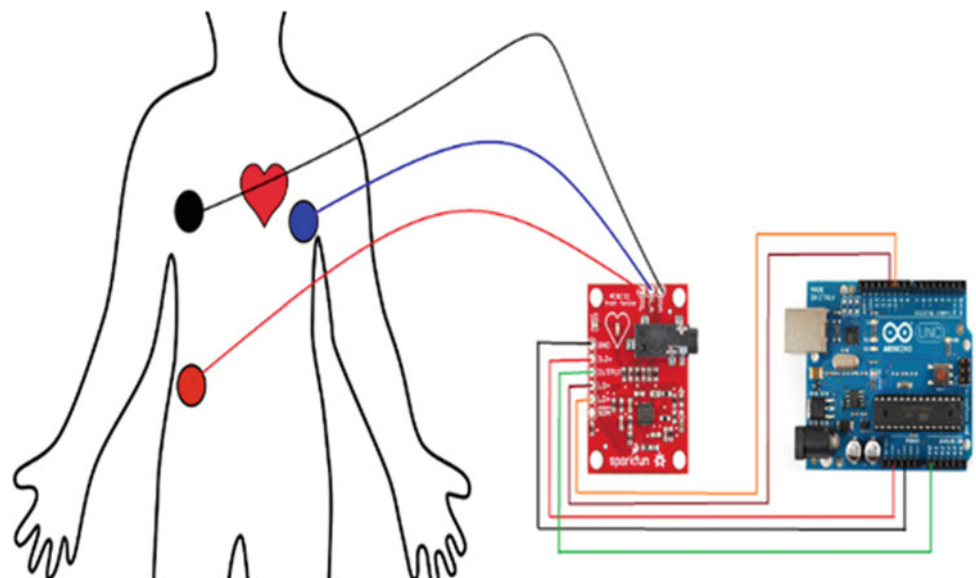
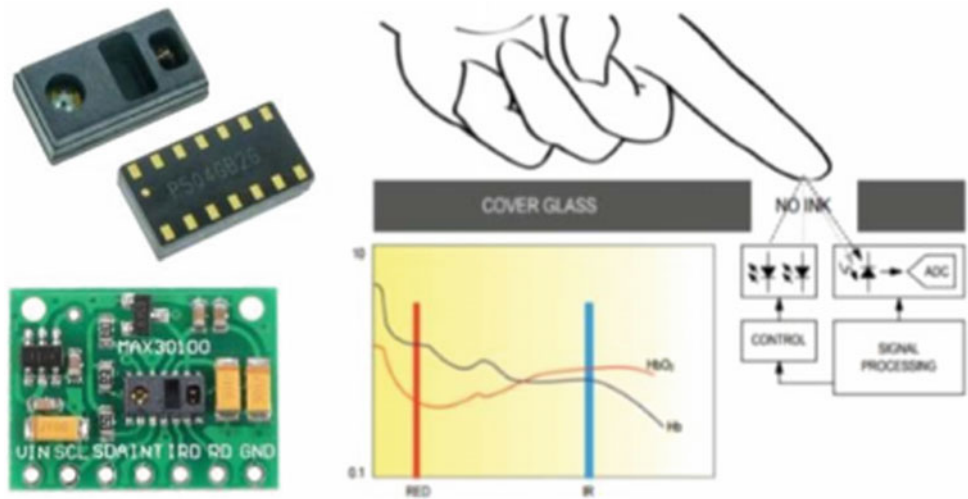


Fig. 3 Max30100—pulse oximeter sensor



The MAX30100 pulse sensor, a plug-and-play sensor, is designed to work with a development board equipped with at least one analogue pin. This product is useful for collecting heartbeat data in different situations, such as during exercise because it is powered at a 5 V low-power voltage (Fig. 3).

The receiving signal from the sensor will connect to port SCL and SDA of the Arduino development platform. At the same time, it can also be placed on the ear lobe or on the finger without damaging the patient's activity (Fig. 4). Pulse monitoring and oximeter is done in real time [8].

The DHT22 sensor is a small, inexpensive and handy temperature sensor. Use a capacitive moisture sensor and a thermistor to measure ambient air and body surface. It can be

placed in the upper limbs, but also in the heart area. It provides a digital signal on the D2 data pin (no analogue pin is needed). It is easy to use, takes care of reading the data, but also interpreting it because it returns two types of values read by the sensor, namely temperature and moisture from the body (Fig. 5).

The GPS module used uses radio waves and satellite navigation to determine the position. It emits satellite signals. The position (latitude, longitude, altitude) is calculated by knowing the position of at least four satellites receiving the GPS signal at different times. Normally, three satellites are sufficient to determine the three coordinates (space position), and the fourth satellite is used to minimize errors.

Fig. 4 The pulse-oximeter sensor wiring diagram

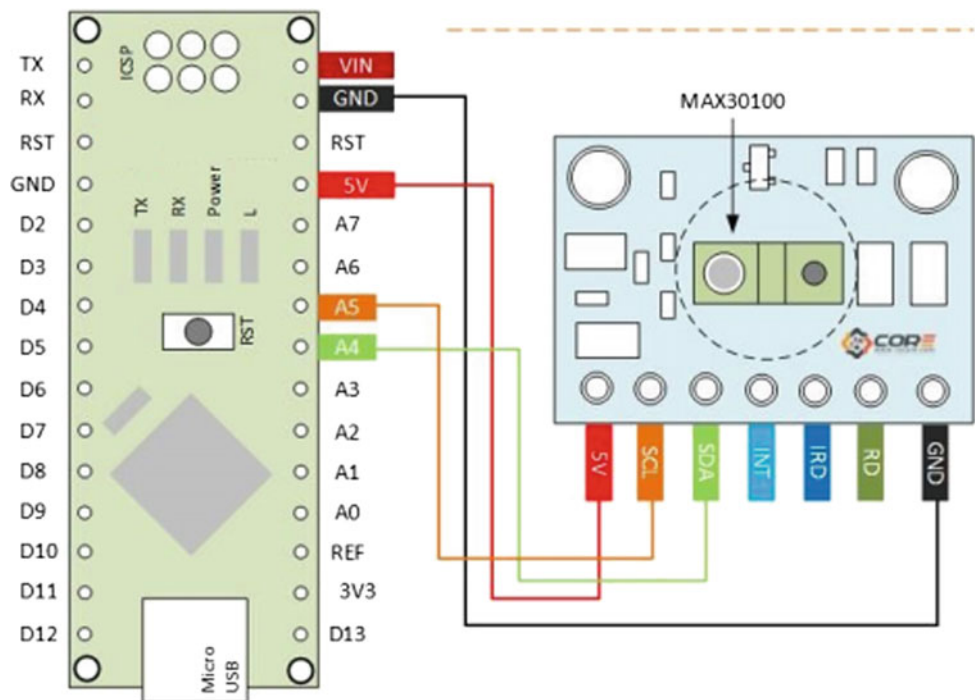


Fig. 5 The temperature sensor DHT22 wiring diagram

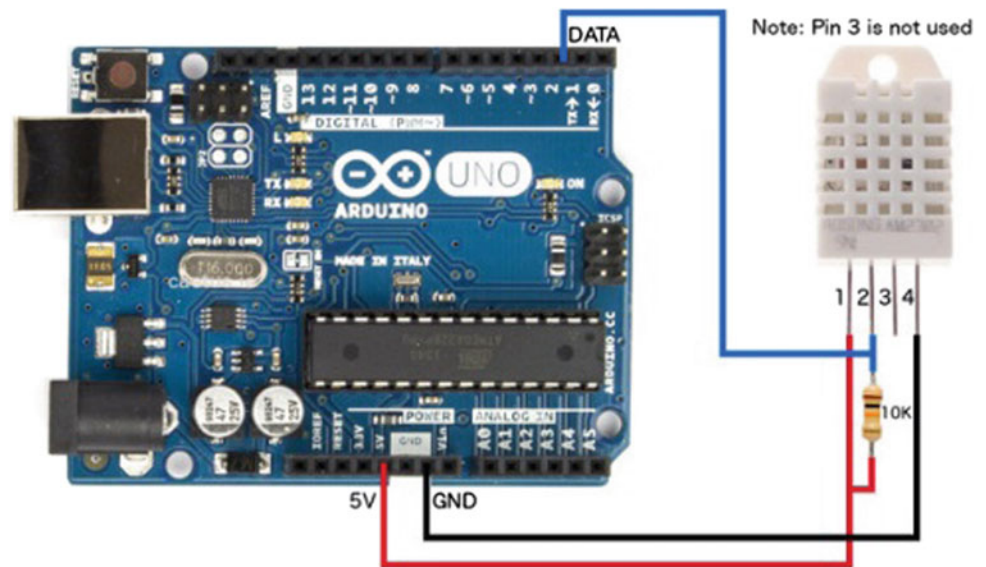
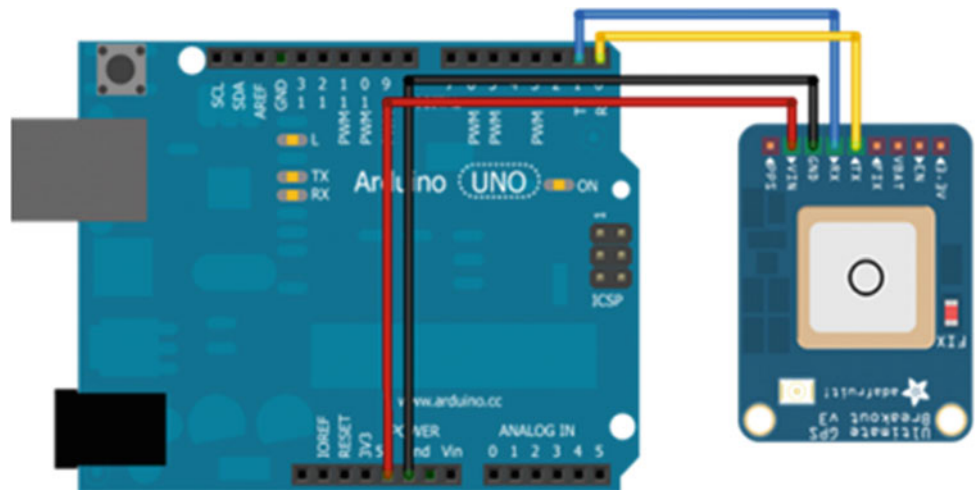


Fig. 6 The GPS module



It communicates via serial transmission of RX and TX ports from the microcontroller, and feeds at a voltage of 5 V (Fig. 6) [7].

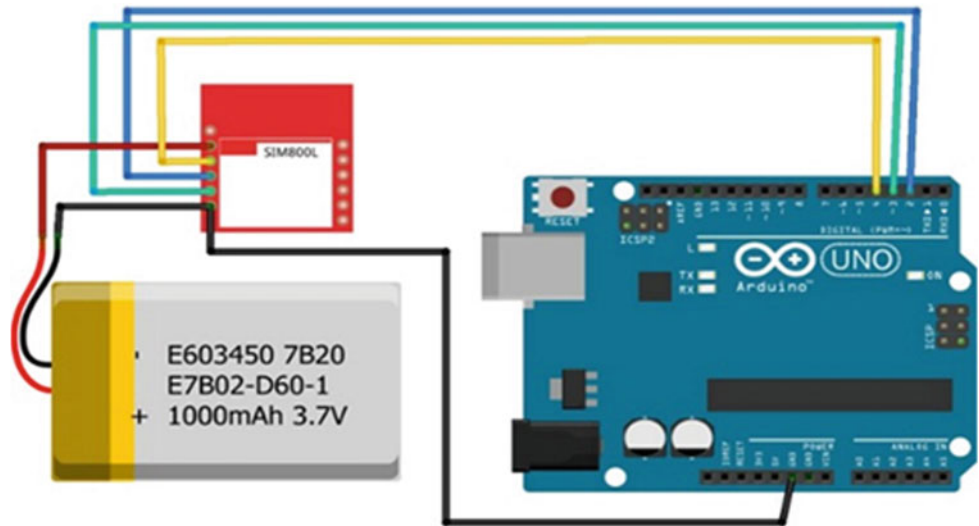
The SIM800L GSM module is powered at a voltage of 3.4–4.4 V and communicates with the Arduino development platform via the serial UART interface. It has the role of having a continuous internet connection of the entire device via the 3G or 4G network, but also sending an emergency message to the emergency service. In the urgent message there is information about the patient's condition and the location provided by the GPS module [9].

The connection of the module is as follows: The VCC pin on the module can be connected to 3.3 V on Arduino either on an external battery or on the GND at the table. The RST port will be linked to D2 to be able to reset the module according to the written program. The RX and TX pin

connected to D3 and D4 are data communication between the Arduino development board and the whole module (Fig. 7). The commands for initializing and verifying the function of the module are made immediately when the whole device is switched on so that if signal connection errors or invalidation of the SIM card are transmitted as a warning message to the patient [7].

The screen used is a touch screen with a 7 “diagonal that is based on a specialized module that connects the Raspberry Pi platform and the display. Having a resolution of 800×480 Requires only two Pi connections are needed; power from Pi's GPIO port and a ribbon cable that connects to the DSI port present on all Raspberry Pi types. Touch screen drivers with 10-finger touch support and a virtual desktop keyboard that can be used when a physical keypad is not connected [10].

Fig. 7 The GSM module and connection configuration



3 Results and Discussion

The source code of the system, in addition to the functions related to the acquisition and processing of biosensors, contains a series of code lines dedicated to the user interface that make the part of the graphics and interpretation of the acquired data (Fig. 8). Once again, one also takes over and processing the physiological signals obtained from the patient. It was desired to obtain a device that does not require complex technical knowledge in use. The graphical interface has been created in its entirety and includes several sub-menus that can access, for example, the record history [3].

When the device is on, it will display the data requested by the attached modules. With auto-run at start-up, the user just needs to wait about a minute until the device is calibrated (Fig. 9). Once the calibration has been successful, it will begin to acquire/record the data. In order to best manage the battery level and battery autonomy when it is only on the battery, the display will go out after about 5 min of inactivity but the data acquisition from the sensors will run in the background [11].

Using the ECG module, we obtained a series of signals that correspond to the physiological graph which are first displayed on the computer through the Processing software to get a better picture and then be shown on the display. This software contains libraries that can process signal processing as it can implement signal processing functions such as Fourier Transform [12].

Calibration of the signal was performed using the Metron PS420 heart simulator to highlight the symptoms and illnesses of a particular cardiac pathology. Such as: ventricular fibrillation, myocardial infarction, these are processed as a

reference by the device, and when such a pathology occurs, it is immediately reported.

The values recorded by the pulse sensor were taken over by the microcontroller and processed using the algorithms to be displayed along with the oxygen saturation calculation. The temperature at which determinations were made ranged from 35.96 to 38.0 °C.

The system designed and built works according to the established requirements. So we've also built design and print a 3D frame. 3D designing was done in Autodesk Fusion 360. It is a discreet, portable device that can be used at home, in the office (Fig. 10).

4 Conclusions

Preliminary results have shown that the device is capable of taking the signals from the attached modules so that we eventually have a complete set of data for the functional evaluation of the patient. Optimization of the device is necessary to achieve accuracy of real-time data but also a patient's safety that can be medically supervised remotely, any alteration of its status being immediately signaled to allow a rapid medical response. The advantages of this system consist of: efficient, quick data acquisition and storage, remote real time monitoring, friendly user interface, possibility of geo-tracking, accessibility for the patients and caretakers [13].

The development of such a system is a wide field of re-search involving medical and engineering knowledge, medical bioengineering being the basis of research in this area of knowledge [14].

```
float height_new = 0;
float inByte = 0;
int BPM = 0;
int beat_old = 0;
float[] beats = new float[500];
int beatIndex;
float threshold = 620.0;
boolean belowThreshold = true;
PFont font;
float temp = 0;

void setup () {

    size(800, 480);

    println(Serial.list());

    myPort = new Serial(this, Serial.list()[2], 9600);
    myPort2 = new Serial(this, Serial.list()[3], 1200);

    myPort.bufferUntil('\n');

    background(0x00);
    font = createFont("Arial", 100, true);
}

void draw () {
    inByte = map(inByte, 0, 1023, 0, height);
    height_new = height - inByte;
```

Fig. 8 Source code



Fig. 9 Graphic user interface

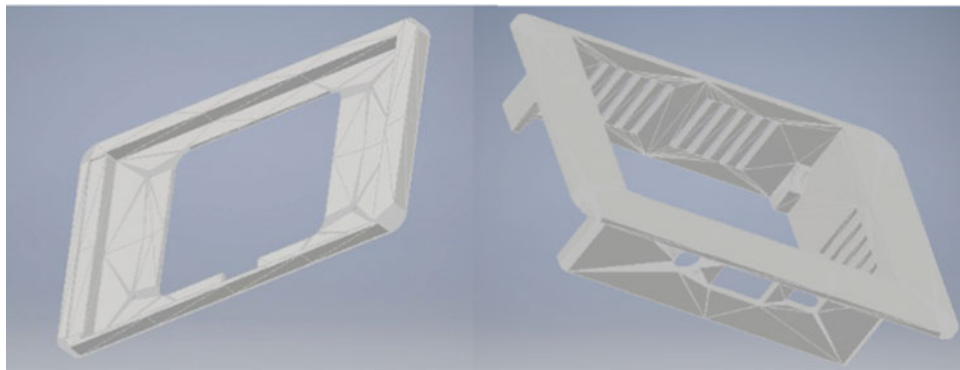


Fig. 10 3D device design project in Fusion 360

References

1. Bovet K.E., Rowland, D.T., Scott, R.C.: Observations on the assessment of cardiac hypertrophy utilizing a chamber partition technique. *Circulation* (2015)
2. Cabrera, E., Gladiola, A.: A critical re-evaluation of systolic and diastolic overloading patterns. *Prog. Cardiovasc. Dis.* (2016)
3. Colombo, A.W., Bangemann, T., Kamouskos, S., Delsing, J., Stluka, P., Harrison, R., Jamees, F., Martnez Lastra, S.L. (eds.): *Industrial Cloud-Based Cyber-Physical Systems, the IMC-AESOP Approach*. Springer, USA (2014)
4. Chan, C.-C., Chen, C.-W., Chou, W.-C., Ho, Y.-L., Haling, Y., Ma, H.-P.: Live demonstration: a mobile ECG healthcare platform. In: *2012 IEEE Biomedical Circuits and Systems Conference (Biomass)*, p. 87 (2012)
5. Gibson, T.C., Miller, S.W., Aretz, T., Hardin, N.J., Weyman, A.E.: Method for estimating right ventricular volume by planes applicable to cross-sectional echocardiography: correlation with angiographic formulas. *Am. J. Cardiol.* (2012)
6. Gao, H.Q., Duan, X.H., Guo, X.Q., Huang, A.P., Jiao, B.L.: Design and tests of a smartphones-based multi-lead ECG monitoring system. In: *35th Annual international conference of the IEEE engineering in medical and biology society (EMBC)* (2013) (in press)
7. ECG: <https://learn.sparkfun.com/tutorials/ad8232-heart-rate-monitor-hookup-guide/understanding-the-ecg>, 2019
8. Max30100: Pulse Oximeter and Heart-Rate Sensor. https://www.maximintegrated.com/en/products/sensors/MAX30100.html/tb_tab0
9. Lau, D.T., Liu, J., Majumdar, S., Nandy, B., St-Hilaire, M., Yang, C.S.: A cloud-based approach for smart facilities management. In: *Proceedings of the 2013 IEEE Conference on Prognostics and Health Management (PHM)*. Gaithersburg, USA (2013)
10. Display 7". <https://www.raspberrypi.org/products/raspberry-pi-touch-display/> (2019)
11. GSM SIM800L: <https://www.optimusdigital.ro/ro/gsm-i-gprs/2019>
12. Xianghan, Z., Wenzhong, G., Guolong, E.: Cloud-based monitoring framework for smart home. In: *Proceedings of the 4th IEEE International Conference on Cloud Computing Technology and Science (CloudCom)*. Taipei, Taiwan (2012)
13. Internet of medical things: a review of recent contributions dealing with cyber-physical systems in medicine. *IEEE J. Mag.* <https://ieeexplore.ieee.org>. Retrieved 23 June 2018
14. Magrassi, P., Berg, T.: A world of smart objects. *Gartner Research Report R-17-2243* (2002)

Bio-behavioral Aspects of Patients with Ocular Problems with Implications for Optometric Comfort

M. I. Baritz, A. M. Lazar, and M. G. Apostoaie

Abstract

The cultural, socio-professional, economic or ideological constraints define and delimit the framework in which human behavior evolves in different situations and which allows the building of a coherent and clear communication system as far as possible. It is therefore important to understand that human subjects are not an image, but that each of them has a reflection of the inner and outer environment to which they relate. In the first part of the paper are presented some general aspects regarding the importance of the optometrist specialist in all stages of interaction with human subjects (information, examination, correction, guidance). The second part of the paper identifies and analyzes a number of important aspects of human bio-behavior in order to establish the coordinates for visual comfort, increase self-esteem or visual aid, where appropriate, in the case of this new profession—optometry developed in Romania. In the final part of the paper are presented the results of this analysis and the conclusions from the processing of the information of a sample of 70 subjects with different parameters for obtaining a more general image related to bio-behavior of patients with ocular problems with implications for the optometric comfort and to find the best solutions for patients.

Keywords

Bio-behavior • Comfort • Self-esteem • Optometry

1 Introduction

Most optometric or ophthalmic medical papers mention the most important aspects of examining the visual function, searching for and identifying solutions for correction, restoration/improvement or visual aid to subjects.

All of these activities are subject to the observance of general principles of observing the rules of experimental research involving a human factor. As it turns out in a series of experimental research on the assurance of behavioral comfort, the personality of a human factor is defined as a unique structure obtained from the combination of genetic parameters, the environmental environment in which it is located and to which is added the educational level acquired by-all of life [1].

All these aspects are focused on the set of components of personal identity that contains three main directions: the cognitive component (the self-concept), the affective component (self-esteem) and the behavioral component (the self-presentation).

The two quantifiable components (cognitive and behavioral) are the objective elements of an analysis related to occupational comfort for the human factor. The affective component, *self-esteem* represents a subjective side that can be evaluated during the interaction of the human subject with the optometrist specialist and which depends on a series of inter-conditional factors. Sometimes this component, by its complexity, is a difficult task to identify, be aware of or be accepted even by the human subject or the optometrist specialist who is looking for all the ways to ensure his visual comfort.

The affective component, *self-esteem* is also a way of modifying human performance in current or professional activities (taking into account all variants—positive or negative) and can induce substantial, temporal and social changes manifested in the daily life. In the specific activities of the optometrist specialist we can find a series of

M. I. Baritz (✉) · A. M. Lazar · M. G. Apostoaie
Product Design, Mechatronics and Environment Department,
Transilvania University from Brasov, B-ul Eroilor, nr. 29, Brasov,
Romania
e-mail: mbaritz@unitbv.ro

connections that are running in the vertical, horizontal or diagonal directions, see Fig. 1.

The way the optometrist specialist interacts with the other partners of the structure is influenced by his experience, the accumulation of knowledge, understanding and communication. In other words, as a human being, every day it becomes more experienced in managing relationships with those around you who have to provide them and provide them with professional and competent activity.

The communication relations represent the mechanism that mediates all interpersonal relations established between employees (optometrists, opticians, doctors), employee–employer (optometrist–manager), employee–client (optometrist, doctor–client). Therefore, it can be appreciated that communication relations have a dual role: information-communication and mutual influence. In the daily action of the optometrist specialist face to face with the subject/patient, self-esteem is identified as a self-sustaining phenomenon. Thus, an optometrist with high self-esteem will act more, realizing several success steps that will value him. If, on the other hand, he is aware of failures his previous self-esteem, which is at a high level, will prevent him from making failures. Instead, the same optometrist specialist but with low self-esteem will hesitate long before launching into professional action. This will immediately affect its actions on the human subject for which optimal solutions are sought in order to ensure the behavioral comfort or correction of its visual function.

As shown in the paper [1] the pillars of self-esteem are: self-confidence, self-conception, self-love. The three components that define self-esteem build relationships and relationships of interdependence, positive in the positive sense as long as they are weighted and applied when needed.

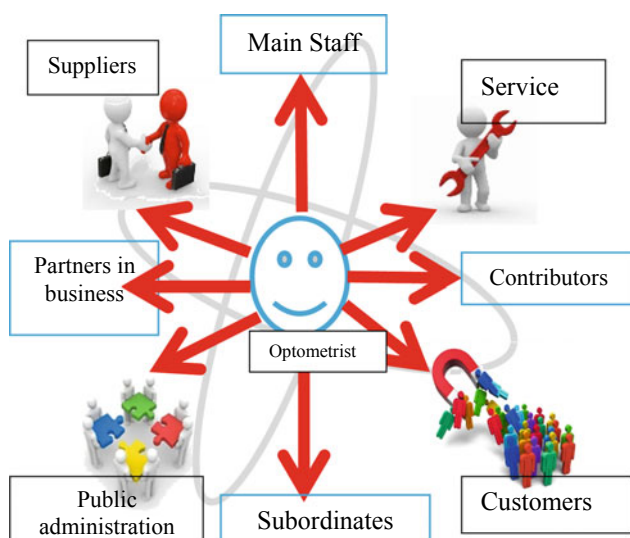


Fig. 1 Optometrist activities structure

One aspect that may be less approached in applied research, regarding the parameters of definition of self-esteem is the degree of their stability correlated with the level and type of self-esteem.

A number of researches have highlighted the need to use permanent learning processes through their cognitive, affective and motivational dimensions in increasing self-esteem [2]. Particularly in the case of a patient with ocular dysfunctions, the learning process associated with understanding and acceptance is supported by a series of parameters in the sensor-motor, mental, intellectual, moral, cultural, affective, social and aesthetic psychomotor levels.

In the case of the optometrist specialist, these levels are complemented by permanent education, which in turn is required by the phenomena of perimetry of professional knowledge, techniques or even discipline in activity, on any post.

The field of optometry, through its technological dynamics and the social impact on the users of specific products, is a rapidly changing, complex and diversified activity area, which makes the optometrists' adaptability process to keep pace and to offer highly qualified specialists to the labor market and with a high level of professional training.

2 Experimental Setup

The purpose of this research is to analyze the influence of age, the environment of origin, gender, and profession, on the level of self-esteem in a procedure of choice and adaptation of contact lenses for the correction of visual impairment. From another point of view, research investigates the link between self-esteem and choice of a correction method for a sample of 70 randomly selected subjects aged between 15 and 60 for both clients in medical optics in the Brasov area as well as in other localities. The tests were applied under the same conditions, respectively, in the same order to all subjects, being presented with the manner of completing the tests, the principle of confidentiality being also mentioned. The investigative methods used in the present research consist in using the SPSS analysis method and the questionnaire survey. The investigative tools used are the test used in an abridged version measuring self-esteem, an observation file (the subject file) and a specific questionnaire. All the subjects provided informed consent prior to the test. The experimental protocol was conducted according to the Declaration of Helsinki [3].

In order to quantify these connections between the evaluation parameters and the level of self-esteem, the following numerical allocations were made:

The age of the subjects: the age between 15 and 20 was given the value of 1, between 20 and 30 years of age 2, 30–

40 years—3, 40–50 years—4, age over 50 years, being assigned a value of 5.

The gender of the subjects (nominal variable): the female gender received the value 1 and the male 2.

The source environment (the nominal variable) of the subjects: the urban environment received the value 1 and the rural one received the value 2.

The subjects' profession (the nominal variable): different values were assigned to the professions that were taken into the analysis.

The studies of the subjects: the average study was assigned the value 1, the general value 2, the professional ones the value 3 and the higher the value 4.

"Diseases of childhood" (measles, rubella, hepatitis, scarlet fever and other illnesses) among the subjects surveyed (the nominal variable): the positive responses were assigned the value 1, 2 being the negative ones.

Refraction vices (myopia, hypermetropia, astigmatism, and presbyopia) among the subjects interviewed (the nominal variable): Positive responses were assigned the value 1, 2 being the negative ones.

Subjects' views on contact lenses (nominal variable): Different values were attributed to the professions that were taken in the analysis.

Subjects looking for eyeglasses (nominal variable): the value 1 was attributed to the wearers, the number 2 of those who claim that the glasses are safer compared to contact lenses, 3 who think they might be uncomfortable, the value of 4 those who claim that they require minimal efforts in use, 5 are those who would like to know more about existing offers, 6 who would use glasses for a change of look, 7 is attributed to those who would use this method of correction in contrast to the other (contact lenses), and those who would not use this correction method have been assigned the value 8.

Self-esteem (the ordinal and numerical variable): First, the gross scores were introduced, so that then the low level of self-esteem was quoted by 1, the average by 2 and the higher by 3.

3 Results and Conclusions

Methods of data analysis of this research included elements of descriptive statistics, comparison tests (difference) for quantitative variables. As elements of the descriptive statistics using the percentage frequency normalized. All of the 70 sample subjects are validated for research, and there are no missing values. Thus, it can be noted that the sample includes 52 female subjects, representing 74.3% of the total interviewed and 18 male subjects, respectively 25.7%. The distribution of the sample of subjects by age group reveals that most subjects are in the interval 20–30 years re-spec 40–50 years (see Fig. 2).

From the point of view of distribution of sample subjects on residential areas, this reveals that an average of 78.57% came from urban areas and only 21.42% from rural areas.

The high percentage of urban subjects indicates the importance of this market segment, the urban environment is a large consumer of resources, characterized by high population density, increased access to information and increased purchasing power compared to rural ones. In a very well developed category as well as consumer proposals, the urban environment offers a variety of information about both the new "trends" in the field and the benefits of the products in question, i.e. the value of their acquisition. The distribution of subjects from the sample chosen for research reveals a high number of students, engineers and administrators who have requested the services of the optician's cabinets, being also in correspondence with the percentages related to the level of education (1% average, 30% general, 8% and 31% higher education). From the point of view of the incidence of refractive vices, it was found that 34.3% had myopia, 15.7% had hyperopia, 10% had astigmatism, and 7.1% had presbyopia manifestations. The total of these variants of ocular dysfunction indicates that not all participants in the research have these ocular problems, and some of them could find combined variants (Fig. 3).

From the analysis of contact lens wearers, participants in the research showed the following: 8.6% of the subjects included in the research believe that contact lenses are discrete, 5.7% consider it awkward, 20% claim to be difficult to use, 12.9% would like to know more about existing offers, 25.7% would use contact lenses for a look of change, 1.4% would use it as a correction method against glasses, and 25.7% would not appeal to them (Fig. 4). By analyzing now the correlated parameters, i.e. age, profession and the option to use contact lenses, most subjects who would use these forms of correction for a change of look come from the respective students and students. Their presence in such a large percentage (44%) demonstrates once again how they choose to implement new technological variants in the field or even to impress and "get out of anonymity." Therefore, in analyzing by occupational categories the way in which they would call for a change of look, it is ascertained that besides the very large percentage of the pupil-student category the other categories are evenly distributed around 5–6%.

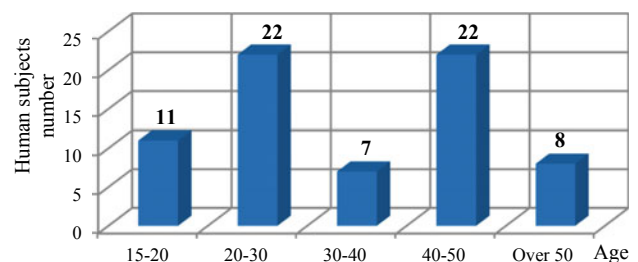


Fig. 2 Distribution based on age

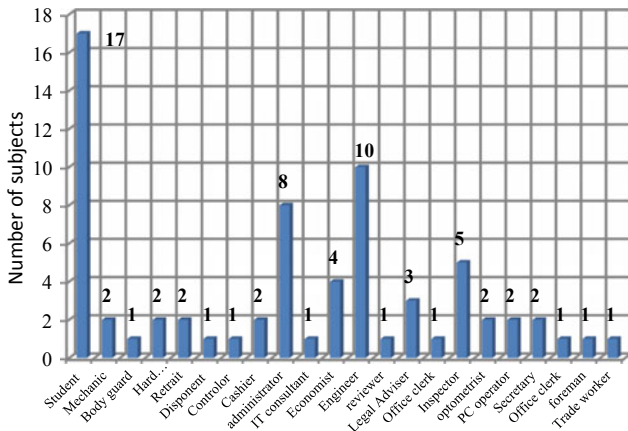


Fig. 3 Distribution based on subjects profession

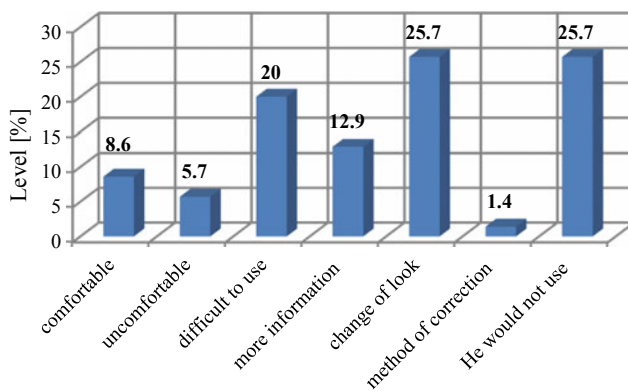


Fig. 4 Distribution based on acceptance level of contact lens

However, from the student to the engineer, from the secretary and to the legal adviser, each of them appeals to this “stratagem” for various reasons. Whether they want to overwhelm, intrude or just make a change, this method seems right. Also in the same context of the change of look is the analysis of the sample in relation to the age, as it is evident that a very high percentage of about 44% of the subjects are aged between 20–30 years.

The professional formation and intellectual training represent, in the same context, another determinant factor evidenced by the percentage of up to 56% of the sample subjects with secondary and higher education.

On the other hand, the subjects in the sample who expressed their opinion and in the situation where they consider the port of the contact lenses to be difficult are 42.4% (6 out of 14 subjects who answered NO) and mostly in the age group 40–50 years old (Fig. 5).

From the viewpoint of glasses we can see that of the total of 70 subjects, 47.1% are glasses, 11.4% think they are safer

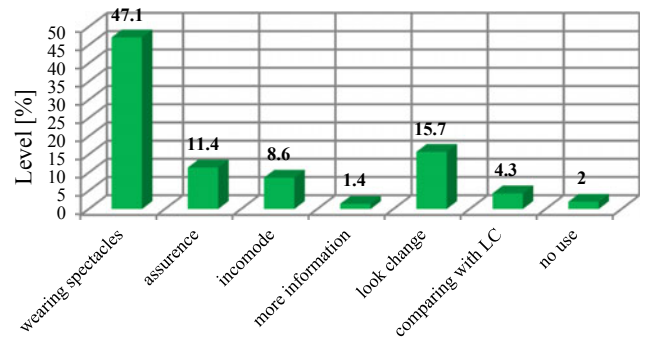


Fig. 5 Distribution based on acceptance level of spectacles



Fig. 6 Levels of coefficient of self-esteem

compared to the other correction method based on contact lenses, 8.6% appreciate that 1.4% would like to know more about existing offers, 15.7% would appeal to them for aesthetic look change, 4.3% would use this correction method to the detriment of the other and only 2% would not call to this correction method. In all cases, patients in the sample were interviewed to define their level of self-esteem in relation to their glasses and/or contact lenses. As shown in Fig. 6, a 1.4% score shows a low self-esteem score (22–27) compared to a 33 (24–33) average score of 33 subjects, i.e. about 47.2%.

The high score (33–41) includes 51.4% of sample subjects with distributions ranging between 5.7 and 12.9%, indicating positive thinking, open to benefit-oriented changes, and also based on a high level of information.

In conclusion the analysis of the level of self-esteem on this sample highlighted the diversity of behaviors and the need for continuous training of optometrists to cope with these new situations current activities.

Acknowledgements In these experiments we’ve developed the investigations with equipment from Applied Optometry Laboratory at University Transylvania of Brasov. **Conflict of Interest** The authors declare that they have no conflict of interest.

References

1. Iurchevici I.: Stima de sine—dimensiunea fundamentală a personalității, *Analele Științifice ale Universității de Stat “B. P. Hasdeu” Din Cahul*, vol. VII (2011)
2. Lepădatu, I.: Psihologia Dezvoltării II. <https://pse-bv.spiruharet.ro/>
3. Donati, M., Cecchi, F., Bonaccorso, F., Branciforte, M., Dario, P., Vitiello, N.: A modular sensorized mat for monitoring infant posture. *Sensors* **14**, 510–531 (2014)

Part VII
Biomedical Signal Processing

Testing the Heart Rate Coherence Function for Detecting and Identifying Atrial Fibrillation

Y. Sokol, P. Shapov, M. Shyshkin, and R. Tomashevskiy

Abstract

Today, one of the main directions in the diagnosis of the heart is the study of long-term registrations and analysis of statistical data of cardintervals (RR-intervals) and amplitudes of various sections of the ECG. However, the processing of a complete cardiogram in real time and its transfer for analysis using wireless communication lines is quite problematic due to the large data volume and high requirements for the processing power of the processing system. The article proposed the method of using coherence functions for a sequence of RR intervals, which make it possible with high accuracy to determine the onset of atrial fibrillation. This type of heart disease is one of the potentially lethal and its occurs mostly hidden. However, atrial fibrillation increases the risk of stroke by 6–8 times. This method does not require the exchange of large amounts of data and can be used in wearable cardiomonitoring devices.

Keywords

Heart rate analysis • Atrial fibrillation • Coherence function • Long-term cardio monitoring

1 Introduction

The prevalence of cardiovascular diseases continues to grow every year, which makes it necessary to develop more effective modern means of their diagnosis and treatment.

The study of new mathematical models and the introduction of more complex, accurate and reliable computer processing algorithms for cardio signals to interpret the results, which give grounds for correct diagnosis, a general

Y. Sokol · P. Shapov · M. Shyshkin (✉) · R. Tomashevskiy
Department of Industrial and Biomedical Electronics, Kharkiv
Polytechnic Institute, National Technical University, 2,
Kyrpychova str., Kharkiv, Ukraine
e-mail: m.shishkin1966@gmail.com

assessment of the human cardiovascular system and the functional class of his disease, are relevant.

Atrial fibrillation (AF) is one of the most common severe cardiac arrhythmias, characterized by uncoordinated electrical activity of the atria and subsequent deterioration of their contractile function [1, 2]. The importance of the problem of AF for cardiology and public health in general lies in the fact that this rhythm disorder leads to a number of complications, among which the most frequent are stroke, heart failure and sudden death [1, 3, 4]. In this regard, the development of informative methods for the early diagnosis of asymptomatic paroxysmal AF is extremely important. Currently, for this purpose, the European Society of Cardiology recommends monitoring ECG of various lengths (from 24 h to several weeks and months) using various equipment (12-channel, 1-3-channel Holter monitors), as well as screening tools. detection of cardiac arrhythmias based on smartphones and other devices [5–7]. Today, however, the problem of early detection of asymptomatic AF at the screening of large population surveys of populations has not been solved. First of all, this is due to the absence in world practice of highly informative methods of automatic detection in real time of this state with a high, pre-planned level of confidence.

2 Literature Review

Currently, one of the main directions in the diagnosis of heart is the study of long-term recording and analysis of statistical data of cardio intervals (RR-interval) and amplitudes of the different sections of the ECG.

The main methods for the study of heart rate variability (HRV) include an assessment of total variability, geometric methods, spectral analysis methods, digital filtering and nonlinear dynamics methods.

Spectral analysis allows you to quantify the different frequency regions of the heart rhythm and identify certain parts of the regulatory mechanism [8, 9].

The most famous example of such a decomposition is the Fourier transform, most often implemented as the fast Fourier transform FFT (Fast Fourier Transform) [10, 11]. Since the cardio signal is non-stationary, the processing of such signals, for example, long-term recordings of Holter monitors, uses the so-called method of spectral-temporal mapping (CRS) [12, 13].

A more modern time-frequency method for analyzing non-stationary signals is the wavelet transform (Wavelet-transform), which is the decomposition of a signal over a set of basis functions that are defined in an interval shorter than the duration of the cardio signal [14]. The advantages of this method include the fact that the multiplication operation by the “window” is contained in the most basic function, and the “window” adapts to the signal as the scale changes.

Despite the potentially large possibilities of using the described methods of analysis, today they are too laborious or insufficiently informative in terms of the effectiveness of the application for complex analysis in real time. In fact, methods of diagnosis used in medical practice are focused on subjective analysis based on the results of post-factum research. In this article, the authors showed the possibility of implementing a model that allows detecting atrial fibrillation solely on the basis of the analysis of sequences of RR intervals and is suitable for continuous online monitoring.

3 Model of Integral Autocoherence of Non-stationary Process

Any processes related to the functioning of the heart and their characteristics (in this case, tachograms) are fundamentally non-stationary, since their probabilistic parameters (average value, dispersion, spectral density, etc.) are not time invariant.

At Fig. 1 typical tachograms of a normal rhythm and with pathology of type AF are presented.

The most important and energetically significant for the processes in Fig. 1 is spectral non-stationarity, the identification of which at local time intervals is an independent problem for both continuous and periodically non-stationary processes. As can be seen, the dispersion and, consequently, the spectrum of the process change significantly at intervals of the AF.

Mathematical models of autocoherence functions, which allow one to detect random modulation of harmonics of periodically non-stationary signals [15–17] at fixed frequencies ω are known. If the non-stationarity frequency ω_0 is known, then for any k -th spectral components associated with the frequency-shifted versions $v(t)$ and $s(t)$ of the original process $x(t)$, you can determine the autocoherence function:

$$\gamma_k(\omega) = \frac{|S_{vs}(\omega)|}{[S_v(\omega) * S_s(\omega)]^{1/2}}, \quad (1)$$

where $S_{vs}(\omega)$ —s the mutual spectral frequency of the processes $v(t)$ and $s(t)$; $S_v(\omega)$, $S_s(\omega)$ —are the spectral power densities of the processes $v(\omega)$ and $s(\omega)$.

The frequency shift $\Delta\omega$ has different signs for versions $v(\omega)$ and $s(\omega)$:

$$\Delta\omega = \pm k \frac{\omega_0}{2} \quad (2)$$

Model (1), in fact, is a mixed second-order cumulant coefficient and characterizes a partial (in k -th harmonic) spectral non stationarity of the initial process $x(t)$.

For integral generalization (in terms of frequency ω and time t), it makes sense to consider parts of the process $x(t)$ localized in a sliding observation window. Such localization impairs the possibility of frequency analysis of the spectral characteristics. However, using the Wavelet transform, the lost information can be recovered (though not completely) thanks to the information about the dynamics of the spectrum over time.

In this case, the wavelet spectrum $W_\xi(a, b)$ [18] of the implementation $\xi(t) \in x(t)$ on the observation interval $T \ll \infty$ can be viewed as a random variable that is correlated not only with the frequency $\omega = a^{-1}$, but also with time $T = b$. If we keep the frequency shift $\Delta\omega$, which provides a constant ratio of the center frequency ω_0 to the width of the frequency window, for any scale values a , then the wavelet transform model will be equivalent to a filter with a constant quality factor [19].

To do this, it is enough to differentiate the process $\xi(t)$, getting a process shifted by a quarter of the period (for each of the corresponding harmonics ω_k):

$$\eta(t) = \frac{d\xi(t)}{dt} \quad (3)$$

We introduce the notation for the spectrums $W_\xi(a, b)$ и $W_\eta(a, b)$ for the processes $\xi(t)$ and $\eta(t)$.

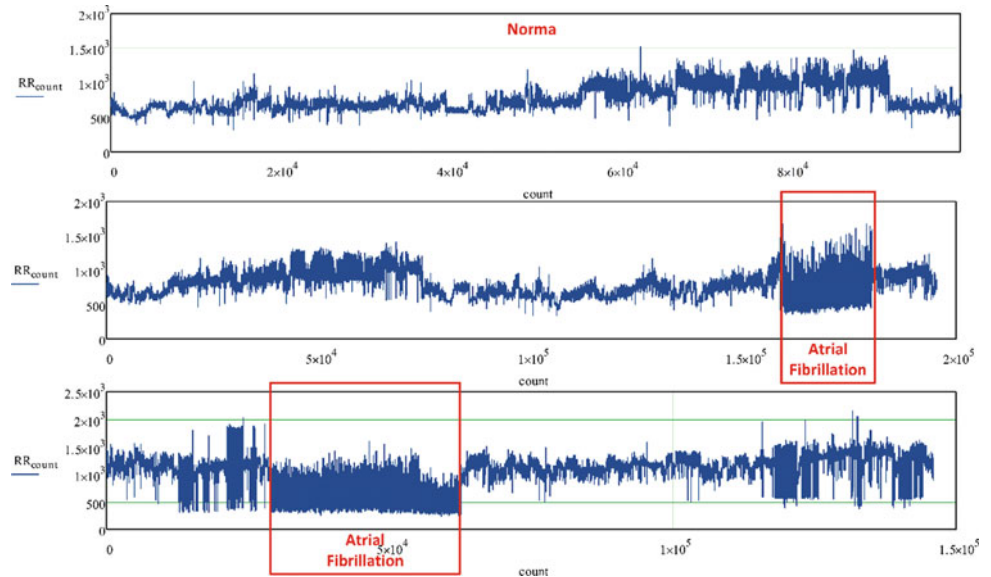
$$\begin{cases} v(\omega_j, t_i) = v_{ji} = W_\xi(a_j, b_i) \\ \zeta(\omega_j, t_i) = \zeta_{ji} = W_\eta(a_j, b_i) \end{cases}, \quad (4)$$

where $j = \overline{1, k}$ (k —number of scales a), $i = \overline{1, n}$ (n —number of shifts b).

We introduce the conditional averages of Wavelet spectrums (4) or fixed frequencies ω_j and time moments t_i :

$$\begin{cases} \overline{v_j} = E[v(\omega_j, t)] \\ \overline{v_i} = E[v(\omega, t_i)] \\ \overline{\zeta_j} = E[\zeta(\omega_j, t)] \\ \overline{\zeta_i} = E[\zeta(\omega, t_i)] \end{cases}, \quad (5)$$

Fig. 1 Tachograms of normal rhythm and rhythms with AF



where $E[\cdot]$ is a sign of the expectation, as a weighted integration operation.

We introduce, also, the common averages of the spectrums (4), as

$$\begin{cases} \bar{v} = E[\bar{v}_j(\omega)] = E[\bar{v}_i(t)] \\ \bar{\zeta} = E[\bar{\zeta}_j(\omega)] = E[\bar{\zeta}_i(t)] \end{cases} \quad (6)$$

Using the model of the variance decomposition [20] of the joint moment of the linear correlation $K_{v\zeta}$ between the Wavelet spectrums v_{ji} and ζ_{ji} , it can be shown, that this moment represents the sum of two components.

For the frequency model of spectral non-stationarity, we will have the following decomposition:

$$\begin{aligned} K_{v\zeta} &= \left(\frac{N-n}{N-1}\right) E[(\bar{v}_j - \bar{v})(\bar{\zeta}_j - \bar{\zeta})] \\ &+ \left(\frac{N-k}{N-1}\right) E[(\bar{v}_{ji} - \bar{v}_j)(\bar{\zeta}_{ji} - \bar{\zeta}_j)] \end{aligned} \quad (7)$$

For the model of spectral non-stationarity in time, we obtain:

$$\begin{aligned} K_{v\zeta} &= \left(\frac{N-k}{N-1}\right) E[(\bar{v}_i - \bar{v})(\bar{\zeta}_i - \bar{\zeta})] \\ &+ \left(\frac{N-n}{N-1}\right) E[(\bar{v}_{ji} - \bar{v}_i)(\bar{\zeta}_{ji} - \bar{\zeta}_i)], \end{aligned} \quad (8)$$

where $N = n * k$.

Expressions (7) and (8) make it possible to obtain measurement information on one of two pairs of particular correlation parameters.

Both pairs are coupled by relation:

$$K_1 + K_2 = K_3 + K_4 = K_{v\zeta}. \quad (9)$$

It is important that the correlation components of any of the pairs are informationally independent (due to the terms of the correlation decomposition). For any of the pairs of expressions (7) and (8), the adequacy of the autocoherece model (1) is preserved.

A distinctive feature of the $K_{v\zeta}$ covariance is the integral nature of the estimated autocoherece due to the operations of averaging the individual correlations separately over frequency and time based on expressions (5) and (6).

At Fig. 2 a tachogram of the development of atrial fibrillation is presented, in which there are both areas of increased rhythm variability that are not a manifestation of arrhythmia and a section of atrial fibrillation.

It also contains the results of calculations (in a sliding window with volume $n_w = 30$) of parameters $K_1 - K_2$ and autocoherece function (1) with shifted versions of the spectral components $v(t)$ and $s(t)$, corresponding to the scales $a = 2$ and $a = 4$.

From Fig. 2 clearly shows, that the parameter K_1 most adequately responds to changes in rhythm, characteristic only for atrial fibrillation.

4 Testing Autocoherece Function

Process K_1 , as follows from Fig. 2 is non-stationary in dispersion. It is obvious that the variance σ_0^2 at the interval,

Fig. 2 Tachogram with areas of increased variability and AF (a); time variations of parameters $K_1 - K_2$ (b, c); auto coherence function (d)

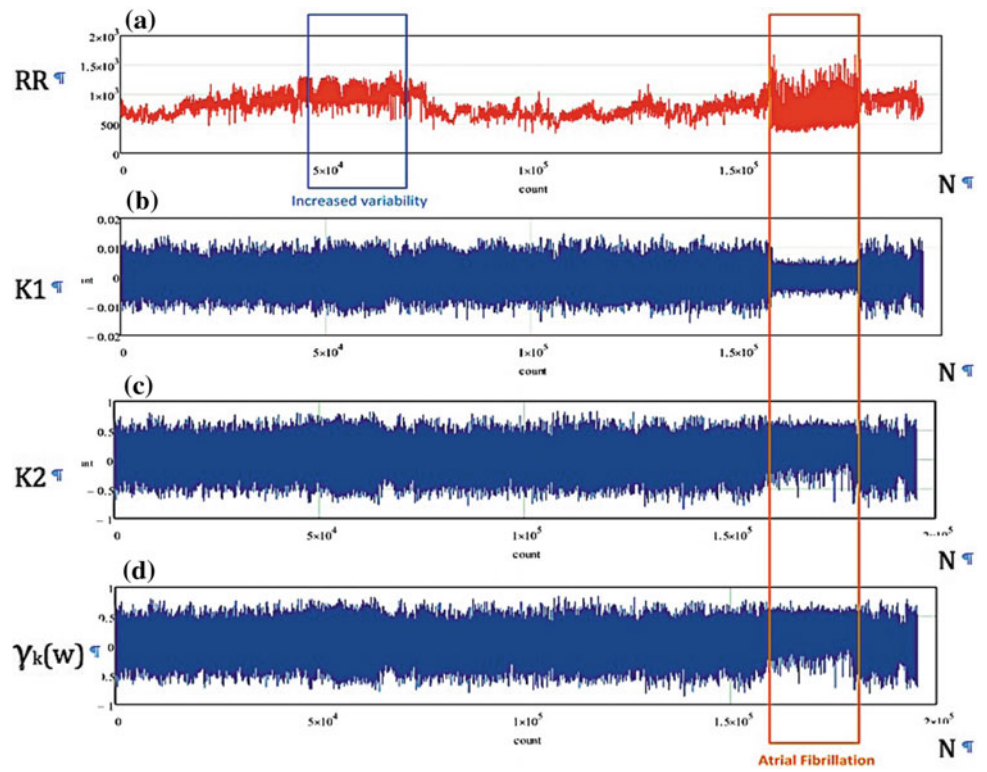
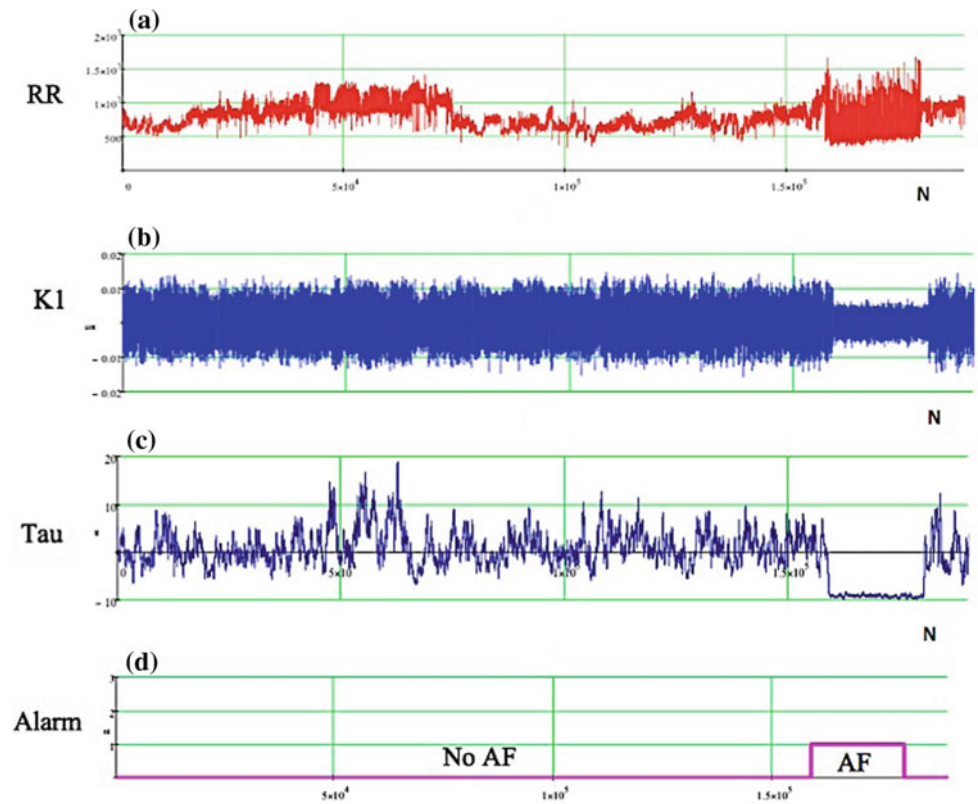


Fig. 3 AF detection procedure. a Original process—RR, b spectral coherence function K_1 , c cumulative function, d alarm function



where AF absence, is much greater than the variance σ_1^2 in the interval of its presence.

To detect changes in the variance, when analyzing the RR intervals in a sliding observation window, classical single-model cumulative T-statistics for the K_1 parameter was used as a function of the conditional shift window time of the observation window:

$$T_n(\hat{t}_j) = \frac{1}{\sqrt{2n}} \sum_{k=1}^{n+j} \left(\frac{\varepsilon_{k+j}^2}{\sigma_0^2} - 1 \right). \quad (10)$$

ε_{k+j}^2 —centered in a sliding observation window value of the process $K_1(w((\hat{t}_j)))$; n —number of measurements in the window; j —number of the sliding window of observation.

If the variance σ_1^2 is known *a priori*, then the conditional the corresponding averages E_0 , E_1 and variances D_0 , D_1 of the statistics T_n are:

$$\begin{cases} E_0 = 0 \\ D_0 = 1 \end{cases} \quad (11)$$

$$\begin{cases} E_1 = \sqrt{\frac{n}{\zeta}} \left(\frac{\sigma_1^2}{\sigma_0^2} - 1 \right) \\ D_1 = \left(\frac{\sigma_1^2}{\sigma_0^2} \right)^4 \end{cases} \quad (12)$$

If E_1 is known, then T_{kp} is most important to find at the risk of type 2 β , which is inversely related to the power of the decision rule [21]. In this case, T_{kp} is determined by the lower $100 * \beta$ —percentage point of the standard normal distribution.

The final use sequence of the proposed method is illustrated by Fig. 3.

This method was tested at 7 patients with AF and give the possibility of increasing the reliability of detection and automatic recording of atrial fibrillation to the level of $P_d > 0.997$.

At the same time, such reliability is ensured for 99 of 100 patients (with a resolution of $\Delta t_j = n/2 = 150$ cardiocycles) with a confidence level of $P_\gamma = 0.99$.

5 Conclusions

1. The information efficiency of using the integrated auto-coherence parameters characterizing changes in the duration of RR intervals when atrial fibrillation occurs is proved.
2. The possibility of using cumulative criteria statistics for sliding testing and detecting changes in the instantaneous power of the integral auto-coherence parameter of the rhythmogram in areas with atrial fibrillation has been proved.

3. The possibility of objective automatic detection of areas with atrial fibrillation in analyzing the sequence of RR intervals at high (more than 0.997) detection accuracy has been statistically proven.

Conflict of Interest Every paper must contain a declaration of conflicts of interest. If there are no such conflicts write “the authors declare that they have no conflict of interest”.

References

1. Kirchhof, P., Benussi, S., Kotecha, D., Ahlsson, A., Atar, D., Casadei, B., Castella, M., Diener, H.-C., Heidbuchel, H., Hendriks, J., Hindricks, G., Manolis, A.S., Oldgren, J., Popescu, B.A., Schotten, U., Putte, B.V., Vardas, P.: ESC scientific document group: ESC guidelines for the management of atrial fibrillation developed in collaboration with EACTS. *Eur. Heart J.* **37**, 2893–2962 (2016). <https://doi.org/10.1093/eurheartj/ehw210>
2. Friberg, L., Bergfeldt, L.: Atrial fibrillation prevalence revisited. *J. Int. Med.* **274**, 461–468 (2013). <https://doi.org/10.1111/joim.12114>
3. Camm, A.J., Corbucci, G., Padeletti, L.: Usefulness of continuous electrocardiographic monitoring for atrial fibrillation. *Am. J. Cardiol.* **110**, 270–276 (2012). <https://doi.org/10.1016/j.amjcard.2012.03.021>
4. Healey, J.S., Connolly, S.J., Gold, M.R., Israel, C.W., Van Gelder, I.C., Capucci, A., Lau, C.P., Fain, E., Yang, S., Bailleur, C., Morillo, C.A., Carlson, M., Themeles, E., Kaufman, E.S., Hohnloser, S.H.: ASSERT investigators. Subclinical atrial fibrillation and the risk of stroke. *N. Engl. J. Med.* **366**, 120–129 (2012). <https://doi.org/10.1056/nejmoa1105575>
5. Mairesse, G.H., Moran, P., Van Gelder, C., Elsner, C., Rosenqvist, M., Mant, J., Banerjee, A., Gorenek, B., Brachmann, J., Varma, N., Glotz de Lima, G., Kalman, J., Claes, N., Lobban, T., Lane, D., Lip, G.Y.H., Boriani, G.: ESC Scientific Document Group. Screening for atrial fibrillation: a European Heart Rhythm Association (EHRA) consensus document endorsed by the Heart Rhythm Society (HRS), Asia Pacific Heart Rhythm Society (APHRS), and Sociedad Latinoamericana de Estimulación Cardíaca y Electrofisiología (SOLAECE). *Europace* **19**(10), 1589–1623 (2017). <https://doi.org/10.1093/europace/eux177>
6. Svennberg, E., Engldahl, J., Al-Khalili, F., Friberg, L., Frykman, V., Rosenqvist, M.: Mass screening for untreated atrial fibrillation. The STROKESTOP study. *Circulation* **131**, 2176–2184 (2015). <https://doi.org/10.1161/CIRCULATIONAHA.114.014343>
7. Copetti, T., Brauchlin, A., Muggler, S., Attinger-Toller, A., Templin, C., Schonrath, F., Hellermann, J.: Accuracy of smart-phone apps for heart rate measurement. *Eur. J. Prev. Cardiol.* **24** (12), 1287–1293 (2017). <https://doi.org/10.1177/2047487317702044journals.sagepub.com/home/ejpc>
8. Surda, J., Lovas, S., Pucik, J., Jus, M.: Spectral properties of ECG signal. In: 17th International Conference. Radioelektronika, 2007, pp. 1–5. Brno, Czech Republic, 24–25 April 2007
9. Murthy, V.K., Grove, T.M., Harvey, G.A., et al.: Clinical usefulness of ECG frequency spectrum analysis. In: Proceedings of the Annual Symposium on Computer Application in Medical Care, 9 Nov 1978, pp. 610–612
10. Bigger, G.T., Fleiss, J.L., Steinman, R.C., et al.: Frequency domain measures of heart rate period variability and mortality after myocardial infarction. *Circulation*. **85**, 164–171 (1992)

11. Himanshu, G., Kedawat, S.: Cardiac arrhythmias detection in an ECG beat signal using fast fourier transform and artificial neural network. *J. Biomed. Sci. Eng.* **4**, 289–296 (2011)
12. Nopadol, U., Sakonthawat, I.: Development of QRS detection using short-time fourier transform based technique. *Comput. Aided Soft Comput. Tech. Imaging Biomed. Appl. (IJCA Special Issue), CASCTP 7–10* (2010)
13. Blaszyk, K., Kulakowski, P., Poloniecki, J., Odemuyiwa, O., Camma, J., Malik, M.: Spectral temporal mapping versus time domain-analysis of the signal averaged electrocardiogram: reproducibility of results. *Eur. Heart J.* **13**, 646 (1992) (Abstract suppl.)
14. Crowe, J.A., Gibson, N.M., Woolfson, M.S., Somekh, M.G.: Wavelet transform as a potential tool for ECG analysis and compression. *J. Biomed. Eng.* **14**(3), 268–272 (1992)
15. Gardner, William A., Napolitano, Antonio, Paura, Luigi: Cyclostationarity: half a century of research. *Sig. Process.* **86**(4), 639–697 (2006). <https://doi.org/10.1016/j.sigpro.2005.06.016>
16. Gardner, W.A.: Exploitation of Spectral Redundancy in Cyclostationary Signals. *IEEE SP Magazine (Signal Processing)*, vol. 8, no. 2, pp. 14–36 (1991). <https://doi.org/10.1109/79.81007>
17. Hurd, H.H.L., Miamme, A.: *Periodically Correlated Random Sequences. Spectral Theory and Practice*, 353 p. Wiley, New Jersey (2007)
18. Merry, R.J.E., Steinbuch, M., van de Molengraft, M.J.G.: *Wavelet Theory and Applications a Literature Study*, 410 p. Department of Mechanical Engineering Control Systems Technology Group, Eindhoven University of Technology (2005)
19. Lee, D.T.L., Yamamoto, A.: *Wavelet Analysis Theory and Application*. Hewlett-Packard Company (1994)
20. Pollard, J.H.: In: J.H. Pollard (ed.) *A Handbook of Numerical and Statistical Techniques*, 344 p. Cambridge University Press, London, New York, Melbourne (1976)
21. Basseville, M., Benveniste, A.: Sequential detection of abrupt changes in spectral characteristics of digital signals. *IEEE Trans. Inf. Theory* **5**, 709–723 (1983)

Dense Array Electroencephalography-Based Electric Source Imaging of Interictal Epileptiform Discharges

S. A. Groppa, D. Ciolac, A. Vataman, and V. Chiosa

Abstract

Electric source imaging (ESI) based on dense array electroencephalography (EEG) is a non-invasive technique for source localization of epileptic activity. However, the diagnostic accuracy of this tool is still debatable. In this study we aimed to investigate the source of epileptiform discharges in a group of epilepsy patients. For this, 20 patients (24.4 ± 8.0 years, 10 males) with drug-resistant focal epilepsy were included. All patients underwent 256-channel EEG recordings and were imaged on a 3T MRI scanner according to a predefined protocol. For spatio-temporal source reconstruction, LORETA (low resolution brain electromagnetic tomography) solution was applied to interictal averaged spikes. Electric sources of epileptiform discharges were detected in all 20 patients. In 18 (90%) patients source localization was concordant with patients' seizure semiology. The most frequent source was identified in the temporal lobe. Dense array EEG is an accurate modality for localization of epileptogenic brain areas in the pre-surgical evaluation of drug-resistant epilepsy patients.

Keywords

Drug-resistant epilepsy • Dense array electroencephalography • Electric source imaging

1 Introduction

Epilepsy is defined as a disease of the brain [1] that affects about 1% of the population or approximately 78 millions people around the world. The epilepsy treatment with antiepileptic drugs has limited effectiveness and 25–30% of patients become drug-resistant [2]. The surgery is the superior option in the treatment of these patients and should be performed as earlier as possible. But in order to perform the surgery it is necessary to accomplish the pre-surgical evaluation of patients with drug-resistant epilepsy for the determination of the epileptogenic zone [3]. This assessment comprises mandatory and optional components. Electrical source imaging (ESI) of interictal epileptiform discharges is an emerging optional non-invasive tool for source reconstruction in drug-resistant epilepsy patients [4].

ESI based on dense array electroencephalography (EEG) is the simultaneous registration of the electric sources of epileptiform discharges with the seizure-generating brain structures as derived either from patient's or template magnetic resonance imaging (MRI). But to render patients seizure freedom after the surgery, the source of patient's epileptic activity should be precisely determined.

In our study we used low resolution brain electromagnetic tomography (LORETA) solution for the source localization of interictal spikes in patients with drug-resistant epilepsy.

2 Materials and Methods

2.1 Participants

We recruited 20 patients with focal epilepsy, who were consulted in the outpatient department of the National Center of Epileptology, Chisinau, Republic of Moldova. The diagnosis of epilepsy was based on clinical and EEG criteria according to International League against Epilepsy

S. A. Groppa (✉) · D. Ciolac · A. Vataman · V. Chiosa
Nicolae Testemițanu State University of Medicine and Pharmacy,
Toma Ciorba 1, Chisinau, Republic of Moldova
e-mail: stgroppa@gmail.com

D. Ciolac
e-mail: dimaciolac@gmail.com

S. A. Groppa · D. Ciolac · A. Vataman
Department of Neurology, Institute of Emergency Medicine,
Chisinau, Republic of Moldova

classification. All participants gave written informed consent prior to the study inclusion.

2.2 Dense Array EEG Acquisition

The interictal dense array EEG recordings was performed at rest and in an alert state for two hours in a dimly lit and quite room as described in [5]. The EEG electrodes were placed according to the international 10/5 system and included in a special net with 20–25 mm interelectrode distance (Hydrogel Geodesic Sensor Net 130, 256 electrodes, Electrical Geodesic, Inc., Eugene, OR) and in reference to anatomical landmarks. The sampling rate of recordings was set to 1000 Hz with low (0.3 Hz) and high (70 Hz) frequency filters. The recorded EEG data were stored using the Net Station 5 software package (Electrical Geodesic). The electrodes' impedance was kept below 10 k Ω .

2.3 MRI Acquisition

All patients were imaged on a 3T MRI scanner (SIEMENS Skyra, Siemens Healthcare) with a 32-channel head coil according to a predetermined Epilepsy protocol used in [6, 7], which comprises 3D T₁-weighted, T₂-weighted and fluid attenuated inversion recovery (FLAIR) sequences.

2.4 Source Reconstruction

The EEG recordings were visually checked and bad channels removed. Interictal spikes in artefact-free epochs (with a duration of ± 500 ms) were manually selected. For each patient at least 20 spikes with similar morphology were marked at the point of maximum negativity. The source localization of interictal spikes was performed by using the LORETA solution [8, 9], which solves the inverse problem by assuming related orientations of neuronal sources and quantifies at each voxel of the grey matter the current density as the linear weighted sum of the scalp electrical potentials [10]. To solve the forward problem we used a template MRI for realistic head model construction (based on finite difference model, FDM). The pipeline of ESI is represented in Fig. 1.

3 Results

3.1 Participants' Characteristics

The mean age of patients was 24.4 ± 8.0 years and mean disease duration was 11.7 ± 7.4 years (Table 1). Seizure semiology varied across the patients, the most predominant type of focal seizures being focal seizures with impaired awareness, mainly due to temporal lobe lesions.

3.2 Neuroimaging Results

Patients presented different structural causes of their focal epilepsy syndromes. Eight (40%) patients displayed imaging signs of hippocampal sclerosis, two (10%) presented with grey matter heterotopia, four (20%) cases of regional gliosis, two (10%) cases of left postsurgical encephalomalacia, one (5%) case of left temporal infiltrative lesion, one (5%) case of right frontal porencephalic cyst and two (10%) cases of normal MRI scans.

3.3 Source Localization Results

Based on dense array EEG, the focal source of discharges was identified in all 20 patients. From ESI analysis we identified only one source of interictal discharges in 17 (85%) patients, two separate sources in two (10%) patients and three sources in one (5%) patient. In seven (35%) cases the source of epileptiform discharges was localized in Brodmann area (BA) 38, in five (25%) patients in BA, in two (10%) cases in BA 25, two (10%) cases in BA 37, one (5%) patient in BA 10, one (5%) in BA 42 and one (5%) in BA 28 (Table 2). Out of 20 patients, in 18 (90%) patients the source was concordant with the presumed epileptic discharges as detected on standard EEG and seizure semiology (Figs. 2 and 3) and in 2 (10%) patients was non-concordant.

4 Discussion

For a successful epilepsy surgery, precise localization of electric sources of the brain's epileptic activity is warranted. Dense array EEG electric source localization is a non-invasive imaging technique that reliably identifies the

Fig. 1 Workflow of the electric source imaging. Left column illustrates the EEG analysis pipeline: selection and averaging of spikes followed by generation of the electric maps (at the rising phase of the averaged spike). Right column illustrates the structural MRI analysis pipeline: segmentation of the brain and grey matter followed by generation of the head model with solution points within the grey matter

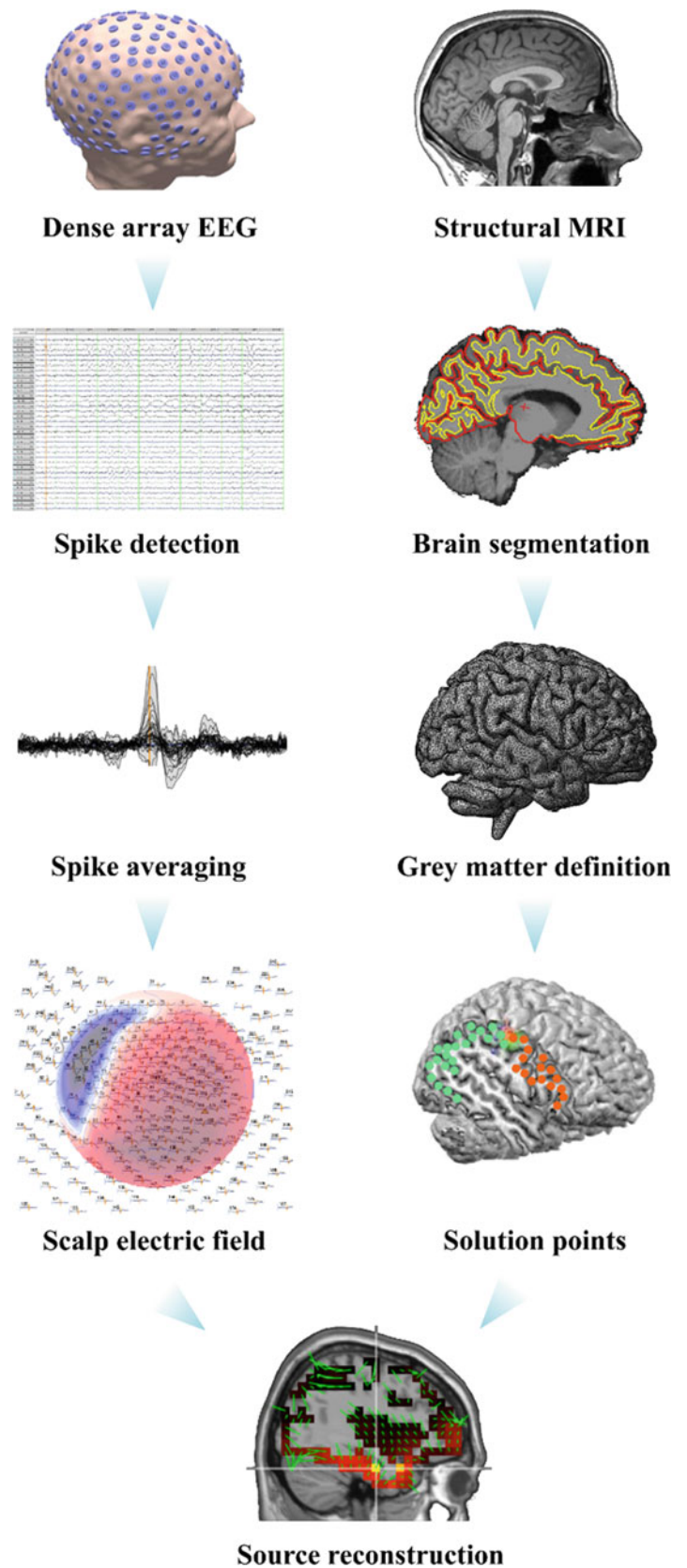


Table 1 Demographic and clinical data of the patients

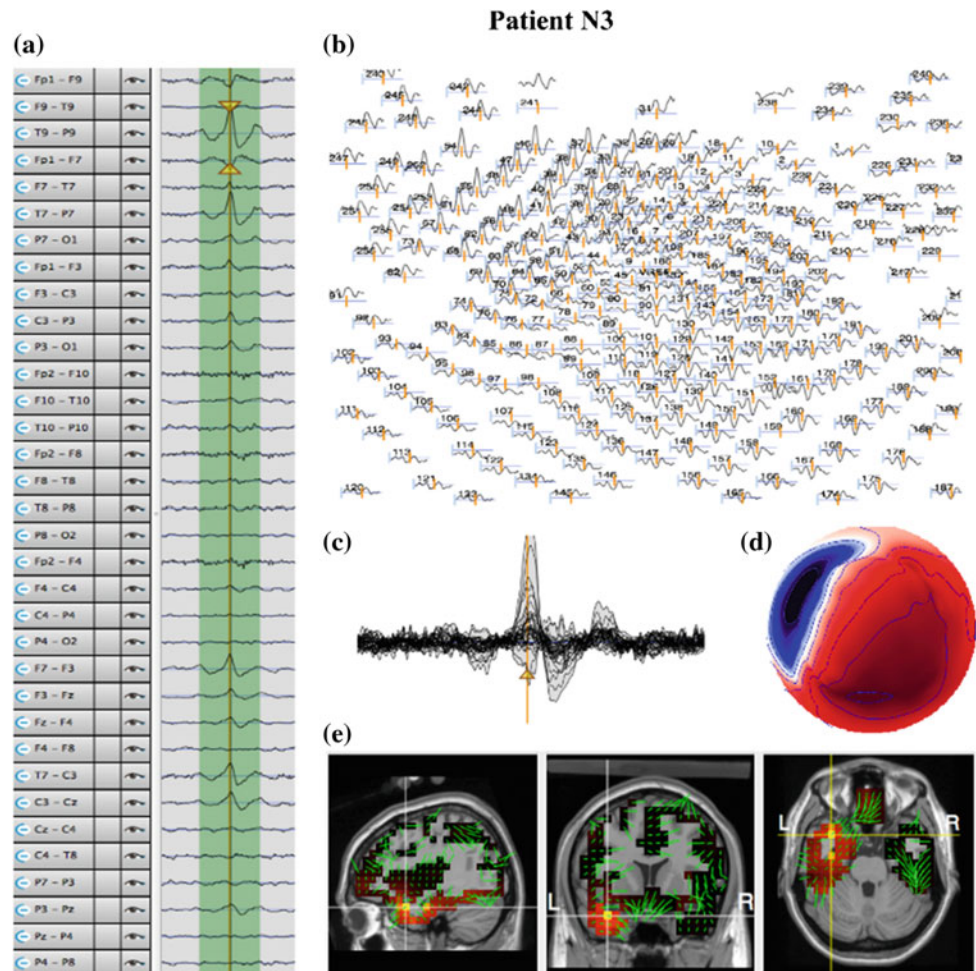
No.	Age	Disease duration	EEG discharges	Antiepileptic drugs
1	22	7	Bilateral F-T	Carbamazepine
2	24	7	Right F-C-T	Lamotrigine
3	14	8	Left F-T	Carbamazepine
4	18	6	Left F-T	Carbamazepine
5	15	13	Left F-C-T	Lamotrigine
6	26	14	Left F-T	Carbamazepine/lamotrigine
7	32	22	Left/right F-T	Carbamazepine/lamotrigine
8	29	17	Left/right F-T	Carbamazepine/lamotrigine
9	32	21	Left F-T	Carbamazepine/levetiracetam
10	22	9	Bilateral P-O	Carbamazepine/levetiracetam
11	27	18	Bilateral F-T	Carbamazepine
12	26	25	Right F-T	Carbamazepine
13	31	24	Bilateral F-T	Carbamazepine/lamotrigine
14	38	3	Right F-C-T	Carbamazepine
15	36	12	Left F-T	Carbamazepine/lamotrigine
16	8	7	Left T	Carbamazepine
17	20	2	Left F-T	Carbamazepine
18	14	3	Left F-T	Carbamazepine/levetiracetam
19	32	14	Left F-T	Carbamazepine
20	23	2	Right F-T	Carbamazepine

Table 2 Results of the 256 channel EEG source localization

No.	Anatomical region	Brodmann area	Concordance
1	Anterior temporal pole	38	Yes
2	Anterior temporal pole	38	Yes
3	Hippocampus	28	Yes
4	Inferior temporal area	20	Yes
5	Temporoparietal area	37	Yes
6	Inferior temporal area	20	Yes
7	Amygdala	25	Yes
8	Inferior temporal area	20	No
9	Inferior temporal area	20	Yes
10	Anterior temporal pole	38	Yes
11	Amygdala	25	Yes
12	Anterior temporal pole	38	Yes
13	Inferior temporal area	20	No
14	Anterior temporal pole	38	Yes
15	Anterior temporal pole	38	Yes
16	Superior temporal gyrus	42	Yes
17	Anterior temporal pole	38	Yes
18	Temporoparietal area	37	Yes
19	Superior frontal gyrus	10	Yes
20	Anterior temporal pole	38	Yes

Fig. 2 Example of correct dense array EEG source localization.

a Segmented interictal spike, **b** topographic waveform plot of 256 EEG channels (common average reference), **c** the average of all selected spikes, **d** topographic map displaying the negative potential in blue color and positive potential in red color and **e** source imaging at the rising phase of the interictal spike with maximum of the estimated source in hippocampus



epileptogenic region. This modality in combination with inverse solution methods has already proved its clinical efficacy in detection of electric sources in patients with intractable epilepsy of temporal as well as extra-temporal origin [4, 10]. In this study we employed LORETA solution for the spatio-temporal source reconstruction of epileptiform activity based on the analysis of interictal spikes in a group of focal epilepsy patients. We were able to localize the sources in all 20 patients but with comparable accuracy, since in two cases we obtained erroneous results, which apparently were non-concordant with patients' clinical profile.

From a methodological point of view electric source imaging consists of a series of steps, whose proper consideration is key for precise localization. The methods aimed for source estimation rely on a theoretical model of propagation of epileptic activity from the brain compartment through skull tissues towards the scalp, which have different conductivity properties [10]. Overall, these methods offer a relatively high diagnostic accuracy. According to a recent systematic review, the accuracy of interictal dense array EEG detection of electric sources for epilepsy surgery

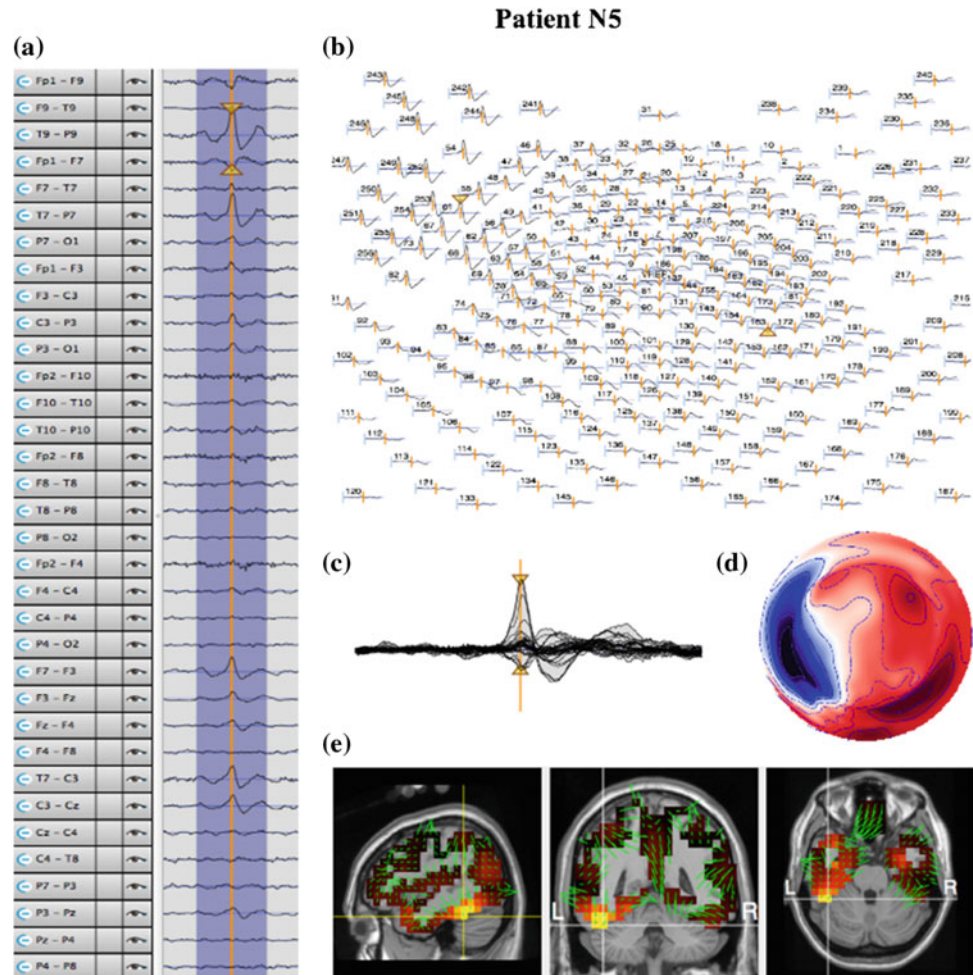
work-up, reaches a sensitivity of 87% (95% CI: 77–93%) and a specificity of 61% (95% CI: 45–74%) [11]. However, in particular cases the existence of constraints inherent to this methodology hinders the use of dense array EEG solely and requires multimodal imaging, frequently invasive ones.

The delimitation of the epileptogenic zone is more accurate when patient's individual MRI but not a brain template (e.g. Montreal Neurological Institute (MNI)) is integrated into the source localization algorithm. This point becomes a substantial issue especially in patients, which have skull or brain defects disturbing tissue conductivity and providing wrong solutions [4]. Here we used the MNI template to construct realistic head models (based on FDM) that is one of our study's limitations.

5 Conclusions

Our findings show that electric source imaging based on dense array scalp EEG is an accurate tool to localize the epileptogenic focus. This technique holds the promise to reduce the need for invasive EEG but we should be

Fig. 3 Example of correct dense array EEG source localization. **a–d** As in Fig. 2. **e** Source imaging at the rising phase of the interictal spike with maximum of the estimated source in temporoparietal junction



confident that at this time point independent diagnostic support from other source localization modalities might be required to proceed to resective surgery in patients with drug-resistant epilepsy.

Acknowledgements We would like to thank all our colleagues who helped us in acquiring and analyzing the data and all our patients who agreed to participate.

Conflict of Interest The authors have no conflict of interest to disclose.

References

1. Fisher, R., Acevedo, C., Arzimanoglou, A., et al.: ILAE official report: a practical clinical definition of epilepsy. *Epilepsia* **55**(4), 475–482 (2014). <https://doi.org/10.1111/epi.12550>
2. Brodie, M., Kwan, P.: Staged approach to epilepsy management. *Neurology* **58**(8 suppl 5), S2–S8 (2002). https://doi.org/10.1212/WNL.58.8_suppl_5.S2
3. Rosenow, F., Lüders, H.: Presurgical evaluation of epilepsy. *Brain* **124**(9), 1683–1700 (2001). <https://doi.org/10.1093/brain/124.9.1683>
4. Brodbeck, V., Spinelli, L., Lascano, A., et al.: Electroencephalographic source imaging: a prospective study of 152 operated epileptic patients. *Brain* **134**(10), 2887–2897 (2011). <https://doi.org/10.1093/brain/awr243>
5. Chiosa, V., Groppa, S., Ciolac, D., et al.: Breakdown of thalamo-cortical connectivity precedes spike generation in focal epilepsies. *Brain Connect.* **7**(5), 309–320 (2017). <https://doi.org/10.1089/brain.2017.0487>
6. Chiosa, V., Ciolac, D., Groppa, S., et al.: Large-scale network architecture and associated structural cortico-subcortical abnormalities in patients with sleep/awake-related seizures. *Sleep* **42**(4) (2019). <https://doi.org/10.1093/sleep/zsz006>
7. Michel, C., Murray, M., Lantz, G., et al.: EEG source imaging. *Clin. Neurophysiol.* **115**(10), 2195–2222 (2004). <https://doi.org/10.1016/j.clinph.2004.06.001>
8. Birot, G., Spinelli, L., Vulliémoz, S., et al.: Head model and electrical source imaging: a study of 38 epileptic patients. *NeuroImage: Clin.* **5**, 77–83 (2014). <https://doi.org/10.1016/j.nicl.2014.06.005>

9. Holmes, M.: Dense array EEG: methodology and new hypothesis on epilepsy syndromes. *Epilepsia* **49**, 3–14 (2008). <https://doi.org/10.1111/j.1528-1167.2008.01505.x>
10. Lascano, A., Vulliemoz, S., Lantz, G., et al.: A review on non-invasive localisation of focal epileptic activity using EEG source imaging. *Epileptologie* **29**, 80–89 (2012)
11. Mouthaan, B., Rados, M., Boon, P., et al.: Diagnostic accuracy of interictal source imaging in presurgical epilepsy evaluation: a systematic review from the E-PILEPSY consortium. *Clin. Neurophysiol.* **130**(5), 845–855 (2019). <https://doi.org/10.1016/j.clinph.2018.12.016>

Cardiorespiratory Coupling: A Review of the Analysis Methods

V. Tonu, V. Vovc, and N. Enache

Abstract

Interaction between cardiovascular and respiratory systems were studied intensively over the last few decades, in order to understand the principles of cardiorespiratory interactions in healthy and non-healthy subjects. Different physiological conditions such as REM sleep, anesthesia, stress, post-stress were used in order to determine and analyze the hidden parameters, that regulate the synchronization between these two integrated physiological systems and their behavior. This paper aims to review the most common methods of analysis of the cardiorespiratory coupling and their capacity to provide additional information for diagnosis and prognosis in medicine.

Keywords

Cardiovascular coupling • Synchronization • Symbolization • Causality • Entropy • Phase transition • Non-linear interactions

1 Introduction

Cardiovascular disease remains the leading cause of death worldwide, although over the past two decades the cardiovascular mortality rate has been reduced in many high-income countries [1]. However, our current understanding of the dynamics of this system and the interaction with breathing is very limited. This is partly due to the fact that there are many different mechanisms that help to control circulation, and direct measurements of the sizes involved in

the cardiovascular system control are very difficult or even impossible. Therefore, we will have to work with hidden or partially hidden variables, and it is desirable to have a model that correlates the “hidden” variables with easily measurable data, such as heart rate variability (HRV) and breathing [2].

Analyzing the synchronization of heart rate variability and respiratory cycles as well as complex heart rate analysis and whether these are simply a consequence of human behavior, such as physical activity or sleep, are just a few of the issues investigated [3, 4]. Recent observational studies have suggested that some indicators describing nonlinear cardiac pace dynamics such as fractal scatter exponents [5], cardiac rhythm turbulence and deceleration may provide useful prognostic information in different clinical settings, and their reproducibility may be better than that of traditional parameters [6]. The disorders of the physiological interaction of these two systems are the cause of many dysfunctions and pathologies. To improve the prophylaxis and treatment of cardiovascular and respiratory diseases, it is necessary to know the laws of cardio-respiratory interaction.

Lots of studies were performed in order to model the interaction between the respiratory and cardiovascular systems [7–12]. In this paper we will give a review and a classification for the most commonly used methods of evaluation of the direct and indirect couplings between respiratory and cardiovascular systems.

2 Methods of Analysis

Synchronization between breathing parameters and heartbeat and has been studied in order to understand the principles of cardiorespiratory interactions in healthy and non-healthy subjects. In order to do that, many methods of investigation, modeling and analyses were developed, some of them use analysis of electrocardiograms and respiratory flow measurements. There are widely discussed statistical approaches to synchronization in noisy and chaotic systems and these are illustrated with numerical examples [13, 14].

V. Tonu (✉) · V. Vovc
Department of Human Physiology and Biophysics, State University of Medicine and Pharmacy “Nicolae Testemitanu”, Nicolae Testemitanu 27, Chisinau, Moldova
e-mail: tonuviorica@gmail.com

V. Tonu · N. Enache
Quantum Optics Laboratory, Institute of Applied Physics of Academy of Sciences, Chisinau, Moldova

There is a classification to all approaches regarding the interactions between the respiratory and cardiovascular systems, it has been grouped in five classes: GC, nonlinear prediction, entropy, symbolization and phase synchronization. We will try to analyze the mechanism of each of these methods of investigation and to highlight their importance for informational prognostic in different clinical settings.

2.1 Granger Causality

In 1956 Wiener [15] defined causality between two-time series in a statistical framework, saying that: “For two temporally measured time series, a series can be called causal for the other if we can better anticipate the second series of time by incorporating knowledge of the first”. Later, Granger adapted this concept to the context of stochastic processes in the economy to analyze linear time series based on an autoregressive pattern (AR). Today, this concept is known as CG. CG for two processes $X_1(t)$ and $X_2(t)$ is defined as: $X_1(t)$ has a causal influence on $X_2(t)$ if the knowledge of the past for both $X_1(t)$ and $X_2(t)$ will reduce the prediction error variance for $X_2(t)$ compared to the situation when knowing the past only for $X_2(t)$ (the past and the present causes the future but not the reverse).

In biomedical applications, evaluation of causality is commonly performed looking for directional dependencies within a set of multiple time series measured from the considered physiological system [16]. Physiological sub-systems measurements are quite difficult to perform using traditional frequency domain methods. Frequency domain Granger causality method based on directed coherence is instead used to analyze the changes in cardiorespiratory coupling like the influence of respiration rates on the cardiovascular parameters.

In their paper [17], Faes and Nollo proposed the utilization of an extended MVAR model including both instantaneous and lagged effects. Their model is used to assess PDC either in accordance with the definition of Granger causality when considering only lagged effects (iPDC), or with an extended form of causality, when they consider both instantaneous and lagged effects (ePDC). It is then applied to representative examples of cardiorespiratory and EEG MV time series. They suggest that ePDC and iPDC are better interpretable than PDC and gPDC in terms of the known cardiovascular and neural physiologies.

An extension of Granger causality to nonlinear bivariate time series was proposed by Ancona et al. [18]. In this frame, if the prediction error of the first time series is reduced by including measurements from the second time series, then the second time series is said to have a causal influence on the first one. They presented an approach with bivariate time series modeled by a generalization of radial

basis functions and show its application to a pair of uni-directionally coupled chaotic maps and to physiological examples, since the first argument for that was that not all the nonlinear prediction schemes are suitable to evaluate causality; indeed, not all of them allow one to quantify how much knowledge of the other time series counts to improve prediction error.

Porta et al. [19] proposed a multivariate dynamical adjustment (MDA) modeling approach to investigate the strength of baroreflex and cardiopulmonary couplings. They compared two models: open loop MDA (OLMDA) and closed loop MDA (CLMDA). The coupling strength was assessed during progressive sympathetic activation induced by graded head-up tilt (15°, 30°, 45°, 60° and 90°). They concluded that both OLMDA and CLMDA models suggested that baroreflex coupling progressively increased with tilt table inclination.

2.2 Entropy

Entropy is often associated with the “disorder” notion, and as one of the most famous examples is a clean room compared with a “messy” room. In this case, the cleaner the room is, the less entropy will describe it. So, one can say that entropy is a measurement of the disorder or using a more scientific approach, entropy represents the number of states that a system can take on and is a tendency for systems to move towards disorder and a quantification of that disorder. Uncertainty or predictability of the signals are reflected by the entropy concept. The higher the entropy is, the greater uncertainty and lower predictability will be.

The first mathematical approach of the entropy was made by Rudolph Clausius in the context of thermodynamics in 1850. Later, Shannon [20] quantified information content in a series of time. $H(x)$ describes the statistical properties of a time series x (stationary) and represents a measure of the uncertainty of a time series based on probabilities.

$$H(x) = - \sum_{k=1}^M p(x_k) \log_2 p(x_k)$$

where $p(x_k)$ is the probability distribution of k th bin of the time series x and M is the total number of all bins.

In 2015 Borowska [21] related some important biomedical signals that can be analyzed by the entropy based methods, such as the brain, the heart, the muscles, or the uterus. Biomedical signal processing methods have become more sophisticated and extract information from signals that is not apparent from visual observation of the signal alone. She stated that in order to conclude that something is wrong or that the patients involved have a disease, further processing is necessary. The algorithms used in biomedical

signal processing try to deal with the unique nature of physiologic signals such as non-stationarities, event detection, and disturbances.

A few studies had the purpose to quantify the complexity or the regularity of a series by means of entropy rates [22–24]. The information carried by the signal is the purpose of all these studies, mentioning that the information cannot be derived from its own past.

Later, Porta et al. [25] introduced an approach extended to a pair of signals to measure the degree of non-linear coupling between them. The approach is based on the calculation of a cross-conditional entropy measuring the amount of information carried by one signal which cannot be derived from the other. Therefore, the cross-conditional entropy can be considered as a measure of unpredictability of one signal when the other is observed. He concluded that the cross-conditional entropy is not completely adequate to measure synchronization. When non-linear interactions induce a coordination different from 1:1 coupling (1: M periodic dynamics) or sliding dynamics, the proposed analysis is a powerful tool to measure the coupling strength between two signals. Indeed, in these situations, linear tools based on the coherence function fail. These dynamics are common when several oscillatory mechanisms linked by coupling parameters compete in a non-linear fashion and/or on different temporal scales (e.g. in the regulation of cardiovascular function performed by the autonomic nervous system) [25].

2.3 Nonlinear Prediction

The prognosis of the future is one of the fundamental tasks of the time series analysis. Linear methods have large applications, however, a nonlinear prediction is more realistic. In their book chapter [26], Fan et al. discussed the general properties of nonlinear prediction, paying particular attention to those features that distinguish nonlinear prediction from linear prediction. It was underlined that sensitivity to initial condition, a key concept in deterministic chaos, plays an important role in understanding nonlinearity. Three types of predictors—namely point predictors, predictive intervals, and predictive distributions—constructed based on local regression was presented.

The study of Faes and Nollo [27] investigated cardiovascular signals from healthy young subjects to characterize the dynamic interaction between short-term spontaneous fluctuations of HR and SBP. A nonlinear prediction method for investigating the dynamic interdependence between short length time series was presented, which was a modification of the nonlinear prediction method based on local linear approximation originally introduced by Farmer and Sidorowich [28]. According to them, the predictability of HR was

low and influenced by nonlinear dynamics in the supine position and given SBP, and that after head-up tilt, the predictability increased significantly. They concluded that their results were related to the larger involvement of the baroreflex regulation from SBP to HR in the upright rather than in the supine position, and to the simplification of the HR–SBP coupling occurring with the tilt-induced alteration of the neural regulation of cardiovascular rhythms.

In 2008 Faes et al. [29] tested three approaches based on cross prediction, mixed prediction, and predictability improvement. They mentioned that the three mutual non-linear prediction schemes were assessed in a common physiological application during known conditions of interaction—the analysis of the interdependence between heart rate and arterial pressure variability in healthy humans during supine resting and passive head-up tilting. Based on simulation results and physiological interpretability of cardiovascular results, they concluded that cross prediction is valuable to quantify the coupling strength and predictability improvement to elicit directionality of the interactions in short and noisy bivariate time series.

2.4 Symbolization

JSD—(Joint symbolic dynamics) was introduced by Baumert et al. [30] where a study of joint symbolic dynamics is presented as a new short-term non-linear analysis method to investigate the interactions between HR and SP. Using the concept of joint symbolic dynamics, HR and SP changes were transformed into a bivariate symbol vector. Subsequently, this symbol vector was transformed into a word series (words consisting of three successive symbols), and the probability of occurrence of each word type was calculated and compared between both groups.

A bivariate analysis of autonomic regulation, based on cardiovascular coupling was developed by Schulz et al. [31] They introduced a new high-resolution coupling analysis method (HRJSD) based on joint symbolic dynamics (JSD), which is characterized by three symbols, a threshold (individual dynamic variability, physiological) for time series transformation and eight coupling pattern families. They concluded that the application of HRJSD revealed detailed information about short-term nonlinear cardiovascular couplings and cardiovascular physiological regulatory mechanisms (patterns) of autonomic function due to the anticholinergic effects of antipsychotics in patients with acute schizophrenia.

Schumann et al. [32] explore a new concept for quantifying information common in two time series by cross-compressibility. First, time series were transformed into symbol vectors, then symbols of the target time series were coded by the symbols of the source series. Their results

indicated that CCE is suitable for the investigation of linear and non-linear coupling in cardiovascular time series. CCE can quantify causal interactions in short, noisy and non-stationary physiological time series.

2.5 Phase Synchronization

Synchronization was mentioned very early in the past in 1665 by Christiaan Huygens. While being sick, he observed that two pendulum clocks, hung from the same wooden structure, will always oscillate in synchronicity. By his explanation at that moment, the effect was being caused by tiny vibrations in the wooden structure on which the clocks were hanging. (<https://phys.org/news/2016-03-huygens-pendulum-synchronization.html>).

Pikovsky et al. [33] gave a classification for three types of synchronization:

1. complete synchronization in which the behavior of the oscillators is the same;
2. generalized synchronization, if the behavior of one coupled system is determined by the behavior of the second system. Ex.: subsystem A has influence on the subsystem B, but subsystem B has no influence on subsystem A;
3. Phase synchronization, if the phase of the coupled systems become locked, however the systems continue to oscillate with different amplitudes. Phase synchronization is often common for systems that exhibit chaotic behavior.

Biological rhythms of the human body, coupled lasers, heart cells and many other examples serve as synchronized oscillating systems. A very large number of studies were performed in order to investigate the cardiorespiratory coupling by the synchronization method of analysis. In order to do that, nonstationary irregular bivariate data, namely, electrocardiograms and measurements of respiratory flow were analyzed [13, 33–38]. The analysis of such experimental records reveals synchronous regimes of different orders $n : m$ and transitions between them.

Different states were investigated, in order to study the influence of the respiratory system parameters on the hearth ones. The impact of meditation on cardiorespiratory synchronization with respect to breathing oscillations and the modulations of heart rate induced by respiration (respiratory sinus arrhythmia, RSA) was investigated by Cyzars et al. in their study [38]. Four different exercises (spontaneous breathing, mental task, Zen meditation, and Kinhin meditation) were consecutively performed by nine subjects mainly without any experience in meditation. An electrocardiogram and a respiratory trace were recorded simultaneously. On this basis the degree of cardiorespiratory synchronization

was quantified by a technique which has been adopted from the analysis of weakly coupled chaotic oscillators.

Phase synchronization between cardiac and respiratory oscillations was investigated during anesthesia in rats by Stefanovska et al. [34]. It appears that the synchronization state may be used to characterize the depth of anesthesia.

The synchrograms of 112 healthy subjects were studied by Bartsch [35] under different physiological conditions that occur during sleep. They found that phase synchronization between heartbeat and breathing is significantly enhanced during non-rapid-eye-movement (non-REM) sleep (deep sleep and light sleep) and reduced during REM sleep.

In their paper, Toledo et al. [36], questioned the true interaction in the cardiorespiratory system reflected by the synchronization. Their primary aim was to determine whether synchronization between HR and respiration rate is a real phenomenon or a random one. An algorithm was applied to recordings of respiration and HR obtained from 13 normal subjects and 13 heart transplant patients. In the result, they concluded that cardiorespiratory synchronization, although not a major feature of cardiorespiratory interaction, seems to be a real phenomenon rather than an artifact.

3 Conclusions

Each of the methods discussed in this paper can provide valuable data about the cardiovascular and respiratory interaction, but in the same time, each of them present some limitations. We have to mention that the cardiovascular and cardiorespiratory systems are complex integrated physiological systems that are interacting between each other directly or indirectly, so that one single method of analysis cannot give a full spectrum of information regarding their synchronization. Some of them give beautiful results, when linear time-series analysis is used, others require a non-linear time series approach. Nonlinear methods are known for studying complex signal interactions, however, linear methods are helpful for the frequency domain representation of biological signals.

We will summarize here the advantages and disadvantages of one of the presented methods of analysis: entropy, based on the study of [21, 24, 25, 32]. Entropy methods can solve important problems in time series analysis, such as: detecting missing points in time series, classifying dynamics, predicting appearance events, identifying directionality and causality and so on. From the other hand, classification of pathological and non-pathological data are quite problematic to asses with the entropy methods. On cannot distinguish two states of a system. A very small knowledge regarding the classification and selection of appropriate data is available at the moment. The reason for that is the choice of

parameter selection concerning the threshold value r , that has an influence on the entropy value.

There are many other methods of prediction, each of them giving very good results when applied in practice. One of them is the Markovian process. In probability theory and related fields, a Markovian process is a stochastic process in which predictions can be made for the future of the process based only on its current state as well as the complete history of the process can be known, that is, conditioned by the current state of the system, its future states and the past being independent.

Applications of such a prediction method are cruise control systems for motor vehicles, prediction of healthy people over a 5-year period, animal population growth, the PageRank algorithm, initially proposed for the Google search engine, is based on a Markovian process [39]. In medicine, Markovian processes have a large and diverse application, exploring such problems as timing of liver transplant [40], breast cancer [41], Hepatitis C [42].

In the last few decades a large number of methods were applied, discussed, improved and developed. These provide a valuable information regarding the oscillatory regulatory physiological processes of the cardiovascular and respiratory systems. Since the interest for the cardiorespiratory interaction have been grow a lot, we would like to see in the nearest future some new methods of approach that will provide the medicine with new possibilities of diagnosis and prognosis.

Conflict of Interest The authors declare that they have no conflict of interest.

References

- Mensah, G.A., et al.: Decline in cardiovascular mortality: possible causes and implications. *Circ. Res.* **120**(2), 366–380 (2017)
- Seidel, H., Herzel, H.: Modelling heart rate variability due to respiration and baroreflex BT—modelling the dynamics of biological systems: nonlinear phenomena and pattern formation. In: Mosekilde, E., Mouritsen, O.G. (eds.) pp. 205–229. Springer, Berlin, Heidelberg (1995)
- Amaral, L.A.N., et al.: Behavioral-independent features of complex heartbeat dynamics. *Phys. Rev. Lett.* **86**(26), 6026 (2001)
- Choi J., Gutierrez-Osuna, R.: Estimating mental stress using a wearable cardio-respiratory sensor, In: *Sensors*, 2010 IEEE, pp. 150–154 (2010)
- Tan, C.O., Cohen, M.A., Eckberg, D.L., Taylor, J.A.: Fractal properties of human heart period variability: physiological and methodological implications. *J. Physiol.* **587**(Pt 15), 3929–3941 (2009)
- Huikuri, H.V., Perkiömäki, J.S., Maestri, R., Pinna, G.D.: Clinical impact of evaluation of cardiovascular control by novel methods of heart rate dynamics. *Philos. Trans. R. Soc. Math. Phys. Eng. Sci.* **367**(1892), 1223–1238 (2009)
- Stefanovska, A.: Coupled oscillators: complex but not complicated cardiovascular and brain interactions. In: 2006 International Conference of the IEEE Engineering in Medicine and Biology Society, pp. 437–440 (2006)
- Milhorn Jr., H.T., Benton, R., Ross, R., Guyton, A.C.: A mathematical model of the human respiratory control system. *Biophys. J.* **5**(1), 27 (1965)
- Chang, H.K.: *Respiratory physiology: an analytical approach*, vol. 40. Marcel Dekker (1989)
- Ursino, M., Magosso, E.: Short-term autonomic control of cardiovascular function: a mini-review with the help of mathematical models. *J. Integr. Neurosci.* **2**(02), 219–247 (2003)
- Dickinson, C.J.: A computer model of human respiration: ventilation, blood gas transport and exchange, hydrogen ion regulation: for teaching, research and clinical use, “MacPuf”. University park press (1977)
- Duffin, J., Mohan, R.M., Vasiliou, P., Stephenson, R., Mahamed, S.: A model of the chemoreflex control of breathing in humans: model parameters measurement. *Respir. Physiol.* **120**(1), 13–26 (2000)
- Schäfer, C., Rosenblum, M.G., Abel, H.-H., Kurths, J.: Synchronization in the human cardiorespiratory system. *Phys. Rev. E* **60**(1), 857 (1999)
- Jensen-Urstad, K., Storck, N., Bouvier, F., Ericson, M., Lindblad, L.E., Jensen-Urstad, M.: Heart rate variability in healthy subjects is related to age and gender, **60** (1997)
- Michael Crump, outcomes in refractory aggressive diffuse large b-cell lymphoma (DLBCL): results from the international SCHOLAR-1 study. ASCO 2016, abstract 7516
- Schulz, S., et al.: Cardiovascular and cardiorespiratory coupling analyses: a review. **371** (2013)
- Faes, L., Nollo, G.: Extended causal modeling to assess partial directed coherence in multiple time series with significant instantaneous interactions. *Biol. Cybern.* **103**(5), 387–400 (2010)
- Ancona, N., Marinazzo, D., Stramaglia, S.: Radial basis function approach to nonlinear Granger causality of time series. *Phys. Rev. E* **70**(5), 56221 (2004)
- Porta, A., et al.: Model-based assessment of baroreflex and cardiopulmonary couplings during graded head-up tilt. *Comput. Biol. Med.* **42**(3), 298–305 (2012)
- Shannon, C.E.: A mathematical theory of communication. *Bell Syst. Tech. J.* **27**(3), 379–423 (1948)
- Borowska, M.: Entropy-based algorithms in the analysis of biomedical signals. *Stud. Log., Gramm. Rhetor.* **43**(1), 21–32 (2015)
- Pincus, S.M.: Approximate entropy as a measure of system complexity. *Proc. Natl. Acad. Sci.* **88**(6), 2297–2301 (1991)
- Cohen, A., Procaccia, I.: Computing the Kolmogorov entropy from time signals of dissipative and conservative dynamical systems. *Phys. Rev. A* **31**(3), 1872 (1985)
- Porta, A., et al.: Measuring regularity by means of a corrected conditional entropy in sympathetic outflow. *Biol. Cybern.* **78**(1), 71–78 (1998)
- Porta, A., Baselli, G., Lombardi, F., Montano, N., Malliani, A., Cerutti, S.: Conditional entropy approach for the evaluation of the coupling strength. *Biol. Cybern.* **81**(2), 119–129 (1999)
- Fan, J., Yao, Q.: *Nonlinear time series: nonparametric and parametric methods*. Springer Science & Business Media (2008)
- Faes, L., Nollo, G.: Bivariate nonlinear prediction to quantify the strength of complex dynamical interactions in short-term cardiovascular variability. *Med. Biol. Eng. Comput.* **44**(5), 383–392 (2006)
- Farmer, J.D., Sidorowich, J.J.: Predicting chaotic time series. *Phys. Rev. Lett.* **59**(8), 845 (1987)
- Faes, L., Porta, A., Nollo, G.: Mutual nonlinear prediction as a tool to evaluate coupling strength and directionality in bivariate time

- series: comparison among different strategies based on k nearest neighbors. *Phys. Rev. E* **78**(2), 26201 (2008)
30. Baumert, M., Walther, T., Hopfe, J., Stepan, H., Faber, R., Voss, A.: Joint symbolic dynamic analysis of beat-to-beat interactions of heart rate and systolic blood pressure in normal pregnancy. *Med. Biol. Eng. Comput.* **40**(2), 241–245 (2002)
 31. Schulz, S., Tupaika, N., Berger, S., Haueisen, J., Bär, K.-J., Voss, A.: Cardiovascular coupling analysis with high-resolution joint symbolic dynamics in patients suffering from acute schizophrenia. **34** (2013)
 32. Schumann, A., Schulz, S., Voss, A., Scharbrodt, S., Baumert, M., Bär, K.-J.: Baroreflex Coupling Assessed by Cross-Compression Entropy. *Front. Physiol.* **8**, 282 (2017)
 33. Pikovsky, A., Rosenblum, M., Kurths, J., Kurths, J.: Synchronization: a universal concept in nonlinear sciences. vol. 12. Cambridge university press (2003)
 34. Stefanovska, A., Haken, H., McClintock, P.V.E., Hožič, M., Bajrović, F., Ribarič, S.: Reversible transitions between synchronization states of the cardiorespiratory system. *Phys. Rev. Lett.* **85** (22), 4831 (2000)
 35. Bartsch, R., Kantelhardt, J.W., Penzel, T., Havlin, S.: Experimental evidence for phase synchronization transitions in the human cardiorespiratory system. *Phys. Rev. Lett.* **98**(5), 54102 (2007)
 36. Toledo, E., Akselrod, S., Pinhas, I., Aravot, D.: Does synchronization reflect a true interaction in the cardiorespiratory system? *Med. Eng. Phys.* **24**(1), 45–52 (2002)
 37. Wu, M.-C., Hu, C.-K.: Empirical mode decomposition and synchrogram approach to cardiorespiratory synchronization. *Phys. Rev. E* **73**(5), 51917 (2006)
 38. Cysarz, D., Büssing, A.: Cardiorespiratory synchronization during Zen meditation. *Eur. J. Appl. Physiol.* **95**(1), 88–95 (2005)
 39. Samarbakhsh, L.: Web search algorithms and PageRank (2008)
 40. Alagoz, O., Maillart, L.M., Schaefer, A.J., Roberts, M.S.: The optimal timing of living-donor liver transplantation. *Manage. Sci.* **50**(10), 1420–1430 (2004)
 41. Maillart, L.M., Ivy, J.S., Ransom, S., Diehl, K.: Assessing dynamic breast cancer screening policies. *Oper. Res.* **56**(6), 1411–1427 (2008)
 42. Faissol, D.M., Griffin, P.M., Swann, J.L.: Timing of testing and treatment of hepatitis C and other diseases. In: Proceedings, p. 11 (2007)

Recording of the Breathing Pattern in the Test with Controlled Hyperventilation in Subjects with a Borderline Type Personality Disorder

S. Lozovanu, I. Moldovanu, V. Vovc, T. Besleaga, and A. Ganenco

Abstract

The study of the variations of breathing pattern components under the influence of physiological or pathological factors allows to deepen the knowledge in the field of physiology of systemic interaction in the whole body as well as in the pathophysiology of functional, psychosomatic diseases. Taking into account the prevalence of 6% of borderline type personality disorder in primary care and up to 20% in specialized psychiatric centers and the considerable impairment caused to patients, the study of the breathing pattern could offer doctors, especially those at the primary level, an alternative to treatment pharmacologically by correcting the psychophysiological mechanisms of systemic dysfunction. The study was conducted on a group of 95 people between March 2017 and February 2019 at the Department of Human Physiology and Biophysics, USMF “N. Testemitanu”. The psychometric assessment preceding the recording of respiratory parameters was performed with the Personality Inventory Test PID-5. The respiratory pattern parameters were recorded using respiratory plethysmography and capnography. The experimental protocol included the recording of respiratory pattern parameters in 3 functional samples (resting breath, hyperventilation test, post-hyperventilation test). In the subjects with borderline type personality disorder group following characteristics of the breathing pattern at rest have been observed—over tidal volume, higher respiratory frequency and lower end-tidal CO₂.

Keywords

Breathing pattern • Borderline type personality disorder • Psychophysiology of respiration

1 Introduction

The process of rhythmogenesis is involved in almost all behaviors and brain functions [1, 2]. This includes generating rhythmic behaviors, communication, memory, attention [3, 4]. Therefore the understanding of rhythmogenesis is the fundamental problem of neuroscience. Mechanisms commonly found in rhythm-generating networks include: reciprocal inhibition [5], pacemaker activity [6] and recurrent excitatory network mechanism [7].

Psychophysiology of respiration is a rapidly advancing field that provides an experimental scaffold in the study of the psychophysiological essence of body-brain interaction. More important are the available experimental tools, which allow the contouring of the specific emotions generated by the body-brain interaction. There are some interesting findings of altered breathing perception in different respiratory patterns and changes in neural activity associated with breathing in individuals with high levels of anxiety, with depression, pain or stress [8, 9]. However, there is still much work to be done to outline the relationship between these functional diseases of the central nervous system and breathing, as well as to assess how nervous system responds to modulation of breathing as a powerful tool in alleviating these disorders.

Simultaneous evaluation of respiratory characteristics and respiratory functional disorders can be applied in the analysis of the role of different brain components and psychological traits in the formation of the respiratory pattern in healthy individuals and patients with psychophysiological respiratory dysfunctions. Highlighting patients with personality disorders and affective disorders (anxiety, depression, obsessive compulsive disorder, etc.) with eminent

S. Lozovanu · I. Moldovanu · V. Vovc · T. Besleaga · A. Ganenco (✉)
State Medical and Pharmaceutical University
“Nicolae Testemitanu”, 27, Testemitanu str, Chisinau,
Republic of Moldova
e-mail: andrei.ganenco@usmf.md

S. Lozovanu
e-mail: svetlana.lozovanu@usmf.md

I. Moldovanu
Department of Headache and Autonomic Disorders within
Institute of Neurology and Neurosurgery, Chisinau,
Republic of Moldova

respiratory symptoms may have an impact on creating patterns of psycho respiratory personality types in healthy individuals and patients with respiratory dysfunctions as well as choosing specific treatment methods, like biofeedback techniques of respiratory reeducation.

The authors of the psychophysiological models of the personality traits that are included in the personality type [10] are of the opinion that the psychophysiological reaction and superior cognition are interconnected. From this perspective, the psychophysiological reaction is a result of both the separate action and the interaction of unconscious cognitive processes and superior cognition. The neurophysiological theories of personality show that psychophysiological reactivity is a pluridetermined construct, where personality traits have a specific neurophysiological substrate and play the role of moderators, generating interindividual variability, which raises great problems for researchers. Modern concepts aim to establish limits between individual psychophysiological manifestations, to define models, general patterns how to analyze the particular characteristics and to highlight the factors that can influence the individual's reactivity.

The method of recording and analyzing the respiratory pattern is widely used in experimental and clinical research. The study of the variations of respiratory pattern components under the influence of physiological or pathological factors allows to deepen the knowledge about systemic interaction in the whole body as well as in the pathophysiology of functional, psychosomatic diseases. The accuracy of the respiratory pattern study by measuring some psychophysiological parameters may be threatened by the presence of factors or variables that may influence the psychophysiological reactivity of the individual [11].

The current study was designed to determine whether there are differences in the breathing pattern of patients with borderline personality disorder compared to the control group at rest, during controlled hyperventilation and during the post-hyperventilation recovery period.

2 Subjects and Methods

The study was conducted on a group of 101 subjects from March 2017 till February 2019 at the Department of Human Physiology and Biophysics, State Medical and Pharmaceutical University "N. Testemitanu" (SMPPhU). The average age of the persons included in the study was 33.5 years (from 19 till 60 years old). The subjects were excluded in the presence of pulmonary and cardiac pathologies. The psychometric assessment, which preceded the recording of respiratory parameters, was performed using the Personality Inventory for DSM-5, PID-5 (DSM-5–Diagnostic and Statistical Manual of Mental Disorders (DSM-5)) which is a

self-assessment tool for personality traits, developed by the American Psychiatric Association (APA) in 2012.

The Personality Inventory for DSM-5 (PID-5) was translated and validated by a working group made up of collaborators of the Department of Human Physiology and Biophysics of SMPPhU "N. Testemitanu" and the Department of Headache and Autonomic Disorders within the Institute of Neurology and Neurosurgery, with the consent of the authors. PID-5 is a questionnaire that contains 220 items, used to measure the personality traits presented in the DSM-5. Responses are selected from a four-point scale, from 0 (very false or false) to 3 ("very true or often true"). Thus PID-5 provides scores evaluated on a 4-point scale for the 25 facets. Each facet includes from 4 to 14 elements. These facets correspond to the disadaptive personality features described in Sect. 3 of DSM-5 and are included in the five higher order domains also described in Sect. 3: Negative Affectivity, Detachment, Antagonism, Disinhibition, and Psychoticism. The score higher than 2 in a certain number of facets is a quantitative index of one of the 6 types of PD: Antisocial, Borderline, Schizotypal, Avoidant, Obsessive-Compulsive or Narcissistic [12, 13].

Finally, based on the results obtained from the PID-5 test, it is possible to allocate the numerical scores for each facet related to the profile of the personality disorder. For the borderline personality disorder we study the distribution of numerical values of 7 facets. For a positive result, 4 out of 7 values on the vertical axis must be higher than 2 (Fig. 1).

Analyzing the distribution of facets and their numerical value, it is possible to separate the examined subjects in two groups:

Group I N—normal, with PID score 0–1.99. The group included 64 subjects 19–60 years old (mean age 35.5 years), 34 women and 30 men.

Group II PDB—with Borderline type of Personality Disorder (with PID score higher than 2.0). Included 37 subjects, 20 women and 17 men, 19–60 years old (mean age 34.7 years).

The recording of breathing pattern was performed with respiratory induction plethysmograph (RIP) VISURESP

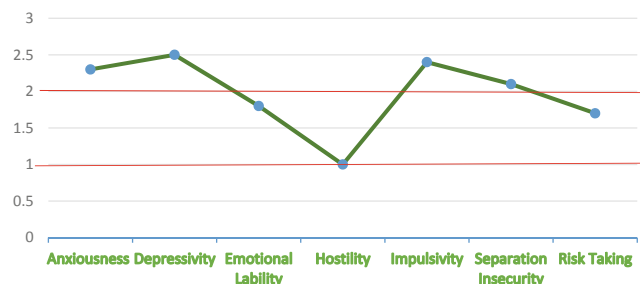


Fig. 1 The profile of the PD borderline

(RBI instruments, France)—for movements of abdomen and thorax [14] and the capnograph CapnoStream™ 20 (Medtronic, USA) for recording of PetCO₂. The RIP activity is based on the principle that a current applied by a the wire loop generates a magnetic field perpendicular to the loop orientation and that a change in a near area creates an opposite current within the loop, directly proportional to the change in that area. An elastic jacket in which two spiral threads is worn around the chest and abdomen. An alternating current is passed through the thread sewn into the vest, generating a magnetic field. The respiratory cycle changes the cross-sectional area of the chest and abdomen and thus modifies the shape of the magnetic field generated by the vest, “inducing” a measurable opposite current. In RIP no electrical current passes through the body, only a weak magnetic field is present, but it does not affect the patient or the surrounding equipment. The produced signal is linear and represents a fairly accurate representation of the changes in the cross sectional areas of the thorax and abdomen [14, 15]. After recording, the files were saved and analyzed using the “Visuresp 3.2” software. Of all breathing cycles, artifacts that resulted from extra movements by subjects, speech, or deep, sighing inspirations were excluded.

Prior to recording the respiratory parameters, the plethysmograph was calibrated for each individual by inspiration of a standard volume of air from a graduated syringe (1 L), recording the changes in the chest box corresponding to this volume, from which the calculations were subsequently made.

The experimental protocol included the recording of the respiratory signals in supine position. During the recording, the subjects were asked to breathe quietly do not talk and avoid additional movements.

1. Resting period (R)—for 5 min in physical, mental and emotional rest periods (the first minute was excluded from calculations to exclude artifacts obtained from application and accommodation movements of subjects in the jacket of the device).
2. Hyperventilation period (HV)—3 min the metronome guided respiration at 20 breaths/min, the subjects were encouraged to breath as deep as possible.
3. Posthyperventilation period (post HV)—subjects were asked to breathe normally again for 5 min.

Respiratory parameters are tidal volumes (V_t), the duration of the respiratory cycle (T_t), respiratory frequency (RF), inspiratory time (T_i), expiratory time (T_e), average inspiratory flow (V_t/T_i), respiratory minute volume (MV), pressure of CO₂ at the end of expiration (PetCO₂).

The statistical analysis (ANOVA) was performed using IMB SPSS Statistics 23.0.

3 Results and Discussion

The results of the study indicate that there are statistically significant differences between the volume parameters of the respiratory pattern between the N group and the PDB group even in the resting state. Subjects with personality disorder breathe with smaller volumes by about 20% compared to the control group ($p < 0.05$) (Fig. 2). Instead, the respiration frequency in PDB group is higher, namely 18.07 ± 0.61 compared to the group N— 16.87 ± 0.48 ($p < 0.05$), fact that exposes that the respiratory minute volume in both groups does not present a statistically correct deviation (Figs. 3 and 4).

During controlled hyperventilation with a frequency of 20 breaths per minute no statistically significant difference is observed in the tidal volume values between in subjects with borderline personality disorder and the control group. This suggests that the differences occurring at rest are caused by changes in the subcortical structures in the control of breathing, during the voluntary control of breathing the differences disappear.

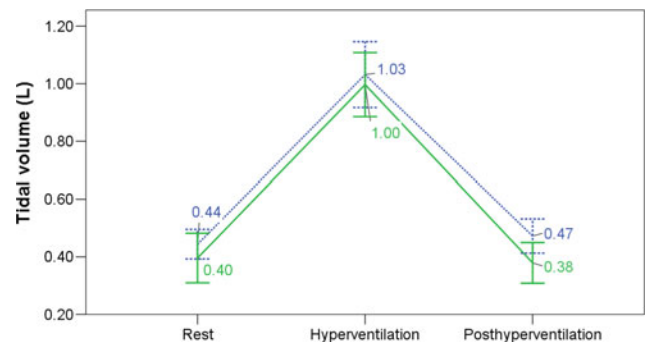


Fig. 2 Tidal volume in subjects in N (dotted line) and PDB (solid line) groups

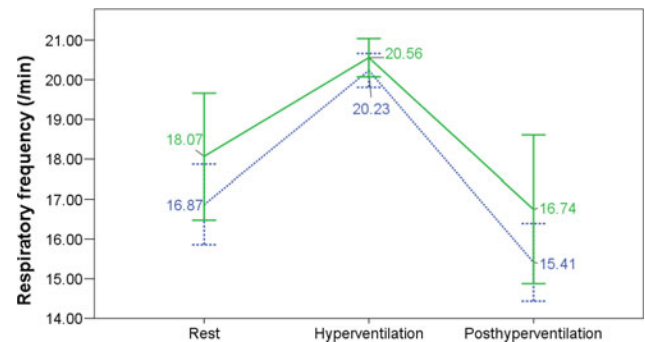


Fig. 3 Respiratory frequency in subjects in N (dotted line) and PDB (solid line) groups

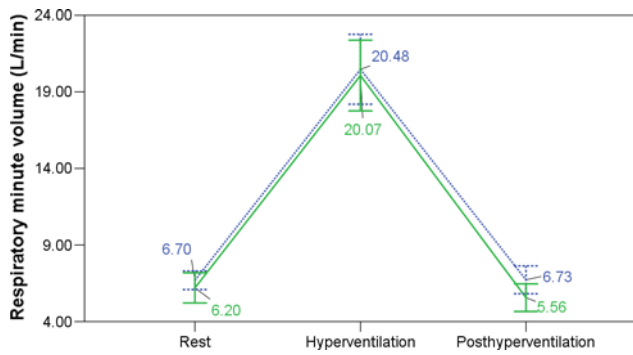


Fig. 4 Respiratory minute volume in subjects in N (dotted line) and PDB (solid line) groups

After the controlled hyperventilation, there were no statistically significant differences between tidal volume values in the subjects in the PDB group and N group.

The time parameters of the respiratory pattern in the subjects from the N group at rest, namely T_i (1.6 ± 0.04 s), differ statistically significantly ($p < 0.01$) (Fig. 5) compared to those in the PDB group (1.54 ± 0.04 s), T_t also has lower values in PDB group ($p < 0.05$) (Fig. 7). No statistically significant difference has been observed in the time parameters of the breathing pattern between the studied groups during controlled hyperventilation test and post hyperventilation period (Fig. 6).

In patients with borderline personality disorder the pressure of carbon dioxide at the end of expiration during resting period was found to be significantly lower (34.88 ± 0.36 mm Hg) than in healthy subjects (36.05 ± 0.44 mm Hg), ($p < 0.05$). During functional tests the changes of carbon dioxide pressure was similar in the subjects of N and PDB group (Fig. 8).

The changes of the average inspiratory flow did not show statistically significant differences between the subjects in N group and PDB group neither at the rest nor during functional tests (Fig. 9).

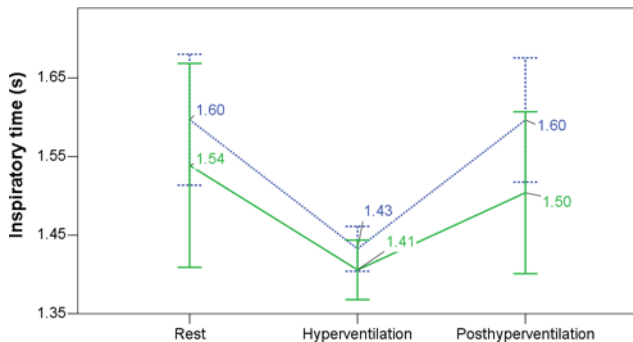


Fig. 5 Inspiratory time in subjects in N (dotted line) and PDB (solid line) groups

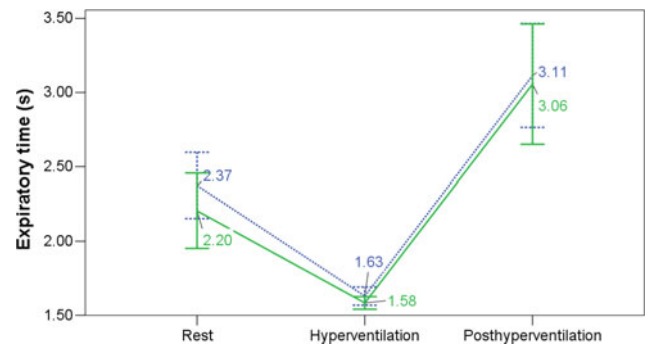


Fig. 6 Expiratory time in subjects in N (dotted line) and PDB (solid line) groups

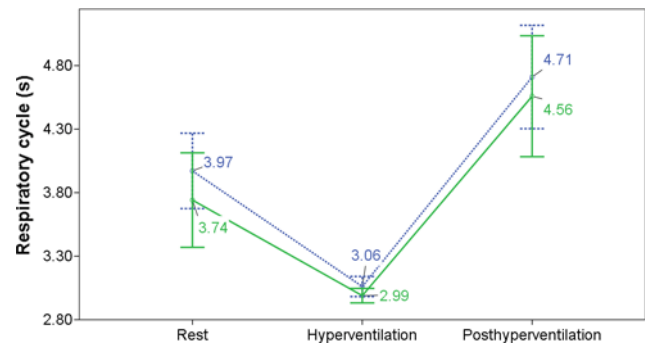


Fig. 7 Duration of respiratory cycle in subjects in N (dotted line) and PDB (solid line) groups

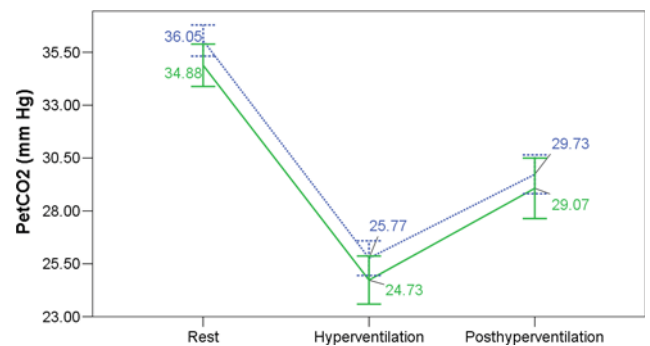


Fig. 8 Pressure of end-tidal CO₂ in subjects in N (dotted line) and PDB (solid line) groups

4 Conclusions

The subjects in PDB group following characteristics of the breathing pattern at rest have been observed—lower tidal volume, higher respiratory frequency and lower end-tidal CO₂.

One of the 7 facets which is include in PDB is anxiousness, and probably this explains the changes of the breathing

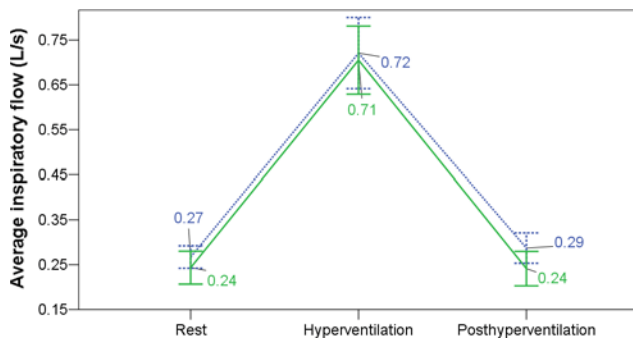


Fig. 9 Average inspiratory flow in subjects in N (dotted line) and PDB (solid line) groups

pattern caused by influences of anxiogenic structures on the brainstem respiratory center.

Conflict of Interest The authors declare that they have no conflict of interest.

References

- Ramirez, J.M., Dashevskiy, T., Marlin, I.A., Baertsch, N.: Microcircuits in respiratory rhythm generation: commonalities with other rhythm generating networks and evolutionary perspectives. *Curr. Opin. Neurobiol.* **41**, 53–61 (2016)
- Mouser, C., Bose, A., Nadim, F.: The role of electrical coupling in generating and modulating oscillations in a neuronal network. *Math. Biosci.* **278**, 11–21 (2016)
- Watson, B.O., Buzsaki, G.: Sleep, memory brain rhythms. *Daedalus* **144**, 67–82 (2015)
- Ramirez, J.M., Tryba, A.K., Pena, F.: Pacemaker neurons and neuronal networks: an integrative view. *Curr. Opin. Neurobiol.* **14**, 665–674 (2004)
- Rosa Jr., E., Skilling, Q.M., Stein, W.: Effects of reciprocal inhibitory coupling in model neurons. *Biosystems*, **127**, 73–83 (2015)
- Shaffer, A., et al.: A critical firing rate associated with tonic-to-bursting transitions in synchronized gap-junction coupled neurons. *Eur. Phys. J. Spec. Top.*, **226**, 1939–1951 (2017)
- Marder, E., Gutierrez, G.J., Nusbaum, M.P.: Complicating connectomes: electrical coupling creates parallel pathways and degenerate circuit mechanisms. *Dev. Neurobiol.* **77**, 597–609 (2016)
- Hölzel, B.K., et al.: Stress reduction correlates with structural changes in the amygdala. *Soc. Cogn. Affect. Neurosci.* **5**, 11–17 (2010)
- Paulus, M.P., et al.: A neuroscience approach to optimizing brain resources for human performance in extreme environments. *Neuro. Sci. Biobehav. Rev.* **33**, 1080–1088 (2009)
- Fiamma, M.N., et al.: Effects of hypercapnia and hypocapnia on ventilatory variability and the chaotic dynamics of ventilatory flow in humans. *Am. J. Physiol. Regul. Integr. Comp. Physiol.* **292**, 1985–1993 (2007)
- Paton, J.F., Nalivaiko, E., Boscan, P., Pickering, A.E.: Reflexly evoked coactivation of cardiac vagal and sympathetic motor outflows: observations and functional implications. *Clin Exp Pharmacol Physiol.* **33**, 1245–1250 (2006)
- Krueger, R.F., et al.: Personality in DSM-5: helping delineate personality disorder content and framing the metastructure. *J. Pers. Assess.* **93**, 325–331 (2011)
- Amad, A., et al.: Genetics of borderline personality disorder: systematic review and proposal of an integrative model. *Neuro. Sci. Biobehav. Rev.* **40**, 6–19 (2014)
- VISURESP system at <http://www.visuresp.com/system.html>
- ClarenbachCF, et al.: Monitoring of ventilation during exercise by a Portable respiratory inductive plethysmograph. *Chest* **128**, 1282–1290 (2005)

Encephalographic Signal LabView Processing

I. C. Roșca, C. Drugă, I. Șerban, and R. D. Necula

Abstract

The research presented in the present paper concern the treatment of signals obtained from monitoring the encephalic function through electroencephalogram. The signal processing is based on the creation of a routine in named Labview software, which allow analyzing both electrocardiographic and electroencephalographic (EEG) signals. Automatic interpretation of an EEG implies analyzing a large diversity of normal and abnormal wave forms on a great number of channels. EEG monitoring aims the detection of significant changes either for slow and fast waves (spikes). A routine was created in LabVIEW software for processing the EEG signal and to indicate anesthesia degree (cerebral state index). After caption and filtering, the signal is distributed through four channels corresponding the electroencephalographic frequencies. Further, the signal was transformed as to be possible its graphic representation and, the Cerebral state index was estimated by implementing its specific formula and expressed by a numerical value. This application has the advantage to save data in different formats as to be visualized and interpreted by other software giving the graphic representations (Excel, Origin etc.). It also allows to be used for a great number of subjects, depending on PC memory, and it is easy and friendly to use for persons that have no specific IT education. The last but not the least, it is very low cost: LabVIEW license and low cost for acquisition board and little other accessories.

Keywords

EEG • LabVIEW • Signal • Routine

1 Introduction

Encephalography (EEG) represents a technique of functional exploration for detecting the bioelectric cerebral activity and its evolution in time.

Electroencephalography is used in nervous system diseases diagnostics as epilepsy, encephalopathies. It can be also useful in monitoring the cerebral activity during surgery or to set the cerebral death.

The first EEG laboratory was first founded in 1936 in general hospital of Massachusetts, after Fischer and Lowenback were the first to register successfully, in 1934, the epileptic spikes on a diagram by an encephalogram.

The encephalographic signal presents different types of waves which, after determining significant statistic relationships between clinical phenomena and these wave forms, can be distinguished in the frequency ranges and amplitude.

A subject in resting state presents a ripple of about 50 μV between the peaks, with the frequency in the range 8–13 Hz. This is a characteristic electric signal, named α rhythm and any concentration or mental effort cancels it. A comprehensive analysis shown five characteristic rhythms [1]:

1. δ -rhythm, in the range 0.5–3 Hz, with amplitude of 50–150 μV and, features babies and adult slow-wave sleep. In waking adult, this rhythm can illustrate different pathological states;
2. θ rhythm, in the range 4–7 Hz, with amplitude of 30–70 μV , characterizing the waking children and as insulated waves for the adult person;
3. α -rhythm, with frequency components in the range of 8–13 Hz and predominant amplitude around 50 μV , but in the encephalographic specter it can be also observed with amplitudes of 30–100 μV . It is specific to the quiet,

I. C. Roșca (✉) · C. Drugă · I. Șerban
Mechatronics and Environment Department, Transilvania
University/Product Design, 1, Universității, Brașov, Romania
e-mail: ilcrosca@unitbv.ro

R. D. Necula
Department of Medical and Surgery Specialties, Transilvania
University, Brașov, Romania

relaxed subject and, when the relaxation is deep enough, the 10 Hz/50 μ V waves are predominant in the two thirds of the posterior scalp and, for this reason, this component is named biologic clock [1, 2];

4. β -rhythm, with frequency components in the range of 14–32 Hz and amplitudes less than 30 μ V, being associated to the mental, logic activity;
5. γ -rhythm has higher frequency components, in the range of 14–32 Hz and amplitudes less than 30 μ V, being associated to the mental, logic activity [1, 2];

In addition to these rhythms an electroencephalogram can present other typical waves. Among them, K complex are defined as waves with minimal amplitudes of 100 μ V, having both phases with a total duration of 0.5–1 s, preceded and followed by at least 2 s of low amplitude encephalic activity. These complexes' amplitudes spindle up and down in fusiform short runs of 0.5–1 s.

2 Signals Acquisition and Treatment

Typically tensions are collected by electrodes applied externally on the head in a standard distribution, which has become traditional. Under very specific conditions, special electrodes are placed directly on or in a deeper cortex of the brain. Ultimately limits bio-systems' engineering exploration brain qualities are given by the coupling circuits and electrodes. Electrodes inserted characteristics determined by the physical-chemical contact phenomena, with potential, drift and other effect thereof.

Modern Electroencephalographs have 64 separate channels—usually they use of 8 to 16 channels simultaneously. The electrodes are fixed with a quick-drying adhesive (colodion) or with a special helmet of rubber twisted strips.

The electrodes are distributed on all head regions and are with the head collection area. Thus, they are: F—frontal electrodes, T—temporal electrodes, C—central electrodes, P—parietal electrodes, O occipital electrodes and, the reference electrode is denoted by A and can be placed either on a nasal fossa or sometimes forehead to the nose, that is an area where brain activity can be considered null.

It is obvious that can be defined voltages between any two points (electrodes) on the head and electrodes potential to a reference potential at a point as close to the explored surface, not participating in the electrical changes guided by brain activity.

EEG direct interpretation provides little useful information to clinician. Semi-automatic analysis assimilates the EEG signal on a limited section, such as two seconds, to a

random process, stationary and ergodic and, thus it uses one embodiment and the analysis in real-time is possible. In terms of information EEG parameters are temporal, statistic in amplitude and frequency. Temporal parameters are the number of zero or constant level intersections and the number of amplitude extremes per time unit and the first and second order temporal averages. The most frequently used temporal averages that can be also statistical averages, are: average, the quadratic dispersion, standard deviation, cross-correlation and autocorrelation functions and coefficients, inter-covariant and covariance functions [1, 2].

Automatic EEG interpretation involves analyzing a wide variety of normal and abnormal waveforms, a large number of channels. EEG monitoring is aimed to detect significant changes in EEG, both slow-wave and spikes. Real time EEG monitoring performs functions as:

Calculation of the correlation function between two EEG channels;

Adaptive filtering comparing the EEG with stored ones;

Digital selective filtering, which makes evident or delete different specific EEG rhythms, for example, rejection $-\alpha$ or $-\alpha$ pass filter,

Monitoring zero cross intervals and spectral density.

3 Labview Signals Treatment

Acquisition, analysis and processing of signals from a complex system of data acquisition, in LabVIEW programming environment, a software complex EEG MONITOR was developed.

Using graphical programming environment LabVIEW to optimize the processing and display signals presents the following advantages, by allowing:

coupling the computer through acquisition boards, of various measuring equipment;

addressing any communication interfaces with acquisition systems coupled to measuring transducers;

simulating physical processes and phenomena, mechanical, electronic, chemical, etc.

creating so-called virtual instruments that can successfully replace a wide range of required instrumentation and control equipment or measuring various parameters,

creating applications both very complex process control in real time, and simulating or controlling them by processes or phenomena on the basis of importing previously generated data files;

developing suitable of applications with parameters measurements flexible character of any physical and mechanical processes.

For all these reasons, using LabVIEW solution proves practical, efficient and inexpensive for many cases where it is necessary to monitor complex processes.

The adopted solution for the EEG signal processing by a LabVIEW application, supposed the use a series of sequences and routines as to represent graphically the results for EEG and the numeric cerebral state index rate. This algorithm can be divided into several program routines as:

- Data acquisition;
- EEG signals treatment;
- Graphic presentation of the EEG;
- Cerebral index rate determination;
- Data saving.

Data acquisition routine used the LabVIEW routine Multi-Function-Synch AI- Read Dig Chan.vi, which are embedded the next components:

1. *DAQmx Create Channel*, creating a channel or a set of virtual channels I/O or for measurement tasks.
2. *DAQmx Timing*, controlling the number of and rate at which samples are acquired from a device, in three different sample modes: finite, continuous, and hardware timed single point.
3. *Get terminal name with device prefix* is a virtual instrument taking a load and a terminal and converting those into a terminal that includes the specified code in the control channel physical DAQmx.
4. *DAQmx*, reading tasks samples from channels or virtual channels. Cases of this virtual instrument specify what format of samples to be returned, if you read a single sample or multiple samples simultaneously or read from one or more channels.
5. *DAQmx clear task*, deleting task. Before deleting, if necessary, stops the charge and the issue all sources reserved.
6. *General error handler*, indicating if an error occurred and returns a description of this.
7. *WHILE-LOOP*, repeating the control flow statement.

EEG signals treatment will act on the EEG signals to transform them by different modules like:

1. *Filter* is a principal sequence of the software and through it, the signal is processed according to the specification.

2. *Spectral measurements*, performing measurements based on FFT as: spectrum, average magnitude, power spectrum, one signal phase spectrum.
3. *Amplitude and level measurements*, measuring voltage on a signal.
4. *Merge signal*, combining two or more signal into a single output one.
5. *Write to measurement*, writing data in text form files on the measuring base .LMV or in binary measuring files .TDM or .TDMS.
6. *Bundle* assembling a group of individual elements or allowing to change in an existing package different values.
7. *Convert from dynamic data* into numerical or matrix form as to be used by other virtual instruments.
8. *Mathematical operators* and *formula* calculate specific mathematical operations or creates mathematical formulas with multiple operations by computer's interface.

Besides these commands, the group concerning signal treatment suppose also different other ones concerning the return data form to operator, computing time etc.

The routines concerning the *graphic presentation of EEG* and *cerebral index rate determination* also suppose a series of different functions/modules as follows:

Filters for the four EEG bands and for the other used virtual instruments. As filter were used δ (delta), α (alpha)/bandpass and, β (beta)/high pass. As other virtual instruments were used: *Spectral Measurements*, *Amplitude and Level Measurements* followed by *Convert from Dynamic Data*. Before displaying, the signal was treated by the module *Index Array* which merges columns on one line and, further connected to Chart.

Cerebral State Index (CSI) is a unitless scale from 0 to 100, where 0 indicates a flat electroencephalographic signal and 100 indicates the awake state. It is used is to monitor the level of consciousness during general anesthesia, where 0 indicates zero cerebral activity and 100 represents the aware state. The suitable range for a normal anesthesia is between 40 and 60. [3]

CSI is calculated according to three parameters:

$$\beta\text{-ratio} = \frac{E_{30-42.5 \text{ Hz}}}{E_{11-21 \text{ Hz}}} \tag{1}$$

$$\alpha\text{-ratio} = \frac{E_{30-42.5 \text{ Hz}}}{E_{6-12 \text{ Hz}}}; \tag{2}$$

$$\beta\text{-ratio} - \alpha\text{-ratio} = \frac{E_{6-12 \text{ Hz}}}{E_{11-21 \text{ Hz}}}, \tag{3}$$

where: $E_{30-42.5 \text{ Hz}}$ is the frequency interval for which the signal was taken from the Beta band, $E_{11-21 \text{ Hz}}$ from the alpha band and, for $E_{6-12 \text{ Hz}}$ from the theta band.

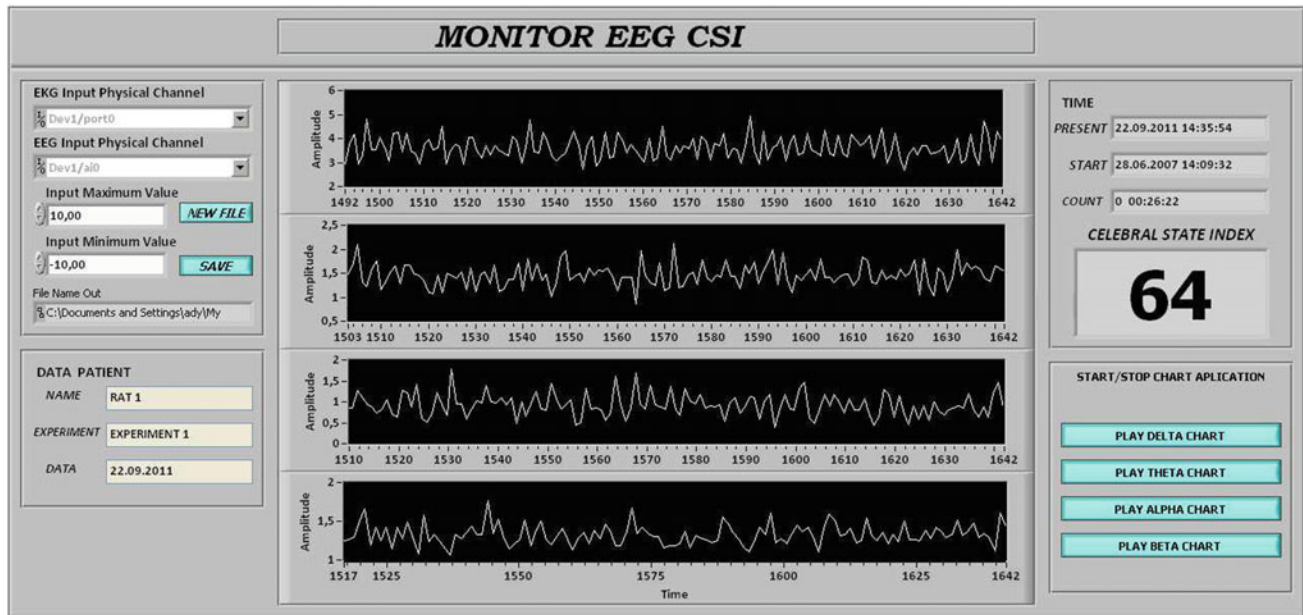


Fig. 1 Display window of the EEG bands and CIS

All calculate d data used the commands *Mathematical operators* and *Formula*, as well as, finally are obtained the program sequence for displaying the EEG and the CSI (Fig. 1).

A LabVIEW sequence that saves EEG data under different formats, in columns, one for each output data type (i.e. four columns) is used for *Data saving*.

4 Conclusions

The aim of the study was to provide an instrument for automatic monitoring EEG and cerebral state index, both for checkups and during surgery.

After filtration, the signal is split in four bands representing the four frequency bands of the EEG and, further it was processed as to be graphically represented. The anesthesia level is evaluated by CSI, determined based on specific formula and numerically displayed.

The application has the advantages of saving data in different formats, creating the possibility to be viewed and interpreted by the physician through different accessible

formats: Excel, origin etc. Depending on the computer hardware capacity, the application can register a high number of subjects.

The application creates a base for further development in the domain of other vital signal analyze and it can be improved accordingly to the computers' software and medical devices' upgrade.

Acknowledgements This study was done with the consistent contribution of student Aurelian Lazarof.

Conflict of Interest The authors declare that they have no conflict of interest.

References

1. Strungaru, R.: *Electronică Medicală*. Editura Didactică și Pedagogică, București, Romania (1982)
2. Hariton, C.: *Electronică Medicală*, Editura Cantes, Iași, Romania (2000)
3. http://journals.lww.com/anesthesiology/Abstract/2006/07000/Cerebral_State_Index_during_Propofol_Anesthesia__A.9.aspx

Multifocal Repetitive Transcranial Magnetic Stimulation—A Novel Paradigm in Migraine Treatment

P. Leahu, S. A. Groppa, M. Bange, S. Scheiter, D. Ciolac, V. C. Chirumamilla, M. Muthuraman, and S. Groppa

Abstract

Transcranial Magnetic Stimulation (TMS) is a non-invasive brain stimulation method used for analyzing structural and functional interactions in brain, assess cortical reactivity, and map functionally relevant brain regions inducing a controlled current pulse in a defined region of the cortex. From a clinical point of view, TMS has shown promising results in the therapeutic approach in a large number of psychiatric and neurological conditions such as anxiety, depression, OCD, headache disorders—migraine being one of the most encountered, etc. In patients with migraine, the pharmacologic therapy can be divided in abortive and preventive treatment of the attack. Usually the treatment is started with simple analgesics and non-steroidal inflammatory; nevertheless, many individuals continue to have attacks refractory to various prophylactic and/or abortive therapies, while others are at high risk of developing medication overuse headache. Among non-pharmacologic therapies TMS has been broadly studied as a preventive migraine treatment with good outcome results.

Keywords

Transcranial • Magnetic • Stimulation • rTMS • Migraine

1 Introduction

Single-pulse transcranial magnetic stimulation (TMS) was introduced for the first time in 1985, as a method of non-invasive stimulation of the human cortex [1, 2]. This technique opened up new ways of studying the functionality, morphology, and connectivity of various cortical regions, especially the motor cortex [3]. In 1990, new technology introduced generators capable of producing rapid, repetitive pulses of magnetic stimulation at frequencies of up to 30 Hz known as repetitive TMS (rTMS) [4]. Nowadays, rTMS is considered a useful tool in the management and treatment of several disorders originating in the cerebral cortex. The electric charges induced by the magnetic field impact various neurochemical mechanisms that play a primordial role in the pathophysiology and chronification of migraine.

The primary mechanisms causing migraine attacks still remain largely unrecognized due to the complex and dynamic organization of processes in the brain neuronal networks. Cortical excitability has been suggested to be dysfunctional in patients with migraine [5]. The ability to modulate cortical activity and induce persistent, plastic effects renders repetitive transcranial magnetic stimulation (rTMS) as a potential therapeutic approach.

Several studies demonstrate that TMS can reduce the frequency and severity of migraine attacks [6, 7]. Possible mechanisms involve induction of long lasting effects on blood-flow (e.g. reducing trigeminally induced meningeal vasodilatation), peripheral nerve sensing (e.g. modulating cortical excitability, ophthalmic and greater occipital nerve (C2) activity, or nociceptive evoked trigemino-thalamic activity), or the release of cytokines or inflammatory peptides (dopamine, serotonin, glutamate, NO, Beta-endorphin, BDNF levels and expressions) [8–10].

Most of the studies conducted so far focused on TMS performed over a single region. The objective of our study was to evaluate the efficacy and tolerability of multifocal rTMS for migraine prevention. We hypothesized that multifocal rTMS

M. Bange · S. Scheiter · V. C. Chirumamilla · M. Muthuraman · S. Groppa
Section of Movement Disorders and Neurostimulation, Biomedical Statistics and Multimodal Signal Processing Unit, Department of Neurology, Focus Program Translational Neuroscience (FTN), University Medical Center of the Johannes Gutenberg-University Mainz, Mainz, Germany

P. Leahu (✉) · S. A. Groppa · D. Ciolac
Department of Neurology, State University of Medicine and Pharmaceutics “Nicolae Testemitanu”, Toma Ciorba 1, Chisinau, Republic of Moldova
e-mail: leahu.pavel@yahoo.com

reduces the frequency and intensity of migraine attacks in comparison to a baseline period, and that this effect exceeds a possible placebo effect. Furthermore, we hypothesized that this stimulation protocol can induce improvements in quality of life measures (HIT-6, MIDAS, HDI).

2 Methods

We conducted a longitudinal, double-blinded, rTMS-intervention study with patients with migraine (both with and without aura, 2–15 attacks per month). After a 4-week baseline period, participants attended 6 intervention sessions within 2 weeks to receive either multifocal rTMS- or a placebo-treatment (randomization has been performed by a researcher blinded to every aspect of the study except randomization codes). The blinding of subjects was performed by means of a specific round biconcave active/placebo coil. Overall baseline data description is presented in Table 1.

2.1 Study Design

Participants were asked to fill out a headache diary for 4 weeks and complete the HDI, HIT-6, and MIDAS questionnaire prior to the first stimulation session. Frequency and severity of migraine attacks within the 8 weeks following the intervention serve as primary outcome variables. Quality of life questionnaires were conducted on several other follow-up dates (Fig. 1).

2.2 Stimulation Protocol

The stimulation protocol consisted of a swipe-stimulation and a spot burst stimulation (Fig. 2). High frequency rTMS comprised 140 pulses/train in trains at 60% of motor

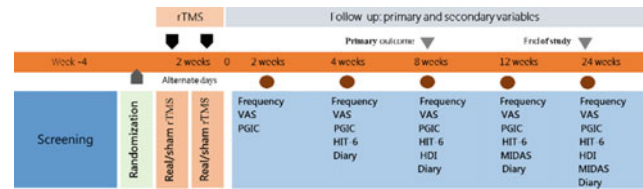


Fig. 1 Study design

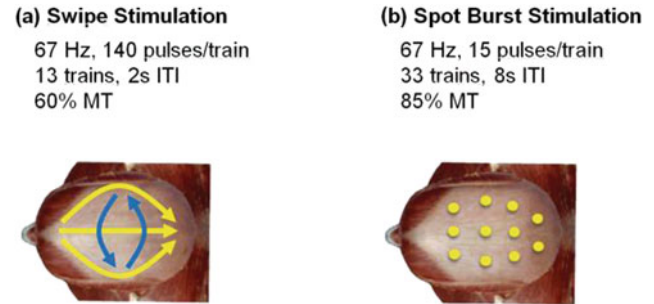


Fig. 2 Stimulation protocol

threshold, followed by 5 pulses/train in trains at 85% of motor threshold applied over cortex within a predefined multifocal delivery scheme consisting of 11 points marked on individual caps according to the 10–20 EEG system during the first session.

2.3 Safety

Stimulation procedures had been performed respecting the IFCN committee safety protocols and re-recommendations [11].

To assess the efficacy of multifocal rTMS we analyzed frequency and intensity of attacks in a 6-month follow-up period in comparison to the 4-week baseline period as

Table 1 Group baseline characteristics

Variables	Total (n = 42)	
	Real (n = 22)	Sham (n = 20)
Female, n (%)	19 (86.3)%	20 (100%)
Age in years (M ± SD)	38.4 ± 10.2	41 ± 12.6
Range	20–58	22–63
Frequency of headache per month (M ± SD)	7.5 ± 3.7	7.3 ± 3.6
Range	2–16	3–16
Pain intensity (M ± SD)	6.7 ± 1.5	6.2 ± 1.2
HIT-6 (M ± SD) ^a	63.4 ± 6.3	64.24 ± 4.4
HDI (M ± SD) ^b	64.2 ± 17.4	55.4 ± 22
MIDA (M ± SD) ^c	36.5 ± 22.9	35.9 ± 23.9

^aHeadache impact test

^bHeadache disability index

^cMigrant disability assessment score

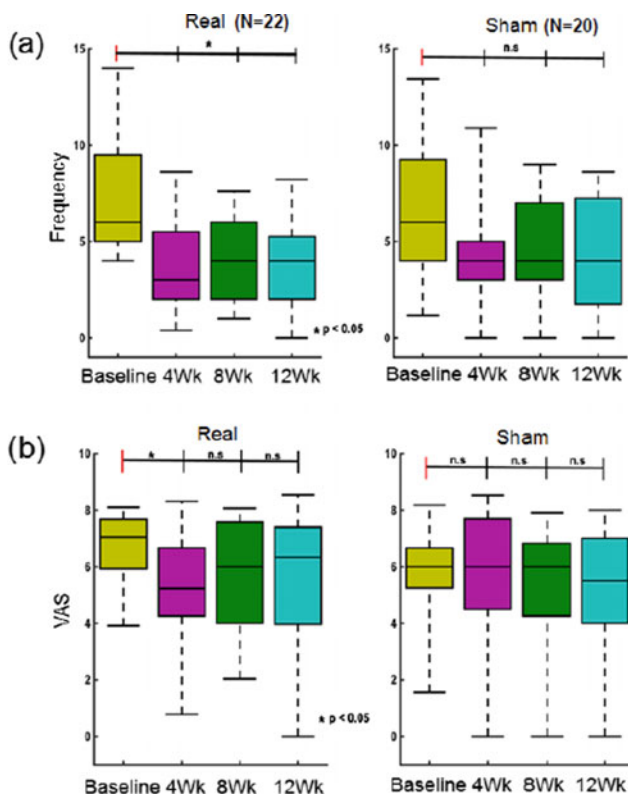


Fig. 3 Primary outcomes

primary outcomes on the basis of a headache diary. To evaluate the impact on everyday life, questionnaires about the quality of life were conducted as secondary variables. Repeated measures ANOVAs were performed separately for both groups.

3 Results

Figure 3 shows the results for frequency and intensity of the attacks from the baseline period until 3 months after the stimulation. In the stimulation group, the number of attacks was significantly reduced following stimulation— 7.5 ± 3.7 at baseline to 3.8 ± 2.7 attacks at 3 months period ($p < 0.05$). This effect lasts for at least three months. The number of attacks was also reduced in the placebo group (7.3 ± 3.6 to 4.4 ± 2.9). However, this was not statistically significant. The severity of attacks was significantly reduced 4 weeks after the treatment exclusively in the treatment group (6.7 ± 1.5 at baseline; 5.3 ± 2.5 at 4 weeks ($p < 0.05$)). Questionnaires suggest that rTMS positively affects quality of life. Screening for possible adverse events after the stimulation revealed no serious side-effects.

4 Conclusions

Our pilot study shows compelling evidence that the studied rTMS paradigm reduces the number and severity of migraine attacks to a larger extent than the placebo treatment. Multifocal rTMS is a novel and effective treatment approach for episodic migraine prophylaxis in adults. Importantly, the experimental protocol is well tolerated, showing no serious adverse events.

Acknowledgements The author thanks all colleagues who helped in processing the data, also all subjects who took part in this study.

Conflict of Interest The authors declare that they have no conflict of interest.

References

- Barker, A.T., Freeston, I.L., Jalinous, R., Jarratt, J.A.: Motor responses to non-invasive brain stimulation in clinical practice. *Electroencephalogr. Clin. Neurophysiol.* **61**, S70 (1985)
- Barker, A.T., Jalinous, R., Freeston, I.L.: Non-invasive magnetic stimulation of human motor cortex. *Lancet* **1**, 1106–1107 (1985)
- Terao, Y., Ugawa, Y.: Basic mechanisms of TMS. *J. Clin. Neurophysiol.* **19**, 322–343 (2002)
- Dhuna, A., Gates, J., Pascual-Leone, A.: Transcranial magnetic stimulation in patients with epilepsy. *Neurology* **41**, 1067–1071 (1991)
- Brighina, F., Cosentino, G., Fierro, B.: Brain stimulation in migraine. *Handb. Clin. Neurol.* **116**, 585–598 (2013)
- Misra, U.K., Kalita, J., Bhoi, S.K.: High-rate repetitive transcranial magnetic stimulation in migraine prophylaxis: a randomized, placebo-controlled study. *J. Neurol.* **260**(11), 2793–2801 (2013)
- Starling, A.J., Tepper, S.J., Marmura, M.J., Shamim, E.A., Robbins, M.S., Hindiyeh, N., Charles, A.C., Goadsby, P.J., Lipton, R.B., Silberstein, S.D., Gelfand, A.A., Chiacchierini, R. P., Dodick, D.W.: A multicenter, prospective, single arm, open label, observational study of sTMS for migraine prevention (ESPOUSE Study). *Cephalalgia* **38**(6), 1038–1048 (2018)
- Cosentino, G., Fierro, B., Vigneri, S., Talamanca, S., Paladino, P., Baschi, R., Indovino, S., Maccora, S., Valentino, F., Fileccia, E., Giglia, G.: Cyclical changes of cortical excitability and metaplasticity in migraine: evidence from a repetitive transcranial magnetic stimulation study. *PAIN®* **155**(6), 1070–1078
- Eller-Smith, O.C., Nicol, A.L., Christianson, J.A.: Potential mechanisms underlying centralized pain and emerging therapeutic interventions. *Front. Cell Neurosci.* **12**, 35 (2018)
- Amgrim, N., Schytz, H.W., Britze, J., Amin, F.M., Vestergaard, M.B., Hougaard, A., et al.: Migraine induced by hypoxia: an MRI spectroscopy and angiography study. *Brain* **139**(Pt 3), 723–737 (2016)
- Groppa, S., Oliviero, A., Eisen, A., Quartarone, A., Cohen, L.G., Mall, V., Kaelin-Lang, A., Mima, T., Rossi, S., Thieckbroom, G. W., Rossini, P.M., Ziemann, U., Valls-Solé, J., Siebner, H.R.: A practical guide to diagnostic transcranial magnetic stimulation: report of an IFCN committee. *Clin. Neurophysiol.* **123**(5), 858–882 (2012)

Part VIII

Biomedical Imaging and Image Processing

Remodeling of Cortical Structural Networks in Multiple Sclerosis

D. Ciolac

Abstract

Multiple sclerosis (MS) is one of the most frequent immune-mediated disorders of the central nervous system. Pathological events occurring within the white matter and gray matter compartments can be reliably tracked in vivo by magnetic resonance imaging (MRI) but conventional imaging parameters do not reflect the remodeling processes of the brain. Here, we sought to investigate the reorganization of cortical structural networks in a group of patients with MS. For this, 40 patients (mean age \pm standard deviation 31.2 ± 7.0 years, 14 males) with relapsing-remitting MS and 40 healthy subjects (27.1 ± 5.0 years, 14 males) were included in the study. From T_1 -weighted MR image-derived cortical thickness values, connectivity matrices were generated and network measures of integration and segregation compared between the groups. MS patients presented higher modularity, clustering coefficient and local efficiency but lower global efficiency when compared to healthy subjects. These results indicate that remodeling of cortical structural networks in patients with MS occurs towards the strengthening of intramodular connectivity and local processing. Presumably, this reorganized network architecture topology is an adaptation response required to maintain brain networks' functionality in conditions of ongoing tissue damage.

Keywords

Multiple sclerosis • Gray matter • Network architecture • Graph theory

1 Introduction

Multiple sclerosis (MS) is a chronic immune-mediated condition that affects central nervous system and is characterized by a neuropathological triad of inflammation, demyelination and degeneration. The ongoing disease progression leads to disruption of short- and long-range network connections, thereby resulting into reorganization of brain networks' structural architecture and functional disconnection. In this respect, addressing brain networks derived from structural and functional neuroimaging provides new insights into pathological processes within the gray matter and white matter compartments [1, 2].

Modelling brain networks by using graph theory is an emerging tool to explore the disease-related reorganization processes that mirror the disease course more accurately than the measures based on conventional magnetic resonance imaging (MRI) [3]. Structural networks can be derived either from T_1 -weighted MR images or from diffusion-tensor imaging. The networks' topological organization is defined based on the relations of nodes and connections and is described in terms of integration and segregation measures [4].

This work aimed to disclose the remodeling of brain structural network architecture in patients with MS. We have postulated that patients show distinct alterations in cortical gray matter networks' organization due to neuroinflammatory and degenerative processes. To address this hypothesis, we constructed group connectivity matrices based on individual cortical thickness measurements from brain MRI and compared the network topological measures between the MS patients and healthy subjects.

D. Ciolac
Nicolae Testemițanu State University of Medicine and Pharmacy,
Chisinau, Republic of Moldova

D. Ciolac (✉)
Department of Neurology, Institute of Emergency Medicine,
Toma Ciorba 1, Chisinau, Republic of Moldova
e-mail: dimaciolac@gmail.com

D. Ciolac
Department of Neurology, Focus Program Translational
Neuroscience (FTN), Rhine-Main Neuroscience Network
(RMN2), University Medical Center of the Johannes Gutenberg
University Mainz, Mainz, Germany

2 Materials and Methods

2.1 Participants

In total, 40 patients with MS (mean age \pm standard deviation 31.2 ± 7.0 years, 14 males) have been included. Diagnosis of relapsing-remitting MS was established according to the 2010 revised McDonald diagnostic criteria [5]. All patients were clinically evaluated, including the Expanded Disability Status Scale score assessment. A control group of age- and gender-matched 40 healthy subjects (27.1 ± 5.0 years, 14 males) without any history of neurological, psychiatric or autoimmune disorders was included.

The study protocol was approved by the Ethics Research Committee of Nicolae Testemitanu State University of Medicine and Pharmacy from the Republic of Moldova (notification no. 81 from 19.06.2018). All participants provided written informed consent (in accordance with the Helsinki Convention) prior to recruitment into the study.

2.2 MRI Dataset Acquisition

Patients with multiple sclerosis and healthy subjects underwent a 3T MRI scanning (Magnetom Tim Trio, Siemens Healthcare, Germany) with a 32-channel head coil by using a standardized protocol [6]. This protocol included sagittal three-dimensional T_1 -weighted magnetization prepared rapid gradient echo with repetition time = 1900 ms, echo time = 2.52 ms, inversion time = 900 ms, echo train length = 1, flip angle = 9° , matrix size = 256×256 , field of view = $256 \times 256 \text{ mm}^2$, slice thickness = 1 mm and three-dimensional T_2 -weighted fluid attenuated inversion recovery with repetition time = 5000 ms, echo time = 388 ms, inversion time = 1800 ms, echo train length = 848, matrix size = 256×256 , field of view = $256 \times 256 \text{ mm}^2$, slice thickness = 1 mm.

2.3 Image Processing and Cortical Thickness Reconstruction

We used FreeSurfer image analysis suit (version 5.3.0, <http://surfer.nmr.mgh.harvard.edu/>) to reconstruct cortical surface from T_1 -weighted images. The FreeSurfer pipeline runs in a fully automated fashion, followed by visual inspection at various processing steps for quality control. At a glance, the surface-based processing stream consists of skull stripping, transformation into Talairach space, optimization of boundaries between gray matter and white matter and between gray matter and cerebrospinal fluid, segmentation of subcortical white matter and deep gray

matter structures, and tessellation [7]. Cortical thickness at each vertex across the cortical mantle was calculated (in mm) as the average of the shortest distance between gray matter-white matter surface and gray matter-cerebrospinal fluid surface. Afterwards, cerebral cortex was parcellated into anatomical labels according to the Desikan-Killiany atlas for regional cortical thickness measurements [8]. The simplified analytical pipeline of the study is represented in Fig. 1.

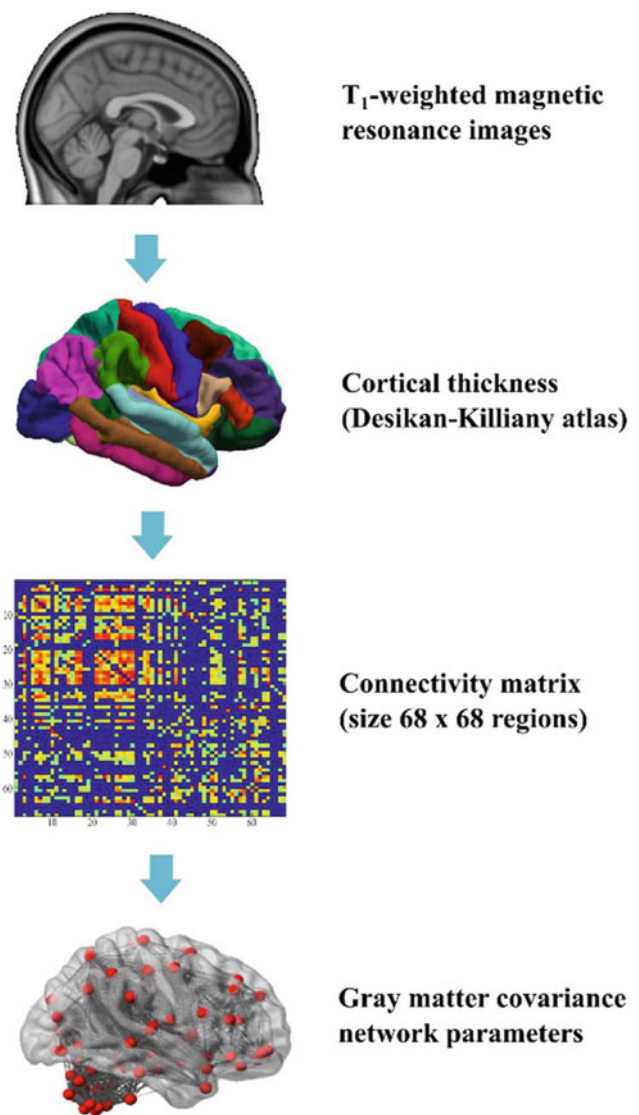


Fig. 1 The flowchart of MRI processing steps. From T_1 -weighted MR images, cortical thickness was quantified for each region and used to construct connectivity matrices, followed by graph theoretical analysis

2.4 Gray Matter Covariance Network Reconstruction

The cortical thickness from each cortical region of interest (according to Desikan-Killiany atlas) was extracted and served for the construction of gray matter connectivity matrices. For MS patients and healthy subjects the connectivity matrices (size 68×68 regions) were obtained by computing the Pearson correlation coefficient between the anatomical regions across the groups [2]. Here, we used Graph Analysis Toolbox to threshold the matrices into multiple densities, ranging from 0.35 to 0.45, and compute the network measures [9].

2.5 Network Topological Measures

Topological organization of gray matter networks was assessed by following parameters: modularity, clustering coefficient, local efficiency and global efficiency [2–4].

Modularity (Q) represents the strength of divisibility of a network into smaller modules, in which nodes are densely interconnected. Modularity is calculated using the Eq. (1).

$$Q = \frac{1}{i} \sum_{ef \in Z} \left[h_{ef} - \frac{g_e g_f}{i} \right] \delta_{m_e m_f} \quad (1)$$

where i is the actual number of links, m_e is the module containing a node e , and $\delta_{m_e m_f} = 1$ if $m_e = m_f$, and 0 otherwise.

Clustering coefficient (C) is the measure of network's local organization that indicates the number of connections between the neighbouring nodes. The clustering coefficient of a node e is represented by Eq. (2).

$$C_e = \frac{2t_e}{g_e(g_e - 1)} \quad (2)$$

where t_e is the number of triangles around the node e .

Local efficiency (E_{loc}) quantifies the efficiency of neural communication within the network at local level. Local efficiency is calculated using Eq. (3).

$$E_{loc} = \frac{1}{z} \sum_{e \in Z} E_{loc,e} \quad (3)$$

where $E_{loc,e}$ is the local efficiency of a node e .

Global efficiency (E) of a network is the average of the inverse distance matrix of all brain networks, estimating the efficiency of information flows through the entire network. Global efficiency is calculated using the Eq. (4).

$$E = \frac{1}{z} \sum_{e \in Z} E_e \quad (4)$$

where E_e is the efficiency of the node e .

2.6 Statistical Analysis

All statistical analyses were performed in MATLAB R2012b (Mathworks, Natick, Mass) and SPSS (version 20.0; IBM, Armonk, NY, USA.) software. The distribution of the analyzed variables was checked for normality by using Shapiro-Wilk test and by inspection of histograms. Assessment of between-group differences in parametric (age, network measures) and non-parametric (gender) variables was based on t-test or Pearson's χ^2 tests, where appropriate. A p value of less than 0.05 was considered as statistically significant.

3 Results

3.1 Participants' Data

The study participants displayed no difference in terms of age ($t = 0.26$, $p = 0.77$) and gender (Pearson $\chi^2 = 0.36$, $df = 1$, $p = 0.54$). Patients with multiple sclerosis had a mean disease duration of 4.5 ± 2 years and a median Expanded Disability Status Scale of 1.5 (range 0–6).

3.2 Structural Gray Matter Network Topology

The analyzed topological parameters of gray matter cortical networks revealed an altered network architecture in MS patients in comparison to healthy subjects (Fig. 2). Compared to healthy subjects, patients with MS showed significantly higher modularity (mean at all densities 0.20 ± 0.009 vs. 0.19 ± 0.005 , $p = 0.004$), higher clustering coefficient (0.68 ± 0.015 vs. 0.61 ± 0.014 , $p = 0.0001$) and higher local efficiency (0.82 ± 0.013 vs. 0.79 ± 0.013 , $p = 0.001$) but significantly lower global efficiency (0.67 ± 0.022 vs. 0.69 ± 0.019 , $p = 0.041$).

4 Discussion

Modern approaches based on neural networks provide a unique framework to describe the intricate organization of brain networks in many neurological disorders, including MS. Application of graph theory in modeling of brain networks offers an exceptional modality to understand the alterations of network architecture at global and local levels induced by MS pathology. In this study we analyzed the reorganization of structural network assemblies within the

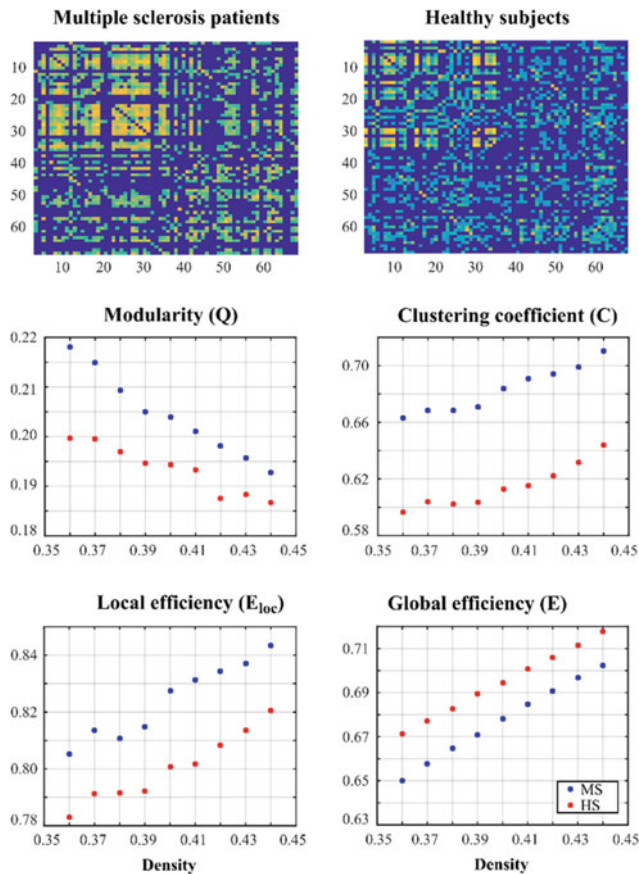


Fig. 2 The generated connectivity matrices (68×68 cortical regions) of multiple sclerosis (MS) patients and healthy subjects (HS) (upper row). Mean values across densities of modularity (Q), clustering coefficient (C), local efficiency (E_{loc}) and global efficiency (E) in MS patients compared to HS

cortical gray matter in patients with relapsing-remitting MS. The identified alterations of network topology in MS patients points towards a pattern of increased intramodular connectivity and intermodular segregation.

The findings of our study showed increased modularity, clustering coefficient and local efficiency but decreased global efficiency in MS patients. Modularity as a measure of segregation reflects the strength of division of a network into smaller units – modules, which represent conglomerates of nodes with strong connections within the module and weak connections with the nodes of other modules. An increase in modularity indicates a stronger partition of networks with enhanced connectivity within the module and breakdown of

between-module connections [1]. As evidenced by recent studies, progression of MS leads to the remodeling of brain neural circuits towards a topology of higher modularity with long-range disconnections and increase in local connectivity [2, 3]. Increased modularity could be explained by the presence of disseminated demyelinating lesions interrupting the neural tracts and thus might represent a sensitive signature of network reorganization in response to deleterious effects of the disease [1].

Clustering coefficient is also a parameter of network's segregation that quantifies the number of connections between the neighboring nodes. Higher clustering coefficient in MS patients indicates the strengthening of short-range connections and is in line with the increased modularity. A combined structural-functional study showed that cortical gray matter networks in MS patients exhibit an increased clustering coefficient as well as characteristic path length in comparison to healthy subjects [10]. Perhaps, increases in clustering coefficient occur independently on disease duration or lesion load [3]. In conditions of increased clustering coefficient the network nodes are more likely to be connected to each other in order to maintain the local information processing [1, 3].

Local efficiency describes the connectivity and information processing in the immediate proximity of a node. Despite the fact that in patients with MS networks become more segregated and remotely “isolated”, the information processing within the modules is preserved at a high level that is reflected by the increased local efficiency. However, on the other hand the global efficiency, which is a measure of integration across the whole brain networks, was decreased in our patients, perhaps driven by the loss of long-distance paths. In contrast, several studies failed to find any significant differences in global efficiency between patients and healthy subjects [2, 3].

5 Conclusions

Overall, patients with MS exhibited an altered topological reorganization pattern of cortical structural networks. This compromised network architecture profile in patients with MS was directed towards an increased number of connections within the network modules and enhanced local processing. The reorganized network topology might serve a

compensatory mechanism in order to maintain proper functioning of brain networks under deleterious conditions of disease-induced diffuse tissue injury.

Acknowledgements I would like to thank Sergiu Groppa, Stanislav Groppa, and Muthuraman Muthuraman for the support.

Conflict of Interest The author has no conflict of interest to disclose.

References

1. Fleischer, V., Radetz, A., Ciolac, D., et al.: Graph theoretical framework of brain networks in multiple sclerosis: a review of concepts. *Neuroscience* **403**, 35–53 (2019). <https://doi.org/10.1016/j.neuroscience.2017.10.033>
2. Muthuraman, M., Fleischer, V., Kolber, P., et al.: Structural brain network characteristics can differentiate CIS from early RRMS. *Front. Neurosci.* **10**, 14 (2016). <https://doi.org/10.3389/fnins.2016.00014>
3. Fleischer, V., Gröger, A., Koirala, N., et al.: Increased structural white and grey matter network connectivity compensates for functional decline in early multiple sclerosis. *Mult. Scler.* **23**(3), 432–441 (2017). <https://doi.org/10.1177/1352458516651503>
4. Rubinov, M., Sporns, O.: Complex network measures of brain connectivity: uses and interpretations. *Neuroimage* **52**(3), 1059–1069 (2010). <https://doi.org/10.1016/j.neuroimage.2009.10.003>
5. Polman, C., Reingold, S., Banwell, B., et al.: Diagnostic criteria for multiple sclerosis: 2010 revisions to the McDonald criteria. *Ann. Neurol.* **69**(2), 292–302 (2011). <https://doi.org/10.1002/ana.22366>
6. Droby, A., Lukas, C., Schänzer, A., et al.: A human post-mortem brain model for the standardization of multi-centre MRI studies. *Neuroimage* **110**, 11–21 (2015). <https://doi.org/10.1016/j.neuroimage.2015.01.028>
7. Fischl, B., Salat, D.H., Busa, E., et al.: Whole brain segmentation: automated labeling of neuroanatomical structures in the human brain. *Neuron* **33**(3), 341–355 (2002)
8. Desikan, R., Ségonne, F., Fischl, B., et al.: An automated labeling system for subdividing the human cerebral cortex on MRI scans into gyral based regions of interest. *Neuroimage* **31**, 968–980 (2006). <https://doi.org/10.1016/j.neuroimage.2006.01.021>
9. Hosseini, S., Hoeft, F., Kesler, S.: GAT: a graph-theoretical analysis toolbox for analyzing between-group differences in large-scale structural and functional brain networks. *PLoS ONE* **7**, e40709 (2012). <https://doi.org/10.1371/journal.pone.0040709>
10. Tewarie, P., Steenwijk, D., Tijms, M., et al.: Disruption of structural and functional networks in long-standing multiple sclerosis. *Hum. Brain Mapp.* **35**(12), 5946–5961 (2014). <https://doi.org/10.1002/hbm.22596>

Polarization Tomography of Synovial Fluids Polycrystalline Layers

V. V. Protsiuk, V. L. Vasiyk, Y. M. Vasylichshyn, O. G. Ushenko, M. V. Shaplavskiy, O. B. Bodnar, A. V. Dubolazov, Yu. O. Ushenko, and Yu. Ya. Tomka

Abstract

The experimental and diagnostic capabilities of the polarization tomography method of linear birefringence distributions of polycrystalline films of the synovial fluid of a human joint in the differentiation of its pathological states are considered. Present the structural-logical scheme and analytical description of the differential diagnosis of aseptic and septic loosening of the artificial hip joint endoprosthesis using the methods of differential Mueller-matrix mapping.

Keywords

Polarization • Linear birefringence • Polycrystalline films • Tomography

1 Introduction

This article contains:

- Structural-logical scheme and analytical description of the differential diagnosis of aseptic and septic loosening of the artificial hip joint endoprosthesis using the methods of differential Mueller-matrix mapping [1–3] of linear birefringence (LB) distributions of polycrystalline synovial fluid (SF) films.
- Results of statistical analysis of the distributions of LB of polycrystalline SF films of patients from the control

V. V. Protsiuk · V. L. Vasiyk · Y. M. Vasylichshyn · M. V. Shaplavskiy · O. B. Bodnar
Bukovinian State Medical University, Chernivtsi, Ukraine

O. G. Ushenko (✉) · A. V. Dubolazov · Yu. O. Ushenko · Yu. Ya. Tomka
Chernivtsi National University, 2 Kotsyubinskogo Str., Chernivtsi, Ukraine
e-mail: a.dubolazov@chnu.edu.ua

Yu. O. Ushenko
e-mail: o.ushenko@chnu.edu.ua

group and groups with different severity of the hip joint pathology.

- Results of establishing the strength of the differential Mueller-matrix mapping method of the distributions of LB polycrystalline films of SF by means of information analysis based on sensitivity determination, specificity and accuracy of the polarization tomography technique.

2 Structural-Logical Scheme of Differential Mueller-Matrix Tomography of Polycrystalline Structure of Films of SF

See Table 1.

3 Differential Diagnosis of Aseptic and Septic Loosening of the Artificial Hip Joint Endoprosthesis Cup by the Method of Mueller-Matrix Reconstruction of LB Size Distributions of Polycrystalline Films of Synovial Fluid of the Knee Joint

This part of the article contains materials on the experimental implementation of polarization reproduction with a comprehensive statistical and correlation analysis of the coordinate distributions of the magnitude of circular birefringence of polycrystalline films of synovial fluid of the hip joint of patients from the control group 1 and research groups 2 and 3:

- Group 1—Deforming osteoarthritis of the right and left hip joint of the third stage; coxarthrosis on the right and left of the third stage; aseptic necrosis of the head of the left and right femur of the IVth stage—group 1 (25 patients);
- Group 2—Aseptic fracture of components of the left and right artificial hip joint endoprosthesis—group 2 (25 patients);

Table 1 Structural-logical scheme of differential Mueller-matrix tomography of polycrystalline films of SF in the differential diagnosis of aseptic and septic loosening of the endoprosthesis cup of an artificial hip joint

Polycrystalline films of synovial fluid (SF)		
Differential Mueller-matrix mapping of polycrystalline SF films		
LB maps		
Statistical and correlation analysis		
Mean values and fluctuations of the magnitude of the statistical moments of the 1st–4th orders characterizing the distribution of the LB value of the samples of the SF		
Information analysis of the Mueller-matrix polarization tomography method for polycrystalline structure of SF films		
Sensitivity, Se	Specificity, Sp	Accuracy, Ac

- Group 3—septic laceration of the left and right hip joint endoprosthesis components—group 3 (25 patients).

An experimental method for determining the coordinate distributions of the magnitude of the CB of samples of SF polycrystalline films is presented in [4–6].

A series of Figs. 1, 2 and 3 illustrates the LB maps (left sides), the coordinate distributions of the LB values (right sides), and two-dimensional autocorrelation functions, which are determined by Mueller-matrix reproduction of linear birefringence of fibrillary networks of a set of polycrystalline films of SF hip joint of patients from control group 1 (Fig. 1), research group 2 (Fig. 2) and research group 3 (Fig. 3).

Quantitative characteristics of the statistical and correlation analysis of the entire set of maps of the distribution of

linear birefringence of polycrystalline films within representative samples of each of the control and experimental groups of samples of synovial fluid smears of patients with different severity of hip joint pathology are presented in Table 2.

Analysis of the results of statistical (SM_{1-4}) and correlation ($KM_{2,4}$) analysis of the distributions of the LB value of polycrystalline films of the SF found:

- high efficiency of differential diagnostics of aseptic and septic loosening of the artificial hip joint endoprosthesis cup based on the calculation of the 1st to 4th order statistical moments characterizing the linear birefringence distributions;
- for each of the statistical parameters SM_{1-4} within all three groups the magnitude $p < 0.001$;

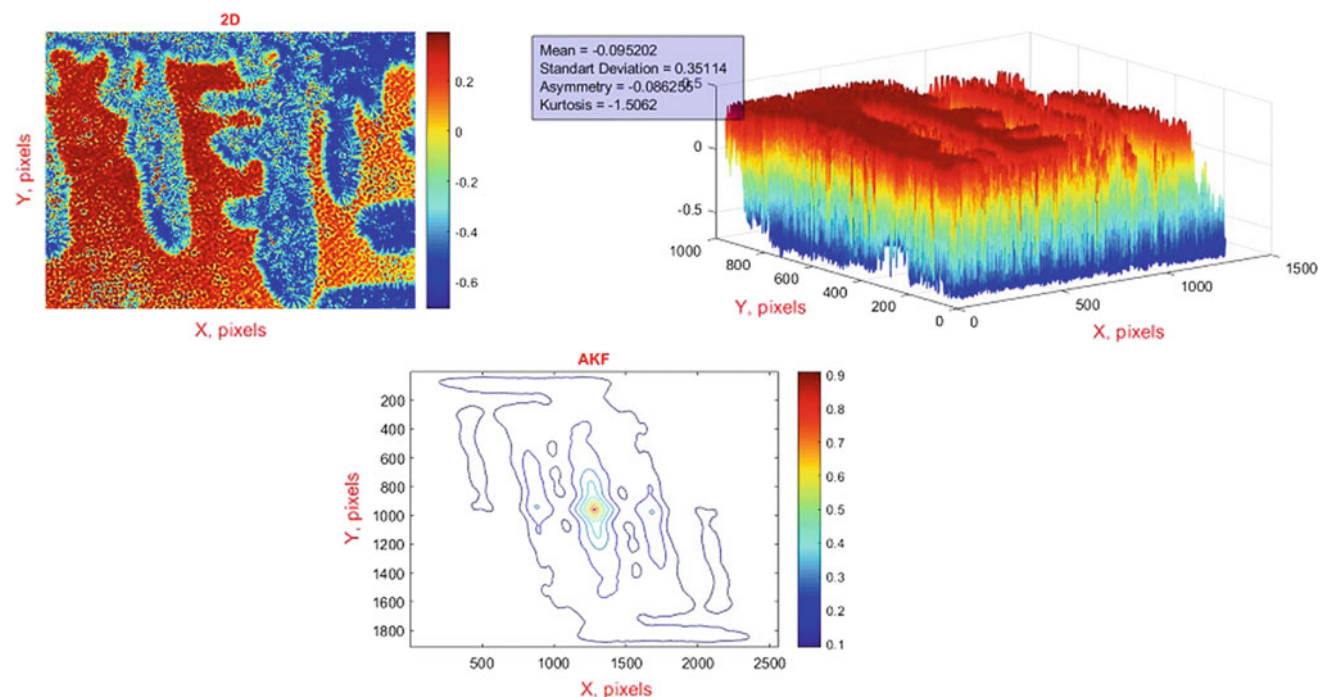


Fig. 1 Map (left part), coordinate distribution (right part) and autocorrelation function (bottom part) of random variables LB of the patient's SF polycrystalline film from group 1

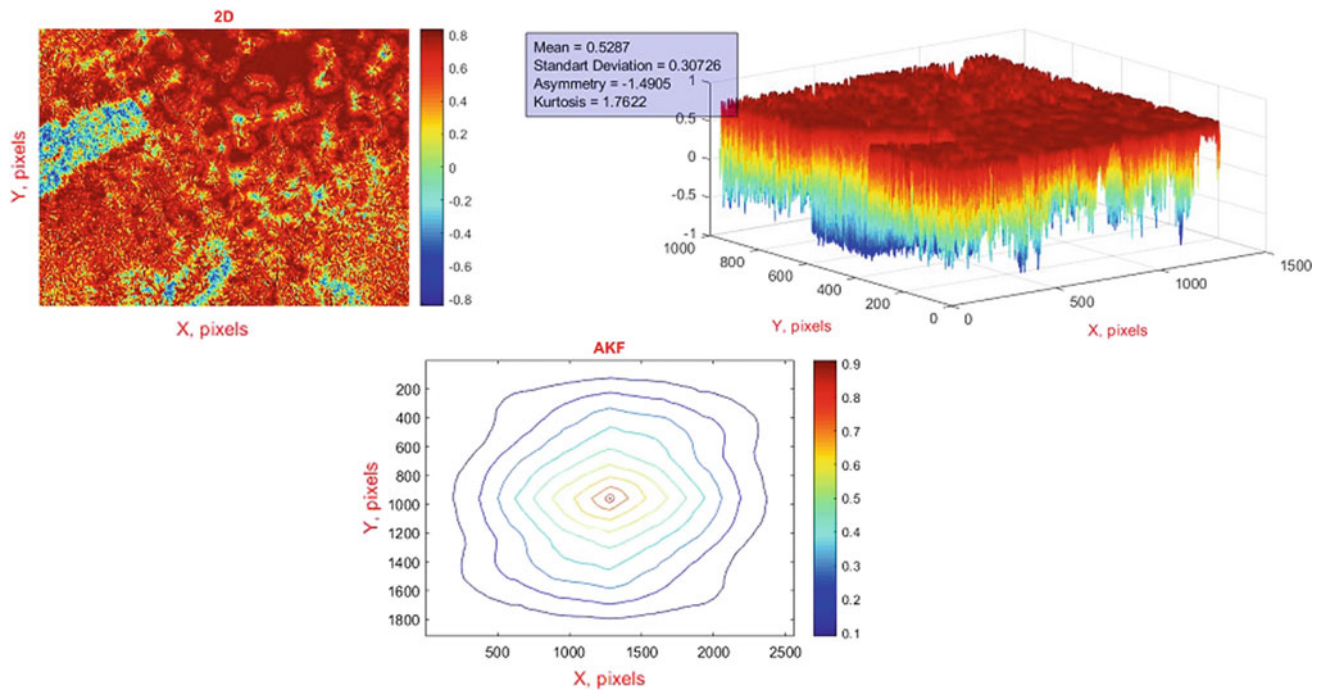


Fig. 2 Map (left part), coordinate distribution (right part) and autocorrelation function (bottom part) of random variables LB of the patient's SF polycrystalline film from group 2

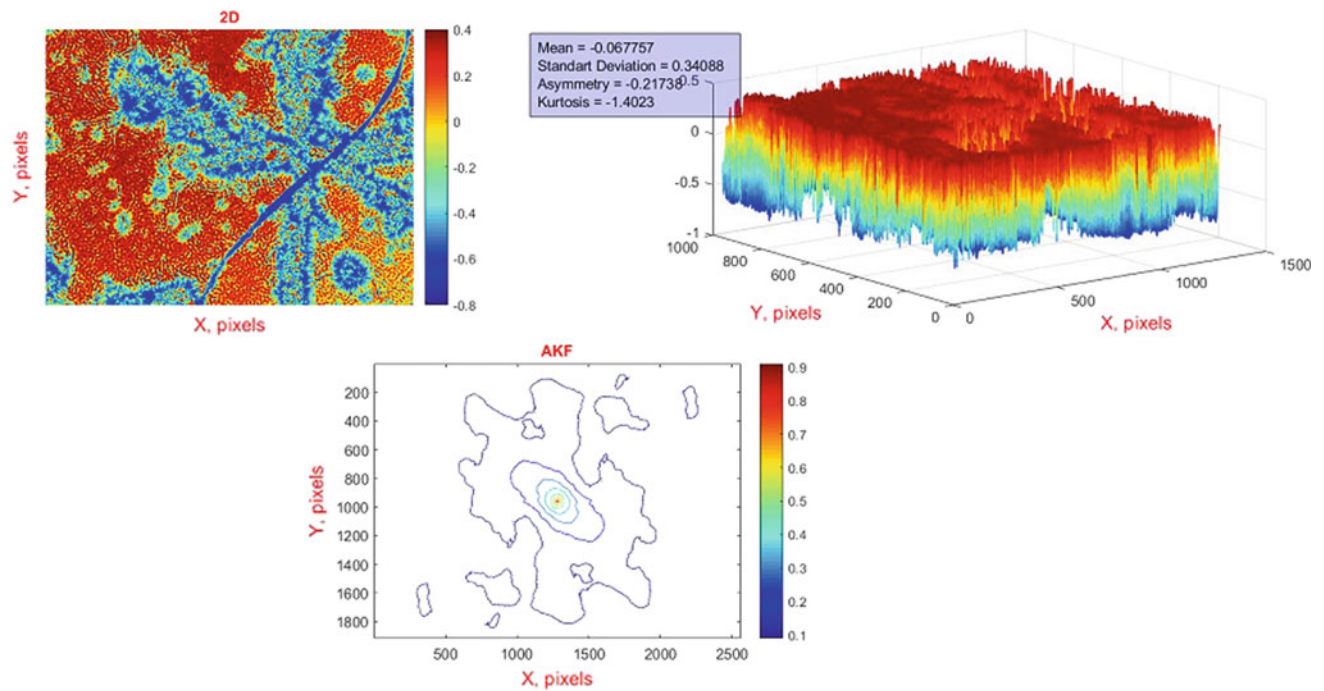


Fig. 3 Map (left part), coordinate distribution (right part) and autocorrelation function (bottom part) of random variables LB of the patient's SF polycrystalline film from group 3

- for the correlation parameters characterizing the half-width and sharpness of the peak of the autocorrelation function of the coordinate distribution of the linear birefringence of SF polycrystalline films from group 2 and group 3, the parameter also changes to a magnitude $p < 0.001$.

Table 2 Statistical SM_{1-4} and correlation moments $KM_{2,4}$ that characterize the distribution of LB values of polycrystalline films of the SF

Statistical moments	Control group	Experienced groups	
	Group 1 (n = 25)	Group 2 (n = 25)	Group 3 (n = 25)
Average, SM_1	0.75±0.041	0.51±0.027	0.32±0.019
P ₁		$p < 0.05$	$p < 0.05$
P ₂		$p < 0.05$	
Dispersion, SM_2	0.41±0.023	0.29±0.016	0.18±0.011
P ₁		$p < 0.05$	$p < 0.05$
P ₂		$p < 0.05$	
Asymmetry, SM_3	0.24±0.014	0.38±0.021	0.49±0.026
P ₁		$p < 0.05$	$p < 0.05$
P ₂		$p < 0.05$	
Excess, SM_4	0.41±0.022	0.61±0.034	0.88±0.046
P ₁		$p < 0.05$	$p < 0.05$
P ₂		$p < 0.05$	
Dispersion, KM_2	0.08±0.005	0.06±0.004	0.04±0.002
P ₁		$p < 0.05$	$p < 0.05$
P ₂		$p < 0.05$	
Excess, KM_4	0.67±0.012	0.99±0.047	1.12±0.063
P ₁		$p < 0.05$	$p < 0.05$
P ₂		$p < 0.05$	

4 Information Analysis of the Mueller-Matrix Data Reconstruction of the Distributions of the Magnitude of the Circular Birefringence of Polycrystalline Films of SF

The values of sensitivity, specificity and accuracy of the Mueller-matrix method of reproducing the LB distributions for SF samples of all three patient groups are presented in Table 3.

As can be seen, the overall level of the operational characteristics of the polarization tomography technique (sensitivity, specificity and balanced accuracy) of the linear birefringence distributions of fibrillar networks of polycrystalline films of SF reaches the highest possible level 95–97%.

Table 3 Operational characteristics of the method Mueller-matrix tomography LB

	Se	Sp	Ac
ST1	88	84	86
ST2	92	92	92
ST3	96	88	92
ST4	96	92	94
KT2	92	84	88
KT4	96	96	96

Identified:

- the range of variation of the sensitivity value of the polarization reproduction of the linear birefringence distributions is $88\% \leq Se \leq 96\%$;
- the range of variation of the specificity of the polarization reproduction of the linear birefringence distributions is $88\% \leq Sp \leq 96\%$;
- the range of variation of the magnitude of the balanced accuracy of the polarization reproduction of the linear birefringence distributions is $88\% \leq Ac \leq 96\%$.

As can be seen, the overall level of the operational characteristics of the polarization tomography technique (sensitivity Se , specificity Sp and balanced accuracy Ac) of the linear birefringence distributions of fibrillar networks of polycrystalline films of SF reaches the highest possible level 95–97%.

5 Conclusions

1. A structural-logical scheme and a description of the differential diagnosis of aseptic and septic loosening of the artificial hip joint endoprosthesis cup have been developed and substantiated by Mueller-matrix reproduction (reconstruction) distributions of the linear birefringence polycrystalline SF films.

2. In the framework of the statistical approach to the analysis of the structure of the coordinate distributions of the LB values of SF polycrystalline films of patients from the control group (group 1) and research groups (group 2 and group 3) of patients with different severity of the knee joint pathology:

- the effectiveness of the Mueller-matrix method of tomographic reconstruction of the coordinate distributions of the magnitude of LB in the differentiation of aseptic and septic loosening of the endoprosthesis cup of an artificial hip joint.

Conflict of Interest The authors declare that they have no conflict of interest.

References

1. Ushenko, Y.A., Dubolazov, A.V., Angelsky, A.P., Sidor, M.I., Bodnar, G.B., Koval, G., Zabolotna, N.I., Smolarz, A., Junisbekov, M.S.: Laser polarization fluorescence of the networks of optically anisotropic biological crystals. *Proc. SPIE—Int. Soc. Opt. Eng.* **8698**, 869809 (2013)
2. Ushenko, Yu.A., Bachynsky, V.T., Vanchulyak, O.Ya., Dubolazov, A.V., Garazdyuk, M.S., Ushenko, V.A.: Jones-matrix mapping of complex degree of mutual anisotropy of birefringent protein networks during the differentiation of myocardium necrotic changes. *Appl. Opt.* **55**(12), B113–B119 (2016)
3. Ushenko, Yu.A., Dubolazov, A.V., Karachevtcev, A.O., Zabolotna, N.I. A fractal and statistic analysis of Mueller-matrix images of phase inhomogeneous layers. *Proc. SPIE—Int. Soc. Opt. Eng.* **8134**, 81340P (2011)
4. Dubolazov, A.V., Pashkovskaya, N.V., Ushenko, Yu.A., Marchuk, Yu.F., Ushenko, V.A., Novakovskaya, O.Yu.: Birefringence images of polycrystalline films of human urine in early diagnostics of kidney pathology. *Appl. Opt.* **55**(12), B85–B90 (2016)
5. Dubolazov, A.V., Koval, G.D., Zabolotna, N.I., Pavlov, S.V.: Fractal structure of optical anisotropy Mueller-matrices images of biological layers. *Proc. SPIE—Int. Soc. Opt. Eng.* **9066**, 90661W (2013)
6. Ushenko, V.A., Sidor, M.I., Marchuk, Yu.F., Pashkovskaya, N.V., Andreichuk, D.R.: Azimuth-invariant mueller-matrix differentiation of the optical anisotropy of biological tissues. *Opt. Spectrosc.* (English translation of *Optika i Spektroskopiya*), **117**(1), 152–157 (2014)

Differential Muller-Matrix Microscopy of Protein Fractions of Vitreous Preparations in Diagnostics of the Pressure of Death

Yu. Sarkisova, V. T. Bachinskyi, M. Garazdyuk, O. Ya. Vanchulyak, O. Yu. Litvinenko, O. G. Ushenko, B. G. Bodnar, A. V. Dubolazov, Yu. O. Ushenko, Yu. Ya. Tomka, I. V. Soltys, and S. Foglinskiy

Abstract

The material of experimental approbation of the Muller-matrix mapping method of polycrystalline structure of vitreous preparations in the task of diagnosing its temporary necrotic changes is presented.

Keywords

Polarization • Mueller matrix • Optical anisotropy • Vitreous body

1 Introduction

Mueller-matrix polarimetry (MMP) is one of the important information-full areas of non-destructive diagnostics of the polycrystalline structure of biological layers, among the many directions of optical diagnostics of biological tissues. As a result of such studies, the relationships between indicatrix and Mueller-matrix images and the morphological structure of diffuse biological tissues are determined [1–3]. For non-depolarizing biological layers two-dimensional tomography techniques are developed—the reproduction of dual-beam refraction maps and dichroism. The aim of this work is to develop and to test experimentally the differential Mueller-matrix mapping^{26–31} of distributions of optical anisotropy parameters of partially depolarizing layers of biological tissues of different morphological structures [4, 5].

Yu. Sarkisova · V. T. Bachinskyi · M. Garazdyuk · O. Ya. Vanchulyak · O. Yu. Litvinenko · B. G. Bodnar
Bukovinian State Medical University, Chernivtsi, Ukraine

O. G. Ushenko (✉) · A. V. Dubolazov · Yu. O. Ushenko · Yu. Ya. Tomka · I. V. Soltys · S. Foglinskiy
Chernivtsi National University, 2 Kotsyubinskogo Str., Chernivtsi, Ukraine
e-mail: o.ushenko@chnu.edu.ua

A. V. Dubolazov
e-mail: a.dubolazov@chnu.edu.ua

2 Methods and Results

Presented research materials:

- temporal dynamics of necrotic changes in the coordinate distributions of the magnitude of the differential matrix element (DME) [4–8] of the protein fraction of vitreous body (VB) layers of the dead;
- magnitudes and ranges of temporal changes in the statistical moments of the 1st to 4th orders characterizing the distributions of the differential matrix element of the protein fraction of the layers of CT of the dead;
- efficiency and accuracy of determining the VB by the method of differential Muller matrix mapping of the protein component of the layers of age death (AD) of the dead;

Differential matrix images and temporal dynamics of changes in the protein component of the vitreous preparations of the dead with different AD.

The following groups of samples were investigated:

AD = 1 h—group 1 (21 samples);
AD = 3 h—group 2 (21 samples);
AD = 6 h—group 3 (18 samples);
AD = 12 h—group 4 (20 samples);
AD = 18 h—group 5 (22 samples);
AD = 24 h—group 6 (19 samples).

In Fig. 1 show maps (fragments 1) and histograms (fragments 2, 3) of the distributions of the DME value of the layers of the CT of the dead from group 1.

The results of the differential Muller matrix mapping of the coordinate distributions of the DME value illustrate the presence of differences between the optical anisotropy of the CT protein complexes of the deceased with different AD.

We have shown that the coordinate distributions of the DME value of a 12-h sample of a VB layer are characterized

Fig. 2 Time diagrams of changes in the magnitude of the statistical moments of the 1st to 4th orders, which characterize the distributions of the differential element of the protein fraction of the layers of VB of the dead with different AD

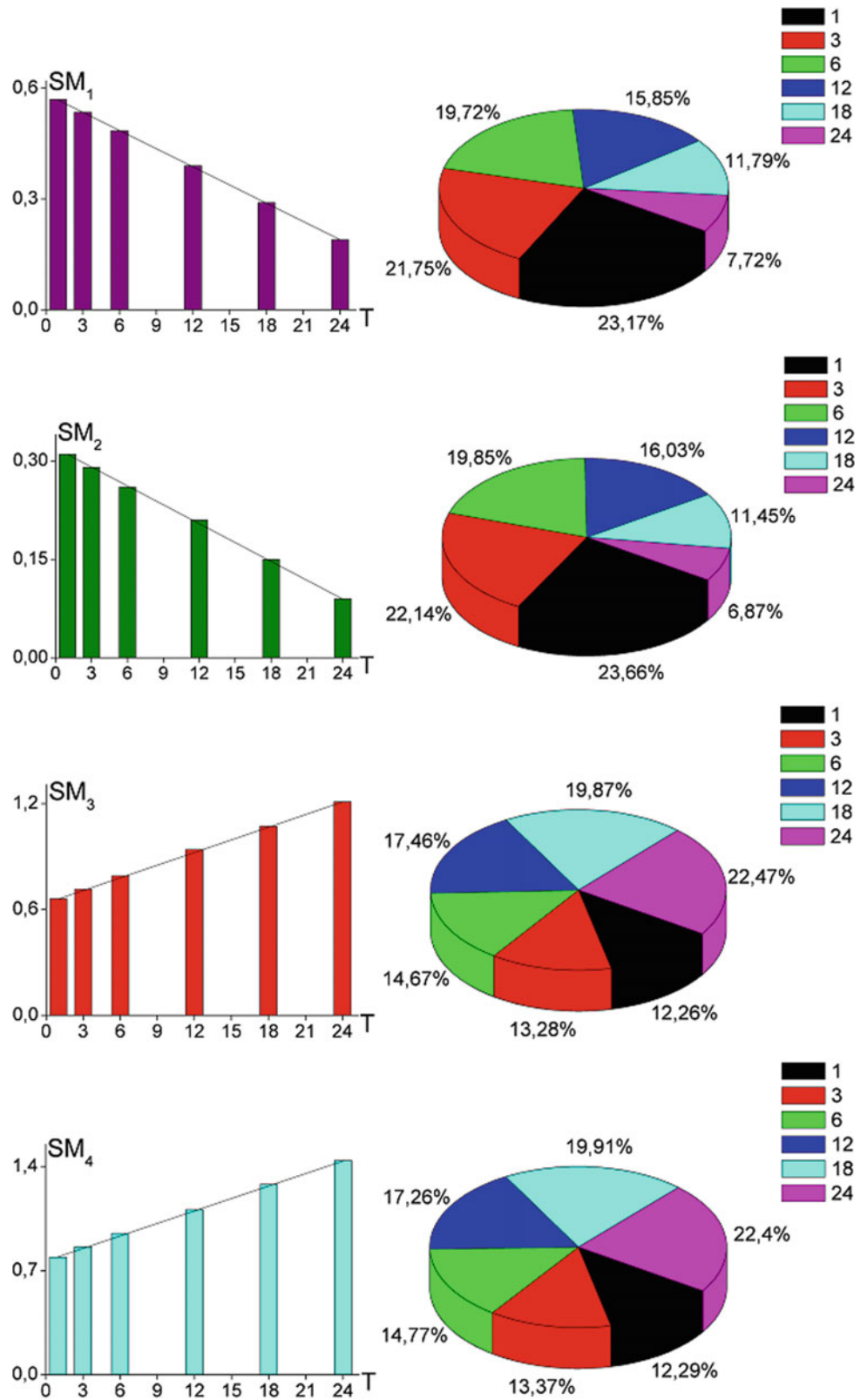


Table 2 Accuracy ($\pm \Delta T$) determination of AD by the matrix differential mapping method of the protein component of the layers of VB

SM_i	$T = 1$	$T = 3$	$T = 6$	$T = 12$	$T = 18$	$T = 24$
SM_1	54 min	54 min	55 min	55 min	56 min	56 min
SM_2	50 min	52 min	52 min	53 min	54 min	54 min
SM_3	44 min	43 min	44 min	43 min	45 min	45 min
SM_4	40 min	40 min	41 min	40 min	40 min	42 min

The analysis of the data obtained on the method of differential Muller matrix mapping of data on necrotic changes in the protein fraction of VB layers revealed a linear range of variation of the magnitude of the statistical moments of the 1st to 4th orders, which characterize the coordinate distributions of the DME of those who died by the magnitude of the AD is 24 h.

Figure 2 illustrates linear and pie charts of changes in the magnitude of a set of statistical moments $SM_{1,2,3,4}$.

From the data obtained (Fig. 2), it can be seen that the values of the statistical moments of the 1st to 4th orders (average 1, variance 2, asymmetry 3 and kurtosis 4) characterizing the polarization maps of the protein fraction layers of VB of the dead with different AD, linearly vary within 24 h.

At the same time, the most sensitive to the necrotic changes of the polycrystalline structure of such samples turned out to be temporary changes in the statistical moments of the 3rd and 4th orders—*asymmetry* SM_3 and *excess* SM_4 , characterizing the distributions of the DME value.

Quantitatively, the improvements in the sensitivity of the differential Muller matrix mapping are found in the growth of tilt angles of the linear dependencies of the necrotic changes in the magnitude of the statistical moments of higher orders characterizing the distributions of the DME of the layers of VB of the dead with different AD—Table 2.

Analysis of the obtained data on the time dependences of the set of statistical moments of the 1st - 4th orders, characterizing the distribution of the differential element of the protein fraction of the layers of VB in different intervals of the AD, found the maximum level (highlighted in gray) in determining the LD within 40–42 min, which corresponds to the accuracy of laser polarimetry methods [5, 6].

3 Conclusions

A set of maps and histograms of the distributions of random values of the differential element of the protein fraction of the layers of VB of the dead with different duration of death

occurred by the method of differential Muller-matrix mapping.

The temporal dynamics of changes in the magnitude of the statistical moments of the 1st - 4th orders, which characterize the differential element of the protein fraction of the layers of VB of the dead with different AD, was studied.

Established: sensitivity range (24 h) and accuracy (40 min) of the differential Muller-matrix mapping method of the protein fraction of VB layers in certain AD.

Conflict of Interest The authors declare that they have no conflict of interest.

References

1. Wang, X., Wang, L.-H.: Propagation of polarized light in birefringent turbid media: a monte carlo study. *J. Biomed. Opt.* **7**, 279–290 (2002)
2. Tuchin, V.V.: *Handbook of Optical Biomedical Diagnostics*. SPIE Press, Bellingham, 1110 p. (2002)
3. Yao, G., Wang, L.V.: Two-dimensional depth-resolved Mueller matrix characterization of biological tissue by optical coherence tomography. *Opt. Lett.* **24**, 537–539 (1999)
4. Ushenko, Yu.A., Tomka, Yu.Ya., Dubolazov, A.V., Telen'ga, O. Yu.: Diagnostics of optical anisotropy changes in biological tissues using Muller matrix. *Quantum Electron.* **41**(3), 273–277 (2011)
5. Ushenko, Yu.A., Tomka, Yu.Ya., Dubolazov, A.V.: Laser diagnostics of anisotropy in birefringent networks of biological tissues in different physiological conditions. *Quantum Electron.* **41**(2), 170–175 (2011)
6. Ushenko, Y.A., Dubolazov, O.V., Karachevtsev, A.O.: Statistical structure of skin derma Mueller matrix images in the process of cancer changes. *Opt. Mem. Neural Netw. (Inf. Opt.)* **20**(2), 145–154 (2011)
7. Ushenko, V.A., Dubolazov, A.V.: Correlation and self similarity structure of polycrystalline network biological layers mueller matrices images. *Proc. SPIE—Int. Soc. Opt. Eng.* **8856**, 88562D (2013)
8. Ushenko, A.G., Dubolazov, A.V., Ushenko, V.A., Novakovskaya, O.Y.: Statistical analysis of polarization-inhomogeneous Fourier spectra of laser radiation scattered by human skin in the tasks of differentiation of benign and malignant formations. *J. Biomed. Opt.* **21**(7), 071110 (2016)

Laser Autofluorescent Microscopy of Histological Sections of Parenchymatous Biological Tissues of the Dead

O. G. Ushenko, A.-V. Syvokorovskaya, V. T. Bachinsky,
O. Ya. Vanchuliak, A. V. Dubolazov, Yu. O. Ushenko, Yu. Ya. Tomka,
and M. L. Kovalchuk

Abstract

The results of experimental testing of the diagnostic capabilities of the method of spectral-selective fluorescence microscopy of temporary necrotic changes in histological sections of kidney internal organs are presented.

Keywords

Laser • Fluorescence • Microscopy • Statistical moments • Kidney

1 Introduction

The results of laser autofluorescence microscopy of the distribution of the intensity of the multidimensional laser autofluorescence (MLA) microscopy of polycrystalline structures [1–3] of biological tissue preparations are presented. The data of a statistical analysis of the distribution of the magnitude of the intensity of MLA networks of biological crystals of histological sections of tissues of the kidney with the parenchymal morphological structure of the dead with different levels of blood loss are presented.

2 Functional Diagram of Multidimensional Laser Autofluorescence (MLA) Microscopy of Biological Preparations

The multidimensional laser autofluorescence (MLA) microscopy of biological preparations include a next functional block diagram of spectrally selective laser autofluorescence microscopy of parenchymal biological tissues [4–7].

1. The illumination block IB of biological preparations, which ensures the formation of a polarized laser beam parallel to 2 mm in diameter with a wavelength of 0.405 μm , which excites the intrinsic fluorescence of the fluorophores of biological preparations;
2. The object block OB is a microscopic table with a two-coordinate movement on which the biological preparation BP is attached;
3. Projection block PB, which with the help of the micro-lens MO (4X) ensures the formation of an autofluorescent microscopic image of a biological preparation BP excited by a laser beam in the plane of the digital camera DC.
4. The block of spectral filtration of BF, which includes the interference light filters F for the spectral selection of the excited autoluoercent polychromatic radiation of an ensemble of BP fluorophores;
5. A block of photoelectron registration BFR of microscopic fluorescent images of biological preparations BP, which includes the CC and provides the formation of the coordinate digital distribution of the intensity value in the computer interface;
6. A data processing block DPB that, using a personal computer PC, provides a calculation of the magnitude of the statistical moments of the 1st to 4th orders characterizing the intensity distribution of the spectrally selective autofluorescence of biological preparations BP.

O. G. Ushenko (✉) · A. V. Dubolazov · Yu. O. Ushenko · Yu. Ya. Tomka · M. L. Kovalchuk
Chernivtsi National University, 2 Kotsyubinskogo Str., Chernivtsi, Ukraine
e-mail: o.ushenko@chnu.edu.ua

A. V. Dubolazov
e-mail: a.dubolazov@chnu.edu.ua

A.-V. Syvokorovskaya · V. T. Bachinsky · O. Ya. Vanchuliak
Bukovinian State Medical University, Chernivtsi, Ukraine

3 Samples

Depending on the level of blood loss (V), the following groups of samples of histological sections of the spleen and kidney with the subsequent level of blood loss were considered:

- $V = 0 \text{ mm}^3$ —group 1 (20 samples);
- $V = 500 \text{ mm}^3 \pm 100 \text{ mm}^3$ —group 2 (22 samples);
- $V = 1000 \text{ mm}^3 \pm 100 \text{ mm}^3$ —group 3 (27 samples);
- $V = 1500 \text{ mm}^3 \pm 100 \text{ mm}^3$ —group 4 (32 samples);
- $V = 2000 \text{ mm}^3 \pm 100 \text{ mm}^3$ —group 5 (22 samples);
- $V = 2500 \text{ mm}^3 \pm 100 \text{ mm}^3$ —group 6 (25 samples).

Maps (fragments 1, 3) and histograms (fragments 2, 4) distributions of the magnitude of the intensity of MLA polycrystalline structures of samples of histological sections of the kidneys of the dead from group 1 (fragments 1, 2) and group 3 (fragments 3, 4), obtained by the method of spectral-selective laser autofluorescence microscopy, are shown in a series of dependences in Fig. 1.

Analysis of the obtained data revealed that with an increase in blood loss and a corresponding decrease in the concentration of blood cells, the fluorescence intensity of the optically anisotropic collagen networks of the kidney of the deceased decreases (Fig. 1, fragments 2, 4). Such changes are manifested in a decrease in the magnitudes of the corresponding statistical parameters—the mean and variance,

which characterize the distribution of the intensity of the MLA of histological sections of the kidney tissue of all groups of the dead. In parallel with this, the magnitudes of the 3rd and 4th order statistical moments, which characterize the asymmetry and excess of distributions of the corresponding MLA histological sections of the kidney of the dead in the range of blood loss $0 \text{ mm}^3 \div 2500 \text{ mm}^3$, increase.

The data of statistical analysis of changes in the structure of MLA samples of histological sections of the kidney of the dead with varying degrees of blood loss illustrate the statistical moments of the 1st to 4th orders, the magnitudes of which are shown in Table 1.

Established:

- the range of changes in the magnitude of the 1st to 4th order statistical moments, characterizing the distribution of the intensity of the MLA of histological sections of the kidney, in terms of the volume of blood loss is $0 \text{ mm}^3 \div 2500 \text{ mm}^3$;
- the statistical moment of the 1st order SM_1 changes within the range of variation of averages magnitudes from 0.32 to 0.04;
- the statistical moment of the 2nd order SM_2 changes within the range of variation of averages magnitudes from 0.26 to 0.03;
- the statistical moment of the 3rd order SM_3 changes within the range of variation of averages magnitudes from 0.97 to 2.51;

Fig. 1 Maps (1, 3) and histograms (2, 4) distributions of the autofluorescence intensity of histological sections of the kidney of the control (1, 2) and research (3, 4) groups the dead

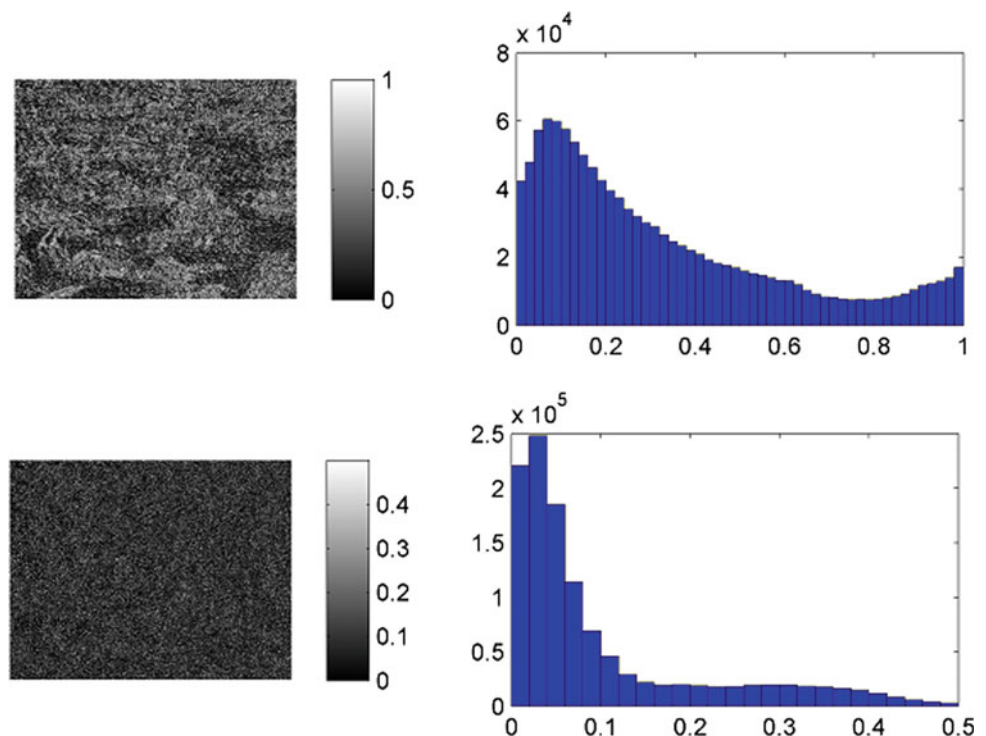


Table 1 Statistical structure of autofluorescence intensity maps of histological sections of the kidney of the dead with varying degrees of blood loss

Blood loss, mm ³	0	500 ± 100 mm ³	1000 ± 100 mm ³
The average, SM ₁	0.32 ± 0.013	0.26 ± 0.012	0.21 ± 0.011
Criteria, t, p	p < 0.05	p < 0.05	p < 0.05
Dispersion, SM ₂	0.26 ± 0.012	0.21 ± 0.011	0.16 ± 0.07
Criteria, t, p	p < 0.05	p < 0.05	p < 0.05
Asymmetry, SM ₃	0.97 ± 0.045	1.33 ± 0.062	1.61 ± 0.074
Criteria, t, p	p < 0.05	p < 0.05	p < 0.05
Excess, SM ₄	0.51 ± 0.022	1.04 ± 0.043	1.69 ± 0.078
Criteria, t, p	p < 0.05	p < 0.05	p < 0.05
Blood loss, mm ³	1500 ± 100 mm ³	2000 ± 100 mm ³	2500 ± 100 mm ³
The average, SM ₁	0.16 ± 0.007	0.09 ± 0.004	0.04 ± 0.002
Criteria, t, p	p < 0.05	p < 0.05	p < 0.05
Dispersion, SM ₂	0.11 ± 0.005	0.07 ± 0.003	0.03 ± 0.001
Criteria, t, p	p < 0.05	p < 0.05	p < 0.05
Asymmetry, SM ₃	1.92 ± 0.089	2.23 ± 0.11	2.51 ± 0.12
Criteria, t, p	p < 0.05	p < 0.05	p < 0.05
Excess, SM ₄	2.02 ± 0.096	2.43 ± 0.11	2.89 ± 0.13
Criteria, t, p	p < 0.05	p < 0.05	p < 0.05

- the statistical moment of the 4th order SM₄ changes within the range of variation of averages magnitudes from 0.51 to 2.89.

In Fig. 2 shows diagrams of changes in the set of statistical moments of the 1st to 4th orders SM_{1;2;3;4}, which characterize the coordinate structure of the distributions of random laser autofluorescence intensity (MLA) values of optically anisotropic collagen networks of a set of

histological sections of the kidney of the dead from all groups according to the level of blood loss.

Statistical analysis of laser spectral-selective laser autofluorescence microscopy of optically anisotropic grids of biological crystals found (Fig. 2; Table 1) a decrease in average, dispersion, and, conversely, an increase in asymmetry and excess, which characterize the distributions of the intensity of MLA of histological sections of the kidney of the deceased, within volume of blood loss 0 mm³ ÷

Fig. 2 Dependences of the magnitude of the average (1), dispersion (2), asymmetry (3) and excess (4), which characterize the autofluorescence intensity maps of histological sections of the kidney of the deceased with varying degrees of blood loss

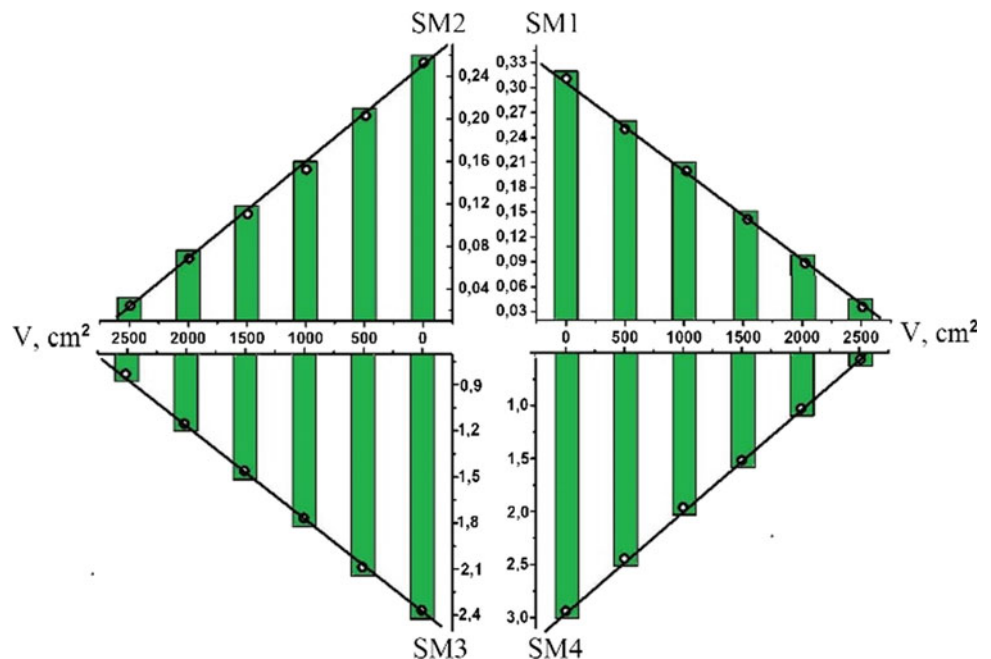
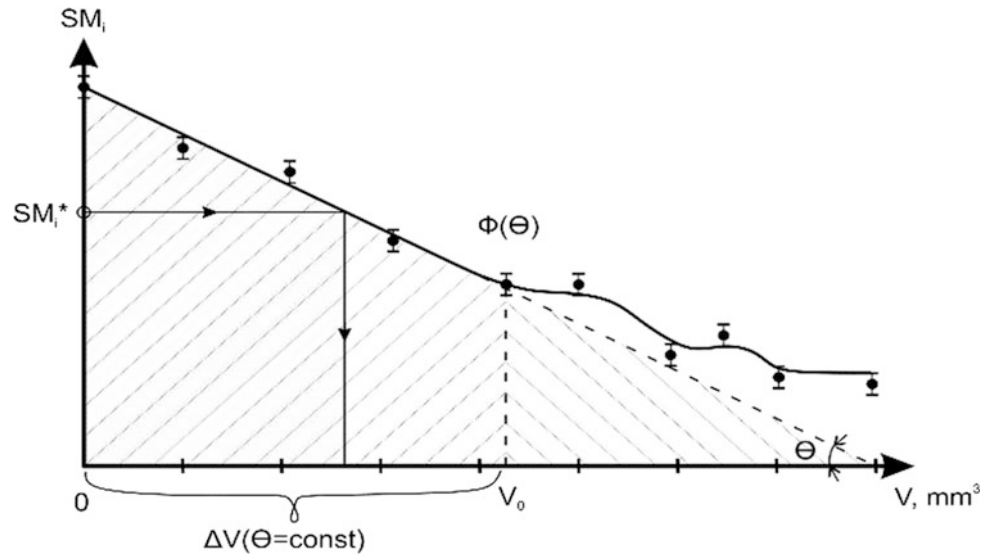


Fig. 3 Analytical scheme for determining the volume of blood loss of the dead according to the method of laser autofluorescence microscopy



2500 mm³. The most sensitive to changes in the fluorescence intensity of histological sections of the kidney with blood loss of varying volume were the statistical moments of the 1st, 2nd, and 4th orders.

4 The Effectiveness of the Differential Diagnosis of the Degree of Blood Loss by Laser Autofluorescence Microscopy

For each statistical moment that characterizes the distribution of the MLA intensity values of a set of spleen samples from different groups of deceased, the accuracy of determining the blood loss volume was found on the basis of a series of nomograms presented in Fig. 3.

The analysis of the obtained data revealed the following parameters of the diagnostic efficiency of the statistical analysis of the results of the method of spectrally selective laser autofluorescence microscopy of histological sections of parenchymal biological tissues (Table 2):

1. For all studied biological preparations, the range of sensitivity of the method of spectral-selective laser autofluorescence microscopy to changes in the volume of blood loss of the dead is the maximum level 0 mm³ ÷ 2500 mm³.

2. The accuracy of the method of spectral-selective laser autofluorescence microscopy of biological samples varies in the range: $\Delta V = 0 \text{ mm}^3 \div 2500 \text{ mm}^3 \Leftrightarrow 86\% - 92\%$;
3. The maximum level is reached for the following statistical parameters characterizing laser autofluorescence maps of histological sections of the kidney

$$\begin{cases} SM_1 \Leftrightarrow 94\% - 96\%; \\ SM_2 \Leftrightarrow 94\% - 96\%; \\ SM_4 \Leftrightarrow 90\% - 94\%. \end{cases}$$

5 Conclusions

1. A set of maps and histograms of random fluorescence intensity distributions of blood corpuscles of the polycrystalline component of histological sections of parenchymal biological tissues of the spleen and kidney of the deceased with varying degrees of blood loss were studied using spectral-selective laser autofluorescence microscopy.
2. The dynamics of changes in the magnitude of the statistical moments of the 1st to 4th orders, characterizing

Table 2 Accuracy of determining the volume of blood loss in the kidney

Blood loss, mm ³	500 ± 100 mm ³	1000 ± 100 mm ³	1500 ± 100 mm ³	2000 ± 100 mm ³	2500 ± 100 mm ³
Average, SM ₁	96	96	96	94	94
Dispersion, SM ₂	96	96	94	92	92
Asymmetry, SM ₃	84	86	86	86	84
Excess, SM ₄	94	94	92	90	90

the distribution of MLA histological sections of parenchymal (spleen, kidney) tissues of the deceased with different blood loss— $\Delta V = 0 \text{ mm}^3 \div 2500 \text{ mm}^3$, was studied.

3. The magnitudes and ranges of accuracy of the method of spectral-selective laser autofluorescent microscopy of biological preparations of the spleen are determined

$$\begin{cases} SM_1 \Leftrightarrow 94\% - 96\%; \\ SM_2 \Leftrightarrow 94\% - 96\%; \\ SM_4 \Leftrightarrow 90\% - 94\%. \end{cases}$$

Conflict of Interest The authors declare that they have no conflict of interest.

References

1. Ushenko, A.G., Dubolazov, A.V., Ushenko, V.A., Novakovskaya, O.Y.: Statistical analysis of polarization-inhomogeneous fourier spectra of laser radiation scattered by human skin in the tasks of differentiation of benign and malignant formations. *J. Biomed. Opt.* **21**(7), 071110 (2016)
2. Ushenko, Y.A., Dubolazov, A.V., Angelsky, A.P., Sidor, M.I., Bodnar, G.B., Koval, G., Zabolotna, N.I., Smolarz, A., Junisbekov, M.S.: Laser polarization fluorescence of the networks of optically anisotropic biological crystals. *Proc. SPIE— Int. Soc. Opt. Eng.* **8698**, 869809 (2013)
3. Ushenko, Yu.A., Bachynsky, V.T., Vanchulyak, O.Ya., Dubolazov, A.V., Garazdyuk, M.S., Ushenko, V.A.: Jones-matrix mapping of complex degree of mutual anisotropy of birefringent protein networks during the differentiation of myocardium necrotic changes. *Appl. Opt.* **55**(12), B113–B119 (2016)
4. Ushenko, Yu.A., Dubolazov, A.V., Karachevtcev, A.O., Zabolotna, N.I.: A fractal and statistic analysis of mueller-matrix images of phase inhomogeneous layers. *Proc. SPIE— Int. Soc. Opt. Eng.* **8134**, 81340P (2011)
5. Dubolazov, A.V., Pashkovskaya, N.V., Ushenko, Yu.A., Marchuk, Yu.F., Ushenko, V.A., Novakovskaya, O.Yu.: Birefringence images of polycrystalline films of human urine in early diagnostics of kidney pathology. *Appl. Opt.* **55**(12), B85–B90 (2016)
6. Dubolazov, A.V., Koval, G.D., Zabolotna, N.I., Pavlov, S.V.: Fractal structure of optical anisotropy mueller-matrices images of biological layers. *Proc. SPIE— Int. Soc. Opt. Eng.* **9066**, 90661W (2013)
7. Ushenko, V.A., Sidor, M.I., Marchuk, Yu.F., Pashkovskaya, N.V., Andreichuk, D.R.: Azimuth-invariant mueller-matrix differentiation of the optical anisotropy of biological tissues. *Opt. Spectrosc.* (English translation of *Optika i Spektroskopiya*), **117**(1), 152–157 (2014)

Statistical Analysis of Polarization Images of Histological Cuts of Parenchymatic Tissues in Diagnostics of Volume of Blood Loss

N. Sivokorovskaya, V. T. Bachinskyi, O. Ya. Vanchulyak, O. G. Ushenko, A. V. Dubolazov, Yu. O. Ushenko, Yu. Ya. Tomka, and L. Ya. Kushnerik

Abstract

The results of polarization mapping of the distribution of the parameters of the Stokes vector of microscopic images of histological sections of parenchymal tissues of human organs in the problem of determining the level of blood loss are presented.

Keywords

Polarization • Stokes parameters • Optical anisotropy • Blood loss

1 Introduction

The results of a statistical analysis of the distributions of the value of the fourth parameter of the Stokes vector (hereinafter the “phase parameter”—FP) of microscopic images of histological sections of spleen tissues with parenchymal morphological structure of the dead with varying degrees of blood loss are presented.

2 Functional Diagram of Multidimensional Polarization Microscopy of Biological Preparations

In Fig. 1 shows a functional block diagram of polarization microscopy [1] of histological sections of biological tissues, which operates in Stokes polarimetry mode [2–4].

N. Sivokorovskaya · V. T. Bachinskyi · O. Ya. Vanchulyak
Bukovinian State Medical University, Chernivtsi, Ukraine

O. G. Ushenko · A. V. Dubolazov ·
Yu. O. Ushenko (✉) · Yu. Ya. Tomka · L. Ya. Kushnerik
Chernivtsi National University, 2 Kotsyubinskogo Str., Chernivtsi,
Ukraine
e-mail: o.ushenko@chnu.edu.ua

A. V. Dubolazov
e-mail: a.dubolazov@chnu.edu.ua

Here:

1. the illumination block IB of biological preparations, which provides the formation of a parallel, diameter 2 mm, polarized, laser beam with a wavelength of 0.63 μm ;
2. the PF polarization filter, using a polarizer P and a quarter-wave phase plate of the FP, ensures the formation of azimuthally invariant circular polarization;
3. the object block OB is a microscopic table with a two-coordinate movement on which the biological preparation BP is attached;
4. projection block PB, which with the help of a polarizing microtitre VET (4X) provides for the formation of a microscopic image of the biological preparation BP in the plane of the digital camera DC;
5. the block of polarization analysis BPA, consisting of the FP and P and provides measurement of the intensity of linearly polarized azimuths of $\pm 45^\circ$ and right and left circularly polarized laser beams;
6. a block for photoelectron registration of BPR of microscopic images of biological preparations BP, which includes the DC and ensures the formation of a coordinate digital distribution of the intensity value at the computer interface
7. the data processing unit DPU, which, using a personal computer PC, provides the calculation of the parameters of the Stokes vector of biological preparations and the statistical analysis of the distributions of their size using known methods, which are described in detail in [5–7].

3 Objects of Study

Samples were investigation (histological sections with a geometric thickness of 30 μm) of the spleen with varying degrees of blood loss:

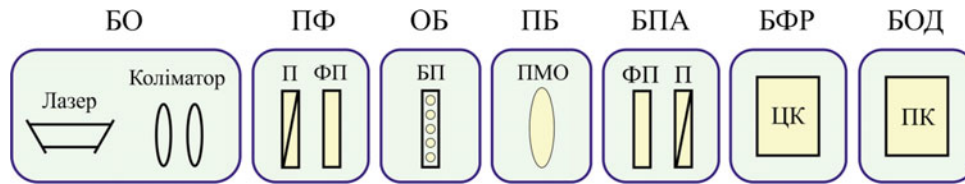


Fig. 1 Functional block diagram of multidimensional polarization microscopy

- $V = 0 \text{ mm}^3$ —group 1 (18 samples);
- $V = 500 \text{ mm}^3$ —group 2 (22 samples);
- $V = 1000 \text{ mm}^3$ —group 3 (15 samples);
- $V = 1500 \text{ mm}^3$ —group 4 (27 samples);
- $V = 2000 \text{ mm}^3$ —group 5 (24 samples);
- $V = 2500 \text{ mm}^3$ —group 6 (22 samples).

4 Analysis and Discussion of Experimental Data

In Fig. 2 shows the coordinate distributions (fragments 1, 3) and histograms (fragments 2, 4) of random values of the FP value of microscopic images of histological sections of the spleen of the dead from group 1 (fragments 1, 2) and groups 3 (fragments 3, 4).

Quantitatively, the scenario of changing the distributions of the coordinate phase structure of a set of points in the plane of microscopic images of histological sections of the

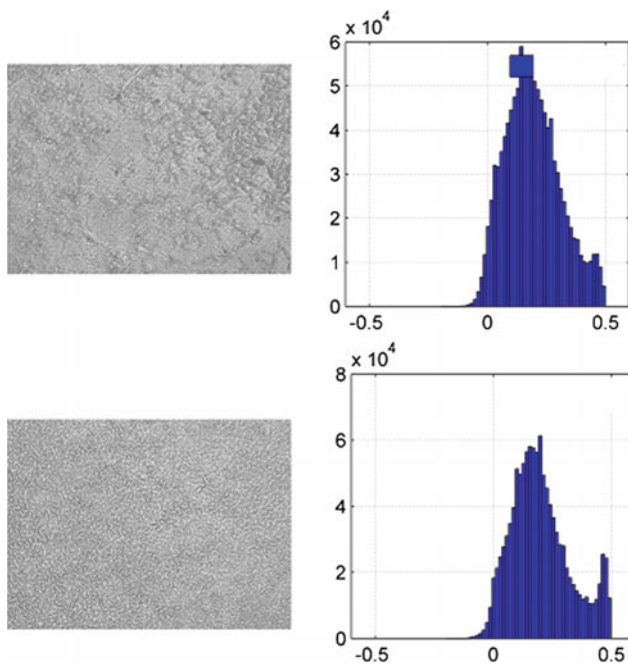


Fig. 2 Maps (1, 3) and histograms (2, 4) of the distributions of the value of the third parameter of the Stokes vector of microscopic images of histological sections of the spleen control (1, 2) and studied (3, 4) groups of decease

spleen of the dead with varying degrees of blood loss is illustrated by the statistical moments of the 1st to 4th orders, which characterize the Stokes polarimetric maps shown in Table 1.

Established:

- the range of changes in the magnitude of the statistical moments of the 1st to 4th orders, characterizing the distribution of FP microscopic images of histological sections of the spleen, according to the level of blood loss is $0 \text{ mm}^3 \div 1000 \text{ mm}^3$;
- average varies from 0.19 to 0.21;
- dispersion ranges from 0.12 to 0.125;
- asymmetry varies from 0.55 to 0.39;
- excess varies from 0.35 to 0.26.

In Fig. 3 shows diagrams of changes due to spleen blood loss a set of statistical moments $SM_{1;2;3;4}$.

From the data obtained (Fig. 3), it can be seen that the dynamics of changes in the magnitude of statistical moments (average 1, variance 2, asymmetry 3 and excess 4) characterizing the Stokes polarimetric maps of histological sections of the spleen of the deceased vary in limits of blood $0 \text{ mm}^3 \div 1000 \text{ mm}^3$. The asymmetry (SM_3) and excess (SM_4) turned out to be the most sensitive to such changes in the optical anisotropy of histological sections.

5 Determination of the Degree of Blood Loss

The algorithm for determining the degree of blood loss is illustrated in Fig. 4.

Analysis of the obtained data revealed the following parameters of the diagnostic efficiency of statistical analysis of the results of the method of polarization microscopy of histological sections of parenchymal biological tissues (Table 2).

1. For all studied biological preparations, the range of sensitivity of the Stokes polarimetry method of microscopic images to changes in the blood loss of the dead is $0 \text{ mm}^3 \div 1000 \text{ mm}^3$.
2. The accuracy of the Stokes polarimetric method ranges from
 - $\Delta V = 0 \text{ mm}^3 \div 1000 \text{ mm}^3 \Leftrightarrow 86\% - 92\%$;
 - $\Delta V = 1500 \text{ mm}^3 \div 2500 \text{ mm}^3 \Leftrightarrow 56\% - 68\%$.

Table 1 Statistical structure of the Stokes polarimetric maps of histological sections of the spleen of the dead with varying degrees of blood loss

Blood loss, mm ³	0	500 ± 100 mm ³	1000 ± 100 mm ³
The average, SM ₁	0.19 ± 0.008	0.195 ± 0.008	0.21 ± 0.009
Criteria, t,p	p < 0.05	p < 0.05	p < 0.05
Dispersion, SM ₂	0.12 ± 0.006	0.12 ± 0.005	0.125 ± 0.005
Criteria, t,p	p < 0.05	p < 0.05	p < 0.05
Asymmetry, SM ₃	0.55 ± 0.024	0.48 ± 0.021	0.39 ± 0.017
Criteria, t,p	p < 0.05	p < 0.05	p < 0.05
Excess, SM ₄	0.35 ± 0.015	0.305 ± 0.013	0.26 ± 0.011
Criteria, t,p	p < 0.05	p < 0.05	p < 0.05
Blood loss, mm ³	1500 ± 100 mm ³	2000 ± 100 mm ³	2500 ± 100 mm ³
The average, SM ₁	0.19 ± 0.008	0.24 ± 0.011	0.18 ± 0.008
Criteria, t,p	p > 0.05	p > 0.05	p > 0.05
Dispersion, SM ₂	0.11 ± 0.005	0.14 ± 0.006	0.13 ± 0.006
Criteria, t,p	p < 0.05	p < 0.05	p < 0.05
Asymmetry, SM ₃	0.33 ± 0.014	0.41 ± 0.018	0.35 ± 0.015
Criteria, t,p	p < 0.05	p < 0.05	p < 0.05
Excess, SM ₄	0.22 ± 0.009	0.25 ± 0.11	0.21 ± 0.009
Criteria, t,p	p < 0.05	p < 0.05	p < 0.05

Fig. 3 Dependences of mean (1), dispersion (2), asymmetry (3) and excess (4), characterizing Stokes polarimetric maps of histological sections of the spleen of the deceased with varying degrees of blood loss

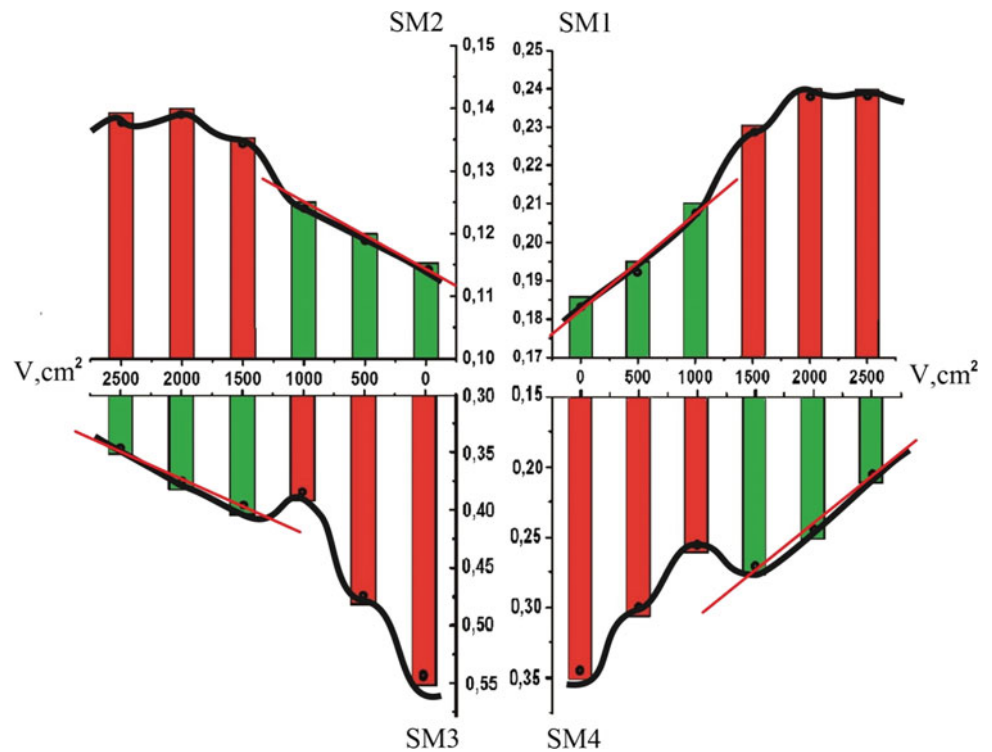


Fig. 4 Analytical scheme for determining the volume of blood loss of the dead according to the method of polarization microscopy

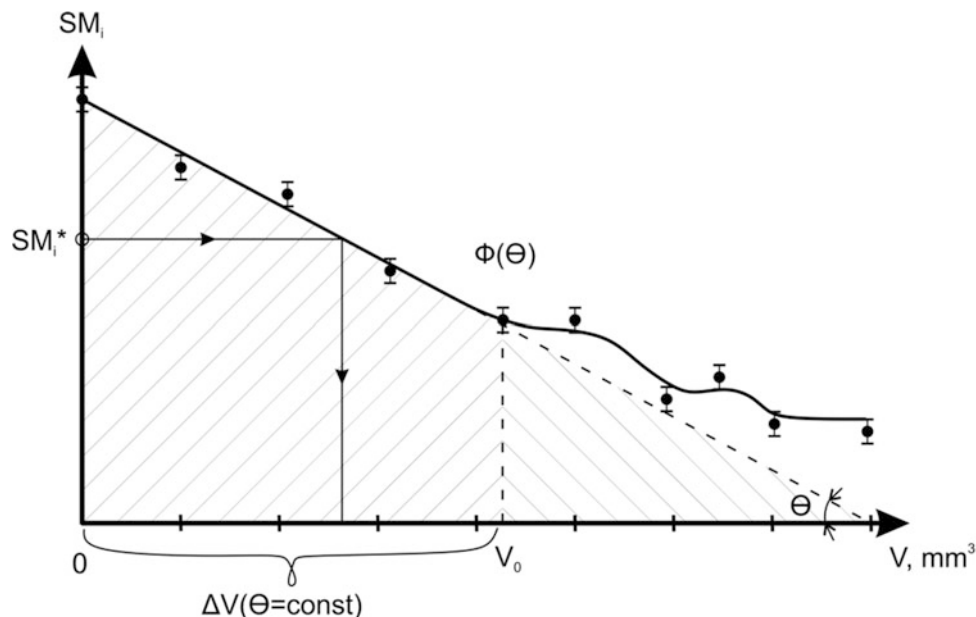


Table 2 Accuracy of determining the volume of blood loss in the spleen

Blood loss, mm ³	500 ± 100 mm ³	1000 ± 100 mm ³	1500 ± 100 mm ³	2000 ± 100 mm ³	2500 ± 100 mm ³
Average, SM_1	68	67	62	60	60
Dispersion, SM_2	70	68	64	60	62
Asymmetry, SM_3	80	82	70	62	60
Excess, SM_4	88	86	68	63	61

3. The maximum level is achieved for the following statistical parameters characterizing polarization maps of histological sections.

- Spleen— $SM_3 \Leftrightarrow 80\% - 82\%$;
 $SM_4 \Leftrightarrow 86\% - 88\%$;

6 Conclusions

A set of polarization maps and histograms of distributions of random values of the phase parameter of microscopic images of histological sections of parenchymal biological tissues of the deceased with varying degrees of blood loss was studied by the Stokes polarimetric mapping method.

The dynamics of changes in the magnitude of the statistical moments of the 1st to 4th orders, characterizing the distribution of the phase parameter of polarizing microscopic images of histological sections of the spleen of the dead with varying degrees of blood loss— $\Delta V = 0 \text{ mm}^3 \div 2500 \text{ mm}^3$.

The range of sensitivity of the method of Stokes polarimetry of microscopic images to changes in the level of blood loss of the dead is established— $\Delta V = 0 \text{ mm}^3 \div 1000 \text{ mm}^3$.

It is shown that the maximum level is reached for statistical moments characterizing polarization maps of microscopic images of histological sections of the spleen— asymmetry and excess $SM_{3,4} \Leftrightarrow 86\% - 88\%$.

Conflict of Interest The authors declare that they have no conflict of interest.

References

1. Ushenko, Yu.A., Dubolazov, A.V., Karachevtcev, A.O., Zabolotna, N.I.: A fractal and statistic analysis of mueller-matrix images of phase inhomogeneous layers. Proc. SPIE— Int. Soc. Opt. Eng. **8134**, 81340P (2011)
2. Dubolazov, A.V., Pashkovskaya, N.V., Ushenko, Yu.A., Marchuk, Yu.F., Ushenko, V.A., Novakovskaya, O.Yu.: Birefringence images

- of polycrystalline films of human urine in early diagnostics of kidney pathology. *Appl. Opt.* **55**(12), B85–B90 (2016)
3. Dubolazov, A.V., Koval, G.D., Zabolotna, N.I., Pavlov, S.V.: Fractal structure of optical anisotropy mueller-matrices images of biological layers. *Proc. SPIE— Int. Soc. Opt. Eng.* **9066**, 90661W (2013)
 4. Ushenko, V.A., Sidor, M.I., Marchuk, Yu.F., Pashkovskaya, N.V., Andreichuk, D.R.: Azimuth-invariant mueller-matrix differentiation of the optical anisotropy of biological tissues. *Opt. Spectrosc.* (English translation of *Optika i Spektroskopiya*), **117**(1), 152–157 (2014)
 5. Ushenko, V.A., Pavlyukovich, N.D., Trifonyuk, L.: Spatial-frequency azimuthally stable cartography of biological polycrystalline networks. *Int. J. Opt.* **2013**, 683174 (2013)
 6. Ushenko, V.A., Zabolotna, N.I., Pavlov, S.V., Burcovets, D.M., Novakovska, O.Yu.: Mueller-matrices polarization selection of two-dimensional linear and circular birefringence images. *Proc. SPIE— Int. Soc. Opt. Eng.* **9066**, 90661X (2013)
 7. Ushenko, V.O.: Two-dimensional mueller matrix phase tomography of self-similarity birefringence structure of biological tissues. *Proc. SPIE— Int. Soc. Opt. Eng.* **8487**, 84870W (2012)

Deep Learning in Processing Medical Images and Calculating the Orbit Volume

V. S. Asipovich, O. N. Dudich, V. L. Krasilnikova, A. A. Karakulko, A. L. Radnionok, P. A. Moroz, A. Y. Nikolaev, M. A. Konovalova, and K. D. Yashin

Abstract

A software tool for calculating the volume of a soft-tissue eye orbit using the deep learning of neural network Mask R-CNN has been developed and tested. The result of the development will be in demand when evaluating the results of surgical intervention for the reconstruction of the thin bones of the orbit. It was established that the inaccuracy in constructing the contour of a soft-tissue orbit is 4–8%.

Keywords

Orbit • Orbit volume • Deep learning • Neural network • Biomedical images

1 Introduction

One of the criteria for evaluating the results of surgery to eliminate post-traumatic defects of the orbital bones is the calculation of the volume of the orbit before and after surgery. Currently, the estimation of the orbit volume is carried out using software tools to visualize the results of X-ray computer tomography in three projections and methods of layer-by-layer calculation of the orbit volume based on the spots set by the surgeon [1–3]. Along with the assessment of the orbit volume, there is an assessment of the tendency for changes in the volume of various types of tissue in the orbit [4].

At the same time, the analysis of the images obtained in the MSCT [5–7] in the DICOM [8] format and the

three-dimensional reconstruction of the skull allows the surgeon to more reliably estimate the anatomical features of the individual patient, localization, boundaries and prevalence of the pathological process, and plan the scope of the surgery [9, 10].

The purpose of the project was the development of software tool for calculating the orbit volumes by using neural network machine learning technologies.

2 Experimental Technique

2.1 Initial Data

The results of microspiral computer tomography of 70 patients with fractures of orbit bones of varying severity were used as initial data for neural network learning. For each patient, a set of images in the DICOM format, obtained using the results of the Siemens Emotion 6 Microspiral Computer Tomography Scanner (Germany), was analyzed.

The preparation of images for neural network learning was carried out by layering these images. Before the marking process, DICOM images were converted to RGB images. The VGG Image Annotator application was used as a data marking tool. It is an application for manual annotation of images with the ability to perform multiple marking. The results of the marking are files in csv and json format, which store the information about the coordinates of the points bounding the polygon (the result of the marking of the orbit) in relation to the file name. Figure 1 shows an example of the marking of the initial files.

Initial data was divided into training and test in a percentage of 80 and 20%, respectively. Test initial data was used to test the operation of the neural network after learning. In addition, the test initial data was used as a control experiment to compare the results of the calculation of the volume of the orbit marked by the neural network with the volume of the orbit marked by hand.

V. S. Asipovich (✉) · A. A. Karakulko · A. L. Radnionok · P. A. Moroz · A. Y. Nikolaev · M. A. Konovalova · K. D. Yashin
Human Engineering and Ergonomics, Belarusian State University of Informatics and Radioelectronics, P. Brovki Street, 6, Minsk, Belarus
e-mail: v.asipovich@bsuir.by

O. N. Dudich · V. L. Krasilnikova
Department of Ophthalmology, Belarusian Medical Academy of Postgraduate Education, Minsk, Belarus

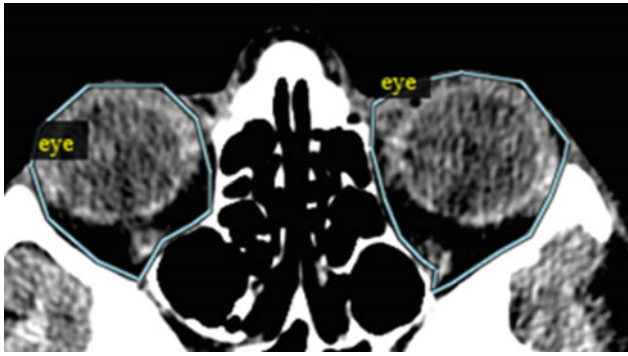


Fig. 1 The result of marking the initial data in one layer

2.2 Neural Network Learning

The task was solved by means of the Python programming language using the Anaconda platform. Tensorflow and Keras were used as the main frameworks for working with neural networks. A ready-made neural network architecture Mask R-CNN was used [5]. The neural network learning was started using the initial COCO weights [6] to ensure a faster learning process. The neural network learning had the following parameters: learning epoch—100, learning rate—0.001, regularization—0.0001, minimum probability at detecting—0.95.

2.3 Software Algorithm

The developed software works in two modes: the learning mode of the neural networks and the search mode for the contours of the orbits and the calculation of their volumes.

The algorithm of the software tool in the search mode for the contours of the orbits and calculation of their volumes consists of the following three procedures: (1) recognition of the contours of the orbit by the neural network by the input images in the DICOM format; (2) checking the correctness of the markings of the right and left orbits, correcting the results of the marking; (3) calculation of the volumes of the orbits and output of the results through the user interface.

The development of an additional procedure for unambiguous identification of the right and left orbits was required due to the fact that as a result of the neural network in some layers, the right orbit and left orbit were noted with an error: left as right, and right as left. Figure 2 shows the flowchart of the algorithm for correcting the recognition results of the orbit contours by the neural network.

In order to calculate the volume of orbits the following formula was used:

$$V = N \times a^2 \times h \quad (1)$$

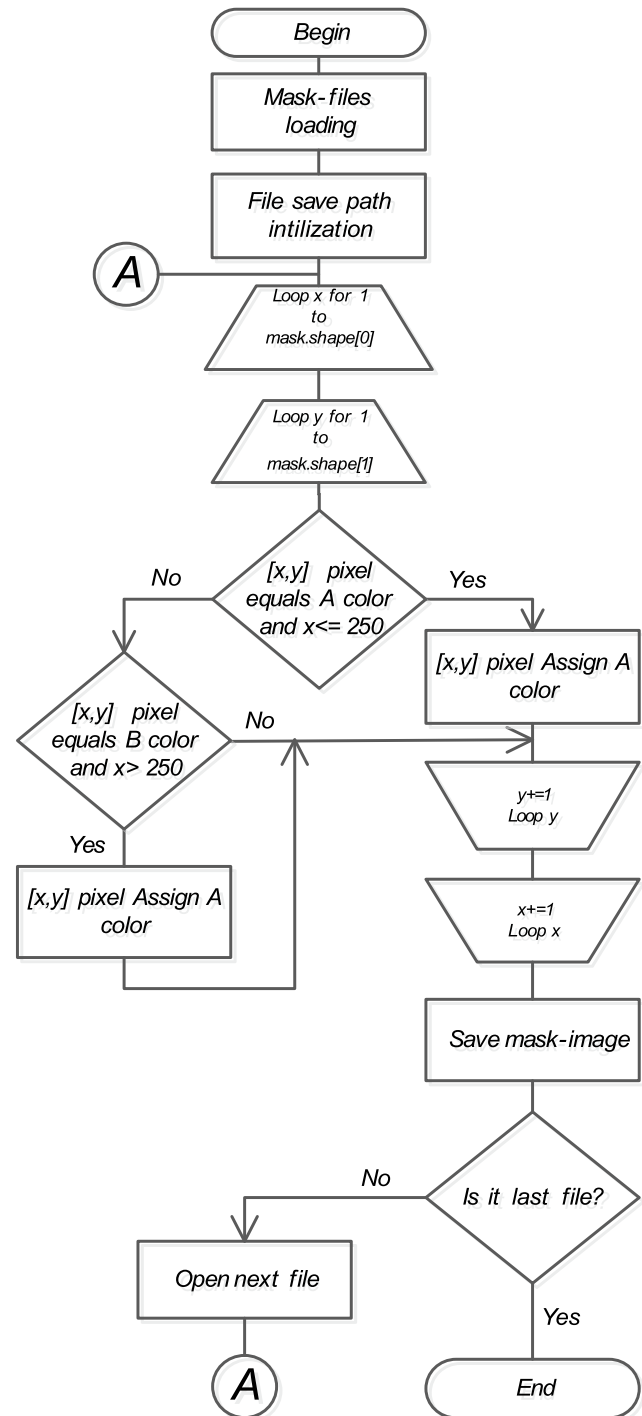


Fig. 2 Flowchart of the algorithm for correcting the results of the search for the orbit contours

where N is the number of pixels marked as part of the orbit; a is the pixel side length, mm; h is the distance between the layers, mm.

The pixel side length a and the distance between the layers h depend on the technical characteristics and resolving

power of the microspiral computer tomography apparatus. In our case, the resolving power of the original DICOM files is 512×512 pixels and $a = 0.455$ mm, and the distance between the layers $h = 0.625$ mm.

The procedures implemented by means of the Python programming language were tested on 14 sets of DICOM files in order to estimate the marking error by the neural network of orbits.

3 Results and Discussion

As a result of neural network learning, a matrix of weights was obtained for each layer of the neural network on the basis of which the orbits were marked in the test data sets.

The typical Grid of ground truth objects and their predictions obtained as a result of the processing of the biomedical image layer are shown in Fig. 3.

After processing the images of the test data sets using the trained neural network and the procedure for correcting the search results, separate data sets were obtained—files with orbit contours. Figure 4 shows the result of the overlay of the orbit contours constructed by the neural network on the original image of the layer received by the software tool.

Further, based on the sets of files with the orbit contours, the volume of the right and left orbits was calculated using the formula (1).

Comparison of the orbits calculated by the results of the neural network marking with the volumes of the orbits calculated by the results of manual marking showed that the difference is 4–8%. This indicates the high accuracy of the marking of the orbits by the neural network. The proposed software tool is useful for automating the process of calculating the volume of orbits at the stage of preparation for the

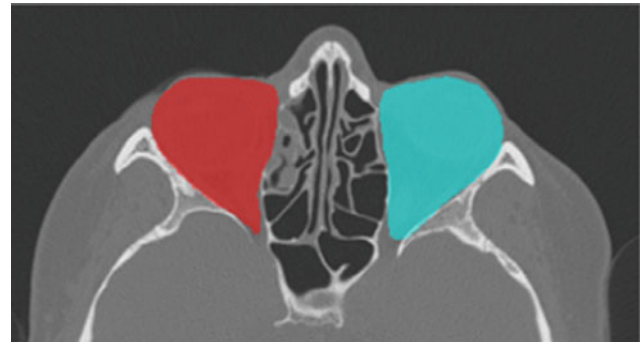


Fig. 4 The result of the search of the orbit by the neural network after learning

operation and in evaluating the results of the operation to replace the thin bones of the orbit.

4 Conclusions

It has been established that the difference in calculations of the volume of orbits based on biomedical images (computer tomography results) using a neural network is 4–8%.

A software tool has been developed and tested to reduce the time spent on preparing for surgery to replace the thin bones of the orbit by 30–40 min.

Conflict of Interest The authors declare that they have no conflict of interest.

References

1. Levchenko, O.V., Krylov, V.V., Davydov, D.V., Lezhnev, D.A., Mikhayliukov, V.M., Sharifullin, F.A., Kostenko, D.I.: The computer tomography for estimation of surgical reconstruction efficacy for treatment of posttraumatic defects and orbit deformations. *Russ. J. Neurosurg.* **1**, 29–33 (2014)
2. Levchenko, O.V., Mikhayliukov, V.M., Davydov, D.V.: Frameless navigation system for surgical treatment of posttraumatic defects and cranioorbital deformations. *Russ. J. Neurosurg.* **3**, 9–14 (2013)
3. Davydov, D.V., Lezhnev, D.A., Kostenko, D.I.: Diagnostic MSCT and planning for surgical treatment for patients with orbital-wall injuries and post-traumatic deformities. *Doctor.ru. Gastroenterol.* **1** (118), 116–120 (2016)
4. IFMBE at <https://studylib.ru/doc/2399666/v.a.-stuchilov-%E2%80%A2-a.a.-nikitin—moskovskij-oblastnoj-nauchno>
5. Masalitina, N.N., Kurochka, K.S.: The automated classificatory of computer tomography results for lumbar spine geometric modeling. *Doklady BGUIR* **3**, 12–19 (2017)
6. Patent 2000125015/14 RF A61B 17/80, A61B 17/56, A61F 2/28. Rybalchenkov's plate for reconstructing damaged bone structures of cheekbone, eye-socket and upper jaw complex and the way of reconstructing damaged bone structures of cheekbone, eye-socket and upper jaw complex with this plate. Rybalchenko, G.N.: Closed joint stock company "KONMET Incorporated". Rybalchenko, G.N.: Application № 2202302, 04 Oct 2000; Published 20 Apr 2003

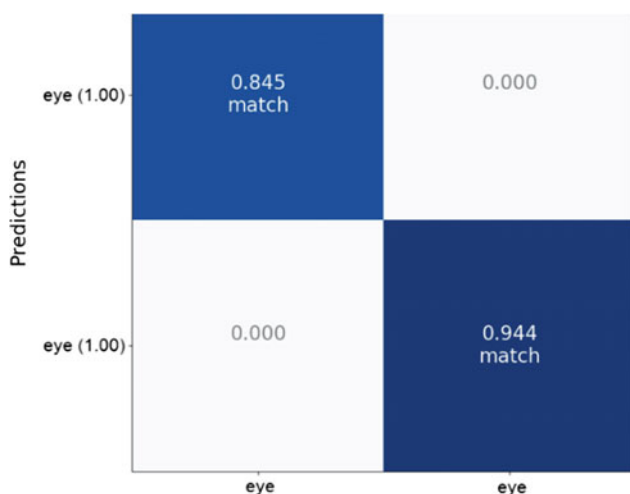


Fig. 3 Grid of ground truth objects and their predictions

7. Patent 2000116451/14 RF A61 F2/28. Method manufacturing an individual precision implant for compensation of complex subtotal polyostotic eye-socket defect. Shalumov, A., S.Z.; Shalumov, A., S.Z.: Application № 2164392, 27 May 2000; Published 27 Mar 2001
8. IFMBE at <https://www.dicomstandard.org/current/>
9. IFMBE at <https://arxiv.org/pdf/1803.01534>
10. IFMBE at https://github.com/matterport/Mask_RCNN/blob/master/samples/coco/inspect_weights.ipynb

Sleep-Related Epilepsy Diagnosis: Standard Video-EEG or Video-EEG Telemetry?

V. A. Chiosa

Abstract

Video-EEG telemetry is a neurophysiological noninvasive method of investigation used for determination of electroencephalogram changes and semiology of paroxysmal events. In this study we aimed to investigate the diagnostic value of video-EEG telemetry in sleep-related epilepsy diagnosis. For this purpose, we have selected 115 patients (18.9 ± 1.3 years old, 71 males) with nocturnal seizures in anamnesis (witnessed level of diagnosis). All patients went through video-EEG telemetry and standard video-EEG according to the IFCN guidelines. The value of video-EEG telemetry was determined using real positive and real negative results. The real positive results of video-EEG telemetry turned to be 79.1% (91 patients), while 12% (14 patients) had no EEG changes in the standard video-EEG nor in video-EEG telemetry. In conclusion, the video-EEG telemetry has a high diagnostic value—79.1% in the diagnosis of sleep related epilepsy and should be performed in patients with nocturnal paroxysmal events.

Keywords

Sleep-related epilepsy • Hyperkinetic seizures • Video-EEG

1 Introduction

Epilepsy still remains a disease [1] with a high incidence and prevalence [2] associated with neurobiological, cognitive, psychological and social impact [3], that affects about 0.6–1% of the population [4]. The prevalence of sleep related epilepsy is rather low, about 1.8–1.9 cases in 100.000 people and corresponds to the definition of a rare disease [5]. However, the importance of diagnosis is high, since the seizures occur during the sleep (especially during the night) and frequently begin in childhood and adolescence, thus presenting difficulties in the correct diagnosis and treatment selection, thereby, increasing the rate of pharmacoresistance.

A controversial topic is the use of video-EEG telemetry (long-term video-EEG) in the diagnosis of nocturnal paroxysmal events [6, 7]. This method is of best choice, but it is expensive and requires admission of the patient into the clinic. Standard video-EEG recordings with scalp electrodes do not always identify the interictal or even ictal epileptiform changes [8], moreover, interictal epileptiform changes may occur as well in some parasomnias [9]. The diagnostic value of video-EEG telemetry remains to be evaluated.

2 Materials and Methods

2.1 Participants and Video-EEG Acquisition

In this study we have included patients who have been consulted by the neurologist or epileptologist and the video-EEG telemetry was performed in the Laboratory of Neurobiology and Medical Genetics and Neurology Department no. 2 (under the leadership of academician Stanislav Groppa), a subdivision of the State University of Medicine and Pharmacy “Nicolae Testemitanu”. During the study period 2850 patients with paroxysmal events were evaluated by video-EEG, of which 875 by using video-EEG telemetry. The long-term video-EEG recording (video-EEG

V. A. Chiosa (✉)

Neurology Department no. 2, State University of Medicine and Pharmacy “Nicolae Testemitanu”, Chisinau, Moldova
e-mail: vachiosa@gmail.com

V. A. Chiosa

Laboratory of Neurobiology and Medical Genetics, State University of Medicine and Pharmacy “Nicolae Testemitanu”, Bd. Stefan Cel Mare 165, Chisinau, Moldova

telemetry) was performed using the Coherence system (Deltamed SA, Natus Medical Incorporated, France) in a semi-dark room for at least 8 h of the nighttime recording. Initially, for each patient standard video-EEG with functional tests was performed, followed by long-term video-EEG recording. For this purpose, the extra-cranial electrodes (Astro-Med Inc Product Group) were used, placed according to international standards (system 10–20) [10], with a digital sampling rate of 256 Hz and with electrodes' impedance below 10 k Ω . The low frequency filter was set to 70 Hz and high frequency filter to 0.3 Hz. The oculography, electrocardiography, deltoid muscle electromyography and respiration were registered at the same time. All patients were under continuous surveillance during the recording. Finally, 115 patients with nocturnal seizures in anamnesis (witnessed level of diagnosis) [8] were selected. The data recorded by video-EEG telemetry has been independently analyzed by 2 neurophysiologists.

2.2 Statistical Analysis

It was performed by using SPSS (version 20.0; IBM, Armonk, NY, USA.) software. Distribution of the variables was analyzed by Shapiro-Wilk test. Summary statistics are presented as mean \pm standard deviation for continuous variables and absolute number (percentage) for categorical variables, where appropriate. The diagnostic value of video-EEG telemetry was determined by employing sensitivity analysis. Following variables were selected as real positive results: no epileptiform discharges during the standard video-EEG—presence of epileptiform discharges during video-EEG telemetry; presence of epileptiform discharges during standard video-EEG—recording of an epileptic seizure during video-EEG telemetry; presence of epileptiform discharges during standard video-EEG—

epileptiform discharges during video-EEG telemetry in new regions). As real negative results type *a* have been considered the results when the presence of epileptiform discharges was determined, both during standard video-EEG and during video-EEG telemetry. As real negative results type *b* have been considered the results with the absence of epileptiform discharges, both during standard video-EEG and during video-EEG telemetry.

3 Results

3.1 Participants' Characteristics

Patients' demographic and clinical information is outlined in Table 1. The mean age of patients at the time of the study was 18.8 ± 1.3 years and mean disease duration was 4.1 ± 0.5 years. All patients presented exclusively nocturnal seizures, the most predominant type of focal seizures being hyperkinetic seizures (witnessed level of diagnosis).

3.2 Diagnostic Value of Video-EEG Telemetry

The assessment of the diagnostic value of video-EEG telemetry was based on the information from standard video-EEG methods and video-EEG telemetry, assessed by the real positive results and real negative results (Fig. 1).

Following the examination of patients from the group with nocturnal epileptic seizures, real positive results were determined in 91 (79.1%) patients with nocturnal epileptic seizures. The real negative results of this method, considered as pathological changes recorded in both standard video-EEG and video-EEG telemetry, were determined in 10 (8.7%) patients. Negative results type *b*, considered as lack of pathological changes in both standard video-EEG and

Table 1 Demographic and clinical data of the patients

Evaluated parameter	The group of patients with nocturnal seizures
Number of patients	115
<i>Gender</i>	
Males	71 (61.7%)
Females	44 (38.3%)
<i>Place of residence</i>	
Urban	90 (78.3%)
Rural	25 (21.7%)
The mean age at the time of study, (M \pm EM) years	18.9 \pm 1.3 (1–64)
The mean age at disease onset, (M \pm EM) years	14.9 \pm 1.33 (1–64)
Disease duration from onset until study, (M \pm EM) years	4.1 \pm 0.55 (0–29)

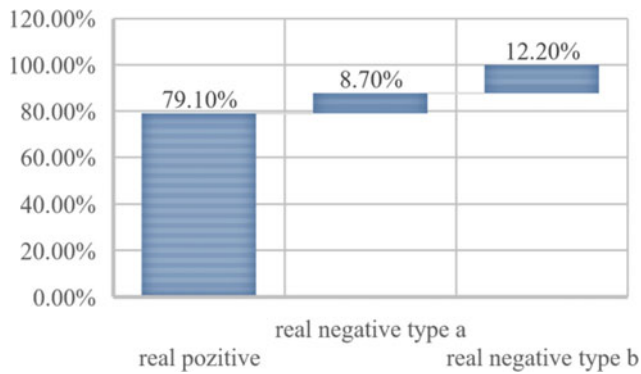


Fig. 1 The value of video-EEG telemetry in the diagnostic workup of nocturnal seizures

video-EEG telemetry, were determined in 14 (12.2%) patients with nocturnal epileptic seizures. Thus, the diagnostic value of the video-EEG telemetry method is quite high in the diagnosis of epilepsy syndromes with nocturnal epileptic seizures and reaches almost 80%, whereas in about 12% of patients with nocturnal seizures the EEG discharges have not been recorded with the standard video-EEG nor with video-EEG telemetry and in 8% of the patients the epileptiform discharges have been recorded during both standard video-EEG and video-EEG telemetry ($\chi^2 = 20.688$, $p < 0.001$).

3.3 Clinical Case

An 11-year-old male (right-handed) was admitted to video-EEG telemetry investigation with presumed diagnosis of sleep-related epilepsy. The onset of epileptic seizures was noted by parents one month before addressing to the neurologist. The patient was born from an uncomplicated full-term second pregnancy. Personal history—insignificant. The objective examination revealed no pathology. During video-EEG telemetry, 9 stereotyped clinical events were recorded, with a duration of 22–63 s. The paroxysmal events were classified as hyperkinetic seizures type II.

The clinical onset was recorded in the second stage of nonREM sleep with vocalizations, followed by repetitive rotational movements of the trunk associated with asymmetric movements in the upper and lower limbs. During the clinical event, the patient was non-responsive with total post-ictal amnesia. At 3T MRI no structural changes were determined. After clinical, neurophysiological and neuroimaging evaluation, the diagnosis of sleep-related epilepsy with type II hyperkinetic seizures was established. The antiepileptic treatment was initiated. Currently epileptic seizures are medically controlled (Fig. 2).

4 Discussion

In this study we evaluated the value of video-EEG telemetry in the diagnosis of sleep-related epilepsy. Thus, the real positive results were 79.1% for patients with nocturnal seizures. According to available data, standard video-EEG sensitivity is quite low, constituting 25–56% [11, 12], and studies conducted to evaluate the comparative utility of video-EEG telemetry reveal an increase in diagnostic possibilities by up to 22% [13]. Twelve percent of patients with nocturnal seizures presented no EEG abnormalities in both standard video-EEG and video-EEG telemetry, which requires us to conclude that not less than 12% of epilepsy patients with epileptic seizures have no intercalated changes on video-EEG telemetry, data congruent with international publications. For example, Licchetta reports up to 24% of patients without interictal EEG discharges [14], and Oldani found even up to 26% [15]. A study conducted by a group of researchers led by Liu [16] demonstrated that epileptiform changes during video-EEG monitoring are reliably identified during the first recording hour, which optimizes the epilepsy diagnosis. And the time or latency from the onset of long-term video-EEG monitoring until the first epileptiform discharge was different depending on the type of epileptic seizure [17]. Thus, in generalized onset epilepsy, a significantly shorter latency was observed compared to the same latency in the assessment of focal onset epileptic seizures. In this study, all patients with generalized epilepsy had the first epileptiform discharge within 10 h, but patients with focal onset epilepsy required monitoring for a longer time in order to register interictal epileptiform discharges [17]. Concerning the characteristic data of the patients depending on gender, male patients predominated (61.7%). These results are comparable to international data, which show a slight predominance of this nosology in males, Menghi reported a ratio of 7–3 [18] and Alqadi—a ratio of 12–5 [19]. If to evaluate the epilepsy epidemiology of sleep-related epilepsy, based on the number of patients with paroxysmal events (9 patients) from the total number of video-EEG telemetries (875), then we can refer to a value of 1.02% of the patients who have investigated by video-EEG telemetry. These data are slightly lower than, e.g., data from Menghi, who reported that patients with hyperkinetic epileptic seizures accounted 13% of all patients with epilepsy referred to perform video-EEG telemetry and 9.4% of all patients with pharmaco-resistant epilepsy [18]. There were no statistically significant differences in the urban or rural living area of the patients in the study group, but still slightly increased addressability of urban patients, probably explained on the one hand by a higher level of health awareness and on the other hand by high accessibility of urban population to the

Fig. 2 Evolution of clinical manifestations in patient with sleep-related epilepsy with hyperkinetic seizures



health services. These data are not reflected in studies, only socio-cultural representations are reported in some African countries [20] and reflect a decrease in the prevalence of epilepsy in rural areas over the last 12 years in China [21].

5 Conclusions

In this study we found that video-EEG telemetry is the method of choice in the diagnosis of patients with the sleep-related epilepsy due to the high diagnostic value of the method, which is 79.1%, being the maximum, compared to the diagnostic value of standard EEG, reported in the literature to be between 22 and 56%. On the other hand, in 12% of patients we have not recorded any epileptic discharges during video-EEG telemetry. This allows us to conclude that approximately in every 7th patient with nocturnal epileptic seizures and sleep-related epilepsy, based on witnessed level of diagnosis, a false negative diagnosis could be established that later would lead to delayed antiepileptic treatment and, as a result, to the development of pharmacoresistance in these patients. It is important that with increase in duration of the disease, on the qualitative and quantitative levels, there were reported increasing rate and frequency of epileptiform changes, which demonstrates the importance of early diagnosis. For patients with real negative results, only recording the epileptic seizure or of any paroxysmal events is helpful for the correct establishment of the diagnosis and starting the appropriate treatment.

Acknowledgements I would like to thank all my colleagues who helped me in acquiring and analyzing of the data and all our patients who agreed to participate.

Conflict of Interest The author has no conflict of interest to disclose.

References

1. Fisher, R.S., et al.: ILAE official report: a practical clinical definition of epilepsy. *Epilepsia* **55**(4), 475–482 (2014). ISSN: 1528-1167 (Electronic), 0013-9580 (Linking)
2. Fiest, K.M., et al.: Prevalence and incidence of epilepsy: A systematic review and meta-analysis of international studies. *Neurology* **88**(3), 296–303 (2017). ISSN: 1526-632X (Electronic), 0028-3878 (Linking)
3. Fisher, R.S., et al.: Epileptic seizures and epilepsy: definitions proposed by the International League Against Epilepsy (ILAE) and the International Bureau for Epilepsy (IBE). *Epilepsia* **46**(4), 470–472 (2005). ISSN:0013-9580 (Print), 0013-9580 (Linking)
4. Beghi, E., Hesdorffer, D.J.E.: Prevalence of epilepsy—an unknown quantity. *Epilepsia* **55**(7), 963–967 (2014). ISSN: 0013-9580
5. Vignatelli, L., et al.: Prevalence of sleep-related hypermotor epilepsy—formerly named nocturnal frontal lobe epilepsy—in the adult population of the Emilia-Romagna Region, Italy. *Sleep* **40**(2) (2017). ISSN: 0161-8105
6. Tinuper, P., Bisulli, F.: From nocturnal frontal lobe epilepsy to sleep-related hypermotor epilepsy: a 35-year diagnostic challenge. *Seizure* **44**, 87–92 (2017). ISSN:1532-2688 (Electronic), 1059-1311 (Linking)
7. Groppa, S., Chiosa V., Ignatenco, A.: Clasificarea și diagnosticul diferențial al crizelor epileptice: studiu clinic-neurofiziologic. *Buletinul Academiei de Științe a Moldovei. Științe Medicale* **1**(29), 65–67 (2011). ISSN:1857-0011

8. Tinuper, P., et al.: Definition and diagnostic criteria of sleep-related hypermotor epilepsy. *Neurology* **86**(19), 1834–1842 (2016). ISSN: 1526-632X (Electronic), 0028-3878 (Linking)
9. Manni, R., Terzaghi, M., Zambrelli, E.: REM sleep behavior disorder and epileptic phenomena: clinical aspects of the comorbidity. *Epilepsia* **47**(Suppl. 5), 78–81. ISSN: 0013-9580 (Print), 0013-9580 (Linking)
10. Jurcak, V., Tsuzuki, D., Dan, I.: 10/20, 10/10, and 10/5 systems revisited: their validity as relative head-surface-based positioning systems. *Neuroimage* **34**(4), 1600–1611 (2007). ISSN: 1053-8119
11. Smith, S.J.: EEG in the diagnosis, classification, and management of patients with epilepsy. *J. Neurol. Neurosurg. Psychiatry* **76** (Suppl 2), ii2–7 (2005). ISSN: 0022-3050 (Print), 0022-3050 (Linking)
12. Pillai, J., Sperling, M.R.: Interictal EEG and the diagnosis of epilepsy. *Epilepsia* **47**(Suppl 1), 14–22 (2006). ISSN: 0013-9580 (Print), 0013-9580 (Linking)
13. Meritam, P., et al.: Diagnostic yield of standard-wake and sleep EEG recordings. *Clin. Neurophysiol* **129**(4), 713–716 (2018). ISSN: 1872-8952 (Electronic), 1388-2457 (Linking)
14. Licchetta, L., et al.: Sleep-related hypermotor epilepsy: long-term outcome in a large cohort. *Neurology* **88**(1), 70–77 (2017). ISSN: 1526-632X (Electronic), 0028-3878 (Linking)
15. Oldani, A., et al.: Autosomal dominant nocturnal frontal lobe epilepsy. A video-polysomnographic and genetic appraisal of 40 patients and delineation of the epileptic syndrome. *Brain* **121**(Pt 2) (2), 205–223 (1998). ISSN:0006-8950 (Print), 0006-8950 (Linking)
16. Liu, X., et al.: The first-hour-of-the-day sleep EEG reliably identifies interictal epileptiform discharges during long-term video-EEG monitoring. *Seizure* **63**, 48–51 (2018). ISSN: 1532-2688 (Electronic), 1059-1311 (Linking)
17. Koc, G., et al.: Latencies to first interictal epileptiform discharges in different seizure types during video-EEG monitoring. *Seizure Eur. J. Epilepsy* **69**, 235–240 (2019). ISSN: 1059-1311
18. Menghi, V., et al.: Sleep-related hypermotor epilepsy: prevalence, impact and management strategies. *Nat. Sci. Sleep* **10**, 317–326 (2018). ISSN: 1179-1608 (Print), 1179-1608 (Linking)
19. Alqadi, K., et al.: Semiology of hypermotor (hyperkinetic) seizures. *Epilepsy Behav.* **54**, 137–41 (2016). ISSN:1525-5069 (Electronic), 1525-5050 (Linking)
20. Mbelesso, P., et al.: Sociocultural representations of epilepsy in the Central African Republic: a door-to-door survey. *Seizure* **67**, 23–26 (2019). ISSN: 1532-2688 (Electronic), 1059-1311 (Linking)
21. Wang, M., et al.: Prevalence of epilepsy in rural China: a decreasing trend over 12 years. *J. Neurol. Neurosurg. Psychiatry, jnnp-2018-320131* (2019). ISSN: 1468-330X (Electronic), 0022-3050 (Linking)

A Real-Time WebGL Rendering Pipeline for MRI Using RayCasting Transfer Functions

R. Ciucu, F. Adochiei, I. Adochiei, F. Argatu, C. M. Larco, and L. Grigorie

Abstract

We present a way to integrate real-time multi-intensity transfer functions in a web browser environment using WebGL. We apply a two-pass rendering in order to establish the opacity and color of the given MRI recording. This pipeline helps viewing high resolution voxel domains and the adjustment of a transfer function for highlighting specific features types of a given DICOM recording. With recent advancements in the augmented and virtual reality domains medical imaging has become a center stage subject by bringing the data closer to the patient and the doctor. Besides virtual reality, visualizing brain reconstructions is vital in brain mapping and neuro research. In conclusion we show a viable approach in rendering, processing and visualizing MRI data in real time in a Web browser.

Keywords

MRI • DVR • RayCasting • WebGL

1 Introduction

Transfer functions are an important feature in the context of volumetric rendering to allow the isolation or highlighting of different biological structures in MRI (Magnetic resonance imaging) datasets. We present an intuitive way of adjusting and rendering in real-time medical imaging transfer functions [1–7].

Direct volume rendering (DVR) is a graphic reconstruction technique used to obtain high-fidelity 3D MRI or CT representations. It uses a series of mathematical functions to

translate the density and optical properties such as ray absorption and transmission through the sparse volume. Post-processing and sample filtering can result in obtaining hard surfaces and geometries from the reconstructed data. DVR can be achieved in modern web browsers through GPU shader development and data structure optimization [8–13].

A transfer function has direct purpose, to translate a specific sample from a set of coordinates into digital optical values such as color and transparency. By doing so a transfer function can isolate a structure by eliminating specific frequencies [7, 14, 15].

Our improved pipeline consists of a volume mapping backend and a two pass DVR viewport for high fidelity reconstruction of MRI datasets. Our main focus will be the process of integrating a second processing layer over the rendered volume with a transfer function that manipulates visibility histograms and optical opacity.

The pipeline's main attributes are the fact that it is platform agnostic and hardware independent, ready to be used on any WebVR supporting browser. With growing interest in Brain-Mapping and functional MRI exams such a fast and reliable platform can be of use in imaging research and scientific data visualization. Augmented reality can also be a point of development for interactive classes where students and teacher can interact directly with data and can highlight biological structures.

The first part of our paper is dedicated to DVR principles and recasting approximations of MRI volumes. An important section will be addressing the many types of transfer functions and their feasibility in raycasting. Furthermore, we will dive deeper in previous work regarding the graphical pipeline and each specific stage.

We will discuss the development results regarding the pipeline. With a comparison to the previous iteration of the platform, where each new stage will be highlighted such as the volume mapping and alpha accumulation function for global opacity correction. The backend stages where the compression and data reduction steps are happening will be

R. Ciucu · F. Adochiei (✉) · F. Argatu
University Politehnica of Bucharest, Splaiul Independenței
nr. 313, Bucharest, Romania
e-mail: felix.adochiei@upb.ro

I. Adochiei · C. M. Larco · L. Grigorie
Military Technical Academy “Ferdinand I”, Bucharest, Romania

illustrated and each modification from the previous pipeline addressed.

The web browser allows for an intuitive experience with medical data and medical imaging. Using a web browser has its own strengths and weaknesses from a performance standpoint. Each issue will be discussed in the final conclusions section of our paper. Moreover, the numerous future improvements of our pipeline and platform will be enumerated.

2 Methods

2.1 Direct Volume Rendering

Volume rendering is the process of constructing three-dimensional images using discrete density domains (voxels) and applying raytracing/raycasting on non-uniform domain. Unlike traditional 3d rendering techniques volume rendering does not have clearly defined surfaces and points and an additional step is needed for reconstructing a surface. Volume processing algorithms such as cube marching, and recasting approximations can be implemented to obtain meshes and surfaces.

Volume Shading is directly depending of the resolution and density of the given domain.

By using a MonteCarlo Raytracing renderer two different types of volumes can be achieved:

Volume Absorption—Which absorbs and dominates the ray intensity over a sparse domain

Volume Scatter—Which acts as a refraction over the ray direction and intensity [4, 5, 13].

Raycasting is a volume approximation method, characterized by sampling individual rays into a sparse volume. It does not affect any optical transmission properties such as volume scatter or absorption but applies a mathematical model per sample to obtain visual aspects and silhouettes (color and opacity). The quality of the representation is directly tied to the number of steps measured within the

volume. In Table 1 a summary analysis of both methods is presented [8, 16].

2.2 Transfer Functions

Opacity Transfer Function:

The transfer function $F(p)$ is a direct translation of MRI data values into RGBA format, where p is the raycasted sample. To achieve color and opacity data a visibility histogram needs to be calculated (*relation 1*).

The visibility histogram takes into account the color channels and opacity of each sample of a given slice.

A global opacity vector is calculated in the domain defined by the ray origin (E) to the domain limit (I). The visibility accumulated in this domain is represented by the integrating the color channel $\tau(t)$ [2, 3, 17]

$$F(p) = e^{-\int_I^E \tau(t)dt} \quad (1)$$

The visibility histogram is represented in Fig. 1 and is a graphical method of visualising color channels and opacity over a given image or domain. Each value is treated as a scalar vector and can be adjusted individually by modifying the coefficients of the volume integral or the F function.

The transfer function in the case of raycasting is implemented as an additional step that changes the visual properties of the MRI reconstruction [12, 14, 15, 18].

2.3 Previous Work

In a previous paper we discussed developing a web platform for medical imaging. The pipeline underwent several modifications to improve overall quality ensure real-time performance for VR headsets.

(a) The pipeline

From the DICOM file container the MRI slices are extracted. A maximum of 128 slices per view are stacked in an array and a binarization algorithm is applied.

Table 1 Comparison between volume rendering methods

	Raytracing	RayCasting
Sampling method	Ray count	Step count
Color output	RGBA	RGBA
Output	Rasterized images	Rasterized images
Applications	Compute physical properties of surface and volume properties	Approximations of volumes and surfaces
Result	PhotoRealistic images	Volume representation
RayCount	Multiple rays per sample	1 per sample

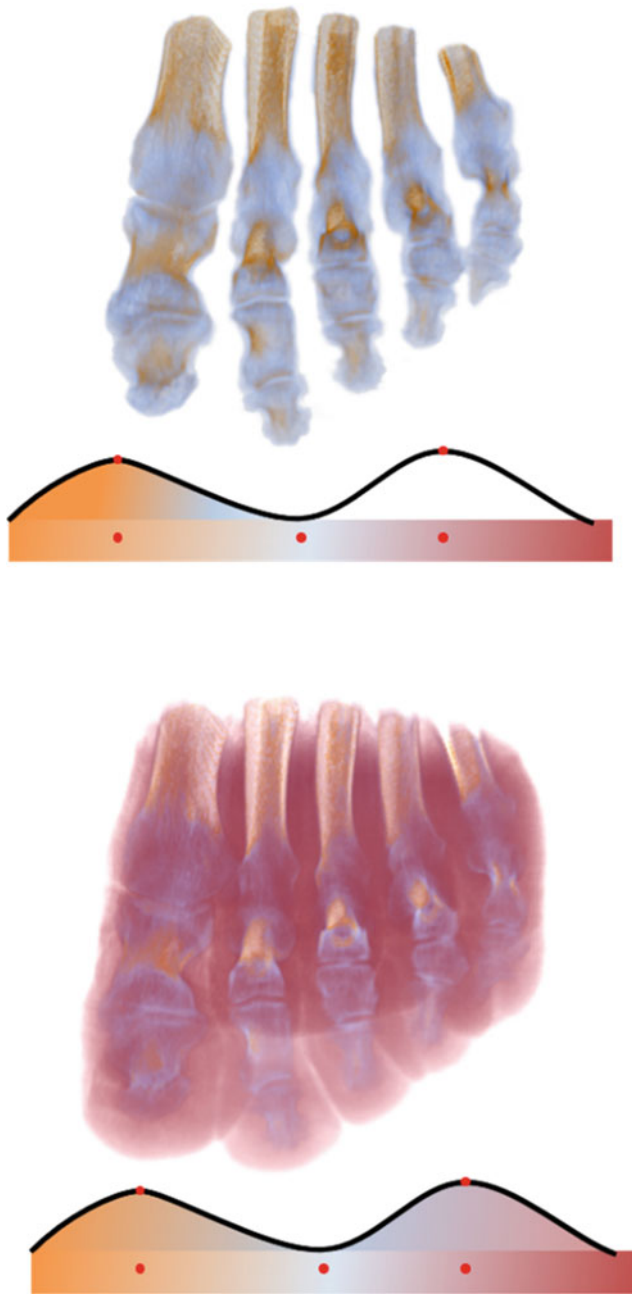


Fig. 1 Visual impact of the transfer functions along side the functional histograms

The adaptive threshold algorithm was previously used in identifying features for machine learning applications and was also integrated in the pipeline. The threshold function worked to highlight specific parts by selecting an interest point on the visibility histogram [6, 7].

The voxel cache/buffer was formed by taking the processed slices, reduced in size based on the user settings and transferred in the browser client (viewport). A monte-carlo raycasting render would produce images based on a simple intensity transfer function. The transfer function would act as

a translation between the intensity of the MRI scan data and the density value represented in our volume rendering. The approach would produce non-colored representations of the MRI scans. The sensibility of the transmission function could be adjusted using a slider on the screen.

3 Results

3.1 Frontend

The frontend components are consisting of a viewport controls of the transfer function, graphical quality and global alpha accumulation.

The viewport is a WebGL canvas solely dedicated to the rendering of the files. The viewport is dynamic and can be adjusted for viewing using VR headsets (rough WEBVR API). The VR functionality renders the image twice (for each eye) with a proper alignment of the viewing angle applied. Thus, our approach for optimizing the render pipelines proves adequate. Our platform main interface is represented in Fig. 2.

Our renderer uses a raycasting approximation of the volume. The main difference is that the ray traversal does not affects the intensity, nor the direction. Raycasting quality is tied to the number of steps the ray is measured within the volume.

3.2 Backend

Our backend solves two main issues, translating data into a fast renderable format (voxel cache) and compressing the data for fast transfer by reducing image sizes, removing DICOM fields and anonymizing the recording.

The voxel cache is represented by a mosaic of slices arranged at different depths. The z-index of our Voxel cache is directly proportional with the depth and number of slices Fig. 3.

The communication between frontend and backend is ensured by a session microservice implemented using Node.js and socket.io. The microservice is contained using the DOCKER virtualization engine.

While the frontend is broken up into independent components, each built using a streamlined JavaScript framework (react-redux). Each component is controlling a specific aspect of the viewport.

3.3 MultiPass

Each time the position in the viewport is changed the volume is recalculated and the subsequent passes applied, a dynamic sample/step counter was implemented to adjust performance

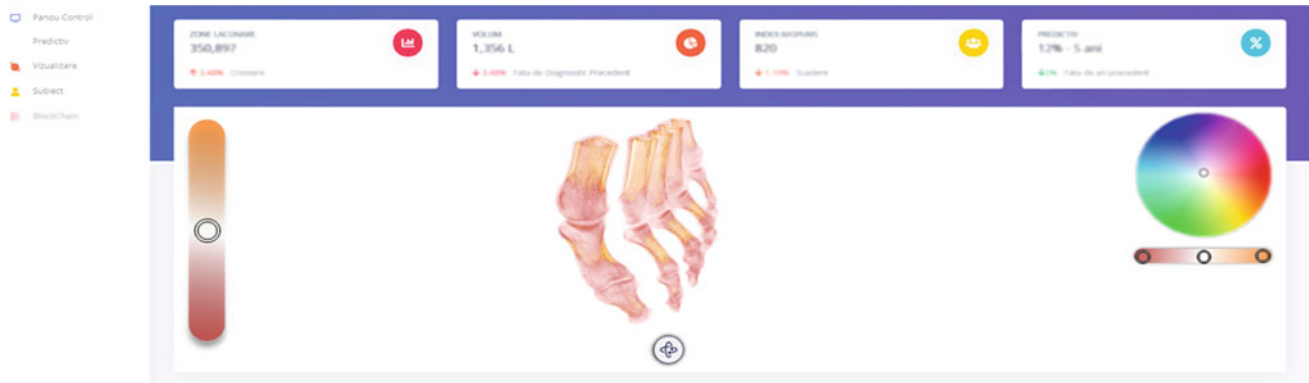
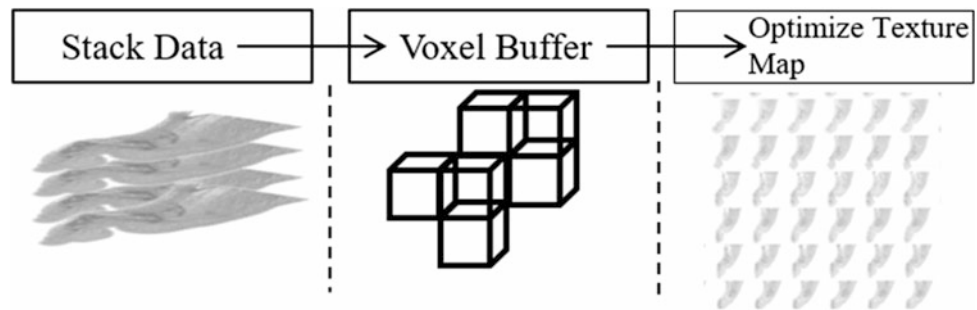


Fig. 2 The frontend view with color adjustment and gradient mapping

Fig. 3 The backend pipeline



at the cost of visual quality. Each pass was implemented as a separate shader in the render pipeline.

The first step is the translation of the intensity of our recording into a visible density of accumulated opacities. The result is a generated multidimensional alpha map. Since we reconstruct the volume using a voxel cache and we do not raytraced our data, the resulting image can have artifacts and opacity issues, we implemented a global alpha correction knob that adjusts the depth our alpha texture map.

The RGB coordinates are separated by linear positions on our transfer function and directly represented by a color gradient in the viewport.

To highlight specific parts of an MRI recording, a transfer functions acts as a differentiator between the ray coordinates and RGB-ALPHA ones, with different sections and different densities being represented individually.

3.4 Changes in the Pipeline

For a more streamlined approach and consistent performance we departed from the stochastic montecarlo raytracing method and we decided that the dynamic lighting feature is no longer needed. Our global illumination is irrelevant as we do not want to render photo-realistic materials but physiological datasets. Furthermore, by removing all dynamic

elements the only two things left to calculate are the volume representation and the render passes.

Our global alpha map can be adjusted in real time as it simply increments or decrements the opacity of the sampled data. Our dataset remains unchanged and the data reduction procedures happen in the backend.

The pipeline was broken in two parts, the optimization of raw voxel data and the visualization renderer where the transfer functions are implemented.

Our transfer functions act as an additional layer over the reconstruction of the voxel cache. The first step is to calculate tissue opacity and construct accumulated transparency vectors for each voxel in the viewport, and the second step is to give each type of tissue a color based on the gradient function Fig. 4.

The colors are obtained by generating a visibility histogram and each accumulation of intensities being represented as a different color. The global opacity map is an array which acts as an individual control over the samples. Thus, correcting transparency artefacts and allowing the adjustment of the reconstruction to the users liking.

The colors can be manually adjusted for an intuitive approach with an arbitrary color (white or black) representing absolute transparency it's opposite absolute opacity. The voxel map can be inverted at the input stages of our frontend pipeline Fig. 5.

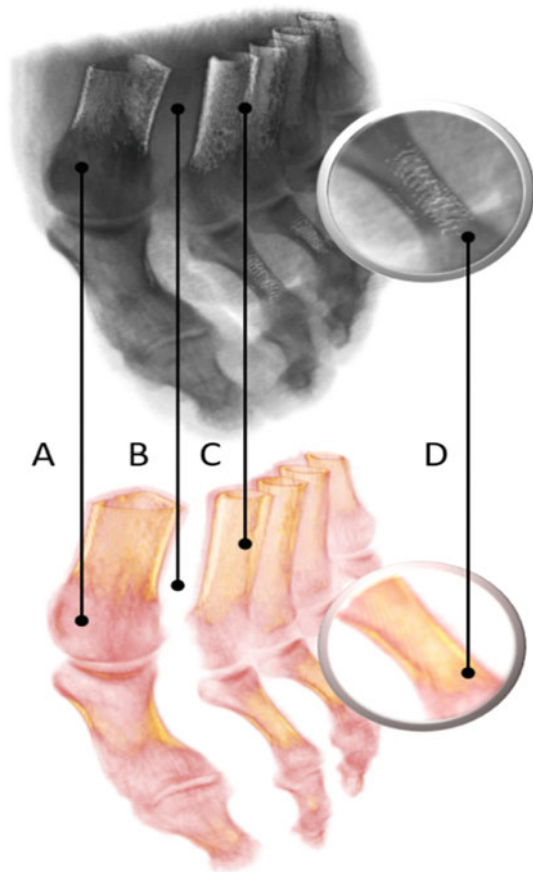


Fig. 4 Visual differences between pipelines. The top image representing the raytracing and the bottom representing the raycasting. **a** Tissue differentiation, **b** channel opacity, **c** contrast, **d** visual consistency

3.5 Performance

Our pipeline offers a base framerate of around 57–60 frames per second when a $256 \times 256 \times 128$ volumes are loaded. To ensure a stable framerate in the VR mode, the volume raycasting steps are lowered. We implemented a maximum of 512 raycasting steps when rendering the volume.

The pipeline suffers if in the input data multiple positioning artifacts are present and the contrast between slices is

shifting, resulting in color artifacts and opacity issues. The transfer functions which are implemented as fragment and vertex shaders would calculate wrong values for each sample.

Regarding the level of detail, we did not allow mipmapping inside the browser viewport since the data is constant and the viewport does not contain any other objects such as geometries and surfaces. Mipmapping would be feasible if the viewing distances change over time, we intended to eliminate any compression and quality reduction measures present in the webgl viewport.

4 Conclusions

In this paper we presented a real-time approach in rendering in visualizing MRI Volumes in a web browser environment.

Our departure from raytracing volume data was a necessary step to ensure that high quality volumes can be represented on both desktop and mobile platforms. We provided a solution for data reduction and voxel caching in the backend while the frontend was solely dedicated to the visualizing functions.

The visual properties of the volume can be directly and independently adjusted without reloading or recalculating the whole domain.

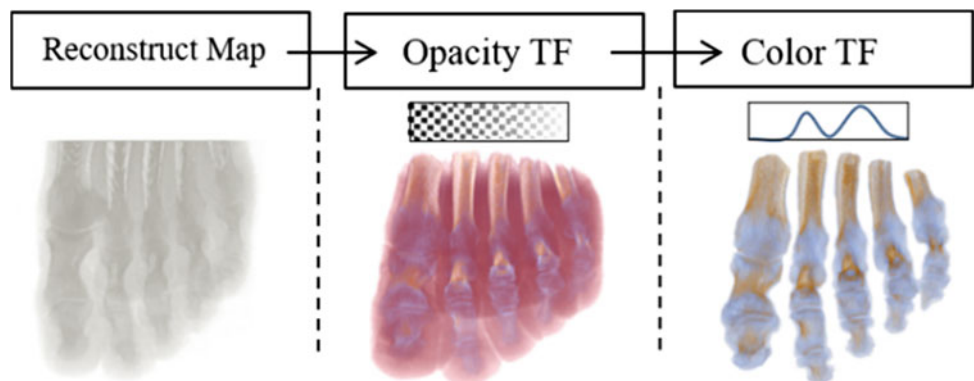
While the raycasting renderer needs an additional post-processing step, it does not hinder the performance since the whole volume is calculated once and the data transferred is buffered in the memory.

The reconstructed image lacks the raytraced sharpness and presents a cloudy texture when multiple color channels are represented in the gradient map.

The opacity accumulation can sometimes provide a fake sense of transparency in some datasets.

With recent announcements by Google to introduce a direct GPU API, we will take into consideration implementing at least a global illumination stage in our renderer. But current APIs do not provide direct access to the texture memory and distributed computing units for per-pixel shading.

Fig. 5 The viewport rendering pipeline



Our shading is limited to the initial voxel cache in the form of fragment shaders and global transforms (opacity function).

In the future we hope to implement additional futures for visualising functional MRIs and Diffusion Tensors of neuronal bundles in our rendering pipeline.

Acknowledgements This paper was developed within the program National Project: GNaC 2018 ARUT no. 19/06.02.2018 from Politehnica University of Bucharest.

Conflict of Interest The authors declare that they have no conflict of interest

References

- Viola, I., Kanitsar, A., Groller, M.E.: Importance-driven volume rendering. In: Proceedings of the IEEE Visualization Conference '04, pp. 139–146 (2004)
- Correa, C.D., Ma, K.: Visibility histograms and visibility-driven transfer functions. *IEEE Trans. Vis. Comput. Graph.* **17**(2), 192–204 (2011)
- Kniss, J., Kindlmann, G., Hansen, C.: Multidimensional transfer functions for interactive volume rendering. *IEEE Trans. Vis. Comput. Graph.* **8**(3), 270–285 (2002)
- Conner, D.B., Snibbe, S.S., Herndon, K.P., Robbins, D.C., Zeleznik, R.C., van Dam, A.: Three-dimensional widgets. In: Proceedings of the 1992 Symposium on Interactive 3D Graphics, pp. 183–188 (1992)
- Drebin, R.A., Carpenter, L., Hanrahan, P.: Volume rendering. In: Proceedings of the 15th Annual Conference on Computer Graphics and Interactive Techniques, pp. 65–74 (1988)
- Adochiei, F., Ciucu, R., Adochiei, I., Grigorescu, S.D., Călin Serișan, G., Casian, M.: A WEB Platform for Rendering and Viewing MRI Volumes using Real-Time Raytracing Principles, (ATEE), Bucharest, Romania, pp. 1–4 (2019)
- Miron, C., Păsărică, A., Arotăriței, D., Costin, H., Bozomitu, R.G., Rotariu, C.: Hand gesture detection using a stereo camera system and simulation of movement. In: 10th International Symposium on Advanced Topics in Electrical Engineering (ATEE), Bucharest, pp. 297–300 (2017)
- Bajaj, C.L., Pascucci, V., Schikore, D.R.: The contour spectrum. In: Proceedings of IEEE 8th Conference Vis., pp. 167–173 (1997)
- Costin, H.: A fuzzy rules-based segmentation method for medical images analysis. *Int. J. Comput. Commun. Control* **8**(2), 196–205, Published: APR 2013
- Kindlmann, G., Durkin, J.W.: Semi-automatic generation of transfer functions for direct volume rendering. In: Proceedings of the IEEE Symposium Vol. Vis., pp. 79–86 (1998)
- Fujishiro, I., Azuma, T., Takeshima, Y.: Automating transfer function design for comprehensible volume rendering based on 3D field topology analysis. In: Proceedings of the IEEE Vis., pp. 467–470 (1998)
- He, T., Hong, L., Kaufman, A., Pfister, H.: Generation of transfer functions with stochastic search techniques. In Proceedings of the IEEE 7th Conference Vis., pp. 227–234 (1996)
- Jonsson, D., Ynnerman, A.: Correlated photon mapping for interactive global illumination of time-varying volumetric data. *IEEE Trans. Vis. Comput. Graph.* **23**(1), 901–910 (2017)
- Lundstrom, C., Ljung, P., Ynnerman, A.: Local histograms for the design of transfer functions in direct volume rendering. *IEEE Trans. Vis. Comput. Graph.* **12**(16), 1570–1579 (2006)
- Pfister, H., Lorensen, B., Bajaj, C., Kindlmann, G.: The transfer function bake-off. In: Proceedings of IEEE Conference Vis., pp. 523–526 (2000)
- Costin, H., Rotariu, C.: Medical image analysis and representation using a fuzzy and rule-based hybrid approach. *Int. J. Comput. Commun. Control* **1**(Supplement: S), pp. 156–162, Published: 2006
- Rotariu, C., Pasarica, A., Costin, H., Andruseac, G., Nemescu, D.: Automatic analysis of the fetal heart rate variability and uterine contractions. In: 8th International Conference and Exposition on Electrical and Power Engineering (EPE), Iasi, Romania, pp. 553–556, 16–18 Oct 2014
- Andruseac, G.G., Pasarica, A., Brezuleanu, C.O., et al.: An intelligent framework to manage and control an autonomous platform for detection, inspection and monitoring applications in chemical environments. In: REVISTA DE CHIMIE **68**(6), 1357–1360. Published: JUN 2017

Alterations of Brain Structure Linked to Myoclonic Epilepsy

A. Vataman

Abstract

Recent neuroimaging studies suggest that frontal lobe and thalamus are the key structures involved in generation of myoclonic seizures. However, data indicating clear structural alterations of other grey matter (GM) regions in this seizure type is limited. Thus, our purpose was to characterize the cortical and subcortical volumes in patients with myoclonic seizures. We quantified brain structural measures (cortical and subcortical GM volumes) extracted from 3T magnetic resonance images (MRI) across 40 patients (mean age \pm standard deviation: 25 ± 7 years; 14 males) with myoclonic seizures and 40 healthy subjects (23 ± 5 years; 14 males). A statistically significant difference in cortical volumes between patients and healthy subjects was found in the following clusters: left superior parietal, postcentral and fusiform; right middle temporal and bilateral precentral, superior frontal and precuneus areas (all $p < 0.05$). Analysis of subcortical volumes revealed significantly smaller volumes of bilateral thalamus and caudate in patients compared to healthy. These findings support the hypothesis of aberrant cortico-thalamic networks in patients with myoclonic seizures and extend these to basal ganglia.

Keywords

Myoclonic epilepsy • Magnetic resonance imaging • Volumetry

1 Introduction

Myoclonus is characterized by sudden, brief, shock-like involuntary movements, associated with bursts of muscular activity (positive myoclonus) or silencing of muscular activity (negative myoclonus) [1]. Epileptic myoclonus is found in 17% of all patients with myoclonus, including cortical myoclonic jerks, which are associated with ictal poly- or spike-and-wave electroencephalography (EEG) discharges, time-locked with and preceding electromyography (EMG)-recorded muscle contractions [2].

Patients with myoclonic epilepsy are expected to have normal neuroimaging findings when studied with conventional MRI scans [3]. However, subtle abnormalities of brain morphology have recently been reported. There are conflicting findings regarding which brain regions are involved and whether the abnormalities consists of increased or reduced volume of particular brain regions. Gray matter atrophy in the putamen [4, 5], pallidum [5], caudate [6] and hippocampus [7] have been identified inconsistently across recent studies. Thus, our purpose was to characterize the cortical and subcortical volumes in patients with myoclonic epilepsy.

2 Materials and Methods

2.1 Participants

This study was performed in the outpatient department of the National Center of Epileptology, Chisinau, Republic of Moldova. Forty participants diagnosed with myoclonic epilepsy (as determined by medical history, clinical features and EEG) were recruited in this study. Inclusion criteria were as follows: myoclonic seizure with or without generalized tonic-clonic seizures (GTCS) or absence seizures; normal neurological examination; normal cognitive function. For group comparison, 40 healthy volunteers matched for age,

A. Vataman (✉)

Nicolae Testemițanu State University of Medicine and Pharmacy,
Toma Ciorba 1, Chisinau, Republic of Moldova
e-mail: anatolie.vataman@usmf.md

A. Vataman

Department of Neurology, Institute of Emergency Medicine,
Chisinau, Republic of Moldova

gender and education years were recruited to serve as controls. All control subjects underwent neurological examination and a detailed interview to ensure that they had no current neurological conditions, no history of neurological, psychiatric, or systemic disorders.

The Research Ethics Committee of the State University of Medicine and Pharmacy “Nicolae Testemitanu” approved this study. After a full explanation of the applied methods, each subject gave written informed consent in order to take part in the study.

2.2 MRI Data Acquisition

All participants were scanned with a 3T MRI machine (Siemens Magnetom Skyra) using a 32-channel head coil according to a predefined Epilepsy protocol used in [8], with the following imaging sequences and parameters: T1-weighted images (repetition time [TR]: 2000 ms, echo time [TE]: 9 ms, inversion time [TI]: 900 ms, slice thickness [ST]: 4 mm, flip angle [FA]: 9°, field of view [FoV]: 256 × 256 mm², acquisition matrix: 256 × 256); T2-weighted images (TR: 3800 ms, TE: 117 ms, ST: 4 mm, FA: 149°, FoV: 100 × 100 mm², acquisition matrix: 384 × 384); and 3D fluid-attenuated inversion recovery (FLAIR) images (TR: 5.000 ms, TE: 388 ms, TI: 1.800 ms, ST: 0.9 mm, FA: 120°, FoV: 100 × 100 mm², acquisition matrix: 256 × 256). Particular attention was taken to center the subject in the head coil and to restrain head movements with cushions and adhesive medical tape. All patients reported no seizure during the scanning procedure.

2.3 MRI Data Processing

The freely available software FreeSurfer (version 5.3.0, <http://surfer.nmr.mgh.harvard.edu/>) was used for processing of T1-weighted images, followed by visual inspection for quality control at various processing steps [9]. The cerebral cortex was then divided into 68 anatomical regions according to the Desikan et al. [10]. Regional cortical surface areas and cortical volumes were extracted. The volumes of subcortical structures directly or indirectly linked to epileptogenesis (thalamus, hippocampus, amygdala, caudate, putamen, pallidum, ventral diencephalon) were included in the subsequent analyses.

2.4 Statistical Analysis

Statistical analysis was performed by using SPSS (version 20.0; IBM, Armonk, NY, USA.) software. Distribution of

the variables was analyzed by Shapiro-Wilk test. Statistical maps of significant differences in structural measures were corrected for multiple comparisons by Monte Carlo permutation cluster analysis at a threshold of $p < 0.05$ ($Z = 1.3$).

3 Results

3.1 Participants

A total of 40 patients (mean age ± SD: 25 ± 7 years; 14 males) with myoclonic seizures and 40 healthy subjects (23 ± 5 years; 14 males) were included in the study. Patients and controls did not differ in age and gender ($p > 0.05$). Subjects' demographical and clinical parameters are outlined in Table 1. The mean disease duration was 10.4 ± 7.4 years. Semiological features included myoclonic seizures in 40 patients (100%), GTCS in 33 (83%) and absence seizures in 7 (18%). The treatment received by patients at the time of study consisted of valproate monotherapy in 12 (30%) patients, lamotrigine monotherapy in 7 (17.5%), carbamazepine monotherapy in 3 (7.5%), topiramate monotherapy in 1 (2.5%); polytherapy with valproate and lamotrigine in 12 (30%), valproate and clonazepam in 2 (5%), valproate, clonazepam and carbamazepine in 1 (2.5%) and none in 2 (5%).

3.2 Cortical Volume Analysis

A statistically significant difference in cortical volumes between patients with myoclonic seizures and healthy subjects was found in several cortical regions. When compared to controls, patients showed significantly lower cortical volumes in following clusters: superior parietal cortex, postcentral cortex and fusiform cortex of the left hemisphere; middle temporal cortex of the right hemisphere and precentral, superior frontal and precuneal cortices of both hemispheres (all $p < 0.05$, Monte Carlo corrected) (Fig. 1).

3.3 Subcortical Volumes Analysis

Analysis of subcortical volumes revealed smaller volumes of bilateral thalamus in patients (right 7043.8 ± 921.8 mm³/left 7697.9 ± 1045.5 mm³) compared to healthy subjects (right 8148.6 ± 720.4 mm³/left 9205.4 ± 1151.4 mm³, $p < 0.05$) (Fig. 2) and reduced volumes of bilateral caudate in patients (right 3542.9 ± 598.1 mm³/left 3536.6 ± 575.2 mm³) compared to controls (right 3817.4 ± 451.1 mm³/left 3960.0 ± 438.9 mm³, $p < 0.05$, Table 2).

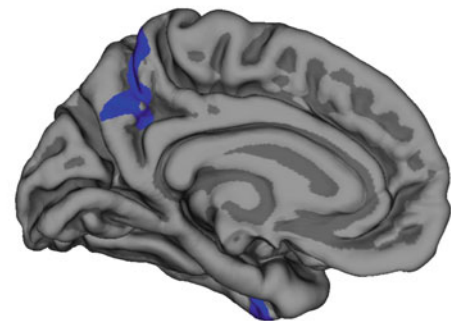
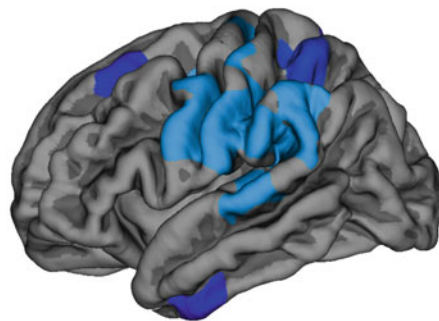
Table 1 Demographical and clinical parameters of patients and healthy subjects

	Patients	Healthy controls
Number of subjects	N = 40	N = 40
Gender (female/male)	26/14	26/14
Age (years)	25 ± 7 years	23 ± 5 years
Handedness (right/left)	37/3	38/2
Disease duration (years)	10.4 ± 7.4 years	
Age of seizure onset (years)	14 ± 7 years	
Seizure semiology	MS (100%), GTCS (83%), AS (18%)	

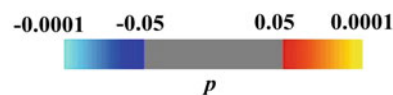
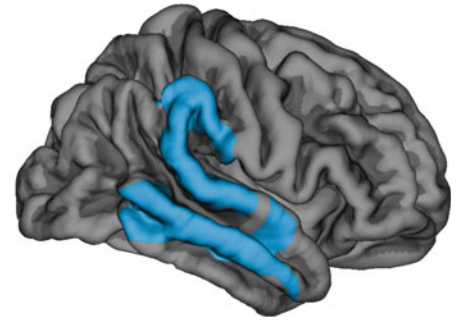
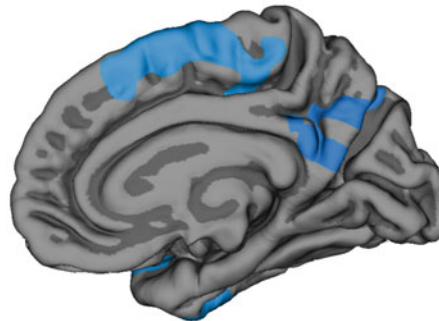
AS absence seizure; GTCS generalized tonic-clonic seizure; MS myoclonic seizure. Data are presented as mean ± standard deviation

Fig. 1 Statistical surface maps in left (LH) and right hemisphere (RH) representing the clusters of significant differences in cortical volumes between patients and controls. Color bar indicates the significance levels in the clusters obtained from Monte Carlo simulation at $p < 0.05$ ($Z = 1.3$)

LH



RH



4 Discussion

In this study, we present clear cut evidence of widespread alterations of cortical and subcortical morphology in a group of patients with myoclonic epilepsy compared to a group of healthy subjects. The underlying pathophysiological mechanisms in myoclonic epilepsy have traditionally been linked to abnormal frontally predominant corticothalamic networks. By definition, the electrophysiological activity in myoclonic

epilepsy captured by using standard EEG recordings shows simultaneous and bilateral involvement of cerebral hemispheres at the onset of seizure activity [11]. However, recent studies using the dense array EEG systems provide evidence that myoclonic epilepsy is not truly “generalized” in the sense of global activation of the cortex at the onset and propagation of epileptiform discharges. Rather, restricted networks within cortical and subcortical circuits are involved in the discharges, predominantly in the cortical areas of frontal and temporal lobes [12]. These observations indicate

Fig. 2 Lower volumes of left and right thalamus and caudate in patients with myoclonic epilepsy (ME) compared to healthy subjects ($p < 0.05$)

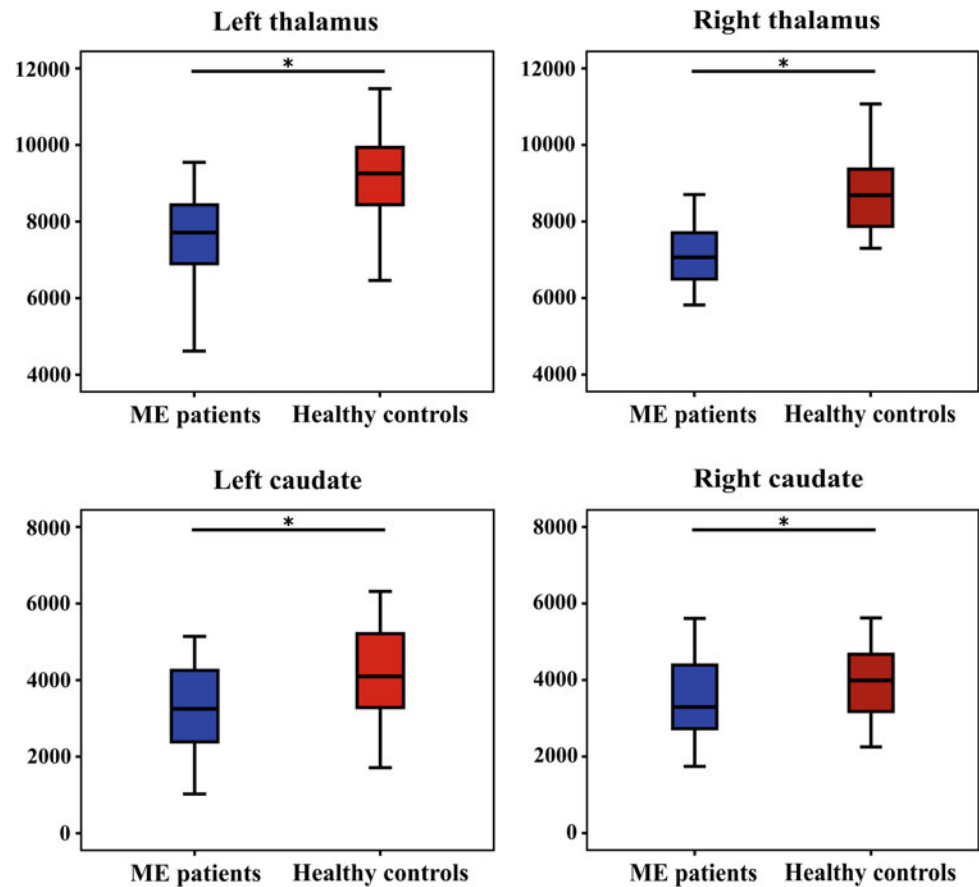


Table 2 Volumetric analysis of the subcortical grey matter structures in patients with myoclonic epilepsy (ME) and healthy controls

Subcortical structures volume (mm ³)	ME patients	Healthy controls
Left amygdala	1720 (721)	1596 (289)
Right amygdala	1690 (291)	1639 (187)
Left hippocampus	4206 (538)	4276 (726)
Right hippocampus	4288 (552)	4548 (348)
Left caudate	3536 (575)	3960 (439)
Right caudate	3543 (598)	3817 (451)
Left pallidum	1437 (271)	1431 (273)
Right pallidum	1427 (249)	1541 (246)
Left putamen	3537 (895)	5538 (1067)
Right putamen	5232 (855)	5581 (683)
Left thalamus	7698 (1045)	9205 (1151)
Right thalamus	7043 (922)	8149 (720)

that the epileptiform discharges in myoclonic seizures can be localized and not necessarily generalized. Our findings also prove that myoclonic epilepsy involves morphological abnormalities within anatomical regions of frontal and temporal lobes but also suggest that it involves cortical and

subcortical structures beyond these regions, comprising basal ganglia, namely thalamus and caudate.

As with most studies in epilepsy, separating out the effect of pharmacology on neuroanatomical morphometric measures or functional circuitry is difficult, so medication

represents a significant confounding variable. Here, we also didn't address the possible effects of anti-seizure medication on brain substrates, this being one of the study limitations. This is further complicated by the fact that the one of the greatest predictors of drug resistance is the occurrence of multiple seizure types, indicating a more severe form of myoclonic epilepsy. Certain alterations of brain morphology could be as well related to the concomitant occurrence of other seizure types that were present in several patients.

We believe that our findings add further evidence to the notion that specific brain networks, implicating in particular cortical and subcortical regions may underlie the origin and propagation of myoclonic seizures.

5 Conclusions

These findings of reduced bilateral thalamus volumes as well as selected cortical volumes support the hypothesis of aberrant cortico-thalamic networks in epilepsy with myoclonic seizures. However, our data suggest that structural alterations may not only be confined to the thalamus and cortex but also affect basal ganglia.

Acknowledgements The author thanks all colleagues who helped in processing the data, also to all patients and participants who took part in this study.

Conflict of Interest No conflict of interest has been done.

References

1. Eberhardt, O., et al.: Myoclonic disorders. *Brain Sci.* **7**(8), 103 (2017)
2. Lozsadi, D.: Myoclonus: a pragmatic approach. *Pract. Neurol.* **12**(4), 215–224 (2012)
3. Schefer, I.E., et al.: ILAE classification of the epilepsies: position paper of the ILAE commission for classification and terminology. *Epilepsia* **58**(4), 512–521 (2017)
4. Kim, J.H., et al.: Subcortical grey matter changes in juvenile myoclonic epilepsy. *NeuroImage Clin.* **17**, 397–404 (2018)
5. Perani, S., et al.: Thalamic volume reduction in drug-naive patients with new-onset genetic generalized epilepsy. *Epilepsia* **59**(1), 226–234 (2018)
6. Seeck, M., et al.: Subcortical nuclei volumetry in idiopathic generalized epilepsy. *Epilepsia* **46**(10), 1642–1645 (2005)
7. Lin, K., et al.: Hippocampal atrophy and memory dysfunction in patients with juvenile myoclonic epilepsy. *Epilepsy Behav.* **29**(1), 247–251 (2013)
8. Chiosa, V. et al.: Large-scale network architecture and associated structural cortico-subcortical abnormalities in patients with sleep/awake-related seizures. *Sleep* (2019)
9. Ronan, L., et al.: Widespread cortical morphologic changes in juvenile myoclonic epilepsy: evidence from structural MRI. *Epilepsia* **53**(4), 651–658 (2012)
10. Desikan, R.S., et al.: An automated labeling system for subdividing the human cerebral cortex on MRI scans into gyral based regions of interest. *Neuroimage* **31**(3), 968–980 (2006)
11. Bauer, P.R., et al.: The topographical distribution of epileptic spikes in juvenile myoclonic epilepsy with and without photosensitivity. *Clin. Neurophysiol.* **128**(1), 176–182 (2017)
12. Holmes, M., et al.: Evidence that juvenile myoclonic epilepsy is a disorder of frontotemporal corticothalamic networks. *Neuroimage* **49**(1), 80–93 (2010)

Part IX
Bioinformatics

Mode of Artemisinins' Action on Oxidative Stress, Genomic and G-Quadruplex DNA

S. G. Ginosyan, G. V. Chilingaryan, H. V. Grabski, L. A. Ghulikyan, N. M. Ayvazyan, and S. G. Tiratsuyan

Abstract

The present study was conducted to evaluate the effect of artemisinins' on the level of lipid peroxidation (LPO), spontaneous chemiluminescence of the S-180 sarcoma homogenate and to study the nature of the interaction with canonical and non-canonical forms of DNA. Artemisinins are secondary metabolites of the medicinal plant *Artemisia annua* have anti-inflammatory, anticarcinogenic, immunomodulatory, antimicrobial, antihelminthic, antiviral, antioxidant and other properties. Our preliminary reverse virtual screening demonstrated that the ligand-binding domain of the human glucocorticoid receptor is the optimal target for artemisinin as well as for dexamethasone. However, the exact molecular targets and mechanisms of action of artemisinins are not well known. We have shown that the introduction of artemisinin leads to increase in LPO and chemiluminescence, which then causes apoptotic cell death in different ways without direct interaction with genomic DNA. We have also shown that artemisinin, dihydroartemisinin, and dimer of dihydroartemisinin interact with 2 sites of the G-quadruplex structure. Artemisinin and dimer of dihydroartemisinin are associated with a groove located between G15 and G21 while dihydroartemisinin binds to a groove located between guanine G5 and G23.

Keywords

Artemisinins • Lipid peroxidation • Chemiluminescence • S-180 sarcoma • Canonical • Non-canonical DNA

1 Introduction

Artemisinins (ART) are sesquiterpene trioxane lactones, the secondary metabolites of the annual wormwood plant *Artemisia annua*. Artemisinins exhibit antioxidant, anti-inflammatory, anticarcinogenic, immunomodulatory, antimicrobial, antihelminthic, antiviral, antimalarial, etc. activities [1, 2]. Our preliminary reverse virtual screening demonstrated that the ligand-binding domain (LBD) of the human glucocorticoid receptor (GR) is the optimal target for ART. At the same time, with the LBD of hGR for ART almost identically overlapping with those of dexamethasone [3].

Experimental data of recent years suggests that ARTs could become a therapeutic alternative in the treatment of highly aggressive, rapidly progressive forms of cancer without acquiring cross-resistance to known anticancer drugs [4]. ARTs also show synergism with other anticancer drugs with no evident toxicity and very few incidences of adverse effects [5], potential to inhibit the growth of solid tumors, suggesting their application in neo-adjuvant therapy. Dihydroartemisinin and artesunate exhibit chemosensitizing effects *in vivo* in breast, lung, pancreas, and glioma cancer cells, proposing the use of ARTs also in combination with anticancer therapy [6]. Different molecular mechanisms of artemisinin action on cancer cells are being considered [7]. ART has been shown to modulate a wide group of signaling molecules or pathways, including TLR, SYK, PLC γ , PI3K/Akt, MAPK, STAT-1/3/5, NF- κ B, Sp1, Nrf2/ARE, etc. [1]. Artemisinins stimulate the formation of free radicals by cleaving the endoperoxide bond with heme iron in its structure to perform antimalarial action and cytotoxic effects

S. G. Ginosyan · H. V. Grabski
Department of Medical Biochemistry and Biotechnology, Institute of Biomedicine and Pharmacy, Russian-Armenian University, 123 Hovsep Emin Street, Yerevan, Armenia

G. V. Chilingaryan · S. G. Tiratsuyan (✉)
Department of Bioinformatics, Bioengineering and Molecular Biology, Institute of Biomedicine and Pharmacy, Russian-Armenian University, Yerevan, Armenia
e-mail: stiratsuyan@bk.ru

L. A. Ghulikyan ·
N. M. Ayvazyan
Laboratory of Toxinology and Molecular Systematics, L.a. Orbeli Institute of Physiology NAS RA, Yerevan, Armenia

against cancer. The exact mechanism of activation and the molecular basis of anti-cancer effects are not fully understood [4, 6, 7]. The involvement of the G-quadruplex DNA motifs of the *Plasmodium falciparum* malaria parasite under the action of antimalarial drugs has also been demonstrated [8]. G-quadruplexes are non-canonical secondary structures of DNA, broadly represented in telomeres and in promoter regions of genes controlling growth, differentiation, splicing, etc. [9, 10]. Stabilization of G-quadruplex structures by interacting with low molecular weight ligands to inhibit telomerase activity or suppress the expression of oncogenes is a new approach in the contemporary anticancer therapy [11]. In this work, we evaluated the effect of artemisinins on the level of LPO and spontaneous chemiluminescence of the S-180 sarcoma homogenate, to study the nature of the interaction with DNA.

2 Materials and Methods

Artemisinin ($\geq 98\%$) TRC (Toronto, Canada); tris(hydroxymethyl)aminomethane (Tris) ($\geq 99\%$) Bobo Biotechnology Co., Ltd. (Shanghai, China); phenylbutazone ($\geq 99.9\%$) Hubei Hengshuo Chemical Co., Ltd. (Hubei, China) were used for the study. ROS' levels were measured by chemiluminescence (ChL) analyzing system Junior LB 9509 portable tube luminometer (Berthold Technologies, Germany). LPOs are unstable and decomposed to a complex series of compounds. The most abundant compound is malonic dialdehyde (MDA). Accumulation of MDA in tissues was determined by spectrophotometric measurement [12] at 532 nm wavelength on the B01-CT-8 spectrophotometer ("E-ChromTech", Taiwan) using the TBA-test. Artemisinin was dissolved in 10 ml of dimethyl sulfoxide (DMSO) to a final concentration of 1, 5, 10, 25, 50, and 100 μM . Line of mice with S-180 sarcoma cells was used for the experiments at the Laboratory of Toxinology and Molecular Systematics of L. A. Orbeli Institute of Physiology (NAS RA). All procedures were done according to the Institution's animal care and use committee (IACUC) rules and ethical guidelines for decapitation of un-anaesthetized mice and rats [13]. Genomic DNA was isolated from a small volume of the S-180 sarcoma tissue using the peqGOLD MicroSpin Tissue DNA Kit (PeqLab Biotechnologie GmbH Erlangen, Germany). Electrophoretic mobility shift assay (EMSA) was performed as previously reported [14]. The DNA concentration was measured by spectrophotometric method (Eppendorf BioPhotometer plus, Germany) and then equal amounts of DNA were mixed with different concentration of artemisinin at a 1:1 (vol:vol) ratio for 30 min, 24 and 48 h. Next, 1% agarose gel electrophoresis (PerfectBlue TM

Horizontal Mini Gel System, PeQlab, Germany) was used to detect the migration of DNA bands under a UV illuminator (E-BOX VX2-VILBER LOURMAT, PeQlab, Germany). The 3D structure of ART [CID: 68827], DHA [CID: 456410], DDHA [CID: 44564070] were obtained from PubChem [15]. The 3D structure of intramolecular human telomere G-quadruplex [PDB ID: 2JSL] in PDB format was obtained from RCSB PDB [16]. Autodock Tools and Autodock Vina used for molecular docking [17], Ligplot⁺—for analysis of hydrogen bonds and hydrophobic interactions [18].

Experimental results were expressed as means \pm SD. All measurements were conducted three to five times. The data were analyzed by a one-way analysis of variance (ANOVA) and the value of $p < 0.05$ was considered as significant.

3 Results

3.1 Lipid Peroxidation

The study of LPO under the action of different concentrations of ART showed that, at the optimal concentration of 40 $\mu\text{M}/\text{ml}$, the level of MDA significantly increased compared to the control (Fig. 1a).

3.2 Chemiluminescence Analysis

The level of chemiluminescence in the presence of ART at the concentration of 40 $\mu\text{M}/\text{ml}$ increased significantly immediately after adding to the cell homogenate and remains above the control level for 90 min (Fig. 1b). Thus, the analysis of the results of LPO and chemiluminescence suggests that ART induced oxidative stress in S-180 sarcoma cells.

3.3 Interaction of Artemisinin with the Genomic DNA of S-180 Cancer Cells

Artemisinin, when interacts with GR, can be imported into the nucleus, and it is extremely important to assess the direct interaction of ART with genomic DNA. This has been carried out by DNA retardation [14].

Different concentrations of ART (1–100 μM) and joint incubation times (up to 48 h) were used when the direct interaction of genomic DNA of S-180 cancer cell line with ART has been tested (Fig. 2). Our results are consistent with data, which claim that there is no direct interaction between them [7, 19].

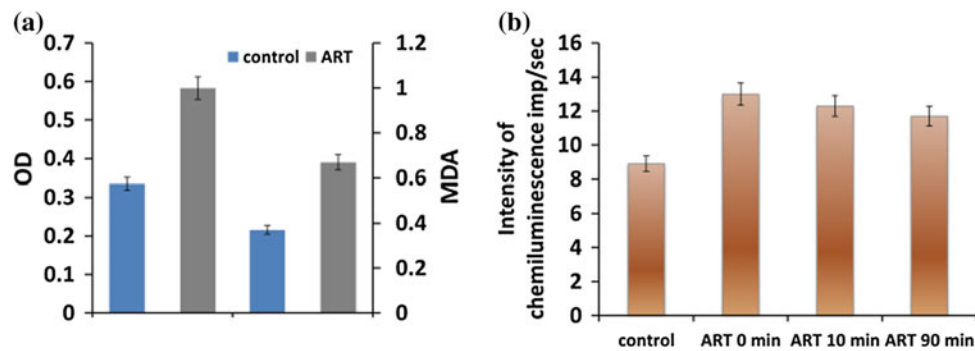
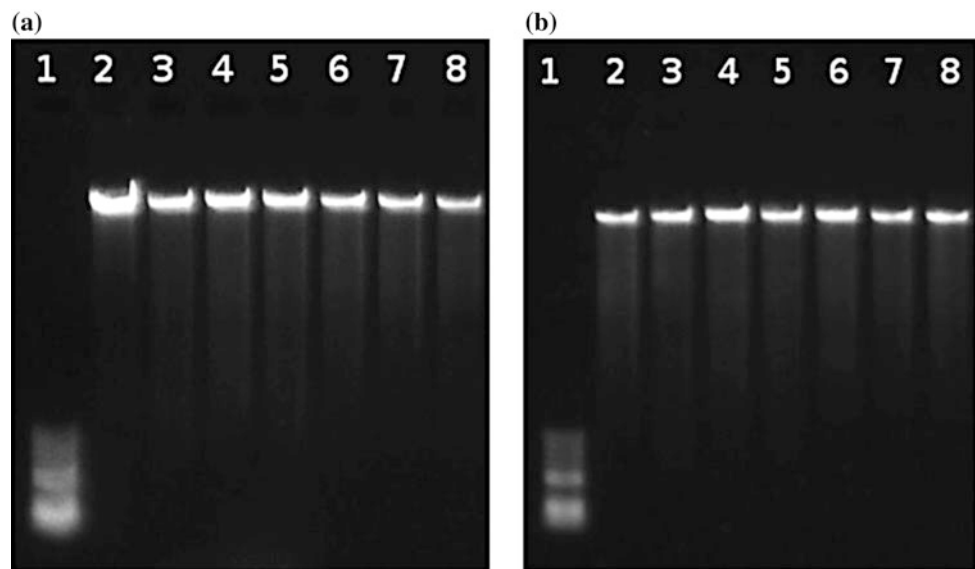


Fig. 1 Content of LPO products (MDA concentration, nM/ml) in control and after adding of the 40 μM/ml ART (a). Intensity of chemiluminescence (imp/sec) of sarcoma cells' homogenate (reference) and after adding ART (40 μM/ml) (b)

Fig. 2 The electrophoretic mobility of DNA after 24 h (a) and 48 h (b) of incubations with ART. 1—ladder; 2—genomic DNA of S-180; 3–8—genomic DNA of S-180 with incubation with increasing concentrations of ART: 3—1 μM; 4—5 μM; 5—10 μM; 6—25 μM; 7—50 μM; 8—100 μM



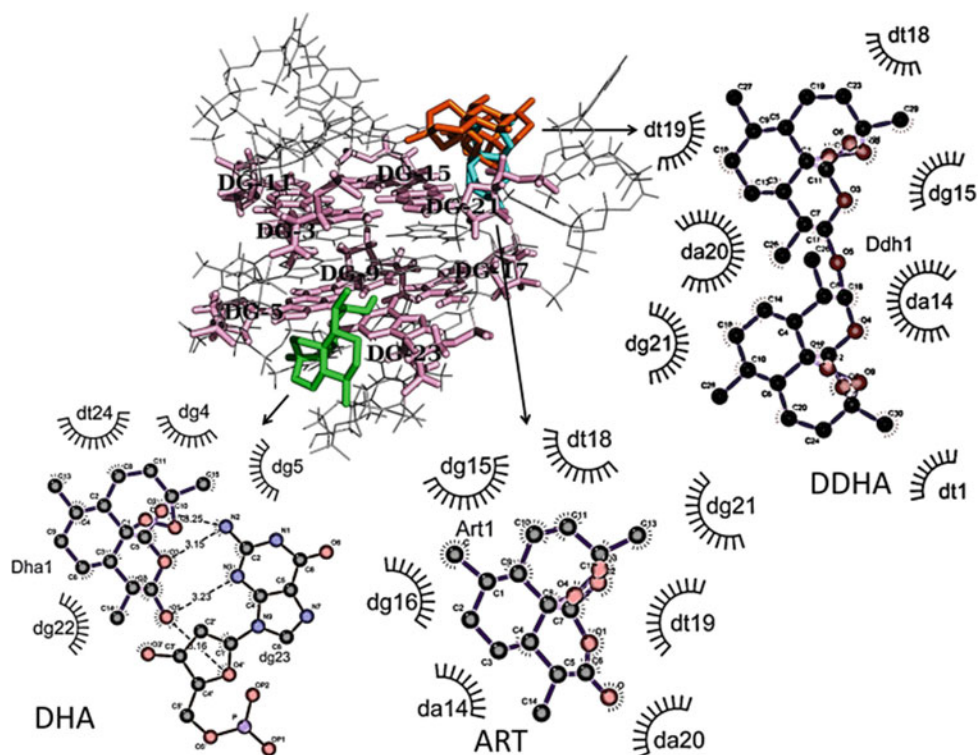
3.4 The Interaction of ART, DHA and DDHA with G-Quadruplex Structures of Human Telomere DNA

The results of the docking analysis show that all three ligands (ART, DHA, and DDHA) interact with 2 sites on G-tetrad of human telomere DNA (Fig. 3), where ART and DDHA interact with the first site (I site), while DHA - with the second (II site). ART and DDHA are associated with a groove located between G15 and G21 with binding energies of -7.4 and -8.4 kcal/mol, respectively. Both ART and DDHA enter into a variety of hydrophobic interactions, including A14, with which DDHA interacts with strong hydrophobic interactions. This nucleotide is a part of a loop formed by T12–T13–A14, which is “K-ion within the loop”. Both ligands also interact with G15 and G21, which are of the top G-tetrad [20].

In the second site, DHA binds to a groove located between guanine G5 and G23. This groove is one of two medium grooves present in the 3D G-quadruplex structure [20]. The binding energy for DHA -7.1 kcal/mol. The results of the Ligplot analysis show that DHA forms 4 hydrogen bonds with G23 and a hydrophobic interaction with G5. These two guanines are part of one of the “three stacked G-tetrads” located on the bottom of the “G-quadruplex core” [20].

Thus, all 3 ligands are associated with extremely important sites of the human telomere G-quadruplex structure DNA. The interaction energy with DDHA is significantly higher than that of DHA and ART, which suggests the preferential interaction of DDHA with non-canonical DNA structures. These interactions can potentially lead to the destabilization of the G-quadruplex structure.

Fig. 3 Docking of human telomere G-quadruplex DNA structure with DHA (green), ART (cyan) and DDHA (orange). Light pink—two G-quadruplexes

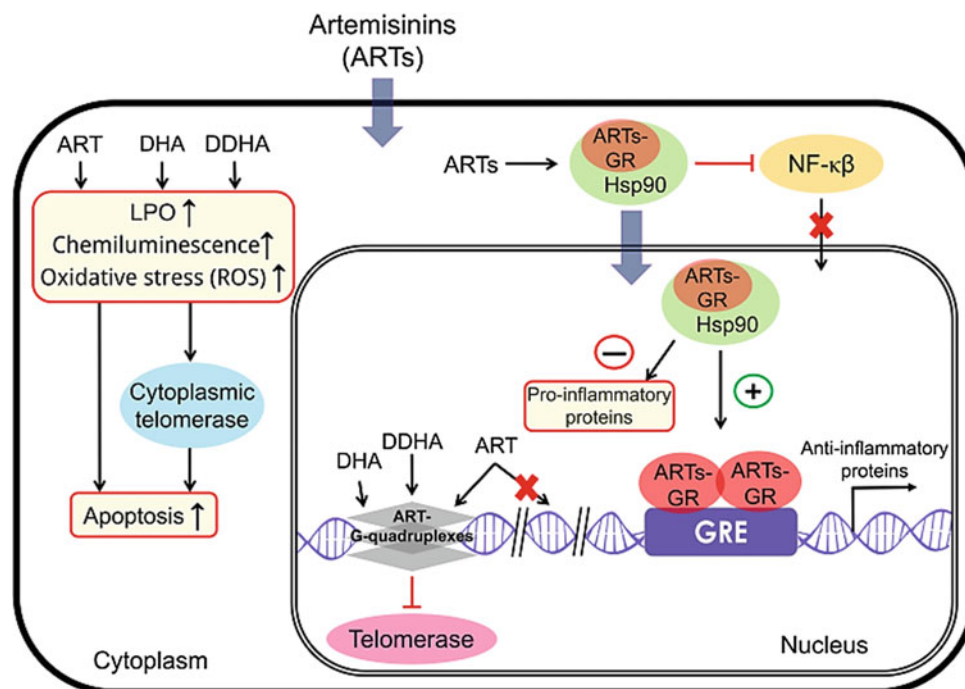


4 Conclusions

We have proposed a scheme (Fig. 4), taking into account the multiple parallel ways of ARTs action, including GR, oxidative stress, and canonical and non-canonical DNAs.

Recent studies have shown that the class of antimalarial drugs has a number of biological characteristics that include anti-cancer properties. The exact mechanism of activation and the molecular basis of these anti-cancer effects are not fully understood [4, 6, 7]. One of the mechanisms may be that ARTs, interacting with GR, binds to Hsp90 and

Fig. 4 Hypothetical scheme of multiple pathways of artemisinin's action in S-180



transduce the signals into the nucleus, affecting multiple molecular pathways, including those associated with anti-neoplastic activity. On the other hand, ARTs-GR interaction in the cytosol can inhibit all inflammatory cytokines via NF- κ B signaling leading to a reduction of necroinflammation [21]. Artemisinins seem to regulate such key factors as NF- κ B, survivin, NOXA, hypoxia-induced factor-1 α , apoptosis, cell cycle arrest with G₀/G₁ and oxidative stress. We have shown that the introduction of ART leads to an almost two-fold increase both in LPO and chemiluminescence levels caused by cell metabolism of S-180 cells. The amplitude of the chemiluminescence signal in the presence of ART correlated with the number of LPO products, determined by the concentration of MDA. The observed positive correlation between the intensity of chemiluminescence accompanying lipid chain oxidation in the presence of ART leads to the conclusion that ART-induced LPO is the main source of chemiluminescence. Oxidative stress is manifested in the accumulation of damaged DNA bases, protein oxidation products and LPO and the associated increased susceptibility of membrane lipids and lipoproteins to the action of pro-oxidants, including ions Fe²⁺ or H₂O₂ [22]. The high level of ROS is a common anti-tumor property of anti-neoplastic drugs since tumor cells are vulnerable to damage induced by free radicals. The formation of ROS can promote the selective action of ART on S-180 cells through DNA damage, enhanced apoptosis, growth arrest and a decrease in angiogenesis [7, 22]. The antitumor effect of ART is associated with either direct DNA damage or indirect, interfering with several signaling pathways involved in carcinogenesis. There are conflicting data regarding the interaction of ART with genomic DNA [23]. Indirect DNA damage is more common than direct. The results of our experiments show the absence of direct interaction of ART with the genomic DNA of S-180 cells. Oxidative stress, induced by ART, can stimulate glyceraldehyde 3-phosphate dehydrogenase (GAPDH) interaction with TERC and lead to the inhibition of telomerase activity, telomere shortening and thereby inducing cancer cell senescence [24]. It is known that the telomerase can localize to the mitochondria and increases hydrogen-peroxide-mediated mitochondrial DNA damage, which can lead to apoptotic cell death and imply a novel function of telomerase in mitochondrial DNA transactions [25]. The other mechanism can be an interaction of ARTs with G-quadruplex DNA motifs [8]. We have shown that ART, DHA, and DDHA interact with the 2 sites of the G-quadruplex structure of human telomere DNA with the preferential interaction with DDHA. Our data corresponded with in vitro studies about increased exhibition of antitumor activity of ARTs dimers [26]. Artemisinin cytotoxicity has also been associated with blocking of cytokines that inhibit tumor invasion, migration, and metastasis in several studies [4].

Acknowledgements We are grateful for the financial support to the Ministry of Education and Science of the Republic of Armenia (grant № 10-2/I-1).

Conflict of Interest The authors declare that they have no conflict of interest.

References

1. Ho, W.E., et al.: Artemisinins: pharmacological actions beyond anti-malarial. *Pharmacol. Ther.* **142**, 126–139 (2014)
2. Dai, Y.F., et al.: The pharmacological activities and mechanisms of artemisinin and its derivatives: a systematic review. *J. Med. Chem.* **26**, 867–880 (2017)
3. Ginossyan, S.V., Grabski, H.V., Tiratsuyan, S.G.: Insights on glucocorticoid receptor modulation through binding of artemisinin. *Biolog J. Armenia* **69**, 104–109 (2017)
4. Das, A.K.: Anticancer effect of antimalarial artemisinin compounds. *Ann. Med. Health Sci. Res.* **5**, 93–102 (2015)
5. Raffetin, A., et al.: Use of artesunate in non-malarial indications. *Med. Mal.* **48**, 238–249 (2018)
6. Wong, Y.K., et al.: Artemisinin as an anticancer drug: recent advances in target profiling and mechanisms of action. *Med. Res. Rev.* **37**, 1492–1517 (2017)
7. Crespo-Ortiz, M.P., Wei, M.Q.: Antitumor activity of artemisinin and its derivatives: from a well-known antimalarial agent to a potential anticancer drug. *Biomed. Res. Int.* 2012 (2011)
8. Harris, L.M., et al.: G-quadruplex DNA motifs in the malaria parasite *Plasmodium falciparum* and their potential as novel antimalarial drug targets. *Antimicrob. Agents Chemother.* **62**, e01828-17 (2018)
9. Trotta, R., et al.: A more detailed picture of the interactions between virtual screening-derived hits and the DNA G-quadruplex: NMR, molecular modelling and ITC studies. *Biochimie* **93**, 1280–1287 (2011)
10. Aksenova, A.Y., Mirkin, S.M.: At the beginning of the end and in the middle of the beginning: structure and maintenance of telomeric DNA repeats and interstitial telomeric sequences. *Genes* **10**, 118 (2019)
11. White, E.W., et al.: Structure-specific recognition of quadruplex DNA by organic cations: influence of shape, substituents and charge. *Biophys. Chem.* **126**, 140–153 (2007)
12. Stalnaja, I.D., Garishvili, T.G.: Method of malonic dialdehyde determination with thiobarbituroacid. *Biochem. Methods Inv.* Moscow, pp. 66–68
13. IACUC at <http://www.utsouthwestern.edu/utsw/cda/dept238828/files/469088.html>
14. Wang, Y.Q., et al.: Biscarbamate cross-linked polyethylenimine derivative with low molecular weight, low cytotoxicity, and high efficiency for gene delivery. *Int. J. Nanomedicine* **7**, 693 (2012)
15. Bolton, E.E., et al.: PubChem: integrated platform of small molecules and biological activities. *Annu. Rep. Comput. Chem.* **4**, 217–241 (2008)
16. Berman, H.M., et al.: The protein data bank. *Nucleic Acids Res.* **28**, 235–242 (2000)
17. Trott, O., Olson, A.J.: AutoDock Vina: improving the speed and accuracy of docking with a new scoring function, efficient optimization, and multithreading. *J. Comput. Chem.* **31**, 455–461 (2010)
18. Wallace, A.C., et al.: LIGPLOT: a program to generate schematic diagrams of protein-ligand interactions. *Protein Eng. Des. Sel.* **8**, 127–134 (1995)

19. O'Neill, P.M., et al.: The molecular mechanism of action of artemisinin—the debate continues. *Molecules* **15**, 1705–1721 (2010)
20. Phan, A.T., et al.: Structure of two intramolecular G-quadruplexes formed by natural human telomere sequences in K⁺ solution. *Nucleic Acids Res.* **35**, 6517–6525 (2007)
21. Wang, Y., et al.: The anti-malarial artemisinin inhibits pro-inflammatory cytokines via the NF-κB canonical signaling pathway in PMA-induced THP-1 monocytes. *Int. J. Mol. Med.* **27**, 233–241 (2011)
22. Valko, M., et al.: Free radicals, metals and antioxidants in oxidative stress-induced cancer. *Chem. Biol. Interact.* **160**, 1–40 (2006)
23. Cai, H.H., et al.: Visual characterization and quantitative measurement of artemisinin-induced DNA breakage. *Electrochim. Acta* **54**, 3651–3656 (2009)
24. Nicholls, C., et al.: Glyceraldehyde-3-phosphate dehydrogenase (GAPDH) induces cancer cell senescence by interacting with telomerase RNA component. *PNAS* **109**, 13308–13313 (2012)
25. Lu, W., et al.: Telomeres—structure, function, and regulation. *Exp. Cell Res.* **319**, 133–141 (2013)
26. Stockwin, L.H., et al.: Artemisinin dimer anticancer activity correlates with heme-catalyzed reactive oxygen species generation and endoplasmic reticulum stress induction. *Int. J. Cancer* **125**, 1266–1275 (2009)

Evaluation of the Quercetin Semisynthetic Derivatives Interaction with ABCG2 and Cyclooxygenase-2

A. E. Manukyan

Abstract

Cancer multiple drug resistance and the inflammatory process are the main problems for successful chemotherapy. In anticancer therapy, plant and semisynthetic compounds are considered as potential modifiers for ABCG2 and COX2 inhibitors. As a result of experiments carried out *in silico*, the possible interaction of ABCG2 and inhibition of COX-2 by semisynthetic derivatives of quercetin were first revealed. The physicochemical parameters of the studied ligands were revealed, after which, for reliability, they were compared with *in vitro* experiments.

Keywords

ABCG2 • COX2 • Quercetin derivatives • Anticancer

1 Introduction

Cancer multiple drug resistance (MDR) and in-flammatory process are the main problems for successful chemotherapy. MDR is an enhanced cellular outflow of antitumor agents due partially to the overexpression of the ATP-binding cassette (ABC) transporters [1]. ABC transporters are characterized by a four-domain structure consisting of two cytoplasmic nucleotide-binding domains (NBD) that bind and hydrolyze ATP, and two transmembrane domains (TMD) that recognize and transport substrates. While the structure and function of NBD are the same in all families, TMD is very heterogeneous, allowing transporters to recognize a variety of substrates and use the energy of ATP hydrolysis to move molecules through membranes,

regardless of the prevailing concentration gradient. Among the 48 currently identified ABC genes, the representatives of B, C & G families [ABCB1 coding for P-glycoprotein or P-gp, ABCC1 coding for protein 1—associated with multidrug resistance (MRP1), and ABCG2 coding for breast cancer resistance protein (BCRP)] are the three main outflow carriers that have been found to be linked with MDR [1]. Recently, special attention has been paid to natural compounds with antitumor and selective inhibitory activity on ABCG2 transporters. Thus, new research is aimed at the synthesis of semisynthetic compounds that can bind to ABCG2, inhibiting the activity of the latter. One of these compounds may be quercetin and its methylated derivatives [2, 3]. Methylation of some naturally occurring phenolic compounds can modulate the activity of multimethoxy substituted phenyl rings which may be an important pharmacophore for MDR [1] and also an inhibitor of cyclooxygenase-2 (COX2), which catalyzing the first stage of prostaglandin synthesis. The released arachidonic acid under the action of COX turns into prostaglandin (PGs)—PGG2, which is reduced to prostaglandin PGH2, and that—to other eicosanoids (prostaglandins, thromboxanes, prostacyclins). PGs are cellular inflammation mediators, the biosynthesis of which may cause the development of severe pathological conditions: participation in the implementation of dysplastic and neoplastic processes (tumor growth), namely, in suppressing apoptotic cell death, pathological neoangiogenesis and invasion, as well as mediating immunosuppressive functions [4].

COX-2 is a homodimer, each subunit of the dimer consists of three domains: a short N-terminal epidermal growth factor (EGF) domain, an α -helical membrane-binding domain, and a C-terminal catalytic domain. The catalytic domain comprises the bulk of protein and contains the cyclooxygenase and peroxidase active sites on either side of the heme prosthetic group. On the opposite side of the protein from the membrane binding domain, the peroxidase active site consists of the heme positioned at the bottom of a shallow cleft. This structure provides considerable solvent

A. E. Manukyan (✉)

Department of Bioengineering, Bioinformatics and Molecular Biology, Russian-Armenian University, Hovsep Emin 123 Street, Yerevan, Armenia
e-mail: amalimnkn@gmail.com

accessibility to the heme with the exception of a cluster of several hydrophobic amino acids that form a dome over part of the cleft [4]. The COX-2 active site lies on the opposite side of the heme from the peroxidase active site at the top of an L-shaped channel that originates in the membrane binding domain. The mouth of the channel consists of the lobby (amino acids R120, Y355, E524), a large volume that narrows to a constriction that must open before substrates or inhibitors can pass deeper into the channel. Amino acids V523 and H513 lead to the formation of an additional side pocket, because of which the active site of COX-2 becomes more accessible, in addition, the last helix D twists up and simplifies access to binding to R120.

The research is aimed at the synthesis of semi-synthetic drugs, the basis of which is quercetin substituted in different positions with methyl, ethyl, etc. groups.

The purpose of this work is to study and evaluate the interaction of quercetin and its derivatives by molecular docking with ABCG2 and COX2.

2 Research Methods

The structural formulas of ligands (1–29) were retrieved from PubChem, and also constructed by MarvinSketch [5]. By SwissADME were determined physicochemical parameters for each ligand [6]. The crystal structure of ABCG2 and COX2 from *Homo sapiens* (PDB: 6ETI, 5f19) were

taken from PDB RCSB [7]. Docking experiments of ligands with proteins were carried out using Autodock Vina [8], and it is based on the use of a rigid receptor. The whole protein conformational space was searched, using grid box dimensions $82 \times 102 \times 90 \text{ \AA}$. Following exhaustiveness values were tested in this study: 8, 16, 32, 64, 128, 256, 512. Exhaustiveness value was increased to a value of 512, and a maximum number of binding modes to generate set to 20. After that, 50 independent docking calculations were carried out with random initial seeds.

3 Result and Discussion

Molecular docking was used for the prediction of binding modes of ligands with ABCG2 and COX2. There are six binding sites with ABCG2-R482, P485; T402; N643, N650; V651. The binding energy for the complex with ABCG2 on the average is -8.2 kcal/mol . The interaction site of ABCG2 is R482, P485 amino acids, T402 is responsible for the transport activity of this protein and N643, N650 and V651 are amino acids that bind to flavonoids [1] (Table 1).

For COX2 there are also six binding sites—S530; R120; Y385; V523; H90; P156 the binding energy on the average is -8.6 kcal/mol (Table 2).

Unfortunately, molecular docking is not appropriate for the prediction of binding affinity or binding poses of protein-ligand complexes. However, by comparing the

Table 1 Results for ABCG2

Ligand-protein binding results		
Derivatives*	Gibbs free energy (kcal/m)	Binding constant (10^6)
4	-8.67	21.1
5	-9.32	62.8
8	-8.72	22.9
10	-9.27	57.7
11	-9.00	36.7
12	-9.40	71.8
15	-9.32	62.8
16	-9.22	53.1
18	-9.30	60.7
19	-9.10	43.4
20	-8.55	17.2
21 4'-O-methylated	-9.47	80.7
26 -3,7-O-dibutylated	-5.72	0.1
29 4',7-O-butylated	-6.95	1.2

*O-methylated quercetin derivatives [4–20: monomethylated (4, 5, 8, 9), dimethylated (10–15), trimethylated (16–18), tetramethylated (19) and pentamethylated (20)]

Table 2 Results for COX2

Ligand-protein binding results		
Derivatives*	Gibbs free energy (kcal/m)	Binding constant (10 ⁶)
4	-9.36	67.12
5	-9.93	174.82
8	-9.4	71.78
10	-9.46	79.39
11	-9.63	105.63
12	-9.36	67.12
15	-9.2	51.30
16	-9.05	39.88
18	-9.16	47.97
19	-8.78	25.34
20	-8.8	26.21
21 4'-O-methylated	-9.4	71.78
26 -3,7-O-ibutylated	-7.2	1.78
29 4',7-O-butylated	-6.5	0.55

*O-methylated quercetin derivatives [4–20: monomethylated (4, 5, 8, 9), dimethylated (10–15), trimethylated (16–18), tetramethylated (19) and pentamethylated (20)]

already performed laboratory studies, docking analysis gives a better estimate [9]. In studies of Yuan and co-authors, it was shown that 3,3',4',7-tetra-O-methylquercetin (19) and 4',4',5,7-penta-O-methylquercetin (20) can be inhibitors for ABCG2 [10] and COX2.

It is important that both the substitution of 3',4'-O-Met, and the presence of a group of 5-OH in the structure of quercetin were necessary to improve the inhibitory properties of new derivatives. Shea and colleagues investigated O-methyl compounds (4), (5) and (8–20) and their ability to inhibit the growth of cancer cells [10, 11]. These studies have shown that the selective masking of the hydroxyl groups of quercetin is crucial in determining antiproliferative activity. It was generally possible to maintain inhibitory effects against cancer cell lines by methylation at the 4'-OH and/or 7-OH positions, while the substitution of 3'- and 4'-O-Me groups increased the activity of the derivatives. In addition, the additional administration of the methoxy group can enhance the inhibition of the growth of cancer cells, with 3',4',7 trimethoxyquercetin (16) showing greater activity than 3',4' dimethoxyquercetin (12). (11), 3,4',7-O-trimethylquercetin tetramethylquercetin (19) slightly increased activity compared with quercetin. In addition, 4'-O-monoalkylated (21–23), 3,7-O-dialkylated (24–26), 4',7-O-dialkylated (27–29) derivatives of quercetin showed good results in relation to human cancer cells [11]. The inhibitory activity of the growth of cancer cells was maintained during the esterification of 3-OH and 4'-OH using a long propyl chain or a short ethyl chain [12].

4 Conclusion

The docking analysis suggests that the majority of modified ligands form bonds with the amino acids active sites on both proteins with a potential subsequent prevention of the outflow of ABCG2 cells and inhibition of COX2. Modification and inhibition of the latter may be a key element in anti-carcinogenic therapy.

Conflict of Interest The authors declare that they have no conflict of interest.

References

1. Jackson, S.M. et al.: Structural basis of small-molecule inhibition of human multidrug transporter ABCG2. *Nat. Struct. Mol. Biol.* **25**(4), 333 (2018). <https://doi.org/10.1038/s41594-018-0049-1>
2. Al-Jabban, S.M.R. et al.: Synthesis and anti-proliferative effects of quercetin derivatives. *Nat. Prod. Commun.* **10**(12) (2015). <https://doi.org/10.1177/1934578x1501001225>
3. Massi, A. et al.: Research progress in the modification of quercetin leading to anticancer agents. *J. Mol.* **22**(8), 1270 (2017). DOI: 0.3390/molecules22081270
4. Leng, J. et al.: Cyclooxygenase-2 promotes hepatocellular carcinoma cell growth through Akt activation: evidence for Akt inhibition in celecoxib-induced apoptosis. *J. Hepatol.* **38**(3), 756–768 (2013). <https://doi.org/10.1053/jhep.2003.50380>
5. Csizmadia F.V (2000) JChem: Java applets and modules supporting chemical database handling from web browsers J of Chemical

- Information and Computer Sciences. 40(2):323–324 <https://doi.org/10.1021/ci9902696>
6. Daina, A. et al.: SwissADME: a free web tool to evaluate pharmacokinetics, drug-likeness and medicinal chemistry friendliness of small molecules. *Sci. Rep.* **7**, 42717 (2017). <https://doi.org/10.1038/srep42717>
 7. Berman, H. et al.: Announcing the worldwide protein data bank. *J. Nat. Struct. Mol. Biol.* **10**(12), 980 (2003). <https://doi.org/10.1038/nsb1203-980>
 8. Trott, O. et al.: AutoDock Vina: improving the speed and accuracy of docking with a new scoring function, efficient optimization, and multithreading. *J. Comput. Chem.* **31**(2), 455–461 (2010). <https://doi.org/10.1002/jcc.21334>
 9. Chen, C. et al.: Quercetin: a potential drug to reverse multidrug resistance. *Life Sci.* **87**(11–12), 333–338 (2010). <https://doi.org/10.1016/j.lfs.2010.07.004>
 10. Madhukar, M. et al.: Design, synthesis and evaluation of mutual prodrug of 4-biphenylacetic acid and quercetin tetramethyl ether (BPA–QTME) as gastroprotective NSAID. *Eur. J. Med. Chem.* **45**(6), 2591–2596 (2010). Doi: 10.1016/j.ejmech.2010.02.047
 11. Shi, Z.H. et al.: Synthesis, biological evaluation and SAR analysis of O-alkylated analogs of quercetin for anticancer. *Bio. Med. Chem. Lett.* **24**(18), 4424–4427 (2014). <https://doi.org/10.1016/j.bmcl.2014.08.006>
 12. Song, X., et al.: Recent advances in the development of organic photothermal nano-agents. *Nano Res.* **8**(2), 340–354 (2015). <https://doi.org/10.1007/s12274-014-0620-y>

Information Analysis of Biochemical Parameters for Glucose Tolerance Tests

Y. I. Sokol, O. V. Chmykhova, V. V. Boyko, P. N. Zamyatin,
and D. P. Zamiatin

Abstract

In the vast majority of existing methods of obtaining parametric biomedical information, it is represented by a finite set of informative parameters (features). Their informational significance is always different and practically not evaluated for the tasks of parametric identification and diagnosis of diabetes mellitus. In this paper, it is proposed to evaluate the informational significance of parameters (features) based on dispersion analysis of changes in their mathematical expectation with respect to residual noise. Fisher's F-statistics were used as a quantitative measure of the changes, with the subsequent conversion of the obtained data into the amount of information expected based on the equations of the information measurement theory.

Keywords

Glucose tolerance testing • Glycemic dynamics • Regression model • Analysis of variance • F-statistics • Correlation

1 Introduction

In the vast majority of existing methods of obtaining parametric biomedical information, the latter is represented by a finite set of informative parameters (features). Such a

Y. I. Sokol · O. V. Chmykhova (✉)

Department of Industrial and Biomedical Electronics, National Technical University "Kharkiv Politechnical Institute, Kyrpychova 2, Kharkiv, 61002, Ukraine
e-mail: zana6732@gmail.com

V. V. Boyko · P. N. Zamyatin

State Institution "V.T. Zaytsev Institute of General and Urgent Surgery of NAMS of Ukraine", Kharkiv, Ukraine

D. P. Zamiatin

Department of Surgery № 1, Kharkiv National Medical University, Kharkiv, Ukraine

presentation, for example, characterizes all, without exception, laboratory methods of biochemical analysis. If we take into account the measured parameters of glucose tolerance tests (the current level of glycemia), then the number of such parameters is at least six. Their informational significance is always different and practically not evaluated for the tasks of parametric identification and diagnosis of diabetes mellitus. Moreover, in practical medicine, the importance of information analysis for minimizing the dimension of the space of informative parameters that carry the maximum diagnostic information is not realized, especially if these parameters are functions of time.

The set of basic parameters used for glucose tolerance testing is known and normatively determined [1, 2], as are the sets of parameters for the general tasks of diabetology [3]. Parameters are widely used for problems of mathematical modeling of the glycemic dynamics [2, 4, 5], which are basic when creating computerized systems for diagnosing diabetic disorders [6].

The purpose of this work is expansion of opportunities for the selection of the most informative diagnostic parameters used in glucose tolerance testing.

2 Experimental

2.1 Medical Significance and Consequences of Diabetes

Diabetes is a serious chronic disease that develops when the pancreas does not produce enough insulin (a hormone that regulates blood sugar or glucose) or when the body cannot effectively use the insulin, it produces.

An estimated 422 million adults worldwide had diabetes in 2014, compared with 108 million in 1980 [7]. The global incidence of diabetes (standardized by age) has almost doubled since 1980, rising from 4.7 to 8.5% among adults. This reflects an increase in associated risk factors such as overweight or obesity. Over the past decade, the incidence of

diabetes has increased rapidly in low- and middle-income countries compared to high-income countries.

In 2012, diabetes caused 1.5 million deaths. A higher compared with the optimal value of glucose in the blood caused another 2.2 million deaths, increasing the risk of cardiovascular and other diseases. Forty-three percent of these 3.7 million deaths occur before the age of 70 years. The proportion of deaths before age 70 as a result of high blood glucose or diabetes is higher in low- and middle-income countries than in high-income countries.

Since a distinction between type 1 diabetes (which requires insulin injections for survival) and type 2 diabetes (which the body cannot properly use the insulin it produces) usually requires complex laboratory tests, there are no separate global estimates of the incidence of diabetes type 1 and type 2 [7].

2.2 Dispersion Model of Glucose Tolerance Test Results

Restoration of the functional dependence, which characterizes the dynamics of glycemia in glucose tolerant testing according to limited empirical data, is an independent task of mathematical statistics, the solution of which is the compression of the primary measurement information in the form of functional dependence.

Most often, this dependence is a regression equation of a sufficiently high order. This means that the coefficients of such a relationship are random variables, and the regression itself is an estimate function, the restoration accuracy of which is characterized by the classical properties of random estimates [8]:

- (a) unbiasedness;
- (b) prosperity;
- (c) efficiency.

Within the framework of glucose tolerance testing, these properties reflect the uncertainty in the restoration of the functional model of a stochastic connection between the glycemia parameter and the time spent in examining a patient.

If we consider, in perspective, the obtained regression model for the subsequent identification of the type of diabetic pathology, then the independent parameters x_1, \dots, x_p of certain types of non-stationarity of the response function $Y(t)$ can be considered the primary identification parameters.

Using a set of such parameters, it is possible to investigate their classification properties when identifying one of the many types of biochemical states. In this case, to assess the impact of changes in the type of biochemical state on the average value of some investigated primary parameter X , standard statistical models of one-factor unilateral classification can be used (model of single-factor analysis of variance at fixed levels of the influencing factor) [9]. In our case, the factor is the type of diabetic pathology, the level of which is the result of glucose tolerance testing in the form of mathematical expectation of functional dependence, restored by incomplete empirical data.

The mathematical model of the measurement result x_{ji} of the parameter X involves the use of a two-dimensional indexation of such a result.

The first index j varies from 1 to k ($j = \overline{1, k}$) and characterizes the level number of the influencing factor Θ (in our case, the specific biological state Θ_j). Index i characterizes the multiple measurement number for a fixed biological state Θ_j .

This approach allows us to present all the measurement results in the form of a table, each row of which corresponds to a selected (from the set k) level of the factor Θ . The number of measurement results for each of the k lines forms a group for which the number of measurements is n_j .

Such a table allows us to check the basic hypothesis $H_0 : \delta_j = 0$, where δ_j —deviation of the mean value x_{ji} of the total average \bar{x} group with the number j . Then the model of the measurement result x_{ji} has the form:

$$x_{ji} = \bar{x} + \delta_j + Z_{ji}, \quad (1)$$

where Z_{ji} is the residual deviation due to random perturbations.

Model (1) allows to make dispersion decomposition of measurement results x_{ji} in accordance with the expression

$$S = S_1 + S_Z \quad (2)$$

The results of this decomposition are presented in Table 1.

In Table 1 the following notation for averaging operations is used:

$$\bar{X}_j = n_j^{-1} \sum_{i=1}^{n_j} x_{ji},$$

$$\bar{X} = N^{-1} \sum_{j=1}^k \sum_{i=1}^{n_j} x_{ji},$$

\bar{x}_j —average value in j group.

Table 1 The results of analysis of variance with one-sided classification

Source of variation	Between groups	Inside groups	Sum
Sum of squares	$S_1 = \sum_{j=1}^k n_j (\bar{X}_j - \bar{X})^2$	$S_Z = \sum_{j=1}^k \sum_{i=1}^{n_j} (x_{ji} - \bar{X}_j)^2$	$S = \sum_{j=1}^k \sum_{i=1}^{n_j} (x_{ji} - \bar{X})^2$
Number of degrees of freedom	$k - 1$	$\sum_{j=1}^k (n_j - 1) = N - k$	
Average square	$\bar{S}_1 = \frac{S_1}{k-1}$	$\bar{S}_Z = \frac{S_Z}{N-k}$	
The ratio of average squares	$\frac{S_1(N-k)}{S_Z(k-1)}$		
Mathematical expectation of the average square	$\sigma^2 + \frac{\sum_{j=1}^k n_j \gamma_j^2}{k-1}$	σ^2	
Fisher's F -statistic	$F_{(k-1), (N-k)} = \bar{S}_1 / \bar{S}_Z$		

2.3 Information Analysis of the Dispersion Model of Glycemic Parameters

Table 1 allows us to estimate the amount of information about the value of the group average \bar{x}_j , which is equivalent to the corresponding level Θ_j of the influencing factor Θ .

Practical use of Table 1: the results of glucose tolerance testing of 120 patients were used for the development of methods and information technologies for identifying variants of the glycemic dynamics (Appendix A) [10].

To separate groups of patients having fixed option of glycemia dynamics were used two glucose tolerance tests embodying traditional [11] and enhanced [10] approaches to the preparation of diagnostic findings.

The results of these types of testing are presented in Appendix A [10]. In this application, the following notation is used to record the diagnostic findings:

- $\forall N$ standard value;
- HTG impaired glucose tolerance;
- g_b basal value of glycemia level;
- g_{120} the value of glycemia level at 120 min;
- α insulin secretion rate;
- β the specific speed of the process of autoregulation.

Involving probabilistic models of the information theory of measurements [12] for further research, we can present this expected information in the form of the basic Eq. (3), where the 1st and 2nd terms of the right-hand side are the initial and residual entropy of the x_{ji} measurement result from Table 1:

$$I = H_x - H_{x/x_N}, \tag{3}$$

where H_x —initial entropy, H_{x/x_N} —residual entropy.

$$H_x = \log\left(\sqrt{2\pi e} \sigma_x\right) - \log \Delta x \tag{4}$$

$$H_{x/x_N} = \log \frac{\sqrt{2\pi e} \sigma_x \sigma_{\Delta x}}{\sqrt{\sigma_x^2 + \sigma_{\Delta x}^2}} - \Delta x \tag{5}$$

In Eqs. (4) and (5) the following notation is used:

- Δx error of the measurement result x_{ji} ;
- σ_x^2 x_{ji} variance before measurement;
- $\sigma_{\Delta x}^2$ x_{ji} variance before measurement.

Using Table 1 and expressions (4) and (5) the amount of information can be expressed in the form

$$I = \log \frac{\sqrt{\sigma_x^2 + \sigma_{\Delta x}^2}}{\sigma_{\Delta x}}, \tag{6}$$

where $\sigma_x^2 = \frac{\sum_{j=1}^k n_j \gamma_j^2}{k-1}$,
 $\sigma_{\Delta x}^2 = \sigma^2$.

The mean squares \bar{S}_1 and \bar{S}_Z of the sums of the dispersion decomposition of S_1 and S_Z in the limit (as $N \rightarrow \infty$) can be expressed in terms of γ_j and the residual dispersion σ^2

$$\begin{cases} \lim_{N \rightarrow \infty} \bar{S}_1 = \frac{1}{k-1} \sum_{j=1}^k n_j \gamma_j^2 = \sigma_x^2 \\ \lim_{N \rightarrow \infty} \bar{S}_Z = \sigma^2 = \sigma_{\Delta x}^2 \end{cases} \tag{7}$$

Since the ratio of the mean squares \bar{S}_1 / \bar{S}_Z is a random variable $F_{(k-1), (N-k)}$, which has a probability distribution density of the central Fisher F-distribution (Snedecor) [9] with $V_1 = k - 1$ and $V_2 = N - k$ degrees of freedom, then Eq. (6) can be represented as

$$I^* = \ln \sqrt{1 + F_{(k-1), (N-k)}} \tag{8}$$

3 Results and Discussions

3.1 Correlation Correction of Information Analysis Results

To identify the completeness of the information content of the entire system, out of the six standard parameters $X_1 - X_6$, an assessment was made of the correlation relationships between the parameters within this system.

For this, the covariance matrix was calculated (Table 2) for all the results of biochemical measurements of the values of the standard parameters made at fixed time intervals (0, 30, 60, 120, 180, 300 min).

Since, as shown in Table 2, the correlation between the first and sixth (0 and 300 min) measurements is equal to 1, then the sixth dimension is informationally non-normative and can be excluded from the results of the subsequent analysis.

3.2 Evaluation of the Information Content of the Parameters of Glucose Tolerance Testing

Using the table of grouped results of glucose tolerance testing allowed us to calculate Fisher’s F-statistics and the corresponding values of the amount of expected information about the type of identifiable state ($\Theta_1, \Theta_2, \Theta_3$). The results of the calculation are presented in Table 3.

Table 2 allows us to test the correlations between the remaining five parameters $X_1 - X_5$. The main hypothesis can

be formulated as a statement about the absence of correlation between the compared parameters.

In this case, it is convenient, for clarity, to construct a matrix of coded solutions that reflect alternatively extreme correlations between any pairs of informative parameters (excluding the X_6 parameter). For such a test, we set a 1% level of significance (the risk of an error of the 1st kind, $\alpha = 0.01$). In this case, the comparison threshold for the correlation coefficients of the Table 2 is the value of $R_{kp} = 0.23423$, obtained from the expression

$$F_{1,(N-2),\alpha} = \frac{R_{kp}^2}{1 - R_{kp}^2} (N - 2), \tag{9}$$

where $F_{1,(N-2),\alpha}$ —upper 1% point of Fisher’s F-distribution [9] for a type 1 risk with $\alpha = 0.01$.

The calculated matrix of correlation coefficients in the form of «0» and «1» are presented in Table 4. At the same time, the decision «0» corresponds to the absence of correlation between pairs of informative features, and the decision «1» corresponds to the presence of correlation.

From Table 4 it follows that all biochemical parameters of standard glucose tolerance testing are linearly correlated, which indicates information redundancy of these parameters. Such a correlation complicates the model of parametric identification [13] of biochemical states, because it forces us to identify not only the model of functional dependence (expected value) of parameters on time, but also to take into account the values of pair correlations from the normalized matrix Table 2.

Table 2 Normalized covariance matrix for biochemical parameters of glucose tolerance testing

	0	30	60	120	180	300
0	1	0.486351	0.324573	0.227308	0.305562	1
30	0.486351	1	0.672842	0.467929	0.228249	0.486351
60	0.324573	0.672842	1	0.638791	0.320516	0.324573
120	0.227308	0.467929	0.638791	1	0.663493	0.227308
180	0.305562	0.228249	0.320516	0.663493	1	0.305562
300	1	0.486351	0.324573	0.227308	0.305562	1

Table 3 Normalized covariance matrix for biochemical parameters of glucose tolerance testing

Parameters	Fisher’s F-statistic	Quantity of information I (nit)
X_1	7,486,012	216,444
X_2	2,750,172	167,498
X_3	1,257,193	130,400
X_4	1,873,255	149,113
X_5	6,521,634	100,889

Table 4 Matrix of statistical decisions regarding the absence of mutual pair correlation between biochemical parameters (significance level $\alpha = 0.01$)

	0	30	60	120	180
0	1	1	1	0	1
30	1	1	1	1	0
60	1	1	1	1	1
120	0	1	1	1	1
180	1	0	1	1	1

4 Conclusions

1. It should be noted that in Table 3 the amount of expected information for biochemical parameters is strictly individual and does not allow the simple summation of information on the set of all parameters due to their non-zero pair correlation. The latter only reduces the total information, the lower limit of which is the value 2.16444 (nit) for the most informative parameter X_1 .
2. The most informative parameters should be considered X_1 and X_4 , for which in the last table obtained a zero correlation with respect to other parameters.

Conflict of Interest The authors hereby declare that they have no conflict of interest.

References

1. Toffolo, G., Bergman, R.N., Finegood, D.T., Bowden, C.R., Cobelli, C. Quantitative estimation of beta cells sensitivity to glucose in the intact organism: a minimal model of insulin kinetics in dog. *Diabetes* **29**, 979–986 (1980)
2. Palumbo, P., Ditlevsen, S., Bertuzzi, A., Andrea De Gaetano, A.: Mathematical modeling of the glucose-insulin system: a review. *Math. Biosci.* **244**, 69–81 (2013)
3. Cobelli, C., Dalla, Man C., Sparacino, G., Magni, L., De Nicolao, G., Kovatchev, B.: Diabetes: models, signals and control. *IEEE Rev. Biomed. Eng.* **2**, 54–96 (2009)
4. De Gaetano, A., Arino, O.: Mathematical modelling of the intravenous glucose tolerance test. *J. Math. Biol.* **40**, 136–168 (2000)
5. Makroglou, A., Li, J., Kuang, Y.: Mathematical models and software tools for the glucose-insulin regulatory system and diabetes: an overview. *Appl. Numer. Math.* **56**, 559–573 (2006)
6. Sokol, Y., Lapta, S., Chmykhova, O., Solovyova, O., Goncharova, O.: Diagnostic biotechnical system of the quantitative diagnostics of malabsorption. *ELNANO*, 255–258 (2017)
7. Globalnyiy doklad po diabetu [Global report on diabetes]. Zheneva: Vsemirnaya organizatsiya zdavoohraneniya. License: CC BY-NC-SA 3.0 IGO (2018)
8. Pollard, J.H.: A Handbook of Numerical and Statistical Techniques, p. 344. Cambridge University Press, New York
9. Dzhonson N.: Statistika i planirovanie eksperimenta v tehnike i nauke: Metodyi planirovaniya eksperimenta. M.: Mir: 520 (1981)
10. Lapta S.S. Metodyi povyisheniya diagnosticheskoy effektivnosti glyukozotolerantnyih testov (na osnove matematicheskogo modelirovaniya dinamiki glikemii): Dis. kand. tehn. nauk: 05.11.17 / Harkovskiy natsionalnyiy un-t radioelektroniki. – H., 2004. – 220 s
11. Saharnyy diabet: doklad Issledovatel'skoy gruppy VOZ (1985). Zheneva: 126
12. Ornatskiy, P.P.: Teoreticheskie osnovy informatsionno-izmeritel'noy tehniki. – K.: Vischa shkola: 455 (1983)
13. Novoselov, O.N.: Identifikatsiya sostoyaniya dinamicheskikh ob'ektov po izmeryaemyim parametram: ot teorii k praktike. *Izmeritel'naya tehnika*. № 2: 20–24 (2010)

Part X

Medical Physics and Biophysics

Theoretical Model of Lipid Peroxidation Kinetics for Complexes of Cytochrome *c* and Cardiolipin with Participation of Antioxidants

E. Yu. Kanarovskii, O. V. Yaltychenko, and N. N. Gorinchoy

Abstract

It is represented the kinetic model of lipid peroxidation process take place in the lipid membranes owing to a peroxidase activity of the complexes of cytochrome *c* and cardiolipine. The theoretical description of the studied kinetics includes two pathways: enzymatic and non-enzymatic, and takes into account the presence of direct-acting antioxidant: the molecules that act as the free radical scavengers, directly exhibiting a relatively high antiradical activity. The enzymatic pathway includes the reactions involving the complexes of cytochrome *c* and cardiolipin. The non-enzymatic pathway includes the reactions involving the free lipid radicals and antioxidant molecules. The obtained system of differential equations allows to simulate the kinetics of the lipid peroxidation process both accounting the inhibitory effect of the antioxidant and without it, and to test the antiradical activity of various types of antioxidants, as well as to find some unknown kinetic parameters by performing a comparison of the theoretical kinetic curves with the experimental ones.

Keywords

Complex of cytochrome *c* and cardiolipin • Lipid peroxidation • Chemical kinetics • Free radicals • Antioxidant

1 Introduction

At the present time, the properties and structures of the complexes of the cytochrome *c* (Cyt *c*) and cardiolipins (CLs) of different types are being intensively studied [1–4]. Great interest in this research area has arisen and continues to grow in connection with the discovery of peroxidase activity (PA) in such complexes. In turn, it is proved that the PA of the complexes of mitochondrial Cyt *c* and CL closely related to such an important phenomenon in a vital activity of cells as an apoptosis. The problem of apoptosis of the cell attracts a special attention of the researchers in the field of the biology and medicine (see the numerous works on this issue cited in the reviews [2, 3]). Apoptosis can be initiated by the lipid peroxidation (LPO), as it causes the pathological disturbances of the barrier properties of the lipid bilayer in the cell membranes. Namely, the oxidized CL is necessary for starting of the release of proapoptotic factors (including the mitochondrial Cyt *c* itself), and this was confirmed experimentally [1]. The results of [1] specify a new way of launching a cell death, when the reactive oxygen species (ROS) accumulate in the cell initiating a formation of the free radicals (FRs) of lipids and their oxidized forms (hydroperoxides and hydroxides), and this is associated with the PA of the complex of Cyt *c* and CL (Cyt-CL) formed in the mitochondrial membranes. The main structural features of such complexes are presented in [4] (see also Refs 103–105 from [3]). It is important to note that Cyt *c* in the absence of CL exhibits the extremely weak PA [4], but namely in the complex with a CL its PA grows substantially, making this complex an active participant in the membrane processes.

First of all, before a representation of the model system of differential equations (DE), which simulates of the LPO kinetics involving the Cyt-CL complex and antioxidants (AOs), a brief description of the components of the Cyt-CL complex to give, as well as to note some common properties of AOs (for more details refer to the reviews [2, 3]).

E. Yu. Kanarovskii (✉) · O. V. Yaltychenko
Institute of Applied Physics, ASM, Academy 5,
Chisinau, 2028, Republic of Moldova
e-mail: kanarovskii@gmail.com

N. N. Gorinchoy
Institute of Chemistry of Physics, ASM, Chisinau,
Republic of Moldova

As known, cytochrome *c* is the smallest and the alone water-soluble protein in the cytochrome family, in which about 30 species. Cytochromes, as the components of mitochondrial membranes, are present in all eukaryotic cells (animals and plants). Cyt *c* contains in its structure a heme type *c*, localized in the internal protein cavity by means of the covalent bonds with the amino-acid residues. Due to this, Cyt *c*, like other cytochromes, plays the role of a catalyst for the oxidation-reduction (redox) reactions. In a living cell, Cyt *c* is usually located (loosely bound) outside the inner mitochondrial membrane, and, above all, it performs two major functions (see Refs 92–95 from [3]). Firstly, it is a single-electron carrier in the respiratory chain, since it is capable of the oxidation and reduction without the oxygen participation. Secondly, it is an activator of apoptosis, since under certain conditions it is able to detach from the membrane, passing into a solution in the intermembrane space, and then from it into the cytosol, thereby activating the apoptosis of the cell.

Further, it should be noted that such a phospholipid as a cardiolipin (diphosphatidylglycerol) in the eukaryotic cells is an important component of the internal mitochondrial membranes [3] (and Refs 96–102 therein)—its fraction from their total lipid composition is about 20%, and it is found even in membranes of bacterial microorganisms. Phospholipids of this type have a dimeric structure in which two phosphatidylglycerols are connected to each other by a glycerol residue, as a “bridge”. CL consists of two residues of the orthophosphoric acid H_3PO_4 (a polar head part) and four long chains of the fatty acids (a nonpolar tail part), and each of these four alkyl chains C_{18} in the majority of the animal tissues has two unsaturated bonds. Owing to the specific physical and chemical properties, the phospholipids play a very important role in the structure and functioning of biomembranes. In the phospholipid molecules, the oxygen-containing head parts are hydrophilic, and the long massive tail parts are hydrophobic. At that, their head part is easily deprotonated, acquiring a negative charge. Thus, CLs belong to the complex (multicomponent) lipids—the products of their hydrolysis are the alcohols and carboxylic acids, and also, the phosphoric acid and carbohydrate. That is to say, in addition to the structural functions, the CLs also perform the metabolic functions.

Besides, note that in the chemical reactions involving the Cyt-CL complex, in addition to the CL, the hydrogen peroxide (H_2O_2) also participates as a substratum. It is important to emphasize that in the LPO process considered here, the hydrogen peroxide (H_2O_2) performs as an activator of the Cyt-CL complex. In the organism, H_2O_2 is the most prevalent reagent from the ROS family, since, being a small, neutral and stable molecule it is able to penetrate almost all cellular structures. In general, the oxidation processes of the various substrates by oxygen on the cellular level, which are

necessary in the organism under the aerobic conditions for the normal course of metabolism, occur due to ROS that are formed in the cell or come from outside [2]. The ways of using the oxidative potential of the oxygen molecule, the main sources and conditions for the appearance of ROS in the organism, and the chemical and physical properties of the various types of ROS are described in detail in [5]. In the organism, under the physiologically normal or close to normal conditions, the system of antioxidant defense (AOD) effectively protects it from the destructive action of the lipid FRs, ROS and lipid peroxides mainly through the control of the concentrations of the FRs of different types and the regulation of the rates of the radical and redox reactions accompanying any process on the cellular level, including the LPO process. In the AOD system containing two main functional branches: the enzyme and non-enzyme branches, the direct-acting AOs are components of the non-enzyme branch, which, unlike the enzyme branch, includes mainly the low-molecular chemical compounds. The direct-acting AOs manifest themselves as the most operative means of the antiradical protection of a living cell. After the interception (scavenging) of the FRs, they pass into oxidized or stable radical forms, and then, under the action of the corresponding enzymes or other AOs, they are again transformed into the reduced forms (synergy). The manifestation of a synergy among the AOs in relation to each other (the enhancement of the antioxidant effect at the joint action and/or the conversion of each other to the reduced forms) is a very important property of the AOD system [2, 3].

2 Theoretical Model, Results and Discussions

At the theoretical description of the LPO kinetics for the Cyt-CL complexes, it is convenient to emphasize two ways of the process—the enzymatic pathway, which is realized as a catalytic cycle, and the non-enzymatic pathway on which the reactions proceed involving the lipid FRs. In the presence of an antioxidant, depending on the features of its action, its influence is taken into account differently in each of these pathways. A catalytic cycle of the Cyt-CL complex is described using the reaction scheme proposed in [2]. The graphical scheme of the reactions shown in Fig. 1 describes the PA of the Cyt-CL complex realized as a catalytic cycle. The continuation of the LPO process caused by the PA of the Cyt-CL complex occurs on the non-enzymatic pathway involving the lipid FRs, which arise in a course of the reactions of the catalytic cycle and initiate the chain reactions of the LPO process.

This scheme shows that the Cyt-CL complex, being initially in the non-activated state E , successively passes through three stages involving the activated states E_1 and E_2 .

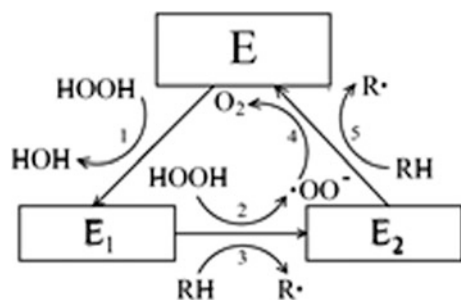


Fig. 1 Scheme of the catalytic cycle of the Cyt-CL complex

The conformational features of these states (E_1 , E_2) a description of the chemical reactions at these three stages are indicated in [2, 3]. Here one should pay attention to one important feature of the Cyt-CL complexes [6], which makes a noticeable contribution to the kinetics of accumulation of the LPO products: the lipid hydroperoxides (ROOH), being the most significant among the LPO products, are also a substratum on the enzymatic pathway of the LPO process, in addition to the lipid molecules (RH). Since the formation of an excessive amount of the ROOH due to the reactions involving the FRs proceeding on the non-enzymatic pathway is an impetus for the initiation of the apoptosis process [1], then using the direct-acting AOs it is possible to achieve the effective control of the LPO process, mainly through its FR stage, and hence, to gain the control over the effect of apoptosis as a whole [2, 3]. Namely, the direct-acting AOs, disrupting the radical reaction chains, inhibit the process of formation of the oxidized product, and are necessary as a means of the operative control of the PA of the Cyt-CL complex.

The most important representative of this class of AOs, protecting the cell from the oxidative stress, which occurs at a deviation from a physiologically normal level of the ROS concentrations involved in a cellular metabolism, is vitamin E. The results of the extensive investigations [3, 6] (and Refs therein), devoted to a study of the various properties of vitamin E, show that vitamin E should be considered as the main fat-soluble antioxidant. In general, the family of vitamin E includes two groups of chemical compounds—tocopherols and tocotrienols (4 species in each group: α -, β -, γ - and δ -) and among them α -tocopherol is considered as the most biologically active form of vitamin E.

Also note that tocopherols in the biomembranes perform a structure-forming function, by means of a modifying action on the phospholipid bilayers. In this connection, an attention should be paid to the ability of α -tocopherol to form the complexes with the phospholipids. In general, the membranotropic effect of tocopherols consists in their ability not only to intercept the lipid FRs, but also modulate the physical properties of the lipid bilayer, maintaining the necessary packing density of phospholipids, and limiting the

access of oxygen to the fatty acid chains, and as well as providing other AOs in the biomembranes the conditions for performing their antioxidant function (synergy). Since at the interaction of tocopherols with the unsaturated phospholipids, such as the CLs, the membranotropic effect manifests itself in the compaction of the lipid bilayer, then in [3] it was suggested that the possibility of the entry of α -tocopherol into the Cyt-CL complex opens another way (the third, associated with the membranotropic effect) to regulate the PA of the Cyt-CL complex in addition to the other two known ways mentioned in [3]. Upon extinguishing the lipid FRs by α -tocopherol after a proton donation the α -tocopherol radical is formed which is stable and, furthermore, is also capable of interacting with the lipid FRs to produce the oxidized molecular products safe for a living cell. In general, the effective control of the LPO process is determined by the well-known characteristic feature of α -tocopherol [3]: α -tocopherol (and its radical) very actively intercepts, namely, the peroxy radicals $ROO\cdot$, whereas the alkyl radicals $R\cdot$ it intercepts much weaker. Besides, the peroxy radical is of decisive importance for the development of the LPO process, since it is it that provides the continuation of radical-oxidation chains and degenerate branching of them. And with this, the amount of other lipid radicals (alkyl $R\cdot$ and alkoxy $RO\cdot$) is determined mainly by reactions involving the peroxy radical, so that the important inequality is fulfilled $[ROO\cdot] \gg [R\cdot]$, $[RO\cdot]$. Thus, α -tocopherol in the membranes is a very potent quencher of the chain radical reactions, protecting the membrane from the LPO. Herewith, its effectiveness as a scavenger of the FRs is enhanced by the synergy that other components of the AOD system manifest in the living cell with respect to α -tocopherol, such as, vitamin C, ubiquinone coenzyme Q_{10} and glutathione: they are able to convert α -tocopherol from the oxidized or radical form to the reduced form [3, 6].

The DE system, which describes the considered LPO kinetics, is presented below by the expressions (1)–(4). Here, a standard approach is used to describe the activity of AO, when the AO is considered solely as a scavenger of FRs on the non-enzymatic pathway of the LPO process, that is, only its antiradical activity (ARA) is taken into account. Thus, in the presence of a direct-acting AO, the catalytic cycle of the Cyt-CL complex remains unchanged (Fig. 1), but the non-enzymatic pathway is expanded by the additional reactions involving the AO. In particular, α -tocopherol (or one of its homologues) is most commonly used as a direct-acting AO. The structural formulas of α -tocopherol and its homologues are represented in [6]: α -C6-chromanol has the shortened tail (C6) and α -C1-chromanol has the shortest tail (PMC). In [6], the experimental kinetics of accumulation of the LPO products of tetralinoleoyl cardiolipin is studied in detail, so that the antioxidant effect of α -tocopherol and its two homologues C6 and PMC is

examined singly for each of them. The radical forms of PMC and C6, as well as of α -tocopherol, are the stable radicals, and they also actively participate in the reactions with the lipid FRs, neutralizing them. It is also important that PMC and C6, like α -tocopherol, can be easily restored with the help of vitamin C, glutathione or ubiquinone coenzyme Q₁₀ [3, 6].

In result of all above, the sought DE system includes four connected subsystems: for the enzyme, radicals, LPO products and AO. This DE system is a base and has the following form:

$$\begin{cases} dE_1/dt = k_1XE - k_2XE_1 - k_3SE_1 + k_{8a}P_1E_2 \\ dE_2/dt = k_2XE_1 + k_3SE_1 - k_4R_0E_2 - k_5SE_2 + k_8P_1E - k_{8a}P_1E_2 \\ dE/dt = -k_1XE + k_4R_0E_2 + k_5SE_2 - k_8P_1E \end{cases} \quad (1)$$

$$\begin{cases} dR/dt = k_3SE_1 + k_5SE_2 - k_6YR + k_7SR_1 + k_9SR_2 - k_{11}R_0R \\ \quad - k_{13}I_1R - k_{16}I_2R \\ dR_0/dt = k_2XE_1 - k_4E_2R_0 - k_{11}RR_0 - k_{22}R_0^2 \\ dR_1/dt = k_6YR - k_7SR_1 - k_{10}R_1^2 - k_{12}P_1R_1 - k_{14}I_1R_1 - k_{17}I_2R_1 \\ dR_2/dt = k_8P_1E + k_{8a}P_1E_2 - k_9SR_2 - k_{15}I_1R_2 - k_{18}I_2R_2 \end{cases} \quad (2)$$

$$\begin{cases} dP_1/dt = k_7SR_1 - k_8EP_1 - k_{8a}E_2P_1 - k_{12}R_1P_1 + k_{14}I_1R_1 \\ dP_2/dt = k_9SR_2 + k_{15}I_1R_2 \end{cases} \quad (3)$$

$$\begin{cases} dI_1/dt = -k_{13}RI_1 - k_{14}R_1I_1 - k_{15}R_2I_1 \\ dI_2/dt = k_{13}RI_1 + k_{14}R_1I_1 + k_{15}R_2I_1 - k_{16}RI_2 - k_{17}R_1I_2 \\ \quad - k_{18}R_2I_2 - k_{19}I_2^2 \end{cases} \quad (4)$$

here E_1 , E_2 , and E denote the concentrations of the two active forms and the inactive form of the Cyt-CL complex, respectively, and for the reagent concentrations the following notations are introduced: $X \equiv [\text{H}_2\text{O}_2]$, $Y \equiv [\text{O}_2]$, $S \equiv [\text{RH}]$, $R_0 \equiv [\cdot\text{OO}^-]$, $R \equiv [\text{R}\cdot]$, $R_1 \equiv [\text{ROO}\cdot]$, $R_2 \equiv [\text{RO}\cdot]$, $P_1 \equiv [\text{ROOH}]$, $P_2 \equiv [\text{ROH}]$, $I_1 \equiv [\text{InH}]$, $I_2 \equiv [\text{In}\cdot]$.

For the numerical calculations (in the first approximation), the concentrations of the substances $[\text{H}_2\text{O}_2]$, $[\text{O}_2]$ and $[\text{RH}]$ are considered to be enough high (i.e., in excess), and so, can be assume: $X \approx X_0$, $Y \approx Y_0$ and $S \approx S_0$. Also, using the matter conservation law for the catalyst, it should be taken into account that: $E_0 = E_1 + E_2 + E$. Then, using the quasi-stationary conditions for the radicals R_0 , R , R_1 , R_2 , this DE system is converted to a simpler and convenient form for the numerical simulation. Also, the DE system in the absence of the AO can be easily obtained from (1)–(4) if the variables I_1 and I_2 are set equal to zero, such a reduced DE system makes it possible to evaluate the effectiveness of the AO influence on the LPO process by comparing the yields of the LPO products in the presence of the AO and without it. Here, it should be noted that, in connection with the

above-mentioned third way of the regulation of the PA of the Cyt-CL complex, the reactions involving the AO are also possible on the enzymatic pathway of the LPO process (in addition to the standard approach) and they were included in the LPO kinetics in our work [3]. Thus, in a more general case considered in [3] the AO molecule is also the reactant in the reactions of the catalytic cycle (Fig. 1). In such case, the corresponding reactions for the AO, where it and its radical are denoted as InH and In \cdot are similar to the reactions 3 and 5 for the lipid (see Fig. 1) and are obtained from them by a formal replacement of the symbols RH, R \cdot on InH, In \cdot , respectively. So that, the additional terms appear in the DE system (1)–(4) in the corresponding kinetic equations, and this extended DE system is given in [3].

3 Conclusions

In view of the foregoing, the DE system (1)–(4) presented in this article is a base model that takes into account the ARA of antioxidant and gives a description of the LPO process, which is caused and developed owing to the PA of the Cyt-CL complexes. This DE system contains the contributions of all key chemical reactions occurring on the enzymatic and nonenzymatic pathways of the LPO process. Their description was made by us earlier in [3], which contains a detailed analysis of the various reaction channels and their contributions at a certain stages of the LPO process. It also (as [2]) contains a brief review of the main experimental methods used in the modern biophysical studies and a discussion of the key aspects of the functioning of the ROS and AOD systems and their optimal interaction in the organism.

Eventually, the use of system (1)–(4) allows to compare the ARAs of different AOs according to the theoretical yields of the LPO products apart for each of the tested AOs. Moreover, using together the base DE system (1)–(4) and the extended DE system from [3], it is possible to study the antioxidant activity of certain AO in a whole by determining the ratio of contributions in its total antioxidant activity, related with its direct antiradical action (quenching of the radical chains of LPO) and its indirect regulative action (regulation of the enzyme activity and/or participation in the enzyme reactions as a competitive substratum). In general, such a versatile comparison of the theoretical data obtained as a result of numerical simulation and the experimental data from [6], with their subsequent analysis, is planned to publish as a continuation of our work [3] (its second part).

In conclusion, it is worth noting that the DE system (1)–(4) provides the ample opportunities for modeling of the kinetics of the LPO process involving the Cyt-CL complex in a presence of the antioxidant. Using this system, in addition to testing the ARA of various types of antioxidants, it is also possible: to find some of the unknown reaction rate

constants using the experimental kinetic curves for the LPO products; to compare the kinetics of the LPO process for the Cyt-CL complexes with the various kinds of CL molecules.

Acknowledgements This work was supported by the CSSDT of ASM, Institutional Project 15.817.02.03A (2015–2019). Since 2018, the project is supervised by National Agency for Research and Development.

Conflict of Interest The authors declare that they have no conflict of interest.

References

1. Kagan, V.E., Tyurin, V.A., Jiang, J., et al.: Cytochrome *c* acts as a cardiolipin oxygenase required for release of proapoptotic factors. *Nat. Chem. Biol.* **1**(4), 223–232 (2005)
2. Proskurnina, E.V., Vladimirov, Yu.A.: Free radicals as the participants of the regulatory and pathological processes. In: Grigoriev, A.I., Vladimirov, Yu.A. (eds.) *Proc.: Fundamental Sciences—for Medicine. Seria: Biophys. Med. Technol.* vol. 1 (in Russian), pp. 38–71. MAX Press, Moscow (2015)
3. Kanarovskii, E.Yu., Yaltychenko, O.V., Gorinchoy, N.N.: Kinetics of the antioxidant activity of α -tocopherol and some of its homologues. Part I. Review of the problem. *Theoretical Model. Surf. Engin. Appl. Electrochem.* **54**(5), 481–497 (2017)
4. Basova, L.V., Kurnikov, I.V., Wang, L., et al.: Cardiolipin switch in mitochondria: shutting off the reduction of cytochrome *c* and turning on the peroxidase activity. *Biochemistry* **46**(11), 3423–3434 (2007)
5. Metelitsa, D.A.: *Activation of Oxygen by Enzyme Systems*. Nauka, Moscow (1982). (in Russian)
6. Samhan-Arias, A.K., Tyurina, Y.Y., Kagan, V.E.: Lipid antioxidants: free radical scavenging versus regulation of enzymatic lipid peroxidation. *J. Clin. Biochem. Nutr.* **48**(1), 91–95 (2011)

Testing Green Silver Nanoparticles for Genotoxicity, Antioxidant and Anticancer Activity

M. Petrosyan, T. Gevorgyan, G. Kirakosyan, L. Ghulikyan, A. Hovhannisyian, and N. Ayvazyan

Abstract

The toxicity of the synthesized nanoparticles (NPs) by various physicochemical methods is one of the main problems for their application. NPs synthesized using plant extracts are less toxic than other methods of their congregation, so, in this regard, the synthesis of this so-called “Green NPs” is very important. Direct interaction of the AgNPs obtained from the 50% ethanol extract of *Ocimum araratum* with the genomic DNA of sarcoma S-180 cells by the method of retardation has been investigated. No genotoxicity of the stabilized green AgNPs has been detected, which extends its use in vivo. Testing of green NPs was carried out on outbred mice with S-180 induced sarcoma. The changes in the intensity of spontaneous chemiluminescence (SChL) of the homogenates of the tumor tissue of the S-180 sarcoma of all groups of mice were investigated. For evaluation of lipid peroxidation (POL), the formation of malonic dialdehyde (MDA) was determined using thiobarbituric acid (TBA-test), and the activity of superoxide dismutase (SOD) was measured for the activity of the endogenous antioxidant enzyme system. The highest values of SChL and MDA were observed in the experimental group, which was administered with a stabilized extract of AgNPs, compared with control animals. SOD activity increases both in the positive control group and in the experimental group. Since the formation of MDA is characteristic of lipid peroxidation reactions and the data obtained correlate with the results of SChL and SOD, it can be argued that AgNPs increase the level of ROS and

cause damage of cellular structures and biopolymers, thus causing degradation of tumor tissue.

Keywords

Green silver nanoparticles • Genotoxicity • Spontaneous chemiluminescence • Malonic dialdehyde • Superoxide dismutase

1 Introduction

NPs are known for several potential hazardous properties, including carcinogenicity, genotoxicity, and cytotoxicity. The extremely small size of NPs underlays to their ability to pass through the skin, lungs, intestinal tract with unknown consequences for human health [1, 2]. The synthesis of NPs using plants is a very cost-effective approach today. Hence, the development of relevant methodology is very actual. Different NPs can generate various ROS, such as superoxide or hydroxyl radical, hydrogen peroxide (H₂O₂) and O₂ [3]. The level of ROS generated by NPs depends on the chemical nature of the NPs themselves. Silver nanoparticles are the subject of research due to their unique characteristics, such as size and shape, which are underlying the optical, antimicrobial and electrical properties [4]. Various methods for the synthesis of AgNPs are known and the extracts of various plants could be used as reducing and stabilizing agents for Green NPs biosynthesis.

There is an increasing interest in studying the properties of plants of the *Ocimum* genus due to the wide distribution and frequent use in national cuisine and traditional medicine, as well as due to the content of a large range of secondary metabolites [5]. The antimicrobial properties of some types of basil have been studied in link with main secondary metabolites found in plants of the *Ocimum* genus: essential oils, phenolic components and anthocyanins [6]. The endemic representative of this genus, *Ocimum araratum*, is widely distributed in Armenia. Its' extracts have strong

M. Petrosyan · T. Gevorgyan · G. Kirakosyan · A. Hovhannisyian (✉)
Department of Medical Biochemistry and Biotechnology,
Russian-Armenian University, IMBiF, 123 Hovsep Emin,
Yerevan, Armenia
e-mail: ashkhen.hovhannisyian@rau.am

G. Kirakosyan · L. Ghulikyan · N. Ayvazyan
L. Orbeli Institute of Physiology NAS, Yerevan, Armenia

antiradical properties, which is one of the necessary criteria for the successful synthesis of NPs by the “green” method [7]. Therefore, *O. araratum* extracts could be very good candidates for the synthesis and stabilization of AgNPs with novel drug design perspectives.

2 Materials and Methods

2.1 Preparation of Plant Extract and Silver Nanoparticles’ (AgNPs) Synthesis

The Armenian plant *O. araratum*, was collected during the flowering period of 2018 in Ararat province of Armenia. The plant material was finely ground until getting uniform and extracted in the 50% water-ethanol solution with 1:30 ratio. A suspension was subjected to ultrasound at 75 W (Ultrasonic Homogenizer, Sonic-150 W, MRC, Israel) 15 min, after which it was incubated 24 h on a shaker in dark conditions (60–70 rpm) and then centrifuged for 15 min at 3000 rpm (Jouan GR412 centrifuge). A silver nitrate solution was added to the plant extract at room temperature. The transition of Ag^{+1} to Ag^0 was confirmed by changing the color of the solution from colorless to brown.

2.2 Scanning Electron Microscopy (SEM) of AgNPs

The scanning electron microscopy was conducted (SEMLEO-1430 VP, Carl Zeiss, Germany). The focal length from the detector is WD, the type of detector used is SE1 (secondary electron detector) and the accelerating voltage is EHT. The samples were pasted on aluminum plates, deposited with gold by the method of cathode deposition in the argon environment and viewed in high vacuum mode. According to the results of this analysis, the formation of AgNP with a size of 12 ± 5 nm was revealed.

2.3 Getting Model of Sarcoma S-180 in Mice

Adult male albino Wistar mice weighing 25 ± 2 g were purchased from the Experimental Center of the Orbeli Institute of Physiology (NAS RA). The animals were kept under standard vivarium conditions at 25 ± 2 °C, 12/12 h light/dark cycle (lights on at 7.00), and with food and water ad libitum. All procedures were done according to our institution’s animal care rules and the IACUC’s ethical guidelines for Decapitation of Unanesthetized Mice and Rats

(<http://www.utsouthwestern.edu/utsw/cda/dept238828/files/469088.html>). For the preparation pure culture of Sarcoma S180 without blood vessels, 3 mL of physiological saline was added and tissue was homogenized. 0.5 mL S-180 sarcoma cells were transplanted subcutaneously into the right axilla of each mouse. When the tumor grew to 100–300 mm³ we randomly divided mice into 3 groups: group I, control group treated with 50% ethanol solution based on saline, group II, which were injected with 50% *Ocimum araratum* ethanol extract (1.75 µg/mL standardized by rosmarinic acid) and group III which were injected with AgNPs stabilized in the *O. araratum* extract. Mice were sacrificed under light ether anesthesia.

2.4 Extraction of Genomic DNA from Sarcoma S-180 Cells and DNA Retardation Method

Isolation of genomic DNA was performed using the apeG-GOLD MicroSpin Tissue DNA Kit (PeQlab Biotechnologie GmbH Erlangen, Germany).

The study of direct interaction of 50% the ethanolic extract of basil (*Ocimum araratum*) and AgNPs with the genomic DNA of S-180 sarcoma cells depend on concentration was carried out by measuring the electrophoretic mobility of genomic DNA in a 0.8% agarose gel [8]. For the preparation of Tris-acetate buffer solution distilled water was added to 20 mL of concentrated $50 \times$ TAE buffer and, thoroughly mixed, then made up the solution to 1 L. 0.8 g agarose was dissolved in 100 ml $1 \times$ TAE buffer [9]. Agarose gel electrophoresis was performed at 100 V, 60 min (PerfectBlue™ Horizontal Mini GelSystem, PeQlab, Germany) to detect the migration of DNA bands under a UV illuminator (E-BOX VX2-VILBER LOURMAT, PeQlab, Germany).

2.5 Method of Spontaneous Chemiluminescent Analysis

Non-purebred white mice were decapitated. Then the localized sarcoma was removed and homogenized for 5 min by the homogenizer of Potter-Elvehjem in Tris-HCl buffer (pH 7.4) with a final concentration of 20 mg/mL [10]. Reactive oxygen species (ROS) levels were measured by a ChL analyzing system: intensities of tissue homogenates were measured on a quantometric device equipped with a photomultiplier, which is an ultra- fast single photon counter with a spectral sensitivity range of 380–630 nm. All the experiments were performed by Junior LB 9509 portable tube luminometer (BERTHOLD Technologies, Germany).

2.6 The Malonic Dialdehyde (MDA) Formation in the Presence of Thiobarbituric Acid: TBA-Test

Lipid peroxides are unstable and decomposed to a complex series of compounds. The most abundant compound is malonic dialdehyde (MDA). MDA level of tissues was determined by spectrophotometric measurement [11], using the TBA-test, based on the reaction of a chromogenic reagent, thiobarbituric acid (TBA) with MDA at 100 °C and two molecules of MDA, reacting with one molecule of TBA to yield a stable three-methine complex dye. MDA concentration was measured at 532 nm, using the B01-CT-8 spectrophotometer (“E-ChromTech”, Taiwan).

The amount of MDA (in nmol per sample) is calculated by the formula:

$$D = \varepsilon cl$$

where, D —optical density, C —MDA concentration, l —cuvette thickness, $\varepsilon = 1.56 \times 10^5 \text{ cm}^{-1} \text{ m}^{-1}$.

2.7 Superoxide Dismutase Activity (SOD) by Adrenaline Photo-Oxidation

Determination of superoxide dismutase (SOD) activity was done using a method of the adrenaline autooxidation reaction in $\text{pH} = 10.2$ [3]. The method is based on the inhibition of adrenochrome formation in epinephrine autooxidation in aqueous alkaline solution ($\text{pH} > 8.5$) to yield a chromophore with a maximum absorbance at 480 nm, using the B01-CT-8 (E-Chrom Tech, Taiwan) spectrophotometer. The kinetic measurement of the 480 nm absorbance change (adrenochrome concentration) was performed after the addition of adrenalin. The SOD activity was determined from the ratio of the autoxidation rates at the presence and absence of SOD. The whole protein amount of the sample was measured by Lowry’s method.

2.8 Statistical Processing of Results

For quantitative estimation of the chemiluminescence and lipid peroxidation intensity, as well as SOD activity levels, the Student’s t -test was used to estimate intergroup differences between values at each time point, considering $P < 0.05$ as an index of significance. All numerical data are presented below as means \pm s.e.m.; n is the number of experiments.

3 Results

3.1 The Interaction of 50% Ethanol Extract of Basil and Green AgNPs with Genomic DNA of Tumor Cells

The results of the DNA retardation experiment (Fig. 1) demonstrated that both 50% ethanol extract of basil and green AgNPs were not able to bind genomic DNA in S-180 sarcoma cells and suppress its electrophoretic mobility (genomic DNA was determined for a series of basil extract and AgNPs concentrations in a SYBR green stained agarose gel). It is obvious that the direct interactions with genomic DNA of Sarcoma S180 cancer line cells within the concentration of the extract from *Basilica Ocimum araratum* and AgNPs from 0.56 to 4.5 mg/mL and with incubation up to 30 min not observed, indicating low genotoxicity of both samples.

These data are in contradictory with a numerous published works, where the direct effect of AgNPs on genomic DNA and quite potent genotoxicity for various AgNPs have been reported. This contradictory could be explained by the possible size-dependent effects, when an increase in DNA damage was correlated with the effect of NPs size, varying between 16 and 25 nm, or 50–200 nm covered with citrate [12–14].

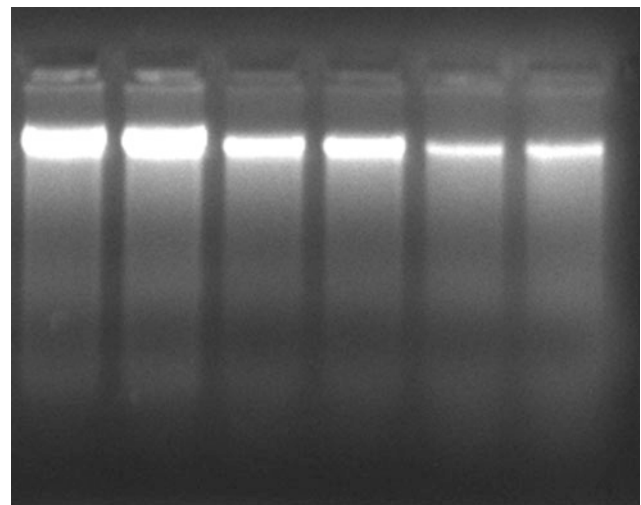


Fig. 1 Electrophoretic mobility of genomic DNA S-180: without adding extract and NPs (control); for 30 min. incubation with basil extract; for 30 min. incubation with increasing concentrations of Ag NPs stabilized with basil extract: 3 - 0,56 mg/ml; 4 - 1,125 mg/ml; 5 - 2,25 mg/ml; 6 - 4,5 mg/ml (left to right)

3.2 Spontaneous Chemiluminescence (SchL) and Lipid Peroxidation (TBA-Test)

The intensity of spontaneous chemiluminescence of tumor tissue homogenates of S-180 sarcoma of all groups of mice (treated and untreated with 50% ethanol extract of basil and green AgNPs) was measured. It was found that, compared to the control groups, the highest level of chemiluminescence was detected in the supernatant of the tumor tissue of the experimental group, which was injected with AgNPs stabilized in 50% of the extract of *Ocimum araratum*—about 1.4 times more over the control. With the introduction of 50% *Ocimum araratum* ethanol extract, the increase of free radical activity in a real time mode was less significant (Fig. 2).

Malonic dialdehyde (MDA) is a product of free radical oxidation of lipids, the accumulation of which reflects the degree of oxidative stress in the body. This indicator is necessary to determine the causes of the development of a pathological process, as well as for further treatment of the disease. The results obtained through the TBA-test showed that the MDA accumulation in the treated sarcoma S-180 tissues compared to the control group is very pronounced, especially a higher value in the experimental group treated with AgNPs is detected—approximately 1.14 times more over the control (Fig. 2). These data are correlated with the SchL results.

3.3 SOD Activity of Treated Sarcoma Tissue Homogenate S-180

Since the analyzed lipid peroxidation processes in sarcoma tissues are associated with the activity of the antioxidant enzyme systems, we, according to the same principle, measured the activity of SOD, a first barrier in the antioxidant system. SOD protects the body from obstructed highly toxic oxygen radicals [15].

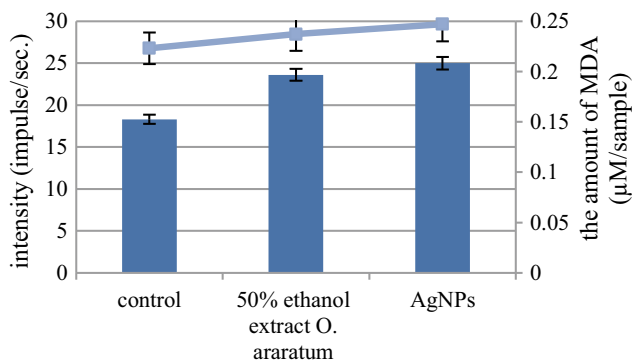


Fig. 2 Changes in the intensity of SCL (impulse/sec) and the amount of MDA ($\mu\text{M}/\text{sample}$) of homogenate tumor tissue sarcoma S-180 under the influence of 50% ethanol extract *Ocimum araratum* and stabilized AgNPs, significant differences, $p < 0.05$

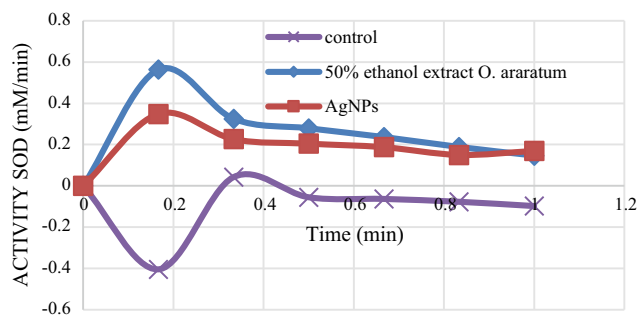


Fig. 3 Investigation of the effect of 50% extract *O. araratum* and stabilized AgNPs on activity superoxide dismutase of the tumor tissue sarcoma S-180, significant differences, $p < 0.05$

In the study of the effect of the extract and AgNPs, a remarkable increase in SOD activity was found in comparison with the control group (Fig. 3).

4 Conclusions

Currently, there is a need to develop environmentally friendly NPs, which do not use toxic chemicals in the NP's synthesis protocols. Green NPs have advantages over physicochemical methods. The selection of environmentally friendly non-toxic reducing and stabilizing agents are the most important issues. AgNPs are of interest due to their unique properties, which may include anticarcinogenic use [16]. Extracts of various plants are used as regenerating and stabilizing agents for the biosynthesis of AgNPs. In the present work, we used *Ocimum araratum* 50% ethanol extract for the synthesis of AgNPs, since we had the highest content of flavonoids, as well as the highest antiradical activity. Our results showed that the green method to obtain AgNPs do not possess genotoxicity, which expands their use as therapeutic agents.

Oxidative stress caused by reactive oxygen species is one of the most important mechanisms contributing to the cytotoxic activity of NPs [17, 18]. ROS are natural by-products of cellular oxidative metabolism and play a significant role in modulating cell survival and death, differentiation and cell signaling. Excessive production of ROS leads to impaired redox homeostasis and, as a result, to oxidative stress, which affects membrane lipids and alters the structure of DNA and proteins [17]. On the basis of the obtained results on parameter estimation, it can be said that the formation of MDA is characteristic of lipid peroxidation reactions and the obtained data correlate with the results of the SchL and SOD, then it can be argued that AgNPs increase the level of ROS, which leads to an increase in the values of the corresponding parameters studied. Our results coincided with the literature data that AgNPs can generate various ROS, such as superoxide or hydroxyl radical,

hydrogen peroxide, etc. [17, 19], which leads to the activation of SOD in the course of the body's defense against oxidative degradation.

Increased levels of ROS formation under the influence of AgNPs can damage cellular structures and biopolymers, thus causing the degradation of tumor tissue.

Conflict of Interest The authors declare that they have no conflict of interest.

References

1. Malabadi, R.B., Mulgund, G.S., Meti, N.T., et al.: Antibacterial activity of silver nanoparticles synthesized by using whole plant extracts of *Clitoria ternatea*. *Res Pharm.* **2**(4), 10–21 (2012)
2. Mukunthan, K., Elumalai, E., Patel, T., et al.: *Catharanthus roseus*: a natural source for the synthesis of silver nanoparticles. *Asian Pac. J. Trop. Biomed.* 270–274 (2011). [https://doi.org/10.1016/s2221-1691\(11\)60041-5](https://doi.org/10.1016/s2221-1691(11)60041-5)
3. Makarevich, O., Golikov, P.: Superoxide dismutase activity of blood during the acute phase of various diseases. *Laboratornoye Delo.* **6**, 24–27 (1983)
4. Singh, M., Singh, S., Prasada, S., et al.: Nanotechnology in medicine and antibacterial effect of silver nanoparticles. *Dig. J. Nanomater. Bios.* **3**(3), 115–122 (2008)
5. Patil, D., Mhaske, D., Wadhawa, G., et al.: Antibacterial and antioxidant study of *Ocimum basilicum* Labiatae (sweet basil). *JAPER* **2**, 104–112 (2011)
6. Deshpande, R., Tipnis, H.: Insecticidal activity of *Ocimum Basilicum* L. *Pesticides* **12**, 21–28 (1997). <https://doi.org/10.17660/ActaHortic.2016.1125.28>
7. Hayyan, M., Hashim, M.A., Alnashef, I.M.: Superoxide ion: generation and chemical implications. *Chem. Rev.* **116**, 3029–3085 (2016). <https://doi.org/10.1021/acs.chemrev.5b00407>
8. Kirakosyan, G., Mohamadvarzi, M., Ghulikyan, L., et al.: Morphological and functional alteration of erythrocyte ghosts and giant unilamellar vesicles caused by *Vipera latifi* venom. *Biochem. Physiol. Part C Toxicol. Pharmacol.* **190**, 48–53 (2016). <https://doi.org/10.1016/j.cbpc.2016.08.006>
9. Wang, Y.Q., Su, J., Wu, F., et al.: Biscarbamate cross-linked polyethylenimine derivative with low molecular weight, low cytotoxicity, and high efficiency for gene delivery. *Int. J. Nanomed.* **7**, 693 (2012). <https://doi.org/10.2147/ijn.S27849>
10. Zaqaryan, N., Ghazaryan, N., Ayvazyan, N.: Dynamic changes in lipid peroxidation and antioxidant level in rat's tissues with *Macrovipera lebetina obtusa* and *Montivipera raddei* Venom Intoxication. *JBC* **5**(4), 152–160 (2014). <https://doi.org/10.4236/jbpc.2014.54017>
11. Stalnaja, I., Garishvili, T.: Method of malonicdialdehyde determination with thiobarbituroacid. In: *Biokhimicheskie metodi issledovania* (Biochemical Methods of Investigations), pp. 66–68 (1985)
12. Che, B., Luo, Q., Zhai, B., et al.: Cytotoxicity and genotoxicity of nanosilver in stable GADD45 α promoter-driven luciferase reporter HepG2 and A549 cells. *Environ. Toxicol.* **32**(9), 2203–2211 (2017). <https://doi.org/10.1002/tox.22433>
13. Dwivedi, S., Wahab, R., Khan, F., et al.: Reactive oxygen species mediated bacterial biofilm inhibition via Zinc oxide nanoparticles and their statistical determination. *PLoS ONE* **9**(11), e111289 (2014). <https://doi.org/10.1371/journal.pone.0111289>
14. Souza, A., Franchi, P., Rosa, R., et al.: Cytotoxicity and genotoxicity of silver nanoparticles of different sizes in CHO-K1 and CHO-XRS5 cell lines. *Mutat. Res. Genet. Toxicol. Environ. Mutagen.* **795**, 70–83 (2016). <https://doi.org/10.1016/j.mrgentox.2015.11.002>
15. Huk, A., Izak-Nau, E., Reidy, B., et al.: Is the toxic potential of nanosilver dependent on its size? Part. *Fibre Toxicol.* **11**, 65 (2014). <https://doi.org/10.1186/s12989-014-0065-1>
16. Gevorgyan, T., Oganian, S., Petrosyan, M., et al.: Study of cytotoxic and genotoxic properties of “green” nanoparticles of silver. *Vestnik RAU.* **1**, 98–110 (2019). ISBN 1829-0450
17. Al-Sheddi, E.S., Farshori, N.N., Al-Oqail, M.M., et al.: Anticancer potential of green synthesized silver nanoparticles using extract of *Nepeta deflersiana* against human cervical cancer cells (HeLA). *Bioinorg. Chem. Appl.* (2018). <https://doi.org/10.1155/2018/9390784>
18. Rudramurthy, R., Swamy, K., Sinniahb, R., et al.: Nanoparticles: alternatives against drug-resistant pathogenic microbes. *Molecules* **21**(7), 836 (2016). <https://doi.org/10.3390/molecules21070836>
19. Wang, Z., Dong, K., Liu, Z., et al.: Activation of biologically relevant levels of reactive oxygen species by Au/g-C3N4 hybrid nanozyme for bacteria killing and wound disinfection. *Biomaterials* **113**, 145–157 (2017). <https://doi.org/10.1016/j.biomaterials.2016.10.041>

Influence of Polarization on Electron Localization in the Coated Tetramer Nanoclusters Used as Elements of Biorecognition Systems

E. Yu. Kanarovskii and O. V. Yaltychenko

Abstract

A quasi-classical theoretical model is proposed for describing the localization dynamics of a common (tunneling) electron in the coated metal-organic nanocluster in an external low-frequency electric field, taking into account the electron-vibrational interaction and the polarization effects on its centers and on the ligand (organic) shell. The case of a square-planar tetramer nanocluster with the tunnel-connected centers is considered. This model allows a detailed study of the controlling role of the electric field, taking into account the contributions from the electron-vibrational interaction and from the polarization effects, in the realization of the various electron localization regimes, and reveals the ability of such a nanocluster to switch between them. This model is actual and suitable for the nanostructured composite systems of such kind, which are widely used as the basic elements in the bio-recognition systems.

Keywords

Tetramer nanoclusters • Electron localization dynamics • Electron-vibrational interaction • Periodic electric field • Polarization

1 Introduction

An enormous number of theoretical and experimental results obtained in the researches on various kinds of clusters and complexes, composite nanoparticles, quantum dots, 1D and 2D nanostructures and nanocomposite materials [1–4] based on them are actively being implemented into biomedicine for the purpose to create various multifunctional hybrid materials for the cell and tissue engineering and the regenerative

medicine. Despite the relative youth, these domains of biomedicine are rapidly expanding, both in the laboratory and in the clinical setting.

It should be emphasized that, namely, methods elaborated in physics, chemistry and computer science with using an incredibly huge array of outstanding achievements and powerful results obtained in these sciences provide such a high potential for the innovations in all domains and directions of biomedical researches [1–10].

In many modern biomedicine studies and applications, the metal nanoparticles coated by the organic shells (including and nanoclusters) extensively used as the key elements in the bio-recognition systems.

In essence, a shell of the metal-organic composite system performs a stabilization of metal core and its protection, as well as, it serves as a platform for linking the corresponding bio-active molecule and its subsequent transportation to the target molecule for the implementation of its bio-recognition. Typically, such a shell, through its external functional groups, provides the linking of cell-identifying labels, fluorescent dyes, enzymes, and drug molecules.

Composite systems containing the metal-organic nano-clusters (MONCs) are relatively new materials that attract the intent attention of both the theoretician and the experimentalists. MONCs belong to the structures of shell-core kind, in which the organic ligands are located on the periphery of metal core forming a shell surrounding of its.

In other words, the organic shell is coordinated to the metal core. Small MONCs, have in its core from one to several dozen atoms. In the most cases, these are atoms (ions) of d- and f-metal, which act as an effective coordination center. So, for example, in a result of a convergence of the transition metal atom (such as Cu, Co, Ni, Pd, etc.) and the organic ligand's shell to form a stable complex owing to the interactions between s- and p- molecular orbitals of the donor-atoms in the ligands (most often these are atoms of oxygen, nitrogen, sulfur, and less often a carbon atom is involved through its π -orbitals) and the d-orbitals of

E. Yu. Kanarovskii (✉) · O. V. Yaltychenko
 Institute of Applied Physics, ASM, Academy 5, MD-2028
 Chisinau, Republic of Moldova
 e-mail: kanarovskii@gmail.com

the metal ions. The condition for the stability of such systems is the existence of local minimum of the free energy. Stability, in a rather wide range of temperatures, manifest the many types of the NCs from the small NCs of different transition metal atoms in the organic shells to the large nanoparticle clusters (as the coated quantum dots). In terms of their shapes, they are conventionally divided into the following types—the flat discs (quasi 2D), as well as the needle (quasi 1D) and globular (quasi 3D) complexes [3–7]. In this paper we propose the theoretical model describing the nonlinear dynamics of electron localized in 4-center (tetramer) metal core of MONC with a organic shell, so that the MONC metal core Me_4^- contains the transition metal atoms (for example, $\text{Me} = \text{Cu}, \text{Co}, \text{Ni}, \text{Pd}$), which may have different oxidation degrees. It should be noted that taking into account the nonlinear and collective effects on the different kinetic processes in the metal-organic nanoclusters and nanoparticles in demand both from a theoretical point of view and for practical developments [1–10]. The purpose of this work is to build a model describing the dynamics of electron localization-delocalization, using as an example a cyclic nanocluster, having square-planar conformation (or linear nanocluster), which can be extended for clusters with a large number of localization centers and having more conformations. The tetramer nanocluster (NC) considered here differs from the dimer and trimer NCs not only a larger number of centers, but also it has more conformations of their mutual arrangement (it can have a tetrahedral conformation, in addition to linear and planar). Thus, is characterized by a larger number of model parameters that determine the electron localization regimes at the account electron-vibrational interaction and polarization caused by the action of an external electric field. Consequently, the tetramer NC has a richer picture of localization dynamics of the internal common electron, tunneling between the NC centers. In the proposed model, to describe the localization and delocalization of the common electron in the NC of this type, in addition to its tunneling between the centers, the external low-frequency electric field, the electron polarization induced by it on the NC centers and on the ligand shell of NC and electron-vibrational interaction are also considered. The interaction of an electron with the vibrational modes of the ligand environment at each of the centers of the tetramer NC, as well as the inclusion of polarization, ultimately leads to nonlinear electron dynamics. In the model represented below, non-linearity appears explicitly in the differential equations describing the electronic subsystem, excluding from them the intracuster vibrational modes of the ligand environment of the NC centers and the polarization displacement modes of the collective electron density at each of the NC centers taking into account its ligand environment.

2 Theoretical Approach

The model Hamiltonian, which makes it possible, taking into account the indicated internal (and external factors, to consider these tetramer NC, has the form:

$$\begin{aligned}
 H = & \sum_{m=1}^4 \varepsilon_m a_m^+ a_m + \sum_{m,n=1}^4 V_{mn} a_m^+ a_n + \\
 & + \sum_{m=1}^4 g_{0m} q_m a_m^+ a_m + \sum_{m=1}^4 g_{sm} s_m a_m^+ a_m \\
 & + \sum_{m=1}^4 e \mathbf{E} \mathbf{r}_m \cos(\Omega t) a_m^+ a_m + \sum_{m=1}^4 e_{\text{eff}} \mathbf{E} \mathbf{s}_m \cos(\Omega t) \\
 & + \frac{1}{2} \sum_{m=1}^4 (p_m^2 + \omega_{0m}^2 q_m^2) + \frac{1}{2} \sum_{m=1}^4 (p_{sm}^2 + \omega_{sm}^2 s_m^2)
 \end{aligned} \tag{1}$$

where: a_m^+ , a_m are the electron creation and annihilation operators at the m th center of the TC; p_m and q_m are the momentum and coordinate of the local intracuster vibrational mode; p_{sm} and s_m are the momentum and coordinate of the local polarization mode; ε_m is the electron energy at the m th center; V_{mn} is the constants of tunneling from the m th to the n th center; g_{0m} is the electron-vibrational interaction constant at the m th center of the cluster; $e \mathbf{E} \mathbf{r}_m \cos(\Omega t)$ is the interaction energy of an electron at the m th center of the NC with an external periodic electric field, g_{sm} is the corresponding constant of interaction of the electron with the polarization displacement \mathbf{s}_m of the collective electron density at the m th center of the NC (vector \mathbf{s}_m is antiparallel to \mathbf{E}). The vector \mathbf{E} and directed from 4th to 1st center in the linear NC conformation and from 3rd to 1st center in the cyclic NC conformation. The vector \mathbf{r}_m counts the position of the electron at the m th center relative to the origin, which is convenient to choose at the center of symmetry of the tetramer NC. This issue is described in more detail in [10]; in the same place, using the generally accepted “jelly” model [5–10], the question of the formation of a potential well for a common electron at each of the NC centers, taking into account its local ligand environment, is discussed. Farther, we make some assumptions that simplify the numerical calculation: all centers are considered energetically equivalent ($\varepsilon_m = \varepsilon$) and the level ε is chosen as the origin of energy, and also the value \hbar is conventionally taken as 1.

As a result, we obtain differential equations for the amplitudes of the probability of detecting an electron at the NC centers $c_m(t)$:

$$\begin{aligned}
 i \frac{dc_m}{dt} = & \sum_{n=1}^4 V_{mn} c_n + g_{0m} q_m c_m + g_{sm} s_m c_m \\
 & + e \mathbf{E} \mathbf{r}_m \cos(\Omega t) c_m
 \end{aligned} \tag{2}$$

The differential equations for the corresponding local vibrational and polarization modes with frequencies ω_{0m} and ω_{sm} , respectively, have the following form:

$$\begin{aligned} \ddot{q}_m + \omega_{0m}^2 q_m &= -g_{0m}|c_m|^2 \\ \ddot{s}_m + \omega_{sm}^2 s_m &= -g_{sm}|c_m|^2 - e_{eff} E \cos(\Omega t) \end{aligned} \quad (3)$$

Using the method of “slowly varying vibration amplitudes”, we assume that $\dot{q}_m \ll \omega_{0m}^2 q_m$ and $\dot{s}_m \ll \omega_{sm}^2 s_m$ then, using this approximation, the vibrational and polarization degrees of freedom can be excluded from (2). As a result, in the Eq. (3), in accordance with the above approximation, we neglect terms with the second derivatives \ddot{q}_m and \ddot{s}_m and substituting in Eq. (2) the results for the values q_m and s_m in a view: $q_m \approx -g_{0m}\omega_{0m}^{-2}|c_m|^2$ and $s_m \approx -g_{sm}\omega_{sm}^{-2}|c_m|^2 - \tilde{e}_{eff} E \cos(\Omega t)$.

As a consequence, the differential equations for the electronic subsystem of the NC are obtained:

$$\begin{aligned} i \frac{dc_m}{dt} &= \sum_{n=1}^4 (V_{mn}c_n - \tilde{g}_{0m}|c_m|^2 c_m - \tilde{g}_{sm}|c_m|^2 c_m \\ &+ e\mathbf{E}\mathbf{r}_m \cos(\Omega t)c_m - \tilde{e}_{eff} E \cos(\Omega t)c_m) \end{aligned} \quad (4)$$

where: \tilde{g}_{0m} , \tilde{g}_{sm} and \tilde{e}_{eff} are the constants renormalized according to the above-mentioned.

Thus, here: $\tilde{g}_{0m} = g_{0m}^2 \omega_{0m}^{-2}$, $\tilde{g}_{sm} = g_{sm}^2 \omega_{sm}^{-2}$ and $\tilde{e}_{eff} \approx e_{eff} \omega_{sm}^{-2}$.

3 Results and Discussion

The resulting system of differential equations (4) is essentially nonlinear, with third degree nonlinearity. Performing a numerical simulation of this system the different values of the external and internal parameters of the modeled MONC allows us to identify various regimes in the nonlinear dynamics of electron localization, as well as the conditions for switching between them.

The numerical simulation using the base model [10] (i.e., without the account of polarization effects) made it possible to identify three characteristic electron localization regimes. The most interesting, in our opinion, of these regimes is shown in Figs. 1 and 2 for the cases of cyclic and linear MONC, respectively. The corresponding values of basic model parameters are indicated there. This regime, which we

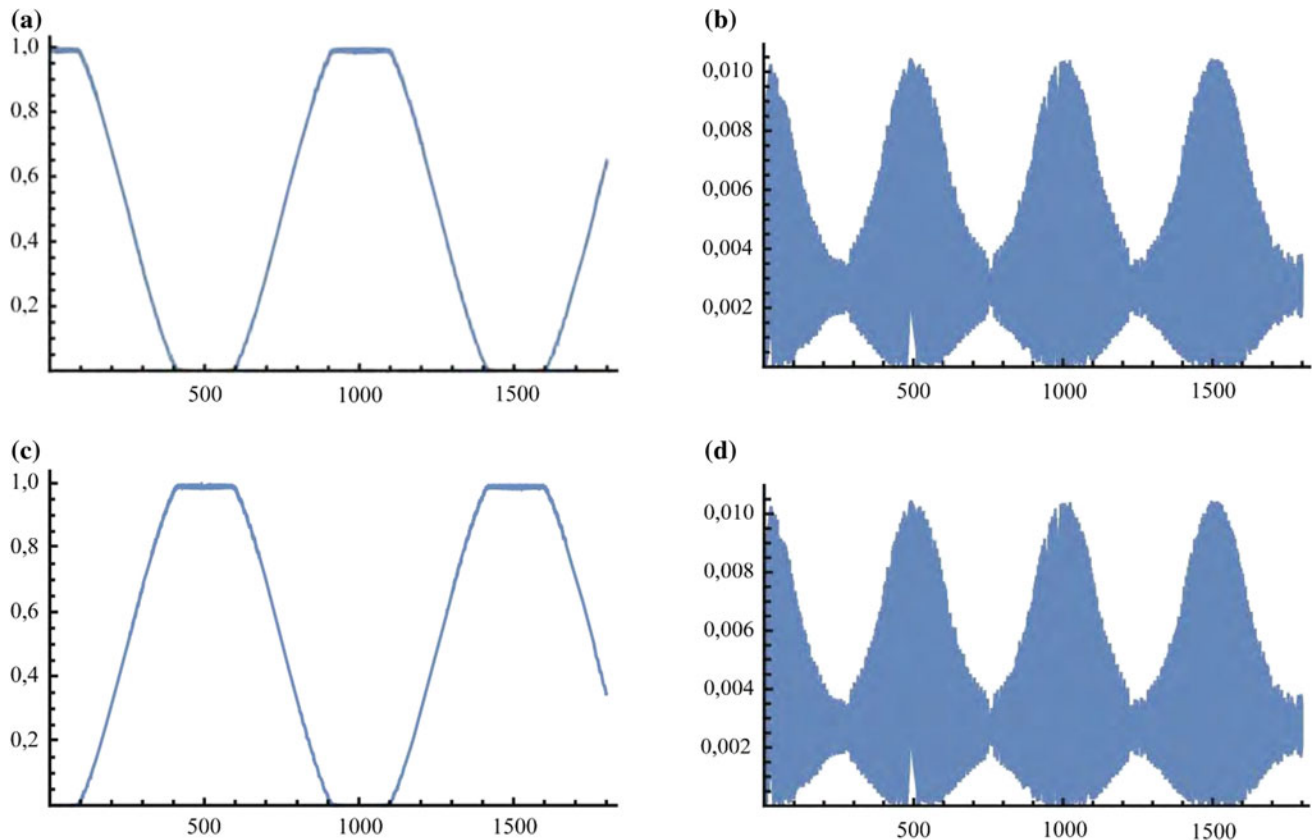


Fig. 1 The time dependence of the probability of localization of an electron at the m th center of the cyclic tetramer (in relative time units) for: $v = 0.2$, $g = 10$, $\Omega = 1/160$, $dE = 6.0$, respectively: **a** $m = 1$, **b** $m = 2$, **c** $m = 3$, **d** $m = 4$

called the regime with the transparency effect of intermediate centers, is periodic.

The preliminary calculations within the framework of given model, which includes the interaction of the tunneling electron with the polarization modes, show, that the polarization effects significantly affects the dynamics of electron localization, in this connection the identified regimes are realized at the another ratios of the values of the basic model parameters.

At the calculations, in addition to the equivalence of the metal core centers mentioned above, it was assumed that all the centers in the MONC have the same ligand environment. From which it follows that in this case all the constants of tunneling are equal, i.e. $V_{mm} = v$, as well as for all local vibrational modes, the frequency equality $\omega_{0m} = \omega_0$. The model parameters are chosen in the units corresponding to the vibrational frequency of the metal-ligand bonds. Time also represented in the dimensionless unit $\omega_0 t$. The calculations and analysis of numerical results of modeling for all four basic model parameters: v —the constant of tunneling, g —the constant of electron-vibrational interaction, Ω —the electric field frequency and dE —the energy interaction of the electron with the electric field, were carried out in a fairly wide range. Comparison of results obtained for the cyclic

(square-planar) tetramer NC and for the linear tetramer NC (see Figs. 1 and 2) leads to the important conclusion that the dynamics of electron localization in such tetramers with different conformations can be very similar at the appropriate ratios of the basic model parameters.

In general, the proposed extended model allows to study in detail the role of polarization effects in the realization and modification of the electron localization regimes identified in [10], as well as to determine the ranges of values of a complete set of model parameters (including the polarization) at which the certain regime is stably realized.

4 Conclusions

As was shown in [10] at the analysis of extensive numerical calculations for various values of a set of model parameters using the system (4) (without taking into account polarization effects), the following characteristic regimes of localization dynamics of an electron can be implemented in the tetramer NCs:

- (1) the regime of periodic switching of the electron density between the 1st and 3rd NC centers (in the cyclic NC)

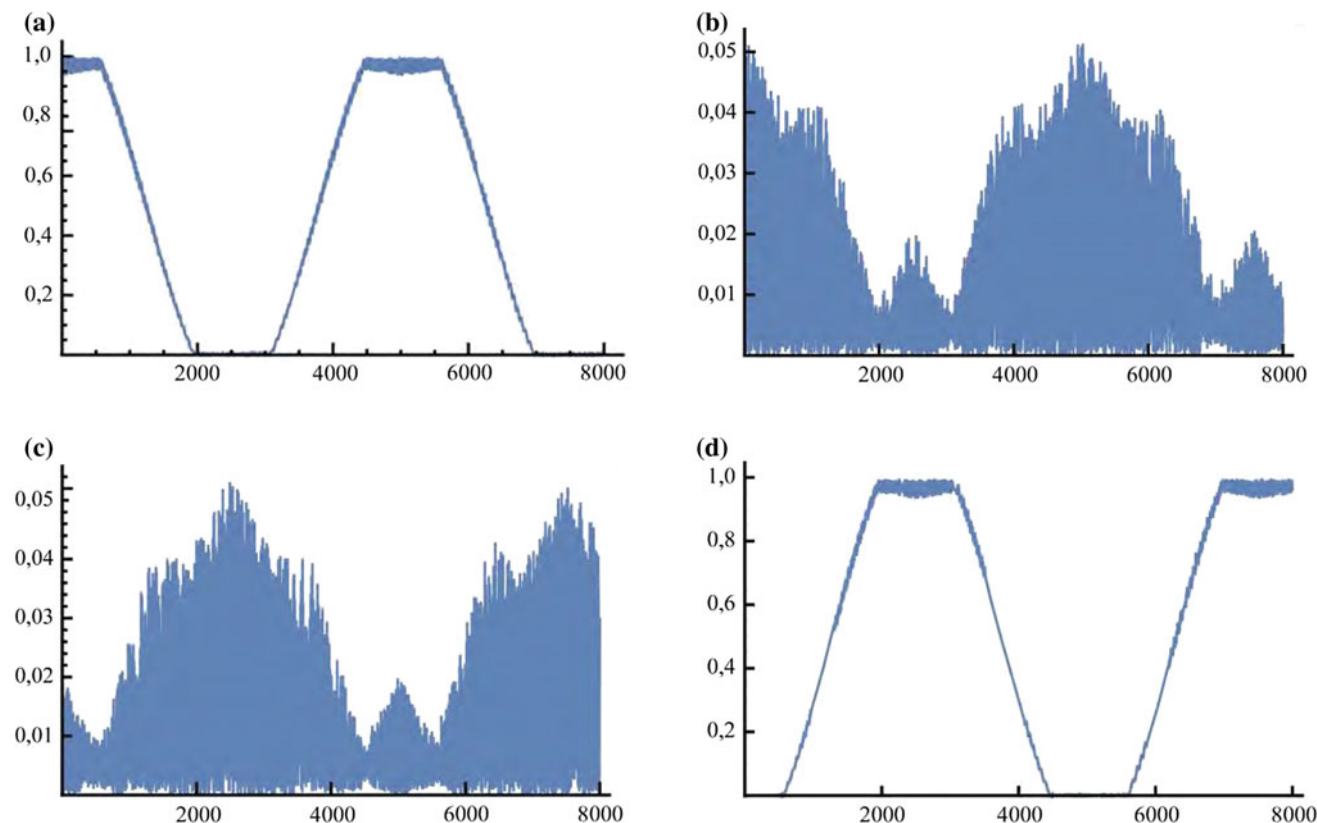


Fig. 2 The time dependence of the probability of localization of an electron at the m th center of the linear tetramer (in relative time units $\omega_0 t$) for: $v = 0.2$, $g = 3.5$, $\Omega = 1/160$, $dE = 1.5$, respectively: **a** $m = 1$, **b** $m = 2$, **c** $m = 3$, **d** $m = 4$

with partial population of intermediate centers (in the linear NC the same switching takes place between the centers of the 1st and 4th);

- (2) the regime with the effect of transparency of intermediate centers (periodic);
- (3) the electron locking regime at one of the centers.

It is important to note that the controlling role of the electric field allows one to realize both regimes with electron localization and regimes with electron delocalization along the direction of the external electric field. In this case, varying the frequency and amplitude of the field adjusts the duration of the full localization at the centers of the NC and switches it from the state with the localized electron to the state with the delocalized electron. Thus, a regulation of the electron density distribution regimes in a tetramer NC (both a square-planar and a linear) by an external electric field becomes more flexible and sensitive when taking into account polarization effects, since on the one hand, the nonlinear response in a NC under the field action takes place, and on the other hand, an increase in the number of adjustable model parameters facilitates the search for the new electron localization regimes and parametric tuning on previously detected in a NC. Eventually, the controlling role of the electric field was revealed, allowing to realize how the regimes of electron localization and as well as the regimes of electron delocalization along the direction of the external electric field. It is shown that a variation of the frequency and amplitude of the field controls the duration of the full electron localization on the definite cluster centers and the cluster can be switched to the states with the different electron localization up to the possibility of being delocalized for a while.

As a consequence of the results obtained in the framework of the model presented here, there is an important conclusion. It consists in the fact that such a NC has a changing dipole moment controlled by an external field taking into account the effects of polarization and electron-vibrational interaction. This will affect the external bio-active molecule linked to the shell not only through the dipole-charge and/or the dipole-dipole interactions, but also due to the polarization displacements of the charge on the shell leads to a redistribution of the charge on the shell near the linkage site of the bio-active molecule. As a result, the bio-active molecule can change the conformational or charge

state of its functional groups or change its spatial position as a whole.

Thus, the parametric regulation of electron localization regimes in the tetramer MONC essentially allows to control the activity of bioactive molecule linked to its shell stimulating its transition from an active state to an inactive state and vice versa.

Acknowledgements This work was supported by the CSSDT of ASM, Institutional Project 15.817.02.03A (2015–2019). Since 2018, the project is supervised by National Agency for Research and Development.

Conflict of Interest The authors declare that they have no conflict of interest.

References

1. Daniel, M.C., Astruc, D.: Gold nanoparticles: assembly, supra-molecular chemistry, quantum-size-related properties, and applications toward biology, catalysis, and nanotechnology. *Chem. Rev.* **104**(1), 293–346 (2004)
2. Deka, A., Deka, R.C.: Structural and electronic properties of stable Aun ($n = 2 - 13$) clusters: a density functional study. *J. Mol. Struct. (Theochem)* **870**(1–3), 83–93 (2008)
3. Martinez-Duart, J.M., Aquillo-Rueda, F., Martin-Palma, R.J.: *Nanotechnology for Microelectronics and Optoelectronics*. Elsevier, Amsterdam (2006)
4. Suzdalev, I.P.: *Nanotechnology: Physical Chemistry of Nanoclusters, Nanostructures, and Nanomaterials*. URSS, Moscow (2009). (in Russian)
5. De Heer, W.A.: The physics of simple metal clusters: experimental aspects and simple models. *Rev. Mod. Phys.* **65**(3), 611–676 (1993)
6. Ivanov, V.K., Kharchenko, V.A., Ipatov, A.N., Zhizhin, M.L.: Optimized “jelly” model for metal clusters. *Letters to JETP* **60**(5), 345–351 (1994). (in Russian)
7. Ivanov, V.K., Ipatov, A.N., Kharchenko, V.A.: An optimized “jellium” model for metallic clusters with screened Coulomb interaction. *JETP* **82**(3), 485–492 (1996)
8. Calvayrac, F., Reinhard, P.-G., Suraud, E., Ullrich, C.A.: Nonlinear electron dynamics in metal clusters. *Phys. Rep.* **337**(6), 493–578 (2000)
9. Gervais, B., Giglio, E., Ipatov, A.N., Douady, J.: Effective numerical method for theoretical studies of small atomic clusters. *Comput. Mater. Sci.* **35**(3), 359–365 (2006)
10. Kanarovskii, E.Yu., Yaltychenko, O.V.: Nonlinear dynamics of electron localization in four-center linear and cyclic type clusters in an external electric field. *Surf. Eng. Appl. Electrochem.* **53**(3), 250–257 (2017)

Use of Physical Methods as an Element of Complex Treatment of Burn Wound Microbiome

V. Nagaichuk, R. Chornopyschuk, O. Yunusova, and M. Onyshchenko

Abstract

According to World Health Organization, burns remain a high priority matter of medicine as the third in the overall structure of traumatism. One of the main causes of death from burn injuries is infectious complications, which require the use of effective antimicrobial agents. In view of the increased resistance of microorganisms to antibiotics, it is expedient to find alternative ways of antimicrobial control, one of which is the use of low-intensity current without external power supplies. This is exactly the purpose of our study. The obtained results allowed to confirm the antimicrobial effect of low-intensity currents without external supplies on the example of a clinical strain of methicillin-resistant *Staphylococcus aureus* in a closed and open electrical circuits with the need for further research in this direction.

Keywords

Burn • Wound • Infection • Treatment • Microcurrent

1 Introduction

According to World Health Organization, burns remain a high priority matter of medicine as the third in the overall structure of traumatism [1]. In Ukraine, as in other developing Eastern European countries, the frequency and

severity of burn injuries in different age groups are increasing [2].

One of the main causes of death from burn injuries is infectious complications, which, according to literature data, constitute 73.0% of fatal cases in the first 5 days after the injury [3]. To date, *Pseudomonas aeruginosa* and *Acinetobacter baumannii* occupy the leading position among the gram-negative microflora emitted from the wounds of burn patients; *Staphylococcus aureus* occupies the leading position among the gram-positive microflora [4]. Therefore, an important component in the complex treatment of this category of patients is the use of antimicrobial agents [5]. At the same time, prolonged and not always rational antibiotic therapy leads to the formation of stable resistance of pathogenic microorganisms which requires the search and development of a new way to fight it [6].

The purpose of our research was to study the effect of low-intensity current without external power supplies on strains of microorganisms in burn patients in vitro.

2 Materials and Methods

The study involved the use of clinical strains of methicillin-resistant *Staphylococcus aureus*, *Pseudomonas aeruginosa* and *Acinetobacter baumannii* which were emitted from the wounds of burn patients at the Clinical Center of Thermal Injury and Plastic Surgery of the Regional Pirogov Clinical Hospital.

To study the effect of biogalvanic current on the culture of microorganisms a device containing a copper, 0.5 mm diameter electrode-donor of electrons and an aluminum–magnesium–zinc composite electrode-acceptor of electrons of the same diameter connected with each other through the measuring device with a conductor of the first kind was designed.

A Petri dish was filled with a dense agar nutrient medium; a culture of microorganisms with a standardized turbidity

V. Nagaichuk · R. Chornopyschuk (✉) · M. Onyshchenko
National Pirogov Memorial Medical University, Pirogov, 56,
Vynnytsya, Ukraine
e-mail: ro_man@mail.ru

V. Nagaichuk
Regional Clinical Hospital named after M.I. Pirogov, Vynnytsya,
Ukraine

O. Yunusova
Regional Laboratory Center of the MOH, Vynnytsya, Ukraine

according to the optical standard (500,000 microorganisms per mL) was uniformly applied on the surface.

The study of the antimicrobial properties of low-intensity current without external power supplies was carried out in conditions of both closed and open electric circuits during 24 h in thermostat conditions at a temperature of 36 °C after the installation of electrodes on the microbial medium. Antimicrobial effect was evaluated after 24 h by the degree of growth retardation of microorganisms around the electrodes under study.

3 Research Results and Their Discussion

The electrodes located on the surface of the nutrient medium generated a constant microcurrent without external power supplies with a force of $12.6 \pm 2.5 \mu\text{A}$; however, a current of $28.05 \pm 3.1 \mu\text{A}$ was recorded on the dishes with methicillin-resistant *Staphylococcus aureus*, currents of 14.2 ± 2.8 and $12.7 \pm 3.4 \mu\text{A}$ were recorded on the dishes with *Acinetobacter baumannii* and *Pseudomonas aeruginosa* accordingly (Fig. 1).

The strength of bactericidal effect of low-intensity currents without external power supplies on the culture of methicillin-resistant *Staphylococcus aureus* in the conditions of a closed loop energy circulation depended on the electrochemical nature of the electrodes and amounted to 16.9 ± 2.2 mm under a positive electrode and 12.7 ± 2.8 mm under a negative electrode (Fig. 2).

In conditions of open loop energy circulation the growth retardation zone amounted to 12.3 ± 1.9 mm under the positive electrode and 12.8 ± 1.7 mm under the negative electrode (Fig. 3).

No growth regions were located around any of the electrodes on dishes with gram-negative microflora of *Acinetobacter baumannii* and *Pseudomonas aeruginosa*, which is



Fig. 2 The diameter of the growth retardation zone of methicillin-resistant *Staphylococcus aureus* on agar under electrodes in a closed loop energy circulation

obviously due to significantly lower current strength without external power supplies on nutrient media with gram-negative microflora (Fig. 4).

4 Conclusions

As a result of the research it was possible to establish the antimicrobial effect of low-intensity currents without external power supplies on the culture of methicillin-resistant *Staphylococcus aureus* under conditions of closed and open loops of energy circulation without visible signs of sensitivity in representatives of gram-negative microflora.

In the future it is advisable to study the effect of low intensity currents without external supplies on the sensitivity of microorganisms to antimicrobial agents with the possibility of enhancing the latter.

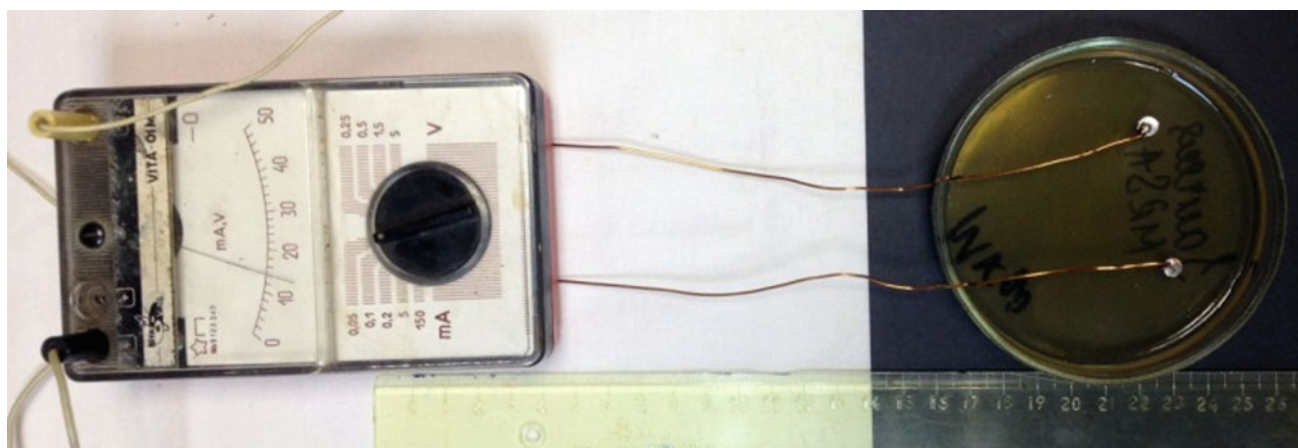


Fig. 1 A device for studying the effect of low-intensity current without external power supplies on the culture of microorganism

Fig. 3 The diameter of the growth retardation zone of methicillin-resistant *Staphylococcus aureus* on agar under positive (left) and negative (right) electrodes in open loop energy circulation

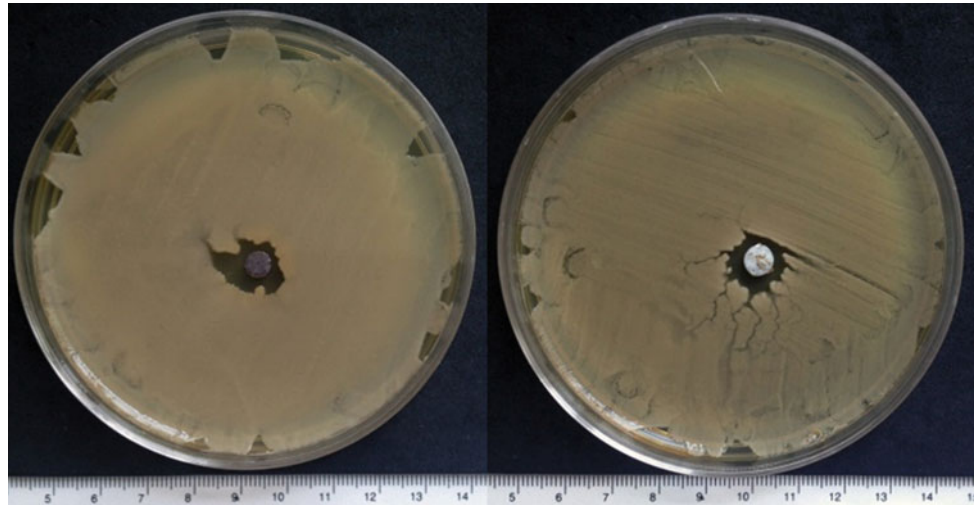


Fig. 4 The diameter of the growth retardation zone of *Acinetobacter baumannii* on agar under electrodes in a closed loop energy circulation

Conflict of Interest The authors declare that they have no conflict of interest.

References

1. Macewicz, L.L., Papuga, A.Ye., Ruban, T.P., et al.: Optimization of containing dermal coverages production for burn wound treatment at in vivo model. *Factors Exp. Evol. Org.* **22**, 287–292 (2018)
2. Vons, B.V., Chubka, M.B., Groshovyi, T.A.: Market analysis of semisolid dosage forms registered in Ukraine and research of excipient included to their formulas. *Pharm. Rev.* **1**, 55–61 (2015)
3. Sabzghabae, A.M., Abedi, D., Fazeli, H., Javadi, A., et al.: Antimicrobial resistance pattern of bacterial isolates from burn wound in an Iranian university hospital. *J. Res. Pharm. Pract.* **1**, 30–33 (2012)
4. Rezaei, E., Safari, H., Naderinasab, M., et al.: Common pathogens in burn wound and changes in their drug sensitivity. *Burns* **37**, 805–807 (2011)
5. Wang, L.F., Li, J.L., Ma, W.H., et al.: Drug resistance analysis of bacterial strains isolated from burn patients. *Genet. Mol. Res.* **13**, 9727–9734 (2014)
6. Tsyganenko, A.Ya., Tkachenko, V.L., Kovalenko, N.I., et al.: Antibiotic susceptibility of pathogens to wound infection in patients with thermal burns. *Exp Clin. Med.* **56**, 6–10 (2012)

Part XI

Molecular, Cellular and Tissue Engineering

Interaction of Quercetin with LasR of *Pseudomonas aeruginosa*: Mechanistic Insights of the Inhibition of Virulence Through Quorum Sensing

H. V. Grabski and S. G. Tiratsuyan

Abstract

Pseudomonas aeruginosa is one of the most dangerous superbugs for which new antibiotics are urgently needed. This bacterium forms biofilms that increase resistance to antibiotics and host immune responses. Current therapies are not effective because of biofilms. Biofilm formation is regulated through a system called quorum sensing, which includes transcriptional regulators LasR and RhIR. These transcriptional regulators detect their own natural autoinductors. It is known that quercetin inhibits *Pseudomonas aeruginosa* biofilm formation, but the mechanism of action is unknown. In the present study, we tried to analyse the mode of interactions of LasR with quercetin. We show that quercetin has two binding modes. One binding mode is the interaction with ligand binding domain. This interaction is not competitive and it has been shown experimentally. The second binding mode is the interaction with the “bridge”, that involves amino acids form ligand binding domain, short linker region and DNA binding domain. This part has not been shown experimentally, because LasR protein is not soluble. In our model the hydroxyl group of ring A interacts with multiple leucines during the second binding mode. This study may offer insights on how quercetin inhibits quorum sensing circuitry by interacting with transcriptional regulator LasR.

Keywords

Pseudomonas aeruginosa • Quorum sensing • Flavonoids • Molecular docking • Molecular dynamics

1 Introduction

Pseudomonas aeruginosa is one of the “ESKAPE” pathogens and has acquired resistance to commonly used antibiotics [1]. It is vital to find ways on how to counteract against it. *P. aeruginosa* is an opportunistic human pathogen and of clinical relevance, because it affects people with cystic fibrosis, cancer, burn victims, with implants and prosthetics, etc. *P. aeruginosa* uses quorum sensing system for the regulation of collective behaviors. This system controls virulence factor production. *P. aeruginosa* is pathogenic because of the synthesis of virulence factors such as proteases, rhamnolipids, hemolysins, production of antibiotic pyocyanin, Hydrogen Cyanide (HCN), secretion systems of Types 1 (T1SS), 2 (T2SS), 3 (T3SS), 4 [2], 5 (T5SS), 6 (T6SS) [3], and biofilm formation [2]. *P. aeruginosa* has four QS circuit system, which involves transcriptional regulator LasR and RhIR, which detect 3OC12 homoserine lactone and C4 homoserine lactone [4]. In our previous research, we show that there are multiple binding modes of the native ligand with the transcriptional activator LasR [5].

There have been numerous attempts for the development of *P. aeruginosa* QS inhibitors [6]. These efforts resulted in the findings of inhibitors that work in vitro, but not in vivo models in animals [7]. Most of these researches assume that the inhibitors bind to the ligand binding domain (LBD). There was also another research involving flavonoids as inhibitors of biofilm formation [8]. Flavonoids are a group of natural products and secondary metabolites of plants that exhibit broad spectrum of pharmacological activities such as antimicrobial, anti-inflammatory, etc. [9]. However, their mechanism of action is not well investigated. One such flavonoid is quercetin, which is considered as generally safe compound [8]. Hence, we analysed the molecular details of the interactions of quercetin with LasR protein. So far this is the first report that shows that the quercetin can interact as well with the “bridge” of LasR, that involves amino acids from LBD, short linker region (SLR) and DNA binding

H. V. Grabski (✉) · S. G. Tiratsuyan
Department of Medical Biology and Biotechnology, Institute of Biomedicine and Pharmacy, Russian-Armenian University, 123 Hovsep Emin str., Yerevan, Armenia
e-mail: hovakim.grabski@rau.am

domain (DBD) [5]. This study may explain why and how quercetin inhibits biofilm formation on a molecular level.

2 Methods

2.1 LasR and Quercetin Model

Previously modeled LasR monomer structure was used for the study [5]. The 2D and 3D structure of quercetin were obtained from PubChem [10] (Fig. 1). The ligand parameters were generated using the acpype tool [11] for the General Amber Force Field [12] with AM1-BCC partial charges [13].

2.2 LasR–Quercetin Ligand Blind Docking Experiments

The docking experiments of quercetin with LasR monomer were carried out using Autodock Vina [14], and it is based on the use of a rigid receptor. The whole protein conformational space was searched, using grid box dimensions $60 \times 62 \times 48 \text{ \AA}$. Following exhaustiveness values were tested in this study: 8, 16, 32, 64, 128, 256, 512, 1024, 2048 and 4096. Exhaustiveness value was increased to a value of 1024, and a maximum number of binding modes to generate set to 20. After that 100 independent docking calculations were carried out with random initial seeds. Later we verified blind docking results with rDock [15] and FlexAid [16].

2.3 Molecular Dynamics Simulations of LasR–Quercetin Systems

The same methodology was used from our previous work [5]. We conducted the MD simulations with the GROMACS suite, version 5.1.2 [17]. Amber ff99SB-ILDN force field [18] was used for the MD simulations. Structures were placed in a dodecahedron box of TIP3P water [19], to which 100 mM NaCl was added, including neutralizing counter-ions. After that two steepest descents minimization

were performed and then equilibrated in two stages. The first stage involved simulating for 200 ps under a constant volume (NVT) ensemble. The second stage involved simulating for 200 ps under a constant-pressure (NPT) for maintaining pressure isotropically at 1.0 bar.

3 Results

3.1 Docking Analysis of Quercetin with LasR Monomer

Molecular docking was used for the prediction of binding modes of quercetin with LasR monomer. Principal component analysis [20] and cluster analysis were performed on docking data using center coordinates of the conformations. There are four binding sites, cluster 1 and 3 correspond to the interaction with LBD, cluster 2 corresponds to the interaction with the “bridge”, cluster 4 is not significant since it only encompasses only 0.5% of the docking simulations.

We generated 1979 docked poses and performed representative structure extraction for use in MD simulations of the LasR-quercetin binding sites. The resulting cluster representative structures were extracted by finding the centroid conformations using method from our previous research [5]. Unfortunately, molecular docking is not appropriate for the prediction of binding affinity or binding poses of protein-ligand complexes, however, they can still provide important information [21]. For molecular dynamics simulations, we only used centroid conformations from cluster 1 and 2, since they encompass 94.29% of the docking data.

Later we corroborated the blind docking with other molecular docking software as well, which includes Autodock Vina [14], rDock [15] and FlexAid [16] (Fig. 2) and cluster 1 and 2 correspond to the common sites.

3.2 Binding Modes of Quercetin

We performed two 300 ns simulations using standard MD protocol. Overall, 600 ns of aggregate simulation data was used for the analysis of the interaction quercetin with LasR monomer. Principal component analysis was performed using conformations obtained from MD simulations. After that several rounds of agglomerative clustering were performed using the simulation data. The accuracy of the cluster analysis and an optimal number of clusters were chosen using the same methodology from our previous work [5].

Interaction of quercetin with LBD. Hydrogen and hydrophobic analysis show that nine amino acid residues interact with the ligand. Three amino acid residues, which

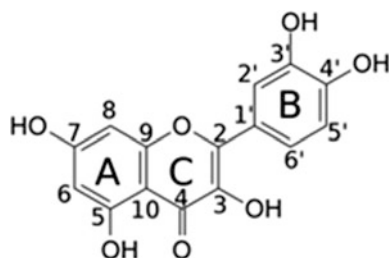
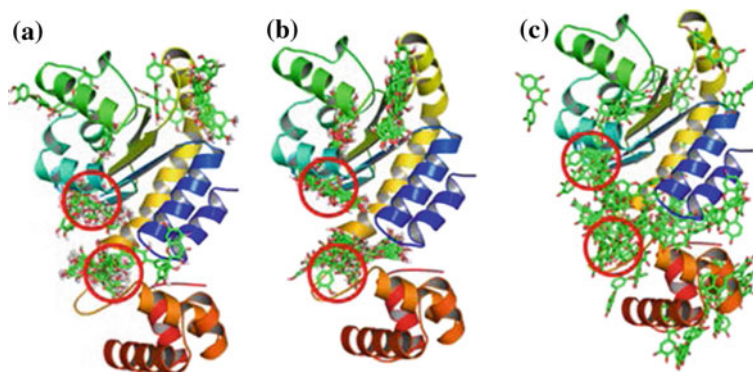


Fig. 1 2D structure of quercetin

Fig. 2 Blind docking with various molecular docking programs: **a** Autodock Vina, **b** rDock, **c** FlexAid. Red circles—binding interactions that are common for all programs



include Arg61, Ala50, Glu48, form hydrogen bonds. Six amino acid residues interact hydrophobically with quercetin (Fig. 3a). Quercetin does not enter the binding pocket, this could suggest for a ternary interaction possibility, so has been shown experimentally [8].

Interaction of quercetin with the “bridge”. Hydrogen and hydrophobic analysis show that thirteen amino acid residues interact with the ligand. Three amino acid residues, which include Glu11, Ser13, Leu177, form hydrogen bonds (Fig. 3b). Ten amino acid residues interact hydrophobically with quercetin.

3.3 Binding Energy of Quercetin to LasR

In order to analyse the binding sites in detail, MMPBSA [22] binding energy calculation was performed for each binding site based on the trajectories. It is also interesting that quercetin does not compete for the LBD (Table 1), which has also been shown experimentally [8]. But the results suggest that the interaction of quercetin with the “bridge” is

not competitive, but allosteric. More detailed analysis of the energy terms showed that Van der Waals, electrostatic interactions, and non-polar solvation energy contribute negatively to the binding energy while polar solvation energy contributes positively. Electrostatic interaction contributes most in the terms of negative contribution for both cases, but for the interaction with the LBD-SLR-DBD “bridge”, the electrostatic interaction is 1.95 times higher than with the LBD interaction.

4 Conclusions

From the simulations, it can be concluded that quercetin can bind both to LBD and to “bridge” of transcriptional regulator LasR. This suggests that there are multiple binding modes rather than one. From experimental studies, it has been shown that hydroxyl group at position 7 of ring A is important for inhibitory activity. In our case, it is visible that quercetin interacts with Leu177 with hydroxyl group at position 7 from ring A. This amino acid residue is a conservative and from the short linker region between LDB and DBD. This could explain that quercetin inhibits DNA binding by preventing hinge rotation of DBD. The interaction with the LBD-SLR-DBD “bridge” is a novel site. The analysis of binding energy shows that the interaction of quercetin with “bridge” is not competitive. Conservative amino acids such as Leu177, Leu236, Lys182, Lys218 contribute most during the interaction with LBD-SLR-DBD “bridge”. This could suggest that the interaction of quercetin with the “bridge” is necessary for the inhibition of DNA binding capability. This study may reveal new insights of the interactions of the quercetin with transcriptional regulator LasR of *P. aeruginosa*. Results from this study may explain why quercetin is effective at inhibiting transcriptional regulator LasR and thus stop biofilm formation and virulence gene expression.

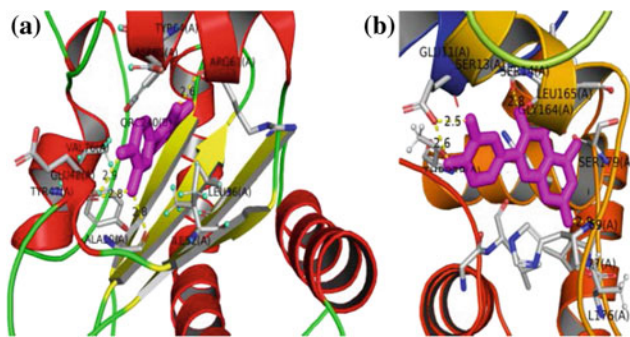


Fig. 3 Schematic and 3D representation of hydrogen and hydrophobic interactions of quercetin with LasR: **a** LBD, **b** LBD-SLR-DBD “bridge”

Table 1 Relative Binding energy using g_mmpbsa on simulation data

Binding sites	Van der waals (kJ/mol)	Electrostatic (kJ/mol)	Polar salvation (kJ/mol)	Non-polar salvation (kJ/mol)	Binding energy (kJ/mol)
3OC12 HSL-LBD	-215.673 ±8.007	-39.586 ±18.817	147.522 ±13.978	-20.840 ±0.794	-128.578 ±18.757
3OC12 HSL- "bridge"	-205.141 ±11.803	-142.974 ±29.032	201.889 ±20.117	-20.230 ±0.842	-166.456 ±20.492
QRC-LBD	-148.890 ±14.038	-123.004 ±33.612	158.564 ±14.347	-16.113 ±0.657	-129.443 ±19.319
QRC-"bridge"	-129.937 ±15.771	-240.057 ±23.884	201.062 ±11.982	-14.983 ±0.545	-183.915 ±16.249

Acknowledgements We thank Yerevan Physics Institute for providing time on the cluster for the molecular dynamics simulations.

Conflict of Interest The authors declare that they have no conflict of interest.

References

- Davies, J., Davies, D.: Origins and evolution of antibiotic resistance. *Microbiol. Mol. Biol. Rev.* **74**, 417–433 (2010)
- Coggan, K., Wolfgang, M.: Global regulatory pathways and cross-talk control *Pseudomonas aeruginosa* environmental life-style and virulence phenotype. *Curr. Issues Mol. Biol.* **14**, 47 (2012)
- Filloux, A.: Protein secretion systems in *Pseudomonas aeruginosa*: an essay on diversity, evolution, and function. *Front. Microbiol.* **2**, 155 (2011)
- Pearson, J.P., et al.: A second N-acylhomoserine lactone signal produced by *Pseudomonas aeruginosa*. *PNAS* **92**, 1490–1494 (1995)
- Grabski, H., et al.: Interaction of N-3-oxododecanoyl homoserine lactone with transcriptional regulator LasR of *Pseudomonas aeruginosa*: insights from molecular docking and dynamics simulations. *F1000Res* **8** (2019)
- Welsh, M.A., et al.: Small molecule disruption of quorum sensing cross-regulation in *Pseudomonas aeruginosa* causes major and unexpected alterations to virulence phenotypes. *J. Am. Chem. Soc.* **137**, 1510–1519 (2015)
- Smith, R.S., Iglewski, B.H.: *Pseudomonas aeruginosa* quorum sensing as a potential antimicrobial target. *J. Clin. Invest.* **112**, 1460–1465 (2003)
- Paczkowski, J.E., et al.: Flavonoids suppress *Pseudomonas aeruginosa* virulence through allosteric inhibition of quorum-sensing receptors. *J. Biol. Chem.* **292**, 4064–4076 (2017)
- Kumar, S., Pandey, A.K.: Chemistry and biological activities of flavonoids: an overview. *Sci. World J.* (2013)
- Bolton, E.E., et al.: PubChem: integrated platform of small molecules and biological activities. *Annu. Rep. Comput. Chem.* **4**, 217–241 (2008)
- da Silva, A.W.S., Vranken, W.F.: ACPYPE-Antechamber python parser interface. *BMC Res. Notes* **5**, 367 (2012)
- Wang, J., et al.: Development and testing of a general amber force field. *J. Comput. Chem.* **25**, 1157–1174 (2004)
- Jakalian, A., et al.: Fast, efficient generation of high-quality atomic charges. AM1-BCC model: II. Parameterization and validation. *J. Comput. Chem.* **23**, 1623–1641 (2002)
- Trott, O., Olson, A.J.: AutoDock Vina: improving the speed and accuracy of docking with a new scoring function, efficient optimization, and multithreading. *J. Comput. Chem.* **31**, 455–461 (2010)
- Ruiz-Carmona, S., et al.: rDock: a fast, versatile and open source program for docking ligands to proteins and nucleic acids. *PLoS Comput. Biol.* **10**, e1003571 (2014)
- Gaudreault, F., Najmanovich, R.J.: FlexAID: revisiting docking on non-native-complex structures. *J. Chem. Inf. Model.* **55**, 1323–1336 (2015)
- Abraham, M.J., et al.: GROMACS: high performance molecular simulations through multi-level parallelism from laptops to supercomputers. *SoftwareX* **1**, 19–25 (2015)
- Lindorff-Larsen, K., et al.: Improved side-chain torsion potentials for the Amber ff99SB protein force field. *Proteins* **78**, 1950–1958 (2010)
- Jorgensen, W.L., et al.: Comparison of simple potential functions for simulating liquid water. *J. Chem. Phys.* **79**, 926–935 (1983)
- Hotelling, H.: Analysis of a complex of statistical variables into principal components. *J. Educ. Psychol.* **24**, 417 (1933)
- Chen, Y.C.: Beware of docking! *Trends Pharmacol. Sci.* **36**, 78–95 (2015)
- Kumari, R., et al.: g_mmpbsa a GROMACS tool for high-throughput MM-PBSA calculations. *J. Chem. Inf. Model.* **54**, 1951–1962 (2014)

Mechanical and Morphological Characterization of Decellularized Umbilical Vessels as Tissue Engineering Scaffolds

T. Malcova, L. Globa, A. Vascan, E. Țugui, A. Stoian, and V. Nacu

Abstract

Cardiovascular diseases are the number one cause of morbidity and mortality globally. Numerous pathophysiological modifications that develop are associated with the stenosis and occlusion of blood vessels and tissue damage due to inadequate nutrient supply. Despite a variety of therapies available today, the preferred treatment for the long-term revascularization is artery bypass surgery. The autologous vessels are considered the “gold” standard treatment for this category of patients; unfortunately, they are often unavailable due to comorbidities or unsuitable for use. Synthetic scaffolds are suitable in large-diameter arteries (>8.0 mm) and medium-diameter arteries (6.0–8.0 mm), but are of limited use in small-diameter vessels (<6.0 mm) due to poor patency rates. However, tissue engineering may be an option to overcome the existing practical issue. Thus, tissue engineered vascular grafts (TEVGs), namely decellularized matrix, are suggested to present an appropriate graft alternative; as a result, increasing interest is dedicated to this field. By decellularization the loss of major histocompatibility complex (MHC) is induced. Consequently, the risk of development of an immunological response by the host is reduced. Undoubtedly, the acellular scaffolds have a lot of advantages. There are reports about different decellularization techniques already, such as physical, chemical and biological methods. Unfortunately, information about combination and comparison between them are not sufficient. This study aimed to contrast three different methods (the enzymatic method with 0.25% trypsin; the chemical method with 1% SDS and the combined method with 0.25% trypsin and 1% SDS) to decellularize umbilical vessels as a TEVG of a small

diameter and test histological and physical properties. In addition, a short overview of advantages and disadvantages of existing protocols is also presented.

Keywords

Cardiovascular diseases • Tissue engineering • Decellularized biological scaffold • Extracellular matrix • Mechanical properties

1 Introduction

Cardiovascular diseases (CVDs) are the leading cause of death worldwide and the number of patients who are suffering from CVD is growing (WHO). According to the latest statistics in the field it is predicted that the annual incidence of CVD—related mortalities will rise to 23.3 million globally by 2030 [1]. Common presentations are cerebrovascular diseases, coronary heart disease, peripheral arterial disease, and deep vein thrombosis. Numerous problems included in the list above are related to a condition called atherosclerosis, pathophysiologically characterized as narrowing or blockage of the luminal diameter by a plaque—a deposition of cholesterol, lipids, and calcium. Because of the presence of this buildup inside the arteries the blood flow through the affected vessels is diminished or inhibited. It leads to tissue damage due to inadequate nutrient and oxygen supply [2, 3].

Treating atherosclerosis is an important clinical issue, because just in this way serious complications may be avoided. A variety of therapies is available today—from dietary and lifestyle modification to pharmaceutical therapies and endovascular or surgical interventions [4]. Unfortunately, changes of living style (healthy eating, weight management, exercise therapy, and smoking cessation) and adequate pharmaceutical therapy (cholesterol-lowering drugs, antiplatelet and anticoagulants, beta-blockers, calcium channel blockers, diuretics, and vasodilators) are not always sufficient to prevent complications and to improve

T. Malcova (✉) · L. Globa · A. Vascan · E. Țugui · A. Stoian · V. Nacu

Laboratory of Tissue Engineering and Cell Cultures, Nicolae Testemitanu State University of Medicine and Pharmacy, 165, Stefan Cel Mare Si Sfânt, Bd., Chisinau, Republic of Moldova
e-mail: malcovatiana92@mail.ru

the patients' life expectancy. In cases when the symptoms are severe interventional procedures are needed, such as endovascular procedures and vascular grafting [5].

Endovascular procedures with percutaneous transluminal balloon angioplasty, stenting or atherectomy offer many advantages, but cannot be accomplished frequently because of impossibility to pass the catheter through the narrowed area or plaque's calcification. In addition, the risk of restenosis is still high [6]. The preferred treatment of advanced atherosclerosis for the long-term revascularization of occluded vessels (when life expectancy is more than 2 years) is more invasive surgery utilizing vascular grafts [7].

Currently, four types of conduits for vascular grafting are available, such as autografts, allografts, xenografts, and synthetic vascular grafts. Autologous vascular substitutes (greater saphenous vein, lesser saphenous vein, radial artery, and internal mammary artery) are considered the gold standard material and the best solution in bypass surgery of blood vessels because they possess the most physiological properties and exhibit excellent patency [8]. However, this approach is not always feasible. For instance, in up to 40% of patients the tissue's sources may be inadequate or unavailable, most vessels being affected by diffuse atherosclerotic abnormalities, previous phlebitis, vessel removal, varicosities, hypoplasia or anatomical unsuitability [9]. Moreover, extraction's procedure adds time, cost and the potential for additional morbidity due to the surgical procedure. In addition, despite good clinical performance, autologous native vessels are also liable to atherosclerosis and intimal hyperplasia occurring throughout the length [10].

Allografts (ascending thoracic aorta, aortic arch, descending thoracic aorta, abdominal aorta) are considered superior to artificial prostheses due to relatively resistance to infection, minimal thromboembolic complications, and avoidance of anticoagulation, but inferior to autologous vascular substitutes. However, restrictions include their limited availability and durability due to calcification, aneurysmal dilatation, and rupture [11].

Published reports about the application of xenografts indicate a high incidence of complications, the main disadvantages of this material are aneurysmal degradation, infections, early thrombosis, considerable cost, and non-availability of the graft in different dimensions [12]. Thereby, use of xenografts cannot be recommended for vascular reconstruction due to not encouraging long-term results.

Synthetic vascular grafts (ePTFE, PET, Polypropylene, Polyamide, and Polyurethanes) are an alternative to autologous vessels, but they are not suitable for small-diameter arteries (<6.0 mm). They fail to "bio-integrate" after implantation in vivo and are accompanied by poor patency rates due to intimal hyperplasia and thrombosis [13].

Because the limitations of currently available conduits are obvious, tissue engineering seems to be an attractive solution for development of an "ideal" conduit for vascular surgery. In this context, decellularized matrices have gained important attention in the field and have already demonstrated good results in animal models [14]. A decellularization technique should satisfy several critical issues: to preserve the composition and 3D-structure of extracellular matrix (ECM), to eliminate the heterogenic antigen, and to reduce the immunogenicity of ECMs. There are different decellularization techniques, such as physical (freezing-thawing, radiation), chemical (acid and alkaline solutions, osmotic shock, detergents) and biological (enzymes, chelating agents). The efficiency of many protocols is evaluated already; however, the best decellularization method for a suitable tissue-engineered small-diameter vascular scaffold still does not exist [9].

In this study we performed decellularization of umbilical vessels by three different methods with respect to biomechanical stability to evaluate their potential for human use.

2 Materials and Methods

Human umbilical arteries for the experiment were extracted under clean conditions during the first 4 h after birth (4 ± 0.8 h). The study was carried out under the approval of the Ethical Committee of the Nicolae Testemitanu State University of Medicine and Pharmacy. After extracting, the vessels were rinsed with phosphate-buffered solution (PBS) to remove blood clots and clean the lumen and then transferred to the Laboratory for processing.

The vessels were cut into short pieces of 4.0 cm in length and randomly assigned to four different groups ($n = 6$), then the tissues were subjected to decellularization using three different methods (one group was used as control). The vessels were connected to an infusion system. The advantage of this system is double concentric effect on the graft wall: the effect of the decellularization solution within the lumen and action from the outside. The solution was continuously infused through the lumen of the vessel immersed in solution, which allowed decellularization through continuous washing with the solution flow passing through the vessel, an effect that intensified the solution action from the outside of the vessel. Due to advantages of this technique it was possible to reduce the overall time of tissue exposure to the action of decellularization solution (the process lasted 3.5 h) and to reduce the damage of the extracellular components (compared to other "traditional" methods the decellularization process requires up to 24 h or even more).

Decellularization was performed using three different methods: chemical with detergent, enzymatic and combined (enzyme + detergent).

Chemical method (1% SDS)

This method consists of treating the vessel in PBS with 1% SDS for 3.5 h.

Enzymatic method (0.25% Trypsin)

The enzymatic method is similar to the previous one, but the vessels were treated in PBS with 0.25% trypsin and 0.01% EDTA (divalent cations Ca^{2+} , Mg^{2+} chelator to prevent cell-cell and cell-matrix adhesion).

Combined method (1% SDS + 0.25% Trypsin)

The method consists of two consecutive steps:

The first step involves the use of 0.25% trypsin and 0.01% EDTA. This solution circulated through the vessel lumen for 30 min. Afterwards the arteries were washed with PBS for 15 min to remove residual enzymatic substances.

The second step consists of treating the vessel with 1% SDS for 3 h, with subsequent washing with PBS to remove the chemical agent.

The decellularized vessels were subjected to morphological macro- and microscopic examination. Then pressure and stretch resistance tests were performed.

Histological and histochemical methods

Primary processing of the material was similar in all morphological and histochemical methods used in the study. The harvested specimens were fixed in 10% buffered formalin for 48 h, then embedded in paraffin according to the standard

method. Then 5 μm thick sections were cut and mounted on usual histological slides for next processing step.

For histological observation the sections were stained with hematoxylin-eosin (HE). In order to highlight the degree of collagenization of vessels, Masson's trichrome staining was performed. In addition silver impregnation was carried out to highlight the reticular fibers.

The microscopic examination and imaging was performed with Nikon Eclipse E600 and Nikon Eclipse 80i microscopes. The images were captured in JPEG format.

3 Results

Morphological examination of umbilical arteries

The umbilical cord contains two arteries and one vein, suspended in an extracellular hydrated matrix known as Wharton's jelly. The umbilical vessels differ structurally from the same caliber vessels in the body. These vessels are free of adventitia, external elastic membrane, and vaso-vasorum. The umbilical arteries' lumen has an irregular and branched outline, while the cross-sectioned vein presents a wide lumen. The umbilical vessels are covered by endothelium, the nuclei of endothelial cells are protruding, versus arteries' ramifications where the endotheliocytes' nuclei are flattened. The intima thickness in arteries is greater than in veins. The internal elastic membrane has a discontinuous structure or is absent in arteries, in contrast to veins, where it is continuous (Fig. 1).

When treating umbilical arteries with different decellularization solutions, variable degree of decellularization was

Fig. 1 Morphological aspects of umbilical vessels, HE staining: **a** umbilical artery with an irregular lumen and vein with a broad lumen; **b–d** umbilical vessels: endothelial cells with prominent nuclei and in areas of artery ramifications flattened nuclei. **a**, **c** $\times 2.5$; **b** $\times 10$; **d** $\times 20$

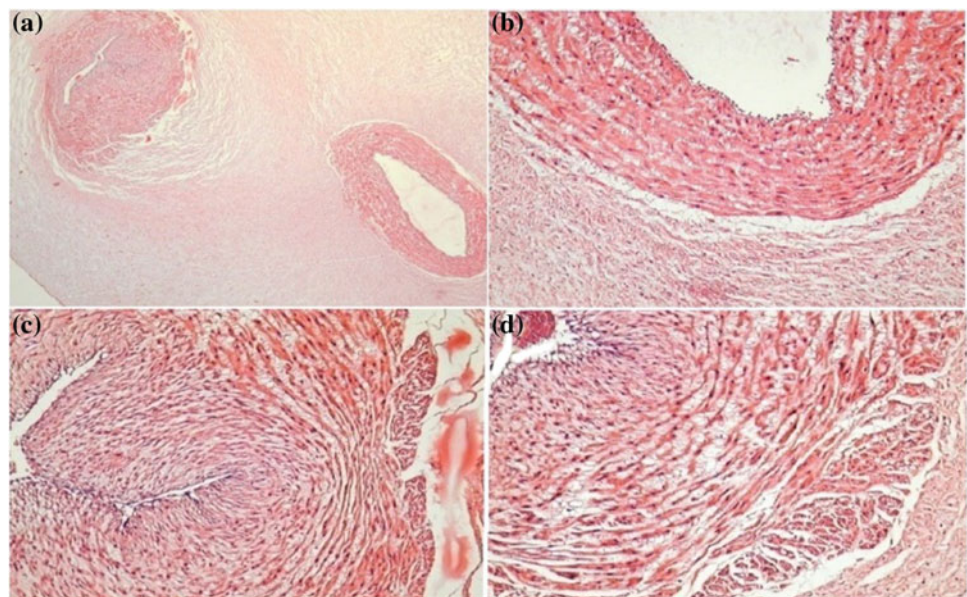
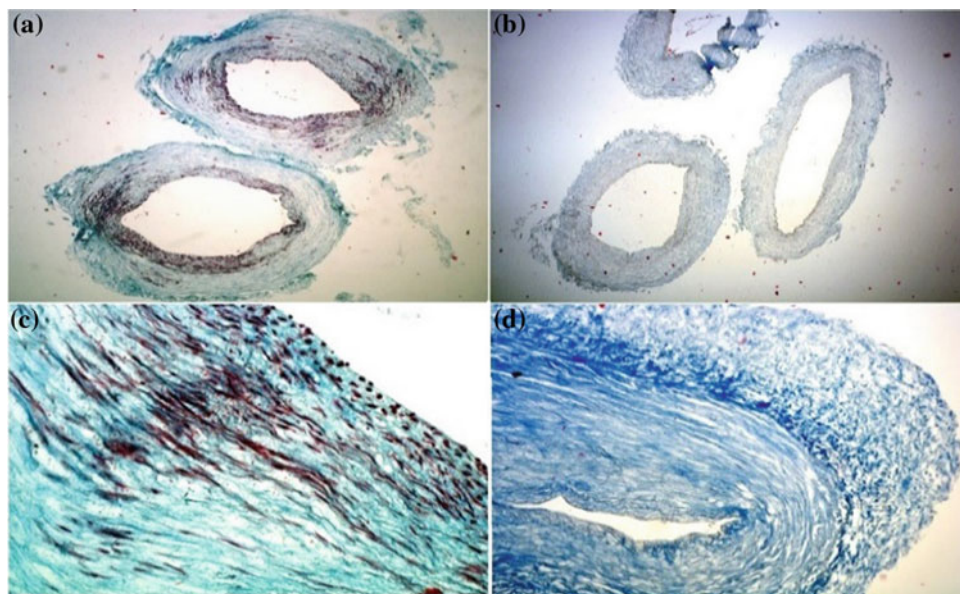


Fig. 2 Cross sections of umbilical artery, Masson's trichrome staining: **a, b** arteries decellularized by the enzymatic method-incomplete and non-uniform decellularization of arterial media, numerous myocytes with changed morphology; **c, d** arteries decellularized by chemical method-complete decellularization, only fibrillary component highlighted. **a, c** $\times 2.5$; **b, d** $\times 20$



observed. The degree of decellularization with 0.25% trypsin is incomplete. In the histological section the cell nuclei were found. Under the action of trypsin the myocytes changed not only quantitatively but qualitatively too, their size reduced, the cytoplasmic volume decreased. The cell became flatter, the nucleus showed a high degree of degeneration, and some myocytes had even pyknotic nuclei.

There was also observed a variability in the morphological character of the collagen matrix depending on the method used. Thus, under the lytic action of trypsin solution the collagen fibers were much thinner and dissociated, arranged discontinuously, and the wavy character of fibers disappeared. Virtually in all areas of the arterial wall the fibers appeared to have low intensity staining. The fibrillary framework in arteries decellularized by the chemical and combined methods showed a low degree of dissociation, being characterized by numerous collagen fibers retaining their wavy feature (Fig. 2).

Stretch test

Nine decellularized fragments were used for stretch test (3 from each group) and 3 arteries from control group. The stretching was done using a dynamometer (maximal force 5 N) and a fastening system. The vessel was stretched until it tore and the rupture force was recorded (Table 1).

Table 1 Rupture force of the umbilical arteries

Stretching	1 (N)	2 (N)	3 (N)	Mean \pm SD
Combined	1.8	1.85	1.75	1.8 \pm 0.05
Trypsin	1.55	1.5	1.55	1.53 \pm 0.03
SDS	1.75	2.0	1.75	1.83 \pm 0.14
Control sample	2.5	2.5	2.0	2.33 \pm 0.29

Pressure resistance test

The air pump device "SANGVINOTEST" was used for this test. One end of the vessel was connected to it and the other end was clamped. The maximum airflow pressure that the device may form and record is 280 mmHg, with an accuracy of ± 0.2 mmHg. The air was pumped to the maximum value or vessel rupture with the subsequent digital recording of the maximum pressure on the device display.

The inflation test was carried out to evaluate the ability of the vessels to withstand the pressure of 280 mmHg, which is unlikely in the recipient's cardiovascular system. All the vessels withstood the maximum inflation pressure.

4 Discussion

Decellularization means complete removal of the cellular and nuclear material from a tissue with preservation of its native ECM and original mechanical properties. By elimination of cell antigens, including HLA antigen, after transplantation of acellular matrix the rejection response can be avoided. The concept of using this complex framework with a relative intact vascular structure for building new organs has piqued researches' imagination already. Decellularization seems to

be an attractive option for development of biocompatible and compliant vascular graft too.

In the present study 3 (three) methods of decellularization were described. An “ideal” method should be focused on dissolving cells and rinsing cell residuals with a less ECM-damaging solution. After comparison of three different techniques, it appears that just combined method can decompose the cellular membrane efficiently with elimination of cellular components and preservation of ECM’s biomechanical properties. The method implies treating the vessel with trypsin, thus ensuring cells’ detachment from the extracellular matrix by the proteolytic action at the level of intercellular proteins. The second solution, SDS, is a detergent which lyses the cell membrane. Thus, the cellular component of tissue appears completely destroyed and its immunogenicity is reduced. The stretch test results show no significant difference between this group and intact vessels ($p > 0.05$). Maximum inflation test of the arteries with 1.00 SANGVINOTEST device indicates a maximum resistance to pressure of 280 mmHg in all cases.

5 Conclusions

1. Combined method (enzyme-detergent) is an efficient decellularization method that can be recommended for development of tissue-engineered small-diameter vessels.
2. By transplantation of a decellularized allograft covered by recipient’s stem cells the rejection reaction can be avoided. These issues will be explored in the future.

Acknowledgements This study was supported by the institutional project 15.817.04.04.F, Laboratory of Tissue Engineering and Cell Cultures, Nicolae Testemitanu State University of Medicine and Pharmacy, Chisinau, Republic of Moldova.

Conflict of Interest The authors declare that they have no conflict of interest.

References

1. Mathers, C., Loncar, D.: Projections of global mortality and burden of disease from 2002 to 2030. *PLoS Med* **3**(11), e442 (2006). <https://doi.org/10.1371/journal.pmed.0030442>
2. Clapp, C.: Senior Project: Evaluation of Decellularization Procedures for Porcine Arteries. Faculty of the Biomedical Engineering Department, California Polytechnic State University, San Luis Obispo (2012)
3. Pashneh-Tala, S., MacNeil, S., Claeysens, F.: The tissue-engineered vascular graft—past, present, and future. *J. Tissue Eng. Part B* **22**(1), 68–100 (2016). <https://doi.org/10.1089/ten.teb.2015.0100>
4. Abdulhannan, P., Russell, D., Homer-Vanniasinkam, S.: Peripheral arterial disease: a literature review. *Br. Med. Bull.* **104**, 21–39 (2012). <https://doi.org/10.1093/bmb/lds027>
5. Benjamin, E., Blaha, M., Chiuve, S., et al.: Heart disease and stroke statistics—2017: a report from the American Heart Association. *Circulation* **135**(10), e146–e603 (2017). <https://doi.org/10.1161/CIR.0000000000000485>
6. Serruys, P., Kutryk, M., Ong, A.: Coronary-artery stents. *N. Engl. J. Med.* **354**(5), 483–495 (2006). <https://doi.org/10.1056/NEJMra051091>
7. Weintraub, W., Grau-Sepulveda, M., Weiss, J.: Comparative effectiveness of revascularization strategies. *N. Engl. J. Med.* **366**, 1467–1476 (2012). <https://doi.org/10.1056/NEJMoa1110717>
8. Chlupáč, J., Filová, E., Bacáková, L.: Blood vessel replacement: 50 years of development and tissue engineering paradigms in vascular surgery. *Physiol. Res.* **58**(Suppl 2), S119–S139 (2009)
9. Boccafoschi, F., Botta, M., Fusaro, L., et al.: Decellularized biological matrices: an interesting approach for cardiovascular tissue repair and regeneration. *J. Tissue Eng. Regen. Med.* **11**(5), 1648–1657 (2017). <https://doi.org/10.1002/term.2103>
10. Ravi, S., Chaikof, E.: Biomaterials for vascular tissue engineering. *Regen. Med.* **5**(1), 107–120 (2010). <https://doi.org/10.2217/rme.09.77>
11. Koskas, F., Goëau-Brissonnière, O., Nicolas, M., et al.: Arteries from human beings are less infectible by *Staphylococcus aureus* than polytetrafluoroethylene in an aortic dog model. *J. Vasc. Surg.* **23**(3), 472–476 (1996)
12. Dale, W., Lewis, M.: Modified bovine heterografts for arterial replacement. *Ann. Surg.* **169**, 927–946 (1969)
13. Li, S., Henry, J.: Nonthrombogenic approaches to cardiovascular bioengineering. *Ann. Rev. Biomed. Eng.* **13**, 451–475 (2011). <https://doi.org/10.1146/annurev-bioeng-071910-124733>
14. Syedain, Z., Meier, L., Lahti, S., et al.: Implantation of completely biological engineered grafts following decellularization into the sheep femoral artery. *Tissue Eng. Part A* **20**, 1726–1734 (2014). <https://doi.org/10.1089/ten.TEA.2013.0550>

The Procedure of Bone Cells Obtaining, Culture and Identification

M. Jian, V. Cobzac, A. Mostovei, and V. Nacu

Abstract

Isolation of bone cells represent a major importance in laboratory research and clinical practice. This work was conducted on six 6 ± 1.5 months Wistar rats from which the diaphysis of long tubular bones were harvested, followed by mechanical removal of all tissues excepting the bone tissue with further chopping. The chopped bone tissue (ChBT) was processed by two ways, each of them was followed by two methods of bone cells isolation and culture: through explant and enzymatic digestion. Obtaining of bone cells through the explant method in both ways, was more effective compared to enzymatic digestion. Also, there was no significant difference between the amounts of cells obtained between both bone processing protocols. The obtained bone cells were identified following morphological changes and Alizarin red staining after cells culture in over-confluence.

Keywords

Bone cells • Isolation • Culture • Identification • Enzymatic digestion • Explant

1 Introduction

Bone tissue exerts important functions of the body: like movement, support and protection of soft tissues, participates in the metabolism of calcium and phosphorus, and shelters the bone marrow [1]. Although, the bone appears to

be an inert organ, he has a great dynamicity, characterized by permanent remodeling, done by bone cells: osteoblasts, osteocytes and osteoclasts [1, 2].

Nowadays, the experimental studies on bone cells are of a high interest in laboratory practice needed for understanding bone biology [1, 2]. Their utilisation in various tests, for in vitro assessment of different substances and structures effects over them. Also, the bone cells can be used in regenerative medicine as source of bone formation [3].

The purpose of this study is to compare two bone processing protocols with further bone cells isolation and culture through explant and enzymatic digestion methods.

2 Materials and Methods

The extraction and experiments with rat cells, tissues and organs was approved by ethics committee of Moldovan State University of Medicine and Pharmacy “Nicolae Testemitanu” on 18.06.2015, No. 60.

2.1 Preparation of Reagents for Isolation, Culture and Preservation of Bone Cells

1. Enzymatic solution I consists of 300 U/ml clostridium histolyticum collagenase (Sigma, UK) in α -MEM with antibiotics-antimycotics (HiMedia, India)
2. Enzymatic solution II consists of 125 U/ml clostridium histolyticum collagenase (Sigma, UK) and 1 U/ml dispase (HiMedia, India) dissolved in α -MEM with antibiotics-antimycotics (HiMedia, India)
3. 0.25% trypsin solution, without EDTA, obtained by dissolving bovine pancreatic trypsin (Sigma, USA) in HBSS without Ca^{2+} and Mg^{2+} , with phenol red (HiMedia, India)
4. 5 mM EDTA solution (Sigma, Germany) with 0.1% albumin from bovine serum (HiMedia, India) with pH 7.2–7.4.

M. Jian (✉) · V. Cobzac · A. Mostovei · V. Nacu
Laboratory of Tissue Engineering and Cells Cultures, State Medical and Pharmaceutical University “Nicolae Testemitanu”,
Bd. Stefan Cel Mare 165, Chisinau, Republic of Moldova
e-mail: mariana.jian@usmf.md

V. Cobzac
e-mail: vitaliecobzac@yahoo.com

5. α -MEM with antibiotics-antimycotics (HiMedia, India)
6. HBSS without Ca^{2+} , Mg^{2+} and phenol red with antibiotics-antimycotics (HiMedia, India)
7. Culture medium α -MEM with antibiotics-antimycotics (HiMedia, India) and 10% FBS (Lonza, Belgium)
8. Culture medium DMEM/Ham's F-12 (Sigma, UK) with antibiotics-antimycotics (HiMedia, India) and 10% FBS (Lonza, Belgium)
9. FBS (Lonza, Belgium) with 5% DMSO (OriGen Biomedical, Germany).

All solutions were filtered through 0.22 μm filtration systems or syringe filters (Sofra, China). During the researches, prepared solutions and culture media was stored in refrigerator at 4–8 °C, and the enzymatic solutions in freezer at –24 °C.

2.2 Isolation and Culture of Cells from Bone Tissue

Before isolation and culture of cells from bone tissue, all solutions and culture media were heated to 37 °C in water bath (BAE-2, RAYPA).

The cells were obtained from long tubular bones of 6 Wistar rats, 6 \pm 1.5 months old. Following the euthanasia, humeral, femoral and tibial bones were harvested. With an osteotome, the meta-epiphyseal areas were dissected, followed by complete periosteum removal from the diaphysis with a scalpel. After, the medullary canal was washed in jet till the complete removal of bone marrow with a syringe filled with α -MEM with antibiotics-antimycotics. Then, the bones were chopped with an osteotome and a scalpel to approximately 1 \times 1 mm, followed by two washings with HBSS without Ca^{2+} , Mg^{2+} and phenol red with antibiotics-antimycotics. The chopped bone tissue (ChBT) was transferred in equal quantities into four wells of a 12-well plate. For bone tissue processing we tested 2 protocols. In each protocol we used three rats.

Protocol I for bone tissue processing: After transfer of ChBT into the plate, into the wells with bone were poured by 2 ml of enzymatic solution I, followed by plate incubation for 25 min on orbital shaker (ES-20, Biosan) at 37 °C, 150 rpm. Bone fragments were washed 3 times with HBSS without Ca^{2+} , Mg^{2+} and phenol red with antibiotics-antimycotics. Collagenase digestion was repeated for two more times, after which ChBT were incubated in 4 ml of 5.5 mM EDTA solution with 0.1% albumin from bovine serum and stirred in the same conditions and washed again for three times. Collagenase digestion was repeated for two more times, with subsequent washes, after which the ChBT were treated again with EDTA and albumin from bovine serum solution. The ChBT from half wells were washed with

5 ml culture medium α -MEM with antibiotics-antimycotics and 10% FBS, followed by transfer of ChBT into 25 cm² cell culture flask (Nunc, Denmark), to obtain bone cells through the explant pathway. The ChBT from the rest of the wells subjected again three times collagenase digestion with subsequent washings and one treatment with EDTA and albumin from bovine serum solution as described above. But, after each digestion and wash, the used solutions were collected in 15 ml tubes, centrifuged at 170 g for 5 min. The supernatant was discarded and the cells were resuspended in 1 ml of culture medium α -MEM with antibiotics-antimycotics and 10% FBS, transferred in 24-well plate and incubated at 37 °C with 5% CO₂ (SMART CELL, Heal Force).

Protocol II for bone tissue processing: Into the plate, in wells with ChBT were poured by 3 ml of 0.25% trypsin solution and incubated for 25 min on orbital shaker at 37 °C, 150 rpm (ES-20, Biosan), followed by washing. The ChBT underwent enzymatic digestion with 2 ml of enzymatic solution II in the same conditions. The digestion was repeated two more times, followed by washings and further incubation of ChBT with 4 ml of EDTA and albumin solution followed by subsequent washings as described above. Collagenase and dispase digestion was repeated twice in the same conditions with washings with repeated treatment with EDTA and albumin solution. As in previous protocol, the ChBT was washed with 5 ml of culture medium, followed by transfer of ChBT into 25 cm² cell culture flask (Nunc, Denmark), to obtain bone cells through the explant pathway. The ChBT from the other wells were digested with enzymatic solution II for three times, treated with EDTA and albumin solution in the same conditions with the subsequent washes. As in Protocol I, after each digestion and wash, the cells were isolated and incubated with 1 ml of the same culture medium in 24 well plates at 37 °C with 5% CO₂ (SMART CELL, Heal Force).

The ChBT introduced into 25 cm² cell culture flask (Nunc, Denmark) and the cells obtained after enzymatic digestions and washings has been cultivated up to a 60–70% confluence, followed by cell detachment through trypsinization. The cells were counted and cryopreserved by 5 \times 10⁵ cells/ml in FBS (Lonza, Belgium) with 5% DMSO (OriGen Biomedical, Germany) at –84 °C.

2.3 Identification of Obtained Cells from ChBT

The preserved cells obtained with Protocol I and II were thawed and cultured with DMEM/Ham's F-12 medium with antibiotics-antimycotics and 10% FBS for 18 days to get a significant over-confluence. Parallel, as control probe were cultivated bone marrow mesenchymal stem cells (BMMSCs), also obtained from rat after washing the

medullary canals of diaphyses and metaphyses of long tubular bones, with subsequent processing and cultivation as described [4]. All cells were grown under the same conditions with the same culture medium in 25 cm² cell culture flask (Nunc, Denmark), in cell incubator (SMART CELL, Heal Force) at 37 °C, 5% CO₂. Cell growth was assessed at 7, 13, and 18 days. At 18th day of culture the over-confluent cells were stained with Alizarin red to determine bone formation [5, 6].

3 Results

Following the isolation and primary culture of cells from bone tissue by explant and enzymatic digestion methods, using both protocols for ChBT treatment, we determined that obtaining the cells from bone tissue by explant method is more efficient, faster and cheaper. However, there was not a big difference between obtained results in cells isolation from ChBT using Protocols I and II, both protocols seem to be equally efficient in cultivation time and number of obtained cells by explant and enzymatic digestion methods ($p < 0.5$) (Figs. 1, 2 and 3).

Isolation of cells from long tubular bones by enzymatic digestion was deficient due to their small number, resulting in a lack of cell growth and multiplication in several wells (Tables 1 and 2). Isolation of bone cells by explant has proven to be more effective, this allowed to obtain during in the same cell culture period 3 times more cells comparatively to enzymatic digestion ($p < 0.0001$).

The cells isolated from ChBT after processing according to Protocols I and II, were identified as bone cells after 18 days of culture to obtain over-confluence. As a control, parallelly under the same conditions, BMMSCs were cultured. Thereby, at the 7th day of cell culture, in flasks with cells obtained from bone were determined formation of cellular bridges as a result of cellular overlapping proliferation. There is also initiation of collagen synthesis and calcium deposition. At 13th day the formation of mineralized nodules is determined, as on the 18th day they becomes more hypertrophied and opaque. After staining the cells obtained from bone tissue with Alizarin red, there was determined a dark red staining of the nodules, confirming

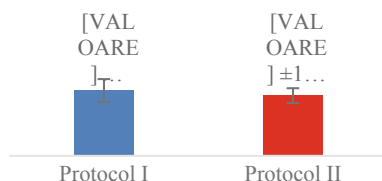


Fig. 1 Obtained cells culture period

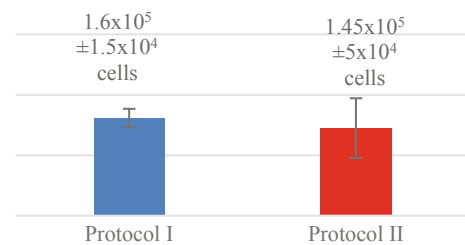


Fig. 2 Cells obtained through enzymatic digestion method

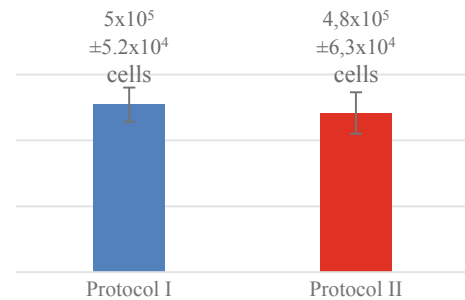


Fig. 3 Cells obtained through explant method

this way the presence of bone cells in the flasks. In the control flask, with BMMSCs cultured in over-confluence, were determined morphological changes different from those of bone cells, and after staining with Alizarin red, the color was not retained (Fig. 4).

4 Discussions

The processing of ChBT with collagenase is the commonly used protocol for obtaining bone cells [2, 5]. Reducing the collagenase concentration from 300 to 125 U/ml and inclusion of 0.25% trypsin free of EDTA and 1 U/ml of Dispase in bone tissue processing process, theoretically should reduce the cytotoxic effect of collagenase on the cells, but also to maintain at the same level or increase the number of obtained cells particularly by enzymatic digestion. However, bone cells obtaining by enzymatic digestion at utilisation of both protocols showed much lower results compared to explant method ($p < 0.0001$).

Intensive processing stages of ChBT by numerous enzymatic digestion, washings and treatment with EDTA with albumin from bovine serum, was performed to obtain a cell culture that will consist largely of bone cells, otherwise it increases the risk of excessive contamination with BMMSCs and fibroblasts [2]. After incubation of ChBT to obtain bone cells through explant method, the remaining ChBT could be processed a few more cycles to isolate more cells. Unfortunately, further isolation of bone cells requires higher costs in enzymes, consumables and time.

Table 1 Isolation and culture of cells from ChBT using Protocol I

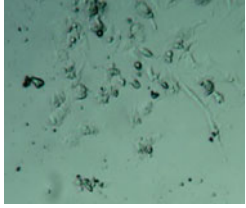
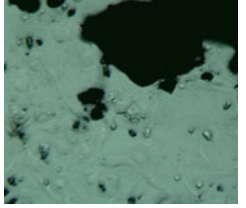
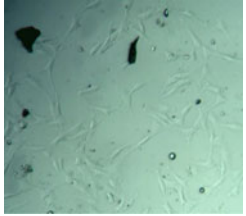
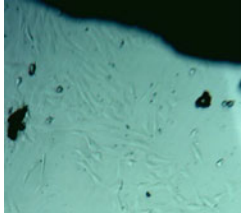
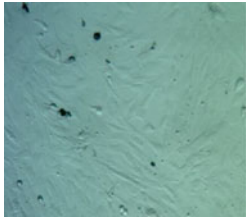
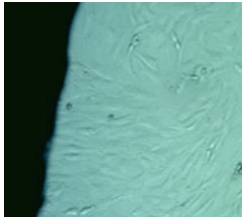
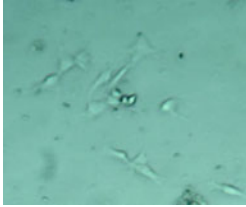

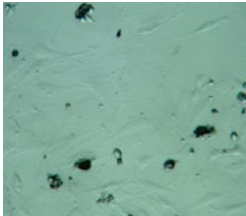
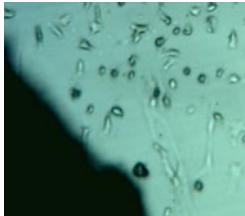
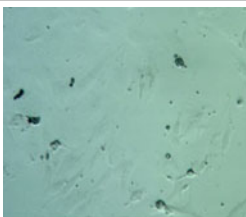
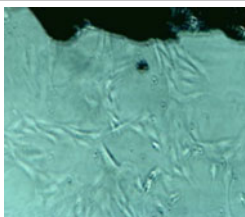
Day	Enzymatic digestion	Explant method
3 days		
5 days		
8 days		

Table 2 Isolation and culture of cells from ChBT using Protocol I

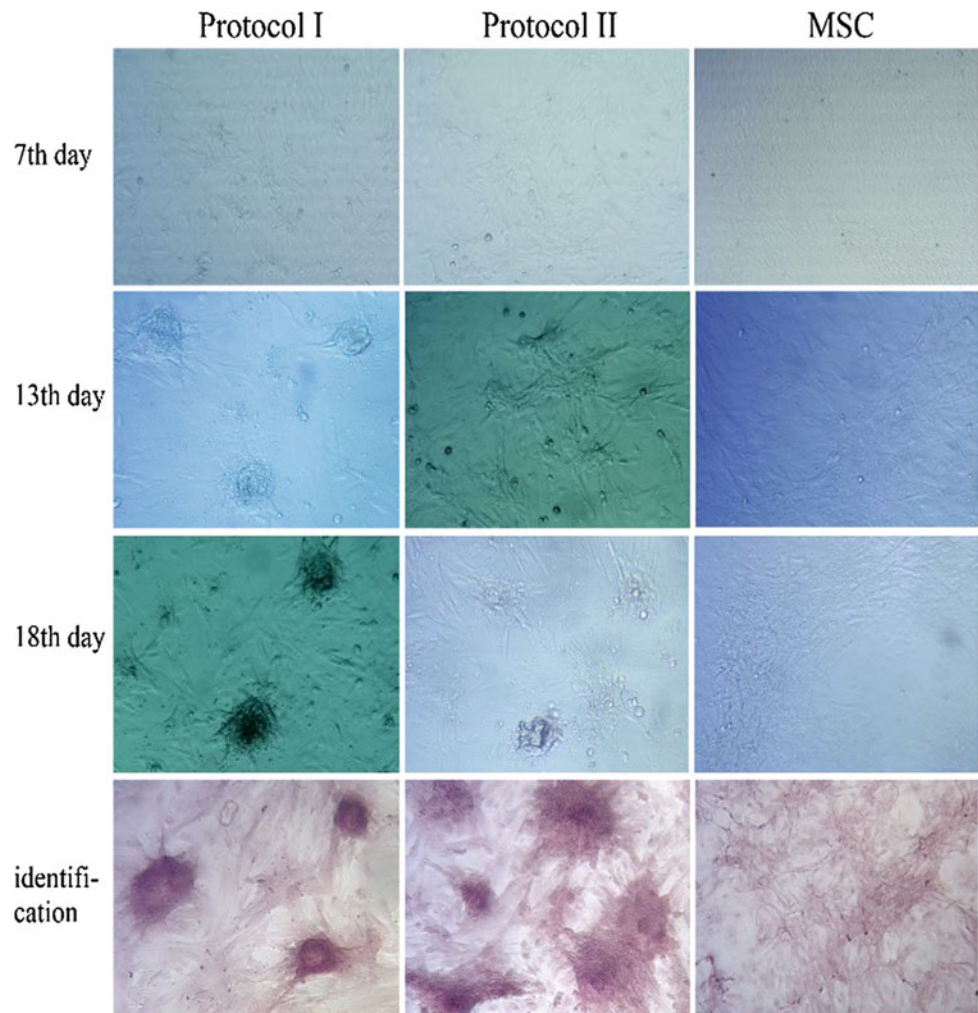
Day	Enzymatic digestion	Explant method
3 days		
5 days		
8 days		

Identification of isolated cells in our opinion is an indispensable component in any cell isolation. It is necessary to document the respective cells before use, regardless of their type [4]. Cell type identification prevents from errors in laboratory research [2] and clinical practice. Obtaining of bone mineralized nodules who were stained with Alizarin red indicates the presence of bone cells [5, 6].

5 Conclusions

Cells obtained from ChBT through both processing protocols have been identified as bone cells, as a result of morphological changes and Alizarin red staining in over-confluent culture. Both protocols used in the experiment

Fig. 4 Bone and mesenchymal stem cells culture in over-confluence for 18 days and their staining with Alizarin red



proved to be equally effective in obtaining bone cells ($p < 0.5$), and obtaining of bone cells by explant method has been more effective compared to enzyme digestion ($p < 0.0001$).

Acknowledgements The authors acknowledge the support from the Ministry of Education, Culture and Research of the Republic of Moldova under the Grants #18.80.07.11A/PS and #18.80012.80.14A.

Conflict of Interest The authors declare that they have no conflict of interest.

References

1. Florencio-Silva, R., Rodrigues da Silva Sasso, G., Sasso-Cerri, E., et al.: Biology of bone tissue: structure, function, and factors that influence bone cells. *Biomed. Res. Int.* **2015**, 421746 (2015). <https://doi.org/10.1155/2015/421746>
2. Rath Stern, A., Stern, M., Van Dyke, M., et al.: Isolation and culture of primary osteocytes from the long bones of skeletally mature and aged mice. *Biotechniques* **52**, 361–373 (2012). <https://doi.org/10.2144/0000113876>
3. Sadat-Ali, M., Azam, M.Q., Elshabouri, M.E., et al.: Stem cell therapy for avascular necrosis of femoral head in sickle cell disease: report of 11 cases and review of literature. *Int. J. Stem. Cells* **10**, 179–183 (2017). <https://doi.org/10.15283/ijsc17019>
4. Cobzac, V., Mostovei, A., Jian, M., Nacu, V.: An efficient procedure of isolation, cultivation and identification of bone marrow mesenchymal stem cells. *Moldovan Med. J.* **62**, 35–40 (2019). <https://doi.org/10.5281/zenodo.2590011>
5. Liu, L., Zhao, G.H., Gao, Q.Q., et al.: Changes of mineralogical characteristics and osteoblast activities of raw and processed pyrites. *RSC Adv.* **7**, 28373–28382 (2017). <https://doi.org/10.1039/c7ra03970k>
6. Orriss, I.R., Taylor, S.E., Arnett, T.R.: Rat osteoblast cultures. *Methods Mol. Biol.* **816**, 31–41 (2012). https://doi.org/10.1007/978-1-61779-415-5_3

Evaluation of the Endothelial Cell Regenerative Proprieties of the Cornea in the Culture Media. Results and Prospects

A. Cociug, O. Macagonova, V. Cusnir Jr., V. Cusnir, and V. Nacu

Abstract

Preservation of the endothelial viability of the cornea is one of the main problems of the non-proliferative corneal transplantation, which creates a well-maintained status with the peripheral cell density decreasing throughout the life, about 30% higher than in the center of the cornea. The disruption of connections between cells adherent junctions correlates with a rapid decline of the proliferation of endothelial monostratified cells during the in vitro culture. The nutritional environment supplemented with EDTA proves that it has the ability to break the adherent junctions of the intercellular endothelial cells. The most widely used method of preservation is the cultured Tissue, “C”. It provides for the endothelial cells viability for 45 day.

Keywords

Keratoplasty • Limbal stem • Endothelial cells • Schwalbe’s line • Descemet membrane • Tissue “C”

1 Introduction

The corneal endothelium is the cell monolayer with a non-proliferative density declining throughout their lives [1]. The corneal epithelial cells divide the limbal stem cells of the corneal endothelium cells and fail to extend in vivo, but expands *slowly* in vitro [2]. Some of the data shows that there are populations of the progenitor cells in the posterior limbus, and the transition zone is on the outskirts of the endothelium and Schwalbe’s line, the part of the trabecular network. These progenitor cells are able to produce endothelial and trabecular cells [3].

There are evidences that the cells of the human corneal endothelium have different features depending on their placement in the cornea. Schimmelpfennig [4] has reported a 30% higher the cells density in the area of 1.6 mm peripheral to the Schwalbe’s line, compared to the center of the cornea. The reason for these differences is unknown, although it has been suggested that the peripheral cornea may provide a physiological backup region and the storage of endothelial cells continues to maintain the life and food for the central cornea [5].

Bednarz et al. [6], have demonstrated that the cells isolated from conglomerates are dense and do exhibit mitogenic activities while the cells derived from the peripheral part of the cornea are characterized by mitogenic activity but their intercellular attachment is stronger in vivo. Konomi et al. [7], have studied the human corneal donors with the various ages and found that the cells from both central and peripheral areas retain the ability, potential proliferation but although the cell doubling time tended to be greater in the center of the old donors of the corneas (Fig. 1) [8].

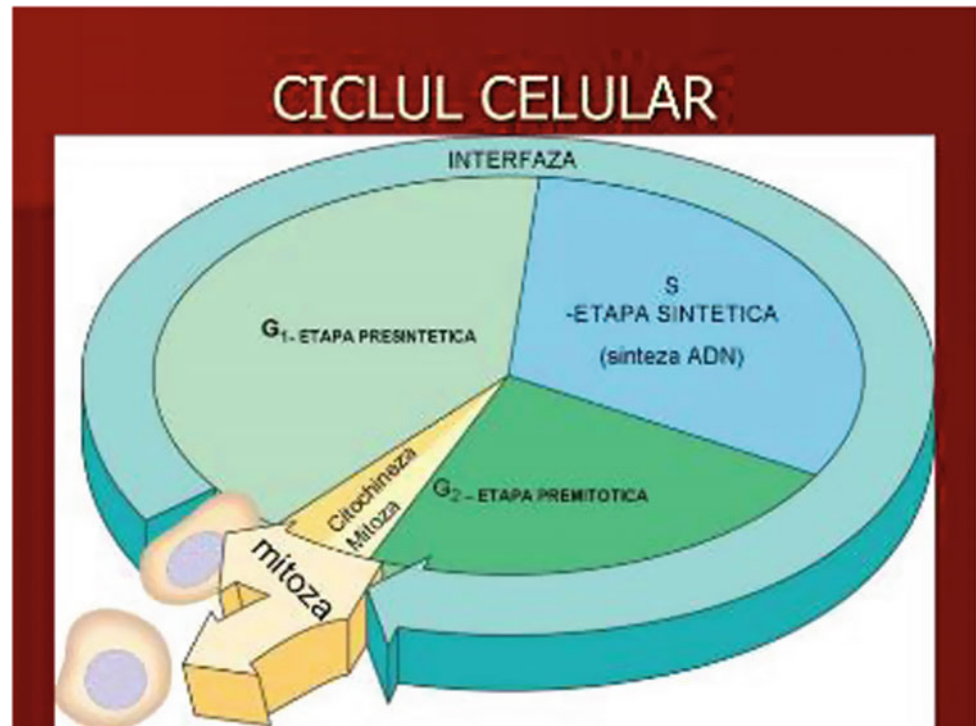
After treatment of the endothelial cells with EDTA (ethylenediaminetetraacetic acid), approximately 17% of the cell population progressed into the S-phase of the cell cycle from their arrested G1-phase. The use of EDTA alone, in combination with the solution of trypsin/EDTA, may allow for a higher survival rate of the cells. Also, the presence of

O. Macagonova · V. Cusnir Jr. · V. Nacu
Tissue Engineering and Cells Cultures Laboratory,
“Nicolae Testemitanu” State University of Medicine and
Pharmacy, Chisinau, Republic of Moldova

A. Cociug (✉) · V. Nacu
Tissue Bank, Chisinau, Republic of Moldova
e-mail: adriancociug77@gmail.com

V. Cusnir
Department of Ophthalmology and Optometry,
“Nicolae Testemitanu” State University of Medicine and
Pharmacy, Chisinau, Republic of Moldova

A. Cociug
“Nicolae Testemitanu” State University of Medicine and
Pharmacy, Bd. Stefan cel Mare 196, Chisinau, Republic of
Moldova

Fig. 1 Cell cycle

L-ascorbic acid 2-phosphate (Asc-2p) in the nutritional environments is useful to increase the proliferation of the endothelial cells [9]. ASC-2p is the derivative antioxidant that stimulates the production of the growth factor of the hepatocytes in vitro [10].

2 Experimental Details

The samples were obtained from the Human Tissue Bank of Moldova, Chisinau. A total of 250 corneas collected from 126 deceased donors after cardiac death were sampled and examined. The samples were subdivided into 3 groups: group I-160 donors—transparent stroma, the edges of the limbal border are well marked, corneas collected up to 20 h after death; group II-60 donors—the surface of the epithelium being poorly edema, his integrity is not compromised, the noticeable edema in the form of a matte opalescence, the lingual contours are well visualized, the corneas collected from 20 to 24 h after death; and group III-30 donors—the corneal-scleral contour is poorly visible, with the vast majority of the opalescent ring at the corneal edge, the cornea taken after 24 h after death. Corneas were severed with a cutting device at 3 mm from the limbus (Fig. 2) [11].

All corneas have been stored in the incubator at 31–37 °C for 30–45 days (Fig. 3).

3 Results and Discussion

The evaluation of the corneas was performed by a device modeled for the preservation of the corneal endothelial cells and examination of the cornea (Fig. 4) [12].

Microscopic examination (Fig. 5) showed the presence of epithelium edema, absolutely transparent stroma, and blunt, rare folds. Descemet membrane was very thin, the endothelial layer completely transparent, intact throughout surface; the areas with the uniform cell redistribution, at the edge of the cornea and preferentially at the corneal edge and middle area; the dead cells (necrosis/apoptosis) that occupy small spaces were identified. The endothelial cells density was greater than 2800 cells/mm², with moderate changes of the cellular pleomorphism, polymegethism, considered as indications for the penetrative keratoplasties.

The corneas from group II (Fig. 6): the epithelium surface with the weak edema, the integrity is not compromised. Its stroma are with the signs of the edema in the lower layers, not wholesale, transparent.

The Descemet membrane has a single flat envelope, located centro-radially; the endothelial layer is intact; generally, over the folds of the Descemet membrane it is only possible to see swelling in the form of a matte opalescence. The endothelial layer is uniformly arranged with the mild,

Fig. 2 Patent. (MD) 1048
Device for cutting of the cornea

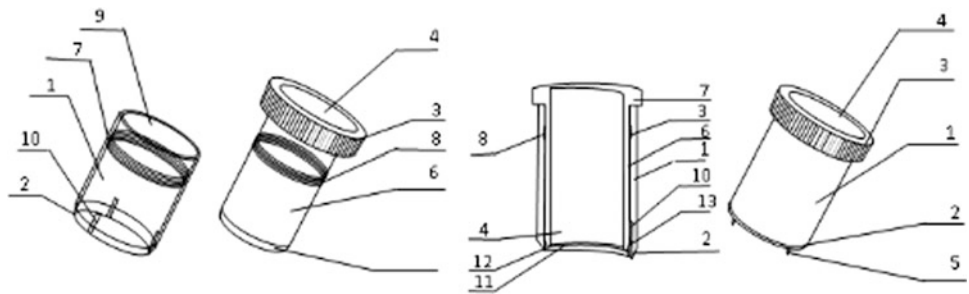


Fig. 3 Incubator for the storing of the cornea

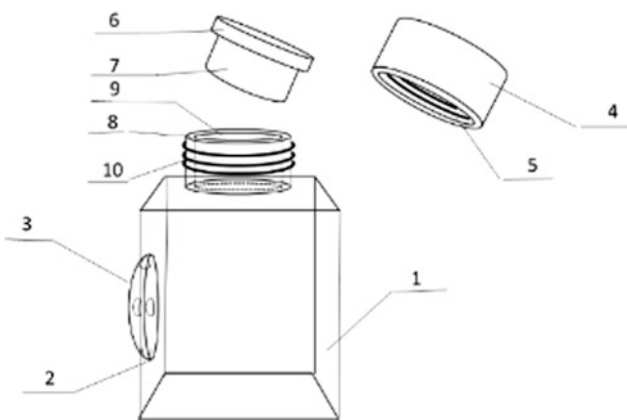


Fig. 4 Patent number 1311 MD. Device for preservation of cornea and corneal endothelial cells examination

slightly swollen mosaic persistence that counts 26 cells per square, averaging. 2600 cells/mm².

The corneas from group III (Fig. 7):—edema of the anterior epithelium, in some areas is exfoliated with the detachment of the Bowman membrane, sometimes mosaic

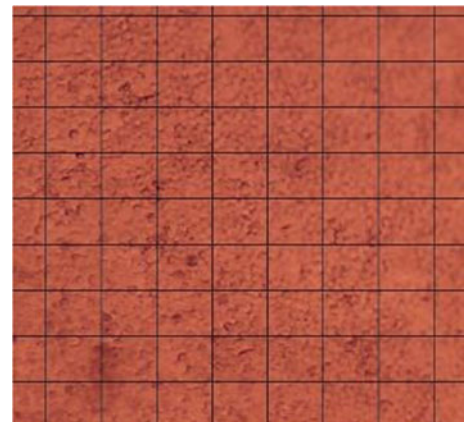


Fig. 5 Patient, 71 YO. Morphological examination of the cornea by the electron microscopy with the inverted phase contrast. The endothelial cells arranged in mosaic form (a), including 28 cells per square, constituting 2800 cells/mm²

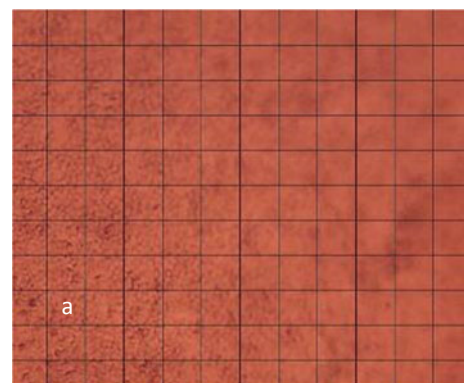


Fig. 6 Patient D, 70 YO. Morphological examination of the cornea by the reversed-phase electron microscopy. The endothelial cells arranged in the mosaic form (a), which include 26 cells per square, constituting 2600 cells/mm²

desquamation is observed. Descemet membrane has pronounced folds, crests directed in different directions of “parquet floor” or “chessboard”. Morphological examination of the cornea was performed by the reversed-phase electron microscopy. The endothelial cells are sectorally persistent with the disappearance of the mosaic (a), which contains 20 cells per square (c), constituting 2000 cells/mm², the epidermis (b).

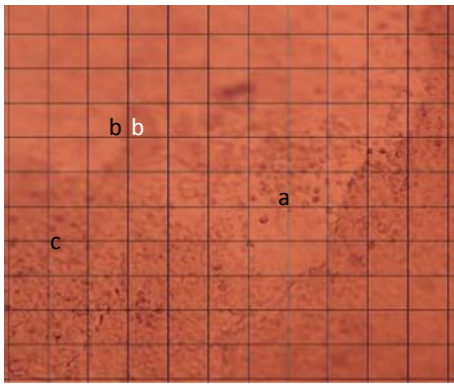


Fig. 7 Patient D, 69 YO. Morphological examination of the cornea by the reversed-phase electron microscopy. The endothelial cells are sectorally persistent with the disappearance of the mosaic (a), which contains 20 cells per square (c) or 2000 cells/mm², the epidermis descending (b)

Corneas of group III (Fig. 8): immunohistochemical staining with Pan-Cytokeratin (AE1/AE3 monoclonal antibody) showed a delineated anterior layer formed by the squamous epithelium (a), intensely chlorated (+++) (b), detachment on some sectors of the anterior layer (c), the stroma with an unframed thickened fibrillar structure (d), uncontaminated fibroblasts (e).

Corneas are stored for up to 4 weeks and their transplantation validity is based on the examination of the corneal endothelium by the light microscopy. This allows assessment of endothelial cell density (ECD). In Bristol city, a minimum ECD of 2200 cells/mm² is considered acceptable for transplants requiring a viable endothelium. Corneas stored in the culture medium for up to 4 weeks have been shown to maintain the integrity of both the endothelial and outer epithelial cells. Although corneal cells may be lost by apoptosis, this seems to affect the external epithelial cells more than endothelial cells.

The other methods of corneal preservation used in the Human Tissue Bank of the Republic of Moldova, such as

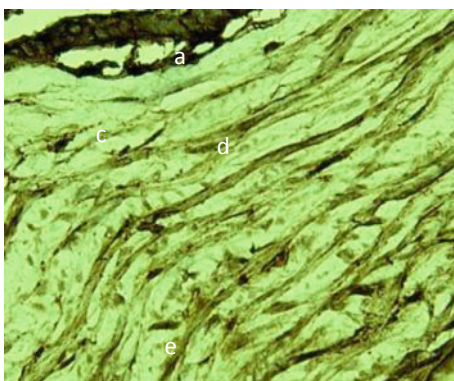


Fig. 8 Patient E, 54 YO. The Cornea from group III. The anterior layer consisting of the weakly contoured epithelium (a), intense staining (+++) with AE1/AE3 (b), detachment on some sectors of the anterior layer (c), the stroma has a unfolded thickened fibrillar structure (d), uncontaminated fibroblasts. x140

lyophilization, 80% glycerol concentration with antibiotic and nutritional medium and decellularization, are nonviable methods in which the viability of cells is lost, only the architectural housing of collagen fibers may be recaptured after transplantation. The nonviable methods are used in the tectonic keratoplasty to restore the integrity of the sclera or some portions of the cornea. The most commonly used preservation method is the Tissue “C” culture medium with a storage temperature of 31 °C and one month’s duration. This medium contains a mixed antibiotic/antimycotic solution that guarantees the effective protection against bacteria and fungi. The phenol red indicator allows rapid viewing of pH variations, and it is not necessary to change the preservation medium during storage of the cornea.

As a perspective in the development of the corneal transplantation, structural corneal tree engineering is used as a source of grafts derived from the animals as a native tissue substrate. Considering that the immune rejection is a major obstacle to widespread use of xenotransplantation, studies are currently being carried out to overcome it. Decellularization of animal tissue provides the ECM three-dimensional structure, favorable for biocompatibility [13–16]. Other animal sources such as cattle [17] and cat [18] are subject to xenotransplantation. Since the decellularized stroma of the cornea retains the basal membrane components, it was also used as a matrix scaffold for in vitro extension of the limb stem cells for epithelial transplantation in the animal models, giving good results [19, 20].

Decellularization can be applied not only to the xenogenic grafts, but also to the allogeneic corneas for transplantation. Theoretically, it would reduce complications associated with allogeneic corneal transplants and improve clinical outcomes.

4 Conclusions

1. Currently, literature suggests that the progenitors of the endothelial cells are precursors, not stem cells. The common features of precursors and adult stem cells are that both have the ability to self-renew and differentiate into the mature effector cells, but stem cells can be renewed endlessly and produce one or more progeny by symmetrical and asymmetric divisions.
2. The most preferred cornea for transfusion keratoplasty and anterior lamellar keratoplasty is the cornea taken up to 24 h after death with a preference being greater than 2000 endothelial cells per mm².
3. Endothelial cells are sensitive to the environment and require pre-nutrition with nutrients and oxygen with the most frequent change of preservation media, allowing them to extend their viability.

Conflict of Interest The authors declare that they have no conflict of interest.

References

- Joyce, N.C.: Cell cycle status in human corneal endothelium. *Exp. Eye Res.* **81**, 629–638 (2005)
- Joyce, N.C., Harris, D.L., Mello, D.M.: Mechanisms of mitotic inhibition in corneal endothelium: contact inhibition and TGF-beta2. *Invest. Ophthalmol. Vis. Sci.* **43**, 2152–2159 (2002)
- Yu, W.Y., Sheridan, C., Grierson, I., Mason, S., Kearns, V., Lo, A. C., Wong, D.: Progenitors for the corneal endothelium and trabecular meshwork: a potential source for personalized stem cell therapy in corneal endothelial diseases and glaucoma. *J. Biomed. Biotechnol.* **2011**, 412743 (2011)
- Schimmelpfennig, B.H.: Direct and indirect determination of nonuniform cell density distribution in human corneal endothelium. *Invest. Ophthalmol. Vis. Sci.* **25**, 223–229 (1984)
- Amann, J., Holley, G.P., Lee, S.B., Edelhauser, H.F.: Increased endothelial cell density in the paracentral and peripheral regions of the human cornea. *Am. J. Ophthalmol.* **135**, 584–590 (2003)
- Bednarz, J., Rodokanaki-von Schrenck, A., Engelmann, K.: Different characteristics of endothelial cells from central and peripheral human cornea in primary culture and after subculture. *Vitro Cell. Dev. Biol. Anim.* **34**, 149–153 (1998)
- Konomi, K., Zhu, C., Harris, D., Joyce, N.C.: Comparison of the proliferative capacity of human corneal endothelial cells from the central and peripheral areas. *Invest. Ophthalmol. Vis. Sci.* **46**, 4086–4091 (2005)
- Senoo, T., Joyce, N.C.: Cell cycle kinetics in corneal endothelium from old and young donors. *Invest. Ophthalmol. Vis. Sci.* **41**, 660–667 (2000)
- Zhu, Y.T., Hayashida, Y., Kheirkhah, A., He, H., Chen, S.Y., Tseng, S.C.: Characterization and comparison of intercellular adherent junctions expressed by human corneal endothelial cells in vivo and in vitro. *Invest. Ophthalmol. Vis. Sci.* **49**, 3879–3886 (2008)
- Kimoto, M., Shima, N., Yamaguchi, M., Amano, S., Yamagami, S.: Role of hepatocyte growth factor in promoting the growth of human corneal endothelial cells stimulated by L-ascorbic acid 2-phosphate. *Invest. Ophthalmol. Vis. Sci.* **53**, 7583–7589 (2012)
- Adrian, C., Nacu, V., Olga, M.: (MD) 1048 (13)Y. A61B 17/56 (2006.01); A61B 17/3205 (2006.01); A61B 17/3209 (2006.01); 2016.02.11. Device for cutting cornea. BOPI, nr. 6/2016, p. 34 (2016)
- Adrian, C., Olga, M., Nacu, V.: 1311 MD Device for corneal preservation and examination of endothelial cells of the cornea
- Elisseeff, J., Madrid, M.G., Lu, Q., Chae, J.J., Guo, Q.: Future perspectives for regenerative medicine in ophthalmology. *Middle East Afr J Ophthalmol.* **20**, 38–45 (2013)
- Tan, D.T., Ficker, L.A., Buckley, R.J.: Limbal transplantation. *Ophthalmol.* **103**, 29–36 (1996)
- Rao, S.K., Rajagopal, R., Sitalakshmi, G., Padmanabhan, P.: Limbal allografting from related live donors for corneal surface reconstruction. *Ophthalmol.* **106**, 822–828 (1999)
- Tsubota, K., Toda, I., Saito, H., Shinozaki, N., Shimazaki, J.: Reconstruction of the corneal epithelium by limbal allograft transplantation for severe ocular surface disorders. *Ophthalmol.* **102**, 1486–1496 (1995)
- Tsai, R.J., Tseng, S.C.: Human allograft limbal transplantation for corneal surface reconstruction. *Cornea.* **13**, 389–400 (1994)
- Dua, H.S., Azuara-Blanco, A.: Autologous limbal transplantation in patients with unilateral corneal stem cell deficiency. *Br J Ophthalmol.* **84**, 273–278 (2000)
- Rao, S.K., Rajagopal, R., Sitalakshmi, G., Padmanabhan, P.: Limbal autografting: comparison of results in the acute and chronic phases of ocular surface burns. *Cornea.* **18**, 164–171 (1999)
- Chen, J.J., Tseng, S.C.: Corneal epithelial wound healing in partial limbal deficiency. *Invest Ophthalmol. Vis. Sci.* **31**, 1301–1314 (1990)

The Influence of Semiconductor Nanoparticles Upon the Activity of Mesenchymal Stem Cells

T. Braniste, V. Cobzac, P. Ababii, I. Plesco, S. Raevschi, A. Didencu, M. Maniuc, V. Nacu, I. Ababii, and I. Tiginyanu

Abstract

In this paper, we report on the viability and proliferation of mesenchymal stem cells after exposure to different types of semiconductor nanoparticles. The nanoparticles used for the tests are based on GaN thin layers grown on commercial ZnO and ZnFe₂O₄ nanoparticles. Different quantities of nanoparticles incubated with mesenchymal stem cells influence the metabolic activity of cells, which was assessed by the MTT assay. The cytotoxic effect of ZnO nanoparticles on MSC was demonstrated and no harmful effect of the other materials.

Keywords

Nanoparticles • Gallium nitride • Mesenchymal stem cells • MTT

1 Introduction

Stem cells represent unspecialized cell type that can differentiate into various specialized cell types under certain physiological or experimental conditions. The mesenchymal stem cells are widely used in cell therapy with a different

success-rate [1]. In order to increase the impact, interdisciplinary research that implies the use of nanoparticles in biomedical applications, like bio-sensing, imaging, or therapy is ongoing [2–7]. The use of nanoparticles in medical applications is widely investigated through different approaches. Nanomedicine is also oriented to cancer treatment with stem cells utilization as drug carriers [8]. One of the actual problems in nanomedicine is the evaluation of nanoparticles cytotoxicity and their potential impact at the cellular level. Our previous investigations have shown that uncoated gallium nitride nanoparticles (GaN) do not affect the viability and proliferation of endothelial cells [9] and can be used for multifunctional therapeutic purposes which include cells spatial redistribution [10].

In this work, we report on the interaction of rat MSC with different types of nanoparticles. We used both commercially available zinc oxide (ZnO) and zinc ferrite (ZnFe₂O₄) as well as synthesized GaN-based nanoparticles. The metabolic activity of cells after exposure to nanoparticles was assessed using the MTT assay, which shows a highly toxic effect of the ZnO nanoparticles and no harmful effect of the other materials.

2 Experimental

2.1 Nanoparticles Synthesis and Characterization

Nanometre-scale thin layers of GaN have been grown on sacrificial zinc ferrite (ZnFe₂O₄) based nanoparticles acquired from Sigma-Aldrich (CAS#12063-19-3). The growth took place in a horizontal hydride vapor phase epitaxy (HVPE) reactor with four temperature zones. In the source zone, at T = 850 °C, the GaCl is formed after the interaction of HCl with metallic Ga. Then, in the reaction zone at 600 °C, the formed GaCl interacts with NH₃ for 10 min in order to initiate the GaN growth on the ZnFe₂O₄

T. Braniste (✉) · I. Plesco · I. Tiginyanu
National Center for Materials Study and Testing, Technical University of Moldova, Bv. Stefan cel Mare, 168, 2004 Chisinau, Moldova
e-mail: tudor.braniste@cnstm.utm.md

V. Cobzac · V. Nacu
Laboratory of Tissue Engineering and Cells Cultures, State University of Medicine and Pharmacy “Nicolae Testemiteanu”, Chisinau, Moldova

P. Ababii · A. Didencu · M. Maniuc · I. Ababii
Department of Otorhinolaryngology, State University of Medicine and Pharmacy “Nicolae Testemiteanu”, Chisinau, Moldova

S. Raevschi
Department of Physics and Engineering, State University of Moldova, Chisinau, Moldova

nanoparticles. The GaN layer growth accompanied by simultaneous reduction of ZnO in the sacrificial substrate nanoparticles occurs at 800 °C for 10 min in the H₂ flow rate of 3.6 l/min. During the growth process, the ammonia and hydrogen chloride flow was kept constant at 500 ml/min and 15 ml/min, respectively. The initial nanoparticles, as well as the resulted material after the GaN growth, have been characterized using the electron microscopy tools, including scanning electron microscopy (SEM) and transmission electron microscopy (TEM).

2.2 Mesenchymal Stem Cells Isolation and Culture

The isolation, culture, and use of rat MSC in the research activities were approved by the Ethics Committee of the Moldovan State University of Medicine and Pharmacy “Nicolae Testemitanu” on 18.06.2015.

The MSC were isolated from the bone marrow of 5 months old Wistar male rat. After rat euthanasia, the bone marrow from long tubular bones has been flushed with warm PBS (HiMedia, India). The suspension was centrifuged for 10 min at 170 g, followed by MSC isolation in mesenchymal stem cells expansion medium HiMesoXL (HiMedia, India) supplemented with antibiotics and antimycotics. The incubation was performed in 25 cm² cell culture flasks (Nunc, Denmark) at 37 °C with 5% CO₂. The cells were cultured in 2 passages followed by cryopreservation by 5 × 10⁵ cells/ml in FBS (Lonza, Belgium) with 10% DMSO (OriGen Biomedical, Germany). The MSC isolation and identification was done following the chondrocytes line differentiation protocol [9].

To perform the experiment, 5 × 10⁵ MSC were cultured in 75 cm² culture flasks (Nunc, Denmark) with 15 ml DMEM/Ham's F-12 medium (Sigma, UK) supplemented with 10% FBS (Lonza, Belgium) and antibiotic-antimycotic solution. The medium was completely changed every 2 days until the culture gained 80–90% of cells confluence. After trypsinization, the cells were counted in hemocytometer with Trypan blue exclusion, followed by cells seeding at a density of 1 × 10⁴ cells/ml in 24 well tissue culture test plates (TPP, Switzerland) for MTT cell viability assay.

The suspension of MSC was prepared using nanoparticles at a concentration of 1 × 10⁴ cells/ml with each type of nanoparticles at a concentration of 50 ng/ml, 25 ng/ml and 10 ng/ml. One milliliter of each nanoparticle-MSC suspension type was moved in wells with glass coverslips (n = 3), and incubated at 37 °C with 5% CO₂, for 2 days under magnetic field influence.

2.3 MTT Assay

The MTT assay started 24 h after the medium supplemented with nanoparticles was added to 24 well tissue culture test plates seeded with MSC and has been performed every day during the incubation period (n = 3). The culture medium was replaced by 1 ml of 2.5 mg/ml MTT (Sigma, UK) solution prepared in DMEM/Ham's F-12 medium (Sigma, UK), followed by two hours incubation at 37 °C with 5% CO₂. After incubation, the MTT solution was replaced by 1 ml of 99,8% isopropanol (STANCHEM, Poland). The plates covered with tinfoil have been shaken for 15 min at 100 rpm (ES-20, Biosan), followed by the color change quantification using the plate reader (Synergy H1, BioTek) at 570 nm.

The cell viability was assessed by the formula:

$$\text{Cell viability (\%)} = \frac{(\text{OD}_{570} \text{ of test nanoparticles}) - (\text{OD}_{570} \text{ of blank})}{(\text{OD}_{570} \text{ of control}) - (\text{OD}_{570} \text{ of blank})} \times 100\% \quad (1)$$

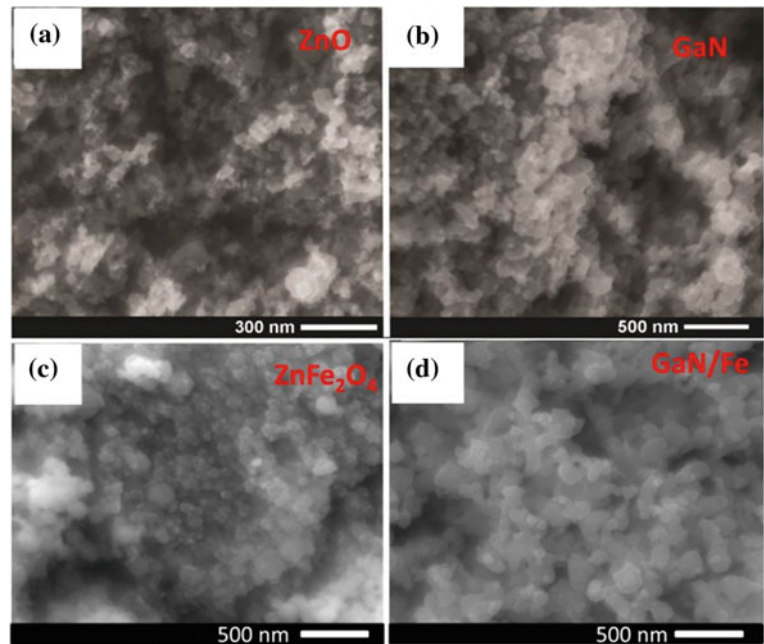
2.4 Cells Preparation for Scanning Electron Microscopy

The morphology of rat MSC cultivated in the presence of nanoparticles exposed to the magnetic field was studied using a Vega Tescan SEM. Before imaging, the cells were fixed in glutaraldehyde, dehydrated with ethanol, dried, and covered with a thin gold (Au) layer in order to avoid charging effects during electron microscopy scanning. The fixation process was done at 4 °C in 2.5% glutaraldehyde for 12 h, followed by other 24 h in a saline buffered solution (NaCl 0.9%). The dehydration process involved incubation in gradually increasing ethanol concentrations from 30 to 97% at room temperature. Since we were more interested in seeing the cells redistribution under magnetic field influence rather than the cell membrane integrity, the drying process has been performed in a normal atmosphere at room temperature. Before imaging, the samples were coated with an ultrathin layer of Au by using a Cressington 108 auto sputter coating machine.

3 Results and Discussion

Figure 1 shows the SEM images of the initial commercial nanoparticles and their morphology after GaN growth. During the epitaxial growth process, the sacrificial layers of ZnO and ZnFe₂O₄ are decomposed due to high temperature

Fig. 1 SEM images of nanoparticles. **a** ZnO, **b** GaN/ZnO, **c** ZnFe₂O₄ and **d** GaN/Fe

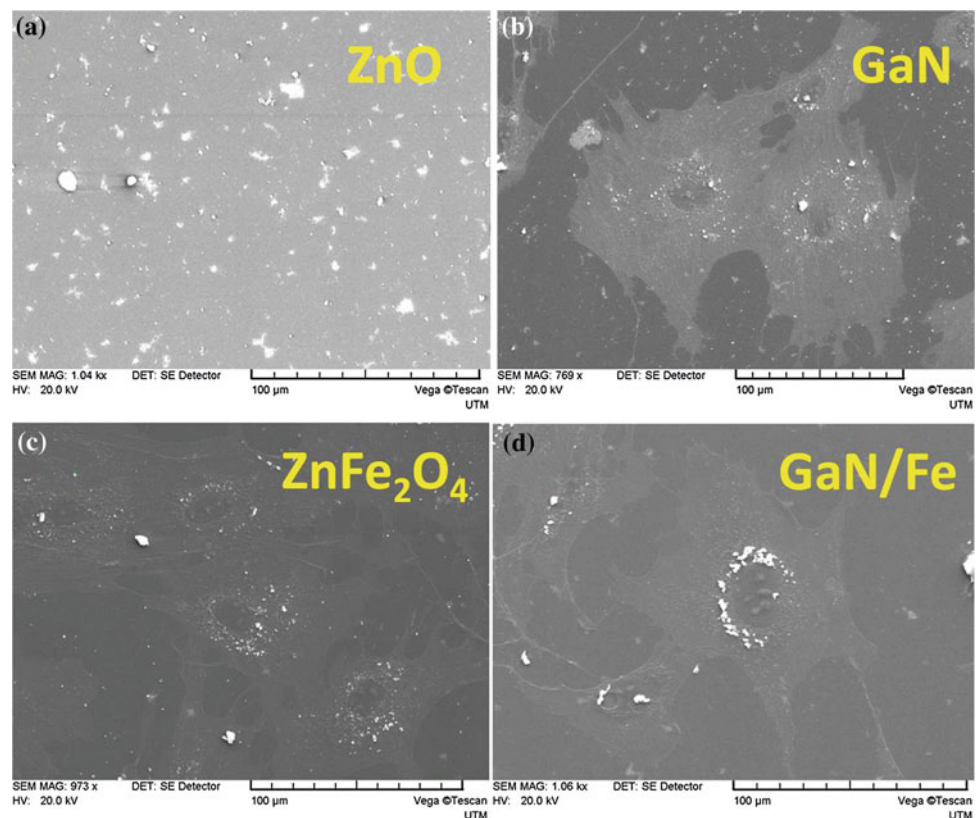


and the harsh environment in which GaN is grown. The chemical composition and crystalline structure have been analyzed in our previous works [10, 11].

The influence of different types of nanoparticles has been assessed by incubating them in different quantities with

living cells. Figure 2 depicts the scanning electron micrographs (SEM) of MSC after three days of incubation with 50 µg/ml of different types of nanoparticles. According to the pictures, one can observe the tendency of cells to collect the nanoparticles and the clusters of nanoparticles from the

Fig. 2 SEM images of MSC after three days of incubation with 50 µg/ml of **a**—ZnO, **b**—GaN, **c**—ZnFe₂O₄ and **d**—GaN/Fe nanoparticles



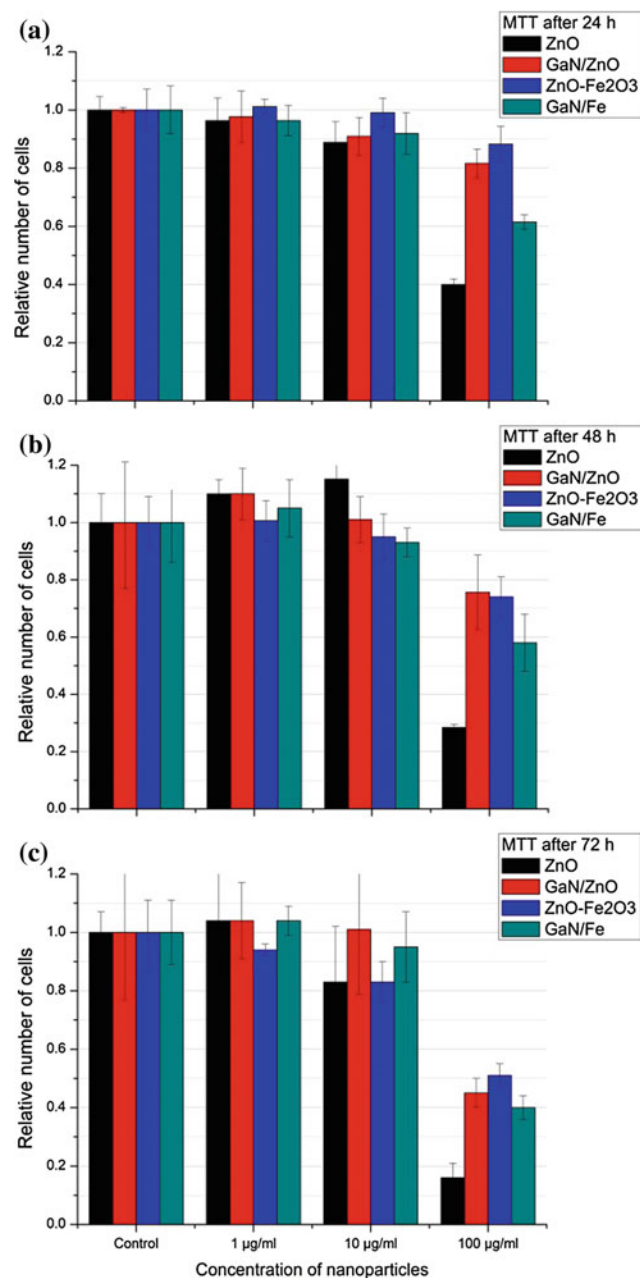
media and deposit in vesicles. The morphology of cells seems not to be affected by GaN-based nanoparticles, while there are no attached cells in the samples incubated with zinc oxide nanoparticles even at concentrations as low as 25 $\mu\text{g/ml}$.

The MTT assay confirms that ZnO becomes highly toxic at higher concentrations, while the other types of nanoparticles are being accepted and uptaken by MSC. Figure 3 presents the dynamic evolution of cells activity during the incubation process with different concentrations of nanoparticles based on different semiconductor materials. One can notice a time-dependent decreasing tendency in

cells metabolic activity for all the nanoparticles used. The concentration-related tendency is also noticeable, and the concentration of 50 $\mu\text{g/ml}$ of nanoparticles incubated for three days leads to a decrease in cells metabolic activity with about 50% comparing to the control group.

The high toxicity of ZnO nanoparticles is attributed to poor chemical stability of the material: the Zn^{2+} ions concentration increases in the growth medium, which lead to cells apoptosis. The GaN nanoparticles grown on ZnO and ZnFe₂O₄ nanoparticles stabilize the remaining oxide layer and increase the material chemical stability and thus are less toxic for living cells.

Fig. 3 MTT product after **a** 24 h, **b** 48 h and **c** 72 h of incubation of cells with 10, 25 and 50 $\mu\text{g/ml}$ of nanoparticles



4 Conclusions

The activity of mesenchymal stem cells is highly affected by ZnO nanoparticles with dimensions less than 50 nm at a concentration higher than 25 µg/ml. The GaN based nanoparticles does not affect the activity of MSC significantly at low concentrations, while at higher concentrations (>50 µg/ml) the metabolic activity of MSC is inhibited by the presence of nanoparticles.

Acknowledgements The authors acknowledge the support from the Ministry of Education, Culture and Research of the Republic of Moldova under the Grants #18TC, #15.817.02.29A and #15.817.04.04F. This work has received partial funding from the European Union's Horizon 2020 research and innovation programme under grant #810652 (NanoMedTwin project).

Conflict of Interest The authors declare that they have no conflict of interest.

References

1. Wei, X., Yang, X., Han, Z., et al.: Mesenchymal stem cells: a new trend for cell therapy. *Acta Pharmacol. Sin.* **34**, 747–754 (2013)
2. Alan, L., Jan, Y.: How interdisciplinary is nanotechnology? *J. Nanopart. Res.* **11**(5), 1023–1041 (2009)
3. Cormode, D.P., et al.: Nanotechnology in medical imaging: probe design and applications. *Arterioscler. Thromb. Vasc. Biol.* **29**(7), 992–1000 (2009)
4. Wenyi, G., et al.: Nanotechnology in the targeted drug delivery for bone diseases and bone regeneration. *Int. J. Nanomed.* **8**, 2305–2317 (2013)
5. Tran, S., et al.: Cancer nanomedicine: a review of recent success in drug delivery. *Clin. Transl. Med.* **6**(1), 44 (2017)
6. Paurush, A., et al.: Nanomedicine in coronary artery disease. *Indian Heart J.* **69**(2), 244–251 (2017)
7. DiSanto, R.M., et al.: Recent advances in nanotechnology for diabetes treatment. *Wiley Interdiscip. Rev. Nanomed. Nanobiotechnol.* **7**(4), 548–564 (2015)
8. Xie, F.-Y., Xu, W.-H., Yin, C., et al.: Nanomedicine-mediated cancer stem cell therapy. *World J. Gastrointest. Oncol.* **8**, 735–744 (2016)
9. Cobzac, V., Mostovei, A., Jian, M., Nacu, V.: An efficient procedure of isolation, cultivation, and identification of bone marrow mesenchymal stem cells. *Moldovan Med. J.* **62**, 35–40 (2019)
10. Braniste, T., Tiginyanu, I., Horvath, T., Raevschi, S., Cebotari, S., Lux, M., Haverich, A., Hilfiker, A.: Viability and proliferation of endothelial cells upon exposure to GaN nanoparticles *Beilstein. J. Nanotechnol.* **7**(1), 1330–1337 (2016)
11. Braniste, T., Tiginyanu, I., Horvath, T., Raevschi, S., Andrée, B., Cebotari, S., Boyle, E.C., Haverich, A., Hilfiker, A.: Targeting endothelial cells with multifunctional GaN/Fe nanoparticles. *Nanoscale Res. Lett.* **12**(1), 486 (2017)

Part XII

**Clinical Engineering, Health Technology
Management and Assessment**

Medical Devices Regulations, Management and Assessment; New Trends New Needs

N. Pallikarakis

Abstract

In the accelerated way that Medical Devices (MDs) are developed and revolutionize health care delivery during the last decades, Regulation, Management and Assessment of Health Technology are of paramount importance. This paper provides a short overview of the recent development in this area and discusses some issues related to the new EU regulatory framework on MDs, the need for a more rigorous management and the importance of Health Technology Assessment for MDs. Study is also focusing on the particular characteristics of MDs that impose a different approach, in these three domains, compared to medicinal products, in order to get the expected benefits right to the patients, in a safe and cost-effective way.

Keywords

Medical devices • Regulations • Management • Health technology assessment

1 Introduction

The rate of growth of health expenses has consistently exceeded GDP growth in each and every decade. In 2009 EU countries spent, on average, 9.6% of their GDP on health, compared to 8.8% in 2008 and 7.3% in 1998. Between 1980 and 2000, medical technology reduced hospital stays by more than 50% and between 2000 and 2008, by an average of an additional 13%. Still, Medical technology accounts for less than 5% of the total health care expenditure.

Medical technology industry is one of Europe's most diverse and innovative high-tech sectors, with more than

13,000 patent applications filed by the European Patent Office (EPO) in 2017, more than double compared with the pharmaceuticals. Medical Technology is amongst the largest technical sectors of Europe, with 27,000 medical technology companies, (95% of them SMEs) employing over 675,000 people in Europe [1]. The global medical device market is estimated to more than 400 billion Euros in year 2017, with more than 500,000 medical technologies available. Europe represents 27% of this market, with a 20 million Euros positive MDs trade balance.

The MDs life cycle starts with an idea and hopefully passes a number of stages before it is placed on the market, used and discarded. These phases include the R&D cycle, usually with the development and testing stages, leading to a prototype, that initially undergoes preclinical tests not involving humans. If successful, clinical trials are performed and conformity with the legal framework is certified in order to get approval for placing on the market. Procurement and use are the final phase and if appropriate, Health Technology Assessment is done. The whole MD life cycle is graphically depicted in Fig. 1.

The medical technology sector today is characterized by a high degree of regulation and standardization, aiming to ensure reliability, safety, and performance, under proper conditions of use and maintenance. All medical devices produced and “placed on the market”, are in accordance with the international standards and have the necessary certification in compliance with the Medical Devices Directives and guidelines for the EU, and/or FDA approval for the US. It should also be stressed that, in contrary with the past, life cycle of MDs is quite short today, sometimes down to two years before an improved product becomes available.

2 The Three Pillars for Patient Safety

There are three major ways that patient safety is assured today: *Regulations* that addresses the issues related to placing safe devices on the market, *Management* that is

N. Pallikarakis (✉)
INBIT Institute of Biomedical Technology, Stadiou, Patras
Science Park, Patras, Greece
e-mail: nipa@inbit.gr

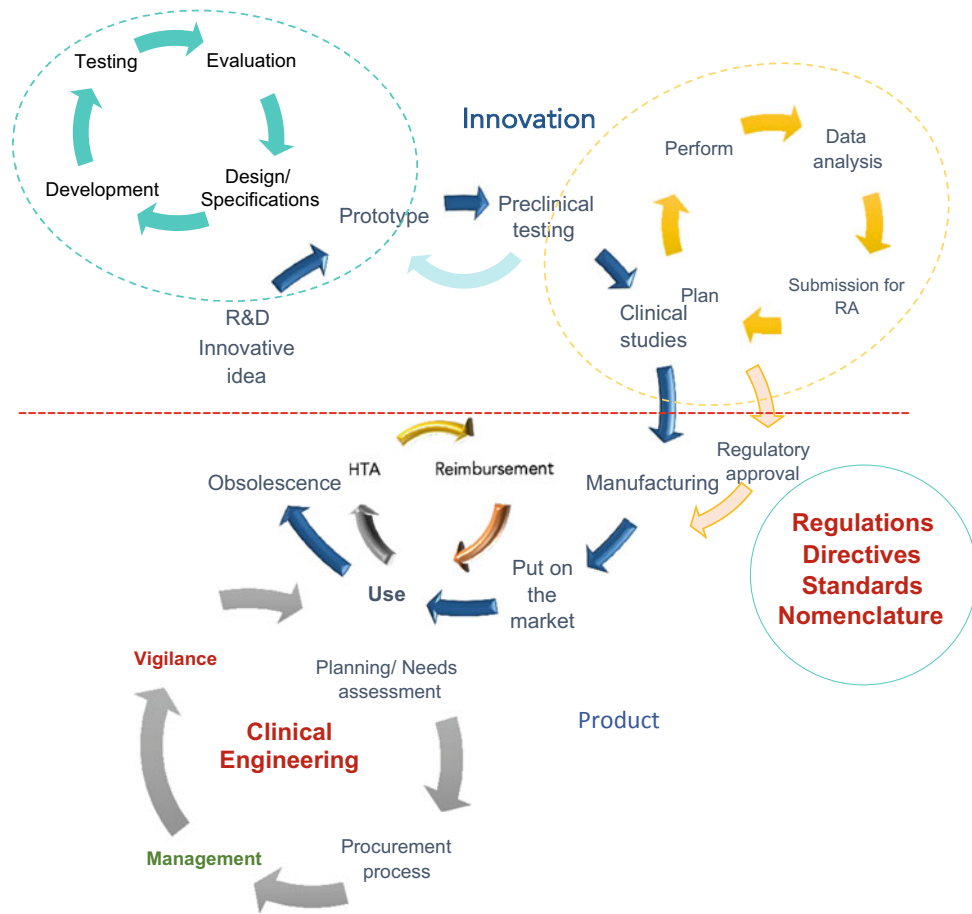


Fig. 1 The MDs life cycle

related to the safe use of the devices and *Assessment* that provides evidence-based information for decision making (Fig. 2).

2.1 Regulations

The path to a common European MDs legal framework started in the 80s with the decisions of the ‘New approach and the preparation of the three central European Directives on: the Active Implantable Medical Devices (AIMDs), the In Vitro Diagnostics (IVDs) and the main Medical Devices (MDs) including all other devices not included in the two

previous mentioned categories. Three Directives were voted by the European Parliament in the nineties:

- AIMDs Directive—90/385/EEC [2]
- MDs Directive—93/42/EEC [3] and
- IVDs Directive—98/79/EEC [4]

These directives were implemented in the form of national laws and therefore harmonization of the European market took place. The Directives are complemented by a number of guidelines (MEDDEVs), like the Risk Classification of MDs or guidelines on Vigilance, and by harmonized standards, that provide technical requirements for

<p>HT Regulation Safety Performance Market control Vigilance</p>	<p>HT Management Procurement Testing Maintenance Safety</p>	<p>HT Assessment Clinical effectiveness Financial implications Ethical & Social issues Organizational aspects</p>
---	--	--

Fig. 2 The three pillars for patient safety

conformity assessment. With these European directives, certification became compulsory, in order to prove compliance of the product with the requirements of the Directives, to put the CE marking, otherwise marketing of the product is not allowed [5]. At the same time the application of Information and Communication Technologies were slowly introduced in the regulatory sector although with a lot of reluctance, until the mid 2000s with the launch European Database on Medical Devices (EUDAMED), in spite of the fact that the basic work was ready ten years ago [6] (Fig. 3).

Following some failure cases for the directives to assure patient safety for devices put on the market with the CE mark, in the late 2010s it was decided to change the regulatory framework. As a result, in 2017, the three directives have been replaced by two regulations:

- 2017/745 on MDs [7]
- 2017/746 on IVDs [8].

Regulations are stricter in terms of implementation and rules of compliance and monitoring. Their scope is broadened in relation to the three Directives. Some main differences introduced are listed below:

- The classification of products shows a general trend of upgrading the risk categories.
- For the certification/licensing of high-risk products, participation of the authorities and/or expert groups is necessary. At the same time the requirements for technical documentation are increasing.
- The Unique Device Identification (UDI) is introduced to improve the recognition and traceability of products.
- The central system of safety and vigilance reports is being upgraded and the role of the European Database on Medical Devices (EUDAMED) becomes more critical.

- A central approach is foreseen for the submission of international clinical investigations and the procedures for the notification of post-clinical valuation.

There is however criticism on the negative impact that this stricter approach will have on innovation. Problems are also faced by the manufacturers with the certification process by the notified bodies that are significantly reduced in number and therefore overcharged and respond to the demand with big delays.

2.2 Management

Health Technology Management, mainly deals with all aspects related to safe and effective use of the devices placed on the market, from the procurement phase up to their withdrawal. Efficient management of technology in the hospital environment starts with good matching between needs and capabilities. To be successful, it must integrate the technology procurement planning and management program at the hospital level, with a final goal to address the needs of proper patient care [9]. Implementing a comprehensive biomedical technology management program is a quite complex and multidimensional process, that depends on the skills and the background of the personnel involved. In principle it contains the tasks briefly outlined below, nowadays performed by the Clinical Engineering Departments:

Medical Equipment Inventorying, consisting of organized records of all medical equipment items belonging to or used in the hospital.

Medical Equipment Procurement Planning, aiming to ensure the availability of appropriate equipment at the right time in the right place.

Fig. 3 The EU legal framework for placing MDs on the market



Medical Equipment Acquisition, including preparation of technical specifications, call for tender, offers evaluation, and contract signing.

Acceptance Testing, to verify that the correct devices have been delivered and properly installed.

Training, to assure proper use of the devices.

Preventive Maintenance, keeping the equipment in good functional condition, through regular inspections and service

Corrective Maintenance, when repairs are necessary for re-establishing the normal operating status.

Quality Assurance, comprising planning and performing quality control and safety tests of medical equipment.

Disposal, when the equipment becomes obsolete.

Management of hospital technology requires creation and continuous update of data files with all interventions performed on each individual equipment, covering its whole life cycle. These data must be easily retrievable and able to be presented to the end users in an appropriate way, i.e. converted into meaningful information. Since the 80s software tools have been created, known as Medical Equipment Management Systems (MEMS) or as Computerized Maintenance Management Systems (CMMS) that assist clinical engineers to perform their tasks, covering all management activities of the CEDs including:

- management of files for medical devices, manufactures, and suppliers
- follow up of equipment acquisition procedures, from the request departments to acceptance testing
- implementation and management of quality and safety protocols and procedures
- scheduling of all routine procedures, inspections and tests
- follow up of all corrective maintenance tasks
- management and monitoring of training activities provided by the CED
- monitoring of the overall performance of the department, using quality and cost indicators
- easy access to and exchange of vigilance-related information
- data analysis and report generation

The ICT evolution has nowadays, provided CMMS operating over networks, interconnected with other hospital information systems and the equipment themselves [10].

2.3 Health Technology Assessment HTA

HTA is multi-disciplinary field of policy analysis that examines the medical, economic, social and ethical implications of the incremental value, diffusion and use of a medical technology in health care. HTA mainly deals and provides information and evidence on:

Comparative clinical effectiveness
 Comparative cost-effectiveness
 Health delivery organisational aspects
 Legal framework
 Ethical, social implications

Balancing access, quality of care and sustainability of a health care system, is a challenging task, especially when deciding on the best use of the limited budgets available. Acceptable levels of safety, cost-effectiveness, may vary in different communities, countries, or circumstances and the overall health benefits for the population should be considered in each case, i.e. what intervention on the adoption of technologies result in the greatest health benefits to a community. Difficult questions like:

- Are the interventions cost effective?
- Is the technology affordable?
- Is context-specific?

should be answered and justified. The problem of «*when-to-assess?*» is also critical. It should be when enough evidence could be gathered on most parameters to be studied. However, it is a “moving target problem” since there is always the risk that a delay in the time HTA is performed and disseminated, could make its findings soon outdated by technological changes.

Although in the past, the methods applied for medicines were also used for MDs, the need for different approaches in HTA of MDs is now recognized [11]. The new regulatory framework for MDs clearly introduces new incentives for HTA [12].

New technologies significantly improve clinical practice, but their rapid growth is making it virtually impossible for care providers to keep in pace with all new advancements. Additionally, reluctance to change long-standing practices, as well as outdated education, restricts the uptake of new and potentially more efficient solutions. Growing concerns about more financial constraints, accountability, transparency, and legitimacy in decision-making processes, imposed more evidence-based approaches. Health Technology Assessment (HTA), emerged exactly from the need to give answers and support decisions on the development, approval, and diffusion of health technologies. Although the scope of HTA is very large and the majority of reports address pharmaceuticals, the medical equipment sector has recently started gaining more attention. Its origin goes back actually in the 1970s, when healthcare institutions were under pressure to apply newly appeared costly medical equipment, especially in the diagnostic imaging area. A kind of precursor was the comparative evaluation trend of MDs that flourished in the 1980s, but was of limited scope and unable to cope with the very rapid changes during the 90s and was therefore

abandoned. The growth and development of HTA and especially the hospital-based HTA, during the two last decades, focusing on medical equipment-related technologies, reflects the importance that this field is gaining. CEs being in the center of technology management, with a profound understanding of the technical issues, are well placed to play a pivotal role as members of the interdisciplinary teams working in HTA worldwide.

3 Future Perspectives

Health technology will continue to grow and contribute to improvements in healthcare delivery. At the same time, it will require more often update of regulations in order to face the explosive changes and continue to assure patient safety without compromising innovation.

Apart from the new impressive medical technologies already announced or still at the R&D stage, very important impact comes also from the developments in Information and Communication Technologies, with mobile applications, distance monitoring and data exchange and retrieval. Today's medical equipment either incorporates embedded computer systems or the equipment is computer-driven. They also started to be interconnected and self-tested or calibrated.

The systematic operation of CMMS will continue to contribute considerably towards the improvement of effective medical technology management in healthcare facilities, with significant benefits relating to cost-effectiveness and safety. However, future CMMS are expected to be directly connected with most of the equipment, with new remote monitoring and diagnostic capabilities.

HTA for medical devices should find its own way and models of conductance, to respond to the large and ever-expanding variety of technologies involved should be created, in order to continue to play its important role.

4 Conclusions

The future of medical technology will continue to provide impressive solutions and possibilities. However, it is important to keep regulation effective, management efficient and HTA adaptable, taking into account their influence to the

financial, social and environmental variables of countries and systems that are directly implemented, but also their indirect impact worldwide.

Acknowledgements The author wants to acknowledge the precious information, inspiring ideas and fruitful discussions, provided by the IFMBE/Clinical Engineering and Health Technology Assessment Divisions which are exceptionally active and productive during the last period. The unique leading role and guidance of the WHO medical devices sector in the field is equally remarkable and extremely motivating.

Compliance with Ethical Requirements The author declares that there is no Conflict of Interest, or any other no compliance with ethical requirements.

References

1. MedTech Europe: <https://www.medtecheurope.org>
2. Council Directive 90/385/EEC: Official Journal of the European Commission L-189 (1990)
3. Council Directive 93/42/EEC: Official Journal of the European Commission L-169 (1993)
4. Council Directive 98/79/EC: Official Journal of the European Commission L-331 (1998)
5. Pallikarakis, N., Moore, R.: Health technology in Europe—regulatory framework and industry perspectives of the “new approach”. *IEEE Eng. Med. Biol. Mag.* **26**(3), 14–17 (2007)
6. Pallikarakis, N., Anselmann, N., Pernice, A. (eds.): *Information Exchange for Medical Devices*. IOS Press, Amsterdam (1996)
7. REGULATION (EU) 2017/745: Official Journal of the European Union, L 117/1, 5.5.2017
8. REGULATION (EU) 2017/746: Official Journal of the European Union, L 117/176, 5.5.2017
9. Medicines and Healthcare Products Regulatory Agency Annual Report and Accounts 2013/14, Medicines and Healthcare Products Regulatory Agency (MHRA), Williams Lea Group, 117 p., Print ISBN 9781474108119, Web ISBN 9781474108126, <https://www.gov.uk/government/publications/medicines-and-healthcare-products-regulatory-agency-annual-report-and-accounts-2013-to-2014>
10. Malataras, P., Bliznakov, Z., Pallikarakis, N.: Re-engineering a medical devices management software system: the web approach. *Int. J. Reliable Qual. E-Healthc.* **3**, 9–18 (2014)
11. Polisen, J., Castaldo, R., Ciani, et al.: Health technology assessment methods guidelines for medical devices: how can we address the gaps? The international federation of medical and biological engineering perspective. *Int. J. Technol. Assess. Health Care* **34**(3), 276–289 (2018)
12. Commission Proposal on Health Technology Assessment: European Commission-Fact Sheet. Retrieved from http://europa.eu/rapid/press-release_MEMO-18-487_en.htm (2018)

Assessment of Human Tissue Transplantation Activities in the Republic of Moldova

T. Timbalari, I. Codreanu, O. Lozan, and V. Nacu

Abstract

The assessment of human tissue transplantation activities in the Republic of Moldova highlights the tissue transplant service as a component part of the national transplant system in the Republic of Moldova. Strengthening the national transplant system and continuous development of the human tissue transplant service has resulted in a significant increase of efficacy of deceased donation process. Implementation of performance indicators for institutions authorized to carry out donation and procurement activities from deceased donors will allow performing the audit of donation and transplantation.

Keywords

Tissue transplantation • Deceased donor • Potential of donation • Performance indicator

1 Introduction

Once the Transplant Agency was established according to the Government Decision nr. 386 of 14 May 2010, there were launched actions aimed to implement the national

policies and programmes for human organ, tissue or cell transplantation, and to guarantee equal access to transplant services to all patients [1]. The national transplant system is still developing in the Republic of Moldova, and its main goal is to improve the quality of healthcare services rendered and the living standards of the patients through human organ, tissue or cell transplantation [2].

The human tissue transplant service is incorporated in and is a component part of the national transplant system of the Republic of Moldova [3]. Transplant of such tissues as cornea, bones, tendons or skin is a well-developed therapeutic technique. Tissues of a deceased donor may be transplanted to up to 100 people [4]. Some tissues may be donated only by living donors, if only such a procedure does not endanger the donor's life. Tissue transplant is a method, efficacy of which varies from life-saving treatment (for instance, in case of severe burns) to improvement of living standards [4]. Deficiency of donated tissues is the main factor impeding the transplant development; hence, it should be thoroughly examined [5]. Getting donated tissues is a complex activity in the healthcare practice and depends on the efforts made, motivation and professional training of the doctors of different specialties [6]. Deficiency of tissue donors is a common problem for all the countries possessing the tissue transplant techniques [7, 8].

According to the Law nr. 103 of 12 June 2014 for amending and completing the Law no. 42-XVI of 6 March 2008 on the transplant of human organs, tissues and cells, such activities as human tissue procurement, storage and transplantation are carried on by medical-sanitary institutions authorized by the Ministry of Healthcare, at the proposal of the Transplant Agency [9, 10]. 16 public and private medical-sanitary institutions were authorized by the Ministry of Health from 2011 to 2017 to carry on tissue procurement and transplantation, including 6 public institutions for conducting procurement and transplantation of tissues, human tissue bank, 2 public institutions for conducting procurement of tissues, 2 public and 4 private institutions for conducting transplantation of tissues, and 2

T. Timbalari (✉)

Transplant Agency, SMPPhU “Nicolae Testemitanu”,
29, N. Testemitanu, Chisinau, Republic of Moldova
e-mail: tatiana.timbalari@gmail.com

T. Timbalari · I. Codreanu
Transplantology Department, Transplant Agency, Chisinau,
Republic of Moldova

T. Timbalari · V. Nacu
Laboratory of Tissue Engineering and Cells Cultures, SMPPhU
“Nicolae Testemitanu”, Chisinau, Republic of Moldova

O. Lozan
School of Public Health Management, Chisinau, Republic of
Moldova

V. Nacu
Human Tissue Bank, Chisinau, Republic of Moldova

laboratories (public and private) to carry out mandatory biologic tests for donors [3].

Eight transplant coordinators for identifying, evaluating the potential donors and organizing procurement activities, 16 doctors responsible for tissue transplantation, and 5 medical assistants responsible for transplantation activities were appointed at the medical-sanitary institutions in order to arrange and supervise human tissue procurement and transplantation, together with the Transplant Agency, in conformity with the effective laws [3].

Hence, the goal of this thesis is to assess for the first time the activities of authorized medical-sanitary institutions dealing with human tissue donation and transplantation during a 7-year period in the Republic of Moldova, in order to develop the criteria for evaluation of efficacy of donation and transplant institutions, and to introduce new performance indicators.

2 Materials and Methods

This study has been based on the information about transplant services rendered by the medical-sanitary institutions, in correspondence with the national (Ministry of Health, Labour and Social Protection, Transplant Agency, National Agency for Public Health, National Bureau of Statistics) and international (Global Observatory on Donation and Transplantation, EURO CET, Newsletter Transplant) data and sources [11–13]. Primary documents of the medical-sanitary institutions and databases of the Transplant Agency have been also used: “TRANSPLANT” Automated Information System, additional automated information systems “Potential of Donation” and “Waiting list for cornea transplantation” [3]. The choice of the assay procedures has been made according to the complexity and particularities of the human tissue transplantation service. Thereby the direct observation, being the form of acquisition of information through direct, uninterrupted experience, obtained from a primary source, contributed to the direct evaluation of the activity of the authorised medical-sanitary institutions, of the way to perform the data processing operations of the primary documents used and their degree of difficulty. The volume and character of human tissue donation and transplantation activities performed in the authorised medical-sanitary institutions has been evaluated.

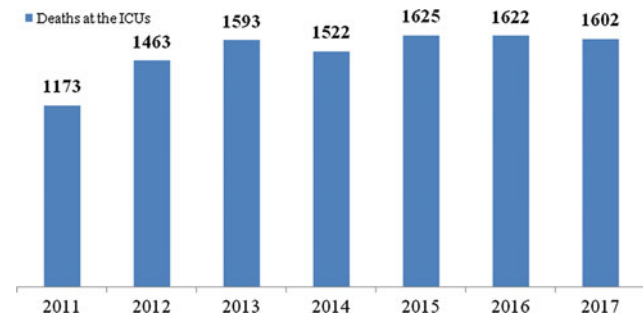


Fig. 1 Number of deaths at the ICUs in the period 2011–2017

3 Results

Transplant coordinators at authorized medical-sanitary institutions are responsible for coordination of procurement and transplant activities, and, as well, for provision of quarterly and annual reports of their activities.

The analysis of the 2011–2017 reports of transplant coordinators at authorized medical-sanitary institutions has been made.

The total number of deaths at Intensive Care Units hereinafter referred to as ICUs, as shown in Fig. 1, varied from 1173 to 1625. The mean number thereof constituted 1515 cases.

The number of potential donors after brain death and circulatory death, as presented in Fig. 2, varied from 36 to 139 from 2011 to 2017, and the mean number of cases was 69.4. Meanwhile, the number of actual donors varied from 5 to 40, and the mean number of cases was 24.9, i.e. 35.9% of potential donors, within the same period of time.

The potential of deceased donation, as calculated based on the number of deaths at ICUs, increased from 4.5% in 2011 to 8.7% in 2013 and then fell to 2.2% in 2017, although the efficacy of the donation process, as shown in Fig. 3, was continuously growing within the same period of time: from 9.4% in 2011 to 72.2% in 2017. The number of potential donors lost due to their families’ refusal decreased from 38.9% in 2014 to 22.2% in 2017.

An organ donor after brain death became also a tissue donor for the first time in the Republic of Moldova in 2014 (3.4% of the total number of actual tissues donors), while in 2016, already 8 organ donors became multi-tissue donors too (25.8% of the total number of actual tissues donors). Then 11 organ donors became multi-tissue donors too in 2017 (47.8% of the total number of actual tissues donors), as presented in Fig. 4.

The analysis of 2011–2017 reports of the persons responsible for tissue transplantation at authorized medical-sanitary institutions has shown that the most often

Fig. 2 Deceased donors after brain death and circulatory death in the period 2011–2017

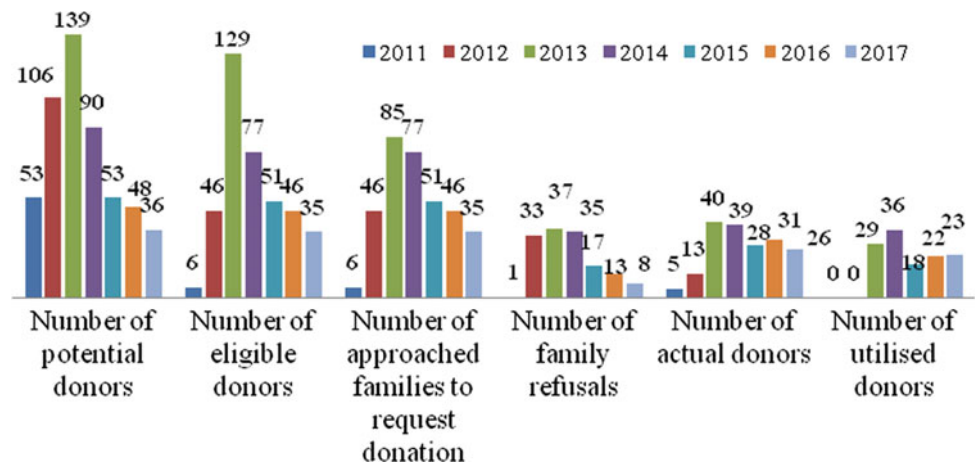


Fig. 3 Indicators related to the potential of deceased donation in the period 2011–2017

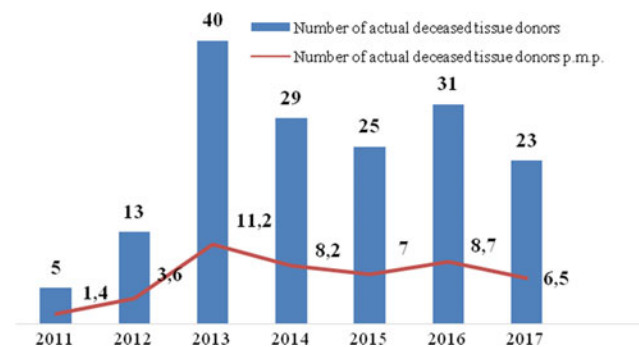
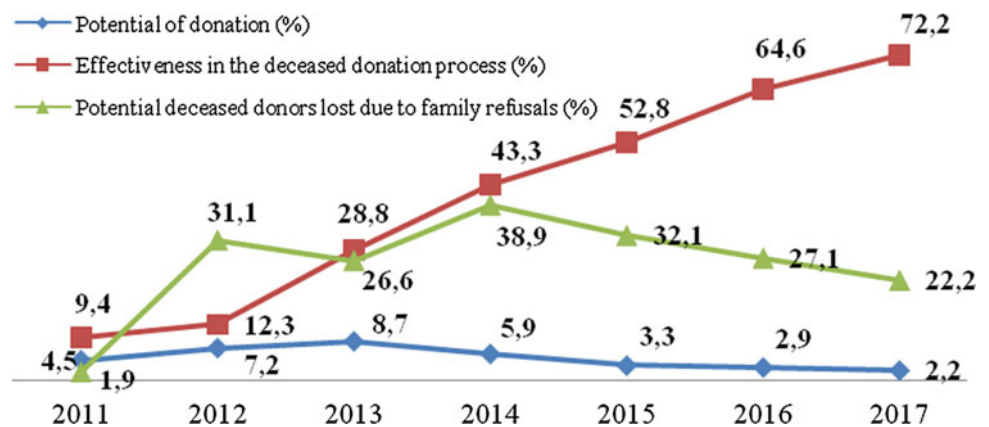


Fig. 4 Actual deceased tissue donors during in the period 2011–2017

transplanted tissue is bone (a mean number of 131.8 surgical interventions), followed by amniotic membrane (a mean number of 64.3 surgical interventions) and cornea (a mean number of 33.2 surgical interventions) and is presented in Table 1.

Relying on the provisions of the National Transplant Programme for 2017–2021, adopted by the Government Decision nr. 258 of 28 April 2017 [14], and on the international practices in implementation of the quality assurance programme in the deceased donation process [15], based on

assessment of the annual reports of medical-sanitary institutions’ activities, showing the potential of donation in each institution, the following performance indicators have been proposed for medical-sanitary institutions, in order to increase the efficacy of human organ and tissue donation from deceased donors:

- The number of actual organ/tissue donors shall make at least 5% of the total number of deaths per ICU,
- The number of actual tissue donors shall make at least 2.5% of the total number of deaths per medical-sanitary institution.

Based on this, the Transplant Agency has suggested to complete the Ministry of Healthcare Order no. 1038 of 23.12.2016 regarding the approval of the List of performance indicators of the medical-sanitary institution’s activity and the Regulation on the evaluation of the performance indicators of the public medical-sanitary institution’s activity, with provisions related to human organ and tissue donation from deceased donors within the medical-sanitary institutions authorized for this purpose [16].

Table 1 Number of tissue transplant procedures

Type of tissue	Year						
	2011	2012	2013	2014	2015	2016	2017
Bone	110	120	130	152	128	119	121
Tendon	6	1	2	3	7	11	10
Skin	–	–	2	24	23	15	20
Cornea	–	–	40	44	18	28	36
Nerve	–	–	14	–	–	–	–
Amniotic membrane	–	–	–	–	63	68	62
Sclera	–	–	–	–	1	–	–
Total	116	121	188	223	240	241	249

In order to assess the degree of achievement of the results during the implementation of the National Transplant Programme for 2017–2021, the following progress and performance indicators have been proposed to be used:

- Tissue transplant rate (bone, tendon, skin, cornea) per million population,
- Cornea transplant patients rate versus patients registered on waiting list,
- Success rate of treatment through tissue transplantation (bone, tendon, skin, cornea),
- The total number of actual deceased donors after brain death in relation to the total number of actual deceased donors,
- The number of actual deceased tissue donors per million population [14].

4 Conclusions

The human tissue transplant service is incorporated in and is a component part of the national transplant system of the Republic of Moldova.

Consolidation of the national transplant system and continuous development of the human tissue transplant service has led to a significant growth of efficacy of the deceased donation process.

Implementation of performance indicators for authorized medical-sanitary institutions dealing with human organ and tissue donation and procurement from deceased donors will allow to analyze the efficacy of functioning of donation and transplant institutions, and, as well, to carry on the audit of this field.

Conflict of Interest The authors declare that they have no conflict of interest.

References

1. Hotărîrea Guvernului nr. 386 din 14.05.2010 cu privire la instituirea Agenției de Transplant. În: Monitorul Oficial al Republicii Moldova, nr. 78–80, art. 4574 (2010). <http://lex.justice.md/md/334622/>
2. Codreanu, I., Romanciuc, G., Timbalari, T., et al.: Development of the national transplant system in the Republic of Moldova. *Organs Tissues Cells* **15**(3), 197–200 (2012)
3. Codreanu, I., Lozan, O., Timbalari, T.: Evaluation of the transplant system in the Republic of Moldova. *Manag. Health* **18**(4), 4–11 (2014)
4. The Guide to the Quality and Safety of Tissues and Cells for Human Application, 3rd edn. Directorate for the Quality of Medicines & Healthcare of the Council of Europe (2017) <https://www.edqm.eu/en/organs-tissues-and-cells-technical-guides>
5. WHO. <http://www.who.int/transplantation/ReportOttawaCTTx.pdf?ua=1>
6. Economic landscape of human tissues and cells for clinical application in the EU. Final report—study. Directorate-General for Health and Food Safety (European Commission), Foundation of European Tissue Banks; Rathenau Instituut; TRIP office for hemo- and biovigilance (2016). <https://publications.europa.eu/en/publication-detail/-/publication/5a0fd429-4a4e-11e6-9c64-01aa75ed71a1>
7. El-Shoubaki, H., Bener, A., Al-Mosalamani, Y.: Factors influencing organ donation and transplantation in State of Qatar. *Transplant. Med.* **18**(2), 97–103 (2006)
8. Maroudy, D., et al.: National transplant centers activities. Procurement of organs from deceased donors: approaching Muslim families. *Organs Tissues* **7**(2), 129–131 (2004)
9. Legea nr. 103 din 12.06.2014 pentru modificarea și completarea Legii nr. 42-XVI din 6 martie 2008 privind transplantul de organe, țesuturi și celule umane. În: Monitorul Oficial al Republicii Moldova, nr. 185–199, art. 438 (2014). <http://lex.justice.md/md/353825/>
10. Legea nr. 42-XVI din 06.03.2008 privind transplantul de organe, țesuturi și celule umane. În: Monitorul Oficial al Republicii Moldova, nr. 81, art. 273 (2008). <http://lex.justice.md/md/327709/>
11. Global Observatory on Donation and Transplantation. <http://www.transplant-observatory.org>
12. EURO CET Project. <http://www.eurocet.org>
13. Newsletter Transplant. International figures on donation and transplantation-2014. In: Matesanz, R., Miranda, B. (eds.) Select Committee of Experts on the Organizational Aspects of Co-operation in Transplantation. Council of Europe. Aula Médica Ed., Madrid, Spain (2015). https://www.edqm.eu/sites/default/files/newsletter_transplant_2015.pdf

14. Hotărîrea Guvernului nr. 657 din 23.08.2017 cu privire la aprobarea Programului național de transplant pentru anii 2017–2021. În: Monitorul Oficial al Republicii Moldova, nr. 322–328, art. 774 (2017). <http://lex.justice.md/index.php?action=view&view=doc&lang=1&id=371164>
15. Dopki Project, European Commission: Guide of Recommendations for Quality Assurance Programmes in the Deceased Donation Process (2009)
16. Ordin Ministerului Sănătății nr. 1038 din 23.12.2016 cu privire la aprobarea Listei indicatorilor de performanță a activității instituției medico-sanitare publice și Regulamentului privind modul de evaluare a indicatorilor de performanță a activității instituției medico-sanitare publice. În: Monitorul Oficial al Republicii Moldova, 03.02.2017, nr. 30–39, art Nr: 100. <http://lex.justice.md/index.php?action=view&view=doc&lang=1&id=368723>

Electro-Acoustical Examination in Noninvasive Monitoring as a Basis for Treatment Selection

S. Diacova

Abstract

Early detection of otitis media and adequate treatment in small children prevent from chronic middle ear disease and complications development. The purpose of this article is to determine the role of the noninvasive electro-acoustical examinations in treatment modality selection in prolonged otitis media forms. Impedance audiometry, brainstem evoked response audiometry and registration of otoacoustical emissions were used for early detection of middle ear pathology and for monitoring of children. Monitoring of small children confirmed high rate of otitis media in this age group. Correct interpretation of the diagnostic tests results, analysis of risk factors background and electro-acoustical monitoring present the basis for differentiation between short-duration otitis media forms and prolonged forms. Any modification of impedance audiometry results in a child with risk factors is indication for further electro-acoustical monitoring of middle ear. Prolonged forms of otitis media in children are treated by ear surgery—myringotomy with tympanostomy tube insertion. Post-surgical electro-acoustical monitoring gives the information of middle ear status and function and is useful in prognosis of otitis media evolution. Post-surgical electro-acoustical monitoring showed the advantages of tympanostomy in children especially in modified version.

Keywords

Noninvasive diagnostic tools • Monitoring • Impedance audiometry • Otitis media prolonged forms • Modified tympanostomy

1 Introduction

Otitis Media (OM) is the middle ear (ME) pathology, which affects 90% of children, especially at early age. Some of OM forms provoke intracranial complications, chronic suppurative OM and chronic hearing loss. The prognostics and detection of those OM forms and intensive treatment including surgical one in small children prevent from the negative disease evolution.

Difficulties of precise diagnostics and unsatisfactory results of therapy evoked application of objective diagnostic tools—electro-acoustical and electrophysiological methods, impedance audiometry (IA), Brainstem Evoked Response Audiometry (BERA) and registration of otoacoustical emissions (OAE), for early detection of ME pathology [1–6]. Are they useful in prognosis of OM negative evolution?

Management of OM prolonged forms such as persistent OM with effusion (POME) and recurrent acute OM (RAOM), presents variety of approaches and technologies in different countries. Traditional approach is standard treatment modality in Eastern Europe. It includes diagnostic tests in children with evident OM manifestations. Treatment usually consists of adenoidectomy with/or without physiotherapy as a first stage. Myringotomy with tympanostomy tube insertion, or tympanostomy (TS) sometimes is performed as a second procedure on a later stage. The effectiveness of this classical intervention is not clear [3–6].

Another approach to POME and RAOM treatment is presented in new Protocols of OM management from USA, Japan, Australia, Finland, etc. [1–3]. Those standards are based on early detection of ME pathology in small children with risk factors (RF) and relatively early surgical intervention—TS as a first and single procedure. Traditional modality of OM management, adenoidectomy, is recommended only in cases of further OM progression or recurrence, in complex with second TS-surgery. Physiotherapy is not included in recommendations. This modality significantly reduces recurrence and complication rates, but

S. Diacova (✉)

Department of Otorhinolaryngology, State University of Medicine and Pharmacy “Nicolae Testemitanu”, Stefan cel Mare, 165, Chisinau, Moldova
e-mail: svetlana.diacova@usmf.md

increases the number of ear surgery and makes TS the most frequently surgery performed in USA, Finland, Australia, etc. [1–3].

In Moldova the chronic suppurative OM, otogenic complications and chronic hearing loss rates are relatively high. Vetricean [5], Diacova and Ababii [9], what indicates necessity of OM researches.

In collaboration with Society “Pediatricians due Monde”, Clermont-Ferrand, France and Mayo Foundation, Mayo Clinic, Rochester, MN, USA we conducted several projects in order to create a system of OM management.

Our system includes ME monitoring in children with RF high score for determination of patients who really need surgical intervention and treatment complex. We elaborated the diagnostic algorithm to highlight the conditions and diseases, which provoke OM. Medical therapy of this pathology helps in differentiation between the symptomatic and independent OM forms. Surgical treatment in our modification, modified tympanostomy (MTS), is designed for better functional results and prevention of secondary persistence or recurrence [9].

Specific goal of OM management is the ME physical and acoustical restoration and prevention of OM recurrence [6–9]. Assessment of the physical, acoustical characteristics, hearing, quality of life and general health characteristics is necessary in order to determine the feasibility of therapeutic activities conducted in this pathology.

The purpose of this article is to formulate the role of the noninvasive electro-acoustical examinations in indication and selection of treatment modalities in persistent and recurrent OM forms.

2 Materials and Methods

2.1 Material

Database selection: Children at 1–7 years of life with chronic pathology: group I—respiratory tract pathology (RTP), group II—gastro-intestinal pathology (GIP), and group III—healthy children.

Methods of selection: Monitoring of ME includes screening IA and screening-otoscopy four times during 1 year (once in 3 months). The presence of pathological changes for at least 3 months we classified as persistent otitis media with effusion (POME). Recurrence of OM signs 3 times during 6 months or 4 times during four has we classified as recurrent acute otitis media (RAOM).

Database: Children with POME and RAOM were selected and three hundred of them were randomly assigned to 3 subgroups according to different modalities of treatment: CTSA—classical TS and Adenoidectomy, MA—

Myringotomy and Adenoidectomy, MTS—Modified TS (MTS) and Adenoidectomy.

Methods: Several noninvasive instruments were used in the study: background characteristics questionnaire; otomicroscopy; impedance audiometry (IA); audiometry, which consists of subjective conventional audiometry and objective methods, such as registration of otoacoustical emissions (OAE) and registration of brainstem electrical response audiometry (BERA); X-ray examination of paranasal sinuses (XPS); bacteriologic examination of palatine tonsils (BT); Computer Tomography (CT) of ME; noninvasive monitoring (NM); quality of life (QOL) and general health (GH) questionnaires before and after the treatment. Statistical analysis (Student-test, Fisher-statistics and discriminate analysis) was performed.

3 Results and Discussions

3.1 Risk Factors (RF)

Background characteristics: For the identifying of the risk factors, associated with the OM prolonged form, we analyzed the anamnesis data and the objective tests results by the statistical comparative methods. Wide range of RF for OM development in children is variable, unspecific and is characteristic for both forms—POME and RAOM. Some of risk factors for OM development (only with $p < 0.001$, and F not less than 15), are presented. Risk factors for OM prolonged forms in children during the first 2 years of life included: maxilla-facial abnormalities, RTP or/and GIP during first year of life, horizontal position in feeding time. Risk factors for RAOM development in children of pre-school age included maxilla-facial abnormalities, physiotherapy of middle ear and paranasal sinuses, recurrent sinusitis, presence of Strep B hemolytic group A and *Staphylococcus aureus* in pharynx.

Microbiological profile differs in three groups of examined patients ($p < 0.001$). The majority of children with POME had in palatine tonsils *Haemophilus influenza* and *Streptococcus pneumonia*, in children with RAOM—*Streptococcus b-hemolytic* and *Staphylococcus aureus*, in difference from the healthy children where predominated *Streptococcus viridans* and other nonpathogen microbes (Fig. 1).

Otomicroscopy test characteristics: Two otoscopy sets were used: “Carl Storz” set and Otomicroscope “Zeiss”. We have designed Otoscopical profile for each child. Each of the examinations included 40 points, such as color, contour, luster, translucence, light reflex, landmarks and others. Results were statistically compared with surgical findings.

Sensitivity of otomicroscopy in OM detection was 98.1%, specificity—48.0%. We found some important for

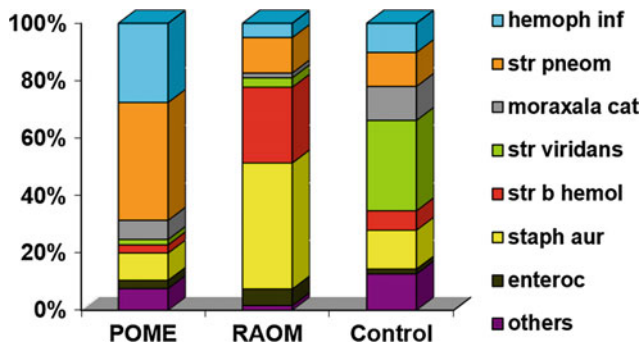


Fig. 1 The most common microorganisms isolated from pharynx. POME—*Haemophilus influenza*, *Streptococcus pneumoniae*; RAOM—*Streptococcus beta-hemolytic group A*, *Staphylococcus aureus*; Control—*Streptococcus viridans*

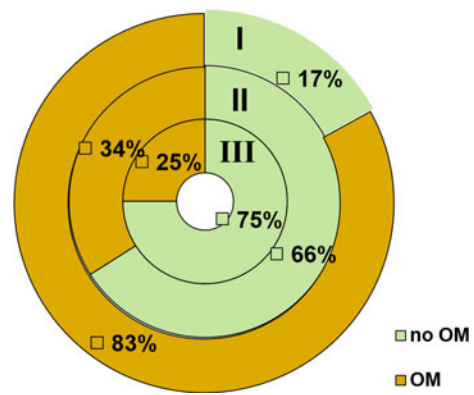


Fig. 2 Otitis media rate in 3 groups of children. I: 83%, II: 34%, III: 25%

OM-diagnostics symptoms. But precise diagnosis of OM, based on otomicroscopical findings alone, is limited. Subjective character of the exam and similarity of signs in POME and RAOM groups and even in healthy infant's ears make this important diagnostic tool not specific.

Electro-acoustical tests characteristics

Two Impedance Audiometers were used: (a) impedance audiometer for screening and monitoring MT-10, (b) clinical impedance audiometer. Both instruments—with a probe tone frequency of 226 Hz and a positive and negative pressure sweep between +200 and -400 daPa and sweep speed—600 daPa/s, near the tympanogram peak—200 daPa/s, and the compliance range—0.1 to 0.6 mL. We perform 3 consecutive tests to get a reliable curve for interpretation. For evaluation of tympanometric curve results we used classification of Jerger J. in modification of Tos M. as type A, B, C1 and C2. Additionally, we evaluated all other tympanometric curve characteristics.

Audiometry—subjective and objective methods: For hearing assessment and topical diagnostics of hearing loss, differentiation between conductive, sensori-neural and mixed hearing loss we used conventional audiometry. Children at early age or with difficulties in communication were examined by objective examination, such as registration of OAE or BERA.

Monitoring of children: ME pathology was detected in majority of children during the period of observation. Clinically ME changes were classified as acute OM (AOM) and OM with effusion (OME) (Fig. 2).

All children with OM received standard treatment according to clinical manifestations and coincident pathology.

Electro-acoustical monitoring: Electro-acoustical monitoring of children, suffered of OMA and OME permitted to diagnose prolonged forms of OM in small children (Fig. 3).

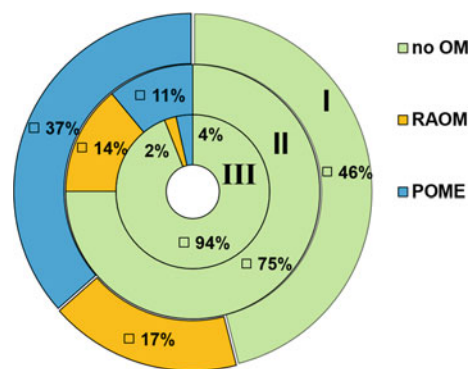


Fig. 3 Prolonged otitis media forms rate in 3 groups of children. I: POME—17%, RAOM—37%; II: POME—14%, RAOM—11%; III: POME—2%, RAOM—4%

Classification of OM: Classification on short-duration forms, such as AOM and OME and prolonged forms, such as POME and OMAR we made on the base of monitoring of electro-acoustical tests results and clinical manifestations.

Short-duration forms, such as AOM and OME were prevalent in children. Persistence of type B or low characteristics of tympanogram with any another type of tympanograms for more than 3 months was classified as POME. Recurrence of these electroacoustical signs 3 times during 6 months or 4 times during 12 months we classified as RAOM. Formation of sub-chronic forms such as POME and RAOM began from 8 to 10 months of life with the maximum at the age 2–3 years of life.

Clinically, prolonged forms of OM have silent course and became evident for a child's parents at the age of 3–4 years of life. Electroacoustical monitoring of small children with RF demonstrates that OM prolonged forms background is formed at 1–2 year children (Fig. 3).

Audiometry: Audiometry revealed mild to moderate conductive hearing loss, which correlated to ME pathology

independently of OM form. Part of small children (15%) were diagnosed as having mixed hearing loss.

Radiology examinations: Clinical signs of sinusitis during for more than 1 month in children aged older than 2 years were an indication for paranasal sinuses analyzing and adequate treatment. All children with prolonged forms of OM were examined by Spiral CT with 3D reconstruction of ME. The analysis of the results demonstrated the presence of effusion in tympanic cavity and mastoid process, and parietal thickness of ME cavities.

Surgery: Prolonged forms of OM, such as POME and RAOM, are indication for surgery. All selected children with POME and RAOM from the Database were randomly assigned to three subgroups according to different modalities of treatment: MA—Myringotomy and Adenoidectomy, CTSA—classical TS and Adenoidectomy, MTSA—Modified TS (MTS) and Adenoidectomy.

Post-surgical monitoring: Post-surgical monitoring included audiometry, otomicroscopy, monitoring of quality of life and general health monitoring.

Post-surgical impedance audiometry: In 12–18 months after surgery, when tympanic perforation is closed, children were examined by IA test and audiometry.

Electro-acoustical test of middle ear in 12–18 months after surgery demonstrated complete restoration of ME function (tympanogram Type A with normal characteristics) in 83% of children after CTSA, 52% of children after MA and in 96% of children after MTSA (Fig. 4).

Tympanogram type B was registered in 10% of CTSA group, 23% of MA group and 2% of MTSA group. Tympanogram type C was found in 4% of children from CTSA group, 25%—from MA group and 2% of MTSA group.

According to electro-acoustical examination, we conclude that majority of small children suffered from OM. Correct interpretation of the diagnostic tests results, analysis

of risk factors background and electro-acoustical monitoring is the basis for differential diagnostics and adequate treatment. Children with risk factors for prolonged OM forms received intensive medical treatment and were included in electro-acoustical monitoring. Development of prolonged modifications was the basis for surgical treatment. Post-surgical electro-acoustical monitoring was included in complex monitoring and showed the advantages of myringotomy with insertion of tympanostomy tube especially in modified version.

4 Conclusions

1. Electro-acoustical examinations of child middle ear majority of small children suffered from OM.
2. Correct interpretation of the diagnostic tests results, analysis of risk factors background and electro-acoustical monitoring is the basis for differential diagnostics and adequate treatment.
3. Electro-acoustical monitoring of middle ear function in children with risk factors presents the collection of data for differential diagnosis between short-duration OM forms and prolonged forms what is the basis for adequate treatment.
4. Post-surgical electro-acoustical monitoring gives the information of ME status and function and is useful in prognosis of OM evolution.
5. Post-surgical electro-acoustical monitoring showed the advantages of tympanostomy especially in modified version.

Acknowledgements The author expresses the appreciation for the support we received from the Mayo Clinic (USA) staff, especially from Dr. Thomas McDonald and from the Society Pediatricians du Monde in Clermont-Ferrand (France), Dr. Desvignes Veronique. We also acknowledge the contributions of the staff and associates in the Department of Otorhinolaryngology at the State University of Medicine and Pharmacy “Nicolae Testemitanu” in Chisinau, Moldova. **Conflict of Interest** The author has no conflict of interest to declare.

References

1. Rosenfield, R., Shin, J., Schwartz, S., et al.: AAO-HNSF updated clinical practice guideline: otitis media with effusion. *Otolaryngol. Head Neck Surg.* **154**(1 suppl.), S1–S41 (2016)
2. Venekamp, R.P., Burton, M.J., van Dongen, T.M.A., van der Heijden, G.J., van Zon, A., Schilder, A.G.M.: Antibiotics for otitis media with effusion in children. *Cochrane Database of Systematic Reviews*, Issue 6. Art. No.: CD009163 (2016) <https://10.1002/14651858.CD009163.pub3>.
3. McDonald, S., Langton, CD., Nunez, DA., et al.: Grommets (ventilation tubes) for recurrent acute otitis media in children.

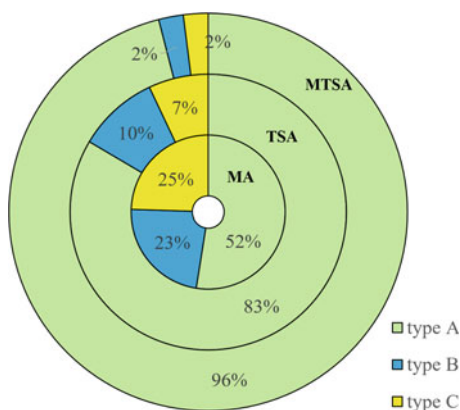


Fig. 4 Tympanograms after surgery in 3 groups of children. MA: type A—52%, type B—23%, type C—25%; TSA: type A—83%, type B—10%, type C—4%; MTSA: type A—96%, type B—2%, type C—2%

- Cochrane Database Syst. Rev. **4**, (2008) <https://doi.org/10.1002/14651858.CD004741.pub2>
4. Lous, J., Ryborg, C., Thomsen, J.: A systematic review of the effect of tympanostomy tubes in children with recurrent acute otitis media. *Int. J. Pediatr. Otorhinolaryngol.* **75**, 1058–1061 (2011)
 5. Vetrician, S.: *Maladia urechii operate*. Monografia, Chişinău (2018)
 6. Diacova, S., McDonald, T., Ababii, I.: Clinical, functional, and surgical findings in chronic bilateral otitis media with effusion in childhood. *Ear Nose Throat J* **95**(8), E31–E 38 (2016)
 7. Kujala, T., Alho, O., Luotonen, J., et al.: Tympanostomy with and without adenoidectomy for the prevention of recurrences of acute otitis media. *Pediatr. Infect. Dis. J.* **31**, 565–569 (2012)
 8. Browning, G., Rovers, M., Williamson, I.: Grommets (ventilation tubes) for hearing loss associated with otitis media with effusion in children. *Cochrane Database Syst. Rev.* **10** (2010), <https://doi.org/10.1002/14651858.CD001801.pub3>
 9. Diacova, S., Ababii, I.: *Metoda de tratament al otitei medii exudative la copii*. Brevet de invenție MD 674Y. BOPI, pp. 24–25, 30 Sept 2013

Functional and Morphological Correlations in Prolonged Otitis Media in Childhood

S. Diacova, I. Ababii, L. Danilov, M. Maniuc, P. Ababii, V. Gavriluta, and A. Levcenco

Abstract

Recurrent and persistent otitis media (OM) in childhood are characterized by prolonged and clinically different courses. The aim of this work is to study functional and morphological features in children with prolonged OM forms. Children with persistent OM with effusion and recurrent acute OM were examined by impedance audiometry, brainstem evoked response audiometry, registration of oto-acoustical emissions, pneumatic otoscopy, otomicroscopy, computer tomography and examination of surgical findings. Surgery consisted of modified version of tympanostomy. Otomicroscopical, cytological and histological examinations revealed the presence of morphological changes characteristic for chronic inflammation in part of recurrent and persistent OM. Duration of the process (more than 3 months) and previous treatment (physiotherapy and adenoidectomy) correlated with chronic changes in both groups. Prolonged OM forms present interrelated stages of the common inflammatory process in the middle ear. Functional changes, indicating the presence of OM for more than 3 months are the basis for comprehensive treatment, including tympanostomy. Modified tympanostomy permits better evacuation of pathological content from tympanic cavity and improves evaluation of morphological changes.

Keywords

Prolonged forms of otitis media • Functional examinations • Histological and cytological findings • Modified ear surgery

1 Introduction

Otitis media (OM) presents the group of the middle ear (ME) pathology, which begins in childhood from short-duration forms, continues to persistent or recurrent forms and progresses to chronic forms. Understanding of transformational mechanism influences on elaboration of treatment preventive approaches [1–4].

Prolonged forms of OM include recurrent acute otitis media (RAOM) and persistent otitis media with effusion (POME). RAOM is defined as three episodes of acute OM in 6 months or four episodes—in 12 months. POME is classified as a presence of liquid behind an intact tympanic membrane. The importance of the middle ear status for the child's development and unclear criteria for the differential diagnosis of various OM forms causes a large variety of treatment methods from “Watchful waiting and monitoring” tactics, long duration antibiotic therapy, antibiotic prophylactics, local physiotherapy in combination of auditory tube catheterization and insufflation, adenoidectomy etc. Existing methods of treatment clinically improve hearing. How those methods influence on the evolution of the inflammatory process in middle ear is unclear. Long-term results do not always correlate with initial clinical positive changes [1–3, 5–7].

Protocols of OM management from USA, Japan, Australia, Finland, advise early ear surgery. Myringotomy with insertion of tympanostomy tube was found by many authors to be the most effective approach in preventing and treating of OM chronic forms. Standard treatment modality in Eastern Europe includes adenoidectomy with/or without physiotherapy as a first stage. Myringotomy with

S. Diacova (✉) · I. Ababii · L. Danilov · M. Maniuc · P. Ababii · V. Gavriluta · A. Levcenco

Department of Otorhinolaryngology, State University of Medicine and Pharmacy “Nicolae Testemitanu”, Stefan cel Mare, 165, Chisinau, Moldova
e-mail: svetlana.diacova@usmf.md

P. Ababii · V. Gavriluta · A. Levcenco
Otorhinolaryngology Division, Pediatric Clinic “Em. Cotaga”, Chisinau, Moldova

tyimpanostomy tube insertion or tympanostomy (TS) sometimes is indicated as a second procedure on a later stage [1–4].

Evaluation of the objective ME functional characteristics with the status of the middle ear tissue at all stages of the OM development is necessary both to clarify the OM pathogenesis and to determine the feasibility of different treatment types carried out in this pathology [1–8].

In collaboration with Mayo Foundation, Mayo Clinic, Rochester, MN, USA we conducted several projects in order to create a system of OM management. Our common clinical, functional, histological and cytological researches of middle ear in children suffered from OM demonstrated significant influence of treatment modality on evolution of the disease [7, 10, 11].

The aim of this work is to study the functional and morphological correlations in children with OM prolonged forms.

2 Materials and Methods

2.1 Material

Database. Our research was carried out in ORL division, Pediatric Clinic “Em. Cotaga”. The study involved 128 patients at the age from 1 to 18 years with different forms of otitis media. The main including criteria consisted of presence of ME pathology during for at least 3 months.

The first group (I) contained children with POME—the presence of otoscopic and functional changes characteristic for the ME fluid for at least 3 months with absence of any acute general or local manifestations. In the second group (II) we included children who suffered from RAOM—three acute otitis media (AOM) for the last 6 months or 4 of the episodes over the past year. Part of children received physiotherapy and adenoidectomy as previous treatment.

2.2 Methods

Methods of noninvasive examination. Noninvasive examination included anamnesis, routine ENT examination, pneumatic otoscopy and otomicroscopy before surgery, functional exams in dynamics—conventional audiometry, impedance audiometry, radiological examinations. Detailed history of the disease containing: beginning, duration, progression and data of previous treatment was collected and analyzed. Results of endoscopy and functional examinations in dynamics were included in database.

Invasive examinations. The work up included invasive examinations: otomicroscopy during surgery, otomicroscopy and revision of tympanic cavity during second-look surgery,

analysis of surgical findings and morphological changes, cytological and histological examinations of pathologic material.

Surgical intervention. Classical tympanostomy (CTS), a microsurgical procedure, schematically consists of some stages: the small incision is created in antero-superior or antero-inferior quadrant of the tympanic membrane (TM), aspiration of the exudate is carried out from tympanic cavity (TC) through this perforation, tympanostomy tube (TT) is inserted and fixated in incision. The positive effect of the surgery consists of tympanic cavity pressure equilibration to atmospheric, drainage of liquid, aeration of tympanic cavity, etc. [3–5, 7–9].

We analyzed some disadvantages of this surgery type. Otorrhea is one of the common complications and outcome of the classical tympanostomy [7, 9–11] (Fig. 1).

One of disadvantages consists in 2 different tasks of the surgery: evacuation of pathological contents and TT fixation. The incision created for fixation of TT corresponds to TT size and has to be very small. Effusion in tympanic cavity is very thick, “glue-like”, in a big amount. The tiny incision is too small for complete evacuation of the viscous, mucous or purulent liquid from the tympanic cavity.

As a result, a part of pathological content remains in TC and manifests in post-surgical period by otorrhea. Additionally, microscopic examination of the TC through the small incision is practically impossible.

Modified tympanostomy (MTS) was elaborated for avoiding of these disadvantages [7, 9]. Modified tympanostomy differs from CTS by the additional incision, which we create in posterior quadrants in order to complete evacuation of pathological content from the tympanic cavity.

This incision opens tympanic cavity larger than classical incision which improves evacuation of pathological material from tympanic cavity. Additionally, the visibility of mucosal modification in tympanic cavity is also ameliorated (Fig. 2).

According to our previous results, the additional incision closes during next few days with no any negative further influence on ME function and/or otoscopic appearance.

3 Results and Discussions

3.1 Noninvasive Examinations

Pneumatic otoscopy and otomicroscopy revealed different changes in tympanic membrane appearance, retraction pockets and thin-film adhesion.

Audiometry and impedance audiometry demonstrated in all groups mild conductive hearing loss. The mean hearing level before surgery in Group 1 was 35 dB (SD 4) and in Group 2—39 dB (SD 6).

Fig. 1 Classical tympanostomy.
1. Small incision—ineffective drainage. 2. Otorrhea after surgery

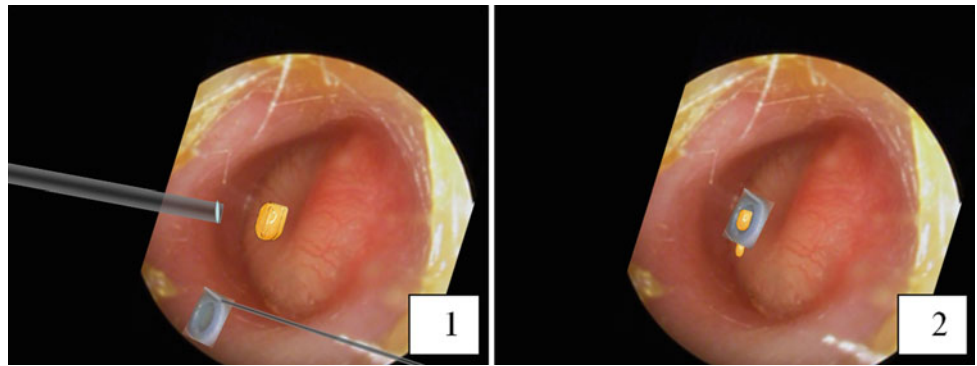
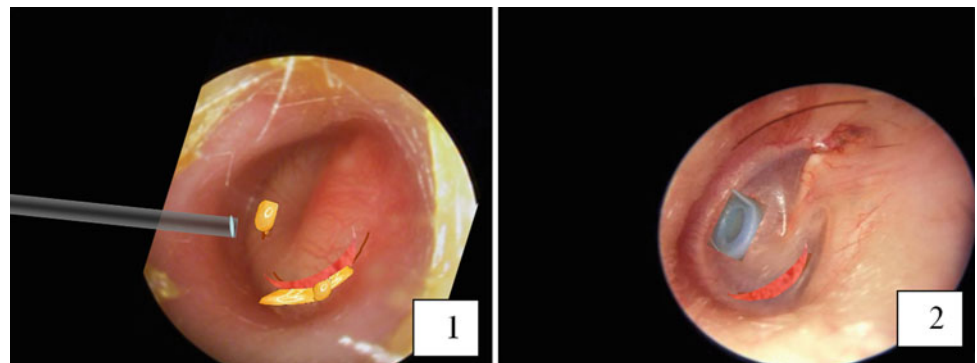


Fig. 2 Modified tympanostomy.
1. Two incisions: small incision for TT and big incision for an effective drainage. 2. After tympanostomy: small incision contains TT and big incision is closing by itself in 10 days



Type B or Type C₂ of tympanogram without acoustical reflex. Type B of tympanogram was registered in 96% of ears from Group 1 and 72% of ears from Group 2, Type C₂—in 4 and 28% accordingly. No any Acoustical Reflex was registered. Noninvasive functional results were practically identical in both groups of patients.

3.2 Invasive Examinations

Surgical findings. Effusion was detected in majority of cases—88% with different amount and quality. Other changes, characteristic for chronic suppurative process were relatively rare in Group I and more often in Group II: retraction pockets, thin-film adhesion to promontory—in 24.6 and 64.5% of cases accordingly, granulations, polyps—in 16.4 and 45.2%, cholesteatoma—in 1.2 and 3.9% of ears. Therefore, in some cases of OME and RAOM we found modifications which characterize adhesive and chronic suppurative OM.

Analysis of surgical findings in the tympanic cavity during surgery demonstrated the presence of a viscous fluid (mucus or muco-purulent).

Cytological examination. There were found 2 types of exudate by cellular composition. The first type had small number of cells (<100 in the field of view with increasing X400), with a predominance of lymphocytes and histiocytes

and a small number of polymorphonuclear leukocytes. Exudate of the second type contains a large number of cells (>1000 in the field of view with increasing X400), with the dominance of polymorphonuclear leukocytes and the relatively small number of lymphocytes and histiocytes. In all cases in both groups were evident fibrotic bands and an increasing number of proteins—changes that are responsible for the viscosity of secretions.

In the most cases, in the ears of the group I was found exudate of the first type (62%) in Group II was dominated by changes in the second type (69%).

Histological examination revealed mucosal hyperplasia, ciliated cells, infiltration of the sub-epithelial layer of leukocytes (mononuclear cells) and goblet cells, large vessels and granulation tissue fibroblasts. Polymorphism of cells—presence of macrophages, polymorphonuclear leukocytes, mast cells, lymphocytes—was found. Were detected threads of fibrin. Such modifications were more often characteristic of patients from group II ($p < 0.05$). Mucous membrane was relatively pale in the presence of proliferative processes. Were found collagen fibers with a small number of vascular and glandular structures, mainly in patients from II groups ($p < 0.05$). In 3 ears (3 children) deep retraction pockets contained cholesteatoma cells.

Correlations. We analyzed the presence of chronic modifications in the middle ear in function of different factors from disease history, including age of the disease

beginning, duration of the disease and previous treatment of the patients.

Correlations of chronic modifications with age of the disease beginning is negative, $r = -0.63$. That indicates indirect correlation: the earliest age of disease beginning more correlated to chronic changes than oldest age of disease beginning.

Duration of the disease was the most important criteria of chronic modifications development. Correlations of chronic modifications with duration of disease was $r = 0.78$. It shows the direct correlation between these characteristics. In many cases, duration of the disease was determined relatively approximately because of silent disease beginning.

The influence of previous treatment on development of chronic middle ear changes was analyzed as adjustment to the duration of the disease. The most significant influence was found for physiotherapy + adenoidectomy. So, duration of disease with the adjustment of physiotherapy + adenoidectomy correlated with chronic modifications in middle ear with $r = 0.82$.

Surgical treatment. Modified tympanostomy performed for treatment of OM prolonged forms was useful also in surgical examination of tympanic cavity. Visualization, morphological evaluation, histological and cytological sampling were carried out through the additional incision in posterior quadrants of the tympanic membrane. Additional incision was closed itself during less than 10 days after surgery in all patients.

4 Discussions

The age of OM onset of our patients was the first 1–2 years of life. This middle ear inflammation manifests with only one single symptom—mild, sometimes undulating, hearing loss, which was not evident for the child and his parents because of early age of the child.

Summarizing the clinical and functional data and comparing them with the results of surgical, cytological and histological studies, we established some clinical and morphological correlations.

Natural OM evolution, observed in the absence of any treatment, depends on age of the child, the pathology of respiratory tract, gastrointestinal tract, etc. It presents progressive development of pathological changes in the middle ear, which may clinically manifest by disease staging from persistent OM with effusion to recurrent acute OM and backward, and resulted in formation of a chronic adhesive OM, in some cases—with purulent content. The bacteria, bacterial products, enzymes, and inflammatory mediators presented in the unresolved OM contribute to progression of local disease and eventually to irreversible changes associated with chronic otitis media.

The disease beginning during the first two years leads to earlier transition from persistent OME to recurrence of acute OM and formation of granulation tissue in most cases. The lack of adequate treatment contributes to the transformation in granulation-adhesive process.

At this stage, the use of physical treatments and adenoidectomy does not stop the further development of chronic adhesive and purulent otitis media, but leads to faster formation of adhesion, which clinically manifested by partial temporal improvement of hearing and latent gradual formation of morphological substrate of chronic pathology.

Modified tympanostomy performed for treatment of OM prolonged forms was useful in surgical examination of tympanic cavity.

5 Conclusions

1. Clinical forms—persistent otitis media with effusion and recurrent acute otitis media—are interrelated stages of evolution of the common inflammatory process in the middle ear, which lead to adhesive otitis media or chronic purulent otitis media.
2. Pathological changes in the middle ear depend on the child's age, duration and dynamics of the process, the adequacy of ongoing medical treatment.
3. Functional changes, indicating the presence of otitis media for more than 3 months corresponds to chronic modifications of middle ear and not only effusion.
4. The physiotherapy and adenoidectomy worsened middle ear chronic changes in children with prolonged OM forms.

Acknowledgements The author expresses the appreciation for the support we received from the Mayo Clinic (USA) staff, especially from Dr. Thomas McDonald and from the Society Pediatricians du Monde in Clermont-Ferrand (France), Dr. Desvignes Veronique. We also acknowledge the contributions of the staff and associates in the Department of Otorhinolaryngology at the State University of Medicine and Pharmacy “Nicolae Testemitanu” in Chisinau, Moldova.

Conflict of Interest The author has no conflict of interest to declare.

References

1. Rosenfield, R., Shin, J., Schwartz, S., et al.: AAO-HNSF updated clinical practice guideline: otitis media with effusion. *Otolaryngol. Head Neck Surg.* **154**(1 supp.), S1–S41 (2016)
2. Venekamp, R., Burton, M., van Dongen, T., van der Heijden, G., van Zon A., Schilder A.: Antibiotics for otitis media with effusion in children. *Cochrane Database Syst. Rev.* **6**(6) (2016)

3. Venekamp, RP., Mick, P., Schilder, AG., Nunez, DA.: Grommets (ventilation tubes) for recurrent acute otitis media in children. *Cochrane Database Syst. Rev.* **5**(4) (2018)
4. Browning, G., Rovers, M., Williamson, I.: Grommets (ventilation tubes) for hearing loss associated with otitis media with effusion in children. *Cochrane Database Syst. Rev.* (10) (2010)
5. Lous, J., Ryborg, C., Thomsen, J.: A systematic review of the effect of tympanostomy tubes in children with recurrent acute otitis media. *Int. J. Pediatr. Otorhinolaryngol.* **75**, 1058–1061 (2011)
6. Vetrician, S.: *Maladia urechii operate*. Monografia, Chişinău (2018)
7. Diacova, S., McDonald, T., Ababii, I.: Clinical, functional, and surgical findings in chronic bilateral otitis media with effusion in childhood. *Ear Nose Throat J.* **95**(8), E31–E 38 (2016)
8. Kujala, T., Alho, O., Luotonen, J., et al.: Tympanostomy with and without adenoidectomy for the prevention of recurrences of acute otitis media. *Pediatr. Infect. Dis. J.* **31**, 565–569 (2012)
9. Diacova, S., Ababii, I.: *Metoda de tratament al otitei medii exudative la copii*. Brevet de invenție MD 674Y. BOPI, pp. 24–25, 30 Sept 2013
10. Diacova, S., McDonald, T., Beatty, C., Wei, J.: Ear drops in preventing otorrhea associated with tympanostomy tubes insertion in children. In: 4th European Congress of Oto-Rhino-Laryngology Head and Neck Surgery, ICC Berlin, Germany. Abstracts, p. 56 (2000)
11. Diacova, S., McDonald, T.: A comparison of outcomes following tympanostomy tube placement or conservative measures for management of otitis media with effusion. *Ear Nose Throat J.* **86**, 552–554 (2008)

The Review of Bipolar Ion Mobility Spectrometers

Y. R. Shaltaeva, A. V. Golovin, V. K. Vasilyev,
E. A. Gromov, M. A. Matusko, E. K. Malkin,
I. A. Ivanov, V. V. Belyakov, and V. S. Pershenkov

Abstract

The review considers the design of ion mobility spectrometers, which allow for the conditionally simultaneous detection of both positive and negative ions. The review of existing serial ion mobility spectrometers with simultaneous detection of substances in both spectrometric modes is carried out. The ways of realization of the bipolar ion mobility spectrometer are analyzed.

Keywords

Ion mobility spectrometry • Ions • Detection of explosives traces • Bipolar mode • Design

1 Introduction

The problem of environmental protection, technological processes for obtaining high-purity substances, health care, biology, forensic medicine requires the ability to identify trace concentrations (10⁻⁹ g and below) of complex mixture components from small volumes of samples in the presence of a large number of known and unknown substances. The variety of tasks and problems arising in the determination of micro- and sub-microquantities of the analyzed components involves both modern instrumental methods and the development of new non-traditional approaches to their implementation, exceeding the existing ones in terms of sensitivity and speed. At the same time, newly created devices should be cheap, reliable, easy to use, and, as a rule, portable, and autonomous.

Y. R. Shaltaeva (✉) · A. V. Golovin · V. K. Vasilyev ·
E. A. Gromov · M. A. Matusko · E. K. Malkin · I. A. Ivanov ·
V. V. Belyakov · V. S. Pershenkov
Institute of Nanoengineering in Electronics, Spintronics and
Photonics, National Research Nuclear University MEPhI
(Moscow Engineering Physics Institute), 31 Kashirskoe shosse,
Moscow, Russia
e-mail: shaltaeva@yandex.ru

The term Ion Mobility Spectrometry (IMS) refers to the principles, methods, and equipment that enable the identification of chemicals by their mobility in the gas phase. Ion mobility is a characteristic of a substance and can be used to detect and identify specific molecules. Possessing unique characteristics (high sensitivity, selectivity, rapidity, small size, and weight, simplicity), modern ion mobility spectrometry [1] solves an extensive range of issues, often impractical to any other analytical methods and techniques.

Ion mobility spectrometers use high voltages to create fields in drift and ionization chambers. It is necessary to ensure that ions move at a sufficient rate, and at the characteristic drift time, there is a slight change in the shape of the ion cloud due to Coulomb proliferation. During the movement of ions, the field in the drift chamber should be stable [2], that is achieved by using electrical capacitors (capacitors) of large nominal value in the high voltage formation block. Therefore, most of the existing ion mobility spectrometers can create a constant electric field in the drift chamber with the possibility of only slow switching. Besides, switching a high voltage causes electrical interference and overloading of a highly sensitive ion current amplifier [3], which does not allow measurements to be made for a long time.

If it is necessary to detect substances from other modes, it is necessary to switch the polarity of the device, which takes from 40 s [4] to several minutes [5], which is unacceptable for operational operation. In some devices, the polarity is set by hardware (design), and it is not possible to switch the mode.

This article reviews the existing serial spectrometers with the possibility of simultaneous detection of both positive and negative polarity substances. The disadvantages of the designs are considered, and a more optimal way of implementing a bipolar spectrometer with alternate detection of both polarity ions on the same spectrometer cell is proposed (pseudo-simultaneous detection).

2 The Review of Commercial Two-Polar Spectrometers

Most detection tasks require a device that can operate in both negative and positive ion detection modes at the same time. Below are some of the most well-known and widely used detectors on the world market.

2.1 IONSCAN 500DT Smiths Detection

IONSCAN 500DT [6] by Smiths Detection (Great Britain) is a two-channel tabletop detector of trace amounts of explosives and drugs, development of the IONSCAN 400B model [7]. The device can operate in three modes: “simultaneous detection of explosives and drugs,” or “explosives only,” or “drugs only.” The sample analysis time is 8 s. Operating temperature range from 0 to 40 °C with a relative humidity of less than 95%. IONSCAN500DT includes a regenerative air purification system (APS) [8], which reduces maintenance time. A distinctive yellow stylus simplifies sample collection by the operator and eliminates direct contact with the smear tampon sampler. Significant disadvantages of the device are the use of a radioactive source of ionization, a large mass of 19 kg, dimensions 40 × 57 × 40 cm, consumption of up to 600 W, power supply only from the mains (the impossibility of autonomous operation). Time of output to the operating mode is 30 min.

2.2 DE-Tector Bruker

The company Bruker (Germany) has developed a modern ion mobility spectrometer DE-tector [9] for detecting trace amounts of explosives and drugs. The advantages of the device include the absence of sources of radioactive ionization. The patented non-radioactive XPITM photoionization source is used [10]. Sampling is carried out with the help of a special Teflon strip for wiping from the surface. Sample analysis time does not exceed 10 s. Operating temperature range from 5 to 40 °C with relative humidity from 5 to 95%. The device is powered by AC 100–240 V AC, 47–63 Hz, but also available with UPS. The disadvantages are the weight of 19 kg, dimensions 52 × 44 × 40 cm, consumption up to 400 W. The time to enter the operating mode is 30 min.

2.3 QS-B220 Implant Science Corporation

Desktop detector QS-B220 [11] by Implant Science Corporation (USA) is designed for simultaneous detection of traces of explosives and drugs. The principle of operation of

QS-B220 is based on the use of ion mobility spectrometry with a photon source of ionization [12, 13]. In order to increase sensitivity, the QS-B220 detector is equipped with a desorber. The advantages of the device include the absence of sources of radioactive ionization, which eliminates licensing, inspection, transportation, and problems associated with disposal at the end of its service life. The automatic and continuous self-calibration function, which does not require a break-in operation, allows you to adapt to changes in the environment. Sampling is done by wiping the surface with special wipes. Sample analysis time does not exceed 10 s. Operating temperature range from –10 to 55 °C with a relative humidity of less than 95%. Can be operated at altitudes of 4572 m above sea level. The disadvantages of the device are the weight of 15.7 kg, dimensions 39.6 × 39.7 × 41.2 cm, power supply only from the mains (the impossibility of autonomous operation). The time of entering the operating mode is 30 min.

2.4 Itemiser DX Morpho Detection

The device [14] provides simultaneous recognition of explosives and drugs. The device has a patented regenerative dryer (patent [15]), which simplifies maintenance. Automatic calibration [16] with verification capability ensures accurate detection. For better search for peroxide explosives, a new patented alloying admixture is used [17]. The sample analysis time is 8 s. Operating temperature range from 0 to 40 °C, storage temperature from 0 to 50 °C, protection class of the device IP20 [18]. The device can be operated from 100–120 V, 200–240 V, 47–63 Hz AC mains power supply, or from 11 to 18 V, 10 A DC power supply unit, or a built-in battery with a duration of 60 min autonomous operation. The power consumption is 150 W. A significant disadvantage of the device is the use of a radioactive source of ionization. The following drawbacks can also be referred to as drawbacks in comparison with portable devices: dimensions 38 × 48 × 50 cm, weight 12 kg, time of output on an operating mode 30 min, small duration of independent work.

2.5 The Subtotal of Review

Thus, the above analysis shows that the existing serial ion-mobility spectrometers with simultaneous detection of substances in both spectrometric modes have significant drawbacks. Most of the devices manufactured based on the ion mobility spectrometry method use ionization sources of molecules based on the ⁶³Ni radioactive isotope, as well as based on tritium ³H [19]. Despite the ease of manufacture, lack of power consumption and stability characteristics, radioactive ionization sources have significant drawbacks.

The main problems are related to the need for certification of the manufacturer and the consumer to work with devices containing radioactive substances, and with the complexity of transportation. The fundamental point is the problem of disposal of devices with a radioactive source, exhausted their life or for some reason have become unusable. Disposal of radioactive materials contained in the detectors can grow into a serious environmental problem with a higher volume of production of such devices. Also, almost all devices of this class (with simultaneous detection of substances in both spectrometric modes) are desktop and have large dimensions, weight, significant energy consumption, inability to work autonomously. That limits the possibility of their use as wearable portable devices, and in comparison with this class of detectors, their characteristics can be considered as shortcomings. This makes the actual task of developing domestic portable wearable devices capable of detecting substances simultaneously in both spectrometric modes, which would allow the detection of explosive, narcotic, and toxic substances in real-time.

3 Installation of Two Drift Chamber in One Spectrometer

In case of necessity of operative detection of substances, for example, at inspection points, it is possible to install two ionization chambers, drift chambers, detecting units, gas purification systems and high-voltage control systems in one device [20] at once, i.e., in fact, to install two parallel devices operating in fixed polarity. Due to a significant increase in size, weight, and energy consumption, such devices are produced only in a stable version, which reduces the efficiency of rapid search for target substances. There is a need for proper organization of sampling and separation of gas flows inside the device for two devices, which leads to complication of the sampling system.

Several detector designs and gas flow separation options are possible:

The first variant (Fig. 1) consists of feeding the sample sequentially through the first and second instruments [21–23]. In this case, the analyzed air through the sampling system first enters the ionization chamber of the first device, from where the ions of appropriate polarity move in the drift chamber to the detecting node 1. The sample then enters the ionization chamber of the second device through the connection channel, from where the ions of different polarity move in the drift chamber to the detecting node 2. This option reduces the sensitivity during measurement by the second device due to ion-exchange reactions in the ionization chamber of the first device. Therefore, in practice, this variant is unsuitable.

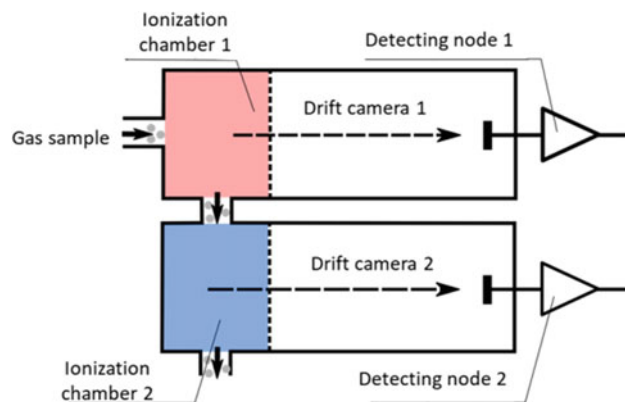


Fig. 1 The block diagram of the device with a serial sample transfer

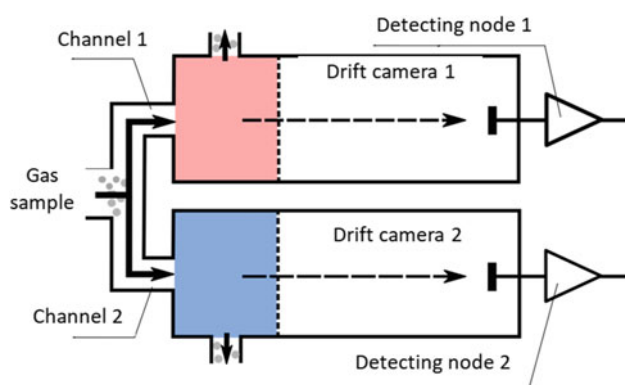


Fig. 2 The block diagram of the device with a shared channel

The second option (Fig. 2) is to install an airflow divider in the sample supply channel [24, 25]. In this case, the analyzed air first enters the sampling system, then is divided into parts and enters the ionization chamber of the first device that detects only positive ions through channel 1, and the ionization chamber of the second device that detects only negative ions through channel 2, respectively. The disadvantages of this variant are:

- The complexity of the sampling system design due to the airflow separator
- Deterioration of the sample transport, due to the increase in the length of the canal and the appearance of additional bends
- Difficulties in monitoring the proportion of substances entering each device
- Reducing the amount of substance supplied to each device, which also leads to a decrease in sensitivity

The third variant (Fig. 3) uses a common ionization chamber [26, 27] for positive and negative polarity ions. Such an ion mobility spectrometer has two drift chambers,

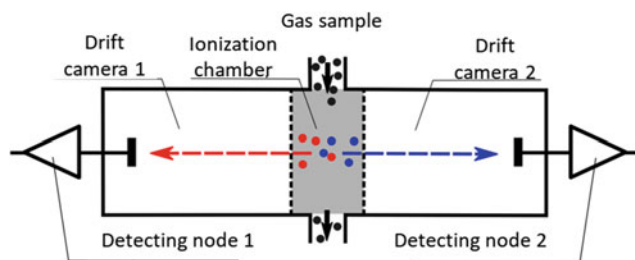


Fig. 3 The block diagram of the device with a common ionization chamber and two drift chambers

two detecting nodes, two gate systems, two collectors, and one standard sampling system and the ionization area. In this case, the obtained ions are retained in the ionization area using gates, then simultaneously injected into the corresponding drift areas. Positive ions enter drift area 1, and negative ions enter drift area 2.

The disadvantages of this variant include the use of complex structures of ion sources and gates. Since traditional sources of ionization are oriented for a single drift tube, such sources will have low efficiency of ionization of sample molecules and ionize a small fraction of molecules when operating in two polarities [28]. Also in this structure, sources of ionization, as a rule, are made based on radioactive isotopes, because of the need for volume ionization. There are known ion sources (patent US 7259369B2 [29]) in which the sample molecules after ionization in the ion chamber located outside the system (in this design, instead of the central ionization chamber there is a separating chamber with an ion trap) are transported by carrier gas to the ion trap in the center of the double drift chamber. The ions in the trap are then injected into the corresponding drift areas. This source is of low efficiency because a large number of ions are lost during transport from the ionization chamber to the ion trap. The double-sided gate (US 8013297 B2 [30]) has disadvantages of a complex production process, strict assembly requirements, and high costs.

4 Directions for the Implementation of a Bipolar Spectrometer

This review of existing designs shows that the implementation of a portable bipolar ion mobility spectrometer can be divided into two main areas—miniaturization of components and development of a set of circuitry solutions to quickly switch the polarity of the device.

The first direction has several limitations:

The resolution of the device directly depends on the drift tube length (since the role of the drift chamber geometry is essential when using the physical principle of ion mobility spectrometry). Therefore, the reduction of length will lead to

a decrease in the resolution, and thus to a deterioration of the device parameters.

The diameter of the drift chamber is connected with ensuring the uniformity of the field [31]. Decreasing the diameter of the drift chamber electrodes will cause a charge loss due to the strong curvature of ion trajectories. In order to maintain the uniformity of the field, it is necessary to reduce the length of the electrodes and place them with more various steps, which will lead to a multi-element structure, complication of the drift tube and an increase in labor intensity and manufacturing cost.

Reducing the effective channel diameter for ion drift will result in a reduction in ion clotting, as the charge density is limited by Coulomb proliferation. Reducing the charge in the clot entering the collector will increase the noise level relative to the value of the useful signal.

Reducing the diameter of the gas channels will result in increased resistance to the gas flow, as well as increased sample losses on the walls due to adsorption and diffusion into the gas channel wall material. It will decrease sensitivity of the instrument.

Miniaturization does not solve the problems associated with the separation of the gas flow in the sample feed channel.

Miniaturization, in general, will cause a significant complication of the technology. For example, switching to multilayer printed circuit boards causes a sharp increase in price and production time. Machining of mechanical parts falling into the next precision class is much more complicated, more expensive and precise machines and more qualified personnel are required. Going beyond standard technology is sometimes impossible because of the lack of necessary prototyping services and manufacturing plants. In general, miniaturization of components increases the complexity, manufacturing time, and price of the device, which is undesirable for mass production.

The second option is to upgrade the ion mobility spectrometer units. It makes it possible to obtain a pseudo-detection of both polarity ions on a single drift tube [32] and has a number of features.

The high-voltage block serves to form a high voltage in the drift chamber. In order to provide bipolar mode, it is necessary to realize fast, continuous, electronic switching of high voltage polarity, as well as providing stability of the drift field level.

The high voltage divider is used to distribute high voltage and form a uniform drift field. In order to ensure fast polarity switching, the divider must have a frequency compensation and low electrical capacitance of the links.

The digital-to-analog conversion of the ion current spectrometric signal allows the subsequent processing and accumulation of data. For simultaneous detection of positive and negative polarity ions, it is necessary to develop a

bipolar trans-impedance charge-sensitive ion current amplifier. It is also necessary to minimize the interference from the high-voltage system to the charge-sensitive amplifier.

The shielding collector mesh allows minimizing the induced current from the ion clot as it approaches the collector. To ensure bipolar mode, it is necessary to develop a scheme of quick polarity switching and formation of stable voltage on the protective grid.

The ion source, where the sample is ionized, must ensure efficient operation in both polarities.

The ion gate allows controlling the start time and duration of the ion injection. The ion gate control unit needs to be upgraded to be compatible with a bipolar high voltage system.

The Ion Mobility Spectrometer Control System synchronizes and controls the electronic units. It is necessary to upgrade the control system to implement bipolar operating algorithms.

The advantage of the circuitry development and modernization option is the following: all elements are preserved within the existing technology, technological operations remain the same at all stages of assembly, no retraining of personnel is required. This development option is less labor-intensive and requires less research.

5 Conclusions

One of the critical requirements of modern inspection equipment is the simultaneous detection of a wide range of substances, long-term autonomous operation, and minimization of mass and size characteristics of the devices.

Almost all instruments capable of detecting substances of different classes simultaneously are desktop instruments with large size, weight, significant energy consumption, and no possibility of autonomous operation. This makes the task of developing portable wearable devices capable of simultaneously detecting substances forming positive and negative ions at ionization, which will allow detecting explosives, drugs, and poisonous substances in real-time.

It is possible to install two ionization chambers, drift chambers, detecting units, gas purification systems, and high-voltage units into one device, i.e., two parallel devices operating in fixed polarity. This variant has a number of disadvantages associated with the increase in size, weight, price, and energy consumption. Also, the organization of sampling and separation of gas flows inside the device becomes more complicated.

The direction of miniaturization of the device components is a technically complicated and expensive development that requires additional research.

The most promising is the implementation of a bipolar ion mobility spectrometer by modernizing the circuitry without any significant changes in design.

Conflict of Interest The authors declare that they have no conflict of interest.

References

1. Wilkins, C.L., Trimpin, S. (ed.): Ion Mobility Spectrometry—Mass Spectrometry: Theory and Applications (2010)
2. Avida, A., Friedman, M.: The Design of an Ion Drift Tube with a Uniform Electric Field. NRCN(TN)-099 (1986)
3. Boylestad, R., Nashelsky, L.: Electronic Devices and Circuit Theory, 11th edn (2012)
4. Samotaev, N., Golovin, A., Vasilyev, V., et al.: IMS development at NRNU MEPhI. In: Lecture Notes in Electrical Engineering, LNEE, vol. 268, pp. 447–451 (2014)
5. Pershenkov, V.S., Tremasov, A.D., Belyakov, V.V., et al.: X-ray ion mobility spectrometer. *Microelectron. Reliab.* **46**(2–4), 641–644 (2006)
6. IONSCAN 500DT: <http://www.smithsdetection.com/>
7. IONSCAN 400B: <http://www.smithsdetection.com/>
8. Gabowicz, T., Ridjosic, D., Nacson, S.: WO2009140812 A1; US H01J49/04, G01N27/62, H01J49/26, G01N27/64, G01N30/16, G01N37/00, G01N27/68. Ion Mobility Spectrometry Analyzer with Improved Sample Receiving Device. Smith Detection Inc., № PCT/IB2006/004307 (2008)
9. «DE-tector»: <http://www.bruker.com/products/cbrne-detection/ims/de-tector/overview.html>
10. Yang, Z., Moeller, R.P., Zanon, S.: Atmospheric pressure ion source with exhaust system. Patent № US 8841607 B2, 23 Sept 2014
11. «QS-B220»: <http://www.implantsciences.com>
12. Bunker, S.N., Krasnobaev, L.: Photoelectric ion source photocathode regeneration system. Patent № US 7576320 B2, 18 Aug 2009
13. Belyakov, V.V., Kekukh, V., Lazarevich, A., Bunker, S.N.: Pulsed ultraviolet ion source. Patent № US 7820979 B2, 26 Oct 2010
14. Detector «Itemiser DX»: <http://www.morpho.com/>
15. Patterson, M.E., Knapp, M.E.: Detection system assembly, dryer cartridge, and regenerator and methods for making and using the same. Patent № CA 2807894 A1, 8 Sept 2013
16. Carey, L., Bistany, K.: Calibration and verification tool and method for calibrating a detection apparatus. Patent № US 7856898 B2, 28 Dec 2010
17. Napoli, J.D.: US 7456393 B2; US20050019220. Device for testing surfaces of articles for traces of explosives and/or drugs. Morpho Detection, LLC, California, G01N1/02, G01N1/04 (2008)
18. International Standard IEC 60529: Degrees of protection provided by enclosures (IP Code), 2.1 edn. IEC, Geneva (2001–02)
19. Leonhardt, J.W.: New detectors in environmental monitoring using tritium sources. *J. Radioanal. Nucl. Chem.* **206**(2), 333–339 (1996)
20. Kafle, G.K., Khot, L.R., Sankaran, S., et al.: State of ion mobility spectrometry and applications in agriculture: a review, *Eng. Agric. Environ. Food* **9**(4), 346–357 (2016)
21. Stimac, R.M., Wernlund, R.F., Cohen, M.J., Lubman, D.M., Harden, C.S.: Initial studies on the operation and performance of the tandem ion mobility spectrometer. Presented at the 1985 Pittsburgh Conference and Exposition on Analytical Chemistry and Applied Spectroscopy, Pittcon 1985, New Orleans, LA, Mar 1985

22. Stimac, R.M., Cohen, M.J., Wernlund, R.F.: Tandem ion mobility spectrometer for chemical agent detection, monitoring and alarm. Contractor Report on CRDEC contract DAAK11-84-C-0017, PCP, Inc., West Palm Beach, FL, AD-B093495, May 1985
23. Eiceman, G.A.: History of Tandem Ion Mobility Spectrometry at or Near Ambient Pressure. New Mexico State University, New Mexico, Mar 2014, 12 с. (Электронный ресурс). <http://ionmobility.nmsu.edu/history/> (дата обращения: 26 Jan 2015)
24. Machlinski, K.J., Pompeii, M.A.: (Chemical agent) point detection system (IPDS) employing dual ion mobility spectrometers. Patent № US 6627878 B1, 30 Sept 2003
25. Wynn, P.G., Breach, J.A.: Ion mobility system comprising two IMS cells operated at different polarities. Patent № US 7345276 B2, 18 Mar 2008
26. Spangler, G.E., Wroten Jr., J.F.: Apparatus for simultaneous detection of positive and negative ions in ion mobility spectrometry. Patent № US 4445038 A, 24 Apr 1984
27. Atkinson, J.R., Clark, A., Taylor, S.J.: Ion mobility spectrometer comprising two drift chambers. Patent № US 8415614 B2, 9 Apr 2013
28. Chen, Z., Li, Y., Peng, H., Zhang, Q., Lin, J.: Double-faced ion source. Patent № US 8217365 B2, 10 July 2012
29. Scott, J.R., Dahl, D.A., Miller, C.J.: Dual mode ion mobility spectrometer and method for ion mobility spectrometry. Patent № US 7259369 B2, 21 Aug 2007
30. Peng, H., Zhang, Q., Lin, J., Li, Y.: Ion gate for dual ion mobility spectrometer and method thereof. Patent № US 8013297 B2, 6 Sept 2011
31. Samotaev, N., Pershenkov, V., Belyakov, V., Vasilyev, V., et al.: Electric modeling of charged particles trajectories in the drift tube of ion mobility spectrometer for hazardous industrial chemicals detection. *Procedia Eng.* **87**, 436–439 (2014)
32. Vasilyev, V., Pershenkov, V., Belyakov, V., et al.: Ion mobility spectrometer for rapid simultaneous detection of positive and negative ions. *IFMBE Proc.* **55**, 515–519 (2016)

Assessing the Safety of Using Incubators for Newborns

C. Pislaru, V. Şontea, and S. Railean

Abstract

This paper presents an analysis of the risks of using the incubator for newborns. In order to use the incubator safely, we must evaluate the risks related to its use, to identify how the patient will be influenced in different circumstances. For evaluation, the criteria have been established that can directly or indirectly influence the quality of the medical act as well as the safety of the user and the patient, the criteria are such as: the age of the medical devices, the degree of use, the people in charge of preventive maintenance, the type of preventive maintenance, the number of users who operate the medical equipment. The basic causes of the occurrence of the incidents are the technical defects, their faulty and incomplete calibration, the lack of preventive maintenance as well as the effects of the human factor on this process.

Keywords

Safety • Analysis • Newborn incubator • Evaluation
• Correct use of medical equipment •
Premature

1 Introduction

Today, the Republic of Moldova and the entire world are facing a major health problem regarding premature birth. According to the report by “Save the Children International” and the World Health Organization, every year there are 15 million preterm births, 85% of them occurring between weeks 32 and 37, with the rate increasing in almost all

C. Pislaru · V. Şontea · S. Railean (✉)
Technical University of Moldova, 166 Stefan cel Mare bd.,
Chisinau, Republic of Moldova
e-mail: serghei.railean@mib.utm.md

V. Şontea
e-mail: victor.sontea@mib.utm.md

countries of the world. Thus, in the US the incidence of premature births constitutes from 10 to 12%, in Europe from 5 to 9%. In Moldova, more than 1700 preterm infants are born each year, which represents about 5% of all births, so this is a considerable value [1].

Newborn babies with complications of health and premature birth have great difficulties in regulating their body temperature for various reasons such as: rapid metabolism caused by diseases, low birth weight or other congenital diseases. In this context, the incubator for newborns is the inevitable medical device for providing favorable conditions and maintaining the lives of newborns. In this early life period, incubators are fundamental tools for reducing the risk of mortality and diseases. The incubator offers an adequate microclimate, so that the newborns can overcome the first occurrences of the diseases, also controlling the skin temperature and relative humidity. Most incubators also include means for controlling oxygen levels and the relative humidity of the air the child breathes. The microprocessors incorporated in most modern incubators help to precisely control the temperature, humidity and oxygen level, while allowing the visualization of the monitoring parameters graphs for 24, 48, 72 h [2]. So, these devices can be considered quite safe in use, but there are a lot of risks associated with their daily use. The risks are related not only to improper use, but also to the inadequacy of these equipment in many medical institutions.

2 The Level of Endowment of Medical Institutions with Incubators for Newborn

At the moment the insufficiency of the medical devices would be one of the basic problem that persists in the Republic of Moldova, but it is a time-resolved one, which requires financial resources and a correct assessment of the needs. Analyzing the situation to date we can identify the following major problems:

Table 1 Distribution of risk score by age of devices

Age of medical device	Risk points
<5 years	1
5–10 years	2
10–15 years	3
>15 years	4

Table 2 Distribution of the risk score according to the degree of use of the medical devices

Grade of use intensity of medical devices	Risk points
Unused	1
Normal use	2
Overused or in lack of spare equipment	3

- Insufficient number of incubators in relation to children born prematurely or newborns with diseases that require this type of equipment taking into account that their number is increasing.
- Use of incubators with the operating deadline exceeded. Incubators have a lifespan of up to 10 years, and many of them after 5 years of operation fail because they are operate continuously.
- Use of incubators that do not comply with European standards and norms that are required by EN 60601-2-19.
- Overuse of incubators due to insufficient number and duration of treatment which can last from 3 days to 7 months for a single patient [3].

Incubators are divided by age is in four categories to which a risk score of use is assigned according to Table 1. Medical devices over 15 years of age will have a maximum risk score.

According to the table and evaluation criteria (Table 1), the incubator for newborns is in the category of devices from 5 to 10 years with 2 assigned points.

Another evaluation criteria would be the degree of use of the incubator that is in the category of overused devices with 3 assigned points (Table 2).

3 The Degree of User Training and Its Importance

The degree of training of the users on the correct use of this equipment is a basic factor to which more attention must be drawn. The newborn incubator is a medical device that is installed in majority of cases in the intensive care departments. In these medical departments, the number of users (nurses, doctors) operating with a single medical equipment is on average greater than three persons per equipment.

Under these conditions, the newborn incubator becomes a vulnerable device that could endanger the patient's health, especially if used incorrectly due to human factor. It is very important that the user is properly trained and follows certain rules of use in accordance with the manufacturer's requirements and clinical protocols such as:

- The setting of the parameters for temperature, humidity and oxygen must be in accordance with the patient's condition and not standardized in all patients [4].
- The calibration of the oxygen sensor must be performed before each use of the O₂ module at the values of 21% and periodically at 100% (according to the procedure described in the user manual) [5].
- The air filter should be changed periodically to prevent dust from entering the incubator and damaging the patient's condition.
- Use and set the correct parameters for the operating mode of the incubator "Air temperature" and in "Child" mode using the temperature sensors placed on the child's body. Often these regimes are mistaken or used incorrectly which can lead to overheating of the newborn. It is worth noting that in any operating mode of the incubator the temperature of the child must be monitored [2].
- Use of water for humidifier without impurities and change of water periodically after each patient. These procedures performed on time would reduce the failure of the incubator as well as the appearance of bacteria (humidifier is a favorable environment for bacteria) [6].
- Cleaning and disinfection of the incubator periodically and after each use. Some manufacturers suggest cleaning the incubator every day with a soap and water solution, others do not. But at least the incubator must be thoroughly cleansed and disinfected after each change of child or at least once a week [2, 4, 7, 8].

Following these simple rules by the user could reduce the number of faults and incidents involving this type of equipment. Regular user training is a priority action for risk prevention.

According to the table and evaluation criteria (Table 3), the incubator for newborns is in the category of devices with 2–5 users and 2 assigned points.

Table 3 Distribution of risk score by number of users on medical equipment

Number of operators per medical device	Risk points
1 user	1
2–5 users	2
>5 users	3

4 Periodic Maintenance

Incubators are devices that directly influence the health of newborns, making important contributions to the implementation of accurate diagnosis and treatment for patients. However, the correct diagnosis and treatment are directly related to the reliability and functionality of the devices. Therefore, the device must be maintained under normal operating conditions by performing the correct periodic preventive maintenance. The people responsible for this process are the bioengineers, who must be equipped with the necessary control devices and tools [9].

A regular incubator maintenance program should take into account the manufacturer's recommendations and include the following preventative measures:

- The measurement of the noise level is a very important parameter that directly influences the patient's health. The auditory, visual and central nervous systems for the premature are at birth in a general immaturity which is then formed in the incubator environment. This is why it is very important for noise limits to be in order and to create a favorable environment for child development. These noises are most often caused by defective fan bearings that need to be changed or lubricated periodically [7, 8, 10].
- Periodic verification of the operating temperatures must be within the limits and be uniform throughout the internal surface of the incubator. Uncalibrated temperatures can lead to hypothermia or hyperthermia of the patient which for a premature child is lethal.
- Periodic visual check and operation of the humidifier. There are several types of humidifiers of internal type, where access for verification and maintenance can only have the technical or removable personnel where the user has full access. The latter type is preferable and involves daily visual verification at the user level. Often these humidifiers are a source of incident production because they operate at high voltages and are subjected to corrosion and oxidation due to water having direct contact with it. More attention should be paid to humidification modules [6].
- Replacement of oxygen sensors and appropriate calibration. The life time of an electro-chemical sensor is one year. A faulty sensor can affect the patient or even cause explosions and fires.
- Verification of audible and visual alarms by simulating different faults. All modern incubators are equipped with intelligent alarm systems in case of failure of a module. Failure to set off alarms can cause major incidents and endanger the patient's life.

Table 4 Distribution of the risk score according to the responsibility of performing the maintenance of the medical devices

Responsible for maintenance of medical device	Points
Biomedical engineering department of institution	1
External companies	2

Table 5 Distribution of the risk score according to the complexity of performing the preventive maintenance

Maintenance complexity	Points
Visual and functional preventive maintenance	1
Basic preventive maintenance	2
Complex preventive maintenance	3

Inadequate maintenance can make the incubator dangerous for children. Incubators that are used for many years, during which they are subjected to shocks and vibrations, as most are mounted on wheels and moved for cleaning and storage from one place to another. In international practice there have been incidents where these mechanical shocks have deteriorated the temperature control mechanisms, which, in turn, overheated the newborns, causing brain injury or death [11].

Incubators with an outdated operating time should not be used, and in the worst case should be subjected to thorough checks to avoid an incident.

Incubators that do not comply with European standards should be discarded because they are not safe to use. Often they do not have alarm systems and patient safety, and many operating modules use old technologies that are no longer used in the medical field.

According to the table and evaluation criteria (Table 4), the incubator for newborns is in the category of devices that can be maintained by the bioengineers of the institution without the involvement of outsourced services, so we assign 1 point.

If we analyze the complexity of performing preventive maintenance (Table 5) then the incubator for newborns is in the category of medical devices with an average or basic complexity, with 2 assigned points.

5 Conclusions

This work represents an analysis of the risks of using the incubator for newborns. In order to use the incubator safely, we must evaluate the risks related to its use, to identify how the patient will be influenced in different circumstances. The basic causes of the occurrence of the incidents are the technical defects, their faulty and incomplete calibration, the

lack of preventive maintenance as well as the effects of the human factor on this process.

For example, electrical defects can cause measurement or display errors. A module for measuring the faulty temperature can lead to hyperthermia or hypothermia of the patient, or cause a fire or danger of electrocution. Uncontrolled oxygen may cause hypoxia or hyperoxia in the patient. A malfunctioning fan can cause choking disease, or it directly affects oxygen saturation, relative humidity and ambient temperature in the incubator [5, 12].

According to the risk assessment criteria, the incubator for newborns accumulated a score of 10 points. The equipment that accumulates a maximum evaluation score (10–15 points) is in the major risk area for the patient and user. With these types of equipment, the most frequent incidents and failures with serious consequences can occur. That is why monitoring the use and periodic checks of incubators for newborns should be a priority for the Departments of Medical Bioengineering. The maintenance plan and the periodicity of the preventive maintenance must be drawn up according to the indicators calculated for each medical equipment provided.

It is very important to evaluate the risks for complex medical devices. Applying this method in a medical institution will reduce the risk of occurrence and increase the quality of the medical act. The safety of the user and the patient is the basic priority of the medical institution.

Conflict of Interest Every paper must contain a declaration of conflicts of interest. If there are no such conflicts write “The authors declare that they have no conflict of interest”.

References

1. Stefan, G., Vera, V., Anatol, S.: Risk factors associated with preterm birth. “Info-Med” J. 2, 27–32 (2015)
2. Kaitano, D.: Interface of a digital temperature microcontroller with an analog incubator. *Instrum. Sci. Technol.* **42**, 38–45 (2013)
3. Sound, V., Morgoci, S., Turcanu, G.H., Pislaru, C.: Medical devices management strategy in the Republic of Moldova. In: *Proceedings of 3rd International Conference on Nanotechnologies and Biomedical Engineering (ICNBME-2015)*, Chisinau, Republic of Moldova, 23–26 Sept 2015. IFMBE Proc. **55**, 478–481. ISBN 978-981-287-735-2 (2016)
4. Heimann, K., Schoberer, M., Orlikowsky T.: Thermomanagement in neonatology and paediatrics: clinical problems and challenges. *Biomed. Eng. (Biomed. Tech.)* **58** (2013)
5. Askie, L.M., Henderson-Smart, D.J., Irwig, L., Simpson, J.M.: Oxygen-saturation targets and outcomes in extremely preterm infants. *N. Eng. J. Med.* **349**, 959–967 (2003)
6. Abdiche, M., Farges, G., Delanaud, S., Bach, V., Villon, P., Libert, J.P.: Humidity control tool for neonatal incubator. *Med. Biol. Eng. Comput.* **36**, 241–245 (1998)
7. Plangsangmas, V., Leeudomwong, S., Kongthaworn, P.: Sound pressure level in an infant incubator. *MAPAN J. Metrol. Soc. India* **27**(4), 199–203 (2012)
8. Roske, K., Foitzik, B., Wauer, R.R., Schmalisch, G.: Accuracy of volume measurements in mechanically ventilated newborns: a comparative study of commercial devices. *J. Clin. Monit. Comput.* **14**, 413–420 (1998)
9. Lalib, A.W., Williams, G.B., O’Conner, R.F.: An intelligent maintenance model (system): an application of analytical hierarchy process and a fuzzy logic rule-based controller. *J. Oper. Res. Soc.* **49**, 745–757 (1998)
10. Alvarez Abril, A., Terrón, A., Boschi, C., Gómez, M.: Review of noise in neonatal care units—regional analysis. *J. Phys. Conf. Ser.* **90**, 1–6 (2007)
11. *Medical Electrical Equipment—Part 2-19: Particular Requirements for Safety of Baby Incubator*, British Standards BS EN 60601-2-19: 2009. European Committee for Electrotechnical Standardization, United Kingdom (2009)
12. Mäkinen, T.M., Juvonen, R., Jokelainen, J., Harju, T.H., Peitso, A., Bloigu, A., Silvennoinen-Kassinen, S., Leinonen, M., Hassi, J.: Cold temperature and low humidity are associated with increased occurrence of respiratory tract infections. *Respir. Med.* **103**(3), 456–462 (2009)

Part XIII

Health Informatics, e-health and Telemedicine

Creation of Regional Telemedicine Diagnostic and Treatment Complex

K. V. Kolisnyk, R. S. Tomashevskiy, T. V. Sokol, S. M. Koval,
and D. M. Deineko

Abstract

Given the extreme prevalence of cardiovascular diseases, which have recently become an epidemic and are the main cause of death, early diagnosis and detection of diseases at the initial stage with subsequent monitoring of the condition of patients is of great importance. The creation of modern high-performance telemedicine diagnostic and treatment complexes to solve these problems should be based on modern advances in telecommunication and medical technologies, and modern methods of designing complex radio engineering geographically-distributed systems.

Keywords

Telemedicine • Medical diagnostics • Cardiovascular diseases • Radio engineering systems

1 Introduction

Nowadays, scientific and technical progress has not only qualitatively changed all spheres of human activity, having provided it with highly efficient technologies, but also gave a fundamentally new understanding of the interaction between the “man-nature-technology” system. Against the background

K. V. Kolisnyk (✉) · R. S. Tomashevskiy
National Technical University “KhPI”, Kyrpychova 2, Kharkiv,
61002, Ukraine
e-mail: kolesniknet@ukr.net

T. V. Sokol
Kharkiv Medical Academy of Postgraduate Education, Kharkiv,
Ukraine

S. M. Koval
Government Agency “National Institute of Therapy named after
L.T. Maloyi of the National Academy of Medical Sciences of
Ukraine”, Kharkiv, Ukraine

D. M. Deineko
New Medical Technologies Ltd., Kharkiv, Ukraine

of a decrease in people’s physical activity, there is a decrease in the quality of food, the state of the atmosphere and water resources, a change in the composition of microflora, which leads to a decrease in the biological potential of the human body. In conditions of sharply deteriorated external conditions of existence, mass chronic diseases and epidemics arise.

When creating modern high-performance telemedicine diagnostic and medical complexes, it is necessary to take into account not only the latest achievements of medical equipment for the diagnosis and treatment of cardiovascular diseases, but also advanced experience in designing and creating modern multi-level special-purpose radio engineering complexes.

The purpose of this study is to determine the concept of integrated solutions to these problems based on the analysis of the best practices in the field of practical medicine and telecommunications.

2 Features of Cardiovascular Diseases

One of the most common chronic diseases of recent general concern is cardiovascular diseases (CVD), which often develops under the background of a deteriorating state of the patient’s immune and endocrine systems.

CVD are the leading cause of death worldwide, and according to the latest data, up to 20 million people die each year, which is more than 30% of all deaths in the world, and more than 2/3 of these deaths occur as a result of heart attack and stroke [1, 2].

People suffering from CVDs or at high risk of such diseases (due to the presence of one or more risk factors such as elevated blood pressure, diabetes, hyperlipidemia, or an already frisky disease) need early detection and assistance by counseling.

The most common forms of CVD include:

- ischemic heart disease—a disease of the blood-nasal vessels supplying blood to the cardiac muscle;

- cerebrovascular disease—a disease of the blood vessels that supply blood to the brain;
- peripheral artery disease—a disease of the blood vessels supplying blood to the hands and arms;
- rheumatic heart disease—damage to the heart muscle and heart valves as a result of rheumatic fever caused by streptococcal bacteria;
- congenital heart disease—deformations of the heart structure existing since birth [2, 3].

In modern conditions, the problem of improving the methods of diagnosing and treating CVD is of particular relevance due to the need to expand the scope of control and monitoring of patients' condition.

This is possible with the early screening of disorders of the cardiovascular system, when changes in the functions of the body are irregular and reversible. At the same time, the patient is often not under constant observation in the hospital, but may lead an active lifestyle.

During the period of active treatment of a patient with confirmation of the diagnosis of CVD, the patient may also not always be under the constant supervision of a physician, and usually after inpatient treatment continues treatment at home or in sanatorium conditions, exercising periodic monitoring of his condition, either independently or by periodic visits medical institutions.

In this case, biomedical tools for remote monitoring of patients with CVD can play an important role in treating the patient, allowing to monitor the main parameters of the patient's body away from the hospital and provide the necessary information to the attending physician for monitoring his condition and taking the necessary medical actions.

For a number of years, the European Society of Hypertension (ESH) and the European Society of Cardiology (ESC) have adopted guidelines for the management of CVD patients developed by the World Health Organization and the International Society of Hypertension. However, research in this area and the search for new methods of control are quite important, as finding new signs that precede the development of various anomalies can significantly reduce the risks and increase the effectiveness of treatment [4–6].

The use of modern telecommunications technologies and means of telemedicine control can significantly expand the capabilities of these studies, given the almost unlimited package of biomedical information, which, along with the use of mathematical statistics and probabilistic forecasting methods, allows you to create models of processes and in some cases anticipate undesirable developments.

3 Modern Diagnostic Methods for Cardiovascular Diseases

For the purpose of early diagnosis and detection of diseases in the initial stages, various functional methods for studying the cardiovascular system are widely used.

Based on the clinical and pathogenic characteristics of CVDs, the following biometrics are of particular importance for telemedicine monitoring: office and home arterial pressure (AP) levels, daily blood pressure monitoring indicators (average systolic, diastolic, average AP and HR values per day, day, night); maximum and minimum values of BP and HR for different periods of the day; time pressure load index; variability of blood pressure and heart rate during the day and night); daily index (degree of nightly decrease in blood pressure); morning rise in blood pressure (magnitude and speed of morning an elevation of blood pressure); hypotonic episodes (hypertonia time index, diagnosis of rhythm disturbances and conduction according to a single-meter ECG study at rest and daily ECG monitoring data) [7–9].

The main functional method is electrocardiography. The ECG provides the physician with evidence supporting the diagnosis and in some cases plays a key role in the choice of treatment. Electrocardiography is the main method for diagnosing cardiac arrhythmias and monitoring the treatment of arrhythmias and helps to understand the causes of chest pain. Based on the ECG, the doctor decides whether to use thrombolytic therapy for myocardial infarction and monitor its treatment. The advantages of this method include its information content, accessibility and ease of implementation.

The next generally accepted method of CVD research is Holter-monitoring—this is the registration of an ECG recording for one or more days using a portable recorder and further decryption using a computer program. Used to diagnose previously undetected arrhythmias, myocardial ischemia, to evaluate the effectiveness of treatment, including surgery, to monitor patients with possible threatening arrhythmias and to predict CVD.

Daily monitoring of arterial pressure (DMAP), along with Holter monitoring, is widely demanded in clinical practice because of its great informativeness for more accurate individual assessment of blood pressure for early diagnosis of arterial hypertension and selection of optimal treatment regimens.

Samples with dynamic exercise include treadmillmetry (TMM) and bicycle ergometry (BEM). These studies are used for the purpose of early detection of cardiovascular pathology during mass surveys of various contingents.

In addition, to identify individual exercise tolerance in individuals with an established CVD diagnosis and to evaluate the effectiveness of treatment and rehabilitation, as well as to diagnose and identify rhythm disturbances and hypertensive reaction to exercise. Samples are carried out using a bicycle ergometer (ride) and treadmill (walking).

The variety and value of diagnostic methods allows you to accurately establish the diagnosis of cardiovascular diseases and adequately prescribe treatment.

4 Concept of Creating a Regional Radiotechnical Telemedical Treatment-Diagnostic Complex

For comprehensive and widest coverage of the population with screening and monitoring of CVDs, taking into account modern scientific and technical capabilities and medical technologies, it is most appropriate to use geo-graphically distributed radiotechnical telemedical treatments-diagnostic complex (RTTDC) created for the particular region.

First, it allows concentrating technical and medical potential in a single structure, which will significantly increase the efficiency of its use. Secondly, this will make it possible to increase the efficiency of the provision of medical services through timely, high-quality and professional medical care, as well as the possibility of promptly obtaining and processing telemedical information.

The complex is a territorially separated radio engineering structure with a central server (CS) of management telemedicine complex (TMC) and cloud storage databases (CSDB), and a number of local points of diagnosis and control (LPDC), distributed according to the demographic needs and the specific features of individual regional structures of the region (Fig. 1).

To increase the efficiency of the resource usage during the creation of the complex, it is assumed that structural and functional parametric optimization is carried out according

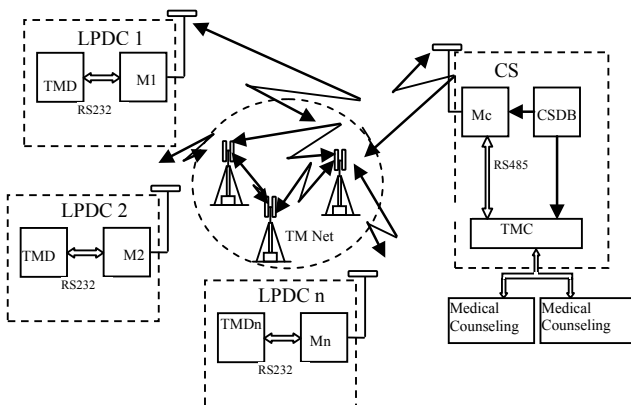


Fig. 1 Example structure of RTTDC

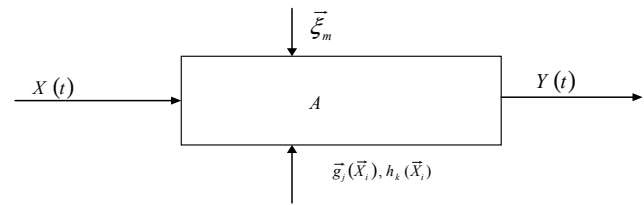


Fig. 2 Generalized model of RTTDC

to the functional criteria and cost indicators of the quality of medical services provided [10, 11].

Parametric optimization of such systems is carried out taking into account the dynamic parameters of the consumer properties of this system and using the technique of geoinformation technologies, which allows taking into account the geographical characteristics of each local point as much as possible along with ethnically-statistical and medical-analytical needs.

The problem of parametric multifunctional optimization is reduced to solving the problem of finding the maximum of the efficiency function of the created system in the environment of the parameters of external and internal perturbing influences considered by the authors in [12, 13].

To define it, use the generalized model of RTTDC (Fig. 2)

The generalized model RTTDC shows that the input actions for it $X(t)$ are a set of medical functional parameters of the set of LRDCs involved in the complex. The output parameter $Y(t)$ is the expected clinical and medical result of a specific medical action determined by the algorithm of the given medical procedure. Own parameters of a specific RTTDC A are determined by the parameters of technological medical systems and the structural scheme of the complex.

It is g_j, h_k —is the vector of the constraint function for the i th factor.

The influence of external environmental influences is determined by the vector of external influences— ξ_m .

Based on the results of the studies, the optimal structure of the system is determined, proceeding from the fact that the objective function $\vec{\Phi}$ of the optimal discrete choice of the elements of the RTTDC structure, depending on the internal parameters of the applied elements and the actual conditions of its application, corresponds to the maximum value of the system quality index \vec{K} , and combines both of the above optimality requirements.

5 Practical Implementation of the Regional Telemedical—Treatment-Diagnostic Complex

As practical example of creating the RTTDC we can consider the regional telemedicine network MedStar Solution. It is network performed on the basis of the technological



Fig. 3 Telemedical mobile diagnostic system IDIS

platform for remote patient monitoring Telemed 24 using intelligent system for remote diagnosis IDIS [14–16].

Creation of a telemedicine web platform and the creation of a common information space in medical diagnostic process is possible only with a special software authorized for primary health care, with the possibility of electronic medical cards management, home teleconsultation with the patient and telemedicine consultations with other doctors, and software complex of customer protection of network connections.

Equipment medical institutions with modern diagnostic equipment using telemetry and telemedicine technologies to create a single information space which will bring the provision of quality early diagnosis and medical care. This will help early detection of diseases and their timely treatment.

CS based of the platform Telemed 24 allows:

- Receive measurements from mobile diagnostic devices and transmit them to the cloud platform.
- Submit the results of the survey through the cloud platform to the electronic medical records of patients.

As a LPDC, for example, it can be used mobile diagnostic system IDIS.

The complex is mobile and can be used directly at the place of provision of primary care, namely: in a family outpatient clinic, in a hospital at home for remote monitoring and rehabilitation.

Telemedical mobile diagnostic system IDIS (Fig. 3) digital interface—is telemedicine, portable, diagnostic system for the collection, processing, transmission, storage and sharing of cloud storage on the state of the patient as well as for remote monitoring of patients and for their rehabilitation [16].

General diagnostics:

- Blood pressure measurement;
- Electrocardiographic study (12 channels);
- Measurement of glucose, cholesterol in the blood;
- Clinical analysis of urine (11 parameters).

A set of features of the complex depends on its purpose and appropriate configuration diagnostic equipment, such as: general diagnosis, hypertension and other cardiovascular diseases, diabetes, pulmonary disease.

Moreover, in each particular case, the LPDC can be equipped with individual tasks, depending on the tasks to be solved.

6 Conclusions

The practical implementation of these Internet technologies for RTTDK allows us to provide a high level of solution to the problems of the examination and diagnosis of patients in the early stages of the disease.

Currently, the Government Agency “National Institute of Therapy ...” together with experts in the field of medical instrumentation, to which the authors of this article belong, are conducting research on the creation of a telemedicine consultative and diagnostic complex CVD on the basis of leading specialized clinics in the eastern region of Ukraine.

Conflict of Interest The authors declare that they have no conflict of interest.

References

1. Cardiovascular Diseases (CVDs): World Health Organization. [https://www.who.int/ru/news-room/fact-sheets/detail/cardiovascular-diseases-\(cvds\)](https://www.who.int/ru/news-room/fact-sheets/detail/cardiovascular-diseases-(cvds))
2. Koval, S., Iushko, K., Starchenko, T.: Relations of apelin with cardiac remodeling in patients with hypertension and type 2 diabetes. *Folia Med.* **60**(1), 117–123 (2018)
3. Koval, S.M., Vysotska, E.V., Strashnenko, A.M., Snihurska, I.O.: Prognosis of essential hypertension progression in patients with abdominal obesity. *Proc. SPIE (USA)* **4**, 115–120 (2018)
4. Holland, W.W., Stewart, S., Masseria, C.: Policy Basics. Screening in Europe. WHO European Center for Health Policy, Belgium (2008)
5. McKeown, T. (ed.): *Screening in Medical Care: Reviewing the Evidence*. Oxford University Press for the Nuffield Provincial Hospitals Trust, Oxford (1968)
6. Zundel, K.M.: Telemedicine: history, applications, and impact on librarianship. *Bull. Med. Libr. Assoc.* **84**(1), 71–79 (1996)
7. Kolesnik, K., Shishkin, M., Koval, S., Iushko, K.: Research of directions of perfection of methods of remote monitoring of patients with arterial hypertension. In: *Proceeding of I International Scientific and Practical Conference “Information Systems and Technologies in Medicine” ISM-2018*, Kharkiv, Ukraine, pp. 160–161 (2018) (in Russian)
8. Gorskaya, L.M.: *Functional Methods of Studying the Cardiovascular System*. <http://www.10gkb.by/informatsiya/stati/funktsionalnye-metody-issledovaniya-serdechno-sosudistoj-sistemy> (in Russian)
9. Vladzimerskiy, A.V.: *Telemedsina (monograf.)*. OOO «Digital pr.», Donetsk, 477 pp. (2011) (in Russian)
10. Kolesnik, K.V., Shishkin, M.A., Kipenskij, A.V., Sitnikova, O.A.: The use of mobile radio engineering complexes in biometrics and

- telemonitoring. In: Proceedings of the Collected scientific works of the 5th International Forum: Applied Radioelectronics. Status and Development Prospects. MYFF 2014. Conference: Problems of Bioengineering. Science and Technology, pp. 166–171. ANPRE, KhNURE, Kharkiv, Ukraine, 14–17 Oct 2014 (in Russian)
11. Sokol, E., Kolisnyk, K., Boyko, V., Zamiatin, P.: Actual problems of information technologies use in the telemedicine services provision in special conditions. In: Proceedings of IEEE International Scientific and Practical Conference: Problems of Information. Science and Technology (PIC S&T-2018), Kharkiv, Ukraine (2018). <https://doi.org/10.1109/infocommst.2018.8632164>
 12. Sokol, E.I., Kipenskiy, A.V., Kolisnyk, K.V.: A formalized approach to assessing the quality of radio engineering systems for monitoring the parameters of biological object. In: Technical Electrodynamics. Thematic Issue, Kiev, part 2, pp. 192–198 (2012) (in Russian)
 13. Kolisnyk, K., Zamiatin, P.: Perfection of methods for constructing remote monitoring systems for patients in emergency situations. In: Proceedings of IEEE 3rd International Conference on Intelligent Energy and Power Systems (IEPS-2018), Kharkiv, Ukraine (2018). <https://doi.org/10.1109/ieps.2018.8559526>
 14. Kolisnyk, K., Sokol, T., Deineko, D., Kutsevlyak, S., Avrunin, O.: Application of modern internet technologies in telemedicine screening of patient conditions. In: Proceedings of IEEE International Scientific and Practical Conference: Problems of Information, Kyiv, Ukraine. Science and Technology. PIC S&T-2019 (2019, in press)
 15. Easy and Secure Telemedicine Solution: https://www.continuous-care.io/telemedicine-software/?gclid=CjwKCAjwwtTmBRBqEiwA-b6c_zE0ocR_9S6CY8c8eqS6WGLtM-FMGUgrZS2kxgidC-cpplr_-ShvBoCJREQAvD_BwE
 16. Intellectual System of Remote Diagnostics IDIS: <https://medstar.ua/ru/resheniya/idis/> (in Russian)



Telemedicine—Advanced Technology at the Service of Society

E. Arama, S. Maximilian, L. Rotaru, and V. Vovc

Abstract

In the conditions of the information society advanced technologies penetrate into different spheres of human activity, including medicine. In the medical field, three branches of telemedicine have already been formed: synchronous telematics, asynchronous telemetry and remote monitoring. Economic calculations demonstrate the efficacy of telemedicine that has benefits for the entire society, both for healthcare beneficiaries and their providers.

Keywords

Telemedicine • Synchronous • Asynchronous telemedicine • Remote monitoring • Efficiency

1 Introduction

In all countries healthcare is the most important field. There can be a lot of explanations, including the fact that healthcare has a direct impact on living standards and the quality of life. It involves major costs both in highly developed countries and in developing countries. In 2011, for example, the US state healthcare spending was more than 2.7 trillion US dollars or 17.9% of US GDP, which that year (2011) exceeded US \$ 15 trillion [1]. The US population is steadily growing. In 2000 it constituted 282 mln people; in 2011 the population exceeded 311 million inhabitants, i.e. in 10 years it increased by over 10 or 1% annually. By 2020, healthcare spending will, according to forecasts, amount to 4638 trillion

US dollars or 20% of GDP, which will reach 17,775 trillion US dollars by 2020 [1].

The increase of medical services cost is generated by the emergence of some principally new diseases; increase of the qualitative drinking water deficit; the necessity of improving the medical system; population growth; increase of the access of the population to medical services; the emergence of new principally new medical technologies; the appearance of poor-quality foods; aggravation of ecological problems (Fig. 1).

Under these circumstances, new solutions, including TELEMEDICINE, are required for the benefit of all the inhabitants of the earth. This (telemedicine) will no longer “recognize” border issues, large distances, incompetence of medical staff, etc. TELEMEDICINE will help to reduce medical errors and increase the quality of medical services; the improvement of the professional level of doctors; timely identification of patients’ diseases; improvement of doctors’ study programs; efficient use of time for doctors; to increase synergistic efficiency; reduction of patients’ time to refer to a doctor and increasing the accessibility of the rural population to medical services (Fig. 2).

TELEMEDICINE is the medicine of the future. “Remote” medical services have also taken place throughout history. People, on the basis of available means of distance communication, have always helped each other.

The first communication system was POST. In spite of all its problems of traveling and transmitting information in the most diverse way, POST was also a “TELEMEDICINE”. In the same time the forms of transmission of information, including medical ones were: TELEGRAPH (1835); Phone (1906); RADIO (1920); TELEVISION (1950); MEDICAL VIDEO COUNSILIUM (1967); INTERNET (1990); TELEMEDICINE (XXI century) (Fig. 3).

E. Arama (✉) · L. Rotaru · V. Vovc
State University of Medicine and Pharmacy “Nicolae Testemitanu”, Bld. Stefan cel Mare si Sfint 165, Chisinau, Moldova
e-mail: aramaefim@yahoo.com

S. Maximilian
State University of Moldova, Chisinau, Moldova

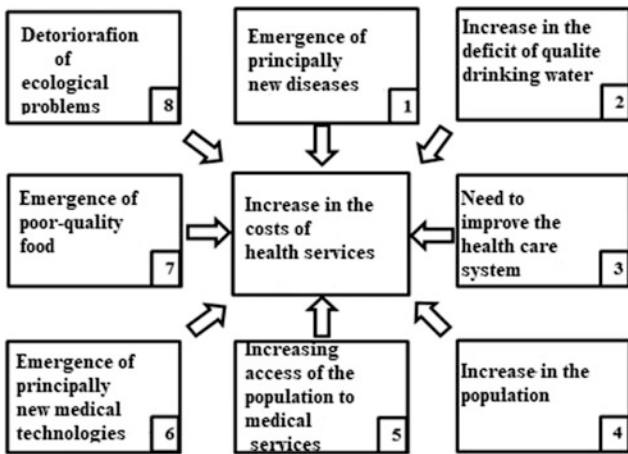


Fig. 1 Block diagram. Causes of increasing the cost of medical service

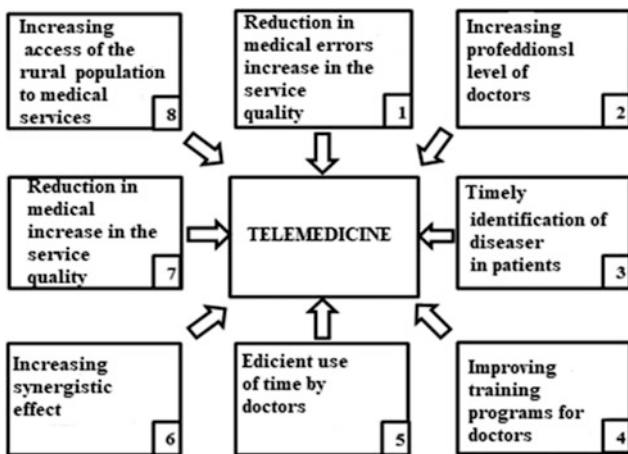


Fig. 2 Block diagram. TELEMEDICINE

2 Methodological Aspects and Discussions

TELEMEDICINE will change the “status” of doctors and employees in the medical system. Some “changes” will also refer patients, being remotely informed of some illness they did not even suspect. The replacement of the traditional system of provision of medical services with a principally new system, called TELEMEDICINE, should be progressively developed. The new system should involve not only doctors and patients, but also university institutions, which have to revise their study programs, must include not only new subjects related to information technologies, but also to train future physicians to develop software necessary in professional activities. Currently there are about 455 telemedicine programs out of which 364 programs are of US, i.e. about 80%. Among these programs there are identified councils, mutual consultations between doctors (200 programs); interpretation of patient analysis results (169

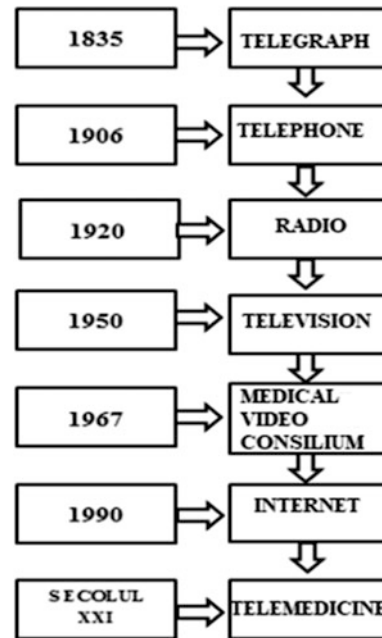


Fig. 3 Block diagram. Evolution of medical services

programs); treatment of chronic diseases (130 programs) [2]. TELEMEDICINE contributes to increasing the quality of medical services, increasing accessibility to healthcare services regardless of distance.

TELEMEDICINE, being still “young”, managed to branch out:

- (1) SYNCHRONOUS TELEMEDICINE;
- (2) ASYNCHRONOUS TELEMEDICINE;
- (3) REMOTE MONITORING. (Fig. 4)

1. SYNCHRONOUS TELEMEDICINE: both the physician and the patient are at a distance at the same time and interactive devices help them to communicate in the current regime. This group also includes visits to the patient’s home, telephone communications via the INTERNET.
2. ASYNCHRONOUS TELEMEDICINE: In this case, the doctor and the patient are not only at a distance but also

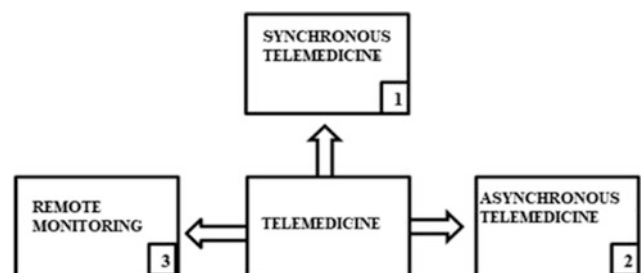


Fig. 4 Block diagram. Medical services

are not communicating. The physician receives information about the patient’s state of health based on the analyses and tests administered in later periods.

- 3. REMOTE MONITORING: deals with the evolution of chronic diseases, informing the patient about the work regime, food, rest, about the new technologies for treating the respective diseases, a kind of “updating” of the patients’ knowledge.

The possibilities of TELEMEDICINE will create “RENT” for the doctor. Some doctors will be overloaded, become “monopolists” with all monopolistic consequences, others will be “underappreciated” by patients.

TELEMEDICINE creates prerequisites for continuous education for all doctors. These (physicians) can “raise”, “increase” their medical qualification level, being in their office by TELECOMMUNICATIONS with highly qualified medical specialists. TELEMEDICINE is currently being promoted more “administratively” in the US and in developed countries. Their experience, the problems faced by Man will serve as “impulses” for the extension of the medical fields of TELEMEDICINE. The transition from traditional medicine, that is to say from the traditional forms of organizing the functioning of the medical system, to other forms based on new technologies, equipment, forms of doctor-patient telecommunication, patient-doctor based on modern information technologies, is an irreversible process. The evolution of this process depends on increasing the cumulative number of buyers of new, principally new information products with long-lasting operation, without being substituted with traditional products that have become “morally” obsolete. Traditional forms of operation of the global medical system, including in developing countries, are on the way to modernizing and streamlining. The evolution of efficiency can be formalized. We develop the mathematical model of the logistic curve for this purpose [3].

Note: $N(t)$ the cumulative number of purchasers of long-term information products at time (t) , $\frac{dN(t)}{dt}$ increase of the number per time unit $N(t)$.

Note: M —the size of the market; m —a share of principally new (up-to-date) products in all these products; k —a share of quasi-modern products.

Probability of purchasing by a “new” consumer:

$$\left[m + k * \frac{N(t - 1)}{M} \right]$$

The number of “new” purchasers (who at the beginning of the period t had not purchased the product yet):

$$[M - N(t - 1)]$$

The increase of the number of purchasers per unit of time at $\frac{dN(t)}{dt}$ is in direct dependence:

- with the probability of purchasing a new consumer,

$$\left[m + k * \frac{N(t - 1)}{M} \right]$$

- with the number of “new” purchasers $\left[m + k * \frac{N(t)}{M} \right]$;
- with the price dynamics $\left[1 + A * \frac{\Delta P(t)}{P(t)} \right]$.

Based on the formulated dependencies, we get:

$$\frac{dN}{dt} = \left(m + k * \frac{N}{M} \right) (M - N) \left(1 + A * \frac{\Delta P(t)}{P(t)} \right) \quad (1)$$

Price evolution $\left[1 + A * \frac{\Delta P(t)}{P(t)} \right]$ can be identified exogenously. We admit the price is expressed by a regression equation $P(t) = a + bt$, for which the elasticity $E_i(p) = \frac{dP}{dt} * \frac{t}{P} = \frac{bt}{a + bt}$. To $a \neq 0$, time elasticity is evaluated:

- if $a > 0; b > 0$, then for the values $t \in (0; \infty)$ the elasticity increases from 0 to +1;
- if $a < 0; b > 0$, then for the values $t \in (-\frac{a}{b}; \infty)$ the elasticity decreases from $+\infty$ to +1;
- if $a > 0; b < 0$, then for the values $t \in (0; -\frac{a}{b})$ the elasticity decreases from 0 to $-\infty$. In the interval $(0; -\frac{a}{2b}) E_i(P) = -1$.

In principle, price evolution over time can be expressed by the most diverse formulas, including: (a) $P = (a - bt)$; (b) $P = \frac{a}{t + b}$; (c) $P = \sqrt{a - bt^2}$; (d) $P = (a - bt)^2$; (e) $P = a - bt^2$; (f) $P = \left(\frac{b}{t - c}\right)^a = \sqrt[a]{\frac{b}{t - c}}$; (g) $P = \frac{1}{b} \ln \frac{a}{t}$

Dependency (1) can be written as follows:

$$\frac{dN}{dt} = \left(m + k * \frac{N}{M} \right) (M - N)(a + bt) \quad (2)$$

We have a differential equation. We make the transformations on the first two factors of Eq. (2):

$$\begin{aligned}
\left(m + k * \frac{N}{M}\right)(M + N) &= Mm + Nm + Nk + \frac{k}{M} * N^2 \\
&= \frac{k}{M} \left(N^2 + MN + Nm \frac{M}{k} + \frac{M^2 m}{k}\right) \\
&= \frac{k}{M} \left(N^2 + 2N \frac{Mk + Mm}{2k} + \frac{M^2(k+m)^2}{4k^2} - \frac{M^2(k+m)^2}{4k^2} + \frac{M^2 m}{k}\right) \\
&= \frac{k}{M} \left[\left(N + \frac{M(k+m)}{2k}\right)^2 - M^2 \left(\frac{k^2 + 2km + m^2 - 4km}{4k^2}\right)\right] \\
&= \frac{k}{M} \left[\left(N + \frac{M(k+m)}{2k}\right)^2 - \frac{M^2}{4k^2} (k^2 - 2km + m^2)\right] \\
&= \frac{k}{M} \left[\left(N + \frac{M(k+m)}{2k}\right)^2 - \frac{M^2}{4k^2} (k-m)^2\right] \\
&= \frac{k}{M} \left[\left(N + \frac{M}{2k}(k+m)\right)^2 - \frac{M^2}{4k^2} (k-m)^2\right] \\
&= \frac{k}{M} \left[\left(N + \frac{M}{2k}(k+m) - \frac{M}{2k}(k-m)\right) \left(N + \frac{M}{2k}(k+m) + \frac{M}{2k}(k-m)\right)\right] \\
&= \frac{k}{M} \left[\left(N + \frac{M}{2} + \frac{Mm}{2k} - \frac{M}{2} + \frac{Mm}{2k}\right) \left(N + \frac{M}{2} + \frac{Mm}{2k} + \frac{M}{2} - \frac{Mm}{2k}\right)\right] \\
&= \frac{k}{M} \left[\left(N + \frac{Mm}{k}\right)(N + M)\right].
\end{aligned}$$

The differential Eq. (2) can be written as follows:

$$\frac{dN}{dt} = \frac{k}{M} \left[\left(N + \frac{Mm}{k}\right)(N + M)\right] * (a + bt)$$

Separate the variables:

$$\begin{aligned}
\frac{dN}{\left(N + \frac{Mm}{k}\right)(N + M)} &= \frac{k}{M} (a + bt) dt \quad \text{or} \\
\frac{dN}{N + \frac{Mm}{k}} - \frac{dN}{N + m} * \frac{1}{M(1 - \frac{m}{k})} &= \frac{k}{M} (a + bt) dt \\
\frac{dN}{N + \frac{Mm}{k}} - \frac{dN}{N + m} &= \frac{k}{M} * \frac{M(k-m)}{k} * (a + bt) dt \\
-\frac{dN}{N + \frac{Mm}{k}} + \frac{dN}{N + m} &= (m - k)(a + bt) dt \\
\ln|N + m| - \ln\left|N + \frac{Mm}{k}\right| &= (m - k)at + \frac{(m - k)}{2} bt^2 + c \\
\ln \frac{(N + M)k}{Nk + Mm} &= (m - k)at + \frac{(m - k)}{2} bt^2 + c \\
\frac{(N + M)k}{Nk + Mm} &= e^{at(m-k)} * e^{bt^2(m-k)} * e^c
\end{aligned}$$

(3)

In the initial period $t = 0$ or in the period, when $m = k$, i.e. in the country the “new” and the quasi-principals have the same share, $N = N_0$. We determine the constant e^c : $\frac{(N_0 + M)k}{N_0k + Mm} = e^c$. The expression (3) can be written like this:

$$\begin{aligned}
\frac{(N + M)k}{Nk + Mm} &= \frac{(N_0 + M)k}{N_0k + Mm} \\
e^{at(m-k)} * e^{bt^2(m-k)} &= \frac{(N_0 + M)k}{N_0k + Mm} (e^{a+bt})^{t(m-k)}.
\end{aligned}$$

Determine the variable N:

$$\begin{aligned}
(N + M)k &= Nk \frac{N_0(N_0 + M)k}{N_0k + Mm} (e^{a+bt})^{t(m-k)} + Mm \frac{(N_0 + M)k}{N_0k + Mm} (e^{a+bt})^{t(m-k)} \\
N + M &= \frac{(N_0 + M)k}{N_0k + Mm} (e^{a+bt})^{t(m-k)} + m \frac{N_0 + M}{N_0k + Mm} (e^{a+bt})^{t(m-k)} M \\
N \left(1 - \frac{(N_0 + M)k}{N_0k + Mm} (e^{a+bt})^{t(m-k)}\right) &= M \left(\frac{(N_0 + M)m}{N_0k + Mm} (e^{a+bt})^{t(m-k)} - 1\right)
\end{aligned}$$

$$N = \frac{M \left(\frac{(N_0 + M)m}{N_0k + Mm} (e^{a+bt})^{t(m-k)} - 1 \right)}{1 - \frac{(N_0 + M)k}{N_0k + Mm} (e^{a+bt})^{t(m-k)}}$$

$$= \frac{M \left(\frac{(N_0 + M)m}{N_0k + Mm} - \frac{1}{(e^{a+bt})^{t(m-k)}} \right)}{\frac{1}{(e^{a+bt})^{t(m-k)}} - \frac{(N_0 + M)k}{N_0k + Mm}}$$

When $t = 0$:

$$N = \frac{N_0m + Mm - N_0k + Mm}{(N_0k + Mm)} * \frac{(N_0k + Mm)}{N_0k + Mm - N_0k - Mk} * M = \frac{MN_0(m-k)}{M(m-k)} = N_0.$$

When $t \rightarrow \infty$:

$$N = M \frac{(N_0 + M)m}{N_0k + Mm} * \frac{N_0k + Mm}{(N_0 + M)k} = \frac{Mm}{k}$$

The evolution of the cumulative number purchasers of durable products shows the graphical logistic curve (Fig. 5), that can be expressed analytically by the function:

$$N(t) = \frac{\frac{(N_0 + M)m}{N_0k + Mm} - \frac{1}{(e^{a+bt})^{t(m-k)}}}{\frac{1}{(e^{a+bt})^{t(m-k)}} - \frac{(N_0 + M)k}{N_0k + Mm}} * M$$

One of the economic interpretations of the above model is illustrated by the following example: the car buyer oriented towards the purchase of modern cars will not return to the Soviet models of cars Zaporozhets, Volga, Lada etc.; purchasers (consumers) of electric, hydrogen, renewable energy vehicles, etc. will not return to internal combustion engine vehicles. In other words, the model involves passing from one system of form of operation to other principally new form.

Some information about system transformations can be identified with the following parameters: M; m; k. Market

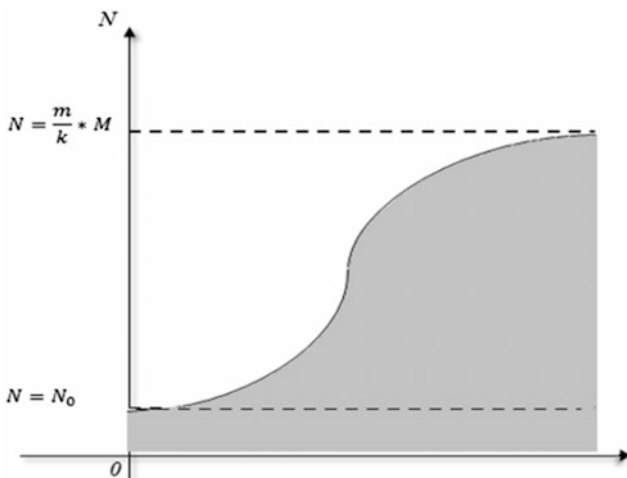


Fig. 5 The evolution of the cumulative number of purchasers of durable products

dimensions (parameter M) are determined exogenously by experts. For this purpose, the most diverse forecasts are used. Parameter M for the TELEMEDICINE model can be estimated based on pharmacy data on the demand structure, and therefore the market. It is difficult to determine the value of parameter M, the range of values can be determined with a high precision.

The share of principally new, up-to-date, relatively more efficient products (cars, systems) in relation to the total of these products (m) and the share of quasi-modern systems are usually used in the decision-making process. In this case, marketing forecasts, sales data from pharmacies can also be used. There is no problem forecasting demand for products, principally new systems. This evolutionary demand will outstrip the demand for products, traditional systems.

TELEMEDICINE cannot be “created somewhere” and implemented in an administrative manner. This (TELEMEDICINE) is the result of research, analysis, and innovations in the profile of medical structures, based on their own strategies (OS). PS is understood as the strategy of innovation activities in the respective medical structure oriented towards the realization of remote medical services based on their own innovations. Such activities of research, innovation, implementation can only take place under the impact of a “driver”, a social, economic mechanism, under the impact of a motivational mechanism.

The experience of the medical structures in the country as well as OS will certainly generate synergistic effects. The medical structures in the process of creating TELEMEDICINE are in a 3C process: CO-opetition; CO-specialization; CO-evolution, which allows them to update their PS. The convergence of local systems (PS), the use of global achievements in the process of creating TELEMEDICINE generates globalization (global + local) phenomenon. Globalization is based exclusively on KNOWLEDGE which is updated systematically and continuously. The processes of creating knowledge are complex, including their dissemination, the involvement of numerous participants, representatives of universities, academic structures, industries and society as a whole. Knowledge is a “good” non-material for the creation of which investment is needed. The knowledge contributes to the emergence of new forms of organization of medical services, it is the subject of discussions, scientific analyses, researches of new principles in new time and space.

Research, analysis and development (RAD) constitute the “effort”, labor productivity, quality while diversification of final products is the “effect” of RAD. The ratio of “effect” to those “efforts” means direct efficiency. Intersectoral (economic, technological) dependencies generate “indirect” efficiencies, which added to the direct one, are the efficiency of total RAD. As a rule, only the direct effects of RAD are included in the feasibility calculations. The chain of

interdimensional dependencies is simple: making consumer goods production technologies more efficient through producing new means of production contributes to lowering the cost and thus increasing the level of competitiveness.

In other words, the investments made in the processes of TELEMEDICINE creation can serve as a driver for the efficiency of the functioning of all branches of the national economy. TECHNOLOGIES of TELEMEDICINE (TTM) can be created in all countries, but their contribution to the efficiency of TELEMEDICINE will be different, due to the level of development of the industries and economy as a whole, specificity and traditions of the population, etc. The success of TELEMEDICINE abroad is of interest to the population in each country. TTM export can be formalized. We draw up the matrix of TTM exports for this purpose (Table 1):

where: EX_{ij} —TTN export by country $j; i = 1, 2, \dots, m; j = 1, 2, \dots, n;$

$\frac{EX_{ij}}{\sum_{i=1}^m EX_{ij}}$ —the share, value of technology exports i by country j in total TTM exports from country j (Tab.2);

$\frac{\sum_{i=1}^m EX_{ij}}{\sum_{i=1}^m \sum_{j=1}^n EX_{ij}}$ —the share, value of technology exports i from all countries in relation to the sum of technologies i exported by all countries (Table 2);

$\frac{EX_{ij}}{\sum_{i=1}^m EX_{ij}} : \frac{\sum_{i=1}^m EX_{ij}}{\sum_{i=1}^m \sum_{j=1}^n EX_{ij}}$ indexes of TTM exports (Table 3).

TELEMEDICINE will contribute not only to the increase of the quality and extension of medical services, but also to the territorial economic growth and reduction of the deficit of doctors in rural areas.

The new forms of functioning of the medical system through TELEMEDICINE will also influence the structure of investments in medicine. There will be new spaces for physician-patient dialogue in addition; computers of

Table 1 Matrix of TTM export

Exporting country	1	2	...	j	...	n	Total of technology export i
TTM							
1	EX_{11}	EX_{12}	...	EX_{1j}	...	EX_{1n}	$\sum_{i=1}^n EX_{1j}$
2	EX_{21}	EX_{22}	...	EX_{2j}	...	EX_{2n}	$\sum_{i=1}^n EX_{2j}$
⋮	⋮	⋮	⋮	⋮	⋮	⋮	⋮
i	EX_{i1}	EX_{i2}	...	EX_{ij}	...	EX_{in}	$\sum_{i=1}^n EX_{ij}$
⋮	⋮	⋮	⋮	⋮	⋮	⋮	⋮
m	EX_{m1}	EX_{m2}	...	EX_{mj}	...	EX_{mn}	$\sum_{i=1}^n EX_{mj}$
Total of technology export by country j	$\sum_{i=1}^m EX_{i1}$	$\sum_{i=1}^m EX_{i2}$...	$\sum_{i=1}^m EX_{ij}$...	$\sum_{i=1}^m EX_{in}$	$\sum_{j=1}^n \sum_{i=1}^m EX_{ij}$

Table 2 TTM exports in relation to total TTM exports in the country

	1	2	...	j	...	n	
1	$\frac{EX_{11}}{\sum_{i=1}^m EX_{i1}} = p_{11}$	$\frac{EX_{12}}{\sum_{i=1}^m EX_{i2}} = p_{12}$...	$\frac{EX_{1j}}{\sum_{i=1}^m EX_{ij}} = p_{1j}$...	$\frac{EX_{1n}}{\sum_{i=1}^m EX_{in}} = p_{1n}$	$\frac{\sum_{i=1}^m EX_{ij}}{\sum_{i=1}^m \sum_{j=1}^n EX_{ij}} = P_{10}$
2	$\frac{EX_{21}}{\sum_{i=1}^m EX_{i1}} = p_{21}$	$\frac{EX_{22}}{\sum_{i=1}^m EX_{i2}} = p_{22}$...	$\frac{EX_{2j}}{\sum_{i=1}^m EX_{ij}} = p_{2j}$...	$\frac{EX_{2n}}{\sum_{i=1}^m EX_{in}} = p_{2n}$	$\frac{\sum_{i=1}^m EX_{2j}}{\sum_{i=1}^m \sum_{j=1}^n EX_{ij}} = P_{20}$
⋮	⋮	⋮	⋮	⋮	⋮	⋮	⋮
i	$\frac{EX_{i1}}{\sum_{i=1}^m EX_{i1}} = p_{i1}$	$\frac{EX_{i2}}{\sum_{i=1}^m EX_{i2}} = p_{i2}$...	$\frac{EX_{ij}}{\sum_{i=1}^m EX_{ij}} = p_{ij}$...	$\frac{EX_{in}}{\sum_{i=1}^m EX_{in}} = p_{in}$	$\frac{\sum_{i=1}^m EX_{ij}}{\sum_{i=1}^m \sum_{j=1}^n EX_{ij}} = P_{i0}$
⋮	⋮	⋮	⋮	⋮	⋮	⋮	⋮
m	$\frac{EX_{m1}}{\sum_{i=1}^m EX_{i1}} = p_{m1}$	$\frac{EX_{m2}}{\sum_{i=1}^m EX_{i2}} = p_{m2}$...	$\frac{EX_{mj}}{\sum_{i=1}^m EX_{ij}} = p_{mj}$...	$\frac{EX_{mn}}{\sum_{i=1}^m EX_{in}} = p_{mn}$	$\frac{\sum_{i=1}^m EX_{mj}}{\sum_{i=1}^m \sum_{j=1}^n EX_{ij}} = P_{m0}$
	$\frac{\sum_{i=1}^m EX_{i1}}{\sum_{i=1}^m EX_{i1}} = 1$	$\frac{\sum_{i=1}^m EX_{i2}}{\sum_{i=1}^m EX_{i2}} = 1$...	$\frac{\sum_{i=1}^m EX_{ij}}{\sum_{i=1}^m EX_{ij}} = 1$...	$\frac{\sum_{i=1}^m EX_{in}}{\sum_{i=1}^m EX_{in}} = 1$	$\frac{\sum_{i=1}^m \sum_{j=1}^n EX_{ij}}{\sum_{i=1}^m \sum_{j=1}^n EX_{ij}} = P_{10}$

Table 3 TTM export indices in country and technology profiles

Country	1	2	...	j	...	n	
TTM							
1	$\frac{P_{11}}{P_{10}} = \hat{P}_{11}$	$\frac{P_{12}}{P_{10}} = \hat{P}_{12}$...	$\frac{P_{1j}}{P_{10}} = \hat{P}_{1j}$...	$\frac{P_{1n}}{P_{10}} = \hat{P}_{1n}$	$\frac{P_{10}}{P_{10}} = 1$
2	$\frac{P_{21}}{P_{20}} = \hat{P}_{21}$	$\frac{P_{22}}{P_{20}} = \hat{P}_{22}$...	$\frac{P_{2j}}{P_{20}} = \hat{P}_{2j}$...	$\frac{P_{2n}}{P_{20}} = \hat{P}_{2n}$	$\frac{P_{20}}{P_{20}} = 1$
⋮	⋮	⋮	⋮	⋮	⋮	⋮	⋮
i	$\frac{P_{i1}}{P_{i0}} = \hat{P}_{i1}$	$\frac{P_{i2}}{P_{i0}} = \hat{P}_{i1}$...	$\frac{P_{ij}}{P_{i0}} = \hat{P}_{ij}$...	$\frac{P_{in}}{P_{i0}} = \hat{P}_{in}$	$\frac{P_{i0}}{P_{i0}} = 1$
⋮	⋮	⋮	⋮	⋮	⋮	⋮	⋮
m	$\frac{P_{m1}}{P_{m0}} = \hat{P}_{m1}$	$\frac{P_{m2}}{P_{m0}} = \hat{P}_{11}$...	$\frac{P_{mj}}{P_{m0}} = \hat{P}_{mj}$...	$\frac{P_{mn}}{P_{m0}} = \hat{P}_{mn}$	$\frac{P_{m0}}{P_{m0}} = 1$

physicians and patients will be installed with additional elements of reception, analysis, memory and transmission of patient-physician data and vice versa.

At present, there is a positive trend of population migration from villages to cities. Given the importance of agriculture, a certain percentage of the country population must be located in rural areas. In the US, for example, more than 60 million people live in rural areas. The creation of medical “comfort” in rural areas will also contribute to the development of agriculture.

Switching from the traditional organization to the TELEMEDICINE system involves solving a number of problems, including financial, technical, technological ones, as well as logistic problems of retooling of medical managers and patients. In the structure of investments considerable expenses will be the costs of software, logistics equipment, “e-government” of the organization of TELEMEDICINE, retooling of “generations” of physicians who have been engaged in other system. The “invasion” of computers in human activities can already be seen in some companies. For example, according to the data of The Reform group, the use of Web sites and application of artificial intelligence bots would eliminate the need for 130,000 recruiting managers of the company Whitehall by 2030 saving GBP 2.6 billion (3 billion euros). Other 90,000 administrative posts in the health service and 24,000 posts of general practitioners could also be replaced in a similar way. Even jobs normally associated with human functions could fall victim to the advancement of robot information technologies, which could replace up to 30% of the average healthcare activities, such as information collection, and administration of non-intravenous medication suitable for automation. Doctors (physicians) will not be “immune” to automation, as computers are already more effective in diagnosing lung cancer, and while robots surpass human surgeons in routine procedures. The report also highlights the goal of increasing automation through drones that monitor crowds and facial

recognition technology, although it recognizes concerns about storing people’s images. The report demonstrates that public services should become more flexible based on an economy where employees are engaged in a variety of flexible, online jobs. Such “contingent labor” platforms would be suitable for hospitals and schools as an alternative to traditional labor agency models as well as organizations experiencing seasonal differences with maximum values.

The processes of automation, “computerization” and implementation of information technologies in human activities should not be given to the market. All human activities are necessary for human society, but the protection of public health will always be the most important one. Health care helps to increase the quality of life and work productivity. The efforts made to create TELEMEDICINE will transform the field of health care into a driver, in a mechanism that indirectly will help create new (principally new) jobs to create useful logistics and to automate human activities and other activities (education, industry, transport, etc.). TELEMEDICINE must be transformed into a strategic goal of governmental structures. But for that to happen, efforts are needed to study the potential, the successes achieved abroad; to identify the financial, human resources needed in the process of implementing experience in highly developed industrial countries in the field of TELEMEDICINE. The Republic of Moldova, in general, is more of a “consumer” of technologies. In this context, the medical system in the country is obliged to follow the trends of the medical development at the global level, to improve its study programs, the organization of the medical services, starting from the new possibilities offered by the scientific and technological progress. No matter how much traditional medicine differs from TELEMEDICINE, this (TELEMEDICINE) must be evolved systematically. As a result of the creation of TELEMEDICINE, those who benefit most are patients. These (patients) will have the access to the most effective forms of diagnosis and treatment of the diseases.

3 Conclusions

In the Republic of Moldova the inertia of the functionaries of medicine regarding the traditional forms of doctor-patient organization and that of TELEMEDICINE can be overcome if in the country mixed scientific-practical structures will be created in which economic, technical, programming (software) aspects will be analyzed, organizational problems will be identified and the transition strategy from the current model to the TELEMEDICINE will be developed.

The transition strategy must include the following measures:

- Creation of the TT Data Base in the Republic of Moldova, in industrialized countries with the contribution of the university scientific potential (SUM, UTM, N.TES-TIMIȚIANU SUMPh, AESM, AS of the Republic of Moldova);
- Monitoring the necessary changes in the education programs and training of doctors;
- Including the study of technologies from foreign countries in the programs of continuing education of physicians;
- Creation of motivation systems for innovations and development of TELEMEDICINE;
- Reprofiled and continuing education of physicians are done “remotely” through the Internet;
- Elaboration of the strategy TT export- import.

In this content the issue of intellectual services, elaboration of the most diverse software, forms of organization of the TELEMEDICINE arises. Metaphorically, any construction should be initially designed. TELEMEDICINE needs its “projects” to find the solution in the problems of intellectual services, software and infrastructure. Another specific point is that training and continuing education of medical staff are done with the identification of the workplace, each medical structure organizes internships, reprofiling, training of its own medical staff. Each medical structure can be a driver for the transition to TELEMEDICINE.

Conflict of Interest The authors declare that they have no conflict of interest.

References

1. Național Health Expenditure Data. Baltimore, MD: Centers for Medicare and Medical Services: <http://www.cms.gov/Research-Statistics-Data-and-Systems/Statistics-Trends-and-Reports/NationalHealthExpendData/downloads/tables.pdf>
2. Ulian, G., Lascu, D.: Sistemul de asigurări sociale de sănătate din România. În rev. Științifică “Studia Universitatis”. Seria Științe Exacte și Economice. 3, 153–158 (2008)
3. Casalino, L., et al.: External incentives, information technology, and organized processes to improve health care quality for patients with chronic diseases. JAMA J. Am. Med. Assoc. **289**(4), 434–441 (2003)

Part XIV

Biomedical Engineering Education

Static Analysis of the Human Body Balance Following an Induced Vertigo

I. Şerban, C. Drugă, A. Tătaru, and B. Braun

Abstract

This paper is aimed towards a static evaluation of the human body balance, on a force platform such as Kistler platform, following an induced vertigo by spinning the subject. Vertigo is the feeling of spinning even when the person stays in place. The environment seems to move vertically or horizontally. Some people feel like they're spinning. The effect may be easy or hardly noticeable, or it may be so severe that the subject may fall to the ground. Vertigo is more severe than dizziness, described as a slight uncertainty in orthostatic position. Dizziness can make the movement difficult, as the feeling of rotation affects the balance. The recorded values were acquired at a frequency of 100 Hz for 30 s, which led to the recording of 3000 values for every different parameter. A specialized numerical analysis software, Interactive Data Language (IDL), was used for the realization of the graphs and the statistical analysis of the results obtained on the Kistler force platform.

Keywords

Kistler • Vertigo • Balance • Dizziness

1 Introduction

Vertigo is a sensation of spinning even when the person stays in place. The environment seems to move vertically or horizontally. Some people feel like they're spinning. The effect may be easy or hardly noticeable, or it may be so

severe that the subject may fall to the ground. Vertigo is more severe than dizziness, described as a slight uncertainty in orthostatism. Dizziness can make the movement difficult, as the feeling of rotation affects the balance. The incidence of vertigo in association with migraine has been reported to range between 50 and 70% [1]. Due to this, vertigo and dizziness are studied in various situations [2–5].

Vertigo is often confused with fear of heights. However, the feeling of dizziness described by people looking down from a high height is different from vertigo, which can occur at any time and can last for many years.

Vertigo can occur suddenly and may take a few minutes or may appear and resolve over several days. For some subjects with severe vertigo, the symptoms may be constant for several days and can make it difficult to carry out daily life.

The symptoms of vertigo can vary in intensity, and may include the feeling that the environment is moving or spinning, nausea, vomiting, difficulty standing and going, feeling unsafe, the feeling that it will not be able to keep a look at the same point for a long time, the feeling that the floor is moving [6, 7].

Causes of vertigo have not yet been demonstrated, but it is assumed that the calcium particles normally present in the inner ear break out and float in the semicircular canal of the inner ear. This disturbs the normal balance and produces vertigo. Drugs, various illnesses, advanced age or cranial trauma are some of the factors that can cause particles to detach from the inner ear. Vertigo can occur at any age and affects men and women equally.

The proposed paper refers to an experimental analysis of a vertigo-induced state, using the force platform Kistler. The parameter taken into consideration is the distribution of the center of gravity influenced by human body balance during a vertigo. A comparison shall be made between before the state of dizziness and during this state.

The hypothesis of this study is that vertigo, or the feeling of dizziness, of imbalance, does not take more than a minute for one person, and then returns to its initial state of equilibrium.

I. Şerban (✉) · C. Drugă · A. Tătaru · B. Braun
Product Design, Mechatronics and Environment Department,
Faculty of Product Design and Environment, Transylvania
University, University Street, No. 1, Braşov, Romania
e-mail: ionel.serban@unitbv.ro

2 Methods and Materials

The stability analysis methods are divided into two categories: when the motion is linear (average, standard deviation, coefficient of variation, standard error) and when motion is non-linear (coefficients of a stabilogram).

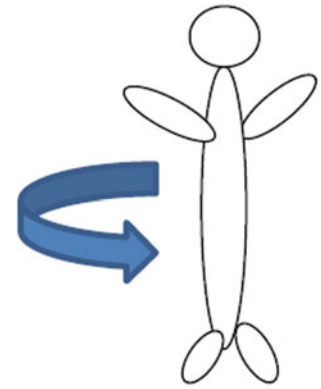
Subjects have undergone rotational movements, the stability and initial posture being altered due to the forces acting on the body during these movements. All the experiments were done with the informed consent from the subjects.

In the experiment, the Kistler plate (Fig. 1) is used to determine the bipedal locomotor function. This type of measurement uses a Kistler measuring device, a signal amplifier, two acquisition boards for digital and analogue signals, and a connection between the PC and the board through a communication interface for data acquisition. The Kistler platform measures the vector of a total force (F) consumed during locomotor activities during contact with the surface of the human body (foot) and the floor surface on which the plate is seated.

The Kistler plate is equipped with four piezoelectric sensors, each positioned in the 4 corners of the plate. Piezoelectric sensors are designed to transform a mechanical action (the force the subject effects on the plate) into an electrical signal without any external energy source. The sensors used by the force plate comprise three overlaps of quartz crystals, piezoelectric sensitive to compressive forces F_z and shear forces F_x and F_y .

In order to carry out the experiment on the Kistler plate the static equilibrium analysis of the human body was carried out measurements of each subject, namely, making two cycles of rotations in place as in Fig. 2.

Fig. 2 Direction of rotation



Ability to maintain balance, stability, is a complex process that holds in the posture reflexes (Fig. 3). The main sensory systems that provide clear information on the body's position in relation to environmental conditions and contribute as input signals for these reflections are the visual system, the vestibular system, and the somatic-sensory system [10].

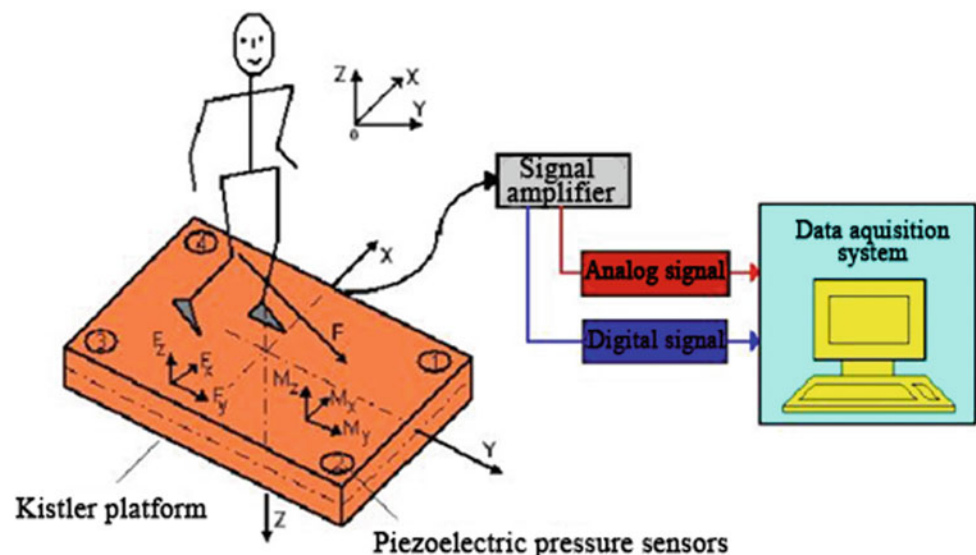
As the next step of the experiment, immediately after rotation, the subject is assisted and then taken to the Kistler plate for postural stability determination.

3 Results and Discussion

Data processing is one of the steps which, like the acquisition of data, needs to be carefully fulfilled, because an inappropriate choice of the evaluated parameters may lead to a misinterpretation and thus, to erroneous conclusions.

The choice of measured parameters is guided by the desired direction at the beginning of the experiment

Fig. 1 Kistler force platform [8, 9]



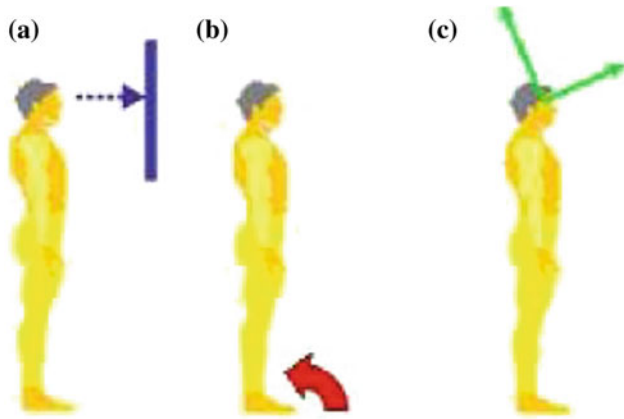


Fig. 3 Posture reflexes: visual stability reflexes (a) proprioception, somatic sensory, stability reflexes (b) vestibular stability reflexes (c)

planning, and is of utmost importance, helping to visualize and understand the measurements made as well as further statistical processing.

The recorded values were acquired at a frequency of 100 Hz for 30 s, which led to the recording of 3000 values corresponding to the different parameters [10].

The stabilization time of the subjects, according to the graphs above, is about 3 s (Figs. 4 and 5). After this period the subject resumes to a stable equilibrium or balance.

Fig. 4 Position of the x coordinate, of the center of gravity in relation to time (subject 1)

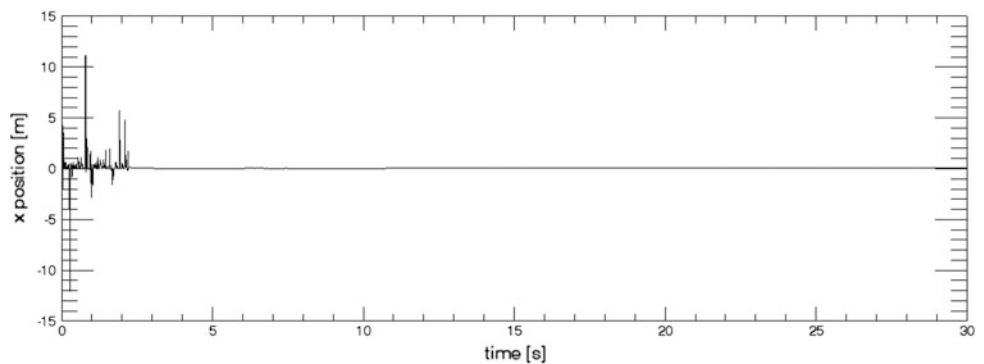
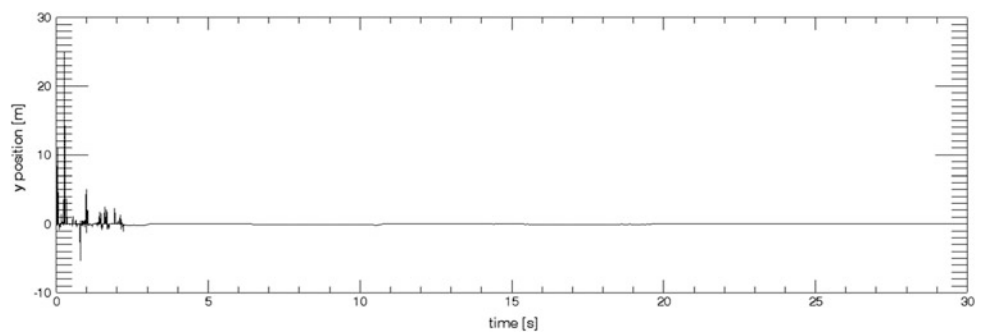


Fig. 5 Position of the y coordinate, of the center of gravity in relation to time (subject 1)



In the case of this experiment, the most important parameters are the coordinates of the center of gravity (Figs. 6 and 7), as well as its variation over time.

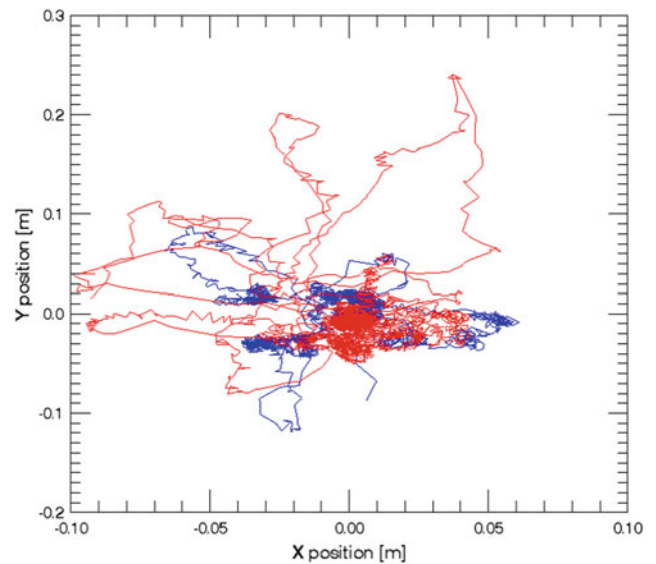


Fig. 6 First subject, comparison between the subject's center of gravity coordinates: before simulating vertigo (blue) and after simulating vertigo (red)

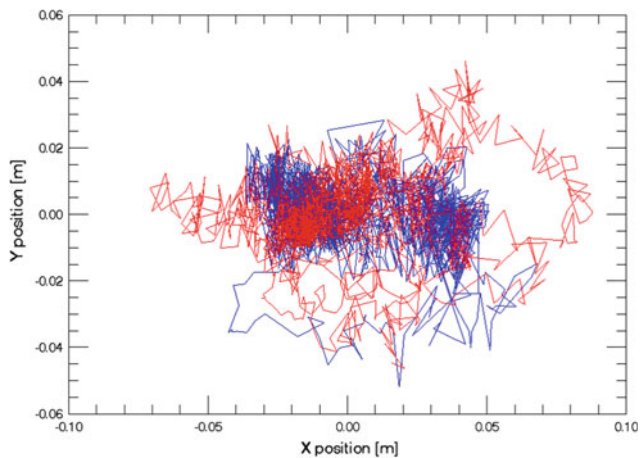


Fig. 7 Second subject, comparison between the subject's center of gravity coordinates: before simulating vertigo (blue) and after simulating vertigo (red)

Table 1 Before and after simulating vertigo for X axis

Subject	Center of gravity average X (m)	Center of gravity STDEV (x)
<i>Before simulating vertigo</i>		
Subject 1	0.051743982	0.028479
Subject 2	0.077564399	0.023455
<i>After simulating vertigo</i>		
Subject 1	-0.01278434	0.026511
Subject 2	0.11384748	0.025371

Table 2 Before and after simulating vertigo for Y axis

Subject	Center of gravity average Y (m)	Center of gravity STDEV (y)
<i>Before simulating vertigo</i>		
Subject 1	-0.03230179	0.02284
Subject 2	-0.13469447	0.010575
<i>After simulating vertigo</i>		
Subject 1	-0.06947604	0.049166
Subject 2	0.065231418	0.012373

For the execution of graphs and static analysis, a specialized numerical analysis software, IDL EXELIS, was used. The data was originally imported into the Microsoft Excel application, and exported from there in a compatible format.

Following the experiments performed, the following results were presented here in tabular form (Tables 1 and 2).

4 Conclusion

A spectral analysis of the signal provides indications of the frequency of these oscillations, in the case of the first subject being able to observe the occurrence of 1 Hz frequency components as a result of spin stimulation. This spectral analysis was carried out by applying the Fourier transformation of the data series to the distance from the center.

The analysis of the histogram of the variation of the center of gravity compared to the mean indicated that the loss of the sense of direction leads to the oscillations of the subject and is numerically manifested by the passage at a higher frequency through the center.

Acknowledgements Practical realization of this project was made possible thanks to funding received in the *My License Project-2019* competition held in the "Transylvania" University of Brașov.

Conflict of Interest The authors declare that they have no conflict of interest.

References

1. Brandt, T.: Migraine and vertigo. In: *Vertigo: Its Multisensory Syndromes. Clinical Medicine and the Nervous System*. Springer, London (1991)
2. Brandt, T., Dieterich, M., Strupp, M.: *Vertigo and Dizziness: Common Complaints*, 2nd edn. Springer, London (2014)
3. Zaidi, S.H., Sinha, A.: *Vertigo. A Clinical Guide*. Springer, Berlin (2013)
4. Kaga, K.: *Vertigo and Balance Disorders in Children*. Springer, Japan (2014)
5. Cesarani, A., Alpini, D.C.: *Vertigo and Dizziness Rehabilitation*. Springer, Berlin (1999)
6. Earassociates Homepage: <http://www.earassociates.com/conditions-balance-dizziness-disorders-san-jose-ca.html>. Last accessed 18 May 2018
7. Șerban, I., Roșca, I.C., Braun, B., Drugă, C.: Environmental effects on the center's offset of the Kistler force plate. In: Vlad, S., Ciupa, R. V. (eds.) *International Conference on Advancements of Medicine and Health Care through Technology 2011. IFMBE Proceedings*, vol. 36, pp. 100–105. Springer, Berlin, Heidelberg (2011)
8. Drugă, C., Radu, C., Barbu, D., Șerban, I.: Determination of dynamical parameters of the human gait using force plate. In: *3rd International Conference on "Computational Mechanics and Virtual Engineering"*, pp. 208–214. Transilvania University Press, Brașov, Romania (2009)
9. Șerban, I., Roșca, I.C., Baritz, M.: Influence of sound frequency on human body stability. *Environ. Eng. Manage. J.* **15**(2), 375–380 (2016)
10. Șerban, I., Roșca, I.C., Braun, B.C., Drugă, C.N.: Analysis parameters base of support and center of mass of the human body. In: *4th International Conference on "Computational Mechanics and Virtual Engineering"*, Brașov, România, pp. 429–434 (2011)

Part XV

**Innovation, Development and Interdisciplinary
Research**

Voltage Management of a Remote Load

A. Penin, Yu. Savva, and A. Sidorenko

Abstract

Accurate regulation and measurement of a load parameters can be difficult when there are significant voltage drops between the power supply and the load. In particular, some methods of the load voltage management or regulation are known. These methods have these or those disadvantages. A new power supply method is offered for the remote load. This method is based on correction of the power supply output voltage by using an invariant relationship of the line. The affine ratio of three points, known in projective and affine geometry, is such invariant. Therefore, three samples of the output voltage and the corresponding samples of the input current are used. The affine ratio value does not depend from the line parameters and the measurement accuracy.

Keywords

Voltage regulation • Supply line • Remote load • Voltage drop • Affine ratio

1 Introduction

Accurate regulation and measurement of a load voltage can be difficult when there are significant voltage drops between the power supply and the load. In particular, even if a regulator produces a perfectly regulated voltage at its own output, variations in load current affect the voltage drop along the line wires, resulting in significant voltage fluctuations at the load.

There are some methods of the load voltage stabilization or accurate regulation [1–3]. The first conventional technique, direct remote sensing, produces excellent load-end regulation, but it requires two pairs of wires: one pair to provide the load current and a second pair to measure the voltage at the load for proper regulation. But adding the second pair is not always desirable, or even possible. The second conventional technique, voltage drop compensation, doesn't require extra wires, but it does require careful estimation of the voltage drop of the line. The supply voltage is adjusted to make up for the estimated interconnection voltage drop. However, since the drop is only an estimated value and not measured, the accuracy of this method is questionable at best. The third conventional technique involves placing a voltage regulator directly at the load. This provides both accuracy and simplified the line, but the regulator consumes valuable space at the load end, reduces overall power system efficiency and power dissipation near the load increases.

The next proposed method, Virtual Remote Sensing VRS, solves the problem of maintaining load regulation at the line end. The VRS solves this problem by using a short test current pulse, direct measurement of the longitudinal line resistance, and correcting of the power supply output voltage. A decoupling capacitor of the load takes on an additional role by filtering out voltage transients from the test current pulse. But, if the line contains lateral resistances or intermediate loads, the measurement of the longitudinal line resistance determines errors of the output voltage correcting.

Due to the explained problems, one more power supply method of a remote load is offered [4]. This method is based on correction of the power supply output voltage by using an invariant relationship of the line. The affine ratio of three points (or cross ratio of four points), known in affine and projective geometry, is such invariant [5]. For our case, we use three samples of the output voltage and the corresponding samples of the input current; one of these samples is the actual (or current) load voltage value, and two other

A. Penin (✉) · A. Sidorenko
D. Ghitu Institute of Electronic Engineering and
Nanotechnologies, Academiei Str. 3/3, Chisinau,
Republic of Moldova
e-mail: aapenin@mail.ru

Yu. Savva
I.S. Turgenev Orel State University, Orel, Russian Federation

samples are test values. Therefore, the affine ratio value does not depend from the line parameters and the measurement accuracy [6]. At first, we calculate the affine ratio by the samples of the input current and then, we find the voltage actual value and correct the power supply output voltage. The basic states of the invariants and offered method are presented in this paper.

2 Input-Output Conformity of a Two-Port

Let us consider a two-port circuit in Fig. 1. A variable voltage source V_1 or variable conductivity Y_{L1} is the load of this two-port. The system of equation of this two-port has the known view

$$I_0 = Y_{00}V_0 - Y_{10}V_1, \quad I_1 = Y_{10}V_0 - Y_{11}V_1, \quad (1)$$

where Y parameters are

$$Y_{00} = y_{10} + y_0, \quad Y_{11} = y_{10} + y_1, \quad Y_{10} = y_{10}.$$

We determine the characteristic value of regime parameters for the short circuit $SC(V_1^{SC} = 0)$ and open circuit $OC(I_1^{OC} = 0)$.

Then,

$$V_1^{SC} = 0, \quad I_1^{SC} = Y_{10}V_0, \quad I_0^{SC} = Y_{00}V_0,$$

$$V_1^{OC} = \frac{Y_{10}}{Y_{11}}V_0, \quad I_1^{OC} = 0, \quad I_0^{OC} = \frac{\Delta_Y}{Y_{11}}V_0.$$

For these parameters, system (1) becomes as

$$I_0 = I_0^{SC} - \frac{I_1^{SC}}{V_0}V_1, \quad I_1 = I_1^{SC} - \frac{I_1^{SC}}{V_1^{OC}}V_1. \quad (2)$$

If the voltage V_1 is an independent quantity, Eq. (2) give the following input and output load straight lines in Fig. 2. As the load characteristics are defined by this linear expression, the affine transformation or mapping $V_1 \rightarrow I_1$, $V_1 \rightarrow I_0$, $I_1 \rightarrow I_0$ takes place. Then, we may determine the running regime parameter by an identical value for the various actual regime parameters (voltages, currents) and for different sections of circuit (input and output).

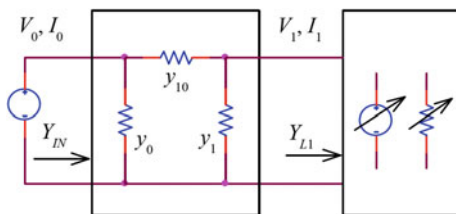


Fig. 1 Two-port with a load voltage source

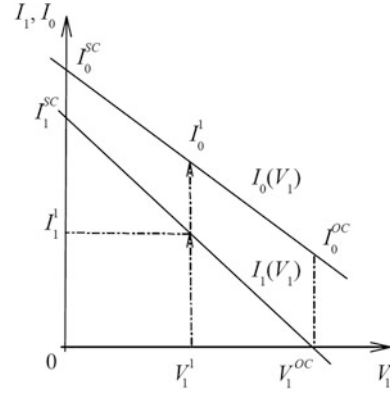


Fig. 2 Conformity of the input and output load straight lines of a two-port

Let an initial regime be given by values V_1^1, I_1^1, I_0^1 . Then, the affine ratio has the form

$$n_1^1 = \frac{V_1^{OC} - V_1^1}{V_1^{OC} - V_1^{SC}} = \frac{I_1^1 - I_1^{OC}}{I_1^{SC} - I_1^{OC}} = \frac{I_0^1 - I_0^{OC}}{I_0^{SC} - I_0^{OC}}. \quad (3)$$

As the first example of the management, the invariant value n_1 represents a practical interest for remote voltage measurement or accurate transmission of voltage sensor signal V_S through an unstable two-port. In this case, the affine ratio value n_1^1 is accepted as a transmitted analog signal, $n_1^1 = V_S$. In a short time slot, the three samples of load voltage are transmitted by connecting two test voltage sources V_1^{SC}, V_1^{OC} and the information voltage source V_1^1 . From (3), the voltage V_1^1 is precomputed by the signal V_S .

In turn, the signal $V_S = n_1^1$ is calculated directly by the measured input currents (3). The structure of this expression shows that errors of measurement are reduced mutually.

3 Proposed Power Supply System

Figure 3a schematically shows a structure of the power supply system for a remote load. Besides a voltage source, supply line with losses, and load, this system contains test units at the input, Fig. 3b, and output of the line in Fig. 3c.

The appliance in Fig. 3 works as follows. Let for an initial state, at a time slot $t_1 - t_0$ in Fig. 4, the voltage V_0 does not change and corresponds to a regulating voltage V_{REF} . The voltage V_{REF} is equal to the nominal value of the reference voltage source V_{NOM} . Also, let the load voltage $V_1 > V_{NOM}$ begin to decrease due to the load current I_1 increase. The control generator (of the receiving test unit) turns on the trigger shaper at moment t_1 , which provides a short pulse at time slot $t_2 - t_1$. This short pulse is being summed with the voltage of the reference voltage source V_{NOM} . Therefore, the voltage V_0 increases approximately by

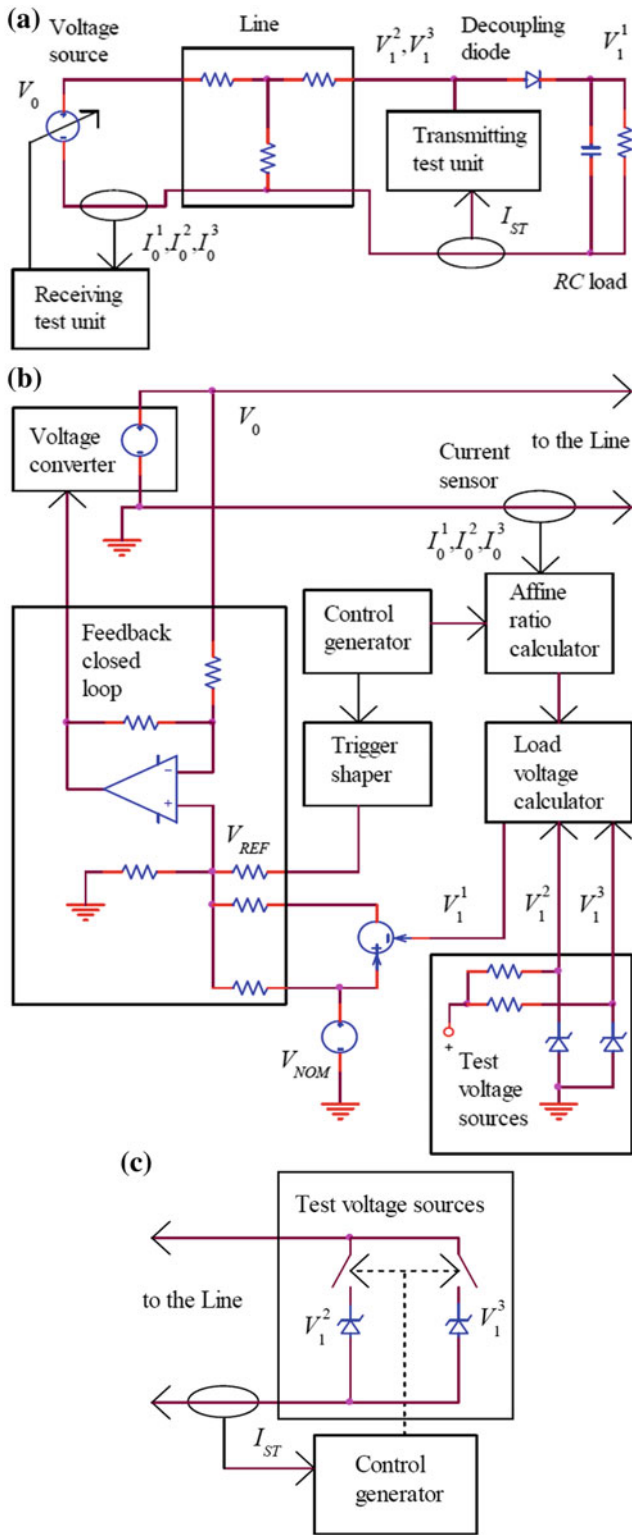


Fig. 3 Power supply system with test units: **a**-general scheme, **b**-receiving test unit, **c**-transmitting test unit

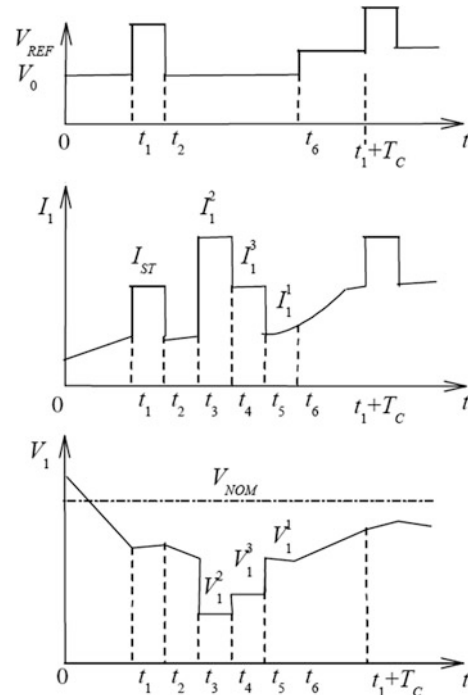


Fig. 4 Diagrams of the voltages and currents of the system

10–20%. But, the load voltage V_1 practically doesn't increase because of the high value of load capacitor. Therefore, the short start pulse of current I_{ST} is obtained. This start pulse turns on the control generator of the transmitting test unit. The control generator connects one after another the test voltage sources $V_1^2, V_1^3 < V_{NOM}$ to the line at the short time slot $t_4 - t_3, t_5 - t_4$ respectively.

But, the load voltage V_1 practically doesn't increase because of the decoupling diode. The pulse currents I_1^2, I_1^3 flow through the current sensor. Further, the actual load voltage V_1^1 and corresponding current I_1^1 are formed at the time slot $t_6 - t_5$. So, we obtain the three voltage samples V_1^2, V_1^3, V_1^1 on the output of the line.

The corresponding samples I_0^2, I_0^3, I_0^1 of the input current enter to the affine ratio calculator of the receiving test unit. Respective control generator permits to calculate this affine ratio in the following view

$$n_1(I_0^1) = \frac{I_0^2 - I_0^1}{I_0^1 - I_0^3}$$

On the other hand, this value is equal to the affine ratio for the line output voltages

$$n_1^1(I_0^1) = n_1^1(V_1^1) = \frac{V_1^2 - V_1^1}{V_1^1 - V_1^3}.$$

Therefore, the load voltage calculator generate voltage value V_1^1 using the same test voltages as V_1^2, V_1^3

$$V_1^1 = \frac{V_1^2 + n_1^1 V_1^3}{n_1^1 + 1}.$$

Finally, we obtain the new value of the regulating voltage

$$V_{REF} = V_{NOM} + (V_{NOM} - V_1^1).$$

This value determines the increased voltage V_0 at the moment t_6 . In this connection, the load voltage V_1 increases also. Through a pulse period T_C , the regulating process repeats at the moment $t_1 + T_C$ and so on. Finally, the load voltage V_1 gradually approaches to the nominal value V_{NOM} .

4 Conclusion

The input- output invariants of a two-port are shown. It allows realizing measurements of remote load parameters. Also, the method of regulation or stabilization of load voltage is offered. In these cases, testing of the load parameters is held by using the power supply line. For these methods, the line parameters are not used obviously and

measurement errors of samples of the input currents and load conductivities are reduced mutually.

Acknowledgements The authors are grateful to A. Osadchuk and D. Maevskii for fruitful discussions. This work was partially supported by A.v. Humboldt Foundation, grant “Kongressbesuch und die Arbeitsbesuche in Jülich und Karlsruhe in der Zeit vom 14. bis 26. Oktober 2018”.

Conflict of Interest The authors declare that they have no conflict of interest.

References

1. Hack, T., Dobkin, R.: Virtual remote sensing improves load regulation by compensating for wiring drops without remote sense lines. *LT J. Analog Innovation* **20**(2), 1–9 (2010)
2. Dobkin, R., Hack, T., Chen, Y.: Voltage regulator compensating for voltage drop along conductors between regulator output and load. US Patent No. 8,754,622 (2014)
3. LT4180—Virtual Remote Sense Controller. <http://www.linear.com/product/LT4180>
4. Penin, A., Sidorenko, A., Donu, S.: Power supply method of a remote load. MD patent 1220 Z (2017)
5. Frank, J.A.: *Schaum's outline of theory and problems of projective geometry*. McGraw-Hill (1967)
6. Penin, A.: Analysis of electrical circuits with variable load regime parameters. In: *Projective geometry method*, 2nd ed. Springer International Publishing AG (2016)

Steady-State Behaviors of a Quantum Oscillator Coupled with a Three-Level Emitter

A. Mirzac and M. A. Macovei

Abstract

A laser-pumped three-level Λ -type system the upper state of which is being coupled with a quantum oscillator characterized by a single quantized leaking mode has been investigated. Two distinct situations leading to lasing effects of the quantum oscillator's degrees of freedom have been identified and the mechanisms behind them have been described. Particularly, the interplay between single- or two-quanta processes accompanied by quantum interference effects among the induced emitter's dressed-states responsible for flexible lasing effects has been proved, respectively.

Keywords

Quantum • Dynamics • Λ -type system

1 Introduction

Quantum dots, quantum wells or other artificially obtained atomiclike systems exhibit properties suitable for modern technology challenges as dipole moments, transition frequency, etc., can be engineered [1–4]. These materials have progressed to appear as promising to generate terahertz waves. The impact of terahertz waves is proved by the growing range of their technological applications: sensing, imaging, detection, data communication. In this context, quantum systems possessing permanent dipoles were proved to manifest terahertz light generation, beside bare-state population inversion and multiple spectral lines and squeezing [5–13]. From this perspective, the increased interest for novel quantum systems displaying lasing in a broad parameter range of micro- or nano-scale devices.

Here, we explore a laser pumped Λ -type three-level system the upper state of which is being coupled with a quantum oscillator described by a quantized single-mode boson field [14]. The frequency of the quantum oscillator is much smaller than all other frequencies involved to describe the model, however, it is of the order of the generalized Rabi frequency specific for the laser-pumped three-level qubit. We have computed the steady-state lasing regimes in both resonance cases for the quantum oscillator's field mode, however, for asymmetrical spontaneous decay rates equivalent to each three-level qubit's transition. If the model contains an electromagnetic cavity mode, describing the quantum oscillator, then its frequency may vary in the terahertz range and, thus, we can demonstrate an effective coherent electromagnetic field source of such photons.

Evidently, lasing effects are known for two-level systems, whereas the three-level ones provide more flexibility for the same parameters involved. Certain practical novel systems are described by a three-level model. As an accurate Λ -type system may be considered a laser-pumped color center emitter embedded on a vibrating membrane where strong coupling strengths can be achieved via vacuum dispersive forces. Few coupled quantum dots are appropriate systems too. Additionally, alternative systems can be asymmetrical real or artificial few-level molecules possessing permanent dipoles, $d_{\alpha\alpha} \neq 0$ [15–17].

2 Theoretical Framework

The Hamiltonian picturing a quantum oscillator of frequency ω coupled with a laser-pumped Λ -type three level system presented in Fig. 1, in rotating wave approximation at $(\omega_{12} + \omega_{13})/2$, is the following:

$$H = \hbar\omega b^\dagger b + \frac{\hbar\omega_{23}}{2}(S_{22} - S_{33}) + \hbar g S_{11}(b + b^\dagger) - \hbar \sum_{\alpha \in \{2,3\}} \Omega_\alpha (S_{1\alpha} + S_{\alpha 1}) \quad (1)$$

A. Mirzac (✉) · M. A. Macovei
Institute of Applied Physics, Academiei str.5, Chişinău, Republic of Moldova
e-mail: mirzacalexandra71@phys.asm.md

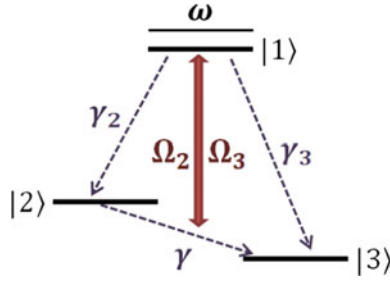


Fig. 1 The schematic of the model

We have considered here that a single laser of frequency ω_L pumping both arms of emitter can act as a pumping electromagnetic field source or, respectively, two laser fields $\{\omega_{L1}, \omega_{L2}\}$ each driving separately the two transitions of the Λ -type sample possessing orthogonal transition dipoles. Also, we have considered that $\omega_{L1} = \omega_{L2} \equiv (\omega_{12} + \omega_{13})/2$, see Fig. 1. Here $\omega_{\alpha\beta}$ are the frequencies of $|\alpha\rangle \leftrightarrow |\beta\rangle$ three level qubit's transitions, $\{\alpha, \beta \in 1, 2, 3\}$.

The terms entering in the Hamiltonian (1) have the usual significance, basically, the first and the second terms are attributed to the free energies of the quantum oscillator and the atomic subsystem, respectively, whereas the third one accounts for their mutual interaction via the most upper-state energy level with g being the respective coupling strength. The atom-laser interaction is represented by the last term and $\{\Omega_2, \Omega_3\}$ are the corresponding Rabi frequencies associated with a particular driven transition. We specially highlight that if the upper state of the investigated model contains a permanent dipole then the external coherent light sources interact with it as well. The related Hamiltonian is:

$$H_{pd} = \hbar S_{11} \sum_{i \in \{2,3\}} G_i \cos(\omega_{L_i} t) \quad (2)$$

where $G_i = d_{1i} \frac{E_i}{\hbar}$ with E_i being the lasers amplitude. Since $\omega_{L_i} \gg G_i$, the Hamiltonian H_{pd} is rapidly oscillating and further is neglected. Thus the Hamiltonian (1) and the analytical approach allows considering both situations simultaneously, specifically, when either a nanomechanical resonator or an electromagnetic cavity as a quantum oscillator. Certainly, the three-level qubit's operators, $S_{\alpha\beta} = |\alpha\rangle\langle\beta|$, verify the commutation relation $[S_{\alpha\beta}, S_{\beta'\alpha'}] = \delta_{\beta\beta'} S_{\alpha\alpha'} - \delta_{\alpha'\alpha} S_{\beta'\beta}$ and the quantum oscillators, as well: $[b, b^\dagger] = 1$ and $[b, b] = [b^\dagger, b^\dagger] = 0$, respectively.

The whole dynamics of this complex model can be treated within Born-Markov approximations via the following master equation:

$$\dot{\rho} + \frac{i}{\hbar} [H, \rho] = - \sum_{\alpha \in \{2,3\}} \gamma_\alpha [S_{1\alpha}, S_{\alpha 1} \rho] - \gamma [S_{23}, S_{32} \rho] - \kappa(1 + \bar{n}) [b^\dagger, b \rho] - \kappa \bar{n} [b, b^\dagger \rho] + \text{H.c.} \quad (3)$$

The term situated in the right-hand side of Eq. (2) corresponds to the emitter's damping due to a spontaneous emission. Also the quantum oscillator's damping effects include the mean oscillators quanta number $\bar{n} = 1/[\exp(\hbar\omega/k_B T) - 1]$, due to the environmental thermostat at temperature T . Here k_B is the Boltzmann constant, γ' 's are the decay rates of the three-level qubit, see Fig. 1, respectively κ describes the quantum oscillator's leaking rate. In the following, we projected our model in the three-level qubit-laser dressed-state picture. Applying this transformation to the Hamiltonian (1) one arrives at the corresponding Hamiltonian's expression in the dressed—state picture:

$$H = H_0 + H_d + H_1 + H_2 \quad (4)$$

where

$$H_0 = \hbar\omega b^\dagger b + \hbar\Omega R_z \quad (5)$$

$$H_d = \hbar g \left(\sin^2 \theta R_{11} + \frac{\cos^2 \theta (R_{22} + R_{33})}{2} \right) (b + b^\dagger) \quad (6)$$

$$H_1 = \hbar g \cos^2 \theta \frac{(R_{22} + R_{33})(b + b^\dagger)}{2} \quad (7)$$

$$H_2 = -\hbar g \frac{\sin \theta}{2\sqrt{2}} (R_{21} + R_{13} + H.C.) (b + b^\dagger) \quad (8)$$

with $R_z = R_{22} + R_{33}$. The dressed-state three-level qubit's operators: $R_{\alpha\beta} = |\Psi_\alpha\rangle\langle\Psi_\beta|$ are obeying the same commutation relations as the old ones. In the interaction picture obtained after a unitary transformation, H_d is an oscillating term, which is dropped off from the dynamics, while the last two Hamiltonians turns into [14]:

$$H_{1I} = \bar{g} (R_{23} e^{2i\Omega t} + H.C.) (b^\dagger e^{i\omega t} + H.C.) \quad (9)$$

$$H_{2I} = -\tilde{g} ((R_{21} + R_{13}) e^{i\Omega t} + H.C.) (b^\dagger e^{i\omega t} + H.C.) \quad (10)$$

where

$$\bar{g} = \hbar g \cos^2 \theta / 2 \quad (11)$$

whereas

$$\tilde{g} = \hbar g \frac{\sin \theta}{2\sqrt{2}}. \quad (12)$$

Investigating the above mentioned Hamiltonians, we explore the quantum dynamics of our model illustrating two resonance cases, namely

- (I) at $2\Omega = \omega$,
- (II) at $\Omega = \omega$.

Therefore, we will interpret these two cases separately. Consequently, the Hamiltonian for the first situation (I), will be

$$H = \bar{\delta} b^\dagger b + \bar{g} (R_{32} b^\dagger + b R_{23}) \quad (13)$$

while for the second

$$H = \tilde{\delta} b^\dagger b - \tilde{g} (R_{22} + R_{33}) b^\dagger + b (R_{22} + R_{33}) \quad (14)$$

where $\bar{\delta} = \omega - 2\Omega$ and $\tilde{\delta} = \omega - \Omega$.

In what follows, we will explore the lasing mechanisms standing behind the two resonance cases, keeping the same parameters range [14].

3 Results and Discussions

The analytical approach developed here allows us to obtain an exact system of equations describing the quantum dynamics of the composed system laser pumped spontaneously damped qubit plus leaking phonon mode within the rotating wave, Born-Markov and secular approximations, respectively, and to extract the variables of interest with the help of the traced density operator over the corresponding degrees of freedom. Figure 2 shows the steady-state behaviors of the mean quanta number and its quantum statistics for realistic parameters. The maximum for $b^\dagger b$ occurs around $\bar{\delta} = 0$, at the resonance when the quanta's frequency ω equals the dressed-state splitting frequency 2Ω due to the pumping lasers. It is necessary to mention here that the quanta's statistics is near Poissonian meaning that we have obtained lasing regimes in our system. Lasing is taking place if $\gamma_3/\gamma_2 \ll 1$ and $\langle R_{22} \rangle > \langle R_{33} \rangle$, that is, we have dressed-state population inversion and this is the reason for lasing effect. Here, via lasing we mean generation of quantum oscillator's quanta possessing Poissonian statistics.

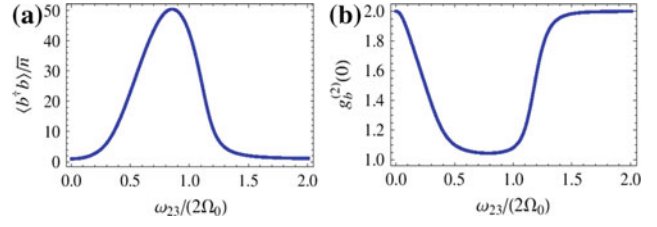


Fig. 2 a The mean quanta number of the quantum oscillator $\frac{b^\dagger b}{\bar{n}}$ and b its second-order correlation function $g_b^{(2)}(0)$ versus $\omega_{23}/2\Omega_0$ for the case (I) $2\Omega = \omega$. Here $\frac{g}{\gamma_2} = 3.9$, $\frac{\gamma_3}{\gamma_2} = 0.09$, $\frac{\gamma}{\gamma_2} = 0$, $\frac{\kappa}{\gamma_2} = 10^{-3}$, $\frac{\omega}{\gamma_2} = 50$, $\frac{\Omega}{\gamma_2} = 20$ and $\bar{n} = 0.9$

We will keep the same parameters and will explore the quantum dynamics for the second resonant case, i.e. (II). Particularly, Fig. 3 shows the mean quanta's number of the quantum oscillator in the resonance case (II) when $\gamma_3/\gamma_2 \ll 1$. Remarkably, one can observe a wide plateau where the quanta's statistics is Poissonian while its quantum oscillator's mean quanta number vary from small to larger numbers. We have a clear lasing effect in this setup. Comparing with the resonance case (I), i.e. Figure 2, there are generated more quanta of the number oscillator followed by a broader regime which is more convenient for the potential application, see Figs. 3 and 2. In this context, if the upper state $|1\rangle$ of the three-level emitter has a permanent dipole then it can couple with a single cavity electromagnetic field mode of terahertz frequency, for instance.

Resonance cases (I) and (II) exhibit lasing phenomena though the mechanisms behind them are totally different. If $\gamma_2 \neq \gamma_3$ and $\gamma = 0$, the first resonance case (I) resembles a two-level system $\{|\Psi_2\rangle, |\Psi_3\rangle\}$ of frequency 2Ω interacting, respectively, with a quantum oscillator of frequency ω , with $2\Omega \approx \omega$, see also [14]. The spontaneous decay acts in both directions, i.e. $|\Psi_2\rangle \leftrightarrow |\Psi_3\rangle$, with a corresponding impact on lasing effects. On the other side, the resonance case (II) is close to an equidistant three-level system $|\Psi_2\rangle \leftrightarrow |\Psi_1\rangle \leftrightarrow |\Psi_3\rangle$, where each transition being of frequency Ω interacts as well with the quantum oscillator possessing the frequency ω , however, with $\Omega \approx \omega$. In this

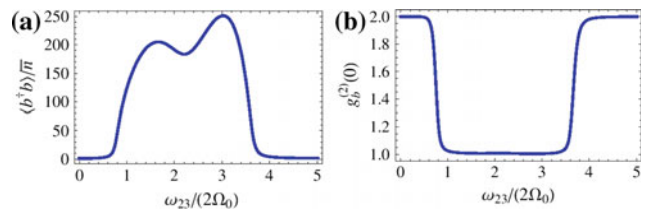


Fig. 3 a The mean quanta number of the quantum oscillator $\frac{b^\dagger b}{\bar{n}}$ and b its second-order correlation function $g_b^{(2)}(0)$ versus $\omega_{23}/2\Omega_0$ for the case (II) $\Omega = \omega$. Here $\frac{g}{\gamma_2} = 3.9$, $\frac{\gamma_3}{\gamma_2} = 0.09$, $\frac{\gamma}{\gamma_2} = 0$, $\frac{\kappa}{\gamma_2} = 10^{-3}$, $\frac{\omega}{\gamma_2} = 50$, $\frac{\Omega}{\gamma_2} = 20$ and $\bar{n} = 0.9$

case transitions may take place via single oscillator's quanta processes among the dressed state $|\Psi_2\rangle \leftrightarrow |\Psi_1\rangle \leftrightarrow |\Psi_3\rangle$ or, respectively, involving two quanta effects among the dressed-states $|\Psi_2\rangle \leftrightarrow |\Psi_3\rangle$. The various decay paths among the dressed-states involved $|\Psi_2\rangle \leftrightarrow |\Psi_1\rangle \leftrightarrow |\Psi_3\rangle$ lead to quantum interference effects. Although the dipole moments corresponding to the two bare transitions of the Λ -type sample are orthogonal to each other. Furthermore, we have observed that lasing effects occur for other parameters ranges, including $\gamma_2 = \gamma_3$ and $\gamma \neq 0$. Finally, the temperatures ranges considered here are within several Kelvins to few hundreds of Kelvins for coherent THz photon generation, respectively [14].

4 Conclusions

Summarizing, we have investigated a laser-pumped three-level Λ -type system the upper state of which is being coupled with a quantum oscillator characterized by a single quantized leaking mode. We have identified two new distinct situations leading to lasing effects of the quantum oscillator's degrees of freedom and have described the mechanisms behind them. Particularly, we have proved the interplay between single- or two-quanta processes accompanied by quantum interference effects among the induced emitter's dressed states are responsible for flexible lasing effects. This leads also to mutual influences between the quantum oscillator's dynamics and the three-level emitter's quantum dynamics, respectively. As well, the coherent terahertz photons generation is identified as one of the possible application resulting from this study.

Acknowledgements We acknowledge the financial support via grant No. 15.817.02.09F.

Conflict of Interest The authors declare that they have no conflict of interest.

References

1. Serapiglia, G.B., Paspalakis, E., Sirtori, C., Vodopyanov, K.L., Phillips, C.C.: Laser-induced quantum coherence in a semiconductor quantum well. *Phys. Rev. Lett.* **84**, 1019–1022 (2000). <https://doi.org/10.1103/PhysRevLett.84.1019>
2. Beveratos, A., Abram, I., Gerard, J.M., Robert Philip, I.: Quantum optics with quantum dots: Towards semiconductor sources of quantum light for quantum information processing. *Eur. Phys. J. D* **68**, 377–391 (2014). <https://doi.org/10.1140/epjd/e2014-50717-x>
3. Lau, H.K., Plenio, M.B.: Laser cooling of a high temperature oscillator by a three-level system. *Phys. Rev. B* **94**, 054305–054315 (2016). <https://doi.org/10.1103/PhysRevB.94.054305>
4. Kibis, O.V., Ya, Slepyan G., Maksimenko, S.A., Hoffmann, A.: Matter coupling to strong electromagnetic fields in two-level quantum systems with broken inversion symmetry. *Phys. Rev. Lett.* **102**(2), 023601–023605 (2009). <https://doi.org/10.1103/PhysRevLett.102.023601>
5. Oster, F., Keitel, C.H., Macovei, M.: Generation of correlated photon pairs in different frequency ranges. *Phys. Rev. A* **85**, 063814–063820 (2012). <https://doi.org/10.1103/PhysRevA.85.063814>
6. De Liberato, S., Ciuti, C., Phillips, C.C.: Terahertz lasing from intersubband polariton-polariton scattering in asymmetric quantum wells. *Phys. Rev. B* **87**, 241304(R)–241309 <https://doi.org/10.1103/physrevb.87.241304> (2013)
7. Miri, M., Zamani, F., Alipoor, H.: Two tunneling coupled two-level systems with broken inversion symmetry: tuning the terahertz emission. *J. Opt. Soc. Am. B* **33**, 1873–1880 (2016). <https://doi.org/10.1364/JOSAB.33.001873>
8. Chestnov, I.Y., Shahnazaryan, V.A., Alodjants, A.P., Shelykh, I. A.: Terahertz lasing in ensemble of asymmetric quantum dots. *ACS Photonics* **4**(11), 2726–2737 (2017). <https://doi.org/10.1021/acsp Photonics.7b00575>
9. Macovei, M., Mishra, M., Keitel, C.H.: Population inversion in two-level systems possessing permanent dipoles. *Phys. Rev. A* **92**, 013846–013851 (2015). <https://doi.org/10.1103/PhysRevA.92.013846>
10. Yu, Kryuchyan G., Shahnazaryan, V., Kibis, O.V., Shelykh, I.A.: Resonance fluorescence from an asymmetric quantum dot dressed by a bichromatic electromagnetic field. *Phys. Rev. A* **95**, 013834–013841 (2017). <https://doi.org/10.1103/PhysRevA.95.013834>
11. Anton, M.A., Maede-Razavi, S., Carreno, F., Thanopoulos, I., Paspalakis, E.: Optical and microwave control of resonance fluorescence and squeezing spectra in a polar molecule. *Phys. Rev. A* **96**, 063812–063828 (2017). <https://doi.org/10.1103/PhysRevA.96.063812>
12. Hiluf, D., Dubi, Y.: Phonon as environmental disturbance in three level system. [arXiv:1803.08327v1](https://arxiv.org/abs/1803.08327v1) (2018)
13. Mirzac, A.V., Ciornea, V., Macovei, M.A.: Non-classical light scattered by laser-pumped molecules possessing permanent dipoles. *Mold. J. Phys. Sci.* **17**(1–2), 95–104 (2018)
14. Mirzac, A., Macovei, M.A.: Dynamics of a quantum oscillator coupled with a three-level Lambda-type emitter. [arXiv:1810.09264v2](https://arxiv.org/abs/1810.09264v2) (2019)
15. Abdi, M., Plenio, M.B.: Quantum effects in a mechanically modulated single-photon emitter. *Phys. Rev. Lett.* **122**, 023602–023608 (2019). <https://doi.org/10.1103/PhysRevLett.122.023602>
16. Zhou, F., Niu, Y., Gong, S.: Electromagnetically induced transparency in a three-level lambda system with permanent dipole moments. *J. Chem. Phys.* **131**(3), 034105–034110 (2009). <https://doi.org/10.1063/1.3176018>
17. Kocinac, S., Ikonc, Z., Milanovic, V.: Second harmonic generation at the quantum-interference induced transparency in semiconductor quantum wells: The influence of permanent dipole moments. *IEEE J. Quant. Electr.* **37**(7), 873–876 (2001). <https://doi.org/10.1109/3.929586>

Integration of Cyber Security in Healthcare Equipment

Au. Buzdugan

Abstract

The expansion of digital technologies in operational technologies (OT) has significantly supported the development of new features and capabilities. However, the integration of information technologies (IT) in such environments, has also led to the inheritance of cyber security risks. This has also created new potential operational risks due to the fact that operations are controlled by a computer or digital device. Most of the equipment, such as from healthcare, that has IT systems embedded and performing certain processes, is subject to vulnerabilities and prone to cyber-attacks similar to computers. The developing capabilities and integration of IT in various operations offers the capability to introduce new features and monitoring capacity that were not possible before, or had a very high cost. The applications and integrations are countless, and do bring improvements for the society, both for the healthcare providers, as well as for the patients. However, the healthcare systems were designed with the focus on operation and safety. The security concept was not always known or taken into account due to the technologies used before. In addition, if we refer to healthcare equipment that uses nuclear or radiological sources for treatment, then safety, as well as security, should be of core importance. Even if there are certain cyber security prevention or monitoring capabilities that are possible to be enabled in some devices, these were not always used due to the perceived high risk of an operational risk. Recent research has proven that the compromise of an OT via a cyber security attack is possible, and thus, security controls and mitigation are not to be neglected anymore [1]. In this paper we will look into the current issues that

cyber security risks could create to operational technologies, with a focus on the healthcare sector.

Keywords

Cyber security • Healthcare • Operational technologies • Security requirements

1 Introduction

The development of IT has triggered a revolutionary process in all industries in embedding these technologies for making use of new features and capabilities. This has also positively impacted the healthcare domain and is one of the leading areas where digital innovations have changed on how systems are being used and their efficiency. The computerized devices help to read and analyze the input, as example the x-ray, process it and provide the diagnosis or certain data that would help the practitioner. The computer is therefore an intrinsic part of the medical device.

The direct benefits of using IT technologies are in supporting the operator and improving the diagnosis quality, as well as serve as a database and recommend certain treatment based on detected anomalies. These types of medical devices are helpful in alerting when certain conditions are met and enhance the chances of an early detection and prevention of certain scenarios. The technological part on how these are programmed in the background are relatively simple. For example, machine learning and analytics can be used to collect, aggregate and analyze data. These systems can also process large data sets, for example previous scans and their diagnosis, as well as type of treatment for each type of anomaly detected.

The digitalization of these technologies is manifold. For example, many smart wearable devices have sensing capabilities and are also used to monitor and collect health data about the user. By collecting and processing this data there are a number of use cases that can be developed. In addition,

Au. Buzdugan (✉)
National Nuclear Security Support Center, Technical University of
Moldova, 9/7, Studentilor St., Block 3, MD2045 Chisinau,
Republic of Moldova
e-mail: aurelian.buzdugan@yahoo.com

should these devices be interconnected with other ones, such as with healthcare operators, then it offers opportunities and capabilities for both the user, as well as the healthcare institution. Another example of such technologies would be the data interconnection between the operators, such as clinics and drug stores—where the network between these entities would help for live data exchange and provide additional functionalities.

A general assumption on the architecture, taking into account nowadays trends, is also being confirmed by other research done in this area [2]. Therefore, these devices make use of cloud technology for interconnecting wearable patient devices and healthcare operators. However, in other use cases the same healthcare device could be interconnected within the premises of the operator also using cloud technologies. Analyzing this in the context of devices that use ionizing radiation, the cyber security of entire ecosystem becomes a mandatory requirement due to potential safety risks and implications on the patient, or society in general.

Taking into account the interconnection as well as number of these devices, we consider the security requirement of core importance. This is already a concern, as both as a priority nowadays for many international institutions [3].

If reviewing the type of data that is being collected, shared and used, then in many countries such type of data is already qualified as personal data and is protected by law. Thus, the risks are already identified in certain regions and there are a number of security controls that are enforced via regulations.

Most of personal data regulations, such as GDPR, already cover as well the aspect of reporting to the national authority whenever there was a breach discovered. This type of regulations are a good start as well can serve as a guideline for vendors, as well as operators, in establishing a information security program and cover elements such as data protection, incident response, reporting mechanisms.

We evaluate that in many cases the reality is different and many operators strive for compliance, but leaving security gaps that are not covered by these regulations. In many cases, the security incidents can also lead to safety events, which is much more tangible for the society.

2 Security and Safety in Healthcare

The implications and impact of cyber security incidents in other domains are beyond the traditional IT issues. These could also result in safety incidents. A cyber attack is primarily associated with a data breach, whether the confidentiality, integrity or availability of data is affected. However, in domains such as the nuclear one, and in our case—healthcare, a cyber attack can be used to compromise data, which could lead to a safety event as well. For

example, a medical device that uses nuclear or radiological sources for treatment and is controlled by a compromised computer, could unfortunately lead to a safety incident. Thus, it is not only about information security.

According to Alemzadeh's study from 2013 the majority of incidents (84%) related to healthcare devices reported to the regulatory body were related to hardware issues, and only 16% were linked to software issues [4]. Whereas technology has changed in the past 6 years as well as the understanding of security risks has considerably raised, we still believe that certain hardware failure could be triggered or enhanced by a cyber security attack by making use of functions of operations that were not taken into account at the design phase of the device.

The number of data breaches is on the rise nowadays. The number of interconnected systems and applications is one factor that makes cyber attacks a high risk for these types of systems. The community is working closely together, as well as with the vendors, to identify and integrate potential security controls. However, many times these controls are retrofitted to the systems, which do not correspond to the security by design concept where such risks are identified and taken into account from the design phase of a system. The result is that these controls can be effective, however not in all situations. There are cases where many systems need to be air-gapped, for example without any internet connection, or have all the security monitoring and filtering done outside the system.

As mentioned before, the type of data processed by healthcare institutions and systems are in many jurisdictions qualified as personal data. In the healthcare sector this data would contain various information such as patient's date of birth, ID, insurance number as well as medical related data. By having this confidential data made public could lead to the situation to an increase in fraud attempts, driven by illicit financial gain desires (e.g. fake insurance claims, accessing financial institution accounts using personal data as an intermediate step etc.). Still, in this domain the level of security culture is still relatively low with the cyber risks not being accordingly identified or evaluated. This is mainly due to a low level of security awareness and potential implications and consequences of a data breach.

Looking one step further on the impact of a cyber security incident in healthcare we can relate to safety concerns. According to Y.Mirski et al. [5], it is possible to modify 3D medical imagery results. This can be used for malicious purposes, such as adding elements that would make the scan present a worse diagnosis, or on the other side—to hide parts of the scan that show a medical issue or anomaly. Such attacks can be also used with the goal to disrupt ongoing research, for financial gains even an act of terrorism by impacting the society [5]. This is one of the first proof of concepts that show the reality of such a cyber attack

scenario. A potential attacker could theoretically easily conduct such an attack, with a certain knowledge on how these systems operate. If we link this proof of concept to healthcare devices that make use of nuclear, radiological, chemical and other types of potentially dangerous materials, then any security event could also lead to a safety event. The consequences could be very high.

The computations that are made by computers part of the healthcare devices are programmed using basic logic algorithms. For example, a scan would result in a data set which is saved in a database, and various algorithms and checks are applied. In addition, machine learning and AI can also be used to evaluate this data and output a human readable format, which can be also a diagnostic. As part of this paper we are assuming such concepts are already being applied, as these seem to be basic for other industries. The type and usage of algorithms in healthcare is out of the scope of this paper.

The potential attack vectors can be theoretically deduced. Just like in any other security testing process, initially the data input module is tested whether it accepts other type of input, such as a different format, as well as whether it sanitized properly this data before passing it on to the processing module.

Similar to traditional industries, the operational systems in healthcare were designed and programmed with the belief and assumption that the data input is standard, and it will always be in a certain format and size. The main goal and requirement were to ensure the functionality of the device, without taking other requirements or concerns into consideration, such as cyber security. The next logical step in analyzing the attack vector is data flow. Analyzing the system and understanding how data is being transferred from one module to another would show potential points of failure, or in this case—potential vectors of attack. This was also the attack vector most probably used during the research performed by Y. Mirski et al. [5].

We can evaluate that security vulnerabilities, both known and unknown, of computer systems are also applicable to healthcare. There are number of general recommendations and best practices that can be taken from the IT domain and applied in other domains when evaluating the security of computers, or devices that make use of such computers.

One element is security by design, that is a concept which stipulates the necessity to identify and set the security requirements of a system from the design phase. This often can lead to choosing different architectures and setups in order to meet these requirements—actions which are impossible or very costly to make after a device was already designed and is in production. As an example, having data integrity checks as well as encrypted channels of communication the type of attack from this research would have been prevented. This is just one simple security control,

however it can be easily deduced that just by having a minimum set of security controls a large number of vulnerabilities and such type of attacks would have prevented, or at least, reduce the occurrence and risks.

The example that we have tackled in this paper shows one more time the impact and actuality of a cyber security risk upon the healthcare devices. Thus, it is required a pragmatic and coordinated action plan in order to ensure that the industry, including the medical device industry, acknowledges the current cyber threats and adopts a security-oriented approach as well.

3 Conclusions and Recommendations

From a global perspective further developments and innovation in healthcare sector should have cyber security as a mandatory prerequisite and require interdisciplinary research and cooperation. The reason why healthcare constitutes a target is due to the weak security controls, as well as value of data that is processed or stored. Similar to other sectors, it is necessary to change the mindset and start adopting the security controls without discarding them due to the fear of a malfunction. This is where interdisciplinary or horizontal cooperation is recommended.

We believe current technology can be sufficient to start this process, however it will require updates in the future for both the design, as well as the functionality in order to ensure that healthcare devices have an adequate level of security that minimizes any potential safety threats.

We believe it is necessary to start this on the process side, preferably on a national level, with the goal to ensure that vendors of healthcare equipment meet certain security requirements that are agreed as mandatory. In addition, via national regulations the security requirements for computers, or similar devices used in the industry, could be enforced and regulated. If we compare to the nuclear domain where the regulators as well as operators were facing the situation to adopt and evaluate cyber security controls, this domain could potentially have similar issues and within the same safety context. Therefore, a horizontal cooperation between key institutions at the national level should be enhanced [6].

In addition to this, most of the healthcare data is categorized as personal data or requires connection to personally identifiable information. Therefore, it is recommended to have the protection of such data protected by law. We would like to also reiterate and support regulations to also cover the reporting requirements in case of a data breach for the healthcare sector as well, due to the sensitivity and confidentiality of this data.

However, this can lead to certain differences between countries in terms of maturity level of such regulations as well as depending on the level of the security culture. By

having national, regional and even international certification schemes it would ensure that such systems in healthcare were designed and developed according to best security practices. This ultimately is applicable to other domains from the industry as well. This is also trivial in the context of regional cooperation, where medical records are exchanged between countries, with the goal to provide mobility and access to services no matter of location of a person [5].

The horizontal cooperation is also required for assessing the security stance of medical devices, due to the specific knowledge required to understand the functionality of the devices as well as the impact that an alteration of data flows could have on the device, and patient itself. This was also one of the conclusions of research done for medical devices used in the cardiology domain, and the necessity to inform users of the cyber security risks [7]. This is also applicable for any medical devices such a wearable [8], or those located within the premises of a healthcare operator. The question of security culture comes into play again in order to inform accordingly the users, as well as the operators on what are cyber security risks and how tangible these are to their safety. Our position is that an interdisciplinary cooperation is required when it comes to cyber security due to integration of IT components into OT, the inheritance of cyber security risks by any domains that makes use of IT, as well as joint actions in raising the overall security culture.

We also consider that the international community should take the lead assessing the cyber security risks in other domains and issue recommendations and guidelines for the healthcare industry. This would support countries to adopt and adapt them in their legislative framework. This would ensure that no matter of the resources that a certain country has, it will be able to access up to date best practices and recommendations in securing healthcare devices, which would ultimately positively reflect for the society and its safety. This would satisfy the requirements in terms of processes at the national level, and would trigger direct changes for the operators as well as vendors of such equipment. This topic becomes even more important when speaking of devices that make use of ionizing radiation, and could impact the safety of society. The nuclear industry is an example where safety threats have convinced member states to support the development of regulations in terms of cyber security for nuclear facilities or operator of nuclear and radiological materials [9].

As a general remark, the good practices in IT security are still applicable in other domains as well as long as these are adapted according to the scope and requirements of the system. This is also the case of the healthcare devices. The

cyber attack example that was referenced in this paper would have been possible to detect and prevent by implementing certain security controls such as data encryption and integrity checks. Therefore, we believe that minimum security requirements should be applicable to the possible extent in all areas of the industry, including healthcare, in order to ensure the vendors as well as operators are following a certain security baseline. The overall goal is to prevent a cyber attack, and most importantly to reduce and prevent any safety incident from which a person or country could suffer from.

Conflict of Interest The authors declare that they have no conflict of interest.

References

1. European Medicine Agency.: Data anonymisation—A key enabler for clinical data sharing, [Workshop report], 2018. Retrieved from https://www.ema.europa.eu/en/documents/report/report-data-anonymisation-key-enabler-clinical-data-sharing_en.pdf (2018). pp 14–15
2. Strielkina, A., Uzun, D., Kharchenko, V.: Modelling of healthcare IoT using the queueing theory. In: 9th IEEE International Conference on Intelligent Data Acquisition and Advanced Computing Systems: Technology and Applications (IDAACS) 2 (2017), pp. 849–852 (2017)
3. European Commission.: Commission makes it easier for citizens to access health data securely across borders, [Press release], 2019. Retrieved from http://europa.eu/rapid/press-release_IP-19-842_en.htm (2019)
4. Alemzadeh, H. et al.: Analysis of safety-critical computer failures in medical devices. IEEE Security and Privacy (14–26 July–Aug. 2013), Co-published by the IEEE Computer and Reliability Societies (2013)
5. Mirsky, Y et al.: CT-GAN: Malicious Tampering of 3D Medical Imagery using Deep Learning. Retrieved from: https://www.researchgate.net/publication/330357848_CT-GAN_Malicious_Tampering_of_3D_Medical_Imagery_using_Deep_Learning (2019)
6. Buzdugan, A.: An overview of cybersecurity in the healthcare sector. In: 6th International Conference Telecommunications—Electronics—Informatics, Chisinau, Moldova (2018)
7. Ransford, B., Kramer, D.B., Foo Kune, D., et al.: Cybersecurity and medical devices: a practical guide for cardiac electrophysiologists. Pacing Clin. Electrophysiol. **40**(8), 913–917 (2017). <https://doi.org/10.1111/pace.13102>
8. Mohan, A.: Cyber security for personal medical devices internet of things. In: IEEE International Conference on Distributed Computing in Sensor Systems, Marina Del Rey, CA, 2014, pp. 372–374. <https://doi.org/10.1109/dcoss.2014.49>. Retrieved from: <http://ieeexplore.ieee.org/stamp/stamp.jsp?tp=&arnumber=6846193&isnumber=6846129> (2014)
9. International Atomic Energy Agency.: <https://www.iaea.org/topics/computer-and-information-security>

Cyber-Physical Systems—Nanomaterial Sensors Based Unmanned Aerial Platforms for Real-Time Monitoring and Analysis (Invited Paper)

A. Vaseashta

Abstract

In the new and transformative era, our surrounding environments are increasingly connected through exponential growth of cyber-physical systems and intelligent technologies. One such example is an Unmanned Aerial Surveillance Platform, also known as drone, for applications such as surveillance, real-time monitoring, emergency augmentation for actionable response, security and enabler of connected communities to bring about new levels of opportunity and growth, safety and security, health and wellness, thus improving the overall quality of life. Based on our previous experience, we present a modality of smart and connected sensors platforms that have a great potential to provide enhanced situational awareness for safety and security.

Keywords

UAVs • Cyber-Physical systems • Safety • Security • Monitoring • Critical-Infrastructure • Situational awareness

1 Introduction

In the new era of transformative progress using exponential growth of intelligent technologies, our surrounding environments are increasingly connected through rapidly changing cyber-physical systems. Based on our previous experience, we present a modality of smart and connected sensors-based platforms that demonstrates potential of providing enhanced situational awareness for safety and security. Our earlier systems are capable of (a): monitoring

environmental pollution using a GIS/GPS based interconnected sensors systems, and (b): capable of spatially sensing and/or detection of waterborne contaminants in real-time using a Contamination Identification and Level Monitoring Electronic Display Systems (CILM-EDS) prototype [1].

We demonstrate modality of an Unmanned Aerial Surveillance Platform (UASP) for applications in surveillance, real-time monitoring, emergency augmentation for actionable response, security and enabler of connected communities to bring about new levels of opportunity and growth, safety and security, and health and wellness. The new system under development has an airborne component to capture relevant information from a Domain of Interest (DOI).

The objectives of this investigation are to; (a): demonstrate feasibility of a mobile UASP that can monitor in real-time, capture, synthesize and analyze observed information and communicate with ground-based systems for a coordinated actionable response. Several commercial off the shelf (COTS) instruments such as hyperspectral imagers, Light Detection and Ranging (LIDAR), Laser-induced Breakdown Spectroscopy (LIBS) and Biometrics systems are discussed along with some innovative nano-sensors based platforms that are still in experimental stage and have potential to serve as payload for sample collection and on-contact detection. (b): Discuss the scalability and transferability of the proposed pilot project for additional solutions. (c): Introduce framework for promoting discovery, innovation, and entrepreneurship in smart and connected communities' initiatives to address infrastructure requirements.

Notwithstanding the fact that highly interconnected world offers great promise for improved wellbeing and prosperity, the technology offers certain societal challenges at the complex intersection of technology and society. Hence one of the objectives is to discuss socio-technical issues supporting understanding of emerging technologies, the use of data analytics to enhance individuals' Quality of Life, improve health and safety, economic prosperity, data-driven

A. Vaseashta (✉)
International Clean Water Institute, Manassas, VA, USA
e-mail: prof.vaseashta@ieee.org
NJCU—A State University of New Jersey, Jersey, NJ, USA

decisions, and policy decisions inclusive of privacy and transparency.

2 Cyber-Physical Domain

2.1 Synopsis of Cyber-Physical Systems

Cyber-Physical domain consists of integrated and networked system-of-systems where physical processes are monitored or controlled by algorithms. Embedded computers and networks monitor and control the physical processes, with feedback loops where physical processes affect computations and vice versa. The physical and software components interact with each other in ways that change with context, within a DOI. Due to its growing significance, the Cyber-Physical systems (CPS) is now a multi-disciplinary technology focused engineering discipline, with a strong foundation in mathematical abstractions. CPS integrates the dynamics of the physical processes with those of the software and networking, providing abstractions and modeling, design, and analysis techniques. The key technical challenge is to conjoin constructs for modeling physical processes with abstractions in computer science that significantly vary over timescale. Advances in CPS have significant applications in terms of capability, scalability, resiliency, safety, security, flexibility and conformity to systems within a DOI, as demonstrated below in the context of connected communities. The economic and societal potential of such systems is vastly greater than what has been realized, and major investments are being made worldwide to develop the technology and hence, CPS will further expand the boundaries of smart and connected communities.

2.2 Connected Communities

Exponential growth in intelligent technologies has created new opportunities to synergistically integrate the entire community services socially, digitally and physically. Rapid innovations in CPS around the world are in a new era of transformational change, in which their people, surrounding structures and natural environments are increasingly connected by smart technologies, leading to new opportunities for innovation, improved services, and enhanced quality of life. Connected systems have enhanced mobility, access and services to include performance based on predictive planning, traffic modeling, parking solutions, geospatial services, environmental services, emergency augmentation, scenario planning and augmented reality, just to name a few. The connected communities' technologies support integrative research at the intersection of intelligent technologies and social sciences to pilot solution pathways that support

productivity, sustainability, knowledge-based economy, data-driven decisions including scalability and transferability of the projected solutions.

In an earlier project, the concept of cyber-physical and connected systems was demonstrated to monitor contaminants in the body of ground and surface water in real-time. The applications described here are in the context of smart and connected systems for real-time monitoring using an unmanned aerial surveillance platform.

3 Background Work—CILM-EDS

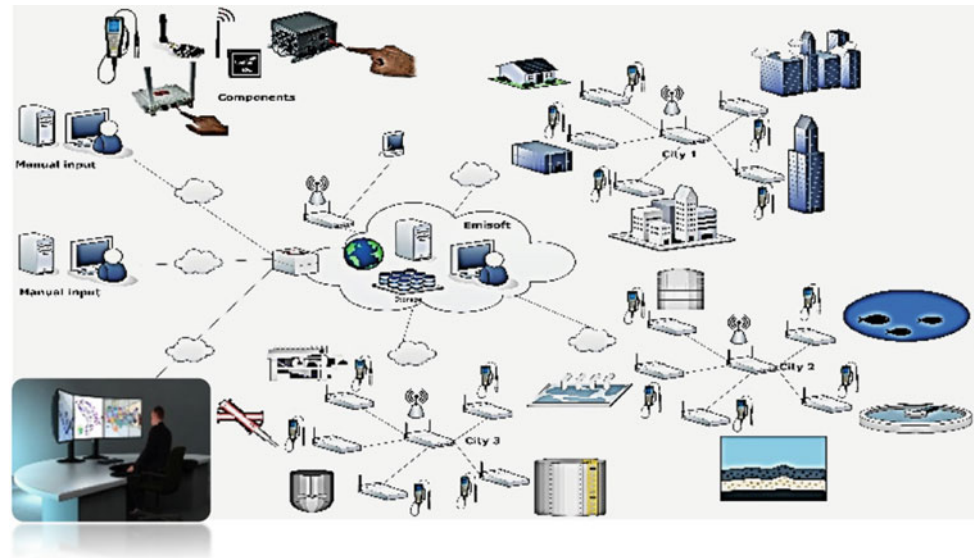
As a part of a North Atlantic Treaty Organization (NATO) Science for Peace and Security project, the proposed activity was to use advanced (Nano) technology and other advanced technology-based sensor platforms to monitor inadvertent and intentional, chemical-biological-radiological-nuclear (CBRN) contamination in water supplies using a stand-alone prototype. In support of the activity, we developed a GPS/GIS based CILM-EDS prototype to spatially monitor contaminants and water levels, for areas that are prone to flashfloods and tsunamis. The research under this program was focused on five distinct, yet unifying areas of the project, viz. sensing and detection of; Metals (As, Hg, Cr, Pb, etc.); pathogenic agents (bacteria, virus, proteins, cryptosporidium etc.); organic compounds (TCE, acetone, degreasers, halogenated organics, etc.); pharmaceuticals; pesticide run-off and compounds with large shelf-life. The sensors deployed for CILM-EDS can identify multiple agents simultaneously in quantities comparable to minimum allowable contamination levels in drinking water, as shown in Fig. 1. The unit required a careful selection of GIS/GPS protocol to provide accurate geographical location of sensors, user-friendly software, and accurate sensors reading so that they provide accurate representation and are reliable, sensitive and have high specificity. An artist's rendition of platform is shown in inset.

Another aspect of the project was centered on monitoring chemical contaminants in groundwater bodies of the Prut river basin. For this investigation, monitoring wells are sampled by several field trials. The results of the chemical analysis are used for the preliminary identification, characterization and classification of groundwater bodies to analyze water quality in acquirers in Moldova to implement the EU Water Framework Directive requirements.

4 Multi-Sensor UAV Sensor Platform

Deploying multiple sensors' payload on a UAV surveillance platform is a disruptive technology. The construct of a platform in conjunction with a ground based mobile

Fig. 1 Distributed sensor system using remote, wireless data transmission and data gathering, (inset—Artist's rendition of CILM-EDS unit) [1]



operations center presents tremendous opportunity and impact of technology, especially for sensing and monitoring. There are several COTS sensors available on the markets for diagnostics. A brief overview of these diagnostic tools along with its capabilities is described below.

4.1 Hyperspectral Imaging

Hyperspectral imaging (HSI) is a spectral imaging acquisition methodology employed to acquire a set of images within certain spectral bands. Each pixel of the image contains certain spectral information, which is added as third dimension to a two-dimensional spatial image, thus generating a three-dimensional data cube, known as hypercube data containing absorption, reflectance, or fluorescence spectrum data for each image pixel. Hyperspectral imaging spectroscopy has now developed into a rugged, compact, reasonably priced tool for a range of process control, monitoring, diagnostic and inspection. It has several applications ranging from spectral radiometry, forensic analysis, bio-agents detection, live-cell microscopy including pre-cancerous cell detection, genomics/proteomics research, and forestry. The multiplexing of wavelengths is achieved either by switching sources to obtain different wavelengths or switching band-pass filters to gate the photons in case of broadband illumination. Recent advances in sensors systems and its integration to near-infrared hyperspectral imager

is equipped with 154 spectral bands and a spectral range of 400–1000 nm. allowing UAV based hyperspectral imaging.

4.2 Lidar

Light detection and ranging (LIDAR) is used for determining the distance to an object by transmitting a laser beam at the object and measuring the time of flight back to the transmitter. In conjunction with GPS and Inertial Measurement Units (IMUs), the data from LIDAR provides topographical maps. With increased miniaturization and high accuracy, UAV based LIDAR sector is growing rapidly. Currently, there are over 12 manufacturers of LIDAR systems with varying capabilities. Most of the latest LIDAR for UAV systems can rotate around their own axis and offer 360° line of sight with very high data rates, e.g. over one million distance points per second. A state-of-the-art integrated Real-Time Kinematic (RTK) GPS and Inertial Navigation System (INS) provides accurate position, velocity, acceleration and orientation under the most demanding conditions. The dual antenna moving baseline RTK GNSS solution ensures that the LIDAR can achieve the highest accuracy possible for the lowest weight. The GPS\INS sensor combines temperature calibrated accelerometers, gyroscopes, magnetometers and a pressure sensor with a multi-channel RTK Global Navigation Satellite System (GNSS) receiver. These are coupled in a sophisticated fusion

algorithm to deliver accurate and reliable navigation and orientation. The applications of LIDARs mounted as payload UAVs range from agriculture and forestry; archaeology and cultural heritage documentation; corridor mapping and inspection; topography; construction site monitoring; structural inspections; surveying urban environments; resource management; collision avoidance; shoreline and storm surge modeling; hydrodynamic modeling to Digital Elevation Models (DEMs), among others.

4.3 Laser Induced Breakdown Spectroscopy

Laser-induced breakdown spectroscopy (LIBS) is essentially atomic emission spectroscopy (AES) utilizing a highly energetic pulse for excitation and ablation of target material. The formation of the plasma attains a finite threshold for breakdown, depending upon the environment and the target material. LIBS uses optical emission spectrometry and hence can analyze any matter regardless of its physical state. These analyses are inherently real-time, require no sample preparation, stand-off detection capability and offer high sensitivity (ngms) and specificity. LIBS provides elemental fingerprinting for the constituents of a material to be analyzed and hence may be used to evaluate the relative abundance of each constituent element, or to monitor the presence of impurities. In practice, detection limits are a function of (a) the plasma excitation temperature, (b) the light collection window, and (c) the line strength of the viewed transition. The miniaturized version of COTS LIBS are available in hand-held size capable of analyzing elements for a wide range of materials, forensics, fingerprinting of conflict materials and biomedical applications.

A summary of specifications of these capabilities are presented in Table 1. Most UASP can take a payload of 3–5 kg. Using quadcopter-based configurations allow payload capacity of up to 15 kg., thus allowing multiple capabilities.

4.4 Other Innovative and Disruptive Platforms

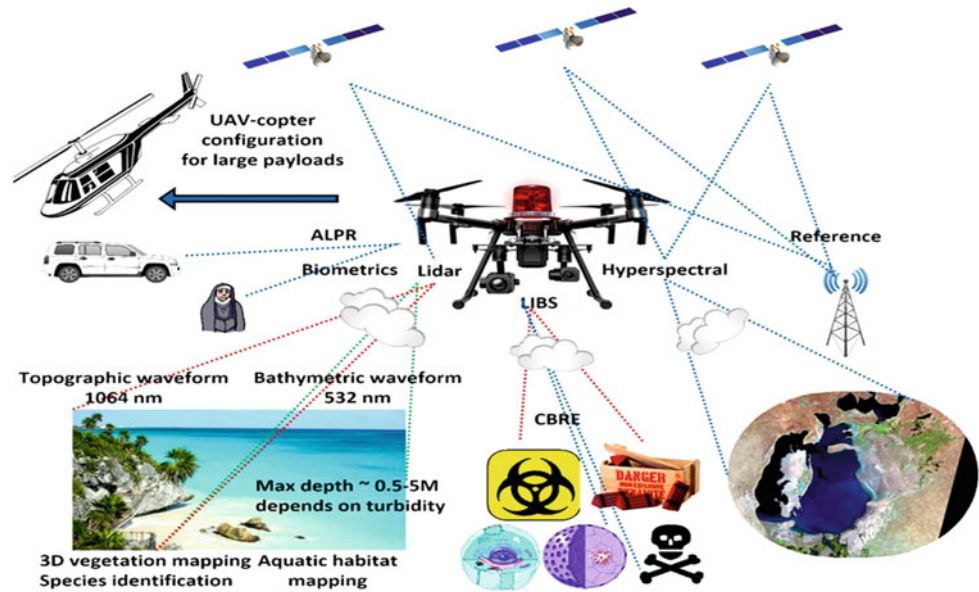
In addition to the COTS sensors, several laboratory-based sensors are also investigated for determine additional range of capabilities. The UASP payload is stand-off platform, however, it demonstrates capability of sampled or contact detection. Nanoscale materials to exhibit unique properties that are attributable to their reduced dimension, which coupled with advances in material synthesis, device fabrication and characterization have provided the means to study, understand, control, or even manipulate the transitional characteristics between isolated atoms, molecules, and bulk materials. Consequently, various “designer” materials capable of producing devices and systems with remarkable, tunable, and desired properties have recently been fabricated. A nanotechnology-based sensor platform enables direct electrical detection of biological and chemical agents in a label-free, highly multiplexed format over a broad dynamic range [2]. From a security standpoint, point and stand-off sensors are used for monitoring pollution, contamination and interrogating hybrid threat-vectors (Fig. 2).

Integration of COTS and several innovative, nanomaterials-based sensors platforms as payload are investigated for various applications in safety, security and monitoring. The core concept focuses on innovative technology solutions to bridge the existing gaps in mission-ready deployability. The platform as discussed above, offers the following mission-ready capabilities, viz: Rapid Decision Making; Collaboration and Communication; Rapid and Adaptable Deployment; Technology Self Sufficiency; Enhanced Situational awareness; Emergency communication infrastructure; and Accessibility of otherwise inaccessible proximities. A single UASP can be equipped with sensors to capture and transmit real-time video, image and other data for a specified coverage area, its overall performance is limited by: sensor range/camera field of view; size/weight/cost of payload; power requirements/flight time; operation by UAVP pilot.

Table 1 Specifications for selected sensing/detection/UAV platforms

Platform	Weight	Scan rate	Power source	Field of view (FOV)	Range (for a typical system)
Lidar	<4 lbs	700 K 3D pts/sec	Nominal	360°	100 m (<20 nm range)
Hyperspectral	~6 lbs	~500 fps	Nominal	Mode dependent	VNIR (380–1000), NR (900–1700), SWIR (950–2500)
LIBS	~3 lbs	<3 s	Lasts 8–10 h	Stand-off detection	Target dependent (1 ppm detection)
Biometrics	~1.5 lbs	4 MP CMOS 60 fps	3330 mA @ 12 V	Y/P/R 300,180,170	F = 4.5 – 135, aperture diameter = 16

Fig. 2 An integrated UAVSP—with an option for heavier payload t



5 Societal Implications and Path Forward

It is demonstrated that an integrated UASP network can be assembled for an operation that supports several integrated and complementary capabilities for monitoring and capturing data which are analyzed at a ground based Mobile Operations Command and Communication Center capable of analyzing data using image and signal processing software. While the rapid democratization of cyber-physical systems connecting communities conjoin opportunities for individuals and entities, it also brings numerous complex challenges and concerns. The question is whether individuals or entities are prepared for the rise of UASPs in their operational ecosystem? Due to versatile nature of the platform described above, there are many considerations that need to be reviewed. A detailed discussion is beyond the scope of this publication and will be presented in a different format elsewhere, however some of such considerations include detect and avoid requirements; human factors in design standards, certification/training and performance analysis of UAS detection technologies. These initiatives will enhance co-existence of USAP with FAA. Rushing to develop applications of drone technology without understanding the complex security risks can result in many unforeseen complex challenges for which the general society.

6 Compliance with Ethical Requirements

- A. *Conflict of Interest*—Author has no conflict of interest.
- B. *Statement of Informed Consent*—This research does not have engagement of human subjects or infringement of personal identifiable information.
- C. *Statement of Human and Animal Rights*—Human subjects or Institutional Animal Care and Use Committees exemptions are not required for this study.

Acknowledgements The project was funded in part NATO: EAP. SFP.984403.

References

1. Nastasiuc, L., Bogdevici, O., Aureliu, O., Culighin, E., Sidorenko, A., Vaseashta, A.: Monitoring water contaminants: case study for Moldova. *Pol. J. Env. Stud.* **25**(1), 221–230 (2016)
2. Vaseashta, A., et al.: Sensors for water safety and security. *Surf. Eng. Appl. Electrochem.* **48**(5), 478–486 (2012)

Bibliometric Analysis of the Nanotechnology Research Area in the Republic of Moldova

A. I. Rosca, I. P. Cojocaru, and A. Gh. Turcanu

Abstract

A bibliometric analysis was performed to evaluate nanotechnology research area in the Republic of Moldova during ten years, 2009–2018. For comparative purposes, the results were benchmarked against the findings of Germany, France, USA, China, Japan, Romania, Russia, and Ukraine. In our research, it was found that the Republic of Moldova holds the first places in the world on two StatNano indicators: national priority and local share in nanoscience, and the fourth position in the world on the number of nano-articles per GDP. Investigations results show that Moldovan nanoscience is defined by a high level of share of international collaboration, the number of nano-articles per million people corresponds to the average figure worldwide and the medium citation per nano-article within the investigated countries is almost at the same level as for Japan. Study of collaboration patterns enables us to identify the active collaborative networks among the scientists from the Republic of Moldova and Germany, USA, Russia, France, Romania. Analysis of the total number of citations to nano-articles and *h*-index shows that the Moldovan nanotechnology scientific community needs to work on improving its research impact.

Keywords

Nanotechnology • Nanoscience • Bibliometric • Citation

1 Introduction

At the beginning of XXI century the scientists proposed to use bibliometrics for understanding the trajectory development of an emerging technology [1]. Bibliometrics, or the study of publication-based output, is a method widely applied in evaluation. The bibliometric investigation of research and development activities remains one of the most challenging issues in program evaluation despite the effort devoted over the last few decades to develop and test reliable and accurate measures of research output [2].

Bibliometric and thematic analyses performed with the use of scientific and technological electronic information resources, such as databases, have shown that the nanotechnology field in the world has been growing exponentially since the early 1990s. Only about 20% of papers in that period used nano-prefixed terms in their titles and abstracts. Toward the end of the second decade of the nanotechnology's emergence, words became more standardized with 80% of papers having nano-prefixed terms in their titles and abstracts [3].

The nanotechnology area is a highly dynamic global phenomenon with a complex inherently interdisciplinary internal structure. The analysis of WoS nano papers shows a concentration of research publications in traditional nanotechnology core disciplines such as physics, chemistry, and materials science. As the same time, there are secondary areas of concentration in bioscience fields on health- and environmental-related research [4].

This specific characteristic significantly complicate the monitoring, the data search, including selection of information resources and formulation of search queries. However, nowadays scientific and technological data systematization is essentially important. Global frameworks include the classification of nanostructures of the International Organization for Standardization (ISO) [5] and several others, for example, the PACS (Physics and Astronomy Classification Scheme) classification of the American

A. I. Rosca (✉) · I. P. Cojocaru
Information Society Development Institute, Ministry of Education,
Culture and Research, 5A Academiei str., Chisinau,
Republic of Moldova
e-mail: alfreda_mail@yahoo.com

A. Gh. Turcanu
University of Petrosani, Ministry of National Education, Petrosani,
Romania

Institute of Physics [6]. All of these frameworks greatly simplify the search for information.

A lot of investigations have been carried out in the field of bibliometric study on nanoscience and nanotechnology. Heinze et al. [7] carried out and identified the research results on nanotechnology and human genetics, Kostoff et al. [8] revealed the structure and infrastructure of the global nanotechnology research output, Lee [9] investigated the nanotechnology patents, Porter (2008) analyzed the research papers and citations on nanotechnology [10]. Interactions between nanotechnology and agriculture have been assessed from a bibliometric point of view, with a focus on co-word analysis to examine aspects of agro-nano applications related to plant protection [11].

Visualizing the global nanotechnology output based on data from WoS, Core Collection database, Thomson Reuters, Philadelphia, the specialists concluded that the maximum numbers of outputs were published by the USA, which ranks first. The next 2 positions have gone to China and Germany (data during 1989–2014) [12]. Spikala and Amudha [13] published in Eureka Journal a bibliometric investigation of nano-articles in IEEE (Institute of Electrical and Electronics Engineers, USA) during 2010–2016. The study analyzed authorship patterns, degree of collaboration among the authors and geographical distribution of papers [13].

The comprehensive statistical database portal StatNano was established in 2010 as a gateway to the latest information and statistics in nano-based Science, Technology and Industry [13]. Its mission is to monitor the status of nanotechnology development and policies in 107 countries. StatNano is today one of the most reliable references of researchers and policymakers around the world. The statistics of nano-articles published by each country are reported by StatNano on a monthly basis taking into account the Web of Science (WoS) platform data.

2 Objectives

The *main aim* of this study was to perform the bibliometric assessment of the nanotechnology area in the Republic of Moldova (RM) in the period 2009–2018.

The *specific objectives* of paper are:

- to identify the country's contribution in international nanotechnology information flow;
- to establish the current country's situation in this field.

3 Methodology

StatNano and the National Bibliometric Instrument (Instrumental Bibliometric Național—IBN) [14] have been used to identify the Moldovan contribution on the field of nanoscience and nanotechnology.

4 Results

According to the data of StatNano database, for the indicator “*National priority in nanoscience*” (ratio of share of nano-articles of a country of total nano-articles to the share of articles of the country of total articles in the same period) [15], the RM is ranked first in the world, being followed by Singapore and North Korea. At international level, the average number is 1.0, the figure for the RM is 2.39 (average data for 2009–2018) Fig. 1.

The analysis of data provided by WoS, SCOPUS and IBN regarding to Moldovan scientists' articles in international journals revealed that they are mostly in collaboration with researchers from Germany, USA, Russia, France, Romania, and in national ones from Ukraine, Russia, Poland.

Among the investigated countries, the RM is ranked first for the indicator “*Share of international collaboration in nanoscience (Percent)*” (Share of joint nano-articles between

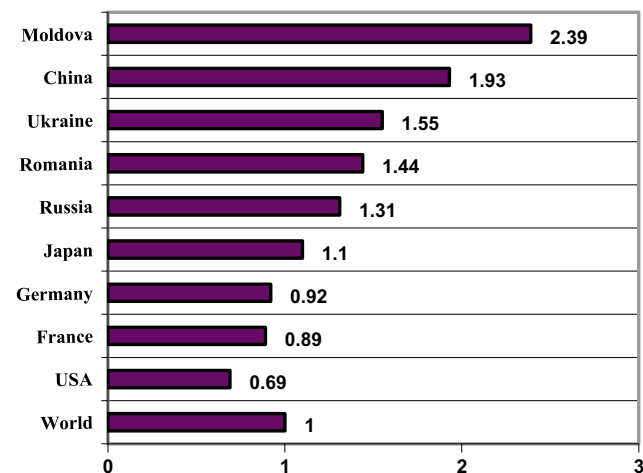


Fig. 1 National priority in nanoscience of selected countries (%), average 2009–2018 StatNano. *Source* Web of Science (ISI Web of Knowledge)

one country and other countries) [16]. In the period 2009–2018 worldwide leaders for this indicator are Liechtenstein, Nepal, and Senegal. The average indicator figure in the world is 66; the data for the RM is 81, with 21% above the average world figure. Less cooperation is characteristic for Iran, China, and India (Fig. 2).

The indicator “*Number of nanotechnology articles indexed in ISI*” is regarded as the simplest and as the same time, the most renowned quantitative indicator for knowledge generation in the field of nano-science. The StatNano database displays that the total number of ISI indexed nano-articles in WoS in the period 2009–2018 was 1,230,738. The leaders in this indicator are China, USA and India [17]. The number of the Moldovan ISI publications in this period represents 0.05% from the global ISI indexed nano-articles.

To the indicator “*Number of nano-articles per Million people*” (Ratio of nano-articles to country population (per million people) the average 2009–2018 figure for the RM is almost the same as for Ukraine and as the world average number, in medium 16 articles per million people per year. Here the world leaders are Singapore, Switzerland, and Finland [18].

Is to be underlined that in the indicator “*Number of nano-articles per GDP*” (Number of nano-articles per billion \$ GDP) [19], the RM outperforms the most developed countries, being ranked fourth in the world, after Singapore, South Korea, Slovenia, the average data for 2009–2018. The world medium number is 1.0 (Fig. 3).

The data analysis of the indicator “*Local share in nanoscience (%)*”, which is the ratio of the nano-articles carried in a country to the total articles of that country, places the RM on the first position in the world (19.3), being followed by Singapore and North Korea (Fig. 4). The world average figure for the investigated period is 8.3 [20].

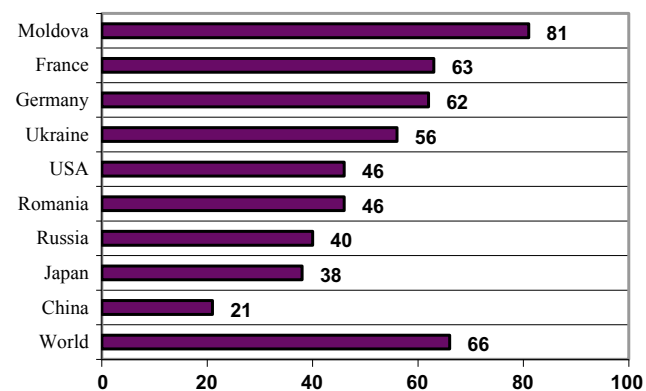


Fig. 2 Share of international collaboration in nanoscience (%), average 2009–2018 StatNano. Source Web of Science (ISI Web of Knowledge)

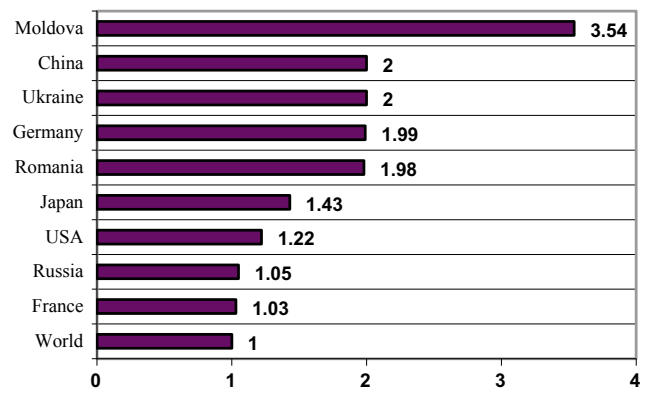


Fig. 3 Number of nano-articles per GDP (ppp), average 2009–2018 StatNano. Source Web of Science (ISI Web of Knowledge)

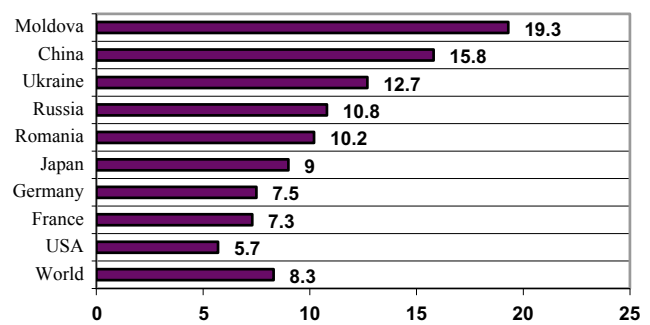


Fig. 4 Share of ISI-indexed nano-articles of total ISI-indexed articles, average for 2009–2018 StatNano. Source Web of Science (ISI Web of Knowledge)

With the reference to the indicator “*Total number of citations to nano-articles (Citation)*”: the total number of times all records have been cited: this field displays the total number of citations to all of the nano-articles in the set of search results [21] the top positions in the list of analyzed countries are held by China, USA and Germany (average data for 2009–2018) (Fig. 5). Moldovan scientists need to

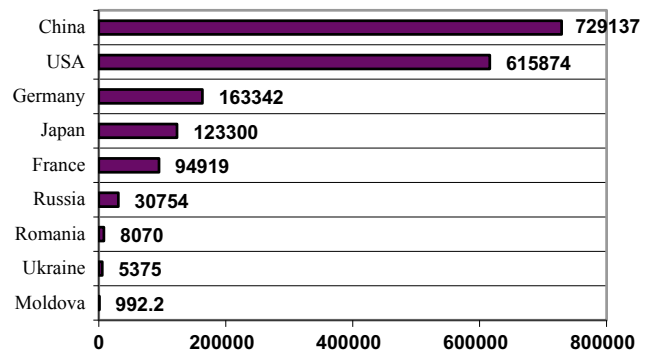


Fig. 5 Total number of citations to nano-articles (Citation), average for 2009–2018 StatNano. Source Web of Science (ISI Web of Knowledge)

make a significant effort to improve their standing regarding to this indicator.

Among the investigated countries to the indicator “Average citation per nano-article (*Citation per article*)” (the average number of times the nano-articles published within a year has been cited in the Journal Citation Reports) [22] the average data for the RM is almost the same as for Japan (Fig. 6). The leaders for the period 2009–2018 are Singapore, USA and Switzerland.

As it is known the *h*-index by comparison rewards both productivity and impact, since a high number of highly cited articles are required to push up the value. While the *h*-index is certainly not a perfect metric for comparing, it is one that has gained enormous popularity in a relatively short period [23]. Thus the *h*-Index of the nano-articles, published by the Moldovan scientists in the period 2009–2018, is 14 [24]. The top countries in this indicator are USA, China and Germany (Fig. 7).

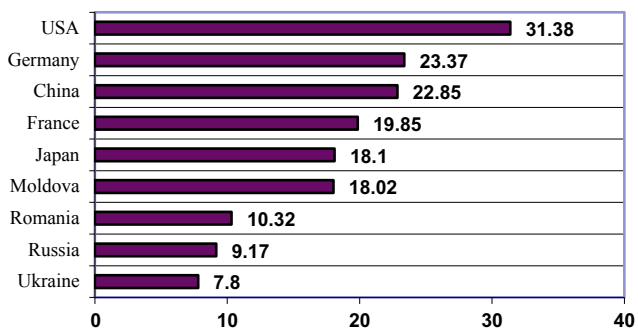


Fig. 6 Average citation per nano-article, average for 2009 – 2018 StatNano. Source Web of Science (ISI Web of Knowledge)

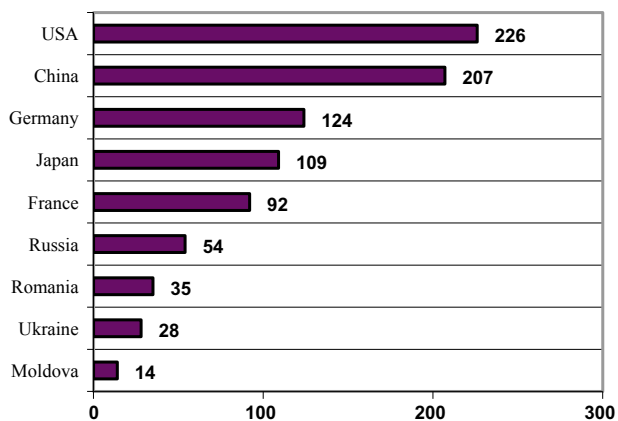


Fig. 7 *h*-Index of nano-articles, average for 2009–2018 StatNano. Source Web of Science (ISI Web of Knowledge)

5 Conclusions

On basis of some bibliometric indicators analyses, for the period 2009–2018, we identified the contribution of the scientists of the Republic of Moldova to the global information flow in nanotechnology area, revealed the country’s situation in this field. We can conclude that the Moldova is relatively well positioned, in terms of global research outputs in this area. According to the StatNano database the Moldovan nanotechnology research area is ranked first in the world for two indicators: national priority in nanoscience and share of ISI-indexed nano-articles of total ISI-indexed articles, it holds the fourth place in the world on the number of nano-articles per GDP. In the period 2009–2018 Moldovan nanoscience features a high share of international collaboration; the number of nano-articles per million people corresponds to the average worldwide figure. The medium citation per nano-article within the investigated countries is almost at the same level as for Japan. Nevertheless, Moldovan nanotechnology researchers need to work on improving their research impact, by means of increasing the total number of citations to nano-articles and *h*-index.

Acknowledgements This study was carried out in the framework of the national SCIFORM project 15.817.06.13A “Pilot platform for quality assurance and visualization of digitized scientific content of the Republic of Moldova”.

Conflict of Interest The authors declare that they have no conflict of interest.

References

1. Guston, D., Sarewitz, D.: Real-time technology assessment. *Technol. Soc.* **24**(1–2), 93–109. [https://doi.org/10.1016/s0160-791x\(01\)00047-1](https://doi.org/10.1016/s0160-791x(01)00047-1) (2002)
2. Hicks, D., Melkers, J.: *Bibliometrics as a tool for research evaluation*. Handb. Theory Pract. Progr. Eval. Georgia Institute of Technology (2012)
3. Arora, S.K., et al.: Measuring the development of a common scientific lexicon in nanotechnology. *J. Nanoparticle Res.* **16**(1), 2014 (2014). <https://doi.org/10.1007/s11051-013-2194-0>
4. Youtie, J. et al.: Lessons from 10 years of nanotechnology bibliometric analysis. In: Hull, M., Bowman, D. (eds.) *Nanotechnology Environmental Health and Safety: Risks, Regulation, and Management*, 3rd edn, pp 11–31. Elsevier, Amsterdam. <https://doi.org/10.1016/b978-0-12-813588-4.00002-6>(2018)
5. Standard ISO/TS 80004-4:2011 at <https://www.iso.org/standard/52195.html>
6. Khokhlyavin, S.: To a single termbase of nanotechnologies. *Nanoind.* **5**, 90–99 (2010)
7. Heinze, T., Shapira, P., Senker, J., et al.: Identifying creative research accomplishments: methodology and results for nanotechnology and human genetics. *Scientometrics* **70**(1), 125–152 (2007)
8. Kostoff, R., Koytcheff, R., et al.: Global nanotechnology research metrics. *Scientometrics* **70**(3), 565–601 (2007)

9. Lee, L., Chan, C., et al.: Nanotechnology patent landscape 2006. *NANO* **1**(2), 101 (2006)
10. Porter, A.L., et al.: Refining search terms for nanotechnology. *J. Nanoparticle Res.* **10**(5), 715–728 (2008). <https://doi.org/10.1007/S11051-007-9266-Y>
11. Stopar, K.: Presence of nanotechnology in agriculture: bibliometric approach. *Acta Agriculturae Slovenica* **107**(2) at <http://ojs.aas.bf.uni-lj.si/index.php/AAS/article/view/282> (2016)
12. Velmurugan, C., Radhakrishnan, N.: Visualizing global nanotechnology research on publication deeds, 1989–2014, *Libr. Philos. Pract.* (e-journal), 1372 (2016)
13. Spikala, S., Amudha, G.: The IEEE transactions on nanotechnology bibliometric analysis. *Int. J. Acad. Res. Libr. Inf. Sci.* **1**(2) at <http://science.eurekajournals.com/index.php/IJARLIS/article/view/29/129> (2018)
14. Latest information and statistics in nano-based Science, Technology, and Industry, at <https://statnano.com/>
15. National Bibliometric Instrument, Republic of Moldova, at: <https://ibn.idsi.md/en/>
16. National priority in nanoscience. Report Toolbox at <http://statnano.com/report/s41>
17. Share of international collaboration in nanoscience. Report Toolbox at <http://statnano.com/report/s82>
18. Number of graduated Masters students whose thesis pertains to nanotechnology regardless of their academic major. Report Toolbox at <http://statnano.com/report/r63>
19. Number of nano-articles per Million people (Article per million people). Report Toolbox at <http://statnano.com/report/s33>
20. Number of nano-articles per GDP(ppp) (Article per billion \$), Report Toolbox at <https://statnano.com/report/s81>
21. Local share in nanoscience. Report Toolbox at <http://statnano.com/report/s75>
22. Total number of citations to nano-articles. Report Toolbox at <http://statnano.com/report/s36>
23. Average citation per nano-article (Citation per article). Report Toolbox at <http://statnano.com/report/s55>
24. Brown, A.: Research Metrics: h-index, *Advanced Science News*. <https://www.advancedsciencenews.com/research-metrics-h-index/>, 15 Mar 2019

Qualitative Method to Control Toxic Impurities in Drinking Water

O. Kulikova, A. Siminel, A. Micu, and N. Siminel

Abstract

This paper presents the capabilities of the laser spectroscopy method for monitoring the concentration of dissolved organic impurities of toxic substances. The method of laser fluorometry that is based on the principle of calibration of the fluorescence signal of a dissolved matter to the internal standard—the Raman scattering signal of water, allows performing a quantitative assessment of the presence of harmful impurities. This method proves to be very promising due to its accuracy and expressiveness. The sensitivity of this method is sufficient enough to detect concentrations of the majority of studied specimens dissolved in water that exceed MCL. The effect of UV light exposure on some specimens was studied as well.

Keywords

PL spectra • Fluorescence • Fluorometry • MCL • Pesticides • Toxins • Water

1 Introduction

The dissolved organic matter (DOM) is a significant part of natural water systems and determines their ecological state. Toxic, harmful and dangerous for human health and the whole ecosystem pesticides that are widely used nowadays often pollute natural waters. When we use natural waters for various industrial and technological purposes or as drinking water, it is of growing importance to develop methods to control the concentration and stability of DOM. Among these diagnostic methods, laser fluorometry is advantageous

due to its expressiveness and high sensitivity for the concentration of pollutants. Fluorescence can be characterised with a range of parameters (e.g. shape and position of fluorescent and excitation bands, time of decay etc.) which can be utilised in the quantitative and qualitative assessment of the organic matter.

In this work, we measured pesticides solution photoluminescence (PL) spectra under the influence of UV laser irradiation. It was established that the intensity of the characteristic photoluminescence bands can be determined for pesticide concentration as low as 10^{-7} – 10^{-8} mg/l. This value is lower than maximum contaminant levels (MCL) of many pesticides dissolved in water.

2 Principles of Method

The method of laser fluorometry is based on the principle of calibration of the fluorescence signal of dissolved matter to the internal standard—the Raman scattering signal of solvent molecules [1, 2]. Normalization to the Raman scattering signal is a basis of quantitative fluorometry.

Nowadays this method is widely used to determine the concentration of pigments of sea phytoplankton (chlorophyll and pheophylline) [3, 4], to control oil pollution in water reservoirs [5, 6], to control the purity of technological fluids for microelectronics [7], and recently this method was applied for monitoring of DOM in natural water [8, 9].

The determination of the concentration of the fluorescent molecules is a difficult task. It requires the absolute calibration of a fluorometer and rigorous control during the process of measurement. Spectra of optical signals depend on two components: the interaction of laser radiation with the solvent molecules (Raman scattering), and the emission of solution's impurities (photoluminescence).

Fluorescence spectrum of DOM in water represents a wide band in a spectral range of 360–500 nm. This band possesses a complex structure that can be clearly seen in Fig. 1. One can see several peaks (in the range 440, 460 and

O. Kulikova (✉) · A. Siminel · A. Micu · N. Siminel (✉)
Institute of Applied Physics, Academy of Sciences of Moldova,
Academiei Str.5, Chisinau, Republic of Moldova
e-mail: olga.kulikova@phys.asm.md

N. Siminel
e-mail: siminel.n@gmail.com

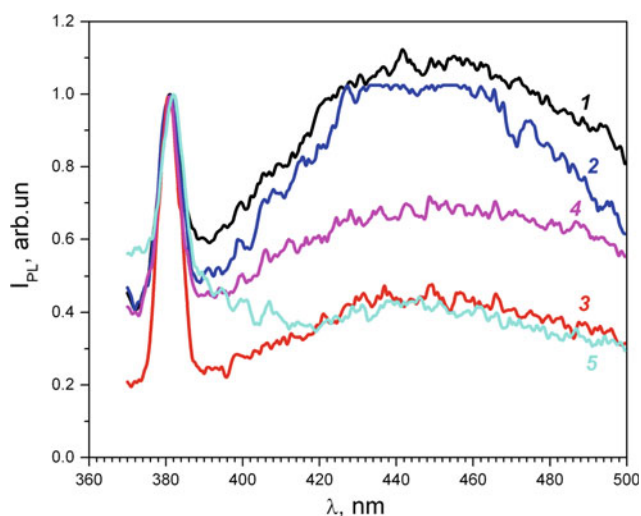


Fig. 1 Fluorescence spectra of water samples: 1—Water-supply network; 2—After boiling; 3—After filter1; 4—After freezing; 5—After filter2

480 nm) on the background of the wide band. It gives evidence of a significant concentration of different impurities in the sample of drinking water [9].

The concentration of impurities in water samples are determined from the expression (1):

$$n_{PL} = \Phi_0 \cdot \xi \cdot \sigma_{RS} \cdot \frac{n_{RS}}{\sigma_{PL}}, \quad (1)$$

where $\Phi_0 = N_{PL} \cdot I / N_{RS}$; N_{PL} , N_{RS} —is the number of detected photons of the fluorescent impurity and Raman scattering, respectively; Φ_0 —can be found geometrically by dividing the areas under the contour of the respective bands in the spectrum of measured signal; I —is a saturation factor of the fluorescence; σ_{RS} , σ_{PL} —cross sections of the interaction processes of the laser radiation with the impurity molecules and the solvent molecules, respectively; n_{RS} —

concentration of the solvent molecules; ξ —gauge factor, which includes the ratio of parameters of respective wavelengths of fluorescence and Raman scattering.

3 Samples

The list of investigated substances is given in Table 1.

3.1 Fuzilade-super (MCL $\sim 3 \times 10^{-7}$ mol/l)

Figure 2 shows the normalized optical signals of water RS peak spectra with various concentrations of Fuzilade-super aqueous solutions. The shape of PL spectra (Fig. 2, curve 1)

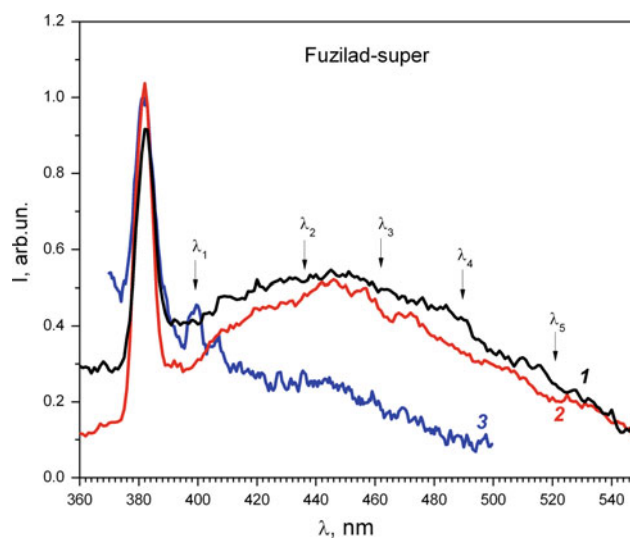


Fig. 2 Fluorescence spectra of aqueous solution of fuzilad: 1—Immediately after preparation; 2—After exposure in dark during 72 h; 3—After exposure in dark for 6 months

Table 1 Samples of pesticides

Pesticides	Chemical formula	Maximum contaminant level (MCL) (mg/l)	Solubility in water (mg/l)	Form of industrial production (%) [*]
Harness	C ₁₆ H ₁₄ Cl ₂ O ₄	0.002	223	c.e. 90
Fusilade-super	C ₁₉ H ₂₀ F ₃ NO ₄	0.01	2	c.e. 12.5
Zollon	C ₁₂ H ₁₅ O ₄ NCIS ₂ P	0.001	10	c.e. 30
Illoxan	C ₁₆ H ₁₄ Cl ₂ O ₄	0.1	50	c.e. 36
Decis	C ₂₂ H ₁₉ Br ₂ NO ₃	0.006	0.002	c.e. 2.5
Metaphos	C ₈ H ₁₀ O ₅ PSN	0.02	50	c.e. 40
Carbophos	C ₁₀ H ₁₉ PS ₂ O ₆	0.05	145	c.e. 10
Ridomil	C ₁₅ H ₂₁ NO ₄	—	0.71%	w.p.25; 35

^{*}c.e.—concentrated emulsions

w.p.—wetable powder

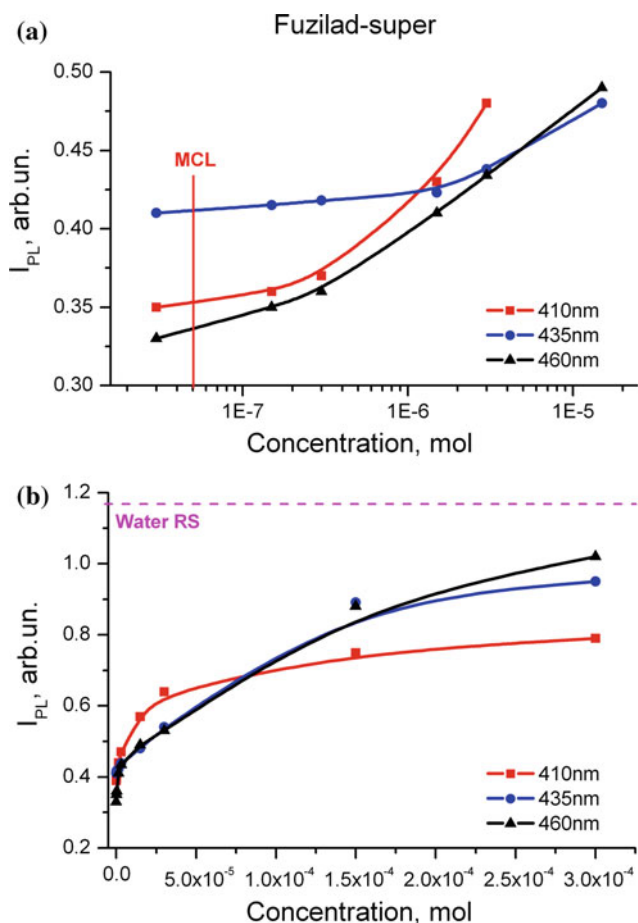


Fig. 3 Concentration nomogram's of the fuzilad-super

suggests a superposition of numerous irradiating processes occurring at a given time. To distinguish these processes we used Gauss function. Peak λ_1 was observed for the concentration of the main compound up to MCL. It was evident that the specimens are stable. PL spectra measured after 72 h and 6-month exposure completely coincide with the initial ones. The material is weakly sensitive to the light action. The exposure of the specimens to the light for 2 h practically did not change the shape and intensity of the fluorescence spectrum (Fig. 3).

3.2 Illoxan (MCL $\sim 3 \times 10^{-7}$ mol/l)

The PL spectra of Illoxan is characterized by intensive fluorescence in a wide spectral range with bands at $\lambda_1 = 400$ nm and $\lambda_2 = 432$ nm (Fig. 4 curve 1). Intensities of λ_1 and λ_2 bands for Illoxan at various concentrations compared with MCL are shown in logarithmic and linear scale in Fig. 5a and b respectively.

The study of light exposure influence has shown that the material is resistant to UV radiation. PL spectra did not

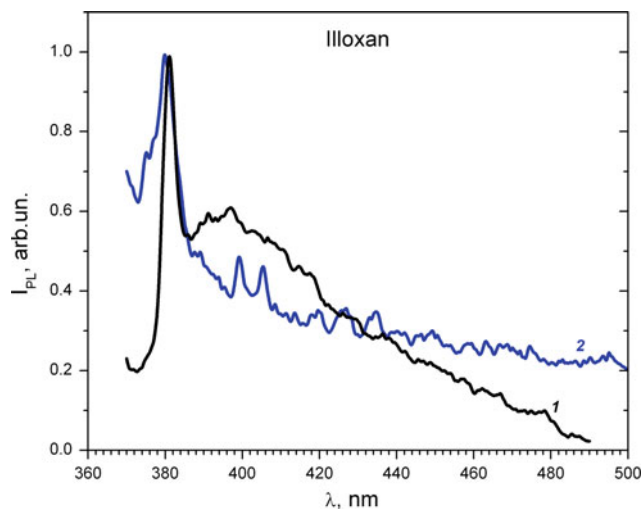


Fig. 4 Fluorescence spectra of aqueous solution Illoxan: 1—Immediately after preparation; 2—After exposure in dark for 144 h

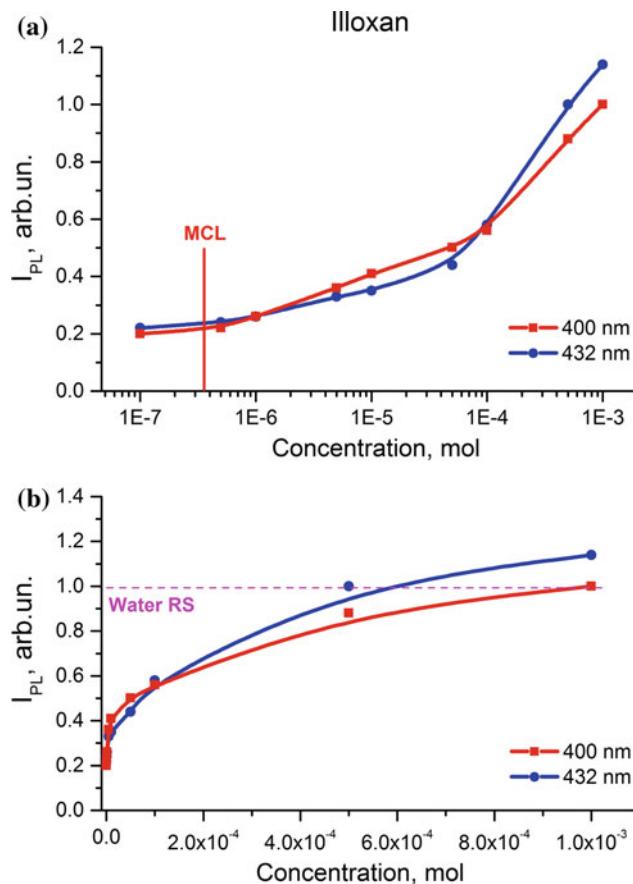


Fig. 5 Concentration nbvograms of the Illoxan

change after the sample exposure to the light for 2 h. Illoxan solutions are not stable. PL spectra of the solutions did not change their shape after 144-hours exposure in the dark Fig. 4. A pronounced decrease of PL intensity of band in the

region 400–430 nm is observed. At the same time, the maximum of fluorescence peak shifts to the long wavelength region.

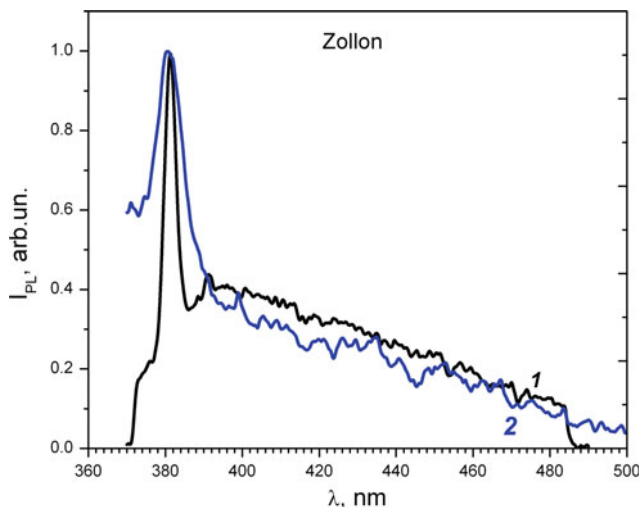


Fig. 6 Fluorescence spectra of aqueous solution Zollon: 1—Immediately after preparation; 2—After exposure in dark for 6 months

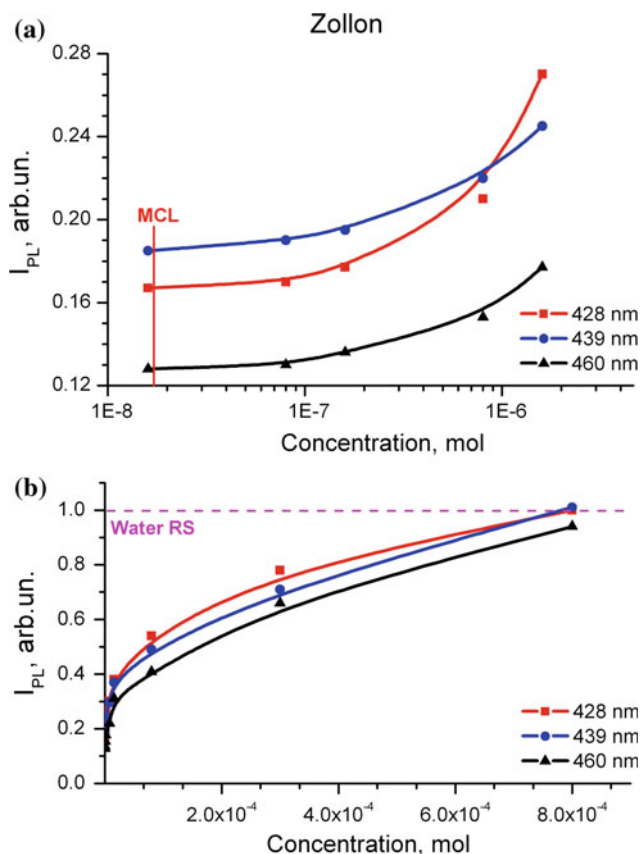


Fig. 7 Concentration momograms of the Zollon

3.3 Zollon (MCL $\sim 10^{-8}$ mol/l)

PL spectra of aqueous Zollon solution are given in Fig. 6. Weakly pronounced PL bands corresponding to the luminescence of Zollon were observed by subtracting the spectrum of the Zollon solution from the spectrum of pure distilled water.

Bands have a complicated structure with peaks at $\lambda_1 = 428$ nm, $\lambda_2 = 439$ nm and $\lambda_3 = 460$ nm. Peak λ_3 is detectable up to the MCL concentrations. The wide band II is more stable than the band I. Optical spectra of the samples measured after 48 h exposure in the dark show weak changes of the peaks λ_2 and λ_4 intensities.

Intensities at maxima λ_1 , λ_2 and λ_3 for Zollon at various concentrations compared with MCL are shown in logarithmic and linear scale in Fig. 7a and b respectively.

The sensitivity of the proposed method is sufficient for the detection of the majority of studied specimens in concentrations exceeding MCL. Some compounds, however, do not possess intense photoluminescence in the given spectral range. For example, the PL spectrum of Metaphos exhibited clear structural characteristics, but the spectrum of Carbophos and Decis could not be measured.

4 Conclusions

The quality of drinking water is extremely important. Dangerous and harmful microorganisms, bacteria and viruses, products of their vital activity-toxins can be present in the water pipe.

In this work, we presented the method of quantitative analysis of the concentration of pesticides in the drinking water. Eight different pesticides and herbicides widely used in agriculture, hence the high risk of them to get into drinking water, were studied. In the present paper, results on three types of pesticides as the most pronounced, are given.

The method proved to be effective and the expressway to control the concentration of dissolved pesticides in water (most of them). Potentially, it can be used to create specialized spectroscopic instruments for express analysis of the quality of drinking water.

Conflict of Interest The authors declare that they have no conflict of interest.

References

1. Klyshko, D.N., Fadeev, V.V.: Reports of the Academy of Sciences of the USSR, v.238, N2 (in Russian) (1978)
2. Abbas, O., Rebufa, C., Dupuya, N., Permyner, A., Kister, J.: Assessing petroleum oils biodegradation by chemometric analysis

- of spectroscopic data. *Talanta* **75**(4), 857–871 (2006). <https://doi.org/10.1016/j.talanta.2007.12.027>
3. Cristescu, L., Pavelescu, G., Carstea, E.M., Savastru, D.: Evaluation of petroleum contaminants in soil by fluorescence spectroscopy. *Environ. Eng. Manag. J.* **8**(5), 1269–1273 (2009). <https://doi.org/10.30638/eeemj.2009.186>
 4. Fadeev, V.V., Chubarov, V.V.: Reports of the Academy of Sciences of the USSR, v.261, N2, p. 342–344 (in Russian) (1981)
 5. Baker, A.: Thermal fluorescence quenching properties of dissolved organic matter. *Water Res.* **39**(18), 4405–4412 (2005). <https://doi.org/10.1016/j.watres.2005.08.023>
 6. Filippova, E.M., Patsayeva, S.V.: Laser fluorescent monitoring of dissolved organic matter in natural water. Physics Department of Moscow State University, Moscow (1994)
 7. Bieroza, M., Baker, A., Bridgeman, J.: Relating freshwater organic matter fluorescence to organic carbon removal efficiency in drinking water treatment. *Sci. Total Environ.* **407**(5), 1765–1774 (2009). <https://doi.org/10.1016/j.scitotenv.2008.11.013>
 8. Carstea, E.M., Baker, A., Bieroza, M., Reynolds, D.M.: Continuous fluorescence excitation emission matrix monitoring of river organic matter. *Water Res.* **44**(18), 5356–5366 (2010). <https://doi.org/10.1016/j.watres.2010.06.036>
 9. Kulikova, O., Siminel, A., Micu, A.: Laser spectroscopy for analysis of water organic pollution. In: Abst. of 8 International Conference on Materials Science and Condensed Matter Physics, MSCMP-2016, Chisinau, p. 276 (2016)

The Cathepsin D as a Potential Biomarker for Survival Rate in Polytrauma. Pilot Research

O. Arnaut, S. Sandru, A. Sauleal, I. Grabovschi, and Gh. Rojnoveanu

Abstract

Trauma represents a major problem affecting the younger part of humanity as shown in several studies. It represents the main cause of deaths or disabilities that could be prevented in children, teenagers and adults younger than 44 years. In Republic of Moldova, trauma has the fourth place after gastrointestinal tract diseases in list of death causes. One of the most complicated and hard to explore domain of trauma is the polytrauma. Except tardive consequences regarding recovery period and other clinical, economic, and social burden aspects of polytraumatized persons, the immediate effects on the patient have a crucial role on patient's life. This is why numerous researches are trying to reveal the key moments and factors in pathogenesis and clinical management of polytrauma patients. Scientists are looking for some predictive models that could estimate the death/survival rate of traumatized/polytraumatized population of patients. Some of these models seem to be based on concentration dynamics of different biomarkers in post-traumatic period. Cathepsin D is one of this enzymes studied in this trial. Using logistic regression technique, it was created a predictive model estimating polytraumatized patients' survival probability based on plasma Cathepsin D concentration (CDEA) at 3 and 48 h after traumatic injury.

Keywords

Polytrauma • Cathepsin D • Predictive model

1 Introduction

Trauma, despite progresses in medicine, remains a world-wide major cause of morbidity and mortality [1]. Thereby, data provided by numerous studies shows that trauma is responsible of the main part of deaths or disabilities that could be prevented in children, teenagers and adults younger than 44 years [2, 3]. According to National Agency for Public Healthcare in Republic of Moldova, trauma determines 8.1% of deaths, being on the fourth place after gastrointestinal tract diseases [4].

One of the most complicated and hard to explore categories of trauma is the polytrauma. Researchers are looking for some predictive models that could estimate the death/survival rate or complication appearance in traumatized/polytraumatized patients' population [1].

Cathepsin D is an intracellular neutrophil's protease, important for apoptosis, processing of various enzymes, antigens, hormones and neuropeptides, being active after releasing in blood plasma. It was demonstrated high levels of Cathepsin D in multiple trauma patients, that caused complement system activation and, as a result, negative effects. Some of them are: compromising of neutrophils and macrophages protective functions (chemotaxis, phagocytosis and free oxygen radical synthesis), activation apoptosis for lymphocytes and synthesis of proinflammatory and adhesion molecules by endothelium [5].

The aim of research was an attempt to solve a serious problem frequently encountered in polytraumatized patient management, namely biomarkers with predictive potential on clinical evolution in this category of patients.

In this prospective study, using logistic regression technique, it was created a predictive model estimating polytraumatized patients' survival probability based on plasma Cathepsin D activity (CDEA).

O. Arnaut (✉) · S. Sandru · A. Sauleal · I. Grabovschi · Gh. Rojnoveanu
Nicolae Testemitanu, State University of Medicine and Pharmacy of the Republic of Moldova, Stefan cel Mare, 165, Chisinau, Republic of Moldova
e-mail: oleg.arnaut@usmf.md

O. Arnaut · S. Sandru · I. Grabovschi · Gh. Rojnoveanu
Emergency Medicine Institute, Chisinau, Republic of Moldova

2 Materials and Methods

Research project was approved by the Ethics Committee of SUMF “Nicolae Testemițanu”. In Emergency Medicine Institute from Chisinau, Republic of Moldova, in a prospective study, was analyzed 63 polytrauma patients admitted in acute period of trauma. Data was collected during 12 months. Criteria for polytrauma were lesions of at least two body regions evaluated with AIS (Abbreviated Injury Scale) ≥ 3 points and SIRS (Systemic Inflammatory Response Syndrome) diagnosed in first 72 h after trauma that persists at least 24 h [6]. Plasma samples (venous blood collection and centrifugation) were collected at 3, 6, 12, 24, 48 and 72 h after traumatic impact. CDEA was determined by spectrophotometric analysis of hemoglobin molecule metabolites resulted by the Cathepsin D processing. The values of ADEA were expressed in ng/s l [7]. Multivariate analysis (logistic regression) for dichotomical and scale data was performed using SPSS 21 (License No. 20130626-3).

3 Results

For a potential predictive model, they were formulated the following hypotheses:

The null hypothesis—covariates included in the model (CDEA at 3, 6, 12, 24, 48 and 72 h after trauma) cannot predict the survival probability of polytraumatized patients better than a model based on only one single constant.

Alternative hypothesis—at least one variable (CDEA at 3, 6, 12, 24, 48 and 72 h after trauma) can predict the survival probability of transported polytraumatized patients better than a model based on only one single constant.

Omnibus Test of Model Coefficients (χ^2 (df = 2) = 38.522, $p < 0.001$), being significant, allows to reject the null hypothesis and to analyze which of the studied covariates is relevant for severe trauma survival prediction.

Nagelkerke R Square coefficient (determination coefficient) = 0.648 (64.8%) shows that variables included in the model determined approximately 2/3 of examined variable dispersion (event occurring probability).

Hosmer—Lemeshow test, analyzing if the model has ability to predict positive and negative results, indicate an insignificant result (χ^2 (df = 8) = 4.462, $p = 0.813$). This shows a high fidelity of obtained results.

Classification chart relies a sensibility of 95.5% (40 of 42 cases), specificity being 78.9% (15 of 19 cases), the mean

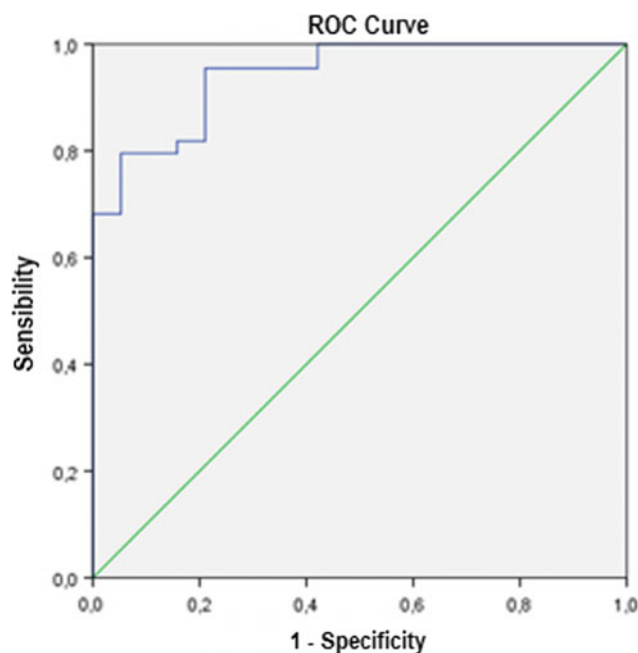


Fig. 1 ROC curve of the predictive model for survival probability in polytraumatized patients

validation appreciated at 87.3%. These results were obtained after analyzing the classification chart and after shifting the cut off value at 0.51.

Area under the ROC curve for the proposed model was 0.943, with a 95% confidence interval (0.889, 0.997) and significant difference from 0.5 value ($p < 0.001$) (Fig. 1). Thus, logistic regression rates the resulted model as significantly better than a random model.

The model includes the constant ($B = 7.399$), CDEA values at 3 ($B = -0.249$) and 48 h. ($B = -0.207$) (Table 1). CDEA at 3 and 48 h was negative factors for survival (OR = 0.779, 95% CI95% 0.667, 0.911 and OR = 0.813, CI95% 0.720, 0.918).

Taking into account Table 1 coefficients, the proposed model has the following mathematical expression:

$$p = \frac{1}{1 + e^{-7.399 + 0.249 \cdot \text{CDEA}_{3\text{ h}} + 0.207 \cdot \text{CDEA}_{48\text{ h}}}} \quad (1)$$

where:

p survival probability in polytrauma;
e (exponent) constant equals to 2.71828

Bootstrapping resampling for stability estimation highlighted the following results. Bootstrap_{CDEA3} ($B = -0.249$, CI95% -0.561; -0.114), Bootstrap_{CDEA48} ($B = -0.207$, CI95% -0.501; -0.110).

Table 1 Equation variables for elaborated predictive model

	CDEA_3 h	CDEA_48 h	Constant
B	-0.249	-0.207	7.399
S.E.	0.080	0.062	1.708
Wald	9.783	11.153	18.768
df	1	1	1
Sig.	0.002	0.001	0.000
Exp(B)	0.779	0.813	1634.386
95% C.I. lower	0.667	0.720	
95% C.I. upper	0.911	0.918	

Constant—equation constant's value, B—B coefficients, S.E.—standard errors, Wald—Wald statistics, df—degrees of freedom, Sig.—significance threshold, Exp (B)—odds ratio values, 95% C.I.—confidence interval for odds ratio

4 Discussions and Conclusions

In this study, it was elaborated a predictive model to determine polytrauma survival rate. As a potential biomarker, where tested plasma CDEA, whose values at 3 and 48 h after trauma can be considered as potential biomarkers to predict patients' the survival probability in polytrauma patients. This predictive model takes part from experimental and mathematical models based on the different elements of proteases/antiproteases system elaborated before [8, 9].

Proposed model, having adequate characteristics and stability, can be recommended for clinical use in polytrauma patients admitted in Emergency Medicine Institute from Chisinau, Republic of Moldova and, evidently, needs coefficient's adjustment for another institution.

In the same time, considering some limits as relative small numbers of respondents, unexplained third of dispersion etc., proposed model can be completed by potential covariates/biomarkers as severity of trauma, time of

admission, different protein's plasma profile etc. Validation of elaborated model follows.

Conflict of Interest The authors declare that they have no conflict of interest.

References

- de Munter, L., Polinder, S., Lansink, K.W.W., Cnossen, M.C., Steyerberg, E.W., de Jongh, M.A.C.: Mortality prediction models in the general trauma population: a systematic review. *Injury* **48**(2), 221–229 (2017)
- Feliciano, D.V., et al.: *Trauma*, 6th edn, p. 987. McGraw-Hill, New York (2008)
- Kunitake, R.C., Kornblith, L.Z., Cohen, M.J., Callcut, R.A.: Trauma Early Mortality Prediction Tool (TEMPT) for assessing 28-day mortality. *Trauma Surg. Acute Care Open* **3**(1), e000131 (2018)
- Population and demographic processes at <http://statbank.statistica.md/pxweb/pxweb/en/?rxid=eb963997-3d38-40e1-86c6-8734d691dcf6>
- Huber-Langa, M., Denka, S., Fuldab, S.: Cathepsin D is released after severe tissue trauma in vivo and is capable of generating C5a in vitro. *Mol. Immun.* **50**, 60–65 (2012)
- Butcher, N., Enninghorst, N., Sisak, K., et al.: The definition of polytrauma: variable interrater versus intrarater agreement—a prospective international study among trauma surgeons. *J. Trauma Acute Care Surg.* **74**(3), 884–889 (2013)
- Gudumac, V.: *Investigatii biochimice*, p. 97. Elaborarea metodică, Tipografia ElenaVI, Chişinău (2010)
- Arnaut, O., Baltaga, R., Rojnovanu, Gh., et al.: Is a2-macroglobulin a new biomarker for ARDS occurrence in polytrauma patients? *Eur. J. Trauma Emerg. Surg.* **44**(Suppl 2), 273, Clinical Research, Poster, ANESTHESIA PR001 <https://doi.org/10.1007/s00068-018-0934-7> (2018)
- Grabovschi, I., Arnaut, O., Saulea, A., et al.: Cathepsin D, elastase and α 1-antitrypsin evaluation in ARDS caused by polytrauma. Experimental model. In: *Physiology. The 12th National Congress of the Romanian Society of Physiology*. Craiova, România. Supliment, p. 45 (2016). ISSN 1223-2076

Comparative Study of the *p*-CdS/*n*-CdTe Photovoltaic Devices with Depleted Intrinsic Layer

A. Al Qassem, L. Gagara, V. Fedorov, I. Lungu, and T. Potlog

Abstract

In fabricating CdS/CdTe photovoltaic devices by close space sublimation method, thermal annealed in CdCl₂ ambient at 400 °C at the interface is deposited an *i*-CdO layer by magnetron sputtering. Comparative analysis of electrical, photovoltaic parameters and photo-response spectral distribution is studied. The insertion of *i*-CdO at the interface of device increases both short circuit current (I_{sc}) and open circuit voltage (V_{oc}). In addition, the experimental results revealed that the insertion of *i*-nanolayer broaden the depletion region of the device and diminish the interface state density, thus improving efficiency of the device.

Keywords

CdS/CdTe • *i*-CdO • Electrical and photovoltaic parameters • Photo-response

1 Introduction

CdTe Photovoltaic (PV) is an important thin film PV technology that has grown rapidly in recent years. CdTe PV provides the lowest carbon footprint and fastest energy payback time of current PV technologies and other energy alternatives. In the overall lifecycle of CdTe PV, it's found to produce minimal environmental emissions (e.g., air emissions of 0.02–0.3 g Cd/GWh compared to 2–3.1 g Cd/GWh from coal burning power plants) compared to other PV systems and energy generation options [1]. In the presence of tellurium, cadmium forms a crystalline lattice that is highly stable (high boiling point, low vapor pressure, low solubility). The performance of a solar photovoltaic cell depends on its fabrication technology, design and material

properties. During the past twenty years, CdTe solar cells have demonstrated long-term stability and competitive performance, and they continue to attract production-scale capital investments. Recently (February 2015), First Solar set a world record for CdTe PV cell conversion efficiency, achieving 21.5% [2]. CdTe has an absorption so high that it takes only a few microns absorb sunlight whereas crystalline silicon requires a layer, which is 100 μ or more thick. Traditional CdS/CdTe solar cells with a p-n heterojunction were normally 5–8 μm thick in total, the emitter layer having slightly less thickness compared to the base so that the junction is closer to the surface. Silicon cells, on the other hand, have thicknesses surpassing 250 μm because of it being indirect band gap semiconductor [3]. One out of the many kinds of basic solar cell structures is the *p-i-n* structure, which consists of p- and n-doped regions at the top and the bottom with an intrinsic layer (*i*-layer) in the middle. It provides a simple way to improve the absorption ability with a thick intrinsic region. However, a thicker *i*-layer may induce more defects degrading the quality of the grown layers and resulting in the formation of dangling bonds. The built in electric field is also dependent on the thickness of the *i*-layer with the field strength decreasing with the increase in its thickness. The paper [4] studied the properties of CdS/CdTe with improved parameters due to the deposition of a Te layer at the back contact. Therefore, the scientific novelty of this paper consists in the insertion at the interface of intrinsic CdO layer and the optimization of its thickness.

2 Fabrication and Characterization Techniques

The close spaced sublimation method is considered as one of the most promising technique for A₂B₆ thin film deposition. Details of the close space sublimation (CSS) technique are widely described in literature [3]. CdS and CdTe materials of 99.999% purity were used as the source materials. The polycrystalline films were obtained in a short time (about

A. Al Qassem · L. Gagara · V. Fedorov · I. Lungu · T. Potlog (✉)
Physics Department and Engineering, Moldova State University
Chisinau, 60, A. Mateevici str, Chisinau, Republic of Moldova
e-mail: tpotlog@gmail.com

30 min) without an additional transport agent gas. The temperature and growth rate are maintained using BPT-3 temperature controllers that allow keeping a constant temperature with a precision of ± 0.5 °C. Our substrate is SnO₂/glass, which we purchased from Solaronix, Swiss. A standard glass cleaning procedure is used. CdO thin film were deposited by the dc magnetron reactive sputtering of cadmium in an oxygen atmosphere. For sample preparation, a Cd target of 99.99% purity was used in the sputtering process. The sputtering chamber was evacuated down to 2×10^{-5} mbar. The distance between the target and the substrate was kept constant at 3 cm. The magnetron discharge was done in a O₂ gas via independent mass-flow controller. The working total pressure was kept at 5×10^{-3} mbar. The substrate temperature was slightly higher than the room temperature (below 90 °C). Using the optimized growth parameter determined for the individual layers, two different heterostructures (HJs) were prepared: SnO₂/CdS/CdTe and SnO₂/CdS/CdO/CdTe. Therefore, the process steps for fabrication of a CdTe thin-film cell with superstrate configuration include SnO₂ layer, formation of a CdS/CdTe stack over the TCO layer, Cl-treatment, cleaning of the CdTe film surface, doping, and formation of a back contact.

3 Results and Discussion

3.1 Current-Voltage Characteristics

Figure 1 provides the illustration of the SEM cross-section image of the SnO₂/CdS/CdTe thin film heterojunctions interface.

The photovoltaic characteristics of the CdTe thin film HJs were investigated through the wide band gap component at the room temperature (300 K) and illumination 100 mW/cm².

The dark current-voltage characteristics of the SnO₂/CdS/CdO/CdTe/Sb/Ni and SnO₂/CdS/CdTe/Sb/Ni heterostructures in log scale are shown in Fig. 2. The introduction of an intrinsic layer CdO at the interface of CdS/CdTe devices does not change the trend of the behavior of the current transfer, but only increases the magnitude of the current.

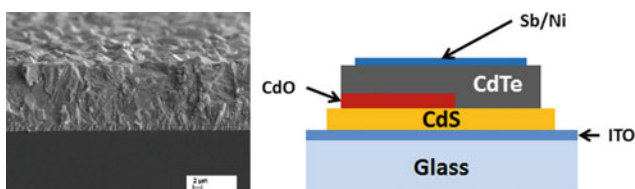


Fig. 1 SEM cross-section image of CdS/CdTe thin film HJ and a schematic diagram of the CdS/CdO/CdTe device

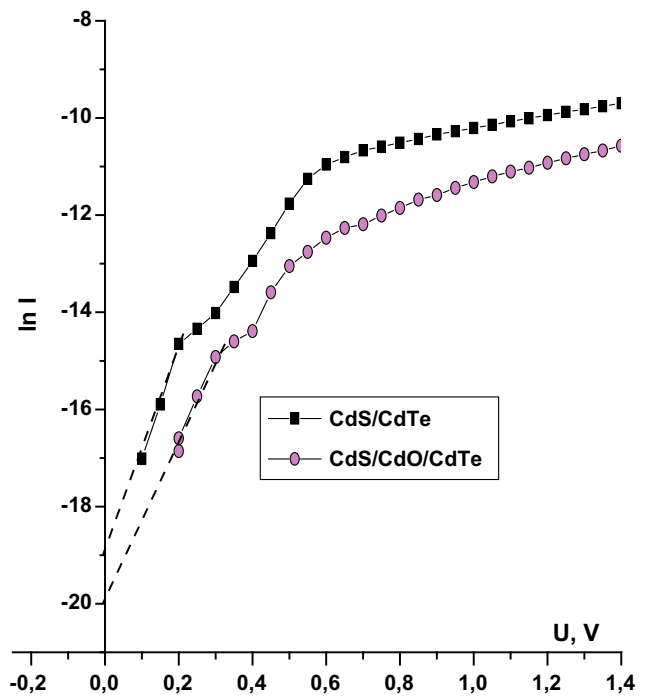


Fig. 2 Dependencies of $\ln I$ versus voltage of SnO₂/CdS/CdO/CdTe/Ni and SnO₂/CdS/CdTe/Ni devices

Table 1 shows the main electrical parameters (the saturation current (I_0), diffusion potential (U_D), series (R_s) and shunt resistances R_{sh}) of CdS/CdTe heterojunctions with and without a CdO layer fabricated in the same technological cycle. The I_0 decreases from 6.2×10^{-9} A to 2.06×10^{-9} A when at the interface is deposited *i*-CdO layer. Moreover, the decrease of I_0 with increasing shunt resistance calculated from formula

$$I = I_0 \left(e^{q(V-IR_s)/AKT} - 1 \right) + \frac{V - IR_s}{R_{Sh}} \quad (1)$$

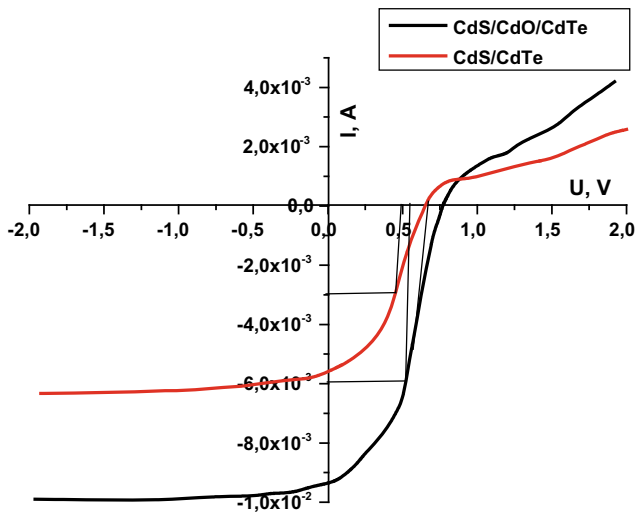
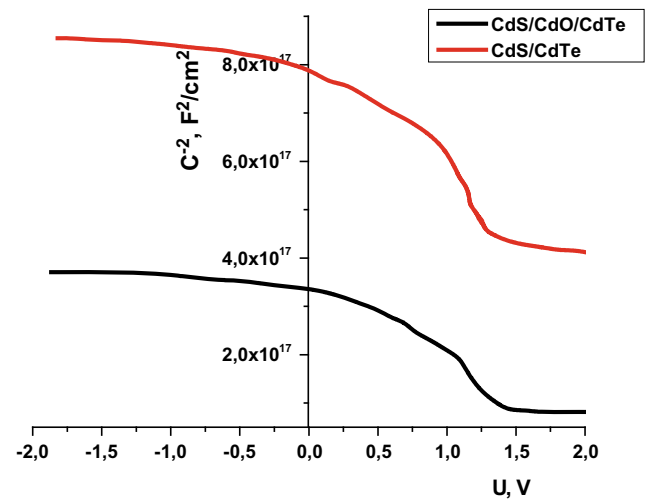
reveals the evolution of shunting effect in the CdS/CdO/CdTe heterojunction.

In Fig. 3 the current-voltage characteristics of devices with an area of 0.35 cm² under 100 mW/cm² illumination showed that *i*-CdO layer increases both short circuit current density (J_{sc}) and open circuit voltage (U_{oc}). The I-U curves indicate non-ideal behavior.

Such I-U behavior are due to the formation of the secondary barrier at the absorber-metal contact interface for both types of devices. CdTe is a p-type semiconductor with a high electron affinity ($\chi = 4.5$ eV) and high band gap (1.45 eV), and thus a metal with a high work-function ($\Phi_m \geq 5.9$ eV) is required to make an ohmic contact to CdTe. Most metals, however, do not have sufficiently high work-functions and therefore form Schottky-barrier contacts to CdTe absorber layers. In the Table 2 the photovoltaic parameters (J_{sc} , U_{oc} , fill factor (FF) and efficiency (η) of both

Table 1 Electrical parameters of photovoltaic devices

Samples	I_0 , A	U_D , V	R_S (Ω)	R_{Sh} (Ω)
CdS/CdO/CdTe	2.06×10^{-9}	1.2	1.4×10^4	5.1×10^6
CdS/CdTe	6.2×10^{-9}	0.95	1.0×10^4	1.7×10^5

**Fig. 3** Voltage of SnO₂/CdS/CdO/CdTe/Sb/Ni and SnO₂/CdS/CdTe/Sb/Ni devices**Fig. 4** Dependence of $1/C^2$ versus voltage for SnO₂/CdS/CdO/CdTe/Ni and SnO₂/CdS/CdTe/Ni devices**Table 2** Photovoltaic parameters of photovoltaic devices

Samples	J_{sc} (mA/cm ²)	U_{oc} , V	FF	η (%)
CdS/CdTe	15.7	0.66	0.37	3.8
CdS/CdO/CdTe	26.5	0.77	0.44	8.9

structures are presented. The FF is low in general. According to the theory the FF is determined by the series resistance (R_s), the saturated dark current density (I_0) and the diode quality factor (n). From Table 1 results that low value of FF is mainly determined by the high value of the series resistance.

3.2 Capacitance-Voltage Characteristics

The study of capacitance-voltage characteristics ($C^{-2} = f(U)$) also indicate the presence of a conduction band secondary barrier at the absorber-metal contact interface (Fig. 4).

The appearance of the minimum at $C^{-2} = f(U)$ characteristics is presented in both types of the devices with and without CdO layer. For analyzing the capacitance data, the following equations were used:

$$W(U) = \frac{\epsilon_0 \epsilon_r S}{C} \quad (2)$$

$$N_{effective}(W) = -\frac{2}{q\epsilon_r} \frac{dU}{d(C^2)^{-1}} \quad (3)$$

where W is the depletion layer width, C is the capacitance per unit area, $\epsilon_r = 9.4$ is the dielectric constant of CdTe, $q = 1.6 \times 10^{-19}$ C, and N is the concentration of uncompensated impurity in the depletion layer. It was found that device with *i*-CdO had wider depletion 37.2 nm in comparison with 24.5 nm for device without *i*-layer. Relatively lower difference in carrier concentration of uncompensated impurity 7.36×10^{13} cm⁻³ in cell with *i*-layer when compared to device without intrinsic layer 7.0×10^{13} cm⁻³ is revealed. The slightly increasing of the ionized-charge concentration in cell with CdO layer suggests to a lowering of density of the states that result at the junction. Although there can exist other mechanisms of recombination interface of CdS/CdTe. So, increase in the open circuit voltage could be explained due to minimizing the number of deep recombination centers from the charge space region of the CdS/CdO/CdTe heterojunction at interface, it is, in general, admitted that the biggest weight can be represented by the structure dislocations, that appear due to mismatching lattice parameters of those 2 materials CdS and CdTe. Measurement of the capacitance of the devices as a function of frequency (Fig. 5) measured under dark condition show considerable frequency dispersion with increasing of applied voltage. The capacitance of the CdS/CdTe heterojunction prepared with CdO at the interface shows higher values in

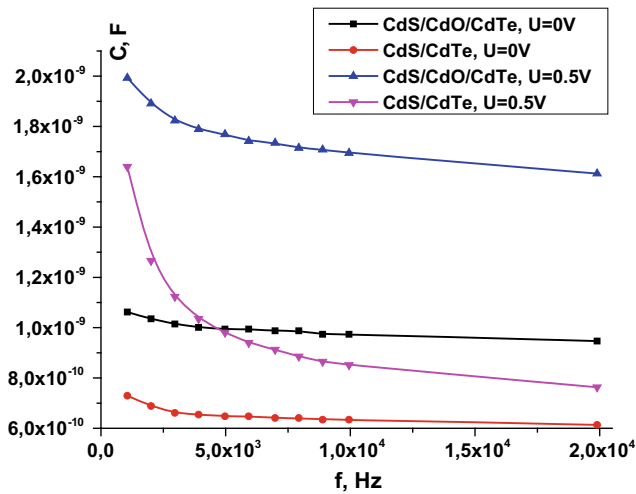


Fig. 5 Dark capacitance versus frequency characteristics of $\text{SnO}_2/\text{CdS}/\text{CdO}/\text{CdTe}/\text{Ni}$ and $\text{SnO}_2/\text{CdS}/\text{CdTe}/\text{Ni}$ devices

comparison without *i*-layer. At applied voltage of 0.5 V the capacitance mainly increases at the lower frequencies for both types of devices is observed.

The decrease in capacitance with frequency indicates the existence of deep levels at or near the CdS/CdTe interface. Variation of the interface state capacitance, C_{it} with frequency is reported in [4].

$$C_{it} = \frac{AqN_{ss} \arctan(\omega\tau)}{\omega} \quad (4)$$

where N_{ss} is the density of interface states, A is the area, ω is the frequency and τ is the relaxation time of the interface state.

We selected a low frequency of 1 kHz and a high frequency of 5 MHz to obtain the detailed interface state density n_{ss} of the CdS/CdTe structures by a high-low frequency method. Here C_{LF} at a low frequency can be determined by

$$C_{LF} = C_{it} + C_{sc}. \quad (5)$$

Thus, the equivalent capacitance becomes the parallel connection of interface state capacitance C_{it} and space charge capacitance C_{sc} ,

$$C_{sc} = C_{HF}. \quad (6)$$

Substituting Eq. (6) into Eq. (5) gives the interface state capacitance (C_{it}) in terms of the measured low frequency (C_{LF}) and the higher frequency (C_{HF}) curves as

$$C_{it} = C_{LF} - C_{HF}. \quad (7)$$

The interface state density n_{ss} can be obtained from Eqs. (5)–(7), and yields

Table 3 The carriers lifetime τ and the interface state density n_{ss} of devices

Samples	τ , s	N_{ss} ($\text{eV}^{-1}\text{cm}^{-2}$)
CdS/CdO/CdTe	1.25×10^{-6}	7.3×10^8
CdS/CdTe	3.35×10^{-6}	7×10^{10}

$$N_{ss} = \frac{C_{it}}{qA} = (C_{LF} - C_{HF})/qA, \quad (8)$$

The interface state density extracted from the C - f plots was $7 \times 10^{10} \text{ eV}^{-1} \text{ cm}^{-2}$ for device without *i*-CdO, while for device with *i*-nanolayer $7.3 \times 10^8 \text{ eV}^{-1} \text{ cm}^{-2}$.

In addition, the value of the lifetime of the carriers and the interface state density n_{ss} at the CdO/CdTe and CdS/CdTe interfaces of the devices are presented in Table 3.

As can be seen from the data from Table 3, the lifetime τ does not change significantly with the introduction of the *i*-CdO nanolayer, which indicates that all the physical processes of the current transfer occur in the CdTe layer, and a thin CdO layer is like a stabilizer of losses of minority current carriers during photoexcitation processes.

3.3 Photo-Response Spectral Distribution Characteristics

In Fig. 6 The photo-response spectral dependences of $\text{SnO}_2/\text{CdS}/\text{CdO}/\text{CdTe}/\text{Ni}$ and $\text{SnO}_2/\text{CdS}/\text{CdTe}/\text{Ni}$ devices are shown.

The photo-response spectral dependences were investigated through the SnO_2 side. The photosensitivity comprises the wavelength range spectral interval of 550–900 nm. The photo-response in the long wavelength region for both devices is limited for photon absorption with a wavelength of around 810 nm that correspond to photon energy 1.57 eV. In the shorter wavelength region for device without

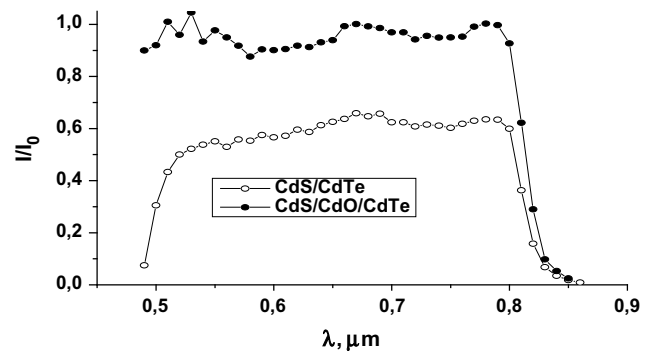


Fig. 6 The photo-response spectral dependences of $\text{SnO}_2/\text{CdS}/\text{CdO}/\text{CdTe}/\text{Ni}$ and $\text{SnO}_2/\text{CdS}/\text{CdTe}/\text{Ni}$ devices

i-layer equals to 2.48 eV, while for device with *i*-CdO it is impossible to estimate. It can be summarized that the introduction of a *i*-CdO layer in CdS/CdTe device increases the absolute value of the photo-response and changing not significant the sensitivity region.

4 Conclusions

Analysis of the current-voltage characteristics of CdS/CdTe device with and without *i*-CdO at the interface show non-ideal behavior. The insertion of *i*-CdO at the interface of device increases both I_{sc} and V_{oc} , show wider depletion region (37.2 nm) in comparison with device without *i*-layer (24. nm). Relatively lower difference in carrier concentration of uncompensated impurity $7.36 \times 10^{13} \text{ cm}^{-3}$ in cell with *i*-layer when compared to device without intrinsic layer $7.0 \times 10^{13} \text{ cm}^{-3}$ is revealed. The interface state density decreases from $7 \times 10^{10} \text{ eV}^{-1} \text{ cm}^{-2}$ for device without *i*-CdO, to $7.3 \times 10^8 \text{ eV}^{-1} \text{ cm}^{-2}$ for device with *i*-nanolayer. The photo-response spectral dependences comprise the wavelength range spectral interval of 550–900 nm.

Acknowledgements The authors would like to thank the Ministry of Education, Culture and Research of Republic of Moldova for supporting this research by funding the grant 15.817.02.39A.

Conflict of Interest The authors declare that they have no conflict of interest.

References

1. Held, M., Ilg, R.: Update of environmental indicators and energy payback time of CdTe photovoltaic systems in Europe. *Progr. Photovolt. Res. Appl.* **19**, 614–626 (2011)
2. <https://www.greentechmedia.com/articles/read/first-solar-hits-record-22-1-conversion-efficiency-for-cdte-solarcell>
3. Glunz, S.W., et al.: Crystalline silicon solar cells: state-of-the-art and future developments. *Compr. Renew. Energy* **1**, 353–387 (2012)
4. Potlog, T.: The production of new types of CdTe photovoltaic devices with high efficiency. In: *Advances in the II-VI Compounds Suitable for Solar Cell Applications*, pp 87–122, Trivandrum-695023, India (2014). ISBN 978-81-308-0533-7

Synthesis and Biological Properties of the Novel Coordination Compound with Rhodanine-3-Acetic Acid

A. Vitiu, D. Chișca, E. Gorincioi, E. Coropceanu, and P. Bourosh

Abstract

The new coordination compound based on rhodanine-3-acetic acid was synthesized, characterized and evaluated as potential antimicrobial agent on a panel of bacteria and fungi. The structure and stereochemistry of the novel 1D coordination polymer $[Zn(5,5'-Rda-Rda)(dmf)_2(H_2O)_2]_n$ (**1**) have been characterized by single crystal X-ray structure, IR- and NMR-spectra.

Keywords

Transition metal • IR spectroscopy • Crystal structure • Antimicrobial activity

1 Introduction

Treatment of bacterial infections remains a challenging therapeutic problem because of the increasing number of multidrug-resistant bacteria. There is still a need for some new antibacterial agents, especially those with unique structural features that can influence by different mechanisms of action.

Heterocyclic compounds have often been used in medicinal chemistry as drugs or as pharmacophore moieties for producing the new potential drugs. In the group of heterocycles there are molecules containing the rhodanine (Rda) ring, which includes the five-membered thiazolidine with exocyclic sulfur and oxygen atoms (Fig. 1a).

Rhodanine moiety is present in many molecules showing various pharmacological activities: antidiabetic [1],

antifungal [2], antimicrobial [3], pesticidal [4] and anticancer [5] activities. Amongst the biologically active compounds, there are also the rhodanine-3-carboxylic acids, which are the rhodanine derivatives. They can be used as substrates in various syntheses of other rhodanine derivatives.

The rhodanine-3-acetic acid (2-(4-oxo-2-thioxothiazolidin-3-yl)acetic acid) (HRda), (Fig. 1b) has become an interesting heterocycle that in addition to the hetero-donor atoms: N, O and S of Rda contains the carboxyl group ligand. In this work, we have studied the impact of the presence of the ring hetero-atoms in ligand upon the structure of complexes. Thus, combination of Zn (II) metal ion and (HRda) resulted in coordination compound $[Zn(5,5'-Rda-Rda)(dmf)_2(H_2O)_2]_n$ (**1**), its structure being characterized by single-crystal X-ray diffraction, IR-, and RMN-spectra. X-ray structural analysis of the metal assemblies reveal polymeric structure that could be obtained based on the used organic ligand. In compound **1** the bridge ligand (*E*)-2,2'-(4,4'-dioxo-2,2'-dithioxo-2H,2'H-[5,5'-bithiazolylidene]-3,3'(4H,4'H)diyl) diacetic acid $(5,5'-Rda-Rda)^{2-}$ was obtained as a result of the autocondensation of HRda. The retrieval of data from the Cambridge Structural Database (CSD) [6] revealed that the structures of HRda and its monohydrate are there present [7, 8]. Also the three structures of Sn(IV) compounds with HRda were found, which coordinate in a bidentate-chelated mode to the central metal atom, leading to the formation of mono-, tetra- and hexanuclear compounds [9].

2 Experimental

2.1 Materials and Methods

All reagents and solvents were obtained from commercial sources and were used without further purification.

Elemental analysis was performed on an Elementary Analysensysteme GmbH Vario El III elemental analyzer.

The IR spectra were obtained in Nujol on a FT IR Spectrum-100 Perkin Elmer spectrometer in the range of $650\text{--}4000\text{ cm}^{-1}$.

A. Vitiu (✉) · D. Chișca · P. Bourosh
Institute of Applied Physics, Academiei 5, Chisinau,
Republic of Moldova
e-mail: vitiualiona@gmail.com

A. Vitiu · E. Gorincioi · E. Coropceanu
Institute of Chemistry, Chisinau, Republic of Moldova

D. Chișca · E. Gorincioi · E. Coropceanu · P. Bourosh
Tiraspol State University, Chisinau, Republic of Moldova

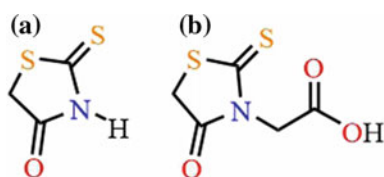


Fig. 1 Structure formulae of: **a** rhodanine and **b** rhodanine-3-acetic acid

2.2 Synthesis of [Zn(5,5'-Rda-Rda)(dmf)₂(H₂O)₂]_n (1)

To a hot solution of Zn(BF₄)₂·nH₂O (0.024 mmol), HRda (0.04 mmol) was added and the mixture was dissolved in H₂O (10 mL), CH₃OH (5 mL) and 10 drops of dimethylformamide (dmf) were subsequently added. The reaction mixture was heated for 10 min, filtered off and then slowly cooled to room temperature giving brown crystals. Yield: 70%. Anal. calc. for C₁₆H₂₂N₄O₁₀S₄Zn₁ (%): C-30.80; H-3.55; N-8.98. Found: C-30.21; H-3.37; N-8.46.

IR (cm⁻¹): 3854(w), 3671(s), 2988(w), 2908(m), 2552(s), 1794(s), 1724(m), 1427(w), 1396(m), 1313(w), 1218(w), 1190(w), 1036(m), 979(s), 856(s), 776(m), 718(s).

2.3 NMR-Spectra

¹H NMR (400.13 MHz, DMSO-*d*₆, δ, ppm): 7.95 (s, dmf), 2.89 (s, dmf), 2.73 (s, dmf), 2.40 (2H, s, HC-CH), 2.53 (s, 4H, N-CH₂). ¹³C NMR (100.61 MHz, DMSO-*d*₆, δ, ppm): 174.63 (C = O), 163.30 (dmf), 35.70 (dmf), 34.91 (N-CH₂), 31.30 (dmf), 29.38 (HC-CH) (the atoms in the C = S and COO groups were not detected).

2.4 X-ray Crystallography

X-ray diffraction measurements for **1** were carried out at room temperature on an “Xcalibur E” diffractometer equipped with CCD area detector and a graphite monochromator utilizing MoK α radiation. Final unit cell dimensions were obtained and refined on an entire data set. All calculations to solve the structures and to refine the proposed models were carried out with the SHELXS97 program package [10]. All non-hydrogen atoms were refined anisotropically and hydrogen atoms refined isotropically.

2.5 Antibacterial Activity

Two bacterial strains and one yeast strain were obtained from the American Type Culture Collection (ATCC). Reference strains included the Gram positive bacteria *Staphylococcus aureus* (ATCC 6538), the Gram negative bacteria

Escherichia coli (ATCC 25922), and one yeast strain, *Candida albicans* (ATCC 10231). The bacterial cultures were maintained on nutrient agar slants. The antibacterial activities of the compound **1** were assessed based on the determination of the Minimal Inhibitory Concentrations (MICs) [11].

3 Results and Discussion

3.1 NMR Data

¹H and ¹³C NMR spectral studies of complex **1** confirmed its structure in DMSO-*d*₆ solution.

The 1D (¹H and ¹³C) and 2D heteronuclear (¹H/¹³C HSQC and ¹H/¹³C HMBC) NMR experiments were performed through standard pulse sequences. The ¹H and ¹³C NMR characterization of compound **1** was presented above. Additionally, it should be mentioned that in the ¹H spectrum many signals are present in 2.71–2.93 ppm region characterizing different species of coordinated dmf molecules, the broad peak of some residual after crystallization methanol at δ 4.03 ppm being also attested (Fig. 2). Long-range correlations found by ¹H/¹³C HMBC NMR experiment corroborated the assignment of signals for ¹H and ¹³C nuclei, also confirming the co-existence of various species of dmf, δ 2.71–2.99/163.3–165.7 ppm (Fig. 3).

3.2 Crystal Structure

Compound **1** was obtained as a result of an unusual condensation of RdaH, which occurred in reaction with zinc tetrafluoroborate hydrate in methanolic solution in the presence of dimethylformamide. The X-ray experiment for

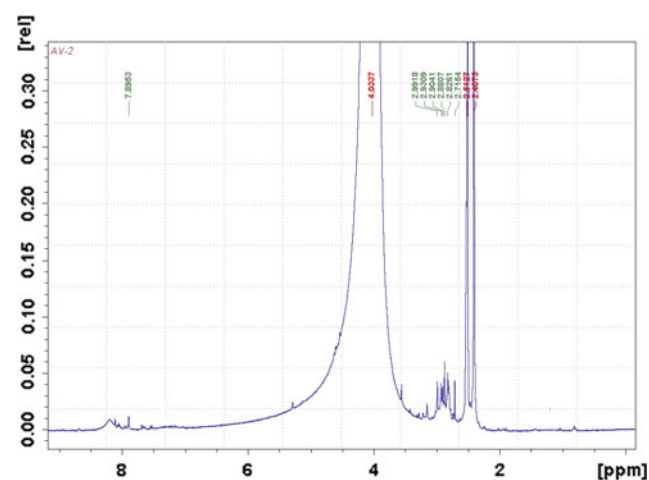


Fig. 2 ¹H NMR spectrum of complex **1**

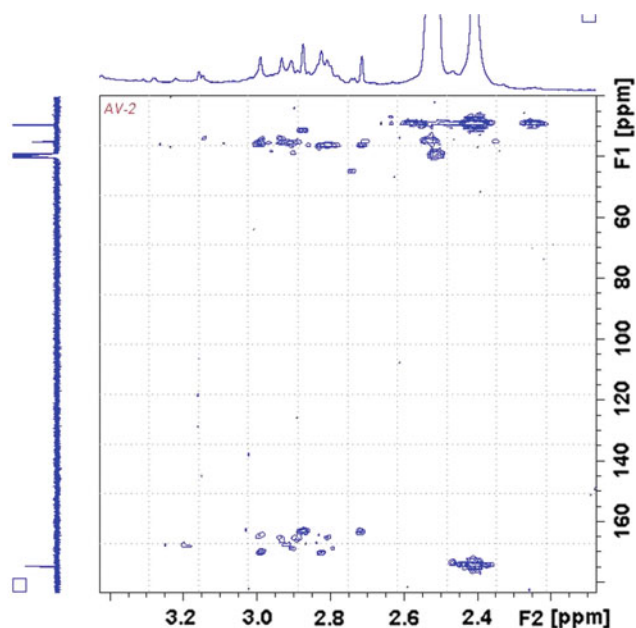


Fig. 3 Fragment of $^1\text{H}/^{13}\text{C}$ HMBC NMR spectrum of complex **1**

compound **1** has shown that it crystallizes in monoclinic $P2_1/c$ spatial group: $a = 15.6602(12)$, $b = 5.1186(3)$, $c = 17.3621(15)$ Å, $\beta = 114.245(10)^\circ$, $V = 1268.97(16)$ Å³ for $Z = 2$.

As a result of the determination of the crystal structure it was established that two metal atoms, two 5,5'-Rda-Rda²⁻ anions, four dimethylformamide molecules and four water molecules were found in the unique cell. Zinc atom is in a special position. Analysis of the structure of the foregoing compound determined that the central metal coordination coordinate takes the form of an octahedron consisting of the set of O6 donor atoms, two oxygen atoms belonging to the two anions 5,5'-Rda-Rda²⁻ and the other four oxygen atoms belonging to the two dmf molecules and the two water molecules (Fig. 4, Table 1).

The crystal of compound **1** consists of centrosymmetric coordinate polymers, the formation of which is caused by the

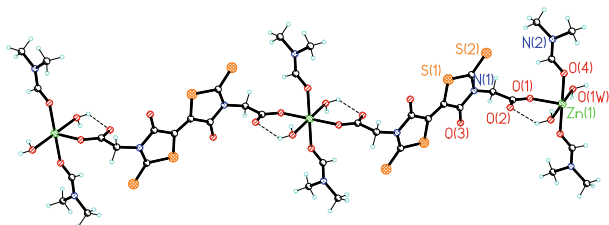


Fig. 4 The structure of a fragment of the coordination polymer $[\text{Zn}(5,5'\text{-Rda-Rda})(\text{dmf})_2(\text{H}_2\text{O})_2]_n$ (**1**)

Table 1 Bond distances (Å) and angles ($^\circ$) between the crystallographic independent atoms in the **1** coordination core

Bond	d (Å)	Angle	ω (deg)
Zn(1)–O(1)	2.087(3)	O(1)–Zn(1)–O(4)	92.3(2)
Zn(1)–O(4)	2.138(4)	O(1)–Zn(1)–O(1w)	88.8(1)
Zn(1)–O(1w)	2.067(3)	O(1)–Zn(1)–O(4)#1	87.7(2)
		O(1)–Zn(1)–O(1w)#1	91.2(1)
		O(4)–Zn(1)–O(1w)	88.5(2)
#1 $-x + 2,$ $-y + 1, -z + 1$		O(4)–Zn(1)–O(1w)#1	91.5(2)

bridge function of the 5,5'-Rda-Rda²⁻ bideprotonate organic ligand, which coordinates in a monodentate mode by two oxygen atoms on two metal atoms (Fig. 4). These 1D polymers are stabilized by a hydrogen bond O(1w)–H \cdots O(2) with the participation of the water molecule, while this hydrogen atom of water molecules is entrained in the intermolecular hydrogen bonding O(1w)–H \cdots O(2)*. As a result, the polymer chains are bonded in layers by means of hydrogen bonds. These layers are also established by C–H \cdots O fine intermolecular hydrogen bonds. The interactions of type S \cdots S (3.493 Å) assemble the layers in a three-dimensional network.

3.3 Antimicrobial Activity

Various infectious diseases and increasing microbial resistance are major concerns in the 21st century, revealing the steadily decreasing potencies of prevalent antibiotics. To combat this problem, there is a need to explore various resources, which can expand the antibiotic spectrum [12, 13]. Keeping this in mind, compound **1** was screened for its antimicrobial potential against two bacterial strains-pathogens of medical relevance, which are difficult to treat and eradicate worldwide, mainly due to their resistance to multiple antibiotics. *Escherichia coli* is a pathogen capable of causing a wide array of infections in humans, including urinary tract infections, neonatal meningitis and rarely hemolytic–uremic syndrome, peritonitis, mastitis and septicemia. *Staphylococcus aureus* is a well-known pathogen, responsible for many hospital and community-acquired infections, producing abscesses filled with pus and damaged leukocytes surrounded by necrotic tissue. The analyzed compound **1** has revealed significant antifungal activity for selected strains of *Candida albicans* species, one of the most important opportunistic fungal pathogens, which can harmlessly colonize the gastrointestinal tract, mouth, skin and

urogenital system [14, 15]. However, it can also cause infections, especially among people with weakened immune systems, attacking the skin, mucous membranes, getting into the blood, and attacking internal organs. Risk factors that are conducive to the development of systemic infections caused by *Candida* include: long-term stay in intensive care units, surgery, broad-spectrum antibiotic intake, and immunosuppressants [16, 17].

The MIC was worked out by the agar dilution method. A stock solution of the studied compound $[\text{Zn}(5,5'\text{-Rda-Rda})(\text{dmf})_2(\text{H}_2\text{O})_2]_n$ (**1**) with 2.00 mmol/L concentration were prepared and incorporated into Muller Hinton agar medium for bacteria, and yeast malt extract medium for *Candida albicans*. These plates were then inoculated with 0.1 mL of the activated bacterial/yeast strains by streaking with a sterile tooth pick. The plates were incubated at 37 °C for bacteria and 25 °C for yeast for 24 h and the lowest concentration of the extract causing complete inhibition of the bacterial growth was taken as the MIC.

The study of antibacterial and antifungal activity showed that compound $[\text{Zn}(5,5'\text{-Rda-Rda})(\text{dmf})_2(\text{H}_2\text{O})_2]_n$ (**1**) presented antifungal activity in the range of all the studied concentrations, the MIC being 1.2 µg/mL (dilution 1:1024) and antibacterial in the case of 1:8 dilutions towards *E. coli* and 1:16 dilutions towards *S. aureus*.

MICs values for the studied compound against gram-positive bacteria *S. aureus* range from 70–413 µg/mL, and gram-negative bacteria *E. coli*—range of 137–413 µg/mL. As a result of the biological assays, it has been demonstrated that compound **1** exhibits excellent antifungal and antibacterial properties at low MIC values (µg/mL), which are well above those characteristic of the reference compounds in the literature [18].

4 Conclusions

The combination of Zn(II) salt with the (2-(4-oxo-2-thioxothiazolidin-3-yl)acetic acid) resulted in new bridge ligand (E)-2,2'-(4,4'-dioxo-2,2'-dithioxo-2H,2'H-[5,5'-bithiazolylidene]-3,3'-(4H,4'H)-diyl)diacetic acid, as a result of the autocondensation of (2-(4-oxo-2-thioxothiazolidin-3-yl)acetic acid). The newly obtained Zn(II) complex **1** represents a 1D polymer. The results of microbiological studies revealed significant activity of compound **1** over *Candida albicans*, *E. coli* and *S. aureus* cultures, indicating its possible use as an antifungal and antimicrobial preparation.

Conflict of Interest The authors declare that they have no conflict of interest.

References

- Murugan, R., Anbazhagan, S., Narayanan, S.: Synthesis and in vivo antidiabetic activity of novel dispiropyrrolidines through [3 + 2] cycloaddition reactions with thiazolidinedione and rhodanine derivatives. *Eur. J. Med. Chem.* **44**, 3272–3279 (2009). <https://doi.org/10.1016/j.ejmech.2009.03.035>
- Inamori, Y., Okamoto, Y., Takegawa, Y., et al.: Insecticidal and antifungal activities of aminorhodanine derivatives. *Biosci. Biotechnol. Biochem.* **62**, 1025–1027 (1998)
- Sortino, M., Delgado, P., Juarez, S., et al.: Synthesis and antifungal activity of (Z)-5-arylidenerhodanines. *Bioorg. Med. Chem.* **15**, 484–494 (2007). <https://doi.org/10.1016/j.bmc.2006.09.038>
- Muro, C., Yasuda, M., Sakagami, Y., et al.: Inhibitory activities of rhodanine derivatives on plant growth. *Biosci. Biotechnol. Biochem.* **60**, 1368–1371 (1996). <https://doi.org/10.1271/bbb.60.1368>
- Azizmohammadi, M., Khoobi, M., Ramazani, A., et al.: 2H-chromene derivatives bearing thiazolidine-2,4-dione, rhodanine or hydantoin moieties as potential anticancer agents. *Eur. J. Med. Chem.* **59**, 15–22 (2013). <https://doi.org/10.1016/j.ejmech.2012.10.044>
- Groom, C., Bruno, I., Lightfoot, M., et al.: The Cambridge structural database. *Acta Crystallogr. A* **72**, 171–179 (2016). <https://doi.org/10.1107/S2052520616003954>
- Barakat, A., Ali, M., Al-Majid, A., et al.: Crystal structure of 2-(4-oxo-2-thioxothiazolidin-3-yl)acetic acid monohydrate, C₅H₇NO₄S₂. *Kristallogr.-New Cryst. Struct.* **232**, 141–142 (2017). <https://doi.org/10.1515/ncrs-2016-0197>
- Tejchman, W., Skorska-Stania, A., Zeslawska, E.: The crystal structures of three Rhodanine-3-Carboxylic Acids. *J. Chem. Cryst.* **46**, 181–187 (2016). <https://doi.org/10.1007/s10870-016-0644-0>
- Zhang, R., Sun, J., Ma, C.: Structural chemistry of mononuclear, tetranuclear and hexanuclear organotin(IV) carboxylates from the reaction of di-n-butyltin oxide or diphenyltin oxide with rhodanine-N-acetic acid. *J. Organomet. Chem.* **690**, 4366–4372 (2005). <https://doi.org/10.1016/j.jorgchem.2005.07.005>
- Sheldrick, G.: Crystal structure refinement with SHELXL. *Acta Crystallogr. A* **71**, 3–8 (2015). <https://doi.org/10.1107/S0108767307043930>
- Babahan, I., Coban, E., Biyik, H.: Synthesis, characterisation and antimicrobial activities of vicdioxime derivatives containing heteroaromatic hydrazine groups and their metal complexes. *Maejo Int. J. Sci. Technol.* **7**, 26–41 (2013). <https://doi.org/10.14456/mijst.2013.2>
- Arora, D., Onsare, J.: In vitro antimicrobial evaluation and phytoconstituents of *Moringa oleifera* pod husks. *Ind. Crop. Prod.* **52**, 125–135 (2014). <https://doi.org/10.1016/j.indcrop.2013.09.016>
- Cardoso, J., Galvão, A., Guerreiro, S., et al.: Carvalho, antibacterial activity of silver camphorimine coordination polymers. *Dalton Trans.* **45**, 7114–7123 (2016). <https://doi.org/10.1039/C6DT00099A>
- Wu, T., Mitchell, B., Carothers, T., et al.: Molecular analysis of the pediatric ocular surface for fungi. *Curr. E Res.* **26**, 33–36 (2003). <https://doi.org/10.1076/ceyr.26.1.33.14253>
- Jackson, B., Wilhelmus, K., Mitchell, B.: “Genetically regulated filamentation contributes to *Candida albicans* virulence during corneal infection. *Microb. Pathog.* **42**, 88–93 (2007). <https://doi.org/10.1016/j.micpath.2006.11.005>
- Kontoyiannis, D., Mantadakis, E., Samonis, G.: Systemic mycoses in the immunocompromised host: an update in antifungal therapy. *J. Hosp. Infect.* **53**, 243–258 (2003). <https://doi.org/10.1053/jhin.2002.1278>

17. Sydnor, E., Perl, T.: Hospital epidemiology and infection control in acute-care settings. *Clin. Microbiol. Rev.* **24**, 141–173 (2011). <https://doi.org/10.1128/CMR.00027-10>
18. Kshirsagar, V., Gandhe, S., Gautam, M.: Synthesis and antimicrobial screening for Rhodanine complexes of Iron, Copper and Zinc. *Asian J. Chem.* **20**, 4955–4956 (2008)

Phenomena of Radiative Recombination in Single Crystals of Cadmium Thiogallate with Cadmium (CdGa₂S₄:Cd) or Sulfur (CdGa₂S₄:S) Excess

E. Arama, V. Pantea, T. Shemyakova, and V. Vovc

Abstract

The experimental results related to the influence of non-stoichiometry on the emission spectra of CdGa₂S₄ single crystals excited by accelerated electrons are presented. Cadmium thiogallate single crystals with the excess of cadmium or sulfur were prepared by the method of chemical transport reactions with iodine, and the cathodoluminescence spectra of CdGa₂S₄:Cd and CdGa₂S₄:S were studied. A model of energy levels and optical transitions for this compound is proposed.

Keywords

Ternary semiconductor • Cadmium thiogallate • Non-stoichiometry • Cathodoluminescence

1 Introduction

Cadmium thiogallate CdGa₂S₄ is a wide-gap semiconductor ($E_g = 3.77$ eV at 10 K [1]) with direct optical transitions. The complex chemical composition, with two types of cations, is responsible for the broad spectrum of local states in the band gap of CdGa₂S₄, the high photosensitivity of this compound [2], intensive photoluminescence [3] and cathodoluminescence [4]. These characteristics are of great interest both for fundamental investigations and for practical applications in nonlinear optics and optoelectronics [5]. The main physical parameters were studied in multiple theoretical and experimental works ([6–9] and references therein).

As for many ternary A^{II}B₂^{III}C₄^{VI} compounds, CdGa₂S₄ crystals can be grown from a vapor phase [10] or by the vertical Bridgman method [11]. These materials are also suitable for many applications, for example, as acousto-optic and electro-optic modulators and switches, optical filters, frequency doublers, optical parametric oscillators and photovoltaic solar cells [12]. Cadmium thiogallate is promising for application in X-ray dosimetry [13], as photoresistors and optical narrow-band filters [14, 15].

A number of research works were accomplished using thin film samples of CdGa₂S₄. Thin polycrystalline films of CdGa₂S₄ were prepared by the vacuum evaporation and flash evaporation methods [16]; their optical absorption spectra were studied in the visible range of radiation. El-Nahass et al. studied the dark electrical conductivity and dielectric properties of cadmium thiogallate films [17]; the structural and optical properties of thermally evaporated CdGa₂S₄ nanostructure films are reported in [18]. Photoelectric properties of cadmium thiogallate films and the influence of γ -radiation on these properties have been investigated [19, 20].

Single crystals of the CdGa₂S₄ ternary compound were grown either from melt or by chemical-vapor deposition. Several types of photosensitive structures—Schottky barriers, heterostructures, photoelectrochemical cells, and natural-protein-CdGa₂S₄ barriers—were formed for the first time on the basis of single crystals of cadmium thiogallate, and their photoelectric properties were studied. The main parameters of these structures are determined, and it is concluded that they can be used in photodetectors [21]. The cadmium thiogallate crystals were also used to produce In/CdGa₂S₄ surface-barrier structures and H₂O/CdGa₂S₄ photoelectrochemical cells [22].

Note, that the parameters of semiconductor materials are closely linked with their structure and may substantially differ in dependence on the method of preparation of the samples and the measurement procedure employed. It was suggested in [20] that annealing of CdGa₂S₄ thin films leads

E. Arama · V. Vovc
University of Medicine and Pharmacy “Nicolae Testemitanu”,
Chisinau, Moldova

V. Pantea
Technical University of Moldova, Chisinau, Moldova

T. Shemyakova (✉)
Institute of Applied Physics, 5 Academiei, Chisinau, Moldova
e-mail: shemyakova@yahoo.com

to decreasing of cadmium content in the films and induces shifts of the curves of intrinsic photoconductivity.

In several works the dependence of physical parameters on the composition of cadmium thiogallate crystals was investigated. In [23] the Raman, cathodoluminescence, and photoconductivity spectra of cadmium thiogallate crystals obtained in synthesis conditions $\text{CdS} + \text{Ga}_2\text{S}_3$ (type A) and for crystals obtained in synthesis conditions $2\text{CdS} + \text{Ga}_2\text{S}_3$ (type B) were studied. The effect of excess CdS in gallium thiogallate (CdGa_2S_4) on the spectrum of defect states in its band gap was investigated. In [24] the variation of photoluminescence (PL) spectra as a function of the composition of cadmium thiogallate crystals was studied. It was stated that the positions of PL bands in blue and near IR spectral ranges are associated with defects in the cation sublattice.

In recent decades semiconductors with bright cathodoluminescence attracted a special attention of researchers since the works on the development of new types of light sources—cathodoluminescent lamps (CLLs)—have been in progress [25–28]. The necessity for these works is determined primarily by the fact that all now existing light sources possess serious limitations [25].

Therefore, it is expedient to test a great variety of semiconducting materials for their applicability as screens for CLLs.

To the best of our knowledge, only a limited number of published papers have been devoted to the study of cathodoluminescence (CL) in CdGa_2S_4 [4, 23, 29, 30]. Since it is important to elucidate the influence of deviations from stoichiometry on the properties of this semiconductor, we manufactured single crystals of cadmium thiogallate with the excess of cadmium ($\text{CdGa}_2\text{S}_4:\text{Cd}$) and with the excess of sulfur ($\text{CdGa}_2\text{S}_4:\text{S}$) and studied their emission spectra excited by accelerated electrons. The technology of preparation of the samples is based on the method of chemical transport reactions where iodine is used as a transport agent. Cathodoluminescence spectra were measured in an installation based on an electron beam microscope UEMB-100K.

2 Results and Discussion

The CL spectra obtained under the excitation of $\text{CdGa}_2\text{S}_4:\text{Cd}$ single crystals by an electron beam at a temperature of 296 K and 80 K are presented in Fig. 1. The cadmium percentage amounts to 0.01%. It can be seen that the blue band is the dominant one at the both temperatures; its maximum shifts from 2.67 to 2.78 eV when the temperature decreases. At the same time, at low temperatures the intensity of the blue band considerably increases, and at a temperature of 80 K it coincides with the red band with the energy maximum at 1.96 eV.

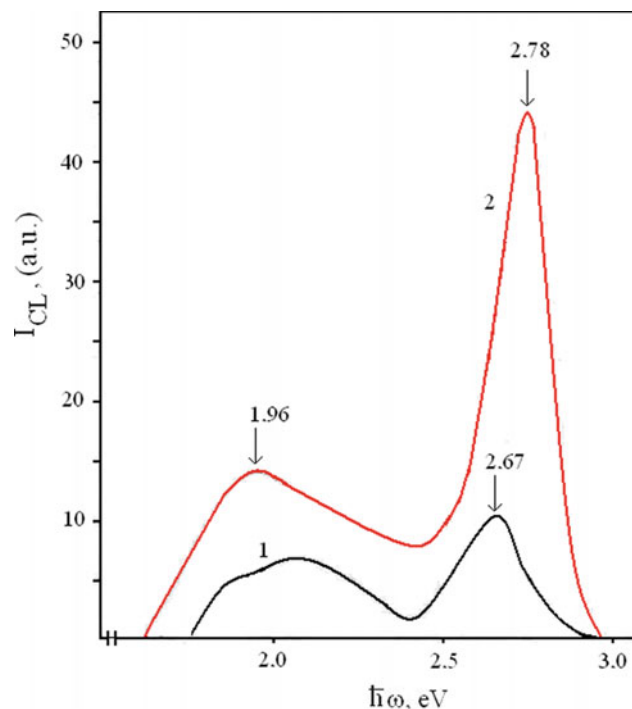


Fig. 1 CL spectra of $\text{CdGa}_2\text{S}_4:\text{Cd}$ (0.01% of Cd). T, K: (1) 296 and (2) 80; $U_a = 60$ keV. The depth of penetration of electrons amounts to $13.6 \mu\text{m}$

The CL spectra of the cadmium thiogallate samples with the excess of sulfur are presented in Fig. 2. Analysis of the experimental results allows one to conclude that the excess

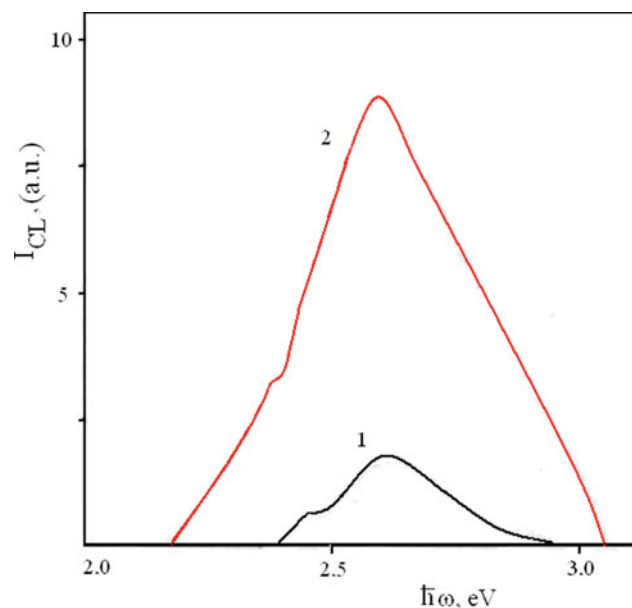


Fig. 2 CL spectra of $\text{CdGa}_2\text{S}_4:\text{S}$ single crystals at 296 K. Sulfur content, %: (1) 0.01, (2) 0.10; $U_a = 60$ keV. The depth of penetration of electrons amounts to $13.6 \mu\text{m}$

of cadmium or sulfur considerably influences the spectral distribution of the integral and radiative energy.

On the basis of the experimental data we can propose a model related to the possible defects associated with the crystal lattice and chemical composition of the ternary compound CdGa_2S_4 . We can suggest the occurrence of the following most simple defects: the sulfur vacancies V_s ; interstitial sulfur ions between the sites of the crystalline lattice S_i ; cadmium vacancies V_{Cd} ; interstitial cadmium between the sites of the crystalline lattice Cd_i ; gallium vacancies V_{Ga} ; interstitial gallium between the sites of the crystalline lattice Ga_i , and substitution defects— Cd_{Ga} and Ga_{Cd} —that appear due to the substitution of the metals in the sites of the crystal lattice. Moreover, the substitution of sulfur by iodine in the sites I_s and interstitial iodine between the sites I_i are possible in CdGa_2S_4 single crystals. Obviously, it is a difficult problem to identify the intrinsic defects if to take into consideration the crystal structure and chemical composition, though it can be solved on the basis of the experimental results.

The preparation of single crystals with deviations from stoichiometric composition, as in our case, and investigation of their luminescence properties can to some degree facilitate the solution of this problem.

When in the initial load prepared for synthesis an excessive amount of one of the components of the ternary compound is introduced, we can suppose that this facilitates the reduction of the concentration of vacancies of the respective element, though the concentration of the substitution defects and interstitial ions between the sites of the crystal lattice should increase. This induces certain changes in the luminescence spectra of the compound with several types of intrinsic defects. The radiation spectrum becomes simpler, since certain bands associated with the defects with predominant concentration dominate. The characteristic luminescent bands of the cadmium thiogallate grown by various methods are presented in Table 1.

The type A crystals are grown by the method of chemical transport reactions; the type C crystals are grown from melted solutions. In our opinion, the blue band in the CL spectrum of the thiogallate with the excess of cadmium (Fig. 1) most probably can be associated with the additional interstitial cadmium Cd_i between the sites of the crystal lattice and the substitution defects Cd_{Ga} . It was proposed and confirmed experimentally in work [30] that the red

luminescent band of the thiogallate is associated with sulfur vacancies. In our case, we can confirm that due to the sulfur excess the concentration of sulfur vacancies decreases; this leads to vanishing of the red band with the maximum at 1.96 eV in the emission spectrum (Fig. 2).

Therefore, we can conclude that the sulfur vacancies can form energy levels of donor type located near the conduction band, though the cadmium vacancies create deep levels of acceptor type.

From the CL spectra of the $\text{CdGa}_2\text{S}_4:\text{Cd}$ samples measured at 296 and 80 K we can see that at low temperature a blue band predominates in the radiation spectrum; its peak shifts from 2.67 eV at a temperature of 296 K to 2.78 eV at 80 K. At the same time, the intensity of the absolute maximum considerably increased, approximately by a factor of 3, and the half-width of the radiation line reduced from 0.40 to 0.30 eV. The high-energy maximum of the CL band 2.78 eV is associated with radiative transitions of free electrons that determine the width of the forbidden energy gap E_g in the range of direct radiative transitions.

The CL spectra measured in $\text{CdGa}_2\text{S}_4:\text{S}$ single crystal samples with different sulfur content (0.01 and 0.10%) have shown that at 296 K a wide emission band with a half-width of (0.5 ± 0.05) eV and energy maximum at 2.61 eV was registered. At the other hand, it was demonstrated that at 80 K the energy distribution in the radiation spectra of the both samples did not change, and in the spectrum a weakly pronounced energy plateau at 2.36 eV was observed. The comparative analysis suggests that: (1) the peak intensities in the spectra of the $\text{CdGa}_2\text{S}_4:\text{S}$ samples are considerably lower than in the spectra of cadmium thiogallate with the cadmium excess; (2) in the radiation spectra of cadmium thiogallate with the sulfur excess the red-orange band is virtually absent; this band is characteristic for CdGa_2S_4 grown by the method of chemical transport reactions when iodine is used as a transport agent.

Generalizing the aforementioned experimental results we propose a model of the energy levels and optical transitions for $\text{CdGa}_2\text{S}_4:\text{Cd}$ and $\text{CdGa}_2\text{S}_4:\text{S}$ single crystals (Fig. 3). Transition (1)—red band (1.96 eV) is identified as a donor-acceptor optical transition; transition (2)—green band (2.33 eV) is a band edge—acceptor transition; transition (3)—an orange band (2.13 eV); transitions 4 and 5 correspond to the blue band with maxima 2.67 and 2.78 eV that we suggest most probably can be associated with interstitial cadmium between the crystal lattice sites and substitution defects Cd_{Ga} .

Table 1 Positions of CL peaks in spectra for two types

Crystal type	Peak position (eV)				
A	2.1	2.33	2.67	2.78	—
C	2.1	2.33	2.67	2.78	3.0

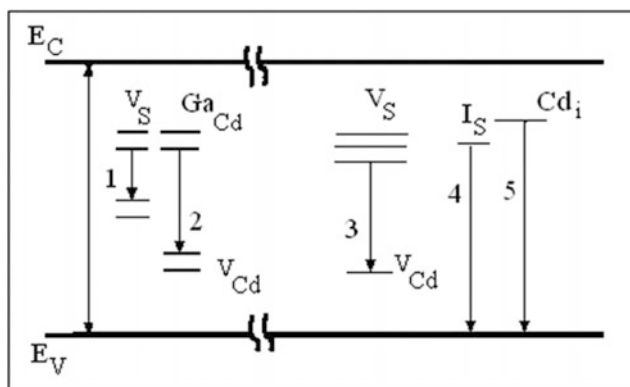


Fig. 3 Scheme of the energy levels and optical transitions related to the emission from CdGa₂S₄:Cd and CdGa₂S₄:S single crystals

3 Conclusions

The correlation between the defects that can possibly form due to the crystal lattice and chemical composition of the ternary compound CdGa₂S₄ was stated. The occurrence of the following simple defects was confirmed: the sulfur vacancies V_s; interstitial sulfur ions between the sites of the crystalline lattice S_i; cadmium vacancies V_{Cd}; interstitial cadmium between the sites of the crystalline lattice Cd_i; gallium vacancies V_{Ga}; interstitial gallium between the sites of the crystalline lattice Ga_i, and the substitution defects—Cd_{Ga} and Ga_{Cd} that appear due to substitution of the metals in the sites of the crystal lattice. Moreover, the substitution of sulfur by iodine in the sites I_s and interstitial iodine between the sites I_i are possible in the CdGa₂S₄ single crystals.

On the basis of the experimental results we can conclude that the excess of Cd or S considerably influences the spectral distribution of the radiative and integral energy. We can also state that the sulfur vacancies can form energy levels of the donor type located near the conduction band, though the cadmium vacancies create deep levels of the acceptor type. A model of the energy levels and radiative optical transitions in CdGa₂S₄:Cd and CdGa₂S₄:S single crystals was proposed.

Conflict of Interest The authors declare that they have no conflict of interest.

References

- Georgobiani, A.N., Ozerov, Y.V., Radautsan, S., Tiginyanu, I.: Modulation spectroscopy study of fundamental optical transitions in CdGa₂S₄. *Fiz Tverd Tela* **23**, 2094–2099 (1981)
- Radautsan, S., Georgobiani, A., Tiginyanu, I.: II-III₂-VI₄ compounds: properties and trends for applications. *Progr. Crystal Growth Charact.* **10**, 403–412 (1984)
- Guzzi, M., Grillii, E.: Localized levels and luminescence of AB₂X₄ semiconducting compounds. *Mater. Chem. Phys.* **11**, 295–304 (1984)
- Machuga, A., Zhitar, V., Arama, E.: Interband emission of cadmium thiogallate. *Semiconductors* **34**, 626–628 (2000)
- Kumar, P., Sahariya, J., Soni, A., Bhamu, K.: Optoelectronic analysis of CdGa₂X₄ (X = S, Se): a promising material for solar cells. *Mater. Sci. Forum* **900**, 69–73 (2017)
- Goryunova, N.A.: *Slozhnyealmazopodobnye poluprovodniki*. Sov radio, Moscow (1968)
- Berger, L., Prochukhan, V.: *Ternary diamond-like semiconductors*. Consultants Bureau, New York (1969)
- Manjon, J., Ursaki, V., Tiginyanu, I. (eds.): *Pressure-induced phase transitions in AB₂X₄ chalcogenide compounds*. Springer, Berlin, Heidelberg (2014)
- Derid, Yu., Radautsan, S., Tiginyanu, I.: *Mnogokomponentnyye khalkogenidy A^{II}B₂^{III}C₄^{VI}*. Stiinta, Kishinev (1990)
- Nitsche, R., Bolsterli, H., Lichtensteiger, M.: Crystal growth by chemical transport reactions-I: binary, ternary, and mixed-crystal chalcogenides. *J. Phys. Chem. Solids* **21**, 199–205 (1961)
- Feigelson, R., Route, R.: Crystal growth and optical properties of CdGa₂S₄. *Progr. Crystal Growth Charact.* **10**, 189–197 (1984)
- Gentile, A.: Devices using ternary or multinary compounds. *Progr. Crystal Growth Charact.* **10**, 241–256 (1984)
- Mustafaeva, S., Asadov, M., Guseinov, D.: X-ray dosimetric properties of vapor grown CdGa₂S₄ single crystals. *Inorg. Mater.* **46**, 587–589 (2010)
- Isaev, V., Serezhkin, V., Avanesov, A.: Correlation between optical and crystal-structure characteristics of single crystals of triple and mixed chalcogenides. *Ekol Vestn Nauchn Tsentrov CHES* **2**, 61–68 (2008)
- Stamov, I., Syrbu, N., Parvan, V., Zalamai, V., Tiginyanu, I.: The band structure of birefractive CdGa₂S₄ crystals. *Opt. Commun.* **309**, 205–211 (2013)
- Kshirsagar, S.: Optical absorption in thin films of CdGa₂S₄ and CdGa₂Se₄. *Thin Solid Films* **45**, L5–L8 (1977)
- El-Nahass, M., El-Shazly, E., El-Barry, A., Omar, H.: *J. Mater. Sci.* **46**, 5743–5750 (2011)
- El-Nahass, M., El-Barry, A., El-Shazly, E., Omar, H.: Structural and optical properties of thermally evaporated cadmium thiogallate CdGa₂S₄ nanostructure films. *Eur. Phys. J. Appl. Phys.* **52**, 10502 (2010)
- Mak, V., Ebragim, A.: Photoelectric properties of cadmium thiogallate films. *Fiz. Techn. Poluprov.* **28**, 1714–1719 (1994)
- Mak, V., Ebragim, A.: Influence of γ -radiation on photoelectric properties of thin cadmium thiogallate films. *Zhurn Tekhn Fiz* **65**, 179–182 (1995)
- Rud, V., Rud, Y., Vaipolin, A., Bodnar, I., Fernelius, N.: Photosensitive structure on CdGa₂S₄ single crystals. *Semiconductors* **37**, 1283–1290 (2003)
- Bodnar, I., Rud, V., Rud, Y.: Growth and properties of CdGa₂S₄ single crystals. *Inorg. Mater.* **40**, 102–106 (2003)
- Venger, E., Ermolovich, I., Milenin, V., Papusha, V.: The effect of composition on the properties and defect structure of the CdS–Ga₂S₃ solid solution. *Semiconductors* **36**, 763–771 (2002)
- Georgobiani, A., Derid, Yu., Radautsan, S., Tiginyanu, I.: Variation of radiative properties of cadmium thiogallate with variation of its composition within the homogeneity range. *Kratkie Soobshcheniya Fiz (FIAN)* **10**, 46–51 (1983)
- Sheshin, E., Kolodyazhnyj, A., Chadaev, N., Getman, A., Danilkin, M., Ozol, D.: Prototype of cathodoluminescent lamp

- for general lighting using carbon fiber field emission cathode. *J. Vac. Sci. Technol.*, B **37**, 031213 (2019)
26. Bugaev, A., Sheshin, E., Ozol, D., Myo, M., Danilkin, M., Vereschagina, N.: Modern trends in the development of UV-sources of germicidal range. *Bull. Moscow State Region. Univ. (Phys. Math.)* **4**, 24–38 (2017)
 27. Ozol, D.: Preliminary study of cathode ray tube phosphors on the basis of nanocrystal quantum dots. In: 29th International Vacuum Nanoelectronics Conference, IVNC, pp. 1–2, Vancouver, BC, 15–16 July 2016 (2016)
 28. Vereschagina, N., Danilkin, M., Kazaryan, M., Ozol, D., Sheshin, E., Spassky, D.: Cathodoluminescent UV-radiation sources. In: Proceedings SPIE 10614, XIII International Conference Atomic and Molecular Pulsed Lasers 106141F, Tomsk, Russia (2017)
 29. Park, H., Kim, Y.-S., Hyun, S.-Ch., Kim, Ch-D, Jin, M.-S., Kim, D.-T., Jang, K., Kim, H.-G., Kim, W.-T.: Anomalous dependence of photoluminescence properties on composition x in $\text{Cd}_{1-x}\text{Mn}_x\text{Ga}_2\text{S}_4$ mixed crystals. *Phys. Stat. Sol. c* **3**, 2915–2918 (2006)
 30. Machuga, A.: Recombination phenomena in single crystals of cadmium thiogallate and zinc-indium sulfides at electron excitation. Extended Abstract of Cand. Phys.-Math. Sci. Dissertation. Kishinev (1986)

Design and Evaluation of a Low Cost Electrical Muscle Stimulator (EMS) with Biopac

I. Şerban, C. Drugă, I. Tătulea, B. Braun, and R. Necula

Abstract

The present paper is aimed towards designing a low-cost electrical muscle stimulation device and evaluating the muscle activity using high performance electromyography device, BIOPAC. The electrical muscle stimulator is essentially an electronic device which has the ability to contract the muscles via electrical current sent to the electrodes. The power of the device is provided by a 9 V battery, which ensures the portability of the device. The electrical muscle stimulation is provided mainly by two timers that are designed to carry electrical impulses and count them, a transformer, a LED that monitors the transmission of the impulse and three potentiometers which are used to change the length, the duration and the amplitude of the impulse that will be sent to the muscle via electrodes. This type of electronic device addresses patients with cervical spine pain, to increase muscle strength, warming and relaxation. By using this EMS device in certain pathologies of the neck, the patients are able to relieve neck pain without using medication. Biopac is used for evaluating and monitoring differences between a natural and an electrical stimulated contraction.

Keywords

Biopac • EMG • EMS • Muscle

1 Introduction

Applying electricity to relieve pain dates back to antiquity. It is assumed that as early as 9000 BC, magnetite and amber were used by ancient Egyptians to treat headaches and arthritis. A very effective approach was the contact with electric fish. There are indications that ancient Egyptians used “the electric catfish of the Nile” for the treatment of severe painful conditions. Their power has been demonstrated in tomb paintings since 2750 BC [1].

Similarly, Hippocrates (420 BC) used the action of electric fish (the torpedo fish). Roman physicist Scribonius Largus was the first in the medical compositions to prescribe direct contact with torpedo fish for pain relief in patients with gout, arthritis or headache. Torpedo fish generate discharges from 8 to 220 V, depending on the species. The average current is about 50 V.

In the 18th and 19th centuries, the treatment of pain with natural electrical energy was replaced by the invention of electrical devices. According to Turrell, the following four phases of electrotherapy must be mentioned: the first phase consists of the application of static or atmospheric electricity, called Franklinism. This phase is characterized by high voltage and low currents in the milliampered order, which were derived from a machine for producing electricity through friction that induced sudden shocks and sparks. The method dates from 1672 when German engineer Otto von Guericke developed triboelectricity through an electrostatic sphere.

The first medical use of static electricity was carried out in 1744 in Europe by German doctor Christian Kratzenstein. A few years later, in 1752, an American scientist and politician Benjamin Franklin invented the “magic square” that is the simple form of a condenser capable of delivering powerful shock to the treatment of various diseases.

The second phase was the galvanic current that occurred around the 1800 s, which allowed the direct contact of dynamic electric energy along the nerves without shocks and sparks.

I. Şerban (✉) · C. Drugă · I. Tătulea · B. Braun
Product Design, Mechatronics and Environment Department,
Faculty of Product Design and Environment, Transylvania
University, University Street, no.1, Braşov, Romania
e-mail: ionel.serban@unitbv.ro

R. Necula
Faculty of Medicine, Transylvania University, Braşov, Romania

The application of galvanic current was not without side effects. Prolonged use has led to necrotic changes in tissues. This harmful action was later used to destroy superficial tumors, including prostate cancer.

The third step was the introduction of faradism. British scientist Michael Faraday, in 1832, used voltaic cells and discovered that the flow of electricity could be intermittently (interrupted) and in alternate directions. Stimulation was performed with a short pulse duration (millisecond), thus preventing any risk of tissue damage. The most important promoter of faradism was the French physicist, Guillaume Duchenne (“the father of electrotherapy”), who used this technique, in particular, to stimulate the muscles.

The fourth phase was the discovery of high frequency currents by the French physician Jacques Arsène d’Arsonval in 1888, who observed that frequencies beyond 5000 Hz decreased excitement of the muscles. Throughout the 19th century, the analgesic effects of electricity have become very popular and have enjoyed the “golden age”. Electrotherapy has been used for many dental, neurological, psychiatric and gynecological disorders.

One potential reason is that when you maximally contract a muscle, at best, only 30% of all your muscle fibers are in a state of contraction. The remaining 70% are dormant and awaiting recruitment when the contracting fibers fatigue. With EMS you can potentially electrically stimulate these resting muscle fibers to improve their strength. Clinically, EMS appears to be more effective when the muscles are very weak and you have difficulty performing normal anti-gravity exercises [2].

The electro stimulator plays an important role in stimulating muscles for toning, vascularization and relieving pain. This device is not intended for people with cancer, with wounds on the skin, heart problems, with very sensitive skin, fever, abnormal blood pressure or people who have implanted a pacemaker [3, 4].

2 Methods and Materials

The drawing design of the circuit was done through a specialized software called OrCAD, which is a software package for computer-aided design of electronic circuits, whose manufacturer is Cadence Design Systems.

The circuit design was designed to simulate this device using the PSpice simulation module included in the OrCAD program. During the design, the cervical muscle stimulation circuit was taken into account, and due to the fact that the program did not incorporate an electrode symbol, they were replaced with a 100 k Ω body resistance.

The purpose of the simulation is to be able to verify the functionality of the electrical circuit of the device and to

provide us with the necessary information to move to the physical part of the device.

In order to perform the simulation, a marker has been placed on the circuit, before the body’s resistance, to be able to observe the stimuli transmitted by the device to the muscle.

Within the stimulus it was chosen a 3-second period and a range of stimulus of 300 ms. Thus, in the resulting graph the duration of a stimulus is 0.05 s, the duration between two stimuli is 0.5 s, and at the output we have a voltage of 80 V (Fig. 1).

Following the simulation, it was noticed the functionality of the device and went over to the next step, practical realization of the device (Fig. 2).

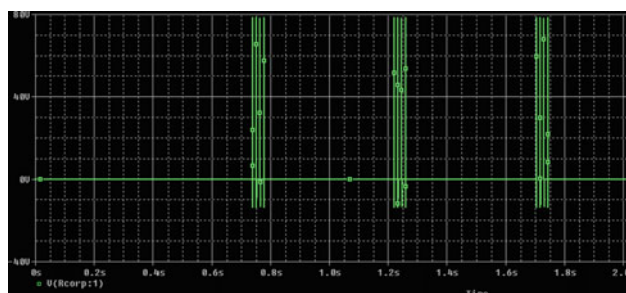


Fig. 1 Pspice simulation

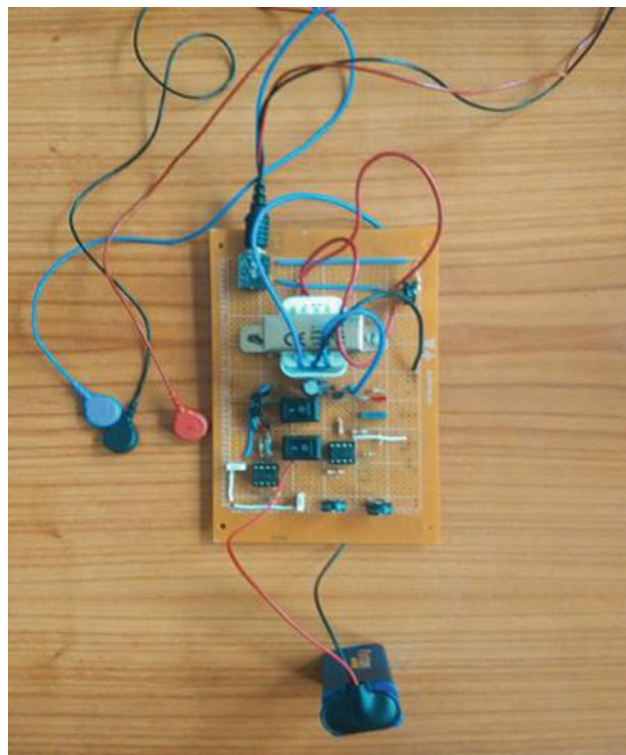


Fig. 2 Cervical muscular electro stimulator

Cervical muscle electrostimulation device consists of the following components: 2 timers 555, 11 different value resistors, one driven to show how pulses are transmitted to the muscles, 3 transistors, 3 potentiometers with which we modulate the signal amplitude, pulse duration and duration between 2 diodes, 5 capacitors, 2 switches used to switch on the device, and 2 electrodes connected to the circuit via the electrodes and designed to transmit the electrical impulses from the device to the muscles.

The current transmitted to the body is of low frequency (50 Hz) because it is in the range 0–1000 Hz.

Following the practical realization it was obtained a maximum current of 1.7 mA and an average current of 0.7 mA.

The value of the output current is changed by a potentiometer which is responsible for changing the amplitude of the signal and another potentiometer has the effect of changing the pulse duration.

Muscle stimulation is performed with a current in the range of 0–80 mA, which means that the value of the device's output current falls within the muscular stimulation range and does not cause any harm to the human body.

The output voltage of the device ranges from 240 to 380 mV.

3 Results and Discussion

Biopac MP 150 acquisition system was used to monitor muscle activity when a natural contraction occurred and when electrical pulses from the electrostimulation device were transmitted to the muscles of the neck [5].

In order to monitor muscle activity, we first need to start the Biopac acquisition system and make the necessary settings (Fig. 3).



Fig. 3 Biopac monitoring system

The acquisition frequency was set between 10 and 500 Hz, Gain to a value of 2000.

The electrodes, noninvasive, were placed on the trapezius muscle (Fig. 4).

EMG 100C bio potential amplification module was used to connect the electrodes to the Biopac EMG module [6]. After connecting the electrodes to the Biopac acquisition system, they were positioned as follows:

- the “-” electrode was placed at the end of the trapezius muscle;
- the “+” electrode was placed in the middle of the trapezius muscle;
- the “ground” electrode was placed on bone structure of the shoulder (Fig. 5).

The EMS electrodes were placed near to the EMG electrodes (plus and minus) (Fig. 6).

After positioning the electrodes, AcqKnowledge 3.9.1 application was set to monitor in real time and record the muscle activity. Monitoring was done in three steps.

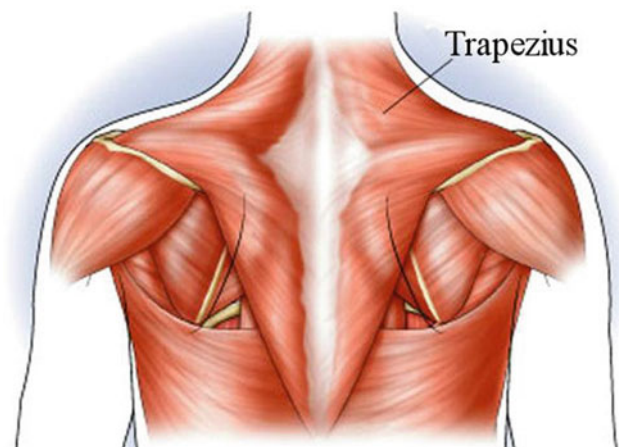


Fig. 4 Trapezius muscle



Fig. 5 Positioning Biopac electrodes



Fig. 6 Positioning Biopac and electrostimulation device electrodes

The first stage is when the muscle is in a state of rest and it can be seen that its activity is null (0% contraction).

In the second stage the muscular contraction is performed by lifting and lowering the shoulder from a small amplitude to a maximum amplitude (100% contraction). The acquisition system receives signals from the muscles and their amplitudes (0–100%) (Fig. 7).

Fig. 7 Muscle contraction following the lift-lowering movement of the shoulder

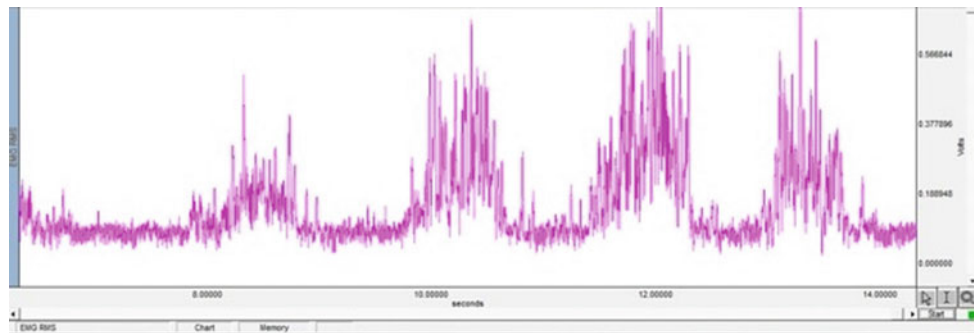
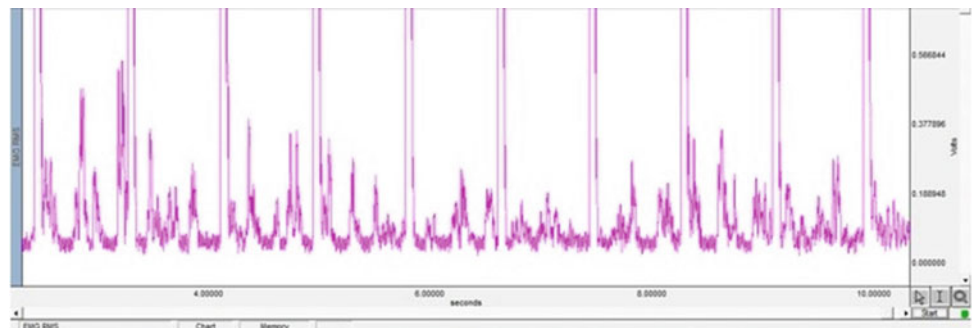


Fig. 8 Muscle contraction induced by the electro stimulator



In the third stage, the electro stimulator electrodes were positioned in order to electro-induce muscle contractions (Fig. 8).

4 Conclusions

The entire circuit is powered by a 9 V battery, at the output displaying a maximum current value of 1.7 mA. The average stimulation current is 0.7 mA and the output voltage of the circuit is in the 240–380 mV range.

Sending pulses to the muscle can be tracked through the LED, which illuminates each time the device sends an electrical impulse. This impulse is sent to the muscle through disposable electrodes.

Following the evaluation of muscle contractions, we could see that the time interval between contractions made by the device is lower than that encountered in a natural contraction.

Following the results obtained on the simulation software, EMG Biopac monitoring and multimeter measurements it can be concluded that the materials and methods used in the realization of the electrical muscle stimulator can be used as a low cost solution with future improvements and optimization. All the experiments were done with the consent of the subject.

Acknowledgements Practical realization of this project was made possible thanks to funding received in the *My License Project-2019* competition held in the “Transylvania” University of Braşov.

Conflict of Interest The authors declare that they have no conflict of interest.

References

1. Finger, S., Piccolino, M.: The shocking history of electric fishes: from ancient epochs to the birth of modern neurophysiology. University Press Scholarship Online, Oxford (2011)
2. Physioworks Homepage.: <https://physioworks.com.au/landing/ems-electrical-muscle-stimulation-machines.htm>. Last accessed 2019/06/10
3. Heidland, A., Fazeli, G., Klassen, A., Sebekova, K.: Neuromuscular electrostimulation techniques: historical aspects and current possibilities in treatment of pain and muscle waisting. *Clin. Nephrol.* **79** (Suppl 1), S12–S23 (2013)
4. Sperelakis, N.: Electrical stimulation of muscle: field stimulation. In: Daniel, E.E., Paton, D.M. (eds.) *Smooth muscle*. Springer, Boston (1975)
5. Biopac Homepage.: <https://www.biopac.com/application/emg-electromyography/>. Last accessed 2019/06/10
6. Biopac Homepage.: <https://www.biopac.com/product/electromyogram-amplifier/>. Last accessed 2019/06/10

Development of the High-Resolution Scintillator Type Imager Using Si GRID Structures

K. Tabata, R. Ohtake, J. Nishizawa, A. Koike, and T. Aoki

Abstract

The scintillator type X-ray image detector is being developed in this paper. The spatial resolution of this detector is not so higher than direct conversion type x-ray image detector because of scattering of luminescence of scintillator in the detector. The diffusion of light emit of scintillator by X-ray irradiated was suppressed by processing the silicon substrate using microfabrication technology. These small hole patterns were machined in a silicon substrate, and the scintillator was filled in the silicon grid holes. These holes reflect the light emitted by the scintillator and suppresses diffusion. The scintillator can be optically separated by this device. And these structures are operated as one detector. The purpose of this study is to prove that the silicon grid structures improve the spatial resolution of the scintillator type detector. Therefore, we measured the spatial resolution of the scintillator using this Si grid structures. In this study, CsI:Tl was buried in grid holes by the melting method. The spatial resolution of the sample in which CsI:Tl was deposited into the inside of the grid structure was measured. From this result, the deposition of the scintillator in the Si grid structures using the melting method has led to an improvement in spatial resolution of the scintillator type X-ray image detector.

Keywords

CsI:Tl • Si grid structures • MTF • Spatial resolution • X-ray image detector

1 Introduction

In this paper, we have been developing the scintillator type X-ray image detector [1]. This detector can be used as large area device in various fields. However the spatial resolution of this detector is not so higher than direct conversion type x-ray image detector because of scattering of luminescence of scintillator in the detector [2, 3]. In preceding study, columnar crystal growth and phase separation scintillator have been developed for reduce scattering of luminescence in the scintillator [4, 5]. In ours study, we are developing the Si-substrate for improvement of spatial resolution. The diffusion of luminescence of scintillator by X-ray irradiated was suppressed by processing the silicon substrate using microfabrication technology. These small hole patterns were processed in a silicon substrate, and the scintillator was filled in the silicon grid holes. These grid holes structures reflect luminescence of scintillator by X-ray irradiated and suppresses diffusion of its luminescence [1, 6]. The purpose of this study is to prove that the silicon grid structures improve the spatial resolution of the scintillator type detector. Therefore, we measured the spatial resolution of the scintillator using this Si grid structures. The deposition methods of the scintillator is melting method. CsI:Tl was put on the Si grid substrate and melted by resistance heating. This method is high packing density. As a scintillator, thallium iodide addition of cesium iodide was used. The spatial resolution of the samples in which CsI:Tl plate made by HAMAMATSU PHOTONICS, this plate with Si grid substrate and the Si grid substrate deposited CsI:Tl into grid structures was measured. The spatial resolution was measured by an edge method using a tungsten edge. From this result, the deposition of the scintillator in the Si grid structures using the melting method has led to an improvement in spatial resolution of the scintillator type X-ray image detector.

K. Tabata (✉) · R. Ohtake · J. Nishizawa · T. Aoki
Graduate Scholl of Science and Technology, Shizuoka University,
3-5-1, Johoku, Hamamatsu-Shi, Shizuoka, Japan
e-mail: tabata.kento.15@shizuoka.ac.jp

A. Koike
ANSeeN Inc., Hamamatsu-Shi, Shizuoka, Japan

2 The Samples and Methods

Our X-ray detector use CsI:Tl as a scintillator because CsI:Tl has high luminous efficiency and sensitivity to the Si-photodiode [7]. It is not easy to fill hole because aspects of the holes are very large. Therefore, the scintillator was filled by the melting method with high packaging density. The melting point of CsI is 894 K, TlI is 713 K [8, 9].

The silicon substrate was processed the small holes patterns by MEMS technique. These grid patterns are constituted by holes in the width of $90\ \mu\text{m} \times 90\ \mu\text{m}$ and depth of $400\ \mu\text{m}$, and the grid substrate is illustrated in Fig. 1. Moreover, we can process the large-size silicon wafers to the grid substrate with high precision semiconductor process, and the structure of this grid holes are made integral with silicon photodiode array, and these structures are operated as one detector. These grid holes structures reflect luminescence of scintillator by X-ray irradiated and suppresses diffusion of its luminescence [10]. CsI:Tl(added Tl 10 mol%) was melted at 973 K and the samples were made at various melting times. The cooling method is natural cooling at about 313 K/min. The Tl concentration of CsI:Tl was changed by the difference heating time. Hamamatsu Photonics CsI:Tl scintillator plate was used as a comparison object and this properties is shown in Table 1. The spatial resolution of the samples in which CsI:Tl plate made by HAMAMATSU PHOTONICS, this plate with Si grid substrate and the Si grid substrate deposited CsI:Tl into grid structures was measured. Modulation Transfer Function (MTF) curves for spatial resolution of the samples were obtained from edge images measured by a CMOS sensor using a 2 mm thick tungsten edge phantom. The experiment condition is shown in Table 2. A distance between X-ray source and the sample was 30 mm detector (Fig. 2).

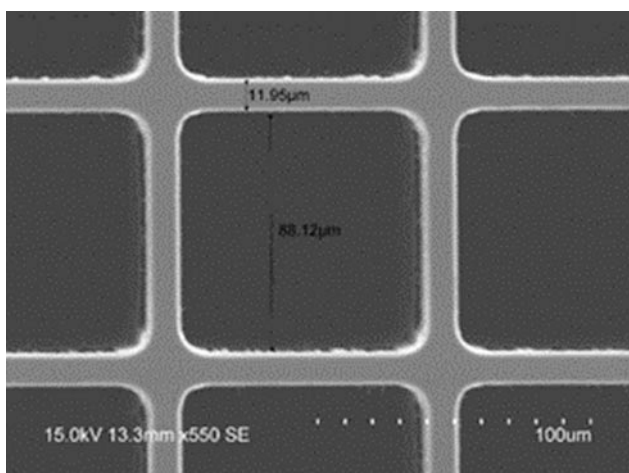


Fig. 1 Surface of the silicon substrate processed the grid holes

Table 1 The properties of CsI:Tl plate made by HAMAMATSU_PHOTONICS

Properties	
Scintillator type	CsI:Tl
External dimensions	$50 \times 50\ \text{mm}$
Effective area	$48 \times 48\ \text{mm}$
Substrate thickness	0.5 mm
CsI thickness	400 μm
Relative light output (Typ.)	320%
CTF (Typ.)	33(at 3 lp/mm) %

Table 2 Experimental condition of obtain edge images

CMOS sensor	Single lens reflex camera (D5300 Nikon)
F-number	5.6
Exposure time	1/30 s
ISO	6400
Condition of X-ray source	
Tube voltage	70 kV
Tube current of HAMAMATSU PHOTONICS	10 μA
Tube current of our sample which CsI:Tl filled in Si grid	500 μA

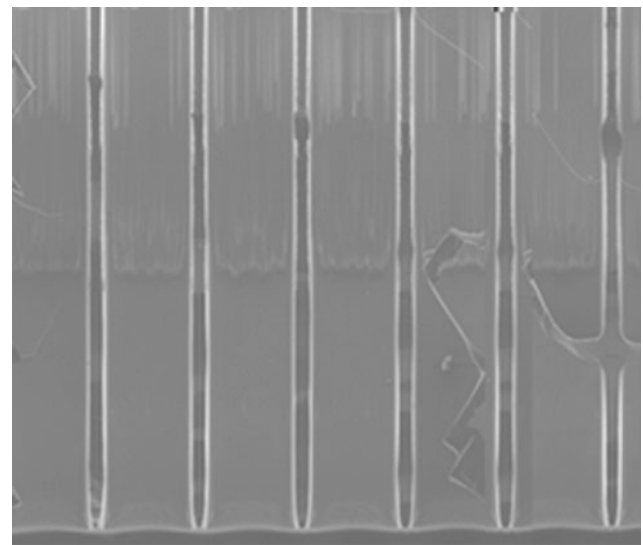


Fig. 2 Cross sectional view of the grid holes

3 The Spatial Resolution of the Scintillator Type Imager Using Si GRID Structures

The spatial resolution was measured by an edge method using a tungsten edge. The edge image of the tungsten plate was projected onto the sample and acquired as an image with a CMOS sensor. Edge images were acquired to obtain edge

Fig. 3 Images of edge phantoms
a CsI:Tl plate made by HAMAMATSU PHOTONICS,
b the Si grid structures was attached on surface of CsI:Tl plate made by HAMAMATSU PHOTONICS,
c CsI:Tl was filled in the Si grid structures by melting method

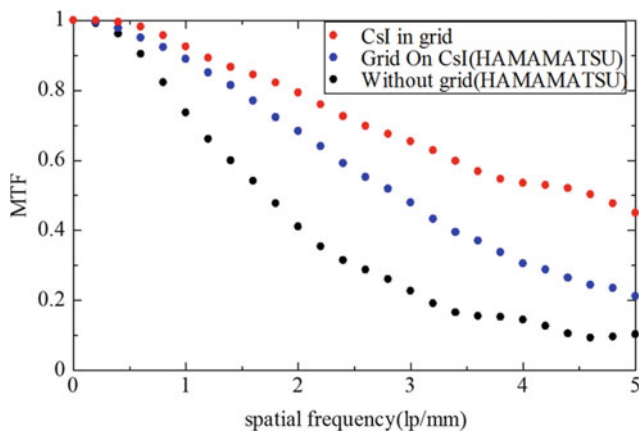
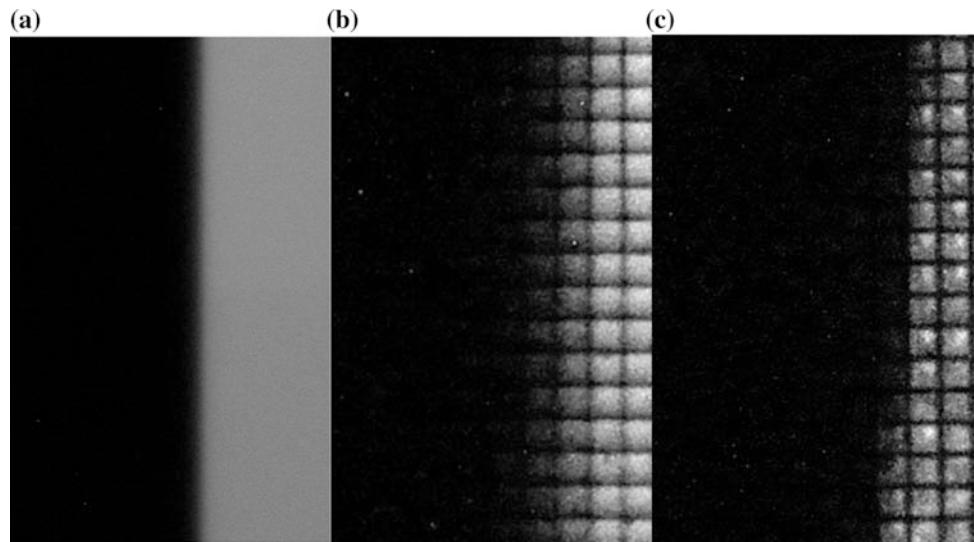


Fig. 4 The spatial frequency of the sample from image of edge phantom

diffusion function (ESF) data. The sloped edge images obtained from the three samples produced are shown in Fig. 3. The ESF was differentiated to obtain line segment distribution function (LSF). The MTF was calculated from the Fourier transform of the LSF data and its value at zero frequency was normalized to unity. Figure 4 shows the measurement results of MTF curves of different samples. When the MTF value is 30%, the spatial frequency of CsI:Tl plate (made by HAMAMATSU_PHOTONICS) is 2.5 lp/mm, and the one layer overlaid the silicon grid substrate is 4.0 lp/mm. The use of a silicon grid substrate improves the MTF value by about 1.4 times up to a spatial frequency of 2.5 lp/mm. And the sample in which CsI:Tl was deposited into the silicon grid hole had an MTF value of 45% at 5.0 lp/mm. When compared the scintillator plate without the Si grid structures, MTF values were improved 1.6 times on

average up to 2.5 lp/mm and 2.7 times on average up to 5.0 lp/mm. As a result, silicon grid substrates of pixel structure appear to be useful in improving the spatial resolution of the scintillator type X-ray image detector.

4 Conclusions

The silicon substrate was processed in the small holes pattern to improve the spatial resolution of the scintillator type X-ray image detector. CsI:Tl scintillation phosphors were used as x-ray transducers and loaded into silicon substrates of pixel structure. And the imaging performance of the sample with the silicon grid structures as X-ray imaging detector for high spatial resolution application was investigated. As a result, the silicon substrate of pixel structure played an important role as an optical separation device to suppress the diffusion of visible light emitted by one pixel. The MTF value was improved about 1.4 times by overlaying the Si grid structures on the scintillator plate. And by filling CsI:Tl in the Si grid structures, the MTF value was improved about 2.7 times. This result indicates that using the Si grid structures substrate leads to an improvement in the spatial resolution of existing scintillator type imaging detectors.

In the future, an X-ray image detector having high sensitivity and high spatial resolution can be developed by a scintillator type X-ray image detector using a more uniform and large-area pixel structure silicon substrate. Since the resolution is improved simply by stacking the substrates, this simple approach to existing scintillator detectors can improve the performance of detectors using various phosphors. And this will enable high-quality and large-area X-ray imaging in the industrial and medical fields.

Acknowledgements This research is partly based on the Cooperative Research Project of Research Center for Biomedical Engineering/Research Institute of Electronics, Shizuoka University. We appreciate Personal communication Annand Sheel, Madu Vora, Nicholas Eib and Brian Rodricks in terapede systems Inc. in USA.

Conflict of Interest The authors declare that they have no conflict of interest.

References

1. Tabata, K., Nishizawa, J., Koike, A., Aoki, T.: SPIE 9968, Hard X-Ray, Gamma-Ray, and Neutron Detector Physics XVIII, 99681H (2016). <https://doi.org/10.1117/12.2238424>
2. Kim, B., Cha, B.K., Jeon, H., Chi, Y.K., Cho, G.: A study on spatial resolution of pixelated CsI(Tl) scintillator. *Nucl. Instrum. Methods Phys. Res. A* **579**, 205–207 (2007)
3. Badela, X., Galeckasa, A., Linnrosa, J., Kleimannb, P., Fröjdh, C., Peterssona, C.S.: Improvement of an X-ray imaging detector based on a scintillating guides screen. *Nucl. Instrum. Methods Phys. Res. A* **487**, 129–135 (2002)
4. Yao-Hu, L., Xin, L., Jin-Chuan, G., Zhi-Gang, Z., Han-Ben, N.: Development of x-ray scintillator functioning also as an analyser grating used in grating-based x-ray differential phase contrast imaging. *Chin. Phys. B* **20**(4)
5. Zhao, W., Ristic, G., Rowlands, J.A.: X-ray imaging performance of structured cesium iodide scintillators. *Med. Phys.* **31**(9) (2004)
6. Lau, H.W., Parker, G.J., Greef, R., Hölling, M.: High aspect ratio submicron silicon pillars fabricated by photoassisted electrochemical etching, and oxidation. *Appl. Phys. Lett.* **67** (1995)
7. Grabmaier, B.C.: Crystal scintillators. *IEEE Trans. Nucl. Sci.* **31**(1) (1984)
8. Liu, Y., Chen, C.P., Li, H.B.: Studies of prototype CsI(Tl) crystal scintillators for low-energy neutrino experiments. *Nucl. Instrum. Methods Phys. Res. Sect. A Accelerators, Spectrometers, Detectors and Associated* **482**(1–2), 125–143 (2002)
9. Sultana, S.: Rfiuddin: electrical conductivity in TiI–TiO₂ composite solid electrolyte. *Physica B* **404**(1), 36–40 (2009)
10. Kim, J.Y., Cho, G., Kim, Y.: High-resolution X-ray imaging based on pixelstructured CsI: Tl scintillating screens for indirect X-ray image sensors. *J. Korean Phys. Soc.* **59**(6), 3670–3673 (2011)

Packing Conditions of Optical Separated CsI: Tl Scintillator by Silicon Collimator

R. Ohtake, K. Tabata, J. Nishizawa, A. Koike, and T. Aoki

Abstract

We have been developing a scintillator type X-ray imaging detector. The spatial resolution of this type detector is lower than that of direct conversion type detectors. This is because X-ray scintillation light spreads in the scintillator. To settle this issue, we proposed optical separations of scintillator by a silicon collimator, which is a silicon substrate processed into grid structure by the semiconductor micro processing technology. The silicon collimator which is filled with scintillators works as an X-ray imaging detector by joining with a photodiode array. In this study, melted Cesium Iodide doped with Thallium (CsI:Tl) was poured into the silicon collimator, and recrystallized. After that, Packing conditions of CsI: Tl in the silicon collimator were observed by Scanning Electron Microscope (SEM) and Computed Tomography (CT). These results suggested that holes on the silicon collimator was closely packed with CsI:Tl. An image of recrystallized CsI:Tl under X-ray irradiation was acquired. From this image we confirmed that CsI:Tl which was recrystallized in the silicon collimator emitted visible light by X-ray excitation. The pixel separation effects of the silicon collimator for light spreading was also confirmed. Moreover, a relative standard deviation of pixel value of the fabricated sample was lower than that of a sample made by the vacuum evaporation method in

the previous study. This result indicated that uniformity of luminescence was improved.

Keywords

X-ray imaging detector • Scintillator • CsI:Tl • Silicon collimator • Recrystallization

1 Introduction

Currently, Scintillator type X-ray imagers are widely used for medical radiography. These are composed of a scintillator material to convert X-ray into visible light, and an optical imager to read out electrical signals from visible light, such as CCD or CMOS image sensor. This type X-ray imager can have a wide detection range easily and take advantage of developments of optical image sensors. On the other hand, it is one of the important issues that a degradation of the spatial resolution caused by light spreads in the scintillator [1–3]. The degradation is remarkably shown in thick scintillators because longer propagation lengths cause wider light spreads [4]. To settle this issue, there are some study on suppressing spreads of light in scintillators with enough thickness for stopping X-ray. For example, columnar crystal growths, developments of pixel structured scintillators, and so on [1, 5].

We have been developing scintillators optically separated by a silicon collimator, which is a silicon substrate have grid structure fabricated by the semiconductor micro processing technology. Walls on the silicon collimator prevent X-ray scintillation light from spreading out to neighborhood pixels. In previous study, we filled CsI:Tl scintillator into the silicon collimator with a bottom in which photodiodes are formed [6]. The melting point of CsI is 894 K [7]. However, there is a restriction that photodiodes cannot be heated to 473 K, so we adopted the vacuum evaporation as a filling method. This article report that the silicon collimator suppresses scintillation light spreading, and improves the spatial

R. Ohtake (✉) · T. Aoki
Graduate School of Integrated Science and Technology, Shizuoka University, 3-5-1 Johoku Naka-Ku, Hamamatsu-Shi, Shizuoka, Japan
e-mail: ohtake.ryota.15@shizuoka.ac.jp

K. Tabata · J. Nishizawa · T. Aoki
Graduate School of Science and Technology, Shizuoka University, Hamamatsu-Shi, Shizuoka, Japan

A. Koike · T. Aoki
ANSeeN Inc., Hamamatsu-Shi, Shizuoka, Japan

T. Aoki
Research Institute of Electronics, Shizuoka University, Hamamatsu-Shi, Shizuoka, Japan

resolution. While, Poor uniformity of luminescence left as an issue.

In this paper, we filled CsI:Tl into the silicon collimator without a bottom. It will work as an X-ray imaging detector by joining with a photodiode array. This substrate can be heated to over 894 K. Therefore, melted CsI:Tl was poured into the silicon collimator, and recrystallized (the melting method). Then, packing conditions of CsI:Tl in the silicon collimator were observed by SEM and CT. Moreover, the X-ray scintillation light from recrystallized CsI:Tl was evaluated.

2 Device Design

Square holes in a grid pattern were fabricated on a silicon substrate by the Deep Reactive Ion Etching (DRIE), as shown in Fig. 1. The size of square holes is 90 μm in pixel width and 400 μm in depth while the walls is 10 μm in thickness. CsI:Tl is used as a scintillator material. This is because it has high conversion efficiencies for X-ray, and its broad emission in range of 400–800 nm with a peak at 550 nm is sensitive to Si-based photodiodes [2, 8]. CsI:Tl is filled in holes on the silicon collimator for optical separation, and joined with a Si-based photodiode array. The light from each scintillator is reflected or absorbed by Walls on the silicon collimator, and propagated to a corresponding photodiode. The sectional schematic of the X-ray imaging detector with silicon collimator is shown in Fig. 2.

3 Experimental

3.1 Filling Silicon Collimator with CsI:Tl

The silicon collimator was filled with CsI:Tl scintillator by the melting method. CsI powder contains 10 mol% Tl was put on the silicon collimator, and it was heated by a hotplate. Then, melted CsI:Tl was recrystallized. The sample was heated at 973 K for 10 min, and then cooled down to about 290 K at a cooling rate of 313 K/min. After recrystallization, scintillators deposited on the surface of the sample was removed by polishing. This experiment was conducted in ambient air.

3.2 Packing Conditions

SEM images of the fabricated sample were acquired to observe the surface of recrystallized CsI:Tl scintillators. Moreover, Tomographic images of the sample were taken by CT. A photon counting X-ray line sensor (XC-HYDRA

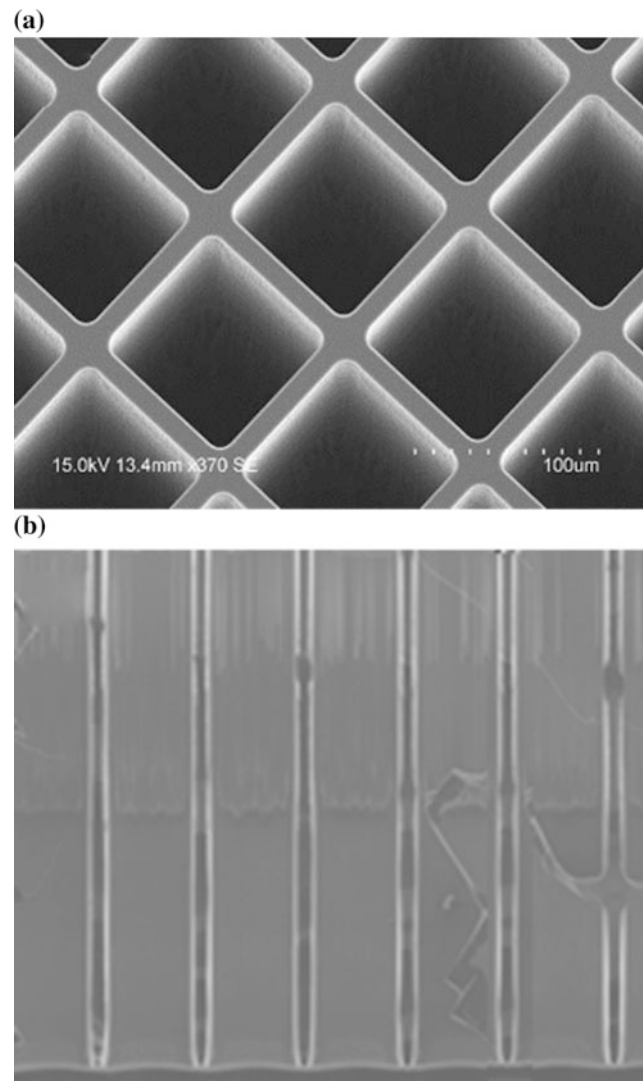


Fig. 1 SEM image of the silicon collimator: **a** Top-view, **b** Sectional-view

FX20, Acrorad) was used for this experiment. From obtained tomographic images, Packing conditions of CsI:Tl in the silicon collimator were investigated. Experimental conditions for CT imaging are shown in Table 1.

3.3 Scintillation

An image of the sample under X-ray irradiation was taken by a digital single-lens reflex camera with CMOS image sensor (D5300, Nikon). A distance between X-ray source and sample was 50 mm. Experimental conditions are shown in Table 2. Based on 20×20 pixels extracted from the acquired image, three statistics (average, sample standard deviation, and relative standard deviation) were calculated.

Fig. 2 Sectional schematic of scintillator type X-ray imager with silicon collimator

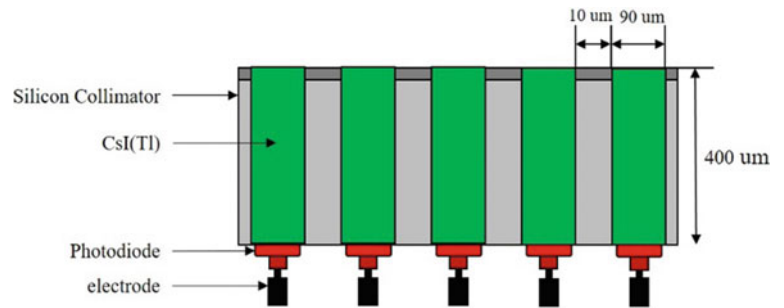


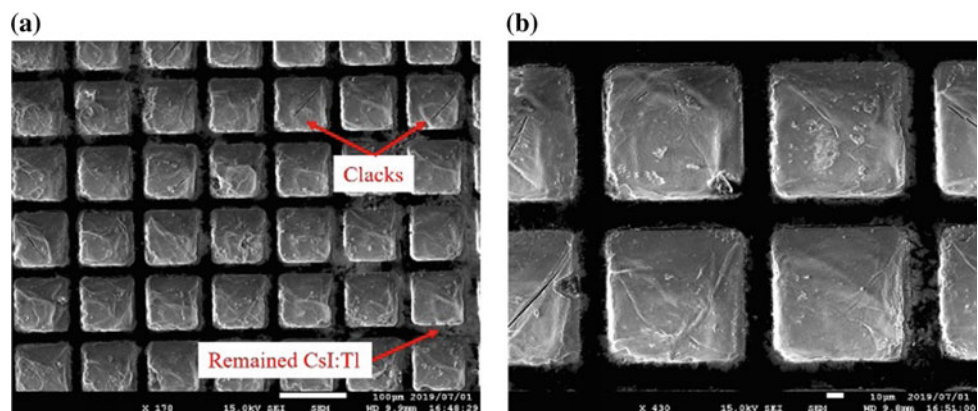
Table 1 Experimental conditions for CT imaging

Image sensor (XC-HYDRA FX20)	
Pixel pitch	100 μm
Sensor area	206 mm × 6 mm
<i>X-ray tube</i>	
Tube voltage	150 kV
Tube current	400 μA
<i>Imaging condition</i>	
X-ray source to detector	1000 mm
X-ray source to sample	90 mm
Number of Frames	2880 Frames
Frame rate	5 Hz
Rotation rate	250 pps
Threshold	10 kV

Table 2 Experimental conditions for observing scintillation light

Single lens reflex camera (D5300, Nikon)	
Exposure time	1/30 s
F-number	5.6
ISO	6400
<i>X-ray Tube</i>	
Tube voltage	150 kV
Tube current	400 μA

Fig. 3 SEM images of the silicon collimator filled with CsI:Tl by the melting method: **a** 170×, **b** 430×



Then, luminescence uniformity was evaluated by the calculated results. This experiment was performed for a sample which was made by the vacuum evaporation method in the previous study.

4 Result and Discussion

CsI:Tl scintillators were filled in the silicon collimator by the melting method. SEM images of the sample are shown in Fig. 3. It can be observed that holes on the silicon collimator are closely packed with CsI:Tl. However, there are some clacks on the surface of crystals. It is assumed that this is because the fast cooling rate caused a quick shrinkage of CsI:Tl at recrystallization. SEM images also shows that CsI:Tl remains on the top of the silicon collimator. These are obstacles when joining the silicon collimator and photodiode arrays. Thus, the polishing method needs to be reconsidered.

The tomographic image of sample acquired by CT, as shown in Fig. 4. Since the attenuation coefficient of CsI:Tl is higher than that of silicon, CT images depicts CsI:Tl in white. Several white rectangles are drawn in the obtained CT image. This result suggested that the inside of square holes was filled with CsI:Tl from top to bottom.

The image of the sample under X-ray irradiation and the line profile of pixels surrounded by a frame are shown in Fig. 3. From this result we observed the scintillation light of CsI:Tl which was recrystallized in the silicon collimator. In the line profile, the gray value dips at every 100 μm. It

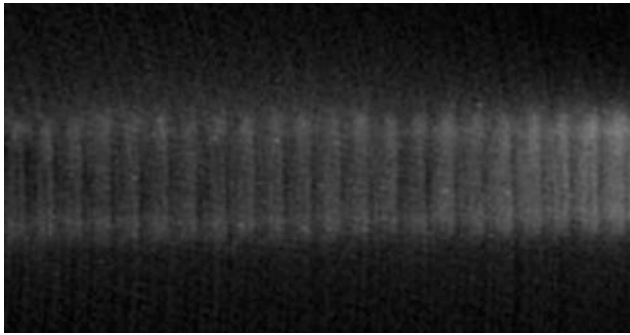


Fig. 4 CT image of the silicon collimator filled with CsI:Tl by the melting method

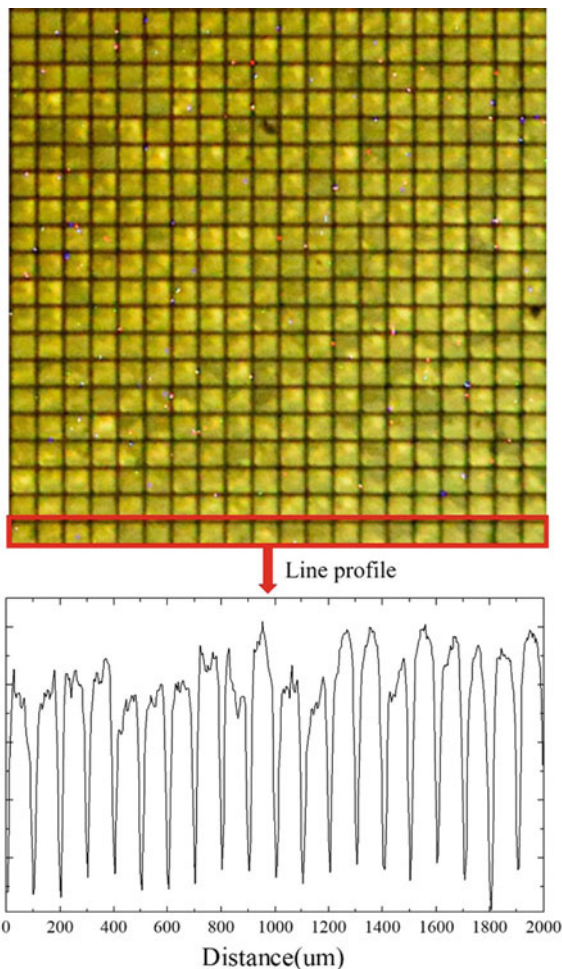


Fig. 5 Scintillation light from CsI:Tl optically separated by the silicon collimator

shows the pixel separation effect of the silicon collimator. Then, 20×20 pixels were extracted from obtained images, and an average (Ave), sample standard deviation (SSD) and relative standard deviation (RSD) of pixel value were calculated. The results were shown in Fig. 5. This table contains above three statistics of a sample which was fabricated

Table 3 Statistics of pixel value (20×20 pixel) on the silicon collimator

Filling method	Ave	SSD	RSD
Melting method	9.3×10^4	7.8×10^3	8.4×10^{-2}
Vacuum evaporation method	4.0×10^4	1.5×10^4	3.9×10^{-1}

by the vacuum evaporation method in the previous study. The RSD of sample made by the melting method is 8.4×10^{-2} , which is lower than a quarter of that of the sample made by the vacuum evaporation method. This result indicated that the uniformity of luminescence was improved (Table 3).

5 Conclusions

In this paper, CsI:Tl scintillator was filled in the silicon collimator by the melting method for optical separations. Packing conditions of CsI:Tl was investigated by SEM and CT. These results indicated that CsI:Tl filled up the square holes on the silicon collimator. However, there were some cracks on the surface of CsI:Tl crystals, and CsI:Tl remained on the top of the silicon collimator. The state of sample under X-ray irradiation was observed. As a result, the scintillation light from recrystallized CsI:Tl, and pixel separation effects of the silicon collimator was confirmed. Furthermore, it showed more uniform luminescence than the sample made by the vacuum evaporation method. It is expected that the silicon collimator filled with CsI:Tl will realize high resolution and wide range X-ray imaging by bonding with a Si-based photodiode array.

Acknowledgements This research was based on the Cooperative Research Project of Research Center for Biomedical Engineering/Research Institute of Electronics, Shizuoka University. We would like to offer our special thanks to Anand Sheel, Madhu Vora, Nicholas Eib, and Brian Rodricks in terapede systems Inc. in USA.

Conflict of Interest The authors declare that they have no conflict of interest.

References

- Kim, B., Cha, B.K., Jeon, H., et al.: A study on spatial resolution of pixelated CsI: Tl scintillator. Nucl. Instrum. Methods Phys. Res. Sect. A **579**(2007), 205–207 (2007)
- Cha, B.K., Lee, D.H., Kim, B., et al.: High-resolution X-ray imaging based on pixel-structured CsI: Tl scintillating screens for indirect X-ray image sensors. J. Korean Phys. Soc. **59**(6), 3670–3673 (2011)
- Badel, X., Galeckas, A., Linnros, J., et al.: Improvement of an X-ray imaging detector based on a scintillating guides screen. Nucl. Instrum. Methods Phys. Res. Sect. A **487**(2002), 129–135 (2002)

4. Kim, B.J., Cho, G., Cha, B.K., et al.: An X-ray imaging detector based on pixel structured scintillator. *Radiat. Meas.* **42**(2007), 1415–1418 (2007)
5. Miller, S.R., Gaysinskiy, V., Shestakove, I et al.: Recent advances in columnar CsI:Tl scintillator screens. *Proc. SPIE 5923, Penetrating Radiation Systems and Application VII*, 59230F (2005)
6. Tabata, K., Nishizawa, J., Koike, A., Aoki, T.: CsI:Tl scintillator separated by Si grid partition wall. *Proc. SPIE 9968, Hard X-Ray, Gamma-Ray, and Neutron Detector Physics XVIII*, 99681H, 2016 (2016)
7. Liu, Y., Chen, C.P., Li, H.B., et al.: Studies of prototype CsI: Tl crystal scintillators for low-energy neutrino experiments. *Nucl. Instrum. Methods Phys. Res., Sect. A* **482**(2002), 125–143 (2002)
8. Cha, B.K., Shin, J.H., Bae, J.H., et al.: Scintillation characteristics and imaging performance of CsI: Tl thin films for X-ray imaging applications. *Nucl. Instrum. Methods Phys. Res., Sect. A* **S604** (2009), 224–228 (2009)

Study on Ferroelectric Thin Film Capacitor for AC-Coupled CdTe X-ray Detector

M. Hayakawa, H. Nakagawa, K. Sakaida, and T. Aoki

Abstract

We present that fabricating ferroelectric thin film capacitor on electrodes of the X-ray detector to make AC-coupled CdTe X-ray imager. In order to determine the capacitance required for the coupling capacitor, radiation spectrum is measured by using some coupling capacitor have different capacitance. As a result, it was found that the more the capacitance is large, we can get correct radiation spectrum. Because small capacitor with large capacitance is required, BaTiO₃ is selected as a high dielectric constant material. We fabricated a ferroelectric thin film capacitor with an area of about 48 μm² and a thickness of about 100 nm by sputtering. As a result of measurement, the capacitance is about 880 pF, and the tendency of variation of dielectric constant with frequency corresponded with past paper. Although the dielectric constant was significantly smaller than the BaTiO₃ film in the papers. We considered that the main issue is quality of BaTiO₃ film. Quality of film is increased by depositing under high substrate temperature. Performance of CdTe as a radiation detector is deteriorated by high temperature. Therefore, we need to consider the way to deposit BaTiO₃ on CdTe at low substrate temperature.

Keywords

CdTe • AC-coupling • X-ray detector • BaTiO₃ • Sputtering

1 Introduction

CdTe can operate at room temperature as an X-ray detector because CdTe has a relatively wide band gap of 1.44 eV. In addition, since it has high sensitivity to high energy X-ray due to its high density and large atomic number, CdTe is expected to use as X-ray imager in wide range of field such as medical, industrial and space observation [1, 2]. Semiconductor X-ray detectors using CdTe perform imaging by reading out a charge from a lot of electrodes on the surface of a CdTe element. In order to reduce the leakage current constantly generated from the detector, CdTe and readout circuit are usually connected by AC-coupling. Because it is necessary to apply AC-coupling to each electrodes, it cannot be used in X-ray imager with integrated electrodes, so DC-coupling has been used. Therefore, we propose to make an AC-coupled X-ray imager by fabricating a capacitor on the electrode using deposition technology. In case connecting by AC-coupling between CdTe and preamplifier, the coupling capacitor which has large capacitance is required to get correct radiation spectrum. We determined to make capacitor on each electrode which has capacitance of 1 nF or more from radiation spectrum measurement. Electrodes of 95 μm × 95 μm are designed at intervals of 5 μm on CdTe because a resolution of 100 μm or more is required in industrial and dental CT. Resistor and capacitor required to be fabricated on electrodes. The area of the resistor is designed to be 1.225 pm² and the area of the capacitor to be 5.625 pm². Assuming that the thickness of the dielectric layer of the capacitor is 30 nm, a dielectric constant of about 600 is required to obtain a capacitance of 1 nF. Therefore, BaTiO₃ with a high dielectric constant was selected as the material.

M. Hayakawa (✉) · K. Sakaida
 Department of Informatics, Graduated School of Integrated
 Science and Technology, Shizuoka University, 3-5-1,
 Johoku Naka-Ku, Hamamatsu-shi, Shizuoka, Japan
 e-mail: hayakawa.mamoru.15@shizuoka.ac.jp

H. Nakagawa · T. Aoki
 Research Institute of Electronics, Shizuoka University,
 Hamamatsu-shi, Shizuoka, Japan

2 Experimental

2.1 Influence of Coupling Capacitance on Radiation Spectrum

In order to investigate how signal be affected by capacitance of coupling capacitor, we measured radiation spectrum by using three different coupling capacitors. We used ^{137}Cs , ^{241}Am and ^{57}Co as radiation sources, and 1 pixel Schottky CdTe of $2\text{ mm} \times 2\text{ mm} \times 0.5\text{ mm}$ as a detector. ^{241}Am and ^{57}Co were used for energy calibration. We used capacitors of 10 nF, 1 nF, 100 pF respectively as a coupling capacitor between CdTe and the preamplifier. The equipment used is shown in Table 1.

2.2 Deposition of BaTiO₃

It is known that BaTiO₃ is crystallized by heating substrate while depositing [3]. Therefore, we deposited BaTiO₃ on Si substrate of 500 °C and Si substrate of no heated by RF magnetron sputtering. Deposition condition common to the each case is shown in Table 2.

2.3 Trial Manufacture of BaTiO₃ Thin Film Capacitor

We fabricated a thin film capacitor by depositing BaTiO₃ on Si substrate of 500 °C. In order to heat the substrate, we used tungsten with a high melting point as lower electrode. Figure 1 shows structure of capacitor. The area of the capacitor is $8\text{ mm} \times 6\text{ mm}$, and the BaTiO₃ film is deposited with a thickness of about 100 nm.

Table 1 Equipment used for radiation spectrum measurement

Detector	Acrorad	Al Schottky CdTe detector
MCA	SEIKO	EG&G MCA7700
CSA	CLEAR-PULSE	Charge sensitive preamplifier 595L
Main amplifier	CLEAR-PULSE	Waveform shaping amplifier 4419HI

Table 2 Common conditions in each deposition

Base pressure	10^{-5} (Pa)	RF power	0.5 (kW)
Gas	Ar, O ₂	Substrate distance	140 mm
Flow rate (Ar)	40 sccm	Deposition time	90 min
Flow rate (O ₂)	10 sccm	Target	BaTiO ₃
Vacuum (deposition)	2.0 Pa	Substrate	Si

3 Result and Discussion

3.1 Influence of Coupling Capacitance on Radiation Spectrum

The spectrum of ^{137}Cs calibrated by using ^{241}Am and ^{57}Co is shown in Fig. 2. The 662 keV peak of ^{137}Cs is shifted to lower energy side as capacitance of the coupling capacitor is reduced. This is considered that the energy calibration cannot be performed correctly because the higher the energy, the spectrum shifts greatly. Since the value closer to the normal energy spectrum was obtained as the coupling capacitor with a large capacitance was used, it was found that it is necessary to use a coupling capacitor with a sufficient capacitance to obtain a correct spectrum.

3.2 Electrode Design of X-ray Imager

Since the resolution of 100 μm pitch or more is required in industrial and dental CT, readout electrodes on the detector is designed with 100 μm pitch. The design of the readout electrode is shown in Fig. 3. Resistor and capacitor exist on the electrode, the area of the resistor is $1.225\text{ }\mu\text{m}^2$ and the area of the capacitor is $5.625\text{ }\mu\text{m}^2$. From Fig. 2, the capacitance of each capacitor is targeted at 1 nF. Assuming that the film thickness of the dielectric layer is 30 nm, a relative dielectric constant of approximately 600 is required to fabricate a capacitor with a capacitance of 1 nF.

3.3 Crystalline Evaluation by X-ray Diffraction

We performed X-ray diffraction measurement to investigate the crystallinity of the sample. Figures 4 and 5 show the

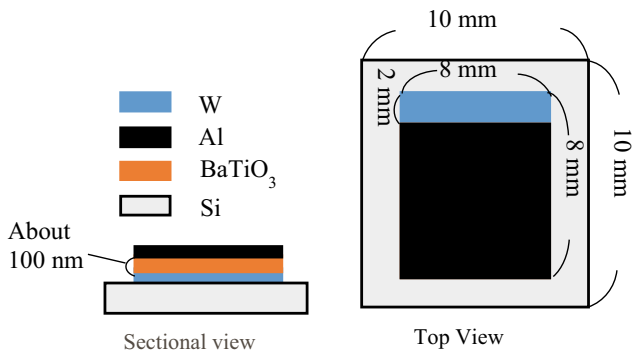


Fig. 1 Schematic of BaTiO₃ thin film capacitor

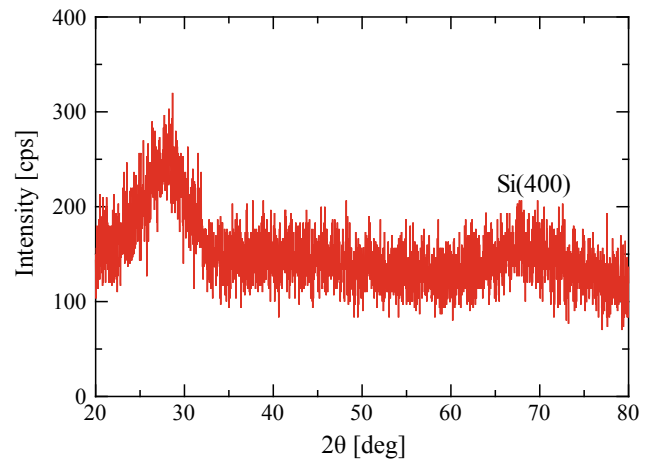


Fig. 4 X-ray diffraction pattern of BaTiO₃ grown at a substrate of room temperature

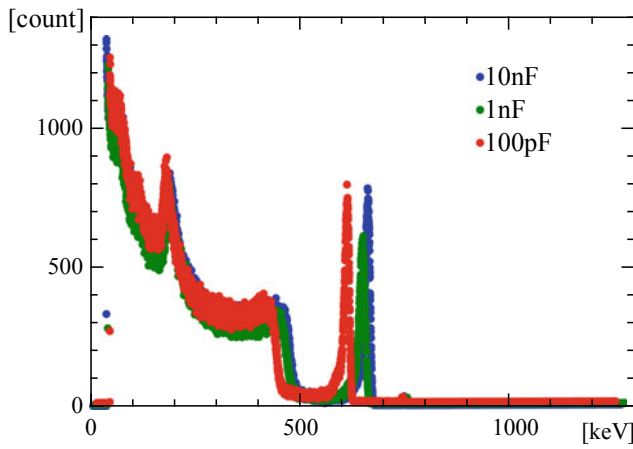


Fig. 2 Gamma ray spectrum of ¹³⁷Cs measured using each coupling capacitor

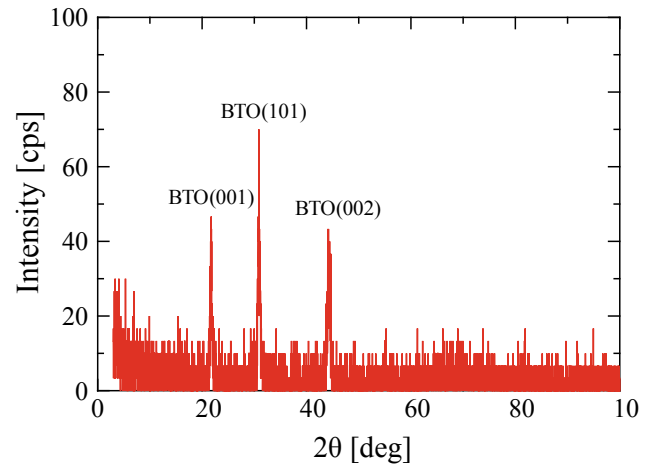


Fig. 5 X-ray diffraction pattern of BaTiO₃ grown at substrate of 500 °C

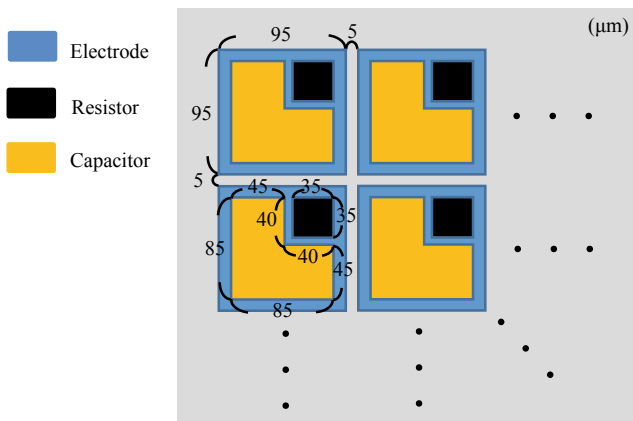


Fig. 3 Design of resistor and capacitor on electrodes

result of X-ray diffraction of the sample without substrate heating and heated 500 °C, respectively. Figure 4 shows that the peak exists at 69°. This is the peak of Si(400) of Si used for the substrate. Figure 5 shows that peaks at around 22°, 31° and 45°, respectively. These indicate BaTiO₃ (001), BaTiO₃ (101), and BaTiO₃ (002), respectively. From these result, it can be confirmed that growing a polycrystalline BaTiO₃ film in which crystall orientation (001) and (101) are mixed when depositing a film on the substrate of 500 °C. It is known that BaTiO₃ is most strongly polarized in the (001)-oriented state [4]. In order to obtain (001)-oriented

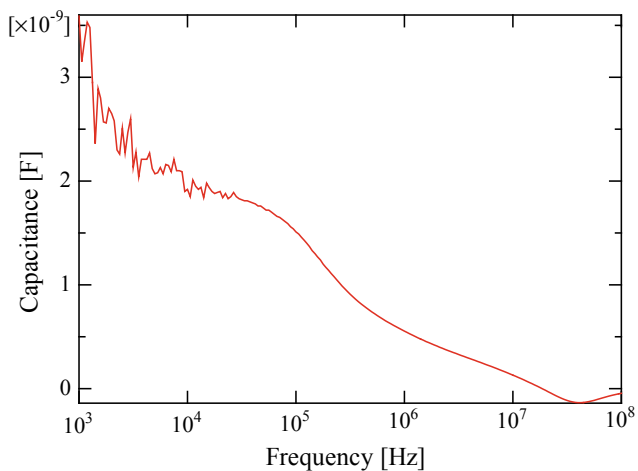


Fig. 6 Frequency dependence on Capacitance of the fabricated capacitor

BaTiO₃ polycrystals, it is necessary to deposit on the substrate of high temperature and close lattice constant. However, if film is deposited on CdTe under these conditions, the performance as a radiation detector will deteriorate due to heating, so it is necessary to study deposition method of BaTiO₃ at low substrate temperature.

3.4 Evaluation of BaTiO₃ Thin Film Capacitors

The capacitance of the fabricated capacitor to the DC power supply was about 880 pF. The relationship between frequency and capacitance was measured in the range of 1 kHz to 100 MHz with an AC power supply of 50 mV. The frequency dependence of capacitance is shown in Fig. 6. It can be confirmed from Fig. 6 that the capacitance decreases as the frequency increases. This is due to the decrease in the dielectric constant as the frequency increases. It is also found that the capacitance decreases around 100 kHz, which coincides with the frequency at which the dielectric constant of the BaTiO₃ thin film capacitor decreases due to the dielectric relaxation shown in the past paper [5]. This supports the fact that a BaTiO₃ capacitor was fabricated.

4 Conclusions

It was found that it is necessary to use a capacitor with a sufficiently large capacitance as a coupling capacitor to obtain a correct radiation spectrum. From the measurement

results, the shift of radiation spectrum is estimated to be large when capacitance is smaller than 1 nF. Therefore, the electrode structure of the X-ray imager was designed for a capacitor has 1 nF. Electrodes size of the X-ray imager is 95 μm × 95 μm, and the area of the capacitor on the electrode is 5.625 μm². Assuming that the thickness of the BaTiO₃ film is 30 nm, the relative dielectric constant needs to be about 600 to obtain a capacitance of 1 nF.

The film was found to be polycrystalline of BaTiO₃ by XRD measurement when the BaTiO₃ was deposited on the Si substrate of 500 °C. The capacitance of the capacitor fabricated by depositing on the substrate of 500 °C was about 880 pF, and the relative permittivity was about 0.207. In order to improve the dielectric constant, depositing at high temperature, annealing BaTiO₃ film, making (001)-oriented BaTiO₃ film, etc. can be considered. Although, CdTe will deteriorate its property as a detector if it is exposed to high temperature for a long time. Therefore, depositing and annealing at high temperature cannot be performed on CdTe. In addition, since it is necessary to deposit a film at high temperature in order to give orientation to the BaTiO₃ film by lattice matching with the substrate, CdTe is also degraded in this case. There is room to consider the crystallization method of BaTiO₃ that can suppress the deterioration of CdTe.

Conflict of Interest The authors declare that they have no conflict of interest.

References

1. Scheiber, C., Giakos, G.G.: Medical applications of CdTe and CdZnTe detectors. *Nucl. Instrum. Methods Phys. Res. A* **458**, 12–25 (2001)
2. Del Sordo, S., Abbene, L., Caroli, E., Mancini, A.M., Zappettini, A., Ubertini, P.: Progress in the development of CdTe and CdZnTe semiconductor radiation detectors for astrophysical and medical applications. *Sensors* **2009**, 3491–3526 (2009)
3. Uchino, K., Lee, N.-Y., Toba, T., Usuki, N., Aburatani, H., Ito, Y.: Changes in the crystal structure of RF-magnetron sputtered BaTiO₃ thin films. *J. Ceram. Soc. Jpn* 1091–1093 (1992)
4. Arakawa, T., Egashira, M., Sameshima, S., Hirata, Y., Matsumoto, Y., Murakami, H.: *Inorganic Materials Science* [Translated from Japanese]. Sankyo Shuppan Co., Ltd. (2012)
5. Zhang, W., Hu, F., Zang, H., Ouyang, J.: Investigation of the electrical properties of RF sputtered BaTiO₃ films grown on various substrates. *Mater. Res. Bull.* **95**, 23–29 (2017)

Aluminium-BSF Versus PERC Solar Cells: Study of Rear Side Passivation Quality and Diffusion Length

A. Schütt, O. Lupan, and R. Adelung

Abstract

The impact of (bulk) material and rear surface (contact) quality to the efficiency is found to be quite hard to measure on a processed solar cell. We will show with this paper that CELLO (solar cell local characterization) photo-impedance-spectroscopy measurements are capable of separating bulk from rear side effects on locally resolved maps. This study focuses on multicrystalline Aluminium-BSF solar cells which have been produced according to a co-firing parameter optimization process with a wide parameter space. It is found that the rear side recombination velocity on some locations of the Al-BSF cell is much better than compared to PERC cells. Thus, the full potential of Al-BSF solar cells is much higher than usually expected and anticipated. In the future paste and co-firing optimizations are required to transfer the excellent local values of Al-BSF cells to the full cell area for excellent global values that result in cell efficiencies higher than today PERC solar cells. Thus, the time of Al-BSF solar cells is for our opinion not over yet.

Keywords

Photovoltaics • Characterization • Diffusion length • PERC • Al-BSF

1 Introduction

Aluminium back surface field (or Al-BSF) silicon solar cells has been the dominant solar cell technology over the past decades. However, newer cell concepts with passivated rear sides like PERC (Passivated Emitter Rear Cell) promise higher solar cell efficiencies with a similar lean process sequence and are a promising candidate for the new industry standard in the coming years ahead. Very crucial for the solar cell research of all concepts are local characterizations methods that are powerful enough to determine and separate the information of the silicon bulk material quality from the passivation quality of the rear side. In this paper the photo-impedance measurement of CELLO-technique will be introduced and demonstrated its capabilities on a multicrystalline Al-BSF cell.

2 Multicrystalline Al-BSF Solar Cells

Multicrystalline Al-BSF solar cells with a wafer thickness of 165 μm are prepared in a commercial like cell production process. The cells discussed in this paper were produced during a co-firing optimization with various belt speeds and changing peak firing temperatures [1].

3 Cello Photo-Impedance-Spectroscopy

3.1 Set-up and Measurement Details

The CELLO set-up is described in full detail elsewhere [1, 2]. In short: Three different lasers are intensity-modulated by four different frequencies and the amplitude and phase shift of the linear response is recorded, while a potentiostat

A. Schütt (✉) · O. Lupan · R. Adelung
Institute for Materials Science, Kiel University, Kaiserstraße 2,
24143 Kiel, Germany
e-mail: asc@tf.uni-kiel.de

O. Lupan
Department of Microelectronics & Biomedical Engineering,
Center for Nanotechnology and Nanosensors, Technical
University of Moldova, Chisinau, Republic of Moldova

keeps short circuit conditions. The lasers are scanned across the solar cell producing amplitude and phase shift maps with a resolution of 1000×1000 pixels.

3.2 Data Preparation and Fit

For a typical measurement, 48 maps were recorded and processed. After a “current-correction” routine that compensates for small non-linearities of the set voltage of the potentiostat the final 24 maps are obtained. These amplitude and phase shift maps were fit to a model called “tSRC3 * 3” that is explained in detail elsewhere [2]. Global fit parameter are set: Minority diffusion coefficient $D = 28 \text{ cm}^2/\text{s}$ (a common value for multicrystalline-material) and $164 \mu\text{m}$ wafer thickness. The resulting maps of the local fit parameters are minority carrier lifetime τ (μs), diffusion length L (μm), rear surface recombination velocity S_B (cm/s), and for the three lasers the $R_{\text{SER}}C$ -time constants (ns).

4 Results and Discussion

The L map is presented in Fig. 1: As expected for good solar cells, the average diffusion length of $160 \mu\text{m}$ is in the range of the wafer thickness of $165 \mu\text{m}$. Nevertheless big local variations are observed. As expected L is shorter at dislocation nests ($\sim 70 \mu\text{m}$), as revealed on the Amplitude map (not presented here). However, at some grains big variations are visible, as well (good: $310 \mu\text{m}$; bad $110 \mu\text{m}$). Here, the effect of Al-P-co-gettering inducing local inhomogeneities is visible. The interplay between bulk material improvement due to gettering and rear side contact formation is nicely resolved in the maps.

The S_B map in Fig. 2 reveals that there exist extremely good local values of -1700 cm/s . As explained in detail in [3] negative values reflect local current flow directions and the smaller the value the better for the cell performance. The pattern of the extremely good areas in Fig. 2 lets to the assumption that the Al-BSF formation on the rear side is not homogeneous. It maybe the consequence of Al-Si-agglomeration [4] that result in inhomogeneously thick back surface fields. However, these values are extremely good. They are better than S_B values from excellent PERC solar cells, e.g. excellent areas of the PERC cells presented [3] have values of -1200 cm/s . However, the global mean

value of the S_B map with 83 cm/s is just average and has still some room for improvement.

The observable effects of local variations of gettering and Al-BSF formation are a direct result of our specially prepared samples from a co-firing optimization with various peak firing temperatures and belt speeds. In a normal industrial production environment these big parameter variations do not exist and the impact of changing process parameters to the local solar cell parameters is not as prominent as in our case. However, our results demonstrated the great potential of further optimization of the complete co-firing process including bulk gettering, Al-BSF-formation and contact formation. Finally our results a hint for the manufacturers of Al-pastes that their pastes are not limiting the performance of solar cells yet and there is still much room for improvement even for standard multicrystalline Al-BSF solar cells.

5 Importance and Outlook

The measurement shows that excellent surface passivation with -1700 cm/s is possible with Al-BSF solar cells. Next, the excellent local values of S_B have to be homogeneously transferred to the complete cell area with paste and co-firing optimizations.

Additionally, also the optimization of the Al-P-co-gettering for excellent lifetimes and diffusion lengths is of major interest for excellent solar cells. As presented here, mastering the rear side contact formation, BSF-formation, and Al-P-co-gettering are essential for the production of efficient silicon solar cells. The optimization potential for the production of (multi-) crystalline Si solar cells cannot be underestimated. A lot of solar manufacturers produce their own solar cell wafers. Thus the cell efficiency improvement opportunities during the cell production during co-firing is for them of great (financial) interest. They get literally more out of every wafer. CELLO-measurements in combination with cell process optimizations Al-BSF solar cells will be possible that are much better than comparable PERC solar cells. Thus, the Al-BSF solar cell age is far from being over. Finally, the presented measurement method might be also promising for the characterization of next generation thin film solar cells [5].

Conflict of Interest The authors declare that they have no conflict of interest.

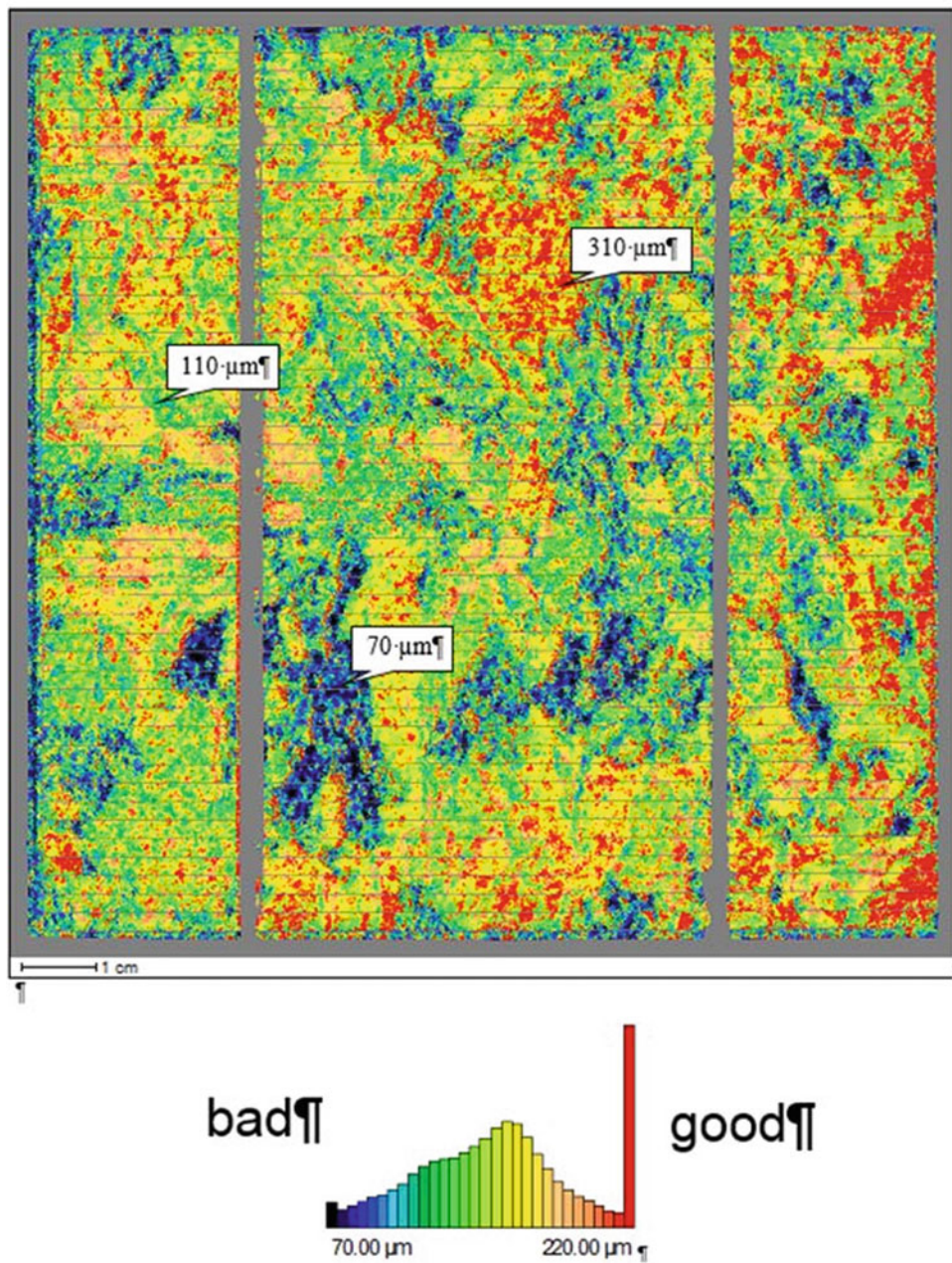


Fig. 1 L-map. The effect of Al-P-co-gettering inducing local inhomogeneities is visible. The interplay between bulk material improvement due to gettering and rear side contact formation is nicely resolved

in the maps. Here the maps are presented as large figures. Thus the reader can clearly see the superior resolution and identify the local variations

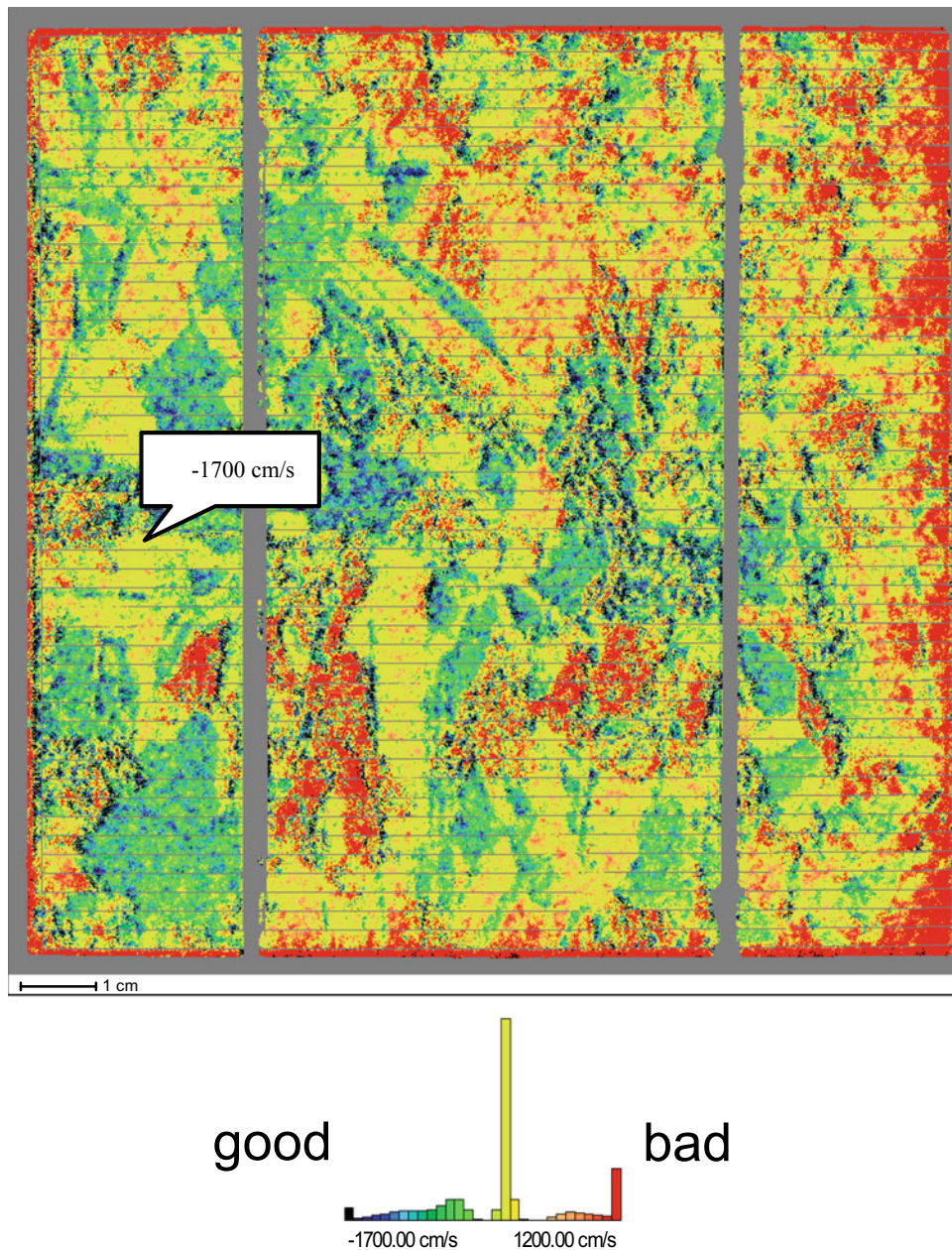


Fig. 2 S_B -map. The pattern of extremely good areas indicates that the back surface field formation on the rear side of the cell is not homogeneous

References

1. Schütt, A. (2015). Ortsaufgelöste Charakterisierung in der Photovoltaik mit der CELLO-Technik (Solar cell local characterization). Dissertation, CAU Kiel, at https://macau.uni-kiel.de/receive/dissertation_diss_00016555
2. Wagner, J.-M., Schütt, A., Carstensen, J., Föll, H.: Series resistance contribution of majority carriers in CELLO impedance analysis: influence of wafer thickness variation Solar Energy Mater. Solar Cells **146**, 129 (2016)
3. Schütt, A.: CELLO photo-impedance-spectroscopy on PERC solar cells: separation of bulk and rear surface defects. Energy Procedia **124**, 161 (2017)
4. Huster, F.: Investigation of the alloying process of screen printed aluminum pastes for the BSF formation on Silicon solar cells. In: Proceedings of 20th European Photovoltaic Solar Energy Conference, 1466, Barcelona (2005)
5. Lupan, O., et al.: Synthesis of nanostructured Al-doped zinc oxide films on Si for solar cells applications. Sol. Energy Mater. Sol. Cells **93**(8), 1417–1422 (2009)

Smart Device for Therapeutic Hypothermia

V. Cojocaru, R. Galus, and T. Fedorisin

Abstract

We describe the construction of a non-invasive hypothermic system for reducing brain temperature used in the treatment of stroke. The device is used by those who offer first medical aid. Its usage helps with the stabilization of the patient's state and stops any aggravations.

Keywords

Peltier element • Hypothermia • Thermo electrical effect • Cooling system

1 Introduction

Hypothermia represents a non-pharmacological method which can improve neurological results in cerebral ischemia. Its benefic effects can be used even in other pathologies as: uncontrolled intracranial hypertension, head injuries, ischemic stroke [1–5].

Mechanisms to protect the brain during hypothermia: re-duction of free radical processes, reducing cerebral edema and intracranial pressure, decreasing the inflammatory response, reduced metabolism of neurons suppress neuro-transmission of glutamate exit toxicity and restriction, limiting activation of apoptosis, also contributes to anticoagulant hypothermia. Authors' goal was to develop a device for cooling the brain, using a thermoelectric cascade of coolers (TEC). Using of TEC eliminates the need to use cryogenic liquid as a cooler. Using systems with thermoelectric cooling offers advantages compared to conventional

methods of cooling with liquid. Advantages include compact size, reduced weight and easy commutation between cooling and warming [6, 7].

2 Methods

The purpose of therapeutic hypothermia is reducing the cerebral consumption of oxygen (CMR O₂—the cerebral metabolic rate of oxygen) by reducing body temperature [8–10].

Depending on the reduction of body temperature there are the next levels of hypothermia:

- (A) maintaining of thermal norm during fever
- (B) light hypothermia (34–36 °C)
- (C) medium hypothermia (32–34 °C)
- (D) deep hypothermia (30–32 °C)
- (E) very deep hypothermia (<30 °C)

Level A is used for relieving fever, in case we can't use antipyretic therapy.

Levels B and C are the most used while being on a relatively safe level of reduction of body temperature [11–13].

Oxidative stress and local inflammation begins to appear within the first 2–3 h of the onset of pathology, reaching a peak in 12–36 h; the long-term down effects are formed, mainly, in 2–3 days [14–17].

Hypothermia for medical therapeutic purposes can be implemented using invasive methods, in case the transfer of heat is directed by a catheter inserted into the femoral vein. It is an efficient method, but requires specially designed rooms and patient care by a specialist. Simple non-invasive methods use water/ice applications in the required zone. It is a cheap method, but the blood temperature in the required area is out of control. For these reasons, a mobile device is required with elements that may form controlled cooling zones with Peltier elements. To reduce the intervention time (which is a major factor in brain attacks), these devices need

V. Cojocaru (✉) · R. Galus · T. Fedorisin
D. Ghitu Institute of the Electronic Engineering and Nanotechnologies, Academiei 3/3, Chisinau, Moldova
e-mail: victor.cojocaru@mib.utm.md

V. Cojocaru
Technical University of Moldova, Chisinau, Moldova

to be mobile to be placed in ambulances. This is a non-invasive method and the device cannot cause harm to the patient. With all the successes of contemporary neurology, the problem of the treatment of cerebral stroke is still not satisfactorily solved. Treatment can be considered successful for most patients only in the initial stages of trauma. A large part of patients are transported too late to clinics, when ischemic trauma is already extended. This is why the priority objectives for this device are to equip the doctors from the emergency hospitals with the technology and equipment needed to deliver the aid as fast as possible, with efficient cooling of the deeper regions of the brain [18, 19].

3 Circuits

The authors have developed a device for hypothermia for controlled cooling of some wounds used for medical purposes. This device functions on the basis of cooling with Peltier elements that are divided into separate cooling zones. The small installation can be used in mobile SMURD stations (emergency vehicles).

Main technical features:

- Nominal voltage—220 to 240 V, 50 Hz
- Energy consumption—1000 W
- Current consumption—33 A
- Size—250 × 250 × 140 mm
- Weight—5 kg

The device does not generate dangerous currents for patient's health. Power sources are galvanically separated and do not represent a danger to health. The device does not generate oscillations and electromagnetic fields dangerous to the health of patients.

The device was tested and it works satisfactorily. Appropriate tests were carried out, namely:

Cooling devices: As cooling elements four Peltier elements are used, with a driver control and feedback with the routing device. It was cooled to 8 °C. The device keeps the temperature constant. After several tests, we found that the heat was best removed by a water cooling system. To cool the Peltier element we used a dune radiator with cooling through a cooling water system pumped from a 15 L water tank. The pump used is an Atman AT-106 pump.

Temperature measurement: As a temperature sensor we use the PZT100 thermosensor and a signal amplification scheme from these modules. The sensors are placed on the scalp and in the ear, also non-invasive.

Control of cooling elements and temperature: The scheme is based on an ATmega128 microcontroller for temperature measurement, routing of Peltier elements and computer communication.

Graphical Interface: Represents software, designed and developed in the laboratory "Medical Technology", installed on a computer to monitor, visualize and change the temperature regime.

Compared with the previous project [20, 21] the construction and the circuit was essentially changed. The main changes were the replacement of four Peltier TEC1-12,706 with dimensions (40 × 40 mm) (Fig. 1) with 20 Peltier elements TEC1-04902 with dimensions (20 × 20 mm) (Fig. 2) and the change in the control system for the cooling. Using of Peltier elements TEC1206 with smaller dimensions allowed the more homogenous temperature distribution. It was also possible to divide the surface of the scalp into four separate areas of the scalp cooling, independently controlled. The last suggestions have been made by medical consultants in the field of using this device to patients after trepanation and when it is necessary to use different temperatures on the surface of the skull.

Taking into account the fact that the installation will be used in the stationary place, but also in the emergency service cars, the technical solutions was to use a power supply capable running from the car's battery to the power supply of the system.

Given that Peltier elements could be controlled separately in the mentioned version of device for hypothermic therapy, we can cool small zones or zones where we need higher precision control after surgery where skull bone was removed. Following the tests, the doctors made an analysis and formed a number of requirements which led to the design of the third version of device (cooling helmet) in Fig. 3.

To provide a high thermal conductivity with the scalp, we used four 4-mm-thick copper plates adjusted to the human head. On the left and right plates, we placed three TEC1-12706 Peltier elements with dimensions of

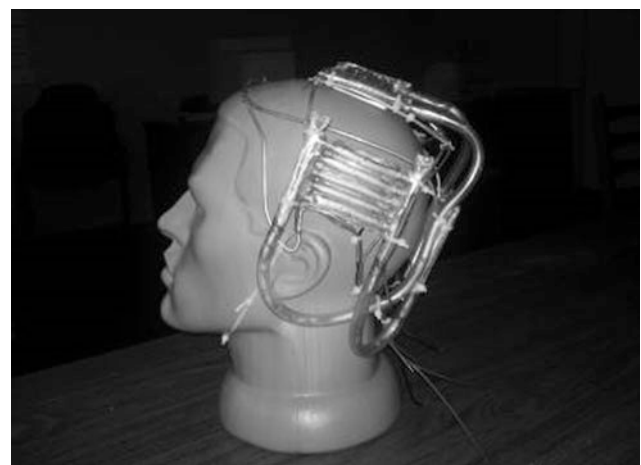


Fig. 1 Model of cooling with four Peltier [25]

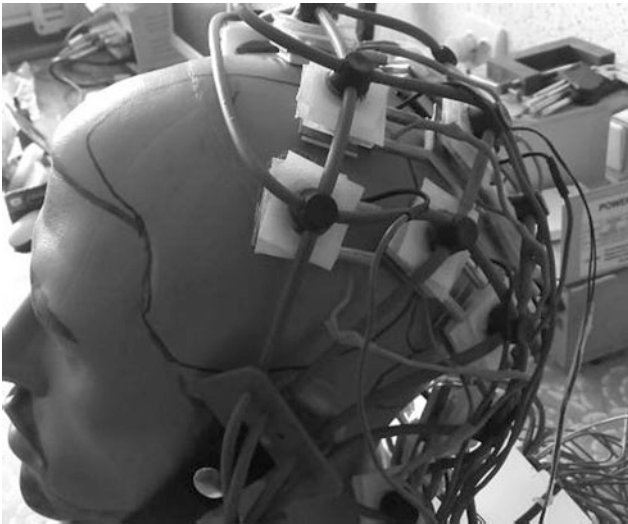


Fig. 2 Model of cooling with twenty Peltier [25]



Fig. 3 The third version of cooling helmet

40 × 40 mm, which provide sufficient thermal power. On the top and back of the scalp, plaques with two TEC1-12706 Peltier elements were placed. To improve the thermal conductivity with the scalp and provide patient's comfort, a heat-conducting gel was placed between the plaque and the scalp.

The power routing scheme for the Peltier elements contains four identical modules (Fig. 4).

The power routing scheme of Peltier elements contains four identical modules (Fig. 4).

Temperature measurement. A temperature measurement and signal amplification scheme from these modules were reported in [20–23]. Sensors are placed on the scalp and in the ear, also non-invasive. The control module diagram is based on an ATmega128 microcontroller for measuring the temperature using the PZT100 thermo-sensor and transmitting the controls to the control module and to the graphics display module [22–26].

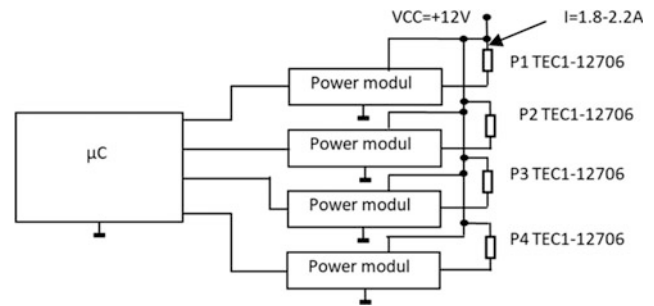


Fig. 4 Module power scheme (from [20–23])

4 Fuzzy Logic Algorithm and Control [20–24]

Comparing to previous project and the control of TEC elements is divided in four zones. The fuzzy control algorithms for the new device consists in the modification of two input variables: “Measured Temperature” and “Preselected temperature by the doctor” in two variables: “Difference in temperature in the ears and preselected temperature” and “Difference of temperature in the ears on the scalp and preselected temperature” (The variables were suggested by H. N. Teodorescu.).

The set of rules is the same for four zones:

1. Left scalp area
2. Right scalp area
3. Top zone
4. Back zone

Rules for one zone looks as [20–24]:

1. If $\Delta t(\text{scalp}) = \text{low}$ and $\Delta t(\text{ear}) = \text{neg}$, then $I(\text{peltier}) = 0$
2. If $\Delta t(\text{scalp}) = \text{negative}$ and $\Delta t(\text{ear}) = \text{any}$, then $I(\text{peltier}) = 0$
3. If $\Delta t(\text{scalp}) = \text{low}$ and $\Delta t(\text{ear}) = \text{low}$, then $I(\text{peltier}) = \text{low}$
4. If $\Delta t(\text{scalp}) = \text{medium}$ and $\Delta t(\text{ear}) = \text{low}$, then $I(\text{peltier}) = \text{low}$
5. If $\Delta t(\text{scalp}) = \text{high}$ and $\Delta t(\text{ear}) = \text{low}$, then $I(\text{peltier}) = \text{low}$
6. If $\Delta t(\text{scalp}) = \text{low}$ and $\Delta t(\text{ear}) = \text{medium}$, then $I(\text{peltier}) = \text{low}$
7. If $\Delta t(\text{scalp}) = \text{low}$ and $\Delta t(\text{ear}) = \text{high}$, then $I(\text{peltier}) = \text{medium}$
8. If $\Delta t(\text{scalp}) = \text{medium}$ and $\Delta t(\text{ear}) = \text{medium}$, then $I(\text{peltier}) = \text{medium}$
9. If $\Delta t(\text{scalp}) = \text{medium}$ and $\Delta t(\text{ear}) = \text{high}$, then $I(\text{peltier}) = \text{high}$

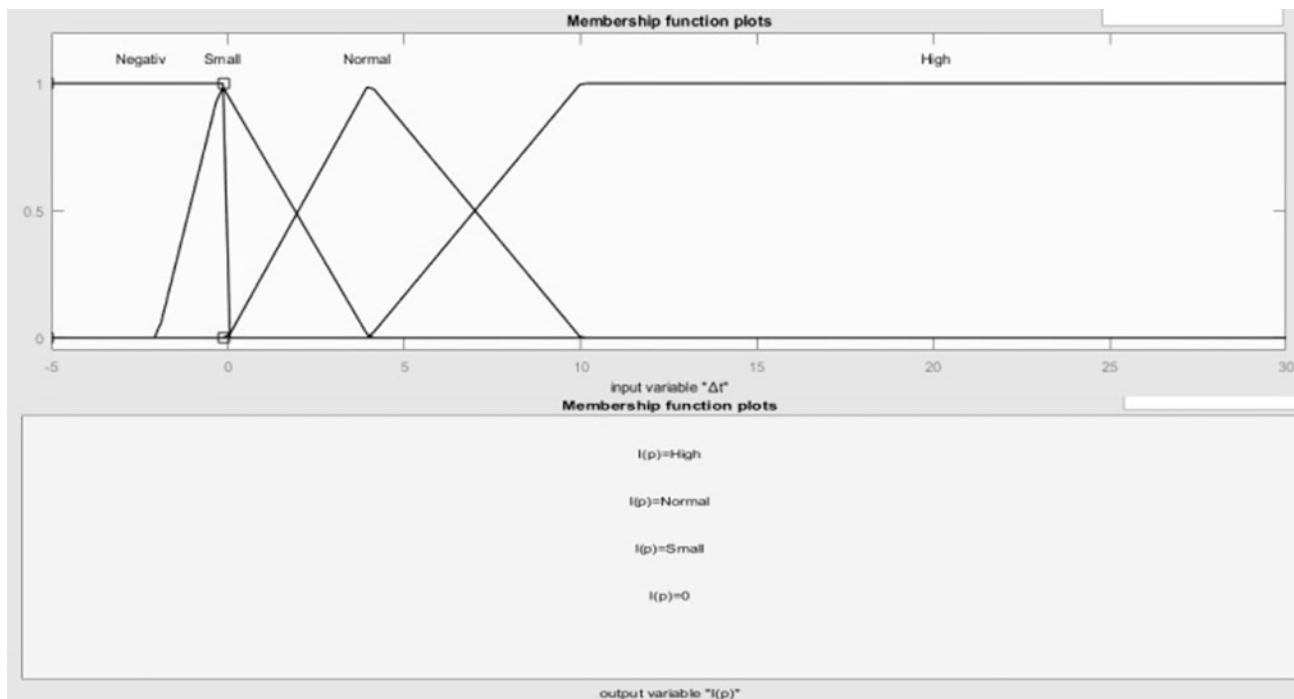


Fig. 5 Input variable Δt —temperature difference on the sensor and preselection (top) and output variable $I(p)$ —current through Peltier elements (back)

10. If $\Delta t(\text{scalp}) = \text{high}$ and $\Delta t(\text{ear}) = \text{high}$, then $I(\text{peltier}) = \text{high}$
11. If $\Delta t(\text{ear}) = \text{higher than } t(\text{preselected})$, then $I(\text{peltier}) = 0$
12. If $\Delta t(\text{ear}) = t(\text{preselected})$, then $I(\text{peltier}) = 0$

Each zone is separately controlled, but the rules are the same for every zone. In Fig. 5 is illustrated one of the input variables.

Choosing of membership functions takes into account the possibility of adjusting the input-output characteristic by using curved triangle functions [27], as well as the restrictions specified in [28].

5 Conclusions

We proposed, designed, built and tested a new version of a hypothermic therapy device used for medical purposes using the Peltier elements.

Second version with 20 Peltier elements TEC1-04902 with dimensions (20 × 20 mm). The use of smaller Peltier elements TEC1-04902 allowed temperature distribution on the scalp to be more homogenous and it was possible to divide the surface that allows the use of this device to patients after trepanning and when it is necessary to use different temperatures on the surface of the skull.

The third version of cooling helmet was designed after medics' recommendations to improve the treatment of patients.

Acknowledgements We thank H.-N. Teodorescu for advice and critic on several versions of the article, and for many suggestions. Authors took advantage of financing of the scientific project "Elaboration and design of medical devices". V.C. acknowledges seven research exchanges supported by the Romanian Academy.

Conflict of Interest The authors declare that they have no conflict of interest.

References

1. Holzer, M.: Mild hypothermia to improve the neurologic outcome after cardiac arrest. *New Engl. J. Med.* **346**(8), 549–556 (2002)
2. Muresan, A., Macovei, R., Alexianu, D., Prazaru, M.: Hipotermiametodaterapeuticaneuroprotectoare, intrebeneficiisiriscuri. *Terapeutica, Farmacologie si Toxicologie Clinica* **12**(3) (2008)
3. Lei, J., Gao, J., Mao, Q., Feng, J., Wang, L., You, W., Jiang, J.: Rationale, methodology, and implementation of a nationwide multicenter randomized controlled trial of long-term mild hypothermia for severe traumatic brain injury (the LTH-1 trial). *Contemp. Clin. Trials* **40**, 9–14 (2015)
4. Wu, X., Lu, X., Lu, X., Yu, J., Sun, Y., Du, Z., Wu, X., Mao, Y., Zhou, L., Wu, S., Hu, J.: Prevalence of severe hypokalaemia in patients with traumatic brain injury. *Injury* **46**(1), 35–41 (2015)

5. Demirela, H., Gökaşb, H.H., Erkala, B., Çiyilanc, B.: Prediction of the brain temperature from other body temperatures in hypothermia induced rats by using artificial neural networks. *Comput. Biol. Med.* **42**(7), 772–777 (2012)
6. Morizanea, K., Ogataa, T., Morinoa, T., Horiuchi, H., Yamaokaa, G., Hino, M., Miura, H.: A novel thermoelectric cooling device using Peltier modules for inducing local hypothermia of the spinal cord: the effect of local electrically controlled cooling for the treatment of spinal cord injuries in conscious rats. *Neurosci. Res.* **72**(3), 279–282 (2012)
7. Cojocaru, V., Mardari, V.: Device for hypothermic therapy. In: 2nd International Conference on Nanotechnologies and Biomedical Engineering, Chişinău. ISBN 978–9975-62-343-8, 18–20 Apr 2013
8. Jiang, J.-Y., Yu, M.-K., Zhu, C.: Effect of long-term mild hypothermia therapy in patients with severe traumatic brain injury: 1-year follow-up review of 87 cases. *J. Neurosurg.* **93**(4), 546–549 (2000)
9. Eldadah, B.A., Faden, A.I.: Caspase pathways, neuronal apoptosis, and CNS injury. *J. Neurotrauma* **17**, 811–829 (2000)
10. Mayer, S., Sessler, D., Decker, M. (eds.): *Thermoregulation and Heat Balance. Therapeutic Hypothermia*, New York (2005)
11. Polderman, K.H.: Application of therapeutic hypothermia in the ICU. *Intensive Care Med.* **30**, 556–575 (2004)
12. Johnson, E.A.C., Bonserand, R.H.C., Jeronimidis, G.: Recent advances in biomimetic sensing technologies. *Phil. Trans. R. Soc. A* **367**, 1559–1569
13. Lee, C., Chuang, H.H.C., Cho, D.Y., Cheng, K.F., Lin, P.H., Chen, C.C.: Applying cerebral hypothermia and brain oxygen monitoring in treating severe traumatic brain injury. *World Neurosurg* **74**(6), 654–660 (2010)
14. Bregy, A., Nixon, R., Lotocki, G., Alonso, O.F., Atkins, C.M., Tsoufias, P., Bramlett, H.M., Dietrich, W.D.: Posttraumatic hypothermia increases double cortin expressing neurons in the dentate gyrus after traumatic brain injury. *Exp. Neurol.* **233**(2), 821–828 (2012)
15. Brennan, A.M., Suh, S.W., Won, S.J.: NADPH oxidase is the primary source of superoxide by NMDA receptor activation. *Nat Neurosci* **12**, 857–863 (2009)
16. Vincent, J.-L. (ed) *Annual Update in Intensive Care and Emergency Medicine*, vol. 796. Springer, Berlin (2014)
17. Keller, E., et al.: Theoretical evaluations of therapeutic systemic and local cerebral hypothermia. *J. Neurosci. Methods* (2009). <https://doi.org/10.1016/j.jneumeth.2008.12.030>
18. Teodorescu, H.N.: Studies should fully report on variables that determinethe dynamics and the temperature gradients during hypothermia. *Crit Care* **22**(1), 219 (2018)
19. Teodorescu, H.N.L.: Design considerations for uniform, fast cooling hypothermia equipment. In: *Proceedings of 10th International Conference on Electronics, Computers and Artificial Intelligence (ECAI)*, Iasi, Romania, 28–30 June 2018
20. Cojocaru, V.P., Tugui, P.S., Fedorisin, T., Postica, I.V., Galus, R.: Hypothermia device used in medicine. In: *3rd International Conference on Nanotechnologies and Biomedical Engineering*. Springer, Singapore, pp. 365–369 (2016)
21. Cojocaru, V., Mardari, V.: Fuzzy controlled system for hypothermic brain therapy. *Proc Romanian Acad Ser A* **15**(4):396–402 (2014)
22. Cojocaru, V.P., Vrabii, D.: Fuzzy logic algorithm for use in controlled hypothermia. In: *The 5th IEEE International Conference on E-Health and Bioengineering—EHB 2015*, Iasi, Romania, Nov 2015, pp. 19–21 (2015)
23. Cojocaru, V.P., Tugui, P.S., Fedorisin, T., Postica, I.V., Galus, R.: Dynamic method of brain cooling. In: *A V-a Conferință Internațională “Telecomunicații, Electronicăși Informatică” ICTEI 2015*, Chisinau, Republic of Moldova, pp. 447–450 (2015)
24. Cojocaru, V.P., Sidorenko, A., Vrabii, D.: 2D/3D heat transport maps of biological tissue in therapeutic hypothermia. *Romanian J. Inf. Sci. Technol.* **19**(1–2), 188–196 (2016)
25. Cojocaru, V., Niguleanu, E., Fedorisin, T., Galus, R.: Intelligent device for controlled therapeutic hypothermia. In: *ECAI 2018 International Conference—10th Edition Electronics, Computers and Artificial Intelligence*, Iasi, 28 June–30 June 2018
26. Cojocaru, V.P., Vrabii, D.: Simulations of the effect of the cooling elements’ temperature on the hypothermia efficiency. In: *The 6th IEEE International Conference on E-Health and Bioengineering—EHB 2017*, p 13
27. Teodorescu, H.N.: Coordinate fuzzy transforms and fuzzy tent maps—properties and applications. *Stud. Inf. Control* **24**(3), 243–250 (2015)
28. Teodorescu, H.N.: On the characteristic functions of fuzzy systems. *Int. J. Comput. Commun. Control* **8**(3), 469–476, Jun 2013

Make Innovation Happen: Scientific and Statistic Tools to Accelerate the Way Toward Technology Readiness Level TRL 9—A Deployed Application

N. Varachiu

Abstract

We consider some tools/methodologies, scientific and statistics based, to design and optimize technological processes and the resulting products, by providing finally a robust design. Being implemented in R&D labs, such tools and methodologies could enable a faster skip from *lab experiments* to *real world* (i.e. Technology Readiness Level TRL 9) by catalyzing innovation, problem solving and even discovery. At the end of the day *to make innovation happen*. We present also a successful example of application of such approach, to open also a larger discussion about the opportunity of intensively using such approach for nano scale organized materials and further products, with application also in biomedical engineering. An usual cause for the difficulty of R&D labs to pass over the TRL 4 (=technology validated in lab) is the approach of testing the realized prototypes in the R&D lab, i.e. not taking into account the effective manufacturing conditions and environment, and the further operation conditions for the proposed and developed concept/product/device. To overpass that, the best practice shows the research scientists/engineers need to find from the beginning of the research and the development process the effective future manufacturing conditions/process parameters and the future real-life utilization of the resulting products (operating conditions) and to test their prototypes in such conditions. But more than only testing, *it is crucial to provide a so called “robust design”* (Taguchi), i.e. to optimize the concepts/products parameters so they perform to expectations under a wide range of operating conditions, meanwhile being possible to be fabricated at lower possible cost and risk.

Keywords

Innovation • Technology readiness level • Design of experiment • Robust design • Six sigma—lean

1 Introduction

At the beginning of the last century, Henry Ford had a dream: “every man having a job to be able to have an automobile for him and his family”. This dream became practically reality in the last decades of the last century, mainly in developed and emerging countries [1]. And that started by implementing the concepts of line assembly and manufacturing process for the famous Ford T model, introduced in 1908. In the so-called Ford system, they fabricated automobiles in large quantities of the same design, delivering cars with low cost, converting the automobile from an expensive curiosity into a practical and affordable transportation mean.

It worth to mention Ford took in his factory the idea of mass production from a slaughterhouse in Chicago: The pigs hung from conveyor belts and each butcher performed only a part of the task of butchering the animal. Henry Ford carried over these principles into automobile production and drastically transformed it in the process. While before one station assembled an entire automobile, now the vehicles were produced in partial steps on the conveyor belt—significantly faster and at lower cost. The discovery of electricity and line assembly line production represent the beginning of the second industrial revolution, starting in the nineteenth century.

Besides above, a crucial role played the adjacent methods developed to sustain this mass production with as low as possible defects and with low fabrication cycle times: in Bell Labs, where in 1940s was invented the transistor, Dr. Walther A. Shewhart invented the *control chart* in the 1920s, droved by a stronger business need, to reduce the frequency of failures and repairs and by engineers

N. Varachiu (✉)

Center for Technology Transfer in Micro Nano Engineering,
National Institute for R&D in Microtechnologies, IMT Bucharest,
126A Erou Iancu Nicolae Str., Bucharest, Romania
e-mail: nicolae.varachiu@imt.ro

observation that to reduce variation in manufacturing process, a continual process-adjustment in reaction to non-conformance actually increased variation and degraded quality [2]. Many other tools using statistics and scientific methods of experiments and testing were further developed to reduce defects and cycle time: these tools were put together in 1980s by Motorola in the Six Sigma concept and philosophy. After, Six Sigma together with Lean manufacturing (having Ford as father) changed the way big companies conducted operations successfully worldwide [2]. One major contribution in that direction was made by Dr. Ronald Fischer who proposed Design of Experiment (DoE), or factorial design, as a new strategy in experimentation, first applied in agriculture; here an experiment could last two years and more, so an experiment should be well prepared. DOE was further an important tool enabling Dr. Genichi Taguchi, a Japanese engineer and statistician, to derive in 1960s the concept of Robust Design, by developing also further the theory and applications of DOE [2–4]. Taguchi had a thorough cooperation with Fisher and Shewhart, also with Dr. Edward Deming who brought and enabled the deployment and development of statistical quality control in Japan in 1950s, from where was spread in the world, initially mainly to industrial corporations.

2 Principles and Strategies of Experimentation

2.1 Experiments and Kind of Inputs

An *experiment* or a test represents a set of systematic actions to manipulate the input variables into a process or device/product/system, even service, to determine/measure the output responses and the effects. A *response* is the punctual value of an output for a particular input setting, while an *effect* represents the difference between output responses for two different settings of input variables [3]. For the estimation of output variability, the effects are of particular interest.

From the perspective of analysis of variation, inputs in a process or in a product are classified in two categories:

- *controllable* inputs: their values could be “controlled”, i.e. set at the desired level.
- *uncontrollable* inputs: that cannot be at all controlled (i.e. their values; e.g. environmental temperature, pressure, humidity, etc.) or cannot be easily controlled during manufacturing process and/or in future real operational conditions.

2.2 Robust Design

Even in real manufacturing environment and in real operating conditions/environment we could not control some input factors, or we choose not to control others difficult or too expensive to control their settings, in the R&D labs we could control in experiments the settings of such uncontrollable (in manufacturing and in real operating condition) inputs, together with the already controllable inputs (e.g. we could test the influence of humidity variation in a manufacturing process or functionality of a device/product and to estimate the output effects of them). If, by design when the concept is researched and developed, we will provide a very low sensibility of the output values in respect with the variation of uncontrollable inputs, we say we provided a Robust Design (Taguchi) [3, 4]. In general optimization is the process of making a design “best” according to some set of objective value measures. Robustness is a special type of optimization: optimizing a concept/design so it is not sensitive to uncontrollable inputs. Figure 1 is a visual representation for the concept of Robust Design.

2.3 Basic Principles of Experimental Design

There are three basic principals: *replication*, *randomization* and *blocking* [3]. *Replication* represents a repetition of basic experiment, in order to obtain an estimate of the experimental error, and when we use the sample mean to estimate the effect of an input to experiment, we obtain a more precise estimate of this effect.

By *randomization* we enable the observations of errors to be independently distributed random variables, and more, very important, helping in “averaging out” the effect of hidden external factors (we don’t know they exist).

A *block* is a part of the experimental material and/or set-up that should be more homogeneous than entire material and/or set-up. *Blocking* take into consideration the observed blocks and making comparisons within each block increase

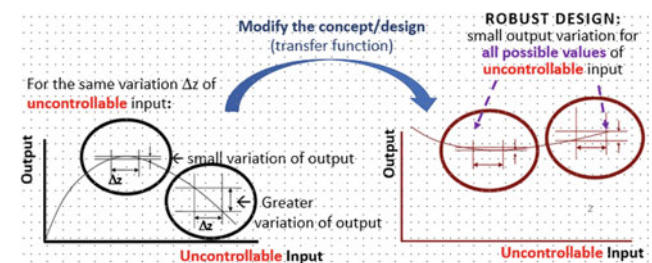


Fig. 1 The robust design concept

the precision of an experiment. A general rule for experiments: *block what you can and randomize what you cannot!*

We used all these principles in the further deployed experiment presented in Sect. 3.

2.4 Strategies of Experimentation

The generally used strategies in experiments are:

- the best-guess approach (trial and error),
- one-factor-at-a-time (OFAT): elect a baseline for the values of each input factor and, successively, vary each factor with all other factors held at the fixed levels initially selected (from the baseline). Major drawback: it can not capture *interactions* between inputs
- factorial design (DOE, Design of Experiment): the input factors considered in the experiment are varied together (=all possible combinations of the considered input levels are considered), so it could capture interaction of inputs, if it does exist. There is an *interaction* of two independent inputs when the effect on output (difference between two output responses) due to the variation of an input depends on the setting of the other input. *Using interaction, when exists, is crucial to implement a robust design, as we will show further.*

In a DOE experiment we usually use two levels for each factor, noted as Low (L) and High (H) respectively. Let's compare, OFAT and DOE for an experiment with three input factors and two levels for each factor:

OFAT	DOE
L L L	L L L
H L L	H L L
L H L	L H L
L L H	H H L
	L L H
	H L H
	L H H
	H H H

In our further experiment we use DOE as strategy.

3 Implemented Experiments and Results

Starting from material science and engineering, after research and lab experiments, a specific formulation was established for a friction material. Next step was to optimize the designed fabrication process, to make it robust, i.e. to

provide at the end of the day cheaper products (brakes) while maintaining the required quality for this safety critical part in an automobile. For the purpose of this experiment, the particular formulation of the material is not significant, and we will not present it. There were established the parameters of a full factorial DoE (Design of Experiment) as:

Output: *Compressibility* (measured in micrometers)

Inputs:

Pressure: Low = 300 kPa, High = 400 kPa

Cycle (attribute data, two different process sequences)

Low = 5-5-5-5-120, High = 5-5-5-5-5-100

(the meaning of the above notation is not significant)

Temperature: Low = 155 °C, High = 165 °C

The full factorial experiment has the $2^3 = 8$ run variants (in standard order), as in Table 1.

The experiment was performed using a molding with four cavities; using the experimental principle of *blocking* we consider each cavity as a separate block. Using the *replication* principle we deployed 13 trials for each variant run, getting 416 samples (=8 variants × 4 blocks × 13 runs), measuring for each the *compressibility*. We also *randomized* the trials. Finally, we consider the average (noted *Ave*) and the standard deviation for each row of 13 runs, as in Table 2.

For *Ave*, the below residual plots look good; as R-squared [2, 4] are higher than 80%, we could trust the model we get (Fig. 2).

The results for analysis of variance for *Ave* are shown in Table 3.

Together with *Cavities* (*Blocks* in table), only two input factors *Temp* (temperature) and *Cycle* and their interaction *Temp * Cycle* are statistically significant, as their F value are high and consequently p-values are very low (much lower than 0.01, a large accepted threshold for that in statistics).

Also, for computed output *Lognormstdev* (for normalization, we use the natural logarithm of Standard Deviation) we get good looking residual plots and borderline acceptable

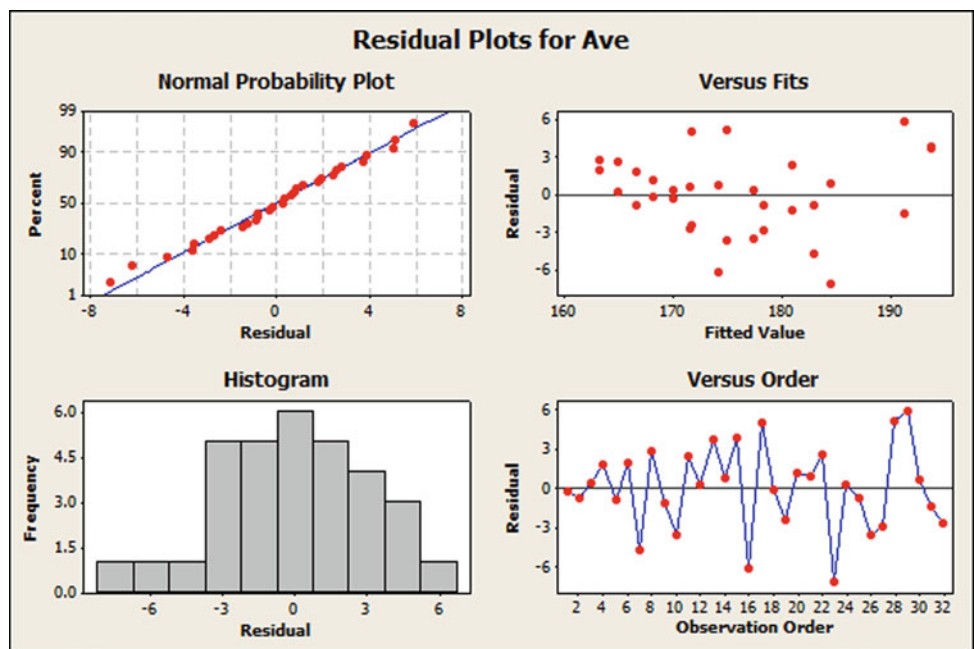
Table 1 Full factorial experiment

Run variant	Pressure (kPa)	Cycle	Temp. (°C)
A	300	5-5-5-5-120	155
B	400	5-5-5-5-120	155
C	300	5-5-5-5-5-100	155
D	400	5-5-5-5-5-100	155
E	300	5-5-5-5-120	165
F	400	5-5-5-5-120	165
G	300	5-5-5-5-5-100	165
H	400	5-5-5-5-5-100	165

Table 2 Full factorial DOE implementation (presented in standard order)

Run	Block = cavity		Factors					Run / Setting variant													Average and St. Deviation for 13 cycles	
	C4	C5	C6	C7-T	C8	run	C9	C10	C11	C12	C13	C14	C15	C16	C17	C18	C19	C20	C21	C22	C23	
	Blocks	temp	pres	cycle	run		Cy1	Cy2	Cy3	Cy4	Cy5	Cy6	Cy7	Cy8	Cy9	Cy10	Cy11	Cy12	Cy13	Ave	StDev	
1	1	155	300	5-5-5-5-120	A		177.5	169.0	169.0	166.0	167.5	169.5	165.0	165.5	168.0	172.5	165.5	175.0	175.5	169.654	4.18522	
2	1	165	300	5-5-5-5-120	E		171.5	166.5	164.5	170.5	167.5	168.0	168.5	169.0	162.0	161.5	160.0	162.5	161.0	165.615	3.89526	
3	1	155	400	5-5-5-5-120	B		179.0	169.0	174.0	170.5	175.0	171.5	167.0	169.0	166.0	172.0	168.5	165.0	167.5	170.308	3.95568	
4	1	165	400	5-5-5-5-120	F		172.0	169.5	168.5	168.5	175.0	177.5	166.0	164.0	163.0	164.0	167.0	163.5	168.5	168.231	4.47034	
5	1	155	300	5-5-5-5-5-100	C		185.5	180.0	179.0	184.5	188.5	191.0	183.0	176.0	179.5	175.0	182.5	185.0	175.5	181.923	4.98684	
6	1	165	300	5-5-5-5-5-100	G		165.5	165.0	169.0	164.0	168.5	167.5	168.5	161.5	162.5	162.0	157.0	169.5	165.042	3.81062		
7	1	155	400	5-5-5-5-5-100	D		183.5	180.5	172.0	185.0	188.0	176.0	175.0	178.0	176.0	171.0	181.5	175.0	173.5	178.077	5.23548	
8	1	165	400	5-5-5-5-5-100	H		172.0	163.0	173.5	168.5	164.5	165.0	169.5	162.0	167.0	166.5	162.5	166.5	156.5	165.923	4.49929	
9	2	155	300	5-5-5-5-120	A		182.0	178.5	180.5	181.5	177.5	181.0	181.0	177.5	181.0	175.0	180.5	182.0	177.0	179.615	2.24679	
10	2	165	300	5-5-5-5-120	E		179.0	178.5	168.5	175.0	170.5	177.0	173.0	174.0	171.5	173.0	172.5	173.0	173.5	173.769	3.01120	
11	2	155	400	5-5-5-5-120	B		183.5	175.5	180.5	183.0	184.5	187.5	184.0	186.5	182.5	187.0	178.0	183.5	186.5	183.269	3.55091	
12	2	165	400	5-5-5-5-120	F		173.5	179.0	181.0	179.5	184.0	176.5	177.0	173.0	180.5	178.0	174.5	172.5	180.5	177.654	3.53780	
13	2	155	300	5-5-5-5-5-100	C		210.0	194.5	200.5	201.5	178.5	184.5	199.5	202.0	203.5	197.5	192.5	206.0	196.0	197.423	8.56311	
14	2	165	300	5-5-5-5-5-100	G		180.5	176.0	179.5	177.0	167.0	172.0	163.0	178.5	171.0	176.5	175.5	181.5	174.833	5.60168		
15	2	155	400	5-5-5-5-5-100	D		211.5	197.5	207.0	194.5	201.0	197.0	196.0	190.5	198.5	200.5	185.5	191.0	198.5	197.615	6.80733	
16	2	165	400	5-5-5-5-5-100	H		176.0	167.5	167.5	167.0	169.5	170.0	171.0	162.0	167.5	166.5	166.0	168.0	163.0	167.808	3.50915	
17	3	155	300	5-5-5-5-120	A		183.0	175.0	173.5	178.0	181.5	172.0	173.5	172.5	179.0	174.5	172.5	183.0	177.5	176.577	4.03560	
18	3	165	300	5-5-5-5-120	E		169.5	170.0	179.5	169.0	170.0	172.0	166.0	166.0	163.5	162.0	166.0	168.5	162.0	167.923	4.68084	
19	3	155	400	5-5-5-5-120	B		170.5	168.5	167.5	171.5	169.5	172.0	162.5	166.0	170.0	169.0	171.5	164.5	175.5	169.115	3.42876	
20	3	165	400	5-5-5-5-120	F		171.0	177.5	168.5	169.5	171.5	167.5	168.5	165.0	170.0	165.5	167.5	169.5	168.0	169.192	3.13275	
21	3	155	300	5-5-5-5-5-100	C		185.0	178.0	182.5	175.0	195.0	196.0	189.5	187.5	185.5	185.0	188.0	180.0	181.5	185.269	6.11220	
22	3	165	300	5-5-5-5-5-100	G		167.0	168.5	167.0	163.5	170.5	160.0	171.5	162.5	169.0	163.5	166.5	178.5	167.333	4.89589		
23	3	155	400	5-5-5-5-5-100	D		177.0	172.0	172.0	179.0	184.0	175.5	183.5	173.5	182.5	175.5	184.0	173.0	172.0	177.192	4.84570	
24	3	165	400	5-5-5-5-5-100	H		166.5	166.0	169.0	165.5	164.5	162.0	163.0	163.0	162.0	162.5	167.5	164.0	169.5	165.000	2.57391	
25	4	155	300	5-5-5-5-120	A		182.5	180.5	176.5	175.0	178.5	172.5	178.0	173.5	175.5	172.0	174.0	182.5	186.0	177.462	4.35154	
26	4	165	300	5-5-5-5-120	E		172.5	177.0	171.0	176.0	169.5	171.0	168.5	171.5	168.5	169.5	172.0	165.5	172.5	171.154	3.07804	
27	4	155	400	5-5-5-5-120	B		176.0	176.5	170.5	174.5	177.0	175.5	177.5	179.0	175.5	172.0	174.0	175.5	176.0	175.342	2.23965	
28	4	165	400	5-5-5-5-120	F		179.0	181.0	177.5	182.0	186.5	184.5	172.5	179.0	184.0	176.5	179.5	172.5	185.0	179.962	4.48823	
29	4	155	300	5-5-5-5-5-100	C		209.5	198.0	196.5	204.5	187.0	178.0	203.0	205.0	200.0	195.0	196.5	193.0	195.5	197.038	8.19670	
30	4	165	300	5-5-5-5-5-100	G		174.5	171.0	178.0	177.5	163.5	168.5	157.0	172.5	170.0	177.0	173.5	182.5	172.125	6.90561		
31	4	155	400	5-5-5-5-5-100	D		198.5	189.5	182.5	198.0	193.5	199.0	187.0	188.0	196.0	193.0	173.5	183.5	183.5	189.654	7.63322	
32	4	165	400	5-5-5-5-5-100	H		170.0	166.5	171.5	171.0	170.0	170.5	170.5	171.0	167.5	166.5	168.0	168.5	162.5	168.769	2.56453	

Fig. 2 Residual plots for Ave



Tabel 3 Analysis for variance for *Ave*

Source	DF	Seq SS	Adj SS	Adj MS	F	P
Blocks	3	658.9	658.9	219.62	17.51	0.000
Main effects	2	1253.3	1253.3	626.63	49.96	0.000
Temp	1	1071.9	1071.9	1071.90	85.46	0.000
Cycle	1	181.4	181.4	181.35	14.46	0.001
2-way interactions	1	524.2	524.2	524.17	41.79	0.000
Temp * cycle	1	524.2	524.2	524.17	41.79	0.000
Residual error	25	313.6	313.6	12.54		
Lack of fit	9	125.3	125.3	13.93	1.18	0.368
Pure error	16	188.2	188.2	11.77		
Total	31	2749.9				

R-squares, so we could trust the model obtained by DOE for this output too (in respect with considered inputs).

From DOE, we get by linear regression [3, 4] two linear transfer functions as:

$$Ave = 163.25 - 2.4 Temp + 0.67 Cycle - 27.58 Temp * Cycle \quad (1)$$

$$LogNormstdev = 4.89 - 0.01 Temp - 0.0016 Pres + 0.05 Cycle - 0.27 Temp * Cycle - 0.0014 Pres * Cycle \quad (2)$$

By using DOE, to get a robust design, it is important to check if does exist interaction between inputs and to use it.

Figure 3 is presenting one interaction plot for *Ave* and Fig. 4 the two interaction plots for *LogNormstdev*.

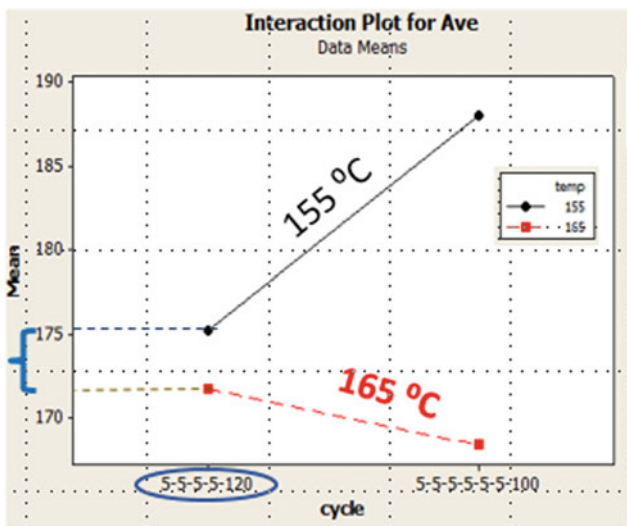


Fig. 3 Interaction plot for *Ave*

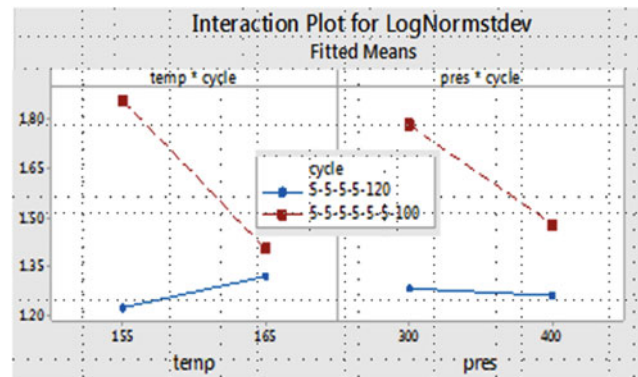


Fig. 4 Interaction plots for *LogNormstdev*

4 Discussions

In all three interaction plots the lines are not parallel, and it tells us graphically the interaction between independent inputs does exist (if not, the line would be parallel).

Analytically, in Eqs. (1) and (2) of the transfer function of *Ave* respective *LogNormstdev* we recognize the inputs that interact because they are in product: so, by changing the value of one term from product, we offer a different slope for the second term from product.

Finding it does exist the above-mentioned interactions, we further use it to provide a robust design in respect with temperature and pressure variation, parameters expensive to control with high precision for such kind of installation: in Fig. 3 we observe that if the temperature varies from 155 to 165 °C, the variation for the output *Ave* is smaller for Cycle setting of 5-5-5-5-120 than for 5-5-5-5-100 Cycle. Also, in *LogNormstdev* interaction plot we observe that for the same cycle 5-5-5-5-120 the variation of the output is smaller than variation from the other cycle for both variation of temperature and pressure. So, choosing 5-5-5-120 variant, we get a robust design in respect with temperature and pressure.

Best practice of using such scientific and statistics methods to enable innovation where reported also in [5, 6].

5 Conclusions

In R&D labs we try to do most a “proof of concept” for a new product, which can be demonstrated by building only few products, sometimes only one. Further, when R&D Lab’s direct customer, i.e. fabrication facility will ask “how producible is the concept lab proposes?” and the market will ask about future behavior of the product in “real life” (operating conditions), the answer will depend on the expected variation of the fabrication process and of the product in operating conditions, in respect with controllable but rather with uncontrollable inputs. So, R&D lab needs to deploy variation analysis and estimate it, in order to produce a robust design: in this way the lab could systematically get high levels of TRL 7–8. Products being prepared technically for real life and responding to effective customer needs, the chance to get market success i.e. TRL 9 increases dramatically.

Last but not least is the question if such methods, DOE in special as an enabler of robust design, could be applied at nano-scale? The answer is YES, as the mathematical background cope and is suitable to model materials and corresponding processes at nano-scale too. There are many articles in the field, e.g. [7, 8]—published in outstanding

journals- being two important examples of applying DOE at nano-scale, in areas of farma, medicine and bioengineering.

Conflict of Interest The authors declare that they have no conflict of interest.

References

1. <https://www.autonews.com/article/19991227/ANA/912270725/henry-ford-s-dream-reshaped-the-world>
2. Breyfogle, F.: *Implementing Six Sigma—Smarter Solutions Using Statistical Methods*, 2nd edn. Wiley, New York (2003)
3. Montgomery, D.: *Design and analysis of experiments*, 5th edn. Wiley, New York (2001)
4. Box, G.E., Hunter, W.G., Hunter, J.S.: *Statistics for Experimenters—Design, Innovation, and Discovery*, 2nd edn. Wiley, New York (2005)
5. Varachiu, N., Benamrouche, B., Noullet, J.-L., Rumeau, A., Dragomirescu, D.: ASIC for an energy efficient impulse radio ultra-wideband transceiver. Testing and statistic assessment. In: *Proceedings of CAS 2018, Romania*, pp. 169–172 (2018)
6. Varachiu, N., Noullet, J.-L., Rumeau, A., Dragomirescu, D.: Process capability evaluation for fabrication of ASIC IR-UWB transceivers. In: *Proceedings of CAS 2019—Romania* (in press, 2019)
7. Arafa, M., et al.: DOE optimization of nano-based carrier of pregabalin as hydrogel: new therapeutic & chemometric approaches for controlled drug delivery systems. *Scientific Reports*, vol. 7. <https://www.nature.com/> (2017)
8. Draheim, C., et al: A design of experiment study of nanoprecipitation and nano spray drying. In: *Pharm. Res.* **32**(8), American Association of Pharmaceutical Scientists (2015)

Investigation into Interlayer Water Structure in Na⁺- and Ca²⁺-Montmorillonite: A Molecular Dynamics Study

N. Siminel

Abstract

Swelling clays play significant roles in current industry. Molecular dynamics simulations have been performed to investigate the swelling properties, hydration behaviour and mobility of interlayer molecules of Na⁺- and Ca²⁺-montmorillonites. More specifically, to characterize the structure and energetics of Na⁺ and Ca²⁺ adsorption as functions of water content; the relationships between the coordination environments of clay surface–interlayer water–exchangeable cations; the influence of cation hydration energy on the dynamics and swelling mechanism of clays; and the influence of charge distribution on all of the above. Establishing an understanding of these clay/water systems is viewed as a sensible foundation for the more complex systems.

Keywords

Molecular dynamics • Montmorillonite • Clay • Water • Diffusion

1 Introduction

Swelling is the process of expansion of clay layers due to increasing incorporation of polar molecules (e.g. water, polymers) in the interlayer region. This property is determined by many factors such as chemical composition of the clay mineral, nature of the surface atoms, exchangeable cations, and the magnitude and location of the layer charge. For example, if the layer charge is too high (micas, chlorites) or zero (kaolinite, pyrophyllite, talc), swelling of the layers does not occur. Therefore, studies of clay swelling are mostly focused upon 2:1 smectite clays in particular montmorillonites (Mt) [1–3].

N. Siminel (✉)
 Institute of Applied Physics, Academy of Sciences of Moldova,
 5 Academiei, Chisinau, Moldova
 e-mail: siminel.n@gmail.com

Swelling clays play significant roles in current industry. It has been observed [3] that smectite clays are candidate systems for the intercalation and capture of substances such as CO₂ and nuclear waste as well as for dehydration of laboratory samples. Furthermore, the process of interlayer swelling is directly related to the formation of polymer-clay nanocomposites. In order to enhance and control this formation, an understanding of the clay swelling mechanisms is required.

It is believed that hydration of interlayer cations is the main driving force in the process of adsorption of water by clays [1], the importance of understanding this phenomenon at a molecular level becomes evident. In particular, the influence of the clay's structure on the thermodynamics of this hydration process is a key factor. Previously reported simulation data investigating the effect of layer charge location and magnitude on hydration is limited, and some of the conclusions drawn are contradictory.

In this work we use the atomistic Molecular Dynamics (MD) approach to investigate the effect of the layer charge location and magnitude on the hydration properties of a range of clay minerals and to relate simulation and experimental results for swelling–deswelling behaviour of clay, and gain a molecular level understanding of such behaviour.

2 Methodology

The model framework for Montmorillonite (Mt) was generated from a pyrophyllite crystal structure. A number of Mt models were investigated with a selection of charge locations and two exchange cations (Na⁺, Ca²⁺). The network of negative layer charge was created by substituting Mg²⁺ for Al³⁺ in the octahedral sheet, giving rise to octahedral charge (Oh), or Al³⁺ for Si⁴⁺ in the tetrahedral sheet (Th charge). Mixed substitutions in octahedral and tetrahedral sheets (Oh/Th) were also considered. To balance the negative layer charge, an appropriate number of Na⁺ cations were initially placed in the gallery between clay layers. To generate a

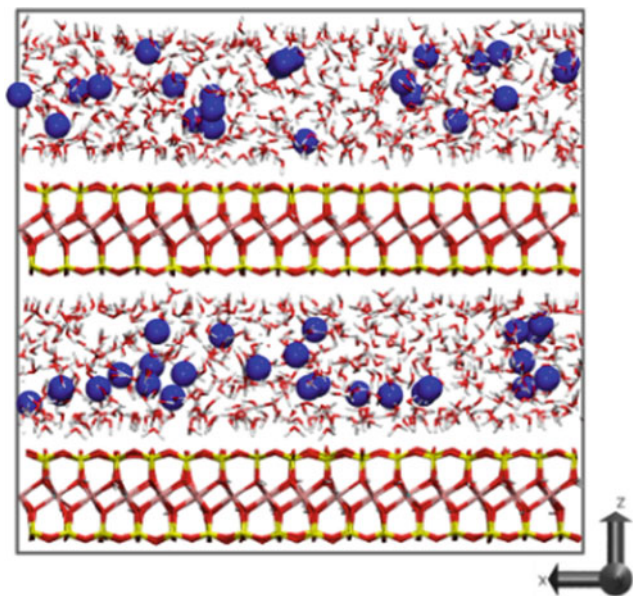


Fig. 1 NaMt simulation cell containing $30.5 \text{ H}_2\text{O uc}^{-1}$ in the interlayers. Colours: Na blue; Si, yellow; Mg cyan; Al pink; O red; H white

CaMt structural model, every pair of Na^+ cations in the initial model was replaced by a single Ca^{2+} cation. The structural formulas and net negative structural charges of the developed clay models are $(\text{Na}_{2x}, \text{Ca}_x) [\text{Al}_{(4-x)}\text{Mg}_x][\text{Si}_{(8-x)}\text{Al}_x]\text{O}_{20}(\text{OH})_4$. The simulation supercell was constructed from two orthogonal clay layers each containing 32 unit cells in an 8×4 expansion. The lateral dimensions (x, y) for all simulated systems were approximately $41.5 \times 36.0 \text{ \AA}^2$ (Fig. 1).

Molecular Dynamics simulation is a technique used to compute the equilibrium and transport properties of a classical many-body system by using essential information about a system's dynamics, usually resolved at atomistic detail. Molecular dynamics simulations were performed using the Nosé-Hoover thermostat and DL_POLY simulation package [4] with a 1.0 ps relaxation time. For the NPT simulations, a Nosé-Hoover barostat was utilised to control the pressure. Interatomic interactions were evaluated using a time step of 0.001 ps, and three-dimensional periodic boundary conditions were employed with a cutoff of 15 Å for short-range interactions. Interatomic potentials for the clay and interlayer ions were obtained from the CLAYFF force field developed by Cygan et al [5]. Each atom in CLAYFF force field has an assigned partial charge derived from DFT calculations, and the flexible TIP3P/Fs water model [6] is incorporated to describe water.

3 Results and Discussion

3.1 Swelling and Hydration Energetics

Figure 2a presents the results of the current series of simulations for the hydration of NaMt. The calculated basal spacing of clay is plotted as a function of water content along with experimental data. The results are in very good agreement, both qualitatively and quantitatively, and indicate that the swelling of clay layers occurs in a stepwise manner, with formation of plateaux around water contents of 0.1 and 0.2 $\text{g}_{\text{H}_2\text{O}}/\text{g}_{\text{clay}}$.

For CaMt, comparison with experimental swelling curves is challenging due to a dearth of data on swelling behaviour with reported interlayer water content. Therefore, our simulated data for basal spacing of CaMt is presented in Fig. 2b along with recent results obtained from MD simulation [8]. The inset axes show the experimental swelling behaviour of CaMt with predominantly octahedral charge [2] as a function of relative humidity (RH). Analogous to the NaMt simulations, CaMt demonstrates a non-linear increase in d-spacing with increasing water content, although this reveals only a single plateau at around 0.15 $\text{g}_{\text{H}_2\text{O}}/\text{g}_{\text{clay}}$. Discrepancies between the expansion behaviours of NaMt and CaMt upon hydration have been previously noted through multiple experimental [2, 9] and theoretical [8] studies. This good agreement with experimental findings and previous simulations ensured the appropriateness of developed potential model.

Six simulated swelling curves for NaMt and CaMt models with a range of layer charges are shown in Fig. 3. The overall stepwise swelling behaviour of NaMt suggests the potential for formation of a well-defined monolayer hydrate (1 W) with partially and fully filled interlayers, a bilayer hydrate (2 W), and three layer hydrate. The observed values of basal spacings of 9.3–9.7 Å for the anhydrous interlayer, 12.15–12.27 Å for the monolayer hydrate and 14.55–14.92 Å for the bilayer hydrate are in very good agreement with reported values from experimental observations. Trends in basal spacing for NaMt with the selected charge locations and magnitudes are virtually identical (Fig. 3a). The d-spacing of clay with tetrahedral charge (Th) is smaller than that of clay with octahedral charge (Oh) by as little as 0.1 Å at monolayer hydrate and 0.3 Å at bilayer hydrate water content. This indicates that neither clay layer charge magnitude nor its location appear to have a significant influence on the swelling behaviour of Na^+ -montmorillonite clay. Siloxane surface of smectites are

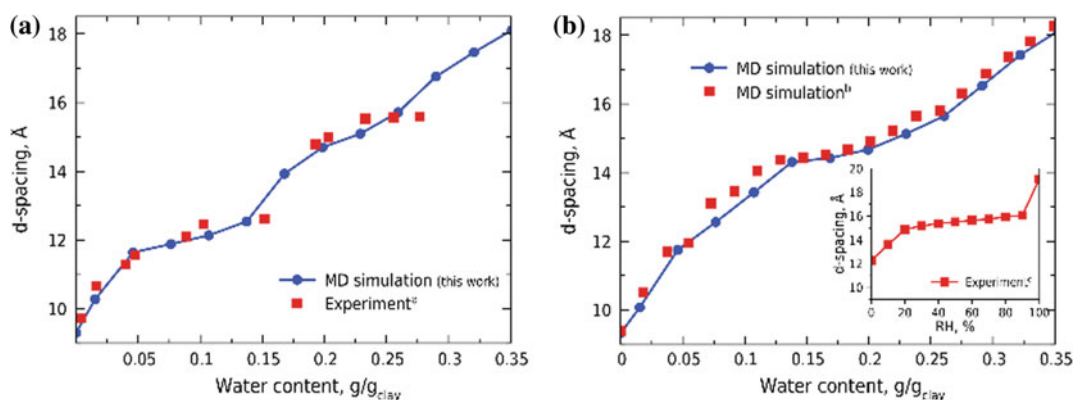


Fig. 2 Simulated and experimental basal spacing of **a** NaMt and **b** CaMt with octahedral charge as a function of increasing water content. Experimental data are taken from ^a[7], ^b[8], ^c[2]

predominantly hydrophobic, especially in locations where no isomorphous substitutions in octahedral or tetrahedral sheet have occurred [1]. Therefore, the main mechanism by which montmorillonites adsorb water is through hydration of exchangeable cations.

Since the ionic radii of Na^+ and Ca^{2+} cations are similar ($\sim 1.15 \text{ \AA}$ [10]), the simulated basal spacings of dehydrated NaMt and CaMt are also very similar (Fig. 3b) and equal to $9.3 \pm 0.05 \text{ \AA}$ for all studied types of clay. Experimentally, however, it is very difficult to obtain completely dry CaMt at room temperature due to the high hydration enthalpy of the divalent cation (1577 kJ mol^{-1} for Ca^{2+} and 406 kJ mol^{-1} for Na^+ [10]). In normal conditions, the interlayer of CaMt with octahedral charge contains two water layers [1] which is consistent with the simulated swelling behaviour of this mineral. There is no stable plateau corresponding to a monolayer hydrate on swelling curves of octahedrally charged CaMt (Fig. 3b); swelling to the bilayer hydrate with basal spacing of 14.5 \AA occurs at $\sim 0.12 \text{ g}_{\text{H}_2\text{O}}/\text{g}_{\text{clay}}$, much lower than that for NaMt. Most clearly, this difference relates to the hydration energies of the exchangeable cations.

Upon introducing tetrahedral charge to CaMt systems, the basal spacing reduces down to 12.5 \AA corresponding to a monolayer hydrate. The high hydration energy of divalent calcium, results in a strong interaction with substitution sites in the tetrahedral sheet close to the clay surface, breaking up the hydration shell of the cation and constraining the basal spacing.

3.2 Interlayer Structure of Hydrated Montmorillonites

From the MD simulations it can be clearly seen that, if charge deficit occurs in the tetrahedral sheet, adsorption of cations is favoured near to the tetrahedral sheet and presumably to the sites of isomorphous substitution. The bilayer hydrate, on other hand, is characterised by four layers of water hydrogens located at 1.7 and 2.4 \AA from both basal surfaces. As in the monolayer hydrate, some hydrogen atoms point toward the basal surface, but, due to the larger space available and the full hydration of the cation, the orientations

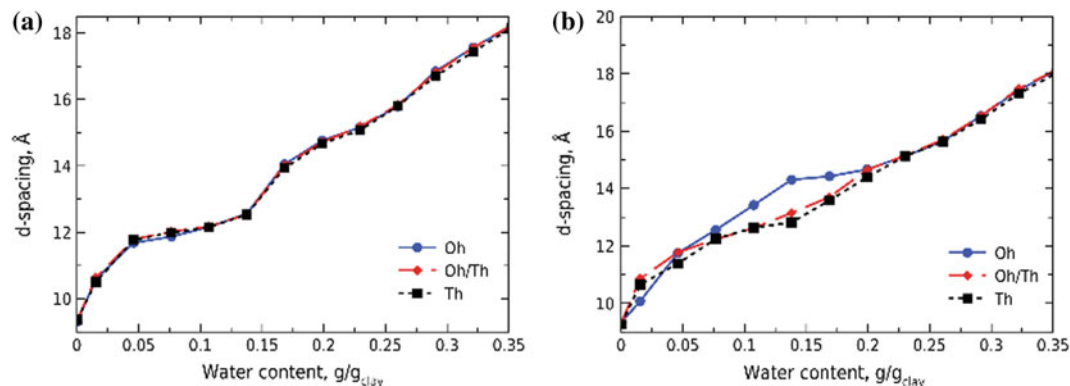


Fig. 3 Simulated swelling curves of **a** NaMt and **b** CaMt as a function of water content and clay charge location. MD simulations were performed at 300 K and 1 atm

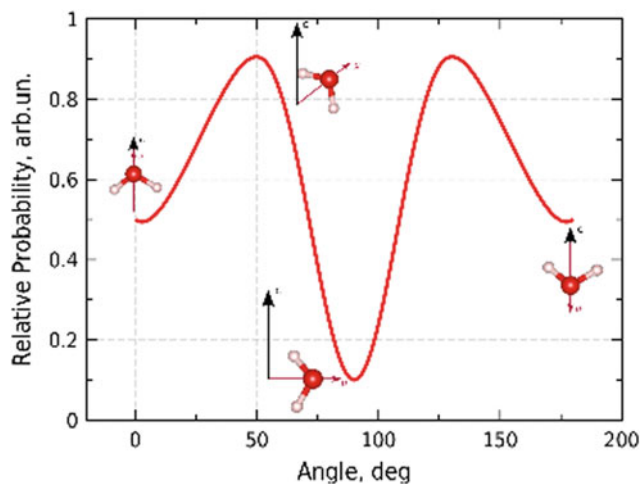


Fig. 4 Distribution of water dipole showing major orientations of water molecules in the bilayer hydrate interlayer. Note that angle is with respect to the c -axis vector which is perpendicular to clay layer

of the water dipole moment are more diverse. To quantify this, the distribution of dipole moments of the water molecules forming the hydration shell of each cation as a function of the angle between the dipole moment vector and the c -axis is presented in Fig. 4. Water orientations in which one of the $\text{OH}_{\text{H}_2\text{O}}$ bonds point toward the clay surface and other being nearly parallel to it were the most frequent. These are followed up by the configuration in which both hydrogen atoms are oriented toward the basal surface of clay. A NMR spectroscopy investigation into the water dynamics at the smectite/water interface suggested similar water orientations in bilayer hydrates [11].

3.3 Dynamics of the Interlayer

The dynamics of the interlayer species were analysed by overlapping 500 ps trajectory maps of NaMt and CaMt with various water contents in the interlayer and presented in Fig. 5. These illustrate both the mobility and the hydration of exchangeable cations and water in the interlayer.

The obtained patterns clearly indicate that adsorption of water by montmorillonite clays occurs in two stages. Firstly, solvation of the exchangeable cations by either three (in case of Na^+ monovalent cations) or more (in case of Ca^{2+} divalent cations) water molecules takes place (Fig. 5, $0.046 \text{ g}_{\text{H}_2\text{O}}/\text{g}_{\text{clay}}$). At this stage, the water is located predominantly around the cations or close to substitution sites that are the focus of the

net negative charge of the clay layers. Secondly, as the amount of water in the interlayer increases, full hydration shells around the cations are formed. Monovalent sodium cations develop an octahedral solvation complex, whereas divalent calcium form a second solvation shell (Fig. 5, $0.1047 \text{ g}_{\text{H}_2\text{O}}/\text{g}_{\text{clay}}$). Since this hydration process depends only on the hydration ability of the exchangeable cations, the formation of complete monolayers of water is not necessary as indicated by the “non-occupied” region between the hydrated Ca^{2+} cations.

The more negative hydration enthalpy of Ca^{2+} produces a water coordination sphere around that is much more stable than that of Na^+ . The mobility of Ca^{2+} is constrained because of this, in contrast to Na^+ cations, which remain mobile, even at low water contents. Diffusion of Ca^{2+} is further inhibited by a second coordination water shell, which can either be complete or share some parts with those of neighbouring cations. The values of the diffusion coefficients obtained for water and exchangeable cations in Mt are summarised in Table 1.

4 Conclusions

The simulations predicted the swelling behaviours of negatively charged clay layers balanced with sodium and calcium cations with high accuracy. This included prediction of a step-wise mechanism of water absorption by NaMt and swelling from dry to bilayer hydrate of CaMt previously discussed in experimental studies. Additionally, the mechanism of water absorption by CaMt with predominantly tetrahedral charge was shown for the first time in this work.

It was shown that cation coordination complexes are significantly influenced by clay charge location and magnitude. For example, Ca^{2+} adsorbed on the surface of clay with high octahedral charge resides in the dodecahedral cavity of clay surface, reducing separation of clay layers as a result. CaMt interlayers with low water content are characterised by the presence of two layers of water with a layer of cations between them as most of the divalent cations are fully hydrated due to their high hydration affinity. However, introducing as little as -0.3 e uc^{-1} of tetrahedral charge into the clay model, rearranges the cations into two distinct layers sandwiching one single layer of water. This leads to significant reduction in the basal spacing of clay. The driving force of this process is considered to be the interaction between the exchangeable cation and the charged sites in the tetrahedral sheet of clay.

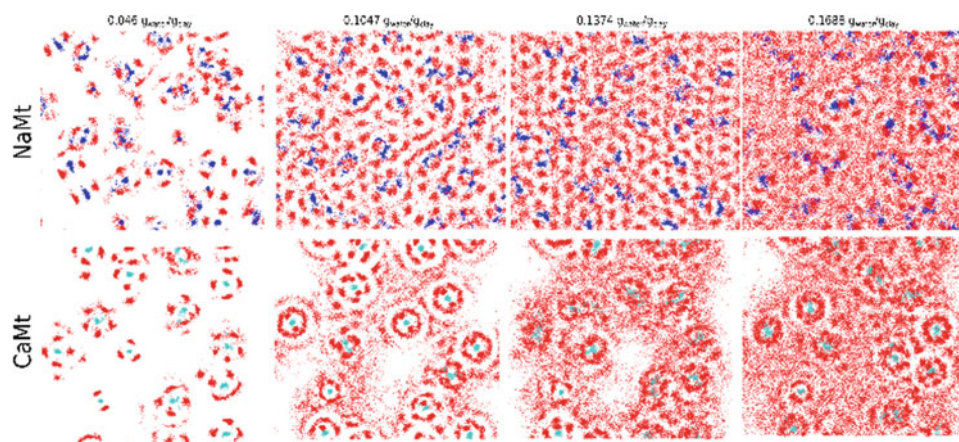


Fig. 5 Overlapped final 500 ps snapshots from MD simulations at 300 K and 1 atm of octahedrally charged NaMt and CaMt at different water contents. It can be observed that the overlapped trajectories of

Ca^{2+} and their accompanying coordinated water molecules are much denser than is the case for Na^+ . Colours are as follows: Na^+ blue, Ca^{2+} cyan, O_{water} red

Table 1 Cation and water (OW) diffusion coefficients ($10^{-10} \text{ m}^2 \text{ s}^{-1}$) from MD simulations and experiment

	D_{OW} (NaMt)	D_{OW} (CaMt)	D_{Na^+}	$D_{\text{Ca}^{2+}}$
1 W	2.4–2.8 (1–3)	1.7–4.2	0.2–1.6 (0.1)	0.02–0.03 (0.06)
2 W	7.5–9.7 (5–10)	3.5–6.7	0.9–2.9 (1)	0.02–0.5
3 W	13.9–15.4	7.6–9.5	2.6–5.2 (2)	0.2–1.2

Experimental values are presented in parentheses and taken from [12]

Acknowledgements Author would like to express his gratitude to Prof Doug Cleaver, Prof Chris Breen and Dr Francis Clegg (Sheffield Hallam University) for provided insight and expertise that greatly assisted the research. This research was supported by New Generation Packaging (NEWGENPAK) project funded by Marie Curie Foundation under seven framework program of European research (agreement no. 290098).

Conflict of Interest The authors declare that they have no conflict of interest.

References

- Bergaya, F., Theng, B.K.G., Lagaly, G.: Handbook of Clay Science, 1st edn. Elsevier Ltd, Amsterdam (2006)
- Sato, T., Watanabe, T., Otsuka, R.: Effect of layer charge, charge location, and energy change on expansion properties of dioctahedral smectites. *Clays Clay Miner.* **40**(1), 103–113 (1992)
- Bujdák, J., Hackett, E., Giannelis, E.P.: Effect of layer charge on the intercalation of poly(ethylene oxide) in layered silicates: implications on nanocomposite polymer electrolytes. *Chem. Mater.* **12**(8), 2168–2174 (2000). <https://doi.org/10.1021/cm990677p>
- Todorov, I.T., Smith, W., Trachenk, K., et al.: DL_POLY_3: new dimensions in molecular dynamics simulations via massive parallelism. *J. Mater. Chem.* **16**, 1911–1918 (2006). <https://doi.org/10.1039/B517931A>
- Cygan, R., Liang, J.J., Kalinichev, A.G.: Molecular models of hydroxide, oxyhydroxide, and clay phases and the development of a general force field. *J. Phys. Chem. B* **108**, 1255–1266 (2004). <https://doi.org/10.1021/jp0363287>
- Wu, Y., Tepper, H.L., Voth, G.A.: Flexible simple point-charge water model with improved liquid-state properties. *J. Chem. Phys.* **124**(2), 024503 (2006). <https://doi.org/10.1063/1.2136877>
- Fu, M.H., Zhang, Z.Z., Low, P.F.: Changes in the properties of a montmorillonite water system during the adsorption and desorption of water: hysteresis. *Clays Clay Miner.* **38**(5), 485–492 (1990)
- Teich-McGoldrick, S.L., Greathouse, J.A., Jove-Colon, C.F., et al.: Swelling properties of montmorillonite and beidellite clay minerals from molecular simulation: comparison of temperature, interlayer cation, and charge location effects. *J. Phys. Chem. C* **119**(36), 20880–20891 (2015). <https://doi.org/10.1021/acs.jpcc.5b03253>
- Sposito, G.: The surface chemistry of soils. Oxford University Press, Oxford, UK (1984)
- Johnston, C.T.: CRC Handbook of Chemistry and Physics, 94th edn, 2013–2014, vol. 53 (2013)
- Bowers, G.M., Singer, J.W., Bish, D.L., et al.: Alkali metal and H_2O dynamics at the smectite/water interface. *J. Phys. Chem. C* **115**, 23395–23407 (2011). <https://doi.org/10.1021/jp2072167>
- Malikova, N., Cadene, A., Marry, V., et al.: Diffusion of water in clays on the microscopic scale: modeling and experiment. *J. Phys. Chem. B* **110**(7), 3206–3214 (2006). <https://doi.org/10.1021/jp056954z>

A Positioning Mechanism Based on MEMS-INS/GPS and ANFIS Data Fusion for Urban Life Mobility Improvement

L. T. Grigorie, N. Jula, C. L. Corcău, I. R. Adochiei, C. Larco, and S. M. Mustață

Abstract

To achieve a positioning mechanism for urban life mobility improvement, a signal processing algorithm was tuned, using an ANFIS (Adaptive-Neuro-Fuzzy-Inference System) data fusion algorithm, with the experimental data collected from platforms equipped with Inertial Measurement Units (IMU) based on MEMS sensors and GPS receivers. In the paper's sections are presented the following aspects of interest: the MEMS-INS/GPS (a GPS unit and a miniaturized Inertial Navigation System) structure and functioning, the fuzzy inference system training procedure, the data evaluation of the proposed structure using experimental data and the testing results. The after-training evaluation of the FISs denoted absolute mean deviations between the reference data and the fuzzy models by order of 10^{-5} degrees for latitude and longitude channels, of 10^{-1} m for the altitude channel and 10^{-1} m/s for all three-speed channels.

Keywords

Mobility improvement • Urban life • Smart positioning • MEMS-INS/GPS • ANFIS data fusion

1 Introduction

Improving the access of people with disabilities and of elderly to all aspects of urban life is a strategic objective of the European Commission [1] and answers to the UN Convention on the Rights of Persons with Disabilities (CRPD) [2–4]. In Europe, more than 80 million people are suffering from different degrees of disabilities. Most of the EU Member States have ratified the UN CRPD and the European Accessibility Act (EAA) and established to create a legislative framework for their accessibility to healthy life [1–4]. EU programs relevant for people with various disabilities offer different thematic funding opportunities, but these refer to cities infrastructures improvements.

Several PC, Android and iOS mobile apps for smartphones are currently helping people to live better lives, by offering traveling guidance or information on different accessibility issues available in certain cities or states of the world, but all the guidance applications use geographic data and positioning signals from the GPS.

In the following are described some popular applications, currently in use. *Brio Nav/Brio Smart (Navability)* [5] is a wheelchair user application, similar to the Google Maps application, based on an algorithm which uses the information on wheelchair's maneuverability, on the environment (gradient, surface, and obstacles) and the user's ability to estimate their best route through the landscape. *NowNav GPS Accessibility* and *GPS for the Blind* [6] are GPS based applications, releasing information on the city's infrastructure, in real time. *TripTripHurray* [7] is another travel planner with special features for people with disabilities, which considers their needs and suggests travel options on a predefined 300 m radius. For visually impaired people, *Map Seeker* is a widely used utility service and location-based application, accessible on Google Play. Other similar apps are "*Better Outdoors*", developed for traveling and visiting Rotterdam, and "*Lost in the City*", available only for iOS 9.0 users.

L. T. Grigorie (✉) · N. Jula · I. R. Adochiei · C. Larco · S. M. Mustață
Faculty of Aircraft and Military Vehicles, Military Technical Academy "Ferdinand I", 39-49 George Cosbuc Blvd, Bucharest, Romania
e-mail: lucian.grigorie@mta.ro

C. L. Corcău
Faculty of Aerospace Engineering, University Politehnica of Bucharest, Bucharest, Romania

All these apps and other similar [8, 9], need precise information related to the user position provided by a GPS. From this perspective many problems are encountered, having in mind that the central area of these applications' using is the urban environment, where the GPS is negatively influenced by many factors, including multiple paths, interferences and signal blockage due to the obstacles.

We propose an everyday life instrument for people with visible and invisible disabilities, like intellectual disabilities, and for persons with reduced mobility, to ease their access to all aspects of urban life, like their workplace, but also parks and stores, public spaces or transport.

The here proposed instrument will have more complex applicability, not only for travel but also for everyday life. It includes MEMS-INS and GPS positioning systems, both fused based on an Adaptive Neuro Fuzzy Inference System (ANFIS) integrated with a Kalman filter. The Fuzzy Inference Systems (FISs) model the errors of navigation in the speed and position channels. In the ANFIS structure, six FISs with one output and ten inputs were considered. The ANFIS is trained during the proper functioning of GPS (training phase) and works together with INS (prediction phase), on short periods, when the GPS signal is lost. Therefore, starting from a person geolocation, the ANFIS algorithms will "learn" from the user everyday walking/traveling itinerary, and offer information on the desired path in a period when the signal from satellites is not accessible. The proposed system was experimentally tested in urban area by using a car as monitored vehicle.

2 MEMS-INS/GPS Data Fusion Mechanism

The data fusion mechanism inside the MEMS-INS/GPS navigator is based on a Kalman filter and on a complex fuzzy inference system which is differently used during two navigation phases: a *Training phase* (Fig. 1 [10]), followed by a *Prediction one* (Fig. 2 [10]). As previously mentioned, *the training phase* takes place when positioning data from the GPS module is available. Then, data packages inputs are

achieved and send to the ANFIS structure: the inertial measurement unit outputs, collected from three accelerometers and three gyros; the global position and the North-East-Down (NED) speed components; the INS attitude solution outputs regarding the angles of attitude (roll, yaw and pitch); the GPS navigation solution and the GPS signal outage time received from the navigator's clock (used as training data packages). The data achieved from the Kalman filter in Fig. 1 include the data received from the integrated navigator and the navigation solution error estimates; these data are used as desired outputs in *the training phase*. The data from the input channels of the ANFIS structure are processed in six FISs. Through this procedure are obtained the navigation errors for the global position parameters (latitude, longitude, and altitude) and for the vehicle speed in NED directions.

In the second stage, the *Prediction phase* (Fig. 2), ANFIS structure uses only the data received from the six inertial sensors, the navigation clock and the INS estimates of attitude angles (roll, pitch and yaw), and offers navigation solution corrections for the position (latitude, longitude, altitude) and for the speed channels (NED channels).

3 The Evaluation of the MEMS-INS/GPS Unit Based on ANFIS with Experimental Data

The MEMS-INS/GPS experimental unit functioning is based on some miniaturized inertial sensors, on a GPS module and on a dsPIC microcontroller (an optimized version of the PIC microcontroller used to facilitate signal processing and control applications). The data from the positioning sensors is achieved with 100 samples per second while the GPS provides data once per second. For evaluation and validation, the proposed navigator was boarded on a car, considered as testing vehicle (Fig. 3).

Initially, the positioning data was used for the ANFIS algorithm tuning, and then, the integrated navigator evaluation, in terms of accuracy and performances, was performed. In this phase, we considered only two scenarios to

Fig. 1 The MEMS-INS/GPS training regime [10]

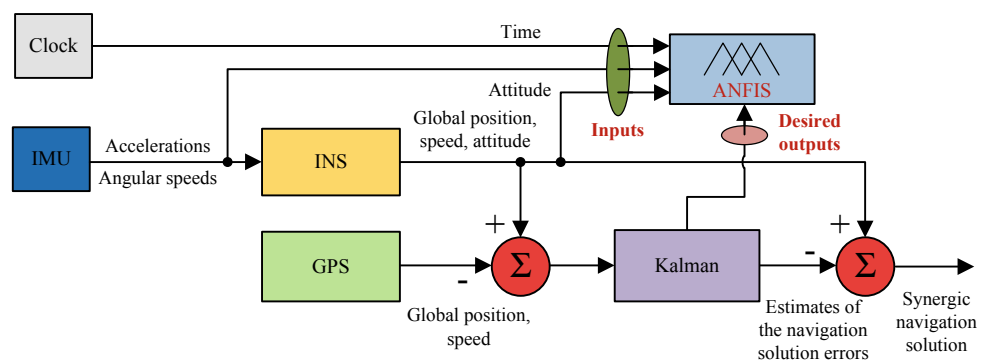


Fig. 2 The prediction regime of the integrated navigator ([10])

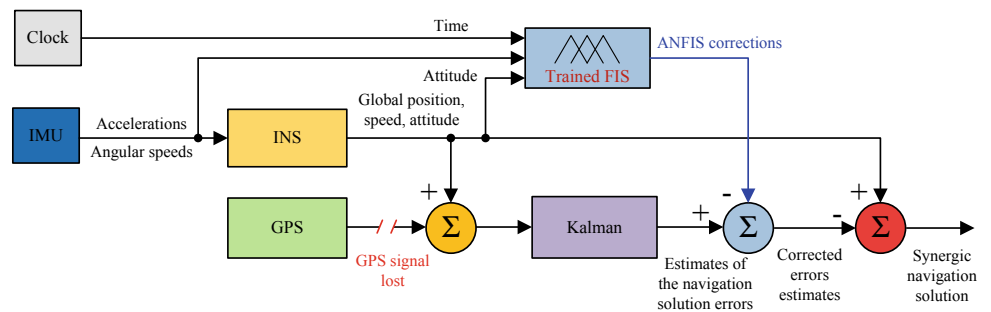
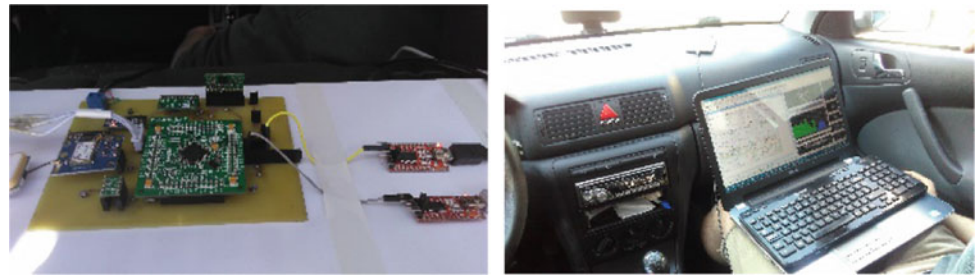


Fig. 3 Testing of the MEMS-INS/GPS experimental unit



be necessary: first, with available GPS signal, and second without a GPS signal, simulating the situations when the GPS signals are off, and the systems based on satellites cannot provide any navigation solution, so it remains only the inertial based ANFIS positioning possibility.

4 The ANFIS

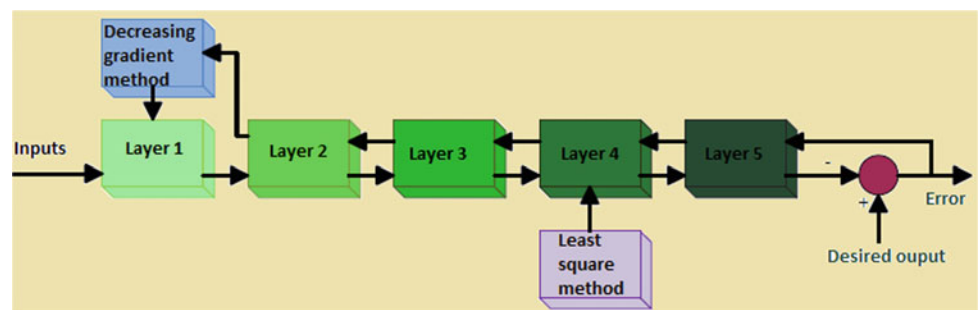
Today, the artificial neural networks, the fuzzy systems, the genetic algorithms, and the expert systems are used complementary: neural networks are used for learning and adapting, but have the disadvantage of the black-box structure; fuzzy logic is used for estimating the probability of occurrence of an event/errors; genetic algorithms perform systematized searches of optimal solutions; and expert systems are used for establishing future operations/control actions. A category of neuro-fuzzy systems, which have been obtained with significant results, are the Adaptive Neuro Fuzzy Systems (ANFIS).

ANFIS type structures are using hybrid learning algorithms through which are generally done both, the linear parameters optimization using the least squares method, and their combination using techniques based on the descending gradient method. A hybrid training algorithm typically has two stages: the forward and backward propagation of the error.

In Fig. 4 is presented one way through which the ANFIS hybrid training can be done. To obtain a FIS structure, the following components are required: a fuzzifier, a knowledge base and rules, an inference engine (deduction), and a defuzzifier. Therefore, the development a FIS based controller involves the following steps: (1) Fuzzification strategy; (2) Building the database (3) Developing the rule base; (4) Elaboration of the inference mechanism; and (5) Defuzzification strategy.

A significant number of experimental data is required to be collected and “learned” in the process of training in order to develop an efficient ANFIS structure, ready to grant a right navigation solution for the situation when the GPS

Fig. 4 ANFIS training



signal is lost, and the MEMS-INS system works in the stand-alone configuration. For this, a laptop and the MEMS-INS/GPS experimental unit were boarded on a vehicle. All the navigation data was registered while performing experimental tests on different runways. All the test regarding the car position were monitored in real-time and marked on a map.

5 System Training and Evaluation Results

Figure 5 is presented the FISs structures training for a data set acquired during the testing stage.

When the GPS signal is available, the integrated system works based on the signals received from the Kalman filtering algorithm and when the GPS signal is lost it switches to the configuration INS/trained ANFIS. In the second scenario, the INS signals are fused with the previously trained ANFIS data. The software model designed for the integrated navigator, having incorporated the Kalman filter and the ANFIS network, has six Fuzzy Inference Systems, offering three global positioning parameters and three NED speeds.

In the following are described the results obtained from the study of the movement of a vehicle, on a U-shaped trajectory on a national road.

Figure 6 depicts the results for the vehicle position evaluation when the GPS signal is available. Shown are the latitude, longitude and altitude components from INS solution of navigation, from GPS solution of navigation and from integrated INS/GPS solution of navigation.

In Fig. 7 is presented the car's navigation evolution when the full integrated system works with GPS signal until the 80th second (the left hand side of each picture), and in the

INS/trained ANFIS configuration (with no GPS signal) after the 80th second (the right hand side of each picture). In the INS/trained ANFIS configuration the position and speed corrections are estimated by combining the ANFIS data and the outputs of the Kalman filter. It can be easily observed that the navigation solution with the integrated navigator in prediction mode follows the reference data, even if the GPS signal is lost. The noisy responses obtained in this configuration after the 80th second are due to the FISs training based on the inertial sensors outputs.

Figure 8 exposes the results for training and evaluation for the latitude FIS included in the ANFIS structure. Shown are the evolution of the training error for 250 epochs, and the deviations between the data and the FIS models.

According to Table 1, the absolute mean deviations between the data and the FISs models are by order of 10^{-5} degrees for latitude and longitude channels, of 10^{-1} m for the altitude channel and 10^{-1} m/s for all three-speed channels.

6 Conclusions

The paper proposed a positioning mechanism based on MEMS-INS/GPS and ANFIS data fusion for urban life mobility improvement. The smart ANFIS data fusion algorithm is used for the navigation solution errors prediction when the GPS signals are unavailable. The training data for the six FISs included in the ANFIS structure were obtained through the boarding on a car of the developed MEMS-INS/GPS experimental unit together with a laptop, and performing experimental tests on different runways. All the test regarding the car position were monitored in real-time and marked on a map.

In the data post-processing stage it was tested various situations for the GPS signal loosing. The paper exposed a situation when the full integrated system worked with GPS signal until the 80th second, and in the INS/trained ANFIS configuration (with no GPS signal) after the 80th second. In all situations, including also the exposed case, has been observed that the navigation solution with the integrated navigator in the prediction mode followed the reference data, even if the GPS signal was lost. The noisy responses obtained after the GPS signal was lost were due to the FISs training based on the inertial sensors outputs. Therefore, the proposed instrument works very well for short time (few minutes), with no GPS signal, and it is suitable to be implemented in various applications for urban life mobility improvement when the GPS signal may be lost or altered due to the blockage, multipath or interferences.

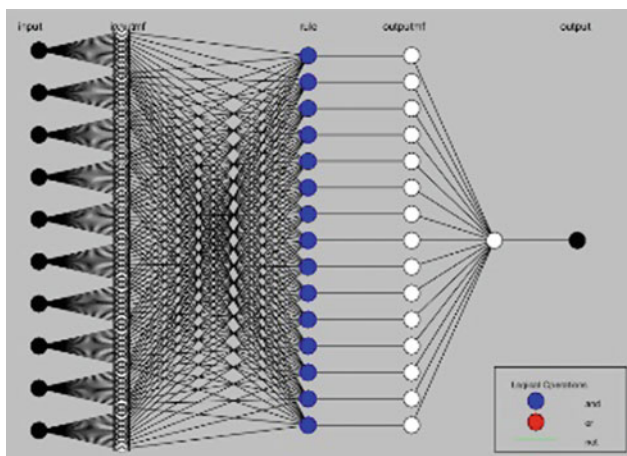


Fig. 5 The FISs training structure

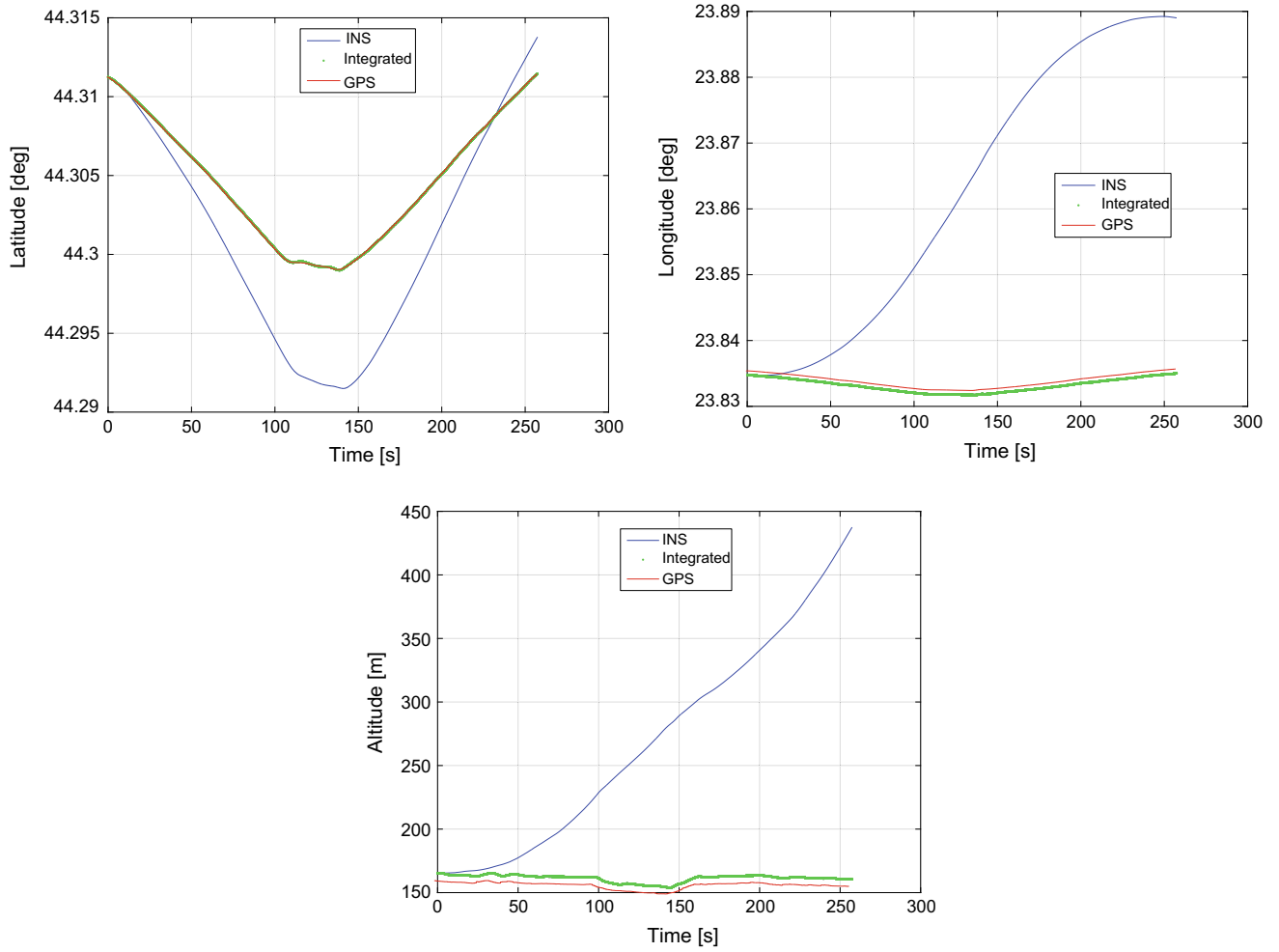


Fig. 6 Vehicle position evaluation when the GPS signal is available

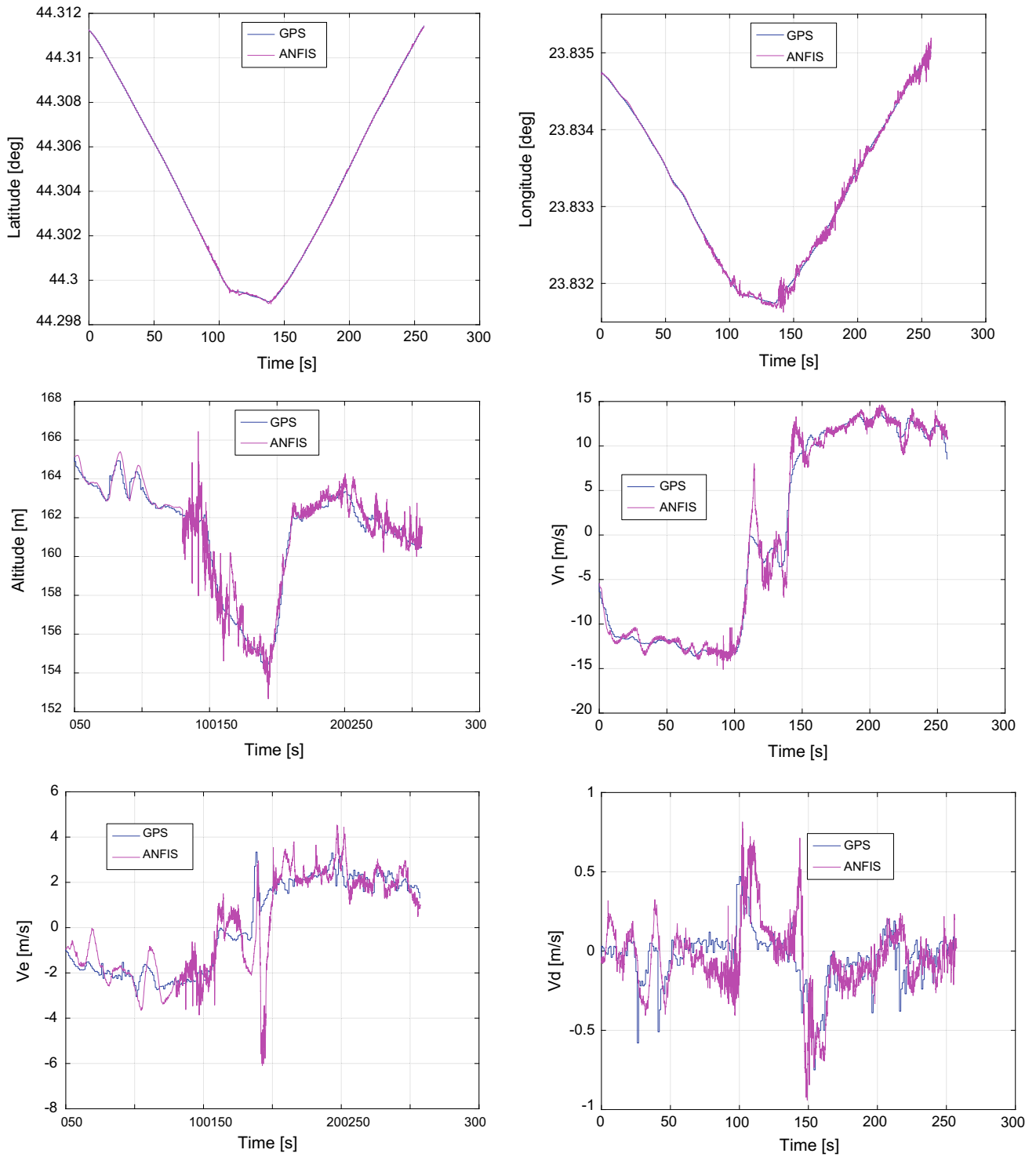


Fig. 7 Navigation solution in a testing scenario

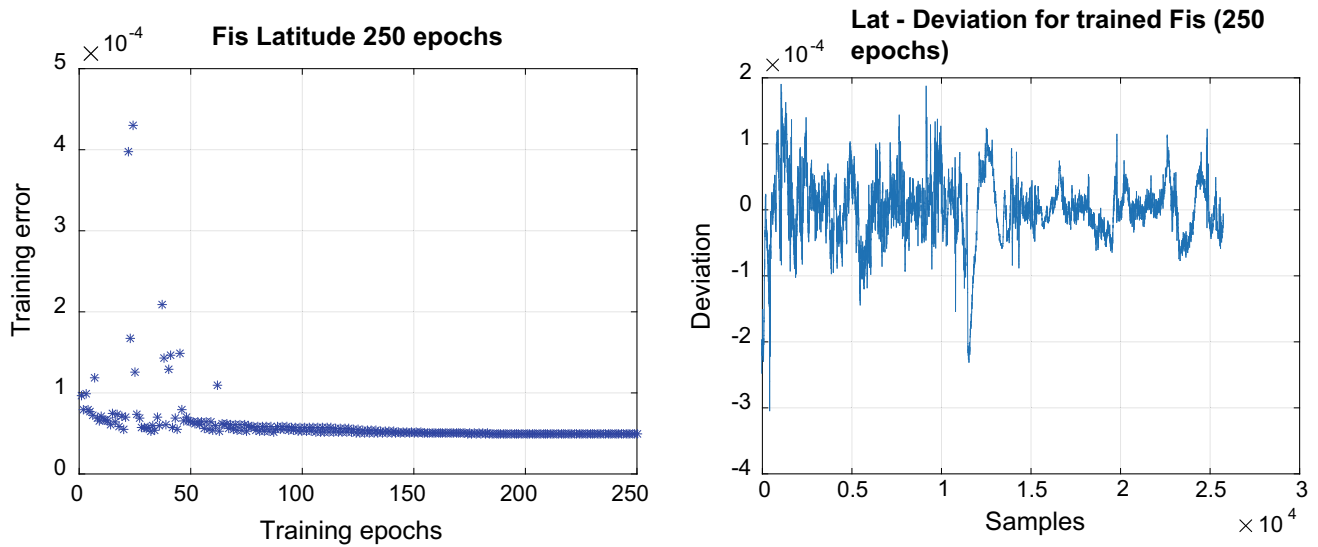


Fig. 8 Results for the training and evaluation of the FIS in latitude channel

Table 1 Absolute mean deviations between data and FIS models

FIS/errors	Latitude (°)	Longitude (°)	Altitude (m)	V-north (m/s)	V-east (m/s)	V-down (m/s)
Untrained	6.6925×10^{-5}	8.6115×10^{-5}	1.1170	0.8746	0.7292	0.0978
50 epochs	3.7229×10^{-5}	5.3801×10^{-5}	0.7235	0.6411	0.4931	0.0894
250 epochs	3.4811×10^{-5}	4.2991×10^{-5}	0.6699	0.5822	0.3985	0.0894

Conflict of Interest The authors declare that they have no conflict of interest.

References

1. A Renewed Commitment to a Barrier-Free Europe. <https://eur-lex.europa.eu/LexUriServ/LexUriServ.do?uri=COM:2010:0636:FIN:en:pdf>
2. Convention on the Rights of Persons with Disabilities (CRPD). <https://www.un.org/development/desa/disabilities/convention-on-the-rights-of-persons-with-disabilities.html>
3. Traveling together: improving the access of people with disability to road infrastructure in Papua New Guinea. <https://dfat.gov.au/about-us/publications/Documents/travelling-together-working-paper.pdf>
4. DOTCOM: The Disability Online Tool of the Commission. <https://www.disability-europe.net/dotcom>
5. <https://www.briometrix.com/>
6. <https://notnav-gps-accessibility.soft112.com/>
7. Paturca, S.V., et al.: Software platform for patients biomonitoring using wearable devices. *Biotech J.* **231**(S), S1044 (2016)
8. Păsărică, A., Andrusac, G.: Remote control of an autonomous robotic platform based on eye tracking. *Rev. Adv. Electr. Comput. Eng.* **16**(4), 95–100 (2016)
9. Pahonie, R., Larco, C., Mustață, Ș.M.: (2018) Aspects on a CubeSat project. In: Proceeding of the International Conference “Scientific Research and Education in the Air Force”—Air Force Academy
10. Grigorie, T.L., Sandu, D.G., Corcau, C.L.: MEMS-INS/GPS data fusion with ANFIS for the prediction of the navigation solution errors during GPS outages. In: *SGEM 2017*, vol. 17(22) (2017)

Scattering Indicatrix for Absorbing Porous Medium with Dark Modes

V. V. Sergentu, E. V. Monaico, and V. V. Ursaki

Abstract

A mathematical model for calculation of the scattered radiation by a highly absorbing porous medium with dark modes is proposed. The contribution of the scattered light from two areas with the same slope was taken into account. It is shown that the previously discovered anomalous retroreflection phenomenon can be observed only in the case when in the porous material the interface between the medium and the vacuum is maintained.

Keywords

Anomalous retroreflection • Scattering indicatrix • Absorbing porous medium • Dark modes

1 Introduction

The anomalous retroreflection phenomenon is observed even in incoherent light [1–4]. Therefore, for a porous medium we use a mathematical model for nonmagnetic case and on average homogeneous porous disordered medium with scattering on the surface with extremely large roughness. The used approach is based on the use of the notion of the generalized Lambert formula and scattering indicatrix [5].

V. V. Sergentu (✉)

Institute of Applied Physics, Academy Str. 5, MD-2028 Chisinau, Republic of Moldova
e-mail: vsergentu@yahoo.com

E. V. Monaico

National Center for Materials Study and Testing, Technical University of Moldova, Chisinau, Republic of Moldova

V. V. Ursaki

Institute of Electronic Engineering and Nanotechnologies “D. Ghitu”, Chisinau, Republic of Moldova

2 Results and Discussions

Further, we assume that the incident waves are converted into scattered radiation, which is satisfactorily described by the scattering indicatrix. In this case, the scattering phenomenon by a transparent disordered medium is formally described by the Lambert law (the law of energy conservation is respected)

$$I(\varphi, \varphi_i) = I_0 \cos \varphi \cos \varphi_i, \quad (1)$$

where, further for simplicity we use the two-dimensional model and assume that the intensity of the incident/scattered radiation $I_0/I(\varphi, \varphi_i)$, φ_i/φ are the angular coordinates for the incidence/scattering angles in spherical coordinates (r, φ). The flat interface between the porous medium and the vacuum is given by the equation for the angle $|\varphi| = \pi/2$ ($\infty > r > 0$).

Accounting for the influence of the medium and the interface in a highly absorbing porous material is formally carried out by introducing a factor into the Lambert law (1) (for more details see Ref. [3]).

Formula (2) correctly describes the behavior of experimental curves in a wide range of angles φ_i, φ and satisfies the general condition of reversibility for the propagation of radiation (mutual replacement $\varphi \leftrightarrow \varphi_i$ does not change anything).

$$I(\varphi, \varphi_i) = C \cos \varphi \cos \varphi_i \exp[-K^{(\pm)} F^{(\pm)}(\varphi, \varphi_i)], \quad (2)$$

where the value

$$F^{(\pm)}(\varphi, \varphi_i) = (\varphi \pm \varphi_i)^2 + a(\varphi \pm \varphi_i)^4 + b(\varphi \pm \varphi_i)^6 + \dots, \quad (3)$$

$K^{(\pm)}$ —describe the form of the scattering indicatrix, the value C sets the order of magnitudes of the radiation intensity in a porous medium, values $a = -0.29$, $b = 0.04$, $I_0 \equiv 1$.

The numerical value of the dimensionless quantity C , $K^{(+)}$, $K^{(-)}$ for our task is estimated by comparing a purely formal approach (2) with an accurate mathematical model in the scattering task of a porous environment to distribute the intensity of the $I(\varphi, \varphi_i)$ at the $|\varphi, \varphi_i| \ll 1$ when the phenomenon of shading is ignored [6].

The indicatrices obtained experimentally on different samples are presented in the recent work [3] (see Fig. 2 from this reference). Samples No. 2, 4, 6 demonstrate that in is necessary to take into account the boundary between a porous environment and a vacuum. The phenomenon of anomalous retroreflection [1–4] is observed in contrast to Ref. [7] only for p-polarization.

Let's divide the scattering process into two components

$$I(\varphi, \varphi_i) = I_{Surf}(\varphi, \varphi_i) + I_{Vol}(\varphi, \varphi_i), \quad (4)$$

where $I_{Surf}(\varphi, \varphi_i)$ —is the scattering in the near surface layer and $I_{Vol}(\varphi, \varphi_i)$ —scattering in the volume.

The boundary of a roughness surface consists from extremely small areas (Fig. 1). The red color indicates area with a flat (planar) surface that forms part of roughness surface [6].

Let consider a more simplified case, when the incident plane waves scattering process occurs only on the surface with extremely large roughness (more wavelengths), which has the form

$$I_{Surf}(\varphi, \varphi_i) = \rho(\varphi_n) |R((\varphi - \varphi_i)/2)|^2, \quad (5)$$

where

$$\varphi_n = (\varphi + \varphi_i)/2, \quad (6)$$

is the angle between the Y axis and the normal to the scattering surface,

$$\rho(\varphi_n) = \rho_0 + \rho_1 \varphi_n^2 + \dots, \quad (7)$$

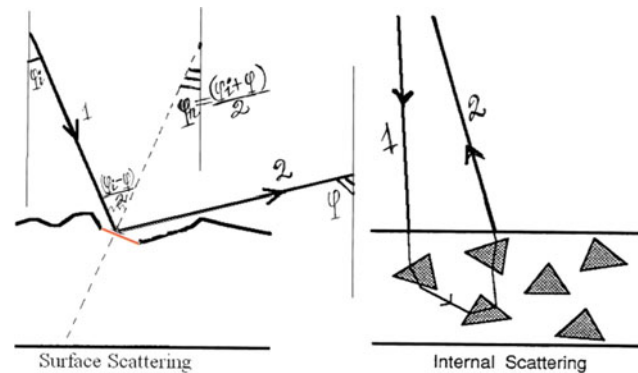


Fig. 1 Scattering in the near-surface layer (a) and internal scattering (b). Red color indicates the area with a tilt angle φ_n

is a function of angle distribution decomposed into its (φ_n) small value. The value of the φ_n is described by the Gauss distribution (the standard deviation for the φ_n is equal to D [8, 9]).

The reflection coefficient is

$$|R((\varphi - \varphi_i)/2)|^2 = |R_0|^2 \left[1 + R_1((\varphi - \varphi_i)/2)^2 + \dots \right], \quad (8)$$

where R_0 , R_1 are dependent on an efficient dielectric constant ϵ_{eff} of porous medium.

Let's write the expression (5) as a expansion in the first non-vanishing order by values $((\varphi \pm \varphi_i)/2)^2$

$$I_{Surf}(\varphi, \varphi_i) = \rho_0 |R_0|^2 \left[1 + \rho_1((\varphi + \varphi_i)/2)^2 + R_1((\varphi - \varphi_i)/2)^2 + \dots \right], \quad (9)$$

Since we use (9) only in the case of small angles φ, φ_i , we will rewrite the Formula (2) in the form

$$I_{Surf}(\varphi, \varphi_i) = \rho_0 |R_0|^2 \left[1 + \rho_1((\varphi + \varphi_i)/2)^2 + R_1((\varphi - \varphi_i)/2)^2 + \dots \right]. \quad (10)$$

Then, in the case of small angles $|\varphi, \varphi_i| \ll 1$, the Formulas (9) and (10) would be identical with each other, and the following equalities must be observed

$$\begin{cases} K^{(+)} = 1/4 + (1/D)^2 + R_1/4, \\ K^{(-)} = -1/4 - R_1/4 \end{cases}, \quad (11)$$

Further, the scattering indicatrices on surface irregularities were obtained for two different polarizations (s, p) and for different values of the parameter D . Note that among them there is no case of anomalous retroreflection, although there are examples when the normalized scattering indicatrix is similar to the Lambert law.

To explain the anomalous retroreflection, it is necessary to take into account scattering on extremely large surface roughness and inside the volume of a porous medium for the case of p-polarization.

In Fig. 2, a ray 1 is incident radiation, ray 2 is the reflected radiation from the interface, ray 3 is transmitted radiation, ray 4 is scattered radiation on internal non-uniformities of the medium and falling on the areas with the same slope, ray 5 is reflected radiation from boundaries, ray 6 is transmitted radiation and scattered according to the Lambert law (ray 9). Herewith, we must take into account the fact that the total radiation of the scattered radiation by the medium is rays 2 + 6 + 9. Then the expression for the total scattered radiation by the medium is described by the formula (4). In

this case, we can write the expression for the magnitude of the radiation

$$I_{Vol}(\varphi, \varphi_i) = \rho((\varphi + \varphi_i)/2)\alpha(\varphi' - \varphi'_i) \left[1 - |R((\varphi - \varphi_i)/2)|^2\right] \left[1 - |R'((\varphi' - \varphi'_i)/2)|^2\right]. \quad (12)$$

which comes of the nanoporous semiconductor material through the areas with the same slope i.e. rays 2 + 6 (where $R'_0 = R_0, R'_1 = -2\sqrt{\epsilon_{eff}}$).

The process of radiation scattering on internal inhomogeneities is described by the function [10]

$$\alpha = \alpha(\varphi' - \varphi'_i) = \alpha_0 + ((\varphi' - \varphi'_i)/2)^2 \alpha_1 + \dots, \quad (13)$$

where the constants $\alpha_0 > 0, \alpha_1 < 0$ depends on the parameters of the medium, wavelength and type of radiation in the medium (transverse (bright modes) or longitudinal (dark modes) [11]), the angle of refraction $\varphi' \approx \varphi/\sqrt{\epsilon_{eff}}$.

Equation (12) is written for the both cases, when the incident and reflected radiation from the medium will leave the interface through areas with the same slope. Overburdened radiation through areas with different slopes will be scattered and will become diffuse (ray 9 with the Lambert distribution), so we will assume that

$$I_{Scatt}(\varphi, \varphi_i) \rightarrow \gamma I_{Scatt}(\varphi, \varphi_i) + (1 - \gamma)(1 - R_0^2) \cos \varphi \cos \varphi_i, \quad (14)$$

where γ is the contribution of areas with the same slope, $(1 - \gamma)$ is the contribution of areas with different slopes.

Power series $I(\varphi, \varphi')$ (4) in the first non-vanishing order by $(\varphi \pm \varphi')/2$ is comparing this with such expansion for the first three non-vanishing order by $(\varphi \pm \varphi')/2$ of (2).

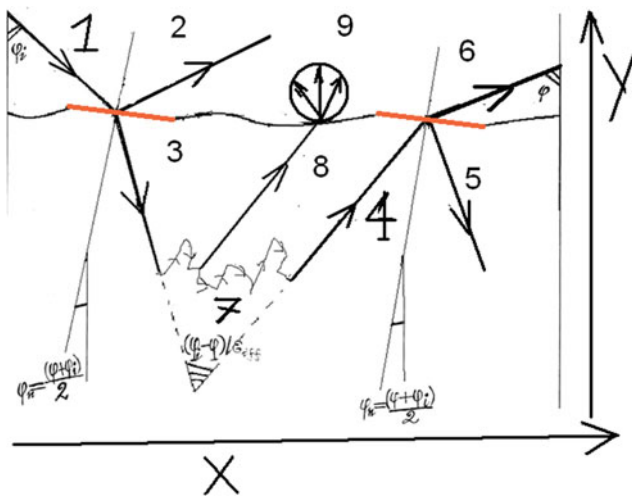


Fig. 2 The scheme for calculating of the total scattered radiation by the medium (in red are marked areas with the same slope)

Then it is easy to obtain expressions for the three values $K^{(+)}, K^{(-)}, C$. Since we are interested in the normalized indicatrix, then the simplified view will be in the following form (for $2 \geq \alpha_0 > 0, |\alpha_1| \gg 1, \gamma \ll 1$).

Let us consider various cases. If we assume that the radiation has the character of a transverse wave (“bright modes” [11, 12]), then it will be strongly absorbed for value $\{\alpha\} \sim 10^{-2} - 10^{-4}$ so that it will give no significant contribution to the light scattering (Eq. (69) from [13]). In this case, the reflected light from the medium forms a sharp ($D \ll 1$) or diffuse ($D \gg 1$) peaks in the specular reflected direction, like any scattered light from a rough surface. If the radiation has the character of a longitudinal wave (“dark modes” [11]), then it will not be absorbed, but a maximum appears related to the backscattering, which in actually is the reason of anomalous retroreflection phenomenon.

The scattering process [10] strictly backwards is described by the value $2 \geq \alpha_0 > 0$. Moreover, in the center of the indicatrix there is not differentiable with $\varphi = \varphi_i$ and therefore, the value $\alpha_1 = \infty$. However, since the scattered light field is averaged over an angular value of 2° , in fact, the observed value will be on the order of $\alpha_1 \sim -10^2$. Therefore, from (14) it follows that

$$K^{(-)} \approx \gamma |\alpha_1| / \epsilon_{eff}, \quad (15)$$

where $\gamma = 1/D\sqrt{K^{(-)}}$ is those part of the radiation that falls on the areas with the same slope. Therefore, for the surface described by the value D

$$K^{(-)} \approx \gamma |\alpha_1| / \epsilon_{eff} = |\alpha_1| / \epsilon_{eff} D \sqrt{K^{(-)}}. \quad (16)$$

Finally

$$\begin{cases} K^{(+)} \approx (1/D)^2 + (R_1 + 1)/4 \\ K^{(-)} \approx [|\alpha_1| / \epsilon_{eff} D]^{2/3} = 20 / (\epsilon_{eff} D)^{2/3}. \end{cases} \quad (17)$$

As $D \rightarrow 0$, we get $K^{(+)} \gg K^{(-)} \gg 1$. The mirrored reflected component will predominate. In the case when $D \rightarrow \infty$, we get $K^{(+)} > K^{(-)} \rightarrow 0$. Both extreme cases are not favorable for the manifestation of anomalous retroreflection. It can be seen from Eq. (17) that the most promising for the manifestation of anomalous retroreflection are highly porous materials ($R_1 = -1$, i.e. small value of ϵ_{eff}) and optimal values of $D \sim 1$.

3 Conclusions

We considered anomalous retroreflection for absorbing nanoporous semiconductor material with p-polarized radiation. This phenomenon is expected to be possible in an absorbing medium, as a result of multiple scattering, due to

longitudinal electromagnetic waves (dark modes) generated at the interfaces. Repeated scattering of these waves of a short wavelength ensures backscattering.

The optimal scheme for the detection and observation of anomalous retroreflection is shown. Based on these calculations, a new technology for obtaining highly porous materials with the preservation of the interface between the medium and the vacuum should be elaborated.

Acknowledgements The authors acknowledge the support from the National Agency for Research and Development under the Grant #19.80013.50.07.03A/BL.

Conflict of Interest The authors declare that they have no conflict of interest.

References

1. Ya, Prislowski S., Naumenko, E.K., Tiginyanu, I.M., et al.: Anomalous retroreflection from strongly absorbing nanoporous semiconductors. *Optics Lett.* **36**, 3227–3229 (2011). <https://doi.org/10.1364/OL.36.003227>
2. Ya, Prislowski S., Naumenko, E.K., Tiginyanu, I.M., et al.: Retroreflection of light from nanoporous InP: correlation with high absorption. *Appl. Phys. A* **117**, 467–470 (2014). <https://doi.org/10.1007/s00339-014-8683-x>
3. Gaponenko, S.V., Monaico, E., Sergentu, V.V., et al.: Possible coherent backscattering of lightwaves from a strongly absorbing nanoporous medium. *J. Opt.* **20**, 075606 (2018). <https://doi.org/10.1088/2040-8986/aac841>
4. Prislowski, S.Y., Gaponenko, S.V., Monaico, E., et al.: Polarized retroreflection from nanoporous III-V semiconductors. In: 26th International Symposium “Nanostructures: Physics and Technology” Minsk, Belarus, 18–24 June 2018, poster NC, 11 p (2018)
5. Rogatkin, D.A.: Rasseyanie elektromagnitnykh voln na sluchajno-sherokovatoj poverhnosti kak granichnaya zadacha vzaimodejstviya lazernogo izlucheniya so svetorasseyivayushhimi materialami i sredami. *Optika i spektroskopija* **97**, 484–493 (2004)
6. Bass FG, Fuks IM (1972) Rasseyanie voln na statisticheski nerovnoj poverhnosti. M Nauka
7. Maradudin, A.A., Mendes, E.R.: Primenimost' impedansnykh granichnykh uslovij v zadache o rasseyanii sveta ot odnomernoj sherohovatoj poverhnosti dijelektrikov. *Optika i spektroskopija* **80**, 459–470 (1996)
8. Sel'kin A V, Kosobukin V A, Lazareva Ju N (2011) Rezonansnoe diffuznoe otrazhenie sveta ot statisticheski sherohovatykh interfesjov fotonnykh kristallov. *Opticheskij zhurnal* **78**:65-71
9. Bhushan, B.: *Modern tribology handbook*, 1 edn. CRC Press (2001)
10. Akkermans, E., Wolf, P.E., Maynard, R.: Coherent backscattering of light by disordered media: analysis of the peak line shape. *Phys Rev Letters* **56**, 1471 (1986). <https://doi.org/10.1103/PhysRevLett.56.1471>
11. Sergentu, V.V., Ya, Prislowski S., Monaico, E.V., et al.: Anomalous retroreflection from nanoporous materials as backscattering by ‘dark’ and ‘bright’ modes. *J. Opt.* **18**, 125008 (2016). <https://doi.org/10.1088/2040-8978/18/12/125008>
12. Sergentu, V.V., Ursaki, V., Monaico, E., et al.: “Dark” modes backscattering as possible rationale for anomalous retroreflection from strongly absorbing porous nanostructures: reviews and short notes to Nanomeeting-2017. *Phys. Chem. Appl. Nanostruct.*, 30–33. https://doi.org/10.1142/9789813224537_0006
13. Iljushin, A.I.: Kogerentnoe obratnoe rasseyanie i slabaja lokalizacija voln v sluchajnykh sredah. Izdatel'stvo fizicheskogo fakul'teta Moskovskogo gosudarstvennogo universiteta, Moskva (2011)

Static Versus Novel Dynamic Biofouling-Testing of Fouling-Release Coatings for Marine Applications: Pros and Cons

H. Qiu, I. Hölken, A. Gapeeva, R. Adelung, and M. Baum

Abstract

With increasing numbers of seaborne transportation of goods worldwide, the exploitation of the ocean is rising. More and more ships and marine equipment with biocide-containing antifouling coatings are in contact with the ecosystem “ocean”. The development of environmentally friendly coatings preventing or allowing a management of biofouling is therefore an urgent issue. To achieve this aim, it is essential to have access to appropriate immersion testing methods to evaluate the fouling-release properties of novel coating systems under most realistic conditions. In this study, a novel dynamic biofouling-test stand was designed and constructed to simulate the movement of a ship and to provide a reproducible testing method for marine coatings. Mechanically durable and environmentally friendly polythiourethane (PTU)/tetrapodal zinc oxide (t-ZnO) microparticle composite as well as reference materials such as AlMg3 alloys and pure polydimethylsiloxane (PDMS) were immersed in the Baltic Sea under static and dynamic conditions for 22 weeks. Strong differences in the degree of biofouling subjected to those conditions were found.

Keywords

Marine coatings • Antifouling • Fouling-release • Dynamic biofouling testing • Tetrapodal zinc oxide

1 Introduction

Due to increased numbers of ships and offshore equipment in the marine sector during recent years, a lot of effort has been done to develop novel environmentally friendly systems for biofouling prevention and fouling-release (FR) as an alternative to conventional antifouling paints, which are known to cause ecological problems [1, 2]. This necessity has driven scientists to shift their research focus from biocide-containing antifouling coatings to so-called fouling-release coatings [3–5]. A fouling-release coating allows a marine organism to attach to its surface, however due to physico-chemical properties of the surface such as low surface energy and/or surface topography, the adhesion forces are so low in between the organism and the surface, that the shear forces generated from the water flow of a moving ship is strong enough to easily release them. For the evaluation of such kind of FR coatings, a conventional testing approach where samples are statically immersed into sea water might not be appropriate [1, 6]. In order to simulate the operational conditions of a ship the dynamic immersion test approach was suggested [7–9].

In this work a novel dynamic biofouling-test stand was used as an alternative testing method for the evaluation of fouling-release materials under more realistic conditions. Those results were compared to the data gained from a static immersion testing to evaluate the impact of frequent changes in water flow comparable to ship movement. Therefore, the recently developed polythiourethane (PTU)/tetrapodal zinc oxide (t-ZnO) composite and pure PTU were tested under both, static and dynamic immersion conditions. Additionally, the pure AlMg3 substrate and the well-known fouling-release material polydimethylsiloxane (PDMS) was chosen as reference materials.

H. Qiu · A. Gapeeva · R. Adelung · M. Baum (✉)
Functional Nanomaterials, Faculty of Engineering,
Institute for Materials Science, CAU Kiel,
Kaiserstraße 2, 24143 Kiel, Germany
e-mail: marb@tf.uni-kiel.de

H. Qiu · I. Hölken
Phi-Stone AG, Kiel, Germany

2 Materials and Methods

2.1 Materials and Sample Preparation

Tetrafunctional pentaerythritoltetrakis (PETMP) and aliphatic 1,6-diisocyanatohexane (HDI) were purchased from Fluid-&Prozesstechnik GmbH (Waltershausen, Germany). The production of the polymer matrix PTU by polyaddition reaction of PETMP and HDI was described in previous works [10, 11]. T-ZnO particles with a mean arm length of ca. 50 μm (Fig. 1) were produced by the flame transport synthesis (FTS) approach [12] at Phi-Stone AG (Kiel, Germany). One component PDMS Elastosil E43 was purchased from Wacker Chemie AG (Munich, Germany).

For polymer composite preparation, t-ZnO particles were first pre-mixed into the PETMP component for 15 min at 6000 rpm by using the MiniMaster disperser machine from Netzsch-Feinmahltechnik GmbH (Selb, Germany). In the next step, the HDI component was added to the pre-mixture and stirred-in manually. The mixing ratio of 58 wt% HDI to 42 wt% PETMP was kept constant, while the amount of t-ZnO was set to 1 wt% of the total polymer composite weight. PTU/t-ZnO composite as well as pure PTU and pure PDMS coating were applied by brush on 10 cm \times 10 cm AlMg3 substrates. Same sets of each 3 samples were prepared for static and dynamic immersion testing.

2.2 Static Biofouling Test Setup

Three coated samples of each material variation (PDMS, PTU, PTU/1 wt% t-ZnO) as well as uncoated AlMg3 reference samples were randomly distributed on a PVC plate and fixed by plastic screws. The whole sample plate was immersed into the Baltic Sea (Strande harbor, Germany) at a

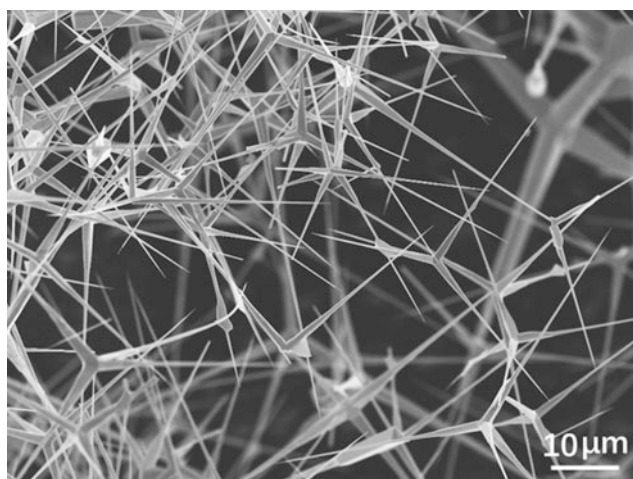


Fig. 1 Scanning electron microscope image of t-ZnO microparticles

depth of 0.6 m, detailed description can be found in the previous study [5]. The mean annual water temperature was 10.5° C (max. 20.6° C, min. -0.3° C). The biofouling on material variations was weekly documented by an underwater camera (Olympus TG-4, Olympus Corporation, Japan).

2.3 Dynamic Biofouling-Test Setup

The dynamic biofouling-test stand was constructed by Kai Rubin Yacht- und Segelservice (Altenholz, Germany). The setup consists of four rotating plates with different diameters (0.4, 0.6, 0.8, and 1 m) (Fig. 2a). The plates are situated at four depth levels: 0.2, 0.4, 0.6 and 0.8 m and 12, 16, 24 and 30 samples can be mounted respectively. Each sample is fixed by plastic screws. A sacrificial zinc anode is used in order to prevent corrosion of metal parts. A 230 V electric motor is mounted on top of the rotating axis. Rotational speed can be adjusted via a control panel. The samples can achieve a linear velocity up to 7 knots. The samples are fixed perpendicularly to the rotational plane and are far sided from the axis. Due to different diameters of rotating plates, samples at each level are rotated with different speed, which allows the investigation of the influence of rotational speed on fouling-release properties. The distance of 20 cm in

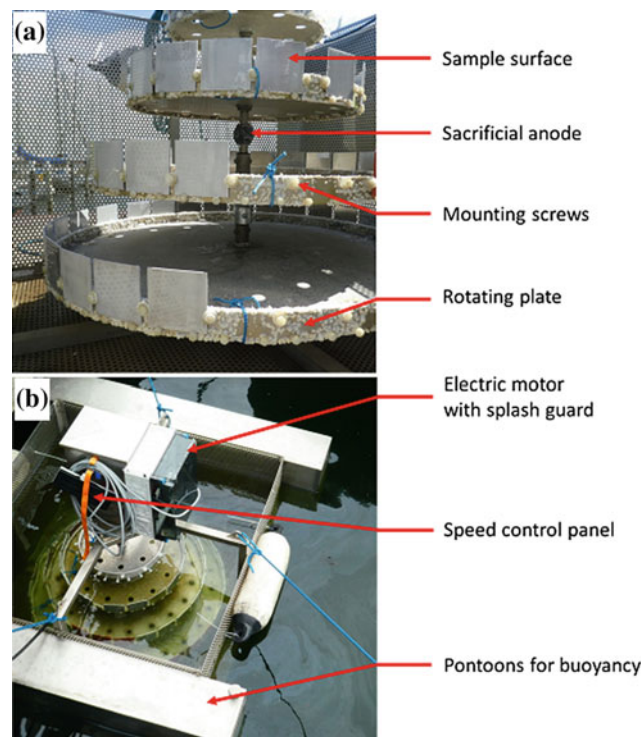


Fig. 2 Dynamic biofouling-test stand: **a** side view of the single plates and the sample mounting equipment, **b** top view of the setup in the Baltic Sea

between the plates was chosen to avoid flow interactions between the levels. The whole setup is floating due to two pontoons and the immersion depth can be adjusted by ballast water. The test stand is fixed by ropes and can be maneuvered by those (Fig. 2b).

In this experiment plates at corresponding depth levels of 0.4, 0.6 and 0.8 m were chosen to fix samples. One of each material variation (AlMg3, PTU, PDMS, PTU/1 wt% t-ZnO) was mounted on each of the three plates. The dynamic biofouling-test stand was immersed in June 2018 for 22 weeks. Rotation at maximum speed was carried out every week for 30 min. The degree of biofouling was recorded by an underwater camera before and after the rotation.

3 Results and Discussion

After 6 weeks of immersion all material variations under dynamic test conditions got fouled by marine organisms, mostly algae, whereby the surface of pure PDMS showed the lowest degree of biofouling compared to other variations (Fig. 3). While some barnacles were found on AlMg3, PDMS and PTU, no barnacles were observed on PTU/1 wt% t-ZnO composite surfaces. During the 30-min rotation, the algae started to detach from the materials surface. When comparing images in row (a) and (b) it becomes apparent that all sample surfaces exhibited a lower degree of biofouling after rotation. However, no barnacles were released from polymer and metal surfaces during the rotation. According to the literature [13] biofouling like barnacles starts detaching from PDMS surfaces at a velocity of approx. 15 knots, which could not be reached by our test stand due to technical and safety reasons.

To evaluate the difference in the degree of biofouling on material variations subjected to static and dynamic conditions, the results recorded after 9 weeks of immersion were compared (Fig. 4). It can be stated that there is a significant difference in the degree of biofouling between material variations, which were immersed under static conditions and those which experienced shear forced due to dynamic testing. Under the static immersion condition, although PDMS showed a slightly less biofouling compared to other material variations, it is difficult to evaluate and compare the performance of other material variations due to a similar degree of biofouling. From the dynamic experimental setup, it can be observed that PDMS as well as PTU/t-ZnO showed a cleaner surface compared to pure PTU.

Although static immersion testing is a well-established and simple method to evaluate the performance of maritime coatings, which is suitable for a large number of applications, this study shows that it is advantageous to conduct dynamic biofouling testing, if fouling-release properties are in focus of investigation. In this study, due to security regulations of the harbour it was prohibited to leave the running dynamic biofouling-test stand unattended and therefore the maximum duration of the dynamic biofouling-test stand operation was limited to 30 min per week. For leisure ships the 30 min-rotation per week is a good approximation, however, to approach real-life conditions for other ships like ferries a more frequent operation of the dynamic biofouling-test stand would be desirable. Another factor limiting the effectiveness of the approach proposed in this paper is the speed of the dynamic biofouling-test stand reaching max. 7 knots, which is high enough for simulation of relatively slow-moving ships like leisure ships while operation speeds of commercial ships like cruises and freighters lie usually above 10 knots. Furthermore, the

Fig. 3 Underwater images of different material variations in dynamic biofouling testing conditions (immersed in 0.6 m depth), after 6 weeks of dynamic immersion: row **a** before rotation and **b** after 30 min rotation

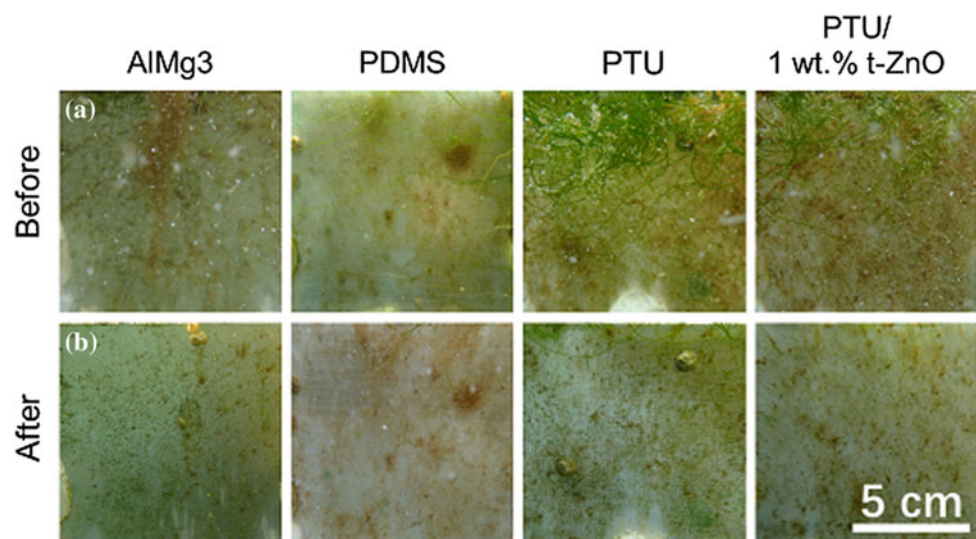
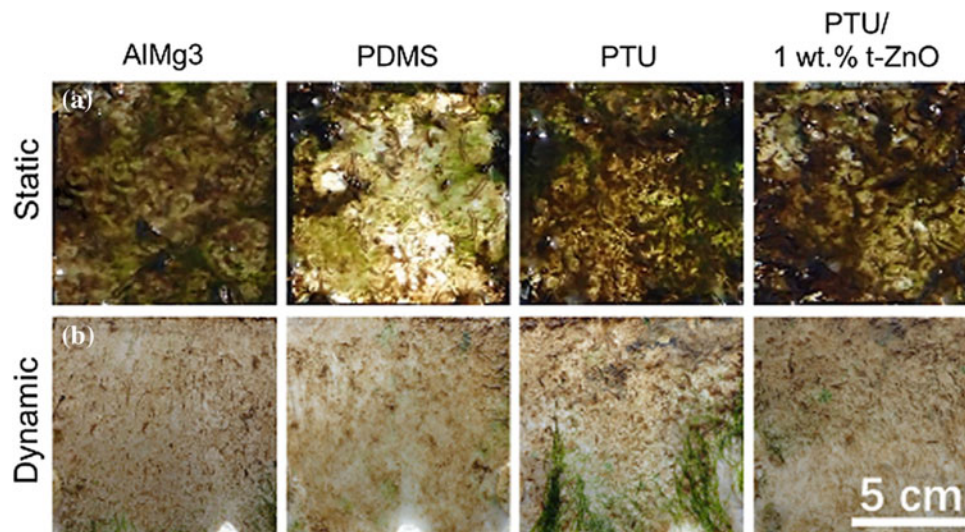


Fig. 4 Images of different material variations, immersed in 0.6 m depth originating from static and dynamic test conditions, after 9 weeks of: row **a** static and **b** dynamic immersion testing



fluctuations in the sea water temperature, salinity, as well as UV light intensity during the movement of the ships from one place to another which can influence the biofouling formation could not be taken into account in this study. In a previous study on the influence of dynamic biofouling-testing by Cassé and Swain [7], the antifouling performance of coatings was evaluated under static condition for two months, followed by a dynamic immersion at periphery velocity of 7.7–9.7 knots for 15 days, which is not comparable with the actual periodic motion of ships. Another difference of their experiment is that the dynamic immersion was conducted in a polyethylene tank with seawater instead of natural conditions found directly in the sea. Nolte et al. [9] conducted dynamic immersion tests in the harbour. However, the linear motion velocity of their test stand was less than 1 knot and therefore much slower than a real ship. Additionally, the sample size was limited to 2.5 cm in width, which implies a strong influence of macrofoulers that attach to the edges of the single testing areas, influencing the overall biofouling occurrence. Unlike our approach, they focused on the degree of microfouling and therefore the immersion period lasted for only 5 days.

Comparing our novel biofouling-test stand to the previously mentioned ones, we can state, that this is the first of its kind offering the possibility for long-term dynamic immersion tests under natural sea conditions for up to 27 material variations with maximum dimensions of 10 cm × 10 cm, vertical sample orientation and a maximum rotational speed of up to 7 knots. Nevertheless, there is a general challenge, when shear forces within a dynamic test stand are generated by rotation. Due to the continuous rotation of the test stand the water in direct contact with the test stand surfaces is accelerated, leading to reduced relative difference in shear forces between the test area surfaces and the surrounding water over time. Therefore, for future investigations we

consider to perform alternating directions of acceleration of the rotation to eliminate this effect. Implementing this intermittently changes in shear forces, this test stand provides a legitimate possibility to evaluate fouling-release properties of e.g. potential ship coatings under a good approximation of realistic ship operation conditions.

4 Conclusions

In this study, the dynamic biofouling-test stand with a maximum rotational speed of 7 knots for testing of marine coatings was introduced. Immersion results revealed that dynamic biofouling testing provides more realistic information on the performance of marine coatings with fouling-release properties, than conventional static immersion testing. Uncoated AlMg3 substrates as well as PTU, PDMS, and PTU/1 wt% t-ZnO composite coatings were tested under both, static and dynamic conditions and the results were compared. Even though the operation time of the dynamic biofouling-test stand was limited to 30 min per week, it was obvious that shear forces generated during rotation were strong enough to release marine organisms from the sample surfaces resulting in a much lower degree of fouling, when compared to sample surfaces subjected to static immersion.

In conclusion, one can state that even though it is difficult to simulate real-life conditions of an operating ship, the approach described in this study provides evidence of the relevance of dynamic testing for materials with fouling-release properties.

Acknowledgements This research was funded by the Federal Ministry for Economic Affairs and Energy within the ZIM-program (16KN015431 and 16KN021267) and the Cluster of Excellence 80

“The Future Ocean”. The “Future Ocean” is funded within the framework of the Excellence Initiative by the Deutsche Forschungsgemeinschaft (DFG) on behalf of the German federal and state governments.

Conflict of Interest The authors declare that they have no conflict of interest.

References

1. Liu, C., Xie, Q., Ma, C., Zhang, G.: Fouling release property of polydimethylsiloxane-based polyurea with improved adhesion to substrate. *Ind. Eng. Chem. Res.* (2016)
2. Lejars, M., Margaillan, A., Bressy, C.: Fouling release coatings: a nontoxic alternative to biocidal antifouling coatings. *Chem. Rev.* (2012)
3. Selim, M.S., et al.: Recent progress in marine foul-release polymeric nanocomposite coatings. *Prog. Mater. Sci.* (2017)
4. Gapeeva, A., Hölken, I., Adlung, R., Baum, M.: Characterization of a polydimethylsiloxane-polythiourethane polymer blend with potential as fouling-release coating. In: *Proceedings of the 2017 IEEE 7th International Conference on Nanomaterials: Applications and Properties, NAP 2017* (2017)
5. Qiu, H., Hölken, I., Gapeeva, A., Filiz, V., Adlung, R., Baum, M.: Development and characterization of mechanically durable silicone-polythiourethane composites modified with tetrapodal shaped ZnO particles for the potential application as fouling-release coating in the marine sector. *Materials* (Basel) (2018)
6. Camós Noguier, A., Olsen, S.M., Hvilsted, S., Kiil, S.: Field study of the long-term release of block copolymers from fouling-release coatings. *Prog. Org. Coat.* (2017)
7. Cassé, F., Swain, G.W.: The development of microfouling on four commercial antifouling coatings under static and dynamic immersion. *Int. Biodeterior. Biodegrad.* (2006)
8. Zargiel, K.A., Swain, G.W.: Static vs dynamic settlement and adhesion of diatoms to ship hull coatings. *Biofouling* (2014)
9. Nolte, K.A., et al.: Dynamic field testing of coating chemistry candidates by a rotating disk system. *Biofouling* (2018)
10. Hölken, I., Hoppe, M., Adlung, R., Baum, M.: Functional ecofriendly coatings for marine applications. In: *IFMBE Proceedings* (2016)
11. Hölken, I., Hoppe, M., Mishra, Y.K., Gorb, S.N., Adlung, R., Baum, M.J.: Complex shaped ZnO nano- and microstructure based polymer composites: mechanically stable and environmentally friendly coatings for potential antifouling applications. *Phys. Chem. Chem. Phys.* (2016)
12. Mishra, Y.K., et al.: Fabrication of macroscopically flexible and highly porous 3D semiconductor networks from interpenetrating nanostructures by a simple flame transport approach. *Part. Part. Syst. Charact.* (2013)
13. Larsson, A.I., Mattsson-Thorngren, L., Granhag, L.M., Berglin, M.: Fouling-release of barnacles from a boat hull with comparison to laboratory data of attachment strength. *J. Exp. Mar. Biol. Ecol.* (2010)

Comparison the Marginal Fit of Metal Coping Cast Made Through Different Methods

A. Badarau, A. Gumeniuc, and E. V. Monaico

Abstract

The present work the evaluation and comparison of the marginal fit of chromium-cobalt (Cr-Co) copings fabricated through three different methods are investigated. There are some technical factors that we cannot get less than 40–50 μm for marginal adaptation. The marginal gap in case of traditional methods is smaller than digital ones, even so the gap produced by the DLMS was not significantly greater and it was not exceeded the clinically acceptable range. Taking into account the advantages of DLMS, it is superior to traditional methods.

Keywords

Conventional and digital impressions • Copings • Lost wax technique • Direct selective laser sintering

1 Introduction

Marginal fit is one of the most important factor for long term success of a restauration in fixed prosthodontics. Improper marginal adaptation of the prosthetic restauration will increase the cement dissolution. As a result, microleakage may cause pulpal inflammation and increase plaque retention

is potentially detrimental to both the tooth and the supporting periodontal tissues [1–5].

Marginal fit can be defined the perpendicular distance from the internal surface of the coping to the axial wall of the preparation at the margin measured at various points between the coping and the tooth. Marginal discrepancy is the angular combination of marginal gap and any extension error [6]. Marginal fit and cement thickness depend on tooth preparation design [5, 7, 8], alloy types [4], casting processes [9], cementation procedures [7, 8, 10–13], porcelain firing cycles [14, 15] and as well as professional factor [16].

Which is the acceptable range of marginal gap? McLean and Fraunhofer studied more than one thousands of crowns during the 5 years. They established that the acceptable range of marginal adaptation is less than 120 μm [17]. Christensen writes that a doctor can reach that marginal fit of gold inlay castings of 40 μm without magnification [18]. Most of the articles relate an average between 60 and 100 μm .

The porcelain-fused-to-metal crowns are most widely used fixed dental prosthesis. It is a one from the significant factors that influence the final porcelain-fused-to-metal crowns marginal gap. High temperature during porcelain firing over the top of the core when producing metal-ceramic crown increase the marginal gap by 10–15 μm [19]. In this study the aim is to study the marginal fit of metal copings which in our days dental practice are most usually fabricated through 3 protocols.

Computer-aided design/computer-aided manufacturing (CAD/CAM) techniques have rapidly replaced the lost wax (LW) technique in dentistry and dental technology. The advantages of the digital workflow are the removal of some intermediate steps that may determine some errors that can affect final result. Traditionally metal copings have been fabricated by the lost wax technique and casting method. This protocol can get some errors at different stages as we may obtain inaccurate marginal fit may result from contraction of impression material, distortion of wax patterns, or irregularities in the cast metal. An opportunity is direct metal

A. Badarau (✉)

Faculty of Dental Medicine, State University of Medicine and Pharmacy “Nicolae Testemițanu”, Florilor 14th Street, Chisinau, Republic of Moldova
e-mail: adrian.badarau@mail.ru

A. Gumeniuc

Department of Orthopedic Dentistry “Ilarion Postolachi”, Faculty of Dental Medicine, State University of Medicine and Pharmacy “Nicolae Testemițanu”, Chisinau, Republic of Moldova

E. V. Monaico

National Center for Materials Study and Testing, Technical University of Moldova, Chisinau, Republic of Moldova

laser-sintering (DMLS) system. It is an additive metal fabrication technology, which use data from computer designing soft based. As against to lost wax technique, direct metal laser-sintering system require an expensive equipment. It is easier for fabrication of complicated shapes, automatic system and get less time. Also less metal is waste by selectively shooting for DMLS system in comparison with LW technique.

2 Materials and Methods

For this study, a dental implant abutment was taken to simulate a perfectly prepared crown. Nine chromium-cobalt (Cr-Co) copings were fabricated through 3 different methods and were selected in three group cast.

In the first group, copings were made by lost-wax technique. Three conventional impression were taken and the dental technician made three gypsum cast. Wax pattern was fabricated by a skilled dental technician. The wax was replaced by metal and the first three copings metal framework were ready. For the next three copings fabrication, clinical steps represent the conventional workflow, but technical ones were like in digital workflow. As with the first method, three conventional impressions were taken three gypsum cast were made. So further the technical steps are different from that passed for the first method. After the casts were fabricated, it was scanned in laboratory scan, Amann Girsch. A frame work of future copings were made on digital model in Exocad Matera 2.3, Dental CAD Software. The thickness was set at 40 μm , starting behind 1 mm the margin. Cobalt-chromium (Co-Cr) piece was fabricated with the direct laser metal sintering technology (DLMS). Specific for the third group is that here we went fully. The dental implant abutment was scanned with intraoral scanner 3 shape TRIOS in the dental office. The digital cast was sent to the dental technician for the direct laser metal copings sintering. The settings were identically like in second method.

After 9 copings were ready, the next step is misfit measurement. We decided to not fix the copings with luting cement as this can generate additional error [20]. The marginal fit may be evaluated by direct visualization of tooth/restoration interface or indirectly through seating of artificial crowns in their respective tooth preparation. We went by the direct visualization. Assessment of marginal fit can be qualitative, which mean by inspection of marginal discrepancy, exploratory probing, radiographic examination, or quantitative with a variety of tools required for this purpose for this type of appreciation [20]. The quantitative measurement were performed with scanning electron microscope (SEM) VEGA Tescan 5130 MM. An example of measurement of marginal discrepancy, for a coping from the third group (dental office scanning and SLS Co-Cr) is

demonstrated in Fig. 1. There is a marked area in the first figure. It represents the chosen zone for measurement (Fig. 2). The basic requirements for the investigation in SEM are that the specimens should adequately prepared and positioned in the way that studied structures to be in a specific focus plane.

In some research, the specimens were sectioned. The cross-section can be done with special cutting disc with different thicknesses and polished with progressively finer grit sandpaper, 240–600 grit, toward the crown to eliminate flash. Another way is using a laser. In contrast to the cutting disc, the laser doesn't create flash, but it heats the metal to an extremely high temperature. We decided to not cut the specimens, as this stage generate a supplemental fault error.

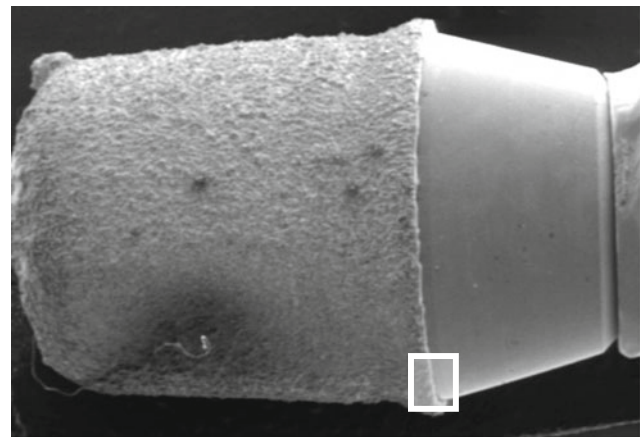


Fig. 1 SEM image of the second coping from the third group (dental office scanning and SLS Co-Cr)

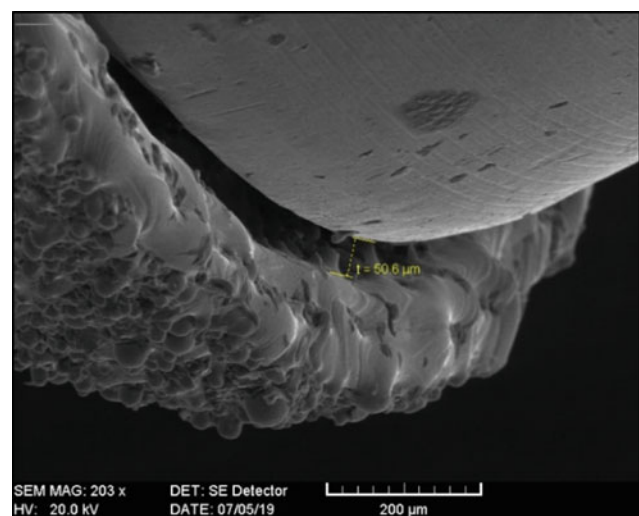


Fig. 2 SEM image, 203 \times magnification, of marginal adaptation for the second coping from the third group (dental office scanning and SLS Co-Cr)

All result were introduced in the Microsoft Excel file. After all the calculations were made in this program, the result were examined.

3 Results

The representative SEM image of the coping from the third group is presented in Fig. 1 as well as magnified view can be found in Fig. 2.

The marked area magnification is represented in Fig. 2.

The mean discrepancy of fit and standard deviation was measured for each coping adaptation. The averages of the calculation were introduced in Table 1. All results were schematically represented as a diagram (Fig. 3).

All studied specimen didn't exceed the acceptable clinical range. We found that in first group, Conventional impression and Cast Co–Cr, we measured the smallest misfit. This fact reveal that direct laser metal sintering is a little bit less precise than traditional method, lost wax technique. Considering the great number of direct laser metal sintering and entire digital protocol on conventional one, the difference in misfit of 15 μm , it is not enough substantial to conclude that lost wax technique is superior on direct laser metal sintering.

Table 1 The mean and standard deviation of marginal gap for three groups

Groups	Mean (SD)
Conventional impression and cast Co–Cr	41.1 (8.1) μm
Conventional impression, laboratory scanning and SLS Co–Cr	61.4 (9.1) μm
Dental office scanning and SLS Co–Cr	55.3 (7.2) μm

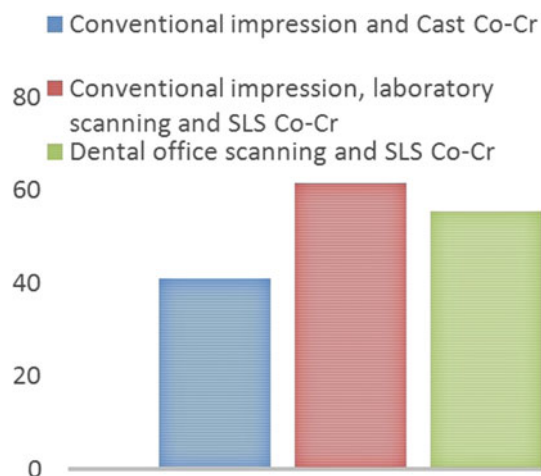


Fig. 3 Marginal gap

A bigger misfit was found in second group, conventional impression, laboratory scanning and SLS Co–Cr, in comparison with the third group. It can be due to extra steps, conventional impression and gypsum cast fabrication which may cause additional errors.

The vertical marginal discrepancy was evaluated on different surfaces (buccal, distal, lingual and mesial) in case of each studied specimen there was no found important difference between different surfaces.

4 Discussions

In this research, we look for the marginal gap as a direct projection of seating the copings on reference abutment, in a two-dimensional image get from SEM. There are different methods of studying, two-dimensional: after cutting it and observing the cross-section under microscope, or by using the silicon replica technique [21, 22] and three-dimensional using a special software (Delcam, Birmingham, UK). All this methods are accurate, some of them more, another less, some of them need cutting and are destructive, some of them need fluid silicone material (two-dimensional or three dimensional replica technique). We chose to measure directly without cementing as this can afford supplementary micros between margins of the copings and reference abutment.

How much points for measurement we need for an objective result? Somebody measured the marginal discrepancy in 6 point, other research say that we must look on for 50 points one tooth [23]. We measured in 4 points as we measured a dental implant abutment which is almost perfectly round, it just has an anti-rotational element. The purpose of this investigation was of copings accuracy made through three different methods.

In this work we evaluated the marginal gap, internal one is not important? It is not so important for a porcelain-fused-to-metal crowns as in case of bondable restauration. In the case of a ceramic veneer restoration that has a small thickness, we need to fix them adhesive to enamel for a long term stability. If it will be fixed to dentin or on a too big thickness of compound than it is a great risk of a crack. The porcelain-fused-to-metal crowns are more resistant constructions. It is desirable a good internal adaptation but not in the same way as in case of a thin ceramic veneer.

Nowadays this type of indirect restauration is still widely used. Weak point of each type of restauration is marginal adaptation. Metal core can be fabricated by lost wax technique or direct laser metal sintering as both method are enough precise to have an acceptable clinically marginal misfit.

5 Conclusions

There are some technical factors that we cannot get less than 40–50 μm for marginal adaptation. The marginal gap in case of traditional methods is smaller than digital ones, even so the gap produced by the DLMS was not significantly greater and it was not exceeded the clinically acceptable range. Taking into account the advantages of DLMS, it is superior to traditional methods. Even if the gap for sintering group was greater, it not exceeded the clinically acceptable range. If the coping will be fabricated by direct laser metal copings sintering, better to go full digital.

Conflict of Interest The authors declare that they have no conflict of interest.

References

- Gardner, F.M.: Margins of complete crowns: literature review. *J. Prosthet. Dent.* **48**, 396–400 (1982)
- Kashani, H.G., Khera, S.C., Gulker, I.A.: The effects of bevel angulation on marginal integrity. *J. Am. Dent. Assoc.* **103**, 882–885 (1981)
- Rosenstiel, S.F., Land, M.F., Fujimoto, J.: *Contemporary fixed prosthodontics*, pp. 475–492. Mosby, St Louis (1988)
- Rosenstiel, S.F., Land, M.F., Fujimoto, J.: *Contemporary fixed prosthodontics*, pp. 579–588. Mosby, St Louis (1988)
- Schwartz, I.S.: A review of methods and techniques to improve the fit of cast restorations. *J. Prosthet. Dent.* **56**, 279–283 (1986)
- Holmes, J.R., Pilcher, E.S., Rivers, J.A., Stewart, M.: Marginal fit of electroformed ceramometal crowns. *J. Prosthet. Dent.* **5**, 111–114 (1996)
- Eames, W.B., O’Neal, S.J., Monteiro, J., Miller, C., Roan Jr., J.D., Cohen, K.S.: Techniques to improve the seating of castings. *J. Am. Dent. Assoc.* **96**, 432–437 (1978)
- Grajower, R., Zuberi, Y., Lewinstein, I.: Improving the fit of crowns with die spacers. *J. Prosthet. Dent.* **61**, 555–563 (1989)
- Pascoe, D.F.: Analysis of the geometry of finishing lines for full crown restorations. *J. Prosthet. Dent.* **40**, 157–162 (1978)
- White, S.N., Kipnis, V.: The three-dimensional effects of adjustment and cementation on crown seating. *Int. J. Prosthodont.* **6**, 248–254 (1993)
- White, S.N., Yu, Z., Tom, J.F., Sangsurasak, S.: In vivo marginal adaptation of cast crowns luted with different cements. *J. Prosthet. Dent.* **74**, 25–32 (1995)
- Kern, M., Schaller, H.G., Strub, J.R.: Marginal fit of restorations before and after cementation in vivo. *Int. J. Prosthodont.* **6**, 585–591 (1993)
- Gavelis, J.R., Morency, J.D., Riley, E.D., Sozio, R.B.: The effect of various finish line preparations on the marginal seal and occlusal seat of full crown preparations. *J. Prosthet. Dent.* **45**, 138–145 (1981)
- Shillingburg Jr., H.T., Hobo, S., Fisher, D.W.: Preparation design and margin distortion in porcelain-fused-to-metal restorations. *J. Prosthet. Dent.* **29**, 276–284 (1973)
- Faucher, R.R., Nicholls, J.I.: Distortion related to margin design in porcelain-fused-to-metal restorations. *J. Prosthet. Dent.* **43**, 149–155 (1980)
- Marker, V.A., Miller, A.W., Miller, B.H., Swepston, J.H.: Factors affecting the retention and fit of gold castings. *J. Prosthet. Dent.* **57**, 425–430 (1987)
- McLean, J.W., von Fraunhofer, J.A.: The estimation of cement film thickness by an in vivo technique. *Br. Dent. J.* **131**(3), 107–111 (1971). <https://doi.org/10.1038/sj.bdj.4802708>
- Christensen, G.J.: Marginal fit of gold inlay castings. *J. Prosthet. Dent.* **16**(2), 297–305 (1966). [https://doi.org/10.1016/0022-3913\(66\)90082-5](https://doi.org/10.1016/0022-3913(66)90082-5)
- Campbell, S.D., Pelletier, L.B.: Thermal cycling distortion of metal ceramics: part I-metal collar width. *J. Prosthet. Dent.* **67**(5), 605–608 (1992)
- Dimashkien, M.R., Davies, E.H., von Fraunhofer, J.A.: Measurement of the cement film thickness beneath full crown restoration. *Br. Dent. J.* (1974)
- Kohorst, P., Brinkmann, H., Dittmer, M.P., Borchers, L., Stiesch, M.: Influence of the veneering process on the marginal fit of zirconia fixed dental prostheses (2010)
- Laurent, M., Scheer, P., Dejou, J., Laborde, G.: Clinical evaluation of the marginal fit of cast crowns—validation of the silicone replica method. *J. Oral. Rehabil.* (2008)
- Groten, M., Axmann, D., Pröbster, L., Weber, H.: Determination of the minimum number of marginal gap measurements required for practical in-vitro testing. *J. Prosthet. Dent.* **83**(1), 40–49 (2000)

Synthesis of New Zinc Phthalocyanine with Block Copolymers in Nanomedicine Applications

P. Tiuleanu, S. Robu, V. Prisakari, V. Furtuna, R. Rusnac, and T. Potlog

Abstract

Synthetic routes towards new conjugates of hydrophilic zinc phthalocyanine (ZnPc) with N-vinylpyrrolidone (NVP) and acrylic chloride (CIAC), are described. For this purpose, a copolymer of N-vinylpyrrolidone (NVP) with acrylic chloride (CIAC), according to the Friedel-Kravts method, was grafted to the benzene nucleus of zinc phthalocyanine (ZnPc). The paper contains the analysis of polymer analogs of NVP-CIAC-ZnPc with IR and UV-VIS spectroscopies.

Keywords

Zinc phthalocyanine • N-vinylpyrrolidone • Acrylic chloride • FTIR analysis • Absorbance

1 Introduction

One of the most interesting groups of porphyrin-like compounds, considering physicochemical properties, are the zinc phthalocyanines—light-sensitive molecules, known for their exceptional stability and light absorption properties in the red/near IR region (ϵ may exceed $10^5 \text{ M}^{-1} \text{ cm}^{-1}$ for the Q band, often located at 650–700 nm). Phthalocyanines of transition metals are attractive for PDT because when reacting with oxygen, or rather, when they absorb a quantum of light, a photochemical reaction occurs and causes a conversion of oxygen from the usual triplet state to the singlet form (oxygen with a spin multiplicity equal to one), which has much higher activity [1, 2]. There are two forms of this oxygen, existing 7.1 s and 40 min

This form of oxygen is the cause of the biological activity of photosensitizers, as interacting with the chemistry of a tumor cell, it becomes an oxidizing agent with a reactive capacity that is much higher than that of a standard triplet state [3].

As practice has shown, polymers and other soluble forms of phthalocyanines, as well as other types of photosensitizers, have the ability to produce singlet oxygen [4]. This happens because the phthalocyanine molecule is rather cumbersome, as well as due to relatively mobile hydrogen atoms in the benzene rings, and also due to the fact that, because of good crystallization and sublimation, they become “crystals”. As is well known, in pure form, they have high quantum activity, and are capable of producing a narrowly directed “beam” of photons. The problem of phthalocyanines is their low solubility in water and in other solvents used in medicine for the treatment of tumor diseases. Therefore, the purpose of this study was to obtain at least partially soluble forms of zinc phthalocyanine compounds and to test their antibacterial activity with the prospect of further use in the medical industry.

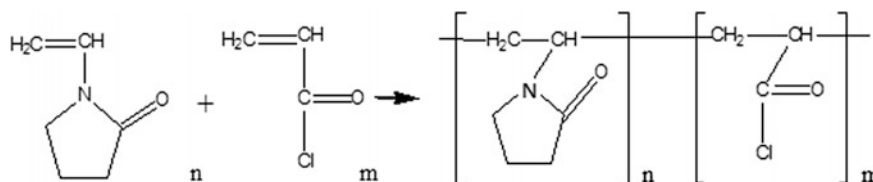
2 Synthesis of a Polymer Analogue of Poly-N-Vinylpyrrolidone-Acrylic Chloride-PcZn

It is well known that polymeric N-vinylpyrrolidone (NVP) is perfectly soluble in water and completely non-toxic [5]. Based on these considerations, it was decided to combine it with a phthalocyanine molecule through a substitution reaction in benzene nucleus using the Friedel-Kravts method [6]. This synthesis in two stages is as follows:

1. At the first stage, NVP was polymerized with CIAC by a radical mechanism in the presence of azo-bis-isobutyronitrile (AIBN) initiator and at a temperature of 80 °C according to Scheme 1. At this stage, a polymer of the composition, where n-mol% N-Vp and m-mol%

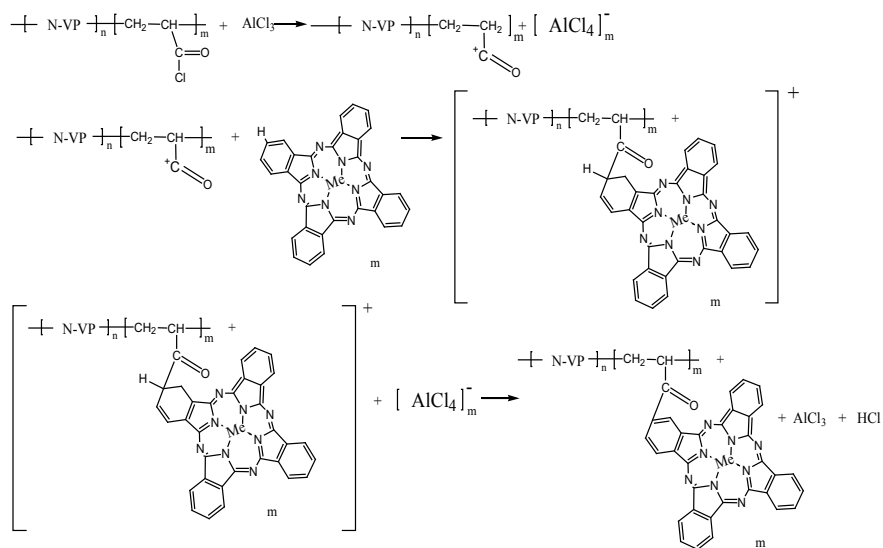
P. Tiuleanu · S. Robu (✉) · V. Furtuna · R. Rusnac · T. Potlog
Physics Department and Engineering, Moldova State University,
60, A. Mateevici Str., Chisinau, Republic of Moldova
e-mail: stefan_robu@yahoo.com

V. Prisakari
Nicolae Testemițanu State University of Medicine and Pharmacy,
Chisinau, Republic of Moldova



Scheme 1 Synthesis of copolymers (N-VP) and (ClAC)

Scheme 2 Synthesis of polymer grafted with phthalocyanine



ClAC, is obtained and followed by the second stage of the synthesis, that is the polymer substitution reaction in PcZn.

2. Synthesis of the polymer grafted with phthalocyanine according to Scheme 2, according to the Friedel-Crafts reaction in the presence of a catalyst—aluminum trichloride. Moreover, the concentration of mol% phthalocyanine should be the same as that of acrylic chloride. After this reaction, a substance that will contain phthalocyanine and will be at least partially soluble in water should be obtained. The conditions must be maintained as close as possible to those indicated, because the polymer may be vulcanized and become unsuitable for further research.

C–H bond stretching motion occurs, while between 600 and 900 cm^{-1} , the out-of-plane bending of this bond is found. The ZnPc macrocycle can interact with water molecules in different ways. These interactions may comprise interaction with the central metal atom (Zn), H-bond interactions (O–H...N) between the water molecule and the bridging nitrogen atoms as well as H-bond interactions.

Compared to pure ZnPc spectrum in the ZnPc-NVP-ClAC the new peaks appear. As follows from (Fig. 1) in the IR spectrum of the polymer analog, new absorption bands are observed at a frequency of 1720 cm^{-1} , characteristic for carbonyl group, and also the disappearance of some bands, for example, at a frequency of 843 cm^{-1} , characteristic for C–Cl bond, etc.

Absorption spectra for the pure ZnPc and mixed with N-vinylpyrrolidone (NVP)—acrylic chloride (ClAC) are presented in Fig. 2.

With increasing of the concentration of N-vinylpyrrolidone (NVP)—acrylic chloride (ClAC) the intensity of the Q band of ZnPc in the ZnPc-NVP-ClAC water solutions samples increases and the position shifted to longer wavelength. On the spectrum of the visible area, absorption is clearly visible at a wavelength of 650–700 nm, which indicates the presence of ZnPc in the copolymer. The band-gap values were estimated using the $(\alpha h\nu)^2$ versus $(h\nu)$

3 Spectral Studies: IR, Visible Spectrum

The FT-IR spectra are essential and useful method to testify bonds of samples. Therefore, IR spectroscopy measured in region (400–4000 cm^{-1}) was involved to characterize chemical structural properties. IR spectra of the ZnPc and obtained polymer analogs are illustrated in Fig. 1. The IR bands of ZnPc in the 700–800 cm^{-1} region can be assigned to N–H bond. In the 3000–3100 cm^{-1} region benzenoid

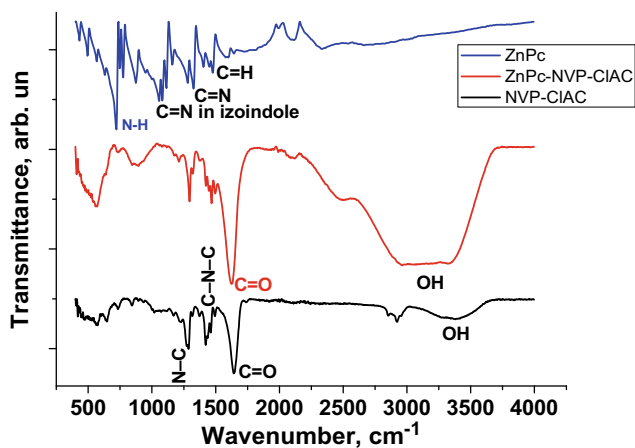


Fig. 1 FTIR spectra of the ZnPc and NVP-CIAC-ZnPc in 400–4000 cm^{-1} region

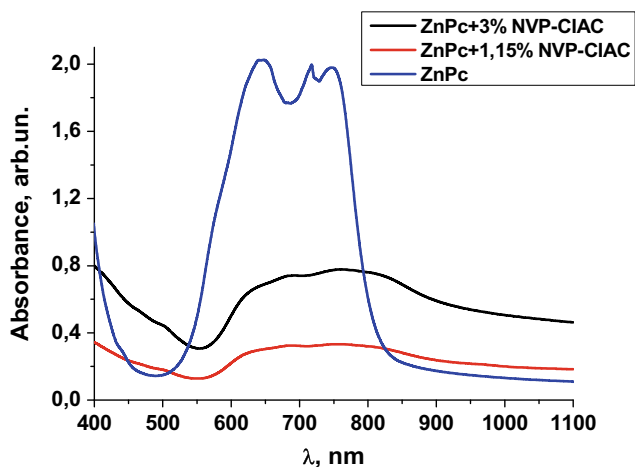


Fig. 2 UV-VIS absorbance spectra of the ZnPc (thermal evaporated) and ZnPc-NVP-CIAC water solutions samples

plots by extrapolating the linear part of the absorption edge to the intersection with the energy axis as shown in Fig. 3.

The estimated values of the band gap in the visible region of the ZnPc-NVP-CIAC water solutions samples were relatively lower in comparison with of pure ZnPc. Thus, the optical studies indicated the presence of direct interband transition across a bandgap whose value depends on the concentration of NVP-CIAC and NVP-CIAC-ZnPc samples.

4 The Process of Dissolving in Water

The obtained compound is initially a green solid with the remains of reaction impurities and of the solvent in which the reaction was carried out—chloroform. After the substance was immersed in water, the water partially became

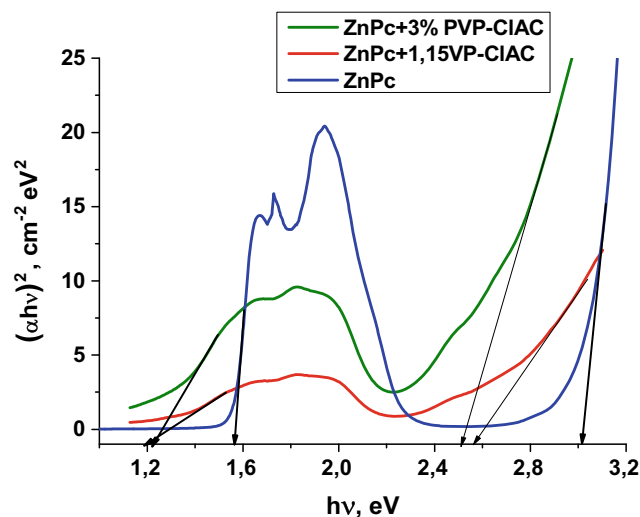


Fig. 3 Dependencies of $(\alpha hv)^2$ versus $h\nu$ of the ZnPc and NVP-CIAC-ZnPc samples

colored blue, and the substance turned into a liquid floating on the bottom, which, after purification from impurities, turned out to be well soluble in chloroform and dimethylformamide, and also perfectly soluble in water. It is worth noting that another factor proving the reaction is that when the substance is dissolved in various solvents, zinc phthalocyanine crystals did not precipitate, which confirms the conclusion about the formation of a chemical bond.

5 Conclusions

In conclusion, can be drawn the following:

1. The polymer compound of zinc phthalocyanine is soluble in water and organic solvents.
2. Using IR spectroscopy, as well as other physical and chemical methods, the occurrence of a chemical bond between NVP-CIAC and zinc phthalocyanine was verified.
3. From absorbance spectra were established that Q band of ZnPc in the ZnPc-NVP-CIAC water solutions samples increase with increasing the concentration of copolymer and the position of band shifted to longer wavelength.

Acknowledgements The authors would like to thank the Ministry of Education, Culture and Research of Republic of Moldova for supporting this research by funding the grant 15.817.02.39A.

Conflict of Interest The authors declare that they have no conflict of interest.

References

1. Photodynamic Therapy. American Cancer Society, 18 Mar 2015
2. Krasnovsky, A.A.: Photodynamic action and singlet oxygen. *Biophysics* **49**(2), 305–321 (2004)
3. Martusevich, A.A., Peretyagin, S.P., Martusevich, A.K.: Molecular and cellular mechanisms of the action of singlet oxygen on biosystems. *Sovrem. Technol. Med.* **2** (2012)
4. Morozova, N.B., Yakubovskaya, R.I., Chissov, I.I., Negrimovsky, V.M., Yuzhakova, O.A.: Photoinduced in vivo activity of positively charged phthalocyanine zinc intended for photodynamic therapy of malignant neoplasms. *Russ. Oncol. J.* **1** (2012)
5. Gorbunova, M.N.: Applied aspects of chemistry of N-vinylpyrrolidone and its polymers. *Perm Sci. Cent. Bull.* **1** (2012)
6. Agronomov, A.E., Shabarov, Yu.S.: *Laboratory Work in the Organic Practice*, 2nd edn, Ext. and pererabat. Chemistry, Moscow (1974)

Portable Campimeter to Evaluate Visual Field Modifications of Subjects with Low Vision State

M. I. Baritz, M. G. Apostoaie, and A. M. Lazar

Abstract

The low vision state that can be installed at the visual function level causes a change in a series of important visual system parameters, as well as a decrease in the quality of life of human subjects. Mostly, lowering the visual function level should be evaluated periodically in any kind of condition (at home, medical clinic or screening center) and in all cases the investigator optometrist should identify the situations in which subjects develop visual field limitations. These visual field limitations may indicate the onset of a wide range of ocular pathologies, which, if detected early, can control procedures of management evolution or even improve with various visual aids. In the first part of the paper are presented some general aspects regarding the field of vision and also its parameters to the human visual system. The second part describes the construction of a visual field assessment system based on the primary requirement of being portable and easy to use device. In the final part of the paper are presented the results obtained using this visual field evaluation device and the way it can be programmed for several types of evaluations.

Keywords

Visual field • Arduino board • Device • Low vision

1 Introduction

The procedures developed in the field of visual field determinations are named perimeter and represent, as specialists say “a standard method used in ophthalmology and

optometry to assess a patient’s visual field. It provides a measure of the patient’s visual function throughout their field of vision.

The devices used to perform this evaluation are called perimeters. Perimetry is performed for several reasons: detection of pathologies; evaluation of disease status; follow-up of pathologies over time to determine progression or disease stability; determination of efficacy of treatment and visual ability testing” [1].

The strategies and procedures used in the structure of the various forms of the visual field evaluation equipment start from the monocular and then binocular determinations to obtain the visual insensitivity areas (scotoma). The monocular and binocular visual fields are defined as the view area of the subject in which the visual capabilities are good while keeping the fixation direction and without eye or head movements. According to those determined by specialists “on average, the monocular visual field extends from 60° nasally to approximately 90° or more temporally, and from approximately 60° superiorly to 70° inferiorly” [1], see Fig. 1.

Normally, in subjects with normal vision, the visual field is monocular for each eye and contains a central area in which vision and visual perception is binocular and spatial (Fig. 2).

The magnitude that can assess the level of normality of the field is the sensitivity to light that is not uniform across the area. For the normal visual system and a typical photopia illumination, the maximum sensitivity is at the center of the visual field and decreases progressively towards the periphery.

When the sensitivity levels of both the central and peripheral areas do not respect this variation on the normal level curves, then the existence of scotomas or sensitivity-lowering areas can be identified. A scotoma is an area of partial alteration in the visual field consisting of partially dimmed visual acuity or entirely, which is surrounded by a normal or relatively well-conserved field of vision. When photoreceptors are affected, the defect in the visual field

M. I. Baritz (✉) · M. G. Apostoaie · A. M. Lazar
Product Design, Mechatronics and Environment Department,
Transilvania University from Brasov, B-ul Eroilor, nr. 29, Brasov,
Romania
e-mail: mbaritz@unitbv.ro

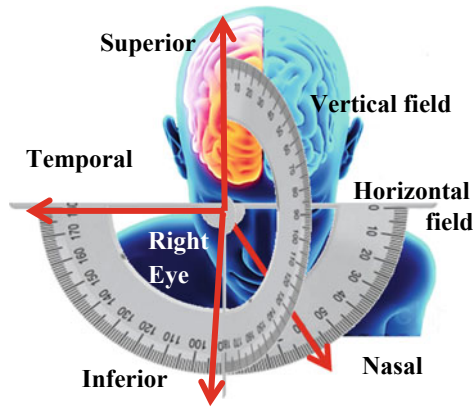


Fig. 1 The monocular visual field

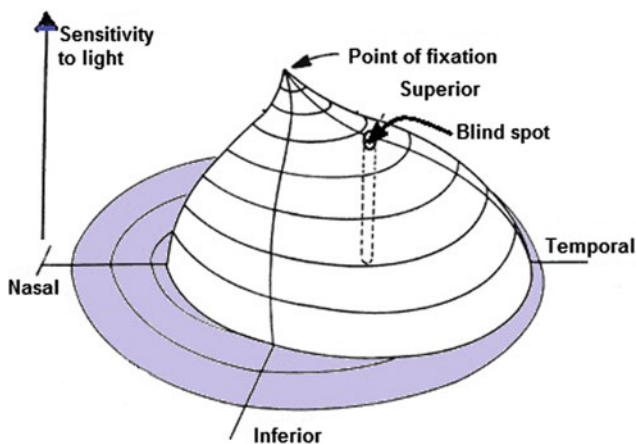


Fig. 2 The hill of vision is a three-dimensional representation of the visual field

corresponds to the retinal defect in position, shape, magnitude and intensity. These scotomas indicate the existence of a local pathology at the retinal level and as such the patient requires an immediate ophthalmologic intervention.

2 Experimental Setup

2.1 The Constructive Principle of the Portable Campimeter

In the design of this portable device, the horopter principle was set as the optimal viewing space for the visual function. Horopter “can be defined theoretically as the points in space which are imaged on corresponding points in the two retinas, that is, on anatomically identical points” [2] (Fig. 3).

The name of the system design in this paper is *Mobile Geriatric Help for Low Vision (MGH-LV)*, a name that encompasses the most important properties of the device. It is mainly addressed to people with low vision. All the

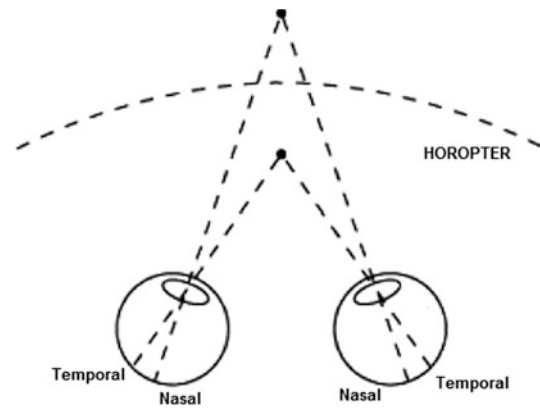


Fig. 3 The representation of horopter principle

distances required for a correct assessment are adjustable, making the system adaptable to any kind of body dimensions and any location of examination.

2.2 Experimental Construction of Campimeter (Perimeter)

The system is mounted on a table; the coarse vertical positioning can be done by adjusting the adjustable seat vertically and the fine mantle (the chin and the front of the subject). The distance from the head of the subject to the appliance is adjustable slightly because the appliance is fixed only to the holder or can be mounted at the distance required for the tests. The device is designed for anthropometric dimensions of the human head and for pupil distances between 55 and 65 mm (for the adult subject). The system is positioned in front of the subject at approximately 30–40 cm, this being the optimal distance for near-vision. The subject’s eyes should be positioned with visual axis to the Amsler grid, this adjustment being made both from the chair and from the device which the subject will support his chin (see Fig. 4).

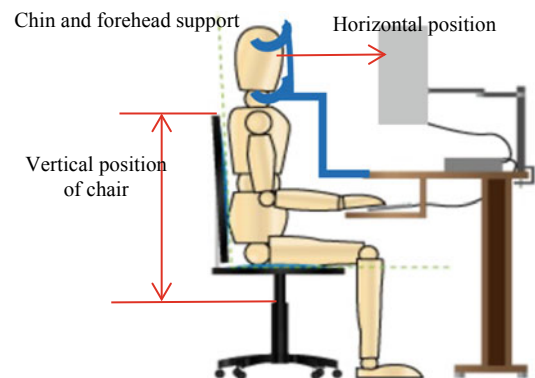


Fig. 4 The experimental setup

In terms of system construction, a number of 48 LEDs have been chosen to cover a field of vision as high as possible. These LEDs are mounted on a white background at distances determined by the uniform distribution calculation on the display surface.

The total number of LEDs was divided into 3 groups: 28 of them form the main body of the device, 10 are positioned on the right side and 10 on the left side (Fig. 5) The device has an Amsler grid in the center, as it is a way of initially assessing the possible positions of the scotomas.

The 20 LEDs on the mobile bodies are intended for the peripheral side and vertical field of vision because many of the visual acuity problems begin in this part of the field of vision. Three dimensional LED construction and positioning variants were created on the three visual field areas (center and sides). Following the determinations was chosen variant no. 3 (see Fig. 5) which allows a better placement of the luminous stimuli on the perimeter areas so that the subject is covered by the entire field of vision, both monocular and binocular [3]. The construction of the device is based on a set of LEDs (that are placed on the central and lateral areas of the perimeter) and which are ordered by a Arduino Mega plate to illuminate randomly according to the procedure selected for visual field evaluation (see Fig. 6).

For the construction's efficiency, the LEDs were linked separately, each on an individual port, and this is also necessary in developing the process of programming the working procedure.

Also, the two sides can be positioned at the center of the body at different angles with respect to the initial parameters of the visual function of the subjects to be assessed.

The ideal position of the system is set at 40 cm to the position of the subject's system.

For a complete and comfortable test, a mentoring is required for the subject to support his chin and forehead and have a correct position on the device, see Fig. 7 (MGH-LV

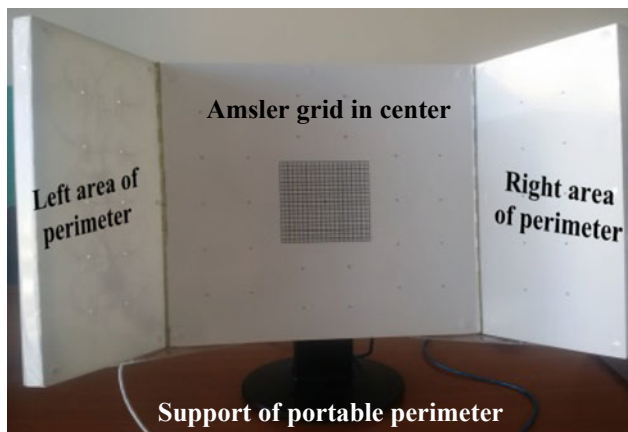


Fig. 5 The perimeter construction

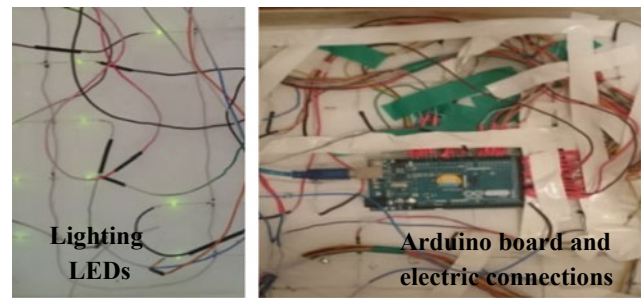


Fig. 6 Back side of the portable perimeter

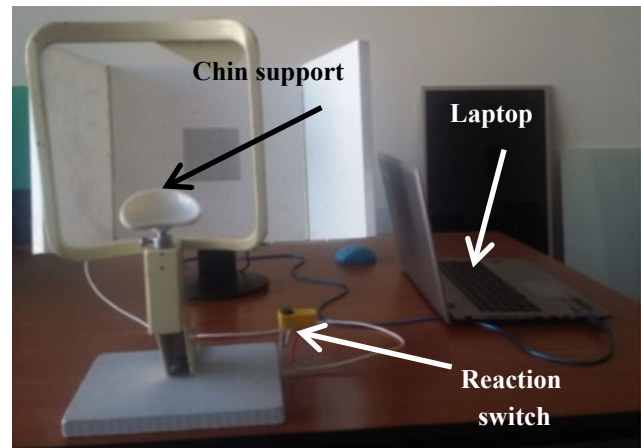


Fig. 7 Integral construction of portable perimeter prototype

prototype accompanied by the reaction button, a laptop for dialing program and a USB cable to connect the laptop to the perimeter system).

3 Results

The device made in the variant presented by the prototype was checked to find and correct the constructive aspects and the poor use.

Thus, various positions of the subject were tested, placed with the head in the chin support to identify the ideal position and the adjustment areas needed to adjust it [4].

The erroneous position of the chin in the support, the head inclination or the position relative to the prototype device were corrected by adjusting the chin support by placing it at the distance and height corresponding to the anthropometric dimensions of the subject and by initial instruction, respectively (see Fig. 8). At the end of the positioning setting, the subject should be placed on the support bracket, with the forehead supported and with a position of the axis of sight forming an angle of 15–20° from the horizontal to be able to carry out the fixation process at the center of the Amsler grid, see Fig. 9.

Fig. 8 Positive positions of the subject towards the menton of the device

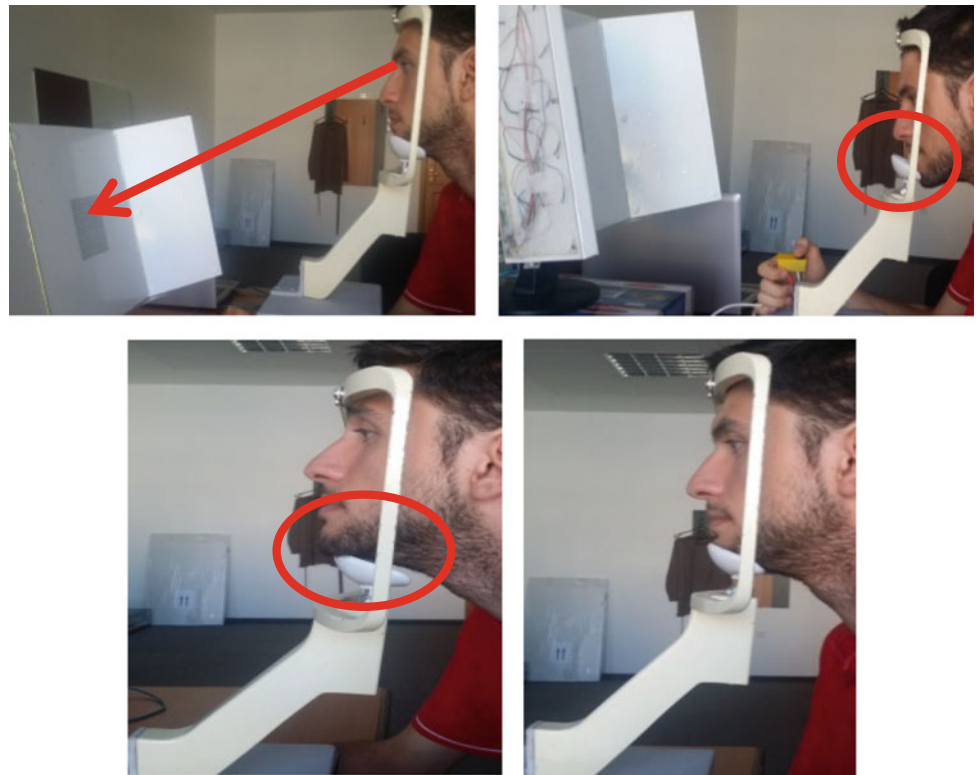
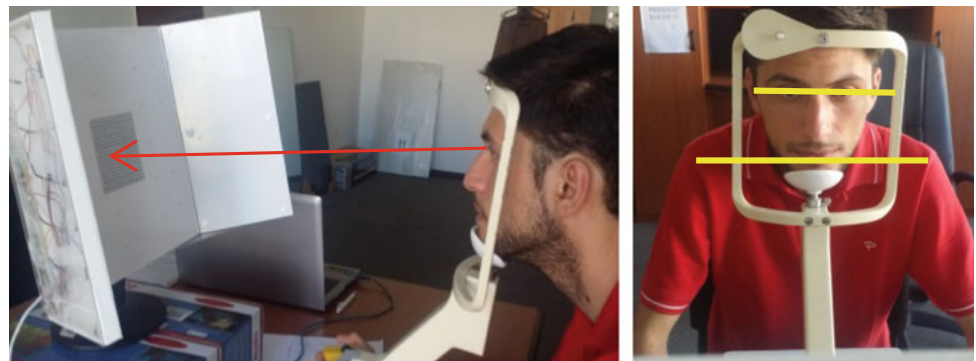


Fig. 9 Correct positions of the subject to use portable perimeter



In addition, the subject should have a good metabolic state, be in a form of behavioral comfort, affective affectivity, and effective testing.

The prototype command and control unit is designed to run the program routine without the need for system surveillance, which gives it freedom of movement to the optometrist conducting the test. It can track the subject's behavior for the duration of the recording.

The activity of using the portable perimeter prototype, displaying LED-based light stimuli, and registering the subject's responses were managed by the software code

created specifically for this prototype and loaded with the Arduino Mega plate, see Fig. 10.

Also, with this code, the Arduino Mega development board has also commissioned the portable perimeter to work alongside the participant's recordings of the test subjects so as to obtain comparable results to those from a computerized campimeter [5].

Comparison of recorded data has highlighted the correlation of these data and therefore the usefulness of such a portable campimeter.

```

#define MAX_INT 100000
const int buttonPin = 0; // the constant that indicates the ID of the
pin to which the button is connected
const int ledPins[] = {2, 3, 4, 5, 6, 7, 8, 9, 10, 11, 12, 13, 14, 15,
16, 17, 18, 19, 22, 23, 24, 25, 26, 27, 28, 29, 30, 31, 32, 33, 34, 35,
36, 37, 38, 39, 40, 41, 42, 43, 44, 45, 46, 47, 48, 49, 51, 53, }; // a
string of constants indicating the IDs of the pins to which the LEDs
are connected const int ledsCount = 48; // constant indicating the
number of LEDs
.....
.....
.....
// note that it was first pressed
buttonFirstPress = true;
// stingem LED-ul
digitalWrite(ledPins[activeLedIndex], LOW);
// we keep the time when the LED was pressed
endTime = millis();
// send a message with the reaction time in milliseconds to PC
Serial.print(endTime - startTime);
Serial.print(" milliseconds\n");
// generate a new LED
generateNewLed();
}
}
// send a delay to Arduino not to call this method sooner than once
100 de milisec
delay(100);
}

```

Fig. 10 Software code (short file) from Arduino Mega board

4 Conclusions

The system built in campimeter/perimeter principle is a portable device made of lightweight and easy-to-use materials, with the possibility of further development through the constructive modification of the command and control process. The design and development of the prototype is done in an accessible programming environment based on C++, and the software application can make it possible to use multiple

testing routines and related applications. The system can be used to test, evaluate, and train subjects with visual field dysfunction, but can also be used to drive performance. Human visual reflexes can be tested and trained in both adults and children, and the prototype can be considered as a game due to its size, but also the colorful and flashing stimulus. This system combines mechatronic engineering with optometry, through the complexity/simplicity of construction with benefits in optometric procedures. Also this device is portable, easy to storage and transport, but very good to make screening of visual field and daily training with Amsler grid.

Acknowledgements In these experiments we've developed the investigations with equipment Applied optometric Laboratory at University Transylvania of Brasov.

Conflict of Interest The authors declare that they have no conflict of interest.

References

1. Racette, L., Fischer, M., Bebie, H., Holló, G., Johnson, C., Matsumoto, C.: VISUAL FIELD DIGEST. A guide to perimetry and the Octopus perimeter. Haag-Streit AG, Kőniz, Switzerland (2016)
2. Vojnikovic, B., Tamajo, E.: Horopters—definition and construction. Coll. Antropol. **37**(Suppl. 1), 9–12 (2013)
3. Apostoaie, M.: Project licenta, coordinator BaritzM. University Transilvania Brasov (2017)
4. Donati, M., Cecchi, F., Bonaccorso, F., Branciforte, M., Dario, P., Vitiello, N.: A modular sensorized mat for monitoring infant posture. Sensors **14**, 510–531 (2014)
5. <http://www.me.umn.edu/courses/me2011/arduino/arduinoGuide.pdf>. Accessed June 2019

Nanotechnological Aspects at Electro-activation of Secondary Dairy Products

E. G. Vrabie, M. K. Bologa, I. V. Paladii, V. G. Vrabie, A. Policarpov,
V. Gonciaruc, C. Gh. Sprincean, and T. Stepurina

Abstract

The study of the electro-activation processing of whey, with the recovery of the PMCs and simultaneous isomerization of lactose into lactulose, reveals the necessity of certain technical requirements in order to ensure management and control of a technological process that takes place in an electrolyzer. Electro-activation of secondary dairy products and obtaining protein mineral concentrates (PMCs), with the simultaneous isomerization of lactulose allows not only to specifically mobilise proteins at the formation of protein compounds but also isomerization of lactose into lactulose. As is well known, a lactulose molecule is about 5 nm. Whey, a secondary dairy product, has over 200 components, a part of which are in nano-quantities. Electro-activation triggers a number of inter- and intramolecular reactions at the nanoscale level. The results may be of interest for dairy factories that can use the proposed installation and apply the whey processing wasteless technology and for other food industry companies, as well as for those in pharmaceuticals—in valorification technologies for obtaining the PMCs with the desired content of protein fractions and amino acids.

Keywords

Electro-activation processing • Protein mineral concentrates • Electrolyzer • Whey • Whey proteins

E. G. Vrabie (✉) · M. K. Bologa · I. V. Paladii · A. Policarpov · V. Gonciaruc · C. Gh. Sprincean
Institute of Applied Physics, Str. Academiei, 5, MD 2028,
Chisinau, Republic of Moldova
e-mail: vrabie657@yahoo.com

T. Stepurina
Moldova State University, Chisinau, Republic of Moldova

V. G. Vrabie
Institute of Physiology and Sanocreatology, Chisinau, Republic of Moldova

1 Introduction

Various issues of whey processing are both topical and controversial, thus requiring more efficient technical and technological solutions. Major techniques for the recovery of whey proteins are combinations of membrane and ion-exchange ones. However, they do not make it possible to isolate all whey fractions and only deal with whey sequential processing, with the recovery of protein fractions, and a subsequent treatment of lactose. Electro-activation (electrochemical activation—ECA) means getting metastable states of the analyzed substances at the unipolar electrochemical action (anodic or cathodic), for those substances to be used in different technological processes when maintaining catalytic activation and high level of physical-chemical properties [1–3].

ECA of secondary dairy products and obtaining protein mineral concentrates (PMCs), with the simultaneous isomerization of lactulose allows not only to specifically mobilise proteins at the formation of protein compounds but also isomerization of lactose into lactulose. As is well known, a lactulose molecule is about 5 nm. Whey, a secondary dairy product, has over 200 components, a part of which are in nano-quantities. ECA triggers a number of inter- and intramolecular reactions at the nanoscale level. Different purposes of technological processes infer application of different methods and technical solutions [4]. Devices for ECA are called electro-activators or electrolyzers (electrolytic equipment). Electrolyzers are chemical apparatuses designed to perform electrolysis. They differ by: areas of applications; technological purposes; types of treated liquids; principles of work and separation of treated liquids; regime of intake of the primary and secondary liquids; constructive design parameters; and quantity of working cells [5]. According to their intended use, electrolyzers can be: laboratory models, commercial prototypes, industrially and designed, household models. According to the technological purposes they are classified into those for generating

a catolyte or anolyte, as well as without separation of the products of electrode reactions. According to the principles of work, electrolyzers are classified into two groups: those for batch or continuous operations. The former ones are further subdivided in the following way: according to the way of the intake of primary and secondary liquids—they are mixed, general, and separated; according to the direction—the intake can be central, lateral, peripheral, and combined; according to the flow of liquid in between the electrodes—it can be of a horizontal, angular, spiraling, and vertical structure, with the intake from the top or from the bottom. Electrolyzers with the periodic intake are with an array of individual cells used for cycling processing of the working liquid; and with immersed cells used for processing in a continuous regime. The mode of the liquid intake can be: pulsed, continuous, batch-wise, forced, free, crowding, and voluntary. Some electrolyzers have a controlled inter-electrode distance while others have a non-controlled one. The geometry of the working cell may be non-uniform, helical, conical, cylindrical, or shaped as parallelepiped or disk. Electrolyzers may have one or many cells, the connection of the cells being parallel or serial; they may have no separating element, or have one diaphragm/membrane, or many [6]. When a heterogeneous mixture is to be treated, the separating element is rapidly worn up as its pores become filled up with products of chemical reactions. For these treatments, if it is technologically admissible, electrolyzers without membranes are used [7]. The quality of the liquid processing, energy consumption, and the efficiency of the process depend on the duration of the processing and the volume of the liquid passed through the diaphragm from the chamber with the secondary electrode into that with the primary one [8]. To control the liquid flow from a chamber into another multilayered diaphragms are used [9].

2 Materials and Methods

The study of the electro-activation processing of whey, with the recovery of the PMCs and simultaneous isomerization of lactose into lactulose, reveals the necessity of certain technical requirements in order to ensure management and control of a technological process that takes place in an electrolyzer.

In the framework of the experiments of electro-activation processing, various types of whey were used provided by the “JLK” Joint Stock Company, Chisinau, Moldova.

The recovery of whey proteins in the PMCs was investigated with 6 membrane electrolyzers named in the paper as: EDP-0.5, EDP-sectional, EDC-3, EDP-2, EDP-4, and EDP-5 (Fig. 1).

The electrolyzers EDP-0.5 and EDP-sectional have the same distance between the electrodes and between each of

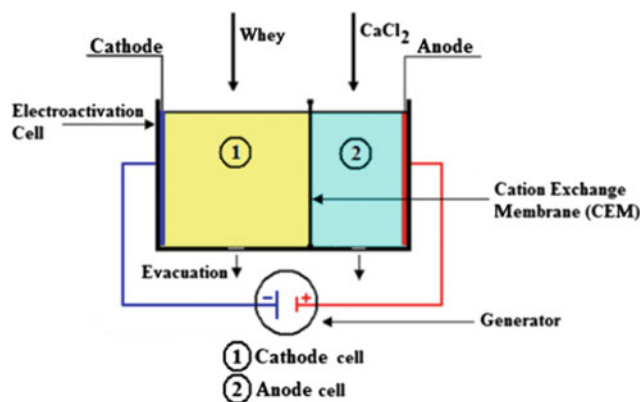


Fig. 1 Layout of experimental membrane electrolyzer

them and the membrane, but the ratio of the volume of the processed whey on the surface of the electrodes V/S is different—5 and 4, respectively (Fig. 2).

The same is the case of the electrolyzers EDP-2 and EDP-4, with the same distance between the electrodes and between each of them and the membrane, but the ratio of the volume of the processed whey on the surface of the electrodes V/S is 1.4 and 1, respectively.

The authors have designed and constructed a slot electrolyzer EDP-5, with the aim, first of all, of fixing the cation-exchange membrane MK-40 that can be deformed in a liquid medium, and also of shortening the distance between the electrodes so as to diminish the resistance and, hence, the energy consumption. EDP-5 is meant to be used for processing in the continuous flow regime. The ratio V/S with EDP-5 is 0.3.

EDC-3 has the frame on which the cathode and the semi-cylindrical membrane are fixed. It was designed and constructed so as to work in two whey processing regimes: continuous and periodic.

At first, it was constructed without slots, but during investigations, it became clear that slots would be necessary

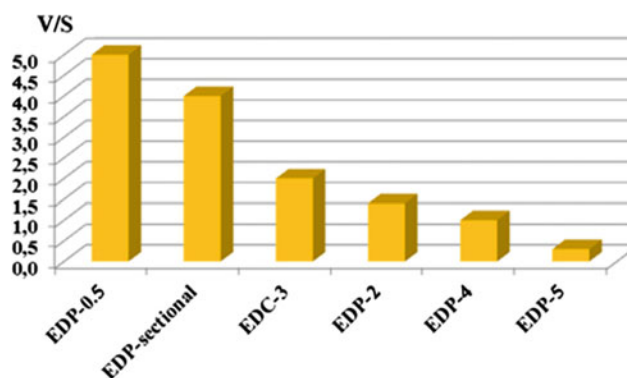


Fig. 2 Variations of ratio of volume of processed whey (V) on electrode surface (S) with 6 electrolyzers

to fix the membrane and to enlarge the working area in order to raise the degree of recovery of whey proteins in the PMCs and to reduce the energy consumption.

The quantity of proteins isolated in the PMCs (or—the degree of the recovery of proteins in the PMCs) was calculated by the difference of the protein content in the initial whey (IW) and that remained in the deproteinized whey (DW):

$$Q = Q_{IW} - Q_{DW}, \% \quad (1)$$

where: Q—protein content in the PMCs; Q_{IW} —protein content in IW; Q_{DW} —protein content in DW.

3 Experimentals

The main electrical parameters at the electro-activation whey processing are: electric current density (j) that is constant during processing, being 10 or 20 mA/cm²; however, the current strength fluctuates showing the conductivity of the processed medium, which is stipulated by several factors, such as: the distance between electrodes, the membrane type (in our case action-exchange membrane MK-40 was used, which allows passing of only cations), the volume of the processed whey (mainly the ratio of the working volume to the electrodes surface V/S), the content of the secondary (anodic) liquid, which allows both keeping the charge carries and ensuring the efficacy of the formation of protein compounds (called salinity of proteins). Raising conductivity or decreasing the resistance of the processed medium is aimed at reducing energy consumption during processing.

The degree of the recovery of proteins (Q, %) in the PMCs during processing in the stationary regime, at a current density of 20 mA/cm² is different in different

electrolyzers, the maximal one being in EDC-3, in which it attains about 70% (Fig. 3).

The content of protein fractions in the PMCs from the liquid phase (CC) is at a different level of recovery in the electrolyzers used in the experiments, the best situation being in EDC-3, which means an increased presence of protein fractions in the liquid phase (Fig. 4).

The degree of the recovery of proteins (Q, %) in the PMCs during processing in the stationary regime, at a current density of 10 mA/cm², is vividly different in different electrolyzers, indicating a lower degree of the recovery of protein than at processing at 20 mA/cm² (Fig. 5). The degree of the recovery of protein fractions (Q, %) in the PMCs during processing in the stationary regime, at a current density of 10 mA/cm², in EDC-3 is much higher at 30 min of processing, in the liquid phase (CC) than at

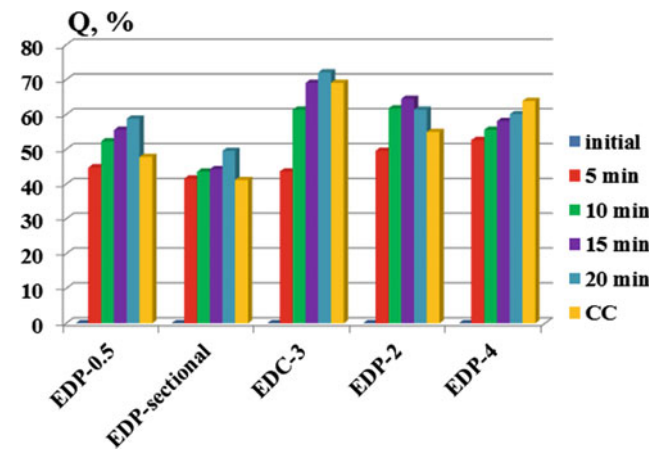


Fig. 4 Variations of degree of recovery of proteins (Q, %) in PMCs at whey processing in stationary regime, at current density 20 mA/cm², in different electrolyzers (CC—content of cathode cell)

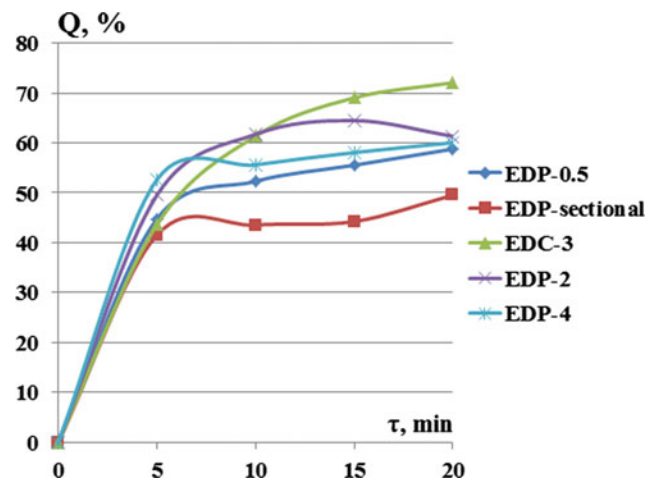


Fig. 3 Variations of degree of recovery of proteins (Q, %) in PMCs at whey processing in stationary regime, at current density 20 mA/cm², in different electrolyzers

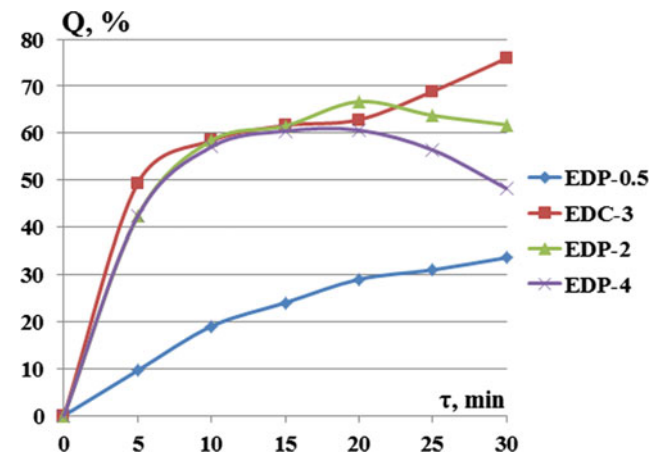


Fig. 5 Variations of degree of recovery of proteins (Q, %) in PMCs at whey processing in stationary regime, at current density 10 mA/cm², in different electrolyzers

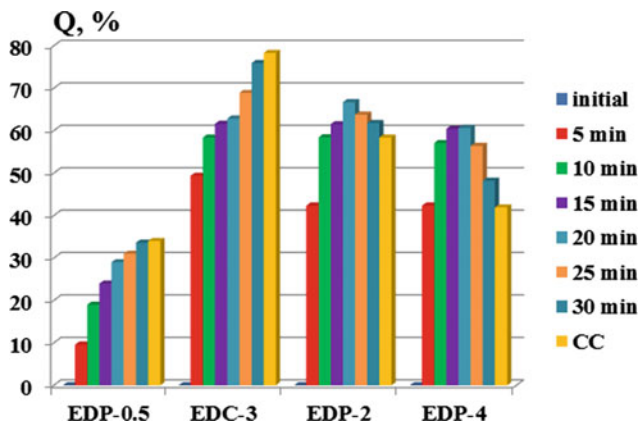


Fig. 6 Variations of degree of recovery of proteins (Q , %) in PMCs at whey processing in stationary regime, at current density 10 mA/cm^2 , in different electrolyzers (CC—content of cathode cell)

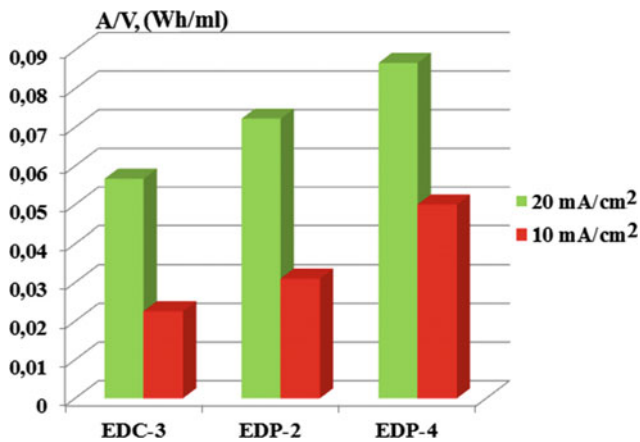


Fig. 7 Variations of total specific energy consumption per a unit of volume A/V , (W h/ml) at whey processing in stationary regime at current density 10 and 20 mA/cm^2 in different electrolyzers

processing at 20 mA/cm^2 , for a shorter duration of processing—20 min; so the general duration of processing becomes longer, which is not economically reasonable (Fig. 6).

For different electrolyzers, the calculations were made of the following: the energy consumption— A , (W h); the specific energy consumption per a unit of volume— A/V , (W h/ml); the specific energy consumption per mass of the PMCs— A/Q_{PMC} , (W h/g).

Comparison of the total specific energy consumption per a unit of volume A/V (W h/ml) at processing in the stationary regime, at current densities of 10 and 20 mA/cm^2 , in different electrolyzers, also contributes to the choice of EDC-3 as the most efficient in our case (Fig. 7). Comparison

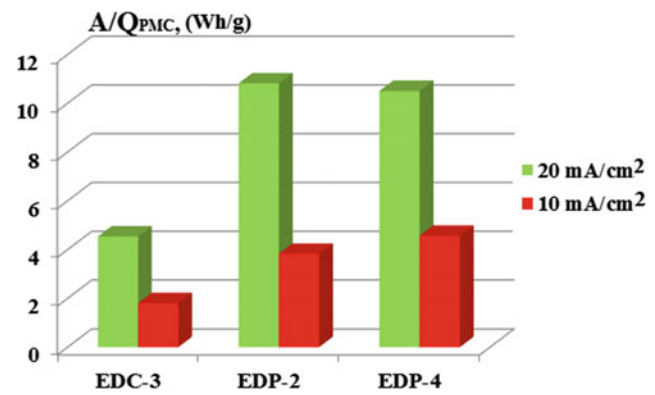


Fig. 8 Variations of total specific energy at a mass of PMCs A/Q_{PMC} (W h/g) at whey processing in stationary regime, at current density 10 and 20 mA/cm^2 , in different electrolyzers

of the total specific energy per a mass of PMCs— A/Q_{PMC} (W h/g), at processing in the stationary regime, at current densities of 10 and 20 mA/cm^2 , in different electrolyzers, also demonstrates the preference of EDC-3 (Fig. 8).

4 Conclusions

The main factors that influence whey processing were specified and described, such as: constructive/geometric parameters (the shape of the frame where the cathode and semi-cylindrical membrane are fixed); the volume of the processed whey and the ratio of this to the electrode surface V/S ; the distance between electrodes and between each of them and the membrane; the stationary (periodic) and the continuous regimes of the whey flow; the content of the CC—studied with three types of whey and that of the AC—with the secondary liquid; at current densities of 10 and 20 mA/cm^2 used in whey processing; the cation-exchange membrane MK-40 was chosen because it allows the migration of bivalent ions from the AC into the CC. The results may be of interest for dairy factories that can use the proposed installation and apply the whey processing wasteless technology and for other food industry companies, as well as for those in pharmaceuticals—in valorification technologies for obtaining the PMCs with the desired content of protein fractions and amino acids.

Acknowledgements The authors acknowledge the technical assistance of Dr. O. Iliasenco.

Conflict of Interest The authors declare that they have no conflict of interest.

References

1. Mashkov, O.A., Baldin, V.P., Krylov, K.P., et al.: Equipment for sorption of toxic ingredients from biological liquids. USSR Author's Certificate № 1680209. Published: Mar 29, in Russian. www.fips.ru (1988)
2. Khrantsov, A.G., Ryabtseva, S.A., Myachin, A.F.: Investigations of the Process of Electro Activation of Lactose Solutions. Collected Works, Ser. "Foodstuffs", Issue 4, pp. 46–51. State Educational Organization "North Caucasus State Technical University (NCSTU)", Stavropol (in Russian) (2001)
3. Dogareva, N.G., Bogatova, O.V., Bogatov, A.I.: Application of electrochemical activation in dairy industry. In: Proceedings of the International Scientific-Practical Conference "Dairy Industry—2009", p. 118, Moscow (in Russian) (2009)
4. Bakhir, V.M., Zadoprojnnii, Yu.G.: Electrochemical RFE Reactors, 35 pp. Giperox, Moscow (1991) (in Russian)
5. Borisenko, A.A., Shamanaeva, E.A.: Classifications of Installations for Electrochemical Activation of Liquids, vol. 1(6), pp. 119–124. Collection of Scientific Papers. Series "Foodstuffs". State Educational Organization "North Caucasus State Technical University (NCSTU)", Stavropol (in Russian) (2003)
6. J Eliseeva, T.V., Tekuchee, T.V., Shaposhnik, V.A., Luschik, I.G.: Electrolysis of amino acids solutions using bipolar ion exchange membranes. *Electrochemistry* **37**(4), 492–495 (2001). (in Russian)
7. Shironosov, V.G., Shironosov, E.V.: Noncontact electrochemical water activation experiments. In: II International Symposium "Electrochemical Activation (ECA) in Medicine, Agriculture Economy, Industry", p. 68, Moscow, 28–29 Oct (1999)
8. Ctryuk, A.I., Shestakov, I.Ya., Fadeev, A.A., et al.: Technique of electrochemical neutralization of alkaline water and aqueous solutions. RF Patent № 2206515. Published on 20 June 2003 (in Russian) (2003). www.fips.ru
9. Kotvov, V.B., Peregonchaya, O.V., Tkachenko, S.V., Nikulin, S.S.: Potential barrier on the surface of cation exchange membranes and their selectivity. *Sorption Chromatogr. Process.* **2**(1), 54–62 (2002). (in Russian)

Part XVI

Nuclear and Radiation Safety and Security

Evaluation of Radiation Hardness of the Bipolar Devices in the Space Conditions

A. S. Rodin, A. S. Bakerenkov, V. A. Felitsyn,
V. S. Pershenkov, and V. A. Telets

Abstract

Real time dependence of operation temperature, which is typical for space environment, was taken into account in the numerical simulation of radiation degradation of LM111 bipolar voltage comparator input current. The technique and results of performed numerical analyses are presented and discussed.

Keywords

Radiation hardness • LM111 • Voltage comparator • Operating temperature

1 Introduction

The dose rate of ionizing radiation of space environment, effects on radiation degradation rate of electrical parameters of electronic equipment of spacecrafts and satellites together with operation temperature [1–5]. In the simulation of electronic devices operation performance in space it is necessary to consider possible variations of irradiation dose rate and operation temperature. As it was shown in [6], to estimate the operational lifetime of electronic equipment at radiation impact with various dose rate we can use the averaged value of the dose rate. In this case, it is necessary to consider only the dependence of temperature on time for a specific orbit, which the satellite equipment is located on.

Using values of the conversion model parameters experimentally extracted [7, 8] for an electronic device and actual dependence of the temperature of electronic equipment on time for actual operating conditions of a spacecraft, we can obtain a total dose dependence of a radiation-sensitive

parameter of the electronic device, which takes into account the actual time dependence of temperature.

Currently, in space conditions telecommunications networks for spacecrafts are widely used. The network architecture of communications standards for onboard space systems involves the use of routing switches, which include analog bipolar voltage comparators, among which become widely used the LM111 comparator. Input current is the most radiation-sensitive parameter in this device. When under ionizing radiation impact input currents of voltage comparators drift out of manufacture specification limits, the operation of onboard space equipment may be failure.

For the most accurate prediction of the operational lifetime of electronic systems under ionizing radiation of space environment, it is necessary to perform numerical calculations to estimate the radiation hardness of the electronic system taking into account actual dependence of operation temperature on time.

2 Evaluation of Radiation Hardness of LM111 Voltage Comparator at Variable Irradiation Temperature Paper

The methodology of estimation of the radiation hardness of semiconductor devices operating at various conditions of space environment is proposed in this paper. The basis of this estimation methodology is the conversion model of ELDRS-effect (Effect Low Dose Rate Sensitivity). According to this model, the radiation-induced positive charge accumulated in the oxide is converted into interface states due to the interaction with electrons tunneling from of the silicon substrate. The shallow and deep positive charged traps are supposed to exist. During short period of high dose rate irradiation only shallow traps are converted. An additional conversion of deep traps occurs during long period of low dose rate irradiation. It leads to an increase of the base current degradation in bipolar structures. The main thesis of the conversion model of ELDRS is described in detail in [7–9].

A. S. Rodin (✉) · A. S. Bakerenkov · V. A. Felitsyn ·
V. S. Pershenkov · V. A. Telets
National Research Nuclear University MEPhI (Moscow
Engineering Physics Institute), Kashirskoe Shosse, 31, Moscow,
Russian Federation
e-mail: ASRodin@mephi.ru

To perform radiation tests for bipolar analog ICs (Integrated circuits) for extracting the parameters of the conversion model is a very hard problem. To provide measurement functions and set electrical modes of the ICs during radiation tests, the measuring equipment presented in [10, 11] can be used. The parameters of the conversion model for the comparator LM111 are presented in below table. These parameters and Eqs. (1) and (2), which are used to modeling the dose dependence of LM111 input current were obtained in [6].

Parameter	K_D , A/rad (SiO ₂)	E_A , eV	τ_{D0} , s	K_S , A/rad (SiO ₂)
Value	6.0×10^{-11}	0.47	3.74×10^{-8}	5.0×10^{-13}

$$Q'_{ot}(t + \Delta t) = \left(qK_D\gamma(t) - \frac{Q'_{ot}(t)}{\tau_D(T)} \right) \cdot \Delta t + Q'_{ot}(t) \quad (1)$$

$$X(t + \Delta t) = \left(K_S\gamma(t) + \frac{1}{q} \frac{Q'_{ot}(t)}{\tau_D(T)} \right) \cdot \Delta t + X(t) \quad (2)$$

Q'_{ot} —value, which linearly related to the charge of deep traps in the oxide, q —electron charge (C), γ —dose rate (rad/s), X —radiation-sensitive parameter, K_D and K_S —coefficients which describe the accumulation of deep and shallow traps in SiO₂, respectively (A/rad), τ_D —conversion time, Δt —a time step of modeling.

Data of the onboard thermometer of TechEdSat satellite (Fig. 1) [12] is used in modeling of the dependence of LM111 input current on time under ionizing radiation impact of space environment.

The methodology of estimation of the radiation hardness of bipolar devices, which takes into account the actual temperature dependence on time in space conditions, includes the following steps:

1. Identification of the most radiation-sensitive parameter of the LM111 and the electrical mode during irradiation impact (the input current was selected).

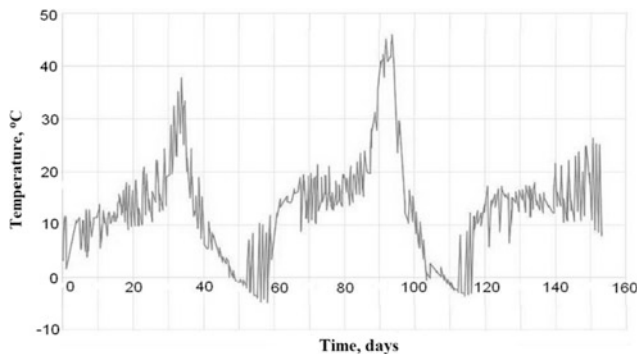


Fig. 1 The dependence temperature on time for satellite TechEdSat [12]

2. The extraction of the conversion model parameters from the experimental data obtained during the radiation tests of the comparator.
3. Using the actual dependence of the temperature of the spacecraft on time and the average value of dose rate for a fixed period of time and previously obtained parameters of the conversion model to calculate the value of $Q'_{ot}(t)$ by expression (1) ($Q'_{ot}(0) = 0$).
4. To calculate the value of the radiation-sensitive parameter $X(t)$ by expression (2), assuming the initial value $X(0)$ is equal to the input current of the comparator before irradiation.
5. To calculate $Q'_{ot}(t + \Delta t)$ taking into account the value of $Q'_{ot}(t)$, which was calculated at the previous step.
6. To calculate $X(t + \Delta t)$ taking into account the value of $X(t)$, which was calculated at the previous step.
7. The fifth and sixth steps must be repeated until the time will become equal to the duration of corresponding space mission which is the electronic device proposed for.

A block diagram of the algorithm for modeling of the radiation degradation of the electrical parameter considering

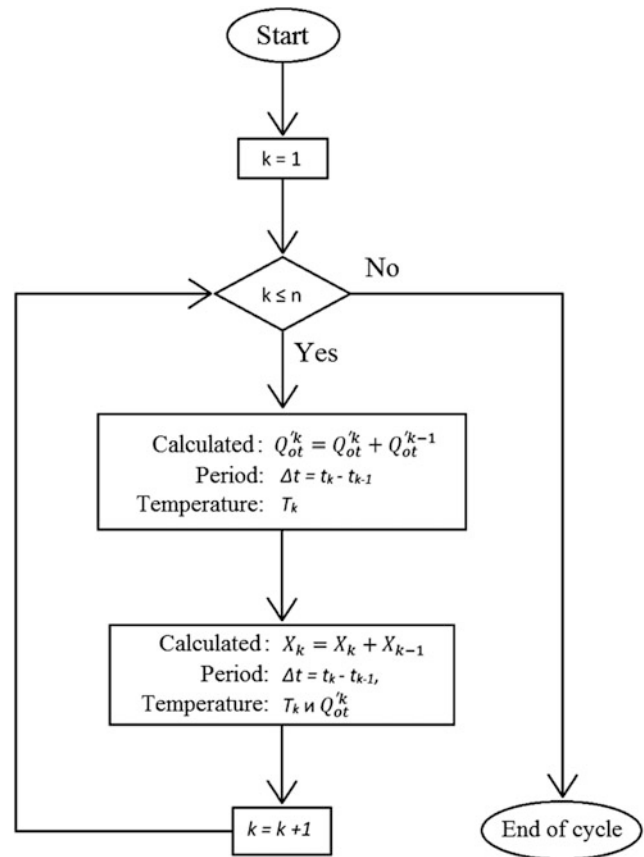


Fig. 2 A block diagram of the algorithm for modeling of the radiation degradation of the electrical parameter considering the actual temperature dependence on time in space conditions

the actual temperature dependence on time in space conditions is presented in Fig. 2. During the simulation, it is assumed that the radiation rate and temperature keep almost unchanged for a short period of time Δt . Therefore, it is necessary that Δt was significantly less than the conversion time of the deep traps τ_D .

To reduce the modeling step ($\Delta t \ll \tau_D$) it is necessary to find intermediate values of time t and their corresponding temperature values T using a known discrete series of time values.

To solve this problem, the linear interpolation of the temperature dependence on the electronic device operational lifetime was performed. For the automation of numerical simulating, a special computer program was developed. This approach allows quickly to estimate the radiation hardness of integrated circuits considering the true dependence temperature on time for space conditions. The prediction correcting of electronic device operational lifetime can be performed in real time.

The simulation results of radiation degradation of the input current of the bipolar voltage comparator LM111 for the irradiation dose rate $\gamma = 10^{-3} \text{ rad}(\text{SiO}_2)/\text{s}$, considering the actual temperature dependence on time is presented in Fig. 3. Using the approach described above we have performed the estimate of the rate of radiation degradation of the input current LM111 for the temperature $+25^\circ\text{C}$ (at which the accelerated radiation tests were performed) and the average temperature for the period of operation of the spacecraft. The simulation result is presented in Fig. 4.

From Fig. 4, it is evident that there is a difference between the results obtained for a fixed temperature value ($+25^\circ\text{C}$, radiation test temperature) and the results obtained for the actual time dependence of temperature. In addition, there is a difference between the results obtained for average temperature and the results obtained for the actual time dependence of temperature.

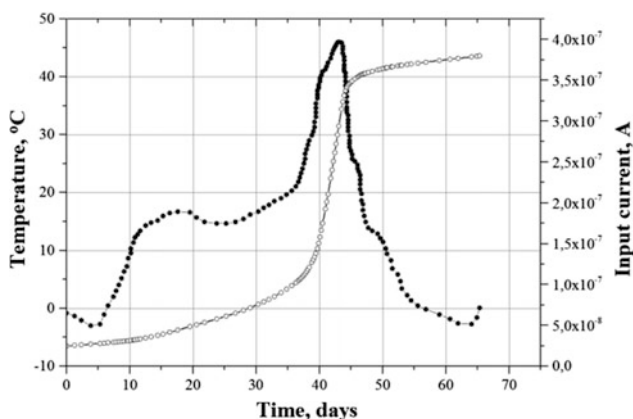


Fig. 3 The calculated dependence of radiation degradation of the LM111 input current on the exposure time (○) taking into account the actual temperature dependence on time (●) for the TechEdSat satellite

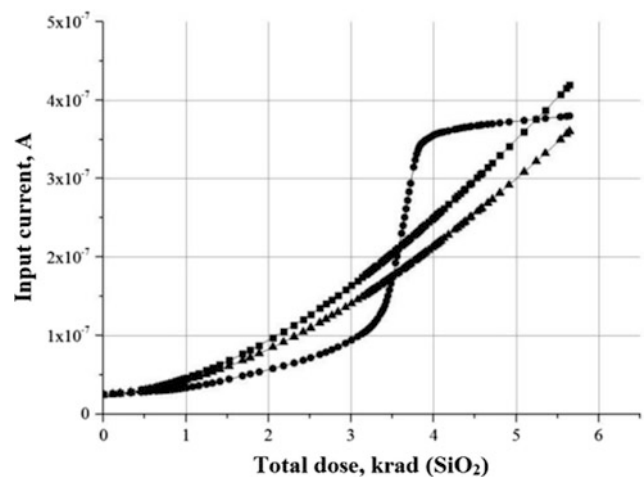


Fig. 4 The calculated dependence of radiation degradation of the LM111 input current at a temperature $+25^\circ\text{C}$ (■), taking into account the actual temperature dependence on time (●), at the average temperature for the period of operation of the spacecraft $+22.6^\circ\text{C}$ (▲)

3 Conclusions

The numerical simulation results demonstrate the impact of the time dependence of temperature for actual operating conditions of a spacecraft on the radiation degradation rate of LM111 input current. Thus, when estimating the operational lifetime of electronic equipment at radiation impact in space conditions it is necessary to take into account the dependence of temperature on time for a specific orbit which the satellite equipment is located on. Using the approach described above we can correct prediction of electronic device operational lifetime in real time taking into account actual dependence of operation temperature on time.

Conflict of Interest The authors declare that they have no conflict of interest.

References

1. Turflinger, T.L., Schemichel, W.M., Krieg, J.F., Titus, J.L., Campbell, A.B., Reeves, M., Walters, R.J., Marshall, P.W., Pease, R.L.: ELDRS in space: an updated and expanded analysis of the bipolar ELDRS experiment on MPTB. *IEEE Trans. Nucl. Sci.* **NS-50**(6), 2328–2334 (2003)
2. Barth, J.L.L: Modeling space radiation environments. *IEEE Nucl. Space Radiat. Eff. Short Course* (1997)
3. Bourdarie, S., Xapsos, M.: The space radiation environment. *IEEE Trans. Nucl. Sci.* **55**(4), 1810–1832 (2008)
4. Harris, R.D., McClure, S.S., Rax, B.G., Evans, R.W., Jun, I.: Comparison of TID effects in space-like variable dose rates and constant dose rates. *IEEE Trans. Nucl. Sci.* **55**(6), 3088–3095 (2008)

5. Borisov, A., Belova, M., Kessarinskiy, L., Boychenko, D., Nikiforov, A.: Analysis of total dose effects in modern analog ICs. In: RAD Conference Proceedings, pp. 427–431 (2015, June)
6. Pershenkov, V.S., Bakerenkov, A.S., Solomatin, A.V., Rodin, A.S., Belyakov, V.V., Shurenkov, V.V.: Prediction of bipolar devices behavior during space mission. *Sens. Syst.* **188**(1), 76–81 (2015)
7. Pershenkov, V.S., Savchenkov, D.V., Bakerenkov, A.S., Ulimov, V.N., Nikiforov, A.Y., Chumakov, A.I., Romanenko, A.A.: The conversion model of low dose rate effect in bipolar transistors. RADECS, paper № 5994661, pp. 290–297 (2009)
8. Pershenkov, V.S., Savchenkov, D.V., Bakerenkov, A.S., Ulimov, V.N.: Conversion model of enhanced low-dose-rate sensitivity for bipolar ICs. *Russ. Microelectron.* **39**(2), 91–99 (2010)
9. Pershenkov, V.S., Sogoyan, A.V., Telets, V.A.: Conversion model of radiation-induced inter-face-trap buildup and the some examples of its application. In: IOP Conference Series: Materials Science and Engineering vol. 151, no. 1, paper № 012001 (2016)
10. Bakerenkov, A.S., Chubunov, P.A., Anashin, V.S., Rodin, A.S., Felitsyn, V.A.: Multifunctional equipment and test results for total ionizing dose testing of analog integrated circuits. In: IEEE Radiation Effects Data Workshop, № 7891724 (2016)
11. Demidova, A.V., Borisov, A.Y., Kessarinskiy, L.N., Boychenko, D.V.: Automated test complex for operational amplifier ICS parametric and functioning monitoring. In: Proceedings 2015 International Siberian Conference on Control and Communications, SIBCON 2015 Omsk; Russian Federation; May 21–23, 2015, article number 6937407
12. Earth Observation resources (eoPortal), ESA. <https://directory.eoportal.org>

Integral Estimate of LSI Radiation Hardness as a Fuzzy Number of Multiplicity of Nodes

V. M. Barbashov, N. S. Trushkin, and A. K. Osipov

Abstract

The analysis of the LSI behavior under radiation exposure at functional and logical level of description was carried out. It is shown that there are deterministic and non-deterministic failures typical when exposed to ionizing radiation. In the first case, the behavior of complex devices is determined by the specific ratio of the radiation-sensitive parameters of the elements, in the second case—the statistical variation of the failure threshold levels for the same type of samples.

Keywords

Topological probabilistic models • Fuzzy probability
• Uncertainty zone

1 Introduction

Design of complex LSI systems resistant to radiation destabilizing factors is currently impossible without active use of logical modeling, which ensures the necessary adequacy of description and accuracy of calculations. Real nature of a complex electronic system behavior under radiation exposure is determined by the specific ratio of the radiation-sensitive parameters of its elements and by taking into account the effect of their statistical scatter. The relationship between the distribution probability density function of the spread and the criterion membership function (CFP) determines, ultimately, the feasibility of functional-logical models of the LSI radiation behavior as applied to each specific case [1]. Such a comparison is a necessary step in the general procedure for analyzing the

V. M. Barbashov (✉) · N. S. Trushkin · A. K. Osipov
National Research Nuclear University MEPHI, Kashirskoe
Shosse, 31, Moscow, 115409, Russia
e-mail: VMBarbashov@mephi.ru

N. S. Trushkin
e-mail: Ntrushkin@gmail.com

capability of the LSI. It should be borne in mind that the parameters of the distribution function, characterizing uncontrolled statistical processes, are themselves dependent on radiation. Moreover, the nature of their changes during irradiation depends on many factors, including the type of radiation, its intensity and spectrum, the type of criterion parameter characterizing the radiation resistance of the LSI, the operation mode, etc.

2 Modeling Environment

Let m branches come out of the node n . Then the multiplicity of a node during normal operation is equal to m [1]. When exposed to external factors (radiation, microwave radiation, etc.), the thresholds for the triggering of logical elements associated with the node under consideration $l_{nj}^m, j = 1, 2, \dots, m$ begin to degrade. In addition, the amplitude levels of logical zero and unity (U^0, U^1), change, which leads to a decrease in the pulse l_n . Thus, the performance of the circuit depends on the magnitude of the excess $\Delta_{nj} = l_n - l_{nj}^m, j = 1, 2, \dots, m$.

In this case, each threshold has a zone of uncertainty, in which the logical element begins to switch randomly and the multiplicity of the node becomes uncertain and can be quantitatively expressed as a fuzzy number.

In this paper, as in [2], we use triangular $L - R$ numbers, which greatly simplifies the estimates.

The zone of uncertainty, l_n, l_{ij}^m are random values. Therefore, to simplify the task, the further calculations will use the maximum value of the uncertainty zone $q_{ij\max}$ for each branch, which is determined experimentally and can be used by default while creating a CAD system.

In [2], when determine the fuzzy multiplicity number, the distribution of quantities l_n only was considered. In fact, the values l_n, l_{ij}^m change simultaneously with the change in the absorbed dose of radiation.

Let, $\Delta_{nj} \rightarrow q_{\Pi j_{max}}$ then the mode of a fuzzy number is determined by the probability of exceeding Δ_{nj} of the number $q_{\Pi j_{max}}$, that is $P(\Delta_{nj} > q_{\Pi j_{max}})$. The blurring of a fuzzy number obviously depends on $P(\Delta_{nj} < q_{\Pi j_{max}})$. The laws of the distribution of numbers l_n and $l_{\Pi j}$ denote, respectively, $F_n(x)$ and $G_j^n(x)$, i.e.

$$\begin{cases} F_n(x) = P(l_n < x) = \int_{-\infty}^x f_n(\xi) d\xi \\ G_j(x) = P(l_{\Pi j} < x) = \int_{-\infty}^x g_j(\xi) d\xi \end{cases} \quad (1)$$

Given the specific conditions of solving the system, we can assume:

$$f_n(x) = \begin{cases} 0 \\ \text{convex differentiable function, } 0 < x \leq 1 \\ 0, x > 1 \end{cases}$$

$$g_j(x) = \begin{cases} 0, x \leq 0 \\ \text{convex differentiable function, } 0 < x < 1 \\ 0, x > 1 \end{cases}$$

Graphs of distribution densities described by expression (1) are shown in Fig. 1.

With an increase in the dose of radiation, the function $g_j(x)$ shifts to the right and $f_n(x)$ to the left. In this case, the excess Δ_{nj} decreases and has its own distribution, which can be taken as a criterial function, as a fuzzy probability.

We denote the excess probability distribution density Δ_{nj} by $\delta_{nj}(x)$.

Then

$$\delta_{nj}(x) = \int_{-\infty}^{\infty} f_n(\xi) \cdot g_j(x + \xi) d\xi \quad (2)$$

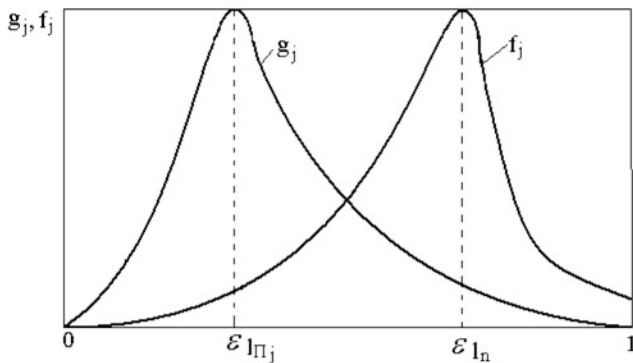


Fig. 1 Density distribution of values l_n and $l_{\Pi j}$: $\epsilon_{\Pi j}$ —expectation $l_{\Pi j}$, ϵ_{ln} —expectation l_n

Considering the previously imposed restrictions on the functions and, equality (2) takes the form:

$$\delta_{nj}(x) = \int_0^{1-x} f_n(\xi) \cdot g_j(x + \xi) d\xi \quad (3)$$

As shown by the experimental data in Figs. 2, 3 distributions f_n and g_j are close to the normal law.

The analysis of the LSI radiation behavior shows that, in some cases, for failures in terms of both functional and electrical parameters, there is a significant statistical variation in the threshold of failure levels for similar types of

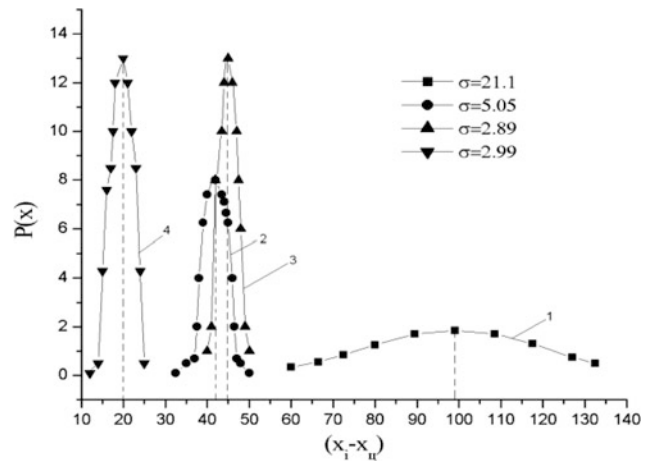


Fig. 2 The distribution of averaged over the plate static current transfer ratio of the base (B_N) 30 bipolar ADS (advanced low power Schottky) transistors test structure 556PT7 between 10 plates of the same batch with different electron fluence: 1— $F_e = 0$, 2— $F_e = 10^{14}$ e/cm², 3— $F_e = 5 \times 10^{14}$ e/cm², 4— $F_e = 10^{15}$ e/cm² ($j = 10^2$ A/cm², $S_{\text{SM}} = 12 \times 12 = 144$ μm², $E_e = 5$ MeV)

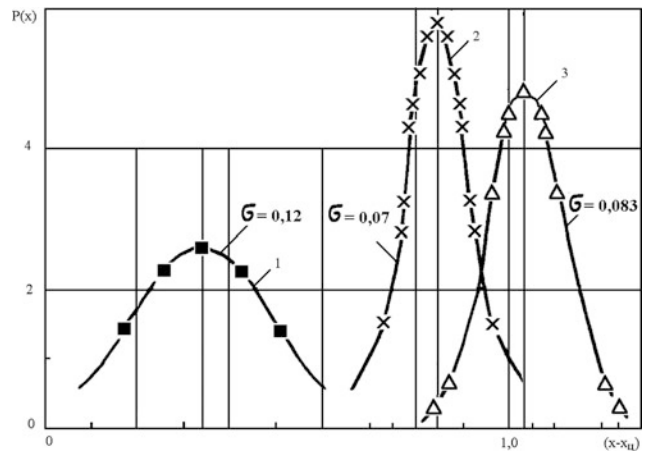


Fig. 3 Distribution of averaged U_{OUT}^0 CMOS chip LSI RAM 1617PV6 dose of (1), Uthr n-channel and p-channel MOS transistors (2, 3), obtained at an electron accelerator with $E = 130$ keV

samples. At the same time, a decrease in the dispersion of the variation of the failure threshold during irradiation was observed with the volume effects of displacement in bipolar structures (Fig. 2), the radiation sensitivity of which is determined by the change in the lifetime.

At the same time, with respect to dose effects in CMOS LSI structures, there is most often a reversal of the dependence of the dispersion on the level of radiation (Fig. 3). Therefore, in different ranges of exposure levels, an object model can be both fuzzy and probabilistic [1]. In general, it can be assumed that fuzzy descriptions of the LSI radiation behavior become more reliable for the volume effects of displacement and ionization effects with increasing levels and intensity of exposure, while for surface effects it is often preferable to use probabilistic models. However, a definite assessment of the radiation behavior requires joint consideration of parameters that are described by fuzzy and probabilistic models.

With reference to the normal distribution law, Formula (3) can be rewritten in the form:

$$\delta_{nj}(x) = \frac{1}{2\pi\sigma_n \cdot \sigma_{\Pi j}} \int_0^{1-x} e^{-\left[\frac{(\xi-\varepsilon_n)^2}{2\sigma_n^2} + \frac{(x+\xi-\varepsilon_{\Pi j})^2}{2\sigma_{\Pi j}^2}\right]} d\xi$$

where— σ_n and $\sigma_{\Pi j}$ —are the dispersions f_n and g_j , ε_n and $\varepsilon_{\Pi j}$ are shown on Fig. 1.

After the transformations, the resulting expression will take the following form:

$$\begin{aligned} \delta_{nj}(x) &= \mu_n^j \cdot \frac{1}{\sqrt{2\pi}\sigma_\Sigma} \int_0^{1-x} e^{-\frac{(\xi-\varepsilon_\Sigma)^2}{2\sigma_\Sigma^2}} d\xi, \\ \mu_n^j &= \frac{1}{\sqrt{2\pi}\sqrt{\sigma_n^2 + \sigma_{\Pi j}^2}} e^{-\sigma_\Sigma^2(\varepsilon_n - \varepsilon_{\Pi j} + x)^2} \\ \sigma_\Sigma &= \frac{\sigma_n \cdot \sigma_{\Pi j}}{\sqrt{\sigma_n^2 + \sigma_{\Pi j}^2}}. \end{aligned} \tag{4}$$

If we express the integral (4) in terms of integrals of probabilities, we finally get:

$$\delta_{nj}(x) = \mu_n^j \left[\Phi\left(\frac{\varepsilon_\Sigma}{\sigma_\Sigma}\right) + \Phi\left(\frac{1-x-\varepsilon_\Sigma}{\sigma_\Sigma}\right) \right] \tag{5}$$

where— $\varepsilon_\Sigma = \sigma_\Sigma^2 \left[\frac{\varepsilon_n}{\sigma_n^2} + \frac{\varepsilon_{\Pi j} - x}{\sigma_{\Pi j}^2} \right]$, $\Phi(z)$ —is the integral of probability.

The function turns out to be monotonously decreasing while x is changing from “0” to “1”. Then the probability $P(x < q_{\Pi j \max})$ is

$$P(x < q_{\Pi j \max}) = \int_0^{1-q_{\Pi j \max}} f_n(\xi) \cdot g_j(q_{\Pi j \max} + \xi) d\xi, \tag{6}$$

$$P(x > q_{\Pi j \max}) = 1 - P(x < q_{\Pi j \max})$$

Formulas (5) and (6) allow us to find the parameters of the desired fuzzy number n of a node multiplicity: mod_n and blur σ_{rn} . For a normal distribution law, the parameters of a fuzzy number are as follows:

$$\text{mod}_n = \sum_{j=1}^m [0.5 + P(x > q_{\Pi j \max})],$$

$$\sigma_{rn} = \sum_{j=1}^m P(x < q_{\Pi j \max}),$$

$$P(x > q_{\Pi j \max}) = \mu_n^j \left[\Phi\left(\frac{\varepsilon_\Sigma}{\sigma_\Sigma}\right) + \Phi\left(\frac{1 - q_{\Pi j \max} - \varepsilon_\Sigma}{\sigma_\Sigma}\right) \right] \tag{7}$$

$$\mu_n^j = \frac{1}{\sqrt{2\pi}\sqrt{\sigma_n^2 + \sigma_{\Pi j}^2}} \cdot e^{-\frac{\sigma_\Sigma^2}{2}(\varepsilon_n - \varepsilon_{\Pi j} + q_{\Pi j \max})^2}$$

$$\varepsilon_\Sigma = \sigma_\Sigma^2 \left[\frac{\varepsilon_n}{\sigma_n^2} + \frac{\varepsilon_{\Pi j} - q_{\Pi j \max}}{\sigma_{\Pi j}^2} \right]$$

Each branch emanating from an n node generates fuzzy numbers in the corresponding nodes of higher rank in the tree. In this case, it is necessary to take into account some degradation of the pulse at the output of the corresponding logic element. After such an account of the pulse state, the components of Formula (7) are summed over all nodes of the critical tree, which gives the integral criterion of radiation resistance in the form of the tree power spectrum.

Another approach to estimating stability with fuzzy numbers is possible, that deals with fuzzy numbers for each node branch. In this case, the logic of elements, working with fuzzy impulses, becomes fuzzy. It helps to identify system failures and bottlenecks, by analogy with the Monte Carlo method.

3 Conclusion

Ensuring the stability of the LSI under ionizing radiation exposure is determined by the specific tree spectrum of the LSI topology and the ratio of radiation-sensitive parameters: the multiplicity of nodes, the power of the tree spectrum, the mode of a fuzzy number. In this case, the ratio between the distribution function of the spread and the fuzzy number

mode determines, ultimately, the expediency of using functional logical models of the LSI behavior for each specific case. Such a comparison is a necessary step in the general procedure for analyzing the radiation stability of an LSI. It should be noted that in different ranges of levels or intensity of exposure, the power estimate of the LSI topology tree spectrum can be both fuzzy and probabilistic. At the same time, the fuzzy multiplicity can be specified in n-dimensional space with preservation of the basic parameters of the model, and the radiation effects occurring in the LSI at different radiation levels are evaluated in it by changing the same system parameter. Such a model structure is probabilistically fuzzy with probabilistic type operators, and the criterion membership function is a superposition of the statistical and deterministic criterion-membership function. At the same time, the interrelation of fuzzy multiplicity

and probabilistic logic was defined, which makes it possible to most accurately quality estimates of the LSI functioning under the influence of radiation.

Conflict of Interest The authors declare that they have no conflict of interest.

References

1. Frank, M.J.: Associativity in a class of operations on spaces of distribution functions. *Aequationes Math* **12**, 121–144 (1975)
2. Barbashov, V.M., Trushkin, N.S.: Evaluation performance of digital integrated circuits while exposed to radiation. In: IOP Conference Series: Materials Science and Engineering, vol. 151, p. 012011 (2016)

Revision of the Curriculum on Nuclear Safety and Security in the Light of Recent International Recommendations

Ar. Buzdugan and Au. Buzdugan

Abstract

The University is the place where it is necessary to further develop the foundations of what we have come to call the general culture. The issue of non-proliferation is not studied as a special discipline at any University in Moldova. To fill this gap, the National Nuclear Security Support Centre of the Technical University of Moldova has developed and introduced a new optional curriculum (ECTS 4) that reflects the synergy of security, safety and safeguards (3S). Because 3S is inextricably linked, the updated curriculum makes the master students aware of the actuality and need for nuclear non-proliferation policy. Cybersecurity that has become a pillar for every on 3S components is also reflected in this optional curriculum. This optional discipline was introduced to the Master of Science in Microelectronics, Nanotechnologies and Biomedical Engineering because nuclear or radioactive materials are parts of microelectronics and also largely used in medical investigations and treatments. The evaluation showed that master's students have higher knowledge of non-proliferation than graduate license holders.

Keywords

Curriculum • Cyber security • Nuclear safety • Safeguards • Non-proliferation

1 Introduction

The international instruments and the recognized principles for multidimensional control of nuclear materials and high-level radioactive substances are the pillars of international jurisprudence on nuclear safety worldwide. Thus, the responsibility for nuclear safety lies entirely with the state, which has signed or recognized in one or another the instruments and principles. We note however, that a number of states have not effectively implemented them through national law or did not abide by them. This creates gaps in the global nuclear safety system that can be exploited by terrorist or criminal elements.

To our knowledge, there is no universal international instrument to address nuclear security in a comprehensive way. The International Regulatory Framework for Nuclear Safety is mainly based on:

- the Convention on the Physical Protection of Nuclear Material (CPPNM),
- the Code of Conduct on the Safety and Security of Radioactive Sources with the Guide on the Import and Export of Radioactive Sources,
- the Safeguard Agreements and their Additional Protocols,
- the Convention on the Suppression of Acts of Nuclear Terrorism,
- United Nations Security Council Resolutions 1540 and 1373.
- However, the evolution of the international situation has led to the development of a series of new international instruments relevant to nuclear security and verification, such as:
- the adoption of UNSCR 1540 on Weapons of Mass Destruction and the growing role of non-state actors (April 2004);
- opening for signature of the International Convention on the Suppression of Nuclear Terrorism (September 2005);

Ar. Buzdugan (✉)
Technical University of Moldova, 9/7, Studentilor St., Block 3,
MD2045 Chisinau, Republic of Moldova
e-mail: artur_buzdugan@yahoo.com

Ar. Buzdugan · Au. Buzdugan
National Nuclear Security Support Centre, Chisinau, Republic of
Moldova

- the adoption by States Parties of the Amendment of the Convention on the Physical Protection of Nuclear Material (July 2005).

Achieving universalism of relevant instruments, harmonizing national legislation and effectively implementing measures would essentially contribute to fighting nuclear terrorism and proliferation of weapons of mass destruction. In this regard, we mention the importance of the International Atomic Energy Agency's (IAEA) statutory functions of informing and advising States on relevant international legal instruments and encouraging their accession and implementation as soon as possible.

The proliferation risk may be from the following 4 categories of countries

- new countries holding nuclear weapons but not officially part of non-proliferation treaty (NPT) in that subject;
- countries whose top politics have decided to manufacture their own nuclear weapons and which have the respective economic and technical base;
- countries that have their own nuclear weapons manufacturing program, but do not have full potential for implementation or high-level political decision-making;
- a new category of countries that had nuclear weapons in the past, reduced or destroyed them on the basis of multilateral agreement, but which can restore their status as a nuclear country (have the technology and economic potential) because of the violation of these agreement by one of the parts.

These are the general international instruments upon which the legal framework as well as educational system in this area is based on in Republic of Moldova.

2 International Trends

The proliferation trends at the regional level are of major concern for Republic of Moldova [1, 2], as the possible return to the nuclear status of a neighboring country could lead to and stimulate similar programs in third countries in the Black sea region. We mark countries that, being part of the Black sea basin, have scientific, economic and technical potential for these purposes. Historical explications of such competitions already exist on the example of Brazil and Argentina, which developed parallel nuclear programs, although they were not in military constellations nor had any territorial claims.

The above-mentioned factors and dynamics could lead to the increase in illicit trafficking in nuclear and radioactive materials and the risk of nuclear terrorism.

For these reasons, the initiation of Nuclear Summit (April 2009, Prague) by USA President Barack Obama led to a significant strengthening of the nuclear security architecture and sensitized top-level politics attention to the risk posed by nuclear terrorism. The launch of the Nuclear Summit idea can be compared to the Atoms for Peace slogan—the speech of US President Dwight D. Eisenhower at the UN General Assembly (8 December 1953). This speech has sensitized worldview and catalyzed the establishment of the IAEA in 1957 under the UN aegis to control the nuclear activities of all the world's states.

The four Nuclear Summits (Washington, DC, 2010, 2016, Seoul, 2012, The Hague, 2014) gathered world leaders from about 50 countries, resulting in new commitments for the adoption of specific remedial measures in the global nuclear safety system. Among these, the following tangible achievements could be mentioned:

- Removing about 32 metric tons of enriched uranium and plutonium globally;
- Definitive removal of enriched uranium from 12 countries, as well as the end of use or its replacement for low-enriched uranium in 15 countries;
- Improving physical security at 32 strategic objects storing fissionable material for nuclear weapons;
- Putting into operation 328 ionizing radiation detectors at international crossing points, airports, seaports;
- 30 states have passed new laws or updated existing regulations to strengthen nuclear security;
- 32 states reiterated their support for the full and universal implementation of UNSCR 1540;
- 28 countries signed a Joint Statement on the Security of High Activity Radioactive Sources;
- 17 countries signed a Joint Statement on Sustainability of Information Sharing and Reporting, which includes a template of a Consolidated National Nuclear Security Report.
- About 20 national Nuclear Security (Support) Centers were organized.

Summits were finalized through consensus communiqués, country commitments, and a work plan. The Washington (2010) work plans, for example, lays out specific steps for realizing the goals of communicate among which could be mentioned the development of corporate and institutional cultures that prioritize nuclear security, education and training, and also assurances of cybersecurity of nuclear (radioactive) objects.

These commitments have accelerated the recovery and elimination of nuclear materials. As a result, three entire geographic regions—South America, South-East Asia, and Central-Eastern Europe—have eliminated enriched uranium

from ground storage. States are also committed to stepping up monitoring of nuclear and radioactive sources at the border and ensuring adequate cybersecurity at nuclear facilities. The echoes of the Summits also positively influenced the ratification of the Amendments to the CPPNM, which allowed their entry into force, as well as an increase in the number of states that have joined the Convention on the Suppression of Nuclear Terrorism.

3 Curriculum on Nuclear Safety and Security

In the Republic of Moldova there were also certain actions taken in line with the international community. The Technical University of Moldova Senate's Decision from 26 February 2013 established the National Nuclear Security Support Centre (NNSSC). The NNSSC is staffed with professors from the Technical University of Moldova (TUM), the State University of Medicine and Pharmacy "N. Testemitsanu", as well as international relations and cybersecurity consultants. With the support of the IAEA, NNSSC became a member of International Nuclear Security Education Network (INSEN). The aim and core objectives of the NNSSC are determined by the need to contribute to the long-term efficiency of education and the implementation of a nuclear safety and security culture in the Republic of Moldova [3].

There is also a direct link between nuclear security, non-proliferation and illicit trafficking with engineering disciplines, such as clinical engineering, biomedical engineering.

The types of radioactive sources used in radiotherapy and radio diagnostic consist of IAEA safety classification I, II, III, and IV category sources [4]. They were used e.g. in teletherapy machines for tumor treatment (Co-60 sources, typical activity 370 TBq), blood and research irradiators (Cs-137, 100 TBq), afterloading units for brachytherapy (Ir-192, 370 GBq), capsules for therapeutic thyroid applications (I-131, 5.5 GBq), seeds for prostate brachytherapy (I-125, 30 MBq).

Cesium-137 is the most dangerous of all radioactive isotopes. If used in a dirty bomb, the highly dispersible powder would contaminate an area for years, with very high costs for evacuation, demolition and clean-up. So, is necessary to improve nuclear security culture in hospitals, industry and decision-making authorities to raise awareness about this threat and the availability of safe and effective future alternative technologies to cesium-137 use.

Such sources differ greatly in their radioactive effect, in their physic-chemical form and thus may cause due to negligence radiological attacks with large scale

contaminations created by the explosive dispersal of the radiological device with high activity sources [5].

The lack of nuclear security awareness is problematic, especially in hospital environments as these are public spaces with a large flow of people. On the other hand, privacy concerns prevent hospitals from wide spreading the use of technical security systems, such as video cameras. This particularly applies especially to the diagnostic and treatment areas where most of the radioactive sources are located. During working hours intrusion sensors are not widely deployed or enabled. In some hospitals, access policies in areas where radioactive sources are available become useless due to insufficient access to the keys of these areas [6, 7]. In low-budget countries, there are also problems in contracting interdepartmental security due to insufficient financial resources.

There are, however, a number of steps that can be taken to better secure—and in some cases even eliminate—vulnerable radiological materials. One of these can be achieved by raising the level of education of master and PhD students in the field of nuclear safety, security and non-proliferation, periodical updating of the university courses in the field, and promoting the implementation of nuclear safety subjects in the cycle of studies through masters or doctorates.

Guided by these goals and by IAEA recommendations and ESARDA courses [8, 9], the curriculum for the Nuclear Safety and Security subject (ECTS 4) has been developed and is designed for master's degree students and includes theoretical lectures, seminars and individual tutorials.

- New Curriculum contains 15 theoretical modules that relate to the following topics:
- Atomic structure and models;
- Ionizing radiation classification;
- Interaction with biological matter and effects;
- Dosimetry units;
- Instruments and the principle of ionizing radiation detection;
- Use of ionizing radiation;
- Radiation safety fundamental;
- National regulatory framework in relation to IAEA and Euroatom standards;
- Nuclear and radioactive waste management policy. Orphan sources;
- Nuclear Security, Safety and Safeguards (3S);
- Non-proliferation and 3S interaction.
- Cybersecurity and interaction with nuclear safeguards, security and non-proliferation;
- Illicit trafficking;
- Case study of Moldova: Incidents with MNR, illicit trafficking;
- Introduction to nuclear forensics.

The NNSSC has a special emphasis on training the teaching personnel on the synergy of nuclear safety, non-proliferation and cybersecurity (with IAEA support). Furthermore, the NNSSC is also engaging master students to participate in yearly summer schools at the Center for Non-Proliferation (Odessa, Ukraine) or ESARDA training course in Trieste (Ispra, Italy), supported by the Swedish Radiation Safety Authority.

Increasing interest in nuclear security and non-proliferation has led to the program restructuring of curriculum in the past three years. Thus, nuclear safety modules were initially included with nuclear safeguards along with the interdependence of security, safety and safeguards. A new topic, dictated by regional realities, was addressed by including the nuclear forensics module.

Subsequently, the increasing role of cybersecurity in nuclear and radiological activities has forced the NNSSC to review the content of the course. Upon its review, the updated curriculum included the new 4S synergetic modules (cyber security, nuclear safety, security and safeguards) in the global context of non-proliferation.

With the increasing role and functionality of computer networks and computing systems, these have become an attractive target for malicious acts and medical radiological objectives. Securing the cyberspace, including such devices used to handle operations or store information regarding to nuclear or radiological materials, it has become a difficult strategic mission. This requires the coordination and concentration of efforts by several national authorities, not only staff from hospital objectives, with the aim to:

- Prevent cyber-attacks against critical infrastructures by identifying threats;
- Reduce vulnerability to cyber-attacks;
- Minimize the potential damage and time to rebuild the system as a result of cyber-attacks.

A cyber-attack could also impact the physical security and lead to a safety event, as well as the implications for a nuclear or radiological target. As a general best practice, reducing the impact of a cybernetic attack may be by adopting specific requirements advanced to the licensing of non-radiological/radiological activities. Such requirements should take into account the main IAEA recommendations [8, 9] with regards to the role of cyber security, as well as the recommendation of a separate security plan besides the physical security one.

The role of cybersecurity in nuclear technology is not exclusively dictated by non-proliferation and nuclear safety,

but also by other factors of nuclear medicine, radio-diagnostics or treatment such as:

- protecting the personal data of the patient;
- ensuring the security of medical imaging data for remote transmission in cases of telemedicine;
- ensuring the safe operation of the device and its protection from cyber-attacks;
- post-treatment or post-interventional real-time monitoring, etc.

Overall, we estimate that the new curriculum has a holistic approach in covering the topics relating to nuclear security and safety, and create a valuable baseline from the educational point of view with the aim to raise the overall security culture. The topics covered are of core importance for young professionals in multiple fields. There is also a high demand of these course, in relation to the needs of such specialists in various domains on a national level.

4 Conclusions

As a result of the actions taken by the NNSSC the curriculum has been updated and reflects the current recommendations on nuclear security and safety, non-proliferation and related topics. The work carried out in the NNSSC in the course improvement was possible with the support of the Swedish Radiation Safety Authority [10]. The new curriculum is intended for students in Biomedical Engineering and Microelectronics and Nanotechnology Programs, and to periodical professional training courses.

At the end of the Master's degree course, students have to write a thesis, about 30% of which are focused on nuclear security, non-proliferation, safeguards and their interaction. The course is followed by a test grid exam. These consist the evaluation process used by higher educational institutions.

The results have shown that master students possess a greater degree of awareness of nuclear safety, security and non-proliferation compared to post-graduate students. This optional discipline (Nuclear Safety and Security) is also required by the graduates of other Universities in Moldova, totaling 20–25 master students per year.

Acknowledgements The authors thank the Swedish Radiation Safety Authority for continuously multi-sided support in development of the educational process in non-proliferation at the Technical University of Moldova.

Conflict of Interest The authors declare that they have no conflict of interest.

References

1. Nuclear Security in the Black Sea Region. Contested Space, National Capacities and Multinational Potential. SIPRI Policy Paper no. 49. Vitaly Fedchenko, Ian Anthony, Dec 2018
2. Zaitseva, L. Steinhäusler, F.: Nuclear trafficking issues in the Black Sea region, EU Nonproliferation Consortium, Non-proliferation Paper no. 39, Apr 2014
3. IAEA Nuclear Security Series No. 7. Implementing Guide. Nuclear Security Culture. IAEA (2008)
4. IAEA Safety Standards. Categorization of Radioactive Sources. Safety Guide RS-G-1.9, IAEA, Vienna (2005)
5. Rozental, J.J.: Two decades of radiological accident direct causes, roots causes and consequences. *Braz. Arch. Boil. Technol.* **45**(spe Curitiba) (Sept 2002)
6. Bielefeld, T., Fisher, H.W.: The Security of Medical and Industrial Radioactive Sources Conference paper: Institute for Nuclear Materials Management 49th Annual Meeting, Nashville, Tennessee, 13–17 July 2008. Northbrook, Ill.: Institute for Nuclear Materials Management, 17 July 2008
7. Waller, E., Maanen, J.: The role of the health physicist in nuclear security. *Health Phys.* **108**(4), 468–476 (Apr 2015)
8. IAEA Nuclear Security Series No. 12. Technical Guidance. Educational Programme in Nuclear Security. IAEA (2010)
9. Janssens-Maenhout, G. (ed.): Nuclear safeguards and non-proliferation. Syllabus Course of ESARDA Course (Dec 2018)
10. Nuclear Security, Safety and Non-Proliferation: Sweden's International Cooperation in 2017, p. 19, ed. SSM (2018)

National Nuclear Security Support Centre and Non-proliferation of Weapon of Mass Destruction

Ar. Buzdugan and A. Țurcanu

Abstract

The paper reviews the need of customs control for dual-use goods and services, including those that belong to medicine, pharmaceuticals, and micro-nanoelectronics. In this regard, a project is ongoing in the Republic of Moldova, with the aim to develop a practical guide in line with requirements on export control systems of the World Customs Organization. The guide is intended for customs service employees, responsible government agencies, universities, academic institutions and relevant business communities involved in international trade of strategic goods. It will enhance the effectiveness of export control systems of dual-use items, combat the proliferation of weapons of mass destruction and related materials, equipment and technologies as well as assist students in training.

Keywords

Customs control • Dual-use goods and services • Export control systems • Non-proliferation • Security • Weapon of mass destruction

Used for the first time in 1937 (Cosmo Gordon Lang, Archbishop of Canterbury, in reference to the aerial bombardment of Guernica, Spain) the actual definition of “weapons of mass destruction (WMD)” was proposed in 1948 by the United Nations Commission on Conventional Arms. Official definition refers to “atomic explosive weapons, radioactive material weapons, lethal chemical and biological weapons, and any weapons developed in the future, which have characteristics comparable in destructive effect to those of the atomic bomb or other weapons mentioned above” [1].

Ar. Buzdugan (✉)
Technical University of Moldova, 9/7 Studenilor St., Block 3,
Chisinau, Republic of Moldova
e-mail: artur_buzdugan@yahoo.com

A. Țurcanu
University of Petrosani, Petrosani, Romania

Since its establishment, the United Nations had as a purpose to eliminate all categories of WMD. The First Committee of the General Assembly has been mandated to deal with disarmament, global challenges and threats to peace that affect the international community. Other UN bodies were mandated with negotiating the elimination of WMD.

In scientific literature the WMD are also referred to the CBRN (Chemical, Biological, Radiological and Nuclear) weapons.

Since the beginning of the 21st century, the WMD proliferation has been seen as one of the world’s most important security threats. This subject is widely presented in speeches, statements, documents, as well as in the policies of major international actors since 1998, with an increasing intensity since the September 11, 2001 terrorist attacks in the USA.

When talking about the proliferation of WMD, two aspects are considered: *horizontal proliferation*—the production and/or purchase of WMD, and *vertical proliferation*—increase of WMD number and/or existent technology improving. The question is what the proliferation is, and especially, what do we mean when talking about proliferation? In general, there are distinguished several stages in obtaining a certain type of WMD: basic research, testing, development, mass production and deployment of the respective WMD and/or military technology.

In this sequence of activities, the basic research plays a very important function. It is worth mentioning that the results of basic investigations connected to WMD are not a secret, and as a rule, the knowledge is openly available and can easily be found in scientific literature. Sometimes these developments satisfy more than one goal and can be used for both peaceful and military aims, being called dual-use goods and technologies. For example, peaceful space research programs may allow creation of the ballistic missiles for WMD transportation; the chemical-pharmaceutical industry can produce substances or microorganisms useful in chemical or biological warfare.

It is not correct to speak only about the WMD proliferation itself in a particular country, without considering the production capacity, the existing knowledge, as well as the highly qualified human resources. Even if some states would abandon the deployment of a certain type of WMD, the others would accept to develop weapons and be involved in arming, following a political decision. Table 1 [2] presents the risk assessment of WMD proliferation from CBRN components.

In nuclear or radiological field, the non-proliferation regime focuses on the Non-Proliferation Treaty of 1968, which defines two categories of states: arms holders (a) and those who undertake measures not to develop military technologies (b). The international non-proliferation regime is often challenged due to the gaps in the inspection system and the absence of transparent sanctions. Unlike nuclear weapons, the use of chemical and biological weapons is prohibited since 1925. Two later conventions Prohibition of the Development, Production and Stockpiling of Bacteriological (Biological) and Toxin Weapons and on Their Destruction (BTWC) and Chemical Weapons Convention (CWC) do not allow the development of chemical and biological (bacteriological) arsenals.

Sometimes there are differences encountered in the structuring and functioning of these regimes. As far as chemical weapons are concerned, it is covered by a disarmament treaty, which forces the states to destroy the existing weapons. What is connected to biological weapons, the capacities are difficult to assess and monitor and the non-proliferation regime allow defensive research.

The basic reason for controlling WMD commodities and technologies is to ensure that trans-border transfer will be

used exclusive for peaceful purposes and will not contribute to the proliferation of WMD. Blocking this path leads to slowing down the process, price increase, and requires new alternative ways identifying for obtaining WMD. The control of exported materials and technologies facilitate WMD program monitoring. Thus, export control (but also import, transit and re-export) has become an important tool in non-proliferation. The greatest shortcoming in this supervision are the difficulties in evaluating training of human resources in research and engineering in these areas, since such kind of trainings take place in third countries universities or scientific centers.

The obstacles of ensuring non-proliferation at border crossing are different and depend on the type of nuclear, radioactive, chemical or biological material. Nuclear and radioactive substances undergo effective control due to the existent high sensitivity methods and detectors. Unlike biological goods, a relatively good control can be achieved for chemical materials. Export control, re-export, import and transit control is an extremely complex domain, conceptually recognized as a common standard in the European Union countries since 1994. The international dimension of global security aims to control products, technologies and services that can be used in development, manufacture, storage and use of WMD.

Developments in this area are strongly influenced by globalization trends, including those related to export of arms and dual-use items, both civilian and military. The strategic products operations are characterized by continuous increased dynamics and sensitivity. Taking this into consideration, the Council of the European Union adopted (2000) Regulation no. 1334 on the establishment of a

Table 1 Risk of proliferation of weapons of mass destruction [2]

	Nuclear	Biological	Chemical
<i>Nuclear material or lethal agent production</i>			
Feed materials	Uranium ore, oxide widely available. Pu and partly enriched U dispersed through NPP programs, mostly under international safeguards	Potential biological warfare agents are available	Basic chemicals available for commercial purposes
Scientific and technical personnel	Requires wide variety of expertise and skillful systems integration	High-level research and development unnecessary to produce lethal agents. Microbiological personnel widely available	Chemical engineers widely available
Design and engineering knowledge	Varies by process, but specific designs for producing equipment technology of enrichment very difficult	Widely published. Basic techniques to produce known agents not difficult to obtain	Widely published. Some processes difficult
Equipment	For processes is specialized and difficult to buy or build	Widely available for commercial uses	Most has legitimate industrial application

Community regime for the exports of dual-use items and technology control [3] as a basic condition for combating the proliferation of WMD, while respecting the principle of free movement of goods within the EU.

Today, it is recognized that The Black Sea region is one of the world's critical crossroads, a strategic intersection of east–west and north–south corridors that enable the free flow of people, ideas, and goods from Asia to Europe and from former Soviet territory to the Middle East and Africa. It is also the center of the world's nuclear black market [4, 5].

If we talk about nuclear and radioactive materials, two important databases that list illicit nuclear-trafficking incidents underscore the Black Sea region's dark nuclear image. The International Atomic Energy Agency's (IAEA) Illicit Trafficking Database (reports only incidents that have been confirmed by the governments of member states. The University of Salzburg's Database on Nuclear Smuggling, Theft, and Orphan Radiation Sources lists incidents that have been the subject of investigation and verification by independent proliferation experts and academics, but not fully confirmed [4].

With the aim of securing borders in the new independent countries of Eastern Europe, and unifying verification processes, a Science and Technology Center in Ukraine project was launched in 2018. The main objective is to develop a Customs Guide (Handbook) on WMD non-proliferation.

The National Nuclear Security Support Center (NNSSC) of the Technical University of Moldova (TUM) was selected for project implementation in the Republic of Moldova. Similar projects are ongoing in Georgia, Ukraine and Azerbaijan.

The statutory goal of the NNSSC is to strengthen nuclear non-proliferation and security by study and sharing international experiences accumulated in the peaceful use of nuclear energy. The main roles in support of this goal emphasize:

- building and applying human resources and expertise;
- serving as a partner for international activities, through personnel exchange, joint research, and international collaboration.

The new non-proliferation task of dual destination goods offers the opportunity of extension of NNSSC goals, as other topics develop and are connected to nuclear safety to WMD non-proliferation based on chemical and biological materials.

For project implementation, the NNSSC established a consortium made of professionals from TUM, Customs Service and Ministry of Economy and Infrastructure.

The structure of the guide, following consultations with international experts, will cover the following topics:

- international commitments of the Moldova;
- national and international control regime;
- strategic goods and their classification;
- complementary services to export, import of strategic goods;
- sanctions and embargoes applied;
- national permissive acts in the field of dual-use goods;
- development and maintenance of human resources;
- attachment, reflecting models of permissive acts, as well as lists of dual-use items.

The guide on export control, re-export, import and transit of strategic goods is designed as a reference point for economic entities as well as for licensing and controlling authorities for the export, re-export, import and transit of dual-use strategic goods, items of CBRN materials. The guide briefly describes the objectives, the control policy in this area, and the ways the Government can impose prohibitions on export, re-export, import and transit of strategic goods, or regulate them through the existing authorization system. Similar guides exist in the most EU countries and describe the domestic regulatory framework, international commitments, and types of authorizations for export, re-export, import and transit of dual-use goods, as well as lists of items covered by dual destination materials. These lists are periodically updated with a focus on Community legislation. All of these are set out in the exhaustive list of Council Regulation (EC) No 428/2009 of May 5, 2009 setting up a Community regime for the control of exports, transfer, brokering and transit of dual-use items [6] (with last modification by Commission Delegated Regulation (EU) 2018/1922 of October 10, 2018 [7]). This document contains a wide range of products for micro-nanoelectronics, medicine, and pharmacy. The EC Regulation provides that dual-use items are subject to operational control when exported from the EU, transit through the EU or delivered to a third country as a result of brokering services provided by an intermediary resident in the EU.

The official declarations of the Moldovan leadership on integration into the European Union a priori presuppose the sustainable formation of a developed export product control system as well as a national authority able to efficiently manage this area. For these reasons, the National Strategic and Dual Destination Goods List is periodically updated as recommended by the EU and implemented on basis of Government Decisions [8].

The Republic of Moldova is a signatory to several international treaties and conventions, being unofficially associated with export control, re-export, import and transit goods control regimes.

Regulating activities in this area serves the following major issues:

- regional and national security;
- the need for foreign policy;
- obligations arising from treaties and international commitments;
- non-proliferation policy on WMD;
- growing concern about the development and geographical spread of terrorism.

The guide briefly reflects the non-proliferation treaties, international agreements, and the UNSCR 1540 on WMD non-proliferation, which provides international standards, supported by most national governments and legal obligations for signatory states. In the regard of WMD to which the Republic of Moldova is party, can be mentioned:

- Nuclear Non-Proliferation Treaty (NPT);
- The Comprehensive Nuclear-Test-Ban Treaty;
- Convention on the Prohibition of the Development, Production, Stockpiling and Use of Chemical Weapons and their Destruction;
- Convention on the Prohibition of the Development, Production and Stockpiling of Bacteriological and Toxin Weapons and Destruction;

The Republic of Moldova is not the member or adherent party to the Multilateral Export Control Regime.

Following the recent reforms, the responsible regulatory body for permissive acts for strategic goods issuing is nominated the Public Services Agency of the Republic of Moldova. Regulatory reform has substantially reduced the bureaucratic process. In order to obtain the permissible export, re-export, import, transit and transit of dual-use goods, the applicant or the authorized representative, according to the law, submits a request to the Public Services.

The guide indicates the organizations authorized to issue permissive documents on this area. Allowing acts in nuclear and radiological field are issued by the National Agency for Regulation of Nuclear and Radiological Activities. The possession of the permissive act in this area does not exonerate the applicant from the necessary document for import, export, re-export, and transit obtaining from the Public Services Agency.

In order to have the export, re-export, import or transit authorization for strategic or military goods, the applicant submits to the Public Services Agency a request, accompanied by the documents certifying the origin of the goods:

- the documents on the qualitative and technical characteristics of the goods and, optionally, the commodity code, according to the Nomenclature of strategic goods under control;

- a copy of the contract concluded with the foreign company or the commercial document importing or exporting the strategic goods;
- the copy of authorization certifying permission for foreign company to carry out export-import operations with strategic goods, issued by the authorized body of the country where the company is registered;
- end user certificate (on request);
- international import certificate (on request).

The Public Services Agency checks the documents certifying the applicant's registration as an economic agent, as well as the permissive acts related to the agent's field of activity, which will then be attached to the file. An inter-departmental commission shall make the proposal for issuance or refusal the permissive act. The decision on the authorization of transactions with strategic goods is taken by the commission, also taking into account the application of international restrictive measures according to Law no. 25/2016 on the application of international restrictive measures, updated periodically after consultations with the EU. The proposal, with the appropriate arguments, is submitted to the Public Services Agency, which issues (or refuses to issue) the requested permissive act. The permissive documents obtained are handed over by the applicant for import/export to the Customs Service.

Taking into account that more than one person is involved in the authorization and customs control processes, it is necessary to ensure not only that they are regularly proficient in customs control procedures, but also providing them with a guide that would give ad hoc express advice.

The guide is intended for state officials dealing with licensing activities, but also for economic agents wishing to export, re-export, imports, transit dual-use goods. The guide will be useful in the teaching process at the courses presented to the master students, as well as at the Training Center of the Customs Service.

Acknowledgements The authors thank the consortium of experts and STCU experts for their contribution to elaboration of the Guide on the export, re-export, import and transit of strategic goods.

Conflict of Interest The authors declare that they have no conflict of interest.

References

1. General Assembly, General and complete disarmament, A/RES/36/97, 09.12.1981. <https://www.un.org/documents/ga/res/36/a36r097.htm>
2. U.S. Congress, Office of Technology Assessment, Proliferation of Weapons of Mass Destruction: Assessing the Risk, OTA-ISC-559 (Washington, DC: U.S. Government Printing Office, Aug 1993)

3. Council Regulation (EC) No 1334/2000 of 22 June 2000 setting up a Community regime for the control of exports of dual-use items and technology. Official Journal of the European Union. L 159, 30/06/2000
4. Zaitseva, L., Steinhausler, F.: Nuclear trafficking issues in the Black Sea region. Non-Proliferation Papers, no. 39, Apr 2014. https://www.files.ethz.ch/isn/187240/April_2014_39.pdf
5. Schmid, A.P., Spencer-Smith, C.: Illicit radiological and nuclear trafficking, smuggling and security incidents in the Black Sea Region since the fall of the iron curtain—an open source. *Perspect. Terror.* 6(2) (2012). <http://www.terrorismanalysts.com/pt/index.php/pot/article/view/schmid-illicit-radiological/html>
6. Council Regulation (EC) No 428/2009 of 5 May 2009 setting up a Community regime for the control of exports, transfer, brokering and transit of dual-use items, Official Journal of the European Union. L 134/1, 29.5.2009
7. Commission Delegated Regulation (EU) 2018/1922 of 10 October 2018 amending Council Regulation (EC) No 428/2009 setting up a Community regime for the control of exports, transfer, brokering and transit of dual-use items, Official Journal of the European Union. L 319/1, 14.12.2018
8. Government Decision no. 606 from 15.05.2002 on National System of Export, Re-export, Import and Transit of Strategic Goods in the Republic of Moldova (last upgraded on April 2019). <http://lex.justice.md/index.php?action=view&view=doc&lang=1&id=296547>

Li₂B₄O₇ for Thermoluminescent Dosimetry: A New Life of an Old Material

M. I. Danilkin, N. Yu. Vereschagina, A. S. Selyukov, and D. I. Ozol

Abstract

The effect of doping conditions on the properties of Li₂B₄O₇-based thermoluminescent materials is studied. It is shown that suppression of Mn clustering improves the linearity of the radiation dose response. Moreover, the order of doping is essential to achieve the formation of trapping and luminescence centers: simultaneous co-doping with Mg degrades the sensitivity of detectors by a factor of 10, while sequential Mg co-doping doesn't diminish the sensitivity but decreases the dispersion of properties in the batch. The origin of the observed technological effects is discussed.

Keywords

Thermoluminescent detectors • Lithium tetraborate • Manganese segregation • Pulsed cathodoluminescence

1 Introduction

Lithium tetraborate (Li₂B₄O₇, LTB) is known for many useful properties, and the idea of application of LTB-based materials in thermoluminescent (TL) dosimetry is very promising despite being an old story [1, 2]. LTB-based luminophores indeed have a rich history of investigations [3–20] and technological improvements [13, 21–25]. Let us consider the reasons why these materials are so attractive and why they have not yet been developed for large-scale commercial production.

When applied to a radiation detector, the term “tissue equivalence” means that the absorbed dose measured by a detector is equal to the absorbed dose in human tissue. More specifically, the dependence of the detector response on the radiation energy should be the same as that of biological tissue. When this is true, the detector calibrated with a radiation source of some kind can be used to measure radiation of different energies. Li₂B₄O₇ has perfect tissue equivalence [4–6], and this makes Li₂B₄O₇-based thermoluminescent detectors very attractive for personnel dosimetry.

However, the properties of a Li₂B₄O₇-based luminophore depend not only on the impurities it is doped with but also on how this doping is performed. The latter affects the features of material so strongly that one can obtain absolutely different materials with exactly the same overall chemical composition. That is why a long history of studies often was a tortuous path in the dark. Recent results have demonstrated the crucial role of doping order in obtaining LTB-based luminophores with the desired properties [24, 25]. The intricacy of this material lies in the ability of its crystal lattice to adopt a complex of either the same or two different impurities occurring at essentially different positions: one impurity being incorporated into the boron-oxygen network and the other residing closely to the former at a displaced cationic position, thus providing charge compensation and increasing the stability of the whole complex. The existence of such structures follows from many indirect experimental facts and some chemical insights. We shall discuss here only those necessary for the development of advanced radiation detectors.

2 Materials and Methods

Li₂B₄O₇ was prepared in the form of ceramic tablets by the procedure described in [24, 25]. The LTB was doped with impurities (Mn and Mg) either in a single stage or in two stages, with Mn always being added at the first stage, and

M. I. Danilkin (✉) · N. Yu. Vereschagina · A. S. Selyukov
Department of Optics, P.N. Lebedev Physical Institute of the
Russian Academy of Sciences, 53 Leninskiy pr., Moscow, Russia
e-mail: mihhail.danilkin@ya.ru

D. I. Ozol
Department of Vacuum Electronics, Moscow Institute of Physics
and Technology, Dolgoprudny, Moscow Region, Russia

with three different ways of Mg doping: either single-stage, together with Mn (LTB:Mn, Mg), or at the second stage after Mn introduction (LTB:Mn + Mg), or with no Mg added (LTB:Mn). An old-style LTB:Mn ceramics was also prepared for comparison, with Mn still added in a single stage but not dropwise.

Pulsed cathodoluminescence (PCL) was measured at excitation with a Radan-expert portable electron accelerator (2 ns pulse duration, 60 A amplitude) with a maximum electron energy of 200 keV and the energy distribution peaked at 110–120 keV. The radiation dose absorbed by the sample was about 0.8 kGy per pulse. The PCL spectra were recorded using an Ocean Optics Maya2000 Pro spectrometer.

To measure the TL curves and dose dependences, the samples were irradiated either with different $^{90}\text{Sr}/^{90}\text{Y}$ beta-radiation sources or with an electron beam from the Radan-expert accelerator. ^{137}Cs was used to give reference doses of γ radiation. The TL curves were measured using different TLD readers with heating rates ranging from 0.3 to 2 K/s. A DVG-2M modified TLD reader was used to record the luminescence spectra during the TL measurements. One end of a quartz UV-waveguide (1.1 mm in diameter) was inserted behind a lens in the gap between the heater and the photomultiplier (9924B, 280–680 nm spectral range). The other end of the waveguide was attached to the Maya2000 Pro spectrometer. The photomultiplier provided TL curves (integrated intensity vs. temperature), while the spectrometer measured spectrally resolved TL.

3 Results and Discussion

3.1 Uniformity of Impurity Distribution

The effect of non-uniformity of Mn distribution on the dose response of detectors is illustrated in Fig. 1.

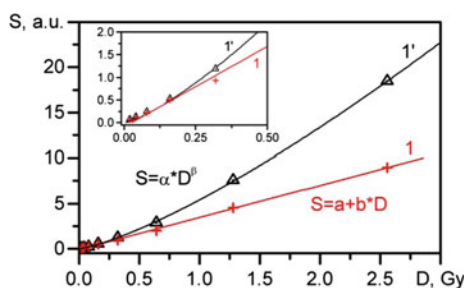


Fig. 1 Dose response (area under TL peak) for LTB:Mn detectors of types (1') and (1). Non-linear response for detectors (1') is fitted by power function; the dose response for detectors (1) is linear. Inset gives a more detailed view of the low-dose region

Detectors (1') were prepared in an old-style manner, with the total amount of the dopant added simultaneously to a hot solution of boric acid. Detectors (1) were made from the material prepared more carefully, with dropwise Mn addition in the course of the reaction between boric acid and lithium carbonate. Simultaneous addition of all Mn causes manganese segregation in the LTB crystal lattice. In this case, powerful and continuous stirring cannot help improve Mn distribution anymore. A supra-linear dependence of the response of detectors to the radiation dose is not the only trouble resulting from the non-uniform impurity distribution. In addition, the displacement of TL peaks and increased radiation damage of the detectors is observed [26, 27].

3.2 Effect of Mg Co-doping on LTB:Mn Properties

As we mentioned above, Mg was added in two ways: either in a single stage together with Mn (LTB:Mn, Mg), or separately—Mn at the first stage, and Mg at the second stage (LTB:Mn + Mg). The interchange of addends drastically affects the result. In Fig. 2a, the PCL spectra of three samples are compared: LTB:Mn (1), LTB:Mn, Mg (2), and LTB:Mn + Mg (3). When magnesium is added after manganese, at the second stage, the intensity of Mn^{2+} PCL (at 600 nm) decreases, while the luminescence of excitons (at ~ 325 nm) remains unchanged (Fig. 2a, curve 3 vs. 1). This means that Mg addition diminishes the number of structures where one Mn is incorporated into the boron-oxygen network, while the other is located close to the former. Such complexes are responsible for energy transfer at PCL and also involved in the low-temperature TL peak. When Mn and Mg are added simultaneously (LTB:Mn, Mg), the luminescence of Mn^{2+} is further suppressed, while the excitonic luminescence is enhanced. This means that Mg^{2+} replaces Mn^{2+} at cationic positions in the majority of such complexes, and effective Mn^{2+} excitation is no longer possible. When excitons are captured, they produce luminescence themselves instead of transferring energy to Mn^{2+} .

TL curves for LTB:Mn (1) and LTB:Mn, Mg (2) are plotted in Fig. 2b together with the luminescence spectra of the corresponding TL peaks (insets). There is no difference in the luminescence spectra for samples (1) and (2), a broad luminescence band near 600 nm is observed in all events due to the spin- and parity-forbidden transition ${}^4\text{T}_1(\text{G}) \rightarrow {}^6\text{A}_1(\text{S})$ of Mn^{2+} . The TL intensity decreases by an order of magnitude when Mn and Mg are added together in a single stage. Also, the TL peaks get closer in this case. In sample (2), the low-temperature peak (which suffers from fading and is not used in dosimetry) is suppressed even stronger than the high-temperature one. This indicates that the mixed complexes are formed, with Mn incorporated into the

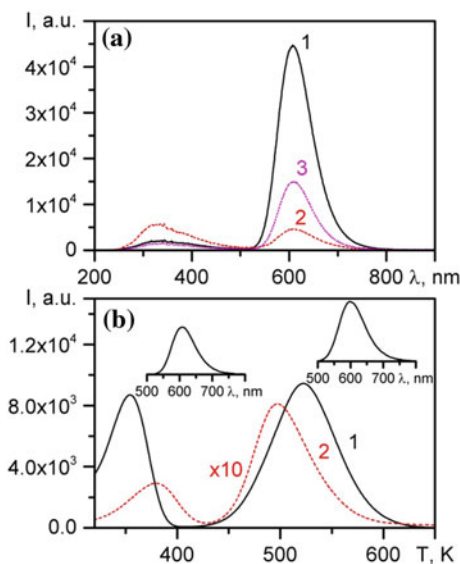


Fig. 2 **a** PCL spectra for LTB:Mn (1), LTB:Mn, Mg (2), and LTB:Mn + Mg (3). **b** TL curves for LTB:Mn (1) and LTB:Mn, Mg (2). Insets show luminescence spectra for corresponding TL peaks

boron-oxygen network and Mg located closely at the cationic position. The amount of such structures increases with sacrifice in the number of Mn–Mn complexes and clusters. This accounts for the decrease in the Mn²⁺ luminescence intensity in the PCL spectra, as well as for the suppression of TL peaks, especially the low-temperature one. We should note that Mn in the boron-oxygen network becomes dead for luminescence and EPR, and the reasons for this lie in the character of chemical bonds; however, this question is beyond the scope of this paper.

And finally, should we regard Mg as a detrimental impurity for LTB:Mn thermoluminescent detectors? The answer is ambivalent and quite surprising: ‘Yes’, if this impurity is already present in the initial materials: ‘No’, if Mg is added later, at the second stage. The former statement was clearly illustrated, while the latter follows from Fig. 3.

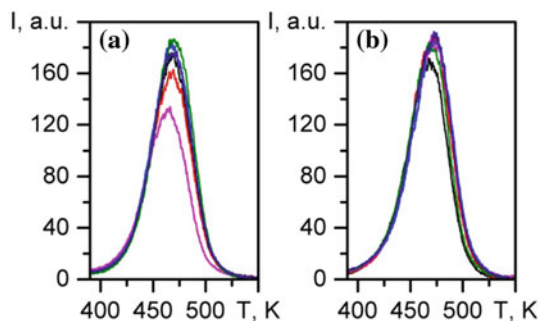


Fig. 3 Dosimetric TL peak for two batches of 6 randomly chosen samples: **a**—LTB:Mn; **b**—LTB:Mn + Mg. Detectors were irradiated using ¹³⁷Cs reference source, γ radiation dose was 200 mGy

When the material is co-doped with Mg at the second stage, the sensitivity to a given radiation dose becomes more homogeneous in the batch of detectors. At the same time, the intensity of the dosimetric TL peak is not affected by this procedure. The addition of Mg at the second stage does not diminish the amount of isolated Mn responsible for the dosimetric TL peak whereas both TL peaks suffer when the co-dopant is added together with Mn in a single stage. One can also expect better dose-response linearity of the co-doped material due to the improved uniformity of Mn distribution.

4 Conclusions

We have demonstrated here that the properties of LTB-based thermoluminescent materials strongly depend on the procedure of doping with impurities, as much as on what impurities the materials are doped with. *Praemonitus—praemunitus*, and the obtained knowledge becomes our armament, so necessary for mastering the technology of advanced radiation detectors based on a well-known material being so unpredictable in the past. Since ceramic detectors are much cheaper than the single-crystal ones, the obtained data on the studied materials would provide a basis for commercial production of general-purpose radiation detectors. From the scientific point of view, our results can be used to extend the developed approach to the study of Cu-doped LTB, the emission spectrum of which better corresponds to the photomultiplier sensitivity.

Acknowledgements This work was supported by the Russian Foundation for Basic Research, projects nos. 18-02-00811 a and 16-29-11805 ofi_m. The authors are grateful to the Laboratory of detectors of the JSC ‘SNIIP’ for providing the facilities for conducting the radiation measurements and obtaining the reference doses.

Conflict of Interest The authors declare no conflict of interest.

References

1. Thompson, J.J., Ziemer, P.L.: The thermoluminescent properties of lithium borate activated by silver. *Health Phys.* **25**, 435–441 (1973). <https://doi.org/10.1097/00004032-197310000-00009>
2. Langmead, W.A., Wall, B.F.: A TLD system based on lithium borate for the measurement of doses to patients undergoing medical irradiation. *Phys. Med. Biol.* **21**, 39–51 (1976). <https://doi.org/10.1088/0031-9155/21/1/003>
3. Prokić, M.: Dosimetric characteristics of Li₂B₄O₇:Cu, Ag, P solid TL detectors. *Radiat. Prot. Dosim.* **100**, 265–268 (2002). <https://doi.org/10.1093/oxfordjournals.rpd.a005863>
4. Selvam, T.P., Keshavkumar, B.: Monte Carlo investigation of energy response of various detector materials in ¹²⁵I and ¹⁶⁹Yb brachytherapy dosimetry. *J. Appl. Clin. Med. Phys.* **11**, 70–82 (2010). <https://doi.org/10.1120/jacmp.v11i4.3282>

5. Kitis, G., Furetta, C., Prokić, M., et al.: Kinetic parameters of some tissue equivalent thermoluminescence materials. *J. Phys. D Appl. Phys.* **76**, 1252–1262 (2000). <https://doi.org/10.1088/0022-3727/33/11/302>
6. Furetta, C., Prokić, M., Salamon, R., et al.: Dosimetric characteristics of tissue equivalent thermoluminescent solid TL detectors based on lithium borate. *Nucl. Instrum. Meth. A* **456**, 411–417 (2001). [https://doi.org/10.1016/S0168-9002\(00\)00585-4](https://doi.org/10.1016/S0168-9002(00)00585-4)
7. Kelemen, A., Ignatovych, M., Holovey, V., et al.: Effect of irradiation on photoluminescence and optical absorption spectra of Li₂B₄O₇: Mn and Li₂B₄O₇: Ag single crystals. *Rad. Phys. Chem.* **76**, 1531–1534 (2007). <https://doi.org/10.1016/j.radphyschem.2007.02.067>
8. Corradi, G., Nagirnyi, V., Kotlov, A., et al.: Investigation of Cu-doped Li₂B₄O₇ single crystals by electron paramagnetic resonance and time-resolved optical spectroscopy. *J. Phys.-Condens. Mat.* **20**, 025216 (2008). <https://doi.org/10.1088/0953-8984/20/02/025216>
9. Corradi, G., Nagirnyi, V., Watterich, A., et al.: Different incorporation of Cu⁺ and Cu²⁺ in lithium tetraborate single crystals. *J. Phys. Conf. Ser.* **249**, 012008 (2010). <https://doi.org/10.1088/1742-6596/249/1/012008>
10. Brant, A.T., Kananan, B.E., Murari, M.K., et al.: Electron and hole traps in Ag-doped lithium tetraborate (Li₂B₄O₇) crystals. *J. Appl. Phys.* **110**, 093719 (2011). <https://doi.org/10.1063/1.3658264>
11. Brant, A.T., Buchanan, D.A., McClory, J.W., et al.: EPR identification of defects responsible for thermoluminescence in Cu-doped lithium tetraborate (Li₂B₄O₇) crystals. *J. Lumin.* **139**, 125–131 (2013). <https://doi.org/10.1016/j.jlumin.2013.02.023>
12. Buchanan, D.A., Holston, M.S., Brant, A.T., et al.: Electron paramagnetic resonance and thermoluminescence study of Ag²⁺ ions in Li₂B₄O₇ crystals. *J. Phys. Chem. Solids* **75**, 1347–1353 (2014). <https://doi.org/10.1016/j.jpcs.2014.07.014>
13. Holovey, V.M., Sidey, V.I., Lyamayev, V.I., Birov, M.M.: Influence of different annealing conditions on the luminescent properties of Li₂B₄O₇: Mn single crystals. *J. Phys. Chem. Solids* **68**, 1305–1310 (2007). <https://doi.org/10.1016/j.jpcs.2007.02.005>
14. Danilkin, M., Jaek, I., Kerikmäe, M., et al.: Storage mechanism and OSL-readout possibility of Li₂B₄O₇: Mn (TLD-800). *Radiat. Meas.* **45**, 562–565 (2010). <https://doi.org/10.1016/j.radmeas.2010.01.045>
15. Ratas, A., Danilkin, M., Kerikmäe, M., et al.: Li₂B₄O₇: Mn for dosimetry applications: traps and mechanisms. *Proc. Est. Acad. Sci.* **61**, 279–295 (2012). <https://doi.org/10.3176/proc.2012.4.03>
16. Kelly, T.D., Kong, L., Buchanan, D.A., et al.: EXAFS and EPR analysis of the local structure of Mn-doped Li₂B₄O₇. *Phys. Status Solidi B* **250**, 1376–1383 (2013). <https://doi.org/10.1002/pssb.201349013>
17. Kerikmäe, M., Danilkin, M., Lust, A., et al.: Hole traps and thermoluminescence in Li₂B₄O₇:Be. *Radiat. Meas.* **56**, 147–149 (2013). <https://doi.org/10.1016/j.radmeas.2013.02.002>
18. Nagirnyi, V., Aleksanyan, E., Corradi, G., et al.: Recombination luminescence in Li₂B₄O₇ doped with manganese and copper. *Radiat. Meas.* **56**, 192–195 (2013). <https://doi.org/10.1016/j.radmeas.2013.02.005>
19. Romet, I., Aleksanyan, E., Brik, M., et al.: Recombination luminescence of Cu and/or Ag doped lithium tetraborate single crystals. *J. Lumin.* **177**, 9–16 (2016). <https://doi.org/10.1016/j.jlumin.2016.04.014>
20. Romet, I., Buryi, M., Corradi, G., et al.: Recombination luminescence and EPR of Mn doped Li₂B₄O₇ single crystals. *Opt. Mater.* **70**, 184–193 (2017). <https://doi.org/10.1016/j.optmat.2017.05.032>
21. Kelemen, A., Mesterházy, D., Ignatovych, M., Holovey, V.: Thermoluminescence characterization of newly developed Cu-doped lithium tetraborate materials. *Radiat. Phys. Chem.* **81**, 1533–1535 (2012). <https://doi.org/10.1016/j.radphyschem.2012.01.041>
22. Kayhan, M., Yilmaz, A.: Effects of synthesis, doping methods and metal content on thermoluminescence glow curves of lithium tetraborate. *J. Alloy. Compd.* **509**, 7819–7825 (2011). <https://doi.org/10.1016/j.jallcom.2011.04.137>
23. Annalakshmi, O., Jose, M.T., Amarendra, G.: Dosimetric characteristics of manganese doped lithium tetraborate—an improved TL phosphor. *Radiat. Meas.* **46**, 669–675 (2011). <https://doi.org/10.1016/j.radmeas.2011.06.016>
24. Vereschagina, N.Y., Danilkin, M.I., Kazaryan, M.A., et al.: Cathodoluminescent UV-radiation sources. In: Proceedings SPIE, 10614, International Conference on Atomic and Molecular Pulsed Lasers XIII, 106141F, 16 Apr 2018. <https://doi.org/10.1117/12.2303579>
25. Vereschagina, N.Y., Danilkin, M.I.: Method for obtaining luminescent ceramics, luminescent ceramics and the detector of ionizing radiation. Patent RU 2660866 (C1) (2018). https://ru.escapenet.com/publicationDetails/biblio?II=0&ND=3&adjacent=true&locale=ru_RU&FT=D&date=20180710&CC=RU&NR=2660866C1&KC=C1#
26. Danilkin, M.I., Koksharov, YuA, Romet, I., et al.: Manganese agglomeration and radiation damage in doped Li₂B₄O₇. *Radiat. Meas.* **126**, 106134 (2019). <https://doi.org/10.1016/j.radmeas.2019.106134>
27. Vainer, Y.G., Vereschagina, N.Y., Danilkin, M.I., et al.: Destruction of doped lithium tetraborate under exposure to ionizing and laser radiation. *Opt. Spectrosc.* **127**, 113–120 (2019). <https://doi.org/10.1134/S0030400X19070257>

Author Index

A

Ababei, G., 305
Ababii, I., 367, 607, 633
Ababii, N., 3, 285
Ababii, P., 607, 633
Abaskin, V., 111, 269, 275
Abes, M., 187
Achimova, E., 111, 269, 275
Adelung, R., 3, 57, 93, 253, 263, 285, 745, 779
Adochiei, F., 529
Adochiei, I.R., 529, 767
Agustini, D.M., 225
Akinsinde, L.O., 57
Al-Mamoori, M.H., 333
Al Qassem, A., 707
Ananiashvili, N., 97
Andrițoi, D., 439
Andronic, S.C., 121, 199
Anzin, V.B., 7
Aoki, T., 731, 735, 741
Apostoaie, M.G., 447, 793
Arama, E., 657, 719
Argatu, F., 529
Arkhiereieva, E.H., 411
Arnaut, O., 703
Arotăriței, D., 433
Asipovich, V.S., 519
Ayvazyan, N.M., 543, 567

B

Babusca, D., 305
Bachinsky, V.T., 503, 507, 513
Badarau, A., 785
Bakerenkov, A.S., 61, 399, 807
Balan, V., 325
Bange, M., 485
Baraban, S.V., 393
Bărar, A., 299
Barbashov, V.M., 811
Barbos, Z.A., 149
Baritz, M.I., 447, 793
Baum, M., 779
Bazgan, S., 373
Bednyakov, P., 7
Bedran, Z.V., 7
Belyakov, V.V., 61, 399, 427, 639
Belyanchikov, M.A., 7

Benchea, C.A., 305
Beril, S.I., 167
Besleaga, T., 475
Bichel, T., 37
Bîrnaz, A., 253
Bodduluri, M.T., 263
Bodnar, B.G., 503
Bodnar, O.B., 497
Bologa, M.K., 799
Bordian, O., 161
Botnariuc, V., 53, 83, 89
Bourosh, P., 713
Boyko, V.V., 553
Braniste, T., 89, 607
Braun, B., 667, 725
Bucuman, C., 379
Bulhac, I., 161
Butnaru, Maria, 385
Buzdugan, Ar., 815, 821
Buzdugan, Au., 681, 815

C

Caraman, I., 207, 247
Caraman, M., 207
Carstens, N., 71
Casian, A.I., 121, 199
Cavers, H., 93
Ceban, V., 155
Cebotari, I.D., 181
Chetrus, P., 53
Chezan, H., 379
Chichikalo, N.I., 411
Chilingaryan, G.V., 543
Chiosa, V.A., 461, 523
Chirita, A., 247
Chirumamilla, V.C., 485
Chișca, D., 713
Chistol, V., 19
Chmykhova, O.V., 553
Chornopyschuk, R., 579
Cinic, B., 53
Ciobanu, Vladimir, 203
Ciolac, D., 461, 485, 491
Ciucu, R., 529
Cobzac, V., 595, 607
Cociug, A., 601
Codreanu, I., 621

Cojocari, O., 319
 Cojocaru, I.P., 691
 Cojocaru, S., 23
 Cojocaru, V., 749
 Corcău, C.L., 767
 Corciovă, C., 433, 439
 Coropceanu, E., 713
 Cosman, B.P., 385
 Coval, A., 53
 Creanga, D., 237, 305
 Cretu, V., 285
 Culeac, I.P., 161
 Cusnir, V., 601
 Cusnir, V. Jr., 601

D

Dabaghyan, V., 127
 Dănilă, O., 299
 Danilkin, M.I., 313, 827
 Danilov, L., 367, 633
 Dankwort, T., 57
 Datsko, T. Ya., 143
 Deineko, D.M., 651
 Dementiev, I., 133
 Diacova, S., 627, 633
 Dick, S.K., 421
 Didencu, A., 607
 Dmitroglu, L., 207
 Dorogan, A.V., 167
 Dorohoi, D., 237
 Drapeza, V.Y., 421
 Dressel, M., 7
 Drugă, C., 481, 667, 725
 Dubolazov, A.V., 497, 503, 507, 513
 Dudich, O.N., 519
 Dudka, A., 7
 Dvornikov, D.P., 143

E

Emelchenko, G.A., 193
 Enache, N., 469
 Enachescu, M., 161
 Enaki, N.A., 373
 Evtodiev, I., 247

F

Faupel, F., 71
 Fedorisin, T., 749
 Fedorov, V., 707
 Felitsyn, V.A., 61, 399, 807
 Fischer, J.K.H., 7
 Foglinskiy, S., 503
 Forsh, P.A., 243, 405
 Fosa, D., 417
 Fuior, R., 439
 Furtuna, V., 789

G

Gachechiladze, M., 97
 Gagara, L., 707
 Galus, R., 749
 Ganenco, A., 475

Gapeeva, A., 263, 779
 Garazdyuk, M., 503
 Gaugas, P., 53
 Gavriluta, V., 633
 Gavzer, S.I., 137
 Gevorgyan, T., 567
 Gheorghită, A., 433
 Ghimpu, L., 291
 Ghulikyan, L.A., 543, 567
 Ginosyan, S.G., 361, 543
 Giorgadze, N., 97
 Globa, L., 589
 Goglidze, T., 133
 Golovan, L.A., 101
 Golovin, A.V., 427, 639
 Goncareenco, E., 133
 Gonciaruc, V., 799
 Gonta, A., 355
 Gonta, M., 355
 Gorceac, L., 53, 89
 Gore, A.I., 137
 Gorinchoy, N.N., 561
 Gorincioi, E., 713
 Gorshunov, B., 7
 Grabco, D.Z., 149
 Grabovschi, I., 703
 Grabski, H.V., 349, 361, 543, 585
 Grigoras, M., 237
 Grigorie, L.T., 529, 767
 Gromov, E.A., 427, 639
 Gronenberg, O., 71
 Groppa, S., 485
 Groppa, S.A., 461, 485
 Gumeniuc, A., 785

H

Hambardzumyan, Y., 361
 Hansen, S., 93
 Hartnagel, H.L., 213, 219, 231
 Hayakawa, M., 741
 Hicke, M., 37
 Hoefle, M., 319
 Hölken, I., 779
 Hoppe, M., 253, 285
 Hovhannisyán, A., 127, 349, 567
 Hrkac, S.B., 187
 Hrkac, V., 187

I

Ikim, M.I., 405
 Ilin, Alexander S., 243, 405
 Iovu, M.S., 79, 161
 Iurieva, T., 133
 Ivanov, I.A., 427, 639

J

Jian, M., 595
 Jordt, P., 187
 Jula, N., 767

K

Kadyrov, L.S., 7

Kaminskaya, T.P., 101
 Kamp, M., 37
 Kanarovskii, E. Yu., 561, 573
 Kaps, S., 263
 Karakulko, A.A., 519
 Karaseva, E.V., 193
 Kashaev, F.V., 101
 Kashkarov, P.K., 101, 243, 405
 Kazaryan, Sh., 127
 Kienle, L., 37, 57, 71, 93, 187
 Kirakosyan, G., 567
 Kirillin, M. Yu., 101
 Klokishner, S.I., 33, 43, 67
 Kohlstedt, H., 187
 Koike, A., 731, 735
 Kolchin, A.V., 101
 Kolisnyk, K.V., 651
 Kolosnitsyn, V.S., 193
 Konovalova, M.A., 519
 Koops, C.T., 187
 Korchovyi, A., 111
 Koroleva, A.V., 405
 Kovalchuk, M.L., 507
 Koval, K.O., 393
 Koval, S.M., 651
 Krasilnikova, V.L., 519
 Kremer, R.K., 7
 Kulikova, O., 697
 Kulyuk, L., 279
 Kumeda, M.O., 343
 Kushnerik, L. Ya., 513
 Kuzmina, E.V., 193

L

Larco, C.M., 529, 767
 Larina, E. Yu., 411
 Lazar, A.M., 447, 793
 Leahu, P., 485
 Levcenco, A., 633
 Litvinenko, O. Yu., 503
 Loghina, L., 269, 275
 Loidl, A., 7
 Loiko, V.A., 299
 Loşmanskii, C., 275
 Lozan, O., 621
 Lozovanu, S., 475
 Luca, C., 439
 Lucaci, A.M., 385
 Lungu, I., 53, 83, 707
 Lunkenheimer, P., 7
 Lupan, C., 253
 Lupan, O., 3, 263, 285, 745
 Lupashku, G.A., 137
 Lupu, N., 305

M

Macagonova, O., 601
 Machavariani, M., 97
 Macovei, M.A., 155, 677
 Magariu, N., 259, 285
 Magnussen, O.M., 187
 Majdi, H. Sh., 333
 Malcova, T., 589
 Malkin, E.K., 427, 639

Mänäilä-Maximean, D., 299
 Maniuc, M., 607, 633
 Manukyan, A.E., 549
 Marsagishvili, T., 97
 Martyshov, M.N., 243, 405
 Masalov, V.M., 193
 Maslobrod, S.N., 137
 Matusko, M.A., 427, 639
 Maximilian, S., 657
 Meshalkin, A., 111, 269, 275
 Metreveli, J., 97
 Mezhenyaya, M.M., 421
 Micu, A., 279, 697
 Mihai, G., 105
 Mihailescu, I.N., 373
 Mihalache, A., 29, 47
 Mimura, H., 83
 Mirgorod, Yu. A., 137
 Miron-Borzan, C., 379
 Mirzac, A., 677
 Mkrtchyan, T., 361
 Mocanu, L., 355
 Moise, C.I., 325
 Moldovanu, I., 475
 Monaico, Ed., 105
 Monaico, E.V., 117, 775, 785
 Mopro-Melgar, D., 319
 Morari, V., 105
 Morosanu, C., 237
 Moroz, P.A., 519
 Moskalenko, S.A., 13
 Mostovei, A., 595
 Muntyanu, F.M., 19
 Murphy, B.M., 187
 Mustață, S.M., 767
 Muthuraman, M., 485

N

Nacu, V., 589, 595, 601, 607, 621
 Nagaichuk, V., 579
 Nakagawa, H., 741
 Nasir, M., 225
 Necula, R.D., 481, 725
 Nedelea, V.V., 161, 279
 Nedeoglo, D., 133
 Nedeoglo, N., 133
 Nenkov, K., 19
 Nicorici, V.Z., 149
 Nielsch, K., 105
 Nikolaev, A.Y., 519
 Nisbet, G., 187
 Nishizawa, J., 731, 735
 Nistreanu, A., 373
 Novikov, B.V., 13

O

Ohanyan, S., 349
 Ohtake, R., 731, 735
 Oleksenko, P., 111
 Onyshchenko, M., 579
 Oprea, I., 319
 Oprica, L., 305
 Osadchuk, O.V., 393
 Osipov, A.K., 811

Osipov, A.N., 421
 Ostrovsky, S.M., 43
 Ozol, D.I., 313, 827

P

Paiuk, O., 111
 Paladii, I.V., 799
 Palistrant, M.E., 181
 Palistrant, S.A., 181
 Pallikarakis, N., 615
 Pantea, V., 719
 Paslari, T., 373
 Penin, A., 673
 Pershenkov, V.S., 61, 399, 427, 639, 807
 Petraru, A., 187
 Petrosyan, M., 127, 567
 Pislaru, C., 645
 Platonov, V.B., 243
 Plesco, I., 607
 Podlepetsky, B.I., 399
 Podlesny, I.V., 13
 Policarpov, A., 799
 Popa, M.E., 173, 177
 Popescu, L., 237, 305
 Postica, V., 285
 Postolache, V., 105
 Potlog, T., 83, 707, 789
 Presnov, D.E., 101
 Preu, S., 219
 Prisacar, A., 111, 269, 275
 Prisakari, V., 789
 Prokleska, J., 7
 Proschek, P., 7
 Protsiuk, V.V., 497

Q

Qiu, H., 779

R

Radnionok, A. L., 519
 Raevschi, S., 53, 83, 89, 607
 Railean, S., 645
 Rasch, F., 263
 Reu, O.S., 33
 Rickes, M., 319
 Ristoscu, C., 373
 Robu, S., 83, 355, 789
 Rodin, A.S., 61, 399, 807
 Rojnovceanu, Gh., 703
 Roman, M.A., 67
 Rosca, A.I., 691
 Roşca, I.C., 481
 Rotaru, L., 657
 Rozorinov, H.N., 411
 Rshtuni, L., 127, 349
 Rübhausen, M.A., 57
 Rusnac, D., 291
 Rusnac, R., 789
 Rusu, E.V., 105, 117

S

Sabau, E., 379

Sacarescu, L., 237
 Sakaida, K., 741
 Saleem, K., 93
 Sandru, S., 703
 Sanduleac, I.I., 121, 199
 Sarkisova, Yu., 503
 Saud, A.N., 333
 Sauleal, A., 703
 Savinov, M., 7
 Savva, Yu., 673
 Savvytskyi, A. Yu., 393
 Scheiter, S., 485
 Scheitz, S., 57
 Schürmann, U., 37, 57, 93
 Schütt, A., 253, 745
 Seeck, O.H., 187
 Selyukov, A.S., 827
 Semenov, Andriy O., 393
 Semenova, O.O., 393
 Şerban, I., 481, 667, 725
 Sergeeva, E.A., 101
 Sergentu, V.V., 775
 Shaltaeva, Y.R., 427, 639
 Shaplavskiy, M.V., 497
 Shapov, P., 455
 Shemyakova, T., 719
 Sheshin, E.P., 313
 Shikimaka, O.A., 149
 Shyshkin, M., 455
 Sidorenko, A., 673
 Siebert, L., 3, 57
 Sierck, J. K., 57
 Siminel, A., 279, 697
 Siminel, N., 161, 279, 697, 761
 Sipitco, N., 417
 Sirbu, E., 355
 Sirkeli, V.P., 213, 219, 231
 Sivokorovskaya, N., 513
 Skobelkina, A.V., 101
 Smetanca, V., 367
 Sokol, T.V., 651
 Sokol, Y.I., 455, 553
 Soltys, I.V., 503
 Şontea, V., 285, 417, 645
 Sprincean, C. Gh., 799
 Sprincean, V., 207, 247
 Stamov, I.G., 167
 Stan, C., 237
 Starodub, E., 373
 Stepurina, T., 799
 Stettner, J., 187
 Stoian, A., 589
 Stronski, A., 111
 Sugatri, R.I., 225
 Sukhinina, N.S., 193
 Sukhodub, L.B., 343
 Sukhodub, L.F., 343
 Suman, V., 291
 Sushkevich, K., 279
 Syrbu, N.N., 79, 117, 167
 Syvokorovskaya, A.-V., 507

T

Tabata, K., 731, 735
 Tătaru, A., 667

Tatishvili, G., 97
Tătulea, I., 725
Telets, V.A., 61, 807
Terasa, M.L., 3
Thomas, V., 7
Thostov, M. X.-M., 421
Tiginyanu, I.M., 105, 231, 607
Timbalari, T., 621
Tiratsuyan, S.G., 349, 361, 543, 585
Tiron, A.V., 75, 79, 117
Tiuleanu, P., 789
Tomashevskiy, R.S., 455, 651
Tomka, Yu. Ya., 497, 503, 507, 513
Tonu, V., 469
Topal, D., 149
Torgashev, V.I., 7
Trakhtenberg, L.I., 405
Triduh, G., 111
Trushkin, N.S., 811
Tskhakaia, E., 97
Țugui, E., 589
Turcan, M., 373
Țurcanu, A., 821
Turcanu, A. Gh., 691
Turnea, M., 433

U

Ungureanu, S., 417
Untila, D., 207, 247
Ursaki, V.V., 105, 775
Ushenko, O.G., 497, 503, 507, 513
Ushenko, Yu. O., 497, 503, 507, 513
Uykur, E., 7

V

Vahl, A., 71
Vanchuliak, O. Ya., 507
Vanchulyak, O. Ya., 503, 513
Varachiu, N., 755
Vascan, A., 589
Vaseashta, A., 685
Vasilyev, V.K., 427, 639
Vasiyk, V.L., 497
Vasylchishyn, Y.M., 497

Vataman, A., 461, 535
Vatavu, E., 207
Vereschagina, N. Yu., 313, 827
Verestiuc, L., 325, 385
Verjbitki, V., 285
Verlan, V.I., 161
Vetrician, S., 367
Vidiborschii, V., 417
Vitiu, A., 713
Vlcek, M., 269, 275
Voß, L., 37
Vorobey, A.V., 421
Vovc, V., 469, 475, 657, 719
Vrabie, E.G., 799
Vrabie, V.G., 799

W

Wagner, B., 263
Wolf, N., 187
Worasawat, S., 83

Y

Yakovleva, A., 269, 275
Yaltychenko, O.V., 561, 573
Yashin, K. D., 519
Yilmazoglu, O., 219
Yunusova, O., 579

Z

Zabotnov, S.V., 101
Zalamai, V.V., 79, 117
Zaleski, A.J., 19
Zamiatin, D.P., 553
Zamyatin, P. N., 553
Zelentsov, V.I., 143
Zhokhov, A. A., 193
Zhugayevych, A., 7
Zhukova, E.S., 7
Zhukov, S.S., 7
Zimoch, L., 57
Zubac, I.A., 13
Zubareva, V.E., 161